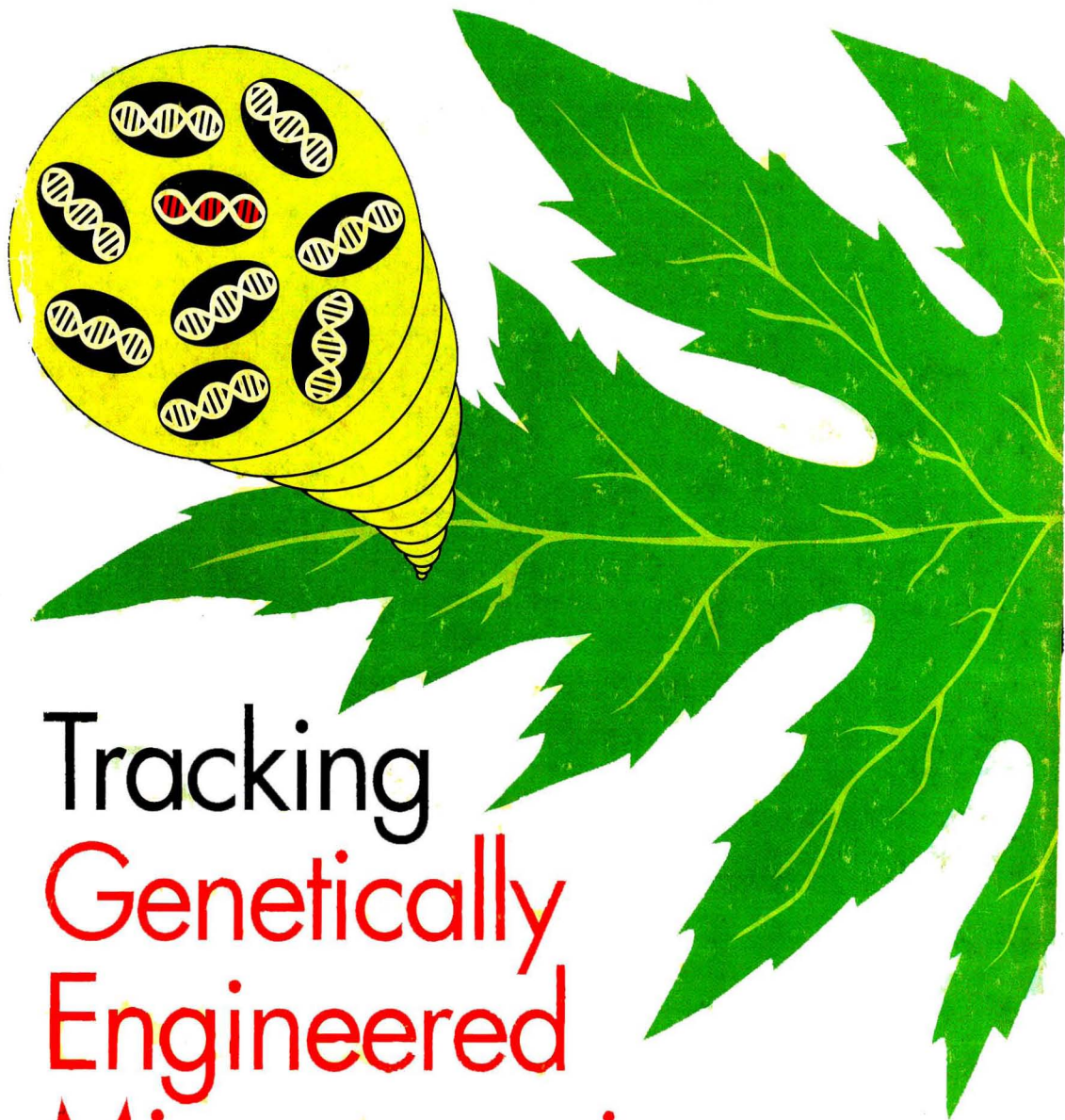


SEPTEMBER 1, 1989

# Analytical CHEMISTRY



## Tracking Genetically Engineered Microorganisms

1001 A

# Clean solutions for troubled waters.

Environmental sample matrices can be hazardous to your productivity.

If you're struggling to detect water contaminants at the required levels, you'll be glad to know Dionex has an easier way.

## Crash the ppb barrier in complex matrices.

Alkali and alkaline earth metals rob ICP spectroscopy of its sensitivity for measuring transition metals in sea water — unless you do a lot of sample prepping.

Couple Dionex Chelation Ion Chromatography to an ICP spectrometer and get those fractional ppb levels with a *direct introduction* of your sea water or acid digest sample.

## Find a drop of chromium in a bucket of interferences.

Hexavalent chromium<sup>6+</sup> in waste water is not unlike a needle in a haystack: so elusive, it devours your time.

With our new IC method, incorporating a very high-



### Direct Metals Detection in Sea Water\*

Metal	Detection Limit (ppb)	
	Direct Nebulization <sup>1</sup>	Chelation Concentration <sup>2</sup>
Cd	10	0.1
Co	10	0.1
Cu	10	0.1
Fe	10	0.1
Mn	5	0.1
Ni	10	0.1
Pb	50	0.9
Zn	10	0.1

<sup>1</sup> With background correction

<sup>2</sup> 11 ml. concentrated

\*IC, ICP under EPA review.

Dionex Chelation IC provides a 100-fold improvement in ICP detection limits.

capacity ion exchange column, non-metallic postcolumn chemistry, and photometric detection, you'll get 0.1 ppb sensitivity and no interferences in a 6-minute analysis.

### Oxy-Halides Detection in Drinking Water†

Adequate separation between the chlorate and nitrate peaks could not be achieved with past anion columns. The new IonPac AS9 column provides the resolution needed for reliable detection of chlorite and chlorate.

Peaks	ppm
1. F <sup>-</sup>	5.66
2. ClO <sub>2</sub> <sup>-</sup>	0.50
3. Cl <sup>-</sup>	45.45
4. NO <sub>2</sub> <sup>-</sup>	0.06
5. Br <sup>-</sup>	0.08
6. ClO <sub>3</sub> <sup>-</sup>	0.14
7. NO <sub>3</sub> <sup>-</sup>	42.11
8. HPO <sub>4</sub> <sup>2-</sup>	0.17
9. SO <sub>4</sub> <sup>2-</sup>	5.00

Column: IonPac AS9  
Eluant: Na<sub>2</sub>CO<sub>3</sub>/NaHCO<sub>3</sub>  
Detection: Suppressed Conductivity

with chemically suppressed conductivity detection, does the job in one easy run.

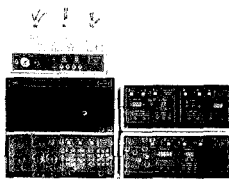
## Series 4500i. The right solutions. Right now.

### Determine chlorite and chlorate in a single run.

How do you measure oxy-halides in drinking water to the required 0.1 ppm? Until now, with great difficulty and not much reliability. Fortunately, the new, highly selective Dionex IonPac® AS9 column, combined

When you want solutions, you need Dionex. Find out how Dionex columns and the Series 4500i Systems can solve your environmental analysis problems — wet or dry. Contact your local Dionex representative or (in U.S.A.) call **1-800-227-1817, ext. 42** today.

## Series 4500i Ion Chromatograph



**DIONEX**  
A BETTER SOLUTION

Dionex Corporation, P.O. Box 5603, Sunnyvale, CA 94088-3503, Canada Dionex Canada, Ltd., (416) 620-0077, England Dionex (UK) Ltd., (276) 691722, West Germany Dionex GmbH, (612) 66036, France Dionex S.A., (1) 4621-6666, Italy Dionex S.r.l., (06) 3792979, Netherlands Dionex B.V. (75) 714800, © 1989 Dionex Corporation

CIRCLE 34 ON READER SERVICE CARD

†Method under EPA review

# MODEL 305 Modular HPLC Pump



**The new Gilson Model 305 Master Pump. For analytical or preparative HPLC in the isocratic, binary or ternary modes.**

#### **The Pump.**

Now you can program gradients without a computer. Upgrade your isocratic system without major expense. Switch from analytical to preparative and back again. Use the special dispense mode for repetitive injection in automatic preparative systems.

#### **The heads.**

For micro-analytical up to laboratory preparative scale (0.025 - 200 mL/min). For aqueous or salt-concentrated solutions. In titanium for ion-free work. All completely interchangeable so you can choose the optimum combination for your separation.

This compact new pump (only 32 cm wide) can handle any HPLC application.

*To find out more about Gilson's new Master Pump, please contact your nearest Gilson representative.*

# THE MASTER PUMP

with built-in gradient controller

 **GILSON**

U.S.A. - Box 27, 3000 West Beltline Hwy - Middleton, WI 53562 - Tel. : 608-836-155  
Tlx : 26-5478 - Fax : 608-831-4451 - FRANCE - BP 45 - 95400 Villiers-le-Bel - Tel. : (1) 34 29 50 0  
Tlx : 606 682 - Fax : (1) 39 94 51 83

CIRCLE 61 ON READER SERVICE CARD

**Because each step  
is critical for peak  
performance in  
chromatography.**

### **J.T.Baker High Purity Solvents**

For HPLC and GC analyses that place you on the leading edge of separations technology, J.T.Baker high purity solvents assure you accurate, reproducible results.

J.T.Baker manufactures high purity solvents by methods that push purification technology to the limits.

When there's no time to retrace your steps, select the high performance solvents that are manufactured and characterized for your specific application: 'BAKER ANALYZED'<sup>®</sup> HPLC grade for HPLC mobile phases; 'BAKER RESI-ANALYZED'<sup>®</sup> and 'BAKER CAPILLARY-ANALYZED'<sup>\*</sup> grades for demanding trace analyte extractions.

Specify J.T.Baker high purity solvents for your next requirement.

▶ *World leading rock climber Stefan Glowacz of West Germany, during his free ascent of the 5.12C rated (Extreme Difficulty) world class "Chain Reaction" at Smith Rocks, Oregon.*

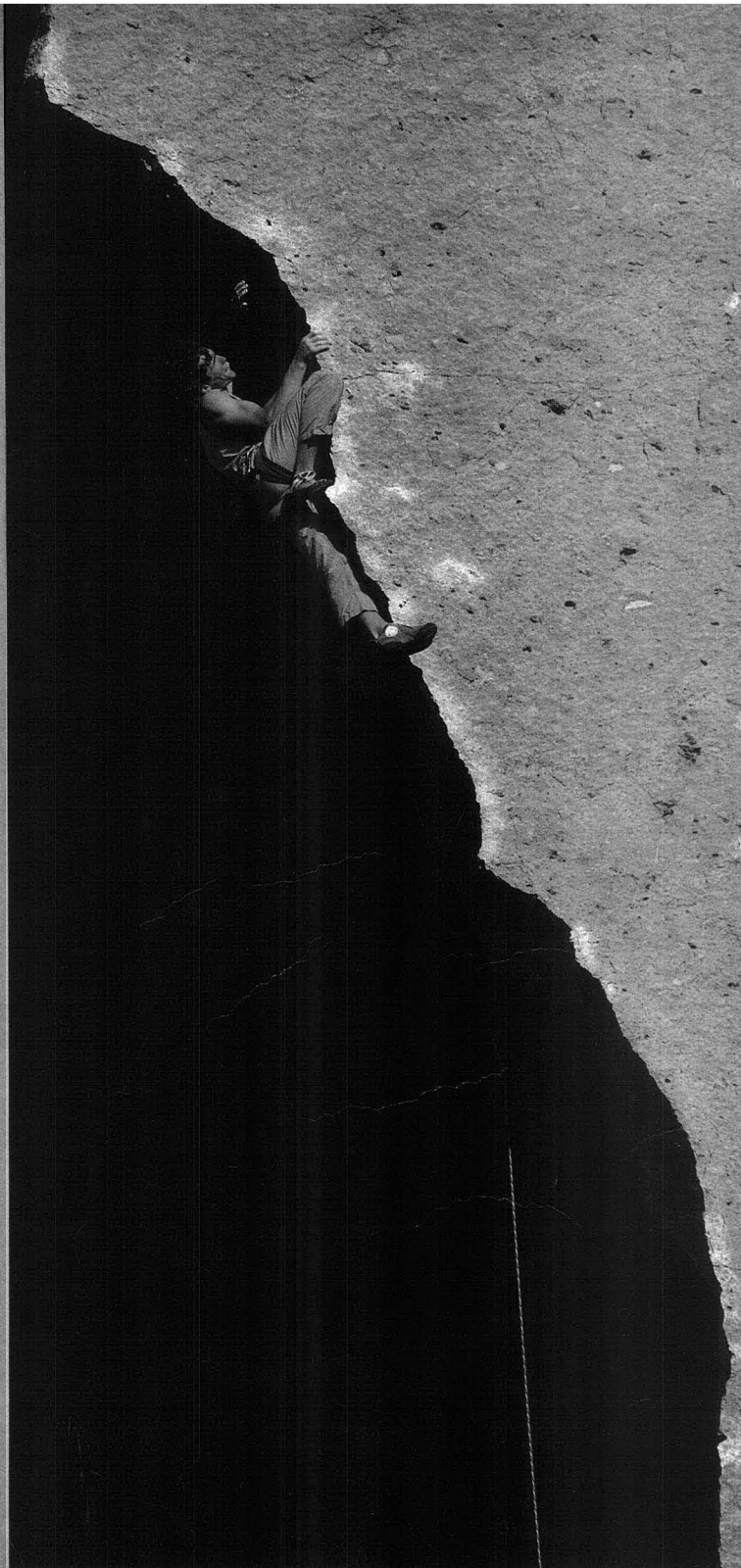


**J.T.Baker Inc.** ■ 222 Red School Lane  
Phillipsburg, NJ 08865

1-800-JTBAKER; in NJ 201-859-2151  
Telex: 299514 BAKR UR ■ FAX: 201-859-9318

CIRCLE 18 ON READER SERVICE CARD

'BAKER ANALYZED'<sup>®</sup>, 'BAKER RESI-ANALYZED'<sup>®</sup> and 'BAKER CAPILLARY-ANALYZED'<sup>\*</sup> are trademarks of J.T.Baker, Inc.



**SEPTEMBER 1, 1989**  
**VOLUME 61**  
**NUMBER 17**



ANCHAM  
 61(17)931A-1008A/1793-2000 (1989)  
 ISSN 0003-2700

Registered in U.S. Patent and Trademark Office; Copyright 1989 by the American Chemical Society  
 ANALYTICAL CHEMISTRY (ISSN 0003-2700) is published semimonthly by the American Chemical Society at 1155 16th St., N.W., Washington, DC 20036. Editorial offices are located at the same ACS address (202-872-4570; FAX 202-872-6325; TDD 202-872-6733). Second-class postage paid at Washington, DC, and additional mailing offices. Postmaster: Send address changes to ANALYTICAL CHEMISTRY Member & Subscriber Services, P.O. Box 3337, Columbus, OH 43210.

Claims for missing numbers will not be allowed if loss was due to failure of notice of change of address to be received in the time specified; if claim is dated (a) North America: more than 90 days beyond issue date, (b) all other foreign: more than one year beyond issue date, or if the reason given is "missing from files."

**Copyright Permission:** An individual may make a single reprographic copy of an article in this publication for personal use. Reprographic copying beyond that permitted by Section 107 or 108 of the U.S. Copyright Law is allowed, provided that the appropriate per-copy fee is paid through the Copyright Clearance Center, Inc., 27 Congress St., Salem, MA 01970. For reprint permission, write Copyright Administrator, Publications Division, ACS, 1155 16th St., N.W., Washington, DC 20036.

**Registered names and trademarks, etc.,** used in this publication, even without specific indication thereof, are not to be considered unprotected by law.

**Advertising Management:** Centcom, Ltd., 500 Post Rd. East, Westport, CT 06880 (203-226-7131)

1989 subscription rates include air delivery outside the U.S., Canada, and Mexico

	1 yr	2 yr
<b>Members</b>		
Domestic	\$ 27	\$ 45
Canada and Mexico	56	103
Europe	83	157
All Other Countries	120	231
<b>Nonmembers</b>		
Domestic	49	83
Canada and Mexico	78	141
Europe	155	280
All Other Countries	192	354

Three-year and other rates contact: Member & Subscriber Services, ACS, P.O. Box 3337, Columbus, OH 43210 (614-447-3776 or 800-333-9511).

**Subscription orders by phone** may be charged to VISA, MasterCard, Barclay card, Access, or American Express. Call toll free 800-ACS-5558 in the continental United States; in the Washington, DC, metropolitan area and outside the continental United States, call 202-872-8065. Mail orders for new and renewal subscriptions should be sent with payment to the Business Management Division, ACS, P.O. Box 57136, West End Station, Washington, DC 20037.

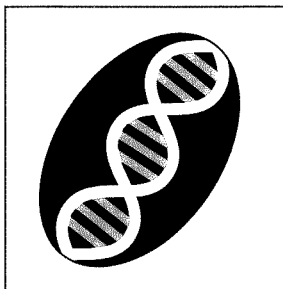
**Subscription service inquiries and changes of address** (include both old and new addresses with ZIP code and recent mailing label) should be directed to the ACS Columbus address noted above. Please allow six weeks for change of address to become effective.

**ACS membership information:** Lorraine Bowlin (202-872-4567)

**Single issues, current year, \$7.00** except review issue and LabGuide, \$12.00; **back issues and volumes and microform editions** available by single volume or back issue collection. For information or to order, call 800-ACS-5558 or write the Microform & Back Issues Office at the Washington address.

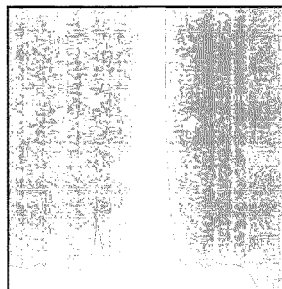
**Nonmembers rates in Japan:** Rates above do not apply to nonmember subscribers in Japan, who must enter subscription orders with Maruzen Company Ltd., 3-10 Nihonbashi 2-chome, Chuo-ku, Tokyo 103, Japan. Tel: (03) 272-7211.

# Analytical



**FOCUS 1001 A**

**On the cover. Tracking genetically engineered microorganisms.** Field tests of recombinant DNA microorganisms are finally under way. To assess the environmental impact of these unique organisms, researchers are closely monitoring them by adapting traditional analytical methods and developing some clever new ones



**INSTRUMENTATION 951 A**

**LC detector linearity.** Failure to take note of nonlinear detector response or to use appropriate data reduction methods can lead to serious inaccuracies in quantitative determinations. Brian A. Bidlingmeyer and co-workers of Waters Chromatography Division of Millipore Corporation examine the problem and propose solutions

**BRIEFS 934 A**

**EDITORIAL 945 A**

**Planetary rock analysis.** Twenty years ago, Apollo 11 returned the first lunar samples (48 pounds of rocks and soil), giving analytical chemists the chance to make unique contributions toward the understanding of our solar system

**NEWS 947 A**

**1990 ACS award winners** include Barry Karger (analytical chemistry), Peter Jurs (computers), John Knox (chromatography), Henry Freiser (separations), and Evan and Marjorie Horning (mass spectrometry). ▶ I. M. Kolthoff Award winners

**MEETINGS 971 A**

**The 16th annual meeting of the Federation of Analytical Chemistry and Spectroscopy Societies** will be held Oct. 1-6 in Chicago, IL. ▶ Conferences. ▶ Short courses and workshops. ▶ Call for papers

**NEW PRODUCTS 1004 A**

**AUTHOR INDEX 1793**

## Articles

### Scanning Electrochemical Microscopy. Apparatus and Two-Dimensional Scans of Conductive and Insulating Substrates 1794

The instrumentation for SECM is described. Topographic information for several different conductive and insulating substrates immersed in electrolytic solution is obtained with micrometer-scale resolution.

Juhyoun Kwak and Allen J. Bard\*, Department of Chemistry, The University of Texas, Austin, TX 78712

### Poly(2-vinylpyrazine) as a Soluble Polymeric Ligand and as an Electrode Coating. Reactions with Pentacyanoferrate(II) 1799

The rate and extent of reaction between  $\text{H}_2\text{OFe}(\text{CN})_5^{3-}$  and poly(2-vinylpyrazine) is measured with both reactants in homogeneous solution and with the polymer in the form of cross-linked coatings on electrode surfaces.

Paolo Ugo and Fred C. Anson\*, Arthur Amos Noyes Laboratories, Division of Chemistry and Chemical Engineering, California Institute of Technology, Pasadena, CA 91125

### Measurement of Nanomolar Dopamine Diffusion Using Low-Noise Perfluorinated Ionomer Coated Carbon Fiber Microelectrodes and High-Speed Cyclic Voltammetry 1805

Electrode noise reduction and signal averaging facilitate detection of 35 nM dopamine with untreated, Nafion-coated carbon fiber voltammetric microelectrodes (10–12  $\mu\text{m}$  o.d.). Response time is evaluated using diffusion analysis.

Margaret E. Rice\* and Charles Nicholson, Department of Physiology and Biophysics, New York University Medical Center, 550 First Avenue, New York, NY 10016

### Transient Infrared Emission Spectroscopy by Pulsed Laser Excitation 1810

IR emission spectra from optically thick samples are obtained by analyzing the emitted radiation from very thin, heated layers produced by a pulsed laser. The spectra are almost saturation-free.

Roger W. Jones and John F. McClelland\*, Center for Advanced Technology Development, Iowa State University, Ames, IA 50011

### Element Selective Detection after Supercritical Fluid Chromatography Using a Radio Frequency Plasma Detector 1815

A He rf plasma detector is evaluated as an element selective detector for capillary SFC. Spectral backgrounds are described for both  $\text{CO}_2$  and  $\text{N}_2\text{O}$ , and selective detection of S and Cl is demonstrated for several pesticides.

R. J. Skelton, Jr., P. B. Farnsworth\*, K. E. Markides, and M. L. Lee\*, Department of Chemistry, Brigham Young University, Provo, UT 84602

### Spin Dynamics in the Analysis of Carbonaceous Deposits on Zeolite Catalysts by Carbon-13 Nuclear Magnetic Resonance with Cross Polarization and Magic-Angle Spinning 1821

Relaxation measurements and other experiments indicate that the carbonaceous deposits formed in cracking reactions on zeolite HY can be analyzed with reasonable confidence, especially for lower reactor temperatures.

Benny R. Richardson and James F. Haw\*, Department of Chemistry, Texas A&M University, College Station, TX 77843

### Characteristics of Aerosols Produced by the Spark Discharge 1826

Compositionally biased aerosols are produced from the spark sampling of brass. The corresponding erosion surfaces on the electrode also differ in composition from the original bulk material.

Robert L. Watters, Jr.\*, James R. DeVoe, Francis H. Shen, John A. Small, and Ryna B. Marinenko, Center for Analytical Chemistry, National Institute of Standards and Technology, Gaithersburg, MD 20899

### Determination of Silicon in National Institute of Standards and Technology Biological Standard Reference Materials by Instrumental Epithermal Neutron Activation and X-ray Fluorescence Spectrometry 1834

Good agreement between the two methods is obtained for 11 different materials at Si concentrations ranging from 100 g/g (the methods' detection limit) to 12,000 g/g (the highest concentration in the samples).

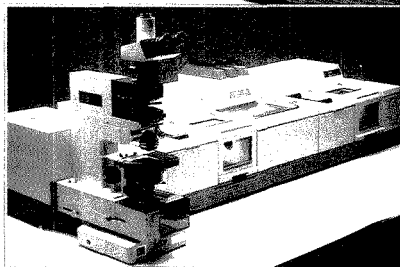
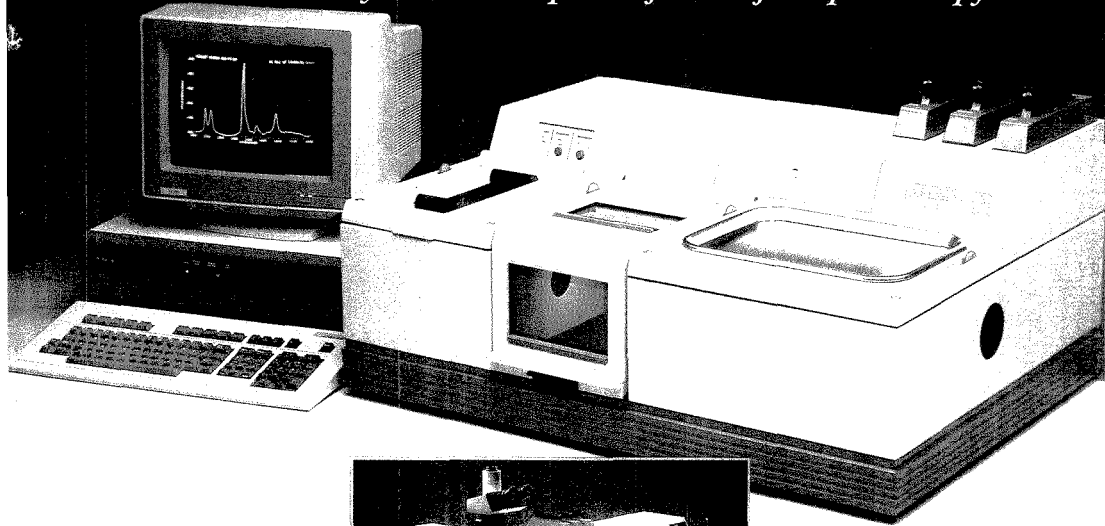
Ernest S. Gladney\*, Health and Environmental Chemistry, Group HSE-9, MS K-484, Los Alamos National Laboratory, Los Alamos, NM 87545 and Peter E. Neifert and Nathan W. Bower, Chemistry Department, Colorado College, Colorado Springs, CO 80903

\* Corresponding author

■ Supplementary material available

# Discover FT-IR 800

*The new Nicolet System 800 shapes the future of FT-Spectroscopy*



The System 800 represents the new generation in research tools. It is the synthesis of advances in optical, electronic and mechanical design. The System 800 combines an ultra-stable interferometer design with a unique dynamic alignment system, for superior data throughout the spectral range.

The System 800 provides the stability, signal-to-noise performance, and repeatability required for demanding applications. Whether your experiments involve long-term data acquisitions or rapid short-term dynamic spectroscopy applications, the 800 has the capabilities to solve your problems with confidence.

The System 800 incorporates the features demanded by leading research investigators throughout the world. Standard features include optical bench

communications, optical bench configuration monitoring and status, rapid spectral range conversion, ultra-quiet electronics train, highest throughput optical design, dynamic alignment, fully expandable optical path, ultra high-output sources, and simplified experimental design for multiple modulation techniques.

The System 800 supports the full range of experiments including FT-Raman, Emission, Microspectroscopy, GC/FT-IR, SFC/FT-IR, and more. Multiple beam paths allow several different experiments or applications to be configured simultaneously.

*Nicolet sets the standard for research performance. Let us show you the future of FT-Spectroscopy.*

**Nicolet**  
INSTRUMENTS OF DISCOVERY

Belgium: 02-762-2511  
Canada: 416-625-8302

France: 1-30-81-3081  
Germany: 069-837001

Japan: 06-863-1550  
Netherlands: 03403-74754

Switzerland: 056-844545  
United Kingdom: 0926-494111

Nicolet Analytical Instruments / 5225-1 Verona Rd. / Madison, WI 53711 / (608) 271-3333 / FAX: (608) 273-5016

*To complement these direct Nicolet offices, Nicolet maintains a network of representatives in countries throughout the world.*

CIRCLE 110 ON READER SERVICE CARD

**Thin-Specimen X-ray Fluorescence Analysis of Major Elements in Silicate Rocks** 1837

Small volumes of finely ground rock, mixed with an internal standard and spread as a monolayer in an organic binder, are analyzed by wavelength-dispersive X-ray spectrometry. The matrix-independent calibrations yield accurate analyses.

**Lewis H. Cohen\***, Department of Earth Sciences, University of California, Riverside, Riverside, CA 92521 and **David K. Smith**, Earth Sciences Department, Lawrence Livermore National Laboratory, Livermore, CA 94550

**Determination of Total Inorganic Carbon in Aqueous Samples with a Flame Infrared Emission Detector** 1841

The detector, using the 4.42- $\mu\text{m}$  (2264  $\text{cm}^{-1}$ ) band emitted by vibrationally excited  $\text{CO}_2$  in a H/air flame, is found to provide accurate TIC results when compared with values obtained from total alkalinity titrations.

**S. Wayne Kubala**, **David C. Tilotta**, **Marianna A. Busch**, and **Kenneth W. Busch\***, Department of Chemistry, Baylor University, Waco, TX 76798

**Limitations of Spectrophotometric Multicomponent Analysis of Metal Ions with Mixed Reagents** 1847

The influence of experimental conditions is studied by computer simulations in a model using a two-component reagent (Tiron and 2-pyridinealdoxime). Fe, Ti, and Cu can be determined simultaneously in aluminum reference samples with errors of < 10%.

**Matthias Otto\***, Department of Chemistry, Bergakademie Freiberg, Akademiestrasse 6, 9200 Freiberg, German Democratic Republic and **Wolfhard Wegscheider**, Institute for Analytical Chemistry, Micro- and Radiochemistry, Graz University of Technology, Technikerstrasse 4, A-8010 Graz, Austria

**Determination of Iron, Cobalt, Copper, Zinc, Rubidium, Molybdenum, and Cesium in Human Serum by Inductively Coupled Plasma Mass Spectrometry** 1851

The accuracy and precision of the technique are tested by the analysis of second-generation human serum reference material. Results obtained by ICP/MS for the seven elements considered show good agreement with the certified values.

**Hans Vanhoe**, **Carlo Vandecasteele\***, **Jacques Versieck**, and **Richard Dams**, Laboratory of Analytical Chemistry, Rijksuniversiteit Gent, Institute for Nuclear Sciences, Proeftuinstraat 86, B-9000 Gent, Belgium

**Determination of Trace Metals in Reference Water Standards by Inductively Coupled Plasma Mass Spectrometry with On-Line Preconcentration** 1857

On-line preconcentration improves the detection limits by a factor of 2-7 times. It is used for the determination of Mn, Co, Cu, Pb, and U in certified riverine water SLRS-1, and Mn, Mo, Cd, and U in reference open ocean water NASS-2.

**Diane Beauchemin\*** and **S. S. Berman**, Analytical Chemistry Section, Chemistry Division, National Research Council of Canada, Ottawa, Ontario K1A 0R9, Canada

**Development of an Optical Relative Humidity Sensor. Cobalt Chloride Optical Absorbency Sensor Study** 1863

The optical absorbency of  $\text{CoCl}_2$  on cellulose as a function of relative humidity exhibits a large hysteresis effect and is dependent on the concentration of  $\text{CoCl}_2$ , temperature, and prior treatment of the substrate.

**Francisca Boltinghouse\*** and **Kenneth Abel**, The ABEL Company, SR 774 Box 192-A, Pembroke, VA 24136

**Atomic Absorption Determination of Lead at Picogram per Gram Levels by Ethylation with in Situ Concentration in a Graphite Furnace** 1867

Tetraethyllead is generated by digestion from natural waters and biological tissues by the reaction of Pb(II) with sodium tetraethylborate. A detection limit of 14 pg is achieved.

**R. E. Sturgeon\***, **S. N. Willie**, and **S. S. Berman**, Division of Chemistry, National Research Council of Canada, Montreal Road, Ottawa, Ontario K1A 0R9, Canada

**Characterization of Single-Ply and Poly laminate Films by Nuclear Magnetic Resonance Spectroscopy** 1870

Solid-state  $^{13}\text{C}$  NMR using cross-polarization and magic-angle spinning techniques is used to obtain structural and morphological information on each layer of multilayer films containing ethylene, Nylon 6, Surlin, and/or ethylene-vinyl acetate copolymers.

**Galen R. Hatfield**, Corporate Technology, Allied-Signal, Inc., Morristown, NJ 07960

**Gas Chromatographic Sample Introduction into the Collision Cell of a Triple Quadrupole Mass Spectrometer for Mass Selection of Reactant Ions for Charge Exchange and Chemical Ionization** 1874

Reactant ions are mass-selected by the first quadrupole and react in the collision cell with the effluent from a gas chromatograph. Highly selective ion-molecule reactions are demonstrated with detection limits in the picogram range.

**Mark E. Hail**, **David W. Berberich**, and **Richard A. Yost\***, Department of Chemistry, University of Florida, Gainesville, FL 32611

**Radio Frequency Powered Glow Discharge Atomization/Ionization Source for Solids Mass Spectrometry** 1879

The use of rf power to sustain the discharge allows for direct analysis of insulating materials. Observed analyte ion currents are similar for both alloy and oxide (glass) matrix materials.

**Douglas C. Duckworth** and **R. Kenneth Marcus\***, Department of Chemistry, Howard L. Hunter Chemical Laboratories, Clemson University, Clemson, SC 29634-1905



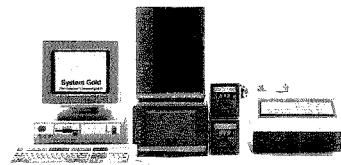
# Ninhydrin by System Gold.™ A classic performed by a master.

Beckman has been doing successful amino acid analysis since Moore, Stein and Spackman pioneered it. So it's only natural we would offer you the first HPLC that really works with the classic methodology:

Ion exchange with ninhydrin derivatization. The preferred method for quantitative results.

It is unaffected by derivative stability during separation, eliminates interference from the sample matrix, and detects both primary and secondary amino acids in one run.

The key to your success is System Gold,™ the Personal™ Chromatograph.



Solvent delivery is precise, data integration easy, and results reliable. It even includes proven methods and a reference chromatogram on disk. So we can *guarantee* successful analyses.

Discover the pleasure of a classic performed by a master. Contact your local Beckman representative. Offices in major cities worldwide.

Call 800/742-2345 in the US.

Or write Beckman Instruments, Inc., Altex Division, 2350 Camino Ramon, P.O. Box 5101, San Ramon, CA 94583.

## BECKMAN

Australia, Sydney Austria, Vienna Canada, Toronto Denmark, Esbjerg France, Gajny Germany, Munich Hong Kong, Aberdeen Italy, Milano Japan, Tokyo Mexico, Mexico City Netherlands, Maastricht Norway, Oslo Puerto Rico, Carolina Singapore South Africa, Johannesburg Spain, Madrid Sweden, Bromma Switzerland, Nyon Taiwan, Taipei United Kingdom, High Wycombe United States, San Ramon © 1988, Beckman Instruments, Inc. AX88-1074

Circle 22 for representative and literature.  
Circle 23 for literature only.

**Determination of the Concentration and Stable Isotopic Composition of Oxygen in Organic Matter Containing Carbon, Hydrogen, Oxygen, Nitrogen, and Sulfur** 1887

A method that measures the concentration and isotopic composition of oxygen in glucose doped with thioguanine (which contains no oxygen) gives the same results as methods that use glucose alone.

**Michael J. DeNiro\*** and **Samuel Epstein**, Division of Geological and Planetary Sciences, California Institute of Technology, Pasadena, CA 91125

**Isomer Discrimination of Disubstituted Benzene Derivatives through Gas-Phase Iron(I) Ion Reactions in a Fourier Transform Mass Spectrometer** 1889

Reactions of Fe<sup>+</sup> with the isomers of several disubstituted benzene derivatives produce spectra that, in many cases, reveal isomer differentiation. EI spectra are too similar and are not helpful in isomer identification.

**Asgeir Bjarnason** and **James W. Taylor\***, Department of Chemistry, University of Wisconsin—Madison, Madison, WI 53706 and **James A. Kinsinger**, **Robert B. Cody**, and **David A. Weil**, Nicolet Analytical Instruments, Madison, WI 53711

**Amino Acid and Tripeptide Mixture Analysis by Laser Desorption Fourier Transform Mass Spectrometry** 1895

The 1064-nm laser desorption efficiencies of amino acids correlate with their sublimation enthalpies. Less discrimination and greater sensitivity are seen with laser desorption than with FAB-MS.

**M. Paul Chiarelli** and **Michael L. Gross\***, Midwest Center for Mass Spectrometry, Department of Chemistry, University of Nebraska, Lincoln, NE 68588

**Dual-Column Immunoassays Using Protein G Affinity Chromatography** 1901

An LC column switching system is used to perform on-line immunoassays. Antibody titers are determined with a precision of ±2%, and a detection limit of 0.7 pmol of human transferrin is obtained with a precision of ±3.5%.

**Linda J. Janis** and **Fred E. Regnier\***, Departments of Chemistry and Biochemistry, Purdue University, West Lafayette, IN 47907

**Direct Coupling of Planar Chromatography to Gas Chromatography by Laser Desorption** 1906

The coupling of TLC to GC is demonstrated using a laser desorption interface. Detection and identification of the TLC separated zones is now possible by a broad spectrum of GC detectors.

**Jianzhong Zhu** and **Edward S. Yeung\***, Ames Laboratory—US-DOE and Department of Chemistry, Iowa State University, Ames, IA 50011

**Resonant Two-Photon Ionization Spectroscopic Analysis of Thin-Layer Chromatography Using Pulsed Laser Desorption/Volatilization into Supersonic Jet Expansions** 1911

Using pulsed laser desorption, it is possible to vaporize TLC spots directly into the gas phase for identification by resonant two-photon ionization spectroscopy and MS.

**Liang Li** and **David M. Lubman\***, Department of Chemistry, The University of Michigan, Ann Arbor, MI 48109

**Examination of the Automated Solute-Independent Calibration Technique** 1915

A universal calibration method for ion chromatography using conductivity detection is examined for long-term use. The completely automated method includes sampling, chromatographic separation, data collection, and analysis.

**Curtiss N. Renn** and **Robert E. Synovec\***, Center for Process Analytical Chemistry, Department of Chemistry, BG-10, University of Washington, Seattle, WA 98195

**Polyamine Detection System for High-Performance Liquid Chromatography Involving Enzymatic and Chemiluminescent Reactions** 1921

The substrate specificity of the enzymes allows the specific detection of polyamines in urine despite the presence of many other coexisting amino compounds. The sensitivity and precision are comparable to the OPA method.

**Sachiko Kamei\*** and **Akiyuki Ohkubo**, Department of Laboratory Medicine, Faculty of Medicine, University of Tokyo, 7-3-1 Hongo, Bunkyo-ku, Tokyo 113, Japan and **Shin Saito** and **Shigeyuki Takagi**, The Medical Equipment Technical and Engineering Division, JEOL, Ltd., 1418, Nakagami-cho, Akisima-shi, Tokyo 196, Japan

**Determination of Chloride in Platinum-Rhenium Alumina-Based Reforming Catalyst by Ion Chromatography** 1924


The chloride is extracted quantitatively with 1 M NaOH at 150 °C in a Parr bomb. The analysis time is 1 h, the detection limit is 0.1% by weight, and the RSD is about 3%. The analysis is confirmed by XRF spectroscopy.

**Raj P. Singh\***, **Khurshid Alam**, **Dawoud S. Redwan**, and **Nur-eddin M. Abbas**, The Research Institute, King Fahd University of Petroleum & Minerals, Dhahran 31261, Saudi Arabia

**Chemically Bonded Liquid Crystals as Stationary Phases for High-Performance Liquid Chromatography. Effects of Mobile-Phase Composition** 1928

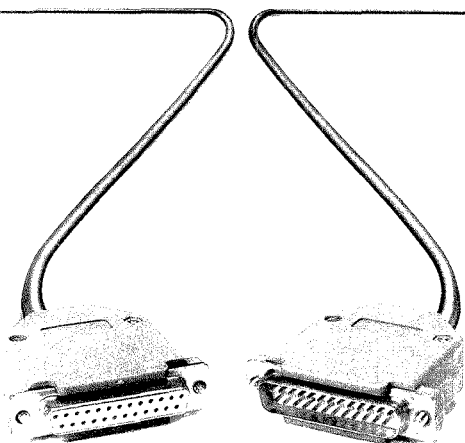
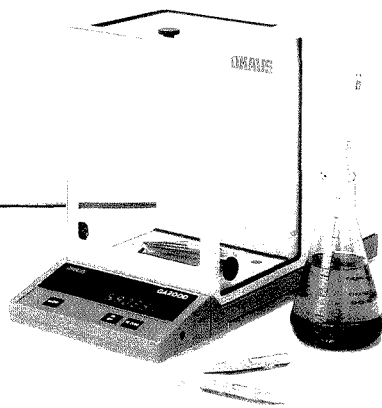
A phase transition in a bonded liquid crystal is detected by examination of the plot of log *k'* versus percentage of organic solvent in the mobile phase. Variable-temperature experiments also support this finding.

**Joseph J. Pesek\***, Department of Chemistry, San Jose State University, San Jose, CA 95192 and **Antoine M. Siouffi**, Laboratoire de Chimie Appliquée, Université d'Aix-Marseille, F13390 Marseille Cedex 13, France



“I switched to Ohaus  
because I needed a  
balance with the brawn to  
withstand heavy use and  
the brains to interface  
with my titrator.”

*Werner Friedrich  
Research Chemist  
Chevron Chemical Co.  
Richmond, CA*



Ohaus GA Series electronic analytical balances are easy to use and ruggedly built to take the abuse of everyday use. RS232C bi-directional data interface connects the balance to Ohaus GP200 printer or any other peripheral equipment for fast, easy, up-to-the-minute calculations. Other features include automatic calibration, variable integration and a large fluorescent display. For more information or a demonstration, call or write Ohaus, P.O. Box 900, Florham Park, NJ 07932, (800) 672-7722.

*Solid, sensible balances & scales*

**HAUS** ★

CIRCLE 120 ON READER SERVICE CARD

**Laser-Based Indirect Fluorometric Detection and Quantification in Thin-Layer Chromatography** 1931

By scanning a low-power He-Ne laser over pretreated TLC plates, analytes can be detected by indirect fluorescence at picogram levels.

Yinfa Ma, Lance B. Koutny, and Edward S. Yeung\*, Ames Laboratory-USDOE and Department of Chemistry, Iowa State University, Ames, IA 50011

**Density Determination of Low-Density Polymer Latexes by Sedimentation Field-Flow Fractionation** 1934

Sedimentation FFF can be used to determine the particle density of copolymer latexes with densities  $<1.02 \text{ g/cm}^3$ . Methanol is used to decrease the density of the mobile phase.

D. J. Nagy, Air Products and Chemicals, Inc., Corporate Research Services, 7201 Hamilton Boulevard, Allentown, PA 18195

**A Different Perspective on the Theoretical Plate in Equilibrium Chromatography** 1937

The differential rate model for equilibrium chromatography is used to derive both the continuous (Martin and Synge) plate model and the stepwise (Craig) model.

Paul J. Karol, Department of Chemistry, Carnegie Mellon University, Pittsburgh, PA 15213

**Robust Statistics and Functional Relationship Estimation for Comparing the Bias of Analytical Procedures over Extended Concentration Ranges** 1942

Two nonclassical statistical methods are applied successively to data from parallel collaborative trials. The benefits of these methods are demonstrated.

Michael Thompson, Department of Chemistry, Birkbeck College, Gordon House, 29 Gordon Square, London WC1H 0PP, U.K.

**Factors Affecting Precision and Accuracy in Quantitative Analysis by Secondary Ion Mass Spectrometry** 1946

Misalignment of samples and differences in ion energy distributions contribute to errors in quantitative analysis by SIMS. Precision is 1.9% RSD from 12 measurements on a carefully aligned sample.

Ray-Chern Deng and Peter Williams\*, Department of Chemistry, Arizona State University, Tempe, AZ 85287-1604

**Linearized Model for Error-Compensated Kinetic Determinations without Prior Knowledge of Reaction Order or Rate Constant** 1949

An algorithm is described for calculating reaction orders, rate constants, and initial and final values of detector signal from several signal-versus-time data points.

Jan A. Larsson and Harry L. Pardue\*, Department of Chemistry, Purdue University, West Lafayette, IN 47907

**Electrochemical Behavior of *N*-Acetylpenicillamine Thionitrate at Glassy Carbon and Carbon Fiber Electrodes** 1954

A detection limit of  $3 \mu\text{M}$  is obtained using square-wave voltammetry in combination with a carbon fiber microcylinder electrode (CFME). The construction and the pretreatment procedure for the CFME are described.

Michael J. Nuwer and Janet Osteryoung\*, Department of Chemistry, State University of New York at Buffalo, Acheson Hall, Buffalo, NY 14214

**Influence of Mass Transfer Kinetics on the Separation of a Binary Mixture in Displacement Liquid Chromatography** 1960

Band profiles in displacement chromatography depend on the displacer concentration, the loading factor, and the combined effect of mass transfer kinetics and axial diffusion. When mass transfer kinetics are slow, the separation is improved by increasing the column length at constant loading factor.

Sadroddin Golshan-Shirazi, Bingchang Lin, and Georges Guiochon\*, Department of Chemistry, University of Tennessee, Knoxville, TN 37996-1600 and Division of Analytical Chemistry, Oak Ridge National Laboratory, Oak Ridge, TN 37831-6120

**Ionic Equilibria of Picric Acid in Mixed Amphiprotic Solvents. The 2-Methoxyethanol/Water Solvent System** 1971

Picric acid is used to verify the applicability of an empirical treatment describing the dependence of the dissociation constant on temperature and composition of the solvent mixture. The dissociation constants are evaluated by the conductometric method at temperatures from  $-10$  to  $80^\circ\text{C}$ .

Andrea Marchetti, Emanuele Picchioni, Lorenzo Tassi, and Giuseppe Tosi\*, University of Modena, Department of Chemistry, via G. Campi, 183, 41100 Modena, Italy

**Correspondence****Voltammetric Detection with Gradient Elution for Open Tubular Liquid Chromatography** 1977

Mary D. Oates and James W. Jorgenson\*, Department of Chemistry, University of North Carolina, Chapel Hill, NC 27599-3290

**Crystal-Face-Specific Response of a Single-Crystal Cadmium Sulfide Based Ion-Selective Electrode** 1980

Kohei Uosaki, Yasuyuki Shigematsu, Hideaki Kita, and Yoshio Umezawa\*, Department of Chemistry, Faculty of Science, Hokkaido University, Sapporo 060, Japan and Ryutaro Souda, National Institute for Research in Inorganic Materials, Namiki, Tsukuba 305, Japan

**Pseudo Molecular Ions in Ion Trap Detector Electron Impact Mass Spectra: Practical Consequences** 1983

Ian Horman\* and Helmut Trautler, Nestlé Research Centre, Nestec Ltd., Vers-chez-les-Blanc, CH-1000, Lausanne 26, Switzerland



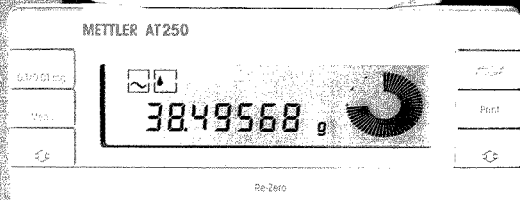
If it did any more, you'd be obsolete.

Perhaps the new METTLER AT does a little too much.

After all, it self-calibrates with FACT, the fully automatic calibration technology. So you never have to remember to do it. Much less, worry about when to do it. It opens its draft shield automatically. So you can weigh something in half the number of steps. In half the time. It comes complete with a stability detector and a vibration adapter. Which enables you to adjust the balance to your lab conditions, so you don't have to adjust your lab conditions to the balance. It's even equipped with METTLER Delta-Trac. So you can see where you are in the weighing range, rather than guess at it. With the new AT, what's left for you to do? Well, someone still has to turn it on. To find out more about the AT, call us.

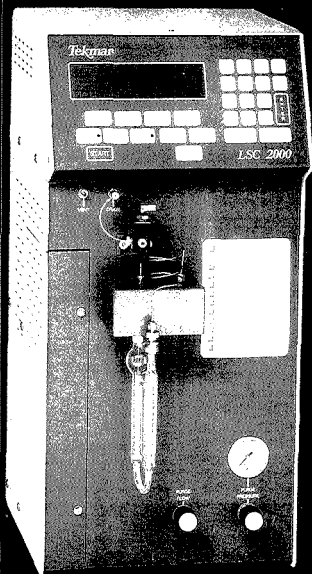
**Mettler Instrument Corporation**  
Box 71, Hightstown, N.J. 08520  
Phone 1-800-METTLER  
in New Jersey 609-448-3000

CIRCLE 96 ON READER SERVICE CARD



**METTLER**

**MAXIMIZE YOUR  
SENSITIVITY...  
for Volatile Organic  
Compounds by Dynamic  
Headspace Concentration**



5 ml **Coffee** on Tekmar's LSC 2000 and Capillary Interface

**Flavor/Fragrance  
Competitive Analysis  
Off Flavor/Odor Analysis  
Packaging Materials  
Pharmaceuticals/Residual Solvents  
Building Products/Outgassing Studies  
Polymers  
Residual Monomers/Solvents**

Ask for our FREE bibliography of reprints  
on a wide range of applications

P.O. Box 371856 • Cincinnati, OH 45222-1856  
(800) 543-4461 Sales • (800) 874-2004 Service  
Fax (513) 761-5183 • Telex 21-4221

CIRCLE 156 ON READER SERVICE CARD

**BRIEFS**

**Optical Resolution of Enantiomers with Chiral Mixed Micelles  
by Electrokinetic Chromatography 1984**

Akira Dobashi, Tamami Ono, and Shoji Hara\*, Tokyo College of Pharmacy, 1432-1 Horinouchi, Hachioji, Tokyo 192-03, Japan and Junko Yamaguchi, Gasukuro Kogyo, Inc., 237-2 Sayamagahara, Iruma, Saitama 358, Japan

**Quantitative Supercritical Fluid Extraction/Supercritical Fluid  
Chromatography of a Phosphonate from Aqueous Media 1986**

J. Hedrick and L. T. Taylor\*, Department of Chemistry, Virginia Polytechnic Institute and State University, Blacksburg, VA 24061-0212

**Technical Notes**

**In Situ Laser Activation of Glassy Carbon Electrochemical  
Detectors for Liquid Chromatography: Demonstration of  
Improved Reversibility and Detection Limits 1989**

Kent Sternitzke and Richard L. McCreery\*, Department of Chemistry, The Ohio State University, 120 West 18th Avenue, Columbus, OH 43210 and Craig S. Bruntlett and Peter T. Kissinger, Bioanalytical Systems, 2701 Kent Avenue, West Lafayette, IN 47906

**Diffusion Apparatus for Trace Level Vapor Generation of  
Tetramethyllead 1993**

P. R. Fielden\* and G. M. Greenway, Department of Instrumentation and Analytical Science, UMIST, P.O. Box 88, Manchester M60 1QD, U.K.

**Preparation of Organic Matter for Stable Carbon Isotope  
Analysis by Sealed Tube Combustion: A Cautionary Note 1996**

Michael H. Engel\* and Rick J. Maynard, School of Geology and Geophysics, The Energy Center, 100 East Boyd Street, The University of Oklahoma, Norman, OK 73019

**Foam Countercurrent Chromatography of Bacitracin with  
Nitrogen and Additive-Free Water 1998**

Hisao Oka, Ken-ichi Harada, Makoto-Suzuki, Hiroyuki Nakazawa, and Yoichiro Ito\*, Laboratory of Technical Development, National Heart, Lung, and Blood Institute, National Institutes of Health, Bethesda, MD 20892

# LIQUID CARBONIC SPECIALTY GASES

**At Liquid Carbonic  
we don't just analyze  
specialty gas...**

**We guarantee it**

When you order a specialty gas, you don't want any surprises. That's why Liquid Carbonic makes sure you get exactly what you expect. Our chemists accurately analyze our specialty gases. And we issue a certificate of analysis so you can be certain of the purity and content of every cylinder.

And when you order our specialty gas you also receive the technical expertise and consistently superior service that Liquid Carbonic has been providing to customers for over 100 years.

For more information about the quality specialty gas and specialty gas services we offer, return the coupon today!

CIRCLE 88 ON READER SERVICE CARD

Send me your catalog and information on:

- |  |   |
|--|---|
| <input type="checkbox"/> Calibration Gas Standards | <input type="checkbox"/> Silane           |
| <input type="checkbox"/> High Purity Gases         | <input type="checkbox"/> Electronic Gases |
| <input type="checkbox"/> Emission Gases            | <input type="checkbox"/> Fluorocarbons    |
| <input type="checkbox"/> Sterilizing Gases         | <input type="checkbox"/> Research Gases   |



**LIQUID CARBONIC**  
SPECIALTY GAS CORPORATION

135 SOUTH LA SALLE STREET  
CHICAGO, ILLINOIS 60603-4282

Name \_\_\_\_\_  
 Title \_\_\_\_\_ Phone (\_\_\_\_) \_\_\_\_\_  
 Company \_\_\_\_\_  
 Address \_\_\_\_\_  
 City \_\_\_\_\_  
 State \_\_\_\_\_ Zip \_\_\_\_\_  
 Have your local representative contact me



# SURE THINGS

Trust Parker quality  
throughout your operation.

You've learned to be certain of Parker column end fittings and valves for critical chromatography applications.

Now extrapolate.

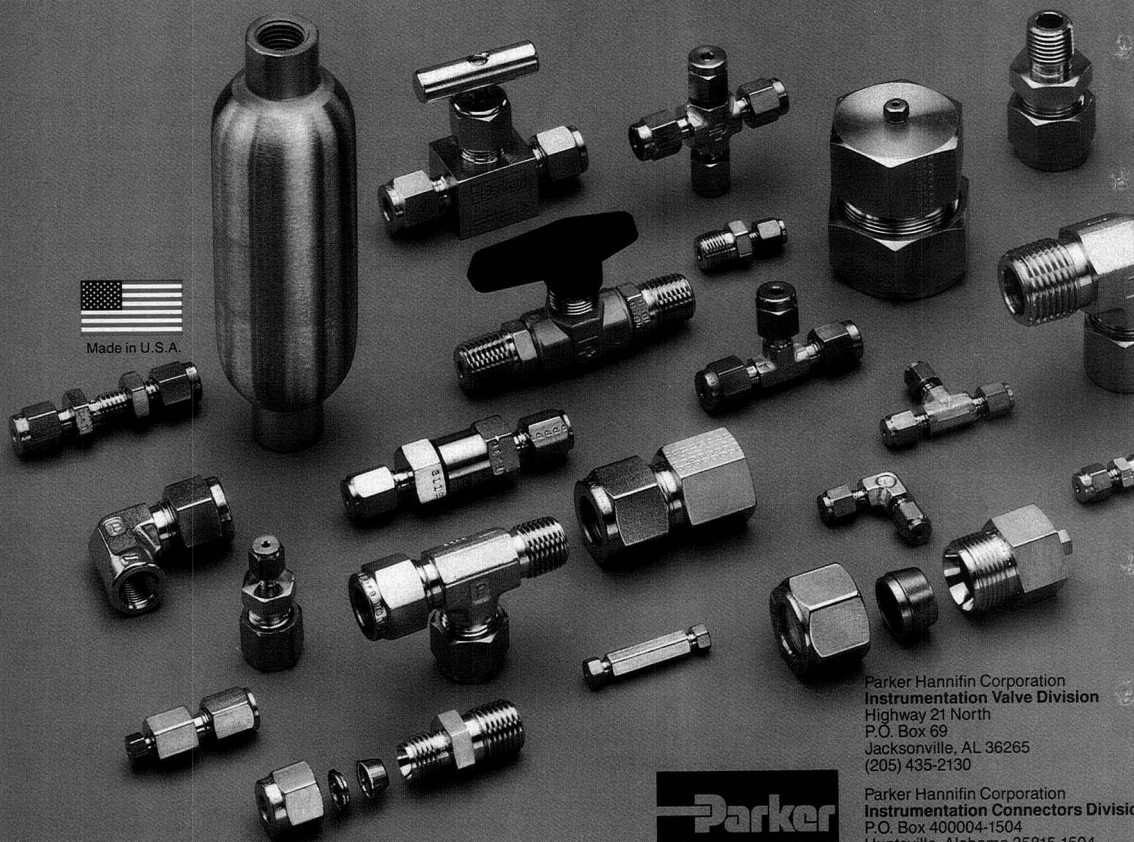
You will enjoy all that quality and accuracy, all that craftsmanship and performance in the total Parker line for all your analytical, laboratory and instrumentation applications.

Parker's complete line includes compression, welded and face-seal fittings, sizes from  $\frac{1}{16}$ " to 1" O.D., in a broad range of materials and configurations. It also includes a full line of needle, ball, bellows, check valves and filters, plus sample cylinders, transfer coils, and more.

All Parker. All sure things. Contact the Instrumentation Divisions or your independent Parker Distributor.



Made in U.S.A.



Parker Hannifin Corporation  
Instrumentation Valve Division  
Highway 21 North  
P.O. Box 69  
Jacksonville, AL 36265  
(205) 435-2130

Parker Hannifin Corporation  
Instrumentation Connectors Division  
P.O. Box 400004-1504  
Huntsville, Alabama 35815-1504  
(205) 881-2040

  
FluidConnectors

CV-926

See you at Booth #4149 at the ISA Show. CIRCLE 129 ON READER SERVICE CARD



## **Planetary Rock Analysis**

This past July 20 marked the twentieth anniversary of the first landing of man on the moon. Apollo 11 astronauts Neil Armstrong, Edwin (Buzz) Aldrin, Jr., and Michael Collins returned to Earth with 48 pounds of lunar rock and soil. These samples were then studied by 142 principal investigators from laboratories around the world who had been selected by the National Aeronautics and Space Administration (NASA) for the Lunar Analysis Program. Between 1969 and 1974 a total of six missions (Apollo 11, 12, 14, 15, 16, and 17) returned a wealth of samples from different locations on the moon.

Study of the Apollo lunar samples represented a unique scientific adventure and an intellectual challenge of the first magnitude. As one might expect, chemical analysis—particularly trace analysis—played a very important role in the Lunar Analysis Program. In addition to chemical and isotopic analysis, mineralogy and petrology, physical studies, and organic and biochemical analyses were performed.

By comparing the elemental abundance patterns of lunar material with those of solar, meteoritic, and terrestrial materials, some insight into the cosmological history of the moon was obtained. The chemical composition of the lunar surface was found to reflect at least three major processes: chemical fractionations

during accretion of the moon from the solar nebula, magnetic differentiation, and infall of meteorites and cosmic dust.

Among the analytical techniques used to study lunar materials were activation analysis, atomic spectroscopy, Auger spectroscopy, gamma spectrometry for radioactive isotopes, inert gas fusion and combustion chromatographic analysis, mass spectrometry, electron and ion microprobe analysis, Mössbauer spectroscopy, scanning electron microscopy, spectrophotometry, wet chemistry, and X-ray fluorescence spectroscopy.

This monumental analysis program has contributed significantly to our current knowledge of the moon. However, further planetary studies are vitally needed to better understand our solar system. Much of the future success of such studies will depend upon high-quality chemical analysis.

For historical interest, I suggest seeing a 16-mm film, "Museum of the Solar System," which was presented by the American Chemical Society in 1971. The film presents scientific studies of the lunar samples by seven investigators, including the Nobel laureate Harold C. Urey.



## The LDC spectroMonitor® 5000 Diode Array Detector for HPLC

LDC introduces a new, truly powerful PDA detector for high performance liquid chromatography. The spectroMonitor® 5000 provides complete spectral information on your LC separation including 4 channels of simultaneous absorbance data. The stand-alone detector stores up to 300 scans or can transmit 10 scans per second to a microcomputer for post-run analysis. LDC also provides PC compatible software for data transfer and analysis.

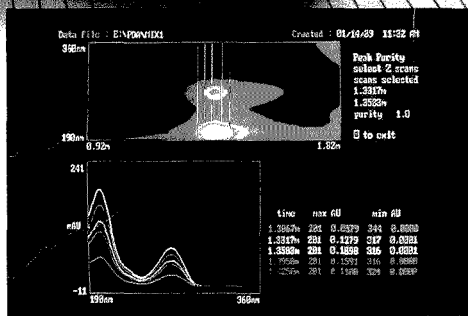


Shown to the right is the LDC peak purity program which enables comparison of up to 5 selected spectra within an LC run.



20 Years of Quality  
in HPLC

To put the power of the spectroMonitor® 5000 to work for you call (800) LDC-HPLC.



## LDC ANALYTICAL

A Subsidiary of Thermo Instrument Systems, Inc.

HEADQUARTERS, P.O. Box 10235, 3661 Interstate Park Road, Riviera Beach, Florida 33419 Toll-free: 800-LDC-HPLC, In Florida: (407) 844-5241 Telex: 441098

UNITED KINGDOM, Diamond Way, Stone Business Park, Stone, Staffordshire, ST 15 0HH, England Telephone: (0785) 813542 Telex: 36623

FRANCE, 15 rue Guyton de Mornveau, Paris 75013, France Telephone: (1) 45 88 28 00 Telex: 205331

FEDERAL REPUBLIC OF GERMANY, Jahnstrasse 22-24, 6467 Hasselroth2, FRG Telephone: 06055-3355 Telex: 4184357

JAPAN, Takanawa Dai-Ichi Building 21-41, Takanawa 2-Chome, Minato-Ku, Tokyo 108, Japan Telephone: (03) 473-3181 Telex: 242-4296

## 1990 ACS Award Winners

Six researchers in the analytical chemistry community have been selected to receive five of the 1990 American Chemical Society Awards. All of the awards will be presented in April 1990 at the 199th ACS Spring National Meeting in Boston, MA.

Barry L. Karger of Northeastern University will receive the ACS Award in Analytical Chemistry. Sponsored by the Fisher Scientific Company, the award recognizes outstanding contributions to the science of pure or applied analytical chemistry.

Peter C. Jurs of The Pennsylvania State University has been selected to receive the ACS Award for Computers in Chemistry, sponsored by the Digital Equipment Corporation. The award recognizes and encourages the use of computers for the advancement of chemical science.

John H. Knox of the University of Edinburgh (U.K.) will receive the ACS Award in Chromatography, sponsored by Supelco, Inc. The award honors outstanding contributions made to the field of chromatography.

Henry Freiser of the University of Arizona will receive the ACS Award in Separations Science and Technology. The award, which recognizes outstanding accomplishments in fundamental or applied research directed toward separations science and technology, is sponsored by the Rohm and Haas Company.

Evan C. Horning and Marjorie G. Horning, both members of the faculty of the Baylor College of Medicine, will be the co-recipients of the Frank H. Field and Joe L. Franklin Award for Outstanding Achievement in Mass Spectrometry. Sponsored by the Extrel Corporation, the award recognizes outstanding achievement in the development or application of mass spectrometry.

Brief biographical sketches of the awardees follow.

**Barry L. Karger** received a B.S. degree from the Massachusetts Institute of Technology (1960) and a Ph.D. from Cornell University (1963) before joining the faculty of Northeastern University in 1963. He became the founding director of Northeastern's Barnett Institute of Chemical Analysis and Materials Science in 1973.

Karger was involved with the development of HPLC in the 1970s and has devoted his research efforts to the study of biochemical separations and analytical biotechnology. He has been instrumental in the development and application of HPLC to peptide and protein separations and in the development of hydrophobic interaction chromatography. More recently, Karger has studied protein aggregation, the measurement of protein fluorescence on chromatographic surfaces, and capillary electrophoresis.

Along with Fred Regnier, Karger organizes an annual analytical biotechnology seminar that brings together analytical chemists, biochemists, biotechnologists, and immunologists to advance the field of analytical biotechnology. In ad-



dition, he was the organizing chairman of the first international symposium on high-performance capillary electrophoresis (see FOCUS, p. 795 A).

Karger has received numerous awards and honors including the Dal Nogare Award (1975), the ACS Award in Chromatography (1982), and the Tswett Chromatography Award (1986) and is a former member of the ANALYTICAL CHEMISTRY Advisory Board (1977-79).



**Peter C. Jurs** joined the faculty of The Pennsylvania State University as an assistant professor in 1969, was appointed associate professor in 1972, and professor in 1978. He received a B.S. degree from Stanford University (1965) and a Ph.D. in chemistry from the University of Washington (1969). He is best known for his work in analytical data analysis using pattern recognition methods, molecular structure-physicochemical property relationship studies, and molecular structure-biological activity relationship studies. A member of the research group that published the first paper on pattern recognition analysis of low-resolution mass spectral data, Jurs applied these methods to other analytical data such as infrared spectral analysis. His latest work deals with the analysis of complex analytical data that serve as fingerprints for membership classes (e.g., classification of biological samples based on capillary chromatograms).

Jurs has also made contributions in computer-assisted studies of structure-property relationships (SPR) and structure-activity relationships (SAR) that required the development of the automated data analysis and pattern recognition toolkit (ADAPT) computer software system. In addition, Jurs has studied the prediction of  $^{13}\text{C}$  NMR chemical shifts directly from the structure of organic compounds. He is currently serving on the ANALYTICAL CHEMISTRY Advisory Board.

**John H. Knox**, professor emeritus at the University of Edinburgh, received a B.Sc. degree from the University of Edinburgh (1949), a Ph.D. from the University of Cambridge (1953), and a D.Sc. (1963) from the University of Edinburgh. Knox's early interests in chromatography arose from his work on the kinetics and mechanisms of gas-phase reactions using GC. He quickly became interested in the kinetics of chromatography and developed a theory for maximizing the speed of separations. This led to more detailed studies on how band spreading occurred and can be controlled. In 1972, Knox was awarded a grant from the Wolfson Foundation to integrate his expertise in LC with industry, a project that led to the development of several commercial packing materials. Knox has made major contributions to the understanding



of preparative LC, ion-pair LC, and size exclusion LC. Currently he is working on capillary electroseparation systems and the application of porous graphite to LC.

Knox's numerous honors include the 1983 Dal Nogare Award and the 1985 Tswett Chromatography Medal.

**Henry Freiser** received his B.S. degree from the City College of New York (1941) and an M.S. degree (1942) and a Ph.D. (1944) from Duke University. After appointment to the faculties of North Dakota State College and the University of Pittsburgh, he joined the faculty at the University of Arizona in 1958.

Freiser's research has centered around his interest in the role of molecular structural factors affecting chemical and physical properties. Based on systematic studies of solvent extraction processes from a fundamental point of view, he has developed techniques to examine intimate details of the mechanism of such processes; novel, highly selective and sensitive metal extractants; and highly selective and sensitive electrochemical sensors. His studies have made an impact in illuminating the relevance of solvent extraction concepts to surface chemistry at liquid-liquid interfaces.

In 1957, Freiser and G. H. Morrison published the first book on the principles and practices of solvent extraction, *Solvent Extraction in Analytical Chemistry*. This classic work has been translated into five languages and is currently being revised.

Freiser was the recipient of the 1987 Division of Analytical Chemistry Award for Excellence in Teaching.



**Evan C. Horning** received a B.S. degree from the University of Pennsylvania (1937) and a Ph.D. from the University of Illinois (1940). He joined the faculty at the University of Pennsylvania in 1945, and moved to the National Heart Institute (National Institutes of Health) in 1950, where he headed the laboratory of chemistry of natural products.

In 1961, Horning was appointed professor of chemistry at the Baylor College of Medicine. In addition to his current position with Baylor's chemistry department, Horning serves as adjunct professor of biochemistry at Rice University and is the director of Baylor's Institute for Lipid Research.

Horning's numerous awards and honors include the 1975 Tswett Chromatography Medal, the 1979 ACS Award in Chromatography, and the 1980 Dal Nogare Award.

**Marjorie G. Horning** received a B.A. degree from Goucher College (1938), and her M.S. degree (1940) and Ph.D. (1943) from the University of Michigan. She worked as a research chemist at the National Heart Institute from 1951 to 1961 and joined the staff at the Baylor College of Medicine in 1961. She currently serves as a professor of biochemistry with the department of biochemistry and the Institute for Lipid Research and as an adjunct professor of biochemical and biophysical sciences at the University of Houston. She is also a special member of the graduate faculty at the University of Texas Graduate School of Biomedical Sciences.



Horning was the recipient of the Garvan Medal in 1977 and is a former member of the Advisory Board of ANALYTICAL CHEMISTRY (1975-77).

The Hornings were pioneers in promoting and establishing GC/MS as a tool for biochemistry and medicine. Their early research focused on synthetic organic chemistry; in the 1960s, their interests expanded to include GC. They established many procedures for isolating samples from biological matrices prior to GC analysis, and the principles of these procedures have been subsequently applied to the field of GC/MS. The Hornings developed new chemical derivatization procedures to facilitate vapor analysis of a variety of compounds including fatty acids, hydroxamic acids, steroids, phospholipids, and barbiturates.

They were instrumental in developing atmospheric pressure ionization MS in the early 1970s. The success of this technique resulted in methods with detection limits at the femtogram and attomole levels. Specifically, their work has involved trace-level determination of nicotine and other drugs in biological fluids.

## Kolthoff Enrichment Awards

Seven undergraduates have been awarded the first I. M. Kolthoff Enrichment Awards. These awards, sponsored by the ACS Division of Analytical Chemistry, were established in 1987 and are given annually to undergraduates demonstrating a special interest and competency in analytical chemistry. The students are entering their final year of undergraduate studies. Up to \$1000 comes with the award, and the money is to be used for an activity (such as research or meeting attendance) that falls outside the curriculum requirements for a degree.

This year's winners are Cheryl Davis, Mary Washington College; Harvey Fishman, The Pennsylvania State University; Trent Peterson, Fort Lewis College; Mary Staton, Tennessee Technological University; Linda Szabo, Wellesley College; Christopher Thomas, University of Wyoming; and Sheryl Tucker, Kent State University. Honorable mentions were awarded to George Mickelson, State University of New York, College at Brockport; Jeffery Pilgrim, University of Georgia; and Radha Pyati, The Ohio State University.

## For Your Information

Nominations are being solicited for the **Tomas Hirschfeld Award in Near Infrared Analysis**. The \$3000 award is given to a graduate, postgraduate, or industrial researcher who is not employed by an instrument manufacturer. Nominations must be submitted by October 2 to Gabor Kemeny, Bran + Luebbe Analyzing Technologies, Inc., 103 Fairview Park Drive, Elmsford, NY 10523 (914-524-8112).

The American Association of Clinical Chemists (AACC) has formulated **guidelines for instructional materials that accompany home clinical test kits**, such as pregnancy kits. For more information, contact Lynnette Washington (202-835-8718). In addition, AACC is seeking uncommon clinical tests for its 1990-91 **Directory of Rare Analyses**. For more information, contact Tina Edwards, AACC Press, 2029 K St., N.W., Suite 700, Washington, DC 20006 (800-892-1400).

# COMPARE FTIR PERFORMANCE & PRICE

Mattson's Galaxy 6020® FTIR System offers you more.

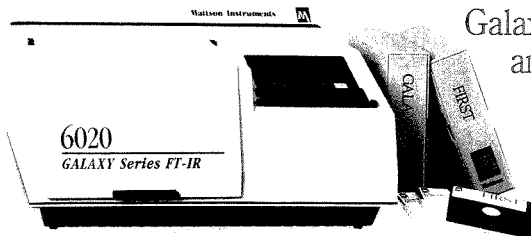
Proof that a better-run company can afford to develop innovative products and competitive prices.

Features & Capability	Mattson 6020	Perkin Elmer 1760	Nicolet 510	Nicolet 800	Digilab FTS-40
Cube Corner Interferometer	Yes	No	No	No	No
Modern User Interface including mouse	Yes	No	No	No	No
High Precision 96 bit FFT	Yes	No (32 Bit)	No (20 Bit)	No (20 Bit)	No (32 Bit)
Macros	Yes	?	Yes	Yes	?
Precision Scan Reference (quadrature)	Yes	Yes	No	Yes	No
Sealed Interferometer	Yes	Yes	No	No	No
19 Bit ADC	Yes	No (16 Bit)	?	No (18 Bit)	Yes
Multi-Component Quantitative Analysis	Yes	Yes	Yes	Yes	Yes
Sadtler Libraries	Yes	Yes	No	No	Yes
MS-DOS Compatibility †	Yes	Third Party	No	No	No
UNIX Compatibility †	Yes	No	No	No	Third Party
Macintosh Compatibility †	Yes	No	No	No	No
<b>Price</b>	<b>\$27,000</b>	<b>\$45,000*</b>	<b>\$30,000*</b>	<b>\$80,000*</b>	<b>\$40,000*</b>

\* Product Comparisons are based on sales information and competitive bid situations. Prices and features may vary significantly with individual negotiations. Please contact vendors directly for more specific information.

† Compatibility meaning primary spectrometer control and data acquisition without intermediate data conversions or alternate operating systems.

See for yourself the extraordinary performance of the Mattson 6020 FTIR System. Then call us for a demo. We'll have a Galaxy 6020 up and running in your lab in 5 minutes.



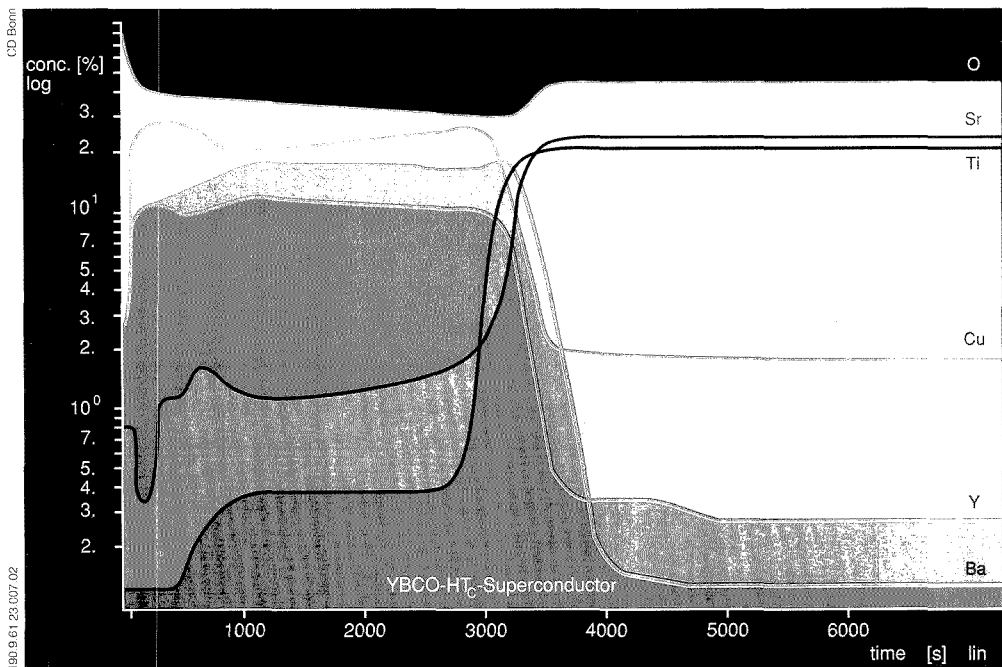
**Mattson**

Mattson Instruments, Inc.  
1001 Fourier Drive  
Madison, WI 53717 U.S.A.  
Tel. (608) 831-5515  
Fax: (608) 831-2093

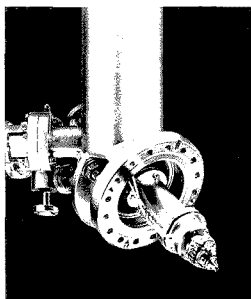
Mattson Instruments, Ltd.  
Green Farm Road  
Newport Pagnell  
Bucks MK16 0AL  
England  
Tel: (44) 908 211414  
Fax: (44) 908 618292  
Telex: 82304 FORUM G

CIRCLE 98 ON READER SERVICE CARD

# REVEALING THE TRUE CHARACTER...



## Sputtered Neutrals Mass Spectrometry (SNMS) – a New Method for Quantitative Depth-Profile Analysis



Homogeneity and chemical composition of different layers determine the quality of the new high-temperature superconductors. Accurate quantification of each individual layer is crucial. One by one, atomic layers are stripped away by ion bombardment. The resultant neutral particles can then be analyzed by the SSM 200 detection system.

Only now is the true character revealed!

In other words, the depth profile. Quantitatively!

All made possible by the SSM 200, whose modular construction can be adapted to both Leybold surface analysis or any other UHV system.

Interested? Call: PA (412) 327-5700

- LEYBOLD VACUUM PRODUCTS INC.  
LAS GROUP  
5700 Mellon Road, Export, PA 15632
- LEYBOLD AG  
Bonner Strasse 498, D-5000 Cologne 51



*Innovative Vacuum Technology*

CIRCLE 92 ON READER SERVICE CARD

A Degussa Company

# Evaluation and Practical Implications of Linearity

Craig A. Dorschel, Juris L.  
Ekmanis, James E. Oberholtzer,  
F. Vincent Warren, Jr., and  
Brian A. Bidlingmeyer

Waters Chromatography Division of  
Millipore Corporation  
34 Maple Street  
Milford, MA 01751

For accurate quantitation in LC, testing for detector linearity is of paramount importance. The relationship between the output signal of the detector and the concentration of the sample in the detector must be defined, and the characteristics of the detector response must be understood.

Scientists expect the LC detector to give a response that is linear to concentration, and conventional calibration procedures often emphasize the fitting of straight lines to calibration data. It is easy to overlook the fact that modern LC detectors may be nonlinear or that system contributions may cause the detector response to become nonlinear. Neither situation is in itself a problem; however, failure to take note of nonlinearity or to use an appropriate method of data reduction can lead to serious inaccuracies in quantitative determinations.

This article will examine the definition of linearity, describe procedures by which the linearity of a detector may

be evaluated, illustrate the practical implications of assumed linearity, and discuss appropriate ways of handling signals from nonlinear detectors so that quantitative analyses can be achieved. The procedures are then applied to two specific cases. The first example will be for the UV-vis photometric detector, the most popular detector for LC. Another commonly used detector, the differential refractive index detector, requires some special considerations that are described as part of the second example. Other LC detectors (e.g., fluorescence, electrochemical, conductivity) will not be discussed but can be evaluated according to the general procedures described here.

## Definition of linear range and dynamic range

The terms linear range and dynamic range are widely used in descriptions of

linear range and dynamic range apply to two distinct concepts (1-5). In casual use, the two terms are often combined or used interchangeably. This can lead to considerable confusion. For example, one author, while stressing that the terms are not synonymous, refers to "dynamic range" and "linear dynamic range" (6). The latter term, if viewed alone, can blur the distinction between the concepts, and the simpler phrase linear range is preferable.

The dynamic range of an LC detector is usually much broader than the linear range. It is defined by ASTM (1) as "that range of concentrations of the

## INSTRUMENTATION

detector performance. A clear understanding of these two terms is a necessity for the discussion that follows. This article follows usage adopted by the American Society for Testing and Materials (ASTM), in which the terms

test substance, over which a change in concentration produces a change in detector signal." (Note that the dynamic range may encompass both linear and nonlinear response behaviors.) The lower limit of the dynamic range is de-

American Chemical Society Announces

# Practical HPLC Method Development

Friday-Saturday  
October 13-14, 1989  
Chicago, Illinois

*A comprehensive Short Course that will teach you strategies, techniques, and methods guaranteed to minimize your time and effort without compromising the goals of method development.*

#### Here's How You'll Benefit:

- Learn when and how to use a particular HPLC method
- Review the simplest techniques for optimizing the solvent in the separation
- Learn the specifications for a good column and how to troubleshoot column problems
- Examine specific monographs for estimating the strength of a different solvent from the known strength of an initial solvent
- Submit actual separations problems of general interest for discussion and solution
- AND MUCH MORE!

**Instructors:** J.J. Kirkland and Lloyd R. Snyder

For more information CALL COLLECT (202) 872-4508, ext 1013. Or, use the coupon below to request a free descriptive brochure on this dynamic course.

American Chemical Society  
Dept. of Continuing Education  
Meeting Code PHM89100  
1155 Sixteenth Street, N.W.  
Washington, DC 20036

Please send me a free brochure on the ACS Short Course, *Practical HPLC Method Development* (PHMD8910), to be held October 13-14, 1989, in Chicago, Illinois

Name \_\_\_\_\_  
Title \_\_\_\_\_  
Organization \_\_\_\_\_  
Address \_\_\_\_\_  
City, State, Zip \_\_\_\_\_

PHM89100

## INSTRUMENTATION

defined as the concentration producing a detector output signal equal to a specified multiple of the detector's short-term noise level (usually 2X). Short-term noise is defined (1-5) as that portion of the signal that consists of random, periodic variations in the detector signal having a frequency of 1 min<sup>-1</sup> or greater. The lower limit of the dynamic range has also been termed the "minimum detectability" (1-5). However, the focus of this article is on linearity rather than detectability, and the latter will not be discussed here in any detail. We note only that the limiting concentrations for linearity and detectability are not necessarily the same.

The upper limit of the dynamic range is the concentration at the point where the slope of the curve obtained by plotting detector response as a function of concentration becomes zero. If the response curve never flattens to zero slope, the highest measured concentration is taken as the upper limit of the dynamic range. (Under ordinary circumstances, this would represent a full-scale response at the detector's least-sensitive setting.)

Before defining the term linear range as it applies to an LC detector, it is first necessary to define a linear detector. A detector is linear when the relationship of the detector output signal to the concentration of the sample in the cell is rigorously described by a linear equation of the form

$$R = SC + R_0 \quad (1)$$

where  $R$  = detector response (signal output)

$S$  = sensitivity (or response factor)

$C$  = concentration

$R_0$  = response at zero concentration

Note that the value for  $R$  is always measured relative to the baseline detector output, either as part of the process of area or height determination for a chromatographic peak or in the measurements required for a static test.

Because, by definition, the detector response must be zero for zero concentration, the intercept,  $R_0$ , must equal zero for a linear detector. The equation then becomes

$$R = SC \quad (2)$$

The slope of the line obtained by plotting response as a function of concentration (i.e., the response curve) is the constant  $S$ . For any point on this line, the value of  $S$  is obtained by dividing response by concentration:

$$R/C = S \quad (3)$$

We therefore define a linear detector as

one for which the sensitivity (or response factor) of the detector, and therefore the slope of the response curve, has a constant value at all concentrations. In practice, the linearity of a detector can be assessed by calculating  $R/C$  over a range of concentrations and observing whether the values thus obtained are in fact constant to within some defined limit.

The linear range of a detector can now be defined as the range of concentrations over which the sensitivity ( $S$ ) is constant to within a defined tolerance. The ASTM practices for evaluating GC detectors (1-5) employ this definition and specify a tolerance of  $\pm 5\%$ . Similar definitions are likely to be included in ASTM practices for LC detectors (7).

Observed linear ranges may vary considerably among detector types, and even from unit to unit. Among commonly used chromatographic detectors, the flame ionization detector used in GC has one of the broadest linear ranges. The sensitivity ( $R/C$ ) for this detector has been reported to be constant over 6 to 7 orders of magnitude (2).

The response of many detectors can be treated according to Equations 2 and 3, at least for a limited range of concentrations. For cases in which non-linearity is found, a different mathematical approach may be required. Later we will discuss an approach that can be applied to the case of an "almost-linear" detector.

#### Experimental considerations

To properly evaluate the detector in an LC system as a component, it is useful to isolate the detector from other system components. For nondestructive, concentration-sensitive detectors such as the LC detectors discussed here, an off-line (static) test is appropriate because it allows the exact concentration of the test solution in the cell to be known at the time of measurement. With the detector disconnected from the LC system, test solutions may be introduced directly into the cell via a syringe, a pump, or another appropriate device. Measurements are then taken in a static mode (i.e., no flow through the detector cell).

Note that a static test is inappropriate for destructive detectors (e.g., electrochemical detectors), which are less commonly used in LC. In cases for which a static test is inadvisable, some workers (8) have removed the LC column and have introduced the test solutions directly into the flowing system. This approach may lead to erroneous conclusions regarding linearity unless care is taken to ensure that all system



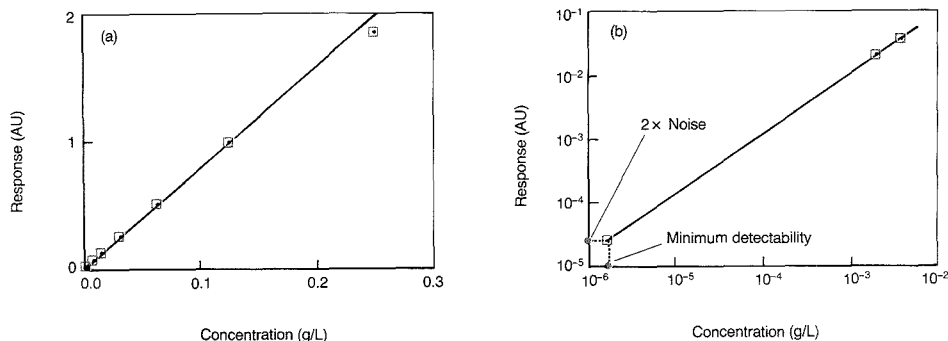


**Figure 1.** Plot of photometric (UV) detector responses at 254 nm obtained from introduction of solution of acenaphthene into the flow cell.

(a) Detector responses plotted as a function of concentration. Data point for lowest concentration omitted for clarity. (b) Enlarged plot on logarithmic axes of photometric detector data.

components (e.g., injector, pump) are operating correctly. However, for destructive detectors, use of a flowing system is the only realistic approach.

The experiment required for the measurement of the linear and dynamic ranges of a nondestructive detector is simple. Solutions of known dilutions of a standard substance having known detection properties (e.g., UV absorbance, refractive index, conductivity) are introduced into the detector cell, and the response is noted. Between test solutions, the detector cell is flushed with clean solvent until a stable baseline is achieved.

The chromatographer must be aware that the choice of test compound and detector operating parameters can affect the results of a linearity test. For instance, Pfeiffer et al. (9) note that the linearity of photometric detectors, which is adversely affected by an increase in the source slit width of the detector, is most pronounced with compounds whose spectra are changing significantly around the nominal wavelength of the detector.

The existing ASTM practice for fixed-wavelength photometric detectors (10) specifies use of a compound having a broad spectral band in the vicinity of the wavelength chosen for the test (e.g., biphenyl or uracil at 254 nm). This could be regarded as a best-case scenario. However, Pfeiffer and co-workers suggest that only rarely will a single wavelength fall at a maximum or on a broad band for each compound in a mixture. They recommend testing under worst-case scenario conditions, such as benzaldehyde at 214 and 254 nm or benzoic acid at 280 nm. The spectra of these substances are sharply

sloped at these wavelengths, and it is anticipated that a narrower linear range would be determined under these conditions relative to the conditions specified by ASTM.

It may be useful to test both the best- and worst-case conditions to obtain the most complete assessment of the detector's performance.

#### Evaluation of a photometric detector

The response curve for a single wavelength photometric detector (i.e., UV detector) operated at 254 nm was obtained from the database collected during development of the existing ASTM standard recommended practice (10, 11). As such, the source of the response data can be considered anonymous with respect to manufacturer, model number, and so forth. For this evaluation, acenaphthene was used as a test substance. Because the spectrum of acenaphthene has a broad, level valley in this wavelength region and because the detector's mercury lamp provides a narrow, intense band at this wavelength, this choice of test substance and wavelength represents the best-case scenario.

The detector response, plotted as a function of concentration in Figure 1a, appears to generate an unexceptional response curve. All data points (except the one at the highest concentration) appear to fall on or near the straight line drawn from the origin to the penultimate data point, implying detector linearity. Because Beer's law fails at high concentrations, the low response corresponding to the highest concentration is not unexpected. However, one needs to look at this situation more closely before conclusions regarding

linearity can be drawn.

We begin by determining the dynamic range of this photometric detector, based on Figure 1a. In keeping with ASTM procedures (7), the highest tested concentration (0.250 g/L) is taken as the upper limit of dynamic range because the curve in Figure 1a does not reach a plateau. The lower limit of the dynamic range (twice the short-term noise) is indicated on the enlarged plot (Figure 1b). Because the noise level is far below the detector response for the lowest measured concentration, a plot with logarithmic axes is used to illustrate the required extrapolation. A concentration of  $1.75 \times 10^{-6}$  g/L is determined to be the lower limit of the dynamic range. The dynamic range is expressed as the ratio of the upper and lower limits and is calculated to be  $1.43 \times 10^5$  in this case.

To determine the linear range for this detector, we note that the points in Figure 1a appear to indicate a linear response that trails off slightly at the highest concentration tested. In this situation, many analysts would exclude the highest concentration standard and fit a least-squares line to the remaining data. The correlation coefficient would then be examined to determine whether the use of a linear model is justified. For Figure 1a,  $r = 0.9999$  according to this approach, and most analysts would conclude that the detector is linear. However, it is well known (12) that nonlinear response curves can lead to  $r$  values of 0.9 or higher. The correlation coefficient provides a useful check on linearity, but it cannot be relied upon exclusively.

Another approach to determining the linear range is provided by ASTM

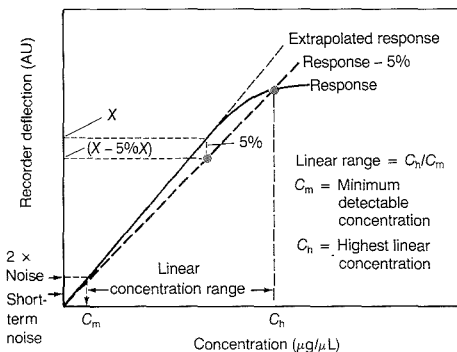


**Figure 2.** Example of plot to determine the linear range of a photometric detector.  
(Adapted with permission from ASTM Standard Practice E685 [10]. Copyright ASTM.)

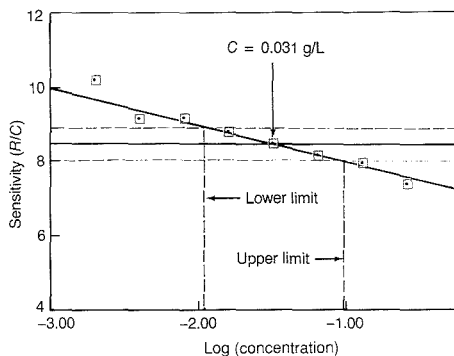


**Figure 3.** Linearity plot for photometric detector.  
The concentration region in which  $R/C$  is within 5% of the value obtained for  $C = 0.031$  g/L appears between the dashed vertical lines.

Standard Practice E685 (10-11). This practice explicitly assumes that a photometric detector will be linear throughout most of its range, becoming nonlinear at high absorbance values because of deviation from Beer's law. The points are first fitted to a smooth curve (which need not be linear) as indicated by the solid trace in Figure 2. The method then specifies that a best-fit line be drawn from the origin through the data points (upper dashed line in Figure 2). A second line having slope equal to 95% of that of the best-fit line is then constructed (lower dashed line in Figure 2). The concentration corresponding to the point where the smooth curve through the data points intersects this second line is taken as the upper limit of the linear range; the lower limit is the same as for the determination of the dynamic range. For the photometric detector, application of this procedure leads to a value of  $1.36 \times 10^5$  for the linear range.

Although the ASTM standard practice provides an approach to linearity assessment that is intuitive, it explicitly assumes the detector to be linear and therefore fails to convincingly demonstrate its linearity. In fact, the process of fitting a straight line tends to smooth the data and obscure any evidence of nonlinearity, especially for the lowest concentration standards (13).

As described earlier, the linearity of a detector is most appropriately determined by noting whether Equations 2 and 3 hold true. Following this reasoning, the linear range was previously defined as the concentration range for which  $S$  is constant to within a tolerance of  $\pm 5\%$ . We now apply this definition to the example photometric detector. For this detector, the response ide-

ally follows the Beer-Lambert law and Equation 2 becomes

$$A = \epsilon b C \quad (4)$$

where  $A$  = absorbance (detector response,  $R$ )

$\epsilon$  = extinction coefficient (a constant)

$b$  = optical pathlength (a constant)

$C$  = concentration

In terms of Equation 2,  $A = R$  and  $\epsilon b = S$ . After making these substitutions, Equation 3 becomes

$$R/C = A/C = \epsilon b = S \quad (5)$$

**The linearity plot.** It is a simple matter to divide each of the measured detector responses by the corresponding concentration and observe whether the resulting sensitivity values are constant. This can be graphically represented by a plot of sensitivity versus the logarithm of concentration. Such a plot, termed a linearity plot, is specified in the ASTM Standard Practices for several GC detectors (1-5) and in the proposed Standard Practice for differential refractive index LC detectors (7). The same plot has previously been recommended over a log-log plot for the evaluation of deviations from linearity (13).

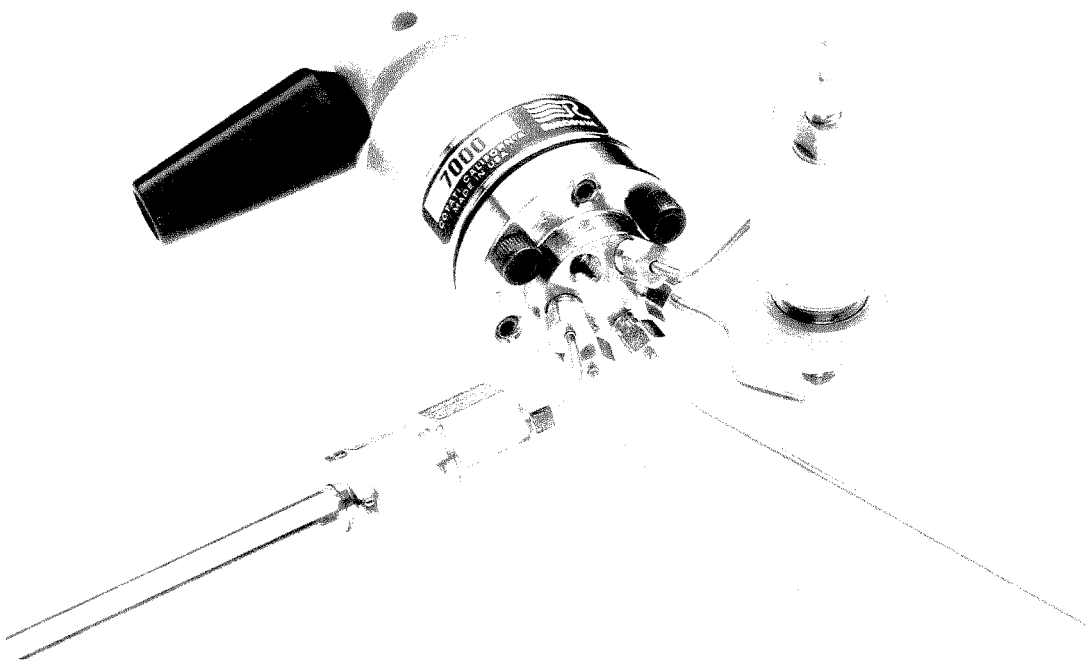
Using calculated values of sensitivity, a linearity plot was prepared for this photometric detector (Figure 3). For comparison, the response curve is presented in Figure 1a. Note that the linearity plot is a straight line sloping downward from left to right with no clearly defined horizontal region; that is, there is no region where the calculated response factor (Equation 5) is constant. The appearance of Figure 3 sug-

gests that the example photometric detector is really not linear at all according to the definitions we have given. This finding may come as a shock to some, especially given that the response curve in Figure 1a appears to be linear with the exception of the last point.

To complete the determination of the linear range, a tolerance of  $\pm 5\%$  must now be applied. Because there is no level portion of the linearity plot, the positioning of the tolerance region must be done arbitrarily. For this example, we select the 0.031 g/L standard to serve as the center of the linear range. The horizontal dashed lines in Figure 3 are constructed at 95% and 105% of the  $S$  value corresponding to the chosen standard. The linear range for the example photometric detector is the concentration range for which the linearity plot lies between the horizontal dashed lines, and this spans just under 1 decade of concentration. Note that similar values for the linear range are determined if other standards are selected as the center of the linear range.

Two treatments of the same data set have now generated strikingly different values for the linear range, ranging from  $1.36 \times 10^5$  for the ASTM Standard Practice to 9.52 for the linearity plot. The significance of this discrepancy becomes apparent only when the linear model is put into practice for the quantitation of unknown samples. The errors that may result from a mistaken assumption of linearity are discussed in the next section and lead to the conclusion that the linearity plot provides the most rigorous and useful evaluation of the suitability of a linear model for the detector response.

# GET RICH QUICK.



The quick way to enrich trace components in an LC sample is to do it on-line with a Rheodyne column switching valve.

The valve, connected after the injector, lets you concentrate the sample in a pre-column, then elute it onto the analytical column by simply turning the valve handle. You eliminate the task of collecting a batch of enriched sample outside the chromatographic system.

The valve also lets you perform

sample cleanup on-line by a similar procedure. You can remove interfering proteins, or polymers, or small molecules present in high concentrations.

Using column switching for enrichment and cleanup is usually faster than batch processing when making repeated analyses. This is especially true when switching is automated under the control of the chromatograph. Indeed, many chromatographs and autosamplers

offer automated column switching as an option, using Rheodyne valves for the purpose.

For more information phone your Rheodyne dealer. Or contact Rheodyne, Inc., P.O. Box 996, Cotati, California 94931, U.S.A. Phone (707) 664-9050.

## RHEODYNE

CIRCLE 142 ON READER SERVICE CARD

As indicated by the linearity plot, the example photometric detector is strictly linear over a narrow concentration range. However, this situation does not preclude the use of this detector for quantitative analysis over a broader concentration range if the calibration method is carefully chosen and properly applied. Even linear calibration methods will give accurate results for selected concentration ranges (see below). A point-to-point or nonlinear calibration may also be used. (One specific nonlinear calibration method is discussed in a later section on almost-linear detectors.) The important contribution of Figure 3 is to facilitate the recognition of nonlinearity. It is not the existence of nonlinearity but rather the analyst's failure to anticipate and adjust for nonlinear behavior that can lead to poor quantitation.

**Possible errors due to assumed linearity.** For the photometric detector used in our example, the foregoing discussion suggests that a nonlinear calibration will provide the best model of detector response as a function of concentration over the full dynamic range. Many chromatography data systems now allow for such calibration methods. Chromatographers, however, tend instinctively to use linear methods or are limited to linear calibration by older data systems. It is useful to examine the extent to which linear approximations may be applied to the photometric detector in question while simultaneously keeping inaccuracies to a minimum. The static test data set of Figure 1a will be used as an example in the discussion that follows.

The simplest form of linear calibration is single-point calibration, in which the calibration line is constructed between the origin and the response for a single standard. If the actual response curve is nonlinear, concentrations predicted on the basis of single-point calibration will only be correct for measured responses that fall within a narrow region centered around that of the calibration standard. The width of this region is determined by the analyst's requirement for accuracy and amounts to about 1 decade for the photometric detector in our example if a 5% tolerance is specified. Response values falling outside this range indicate a need to recalibrate at a concentration closer to that of the unknown and to reanalyze the sample.

The linearity plot of Figure 3 provides a clearer view of the problems introduced by this calibration method. The solid and dashed horizontal lines used previously to determine the linear range also enclose the range in which

the single-point calibration will yield acceptable performance, assuming that the 0.031 g/L standard is now used as the calibration point. Should the actual concentration of acenaphthene in an unknown fall within the linear range indicated in Figure 3, concentrations calculated on the basis of this single-point calibration will be within 5% of the correct value. Outside this region, errors will exceed 5% and will become increasingly large (on a percentage basis) the further the concentration is from the calibration point.

Another common linear calibration approach is the fitting of a least-squares line to several data points. A nonzero intercept is generally allowed in this approach. Use of a least-squares line fitted to all but the highest concentration standard of the present data set expands the concentration range for which acceptable quantitation can be obtained. For example, if the  $\pm 5\%$  tolerance used in the previous discussion is allowed, the concentration range giving acceptable quantitation is expanded from 1 decade to nearly 3 decades by adopting a least-squares line in place of single-point calibration.

The apparent goodness of fit over most of the dynamic range of the detector is seen in Figure 4. At first glance, the least-squares line appears to provide an excellent fit for all but the highest concentration standard. Because chromatographers are conditioned to expect their detectors to be linear, the eye is easily deceived by the appearance of Figure 4 and linearity is accepted. Closer inspection reveals that the least-squares line lies above the responses for both the highest and lowest standards, revealing the underlying curvature of the actual response plot. This lack of fit leads to substantial errors when the least-squares line is used for quantitation of unknowns having concentrations at either extreme of Figure 4. One price that must be paid for the smoothing inherent in the fitting of a least-squares line is the introduction of a nonzero  $y$  intercept value (the  $R_0$  term in Equation 1). This will result in gross errors in calculated concentrations at very low response levels. In fact, negative concentrations would be calculated for observed responses less than the  $R_0$  value (0.0099 AU in this case).

Neither single-point calibration nor a least-squares line provides an adequate model of the detector's response behavior throughout its dynamic range. Alternate mathematical treatments, now available on many chromatography data systems, can provide a much more satisfactory model. One particularly useful mathematical mod-

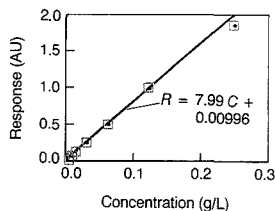


Figure 4. Least-squares calibration line for photometric detector.

el is considered in detail later in this article.

The photometric detector discussed in this section was evaluated using a static test. However, a similar linearity plot can be obtained based on peak heights or integrated peak areas in a flowing system, as will be demonstrated in the next section for a differential refractive index detector. For the specific photometric detector discussed in this section, we conclude that linearity is strictly observed over only a narrow range of concentrations. This conclusion should not be regarded as specific to photometric detectors in general or to one particular manufacturer or design type. It is our experience that many LC detectors exhibit nonlinear behavior that is overlooked by most users. For example, the next section presents evidence of nonlinear behavior in differential refractive index detectors representing different models and manufacturers.

#### Evaluation of differential refractive index detectors

The second most commonly employed detector in LC is the differential refractive index detector. Detection is based on measurement of the difference in refractive index between a solution of an analyte and the pure solvent. The solvent may itself be a mixture, provided that its composition remains fixed throughout the analysis. The response of a differential refractive index detector follows Equation 6 for analyte concentrations of  $\sim 5\%$  or less (14):

$$n - n_2 = v_1(n_1 - n_2) \quad (6)$$

where  $v_1$  = volume fraction of the analyte

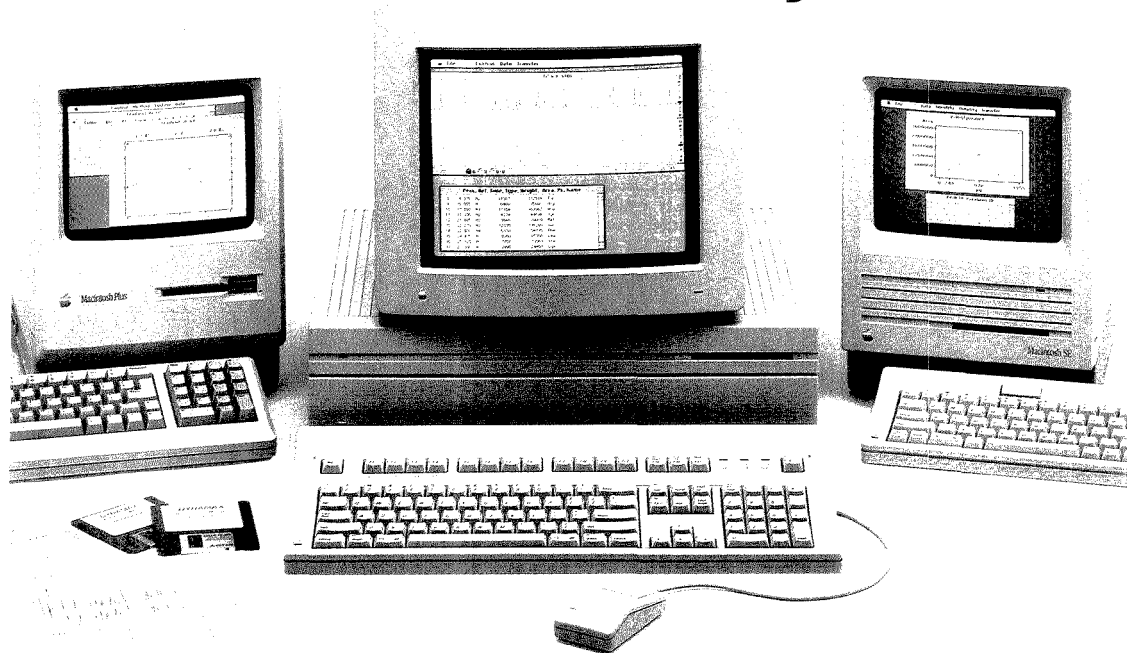
$n_1$  = refractive index of pure analyte

$n_2$  = refractive index of pure solvent (contained in a reference cell)

$n$  = refractive index of solution in sample cell

Equation 6 is in the same form as

# Now any Macintosh™ can be an HPLC data system!



**R**ainin's new Dynamax<sup>®</sup> HPLC Method Manager for the Macintosh incorporates features that significantly expand its chromatographic utility...like total Mac II compatibility...and background operation under MultiFinder<sup>™</sup> so you can do word processing or run other applications simultaneously with data collection and analysis.

Dynamax Method Manager is incredibly easy to use. The Macintosh user interface eliminates complex menu trees. Needed functions are always available, just a mouse click away.

Rainin software and hardware let the Mac<sup>®</sup> acquire data and display the chromatogram on the high-resolution screen. The program locates peaks, identifies analytes, calculates amounts and concentrations, and, uniquely, displays all this information on-the-fly, while data is being collected. No waiting to see results!

After each analysis, the computer prints the chromatogram and report. Complete copies of raw data and method specifications, as well as reported values, can be saved automatically on any Macintosh-compatible storage device.

Dynamax HPLC Method Manager can recall chromatographic data again and again for reprocessing with different integration parameters. Fine tuning processing conditions is easy! Optimum conditions can be saved for later use in real-time analyses.

Automatic calculation of correlation coefficients, peak asymmetries, and efficiencies simplifies quality control of chromatographic methods. A new desk accessory, ChromPic<sup>™</sup>, converts any chromatogram to a PICT-file object for incorporation into graphic and word-processing documents. Report files are compatible with Microsoft Excel and other spreadsheet programs. Contact-closure inputs and outputs facilitate use with automated systems. The list goes on!

As a gradient controller, Dynamax HPLC Method Manager works with any Rainin or Gilson HPLC system. There are no hardware modifications to the Mac, just one convenient connection to the modern port.

If you're getting ready to purchase a complete HPLC system, or just an HPLC data system, let Rainin show you how easy HPLC can be with a Macintosh. Call **800-FOR-HPLC** for a free consultation. (In Massachusetts, call 617-935-3050). Or write:

**RAININ**  
INSTRUMENT CO., INC

Mack Road, Woburn, MA 01801  
617-935-3050  
1715 64th Street, Emeryville, CA 94608  
415-654-9142

\*Macintosh-Plus, Macintosh-SE, or Macintosh II.  
"Dynamax" and "ChromPic" are trademarks of Rainin Instrument Co., Inc.

™Macintosh™, "Mac", and "MultiFinder" are trademarks of Apple Computer, Inc.

© 1988 Rainin Instrument Co., Inc., Mack Road, Woburn, MA 01801

CIRCLE 140 ON READER SERVICE CARD

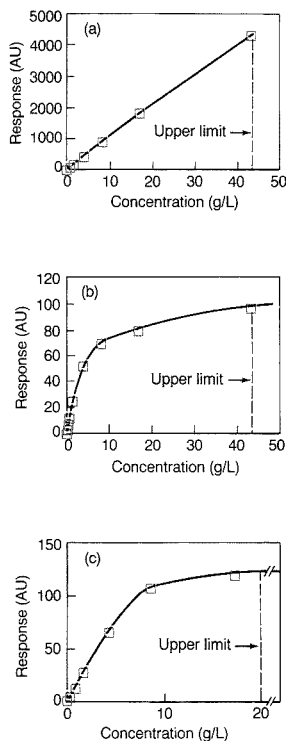


**Figure 5.** Response curves for three differential refractive index detectors. (a) Detector A, (b) Detector B, and (c) Detector C.

Equation 2 ( $R = SC$ ). The refractive index difference,  $n - n_2$ , is the observed detector response ( $R$ ). The volume fraction corresponds to the concentration variable ( $C$ ), and the difference in the refractive indices of pure analyte and solvent corresponds to the sensitivity constant ( $S$ ).

A full method for the evaluation of differential refractive index detectors is not currently available in the literature. Glycerol-water solutions have been used as calibration standards in conjunction with log-log plots of response versus concentration data to estimate linear range (15). For example, a solution of 0.871 g of glycerol in 1 L of water has a refractive index  $10^{-4}$  RIU greater than that of water. Because a log-log plot establishes linearity only if its slope is unity, the existing literature approach was not considered suitable as a general approach to linearity evaluation.

A proposal entitled "Standard Recommended Practice for Refractive Index Detectors Used in Liquid Chromatography" has recently been completed and submitted to the ASTM Committee E19 on Chromatography (7). This proposal incorporates as standards the glycerol-water solutions recommended previously because of the stability of these solutions at room temperature. The standards are used to obtain detector responses, which in turn are used to prepare response curves and linearity plots.

The response curves (Figure 5) and linearity plots (Figure 6) for three commercially available differential refractive index detectors were determined as part of the development of the proposed ASTM Standard Practice (7).

In Figure 5, the three detectors appear at first glance to differ drastically in their linear range. However, the linearity plots of Figure 6 reveal that each of the detectors has a bona fide linear range, spanning 2 or 3 decades. This is much narrower than might be expected on the basis of Figure 5 but is clearly indicated by the linearity plots of Figure 6. Detectors B and C show severe nonlinearity at high concentrations. Detector A, conversely, shows nonlinearity primarily at the lowest concentrations tested, with a trend to increasing values of sensitivity ( $R/C$ ) as concentration is reduced. The overall appearance of Figure 6a is similar to that observed for the photometric detector and will be examined further below.

#### Special considerations when testing differential refractive index detectors

An important difference between the evaluation of differential refractive index detectors and photometric detectors arises from the fact that differential refractive index detectors measure a bulk property of a solution rather than a molecular property of the analyte. The response is therefore influenced by any factor that affects the refractive index of either the sample solution or the reference solvent.

The refractive index of a solution is strongly dependent on changes in solution density, which in turn is dependent on temperature and pressure. In commercial detectors, the temperature at the sample and reference cells is held constant by heat sinks or constant-temperature ovens, thus minimizing this potentially serious problem. Under the static conditions used in the ASTM proposal, there is no possibility of pressure fluctuations from a solvent delivery system affecting the measurements. Atmospheric pressure changes during the course of a measurement

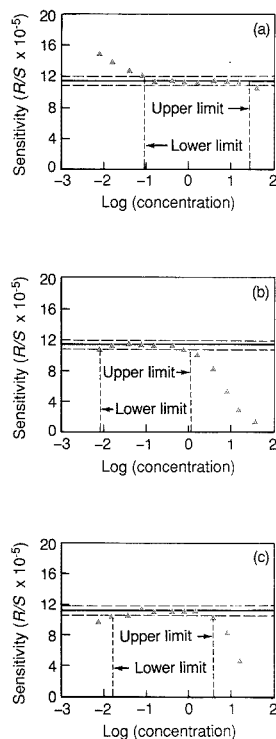


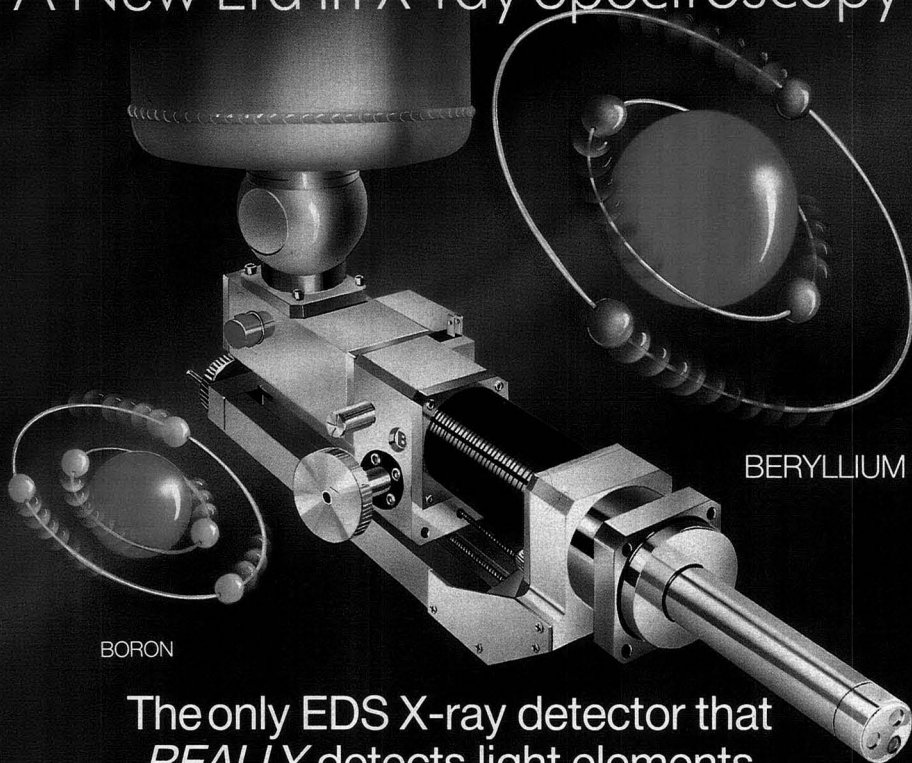
**Figure 6.** Linearity plots for three differential refractive index detectors. (a) Detector A, (b) Detector B, and (c) Detector C.

should also not be a factor.

The most difficult problem to control is that caused by changes in the amounts of dissolved atmospheric gases in the test solutions vis-à-vis the reference solvent (which is normally isolated in a closed reference cell). The refractive index of fully degassed water is greater than the refractive index of water saturated with air at room temperature by  $1.5 \times 10^{-6}$  RIU. As little as 1% of this difference is equivalent to the noise level of many contemporary refractive index detectors, which is on the order of  $10^{-8}$  RIU or less. In practice, it is difficult to maintain fully degassed solvent (and test solutions). Therefore, relatively small changes in the concentration of dissolved gases present in each test solution will lead to substantial baseline disturbances or drift, especially at the most sensitive detector settings.

To assure a stable dissolved air concentration, it is preferable to used air-

# A New Era in X-ray Spectroscopy



BORON

BERYLLIUM

## The only EDS X-ray detector that *REALLY* detects light elements **LZ4** from Link Analytical

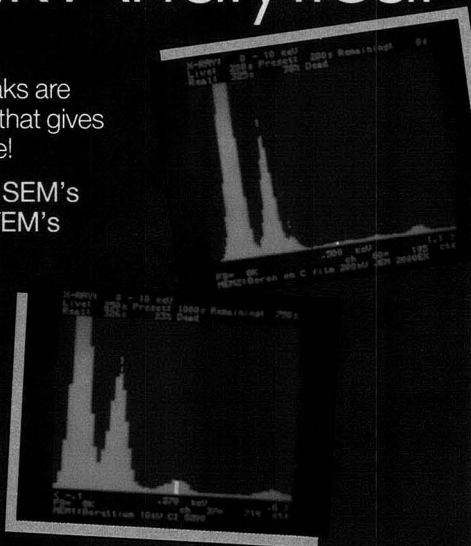
While advertisements showing boron peaks are commonplace, it is *ONLY* Link Analytical that gives an unequivocal guarantee of performance!

We guarantee Beryllium detection on SEM's  
We guarantee Boron detection on TEM's

With detectors specified at better than 133eV resolution *NO* other manufacturer even approaches our quality.

The *NEW* LZ4 detectors for SEM's and the field proven LZ5 detectors for TEM's.

For the analyst who is *REALLY* serious about light element detection.



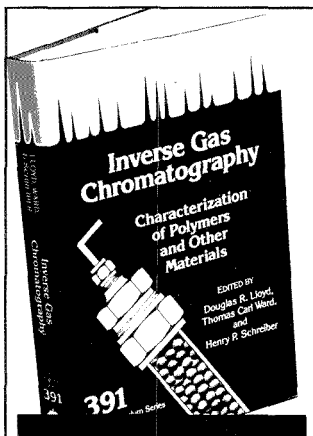
ANALYTICAL EXCELLENCE

ANALYTICAL EXCELLENCE

**Link**  
ANALYTICAL

Link Analytical Inc.  
Old Saw Trails Park,  
8017 Excelsior Drive,  
Madison,  
Wisconsin 53717 USA  
Tel: (608) 836-3200  
Fax: (608) 836-3377

Link Analytical Limited,  
Halifax Road, High Wycombe,  
Bucks HP12 3SE  
England  
Tel: 0494 442255  
Telex: 837542LNKHWG  
Fax: 0494 24129



## Inverse Gas Chromatography

### Characterization of Polymers and Other Materials

**N**o other single reference covers this relatively new subject area so completely! As an extension of conventional gas chromatography, inverse gas chromatography (IGC) has many advantages—simplicity, speed of data collection, accuracy, and low operating costs.

This one volume offers an in-depth look into the most recent advances in theoretical and practical aspects of this approach. Twenty-two chapters provide information on:

- instrumentation and methodology
- characterization of vapor-polymer systems
- polymer-polymer systems
- surfaces and interfaces
- analytical applications
- application of IGC in coal characterization and food science

This valuable title discusses the application of IGC to the thermodynamic and acid-base interaction of components in polymer systems, and the technological advances in the field.

Douglas R. Lloyd, *Editor*, University of Texas  
Thomas Carl Ward, *Editor*, Virginia Polytechnic Institute and State University

Henry P. Schreiber, *Editor*, Ecole Polytechnique

Clara C. Pizana, *Assistant Editor*

Developed from a symposium sponsored by the Division of Polymeric Materials: Science and Engineering of the American Chemical Society and the Macromolecular Science & Engineering Division of the Chemical Institute of Canada

ACS Symposium Series No. 391  
327 pages (1989) Clothbound  
ISBN 0-8412-1610-X LC 89-6628  
US & Canada \$69.95 Export \$83.95

O • R • D • E • R   F • R • O • M

American Chemical Society  
Distribution Office, Dept. 22  
1155 Sixteenth St., N.W.  
Washington, DC 20036

or CALL TOLL FREE

# 800-227-5558

(in Washington, D.C. 872-4363) and use your credit card!

## INSTRUMENTATION

saturated water to prepare the test and reference solutions, as these solutions will be in equilibrium with the atmospheric gases (14). Even with this precaution, small changes in ambient temperature could affect the dissolved gas concentration enough to seriously perturb measurements of the very dilute test solutions required to give responses approaching the noise level. Accordingly, the proposed ASTM Recommended Practice specifies a glycerol-water solution with an expected refractive index differential of  $10^{-6}$  RIU as the most dilute test solution. Unfortunately, in the case of Detectors A and C this results in a need for extrapolation to find the lower limit of dynamic range. Because linearity cannot be assumed without proof, the required extrapolation may set an incorrect lower limit for the linear range of highly sensitive detectors capable of measuring refractive index differences well below  $10^{-6}$  RIU.

### On-line testing of detectors

The static test recommended by the ASTM (7, 10) has the advantage of isolating the tested component (i.e., detector) from the remainder of the chromatographic system. However, an on-line (dynamic) test offers several improvements over the static test in the case of the differential refractive index detector. First, the on-line test is easier to perform, although it does require careful attention to the proper performance of all system components. In addition, an on-line test allows testing of the detector down to its lowest response levels, because dissolved atmospheric gases (or other interfering

components) can be chromatographically resolved from the test solute. The limits imposed by dissolved gases (and other solutes) in the test solutions indicate the need for on-line testing of the differential refractive index detectors considered here.

Although liquid chromatographers rarely regard dissolved atmospheric gases as analytes to be separated, these sample components can in fact be retained under typical chromatographic conditions, as Figure 7 indicates. The separation of dissolved gases is also commonly observed in gel permeation chromatography, where certain "artifact peaks" that elute after the inclusion volume result from dissolved gases. Thus, an on-line LC test enables the assignment of responses to dilute standards without interference from dissolved gases. In this way, extrapolation can be avoided and the detector can be more adequately characterized over its full dynamic range.

On-line testing is carried out by making injections of a series of dilutions of a test substance. The trade-off for the ability to evaluate the full range of detector responses is the possibility that the observed response may be influenced by a system component other than the detector. All system components must be working to specification in order to ensure that conclusions regarding linearity are attributed correctly to the detector.

For on-line testing, the dynamic and linear ranges are determined by treating peak height or peak area data in the manner described for the static test. With proper choice of column and mobile phase, some of the problems en-

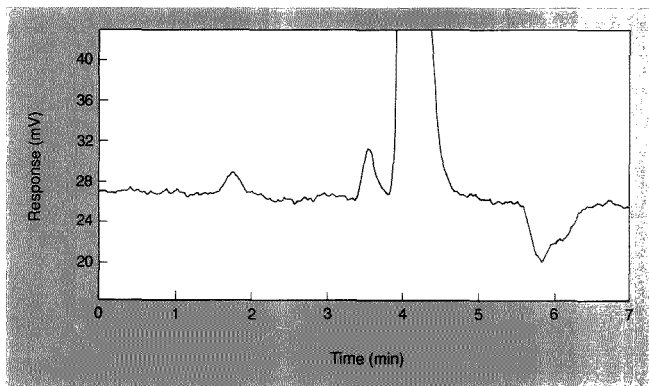


Figure 7. Chromatogram of glycerol and atmospheric gases.

Waters Fast Fruit Juice column:  $7.8 \times 150$  mm; column temperature:  $50^\circ\text{C}$ ; Injection volume:  $20 \mu\text{L}$ ; mobile phase: water, maintained at  $70^\circ\text{C}$ , at  $1.0 \text{ mL/min}$ . Peaks: glycerol (4.2 min) and atmospheric gases (5.90 and 6.15 min). (Column and solvent temperatures selected to emphasize the response for dissolved gases.)

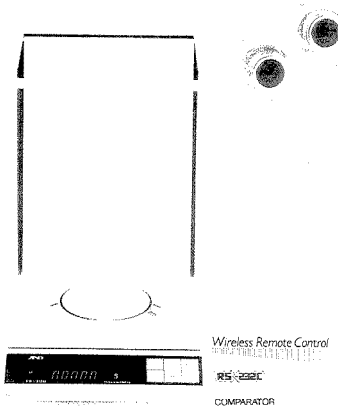




# Ultra-Precise Analytical Tare, Serial, Comparator, Multi-Function Analytical Balances

**Another first from A&D — Analytical precision balances with multi weighing units, multi-functions and optional wireless remote control.**

By using the latest electronic technology combined with easy-to-use multi-function features and extensive ergonomic design — the FR series will revolutionize the ways you can use an analytical balance. Multi weighing units; Comparator mode; Percentage add/subtract mode; Counting mode; Environmental conditions adjustment (including last-digit blanking during course weighing); Auto power ON; — and much, much more.



Start with an optional wireless remote control that simplifies and expands operation of every feature the balance has available — then, enjoy the rest of the full range of options available for the FR Series.

Start with an optional wireless remote control that simplifies and expands operation of every feature the balance has available — then, enjoy the rest of the full range of options available for the FR Series.



## A&D

**A&D ENGINEERING, INC.**

1555 McCandless Drive, Milpitas, CA 95035  
 Fax (408) 263-0119 Telephone (408) 263-0119

**EAST COAST BRANCH OFFICE**  
 2165-A West Park Court, Stone Mountain, GA 30087  
 (800) 426-4480 In Georgia (404) 498-9732  
 Fax (404) 498-4877

CIRCLE 3 ON READER SERVICE CARD

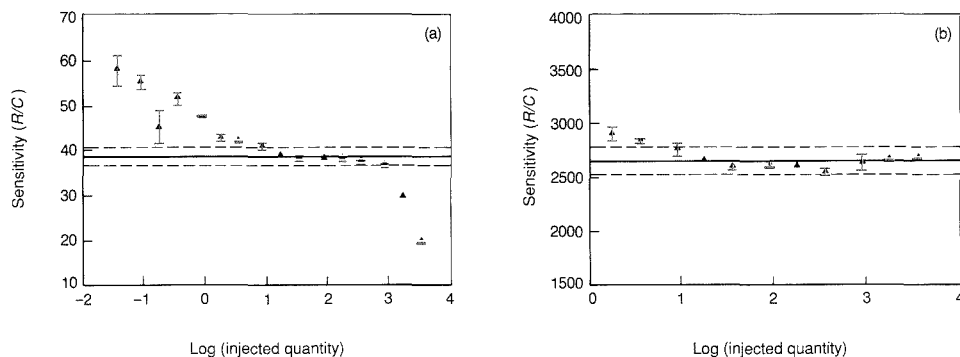


**Figure 8.** Linearity plot for on-line test of differential refractive index Detector D. (a) Peak heights and (b) peak areas.

countered in off-line testing may be obviated. In the case of refractive index detectors, the dissolved atmospheric gases in the sample solution can be made to elute separately from the standard peak(s).

The selection of column, eluent, and solvent for the on-line test should ideally reflect the analysis for which the test detector will be used. For example, if the differential refractometer is most often used for polymer analysis, the on-line test might involve GPC columns, THF eluent, and polystyrene standards. For purposes of this article, the analysis of glycerol was selected to allow the greatest possible consistency with the off-line ASTM test results.

Peak height measurements were obtained for a series of aqueous solutions of glycerol that encompassed those used in the off-line (static) test. Detector D was used in an LC system that included a Waters Fast Fruit Juice column and water as eluent. The linearity plot prepared from this data set is shown in Figure 8a. Note that this figure includes concentrations that correspond to detector responses below the limit of testing for Figure 6 because the LC column separates the atmospheric gases from the glycerol peak.

Inspection of Figure 8a reveals three regions of different behavior: nonlinear regions at the highest and lowest concentrations and a region of linearity at intermediate concentrations. The horizontal portion of the linearity plot spans approximately 2 decades of concentration. Inspection of the chromatograms from which Figure 8a was derived indicated peak broadening for the highest injected quantities. This suggested that column overload might be responsible for the drop in response

factor based on peak heights for the most concentrated standards. To test this, peak areas were determined for the chromatograms corresponding to the top 11 standards in Figure 8a. The resulting linearity plot (Figure 8b) shows 3 decades of linearity for Detector D when peak areas are used, an improvement of 1 decade. This provides a good example of a system contribution to nonlinearity that should not be attributed to the detector.

Also shown in Figures 8a and 8b are the  $\pm 1\sigma$  range for each measurement, centered about the mean of the four individual measurements taken for each standard. Relative standard deviation (RSD) is  $\pm 4\%$  or better across the entire test range for peak heights. For peak areas, precision is better than  $\pm 3\%$  down to the lower limit of the linear range. (Note that the chromatograms obtained for the lowest four standards represent a signal-to-noise ratio of 13 or less. Heights and areas derived from these chromatograms were useful for detector evaluation but would probably not be used for routine quantitation.)

#### The "almost-linear" detector in LC

The preceding discussions of linearity for the two most widely used LC detector types imply that such detectors may be nonlinear in response through a portion of their dynamic range. Depending on the specific detector, a strict linear model can be applied successfully over a 1–3 decade concentration range. If it is necessary to use the detector outside the linear image, more accurate predictions of the concentration corresponding to a given detector response will be obtained when nonlinear functions are used as mathematical

models. Fowles and Scott (16) have devised a mathematical treatment to describe a detector whose response curve displays a small degree of curvature throughout the dynamic range, which has been termed an "almost-linear" detector (6). For this detector, Fowles and Scott suggest that Equation 2 be modified by inclusion of an exponential term as follows:

$$R = S^*C^x \quad (7)$$

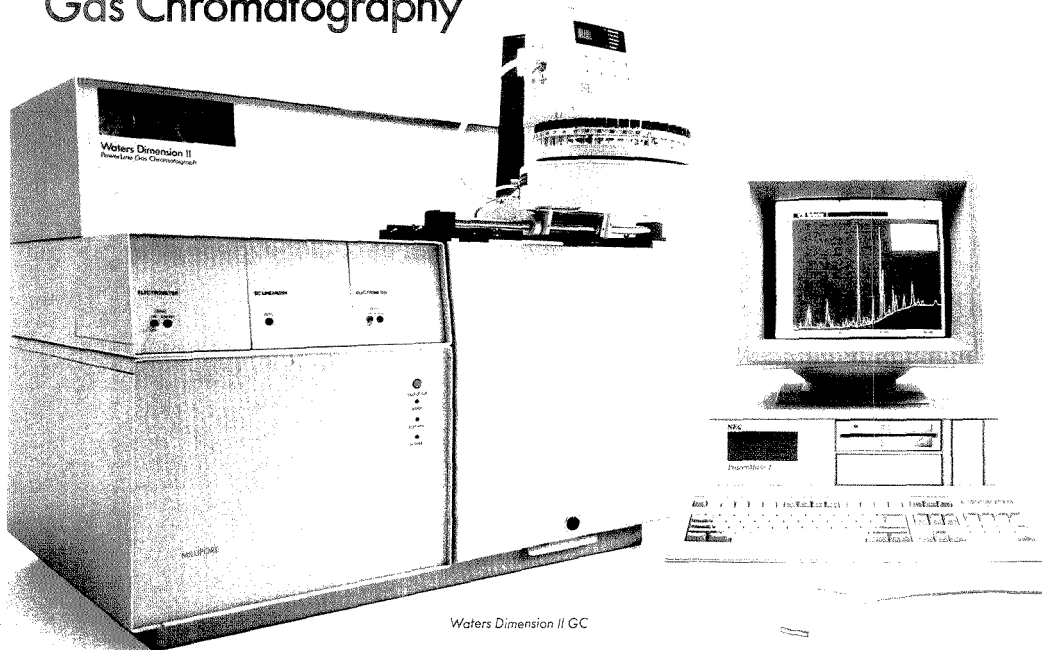
where  $R$  and  $C$  are detector response and concentration as above and  $S^*$  is a constant corresponding to the apparent detector sensitivity at a concentration of 1. The exponent  $x$  (termed the response index by Scott [6]) need not be an integer.

When the response index  $x$  is exactly equal to 1, Equation 7 reduces to Equation 2, and the detector is linear. As the value of  $x$  becomes either progressively greater than or less than 1, the curvature of the response curve increases. It is useful to know the numeric value of  $x$ , which can be determined from a log-log plot of the response data. Taking the logarithm of both sides of Equation 7, we obtain

$$\log(R) = x[\log(C)] + \log(S^*) \quad (8)$$

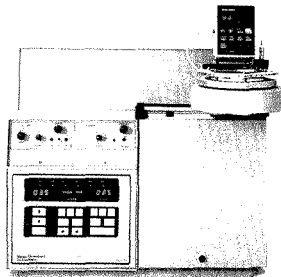
A plot of the log of detector response as a function of the log of concentration will give a straight line with slope  $x$  for detectors having response curves corresponding to Equation 7. Note that a straight line log-log plot implies actual linearity if, and only if, the slope,  $x$ , of the log-log plot is equal to 1. Fowles and Scott claim that detectors having a response index between 0.98 and 1.02 can be treated as linear for most practical purposes (6). The fact that the response behavior of a detector follows

# Waters Adds a New Dimension to Gas Chromatography



Waters Dimension II GC

## Waters Dimension GC Series Takes You Beyond Conventional Performance.



Waters Dimension I GC

**Integrated diagnostics.** Built-in ability to monitor fuel, oxidant, and detector gases saves precious time.

**Increased productivity.** Direct autosampler transfer between independently heated injectors increases throughput.

**Mouse driven software.** Advanced multi-tasking Maxima™ software provides easy mouse driven operation and PowerLine™ system control of either LC or GC systems.

**Convenient column accessibility.** A large dual column oven with independent side-by-side access lets you change columns swiftly.



**Detection versatility.** A complete line of high performance GC detectors provides unmatched versatility. Choose from flame ionization, flame photometric, Ni63 electron capture, electrolytic conductivity, photoionization, nitrogen/phosphorous, discharge ionization and thermal conductivity detection.

**Unique sample cleanup.** Waters MilliLab Workstation couples automated sample cleanup and preparation with GC analytical power. Automate a wide variety of repetitive tasks while feeding autosampler carousels completely unattended.



Only a Waters Dimension I or II GC System can give you all of these performance options, plus the industry's most reputable support program.

Call 1-800-456-WDGC for the Waters representative in your area.

Division of MILLIPORE

Equation 7 rather than Equation 2 can be easily diagnosed from the linearity plot. By dividing both sides of Equation 7 by  $C$ , we obtain Equation 9:

$$R/C = S^* C^{(x-1)} \quad (9)$$

Here  $R/C$  is not a constant but is dependent on concentration (except when  $x = 1$ ). A linearity plot will not be horizontal in this case; a different value of  $R/C$  will be seen for each concentration.

Figure 9 shows linearity plots calculated according to Equation 9 for several values of  $x$ . All of the curves in the figure show a slight concave-up curvature, which becomes more pronounced as the  $x$  value departs from 1. When  $x$  is less than 1, the data points lie on a downward-sloping curve; when  $x$  is greater than 1, the values of  $R/C$  increase with concentration. When the linearity plot of a detector has the general appearance of one of the curves in Figure 9, a log-log plot following Equation 8 should be prepared. If the data points of this log-log plot rigorously fall on a straight line, it may be safely assumed that the response of the detector is described by Equation 7. Values of  $x$  and  $S^*$  are then determined from

the log-log plot, and a nonlinear relationship is prepared.

**Photometric detector.** The linearity plot prepared for the photometric detector in our example (Figure 3) suggests that the response behavior of the tested photometer will follow Equation 7 more closely than Equation 2 and that the value of  $x$  will be less than 1.0. A log-log plot was therefore prepared for this detector. As expected from the appearance of the linearity plot, the log-log data fit a straight line with a high degree of confidence. Linear regression analysis gave a slope of 0.944 for the log-log plot, which is thus the value of the response index  $x$ . A value of 7.00 was determined for  $S^*$ .

After substituting these values into Equation 7, we obtain

$$R = 7.00 C^{0.944} \quad (10)$$

The fit between this nonlinear model and the actual response curve (Figure 1a) can be judged by comparing calculated  $R$  values with actual measurements for each standard. When this is done, an agreement to within 5% of the observed response is observed at each concentration. By comparison, a fitted least-squares line led to predicted re-

sponses that differed by as much as 29% from measured values. This clearly demonstrates the value of using a tool such as the linearity plot to reveal the need for a nonlinear model.

**Differential refractive index detector.** Detector D provides a second example of an almost-linear detector. When peak heights from on-line testing are used, the linearity plot for this detector (Figure 8) has a more complex shape than that of the photometric detector, and it is not initially clear whether Equation 7 can be applied. Note, however, that the curves in Figure 9 for  $x < 1$  resemble Figure 8a over much of the concentration range.

Previous discussions of Detector D indicated that a linear model can be used over a range of about 2 decades for peak height (3 decades for peak area), giving agreement of 5% or better between calculated and measured responses for the standard solutions. Application of Equation 7 might expand the range that can be accurately modelled, perhaps allowing the use of a greater portion of the detector's dynamic range.

Following the same procedure as for the photometric detector, values of  $x$  and  $S^*$  for Equation 7 were determined from a log-log plot prepared from the peak-height data for Detector D. The resulting model was used to calculate a peak-height response corresponding to each standard; the predictions were generally within 15% of the actual response, except for the highest amount injected. The calculated response for this standard was 44% above the actual values. Thus the full 5.3-decade range of tested concentrations cannot be adequately fit by Equation 7. However, removing the two highest standards improved the overall fit dramatically. For this 4.7-decade range of concentrations, predicted peak heights agree to within 8% for all but one standard (the third-lowest standard, which appears to be an outlier). The average deviation for all of the standards is 4.8%.

The 4.7-decade range of concentrations that can be treated by the almost-linear model is contrasted with the 2-decade range for peak heights (3 decades for peak area) over which Equation 2 applies. The use of a least-squares line to model the response of Detector D fails to provide a solution, leading to errors as large as 4682% within the same 4.7-decade range.

As with the photometric detector, the linearity plot provides the essential diagnosis of nonlinear behavior for the differential refractive index detector. The choice of action is then left to the analyst. In this article, we have proposed either that a linear model be ap-

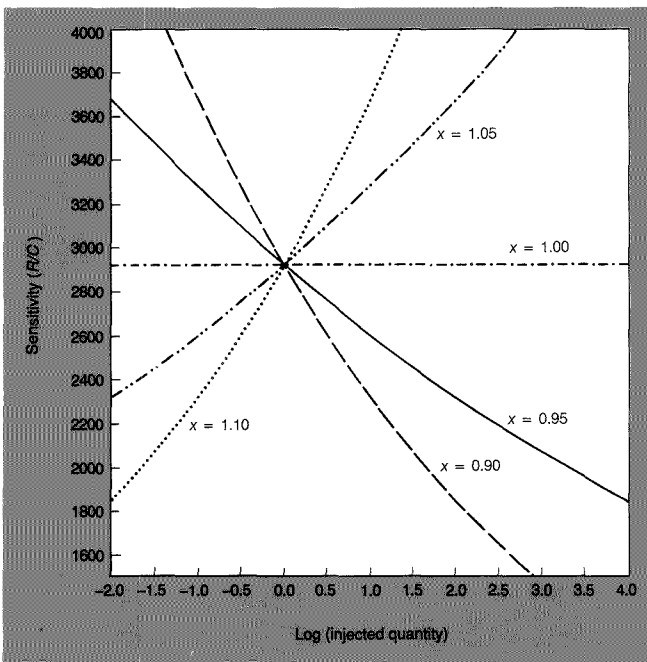
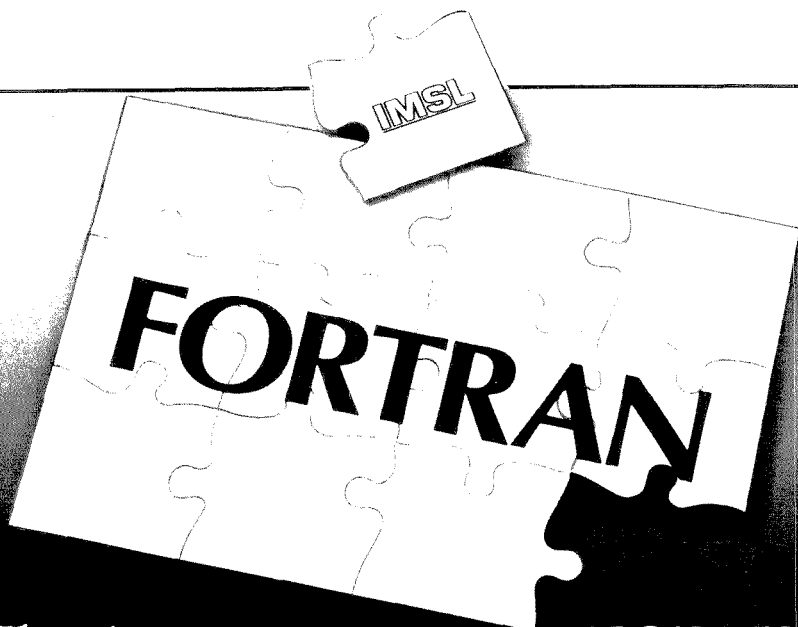


**Figure 9.** Hypothetical linearity plots for a detector conforming to Equation 7, using value of  $S^*$  determined for Detector D.



# What's missing in your FORTRAN problem-solving environment...

## ...IMSL's Mathematical and Statistical Libraries

If you rely on FORTRAN as a problem-solving tool, you recognize the value of the small library of intrinsic functions that came with your FORTRAN compiler. You wouldn't think of coding a routine for a square root, sine, or cosine; you simply call it from the intrinsic function library. But what about the many other standard, more complex mathematical and statistical capabilities you so often need?

What's missing from FORTRAN is a complete, comprehensive library of mathematical and statistical routines...The IMSL Libraries.

IMSL's MATH/LIBRARY, SFUN/LIBRARY, and STAT/LIBRARY comprise more than 800 FORTRAN subroutines covering a broad range of mathematics and statistics. Linear and non-linear systems, differential equations, eigensystems, regression, correlation, and special functions are just a few of the capabilities that can be literally at your fingertips with IMSL's FORTRAN subroutine Libraries.

And that's just part of the story...combined with online documentation and the high-level FORTRAN-like procedures of MATH/PROTRAN and STAT/PROTRAN, IMSL provides the comprehensive mathematical and statistical tools that are missing in your FORTRAN program development.

When you call an IMSL subroutine, you're calling on expert design and development, rigorous testing, and proven reliability demonstrated by hundreds of thousands of hours of use by IMSL customers around the world. To IMSL users this means shorter development time, more robust solutions, and lower costs.

For almost 20 years, IMSL customers in industry, government, research, and education have chosen our high-quality, high-

value FORTRAN Libraries. We'd like to talk to you about how the IMSL Libraries can enhance your FORTRAN application development environment. We have what's missing, contact us today: toll-free 1-800-222-IMSL, or in Texas (713) 782-6060; 2500 ParkWest Tower One, 2500 CityWest Blvd., Houston, TX 77042-3020; FAX: (713) 782-6069.

My interest is in software for:

- Mathematics       Statistics  
 Special Mathematical Functions       Online Documentation

Name \_\_\_\_\_ Title \_\_\_\_\_

Organization \_\_\_\_\_

Department \_\_\_\_\_

Address \_\_\_\_\_

City/State/Country \_\_\_\_\_ Postal Code \_\_\_\_\_

(Area Code) Phone \_\_\_\_\_ Telex or Fax \_\_\_\_\_

Computer Type \_\_\_\_\_ Operating System \_\_\_\_\_

My need for purchasing IMSL software is:

\_\_\_\_ Immediate    \_\_\_\_ 3 Months    \_\_\_\_ 6 Months    \_\_\_\_ 1 Year

IMSL Inc.,  
 Marketing Services Division,  
 2500 CityWest Boulevard,  
 Houston, Texas 77042-3020.

1-800-222-IMSL  
 AC 8909

**IMSL**®  
 We make FORTRAN more useful

CIRCLE 74 ON READER SERVICE CARD

plied over a restricted concentration range or that a nonlinear model be applied over a broader range. Modern data systems permit many additional options that are not addressed here, including logarithmic, polynomial, and point-to-point models. It is not the purpose of this discussion to endorse any one model but rather to emphasize the need for the careful testing of linearity with a tool such as the linearity plot.

**Conclusions**

LC detectors are generally rugged and reliable devices; nonetheless, they may not exhibit linear behavior under all operating conditions. Nonlinearity may be subtle. The usual linear plot of response versus concentration may look good at first glance, but if nonlinearity is not taken into account, sizeable errors in quantitative calculations may result. With today's emphasis on Good Laboratory Practice, Good Manufacturing Practice, and so on, it is important that linearity be verified and not assumed.

The procedure we have described is a straightforward approach to linearity testing that emphasizes deviations from linearity that some testing approaches miss. Furthermore, this procedure avoids the use of columns and separations whenever possible in order to focus the test on the detector itself and to avoid uncertainties introduced by injection and other possible variables. However, problems such as those with dissolved gases may lead to a need for on-line testing for certain detector types. In addition, destructive detectors should be tested on line. The linearity testing and plotting approach presented here is equally useful for on- and off-line testing.

Because linearity can be affected by both the specific operating conditions and the chemical nature of the sample, it is generally recommended that the linearity of an analysis be checked using the exact conditions under which the analysis will be performed. Thus, when developing an analytical method, it is advisable to run a series of standards spanning the expected unknown concentration range and to prepare a linearity plot for the analysis. This exercise will establish the linearity or nonlinearity of the complete chromatographic system for the analysis and guide the user in determining the proper calibration method.

We wish to thank T. Linkkila (Waters) for assistance with data collection, G. Dupré (Exxon) for valuable discussions, and C. Galgano and J. Newman (Waters) for assistance with the preparation of the manuscript.

**References**

- (1) *Annual Book of ASTM Standards*; American Society for Testing and Materials: Philadelphia, 1988; Vol. 14.01, pp. 149-58.
- (2) *Annual Book of ASTM Standards*; American Society for Testing and Materials: Philadelphia, 1988; Vol. 14.01, pp. 178-83.
- (3) *Annual Book of ASTM Standards*; American Society for Testing and Materials: Philadelphia, 1988; Vol. 14.01, pp. 235-45.
- (4) *Annual Book of ASTM Standards*; American Society for Testing and Materials: Philadelphia, 1988; Vol. 14.01, pp. 289-99.
- (5) *Annual Book of ASTM Standards*; American Society for Testing and Materials: Philadelphia, 1988; Vol. 14.01, pp. 344-48.
- (6) Scott, R.P.W. *Liquid Chromatography Detectors*, 2nd ed.; Elsevier: New York, 1986; pp. 13ff.
- (7) ASTM Task Group E 19.90.03. *Proposal for a Standard Recommended Practice for Refractive Index Detectors Used in Liquid Chromatography*. American Society for Testing and Materials: Philadelphia, 1988.
- (8) Guiochon, G.; Moysan, A.; Holley, C. *J. Liq. Chromatogr.* 1988, 11, 2547-70.
- (9) Pfeiffer, C. D.; Larson, J. R.; Ryder, J. F. *Anal. Chem.* 1983, 55, 1622-24.
- (10) *Annual Book of ASTM Standards*; American Society for Testing and Materials: Philadelphia, 1988; Vol. 14.01, pp. 228-34.
- (11) Wolf, T.; Fritz, G. T.; Palmer, L. R. *J. Chromatogr. Sci.* 1981, 19, 387-91.
- (12) Analytical Methods Committee, Royal Society of Chemistry. *Analyst* 1988, 113, 1469-71.
- (13) Colin, H.; Guiochon, G.; Martin, M. In *Practice of High Performance Liquid Chromatography*; Engelhardt, H., Ed.; Springer-Verlag: Berlin, 1986; p. 31.
- (14) Synovec, R. E.; Yeung, E. S. *Anal. Chem.* 1983, 55, 1599-1603.
- (15) Munk, M. N. In *Liquid Chromatography Detectors*; Vickrey, T. M., Ed.; Marcel Dekker: New York, 1983; pp. 165-204.
- (16) Fowles, I. A.; Scott, R.P.W. *J. Chromatogr.* 1963, 11, 1-10.



Craig A. Dorschel (front left), a senior applications chemist in the Waters Chromatography Division of Millipore Corporation, received his B.S. in Chemistry degree from the University of Michigan in 1970 and his Ph.D. from Stanford. His research interests include investigation of sample preparation techniques and chromatographic detection methodologies. Dorschel is also a member of the ASTM Committee E19 task group responsible for drafting the practice for refractive index detector evaluation.

F. Vincent Warren, Jr. (front right) is a senior applications chemist in the Waters Chromatography Division of Millipore Corporation. He received his B.S. degree in chemistry from Stanford, his M.A.T. degree from the University of New Hampshire, and his M.A. degree and Ph.D. in chemistry from Boston University. Warren's research interests include retention mechanisms in LC and the use of computers in chromatography and spectroscopy.

James E. Oberholtzer (back left), a senior applications chemist at Waters Chromatography Division of Millipore Corporation, received his B.S. degree in chemistry from Elizabethtown College and his Ph.D. in analytical chemistry from Purdue. His research interest is in the area of new chromatographic separations and detection technologies.

Juris L. Ekmanis (back center) is a senior applications chemist at Waters Chromatography Division of Millipore Corporation. He received his B.S. degree in chemistry from MIT, his M.S. degree in organic chemistry from Yale, and his Ph.D. in organic chemistry from Harvard. Ekmanis's research interests include viscosimetric detection of polymers and analysis of polymeric formulations.

Brian A. Bidlingmeyer (back right) is vice president and technical director of Waters Chromatography Division of Millipore Corporation. He received his A.B. degree cum laude in chemistry from Kenyon College and his Ph.D. in analytical chemistry from Purdue. Bidlingmeyer's research interests include the investigation of chromatographic retention mechanisms and the development of specialized applications. He is currently chairman of ASTM Committee E19 on Chromatography.

**LC-MS**  
**ONLY VESTEC**  
**REALLY MAKES IT**  
**WORK**  
**FOR YOU.**

How? By utilizing the technology and design know-how unique to the people who invented thermospray LC-MS!

The Vestec Model 201 is designed to be the ultimate LC detector. This instrument can detect and assist in identification of compounds in low picogram quantities, over a wide range of flow rates and solvents, including 100% water. You can eliminate tedious extraction and sample-preparation procedures and still routinely obtain peak-purity information for coeluting peaks.

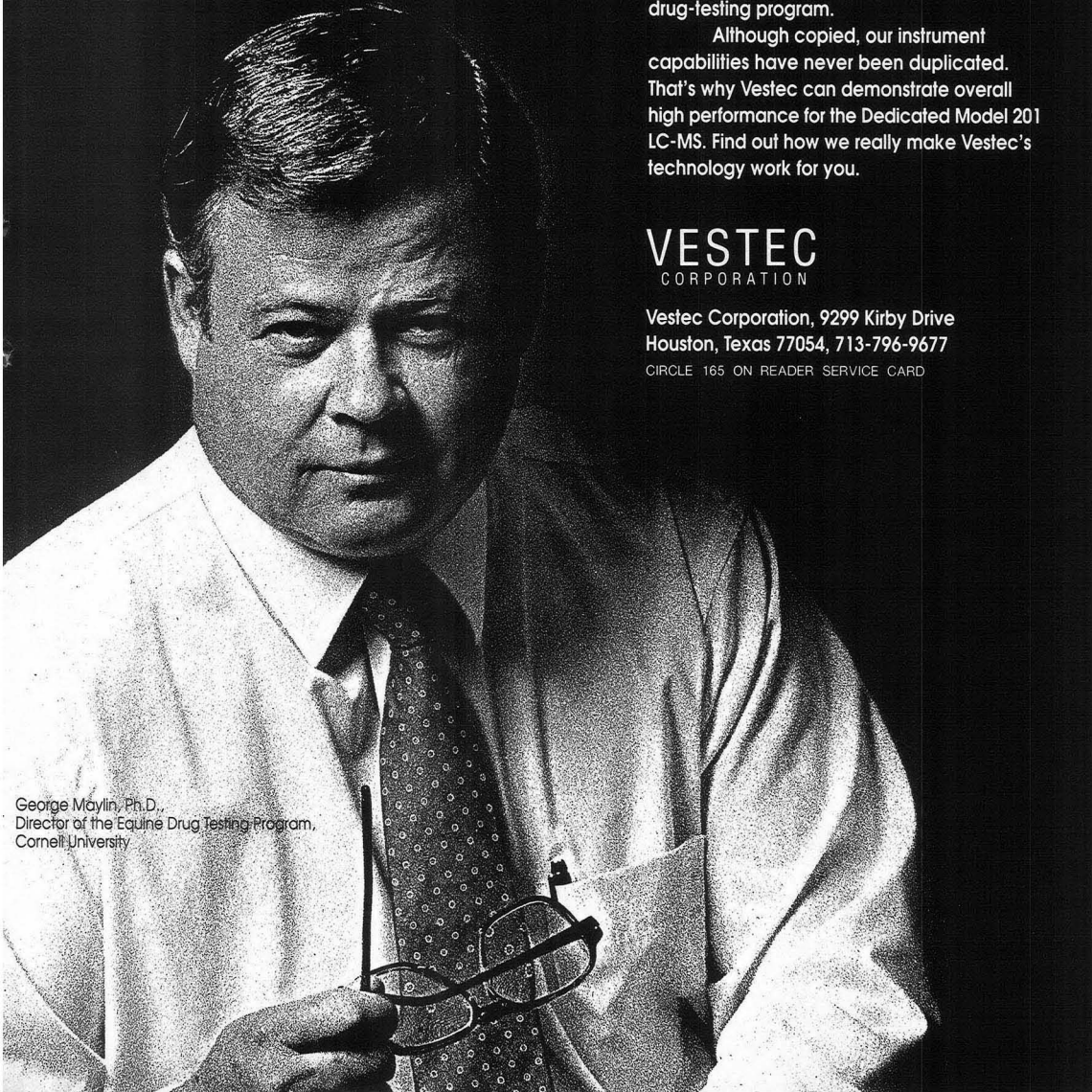
This advanced technology is what works for scientists such as Cornell University's George Maylin, Ph.D., who uses the Model 201 for the productivity required in his equine drug-testing program.

Although copied, our instrument capabilities have never been duplicated. That's why Vestec can demonstrate overall high performance for the Dedicated Model 201 LC-MS. Find out how we really make Vestec's technology work for you.

**VESTEC**  
CORPORATION

Vestec Corporation, 9299 Kirby Drive  
Houston, Texas 77054, 713-796-9677

CIRCLE 165 ON READER SERVICE CARD



George Maylin, Ph.D.,  
Director of the Equine Drug Testing Program,  
Cornell University

# NUPRO Valves and Filters for Analytical Applications

NUPRO Valves and Filters offer these design and performance choices:

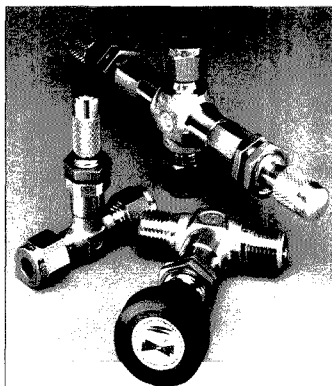
- **End Connections:** SWAGELOK® Tube Fittings, NPT, Tube Stub, Weld, CAJON VCO® & VCR®
- **Service Ratings:** vacuum to 6000 psi; temperatures to 900°F

STOCKED FOR IMMEDIATE DELIVERY BY AUTHORIZED SALES AND SERVICE REPRESENTATIVES.  
Nupro Company, 4800 East 345th St., Willoughby, OH 44094



A SWAGELOK COMPANY

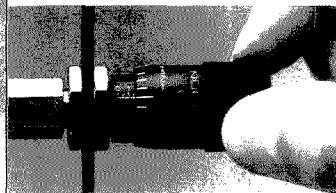
SWAGELOK — TM Swagelok Fitting Company  
CAJON, VCO & VCR — TM Cajon Company  
© 1988 Swagelok Co. all rights reserved N-58



## METERING

Valves for precise flow control in laboratory and instrument systems

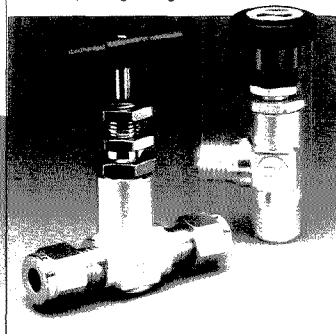
- accurate, repeatable flow adjustment with no initial surge
- compact, low dead space
- stem threads removed from system



## SHUT OFF

Compact valves for reliable flow regulation and shut off

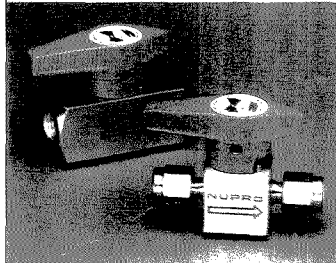
- stem threads removed from system fluid
- compact designs
- ball tip or regulating stems



## FILTRATION

Inline and tee type filters to protect instruments by removing hard particle contamination from fluid lines

- choice of sintered and wire mesh elements from 0.5 to 440 microns
- compact designs
- all metal construction

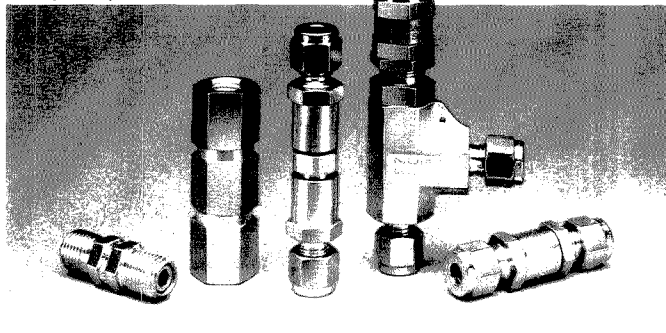


- quick-acting, 1/4 turn
- full flow
- easy maintenance

## CHECK & RELIEF

Relief valves open at pre-set pressure; check valves allow unidirectional flow control

- cracking pressures 1/3 to 6000 psi
- smooth floating poppet
- positive back stop



CIRCLE 154 ON READER SERVICE CARD



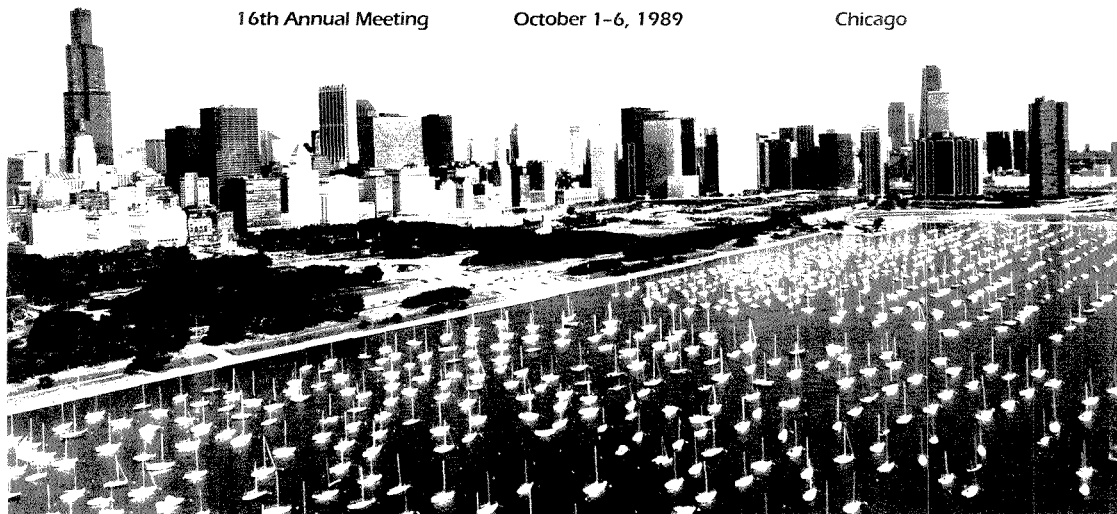
# MEETINGS

# FACSS

16th Annual Meeting

October 1-6, 1989

Chicago



CHICAGO TOURISM COUNCIL/RON SCHRAMM

The 16th annual meeting of the Federation of Analytical Chemistry and Spectroscopy Societies (FACSS) will be held Oct. 1-6 at the Hilton Inn and Towers in Chicago, IL. The meeting is sponsored by the Society for Applied Spectroscopy (SAS), the Division of Analytical Chemistry of the American Chemical Society (ACS), the Association of Analytical Chemists (ANACHEM), the Analysis Instrumentation Division of the Instrument Society of America, the Chromatography Forum of the Delaware Valley, and the Coblenz Society.

More than 800 research papers and 90 poster presentations are scheduled. An instrument exhibit featuring state-of-the-art equipment and services will run for four days in conjunction with the meeting. The exhibition will be housed in the Hilton's Northwest Exhibit Hall.

The program will be highlighted by the presentation of several awards. The ANACHEM Award will be presented

to Harry Pardue at a special symposium on Wednesday, Oct. 4. D. M. Lubman, C. H. Sin, and H. M. Pang will receive the Meggers Award, and G. Horlick, S. Tan, and M. Vaughan will be presented with the Lester Strock Award on Tuesday, Oct. 3. A. C. Albrecht and M. E. Jacox will receive the 1988 and 1989 Lippincott Awards, respectively, on Thursday, Oct. 5. The FACSS Student Award, the Tomas Hirschfeld Scholar Awards, and a number of additional SAS awards will also be presented.

The ACS is offering a series of short courses in conjunction with the meeting. For more information, see p. 999 A of this issue. Three SAS short courses—Plasma Spectrochemical Analysis, FT-IR Spectrometry, and Modern Experimental Spectroscopy—will also be offered. For information on these courses, contact Jo Ann Brown, Society for Applied Spectroscopy, P.O. Box 64008, Baltimore, MD 21264 (301-694-8122).

Thirteen FACSS-sponsored workshops are scheduled, including a complimentary workshop entitled "Professional Analytical Chemists in Industry." For details, contact Jon Carnahan, Dept. of Chemistry, Northern Illinois University, DeKalb, IL 60115 (815-753-6879).

The meeting will feature a scientific software fair in conjunction with the instrument exhibit. Participating firms will display their software packages so that attendees may obtain hands-on experience with a variety of products. In addition, an employment bureau will operate during the meeting. For additional information, contact Foad Mozayani, Akzo Chemicals, Inc., 8401 W. 47th St., McCook, IL 60525 (312-442-7100).

Hours for registration will be Sunday, Oct. 1, from 6 P.M. to 8:30 P.M.; Monday, Oct. 2, from 7:45 A.M. to 4:30 P.M.; Tuesday, Oct. 3, through Thursday, Oct. 5, from 8:00 A.M. to 4:30 P.M.; and Friday, Oct. 6, from 8:00 A.M. to

10:00 A.M. Registration fees are as follows: preregistration, \$75; on-site registration, \$95; single day, \$50; full-time student, \$15. The deadline for advance registration is Sept. 15. For additional information, contact Sydney Fleming, 24 Crestfield Road, Wilmington, DE 19810 (302-695-4572).

Hotel rooms have been reserved at the Chicago Hilton and Towers, Essex Inn, Blackstone, and Congress Hotels. For housing information, contact FACSS Housing Bureau, Chicago Convention and Visitors Bureau, McCormick Place on-the-Lake, Chicago, IL 60616.

Further information about the meeting is available from Paul Bourassa, General Chairman, Memphis Environmental Center, 2603 Corporate Ave., East, Suite 100, Memphis, TN 38132 (901-345-1788) or Robert Michel, Program Chairman, Dept. of Chemistry, University of Connecticut, 215 Glenbrook Rd., Storrs, CT 06269-3060 (203-486-3143). The complete preliminary program follows.

## Program

### MONDAY MORNING

#### Surface Studies of Materials

Arranged by T. Barr

**New Approaches in the Physical Characterization of Globally Amorphous Catalytic Materials.** H. C. Foley, A. Saito, D. Layatis, N. Bamsal, C. Dybowski, U of Delaware

**Characterization of Cobalt Clusters in Zeolites.** S. Suib, U of Connecticut  
P. Stair, Northwestern U

**Advances in Spatially Resolved ESCA.**

B. Tonner, U of Wisconsin, Milwaukee

**Direct Recoil and Ion Scattering Spectroscopy.** A. Krauss, Argonne National Laboratories

**Application of EELS to the Study of Zeolites.** G. Zajac, Amoco Chemical Co.

**Recent Advances in Auger Spectroscopy.** J. Donner, Allied Signal

**Characterization of Green-State Ceramics via Proton (<sup>1</sup>H) NMR Imaging.** S. L. Dieckman, N. Gopalsami, P. S. Wong, W. A. Ellingson, R. E. Botto, Argonne National Laboratories

#### Forensic Applications of MS

Arranged by D. D. Fetterolf

**Explosives Detection by MS.** S. McLuckey, G. Glish, Oak Ridge National Laboratory  
**MS in Urine Drug Analysis.** J. Cody, Dept. of the Air Force

**Forensic Applications of Pyrolysis GC/MS.** T. Munson, St. Cloud State U

**MS of Fentanyl Analogues.** D. Cooper, DEA  
**Forensic Applications of Tandem MS.** D. D. Fetterolf, FBI

## Meeting Officers

**General Chairman:** Paul Bourassa, Memphis Environmental Center

**Program Chairman:** Robert Michel, University of Connecticut

**Chairman of the Governing Board:** Alexander Scheeline, University of Illinois

**Exhibits Chairman:** Edward Brame, Jr., Crippen Consultants

**Secretary:** Keith Olson, General Motors

**Treasurer:** Ronald Schroeder, Wayne State University

### Automation and Robotics in Biological and Chemical Analysis

Arranged by L. B. Fox

**Generic Automated Sample Preparation (GASP).** R. Sharp, Upjohn  
**Automated Approach to the Development of Sample Preparation Procedures.** P. Beals, Waters/Millipore

**Track-Mounted Robot To Prepare Samples for HPLC.** A. Solenki, R. Lipscomb, CyberFluor

**On-Line Quality Control Checking of Pharmaceutical Products.** M. P. Ramsay, R. Lipscomb, Parke Davis

**Smart Cell—An Approach to Networked Automation.** A. Martin, Source for Automation  
**Lab Automation through Intelligent Control and Networking.** D. Cunningham, Ocean Spray Cranberries

**Application of Robotics for Automation of a Water Testing Lab.** R. L. Casselberry, Rohm and Haas

**APOCALYPSE—An Automated Protein Crystallization System.** N. Jones, J. Swartzendruber, J. Deeter, D. Clawson, P. Landis, Eli Lilly

### Advances in New Sources for Atomic Spectroscopy

Arranged by A. Montaser

**Excitation Sources for Analytical Atomic Spectroscopy: Some Views from the Sidelines on a Very Hot Subject.** V. Fassel, Iowa State U  
**Characterization of a Laser-Produced Plasma from a Solid Target.** J. M. Mermet, M. Autin, A. Briand, P. Mauchien, U Claude Bernard

**Atmospheric-Pressure RF Sputtering Source for Direct Analysis of Solid and Liquid Samples.** M. W. Blades, D. C. Liang, U of British Columbia  
**Studies on a New Microwave Plasma Torch as an Excitation Source for AES.** Q. Jin, C. Zhu, M. W. Borer, G. M. Hieftje, Indiana U

**Fundamentals of High-Frequency Plasma Generation Using Electromagnetic Surface Waves.** M. Moisan, J. Hubert, Z. Zakrzewski, U of Montreal

**Hollow Cathode Ion Bombardment Furnace for AES.** S. Tanguay, R. Sacks, U of Michigan  
**Atomic Emission and MS of He ICPs Formed at 6 to 41 MHz.** A. Montaser, I. Ishii, H. Tan, R. H. Clifford, George Washington U

### Fundamentals of the Graphite Furnace

Arranged by J. A. Holcombe

**Temperature Dependence of Atomization Efficiencies in a Spatially and Temporally Isothermal Graphite Furnace.** W. Frech, D. C. Baxter, U of Umea, Sweden

**Study of ETA Profiles.** D. R. Olivares, W. Olivares, Lawrence Berkeley Laboratory

**Energetics of Initial Release and Redesorption of Analyte Atoms in GFAAS.** R. Sturgeon, National Research Council of Canada  
**Carbide Formation and Behavior in GFAAS by Real-Time MS.** D. L. Styris, L. Prell, Battelle Pacific Northwest

**GFAAS Exit Ports.** R. Lovett, West Virginia U  
**Comparison of Experiment and Theory in the Formation of an Absorbance Signal in GFAAS.** O. A. Quell, J. A. Holcombe, U of Texas

**Impact of Kinetics on Analyte Loss and Matrix Decomposition Mechanisms in Graphite Furnace Atomizers.** G. Rayson, M. R. Fresquez, D. A. Lenhoff, New Mexico State U

**Use of Pattern Recognition Techniques To Discern Peak Shape Differences between Standards and Samples.** J. Harnly, U.S. Dept. of Agriculture

### Recent Advances in Analytical Biotechnology

Arranged by N. A. Farid

**Microenvironmental Contributions to the Chromatographic Behavior of Proteins.** F. Regnier, Purdue U

**Application of Capillary Zone Electrophoresis to the Separation and Characterization of Recombinant Protein Products.** R. G. Nielsen, R. M. Riggan, N. A. Farid, E. C. Rickard, Lilly Research Laboratories

**Separation of Immune Complexes of Human Growth Hormone without a Stationary Phase Using Capillary Zone Electrophoresis.** G. S. Sittampalam, R. G. Nielsen, E. C. Rickard, Lilly Research Laboratories

**Recent Advances in LC/MS and CZE/MS in Bioanalytical Chemistry.** R. M. Caprioli, U of Texas Medical School

### Curve Resolution Methods in Chromatography

Arranged by P. J. Gemperline

**Interactive Self-Modeling Multivariate Mixture Analysis: Practical Examples from an Industrial Environment.** W. Windig, Eastman Kodak

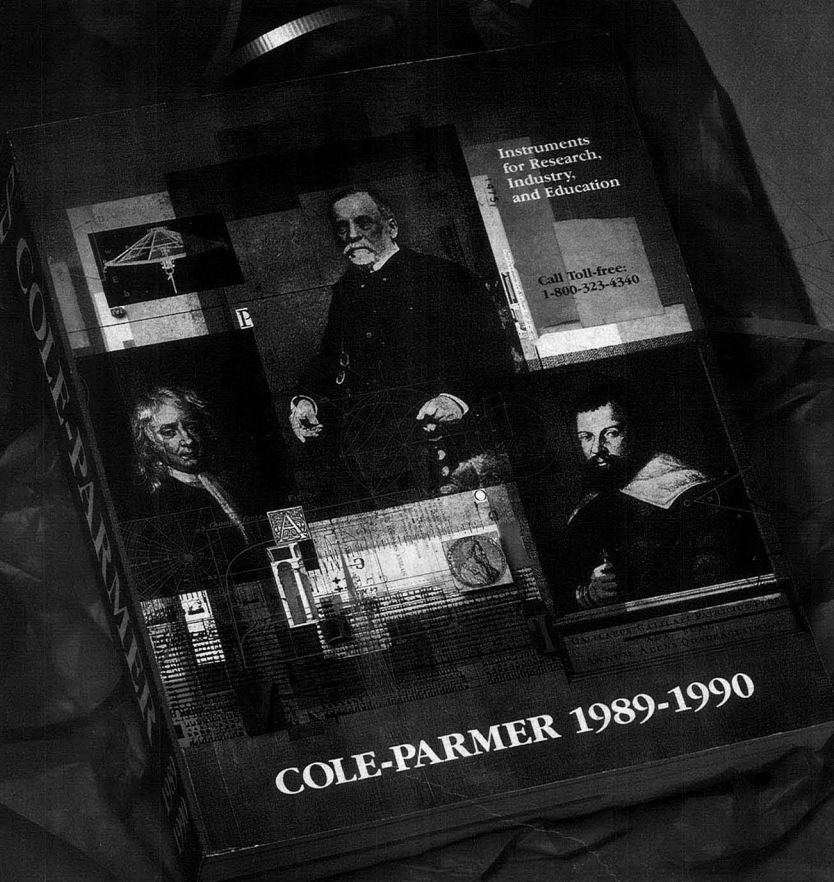
**Kalman Filtering Methods for Curve Resolution in LC and TLC.** S. Rutan, T. L. Cecil, D. D. Gerow, Virginia Commonwealth U

**Purity Analysis in Chromatography:**

**Evaluation of Univariate and Multivariate Approaches.** S. Ramos, Infomatrix  
**Improvement of SVD Properties by Empirical Rank-1 Weights.** R. Shrager, NIH

**Tensorial Approaches to Deconvolution.** E. Sanchez, Infomatrix/U of Washington  
**Least-Squares Chromatographic Baseline Correction and Its Effect on Peak Deconvolution.** R. Lacey, Hewlett-Packard

Our easy-to-use catalog features over 20,000 scientific products for research, industry, and education. For your free copy, mail in the attached card or call us toll-free at 1-800-323-4340.



## This indispensable resource **FREE**

Our many product lines include:

- Balances • Baths and circulators • Biotechnology instrumentation
  - Fermentation • Electrophoresis • Books • Centrifuges
    - Liquid and gas chromatography products
  - Computer software and data acquisition
- Environmental testing equipment • Filtration products • Flowmeters
  - Mixers and stirrers • Ovens, incubators and furnaces
- pH measurement and control • Plasticware • Pumps • Recorders
  - Spectrophotometers • Thermometry • Tubing...and more

COLE-PARMER INSTRUMENT COMPANY • 7425 NORTH OAK PARK AVENUE • CHICAGO, ILLINOIS 60648

Circle Reader Card No. 30

**Curve Resolution Using Nonlinear Optimization.** S. Neal, U of Washington  
**Maximum Likelihood Processing of Three-Dimensional Diode Array Chromatograms.** L. K. DeNoyer, J. G. Dodd, G. E. Barringer, Spectrum Square Associates

### Glow Discharge MS

*Arranged by* W. W. Harrison

**Glow Discharge MS: No Longer "Promising" Technique.** W. W. Harrison, U of Florida

**Glow Discharge MS as a Quantitative Analysis Technique.** W. H. Christie, Oak Ridge National Laboratory

**Ionization and Recombination Processes in a Low-Pressure Glow Discharge Ion Source.** W. A. Vieth, J. C. Huneke, N. J. McKinnon, Charles Evans and Associates

**Planar Magnetron Low-Pressure, High-Efficiency Ion Source for Glow Discharge MS.** L. McCaig, R. Sacks, D. Lubman, U of Michigan

**Applications of the VG 9000 in Inorganic Solids Analysis.** J. Clark, G. Ronan, D. Wheeler, VG MicroTrace

**Glow Discharge MS Employing a Double-Quadrupole Spectrometer.** R. K. Marcus, D. C. Duckworth, Clemson U

**Sputter Ablation Studies in a Glow Discharge Ion Source.** C. M. Barshick, W. W. Harrison, U of Florida

**Analysis of Ceramics by Glow Discharge MS.** D. L. Dugger, G. P. Maklae, GTE Laboratories

### X-ray Spectroscopy

*Arranged by* Y. Gohshi

**Current Trends in X-ray Spectroscopy.** R. Van Grieken, U of Antwerp, The Netherlands

**Trends in Quantification.** B. A. Vrebos, G. T. Kuiperes, Philips Analytical

**Studies on Background X-rays in Wavelength Dispersive Spectrometry.** T. Arai, Rigaku Industrial Corp.

**Total Reflection X-ray Fluorescence—Principles and Applications.** R. Kloockenkaemper, Institute for Spectrochemistry, FRG

**Recent Developments and Results on Total Reflection X-ray Fluorescence Analysis.** P. Wobraschek, Atominstut der Oesterreichischen Universitaet, Austria

**Bragg-Polarized XRF.** H. Alginger, Atominstut der Oesterreichischen Universitaet, Austria

**Thin-Film Characterization by X-ray Fluorescence.** T. C. Huang, IBM

### Hyphenated Analysis Systems: Present Status and Future Prospects

*Arranged by* C. Wilkins

**Alternative Approaches to GC/IR/MS.** C. L. Wilkins, J. R. Cooper, U of California, Riverside

**Fuel Analysis by GC/FT-IR/ITD MS.** E. S. Olson, J. W. Diehl, U of North Dakota

**High-Confidence Qualitative Analysis of Low-Level Components in Industrial Chemicals Using Combined HRGC/FT-IR/MS.** R. Leibrand, W. Duncan, Hewlett-Packard

**Evaluation of GC/Matrix Isolation FT-IR Spectrometry as a Quantitative Technique.** J. F. Schneider, K. R. Schneider, S. E. Spiro, Argonne National Laboratories

**Confirmed Quantitation by GC/IR/MS.** D. Gurka, W. Duncan, I. Farnham, B. B. Potter, S. Pyle, R. Titus, U.S. EPA

**Supercritical Fluid Extraction for SFC/FT-IR and GC/FT-IR Sample Introduction.** P. R. Griffiths, K. L. Norton, H. Makishima, A. J. Lange, U of Idaho

### Atomic Fluorescence and Laser-Enhanced Ionization

*Arranged by* G. J. Havrilla and M. D. Seltzer

**Laser Fluorescence and Ionization Spectroscopy at the Subfemtogram Level.** J. D. Winefordner, B. W. Smith, N. Omenetto, U of Florida

**Determination of Subnanogram per Meter<sup>3</sup> Concentrations of Metals in Air by Impaction Graphite Furnace Laser-Excited Atomic Fluorescence or Atomic Absorption.** Z. Liang, G.-T. Wei, R. L. Irwin, A. P. Walton, J. Sneddon, R. G. Michel, U of Connecticut

**Laser-Excited Atomic and Ionic Fluorescence Spectrometry in the Inductively Coupled Air Plasma.** M. D. Seltzer, R. B. Green, China Lake Naval Weapons Center

**Study of Signal-to-Noise Ratio in Electrothermal Atomizer Laser-Excited Atomic Fluorescence with a 500-Hertz Excimer Pumped Dye Laser.** R. L. Irwin, G.-T. Wei, D. J. Butcher, R. G. Michel, U of Connecticut

**Collisional Transfer between and Quenching of Excited States of the Oxygen Atom Using Two-Photon Laser-Induced Fluorescence.** B. E. Forch, J. B. Morris, A. W. Miziolek, P. J. Dagdigian, Aberdeen Proving Ground

**Laser Atomic Fluorescence with Metal Resonance Line Laser.** J. Simeonsson, J. Vera, B. Smith, U of Florida

**One- and Two-Color Multiphoton Ionization in a Low-Pressure Sampling Cell.** J. M. Ramsey, P. R. Blazewicz, W. B. Whitten, Oak Ridge National Laboratory

**Novel Sensors Applied to Process Analysis**

*Arranged by* J. Stetter and H. Wohltjen

**Ion Mobility Spectrometry: A New Technique for Chemical Detection in Process Control Applications.** A. T. Bacon, J. E. Roehl, Environmental Technology Group

**Near-IR Optical Technology for Process Sensing.** J. B. Callis, U of Washington

**Physical and Chemical Measurements with SAW Devices.** H. Wohltjen, J. Lint, N. L. Jarvis, Microsensor Systems

**Liquid-Absorption Preconcentrators for the Analysis of Trace Air Constituents.** S. Zaromb, K. C. Picoe, R. A. Bozen, H. Carlson, L. S. Criscione, S. M. Spurgash, Argonne National Laboratories

**Solid-State Electrochemical Sensors.** W. Buttner, Argonne National Laboratories

**Membrane Separator Technology for Process Analysis.** R. Bredeweg, Dow Chemical

**Detection and Identification of Pharmaceuticals and Anesthetics by Ion Mobility Spectrometry.** A. P. Snyder, D. A. Blyth, G. A. Elceman, Aberdeen Proving Ground

**Vapor Monitoring with Amperometric Sensors.** J. R. Stetter, Transducer Research

**MONDAY AFTERNOON**

**Characterization of Catalysts**

*Arranged by* S. L. Suib

**Characterization of Zeolite Supported Metal Clusters.** W.M.H. Sachtler, C. Dossi, S. T. Homeyer, L. L. Sheu, Z. Zhang, Northwestern U

**<sup>27</sup>Al NMR Studies of the Dealumination of Moriente.** D. Hasha, J. M. Garces, C. E. Crowder, G. S. Lee, Dow Chemical

**Raman Spectroscopic Studies of Zeolites.** P. K. Dutta, Ohio State U

**Recent Developments in the Characterization of Heterogeneous Catalysts.** R. Von Ballmoos, Engelhard

**Imaging SIMS and Image Processing Methods for Petroleum Cracking Catalyst Characterization.** D. Letta, E. L. Kugler, Exxon

**Composition, Processing, and Aging Effects on a Regenerable H<sub>2</sub>S Absorbent.** P. F. Schubert, F. M. Brinkmeyer, G. A. Detzer, Phillips Petroleum

**EPR Studies of Zeolite Catalysts.** L. Iton, Argonne National Laboratories

**XPS Studies of Pt Metal Catalysts.** T. Barr, U of Wisconsin

### NMR of Surfactants

*Arranged by* F. D. Blum

**Recent Results in Surfactant NMR.** F. D. Blum, U of Missouri, Rolla

**Nuclear Magnetic Relaxation in Surfactant Liquid Crystals.** T. C. Wong, U of Missouri

**<sup>19</sup>F NMR Study of Molecular Exchange in Micellar Systems.** B. M. Fung, W. Guo, E. K. Guzman, S. D. Christian, U of Oklahoma

**Diffusion in Microemulsions.** W. G. Miller, U of Minnesota

**Phase Continuity and Surface Properties of Dispersions of AOT/Water Liquid Crystals.** E. I. Frances, A. H. Alexopoulos, J. E. Puig, Purdue U

**Deuterium Quadrupole NMR of Hexagonal to Bixial Ribbon Phase Transitions in Alkali Metal Carboxylate-Water-Cosurfactant Mixtures.** P. K. Kilpatrick, J. C. Blackburn, North Carolina State U

**<sup>2</sup>H NMR and X-ray Studies of Polymerizable Liquid Crystals.** F. D. Blum, Y.-J. Uang, U of Missouri, Rolla

### Environmental/Dioxin Applications of MS

*Arranged by* D. Kuehl

**Factors Affecting the Choice between High-Resolution MS and Low-Resolution MS in the GC/MS Analysis of Complex Samples for Specific PCDD—PCDF Isomers.** T. O. Tiernan, J. H. Garrett, G. F. Van Ness, J. G. Solch, D. J. Wagle, Wright State U

**Identification of Nonpolar Organic Toxicants in Effluents Using Toxicity-Based Fractionation with GC/MS.** L. P. Burkhardt, E. J. Durhan, M. T. Lukaszewicz, U.S. EPA

**Analysis of Polychlorinated Dibenzofurans and Polychlorinated Dibenzop-dioxins in Samples from the Pulp and Paper Industry.** S. E. Swanson, Argonne National Laboratories

**GC/MS Techniques Applied to the U.S. EPA National Dioxin Study—Phase II.** P. J. Marquis, L. G. Holland, M. L. Larsen, D. W. Kuehl, U of Wisconsin, Superior

**Application of LC/Electron Impact MS to Environmental Analyses.** W. Budde, U.S. EPA

### Availability of Basic Spectroscopic Data for Analytical Atomic Spectroscopy

*Arranged by* P. W. Boumans and A. Scheeline

**Review of Data on Atomic Wavelengths, Energy Levels, and Transition Probabilities.** W. C. Martin, National Institute of Standards and Technology

**Measurement and Simulation of Atomic Spectra for Spectrochemical Analysis: An Electronic Publication.** P. W. Boumans, Philips Research Laboratories

**Databases of Atomic Collisions Cross-Sections.** J. W. Gallagher, National Institute of Standards and Technology

# DIALOG INTRODUCES ANOTHER TABLE OF BASIC ELEMENTS FOR YOUR LAB.



There's no symbol for *information* in the Periodic Table. Yet nothing could be more crucial to your research than complete, accurate technical and business information.

That's why many chemists consider DIALOG<sup>®</sup> an essential element in the modern lab.

As the world's largest online knowledgebank, DIALOG gives you access to a whole world of critical information. Right in your own lab.

For starters, you can tap into the crucial scientific data. DIALOG has detailed information on everything from

compound identification to chemical safety data, property data, substance and substructure.

Then you can expand your focus by accessing important, related data that will enable you to look at your work in a broader context.

For example, you can investigate patents, competitive projects, new product markets, and worldwide industry trends. In fact, you can investigate any topic, anytime.

And you won't have to sacrifice depth for the sake of breadth. DIALOG is updated continuously, so the data is

always comprehensive and current. And many citations can be conveniently retrieved in full text.

Call today for more information and a free Periodic Table Reference Card. Once you've examined them, you'll see how DIALOG can become a basic element of all your research.

Call us toll free at 800-3-DIALOG, (800-334-2564). Or request information by Fax at 415-858-7069.

**DIALOG** INFORMATION SERVICES, INC.  
A Knight-Ridder Company

*The world's largest online knowledgebank.*

**Laser and FT Techniques for the Measurement of Atomic Transition Probabilities.**  
J. E. Lawler, U of Wisconsin, Madison

### Spectroscopic Studies in Organized Media

*Arranged by* I. M. Warner

**Luminescent Assays Utilizing Organized Assemblies.** W. L. Hinze, Wake Forest U  
**Studies of Organized Bile Salt Media.** L. B. McGown, Duke U  
**Interactions in Solid Matrix  $\beta$ -Cyclodextrin Luminescence Analysis.** R. J. Hurtubise, M. D. Richmond, U of Wyoming  
**Counterions and the Properties of Ionic Micelles.** A. L. Underwood, Emory U  
**Study of Solute Micelle Interactions by Various Laser Spectroscopic Measurements.** M. Wirth, S.-H. Chou, J. Burbage, U of Delaware  
**Rotational Dynamics Studies in Organized Media.** F. V. Bright, T. A. Betts, G. C. Catena, J. Huang, K. S. Litwiler, D. P. Paterniti, J. Zagrobelney, J. Zhang, SUNY, Buffalo  
**Fluorescence and Thermal Lensing Detection of Lanthanide Ions Through Solvent Extraction Using Crown Ethers.** C. D. Tran, Marquette U  
**Fluorescence Studies in Cyclodextrin Solutions.** I. M. Warner, G. Nelson, J. Zung, V. Smith, Emory U

### The Graphite Furnace

*Arranged by* J. A. Holcombe

**Comparison of Atomization from Graphite and Metal Surfaces.** B. Welz, B. Radziuk, Bodenseewerk Perkin-Elmer and Co. GmbH  
**Study of Some Gas-Phase Reactions in GFAAS.** C. L. Chakrabarti, G. Gilcrest, Carleton U  
**Ion-Trap MS Using a Graphite Furnace Atom Source.** M. W. Blades, B. Daigle, U of British Columbia  
**Flow-Injection Therospray Sample Deposition for Electrothermal Atomization AAS.** P. C. Bank, M.T.C. deLoos-Vollebregt, L. de Galan, Delft U of Technology, The Netherlands  
**Rotating Arc Tube Furnace for Atomic Emission Analysis of Sulfur Residue Samples.** D. Slinkman, R. Sacks, U of Michigan  
**Atmospheric Pressure Plasma Excited Atomic Emission Inside a Graphite Furnace (Photoatomization Thermal Excitation Source—FATES).** M. W. Blades, D. C. Liang, U of British Columbia  
**Preliminary Studies Comparing Aluminum Atomization Efficiencies in GFAAS Using Ta vs. Pyrolytic Graphite.** D. A. Redfield, W. Frech, A. Cedegen, Northwest Nazarene College  
**Surface and Gas-Phase Investigation of Steps Leading to Atomization of Palladium in a Graphite Furnace.** J. A. Holcombe, V. Majidi, D. C. Hassel, U of Texas  
**Spatial Mapping of Diatomic Molecules within the Graphite Furnace Atomizer.** C. Huie, SUNY

### Recent Advances in Analytical Biotechnology

*Arranged by* N. A. Farid

**New Methods for Carbohydrate Analysis of Recombinant Glycoproteins.** M. Spellman, Genentech  
**Micropurification of Proteins for Structural Analysis.** J. Pearson, Upjohn  
**Mapping and Sequencing the Human Genome: New Challenges in Analytical Chemistry.** L. M. Smith, U of Wisconsin  
**Development of a Validated Assay for Residual DNA in a Protein Pharmaceutical Product.** B. F. Ghrist, K. E. Roehr, Lilly Research Laboratories

### FT-IR Spectrometry

*Arranged by* J. A. de Haseth

**Vibrational Circular Dichroism Techniques and Applications to Conformational Analysis.** T. A. Keiderling, U of Illinois, Chicago  
**Role of Surface Contact in Quantitative Internal Reflection Spectroscopy.** F. M. Mirabella, Quantum Chemical  
**Recent Advances in FT-IR Technology.** I. M. Hamadah, Perkin-Elmer  
**Can IR Reflectance Spectroscopy Determine Monolayer Structure at Solid and Liquid Interfaces?** R. A. Dluhy, Battelle Laboratories  
**FT-IR Applications with a Step-Scanning Interferometer.** P. R. Griffiths, J. Perkins, B. Lerner, U of Idaho  
**Fiber Optics Applications in the Mid-IR.** J. A. de Haseth, J. E. Andrews, U of Georgia

### Glow Discharge MS and Atomic Absorption

**Effectiveness of a Low-Resolution Analyzer as Applied to Glow Discharge MS.** R. C. Hoodless, NG MicroTrace  
**Application of a Computer-Controlled Langmuir Probe in Glow Discharge Plasma Diagnostics.** R. K. Marcus, D. Fang, Clemson U  
**Design and Characterization of a Direct Insertion Probe for Radio Frequency Powered Glow Discharge MS.** D. C. Duckworth, R. K. Marcus, Clemson U  
**Fast Sequential Multielement AAS Analysis of Complex Alloys Using Sputter Rate Corrected Glow Discharge Atomization.** H. L. Kahn, A. E. Bernhardt, T. Sciutto, MARS Co.  
**Use of Atomic Absorption for the Determination of Multiple Elements in Powder, without Dissolution and in Rapid Sequence.** A. E. Bernhardt, W. Batie, H. L. Kahn, MARS Co.  
**Multielement AAS Analysis of Oils for Metals, Using a Single 1-Minute Aspiration for Each Sample.** W. Batie, A. E. Bernhardt, H. L. Kahn, MARS Co.  
**Automatic Sample Dilution and Preconcentration for Flame AAS Using Continuous Flow Techniques.** J. F. Tyson, S. R. Bysouth, P. B. Stockwell, U of Massachusetts  
**Study of Ligand Interferences in Flames by Atomic Fluorescence Using Uniform Isolated Droplet Introduction.** G. L. Klunder, C. B. Boss, North Carolina State U  
**Comparative Study of Furnace Atomic Absorption and Differential Pulse Stripping Voltammetry for Determination of Selected Metals.** M. Z. Mesmer, D. E. Braunlich, Southeastern Massachusetts U

### X-ray Spectroscopy

*Arranged by* Y. Gohshi

**Chemical State Analysis by X-ray Emission Spectroscopy (XES).** G. Andermann, U of Hawaii  
**Compact SR Light Source for Soft X-ray to UV Region.** H. Nakabushi, Sumitomo Heavy Industries  
**Future Trends in X-ray Spectroscopy.** Y. Gohshi, U of Tokyo  
**Energy Dispersive X-ray Fluorescence Using an Electrically Cooled Detector.** A. R. Harding, D. Leland, B. Glynn, Tracor X-ray  
**Energy Dispersive X-ray Fluorescence (EDXRF) Determination of Lanthanides after Chemisorptive Preconcentration on 1-(2-Pyridylazo) Naphthol Modified Naphthalene.** T. P. Rao, V. Bhagavathy, M.L.P. Reddy, A. O. Damodaran, CSIR, India

### ICP-OES

**Induction Plasma Dynamics: Modeling and Measurements.** M. I. Boulos, U of Sherbrooke  
**Computerized Tomography for Studying Plasmas.** L. Ebdon, B. Fairman, S. Hill, Polytechnic South West, Great Britain  
**Effect of Easily Ionized Elements on the Fundamental Parameters in the ICP.** M. Huang, D. S. Hanselman, G. M. Hieftje, Indiana U  
**Statistical-Mechanical Theory of Electron Density in Plasmas.** F. R. Meeks, U of Cincinnati  
**Applications of High-Resolution FT Spectroscopy in Diagnostic Studies of Non-Argon ICP Discharges.** A. Montaser, I. Ishii, B. A. Palmer, L. R. Layman, D. E. Hof, George Washington U  
**Fluorescence and Emission Studies of Easily and Non Easily Ionizable Element Matrix Effects in the ICP.** E. J. Williamson, J. W. Olesik, U of North Carolina  
**Recent Studies on Extraction Discharge Sources for Argon and Helium ICP-AES.** H. Tan, A. Montaser, George Washington U  
**Spectral Line Profile Recognition and Analysis for ICP Spectrometry Using a Photodiode Array-Based Spectrometer.** S. W. McGeorge, R. W. Phillips, A. K. Weiss, Leco Instruments

### Atomic Fluorescence and Laser-Enhanced Ionization

*Arranged by* G. J. Havrilla and M. D. Seltzer

**Nonlinear Laser Wavemixing Spectroscopy for Trace Elemental Analysis.** W. Tong, K. Weed, G. Luena, San Diego State U  
**Nonlinear Spectroscopy in Flames.** J. C. Wright, B. K. Winker, U of Wisconsin  
**Multiphoton Ionization and Stepwise Laser-Enhanced Ionization of PO in Flames for the Determination of Phosphorus.** G. C. Turk, National Institute of Standards and Technology  
**Laser-Enhanced Ionization in a Graphite Tube Furnace with Probe Atomization.** D. J. Butcher, S. Sjöström, R. G. Michel, U of Connecticut  
**Laser Atomic Fluorescence and Resonance-Enhanced Ionization Detection in Graphite Furnaces and Flames.** G. Petrucci, C. Stevenson, J. Vera, N. Omenetto, B. Smith, J. D. Winefordner, U of Florida  
**Laser Atomic Photoionization Spectroscopy as a Tool for Trace Element Analysis.** C. Stevenson, G. Petrucci, J. D. Winefordner, U of Florida  
**Investigation of a Pulsed ICP for Laser-Enhanced Ionization Spectroscopy.** Y.-L. Jian, R. L. Watters, Jr., G. C. Turk, J. C. Travis, National Institute of Standards and Technology  
**Trace Detection in Conducting Solids Using Laser-Induced Fluorescence in a Cathodic Sputtering Cell.** J. C. Travis, G. C. Turk, R. L. Watters, Jr., Y.-L. Jian, National Institute of Standards and Technology

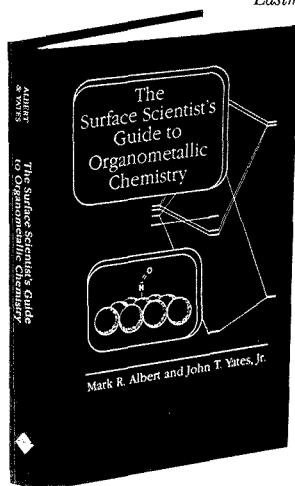
### Advances in HPLC Column Technology

*Arranged by* R. K. Gilpin

**Internal Surface Reversed-Phase HPLC Column: Concepts and Applications.** J. A. Perry, Regis Chemical Co.  
**Developments in LC Columns for Proteins and Related Substances.** F. E. Regnier, Purdue U  
**Applications of Aligned Fiber Columns.** R. K. Gilpin, M. E. Gangoda, Kent State U  
**Developments in Aligned Fiber Column Technology.** R. Beaver, D. Coyne, PPG Industries  
**Adamantyl and Other Novel Nonpolar HPLC Phases.** M. E. Gangoda, R. K. Gilpin, Kent State U

“ The book is rich in content and well written. It is difficult to resist the temptation of reading it all. ”

Dr. Evgeny Shustorovich  
Eastman Kodak Company



# Surface Scientist's Guide to Organometallic Chemistry

“ This book does an excellent job of systematizing available data in the surface science and organometallic literature in an understandable and readable manner. ”

Professor Cynthia Friend  
Harvard University

“ This is the most useful volume for those of us who work in the field of structural surface chemistry. More and more it appears that the cluster bonding is best to describe the nature of the surface chemical bond. This book describes the various cluster bonding possibilities starting with good sound organometallic chemical principles. The book is well written . . . broad, and most useful to those surface chemists who are interested in bonding and applications of bonding to a variety of macroscopic surface phenomena. I am delighted to have this book on my book shelf. ”

Professor Gabor A. Somorjai  
University of California, Berkeley

**W**ithin the field of surface science, concepts from the fields of organometallic and coordination chemistry are becoming more important as a means of understanding chemisorption systems. This valuable resource was written as a means of communicating to surface scientists the aspects of organometallic chemistry that are relevant to current surface science research. This book, divided into three sections, makes relevant organometallic chemistry issues understandable to the surface scientist. Specific topics covered include:

- basic coordination chemistry
- coordination ligands
- bonding sites in clusters and their relationships to surface bonding sites
- application of orbital symmetry and orbital overlap to surface band structure calculations

*Surface Scientist's Guide to Organometallic Chemistry* serves the dual purpose of being both a reference work and an overview of selected aspects of organometallic and coordination chemistry. Surface scientists whose backgrounds include physics, physical chemistry, and engineering will find this book an important addition to the literature of organometallic and coordination chemistry.

by Mark R. Albert and John T. Yates, Jr.

214 pages (1986) Clothbound  
LC 87-25937 ISBN 0-8412-1003-9  
US & Canada \$49.95, Export \$59.95

**Order today!** Mail the coupon below, or call **TOLL FREE** 800-227-5558 and charge your credit card.

## Order Form

Please send me:	Qty.	US & Can.	Export	Total
<i>Surface Scientist's Guide to Organometallic Chemistry</i>	OTB	\$49.95	\$59.95	_____
			Total	_____

Payment Enclosed (make checks payable to ACS).  
 Purchase Order Enclosed. P.O.# \_\_\_\_\_

Charge my  VISA/MasterCard  American Express  
 Diners Club/Carte Blanche  ACCESS  
 Barclaycard

Account # \_\_\_\_\_

Expires \_\_\_\_\_ Interbank # \_\_\_\_\_ (MC/ACCESS)

Cardholder \_\_\_\_\_ Phone # \_\_\_\_\_

Signature \_\_\_\_\_

Name \_\_\_\_\_

Address \_\_\_\_\_

City, State, Zip \_\_\_\_\_

**ORDERS FROM INDIVIDUALS MUST BE PREPAID.**  
Prices subject to change without notice. Please allow 4-6 weeks for delivery. Foreign payment must be made in US currency by international money order, UNESCO coupons, or US bank draft. Order through your local bookseller or directly from ACS.

Mail this order form with your payment or purchase order to:  
American Chemical Society, Distribution Office Dept. 241, P.O. Box 57136, West End Station, Washington, DC 20057

## MEETINGS

### Sensors

**Miniature Fiber-Optic Biosensor for Glutamate Based on Fluorimetric Ammonia Gas Detection.** S. Kar, M. A. Arnold, U of Iowa

**Design of a Fiber-Optic Neodymium pH Sensor.** T. B. Colin, W. C. Stwalley, U of Iowa  
**Acoustic Emission: On Sampling, Sensors, and Signal Interpretation.** A. P. Wade, S. J. VanStyke, I. H. Brock, P. D. Wentzell, U of British Columbia

**Development and Application of a Glutamate-Selective Fiber-Optic Biosensor.** M. A. Stuever, M. A. Arnold, U of Iowa

**Planar Waveguide Optical Sensors.** S. J. Choquette, R. Durst, L. Locascio-Brown, National Institute of Standards and Technology

**Spectrometric Analysis of Samples under Vacuum Using a Diffuse-Reflectance Fiber-Optic Probe.** J. K. Drennen, B. D. Gebhart, R. A. Lodder, U of Kentucky

**Fiber-Optic Probes for Cyanide Using Porphyrins.** M. K. Freeman, L. G. Bachas, U of Kentucky

### TUESDAY MORNING

#### New Developments in Chromatographic Detectors and Systems

Arranged by N. D. Danielson

**Laser Fluorescence and Photoionization Detectors for LC.** V. L. McGuffin, J. W. Judge, Michigan State U

**Flame IR Emission Detection (FIRE) in GC.** M. K. Hudson, T. Fau, R. Henson, K. Underhill, S.

**Appelquist.** Southwest Missouri State U  
**Optical Detection in Capillary Electrophoresis Using Photodiode Arrays.** M. J. Sepaniak, D. F. Swails, U of Tennessee

**Chemiluminescent Detection of Biomolecules Using Tris(bipyridine)ruthenium(II).** N. D. Danielson, Miami U

**Practical Full Bandwidth IR Detector for LC.** J. de Haseth, U of Georgia

**Use of Dichroic Ratios To Determine the Interactions between RPLC Stationary Phases and PAH Solutes.** D. Cropek, P. W. Bohn, U of Illinois

**High-Speed GC System with Recycle Backflush for the Analysis of Common Solvents.** M. Klemp, R. Sacks, S. Levine, U of Michigan

**High-Speed Repetitive GC System for Vapor Analysis.** C. Rankin, R. Sacks, S. Levine, U of Michigan

#### Optical Studies of Ceramics and Semiconductors

**Spectroscopic Studies of Ceramic Binder Decomposition.** R. L. White, A. Nair, U of Oklahoma

**Growth and Characterization of Microwave-Assisted Chemical Vapor Deposited Free-Standing Diamond Films.** W. A. Weimer, C. E. Johnson, China Lake Naval Weapons Center

**Picosecond Transient Absorption Spectroscopy of Semiconductor Colloids.** P. V. Kamat, Notre Dame Radiation Laboratory

**IR Microanalysis of Thermally Sensitive Materials.** S. L. Hill, Digilab Division, Bio-Rad Laboratories

**IR ATR Spectroscopic Studies on Hydrated Dielectric Thin Films.** S. Badilescu, P. V. Ashrit, F. E. Girouard, T. Vo-Van, U of Moncton

**Determination of Optical Constants through Resonant Eigenmode Excitation in High-Speed Semiconductors.** S. R. Kisting, J. E. Maslar, P. W. Bohn, U of Illinois

**Diffuse/Specular Reflectance Measurements of Coatings and Surfaces.** L. Ellis, P. Beauchesne, F. Baudais, Bornem International

**Real-Time Studies of Case II Diffusion in Thin Organic Films with Optical Guided Waves.** N. F. Fell, Jr., P. W. Bohn, U of Illinois

**Characterization of Solids in Three Dimensions by Optical Microscopy.** R. M. Miller, S. Singleton, V. Howard, M. Moss, Unilever Research

#### NMR of Catalysts and Surfaces

Arranged by T. W. Root

**<sup>13</sup>C NMR Studies of Silica-Supported Ru Multicarbonyl Species.** T. M. Durcan, A. M. Thayer, AT&T Bell Laboratories

**Quantum Size Effects and the NMR of <sup>13</sup>CO on Supported Metal Catalysts.** K. W. Zilm, Yale U

**Quantum Size Effects in Catalyst Particles.** D. Durand, C. P. Slichter, U of Illinois

**<sup>13</sup>C High-Resolution NMR Studies of Adsorption and Reaction of Hydrocarbon Molecules on Supported Metal Catalysts.** T. S. King, M. Pruski, J. C. Ketzenberg, B. C. Gerstein, Iowa State U

**Magnetic Resonance Applied to the Study of Zeolites: Xe, <sup>13</sup>C, <sup>2</sup>H, and <sup>1</sup>H Measurements of Adsorbed Material.** C. Dybowski, C. J. Tsiao, J. S. Kauffman, U of Delaware

For Those Involved in the Vital Field  
of Surface and Colloid Chemistry

# Langmuir

The ACS Journal of Surfaces and Colloids

Langmuir is a bimonthly journal of broad coverage that brings together research from all aspects of the field: ultra-high vacuum surface chemistry and spectroscopy, heterogeneous catalysis, and all aspects of interface chemistry involving fluids, and disperse systems.

Langmuir publishes peer-reviewed research in:

- \* "Wet" Surface Chemistry \* "UHV" Surface Chemistry
- \* Disperse Systems \* Electrochemistry
- \* Surface Structure; tunneling electron microscopy

#### EDITOR

Arthur W. Adamson, University of Southern California

#### ASSOCIATE EDITORS

A.T. Hubbard, University of Cincinnati  
R.L. Rowell, University of Massachusetts

1989 Rates	ACS Members*		Non-members 1 year
	1 year	2 years	
U.S.	\$58	\$104	\$376
Can. & Mex.	\$69	\$126	\$387
Europe**	\$74	\$136	\$392
All Other Countries**	\$84	\$156	\$402

\* Member rate is for personal use only.  
\*\* Air service included.

For more information or to subscribe, write:  
American Chemical Society  
Marketing Communications Dept.  
1155 Sixteenth Street, NW  
Washington, DC 20036

**In a hurry?**

**Call Toll Free 1-800/227-5558**



**NMR Studies of Modified Zeolites.** T. Apple, P. Molitor, U of Nebraska

**Hydrodenitrogenation Catalysis over Metal Nitrides.** J. A. Reimer, P. Armstrong, U of California, Berkeley

**NMR Studies of <sup>13</sup>CO Adsorbed on Alkali-Promoted Metal Catalysts.** T. W. Root, D. B. Compton, U of Wisconsin

#### The Graphite Furnace

**Measurement of Atomic Absorption Linewidths in the Graphite Furnace.** T. C. O'Haver, J.-C. Chang, U of Maryland

**Graphite Surface and Gas-Phase Studies of Phosphate Matrix Modifiers for GFAAS.** D. C. Hassell, J. A. Holcombe, U of Texas

**Analyte Losses for Group IIA Elements in GFAAS.** L. J. Prell, D. A. Redfield, D. L. Styris, Pacific Northwest Laboratory

**Optimization of Signal-to-Noise Ratio in GFAAS.** J. A. Holcombe, O. A. Guehl, U of Texas  
**Flow Injection—The Quantum Jump in GFAAS.** B. Weiz, Z. Fang, M. Sperling, Perkin-Elmer and Co. GmbH

**Determination of Arsenic in Nickel-Based Alloys Using FI-HGAAS Incorporating On-Line Matrix Removal.** P. G. Riby, R. Grzeskowiak, S. J. Haswell, Thames Polytechnic, Great Britain

**Determination of Lead in Natural Waters Following Ethylation and In Situ Concentration in a Graphite Furnace.** S. N. Willie, R. E. Sturgeon, S. S. Berman, National Research Council of Canada

**Identification and Effect of Preatomization Losses on the Determination of Aluminum by GFAAS.** D. A. Redfield, W. Frech, Northwest Nazarene College

#### Sample Introduction into Plasmas

Arranged by C. W. McLeod

**Drop Size, Desolvation, and Transport: Is It Blowing Hot and Cold?** R. F. Browner, C. Pan, G. Zhu, Georgia Institute of Technology

**Phase Doppler Technique for Simultaneous Measurements of Drop Size and Velocity Distributions of Aerosols Produced by ICP Nebulizers.** A. Montaser, R. H. Clifford, H. Tan, I. Ishii, George Washington U

**Phase Doppler Laser Anemometry as a New Tool for Aerosol Characterization Spectrometry.** G. Meyer, Dow Chemical

**Aerosol Effects on FIA and HPLC Interfacing to ICP-AES.** J. A. Koropchak, L. Allen, Southern Illinois U

**Samples and Nebulizers, The Inseparable Combination.** B. Sharp, Macaulay Land Use Research Institute

**Improved Analytical Capabilities of Spectrometry Using Sample Introduction Interfaces.** A. Gustavsson, Royal Institute of Technology, Sweden

**Investigation of an Organic Desolvation System in ICP Spectrometry.** C. Pan, G. Zhu, R. F. Browner, Georgia Institute of Technology

#### Automation and Robotics in Biological and Chemical Analysis

Arranged by L. D. Kissinger

**Purdue Automated Synthesis System.** G. Kramer, P. Fuchs, Purdue U

**Lab Automation Using an Industrial Robot.** K. Stelling, W. A. Schmidt, M. F. Fischer, Midwest Research Institute

**Increased Sample Throughput: The Combination of a Robotic Arm with a High-Capacity Overhead Manipulator for Microbiological Vitamin Assay.** J. Zdunek, Kraft

**Emerging Trends in Robotic Dissolution Testing.** E. C. Lewis, T. M. Chen, R. E. Daly, Warner Lambert

**Rotary or Cartesian Robots—Comparison and Contrast.** G. Schoenhard, M. Chang, L. Kosobud, R. Schmidt, G. D. Searle

**Application of Robotics in the Clinical Chemistry Lab.** C. Pippenger, Cleveland Clinic Foundation

**Strategic Opportunities for Automation in the Biotechnology Lab.** G. Hawk, Century International

**Automation and Economic Justification of the Chemical Oxygen Demand Assay for Environmental Samples Using Pyrotechnology Robotics.** L. W. Lindquist, F. X. Dias, B. R. Hill, WMI Environmental Monitoring Laboratories

#### Meggors Award Symposium: Pulsed High-Pressure Liquid Injection of Biological Molecules into Supersonic Beam/MS with Resonant Two-Photon Ionization Detection

Arranged by P. N. Keliher

**Recent Developments in Sample Introduction for MS Using Pulsed High-Pressure Liquid Injection.** D. M. Lubman, U of Michigan

**SFC/Supersonic Jet Spectroscopy.** C. H. Sin, S. R. Goates, K. E. Markides, M. L. Lee, Brigham Young U

**Laser-Enhanced Ionization as a Diagnostic Tool in Laser-Generated Plumes.** H. M. Pang, E. S. Yeung, Iowa State U

**Laser Desorption MS of Biological Materials.** P. Savickas, Dow Chemical

**Reaching Perfection  
in MS and SEM.**

*"A man's reach should  
exceed his grasp..."*  
Robert Browning

Galileo detectors for Mass Spectrometry and Electron Microscopy.

What silicon chips did for computers, Galileo high-performance detectors are doing for GC/MS, MS and SEM analysis.

Whether your projects involve environmental or pharmaceutical analysis, analysis of organic compounds or general spectroscopy applications, a Galileo detector will speed sample identification while providing accurate and precise analysis.

When research projects require frequent sample analysis over a long period of time, you'll want the latest and best technology backing you up. Galileo is the innovator in analytical instrument detectors. If you demand high performance and are concerned about down time, rapid analysis, dynamic range and cost, insist on Galileo scientific detectors. You'll wonder how you ever got along without us.

Write us and ask how to ensure that your instruments have Galileo scientific detectors.

Galileo Electro-Optics Corp.  
Scientific Detector Products Group  
P.O. Box 550, Dept. AA  
Sturbridge, MA 01566  
(508) 347-9191

**GALILEO**  
Galileo Electro-Optics Corp.

CIRCLE 58 ON READER SERVICE CARD

## MEETINGS

**FTMS: Shedding New Light on Old Problems.** R. B. Cody, Nicolet Analytical Instruments  
**Vaporization and Ionization Processes in Particle Beam MS.** R. F. Browner, J. D. Kirk, E. W. Harris, Georgia Institute of Technology

### IR Spectroscopy

**SMATCH/FT-IR (Simultaneous Mass and Temperature Change/FT-IR) Studies of Polymers Undergoing Fast Thermolysis.** T. B. Brill, M. D. Timken, J. K. Chen, U of Delaware  
**LC/FT-IR: Particle Dynamics of the MAGIC Interface.** K. R. Edman, R. F. Browner, J. A. de Haseh, Georgia Institute of Technology  
**MAGIC-LC/FT-IR: No Compromise.** R. M. Robertson, G. K. Ferguson, J. A. de Haseh, R. F. Browner, U of Georgia

**Optimization of Desolvation Parameters for MAGIC-LC/FT-IR Spectrometry.** G. K. Ferguson, J. A. de Haseh, R. F. Browner, U of Georgia  
**Studies of Enantioselective Interaction in Chiral Separations by FT-IR Spectrometry.** X.-J. Lu, L. B. Rogers, J. A. de Haseh, U of Georgia  
**Advances in FT-IR Spectroscopy Using Photoacoustic Detection.** J. F. McClelland, R. W. Jones, Iowa State U

**FT-IR, NMR, and Thermal Studies of Mesogenic Compounds in Contact with Chemically Modified Surfaces.** C. J. Hann, M. E. Gangoda, R. K. Gilpin, Kent State U

**New Measurement Technique for Highly Scattering Samples in FT-IR Spectroscopy.** M. Kaihara, H. Marnetasuka, N. Gunji, Y. Gohshi, NKK Corp. (Nippon Kokam)

**Investigation of Spectral Interferences in Digitally Filtered FT-IR Interferogram Data.** A. S. Barber, G. W. Small, U of Iowa

### Analysis of Organic Compounds in the Environment

*Arranged by R. A. Hites*

**Determination of Ionic Pesticide Residues in Foods by Ion-Pair HPLC.** D. M. Gliviydis, T. M. Chichila, S. M. Walters, U.S. FDA

**Application of Particle Beam LC/MS Systems to Environmental Analysis.** T. D. Behymer, T. A. Bellar, W. L. Budde, U.S. EPA

**Environmental Applications of Open Tubular LC/MS.** K. B. Tomer, National Institute of Environmental Health Sciences

**Application of MS/MS for the Rapid Analysis of Organic Contaminants in Environmental Samples.** E. T. Furlong, U.S. Geological Survey

**Analysis of Halogenated Dibenzo-*p*-dioxins and Dibenzofurans by Hybrid MS.** M. J. Charles, G. D. Marbury, B. N. Green, V. G. Tondeur, J. R. Hass, U of North Carolina

**Gas-Phase and Surface-Catalyzed Reactions of PAH in Negative Ion Chemical Ionization MS.** E. A. Stemmler, M. V. Buchanan, Bowdoin College

**Isolation and Identification of Anthropogenic Chemical Contaminants in Marine Mammals.** D. W. Kuehl, B. C. Butterworth, P. Marquis, E. Lundrmark, M. Larson, L. Holland, J. Lindberg, U.S. EPA

**Absorption Characteristics of Atmospheric Polychlorinated Biphenyls by Tree Bark.** M. H. Hermanson, R. A. Hites, Center for Great Lakes Studies

### Electroanalysis in Gases, Solids, Fluidized Beds, and Supercritical Fluids

*Arranged by D. R. Rolison*

**Fluidized Beds and Related Electrode Structures.** M. Fleischmann, The University, Southampton, Great Britain

**Fluidized-Bed Electrochemistry and the Characterization of Particles and Electrolyte With In Situ Indicator Electrodes.** J. W. Evans, F. M. Doyle, U of California  
**Dispersion Electrolysis at Nanometer-Sized Electrodes.** D. Rolison, Naval Research Laboratory

**Electrochemistry in the Gas Phase.** S. Pons, U of Utah

**Solid-State Electrochemistry: Use of Poly(ethylene oxide) as a Polymer Electrolyte Solvent.** M. L. Longmire, M. Watanabe, R. W. Murray, U of North Carolina

**Solid-State Voltammetric Measurements and Polymer Electrolyte Plasticization as a Basis for an Electrochemical Gas-Liquid Chromatography Detector.** C. J. Barbour, J. F. Parcher, R. W. Murray, U of North Carolina

### Certification and Use of Reference Materials: An Overview of International Programs

*Arranged by M. S. Epstein*

**Marine Certified Reference Materials: The Fishy Side of the Business.** S. Berman, National Research Council of Canada

**NIES Certified Reference Material Program: The First Decade.** K. Okamoto, National Institute for Environmental Sciences, Japan

**Certification of Reference Materials at NIST (NBS).** S. D. Rasberry, National Institute of Standards and Technology

**Standards in Microanalysis.** R. A. Velapoldi, D. E. Newbury, National Institute of Standards and Technology

### Molecular Fluorescence Spectrometry

**Molecular Fluorescence Spectrometer That Corrects for the Effects of Quenching.** L. E. Bowman, S. R. Crouch, Michigan State U

**Compact Photodiode Array Fluorescence Spectrophotometer for HPLC.** J. Wegryzn, M. Ford, I. M. Warner, Emory U

**Fluorescence Detection with a Charge-Coupled Device Detector.** K. J. Rubelowsky, R. Kaminski, Spex Industries

**Time-Resolved Fluorescence Microscopy Using Multichannel Photon Counting and CCD Detection.** D. M. Coleman, W.-X. Feng, T. Uchida, S. Minami, Wayne State U

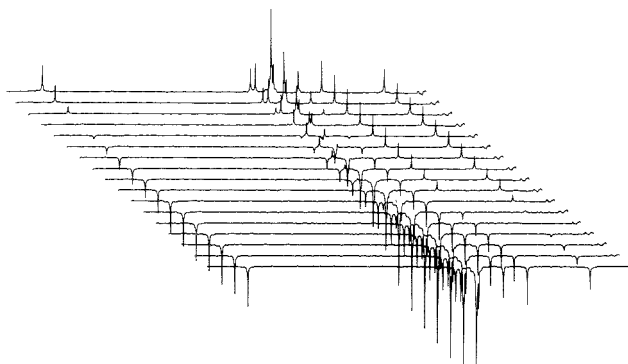
**Electrogenerated Chemiluminescence Detection Using Immobilized Tris-(2,2'-bipyridine) Ruthenium(II).** T. Downey, T. A. Nieman, U of Illinois



Chicago's historic Water Tower on the Magnificent Mile.

CHICAGO: TORRES/ALAN ROSE/SIPA

# Search spectra online



## C13-NMR/IR Now available on STN®

Now there's a new way to identify chemical substances online through their CNMR or IR spectra. Discover the Carbon 13 Nuclear Magnetic Resonance/Infrared file and see how invaluable it can be in your research!

### The file and its sources

In C13-NMR/IR you'll find almost 120,000 spectra for 90,000 compounds. Data are drawn from significant journals, spectral catalogs, and unpublished spectra from BASF and other industrial labs.

**The workshop** Not familiar with searching spectra online? Our workshop shows

you how to

- find spectra by searching a substance name or molecular formula
- predict a C13 spectrum or shift
- find exact or similar structures
- find substances using CAS Registry Numbers

**How to get started** The C13-NMR/IR file is available only through the STN International network. If you're already an STN user, arrange access to C13-NMR/IR by calling Customer Service at 800-848-6538 or 614-447-3600. If you aren't yet using STN, return the enclosed coupon.

**Yes!** I'd like more information about C13-NMR/IR on STN International. Please rush me my FREE information package.

Name \_\_\_\_\_

Organization \_\_\_\_\_

Address \_\_\_\_\_

Phone \_\_\_\_\_

Mail to: STN International, c/o Chemical Abstracts Service,  
Dept. 38389, P.O. Box 3012, Columbus, OH 43210 U.S.A.

In Europe, contact STN International c/o FIZ Karlsruhe, P.O. Box 2465,  
D-7500 Karlsruhe 1, Federal Republic of Germany. Telephone: (+49)  
7247/808-555.



**STN®**  
INTERNATIONAL  
The Scientific & Technical  
Information Network

*STN is operated in North America by Chemical Abstracts Service, a division of the American Chemical Society; in Europe, by FIZ Karlsruhe; and in Japan, by JICST, the Japan Information Center of Science and Technology.*

**Studies on the Luminal Reaction with Various Metallo-catalysts.** T. A. Nieman, U of Illinois

**Investigation of Microscopic Solute Interactions with Mixed Solvent Systems.** G. J. Blanchard, Bell Communications Research

**Industrial Use of the Fluorescence Microscope.** D. A. Krueger, Dow Chemical

**Liquid-Liquid Extraction and Molecular Absorption Spectrophotometric Determination of Neodymium with 5,7-Dichlorooxine and Rhodamine 6G.** T. P. Rao, V. Bhagavathy, M.L.P. Reddy, A. D. Damodaran, CSIR, India

**Supercritical Fluid and Ion Chromatographies**

**Determination of Toluene Diisocyanates in Polyurethane Prepolymers Using Capillary SFC.** R. G. Ridgeway, Jr., A. R. Bandy, J. R. Quay, P. J. Marouli, Drexel U

**Supercritical Fluid/Supersonic Jet Spectroscopy with a Sheath Flow Nozzle.** S. R. Goates, C. H. Sin, M. R. Linford, Brigham Young U

**Optimization of Gas-Phase Detectors for SFC.** D. J. Bornhop, J. G. Wangsgaard, N. L. Porter, B. E. Richter, Lee Scientific

**Evaluation of a He-HEMIP as a Detector for SFC.** C. B. Motley, G. L. Long, Virginia Polytechnic Institute and State U

**Application of Supercritical Fluid Extraction as a Sample Preparation Tool for Environmental Problems.** R. Houck, M. L. Kumar, A. Rosselli, D. Boyer, Suprex

**Separation of Hf from Zr in Geologic Materials by Extraction Chromatography.** J. C. Cousins, C. M. Johnson, U of Wisconsin

**Effect of Operational Variables on the Efficiency of Ion Chromatographic Separations.** D. R. Jenke, Baxter Healthcare

**UltraTrace Analysis of Inorganic Anions in N-Methylpyrrolidone by Preconcentration High-Performance Ion Chromatography.** R. M. Ianniello, GAF Chemicals

**Spectroscopic Instrumentation in Process Analytical Chemistry**

*Arranged by G. Meyer and F. DeThomas*

**Raman and Near-IR Spectroscopies as Noninvasive Techniques for Process Analytical Chemistry.** J. B. Callis, D. A. Mayes, D. B. Dahlberg, U of Washington

**Argon/Helium ICP for Process Control.** R. Romanoski, U.S. DOE

**On-Line Analysis Is Elemental with XRF: Technology, Applications, and Case Studies.** R. Ramamujam, D. Kalinicky, Princeton Gamma-Tech

**Continuous Real-Time Monitoring of Airborne Metals Using an Inductively Coupled Air Plasma Spectrometer.** M. D. Seltzer, R. B. Green, China Lake Naval Weapons Center

**Applications of a Photodiode Array Spectrometer to Process Control.** R. S. Saltzman, Du Pont

**On-Line IR for Measuring Polymer Coatings on Aluminum.** C. Dobbs, J. Szalanski, K. Bowman, Alcoa

**Developments in the Use of Near-IR Spectrophotometers for Process/Product Control.** T. Hosegood, Du Pont

**Moisture Measurements in a Powdered Pharmaceutical Using a Fluidized Bed Dryer with a Novel Sampling Device.** M. Gardell, Moisture Systems

**Variable Matrix Problems in Process Control.** L. Weyer, Hercules

**Single-Fiber Near-IR Measurements Using a Grating Instrument.** D. Honigs, Pacific Scientific

**TUESDAY AFTERNOON**

**Laser-Based Molecular Spectroscopy**

*Arranged by T. Vo-Dinh*

**Laser-Induced Ionization Spectroscopy of Small Biological Molecules in Supersonic Beams.** D. M. Lubman, U of Michigan

**Nonlinear Laser-Excited IR Absorption as an Added Dimension for Speciation.** S. E. Bialkowski, G. R. Long, Utah State U

**Linear and Nonlinear Spectroscopy of Surface Adsorbates.** J. K. Steehler, U of Virginia

**Uranium Analysis Using Time-Resolved Laser Luminescence with Evaluation of Interferences.** D. Eastwood, R. L. Lidberg, A. Miller, Lockheed Engineering Sciences Co.

**Environmental Analysis with High-Resolution Spol'skii Spectroscopy.** J. W. Hofstraat, DGW, The Hague

**Analysis of Multicomponent Samples by Thermal Lens Techniques.** C. D. Tran, Marquette U

**Analytical Laser Spectroscopy of Nitrogen Oxides over Aging Solid Nitric Esters.** C. J. Seliskar, D. J. Schneider, L. R. Dossier, U of Cincinnati

**Laser-Induced Fluorescence Determination of Drugs at Picogram-per-Milliliter Concentrations in Plasma.** T. G. Nolan, C. H. Kiang, B. L. Huang, Syntex

**Deducing Molecular Structures Using Lasers and MS.** M. V. Johnston, U of Colorado

**Organic Films and Polymers**

**Fluorescence Photobleaching in the Study of Surface Diffusion and Deposition.** R. M. Miller, J. J. Birmingham, Unilever Research

**Use of FT-IR Spectroscopy in Polymer Chemistry.** D. Prakash, Detroit Edison Co.

**Characterization of Dynamic Systems Using CCD Cameras.** R. M. Miller, S. C. Joyce, S. Singleton, G. M. Hieftje, C. Monnig, Unilever Research

**Investigation of Polymer Kinetics with IR Fiber Optics.** J. E. Andrews, J. A. de Haseth, U of Georgia

**Nondestructive Three-Dimensional Surface Characterization of High-Refractive-Index Polymers.** R. J. Samuels, R. E. Pepper, Georgia Institute of Technology

**Direct Pyrolysis/FT-IR for Polymer Analysis.** J. W. Washall, T. P. Wampler, CDS Instruments

**FT-IR Analysis of Nylon-6 Chain Conformations.** G. E. Rotter, H. Ishida, Case Western Reserve U

**Dynamic Monitoring of Chromophore Distribution Using Thermal Wave Spectroscopy.** R. M. Miller, S. A. Johnson, Unilever Research

**Study on the Effect of CaZn Stabilizer on Thermal Stability of PVC.** A. M. Aitani, J. H. Khan, S. H. Hamid, King Fahd U of Petroleum and Minerals

**Biological Applications of NMR**

*Arranged by A. C. Bach*

**Structure-Activity Relations in Catalytic RNAs.** A. Pardi, H. Heus, O. C. Uhlenbeck, U of Colorado

**Synthesis and Conformational Analysis of Cyclosporin A Analogs.** D. H. Rich, D. Guillaume, J. Aebi, D. Deyo, C. Q. Sun, K. Miller, U of Wisconsin, Madison

**Solution Structure of Transforming Growth Factor-Alpha by NMR Methods.** L. Mueller, S. C. Brown, T. T. Kline, F. K. Brown, J. C. Hempel, SmithKline and French Laboratories

**Isotope Edited Proton NMR Studies of Enzyme/Inhibitor Complexes.** S. W. Fesik, E. R. Zunderweg, R. T. Grampe, Jr., E. T. Olejniczak, Abbott Laboratories

**MS**

**Ion Dissociation Studies with a Tandem Time-of-Flight Fourier Transform Mass Spectrometer.** D. A. Laude, Jr., S. C. Beu, D. Riegner, U of Texas, Austin

**Organic Analysis of Individual Meteorite Inclusions by Two-Step Laser MS.** R. Zenobi, Stanford U

**Fourier Transform Ion Cyclotron Resonance MS Study of the Gas-Phase Reactions of Nb<sup>+</sup> and Rh<sup>+</sup> with Alcohols.** J. R. Gord, S. W. Buckner, J. H. Ng, A. Chen, B. S. Freiser, Purdue U

**Phase Synchronization of an Ion Ensemble by Frequency Sweep Excitation in Fourier Transform Ion Cyclotron Resonance.** C. Hanson, M. E. Castri, D. H. Russell, Texas A&M U

**Progress Toward a Perfect Ion Trap for Fourier Transform Ion Cyclotron Resonance MS.** M. Wang, A. G. Marshall, Ohio State U

**Comparison of Activation Methods: The Fe<sup>+</sup>-Nitrile System.** L. M. Roth, B. S. Freiser, Purdue U

**Physical and Chemical Properties of Se<sup>+</sup>-Benzene in the Gas Phase.** Y. D. Sun, Y. Huang, B. S. Freiser, Purdue U

**Improved Resolution in Time-of-Flight MS/MS.** S. M. Colby, J. P. Reilly, Indiana U

**Gas-Phase Ion Chemistry of AgFe<sup>+</sup>: Reactivity with Small Hydrocarbons and Absorption and Binding Characteristics.** J. H. Ng, J. R. Gord, B. S. Freiser, Purdue U

**Molecular Ionization in Hyperthermal Supersonic Molecular Beams: A Novel Mass Spectrometric Approach.** A. Amirav, A. Danon, Tel Aviv U

**Sample Introduction into Plasmas**

*Arranged by C. W. McLeod*

**Automated Liquid and Direct Solid Sampling in Mixed-Gas ICP Spectrometry.** K. Ohls, Hoeschstaht AG, FRG

**ICP Spectrometry: The Merits of Flow Injection and Laser Ablation.** C. W. McLeod, Sheffield City Polytechnic, Great Britain

**Low-Cost Ultrasonic Nebulizer for Plasma Spectrometry.** R. H. Clifford, A. Montaser, George Washington U

**Analysis of Biological Material by ICP-AES Employing Ultrasonic Nebulization for Sample Introduction.** F. D. Bulman, D. D. Nygaard, Baird Corp.

**Enhancement Techniques for Detection of Iodine in Foods by ICP Spectrometry.** S. A. Sinex, S. G. Capar, A. Montaser, R. H. Clifford, U.S. FDA

**Hybrid Thermospray Nebulizers for Sample Introduction to ICP-AES.** J. A. Koropchak, S. Majumdar, Southern Illinois U

**Testing and Performance of Crossflow Nebulizers for ICP Spectrochemistry.** J. Ivaldi, W. Slavin, Perkin-Elmer

**Lester Stock Award Symposium: New Developments in Optical Spectrometry with Glow and Sputtering Discharges**

*Arranged by G. M. Hieftje*

**Glow Discharge FT-AES.** G. Horlick, Y. Shao, U of Alberta

**Trends of Development in Glow Discharge Optical Emission Spectrometry.** J. A. Broekaert, G. M. Hieftje, Institut für Spectrochemie, FRG

**Dissociation of Oxide Analyte Species in Glow Discharge Devices.** R. K. Marcus, M. R. Winchester, Clemson U

**Use of a Solid-State Photodetector Array for Glow Discharge AES.** K. R. Brushwyler, G. M. Hieffje, Indiana U

**Jet-Enhanced Glow Discharge for Atomic Absorption and Emission.** E. H. Piepmeier, H. J. Kim, C. E. Crandall, A. E. Bernard, Oregon State U

**Characterization of a Jet-Assisted Glow Discharge for AES.** M. W. Blades, P. Banks, U of British Columbia

**Planar Magnetron Glow Discharge for Atomic Spectroscopy at Millitorr Pressures.** L. McCaig, N. Sesti, R. Sacks, U of Michigan

#### Electroanalysis in Gases, Solids, Fluidized Beds, and Supercritical Fluids

*Arranged by* D. R. Rolison

**Electrochemistry in Frozen Electrolytes.** Z. Borkowska, L.-P. Cheng, E. Kriegsmann, U. Stimming, Columbia U

**Oxygen Reduction at Perfluorosulfonate Ionomer Film-Coated Ultramicroelectrodes: Transport and Kinetics.** A. Parthasarathy, C. R. Martin, Texas A&M U

**Electrochemistry in Supercritical Fluids.** R. M. Crooks, E. Garcia, C. R. Cabrera, A. J. Bard, MIT

**Gas-Phase and Solid-State Electrochemistry Using Zeolite Matrices at Elevated Temperatures.** K. E. Creasy, B. R. Shaw, U of Connecticut

**Hydration Effects in Ion Conduction on Clay-Modified Electrodes.** A. Fitch, S. A. Lee, Loyola U of Chicago

**Electrochemistry in Water Tubules and Oil Phases of Bicontinuous Microemulsions.** J. F. Rusling, M. Iwunze, U of Connecticut

**Microinterface—An Answer to Microelectrodes in Electrochemistry on Immiscible Liquid Interfaces.** I. C. Hernandez, P. Vanysek, Northern Illinois U

#### IR Spectroscopy

**Quantitative Analysis of Digitally Filtered FT-IR Interferograms.** J. M. Bjerga, G. W. Small, U of Iowa

**Quantitative Analysis of Single Copolymer Fibers Using IR Microscopy.** E. G. Bartick, M. W. Tungol, A. Montaser, FBI Academy

**Chemical Kinetics of Triplet Methylene from Tunable IR Diode Laser Flash Kinetic Spectroscopy.** D. Darwin, U of California

**Detection of Transient Species Produced in a Thermal Plasma by IR Spectroscopy and MS.** N. W. Currier, A. G. Severdia, G. A. Totten, Pitman-Moore

**Matrix-Isolation IR Spectroscopy of Mass Selected Ions.** R. L. White, R. E. Fields III, U of Oklahoma

**Comparison of the Analytical Utility of IR Emission, Absorption, and Fluorescence from Combustion Flames.** D. C. Tiliotta, M. A. Busch, K. W. Busch, Baylor U

**Theoretical Investigation of IR Emission from Combustion Products in Hydrogen/Air Flames.** D. C. Tiliotta, C. Lam, M. A. Busch, K. W. Busch, Baylor U

**Principal Component Regression Analysis of Polyurethane Plaques Using Attenuated Total Reflectance Spectra.** J. W. Sherman, G. K. Ferguson, J. A. de Haseth, U of Georgia

**In Situ IR Chemical Analysis: A Progress Report.** W. M. Doyle, B. C. McIntosh, Axiom Analytical

#### Environmental Applications of ICP Atomic Emission and Mass Spectrometry

*Arranged by* F. L. Fricke

**Alternative Sources for Plasma MS.** J. A. Caruso, J. Creed, T. M. Davidson, B. Sheppard, W. L. Shen, U of Cincinnati

**Comparison of ICP/MS and ICP-ES for the Analysis of Environmental Samples.** S. E. Long, E. Martin, T. D. Martin, U.S. EPA

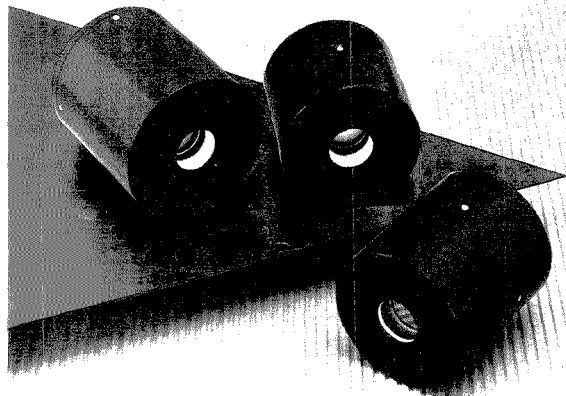
**Investigation of a Tangential Flow Torch with Coupling Probe Injector for Microwave-Induced Plasma MS.** R. D. Satzger, T. W. Brueggemeyer, F. L. Fricke, U.S. FDA

**Applications of a Low-Power Low-Flow ICP to the Analysis of Complex Matrices.** D. G. Goightly, F. B. McGee, A. S. Szabo, Ross Laboratories

**Constant-Pressure Microwave Oven Digestion of Inorganic Analysis Samples.** D. W. Mincey, R. C. Williams, Youngstown State U

**Reduced-Pressure Helium ICP as a GC Detector.** C. Story, J. Caruso, K. Wolnik, F. L. Fricke, U of Cincinnati

## Ultimate Detector: 300 psec for < \$15K with single photon sensitivity!



That's the beauty of our ultra high speed MCP-PMT's.

Hamamatsu microchannel plate Photomultiplier Tubes (MCP-PMTs) offer a broad spectral response, using various cathodes and windows from 115 to 1500 nm,\* with rise times of less than 150 psec. Some tubes feature an IRF faster than 30 psec.\* plus a dynamic range greater than  $10^5$ .\* Gatable types can switch >4 decades with <3 nsec. rise time, using low gate voltages. Multianode configurations are also available.

These affordably priced tubes are ideal for making optical measurements in a variety of studies, including:

- Analog/Phase Fluorescence Decay
- Time Correlated Photon Counting (T.C.P.C.)
- Laser Radar Research (L.R.)
- Optical Communications (O.C.) at 1.3 or  $1.5\mu\text{m}^*$
- Synchrotron Radiation (S.R.)
- Other fast timing applications

\*Measured in TCPC mode.

For application information call David Fattowitz, Special Image Tubes Product Line Manager, at 1-800-524-0504, 1-201-0960 in New Jersey.

# HAMAMATSU

HAMAMATSU CORPORATION • 360 FOOTHILL ROAD P O BOX 6910 BRIDGEWATER, NJ 08807 • PHONE 201/231-0960  
UNITED KINGDOM: Hitachi International(UK) Ltd (phone: 0992-789090) • FRANCE: Hamamatsu Photonics France (phone: 46 55 47 50)  
ITALY: Ivesis S. P. A. (phone: 02/34 52 679) • GERMANY: Hamamatsu Photonics Deutschland GmbH (phone: 09165-319-0)  
SWEDEN, NORWAY, FINLAND, DENMARK: Lambda Electronics AB (phone: 08-620610) • JAPAN: Hamamatsu Photonics K.K.

© 1988, Hamamatsu Corporation

CIRCLE 63 ON READER SERVICE CARD

**Modeling of Inorganic Ion Distribution in the Mahoning River.** D. W. Mincey, S. C. Martin, L. A. Schroeder, Youngstown State U

**Application of ICP to the Analysis of Brines.** J. D. Hwang, G. D. Guenther, J. P. Diomigiuardi, H. P. Huxley, W. J. Vaughn, Occidental Chemical

**Bioanalytical Chemistry**

**Use of a Biochemical Oscillator for Quantitative Analysis.** D. L. Olson, A. Scheeline, U of Illinois

**Protein Conformational Effects in Reversed-Phase HPLC: A Direct Spectroscopic Investigation.** A. W. Grobin, C. H. Lochmuller, Duke U

**Determination of Amphotericin-B in Plasma by Reversed-Phase HPLC.** A. M. Rustum, Abbott Laboratories

**LC Analysis of Amphetamines and Related Compounds in Forensic Samples.** F. T. Noggle, Jr., C. R. Clark, J. DeRuiter, Alabama Dept. of Forensic Sciences

**Improving the Detection Limits of Enzyme Immunoassays through the Use of Modified Binders.** L. G. Bachas, M. Barbarakis, S. Daunert, U of Kentucky

**Measurement of Interstrand Distances Using Bis-Analytes.** R. S. Readnor, W. H. Pirklie, U of Illinois

**Electric Birefringence Densitometry of DNA.** M. Lanan, R. A. Shick, S. Parus, M. D. Morris, U of Michigan

**Properties and Applications of Analyte Velocity Modulation Capillary Electrophoresis.** C.-Y. Chen, M. D. Morris, U of Michigan

**Electric Birefringence Frequency Dispersion of Unseparated DNA Restriction Fragments.** R. A. Shick, M. Lanan, S. J. Parus, M. D. Morris, U of Michigan

**Certification and Use of Reference Materials: An Applications Workshop**

*Arranged by M. S. Epstein*

**Combining Data from Independent Chemical Analysis Methods.** S. Schiller, K. Eberhardt, National Institute of Standards and Technology

**Use of Standard Reference Materials in ICP and AAS Quality Assurance Programs.** R. L. Waters, Jr., National Institute of Standards and Technology

**Use of Ion Chromatography for the Certification of Anions in Standard Reference Materials.** W. F. Koch, National Institute of Standards and Technology

**Sample Preparation of Standard Reference Materials for Atomic Spectroscopy Analyses.** T. C. Rains, T. A. Butler, T. A. Rush, National Institute of Standards and Technology

**"Independent Method" Concept for Certifying Reference Materials. How Realistic?** M. Epstein, National Institute of Standards and Technology

**Analysis of High-Temperature Materials**

*Arranged by F. R. Preli, Jr., and J. Brenner*

**Requirements for Modern Physicochemical Analysis: High-Temperature-Resistant Materials and Structural Ceramics for Use in High-Temperature and Fusion Reactors.** H. Nickel, Nuclear Research Center

**Evaluation of Mixed Gas Plasmas for the Analysis of Refractory Slurries.** I. B. Brenner, G. L. Long, Virginia Polytechnic Institute and State U

**New Approaches to the Analysis of Refractory Ceramics Using the Glow Discharge.** R. Avni, Negev Center for Nuclear Research

**Application of Laser Sampling ICP/MS to the Analysis of High-Temperature Materials.** R. D. Ediger, E. Denoyer, E. Pruszkowski, J. Hagar, Perkin-Elmer

**Determination of Boron and Silicon in High Refractory Metals by Solid Sampling ICP.** F. Preli, Jr., J. P. Dougherty, Pratt and Whitney Aircraft

**Trace Element Analysis of Alumina by GFAAS.** J. Genna, M. Ruschak, J. Stobel, Alcoa Technical Center

**Trace Element Analysis of Nickel-Based Alloys by Laser-Excited Atomic Fluorescence Spectrometry in a Graphite Furnace with Solid Sampling.** J. Takahashi, G. T. Wei, R. L. Irwin, R. G. Michel, U of Connecticut

**Raman Spectroscopy**

*Arranged by T. M. Cotton*

**Surface Raman Spectroscopy in the Study of Electrochemistry.** J. Pemberton, R. L. Sobocinski, D. A. Carter, M. A. Bryant, U of Arizona

**Hadamard Raman Microscopy.** M. D. Morris, P. J. Treado, U of Michigan

**FT Raman Spectroscopy of Biological Assemblies.** I. W. Levin, E. N. Lewis, NIH  
**Dynamics and Reactivity in Hemoglobin: Time-Resolved Raman Studies.** J. M. Friedman, AT&T Bell Laboratories

**Surface-Enhanced Resonance Raman Scattering of Heme-Containing Proteins at Low Temperatures.** V. Schlegel, T. M. Cotton, U of Nebraska, Lincoln

**Spectroscopic Instrumentation in Process Analytical Chemistry**

**Rugged Multiwavelength, Near-IR Analyzer for In-Line Process Measurements.** T. Hyvarinen, J. Malinen, Technical Research Centre of Finland  
**On-Line IR Spectroscopy of Solid Materials in Motion.** R. W. Jones, J. F. McClelland, Iowa State U

**Process FT-IR Spectroscopy—Progress and Potential.** B. McIntosh, D. Peters, Laser Precision Analytical

**Applications of Discriminant Analysis in the Mid-IR.** D. Kuehl, J. Duckworth, Galactec Industries

**Oil Concentrations in "Dirty" Oil-in-Water Emulsions as Determined by Quantitative Near-IR Transflectance Spectroscopy.** K. R. Carduner, A. Ellert, D. L. Wetzel, R. S. Marano, Ford Motor Co.

**Tar Sands Process Analysis Using a Fiber Optic Coupled Spectrometer.** P. Beauchesne, J. Giroux, E. Migneault, G. Tremblay, H. Buijs, F. Baudais, Bomem International

**Quality Control of Amine-Activated Epoxies by IR Microscopy.** D. J. Johnson, S. L. Hill, Digilab Division, Bio-Rad Laboratories

**Poster Session**

**AAS, Biotechnology/Biomedical/Pharmaceutical/Clinical, Chromatography, Molecular Optical Spectroscopy, IR Spectroscopy, Raman Spectroscopy, NMR**

**WEDNESDAY MORNING**

**Laser-Based Molecular Spectroscopy**

*Arranged by T. Vo-Dinh*

**FT Raman and Wavelength-Dependent Sensors.** D. B. Chase, B. Parkinson, Du Pont  
**Ultrasensitive Detection of Molecular Species by Surface-Enhanced Raman Microscopy.** J. J. Laserna, S. Sutherland, J. D. Winefordner, U of Málaga, Spain

**Quantitative Resonance Raman Spectroscopy.** T. J. Vickers, C. K. Mann, Florida State U

**Near-IR Surface-Enhanced Raman Spectroscopy.** S. M. Angel, M. L. Myrick, Lawrence Livermore National Laboratory

**Fiber-Optic Surface-Enhanced Raman Spectroscopy for Environmental Monitoring.** M. M. Carrabba, R. B. Edmonds, P. J. Marren, R. D. Rauh, EIC Laboratories

**Surface-Enhanced Raman Spectroscopy of Biomolecules.** R. L. Garrell, U of Pittsburgh

**Surface-Enhanced Raman Spectroscopy for Chemical and Biological Analysis.** T. Vo-Dinh, J. Belto, D. Stokes, Oak Ridge National Laboratory

**Characterization of a Polydiacetylene by Coherent Inverse Raman Scattering: The Phonon-Mediated Optical Stark Effect.** G. J. Blanchard, J. P. Heritage, A. C. Von Lehmen, M. K. Kelley, G. L. Baker, S. Etemad, Bell Communications Research

**Absorption Effects in Fully Resonant Coherent Four-Wave Mixing Spectroscopy.** R. J. Carlson, J. C. Wright, U of Chicago

**Electroanalysis of Films and Surfaces**

*Arranged by A. Wieckowski*

**Direct Imaging of Surface Structures by Angle-Dependent Auger Microscopy.** A. T. Hubbard, U of Cincinnati

**Recent Advances in Surface Laser Spectroscopy.** R. P. Van Duyn, Northwestern U

**Raman Spectroscopy of Chemically Modified Electrodes.** T. M. Cotton, U of Nebraska

**Time-Resolved FT-IR Spectroscopy at Single Crystal Electrode Surfaces.** M. J. Weaver, Purdue U

**Spectroscopic and Chemical Studies of Organic Thin Films.** R. G. Nuzzo, AT&T Bell Laboratories

**How To Build Structured, Multicomponent Polymer Films on Electrode Surfaces.** J. T. Hupp, Northwestern U

**Open Discussion: Thin Films and Surfaces—Significance, Methods, Focus, and Common Concepts.** L. R. Faulkner, U of Illinois

**Magnetic Resonance in Polymers**

*Arranged by F. D. Blum*

**Deuterium Quadrupole Coupling Constants and the Origin of a Karplus-Type Relationship for Measuring Torsion Angles.** L. G. Butler, Louisiana State U

**Analysis of Free-Radical Species in Maleimides and Bismaleimide Resins Using ESR Spectroscopy.** T. C. Sandreczki, I. M. Brown, McDonnell Douglas Research Laboratory

**NMR Characterization of Protein/Starch Composites.** J. Garbow, J. Schaefer, Monsanto

**<sup>31</sup>P NMR Studies of Polymer Additive Degradation.** A. J. Brandolini, R. E. Truitt, Mobil Chemical Co.

**Solvent Self-Diffusion and Free Volume in Concentrated Polymer Solutions.** R. A. Waggoner, F. D. Blum, U of Missouri, Rolla

**NMR Studies of Compositional Heterogeneity in Copolymers.** H. N. Cheng, Hercules

**Magnetic Resonance of Polyethylene: A New Look at an Old Friend.** C. Dybowski, J. S. Kauffman, U of Delaware  
**NMR Studies of Pressure Effects on Polymer Dynamics.** P. Smith, Dow Chemical

#### GFAAS—Solids and Slurries

Arranged by K. W. Jackson

**Solid and Slurry Sampling in GFAAS—Is It Worth the Effort?** B. Welz, M. Sperling, Bodenseewerk Perkin-Elmer and Co. GmbH  
**Determination of Pb in Soil by Slurry GFAAS with a Fast-Temperature Program.** M. W. Hinds, K. Allen, K. W. Jackson, U of Saskatchewan  
**Quantitative Determination of Au in Blood Plasma of Individuals Treated with Au(I) Drugs Using Zeeman-Corrected GFAAS: Calibration with Solid Standards.** T. Alavosus, Baird Corp.  
**Analytical Errors Unique to Slurry Samples.** J. A. Holcombe, V. Majidi, U of Texas  
**Effects of Charring on Particle Distribution and Atomization Characteristics in Slurry ETAAS.** K. W. Jackson, H. Qiao, SUNY  
**Slurry Sample Preparation for the Determination of Trace Metals.** N. J. Miller-Ihli, U.S. Dept. of Agriculture  
**Rapid Analysis of Fly Ash for Arsenic and Selenium by GFAAS with Slurry Sample Introduction.** D. K. Bradshaw, W. Slavin, Perkin-Elmer  
**Rapid Method for Determination of Gallium and Germanium in Solid Samples by Flame AAS.** R. A. Davidson, D. D. Hammargren, D. D. Harbuck, U.S. Bureau of Mines

#### Excitation Mechanisms in Plasmas

Arranged by J. M. Mermet

**Criterion for LTE in ICP and Consequences on Analytical Results.** J. M. Mermet, U of Lyon  
**Deviations from LTE for the ICP—Measurement and Interpretation.** M. W. Blades, L. L. Burton, U of British Columbia  
**Comparison of LTE and Experimental Behavior in ICPs.** J. W. Olesik, S.-J. Den, L. M. Chen, U of North Carolina  
**Toward an Understanding of the Easily Ionized Element Effect in ICP Spectrometry.** G. M. Hieftje, M. Huang, C. Monnig, P. Yang, U of Indiana  
**Non-LTE Effects in Induction Plasma Modeling.** J. Mostaghimi, M. I. Boulos, U of Sherbrooke  
**Theory and Practice of Common Gas ICP Discharges.** R. M. Barnes, U of Massachusetts  
**Fundamental Studies of ICPs by MS and Vacuum UV Spectroscopy.** R. S. Houk, D. R. Wiederin, J. S. Crain, H. B. Lim, Iowa State U

#### Biomedical Applications of Recent Analytical Chromatographic Techniques

Arranged by L. A. Kaplan

**Biomedical Applications of Microbore HPLC.** T. Annesley, U of Michigan  
**Biomedical Applications of SFC.** S.H.Y. Wong, U of Connecticut Health Center  
**Biomedical Applications of LC/MS.** C. Stacy, Waters Corp.  
**Biomedical Applications of a Secondary Ion Mass Spectrometer (SIMS) Detector for HPLC.** K. Busch, Indiana U

#### ANACHEM Award Symposium: Looking to the Future—A Symposium for Young Analytical Faculty

Arranged by S. R. Crouch

**Macromolecule-Surface Interactions Probed by Surface-Enhanced Raman Spectroscopy.** R. Garrell, U of Pittsburgh  
**Linear and Nonlinear Spectroscopic Studies of Coadsorption at Electrode Surfaces.** R. M. Corn, B. J. Barner, R. V. Cuevel, M. Lynch, U of Wisconsin  
**Chemistry of Quinone Functionalized Vesicles.** C. R. Liedner, M. D. Liu, D. L. Patterson, Purdue U  
**Organized Monomolecular Assemblies: Novel Approaches for Manipulating the Electrochemical Interface.** M. Porter, C. Chihal, C. Chung, Iowa State U  
**Probing and Band Structure of Conductive Polymers via Electrochemical Techniques.** J. G. Gaudiello, Michigan State U  
**Probing the Structure of Electrode Surfaces Using Scanning Tunneling Microscopy.** B. Schardt, Purdue U  
**Award Address: Systems Approach to Analytical Chemistry.** H. L. Pardue, Purdue U

#### Modern Analytical Chemistry of Crop Protection Chemicals

Arranged by J. A. Graham

**Multiresidue Determination of Sulfonylurea Herbicides and Metabolites in Soil and Water by LC/MS.** L. M. Shalaby, Du Pont

**Robotic Sample Preparation of Soil Samples for Herbicide Determination by GC.** S. Adams, Monsanto Agricultural Co.

**Pesticide Residue Analysis Using GC with a Novel Microwave-Induced Helium Plasma Detector.** P. Wylie, Hewlett-Packard  
**Supercritical Fluid Approaches to Pesticide Residue Analyses.** K. Voorhees, J. Franz, Colorado School of Mines

**Use of an HP-1000 GC/MS Data Reduction Environment and Lotus 1-2-3 for the Rapid Evaluation of Low-Level PCB Analysis Data.** B. M. Hughes, D. E. McKenzie, Monsanto  
**LC/MS: Optimizing LC of Pesticides for Mass Spectrometric Analysis.** M. Balogh, Waters Chromatography Division, Millipore  
**Carbamate Pesticide Determinations Using HPLC and Postcolumn Derivatization Techniques.** J. Tschida, Varian Instrument Group

#### Sample Introduction, Ionization, and Data Analysis in FTMS

Arranged by J. R. Eyler

**Chromatography and FTMS.** M. L. Gross, C. B. Jacoby, D. L. Rempel, U of Nebraska  
**Protein Sequence Analysis by Quadrupole FTMS.** D. F. Hunt, J. Shabanowitz, P. R. Griffin, N. Z. Zhu, U of Virginia  
**Application of Correlation Analysis Techniques in MS.** K. G. Owens, J. P. Reilly, Drexel U  
**Laser Ionization for FT-ICR MS.** J. R. Eyler, C. H. Watson, U of Florida  
**Ion Manipulation and Data Reduction in FT-ICR MS.** A. G. Marshall, Ohio State U

## WE MAKE STANDARDS BY THE BOOK.



The metal content in each Conostan oil-based calibration standard is determined by chemical assay methods with results that are traceable to NIST standards (where applicable). This traceability means Conostan

products can serve as reference standards and provide a reliable benchmark for the determination of metals in organics. For a complete list of Conostan single and multi-element standards and special blends for the analysis

of metals in oils, write for our free brochure.



Conostan Division  
Conoco Specialty Products Inc.  
P.O. Box 1267  
Ponca City, OK  
Phone: (405) 767-3078  
Fax: (405) 767-5843

CIRCLE 26 ON READER SERVICE CARD

**Environmental Analysis**

**Nitrate Concentrations of Selected Drinking Water Supplies in New Brunswick.** B. Lo, J. C. Meranger, Health and Welfare Canada

**Novel Approach to the Determination of Chloride Ion, Chlorine, and Organochlorine Compounds in Aqueous Samples by Flame IR Emission.** S. W. Kubala, D. C. Tilotta, M. A. Busch, K. W. Busch, Baylor U

**Evaluation of Sample Holding Times for the Determination of Base, Neutral, and Acid Priority Pollutants in Ground/Surface Waters.** M. D. Wichman, G. M. Breuer, T. G. Cain, G. J. Jacobs, P. M. Mollenhauer, D. R. Seeger, U of Iowa

**Automated Field Analysis of Chemical Waste Sites by GC/Ion Trap MS.** C. P. Leibman, P. H. Hemberger, T. M. Cannon, M. A. Wolfe, Los Alamos National Laboratory

**Particle Size Dependent Chromium Speciation in Environmental Aerosols.** J. A. Koropchak, S. B. Roychowdhury, Southern Illinois U

**Air Sampling and Analysis of Methyl-t-butyl Ether (MTBE) in Gasoline Vapors.** J. Palassis, R. W. Hartle, J. L. Holtz, NIOSH

**Air Quality Measurements with a New Optimized Gas Cell.** F. Baudais, L. Ellis, J. Giroux, D. Pruss, E. Koche, K. Stotling, Bormem International

**Investigation on the Stability and Sensitivity of the Reagents Used in the Quantitation of Organophosphorus Pesticides in Air.** M. S. Abdel-Latif, G. C. Guilbault, U of New Orleans

**Simultaneous Enrichment of Metal Ions across Supported Liquid Membranes.** A. Bhatnagar, J. Cox, Miami U

**Coupling of Atomic Spectrometric Methods with Chromatography**

*Arranged by P. C. Uden*

**Overview of Atomic Spectral Chromatographic Detection.** P. C. Uden, U of Massachusetts, Amherst

**Evaluation of a Helium Discharge Detector for Gas Chromatographic Determination of Volatile Organohalogen Compounds.** G. W. Rice, D. A. Ryan, College of William and Mary

**Increasing the Chromatographer's Toolbox: Simultaneous Multidimensional/Multielement Analysis.** J. J. Kosman, J. L. Buteyn, R. G. Lukco, BP Research International

**Preliminary Investigations Toward the Determination of Deuterium by GC-MIP.** S. R. Goode, J. J. Gemmill, U of South Carolina

**Elemental Speciation and Removal of Interferences by LC with ICP/MS.** R. S. Houk, F. G. Smith, J. J. Sun, J. S. Fritz, U.S. DOE and Iowa State U

**Comparison of Two Atmospheric Pressure Helium Microwave Plasmas Used in Spectroscopic Detection of Supercritical Fluid Effluents.** Q. Jin, D. M. Chambers, C. Zhu, G. M. Hieftje, U of Indiana

**Helium Microwave-Induced Plasmas as Detectors for SFC.** J. W. Carnahan, L. Zhang, P. H. Neill, R. E. Winans, G. K. Webster, Northern Illinois U

**Element-Specific Chromatographic Detection Employing ICP and DCP Sources.** M. B. Denton, J. D. Kolczynski, M. J. Pilon, U of Arizona

**Surface Wave Plasmas and Multielement Detectors for GC/SWP/AES.** J. Hubert, R. Sing, C. Lauzon, C. T. Khanh, U of Montreal

**Plasma MS for Chromatographic Detection.** J. A. Caruso, B. Sheppard, J. Creed, H. Suyani, T. Davidson, U of Cincinnati

**Circular Dichroism/Polarization**

*Arranged by D. R. Bobbitt*

**Spectrochemical Analysis at Trace Concentrations by Polarization-Modulated Resonant Degenerate Four-Wave Mixing.** W. Tong, Z. Wu, J. Nunes, San Diego State U

**Differential Photothermal Detection of Circular Dichroism.** S. R. Erskine, D. R. Bobbitt, U of Arkansas

**Analytical Applications of CD to Problems in Clinical and Pharmaceutical Chemistry.** N. Purdie, K. A. Swallows, L. H. Murphy, R. B. Purdie, Oklahoma State U

**Chiroptical Studies of Pharmaceutical Compounds.** D. E. Bugay, H. Kadin, H. G. Brittain, E. R. Squibb and Sons

**Fluorescence-Detected Circular Dichroism Measurements in Capillary Zone Electrophoresis.** P. L. Christensen, E. S. Yeung, Ames Laboratory, U.S. DOE and Iowa State U

**Applications of Laser-Based Polarimetry to Biochemical Studies.** D. R. Bobbitt, U of Arkansas

**Chromatography Detectors**

**Electrogenerated Chemiluminescence Detection for Use with HPLC and FIA.** J. Holmstrom, T. A. Nieman, U of Illinois

**Indirect Fluorescence Detection for Velocity Modulated Capillary Electrophoresis.** T. Demana, C-Y. Chen, M. D. Morris, U of Michigan

**Results Obtained with a New Particle Beam-Type LC/MS Interface in Combination with a High-Resolution Magnetic Sector Mass Spectrometer.** W. V. Ligon, Jr., S. B. Dorn, General Electric

**High-Speed Vacuum-Outlet Capillary GC with Element-Selective Plasma Detection.** R. Sacks, L. Puig, S. Levine, U of Michigan

**Flame IR Emission/Flame Ionization Detector (FIRE/FID) for GC.** M. K. Hudson, T. Fau, K. Underhill, S. Applequist, Southwest Missouri State U

**Chlorofluorocarbon-Specific Detector for GC Based on Flame IR Emission (FIRE).** D. C. Tilotta, R. Srinivasan, M. A. Busch, K. W. Busch, Baylor U

**Laser-Induced Fluorescence Detection for the Direct Measurement of Retention and Dispersion in LC.** C. E. Evans, V. L. McGuffin, Michigan State U

**Design and Construction of a Particle Beam-Type LC/MS Interface for a High-Resolution Magnetic Sector Mass Spectrometer.** W. V. Ligon, Jr., S. B. Dorn, General Electric

**Expert System/Column Switching HPLC System.** S. V. Medlin, A. P. Wade, S. R. Crouch, Michigan State U

**Flow Methods and Chromatographic Analyses in the Process Environment**

*Arranged by R. Synovec and E. D. Yalvac*

**FIA in Industrial Applications of Process Control Optimization.** E. D. Yalvac, Dow Chemical

**On-Line Monitoring and Control of Fermentation Processes by FIA.** L. W. Forman, F. S. Jacobson, Genentech

**Renewable Reagent Fiber-Optic-Based Chemical Sensors.** L. W. Burgess, R. J. Berman, U of Washington

**Use of Membranes for Sample Conditioning—Volatiles.** R. A. Bredeweg, M. L. Langhorst, D. R. Dittenhafer, A. J. Strandjord, R. S. Willis, Dow Chemical

**Use of Membranes for Sample Conditioning—Extraction.** R. G. Melcher, P. L. Morabito, D. W. Bakke, E. D. Yalvac, Dow Chemical

**Advances in Process GC.** J. Clemons, Combustion Engineering

**High-Temperature LC in Process Analysis.** R. E. Synovec, C. N. Renn, U of Washington

**Automatic Control of a Biological Wastewater Treatment Plant with Biological Removal of Phosphorus and Nitrogen.** K. M. Pedersen, M. Kummel, H. Soeborg, Technical U of Denmark

**Development of a Simple Ion Chromatograph for On-Line Analysis.** R. Puzic, Esso Chemical Corp.

**WEDNESDAY AFTERNOON**

**Lasers and MS**

*Arranged by D. M. Lubman*

**Nd/YAG Laser Desorption FT-ICR MS.** A. G. Marshall, Z. Liang, Ohio State U

**Multiple Laser Applications and FT-ICR MS.** J. R. Eyley, C. H. Watson, U of Florida

**Gas-Phase Chemistry of Laser-Desorbed Neutral Molecules in a Fourier Transform Mass Spectrometer.** I. J. Amster, U of Georgia

**Developments in Laser-Based Techniques for Ion Trap MS.** D. E. Goeringer, G. L. Glish, K. G. Asano, S. A. McLuckey, W. B. Whitten, M. J. Ramsey, Oak Ridge National Laboratory

**Resonance Ionization Mass Spectrometer To Count Isotopically Selective Atoms and Molecules.** C. H. Chen, Oak Ridge National Laboratory

**Laser Ionization Studies of Sulfides and Organophosphonates.** S. R. Long, Aberdeen Proving Ground

**Multiphoton Ionization MS of Small Biological Molecules Using Pulsed Laser Desorption/Volatilization into Supersonic Beams.** D. M. Lubman, L. Li, U of Michigan

**Stepwise Solvation of Reactive Cations as Studied by Molecular Beam Laser MS.** J. Syage, The Aerospace Corp.

**Electroanalysis of Films and Surfaces**

*Arranged by A. Wieckowski*

**Dynamics in Microstructures at Electrodes.** L. R. Faulkner, U of Illinois

**Imaging of Organic Compounds on Platinum Electrode Surfaces.** B. C. Schardt, Purdue U

**Modeling of the Electrical Double Layer in Ultra-High Vacuum.** F. T. Wagner, GM Research Laboratories

**IR Spectroscopy as a Probe of Electrode Processes.** C. Korzeniewski, U of Michigan

**In Situ IR Spectroscopy of Well-Defined Single-Crystal Electrodes: Adsorption and Electrooxidation of CO on Pt(110), Pt(100), and Pt(111).** S-C. Chang, M. J. Weaver, Purdue U

**Orientation of Complex Adsorbates by Raman Scattering and Linear Dichroism.** P. W. Bohn, U of Illinois

**Electrochemical In Situ Surface Science by Radioactive Labeling.** A. Wieckowski, U of Illinois

**Open Discussion: In Situ and Ex Situ Methods of Surface Electrochemistry.** A. Wieckowski, U of Illinois

**Electroanalytical and Bioelectroanalytical Chemistry**

**Electroreduction of Iron Porphyrin Nitrosyls in the Presence of Substituted Phenols.** Y. Liu, M. D. Ryan, Marquette U





Buckingham Fountain in downtown Grant Park.

Electrochemistry of Iron Porphyrin Complexes with Sulfate. P. W. Crawford, M. D. Ryan, Marquette U

Mn(III)-Porphyrin-Based Thiocyanate-Selective Membrane Electrode: Characterization and Application in Flow-Injection Determination of Thiocyanate in Saliva. D. V. Brown, N. A. Chaniotakis, I. H. Lee, S. C. Ma, S. B. Park, M. E. Meyerhoff, R. J. Nick, J. T. Groves, U of Michigan

Influence of Ionophore Structure on the Anion Selectivity of Membrane Electrodes Based on Diquaternary Ammonium Salts. V. J. Woltring, L. G. Bachas, U of Kentucky

Cathodic Stripping Analysis of Heterocyclic Nitrogen DNA/RNA Bases in Nonaqueous Media. J. Fish, A. Ciszewski, T. Malinski, Oakland U

Electrochemical Determination of Pb<sup>2+</sup> Based on the Transfer Across Liquid/Liquid Interfaces. P. Vanyssek, Z. Sun, Northern Illinois U

Electroanalytical Sub-ppm Aqueous Chlorine Measurements. C. O. Huber, U of Wisconsin, Milwaukee

High-Current and Magnetically Altered Plasmas

Arranged by J. M. Goldberg and R. D. Sacks

Magnetic Field Modulation of a Two-Electrode DCP. R. Sacks, F. Braid, D. Slinkman, U of Michigan

Magnetically Induced Rotation of a Direct Current Arc Plasma. R. Sacks, D. Slinkman, U of Michigan

Investigations of a Low-Pressure Laser-Induced Plasma in a Pulsed Magnetic Field. J. M. Goldberg, F. Dorman, U of Vermont

Progress Toward Quantitative Analysis with a Theta Pinch Discharge. D. Miller, A. Scheeline, U of Illinois

Mass Flow and Analytical Characteristics of a Plasma Gun Atomic Emission Source. J. M. Goldberg, D. Robinson, U of Vermont

Preliminary Characterization of the Thin Films, Vapors, and Smokes Formed in Electrically Vaporized Conductor Plasmas. K. Trivedi, R. D. Sacks, S. Brewer, Jr., U of Michigan

Near-IR/Fluorescence/Absorbance

Arranged by G. Patony

New Instrumentation Concepts for Near-IR Spectroscopy. J. B. Callis, U of Washington

Effect of Moving Nonhomogeneous Samples on Multiwavelength Near-IR Analysis. G. Kemeny, Bran + Luebbe

Near-IR Analysis of Intact Sterile Products. R. A. Loder, U of Kentucky

Fiber-Optic In-Line Process Analyzer. R. Weedon, Bran + Luebbe

# COMPARE THE BETTER MICROPIPETTE

■ **Better Performance** — Swiss precision tolerances — accuracy and CV guaranteed to better than  $\pm 1\%$

■ **Better Quality** — Individually tested and inspected — supplied with verified calibration certificate

■ **Better Design** — Comfortable to operate, easy-to-read precision setting — internal detipping mechanism maintains narrow profile

■ **Better Selection** — Variable and fixed volume, air and positive displacement — in a wide range of sizes

■ **Better Value** — Wheaton high quality micropipettes provide better performance, better features at a better price than the better-known competition



Call Wheaton today  
1-800-225-1437  
and compare the better micropipette.

## WHEATON

Manufacturers Since 1888

1501 N. Tenth Street  
Millville, NJ 08332, USA  
Call Toll-Free: 1-800-225-1437  
Ext. 2527  
TLX: 55-1295 (WHEATON US)  
FAX: 1-609-825-1368

CIRCLE 177 ON READER SERVICE CARD

**Remote Monitoring with Near-IR Fiber Optics.** C. W. Brown, S. M. Donahue, S.-C. Lo, U of Rhode Island

**Near-IR Spectroscopy for the Analysis of Polymers.** P. Brimmer, Pacific Scientific Instrument Division

**Application of Near-IR Fluorophores in Analytical Chemistry.** G. Patony, D. Andrews-Wilberforce, Georgia State U

**Molecular Association and Its Consequences for Quantitation of Mixtures.** M. K. Phelan, J. B. Callis, U of Washington

**Biomedical Applications of Recent Analytical Chromatographic Techniques**

*Arranged by L. A. Kaplan*

**Use of Laser Detectors for Measuring Proteins by HPLC.** E. S. Yeung, Iowa State U

**Biomedical Applications of N-Cell Electrochemical Detectors.** W. R. Masterson, ESA

**Use and Limitations of Photodiode Array Detectors in HPLC.** G. Schmidt, Perkin-Elmer

**ANACHEM Award Symposium: Looking to the Future—A Symposium for Young Analytical Faculty**

*Arranged by S. R. Crouch*

**Underdefined and Ill-Posed Problems in the Spectroscopy of Thin Films.** P. W. Bohn, N. F. Fell, S. R. Kisting, U of Illinois

**Emission, Fluorescence, and Scattering Images in Plasmas: Detection, Results, and Implications.** J. W. Olesik, E. J. Williamsen, L. M. Chen, K. Bradley, S. Den, L. J. Smith, M. S. Denker, U of North Carolina

**Kinetic Energy Release Studies in FT-ICR Spectrometry.** S. W. Buckner, S. L. Van Orden, U of Arizona

**New Techniques for Investigating Transition Metal Cluster Ion Chemistry in the Gas Phase.** D. B. Jacobson, North Dakota State U

**Analytical Chemistry Using Supercritical Fluids: Application of Controlled Variation of the Chemical Potential.** S. V. Olesik, T. Engel, L. Giddings, W. Larkins, G. Mellott, C. Miller, L. Pekay, J. Woodruff, Ohio State U

**Signal-Processing Techniques for Real-Time FT-IR Analysis.** G. Small, U of Iowa

**Solvent Modulation in LC.** V. L. McGuffin, J. H. Wahl, Michigan State U

**Characterization of TLC and HPLC Stationary Phases Using UV-Vis and Fluorescence Solvatochromic Methods.** S. C. Rutan, T. L. Cecil, Virginia Commonwealth U

**ICP/MS**

*Arranged by R. S. Houk*

**Present Status of and Analytical Improvements in ICP/MS.** R. S. Houk, Iowa State U

**Oxide Ion Characteristics in ICP/MS.** G. Horlick, M. A. Vaughan, U of Alberta

**Use of a Center-Tapped Load-Coil Geometry with a Noncommercial Instrument for ICP/MS.** B. S. Ross, P. Yang, D. Chambers, G. M. Hieftje, Indiana U

**Location of the Optimal Skimming Position in an Inductively Coupled Plasma Mass Spectrometer.** D. M. Chambers, B. S. Ross, G. M. Hieftje, Indiana U

**Moderate Power Nitrogen Microwave-Induced Plasma as an Alternative Ion Source for Plasma MS.** W.-L. Shen, J. T. Creed, J. A. Caruso, U of Cincinnati

**Determination of Phosphorus at Trace Levels Using a Reduced-Pressure Helium Microwave-Induced Plasma as an Ion Source for Plasma MS.** W. C. Story, J. T. Creed, J. A. Caruso, U of Cincinnati

**Chemometric Approach to an Analytical Technique: ICP/MS.** M. E. Ketterer, C. A. Ramsey, J. J. Reschl, M. J. Peters, U.S. EPA

**Quantitation without Standards for Laser Ablation-ICP/MS.** J. W. Hager, Sciex

**Spatiotemporal Characteristics of the Sampling Interface in ICP/MS.** R. K. Winge, R. S. Houk, J. S. Crain, Iowa State U

**GFAAS—Matrix Modifiers**

*Arranged by J. M. Harnly and W. Slavin*

**Palladium and the Future of Chemical Modification in GFAAS.** L. M. Beach, T. M. Rettberg, Varian Instrument Group

**Matrix Modifiers: Their Role and History for Furnace AAS.** G. R. Carnrick, G. Schlemmer, S. McIntosh, Perkin-Elmer

**Influence of Modifiers on Atomization Mechanisms in Furnace AAS.** D. L. Styris, Pacific Northwest Laboratory

**Influence of Furnace Design on the Need for Matrix Modifiers.** W. Frech, U of Umea, Sweden

**Plasma Spectroscopy**

**Simultaneous Multiple Species Analysis in a Buffered Silane Plasma.** S. W. Rynders, A. Scheeline, U of Illinois

**Separated Sampling and Excitation Using Spark Ablation with a Pulse-Operated Microwave Plasma Emission Source.** D. M. Coleman, M. M. Mohamed, T. Uchida, S. Minami, Wayne State U

**Novel Capacitively Coupled Plasma Detector for GC.** M. W. Blades, D. Huang, D. C. Liang, U of British Columbia

**Helium ICP: Detection of Halogens in UV and UV Regions.** R. H. Clifford, A. Montaser, S. A. Sinex, S. G. Capar, George Washington U

**Ultra-trace Determination of Cd, Cu, Br, and Cl with Electrothermal Vaporization into a Helium Microwave-Induced Plasma.** M. Wu, J. W. Carnahan, Northern Illinois U

**Determination of Nonmetals in Coal by Direct Powder Injection into a He MIP.** J. M. Gehlhausen, J. W. Carnahan, Northern Illinois U

**Study of Noise Amplitude Spectra Produced by a Newly Designed Microwave Plasma Torch.** C. Zhu, Q. Jin, K. Brushwyler, C. Monnig, G. Hieftje, Indiana U

**Tomographic Image Reconstruction of Spatial Emission Profiles on a Microwave Plasma Torch.** C. Zhu, Q. Jin, P. Galley, C. Monnig, G. Hieftje, Indiana U

**Sample Preparation for Chromatographic Analysis**

*Arranged by C. F. Poole*

**Liquid-Liquid Extractions: Theory and Practical Considerations.** P. C. Sadek, J. T. Przybytek, P. M. Meilinger, C. L. Seaver, Baxter Healthcare

**Practical Aspects of Continuous Liquid-Liquid Extractors as Applied to Aqueous Samples.** T. L. Peters, Dow Chemical

**Steam Distillation.** J. Fritz, Iowa State U

**Characterization of Industrial Wastewater by Solid-Phase Extraction.** M. J. Wells, E. C. Roberts, A. Rossano, West Point Pepperell

**Cleanup Techniques for Pesticides in Fatty Foods.** S. M. Walters, U.S. FDA

**Mechanisms and Results for Solid-Phase Extraction of Organic Compounds.** G. A. Junk, Ames Laboratory—U.S. DOE, Iowa State U

**Solid-Phase Extraction (SPE) of Herbicides from Well Water for Determination by GC/MS.** S. A. Schuette, R. G. Smith, L. R. Holden, J. A. Graham, Monsanto Agricultural Co.

**Rapid and Sensitive HPLC Method To Determine Cyclosporin-A in Whole Blood Using a Short Column.** A. M. Rustum, Abbott Laboratories

**ICP-OES**

**Detailed Precision Studies Using a Photodiode Array-Based ICP Spectrometer System.** S. W. McGeorge, P. S. Wee, H. W. Moak, P. A. Cop, Leco Instruments

**Analytical Characterization of Direct Wavelength Drive Spectrometer for ICP-AES.** S. F. Zhu, Spectro Analytical Instruments

**Excitation Mechanisms of Yttrium in an ICAP.** K. Wheeler, K.-P. Li, U of Lowell

**Closed-Vessel Microwave Digestion of Si<sub>3</sub>N<sub>4</sub>-Based and Al<sub>2</sub>O<sub>3</sub>-Based Ceramic Materials for ICP-AES Analysis.** J. M. Keane, A. F. Valeri, GTE

**Determination of Rare Earth Elements in Rare Earth Matrices by ICP-AES Line Selection.** I. B. Brenner, P. Grosdallion, Geological Survey of Israel

**Determination of TiO<sub>2</sub> and BaSO<sub>4</sub> in Sunscreen Preparations by Surface Nebulization ICP-OES.** G. N. Coleman, C. M. Ashkebousi, Leeman Labs

**New Approach to ICP-AES—A Multichannel Polyscan Analyzer.** R. B. Myers, A. Le Marchand, P. Grosdallion, I. B. Brenner, JY Division, Instruments SA

**Elemental Analysis of Edible Oil by ICP-OES.** G. N. Coleman, C. M. Ashkebousi, Leeman Labs

**Automated Heuristic Selection of ICP Background Correction Wavelengths.** M. L. Salt, Perkin-Elmer

**Raman Spectroscopy**

**Polymer-Coated SERS Electrodes for Neurotransmitter Determination in Biological Matrices.** M. L. McGlashen, M. D. Morris, U of Michigan

**Raman Spectroscopy as a Probe of Immersed and Emersed Electrode Interfacial Solvent Structure.** R. L. Sobocinski, J. E. Pemberton, U of Arizona

**FT-Raman Spectroscopy: Industrial Applications.** J. A. Graham, Hercules

**Line-Narrowed Fully Resonant Four-Wave Mixing Spectroscopy of Organics in Amorphous Media.** G. B. Hurst, J. C. Wright, U of Wisconsin

**Changes in the Raman Spectrum of Silicon Oxide Sol-Gels Caused by Additives and Drying.** M. Bradley, J. Maurer, J. H. Krech, U of Connecticut

**Raman Microprobe Profiles with an Automated Stage.** P. J. Codella, General Electric

**Histamine Determination by Surface-Enhanced Raman Spectroscopy in Microliter Volumes.** K. L. Davis, M. L. McGlashen, M. D. Morris, U of Michigan

**Waveguide Raman Sampling Applied to the Study of Diffusion.** N. E. Schlotter, Bell Communications Research

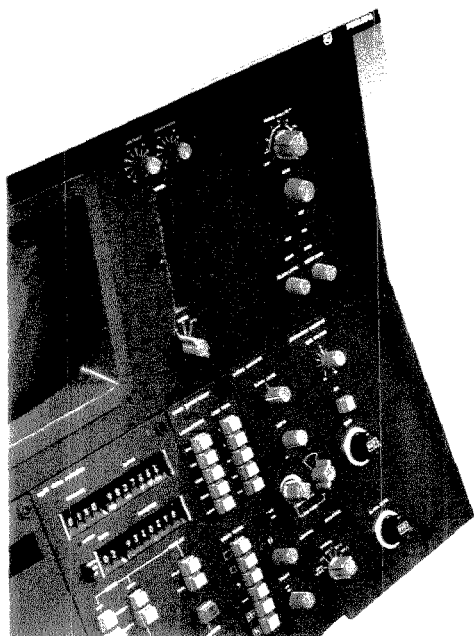
**Recent Developments in FT-Raman Spectrometry.** N. A. Wright, K. Krishnan, Digilab Division, Bio-Rad Laboratories



# PHILIPS

## The World's Leading Family 500 Series SEMs

*Philips Analytical*



*To find out more, contact us today.*

Write to Philips Analytical, Electron Optics Department, Building A/E, 5600 NA, Eindhoven, The Netherlands. Or call your local supplier.  
Austria (0224) 603013/14, Belgium (02) 525011, Denmark (01) 577272, Finland (01) 5025355, France (1) 49420747,  
Germany (0546) 501643, Great Britain (0223) 358986, Italy (02) 674392, Netherlands (040) 782773, Norway (02) 680200,  
Spain (01) 4942200, Sweden (08) 7031385, Switzerland (01) 480270, U.S.A. (703) 5253680.

**PHILIPS  
ANALYTICAL**  
*BIGGER IDEAS FOR  
BETTER ANALYSIS*

CIRCLE 127 ON READER SERVICE CARD

As the  
frontiers  
expand...

# Biochemistry

reflects the most current results of original  
research in all areas of biochemistry.

**Editor**, Hans Neurath, University of Washington

Published biweekly, *Biochemistry* emphasizes the close relationship of chemistry, biochemistry, and molecular and cell biology.

Subject matter covers:

- structure, function and regulation enzymes
- proteins
- carbohydrates
- lipids
- hormones
- receptors
- gene structure and expression
- protein biosynthesis
- viruses
- immunochemistry
- genetics
- bioenergetics
- membrane structure and function
- x-ray crystallography

Over 10,300 pages of original research annually, this internationally renowned journal is vital reading for all scientists in this fast-paced field.

1989 Rates	ACS Members*		Non-Member
	1 Year	2 Years	1 Year
U.S. ....	\$ 80	\$144	\$549
Canada & Mexico .....	\$140	\$264	\$609
Europe** .....	\$237	\$458	\$706
All Other Countries** .....	\$342	\$668	\$811

\* Member rate is for personal use only.

\*\* Air Service Included.

Supplementary material is available for this publication.

This publication is available on microfilm, microfiche, and online through CJO on STN International.

For nonmember rates in Japan, contact Maruzen Co., Ltd.

**For more information** or to subscribe:  
American Chemical Society/Marketing Communications Department  
1155 Sixteenth Street, NW, Washington, DC 20036

**In a hurry?**

Call Toll free (800) 227-5558 (U.S. only)

Outside U.S. (202) 872-4363

Telex: 440159 ACSP UI

89 2582 ACSPUBS

FAX: (202) 872-4615



## Associate Editors

E. W. Davie; *Univ. of Washington*  
E. H. Fischer; *Univ. of Washington*  
M. P. Gordon; *Univ. of Washington*  
W. W. Parson; *Univ. of Washington*

## Editorial Advisory Board

R. H. Abeles; *Brandeis Univ.* • D. S. Auld; *Harvard Medical School* • R. L. Baldwin; *Stanford Univ.* • S. J. Benkovic; *Pennsylvania State Univ.* • G. Blobel; *The Rockefeller Univ.* • T. L. Blundell; *Univ. of London, England* • B. R. Brinkley; *Baylor Coll. of Medicine* • M. J. Coon; *Univ. of Michigan* • D. Davies; *Natl. Inst. of Health* • R. A. Dwek; *Univ. of Oxford, England* • M. Edidin; *Johns Hopkins Univ.* • I. Fridovich; *Duke Univ.* • C. Frieden; *Washington Univ.* • I. H. Goldberg; *Harvard Medical School* • J. Gorski; *Univ. of Wisconsin* • W. F. Harrington; *Johns Hopkins Univ.* • R. Haselkorn; *Univ. of Chicago* • C. H. Heldin; *Ludwig Inst. for Cancer Res., Sweden* • C. Helene; *Museum Natl. d'Histoire Naturelle, France* • J. Hershey; *Univ. of California, Davis* • G. P. Hess; *Cornell Univ.* • P. C. Hinkle; *Cornell Univ.* • F. M. Huennekens; *Scrpps Clinic & Res. Foundation* • T. E. Hughli; *Scrpps Clinic & Res. Foundation* • R. Jaenicke; *Univ. of Regensburg, W. Germany* • H. Jornvall; *Karolinska Inst., Sweden* • H. R. Kaback; *Roche Inst. of Molecular Biology* • N. R. Kallenbach; *Univ. of Pennsylvania* • Y. Kaziro; *Univ. of Tokyo, Japan* • C. B. Klee; *Natl. Inst. of Health* • G. Kohler; *Max-Planck Inst. for Immunobiol., W. Germany* • J. Kraut; *Univ. of California, San Diego* • J. E. Kyte; *Univ. of California, San Diego* • R. J. Lefkowitz; *Duke Univ.* • T. Lindahl; *Imperial Cancer Res. Fund., United Kingdom* • H. Metzger; *Natl. Inst. of Health* • P. L. Modrich; *Duke Univ.* • E. Neufeld; *Univ. of California, Los Angeles* • D. Northrop; *Univ. of Wisconsin* • J. Olgendick; *Roche Inst. of Molecular Biology* • D. Papahadjopoulos; *Univ. of California, San Francisco* • M. L. Pardue; *Massachusetts Inst. of Tech.* • D. C. Phillips; *Univ. of Oxford, England* • J. C. Powers; *Georgia Inst. of Tech.* • J. H. Prestegard; *Yale Univ.* • P. Reichard; *Karolinska Institutet, Sweden* • J. F. Riordan; *Harvard Medical School* • C. A. Ryan; *Washington State Univ.* • R. W. Schekman; *Univ. of California, Berkeley* • H. A. Scheraga; *Cornell Univ.* • P. R. Schimmel; *Mass. Inst. of Tech.* • J. Seelig; *Univ. of Basel, Switzerland* • G. G. Shipley; *Boston Univ.* • A. G. So; *Univ. of Miami* • J. Stubbe; *Univ. of Wisconsin* • B. Sykes; *Univ. of Alberta, Canada* • E. W. Taylor; *Univ. of Chicago* • I. Tinoco; *Univ. of California, Berkeley* • C. L. Tsou; *Academia Sinica, Beijing* • B. L. Vallee; *Harvard Medical School* • K. E. Van Holde; *Oregon State Univ.* • M. Vaughan; *Natl. Inst. of Health* • S. J. Wakil; *Baylor Coll. of Medicine* • Y. L. Wang; *Academia Sinica, Shanghai* • S. Woo; *Baylor Coll. of Medicine* • P. E. Wright; *Scrpps Clinic & Res. Foundation*

**FIA**

**Automation of the DPD Method for Chlorine in Water by Flow Injection.** K. J. Smith, G. Gordon, G. E. Pacey, Miami U

**Automated On-Line Extraction and Determination of Trace Impurities in a Uranium Matrix by Flow Injection/ICP Analysis.** H. Nekimken, D. Gallimore, Los Alamos National Laboratory

**Characterization of Sulphochlorophenol-azorhodamine as a Reagent for Palladium in FIA.** P. M. Shiundu, P. D. Wentzell, A. P. Wade, U of British Columbia

**Peroxide Determinations Using Immobilized Chemiluminescence Reagents.** N. M. Rao, T. A. Nieman, U of Illinois

**Extending the Utility of Gas Diffusion FIA Using Immobilized Enzyme Membranes.** T. A. Spinks, G. E. Pacey, Miami U

**On-Line Preconcentration of Refractory Elements for Determination by Atomizer, Source ICPs in Atomic Fluorescence Spectrometry (ASIA).** J. F. Tyson, S. Greenfield, T. M. Durrani, S. Kaya, U of Massachusetts

**Potentiometric Titration of Mixtures of Nitric, Hydrofluoric, and Acetic Acids in Semiconductor Electrodes.** W. C. Pecklak, SEH America

**On-Line Determination of Dissolved Gases in Liquid Process Streams.** K. G. Schick, P. Karges, FIATron Systems

**Poster Session**

**AAS, AES, Computers and Software, Electroanalytical Chemistry, FIA, IR Spectroscopy, MS, Solid Materials Characterization**

**THURSDAY MORNING**

**Trace Elements in Biological Samples**

*Arranged by* N. Miller-Ihli, S. G. Capar, and F. L. Fricke

**Trace Elements in Biological Samples: A Comparison of Analytical Methods.** M. Stoeppler, KFA Julich

**Programmed Microwave Dissolution Methods for ICP Analysis of Standard Reference Materials.** R. L. Watters, N. M. Kingston, L. J. Wood, T. A. Butler, National Institute of Standards and Technology

**Application of ICP/MS to the Certification of Marine Biological Reference Materials.** J. W. McLaren, S. N. Willie, S. S. Berman, National Research Council of Canada

**Determination of Lead in Foods.** S. G. Capar, W. H. Lamont, S. C. Hight, U.S. FDA

**Laser-Enhanced Ionization Spectroscopy for the Analysis of Standard Reference Materials.** G. C. Turk, H. M. Kingston, National Institute of Standards and Technology

**Dissolution and Separation Methods for DPASV Determinations of Lead and Cadmium in Biological Samples.** K. Pratt, National Institute of Standards and Technology

**GFAAS Determination and Survey of Aluminum in Infant Formulas and Evaporated Milks.** R. W. Dabeka, A. D. McKenzie, Health and Welfare Canada

**Determination of Vanadium in Biological and Environmental Samples.** B. Patel, S. J. Haswell, R. Grzeskowiak, Thames Polytechnic, Great Britain

**Bioelectroanalysis and Miniaturization—In Vivo and Instrumental Use**

*Arranged by* A. Brajter-Toth

**Potentiometric Ion/Gas Selective Sensors for Continuous In Vivo Measurements: Progress and Challenges.** M. E. Meyerhoff, M. E. Collison, U of Michigan

**Enzyme-Modified Ultramicroelectrodes for Monitoring Neurotransmitter Release In Vivo.** W. G. Kuhr, V. Moore, P. Pantano, U of California

**Microdialysis Sampling Probes: The In Vivo Biosensor That Works Today.** P. T. Kissinger, Purdue U and Bioanalytical Systems

**Piezoelectric Deflection of Biological Targets via Enzymatic Amplification Routes.** M. D. Ward, Du Pont

**Physical Electrochemistry**

**Development of a Methodology for High-Pressure Studies of Electrochemical Systems.** W. T. Cruanes, H. G. Drickamer, L. R. Faulkner, U of Illinois

**Characterization of Transport Properties in Ion Exchange Membranes from the Analysis of Nonlinear Diffusion at Ultramicroelectrodes.** M. E. Taylor, L. R. Faulkner, U of Illinois

**Electron Transfer Dynamics at Electrodes Modified by Alternate Adsorption of Isopolyolybdate and Water-Soluble Cations.** C. Li, L. R. Faulkner, U of Illinois

**Controlled Potential Electrolysis at a Modified Electrode.** T. Gray, J. Cox, Miami U

**Voltammetry of Hydrogen Peroxide at a Modified Electrode.** R. Jaworski, J. Cox, Miami U

**Electrochemistry of Charge Transfer Complexes of Copper Chelates and Tetracyanoquinodimethane (TCNQ).** G. J. Pyrka, Q. Fernando, Kent State U

**Electrosynthesis and Characterization of Highly Conducting Poly(3-methylthiophene) on Stainless Steel Substrates.** H. B. Mark, Jr., A. Galai, A. E. Karagozler, D. Cunningham, H. Zimmer, U of Cincinnati

**Photothermal Spectroscopy**

*Arranged by* S. Bialkowski

**Water, A Unique Medium for Thermal Lens Measurements.** C. D. Tran, M. Franko, Marquette U

**Hadamard Transform Photothermal Spectroscopy of Proteins.** P. J. Treado, T. Demana, M. D. Morris, U of Michigan

**New Laser Source for Photothermal Spectroscopy.** T. Imasaka, N. Ishibashi, Kyushu U

**Dynamic IR Spectroscopy Using Step-Scan Interferometry.** R. A. Palmer, C. J. Manning, J. L. Chao, Duke U

**Developments in Pulsed-Laser Photothermal Probe-Beam Deflection Spectroscopy and Radiometry.** A. C. Tam, IBM

**Study of Polymer and Semiconductor Thin Films with Phase Analysis in FT-IR Photothermal Spectroscopy.** L. G. Bertrand, Ecole Polytechnique de Montreal

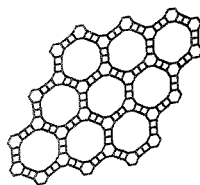
**Photothermal Spectroscopy: Theory and Experiment.** R. Gupta, U of Arkansas

**Multichannel/Multiplex Techniques—Atomic Spectroscopy**

*Arranged by* M. B. Denton

**Studies of Spark Spectroscopy Employing Charge Transfer Device Detectors.** R. S. Pomeroy, M. B. Denton, U of Arizona

**Zeolite Synthesis**



398

Over 600 pages

**Zeolite Synthesis**

Here in one volume is a complete progress report on the various aspects of zeolite synthesis on a molecular level. No other source covers this subject so completely!

This new title provides many examples that illustrate how zeolites can be crystallized and what the important parameters are that control crystallization. A variety of topics covered in this important book include:

- crystallization techniques
- gel chemistry
- crystal signs and morphology
- the role of organic compounds
- novel synthesis procedures

With forty-two chapters, this valuable title offers a complete review of zeolite synthesis as well as the latest findings in this important field. Valuable new methods are highlighted such as VPI—the first 18-membered ring molecular sieve. In addition, examples of modern spectroscopic characterization of reactants and reaction intermediates are provided. Also covered is the chemistry of silicate solutions and reactant effects on crystallization products.

This essential volume contains benchmark contributions from many notable pioneers in the field including R.M. Barrer, H. Robson, and Robert Milton.

Mario L. Occelli, *Editor*, Unocal Corporation  
Harry E. Robson, *Editor*, Louisiana State University

Developed from a symposium sponsored by the Division of Colloid and Surface Chemistry of the American Chemical Society

ACS Symposium Series No. 398  
643 pages (1989) Clothbound  
ISBN 0-8412-1632-0 LC 89-6884  
US & Canada \$139.95 Export \$167.95

O · R · D · E · R · F · R · O · M

American Chemical Society  
Distribution Office, Dept. 33  
1155 Sixteenth St., N.W.  
Washington, DC 20036

or CALL TOLL FREE

**800-227-5558**

(in Washington, D.C. 872-4363) and use your credit card!

**Echelle Spectrometer for Single Spark and Theta Pinch Quantitative Studies.** C. Bye, S. Rynders, A. Scheeline, U of Illinois

**Evaluation of a New Array Detector Atomic Emission Spectrometer for ICP-AES.** M. J. Pilon, M. B. Denton, U of Arizona

**Optical Bandwidth Selection Systems for FT-AES.** G. Horlick, B. Todd, U of Alberta

**Optimized FT Spectrometer as a Multi-element Detection System for GC Using MIP-AES.** R. L. Sing, C. Lauzon, K. C. Tran, J. Hubert, U of Montreal

**Continuum Source AAS with a Pulsed Light Source and Diode Array Detector.** G. Moulton, T. O'Haver, J. M. Harnly, U.S. Dept. of Agriculture

**Corrected Performance of SIT Vidicons Exposed to Transient Radiation.** D. M. Coleman, S. Teruo, T. Uchida, S. Minami, Wayne State U

**Reaching the Read-Out Noise Limit for Diode Array Spectrometry.** G. Moulton, J. Harnly, T. O'Haver, U.S. Dept. of Agriculture

**Present Applications and Future Trends in High-Performance Charge Transfer Device Detectors.** M. B. Denton, U of Arizona

**Chiral Separations for Drug Analysis**

*Arranged by D. A. Roston*

**Opening Remarks.** D. A. Roston, Searle Research and Development

**Characterization of Bulk Samples of New Drug Substances by Achiral and Chiral Separations.** D. Demarest, D. A. Roston, R. Rhineberger, R. Wijayarathne, G. Beck, Searle Research and Development

**Application of Coupled Chiral/Achiral HPLC to Pharmacological Studies of Enantiomeric Compounds.** I. W. Wainer, St. Jude Children's Research Hospital

**Enantiomeric Purity of a Benzidine Prostaglandin.** B. G. Snider, C. P. Clark, P. B. Bowman, Upjohn

**Fast Chiral Chromatography on Pirkle-Concept Columns.** S. R. Perrin, D. N. Baehr, S. E. Lye, Regis Chemical Co.

**Pharmacokinetics of Chiral Nonsteroidal Anti-Inflammatory Drugs.** F. Jamali, U of Alberta

**New Examples of Chiral Separations of Drugs on Polyamides and Cellulose Triacetate.** G. Blaschke, U of Münster, FRG

**Insight into the Chiral Separation Mechanism on Cellulose-Based Materials.** T. Shibata, Daicel Chemical Ind.

**1989 Lippincott Award Symposium: Matrix Isolation and High-Resolution Spectroscopy**

*Arranged by W. E. Blasz*

**Introductory Remarks and Award Presentation to Marilyn E. Jacox.** K. S. Kalasinsky, Mississippi State Chemical Laboratory

**Award Address: Production and Spectroscopy of Small Molecular Ions and Cluster Ions.** M. E. Jacox, National Institute of Standards and Technology

**Electronic and Magnetic Properties of Small Clusters.** W. Weltner, Jr., U of Florida

**Matrix Isolation Studies of Laser-Vaporized Neutral and Charged Radicals.** L. B. Knight, Jr., Furman U

**Ultra-High-Resolution Matrix Spectroscopy.** T. Oka, U of Chicago

**Spectroscopic Studies Applied to Problems of Atmospheric Chemistry.** C. Howard, NOAA

**ICP/MS**

*Arranged by R. S. Houk*

**Analysis of Aerospace and Nuclear Metals by ICP/MS.** G. L. Beck, Teledyne Wah Chang

**High-Resolution ICP/MS.** N. E. Sanderson, N. Bradshaw, E. Hall, VG Elemental

**Formation of a Positive Space-Charge over the Skimmer Cone of an Inductively Coupled Plasma Mass Spectrometer and Its Effects on Analyte Ion Kinetic Energy.** D. M. Chambers, P. Y. Yang, A. Verbeek, G. M. Hieftje, Indiana U

**Comparison of ICP/MS Performance Using Flow Injection and Conventional Sample Introduction.** G. Zhu, C. Pan, R. F. Browner, Georgia Institute of Technology

**Direct Analysis of High-Purity Quartz and Glasses by Laser Sampling ICP/MS.** E. R. Denoyer, G. Wallace, J. W. Hager, Perkin-Elmer

**Laser Ablation ICP/MS: Factors Governing System Sensitivity and Precision.** R. C. Hutton, C. T. Tye, P. D. Blair, VG Elemental

**Laser Ablation ICP/MS Analysis of Environmental Samples: Fundamental Aspects of Analyte Production, Transport, and Detection.** D. W. Koppelaar, M. R. Smith, E. J. Wyse, Battelle—Pacific Northwest Laboratory

**Comparison of Solid Sample Methods for ICP-OES and ICP/MS.** J. F. Tyson, S. Long, S. A. Darke, C. J. Pickford, U of Massachusetts

**Practical Approaches to Oxide Reduction in ICP/MS.** J. W. McLaren, J. Lam, S. S. Berman, National Research Council of Canada

**MS of Fossil Fuels**

*Arranged by K. V. Wood*

**Symposium Overview and Investigation of Homologous Series in Coal-Derived Materials.** K. V. Wood, Purdue U

**Nature of Organosulfur Compounds in Coal.** C. E. Schmidt, Pittsburgh Energy Center

**Characterization of Coal-Derived Materials by FAB High-Resolution MS.** R. E. Winans, Argonne National Laboratories

**Optimization of High-Resolution Mass Spectrometers for Type Analysis.** S. E. Scheppele, G. L. Nutter, D. L. Parisi, Amoco Research Center

**Characterization of Aromatic Hydrocarbons from Oil Shale Extracts by Tandem MS.** M.-I. M. Chou, K. V. Wood, Illinois State Geological Survey

**Special Approaches to Spectral Measurement in SIMS and FAB Analysis of Fossil Fuel-Related Problems: Sample Preparation and Imaging Analyses.** K. L. Busch, Indiana U

**Geological Samples: Current and Future Needs for Chemical Analysis**

*Arranged by M. Thompson*

**Actual and Ultimate Performance from Spectrometric Instruments.** M. Thompson, U of London

**Rare Earth Analysis in Geological Samples—Present Capabilities and Future Requirements.** J. N. Walsh, Royal Holloway and Bedford New College

**Current Status and Future Prospects for ICP/MS in the Analysis of Geological Materials.** G.E.M. Hall, Geological Survey of Canada

**Future Trends in ICP-AES Instrumentation for Routine Analysis.** J. E. Goulter, Messgerate GmbH

**Sample Preparation for Chromatographic Analysis**

*Arranged by C. F. Poole*

**Comparison of Liquid-Liquid and Solid-Phase Extraction Techniques for Drugs in Urine, and the Effects on the Lifetime and Performance of Fused-Silica Capillary Columns.** H. Rood, J. A. Knitter, J and W Scientific

**Novel Sampling and Analysis Techniques for Environmental Analysis.** R. G. Orth, J. M. Wendling, D. Haile, J. McKenzie, F. Hileman, Monsanto

**Configurations of Supercritical Fluid Extractions To Solve Sample Extraction Problems.** L. Kumar, Suprex

**Preparation of Gaseous Standards for GC.** F. Andrews, American Cyanamid

**Sample Preparation in Arson Analysis.** W. Bertsch, G. Holzer, U of Alabama

**Multimodal LC-GC.** H. J. Cortes, Dow Chemical

**On-Line Trace Sample Preparation for HPLC.** U.A.Th. Brinkman, Free U of Amsterdam

**Sample Applications of Ion-Exchange Membranes.** D. Hardy, Bio-Rad Laboratories

**Near-IR Spectroscopy**

**Performance Parameters of a Near-IR Densitometer for TLC.** E. W. Ciurczak, D. M. Mustillo, College of St. Elizabeth

**Isophotonic Data Acquisition for Quantitative Multiple Discrete Wavelength Near-IR Spectroscopy.** D. L. Wetzel, A. J. Eiert, Kansas State U

**Near-IR Spectroscopy for Process Control.** E. Stark, KES Analysis

**Comparison of FT and Principal Components Calibration Methods.** H. Mark, Bran + Luebbe

**Remote Measurements Using an FT-IR Fiber-Optic Spectrometer Operated in the Near-IR.** K. Krishnan, P. J. Stout, J. R. Powell, Digilab Division, Bio-Rad Laboratories

**Recent Developments with a Near-IR FT-Raman Accessory.** R. Rubiniowitz, A. Simon, Bruker Instruments

**Recent Developments in Near-IR FT-Raman.** P. Beuchesse, H. Guy, H. Buifis, Bomem International

**Principles and Applications of Step-Scan Interferometry.** R. Rubiniowitz, A. Simon, Bruker Instruments

**Applications of Artificial Intelligence and Expert Systems in Analytical Chemistry**

*Arranged by M. Riebe*

**Decision Analysis Expert Systems in Analytical Chemistry.** S. N. Deming, U of Houston

**Computer Roles in Structure Characterization.** M. E. Munk, B. D. Christie, V. K. Velu, E. W. Robb, M. S. Madison, Arizona State U

**Mass Spectral Interpretation Using Neural Networks.** B. Curry, Hewlett-Packard

**Interactive, Computer-Assisted IR Spectral Interpretation.** S. A. Tomellini, B. J. Wythoff, U of New Hampshire

**Expert Systems, Databases, and Microwave Dissolution Protocols.** M. A. Pleva, F. A. Settle, H. M. Kingston, Washington and Lee U

**Small Expert Systems in Chromatography: Troubleshooting HPLC Hardware.** T. Jupille, LC Resources

**Application of Artificial Intelligence to Flow Injection and Acoustic Emission Analysis.** A. P. Wade, E. Hemenway, U of British Columbia

**Applications of Expert Systems in Industrial Analytical Chemistry.** M. Riebe, Polaroid

---

**Chemometrics: Fifteen Years after the Revolution**

---

Arranged by B. K. Lavine

- Tensorial Calibration.** B. Kowalski, E. Sanchez, U of Washington
- Investigations of Molecular Structure—Physicochemical Property Relationships.** P. C. Jurs, M. N. Hasan, D. T. Stanton, Pennsylvania State U
- Application of Pattern Recognition Methods to Mass Spectral Data.** W. Dunn III, U of Illinois
- Application of GC/Pattern Recognition Techniques to the Problem of Identifying Africanized Honeybees.** B. K. Lavine, J. H. Han, R. K. Smith, O. R. Taylor, Clarkson U
- Chemometric Applications for Process Control.** L. Wangen, P. Carey, J. Dyke, F. Marsh, Los Alamos National Laboratory
- Comparison of an Expert System vs. SIMCA in Classifying Mass Spectra.** D. R. Scott, U.S. EPA

---

**THURSDAY AFTERNOON**

---

**Trace Elements in Biological Samples**

---

Arranged by N. Miller-Ihli, S. G. Capar, and F. L. Fricke

- Trace Element Imbalances in Alzheimer's Disease.** W. D. Ehmann, W. R. Markesbery, U of Kentucky
- Ultratrace Metal Speciation and Preconcentration Using Biological Organisms.** J. A. Holcombe, V. Majidi, C. Mahan, U of Texas
- Elemental Analysis in the Food Industry.** J. R. Heuser, E. R. Elkins, NFPA
- GFAAS for the Determination of Trace Metals in Biological Materials.** N. J. Miller-Ihli, U.S. Dept. of Agriculture
- Heavy Metal Speciation by HPLC with Plasma MS.** J. A. Caruso, H. Suyant, A. Al Rashdan, D. Heitkemper, J. Creed, U of Cincinnati
- Trace Element Determinations in "Health" Foods.** K. A. Wolnik, C. M. Gaston, B. S. Sheppard, L. K. Olson, J. A. Caruso, F. L. Fricke, U.S. FDA

**Elemental Analysis of Biological Materials Using Nuclear and Atomic Spectrometric Methods.** W. C. Cunningham, D. L. Anderson, S. G. Capar, S. Sinex, National Institute of Standards and Technology

**Study of Aluminum and Iron Distribution in Blood by GFAAS.** R. A. Romero, J. A. Navarro, U del Zulia

---

**Bioelectroanalysis and Miniaturization—In Vivo and Instrumental Use**

---

Arranged by A. Brajter-Toth

- Limits to Spatial and Temporal Resolution in Electrochemistry.** L. R. Faulkner, U of Illinois
- Practical Reference Electrodes for Electrochemical Detectors and Microsensors.** B. R. Shaw, Y. Deng, J. Park, C. L. Wang, U of Connecticut
- Microdialysis as an In Vivo Sampling Technique for LC/EC.** R. Shoup, Bioanalytical Systems
- Direct, Electrochemical Detection of Aliphatic Amines, Amino Acids, Amino Alcohols, and Amino Sugars in LC.** D. C. Johnson, W. R. LaCourse, W. A. Jackson, R. E. Roberts, Iowa State U
- Strategy for the Development of New Surfaces for the Amperometric Detection of Biological Molecules.** A. Brajter-Toth, S. E. Boyette, L. Bodalhai, M. S. Freund, U of Florida

---

**IR Microspectroscopy**

---

Arranged by M. Harthcock

- Sampling Methodologies and Considerations in IR Microspectroscopy.** A. J. Sommer, J. E. Katon, Miami U
- Aspects of IR Microreflectance Spectroscopy.** S. L. Hill, K. Krishnan, Digilab Division, Bio-Rad Laboratories
- Application of IR Microspectroscopy to Archaeological Fabrics and Dyes.** P. A. Martoglio, S. P. Bouffard, A. J. Sommer, J. E. Katon, K. A. Jakes, Miami U
- Studies of Red Blood Cell Disease by IR Microspectroscopy.** W. S. Caughey, A. Dong, R. G. Messerschmidt, J. Refner, Colorado State U
- Functional Group Images (FGI) by IR Microspectroscopy: Recent Applications and Effective Spatial Resolution Enhancement.** M. A. Harthcock, S. Nitzsche, B. L. Davis, J. A. de Haseth, R. M. Robertson, Dow Chemical
- Depth Profiling Using IR Mapping Microspectroscopy.** D. W. Schiering, J. C. Corbett, J. M. Landry, Perkin-Elmer
- Micro-FT-IR in Art Conservation.** J. H. Carlson, Winterthur Museum
- New Hammers for Scientists: A Look into the Future of IR Microspectroscopy.** R. G. Messerschmidt, Connecticut Instrument Corp.

---

**Photothermal Spectroscopy**

---

Arranged by S. Bialkowski

- Characterization of Semiconductor Microstructure Using Photothermal Optical Beam Deflection Imaging.** G. C. Wetsel, Jr., Southern Methodist U
- Thermal Lens Detection with a Deep UV Laser for LC.** Y. Yang, Loyola U of Chicago
- Pulsed-Laser Photothermal Spectroscopy of Strongly Absorbing Liquids and Solids.** E. M. Eyring, S. J. Isak, N. F. Leite, S. J. Komorowski, D. P. Cobranchi, U of Utah
- Differential Thermal Lens Spectrometer for Ultrasensitive Absorption Measurements.** R. E. Russo, J. D. Spear, R. J. Silva, Lawrence Berkeley Laboratory
- Remote Thermal Lens Spectroscopy.** D. Rojas, R. E. Russo, Lawrence Berkeley Laboratory
- Thermal Lens Spectrophotometry Using Right Angle Detection of Scattered Light.** G. R. Long, Indiana U of Pennsylvania
- Evaluation of Pulsed-Laser Excited Photothermal Spectrometric Detection Schemes.** S. Bialkowski, Z-F. He, S. Kalaskar, O. Pagan, C. Erickson, Utah State U
- Photothermal Detection in Capillary Zone Electrophoresis.** N. J. Dovichi, M. Yu, U of Alberta
- Semiquantitative Analysis of the Kinetic Mechanism of Hydrogen Detection by a Palladium-Coated Photopyroelectric Detector.** A. Mandelis, C. Christofides, U of Toronto

---

**Multichannel/Multiplex Techniques—Molecular Optical Spectroscopy**

---

Arranged by M. B. Denton

- Multiplex vs. Multichannel Raman Spectroscopy.** B. Chase, Du Pont
- Near-IR Vibrational and Electronic Raman Spectroscopy with Array Detectors.** T. D. Harris, M. L. Schnoes, AT&T
- Hadamard Transform Spectrometry.** W. G. Fateley, A. P. Bohlike, J. D. Tate, J. White, R. M. Hammaker, Kansas State U

- Near-IR Raman Spectroscopy Employing a Charge-Coupled Device Detector.** R. B. Bihorn, J. L. Lippert, N. S. Ferris, Eastman Kodak
- Expanded Capabilities of a Multichannel HPLC Fluorescence Detector Utilizing a Pulsed Excitation Source.** J. M. Wegrzyn, M. A. Ford, Emory U
- Present and Future Applications of High-Performance Charge-Coupled Device Detectors in Molecular Fluorescence and Chemiluminescence.** R. D. Jalkian, M. B. Denton, U of Arizona
- Novel Crossed Interferometric Dispersive UV to Near-IR Spectrometer.** J. V. Sweedler, M. B. Denton, Stanford U
- Multiplex Disadvantage in UV-Vis Spectroscopy.** E. G. Voigtman, U of Massachusetts
- Limiting Noise Studies in UV-Vis Interferometry.** R. Williams, Clemson U

---

**Chiral Separations for Drug Analysis**

---

Arranged by D. A. Roston

- New Chiral Phases for the LC and GC Resolution of Racemates.** D. W. Armstrong, U of Missouri, Rolla
- Separation of the Enantiomers of Intact Sulfate Conjugates of Adrenergic Drugs by HPLC after Chiral Derivatization.** T. Walle, U. K. Walle, Medical U of South Carolina
- Practical Applications for High-Level Enantioselectivity.** W. H. Pirkle, K. Deming, E. Doherty, U of Illinois
- Considerations for Chiral Method Validation.** R. J. Bopp, S. A. Anliker, T. J. Faulkinbury, Eli Lilly
- NMR Investigation of a Chiral Recognition Mechanism.** J. A. Burke III, W. H. Pirkle, U of Illinois
- High-Level Enantioselectivity on an *N*-Arylamino Ester Based Chiral Stationary Phase.** K. C. Deming, W. H. Pirkle, U of Illinois
- Investigation into the Role of Enantioselective Desolvation in Chiral Recognition.** C. J. Welch, W. H. Pirkle, U of Illinois

---

**1988 Lippincott Award Symposium: Applications of Incoherent Light to Raman Scattering**

---

Arranged by J. A. de Haseth

- Introductory Remarks and Award Presentation to Andreas C. Albrecht.** R. F. Browner, Georgia Institute of Technology
- Award Address: Applications of Incoherent Light to Raman Scattering.** A. C. Albrecht, Cornell U
- Excited-State Structure and Dynamics from Resonance Raman Intensities.** R. A. Mathies, U of California, Berkeley
- Rotational Resonance Raman Effect: A Probe of Subpicosecond Photodissociation Dynamics.** L. D. Ziegler, Northeastern U
- Transform Approach to Resonance Raman Scattering: Theory and Application.** P. M. Champion, Northeastern U

---

**ICP/MS**

---

- Flow Injection ICP/MS—Handling Difficult Matrices.** R. C. Hutton, A. E. Eaton, P. D. Blair, A. Kinsella, R. Henry, VG Elemental
- On-Line Concentration and Cleanup of Natural Water Samples by Chelation Ion Chromatography Prior to Trace Element Analysis by ICP/MS.** L. M. Faires, C. J. Patton, U.S. Geological Survey

**Elimination of Sample Matrix and Enhancement of Analyte Signal for Analysis of Trace Elements by ICP/MS.** J. R. Pretty, T. M. Davidson, J. A. Caruso, U of Cincinnati

**Multivariate Calibration in ICP/MS.** M. E. Ketterer, C. A. Ramsey, J. J. Reschl, M. J. Peters, U.S. EPA

**Determination of Precious Metals in Fire Assay Beads by ICP/MS.** A. W. Varnes, BP Research

**Evaluation of ICP/MS for the Monitoring of Trace Metals in Groundwater.** M. Plantz, B. Warden, P. Duffy, WMI Environmental Monitoring Laboratories

**Determination of Halogens in Plastics by ICP/MS.** J. Marshall, J. Franks, ICI Wilton  
**Considerations in Developing ICP/MS Methods for Trace Element Analysis of Natural Waters.** L. M. Faires, U.S. Geological Survey  
**Direct Analysis of OMVPE Precursors by ICP/MS.** B. J. Streusand, S. W. Govorchin, Bandgap Technology Corp.

**Novel Applications of ICP Spectrometries**

*Arranged by* J.A.C. Broekaert

**Use of ICP Spectrometries for Solving Analytical Problems.** J.A.C. Broekaert, Institut für Spektrochemie, FRG

**Comparative Study of Simultaneous AAS and ICP-OES for Steel Analysis.** K. Ohis, Hoesch Stahl AG, FRG

**Recent Developments in Automated Sample Preparation for ICP-AES Analyses of Geological and Environmental Materials, and Chemometric Data Interpretation.** J. Brenner, M. Borsier, A. le Merchand, Geological Survey of Israel

**Interference or Contaminant: Distinguishing Weak Spectral Interferences and Trace Contaminants in ICP Emission Spectrometry.** R. I. Botto, Exxon

**Determination and Speciation of Pt-Based Antitumoral Drugs in Biological Fluids by Means of ICP-AES.** S. Caroli, C. Dominici, F. Petrucci, A. Alimonti, F. La Torre, M. A. Castello, Istituto Superiore di Sanita, Italy

**Analysis of Human Serum by ICP/MS.** C. Vandecasteele, Rijksuniversiteit van Gent, Belgium

**Plasma Spectroscopy**

**Excitation Parameters and Other Fundamental Parameters of the Inductively Heated Flame.** A. D. Weiss, C. B. Boss, North Carolina State U

**Evaluation of a Cooled Minihollow Cathode Emission Source for the Determination of Several Nonmetals.** F.-Y. Chen, J. C. Williams, Memphis State U

**Electron Density and Electronic Temperature in a Mixed-Gas Hollow-Cathode Discharge.** J. Angus, T. Niemczyk, B. Palmer, L. Layman, D. Hof, Los Alamos National Laboratory

**Simultaneous Determination of Several Elements in Nanoliter Samples of Renal Fluids by an Improved Hollow-Cathode Discharge.** J.-Y. Ryu, J. C. Williams, Memphis State U

**Matrix Effects in the Hollow-Cathode Emission Source.** R. Kuan, J. Williams, Memphis State U

**Study of Interference Effects in a DC Plasma Using Laser-Excited Fluorescence Spectroscopy.** C. LeBlanc, M. W. Blades, U of British Columbia

**Fundamental Studies of a Filament Vaporization Source for Sample Introduction into a DCP.** B. T. Buckley, C. B. Boss, North Carolina State U

**Use of the Ultrasonic Nebulizer with the Direct Current Plasma Spectrometer.** M. W. Tikkanen, S. Peters, R. Starek, Applied Research Laboratories

**Sample Preparation for Chromatographic Analysis**

*Arranged by* C. F. Poole

**Quantitative Sampling of Thymine Dimer from Excess Thymine as Predicted Using a Semi-Ideal Chromatography Model.** R. Ramsey, A. Katti, G. Guiochon, Oak Ridge National Laboratory

**Pyrolysis as a Sample Preparation Method in the Classification of Microorganisms.** G. Holzer, Georgia Institute of Technology  
**Membrane Approach to Solid-Phase Extraction.** D. F. Hagen, 3M

**Techniques for Handling Nanoliter Samples for Analysis by Capillary LC and Capillary Electrophoresis.** J. W. Jorgenson, R. T. Kennedy, M. Oates, B. Cooper, C. A. Monnig, U of North Carolina

**Sample Preparation in Chromatographic Analysis of Pharmaceutical Products.** J. Vessman, S.-O. Jansson, S. Larsson, A.-M. Tivert, O. Gyllenhaal, AB Hassle

**Sample Preparation for Chromatographic Analysis—An Overview.** C. F. Poole, S. K. Poole, Wayne State U

**Liquid Chromatographic Analysis of 3,4-Methylenedioxymethylamylamines, Designer Drugs Related to MDA.** C. R. Clark, F. T. Noggle, Jr., J. DeRuiter, Auburn U

**Chromatographic Methods for the Analysis of Anabolic Steroids in Pharmaceutical Formulations and Forensic Samples.** J. DeRuiter, F. T. Noggle, Jr., C. R. Clark, Auburn U

**Lasers and Laser-Induced Plasmas**

*Arranged by* J. Sneddon

**Spectroscopy in Laser-Generated Plumes.** E. S. Yeung, J. Zhu, Iowa State U

**Characterization of ArF Excimer Laser Ablation of YBa<sub>2</sub>Cu<sub>3</sub>O<sub>7</sub>.** W. A. Weimer, T. J. Geyer, Naval Weapons Center

**Laser-Induced Breakdown Spectroscopy for Rapid Analysis of Asbestos and Thallium Contamination.** D. Cremers, L. J. Radziemski, Los Alamos National Laboratory

**Investigations of Droplets in a Reduced-Pressure Laser-Induced Plasma.** P. J. Galley, G. M. Hieftje, Indiana U

**Combining TLC and GC by Laser Desorption and Pyrolysis.** E. S. Yeung, J. Zhu, Iowa State U  
**Improving Laser Ionization Efficiencies with Picosecond Light Pulses.** C. W. Wilkerson, Jr., S. M. Colby, J. P. Reilly, Indiana U

**Studies on the Use of an Excimer Laser for Sample Introduction in Plasma Emission Spectrometry.** J. Sneddon, Z. W. Hwang, Y. Y. Tang, U of Lowell

**Laser Ablation Sample Introduction and Plasma Source MS.** P. Arrowsmith, IBM  
**Computer Simulation Study of Lasing Dynamics of CVL Pumped Untuned Dye (Rhodamine 6G) Laser, with Consideration for Photodegradation.** A. Kawamoto, Toshiba

**Laboratory Information Management Systems for Analytical Information**

*Arranged by* T. V. Iorns

**LIMS in an Industrial Environment.** J. S. Mras, J. N. Dann, GTE

**Integrating Laboratory and Process Data in a Manufacturing Information Management System.** J. C. Brown, Carolina Eastman Division of Eastman Kodak

**ASTM Subcommittee E-31.40 on Laboratory Information Management Systems.** V. C. Zadnik, Aluminum Co. of America

**Desktop Networking with Macintosh Computers.** R. Williams, Clemson U  
**Design Considerations for AS LIMS—A System Targeted for the Process/Manufacturing Environment.** T. V. Iorns, S. Nathan, Axiom Systems

**Transfer and Manipulation of Atomic Absorption Data into Third Party Software.** F. Delles, T. Holmes, Varian Associates  
**Optimization of Laboratory Data Management through a Modularized PC-Based LIMS System.** R. D. Beatty, L. A. Richardson, Telecaction Associates

**Chemometrics: Fifteen Years after the Revolution**

*Arranged by* B. K. Lavine

**Factor Analysis Using Minimum Entropy Methods.** S. D. Brown, R. Larivee, U of Delaware  
**Applications of Chemometrics to Airborne Particle Source Apportionment Problems.** P. Hopke, U of Illinois

**Signal-Processing Techniques for Quantitative Analysis of FT Near-IR Spectra.** G. W. Small, M. A. Arnold, U of Iowa

**Hypothesis Testing for Multivariate Calibration.** P. J. Gemperline, East Carolina U  
**Optimized Algorithms for Piecewise Linear Discriminant Analysis.** T. F. Kaltenbach, G. W. Small, U of Iowa

**Monte Carlo Simulation of Biopolymer Separation by Micro-HPLC.** C. A. Guell, J. A. Holcombe, U of Texas  
**Evaluation of Amino Acid-Ninhydrin Reaction Kinetics with the Extended Kalman Filter.** C. A. Corcoran, T. T. Nguyen, A. Lankey, S. C. Rutan, Virginia Commonwealth U

**FRIDAY MORNING**

**Applications of Chemometrics in Analytical Chemistry**

*Arranged by* D. Osten

**Applications of Chemometric Methods for On-Line Data Analysis.** S. C. Rutan, Virginia Commonwealth U

**Multivariate Spectral Calibration Applied to Dielectric Thin Films Used in the Microelectronics Industry.** D. M. Haaland, I. Adhichetty, J. McGuire, T. M. Niemczyk, Sandia National Laboratories

**Chemometrics in Process Modeling.** D. Veltkamp, U of Washington  
**Multivariate Analysis Using Spectrometric Regression Techniques.** I. Landa, L. McDermott, LT Industries

**Dynamic Multivariate Calibration.** H. Martens, Norwegian Computing Center  
**Improved Stepwise Regression Using Cross Validation.** D. W. Osten, 3M

**Application of Artificial Neural Networks to Pattern Recognition of Environmental Pollutant Mass Spectra.** R. A. Olivero, D. W. Bottrell, Lockheed Engineering and Sciences



## Chromatographic Applications in Analytical Microbiology and Biotechnology

Arranged by S. L. Morgan

Use of Signature Biomarkers in Defining Microbial Community Structures and Activities in Biofilms. D. C. White, D. E. Nivens, M. W. Middleton, N. Dowling, U of Tennessee

Identification of Furanose and Pyranose Ring Forms of the Reducing Units of Oligosaccharides. F. J. Miskiel, J. H. Pazur, Penn State U

Approach to Automation of Sample Preparation for Profiling of Organic Acids. J. M. Rosenfeld, McMaster U

Preconcentration of Metals by Column Chromatography Using Algal Microorganisms as Ion-Exchange Resins. C. Mahan, V. Majidi, M. Peleties, J. A. Holcombe, U of Texas

Evaluation of Several New Chiral Stationary Phases for Enantiomer Separation. Q. Yang, W. H. Pirkle, U of Illinois

Determination of the Enantiomeric Purity of Carboxyl Activated *N*-Protected Amino Acids by HPLC on Chiral Stationary Phases. J. E. McCune, W. H. Pirkle, Q. Yang, U of Illinois

Gas Chromatographic/Mass Spectrometric Determination of Carbohydrate and Amino Acid Chemical Markers for Bacteria. A. Fox, S. L. Morgan, K. Ueda, J. Rogers, U of South Carolina

Pyrolysis GC/MS as a Tool for Detection and Identification of Chemical Markers for Bacteria. S. L. Morgan, K. Ueda, B. Watt, A. Fox, U of South Carolina

## Process Analysis and Control

Automated Selection of an Optimum Training Set for Discriminant Analysis. S. E. Carpenter, G. W. Small, U of Iowa

Meaning and Significance of Orthogonality. H. Mark, Bran + Luebbe

TGA/FT-IR Evolved Gas Spectral Analysis Using Target Factor Transformation. D. A. Compton, F. Cahn, Digilab Division, Bio-Rad Laboratories

Quantitative Applications of Raman Spectroscopy for Distillation Process Control. A. A. Garrison, E. C. Muly, D. Trimble, M. Roberts, U of Tennessee

Role of Promoters in the Direct Process Reaction. D. M. Sevenich, H. B. Friedrich, U of Iowa

Miniature Diode Array Spectrometers for Process Control Applications. J. T. Brownrigg, C. S. Hatch, T. L. Mikes, American Optical

Use of a Dedicated FT-IR for Quality Control in Industrial Gas Analysis Applications. L. A. Burgess, R. A. Derler, Nicolet

## IR Microspectroscopy

Arranged by M. Harthcock

FT-IR Microbeam Applications. L. Ellis, F. Baudais, D. Gravel, Bomem International

Microspectroscopy of Morphologically Differing Parts of Plant Material. D. L. Wetzel, R. G. Fulcher, Kansas State U

FT-IR Microspectroscopy—Research Applications. L. Ellis, P. Beauchesne, F. Baudais, Bomem International

FT-IR Microspectroscopy—Routine Applications. P. Beauchesne, L. Ellis, F. Baudais, Bomem International

FT-IR Microscopy: The Universal Molecular Spectrometer System. J. A. Reffner, W. T. Wihlborg, J. A. Ryan, Spectra-Tech

Analysis of Polymeric Food Containers by IR Microspectroscopy. R. T. Carl, E. F. Pankau, Nicolet

Reflectance Techniques in FT-IR Microspectroscopy. W. T. Wihlborg, J. A. Reffner, Spectra-Tech

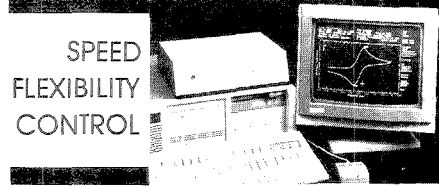
Polarized IR Microspectroscopic Imaging. R. T. Carl, M. J. Smith, Nicolet

Applications of IR Microimaging to Coating Technology. R. T. Carl, L. A. Burgess, Nicolet

Clinical Applications of IR Microsampling. S. L. Hill, K. Krishnan, Digilab Division, Bio-Rad Laboratories

# FACSS

**SPEED  
FLEXIBILITY  
CONTROL**




**For Your Electroanalytical Studies . . .**

- Cyclic Voltammetry
- Linear Scan Voltammetry
- Differential Pulse Voltammetry
- Square Wave Voltammetry
- Chronopotentiometry and Chronocoulometry

The Model CYSY-1 system puts you in complete control of your electrochemical research with its "all-in-one" system design, combining the power and versatility of the personal computer with the three-electrode potentiostat. It gives you an effective, easy-to-use means of electroanalytical control, data acquisition and calculation. The high-sensitivity version is perfect for microelectrode work, down to picoampere current levels. And you can export the data to your other software programs for statistics, spreadsheet analysis, or presentation graphics.

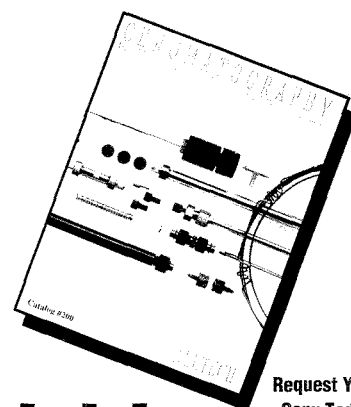
Use of high-resolution color effectively highlights operating functions and experimental results. Pointing with the computer mouse speeds your selection and provides easy zooming and baseline drawing.

*Write or phone now for our free brochure.*




Cypress Systems, Inc.  
P.O. Box 3931  
Lawrence, Kansas 66046  
(913) 842-2511

CIRCLE 28 ON READER SERVICE CARD



**Request Your Copy Today!**

**The most Comprehensive Chromatographic Source available, Alltech's Catalog #200 is filled with over 700 pages of the latest products and applications for all of your Chromatographic needs.**



**ALLTECH**

CIRCLE 1 ON READER SERVICE CARD

## Conferences

1990

- **Winter Conference on Plasma Spectrochemistry.** Jan. 8–13. St. Petersburg, FL. Contact: Ramon Barnes, Dept. of Chemistry, GRC Towers, University of Massachusetts, Amherst, MA 01003-0035 (413-545-2294)
- **6th International Symposium on Separation Science and Biotechnology.** Jan. 16–18. Fort Lauderdale, FL. Contact: Janet Cunningham, Barr Enterprises, P.O. Box 279, Walkersville, MD 21793 (301-898-3772)
- **2nd International Symposium on High-Performance Capillary Electrophoresis.** Jan. 29–31. San Francisco, CA. Contact: Shirley Schlessinger, 400 East Randolph Dr., Suite 1015, Chicago, IL 60601 (312-527-2011)
- **4th International Symposium on Biological and Environmental Reference Materials.** Feb. 5–8. Orlando, FL. Contact: Wayne Wolf, B311 Chemistry Bldg., NIST, Gaithersburg, MD 20899 (301-975-2030)
- **International Symposium on Free Radicals in Biotechnology and Medicine.** Feb. 7. London, U.K. Contact: P. E. Hutchinson, Analytical Division, Royal Society of Chemistry, Burlington House, London W1V 0BN, U.K.
- **41st Pittsburgh Conference on Analytical Chemistry and Applied Spectroscopy.** March 5–9. New York, NY. Contact: Linda Briggs, 300 Penn Center Blvd., Suite 332, Pittsburgh, PA (412-795-7110)
- **3rd Latin American Congress on Chromatography.** March 14–16. São Paulo, Brazil. Contact: Fernando Lanzas, University of São Paulo, Institute of Physics and Chemistry of São Carlos, 13560, São Carlos, SP, Brazil
- **Analytica '90.** March 18–23. Pretoria, South Africa. Contact: J. F. van Staden, Dept. of Chemistry, University of Pretoria, Pretoria 0002, South Africa
- **7th International Symposium on Preparative Chromatography.** April 8–11. Ghent, Belgium. Contact: M. Verzele, RUG-LOS, Krijgslaan 281 (S4), B-9000 Ghent, Belgium
- **20th International Symposium on Environmental Analytical Chemistry.** April 17–20. Strasbourg, France. Contact: M. Frei-Häuser, Postfach 46, CH-4123 Allschwil 2, Switzerland
- **4th Workshop on Chemistry and Analysis of Hydrocarbons.** April 20–21. Strasbourg, France. Contact: M. Frei-Häuser, Postfach 46, CH-4123 Allschwil 2, Switzerland
- **199th National Meeting of the American Chemical Society.** April 22–27. Boston, MA. Contact: Meetings Dept., American Chemical Society, 1155 16th St., N.W., Washington, DC 20036 (202-872-4396)
- **4th Symposium on the Analysis of Steroids.** April 24–26. Pécs, Hungary. Contact: S. Görög, c/o Chemical Works of Gedeon Richter Ltd., P.O.B. 27, H-1475 Budapest, Hungary
- **International Conference on Computer Networks (COMNET '90).** May 8–10. Budapest, Hungary. Contact: COMNET '90 Secretariat, P.O. Box 240, H-1368 Budapest, Hungary
- **12th International Conference on Biochemical Analysis (Biochemische Analytik '90).** May 8–11. Munich, F.R.G. Contact: Biochemische Analytik '90, Nymphenburger Straße 70, D-8000 München 2, F.R.G.
- **International Symposium on High-Resolution and Microcolumn Chromatographic Techniques.** May 13–18. Monterey, CA. Contact: Stuart Cram, Hewlett-Packard, 3000 Hanover St., MS 20BAE, Palo Alto, CA 94304 (415-857-1501)
- **Symposium on Analysis of Paints and Related Materials.** May 14–15. Pittsburgh, PA. Contact: Dorothy Savini, ASTM, 1916 Race St., Philadelphia, PA 19103 (215-299-5413)
- **14th International Symposium on Column Liquid Chromatography.** May 20–25. Boston, MA. Contact: Shirley Schlessinger, 400 East Randolph Dr., Suite 1015, Chicago, IL 60601 (312-527-2011)
- **2nd Scientific Computing and Automation Conference and Exhibition.** May 22–25. Maastricht, The Netherlands. Contact: Robi Valkhoff, Reunion International, Geldersekeade 89, 1011 EL Amsterdam, The Netherlands
- **4th International LIMS Conference.** June 4–7. Pittsburgh, PA. Contact: Gerst Gibbon, LIMS Institute, c/o U.S. DOE/PETC, P.O. Box 109400, Pittsburgh, PA 15236
- **5th World Filtration Congress (Interfilt '90).** June 5–8. Nice, France. Contact: Interfilt '90, c/o IDEXPO, 21 Ave. de la Div. Leclerc, F-94230 Chachan, France
- **3rd Symposium on Computer-Enhanced Analytical Spectroscopy.** June 6–8. Snowbird, UT. Contact: Peter Jurs, Dept. of Chemistry, Penn State University, University Park, PA 16802
- **International Conference on Chirality.** June 7–9. Cancun, Mexico. Contact: D. W. Armstrong or I. W. Wainer, Dept. of Chemistry, University of Missouri—Rolla, Rolla, MO 65401 (314-341-4429)
- **33rd IUPAC International Symposium on Macromolecules (Macro '90).** July 8–13. Montreal, Canada. Contact: Macro '90 Secretariat, Dept. of Chemical Engineering, McGill University, 3480 University St., Montreal H3A 2A7, Canada
- **International Conference and Industrial Exhibition on Ion-Exchange Processes (Ion-Ex '90).** July 9–11. Wales, U.K. Contact: Hayden Hughes, Research Division, The North East Wales Institute, Connah's Quay, Deeside, Clwyd. CH5 4BR, U.K.
- **1st Changchun International Symposium on Analytical Chemistry.** Aug. 7–11. Changchun, People's Republic of China. Contact: Qinhan Jin, Dept. of Chemistry, Jilin University, Changchun, Jilin 130021, People's Republic of China
- **J. Heyrovský Centennial Congress on Polarography and 41st Meeting of the International Society of Electrochemistry.** Aug. 20–25. Prague, Czechoslovakia. Contact: Secretariat, J. Heyrovský Centennial Congress, Czechoslovak Academy of Sciences, J. Heyrovský Institute of Physical Chemistry and Electrochemistry, Dolejškova 3, 182 23 Prague 8, Czechoslovakia
- **6th International Symposium on Bioluminescence and Chemiluminescence.** Aug. 26–30. Cambridge, MA. Contact: L. J. Kricka, Dept. of Pathology and Laboratory Medicine, 3400 Spruce St., 784 Founders Pavilion, Philadelphia, PA 19104 (215-662-6575)
- **Euroanalysis VII.** Aug. 26–31. Vienna, Austria. Contact: D. M. Grasserbauer, c/o Interconvention, Austria Center Vienna, A-1450 Vienna, Austria
- **200th National Meeting of the American Chemical Society.** Aug. 26–31. Washington, DC. Contact: Meetings Dept., American Chemical Society, 1155 16th St., N.W., Washington, DC 20036 (202-872-4396)
- **104th Annual AOAC International Meeting and Exposition.** Sept. 10–13. New Orleans, LA. Contact: Margaret Ridgell, AOAC, Suite 400, 2200 Wilson Blvd., Arlington, VA 22201 (703-522-3032)
- **Eastern Analytical Symposium.** Sept. 23–28. New York, NY. Contact: EAS, P.O. Box 633, Montchanin, DE 19710 (302-453-0785)
- **18th International Symposium on Chromatography.** Sept. 23–28. Amsterdam, The Netherlands. Contact: Symposium on Chromatography, c/o RAI Organisatie Bureau Amsterdam bv, Europaplein 12, 1078 GZ Amsterdam, The Netherlands

## Short Courses and Workshops

■ **Workshop on Advances in Ion-Exchange Chromatography and Electrochemical Detection.** Sept. 21-22. Baltimore, MD. Contact: Nancy Jensen, Dionex Corp., P.O. Box 3603, Sunnyvale, CA 94088 (408-737-0700, ext. 1474)

■ **Workshop on Advanced Experiment Design.** Oct. 24-27. Minneapolis, MN. Contact: Stat-Ease, 3801 Nicollet Ave. South, Minneapolis, MN 55409 (612-822-5574)

■ **Short Course on the Practice of Modern HPLC.** Oct. 16-18, Saddlebrook, NJ; Nov. 27-29, Foster City, CA. Contact: Tom Jupille, LC Resources, 3182 C Old Tunnel Rd., Lafayette, CA 94549 (415-930-9043)

■ **Short Course on Practical HPLC for Biotechnology.** Nov. 29-30. Foster City, CA. Contact: Tom Jupille, LC Resources, 3182 C Old Tunnel Rd., Lafayette, CA 94549 (415-930-9043)

■ **Survey of Industrial Hygiene.** Dec. 12-15, 1989 and April 24-27, 1990. Cincinnati, OH. Contact: Susan Millman, University of Cincinnati Medical Center, Institute of Environmental Health, Kettering Laboratory, 3223 Eden Ave., Cincinnati, OH 45267 (513-558-1732)

■ **Course on Experimental Design for Productivity and Quality in Research, Development, and Manufacturing.** Feb. 19-23, 1990. Houston, TX. Contact: Statistical Designs, 9941 Rowlett, Suite 6, Houston, TX 77075 (713-947-1551)

■ **Short Course on Aerosol Measurement.** April 18-20, 1990. Cincinnati, OH. Contact: Susan Millman, University of Cincinnati Medical Center, Institute of Environmental Health, Kettering Laboratory, 3223 Eden Ave., Cincinnati, OH 45267 (513-558-1732)

## ACS Courses

The following courses are offered in conjunction with the FACSS meeting in Chicago, IL, Oct. 1-6.

■ **Practical HPLC Method Development.** Oct. 6-7. Lloyd Snyder and J. Kirkland

■ **Life Cycle Management for Laboratory Data.** Oct. 6-7. Walter Shackelford

■ **Maintaining and Troubleshooting Chromatographic Systems.** Oct. 6-7. M.P.T. Bradley

■ **Effective Management of Chemi-**

cal Analysis Laboratories. Oct. 6-7. John H. Taylor, Jr., and Mary Routson

■ **Quality Assurance of Chemical Measurements.** Oct. 6-7. John K. Taylor

■ **Capillary Gas Chromatography.** Oct. 6-7. Stuart Cram and Milos Novotny

■ **Analytical Laboratory Operations: Analysis of Water and Waste Samples.** Oct. 6-7. Marcus Cooke

■ **Environmental Laboratory QA/QC Data Validation.** Oct. 6-7. Henry Nowicki and William Purves

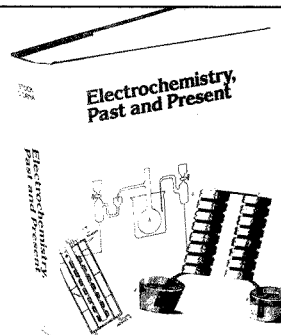
For information on these and other ACS courses, contact the Department of Continuing Education, American Chemical Society, 1155 16th St., N.W., Washington, DC 20036 (202-872-4508).

## Call for Papers

■ **3rd Latin American Congress on Chromatography.** São Paulo, Brazil. March 14-16, 1990. The program will cover fundamental and practical aspects of all modes of chromatography, including HPLC, high-resolution GC, SFC, and GC/MS. Topics include columns, instrumentation, and applications in areas such as petrochemistry, environmental analysis, biochemistry, foods, and polymers. Authors wishing to submit contributions as poster presentations should request forms from Fernando M. Langas, University of São Paulo, Institute of Physics and Chemistry of São Carlos, 13560, São Carlos, SP, Brazil. Deadline for submission of abstracts is Dec. 1.

■ **2nd International Symposium on Applications of Analytical Techniques to Industrial Process Control (ANATECH '90).** Noordwijkerhout, The Netherlands. April 3-5, 1990. The symposium will focus on recent developments in analytical techniques and applications in process control, with particular emphasis on sampling problems, sample preparation, in-line and on-line measurements, and remote sensing. Authors wishing to contribute oral or poster presentations should submit 250-word abstracts by Oct. 15 to Willem van der Linden, Laboratory for Chemical Analysis-CT, University of Twente, P.O. Box 217, NL-7500 AE Enschede, The Netherlands.

These events are newly listed in the JOURNAL. See back issues for other events of interest.



## Electrochemistry, Past and Present

The growing debate over nuclear fusion in a test tube has resulted in a renewed interest in electrochemistry. The development of the battery, pH meter, and pollution control devices has been the result of electrochemistry. This new title highlights key advances in this exciting field—past, present and future.

Thirty-eight chapters capture major events and technologies of classical and fundamental electrochemistry, electrosynthesis, electroanalytical chemistry, industrial electrochemistry, electrode systems and pH measurement. General headings include:

- foundations of electrochemistry
- organic and biochemical electrochemistry
- electroanalytical chemistry
- industrial electrochemistry

This volume presents recent advances in novel electrochemical techniques. Applications in the large-scale production of organic compounds, the elucidation of the biogenesis of natural products by reactions at electrode surfaces, and electrochemical behavior of biological systems are reviewed. Also covered are future possibilities of portable electrolysis, systems for metal recovery and pollution control, and electrochemical machining.

Rich in an array of topics, this title contains many historical photographs and biographical chapters on some of the noted electrochemists.

John T. Stock, *Editor*, University of Connecticut

Mary Virginia Orna, *Editor*, National Institute of Environmental Health Sciences

Developed from a symposium sponsored by the Division of the History of Chemistry and the Division of Analytical Chemistry of the American Chemical Society

ACS Symposium Series No. 390

613 pages (1989) Clothbound

ISBN 0-8412-1572-3 LC 89-15

US & Canada \$89.95 Export \$107.95

O · R · D · E · R · F · R · O · M

American Chemical Society  
Distribution Office, Dept. 21  
1155 Sixteenth St. N.W.  
Washington, DC 20036

or CALL TOLL FREE

**800-227-5558**

(in Washington, D.C. 872-4363) and use your credit card!



## Get realistic about solid waste analysis

### Satisfy SW846 QA/QC requirements with the first commercial reference samples derived from real-world hazardous waste

Valid results are critical in analyzing solid waste. Obtain *certified confidence* with Fisher Scientific's Solid Waste Reference Samples (SWRS). SWRS are produced from *actual* industrial waste streams—homogenized, analyzed and packaged. They are *not* spiked. Their matrices and analytes parallel the analytical samples you receive from clients.

Real-world SWRS let you evaluate how well your lab handles difficult analyses. You can compare your results to an inter-laboratory reference value reliable at the 95% confidence level, assuring the accuracy of your QA/QC methods. For details on our new SWRS, contact your local Fisher Representative or circle the Reader Service number below.

**Expect more from FisherChemical**



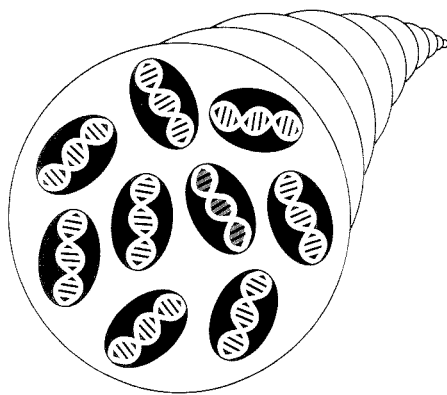
**FisherChemical**

**Fisher Scientific**

Excellence in Serving Science...Since 1902

CIRCLE 50 ON READER SERVICE CARD

# Tracking Genetically Engineered Microorganisms



**A**fter all the preliminary experiments, the ethical debates, the government red tape, and the inevitable legal battles, field tests of genetically engineered microorganisms (GEMs) are finally under way. As biotechnology steps out of the controlled environment of the research laboratory and into the real world, analytical techniques for detecting and monitoring released GEMs must keep pace. The traditional analytical methods of microbiology, such as counting bacterial colonies on a petri dish, will have to be coupled with techniques for monitoring recombinant DNA.

Many of the early field experiments are looking at the environmental impact, if any, following the release of specific GEMs and examining how their presence affects other microbial and, ultimately, plant and animal communities. Analytical methods must provide answers to questions about how successfully GEMs compete with other microorganisms, whether recombinant genes transfer to other organisms, how these engineered microorganisms spread, and how long they survive in various environments. Each new field test of a GEM will present opportunities to experiment with different analytical techniques. Therefore, these early field experiments are as much a test of the analytical procedures being developed as the GEMs being monitored.

In 1987 Steven Lindow and Nickolas Panopoulos of the Department of Plant Physiology at the University of California, Berkeley, directed release experiments with *Ice<sup>-</sup> Pseudomonas syringae*, a genetically engineered bacterium designed to reduce frost damage to plants. Two strains of this GEM were sprayed on potato plant seedlings planted in an experimental agricultural plot at Tulelake, CA.

*Ice<sup>-</sup>* bacteria differ from wild-type *P. syringae* by the partial deletion of the gene encoding an ice-catalyzing protein. Pure water can supercool to  $-40^{\circ}\text{C}$  unless a template of appropriate molecules or particles promotes ice formation. In most plants, freezing at temperatures  $> -10^{\circ}\text{C}$  is catalyzed by the activities of a number of common bacteria, including the expression of the ice protein in wild-type *P. syringae* (labeled *Ice<sup>+</sup>*).

Introducing engineered *Ice<sup>-</sup>* bacteria before *Ice<sup>+</sup>* colonizes the seedlings should minimize wild-type populations of *Ice<sup>+</sup>* through competition. Early results show that the *Ice<sup>-</sup>* sprayed plants

# NEW PRODUCTS



**DeSorb 2300B** is a multiport degassing unit designed for sample preparation for flowing-gas surface area analyzers. Up to three samples can be degassed simultaneously. Micromeritics 401

**Amino acids.** AminoSys HPLC system includes a choice of UV or fluorescence detection, software for system control and evaluation, and an autosampler that provides minimal carryover and allows derivatization using up to eight reagents. Pharmacia LKB 404

**Chromatography.** Midas M888 chromatography data-handling system collects, analyzes, and manipulates data from up to eight chromatographs simultaneously. Postrun and interactive graphics capabilities include chromatogram subtraction and selected area integration. Laboratory Data Systems 405

**Circular dichroism.** Double-CD spectrophotometer, which allows for the acquisition of two CD spectra simultaneously, is also capable of acquiring true absorbance data as a function of wavelength or wavenumber. The two CD channels are independent; only the wavelength range and scanning speed are the same for both samples. Olis 406

**Distillation.** Micro-Dist provides distillation of environmental samples for cyanides and total recoverable phenolics. Disposable tubes are placed into a 21-position heating block and heated to 135 °C; distillations are complete

within 30 and 60 min for cyanides and phenolics, respectively. Lachat Instruments 408

**Pore characterization.** Porometer II features an integrity test that allows testing of cartridge characteristics and a permeability test that measures flow-through characteristics. The instrument also offers bubble-point and flow-rate testing. Coulter Electronics 407

**Detector.** Model LS-40 is a programmable fluorescence LC detector with fluorescence, phosphorescence, chemiluminescence, and bioluminescence capabilities. The system features a 4- $\mu$ L illuminated flow cell optimized for peak resolution and clearance. Perkin-Elmer 409

**FT-IR.** Baseline series of sampling accessories includes a horizontal ATR accessory for sampling gels, pastes, semisolids, and sheet films; a diffuse reflectance accessory for solids sampling; and a specular reflectance accessory for analyzing highly reflective surfaces. Spectra-Tech 410

**AA.** Model Z-8100, a tandem flame/furnace-polarized Zeeman atomic absorption spectrophotometer, includes a built-in CRT and printer/plotter for data presentation. Both the flame and furnace atomizers are permanently installed and aligned. Twenty analytical methods can be stored in non-volatile memory. Hitachi 411

**Titration.** Model DL70 autotitrator provides simultaneous method development and titration, automatic switching of up to four burettes and electrodes, and full control of attached peripherals. The memory is preprogrammed with 10 standard methods and contains room for 25 additional user-developed methods. Mettler 412

**Spectrometer.** SpectraPro-500 contains a triple grating turret that allows one, two, or three gratings to be installed at the same time. Features include direct digital scanning and compatibility with focal plane detectors. Acton Research Corp. 413

## Software

**Hazardous chemicals.** SCS Access contains key regulatory and advisory information on more than 5000 hazardous industrial chemicals. The software allows users to determine which federal and selected state regulations apply and if a chemical is a known carcinogen. Logical Technology 415

**Graphics.** ProPLOT is a 2D graphics package for scientific and engineering applications. The program produces any combination of scatter, line, and bar graphs; there is no limit to the number of graphs per page or to the number of data sets and axes per graph. Cogent Software 416

## Manufacturers' Literature

**Vacuum technology.** *The Vacuum Chronicles* focuses on techniques, tips, and applications in vacuum technology. Vol. 1, No. 1 features an article entitled "Getting the Most Out of Your Cryopump." Danielson Associates 418

**Pyrolyzer.** Brochure describes the Pyroprobe 1000, a digital microprocessor-controlled filament pyrolyzer for GC, MS, and FT-IR analyses of polymers, geological samples, and a variety of other materials. 4 pp. Chemical Data Systems 419

**LC newsletter.** *Interaction Separations*, No. 2, discusses enhancement of detection sensitivity, optimization parameters for anion-exclusion chromatography, and principles of solid-phase extraction. 8 pp. Interaction Chemicals 420

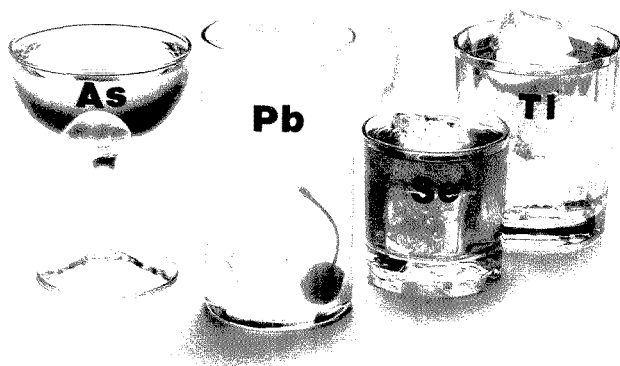
**ICP.** Poster of the periodic table includes information on preparing samples and on choosing appropriate wave-

---

For more information on listed items, circle the appropriate numbers on one of our Readers' Service Cards

---

# Name your poison



Determine these and other  
EPA toxic elements  
simultaneously with Baird ICP.

All-at-once Baird ICP with our UDX ultrasonic sample delivery system could be the answer to almost all of your trace element analysis problems. Meeting CLP detection limits for priority pollutants in drinking water, for example - or verification of sub-ppb ultrapurity in manufacturing process waters.

A UDX-equipped Baird ICP will provide detection limits ten times better than an ICP with a conventional nebulizer - limits approaching those of graphite furnace AA. And the fact that it performs so well for arsenic, lead, selenium and thallium now permits you to determine these and other CLP elements at the same time. No headaches from large sample backlogs. No missed deadlines and contract penalties so often associated with one-at-a-time AA.

Comparative Detection Limits ( $\mu\text{g/L}$ )		
Element	Conventional Nebulizer	UDX Ultrasonic Nebulizer*
As	30	3
Pb	20	2
Se	30	3
Tl	40	4

*\*Data obtained on a Baird Plasma PSQ simultaneous ICP Spectrometer*

Act at once. Call or write right now for complete information on Baird UDX/ICP. Baird Corporation, Analytical Instruments Division, 125 Middlesex Turnpike, Bedford, MA 01730. Telephone (617) 276-6163.

# BAIRD ICP

An Imo Industries Company

## NEW PRODUCTS

lengths for ICP emission analysis. A guide to the recommended stabilizing acid for each element is also provided. Baird 421

LC. Brochure highlights the  $\beta$ -RAM flow-through monitor, which measures radioactivity in HPLC eluates. The system is composed of a liquid scintillation detector interfaced to an AT computer. IN/US Service Corp. 422

Newsletter. *Scan Time Monitor* features news and information about IR applications for methods and process development chemists. Issue No. 1 includes an article on FT-IR in the production laboratory. Spectra-Tech 423

### Catalogs

Instrumentation. Catalog includes air velocity, pressure, water quality, pH, temperature, and humidity meters. Electrical testing equipment is also listed. Davis Instrument Manufacturing Co. 425

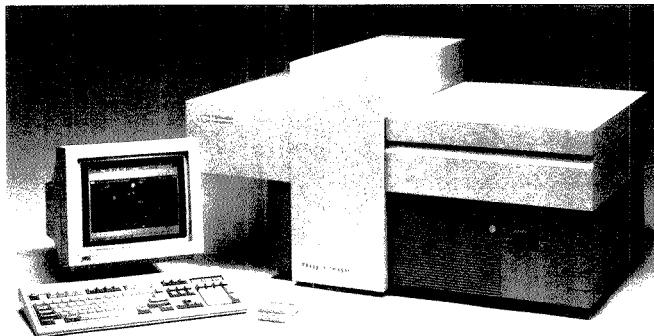
MS. 1989-90 catalog includes electron multipliers; DCI probes; filaments;

heaters; products for FAB and SIMS; gaskets; gas inlet probes; data systems; cryopumps; resistors; and GC/MS, LC/MS, and SFC/MS interfaces. Vacuetrics 427

Laboratory products. Catalog lists acrylic laboratory products, including slide holders, chromatography racks,

safety shields, desiccator storage cabinets, and Pasteur pipet supports. 12 pp. Isolab 428

Computers. Catalog includes optical disks, software, printers, plotters, cables, furniture, terminals, cleaning supplies, and books. 176 pp. Hewlett-Packard 429



400A PhosphorImager uses storage phosphor technology to read images of radioactivity from electrophoresis gels, blotting membranes, and other media. Molecular Dynamics 402

# NEED AN ARTICLE FROM AN EARLIER ISSUE?

GET IT FROM CAS DOCUMENT DELIVERY SERVICE®

Does your research depend on locating an article published in this journal a few years back? The CAS Document Delivery Service can provide copies of articles from **all ACS journals from initial publication to the present.**

You'll also find CAS DDS an excellent source for documents related to chemistry and allied disciplines drawn from **the more than 10,000 scientific and technical publications received at Chemical Abstracts Service each year.**

Order articles, patents, and reports back to

1975 (1970 for Soviet material). Most orders are on their way within 24 hours. Call for more information. Ask about our FREE 1989 Directory of Publications.

Chemical Abstracts Service®  
2540 Olentangy River Road  
P.O. Box 3012  
Columbus, OH 43210

Phone: (toll-free) 800-848-6538, ext. 3670  
or 614-447-3670

Chemical Abstracts Service is a division of the American Chemical Society.



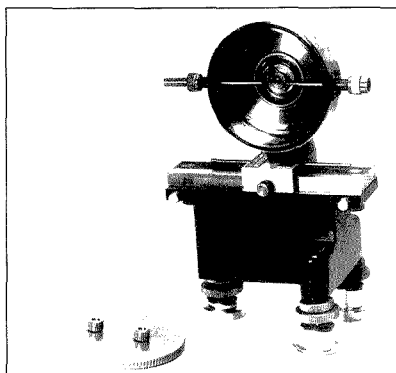
## INDEX TO ADVERTISERS IN THIS ISSUE

CIRCLE INQUIRY NO.	ADVERTISERS	PAGE NO.	CIRCLE INQUIRY NO.	ADVERTISERS	PAGE NO.
3	*A&D Engineering, Inc.	961A	142	Rheodyne, Inc. Bonfield Associates	955A
1	*Alltech Chromad	997A	156	*Tekmar Kenyon Hoag Associates	942A
20	Baird Corporation W. J. Hearn & Company, Inc.	1005A	165	Vestec Corporation Barbeau-Hutchings Advertising, Inc.	969A
18	*J. T. Baker Inc. Stiegler, Wells & Brunswick, Inc.	932A	174	Waters/Division of Millipore Millicom, Inc.	965A
22, 23	*Beckman Instruments, Inc. Cochrane, Chase, Livingston & Company	937A	177	*Wheaton The Wheaton Agency	989A
30	*Cole-Parmer Instrument Company C-P Advertising	973A- 975A	* See ad in ACS Laboratory Guide. ** Company so marked has advertisement in Foreign Regional edition only. Advertising Management for the American Chemical Society Publications		
26	*Conostan Division/Conoco Specialty Products Robert Lamons & Associates	987A	<b>CENTCOM, LTD</b>		
28	*Cypress Systems, Inc.	997A	<i>President</i>		
32	*Dialog Information Services, Inc. Humpal, Leftwich & Sinn, Inc.	977A	<b>Thomas N. J. Koerwer</b>		
34	*Dionex Corporation Rainoldi, Kerzner & Radcliffe	IFC	<i>Executive Vice President Senior Vice President</i>		
50	*Fisher Scientific Hawbaker Communications, Inc.	1000A	<b>James A. Byrne Benjamin W. Jones</b>		
58	*Galileo Electro-Optics Corp. Legasse Associates Advertising, Inc.	981A	<b>Clay S. Holden, Vice President</b>		
60	*Gilson Medical Electronics, Inc.	931A	<b>Robert L. Voepel, Vice President</b>		
61	*Gilson Medical Electronics, SA	931A	<b>Joseph P. Stenza, Production Director</b>		
63	Hamamatsu Corporation Ketchum/Mandabach & Simms	985A	500 Post Road East P.O. Box 231 Westport, Connecticut 06880 (Area Code 203) 226-7131 Telex No. 643310 FAX: 203-454-9939		
74	IMSL, Inc.	967A	<b>ADVERTISING SALES MANAGER</b>		
94	LDC Analytical HRS Communications	946A	<b>Bruce E. Poorman</b>		
92	*Leybold Vacuum Products, Inc. CD Werbeagentur GmbH	950A	<b>ADVERTISING PRODUCTION MANAGER</b>		
90	Link Analytical	959A	Jane F. Gatenby		
88	Liquid Carbonic	943A	<b>SALES REPRESENTATIVES</b>		
98	*Mattson Instruments, Inc. Cunningham & Welch Design Group	949A	<b>Philadelphia, PA . . . Patricia O'Donnell, CENTCOM, LTD., GSB Building, Suite 405, 1 Belmont Avenue, Bala Cynwyd, Pa. 19004. Telephone: 215-667-9666, FAX: 215-667-9353</b>		
96	*Mettler Instrument Corporation Gilbert, Whitney & Johns Inc.	941A	<b>New York, NY . . . John F. Raftery, CENTCOM, LTD., 60 East 42nd St., New York, N.Y. 10165. Telephone: 212-972-9660</b>		
110	*Nicolet Analytical Instruments	935A	<b>Westport, CT . . . Edward M. Black, CENTCOM, LTD., 500 Post Road East, P.O. Box 231, Westport, Ct. 06880. Telephone: 203-226-7131, Telex 643310, FAX: 203-454-9939</b>		
154	*Nupro Company/A Swagelok Company Falls Advertising Company	970A	<b>Cleveland, OH . . . Bruce E. Poorman, John C. Guyot, CENTCOM, LTD., 325 Front St., Suite 2, Berea, Ohio 44017. Telephone: 216-234-1333, FAX: 216-234-3425</b>		
120	*Ohaus Ballotta, Napurano & Company Inc.	939A	<b>Chicago, IL . . . Michael J. Pak, CENTCOM, LTD., 540 Frontage Rd., North- field, Ill. 60093. Telephone: 312-441-6383, FAX: 312-441-6382</b>		
129	*Parker Hannifin Corporation Amundsen/Beier, Inc.	944A	<b>Houston, TX . . . Michael J. Pak, CENTCOM, LTD. Telephone: 312-441-6383</b>		
127	*Philips Analytical	990B	<b>San Francisco, CA . . . Paul M. Butts, CENTCOM, LTD., Suite 1070, 2672 Bayshore Frontage Road, Mountain View, CA 94043. Telephone: 415- 969-4604</b>		
125	*PolyScience	963A	<b>Los Angeles, CA . . . Clay S. Holden, CENTCOM, LTD., Newton Pacific Center, 3142 Pacific Coast Highway, Suite 200, Torrance, CA 90505. Telephone: 213-325-1903</b>		
138	*Radiometer America Inc. Noon, Inc.	OBC	<b>Boston, MA . . . Edward M. Black, CENTCOM, LTD. Telephone: 203-226- 7131</b>		
140	Rainin Instrument Company, Inc. RIC Advertising	957A	<b>Atlanta, GA . . . John F. Raftery, CENTCOM, LTD. Telephone: 212-972-9660</b>		
			<b>Denver, CO . . . Paul M. Butts, CENTCOM, LTD. Telephone: 415-969-4604</b>		
			<b>United Kingdom</b>		
			<b>Reading, England . . . Malcolm Thiele, Technomedia Ltd., Wood Cottage, Shurlock Row, Reading RG10 0QE, Berkshire, England. Telephone: 073-434-3302, Telex #848800, FAX: 073-434-3848</b>		
			<b>Lancashire, England . . . Technomedia Ltd., c/o Meconomics Ltd., Me- conomics House, 31 Old Street, Ashton Under Lyne, Lancashire, Eng- land. Telephone: 061-308-3025</b>		
			<b>Continental Europe . . . Andre Jamar, International Communications, Inc., Rue Mallar 1, 4800 Verviers, Belgium. Telephone: (087) 22-53-85, FAX: (087) 23-03-29</b>		
			<b>Tokyo, Japan . . . Sumio Oka, International Media Representatives Ltd., 2-29 Toranomon, 1-Chome Minato-ku Tokyo 105 Japan. Telephone: 502- 0656, Telex #22633, FAX: 591-2530</b>		

Master the basics of this powerful analytical tool

# X-RAY POWDER DIFFRACTION

Place Your  
Order Today!



An Audio Course produced by the American Chemical Society

From geology to solid state chemistry, here is an easy-to-use audiocassette course that not only addresses basic principles, but also details techniques and procedures used in X-ray powder diffraction. Beginning with a general overview and ending with a discussion on the use of PDF for qualitative phase analysis, this course covers information on all the key subject areas of this analytical method.

## WHAT YOU'LL LEARN

In just a few short hours, you'll gain an understanding of new theories, applications, and techniques. Learn how to set up, align, and run the instrument; how to set up and run diffraction experiments; and how to prepare samples for analysis. Gain a better understanding of how to perform qualitative phase analysis and how to interpret X-ray diffraction data. Plus, these topics will add to your overall understanding:

- principles of X-ray powder diffraction
- instrument selection and parameters
- sample preparation for X-ray diffractometry
- data evaluation
- qualitative methods

## HOW YOU'LL BENEFIT

Because this course teaches you the basic principles involved, you'll improve your on-the-job effectiveness . . . get better data from your X-ray equipment . . . perform analyses faster and more accurately . . . learn special techniques for qualitative phase identification . . . and more!

## ABOUT THE COURSE AUTHOR

Ron Jenkins, JCPDS-ICDO, Swarthmore, Pennsylvania, was formerly Principal Scientist, Philips Electronic Instruments. He has been actively involved in the application of X-ray spectrographic and diffraction techniques and has published six books and more than 100 papers on these methods.

## UNIT (Catalog No. A5)

This audio course comes with four audiocassette tapes (that's 3.7 hours listening time) and a 153-page manual—packaged in a convenient reference-shelf case.

US & Canada: \$440.00; export: \$528.00.  
Additional manuals: \$35.00 each, US & Canada: \$42.00 each, export.

**BACKED BY THE ACS  
GUARANTEE**

ACS guarantees you'll benefit from this course! If you're not completely satisfied with your audio course, simply return it within ten days of receipt for a full refund, charge credit, or cancellation of invoice.

CALL TOLL FREE **1-800-227-5558!**  
In Washington DC area call (202) 872-4363!

## O · R · D · E · R   F · O · R · M

Send this Order Form with your payment or purchase order to:  
**American Chemical Society, Distribution Office, Dept. 06  
PO Box 57136, West End Station, Washington, DC 20037**

	Qty.	US & Can Price	Export Price	Total Amount
X-ray Powder Diffraction (Cat. No. A5)	_____	\$440.00	\$528.00	\$ _____
Additional Manuals	_____	\$ 35.00	\$ 42.00	\$ _____
Total enclosed:				\$ _____

### Ship to:

Name \_\_\_\_\_  
Organization \_\_\_\_\_  
Address \_\_\_\_\_  
City, State, Zip \_\_\_\_\_  
Phone \_\_\_\_\_

### Bill to:

Name \_\_\_\_\_  
Organization \_\_\_\_\_  
Address \_\_\_\_\_  
City, State, Zip \_\_\_\_\_  
Phone \_\_\_\_\_

### Methods of Payment:

Payment enclosed (make checks payable to ACS).  Purchase order enclosed. PO # \_\_\_\_\_  
 Charge my  MasterCard/VISA  American Express  Diners Club/Carte Blanche  
Account # \_\_\_\_\_  
Expires \_\_\_\_\_ Interbank # \_\_\_\_\_  
Name of Cardholder \_\_\_\_\_  
Signature \_\_\_\_\_  
Phone \_\_\_\_\_

Orders from individuals must be prepaid. Please allow 2-3 weeks for UPS delivery. Foreign payment must be made in US currency by international money order, UNESCO coupons, or US bank draft.

EDITOR: **GEORGE H. MORRISON**ASSOCIATE EDITORS: **Klaus Biemann,**  
**Georges Guiochon, Walter C. Herlihy,**  
**Robert A. Osteryoung, Edward S. Yeung****Editorial Headquarters**1155 Sixteenth St., N.W.  
Washington, DC 20036  
Phone: 202-872-4570  
Telefax: 202-872-6325*Managing Editor:* Sharon G. Boots*Associate Editors:* Louise Vores,  
Mary Warner*Assistant Editors:* Grace K. Lee,  
Alan R. Newman*Editorial Assistant:* Felicia Wach*Director, Operational Support:* C. Michael  
Phillippe*Production Manager:* Leroy L. Corcoran*Art Director:* Alan Kahan*Designer:* Amy Meyer Philter*Production Editor:* Elizabeth E. Wood*Circulation:* Claud Robinson*Editorial Assistant, LabGuide:* Joanne Mullican**Journals Dept., Columbus, Ohio***Associate Head:* Marianne Brogan*Journals Editing Manager:* Joseph E. Yurvati*Associate Editor:* Rodney L. Ternos*Staff Editor:* Sharon K. Hatfield**Advisory Board:** Bernard J. Bulkin, Michael S.  
Epstein, Renaat Gijbels, Peter R. Griffiths,  
Thomas L. Isenhour, Nobuhiko Ishibashi,  
James W. Jorgenson, Peter C. Jurs, Mary A.  
Kaiser, David L. Nelson, Lawrence A. Pachla,  
Ralph E. Sturgeon, George S. Wilson, Mary J.  
Wirth, Andrew T. Zander, Richard N. Zare  
*Ex Officio:* Sam P. Perone**Instrumentation Advisory Panel:** James B.  
Callis, Bruce Chase, R. Graham Cooks, L. J.  
Cline Love, Sanford P. Markey, Ronald E. Ma-  
jors, Linda B. McGown, Gary W. Small, R. Mark  
Wightman

*Published by the*  
**AMERICAN CHEMICAL SOCIETY**  
1155 16th Street, N.W.  
Washington, DC 20036

**Publications Division***Director:* Robert H. Marks*Journals:* Charles R. Bertsch*Special Publications:* Randall E. WedinManuscript requirements are published in the  
January 1, 1989 issue, page 91. Manuscripts  
for publication (4 copies) should be submitted to  
ANALYTICAL CHEMISTRY at the ACS Washing-  
ton address.The American Chemical Society and its editors  
assume no responsibility for the statements  
and opinions advanced by contributors. Views  
expressed in the editorials are those of the  
editors and do not necessarily represent the  
official position of the American Chemical  
Society.

- Abbas, N. M., 1924  
Abel, K., 1863  
Alam, K., 1924  
Anson, F. C., 1799
- Bard, A. J., 1794  
Beauchemin, D., 1857  
Berberich, D. W., 1874  
Berman, S. S., 1857, 1867  
Bjarnason, A., 1889  
Boltinghouse, F., 1863  
Bower, N. W., 1834  
Bruntlett, C. S., 1989  
Busch, K. W., 1841  
Busch, M. A., 1841
- Chiarelli, M. P., 1895  
Cody, R. B., 1889  
Cohen, L. H., 1837
- Dams, R., 1851  
Deng, R.-C., 1946  
DeNiro, M. J., 1887  
DeVoe, J. R., 1826  
Dobashi, A., 1984  
Duckworth, D. C., 1879
- Engel, M. H., 1996  
Epstein, S., 1887
- Farnsworth, P. B., 1815  
Fielden, P. R., 1993
- Gladney, E. S., 1834  
Golshan-Shirazi, S., 1960  
Greenway, G. M., 1993  
Gross, M. L., 1895  
Guiochon, G., 1960
- Hail, M. E., 1874  
Hara, S., 1984  
Harada, K.-i., 1998  
Hatfield, G. R., 1870  
Haw, J. F., 1821  
Hedrick, J., 1986  
Horman, I., 1983
- Ito, Y., 1998
- Janis, L. J., 1901  
Jones, R. W., 1810  
Jorgenson, J. W., 1977
- Kamei, S., 1921  
Karol, P. J., 1937  
Kinsinger, J. A., 1889  
Kissinger, P. T., 1989  
Kita, H., 1980  
Koutny, L. B., 1931  
Kubala, S. W., 1841  
Kwak, J., 1794
- Larsson, J. A., 1949  
Lee, M. L., 1815  
Li, L., 1911  
Lin, B., 1960  
Lubman, D. M., 1911
- Ma, Y., 1931  
Marchetti, A., 1971  
Marcus, R. K., 1879  
Marinenko, R. B., 1826  
Markides, K. E., 1815  
Maynard, R. J., 1996  
McClelland, J. F., 1810  
McCreery, R. L., 1989
- Nagy, D. J., 1934  
Nakazawa, H., 1998  
Neifert, P. E., 1834  
Nicholson, C., 1805  
Nuwer, M. J., 1954
- Oates, M. D., 1977  
Ohkubo, A., 1921  
Oka, H., 1998  
Ono, T., 1984  
Osteryoung, J., 1954  
Otto, M., 1847
- Pardue, H. L., 1949  
Pesek, J. J., 1928  
Picchioni, E., 1971
- Redwan, D. S., 1924
- Regnier, F. E., 1901  
Renn, C. N., 1915  
Rice, M. E., 1805  
Richardson, B. R., 1821
- Saito, S., 1921  
Shen, F. H., 1826  
Shigematsu, Y., 1980  
Singh, R. P., 1924  
Siouffi, A. M., 1928  
Skelton, R. J., Jr., 1815  
Small, J. A., 1826  
Smith, D. K., 1837  
Souda, R., 1980  
Sternitzke, K., 1989  
Sturgeon, R. E., 1867  
Suzuki, M., 1998  
Synovec, R. E., 1915
- Takagi, S., 1921  
Tassi, L., 1971  
Taylor, J. W., 1889  
Taylor, L. T., 1986  
Thompson, M., 1942  
Tjotta, D. C., 1841  
Tosi, G., 1971  
Traitter, H., 1983
- Ugo, P., 1799  
Umezawa, Y., 1980  
Uosaki, K., 1980
- Vandecasteele, C., 1851  
Vanhoe, H., 1851  
Versieck, J., 1851
- Watters, R. L., Jr., 1826  
Wegscheider, W., 1847  
Weil, D. A., 1889  
Williams, P., 1946  
Willie, S. N., 1867
- Yamaguchi, J., 1984  
Yeung, E. S., 1906, 1931  
Yost, R. A., 1874
- Zhu, J., 1906

# Scanning Electrochemical Microscopy. Apparatus and Two-Dimensional Scans of Conductive and Insulating Substrates

Juhyoun Kwak and Allen J. Bard\*

Department of Chemistry, The University of Texas, Austin, Texas 78712

**The application of scanning electrochemical microscopy (SECM) in the feedback mode to two-dimensional scans over conductive and insulating substrates to obtain topographic information at the micrometer-level is described. In the feedback mode the effect of the conductivity of the substrate and distance of the substrate from a scanning ultramicroelectrode tip on the current flowing at the tip caused by an electrode reaction is recorded as a function of the tip  $x$ - $y$  position. Experiments with a 50- $\mu\text{m}$  Pt wire on glass, a ca. 50- $\mu\text{m}$  glass fiber on glass, a gold minigrad, a Pt foil, and a KCl crystal in both aqueous and acetonitrile solutions are presented. The construction of the SECM and the hardware and software that control three-dimensional tip movement and data acquisition are also described.**

## INTRODUCTION

Recent papers from our group described the principles of scanning electrochemical microscopy (SECM) (1) and the quantitative theory of the feedback mode of SECM (2). Although the name SECM was not used, similar techniques were also introduced by other groups (3, 4) to study the diffusion layer at electrode surfaces. In SECM an ultramicroelectrode (UME), with a tip radius of the order of micrometers or less, is moved in close proximity to a substrate of interest in contact with a solution containing an electroactive species. The electrode reaction at the tip gives rise to a tip current ( $i_T$ ) that is affected by the substrate. In general, the tip current,  $i_T$ , is controlled by electrochemical reactions at the tip electrode and sample substrate and is a function of the tip/substrate distance,  $d$ , and the conductivity and chemical nature of the sample substrate. The measurement of  $i_T$  can thus provide the information about sample topography and its electrical and chemical properties. In our previous paper (1), we described experiments in which the tip was moved normal to the substrate surface (the  $z$  direction) and showed the variation of  $i_T$  with  $d$  with both insulating and conductive substrates. In the feedback mode,  $i_T$  increases when the tip electrode is moved close to a conductive substrate and decreases when the tip electrode is moved close to an insulating substrate. Therefore, contour information about conductive and insulating sample substrates can be obtained by scanning the tip electrode across the surface of the sample substrate (the  $x$ - $y$  plane) after the tip has been brought into close proximity of the substrate in the  $z$  direction. In this paper we focus on such  $x$ - $y$  (topographic) scans of substrates and describe a new instrument for the control and determination of the three-dimensional location of the tip electrode. This instrument was interfaced with a microcomputer for control of the tip position and potential and processing of the acquired data. With this instrument a platinum wire (50  $\mu\text{m}$  diameter) and a glass fiber (ca. 50  $\mu\text{m}$  diameter) mounted on glass slides were scanned to check the instrument performance. Topographic scans of platinum foil, a gold minigrad, and a

potassium chloride crystal are also presented. Experiments with both aqueous and nonaqueous (MeCN) solutions of electroactive species are described. All of the results are represented in three-dimensional rectangular coordinates, i.e., the  $x$  and  $y$  axes show the location of the tip and the  $z$  axis shows the tip current (which is a function of tip/substrate distance).

## EXPERIMENTAL SECTION

**Hardware.** The instrument, a scanning electrochemical microscope (also abbreviated SECM), was assembled from commercially available and home-built components. A block diagram of the SECM is shown in Figure 1. The instrument was controlled with a 12-MHz Deskpro 286 microcomputer (Compaq Computer Corp., Houston, TX) equipped with a data acquisition board (DT 2821-G-8DI; Data Translation, Inc., Marboro, MA), which has 8 differential analog input channels (12-bit resolution, 250-kHz throughput), 2 analog output channels (12-bit resolution, 130-kHz throughput), and 16 digital I/O lines. For hard copy, an IBM color printer and HP ColorPro graphics plotter (Hewlett-Packard Corp., San Diego, CA) were used. The electrode potentials were controlled by PAR 175 Universal Programmers (Princeton Applied Research Corp., Princeton, NJ) via a home-built bipotentiostat (5, 6).

The DT 2821-G-8DI board was externally connected to a DT752-Y (signal conditioning screw terminal board; Data Translation, Inc.) to acquire the electrochemical signals via the bipotentiostat, the potential of the piezoelectric device (PZT PZ-44, 0-40  $\mu\text{m}$ ; Burleigh Instruments, Inc., Fishers, NY) via a high-voltage dc operational amplifier (Burleigh PZ-70), and the potentials of the piezoelectric devices of the  $x$ ,  $y$ , and  $z$  micro-positioning devices (Burleigh inchworm translators, IW-500-2 for  $x$  and  $y$  movement and IW-702-00 for  $z$  movement; controlled by modified Burleigh inchworm movement controllers (CE-2000-3A00)). To obtain the analog signals and digital signals from the CE-2000-3A00 (which contains an internal Motorola MC6809 microprocessor), the six boards (two boards for each axis; counter board and controller board) were modified (6). These signals were preconditioned with a home-built logic circuit (6) connected to a DT752-Y board. The DT 2821-G-8DI was externally connected to a DT709 (signal conditioning screw terminal board; Data Translation, Inc.) to send the analog signal to control the PZT pusher PZ-44 via PZ-70 and receive the digital signals from the modified CE-2000-3A00 via the home-built logic circuit. These digital signals are needed to obtain the three-dimensional location of the tip electrode as well as to move the tip electrode in a programmed mode.

The inchworm translators (IW-500-2 and IW-702-00) were mounted on a stage capable of three-dimensional motion, which was mounted on an optical table with TS-100 Translation and TS-300  $z$ -axis stages (Burleigh Instruments, Inc.). The stainless steel plate with a PZT pusher housing was also attached to this stage, as shown in Figure 2. The tip electrode holder was glued to the ceramic cap of the PZT pusher with Torr Seal (Varian Associates, Inc., Lexington, MA). With this assembly the tip electrode position above the sample substrate was controlled by both the digital movement of inchworm translators and the analog movement of the PZT pusher.

The resolution of the digital movement of the inchworm translators could be adjusted from  $1/128$  of a "click distance" to

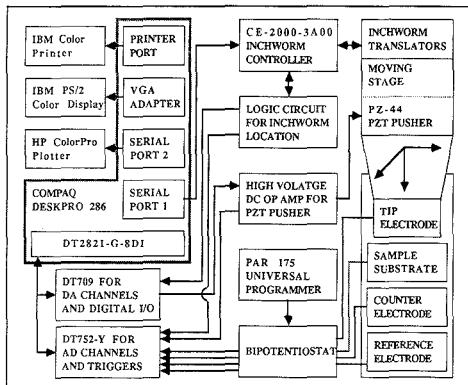


Figure 1. Block diagram of the scanning electrochemical microscope.

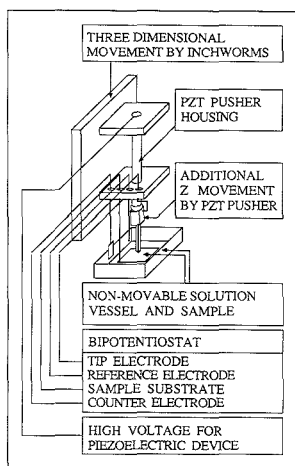


Figure 2. Diagram of electrochemical cell and scanning tip attached to the three-dimensional micropositioning device.

2 "click distances", depending on selection of digital signals from the CE-2000-3A00 (6). The motion of the inchworm translator involves a full contraction and expansion of the cylindrical piezoelectric device along the center shaft as well as clamping and unclamping of this shaft at both ends of the cylindrical piezoelectric. At the moment of clamping and unclamping, a "click" sound is generated. This "click distance" was used as a distance unit (1.1–1.2  $\mu\text{m}$  per click, calibrated as described below) in conjunction with the digital counting unit in the computer program.

**Software.** The hardware was controlled and accessed by the Deskpro 286 via the MS-DOS operating system (Microsoft Disk Operating System version 3.31; Microsoft Corp., Redmond, WA). Programs for this purpose, as well as for data processing, were written in C language and compiled with a Microsoft C Optimizing Compiler (version 5.1; Microsoft Corp.). The ATLAB subroutine library (Data Translation, Inc.) for the DT2821-G-8DI control was incorporated into the programs when necessary (6).

Several different programs were employed. The simplest control program (program 1) was used to acquire electrochemical signals through the DT2821-G-8DI while the tip electrode was held stationary. This program allowed the usual electrochemical experiments (cyclic voltammetry, chronoamperometry, chronocoulometry) to be carried out. The acquired data could be saved on a mass storage device (floppy or hard disk) as a file which could

be imported by Lotus 1-2-3 (Lotus Development Corp., Cambridge, MA) to be plotted in graphics form.

Another control program (program 2) acquired the electrochemical signals as well as data about the tip location via DT2821-G-8DI, while it also controlled the movement of the tip via the programmed or step mode of the CE-2000-3A00 through a serial port 1 (see Figure 1). The programmed mode allowed a two-dimensional scan over the sample substrate, while the step mode was used to move the tip electrode to the sample substrate or to perform a single scan over the sample substrate before obtaining a two-dimensional scan. The acquired data and control parameters were saved in random access memory, graphically displayed on the monitor screen, and optionally saved on a floppy or hard disk.

A processing program (program 3) was used to convert the data obtained from program 2 to a binary data format, which was adaptable to the commercial Surfer program (Golden Software, Inc., Golden, CO). The Surfer program has many features for data manipulation and presentation, i.e., data smoothing (spline and matrix method), three-dimensional plotting ( $x$ ,  $y$  axis for two-dimensional location and  $z$  axis for current at tip electrode) on hard copy devices and monitor, as well as topographic plotting.

**Chemicals.** Milli-Q reagent water (Millipore Corp., Bedford, WA) was used for the aqueous solutions, with dissolved  $\text{K}_4\text{Fe}(\text{CN})_6$  and  $\text{KCl}$ , as received. Acetonitrile (MeCN, spectrophotometric grade; Mallinckrodt, Inc., Paris, KY), which was equilibrated with Mallinckrodt molecular sieve (grade 514GT 4 Å), was used for the nonaqueous solutions with various supporting electrolytes: tetrabutylammonium fluoroborate (TBABF<sub>4</sub>), tetrabutylammonium fluorophosphate (TBAPF<sub>6</sub>), and tetrabutylammonium perchlorate (TBAP) (Southwestern Analytical Chemicals, Inc., Austin, TX). These were dried overnight in a vacuum oven. Ferrocene (Cp<sub>2</sub>Fe; Morton Thiokol, Inc., Danvers, MA) was used as received.

**Tip Preparation.** Several different tips were used in these experiments. Construction of the Pt disk-in-glass ultramicroelectrode (12.5- and 5- $\mu\text{m}$  radii) has been described previously (1). The carbon disk-in-glass ultramicroelectrodes (5.5- and 3.5- $\mu\text{m}$  radii) were made by a similar procedure as the Pt electrodes. The glass surrounding the Pt or C ultramicroelectrodes was conically sharpened after the usual polishing procedure (1) to avoid contacting the substrate with the insulating glass sheath.

**Sample Preparation.** The Pt wire sample was glued on a microscope slide (1 in.  $\times$  3 in.) by applying epoxy cement only at both ends of a 1.5 cm long Pt wire (50- $\mu\text{m}$  diameter). The glass fiber (ca. 50  $\mu\text{m}$  diameter) was pulled from a Pyrex glass tube and glued on a microscope slide in the same manner. The Au minigrad (7.6  $\mu\text{m}$  wire width and 17.6  $\mu\text{m}$  hole size; Buckbee-Mears Co., St. Paul, MN) (7) was cut as a 2  $\times$  2 mm square and carefully glued to a glass slide only at the edges. The  $\text{KCl}$  crystals were grown from an aqueous saturated  $\text{KCl}$  solution. A sample crystal was glued onto a microscope slide. The solution vessel was a Pyrex tube (1 in. o.d., ca. 1 cm long) that was glued on the microscope slide which held the sample.

**Scanning of Samples.** The microscope slide on which the sample substrate and solution vessel were glued (Figure 2) was placed on a heavy brass plate (3 in.  $\times$  5 in.  $\times$  0.5 in.), which was held on a manually adjustable tripod. With this tripod, the sample substrate was moved to within about 1 mm of the tip electrode. This tripod was also used to level the sample substrate. After this procedure, the sample was not moved during a scanning experiment. After the electrochemical solution was transferred into the solution vessel, the counter electrode (a 2 cm length, 0.5 mm diameter platinum wire) and an appropriate reference electrode (a saturated calomel electrode for aqueous solutions and oxidized silver wire quasi-reference electrode (AgQRE) for nonaqueous solutions) were inserted. A cyclic voltammogram was obtained (with program 1) to check the tip electrode condition. Then, the potential of tip electrode was set at an appropriate potential, and by using program 2, the tip was advanced toward the sample with the  $z$ -axis inchworm monitoring the tip current until it either increased by ca. 10% (for a conductive substrate) or decreased ca. 10% (for the insulating substrate). Then, with the PZT pusher PZ-44 or a slower  $z$ -axis inchworm step mode, the appropriate location of the tip electrode from the substrate was adjusted. Finally, an  $x$ - $y$  scan was executed by the pro-

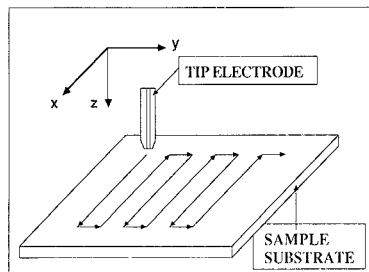


Figure 3. Pattern of two-dimensional movement of tip electrode over the sample substrate.

grammed zigzag movement of  $x$ - and  $y$ -axis inchworms, as shown in Figure 3.

**Calibration.** To obtain the absolute position of the tip, it is necessary to calibrate the inchworm drives and PZT pusher. Every micropositioning device is fundamentally based on its piezoelectric material, which has its own dependent parameters (geometric shape, age, load). After the system was setup, with electrode and solution vessel in place, so that the actual load was known, the inchworm of each axis was moved a relatively long distance (i.e., 200 to 4000 "click distances") and that distance was measured with a micrometer. The linearities of all the inchworms were excellent (better than 0.5%), and the following calibrated click distances were obtained: 1.189  $\mu\text{m}$  per click for the  $x$  axis, 1.181  $\mu\text{m}$  per click for the  $y$  axis, and 1.091  $\mu\text{m}$  per click for the  $z$  axis. These values are in good agreement with the nominal company specification, 1.25  $\mu\text{m}$  without load.

To calibrate the  $z$ -axis PZT pusher (PZ-44), the SECM feedback mode was used. The tip current was monitored while the tip electrode (5  $\mu\text{m}$  radius Pt disk) was moved toward a planar conductive substrate (a 2.5 mm radius Pt disk) immersed in MeCN containing 5 mM ferrocene and 10 mM TBAP by the  $z$ -axis inchworm. The tip movement was stopped when  $i_T = i_{T,1}$ , which was about 50% larger than  $i_T$  when the tip was far from the substrate. The tip was then moved two more clicks toward the substrate with the  $z$ -axis inchworm, and the increased current,  $i_{T,2}$ , was noted. The tip was then moved backward from this location by changing the applied potential of the PZT pusher until the tip current was again equal to  $i_{T,1}$ . From this experiment, the potential change needed to obtain the same distance as two "click distances" of the  $z$ -axis inchworm was obtained, i.e., 26.0 V to the pusher was equivalent to two "click distances" of the  $z$ -axis inchworm. Thus, the calibration factor for the PZT pusher was 42.0  $\mu\text{m}$  per 1000 V. This value is also in good agreement with nominal company specification (ca. 40  $\mu\text{m}$  per 1000 V).

## RESULTS AND DISCUSSION

**Pt Wire on Glass.** The  $i_T$  values for scans over a 50  $\mu\text{m}$  diameter platinum wire on a glass slide immersed in MeCN/0.01 M TBAP, 5 mM  $\text{Cp}_2\text{Fe}$ , are shown in Figure 4. Four scans for the tip at different locations above the sample (different  $d$  values) are shown. The tip electrode was held at 0.8 V vs AgQRE where oxidation of  $\text{Cp}_2\text{Fe}$  to  $\text{Cp}_2\text{Fe}^+$  occurs. When the tip was far from platinum wire,  $i_T$  was independent of  $d$  and showed an anodic current of  $26.5 \pm 0.3$  nA that was independent of the  $x$ - $y$  position. As previously shown (2),  $i_T$  is not affected by the substrate when  $d \gg a$  (where  $a$  is the tip radius). When the tip was moved closer to the sample (i.e.,  $d$  decreased),  $i_T$  was perturbed from its long distance value ( $i_{T,\infty}$ ). When it was over the glass,  $i_T < i_{T,\infty}$ , since the insulating substrate partially blocked diffusion of  $\text{Cp}_2\text{Fe}$  to the tip. When the tip was above the Pt wire,  $i_T > i_{T,\infty}$ , because of the feedback effect, i.e., regeneration of  $\text{Cp}_2\text{Fe}$  at the Pt wire via reduction of  $\text{Cp}_2\text{Fe}^+$ . The maximum anodic currents were 30.6 nA (Figure 4B), 31.3 nA (Figure 4C), and 33.0 nA (Figure 4D). Although the  $z$ -axis calibration provides an accurate measurement of the relative position above the substrate, one

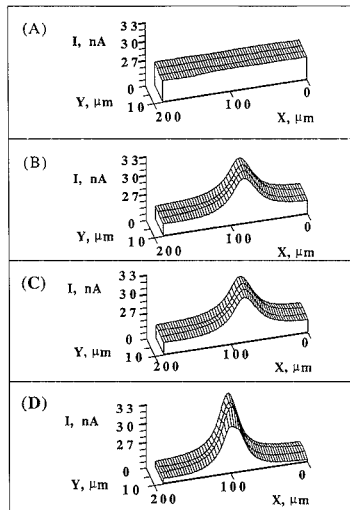


Figure 4. Scans of a 50- $\mu\text{m}$  platinum wire on a glass slide at different tip locations from sample: tip electrode, 5.5  $\mu\text{m}$  radius carbon disk tip electrode at 0.80 V vs AgQRE; solution, 10 mM TBAP, 5 mM ferrocene in acetonitrile; scanning speed, 19.7  $\mu\text{m}/\text{s}$ ; (A) far from sample, (B) close (about 17.8  $\mu\text{m}$ , see text) to sample, (C) 2.18  $\mu\text{m}$  closer than B, (D) 4.36  $\mu\text{m}$  closer than B.

cannot obtain directly an absolute measure of  $d$ . For example, any attempt to move the tip to the substrate until they touch (a "tip crash") would damage both tip and sample. Thus, the best estimate of  $d$  can be obtained from the theoretical treatment of the SECM in the feedback mode (2), where the value of  $i_T/i_{T,\infty}$  can be related to  $d/a$ . Since the theory assumes a planar substrate, the estimated absolute  $d$  value can only be considered an approximation when there is appreciable curvature of the substrate or it consists of insulating and conductive zones with dimensions of the order of the tip radius. Both of these conditions apply for the 50  $\mu\text{m}$  Pt wire on glass substrate under consideration here. On the basis of the theoretical treatment, which yields the following approximate (within 2%) equation for a planar conductive substrate (2)

$$(i_T/i_{T,\infty}) = (\pi/4)(a/d) + 0.901 + 0.099 \exp[-0.16(a/d)] - 0.29 \exp[-0.39(d/a)] \quad (1)$$

the maximum anodic currents in Figure 4, for the tip directly over the Pt wire, can be converted to estimated distances,  $d$ ; the resulting values are  $17.8 \pm 1.5$   $\mu\text{m}$  (Figure 4B),  $15.6 \pm 1.1$   $\mu\text{m}$  (Figure 4C), and  $11.8 \pm 0.7$   $\mu\text{m}$  (Figure 4D). These estimated data are in reasonable agreement with the relative tip location from sample (see figure caption). Note that the errors become smaller as the tip electrode gets closer to the substrate. These nonlinear errors are caused by the intrinsic nonlinearities of tip current vs tip/substrate distance.

**Glass Fiber on Glass.** Five scans at different tip locations above a glass fiber (ca. 50  $\mu\text{m}$ ) on a glass slide are shown in Figure 5. A 5  $\mu\text{m}$  radius Pt tip embedded in a glass sheath and held at 0.50 V vs SCE and immersed in an aqueous 2.5 mM  $\text{K}_4\text{Fe}(\text{CN})_6$ , 0.1 M KCl solution was employed. When the tip electrode was far from the substrate, the tip current was constant at  $2.08 \pm 0.07$  nA. When the tip was brought closer to the sample, the hindered diffusion of ferrocyanide to the tip because of the insulating glass fiber and slide caused a decrease in the currents at the tip electrode. The minimum

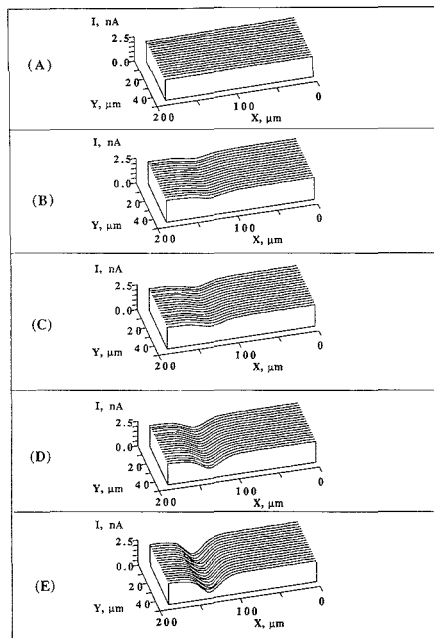


**Figure 5.** Scans of a ca. 50  $\mu\text{m}$  glass fiber on a glass slide at different tip locations from sample: tip electrode, 5  $\mu\text{m}$  radius platinum disk tip electrode at 0.50 V vs SCE; solution, 0.1 M KCl, 2.5 mM potassium ferrocyanide in  $\text{H}_2\text{O}$ ; scanning speed, 25.0  $\mu\text{m/s}$ ; (A) far from sample, (B) close (about 8.05  $\mu\text{m}$ , see text) to sample, (C) 2.18  $\mu\text{m}$  closer to sample than B, (D) 4.36  $\mu\text{m}$  closer to sample than B, (E) 6.54  $\mu\text{m}$  closer to sample than B.

anodic currents were 1.74 nA (Figure 5B), 1.60 nA (Figure 5C), 1.06 nA (Figure 5D), and 0.4 nA (Figure 5E). The distance between tip and substrate,  $d$ , was again estimated from theory (2); the estimated distances between tip and the top of the glass fiber are 8.05  $\mu\text{m}$  (Figure 5B), 5.87  $\mu\text{m}$  (Figure 5C), 3.68  $\mu\text{m}$  (Figure 5D), and 1.50  $\mu\text{m}$  (Figure 5E). These estimates are in excellent agreement with the calibrated relative movements shown in the figure caption. As we reported previously (2), the radius of glass sheath surrounding the disk electrode affects the tip current. In this case, it was about 10 times that of the disk electrode.

**Platinum Foil.** To test the SECM with a larger area conductive substrate, scans with a 5  $\mu\text{m}$  radius Pt tip at 0.5 V over a polycrystalline Pt foil immersed in an aqueous 2.5 mM  $\text{K}_4\text{Fe}(\text{CN})_6$ , 0.1 M KCl solution were carried out. Two scans are shown in Figure 6. As in the previous experiments, the tip was scanned two dimensionally far from the sample both before (Figure 6A, first scan) and after (sixth scan) the closer scans, yielding constant currents of  $2.45 \pm 0.09$  and  $2.32 \pm 0.04$  nA, respectively. The semiinfinite steady-state diffusion current was found to decrease with time compared to the current obtained at the same freshly polished electrode. Since the steady-state current is an important variable in SECM in the estimation of the absolute tip to substrate distance, all the scans should be executed over a minimum period (e.g., an hour or less) or the tips should be frequently polished, either mechanically or electrochemically. In this experiment the time spent obtaining the six scans was about 20 min over which the semiinfinite steady-state diffusion current decreased by about 5%. When the tip was brought closer to the Pt foil and scanned (second scan),  $i_T$  increased to  $2.59 \pm 0.04$  nA. At

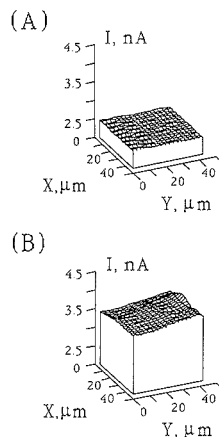


**Figure 6.** Scans of a platinum foil: tip electrode, 5  $\mu\text{m}$  radius platinum disk tip electrode at 0.50 V vs SCE; solution, 0.1 M KCl, 2.5 mM potassium ferrocyanide in  $\text{H}_2\text{O}$ ; scanning speed, 19.7  $\mu\text{m/s}$ ; (A) far from sample, (B) close to sample.

this distance information about the surface topography of the foil could not be obtained. When the tip was brought 10.9  $\mu\text{m}$  closer and scanned (third scan), the current increased to  $2.89 \pm 0.09$  nA, still without obtaining contour information. However, with the tip 6.54  $\mu\text{m}$  closer than in the third scan, the increased tip current produced a scan (fourth scan) that showed the surface structure of a tilted Pt foil (Figure 6B). The fifth scan at the same distance as fourth scan was taken to check reproducibility; scanning data of both matched exactly. From the scan data in Figure 6D, and based on the averaged semiinfinite steady-state diffusion current (2.38 nA), the calculated (2) distance between the tip and platinum foil was in the range of 4.55–6.60  $\mu\text{m}$ . The calculated current ranges for the other locations based on the high-resolution data and estimated distances are 2.93–2.84 nA for the second scan and 2.62–2.65 nA for the third scan, in good agreement with the actual results. These calculated current ranges, which are within the range of variation of the experimental data, illustrate why the tip current data at the distances in the second and third scans do not show the topography of the Pt foil. Variation of  $i_T$  with  $d$  is too small at these distances to show substrate height variations of 2  $\mu\text{m}$ .

**Gold Minigrd.** Figure 7 shows scans of a gold minigrd immersed in an aqueous solution (5  $\mu\text{m}$  radius Pt tip). In both cases the scans clearly show the minigrd structure. Figure 7A is typical of a scan for a sample whose level was not adjusted well. The average for the periodicity of the grids in both directions is  $25.1 \pm 1.8$   $\mu\text{m}$ , which is in good agreement with the manufacturer's specification (25.2  $\mu\text{m}$ ). Since the diameter of the tip disk electrodes was 10, which is bigger than the width of gold lines in the minigrd (7.6  $\mu\text{m}$ ), the current change as the tip electrode moved across the gold lines showed a sinusoidal rather than a step shape. Moreover, when the tip electrode was above a hole between the gold grid lines, the current was not smaller than the semiinfinite steady-state diffusion current. This can be explained qualitatively by the cooperative feedback from all lines surrounding the hole to tip electrode. The extent of feedback is smaller, however, than that when the tip is right above the gold lines.

Parts B–D of Figure 7 demonstrate the reproducibility of the scans. Investigating the data quantitatively, we noticed that the maximum anodic current increased from 4.16 nA (first scan, Figure 7B) to 4.39 nA (second scan, 7C) and 4.49 nA

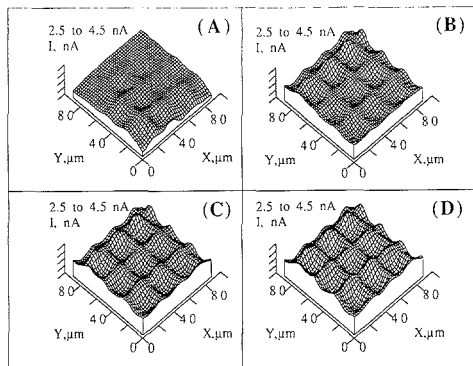


**Figure 7.** Scans of a gold minigrad: tip electrode, 5  $\mu\text{m}$  radius platinum disk tip electrode at 0.40 V vs SCE; solution, 0.1 M KCl, 2.5 mM potassium ferrocyanide in  $\text{H}_2\text{O}$ ; scanning speed, 25.0  $\mu\text{m/s}$ ; (A) close to sample, first scan, (B) same distance as B, but moved to another section of the minigrad, first scan, (C) same location as B, second scan, (D) same location as B, third scan.

(third scan, 7C), while the minimum anodic current did not change ( $3.10 \pm 0.01$  nA). It is difficult to explain these results. Evaporation of the solvent (water) cannot explain them, because only 12 min was required for all of the scans, and also, as discussed above in the Pt foil experiment, the steady-state diffusion current usually decreased with time. It may be that activation (e.g., local electrochemical polishing) occurs at the gold surface, when ferricyanide is reduced back to ferrocyanide. Also, thermal effects of the PZT pusher cannot be excluded. Further studies are needed, however, to understand this effect.

Similar scans were executed in MeCN (5.5  $\mu\text{m}$  radius C tip). In this case, the current increase with time was larger than that in Figure 7, but can mostly be explained by solvent (MeCN) evaporation. Here, the maximum anodic current increased by 11.7% from the first scan to the third scan, while the minimum anodic current also increased by 10.2%. Here, the decrease in the steady-state diffusion current by tip deactivation and the increase of current by gold surface changes, as seen in the aqueous ferrocyanide solution, may have largely cancelled out. The  $x$ - $y$  reproducibility of the scans in Figure 7 shows that drifts in these directions (e.g., attributable to thermal effects, hysteresis, and relaxation in the piezoelectric materials, and voltage drifts in the inchworm power supplies) are negligible at this level of resolution over time periods up to 1 h. This suggests that SECM will be useful for examining the same area of an electrode surface with time following different treatments. The reproducibility also shows that neither the electrode tip nor its surrounding glass sheath contacted the sample and dragged it during the scans. All the data in Figure 7 were smoothed before plotting using the matrix average method. In these cases the averaged current at a given  $x,y$  grid point was obtained by adding half of the raw current data at that point to half of the averaged currents from the raw data at the eight nearby,  $x,y$  grid points. Gray-scale presentation of the data to yield photographic-like images is also possible and is under development.

**Potassium Chloride Crystal.** To illustrate the use of SECM with an insulating substrate, a KCl crystal immersed in a MeCN solution, where the KCl was insoluble, was examined. The single KCl crystal grows with a spiral pattern on the surface. Since the pattern is not periodic, as is the minigrad, and the surface features are spaced apart (ca. 65  $\mu\text{m}$ ), it was difficult to find the desired dislocation steps in a given scan (ca.  $100 \times 100$   $\mu\text{m}$ ). Moreover, the protruding apex

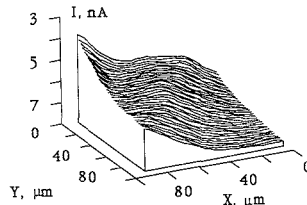


**Figure 8.** Scan of a KCl crystal: tip electrode, 5  $\mu\text{m}$  radius platinum disk tip electrode at 0.80 V vs AgQRE; solution, 0.01 M TBAP, 2.5 mM ferrocene in acetonitrile; scanning speed, 23.8  $\mu\text{m/s}$ .

crystals, which were detected on the surface of a newly grown crystal, sometimes were removed by collision with the scanning tip electrode. In Figure 8 typical crystal surface steps are shown. In Figure 8A the width between steps can be seen to be about 65  $\mu\text{m}$ , even though the steps are not sharp. Analyzing the data in the same way that the glass fiber results were analyzed, we found one step height of about 2.1  $\mu\text{m}$  (current step from 7.6 to 5.6 nA) and another about 1.6  $\mu\text{m}$  or higher (current step from 7.6 to 3.6 nA). Although these results do not show very good resolution, they do demonstrate the ability of the SECM in the feedback mode to scan, non-destructively, an insulating sample.

## CONCLUSIONS

All of the results described above were obtained with the tip scanned at speeds of 7–25  $\mu\text{m/s}$  above the substrate. In all cases the tip currents obtained were considered as steady-state currents, since a theoretical treatment that includes transients and dynamic effects at different scanning speeds is not yet available. Rigorously, only the starting current point of the scan where the tip is held for some time before initiating the  $x$ - $y$  raster is at steady state. However, the fact that the current shows no abrupt changes when the scan is initiated, that the currents during the scan over the flat portions of substrate are essentially the same as the starting point current, and that the currents are insensitive to scan speed over this range suggests that the currents found at tips of this size at the spacings used here can be considered as quasi-steady-state currents for scan speeds  $\leq 25$   $\mu\text{m/s}$ .

The results presented here clearly demonstrate the application of the SECM to obtain three-dimensional scans and topographic information about conductive and insulating surfaces immersed in liquids at the micrometer-resolution level. The achievement of higher resolution mainly depends upon further developments in tip geometry. For the initial studies described here, little effort was made to minimize tip area or study effects of tip geometry (1, 8). Moreover, the application of mathematical approaches (e.g., a two-dimensional spatial deconvolution) may be of use in improving resolution. A one-dimensional temporal convolution was proposed previously (9). Smaller metal tips surrounded by insulators, such as those recently described for use in scanning tunneling microscopy (STM) for samples immersed in liquids (10, 11), might be useful in SECM. For higher resolution scans it will probably be necessary to develop a constant tip current mode, as is frequently used in STM, to avoid crashes of the tip with the surface. In this mode the voltage applied to the  $z$ -axis PZT (pusher) is varied to maintain  $i_T$  constant at some set value (as different as possible from  $i_{T,0}$ ). Information about  $z$ -axis displacement is then obtained from plots of the pusher voltage with  $x$  and  $y$  displacement. While it is very unlikely that SECM will ever attain the atomic resolution found with the STM, submicrometer to 100-Å levels should be possible. For example, the SECM has already been used to deposit



metals with resolution of about 2000 Å (12, 13).

Several other aspects of the SECM are of interest. The ability to study insulators (shared with the atomic force microscope (AFM) (14)) should be of use, for example, in the study of the electrodeposition of insulating features on electrode or in insulator/conductor composites. With further development the SECM should be capable of resolving features and producing images of insulating materials (including biological materials) immersed in liquids with a resolution approaching that of the scanning electron microscope. SECM is unique in its ability to distinguish between insulating and conductive regions by reference to the tip current at long distance ( $i_{T,\infty}$ ). Note that no such reference level exists with the STM or AFM. Moreover, a straightforward and well-developed theoretical approach to calculation of normalized tip current as a function of the tip/substrate distance is available (2). Not only can SECM provide information about the conductivity of the substrate, it should also be possible, by proper selection of solution redox species, to obtain chemical information (e.g., redox potential) about the substrate. For example, the addition of several electroactive species to the solution which span a range of redox potentials and control of the tip potential should allow one to characterize redox-active sites or species on or in an insulating substrate. These aspects of SECM are currently under investigation in this laboratory.

Registry No. Au, 7440-57-5; Pt, 7440-06-4; KCl, 7447-40-7.

#### LITERATURE CITED

- (1) Bard, A. J.; Fan, F.-R. F.; Kwak, J.; Lev, O. *Anal. Chem.* **1989**, *61*, 132-138.
- (2) Kwak, J.; Bard, A. J. *Anal. Chem.* **1989**, *61*, 1221-1227.
- (3) Engstrom, R. C.; Webber, M.; Wunder, D. J.; Burgess, R.; Winquist, S. *Anal. Chem.* **1986**, *58*, 844-848.
- (4) Engstrom, R. C.; Meany, T.; Tople, R.; Wightman, R. M. *Anal. Chem.* **1987**, *59*, 2005-2010.
- (5) Bard, A. J.; Faulkner, L. R. *Electrochemical Methods, Fundamentals and Applications*; Wiley: New York, 1980; p 567.
- (6) Kwak, J. Ph.D. Dissertation, The University of Texas at Austin, 1989.
- (7) Heineman, W. R.; Hawkridge, F. M.; Blount, H. N. In *Electroanalytical Chemistry*; Bard, A. J., Ed.; Marcel Dekker: New York, 1984; Vol. 13.
- (8) Engstrom, R. C.; Wightman, R. M.; Kristensen, E. W. *Anal. Chem.* **1988**, *60*, 652-656.
- (9) Davis, J. M.; Fan, F.-R. F.; Bard, A. J. *J. Electroanal. Chem.* **1987**, *238*, 9-31.
- (10) Gewirth, A. A.; Craston, D. H.; Bard, A. J. *J. Electroanal. Chem.* **1989**, *261*, 477-482.
- (11) Penney, R. M.; Heben, M. J.; Lewis, N. S., submitted for publication in *Anal. Chem.*
- (12) Hüsser, O. E.; Craston, D. H.; Bard, A. J. *J. Vac. Sci. Technol. B* **1988**, *6*, 1873-1876.
- (13) Hüsser, O. E.; Craston, D. H.; Bard, A. J., submitted for publication in *J. Electrochem. Soc.*
- (14) Binnig, G.; Quate, C. F.; Gerber, C. *Phys. Rev. Lett.* **1986**, *56*, 930-933.

RECEIVED for review February 6, 1989. Accepted May 25, 1989. The support of this research by the Robert A. Welch Foundation and Texas Advanced Research Program is gratefully acknowledged.

## Poly(2-vinylpyrazine) as a Soluble Polymeric Ligand and as an Electrode Coating. Reactions with Pentacyanoferrate(II)

Paolo Ugo<sup>1</sup> and Fred C. Anson\*

Arthur Amos Noyes Laboratories, Division of Chemistry and Chemical Engineering, California Institute of Technology, Pasadena, California 91125

The rate and extent of reaction between  $\text{H}_2\text{OFe}(\text{CN})_5^{3-}$  and poly(2-vinylpyrazine) (PVPz) in homogeneous aqueous solutions have been measured and compared with those for the reaction between the corresponding monomeric species ( $\text{H}_2\text{OFe}(\text{CN})_5^{3-}$  and pyrazine). The significant differences observed are attributed to the increasingly negative charge that accumulates on the polymer-metal complex as the reaction proceeds. Solutions of  $\text{PVPz}(\text{Fe}(\text{CN})_5^{3-})_n$  exhibit almost no electrochemical responses in 0.1 M supporting electrolytes but in 1 M solutions a clear response is evident. Stable electroactive coatings of  $\text{PVPz}(\text{Fe}(\text{CN})_5^{3-})_n$  on electrode surfaces can be prepared by exposing cross-linked deposits of PVPz to aqueous solutions of  $\text{H}_2\text{OFe}(\text{CN})_5^{3-}$ . The apparent formal potentials of the redox groups in such coatings vary with the concentration of the supporting electrolyte in the way expected for cation permselective membranes. With homogeneous solutions of PVPz about 30% of the pyrazine groups could be coordinated to  $-\text{Fe}(\text{CN})_5^{3-}$  anions but the maximum extent of binding of  $-\text{Fe}(\text{CN})_5^{3-}$  to cross-linked coatings of PVPz was only about half as large.

Electrochemical studies of polymer-metal complexes adsorbed, or otherwise attached, to electrode surfaces are prominent in research on chemically modified electrodes (1-4). The electrochemistry of soluble polymer-metal complexes has been examined in a few studies (5, 6) but systematic comparisons of the behavior of the same polymer-metal complex when in solution and when attached to electrode surfaces are relatively rare (6). Such comparisons could be useful in judging the effects of attachment on the thermodynamics and kinetic behavior of polymer-metal complexes. One problem that must be overcome in order to carry out comparisons of this type is the instability of electrode coatings prepared from polymer-metal complexes that are soluble in the solvent employed. In this study a water-soluble polymer of 2-vinylpyrazine was reacted with pentacyanoferrate(II) to prepare a soluble polymer-metal complex whose electrochemical and spectroscopic behavior were examined. Stable coatings of the polymer were prepared on electrode surfaces by reacting the 2-vinylpyrazine with dibromohexane to quaternize a small percentage of the nitrogen sites and effectively cross-link the coatings, as described by previous workers (7, 8). The resulting coatings were then readily metalated by exposure to solutions of  $\text{H}_2\text{OFe}(\text{CN})_5^{3-}$ . The versatility of pyrazine as a very weakly basic but effective ligand for back-bonding metals (9) was advantageous because competition with protons for the co-

\* Author to whom correspondence should be addressed.

<sup>1</sup> Permanent address: Dipartimento di Chimica Fisica, Università Di Venezia, Calle Larga S. Marta 2137, 30123 Venezia, Italy.

ordination sites was unimportant at pH values as low as 1.0. One of our objectives was to use the pendant pyrazine groups in the polymer to bind both anionic and cationic electroactive metal complexes to polymer coatings to obtain polyelectrolytes whose ion-exchange properties could be modulated electrochemically. Although we have yet to achieve this goal, some of the novel chemical and electrochemical results obtained in the course of the investigation are described in this report.

### EXPERIMENTAL SECTION

**Materials.** Poly(2-vinylpyrazine) was prepared by radical polymerization of freshly distilled 2-vinylpyrazine (Pyrazine Specialties, Inc.). The polymerization was carried out in the absence of air by adding 0.8 mol % azobis(isobutyronitrile) to 10 mL of a 4 M solution of 2-vinylpyrazine in benzene. The mixture was allowed to react for 48 h at 60 °C. The polymer was obtained by pouring the reaction mixture into hexane and filtering. The initial product was redissolved in benzene and the precipitation procedure repeated. The final product was dried for 24 h in a vacuum oven. The molecular weight of the polymer was not measured, but on the basis of similarly conducted preparations of poly(vinylpyridine) with measured molecular weight, we estimate the molecular weight to be  $1-2 \times 10^5$ .

Other commercially available chemicals were obtained in the purest available forms and used without further purification except for  $\text{Na}_3[\text{NH}_3\text{Fe}(\text{CN})_5]$ , which was recrystallized from concentrated solutions of ammonia.

Complexes of  $\text{Fe}(\text{CN})_5^{3-}$  with pyrazine and poly(2-vinylpyrazine) were prepared in situ by adding the ligand to solutions of  $\text{H}_2\text{OFe}(\text{CN})_5^{3-}$  obtained by dissolution of  $\text{Na}_3[\text{NH}_3\text{Fe}(\text{CN})_5]$  (10). The concentrations of the complexes obtained were monitored spectrophotometrically at 452 and 476 nm for the pyrazine and poly(2-vinylpyrazine) complexes, respectively.

**Apparatus and Procedures.** Electrochemical measurements were conducted in conventional two-compartment cells using standard PAR (EG & G Instruments Co.) instrumentation or a BAS Model 100 electrochemical analyzer (Bioanalytical Systems, Inc.). Cylindrical glassy carbon electrodes (Tokai Carbon Co., Tokyo) 0.20 cm<sup>2</sup> in area were mounted and polished as previously described (11). Potentials were measured and are reported with respect to a KCl saturated Ag/AgCl reference electrode.

Coatings of cross-linked poly(2-vinylpyrazine) (PVPz) were prepared by micropipetting known volumes of freshly prepared tetrahydrofuran solutions of PVPz (1 g/100 mL) and the desired quantity of 1,6-dibromohexane onto the surface of the glassy carbon electrode. After the solvent evaporated, the coated electrodes were kept at 80 °C for 12–14 h to promote the cross-linking reaction (7, 8). The thickness of coatings was estimated from profilometer measurements with dry coatings (Dektak Model 3030). Values of 0.4–0.5  $\mu\text{m}$  were obtained for coatings containing  $5 \times 10^{-7}$  mol cm<sup>-2</sup> pyrazine groups with 10% cross-linking.

Spectra were recorded with a Hewlett-Packard Model 8450A spectrophotometer, which was also employed in spectral monitoring of reaction rates between  $\text{H}_2\text{OFe}(\text{CN})_5^{3-}$  and the pyrazine ligands.

### RESULTS AND DISCUSSION

**Reaction of  $\text{H}_2\text{OFe}(\text{CN})_5^{3-}$  with Poly(2-vinylpyrazine) (PVPz).** The reaction between  $\text{H}_2\text{OFe}(\text{CN})_5^{3-}$  and monomeric pyrazine has been characterized by Toma and Malin (12). It is governed by an equilibrium constant of  $9 \times 10^5 \text{ M}^{-1}$  ( $\mu = 0.5 \text{ M}$ , 25 °C) and exhibits simple second-order kinetics with a forward rate constant of  $380 \text{ M}^{-1} \text{ s}^{-1}$ . The reaction between  $\text{H}_2\text{OFe}(\text{CN})_5^{3-}$  and PVPz proceeds more slowly and exhibits more complex kinetics. The course of the reaction can be followed spectrophotometrically at 476 nm, the absorbance maximum for the complex (Figure 1). (The corresponding  $\lambda_{\text{max}}$  for the complex with pyrazine is 452 nm (12)). With solutions containing 2.5 mM PVPz (the concentration is expressed in terms of pyrazine groups present) and 0.1 mM  $\text{H}_2\text{OFe}(\text{CN})_5^{3-}$  the complexation reaction is complete in about 90 min and the final absorbance matches that expected for an essentially quantitative reaction on the basis of the molar

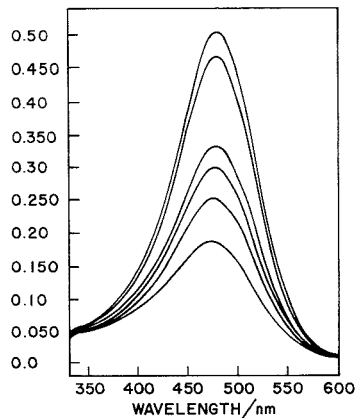


**Figure 1.** Absorption spectra recorded at various times after preparing a solution containing 2.5 mM pyrazine groups as PVPz and 0.1 mM  $\text{H}_2\text{OFe}(\text{CN})_5^{3-}$  in a 0.1 M sodium acetate buffer at pH 5. Times after mixing, from the lowest to the highest spectra, are 5, 10, 15, and 20 s; 30 and 90 min.

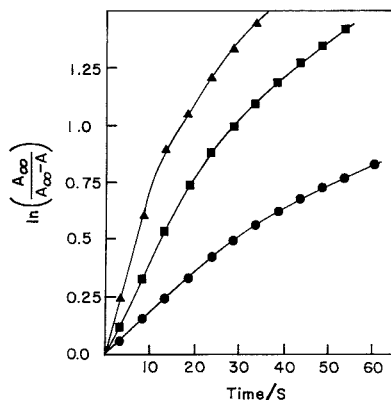


**Figure 2.** Pseudo-first-order kinetic plots for the reaction between PVPz and  $\text{H}_2\text{OFe}(\text{CN})_5^{3-}$  in a 0.1 M sodium acetate buffer at pH 5. Initial concentration of  $\text{H}_2\text{OFe}(\text{CN})_5^{3-}$  was 0.1 mM. Concentration of pyrazine groups in PVPz: ( $\blacktriangle$ ) 5, ( $\blacksquare$ ) 2.5, and ( $\bullet$ ) 1 mM.

absorbance of the monomeric complex ( $\epsilon_{452} = 5.0 \times 10^3$  (12)). Pseudo-first-order kinetic plots of  $\ln(A_\infty / (A_\infty - A))$  vs time, shown in Figure 2, are linear for about 1 half-life with slopes that are proportional to the concentration of the excess PVPz present. The second-order rate constant obtained from these initial rates is  $18 \text{ M}^{-1} \text{ s}^{-1}$ , which is about 20-fold smaller than the constant for the reaction with monomeric pyrazine (12). The smaller reaction rate of the polymeric pyrazine is not unexpected (13) nor is the decrease in reactivity with the extent of reaction (Figure 2) as the electrostatic repulsion between the  $\text{H}_2\text{OFe}(\text{CN})_5^{3-}$  anions and the increasingly polyanionic metallopolymer increases. The rate constants obtained from plots such as that in Figure 2 provide only an approximate measure of the intrinsic reactivity of the co-reactants because the PVPz is expected to consist of molecules having an array of molecular weights and corresponding reactivities. The numerical value of the rate constant quoted above serves mainly to show that the reaction of  $\text{H}_2\text{OFe}(\text{CN})_5^{3-}$  with the polymeric pyrazine proceeds about an order of

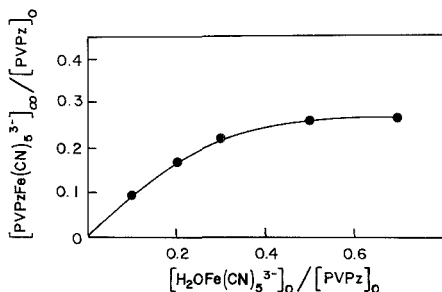


Figure 3. Dependence of the extent of reaction between  $\text{H}_2\text{OFe}(\text{CN})_5^{3-}$  and PVPz on the ratio of the initial reactant concentrations in 0.1 M acetate buffer at pH 5. The initial concentrations of PVPz were between 1.25 and 2.5 mM.

magnitude more slowly than the reaction with monomeric pyrazine.

When the molar ratio of  $\text{H}_2\text{OFe}(\text{CN})_5^{3-}$  to PVPz is increased above 0.1, the complexation reaction is no longer quantitative. As shown in Figure 3, when  $\text{Fe}(\text{CN})_5^{3-}$  groups are coordinated to about 25% of the pyrazine sites available in the polymer, further increases in the ratio cause very little additional complexation to occur. The electrostatic repulsion that presumably underlies this behavior can be diminished by increasing the ionic strength of the solution in which the reaction is carried out. For example, the limiting extent of complexation increases to about 30% in the presence of 0.7 M  $\text{Na}^+$  ion and decreases to about 20% when the concentration of  $\text{Na}^+$  ion is decreased to 0.03 M.

**Protonation of  $\text{PVPz}(\text{Fe}(\text{CN})_5^{3-})_n$ .** Acid-base equilibria in which the polymer-metal complex,  $\text{PVPz}(\text{Fe}(\text{CN})_5^{3-})_n$ , participates can be observed spectrophotometrically. In Figure 4A is shown a series of spectra for solutions of the polyanionic complex at pH values between 1 and 4. The spectra are unaffected by changes in pH between 4 and 9.5. The progressive blue shift as the pH is lowered from 3.9 to 1.5 and the isosbestic point at 446 nm are characteristic of the behavior of a variety of similar  $\text{LFe}(\text{CN})_5^{3-}$  complexes (L = pyridine, pyrazine, and substituted pyrazines (12)). The two species

that are involved in the pH-dependent equilibrium have been identified as the parent complex and a complex in which one of the coordinated cyanide ligands is protonated (12). The extent of the protonation at each pH can be estimated from the measured absorbances at 476 and 428 nm if it is assumed that there is no protonation at pH 3.9 or above and that the protonation is essentially complete at pH 1.5:

$$\frac{C_B}{C_{BH}} = \frac{A_{428}^{BH} - A_{476}^{BH}}{A_{476}^B - A_{428}^B} \quad (1)$$

where  $C_B$  and  $C_{BH}$  are the concentrations of the unprotonated and protonated complex, respectively, and  $A_i$  and  $\epsilon_i$  are the measured absorbances and molar extinction coefficients at the indicated wavelengths. A plot of  $\log(C_B/C_{BH})$ , as evaluated from eq 1, vs pH is shown in Figure 4B. The slope of the linear plot is 1.25 instead of the value of 1.00 that would be obtained with a monomeric acid. This behavior is expected for polymeric acids whose effective dissociation constant decreases with the degree of dissociation (14).

At pH values below 1.5 deviations from the isosbestic point appear (Figure 4A) that may signal a second protonation of the parent complex. Similar behavior is observed with the monomeric complex (5). In addition, a gel is observed to form at pH < 1.5. This observation suggests that the second protonation occurs at the uncoordinated nitrogen of the pyrazine ligand to create a combined polycation and polyanion. Intermolecular bridging between the cationic and anionic centers on separate polymeric chains could be responsible for the precipitation of the insoluble gel. Very similar behavior was observed in an earlier study of polyelectrolytes prepared from protonated poly(vinylpyridine) and  $-\text{Fe}(\text{CN})_5^{3-}$  (15).

**Cyclic Voltammetry of  $\text{PVPz}(\text{Fe}(\text{CN})_5^{3-})_n$  in Solution.** Almost no discernible cyclic voltammetric responses are obtained from 2 mM solutions of  $\text{PVPz}(\text{Fe}(\text{CN})_5^{3-})_n$  in a supporting electrolyte consisting of 0.1 M sodium acetate buffer (Figure 5B). However, increasing the concentration of the buffer to 1.0 M causes a reversible couple to appear with a formal potential close to that for the monomeric complex,  $\text{pzFe}(\text{CN})_5^{3-}$  (12) (Figure 5B). The diminished voltammetric response in the 0.1 M electrolyte suggests that the dissolved polyanionic complex may be prevented from reaching the electrode surface by a layer of similarly charged complex that

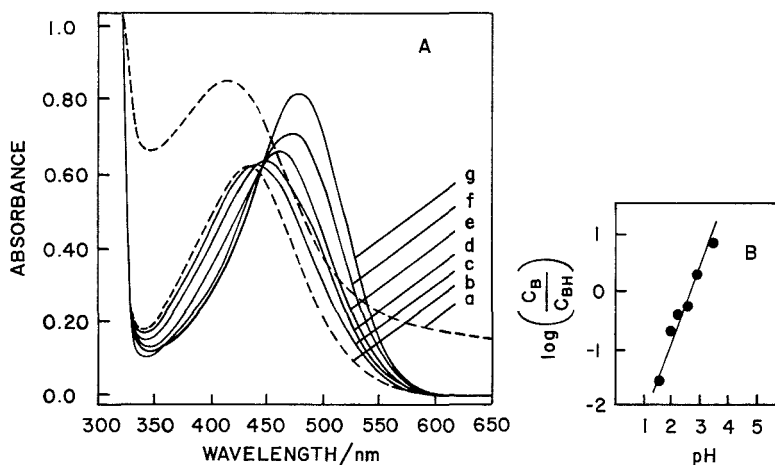
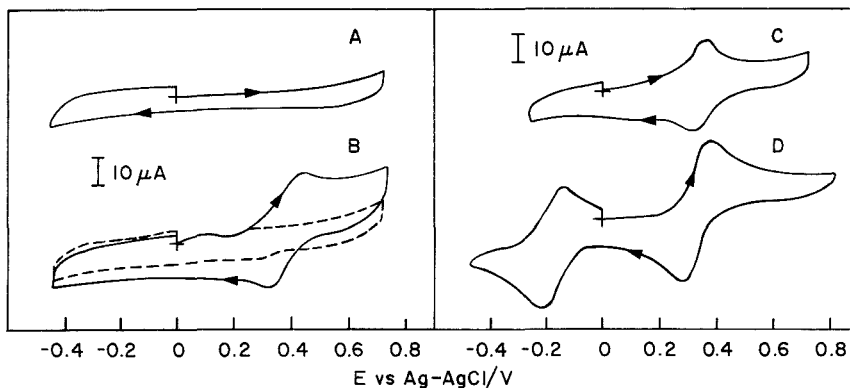


Figure 4. (A) pH dependence of the spectrum of a 0.16 mM solution of  $\text{PVPz}(\text{Fe}(\text{CN})_5^{3-})_n$ . pH of the solutions: (a) 1.0, (b) 1.4, (c) 2.0, (d) 2.3, (e) 2.8, (f) 3.5, (g) 3.9. Buffers employed: (a,b) trifluoroacetate, (c-e) chloroacetate, (f,g) acetate. All solutions contained 0.1 M sodium ion. (B) pH dependence of the ratio of unprotonated to protonated polyanion complex.



**Figure 5.** Effect of supporting electrolyte concentration on cyclic voltammograms for PVPz(Fe(CN) $_5^{3-}$ ) $_n$  at a glassy carbon electrode. Scan rate = 100 mV s $^{-1}$ . (A) Pure supporting electrolyte: 0.1 M sodium acetate buffer at pH 5. (B) Key: dashed line, 25 mM PVPz and 2 mM H $_2$ OFe(CN) $_5^{3-}$  added to the solution from A and allowed to react until equilibrium was attained; solid line, after supporting electrolyte concentration was increased to 1 M. (C) Repeat of B (0.1 M supporting electrolyte) after addition of 1 mM LaCl $_3$ . (D) As in C except 1 mM Ru(NH $_3$ ) $_6$ Cl $_3$  was added.

is adsorbed on the electrode surface. Electron transfer between oxidized  $-\text{Fe}(\text{CN})_5^{2-}$  centers in the adsorbed layer and reduced  $-\text{Fe}(\text{CN})_5^{3-}$  centers in the dissolved polyanion is apparently also impeded by electrostatic repulsion between the highly charged reactants so that the adsorbed layer is not an efficient mediator of electron transfer to the dissolved reactant via self-exchange. With greater concentrations of counterions the highly charged reactant anions are shielded sufficiently to allow them to penetrate the adsorbed layer or to undergo more rapid electron self-exchange reactions with the adsorbed polyanionic layer so that an enhanced voltammetric response is obtained (solid curve in Figure 5B).

The same result can be achieved by addition of much smaller concentrations of more highly charged counterations. For example, addition of even 1 mM La $^{3+}$  or Ru(NH $_3$ ) $_6^{3+}$  cations to the 0.1 M supporting electrolyte used in Figure 5B produces a much more pronounced response from the  $-\text{Fe}(\text{CN})_5^{2-/3-}$  couple (Figure 5C,D). These multiply charged cations are likely to interact with both the dissolved PVPz(Fe(CN) $_5^{3-}$ ) $_n$  complex and that believed to be adsorbed on the electrode surface. The position and magnitude of the voltammetric response for the Ru(NH $_3$ ) $_6^{3+/2+}$  couple in Figure 5D are virtually the same as those obtained at a bare electrode, which might be taken as an indication of relatively weak interactions between the polyanionic complex and the multiply charged cations. However, with slightly higher concentrations of La $^{3+}$  or Ru(NH $_3$ ) $_6^{3+}$ , colloidal precipitates are formed in solutions of PVPz(Fe(CN) $_5^{3-}$ ) $_n$  (but not in solutions of monomeric pzFe(CN) $_5^{3-}$ ) that must result from strong interactions between the polyelectrolyte molecules and the added cations. The colloid that forms in dilute supporting electrolytes (0.05 M sodium acetate buffer) redissolves if the ionic strength is increased to 1 M so that there appears to be competition for binding with the polyanions between the multiply charged cations that yield cross-linked, insoluble colloids and sodium ions that yield soluble polyanionic species.

**Mediated Electron Transfer.** The small voltammetric response obtained for the PVPz(Fe(CN) $_5^{3-}$ ) $_n$  complex in 0.1 M supporting electrolytes (Figure 5B) can also be enhanced by the presence of a redox mediator that can penetrate the adsorbed layer of the polyanionic complex or participate in rapid electron self-exchange reactions with it. A suitable mediator proved to be the monomeric pzFe(CN) $_5^{3-}$  complex whose formal potential is very close to that of the PVPz(Fe(CN) $_5^{3-}$ ) $_n$  complex. In Figure 6 are shown the voltammetric responses for PVPz(Fe(CN) $_5^{3-}$ ) $_n$  alone, pzFe(CN) $_5^{3-}$  alone, and

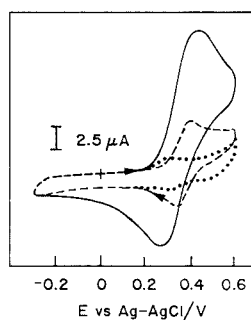


**Figure 6.** Mediated cyclic voltammetry of PVPz(Fe(CN) $_5^{3-}$ ) $_n$  in 0.1 M acetate buffer supporting electrolytes: dotted line, 1 mM polyanion complex alone; dashed line, 0.1 mM monomeric pzFe(CN) $_5^{3-}$  alone; solid line, a mixture (1.0 and 0.1 mM) of the two complexes. Scan rate = 100 mV s $^{-1}$ .

a mixture of the two. The large current obtained with the mixtures shows clearly that the monomeric pzFe(CN) $_5^{3-}$  complex is an effective mediator for both the oxidation and the reduction of the polyanionic complex. The ratio of anodic to cathodic mediated peak currents is near unity for scan rates between 20 and 200 mV s $^{-1}$ . This behavior is qualitatively consistent with that expected for mixtures of two reactants with significantly different diffusion coefficients whose diffusional pathways to the electrode surface are coupled by rapid electron transfer between the rapidly and slowly diffusing species. The current enhancement to be expected in chronoamperometric or chronocoulometric experiments with such systems can be calculated quantitatively from the relationships derived by Andrieux et al. (16). To do so requires that the concentrations and diffusion coefficients for both species be known as well as the equilibrium constant for the reaction between them (16). The diffusion coefficients for complexes were estimated from their voltammetric responses (with the use of 1 M supporting electrolyte for the PVPz(Fe(CN) $_5^{3-}$ ) $_n$  complex), and the electron-transfer cross-reaction was assumed to be a simple self-exchange reaction with an equilibrium constant of unity. The measured slopes of chronocoulometric plots of  $Q$  vs  $t^{1/2}$  were then compared with those calculated from the unnumbered equations at the bottom of p 52 of ref 16. Although the results, given in Table I, clearly show the

**Table I. Enhancement of the Slopes of Chronocoulometric Charge-Reciprocal Time Plots for the Oxidation of PVPz(Fe(CN)<sub>5</sub><sup>3-</sup>)<sub>n</sub> by Monomeric pzFe(CN)<sub>5</sub><sup>3-</sup>**

[PVPz-(Fe(CN) <sub>5</sub> <sup>3-</sup> ) <sub>n</sub> ], <sup>a</sup> mM	[pzFe-(CN) <sub>5</sub> <sup>3-</sup> ], mM	slope of $Q$ vs $t^{1/2}$ plot, $\mu\text{C s}^{-1/2}$		
		calcd, <sup>b</sup> no coupling	calcd, <sup>c</sup> coupling	exptl <sup>d</sup>
1.06	0.39	43.4	52.5	49
1.37	0.38	47.1	57	61
1.32	0.74	73.5	87	76

<sup>a</sup> Concentration of total -Fe(CN)<sub>5</sub><sup>3-</sup> centers present in the polymer. <sup>b</sup> Calculated by using diffusion coefficients of  $5.1 \times 10^{-6} \text{ cm}^2 \text{ s}^{-1}$  and  $0.39 \times 10^{-6} \text{ cm}^2 \text{ s}^{-1}$  for the monomeric and polymeric complexes, respectively. Note that the latter value, which was measured in 1 M supporting electrolyte, probably differs somewhat from the value appropriate for 0.1 M supporting electrolyte where the chronocoulometry was conducted. <sup>c</sup> Calculated from the unnumbered equation at the bottom of p 52 of ref 16. <sup>d</sup> Measured slope for a potential step from 0 to 0.55 V. Supporting electrolyte was 0.1 M acetate buffer. Slopes were reproducible within  $\pm 10\%$  from run to run.

presence of substantial increases in the chronocoulometric slopes compared with those that would have been observed if there were no electron transfer between the monomeric and polymeric complexes, there is only moderate agreement between the observed and calculated values. This behavior could result from several factors: The rate of the electron-transfer reaction between the two types of complex might not be infinitely fast as was assumed in the derivation of the theoretical relationships (16); the PVPz(Fe(CN)<sub>5</sub><sup>3-</sup>)<sub>n</sub> complex is composed of a mixture of varying molecular weights and diffusion coefficients, not a single species as assumed in the derivation of ref 16. Thus, while the ability of the monomeric pzFe(CN)<sub>5</sub><sup>2-/3-</sup> complex to mediate the oxidation and reduction of its polymeric counterpart is clear, it was not possible to account for the mediation quantitatively in terms of the simple self-exchange mechanism considered in ref 16.

**Coatings of Poly(2-vinylpyrazine) on Electrodes.** The solubility of poly(2-vinylpyrazine) in water is so large that coatings of the polymer deposited on electrodes are rapidly lost when the electrode is exposed to aqueous solutions. However, stable coatings can be prepared by introducing alkyl cross-linking bridges between heterocyclic nitrogen atoms by reacting them with alkyl dibromides, as has been done for the case of poly(vinylpyridine) (7, 8). Electrodes coated with the cross-linked polymeric ligand and immersed in solutions containing H<sub>2</sub>OFe(CN)<sub>5</sub><sup>3-</sup> anions exhibit cyclic voltammograms with a single prominent wave that has peak currents which grow continuously as the electrode potential is cycled and a peak potential close to that for the monomeric pzFe(CN)<sub>5</sub><sup>3-</sup> complex prepared independently. (The formal potentials of the coatings of polymeric complex depend on the ionic strength of the supporting electrolytes as is described below.) The voltammograms in Figure 7 were obtained with a coated electrode that had been cycled for 30 min in a solution of H<sub>2</sub>OFe(CN)<sub>5</sub><sup>3-</sup> and then transferred to a solution of pure supporting electrolyte. The voltammetric response is reasonably stable but the peak current decreases to about 70% of its initial value after 3 h of exposure to the pure supporting electrolyte solution. The quantities of -Fe(CN)<sub>5</sub><sup>3-</sup> groups coordinated to the coatings of polymeric ligand were measured coulometrically in pure supporting electrolyte by integrating the charge that passed when the electrode potential was scanned slowly from -0.2 to 1.0 V and held at the upper value until the current decayed to background levels. The extent of coordination depended slightly on the degree of cross-linking employed. As the fraction of the pyrazine groups involved in the cross-linking was increased from 10 to 20%,

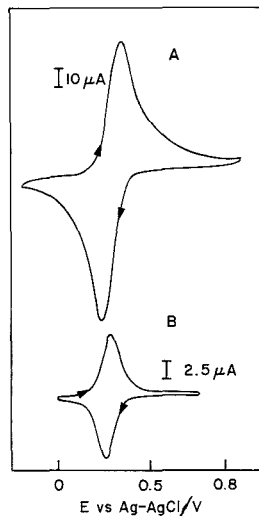


**Figure 7.** Steady-state cyclic voltammograms of a cross-linked coating of PVPz(Fe(CN)<sub>5</sub><sup>3-</sup>)<sub>n</sub> on a glassy carbon electrode. The coating contained  $\sim 10^{-6} \text{ mol cm}^{-2}$  pyrazine centers that had been cross-linked with  $\sim 10^{-7} \text{ mol cm}^{-2}$  1,6-dibromohexane as described in the Experimental Section;  $4.7 \times 10^{-6} \text{ mol cm}^{-2}$  -Fe(CN)<sub>5</sub><sup>3-</sup> centers were coordinated to the coating by 30-min exposure to a 2.5 mM solution of H<sub>2</sub>OFe(CN)<sub>5</sub><sup>3-</sup>. Supporting electrolyte was 0.1 M acetate buffer at pH 5. Scan rate = (A) 50 and (B) 2 mV s<sup>-1</sup>.

the fraction of the groups to which -Fe(CN)<sub>5</sub><sup>3-</sup> centers could be coordinated (from 2.5 mM solutions of H<sub>2</sub>OFe(CN)<sub>5</sub><sup>3-</sup>) decreased from 12 to 10%. This fraction was not sensitive to increases in the concentration of H<sub>2</sub>OFe(CN)<sub>5</sub><sup>3-</sup> or to changes in the ionic strength of the reaction solution. Decreasing the cross-linking below 10% yielded less stable coatings that tended to dissolve from the electrode surface.

The extent of coordination decreased with the thickness of the PVPz coatings. For example, increasing the quantity of PVPz in a coating from  $5 \times 10^{-7}$  to  $2 \times 10^{-6} \text{ mol cm}^{-2}$  decreased the fraction of coordinatable pyrazine groups in 0.1 M supporting electrolyte from ca. 12 to 1%. Increasing difficulty in penetration of the thicker, cross-linked coatings by the solvated H<sub>2</sub>OFe(CN)<sub>5</sub><sup>3-</sup> anions seems the likely origin of this trend.

Much larger fractions of the pyrazine groups in PVPz can be bound to -Fe(CN)<sub>5</sub><sup>3-</sup> centers when the monomer anion reacts with a homogeneous solution of the polymer instead of with a cross-linked coating. Evidently the cross-linking renders a significant portion of the pyrazine sites inaccessible to the H<sub>2</sub>OFe(CN)<sub>5</sub><sup>3-</sup> anions in solution or less reactive toward coordination or both. Attempts to attach the preformed metallopolymer complex to the electrode surface by depositing a coating from aqueous solution, evaporating the solvent, and subjecting the deposit to the cross-linking reaction were unsuccessful.

The shapes of the voltammograms obtained with cross-linked coatings of PVPzFe(CN)<sub>5</sub><sup>3-</sup> are influenced by the scan rate employed to record them. As is evident in Figure 7, the diffusional decay of the current beyond the peaks in Figure 7A is largely eliminated when a very low scan rate is employed (Figure 7B). Estimates of effective diffusion coefficients for the pzFe(CN)<sub>5</sub><sup>3-</sup> centers in the coatings were obtained from measurements of the slopes of chronocoulometric plots and thicknesses of dry coatings obtained from profilometer measurements. The resulting values were in the range (1-5) ×

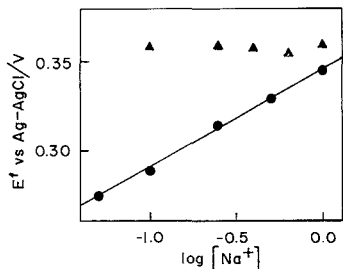
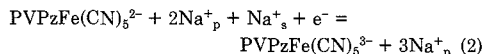


**Figure 8.** Formal potentials for solutions of monomeric  $\text{pzFe}(\text{CN})_5^{3-}$  ( $\blacktriangle$ ) and coatings of  $\text{PVPz}(\text{Fe}(\text{CN})_5^{3-})_n$  ( $\bullet$ ) as a function of the concentration of the supporting electrolyte. The values plotted are the average of anodic and cathodic peak potentials in cyclic voltammograms.

$10^{-10} \text{ cm}^2 \text{ s}^{-1}$ . However, the profilometer measurements showed the coatings to have nonuniform thicknesses so that the values of diffusion coefficients obtained were only approximations.

Coatings of PVPz to which  $-\text{Fe}(\text{CN})_5^{3-}$  groups have been coordinated exhibit cation-exchange activity when exposed to solutions of multiply charged cations such as  $\text{Ru}(\text{NH}_3)_6^{3+}$ . The cation-exchange capacity of such coatings can be controlled by changing the electrode potential at which the cation exchange is carried out. When the electrode potential is held at 0.8 V where the  $-\text{Fe}(\text{CN})_5^{3-}$  centers are oxidized to  $-\text{Fe}(\text{CN})_5^{2-}$ , the quantity of  $\text{Ru}(\text{NH}_3)_6^{3+}$  exchanged into the coatings is about 60% of the quantity incorporated at 0 V where the coordinated anions are present as  $-\text{Fe}(\text{CN})_5^{3-}$ . Similar behavior was reported in an earlier study of coatings based on poly(vinylpyridine) where the net charge carried by the coatings was affected by pH as well as the electrode potential (17). Poly(vinylpyrazine) coatings can be employed over a wider pH range without changes in the coatings' charge because of the much weaker basicity of pyrazine compared with that of pyridine.

The apparent formal potential,  $E_{\text{app}}^f$ , of the  $-\text{Fe}(\text{CN})_5^{2-/3-}$  groups in coatings of  $\text{PVPz}(\text{Fe}(\text{CN})_5^{3-})_n$  on electrodes becomes more positive as the concentration of the supporting electrolyte is increased. A plot of  $E_{\text{app}}^f$  vs  $\log [\text{Na}^+]$  is shown in Figure 8 along with a similar set of measurements at a bare electrode for the monomeric  $\text{pzFe}(\text{CN})_5^{3-}$  complex. The formal potential of the latter complex is essentially constant over the range of concentrations examined while  $E_{\text{app}}^f$  for the  $-\text{Fe}(\text{CN})_5^{2-/3-}$  centers in the coating changes by about 55 mV per decadic change in the concentration of sodium counterions. The changes to be expected in  $E_{\text{app}}^f$  values for redox couples incorporated by ion exchange into electroinactive, permselective polyelectrolyte coatings have been discussed in recent reports (18, 19). If the polyanionic coatings based on  $\text{PVPz}(\text{Fe}(\text{CN})_5^{3-})_n$  are permselective, the measured formal potentials would correspond to the half-reaction



where  $\text{Na}_p^+$  and  $\text{Na}_s^+$  refer to the sodium counterions within the polyelectrolyte and in the bathing solution, respectively. The apparent formal potential for the  $-\text{Fe}(\text{CN})_5^{2-/3-}$  centers coordinated to the PVPz should obey the equation

$$E_{\text{app}}^f = E_p^f - \frac{RT}{F} \ln \frac{[\text{Na}_p^+]}{[\text{Na}_s^+]} \quad (3)$$

where  $E_p^f$  is the formal potential of the couple within the coating. Since the only charged sites within the polyelectrolyte are the electroactive  $-\text{Fe}(\text{CN})_5^{2-/3-}$  centers, the value of  $[\text{Na}_p^+]$

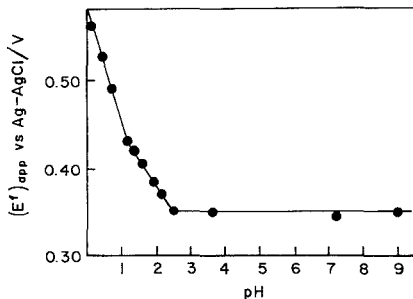


**Figure 9.** pH dependence of  $E_{\text{app}}^f$  for coatings of  $\text{PVPz}(\text{Fe}(\text{CN})_5^{3-})_n$ .

is determined by the maintenance of electroneutrality within the polyelectrolyte:

$$[\text{Na}_p^+] = 3[-\text{Fe}(\text{CN})_5^{3-}] + 2[-\text{Fe}(\text{CN})_5^{2-}] \quad (4)$$

The total concentration of  $-\text{Fe}(\text{CN})_5^{2-/3-}$  groups within the coating,  $C_T$ , is

$$C_T = [-\text{Fe}(\text{CN})_5^{3-}] + [-\text{Fe}(\text{CN})_5^{2-}] \quad (5)$$

and at the formal potential, evaluated as the average of the anodic and cathodic peak potentials:

$$[-\text{Fe}(\text{CN})_5^{3-}] = [-\text{Fe}(\text{CN})_5^{2-}] = \frac{1}{2}C_T \quad (6)$$

Combining eq 4, 5, and 6 allows eq 7 to be rewritten

$$E_{\text{app}}^f = E_p^f - \frac{RT}{F} \ln (2.5C_T) + \frac{RT}{F} \ln [\text{Na}_s^+] \quad (7)$$

Thus, the apparent formal potential is expected to increase by 59 mV (25 °C) for each 10-fold change in the concentration of sodium ion, close to the value (55 mV/decade) observed in Figure 8. This behavior indicates that the coatings have reasonably high permselectivity so that they must be relatively impervious to anions.

According to eq 7,  $E_{\text{app}}^f$  values for the coating should also depend on the concentration of  $-\text{Fe}(\text{CN})_5$  groups coordinated to the polymer. In fact, the values of  $E_{\text{app}}^f$  obtained from the average of the peak potentials do shift to slightly more negative values as electrodes coated with PVPz are cycled in solutions of  $\text{H}_2\text{OFe}(\text{CN})_5^{3-}$ . More quantitative comparisons were not attempted because of the difficulties associated with separation of the effects of residual uncompensated resistance from those attributable to changes in  $C_T$ .

With a fixed concentration of supporting electrolyte,  $E_{\text{app}}^f$  exhibits a pH dependence as shown in Figure 9. The three segments of the plot have slopes of  $-117$ ,  $-61$ , and  $0 \text{ mV/pH}$ . This behavior corresponds to that observed with homogeneous solutions of  $\text{PVPz}(\text{Fe}(\text{CN})_5^{3-})_n$  described above: At pH values above ca. 2.5 oxidation of  $-\text{Fe}(\text{CN})_5^{3-}$  groups to  $-\text{Fe}(\text{CN})_5^{2-}$  occurs without the loss or gain of protons; between pH 2.5 and  $\sim 1.2$  the oxidation is presumably of  $\text{Fe}(\text{CN})_4\text{CNH}^{2-}$  groups to  $\text{Fe}(\text{CN})_5^{2-} + \text{H}^+$ , and at lower pH values two protons are released when  $-\text{HpzFe}(\text{CN})_4\text{CNH}^-$  groups are oxidized to  $-\text{pz}(\text{Fe}(\text{CN})_5^{2-})$ . The intersection points of the three linear segments in Figure 9 depend upon the  $\text{pK}_a$  values governing the protonation of the reduced forms of the complexes within the coatings. However, it would be necessary to know the ion-exchange selectivity coefficient for sodium ion and protons in order to evaluate the  $\text{pK}_a$  values (18), and these coefficients have not been measured. In addition, the non-unit slope of the plot shown in Figure 4B for the soluble  $\text{PVPz}(\text{Fe}(\text{CN})_5^{3-})_n$  complex makes it likely that the apparent  $\text{pK}_a$  values within

the coatings would depend on both the pH of the bathing solution and the potential of the electrode (i.e., the net charge of the polyanionic coating).

### CONCLUSIONS

The potential utility of poly(2-vinylpyrazine) as a polymeric ligand to which suitable metal complexes may be bound is evident from these studies. The observation that no more than 15% of the pyrazine sites in cross-linked coatings of the polymer can be reacted with  $\text{H}_2\text{OFe}(\text{CN})_6^{3-}$  discouraged us from pursuing their application as electrochemically controllable, ion-exchanging polyelectrolytes. Attempts are under way to prepare polymers containing pyrazine ligand sites that swell more extensively in aqueous media in the hope that materials more suitable for electrochemical ion-exchange experiments may result.

### ACKNOWLEDGMENT

We thank Dr. Katsuhiko Sumi for the preparation of poly(2-vinylpyrazine).

Registry No. PVPz, 56217-17-5;  $\text{PzFe}(\text{CN})_6^{3-}$ , 40299-78-3;  $\text{H}_2\text{OFe}(\text{CN})_6^{3-}$ , 18497-51-3;  $\text{Ru}(\text{NH}_3)_6^{3+}$ , 18943-33-4;  $\text{La}^{3+}$ , 16096-89-2;  $\text{Na}^+$ , 17341-25-2; pyrazine, 290-37-9; carbon, 7440-44-0.

### LITERATURE CITED

- (1) Murray, R. W. In *Electroanalytical Chemistry*; Bard, A. J., Ed.; Marcel Dekker: New York, 1984; Vol. 13.
- (2) Faulkner, L. R. *Chem. Eng. News* **1984**, *62*, 135.

- (3) Wrighton, M. S. *Catalysis and Electrocatalysis*; Miller, J. S., Ed.; ACS Symposium Series 192; American Chemical Society: Washington, DC, 1982.
- (4) Hillman, A. R. In *Electrochemical Science and Technology of Polymers*; Linford, R. G., Ed.; Elsevier Applied Science: New York, 1987; Chapters 5, 6.
- (5) Calvert, J. M.; Meyer, T. J. *Inorg. Chem.* **1982**, *21*, 3978.
- (6) Margerum, L. D.; Meyer, T. J.; Murray, R. W. *J. Phys. Chem.* **1986**, *90*, 2696.
- (7) Braun, H.; Storck, W.; Doblhofer, K. *J. Electrochem. Soc.* **1983**, *130*, 807.
- (8) Lindholm, B.; Sharp, M. J. *Electroanal. Chem. Interfacial Electrochem.* **1986**, *198*, 37.
- (9) Creutz, C. *Prog. Inorg. Chem.* **1983**, *30*, 1.
- (10) Emschwiller, M. G. C. R. Acad. Sci. Paris, C **1967**, *282*, 281.
- (11) Sharp, M.; Montgomery, D. D.; Anson, F. C. *J. Electroanal. Chem. Interfacial Electrochem.* **1985**, *194*, 247.
- (12) Toma, H. E.; Malin, J. M. *Inorg. Chem.* **1973**, *12*, 1039, 2080.
- (13) Morawetz, H. *Macromolecules in Solution*; John Wiley and Sons: New York, 1975; Chapters VII, IX.
- (14) Katchalsky, A.; Spitnik, P. *J. Polym. Sci.* **1947**, *2*, 432, 487.
- (15) Shigehara, K.; Oyama, N.; Anson, F. C. *J. Am. Chem. Soc.* **1981**, *103*, 2552.
- (16) Andrieux, C. P.; Hapiot, P.; Saveant, J.-M. *J. Electroanal. Chem. Interfacial Electrochem.* **1984**, *172*, 49.
- (17) Zumbunnen, H.-R.; Anson, F. C. *J. Electroanal. Chem. Interfacial Electrochem.* **1983**, *152*, 111.
- (18) Naegeli, R.; Redepenning, J.; Anson, F. C. *J. Phys. Chem.* **1986**, *90*, 6227.
- (19) Redepenning, J.; Anson, F. C. *J. Phys. Chem.* **1987**, *91*, 4549.

RECEIVED for review February 21, 1989. Accepted May 17, 1989. This work was supported in part by the Dow Chemical Co. and the U.S. Army Research Office. P.U. was the grateful recipient of a supporting grant from the National Research Council of Italy.

## Measurement of Nanomolar Dopamine Diffusion Using Low-Noise Perfluorinated Ionomer Coated Carbon Fiber Microelectrodes and High-Speed Cyclic Voltammetry

Margaret E. Rice\* and Charles Nicholson

Department of Physiology and Biophysics, New York University Medical Center, 550 First Avenue, New York, New York 10016

Several improvements in the fabrication and use of carbon fiber voltammetric microelectrodes (CFVMs) are described. These procedures did not involve oxidative treatment, but resulted in sensitivities and selectivities approaching those of treated CFVMs, without the inherent slow response times associated with the latter electrodes. To accomplish this we reduced CFVM noise by (1) improving the adhesive seal between the 8  $\mu\text{m}$  o.d. carbon fiber and the glass insulation using vacuum, (2) snapping rather than cutting or beveling the fiber to be flush with the glass, and (3) using a concentrated electrolyte solution to make electrical contact with the fiber. System noise was reduced by digital smoothing and signal averaging. Selectivity of the CFVMs for dopamine over ascorbate was enhanced to better than 2000:1 by coating with Nafion, a perfluorinated cation exchange polymer, using a low (+0.5 V vs Ag/AgCl) electroplating potential. This low voltage also prevented electrode surface oxidation. To demonstrate the performance of our CFVMs, we used them in conjunction with high-speed cyclic voltammetry to accurately measure the diffusion coefficient of iontophoretically released dopamine at concentrations as low as 35 nM over distances of less than 200  $\mu\text{m}$  in agarose gel.

### INTRODUCTION

Since the first use of graphite paste electrodes to monitor electroactive substances in brain tissue (1), the design of voltammetric microelectrodes for neurochemical studies has been continually improved with regard to miniaturization, selectivity, and sensitivity. At present, the most successful designs use carbon fibers of 5–35  $\mu\text{m}$  o.d. sealed in pulled glass capillaries (2–8); epoxy resin is commonly added to improve the seal and insulate the fiber (2, 4, 5, 7, 8). Electrical contact between the fiber and a suitable wire is made with a graphite-resin mixture (2, 6, 7, 9) mercury (4), conductive paint (5), or saline (3). The selectivity of such carbon fiber voltammetric microelectrodes (CFVMs) for catechol- and indoleamines can be enhanced by coating the electrode surface with a thin film of the perfluorinated ionomer Nafion (7, 9–12), and the sensitivity can be improved by chemically (13) and/or electrochemically (12, 14–17) treating the carbon fiber surface. Recently, the detection of basal levels (20–50 nM) of dopamine (DA) (15, 16) and serotonin (12) using treated CFVMs in discrete brain regions has been reported.

The introduction of faster sampling techniques like high-speed cyclic voltammetry (18, 19) requires that another characteristic of CFVMs, electrode response time, also be

considered. High-speed cyclic voltammetry has been used to monitor subsecond neurochemical events (20, 21), with substance identification from cyclic voltammograms having a duration of less than 10 ms. Such rapid measurements can be made only with untreated CFVMs (20, 21), however, because the surface adsorption of catecholamines that enhances sensitivity also adds a time constant of seconds or minutes to measurements of concentration change (15–17). Unfortunately, the single-measurement detection limit of untreated, fast-responding, carbon fibers is often about 1  $\mu\text{M}$  for DA (20, 21), so preventing the extension of high-speed techniques to measurements of biologically important concentration changes.

One alternative to electrode treatment for increasing CFVM sensitivity is to improve measurement signal-to-noise ratio by noise reduction. Signal averaging has been used to enable untreated CFVMs, used with high-speed cyclic voltammetry (20–22), to detect 100 nM DA for repetitive stimulation-induced responses (22). Consequently, if the detection limit for unaveraged signals could be improved to 200 nM from the typical 1  $\mu\text{M}$  by decreasing background noise, it should be possible to monitor physiologically relevant DA concentration changes of 20–50 nM with untreated CFVMs.

We have attained such detection limits by use of untreated, low-noise CFVMs. The quality of these electrodes was improved by empirically determining noise sources that were the result of the fabrication procedure (8, 9) and then modifying the procedure to eliminate them. CFVMs were optimized especially for use with high-speed cyclic voltammetry, in which background noise sources (e.g. small, rapid fluctuations in active surface), invisible to slower techniques, become evident. The modifications, however, should be applicable for CFVMs used with other techniques.

An improvement in selectivity was achieved by coating CFVMs with Nafion, using a simple electroplating procedure, which gave a selectivity ratio of better than 2000:1 for DA over ascorbate (AA), the major interferent in the brain. Unlike the original Nafion electroplating procedure of Brazell et al. (7), the plating potential was only +0.5 V vs Ag/AgCl to avoid surface treatment.

Evaluation of CFVM performance required a method that could reliably demonstrate response time and detection limit. In other reports (11, 17), response to a rectangular concentration change in flow injection system was used. In the present study, CFVMs were tested for their ability to follow the time-course of a concentration increase during DA iontophoresis from a nearby source in agarose (23). The resulting concentration-time curves were fitted to a solution of the diffusion equation (9) by using a nonlinear simplex algorithm to extract the diffusion coefficient for DA. Digital smoothing and averaging of the curve permitted analysis of DA concentration maxima of 30–30000 nM.

#### EXPERIMENTAL PROCEDURES

**Electrode Preparation.** Carbon fiber VMs were made by threading a single carbon fiber (5 cm length; 8  $\mu\text{m}$  diameter, Le Carbone Lorraine, France; or 10–12  $\mu\text{m}$  diameter, Thornell, Union Carbide, New York) through a 4 cm length of 2 mm o.d. Pyrex tubing (Fisher Scientific), which was then pulled to a taper with a vertical electrode puller (Model 720, David Kopf Instruments, Tujunga, CA). The glass was stored in acetone and blown dry with a stream of nitrogen gas just before a fiber was inserted and the glass pulled. After several electrodes were pulled, with the fiber partially sealed at the tip, a small (50  $\mu\text{L}$ ) drop of adhesive (either 5:1 918 Epon Resin-triethyltetramine, Polysciences, Inc., Warrington, PA, or Norland Optical Adhesive 60 (NOA 60), Norland Products, Inc., New Brunswick, NJ) was back-filled close to the taper, using a blunt 23-gauge, 1.5-in. syringe needle. To improve the adhesive seal between the glass and the carbon fiber, the open end of the capillary was sealed with wax, then the electrode was placed in a desiccator and the desiccator evacuated. After 5 min under vacuum, adhesive had infiltrated the gaps

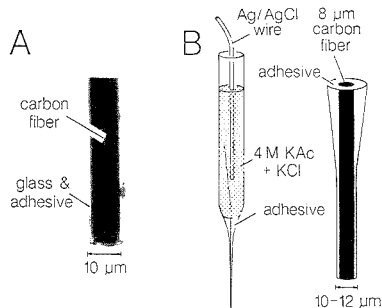


**Figure 1.** Flush-cut carbon fiber microelectrode: (A) photograph of the electrode tip; (B) schematic diagram of electrode features. The back-fill solution was 4 M potassium acetate (KAc) plus 150 mM KCl, adhesive was epoxy or UV-curing optical adhesive (see text).

between the glass and fiber; any external droplets were removed with a cotton swab. Epon resin CFVMs were allowed to cure at room temperature for 48 h before use and were stable for at least several months. NOA 60 CFVMs were cured and ready for use after 10–15 min of UV light exposure using a compound microscope equipped with epi-illumination optics (Zeiss, West Germany).

The glass-epoxy sheath of an electrode tapered over the fiber to an outer diameter of 10–12  $\mu\text{m}$  near the boundary where bare fiber extended beyond the glass. On the day of use, the fiber was manually snapped back to (or slightly within) the glass-epoxy boundary such that the exposed carbon surface was circular and nominally flush with the insulating glass-epoxy wall (Figure 1). CFVMs were back-filled with a solution of 4 M potassium acetate and 150 mM KCl to provide electrical contact between the carbon fiber and a Ag/AgCl contact wire (Figure 1B).

The procedure for electroplating (7) Nafion onto the microelectrode was similar to that reported earlier (9). Briefly, a 4- $\mu\text{L}$  drop of Nafion solution (5% Du Pont 1100 EW Nafion, Solution Technology, Inc., Mendenhall, PA) was held in a 3 mm diameter loop of Ag/AgCl wire that was attached to the reference lead of a two-electrode potentiostat. The CFVM tip was lowered into the Nafion drop for 30 s, with a potential of +0.5 V applied continuously. The CFVM was raised from the drop, allowed to air-dry for 10–15 s, and then dried for 10 min at 60  $^{\circ}\text{C}$ . *Electrodes were not calibrated before coating, because this compromised the effectiveness of the coating procedure.* (For the purpose of comparison, four electrodes were calibrated with increments of 1  $\mu\text{M}$  DA and 100  $\mu\text{M}$  AA before and after coating with Nafion.) The efficacy of the procedure was evaluated by comparing the sensitivity of the CFVM to 200 nM DA and 100  $\mu\text{M}$  AA in phosphate buffered saline (PBS; 100 mM NaCl, 50 mM  $\text{NaH}_2\text{PO}_4$  adjusted to pH 7.4 with NaOH and purged with nitrogen to remove oxygen unless otherwise noted).

**Voltammetric and Diffusion Measurements.** All voltammetric measurements were made by using high-speed cyclic voltammetry with an EI-400 potentiostat (Ensmann Instruments, Bloomington, IN) (Figure 2). Scan rate was 900 V/s with a constant sampling interval of 100 ms. These parameters were found to give the best compromise between measurement frequency and CFVM calibration sensitivity. Resting potential was -0.4 V vs Ag/AgCl; reversal potential was +1.0 V. The potentiostat was used with identical results in either two- or three-electrode mode. The reference electrode was Ag/AgCl wire in 1 M KCl/1% agar bridge; when used, the auxiliary electrode was a Ag/AgCl wire in a pulled glass capillary back-filled with 150 mM NaCl and glued within 1 mm of the CFVM.

Voltammograms were monitored continuously on a digital oscilloscope. The derivative of the applied triangle wave voltage was amplified appropriately and subtracted from the current signal (Figure 2) to offset the large (40–50 nA) charging current component of each voltammogram. This permitted recording of subtraction voltammograms (20–100 pA) for submicromolar DA concentration changes with improved resolution, because more sensitive recording scales could be used. Averaging several





These particles may trap fluid and so cause small fluctuations in surface area, again increasing background noise. We tested several methods for cleaning the surface including beveling (25) or ultrasonically cleaning the tip in a slurry of distilled water and graphite powder. In our hands, beveling led to decreased CFVM sensitivity, possibly because of a layer of epoxy that could be seen on the polished surface under a microscope. The film could be removed with acetone, but this promoted DA adsorption. Ultrasonic cleaning of a cut CFVM was effective, but low noise VMs were more reproducibly made by the simple breaking method described in Experimental Procedures. The most sensitive CFVMs produced by this method were constructed from 8- $\mu\text{m}$  fibers from Le Carbone Lorraine; 8–10- $\mu\text{m}$  Thornell fibers were less sensitive, with DA oxidation peaks at potentials often more anodic than +0.9 V vs Ag/AgCl.

Lastly, good electrical contact with the fiber is essential for undistorted signal transmission to the current monitoring circuitry. In an early paper describing carbon fiber microelectrodes for neurophysiological recording and high-speed cyclic voltammetry, Fox et al. (26), compared the noise levels of electrodes back-filled with mercury, 3 M NaCl or 0.9% NaCl. In that study, mercury and 3 M NaCl were comparable, with 0.9% NaCl CFVMs being somewhat less reliable (26). Similarly, we found that electrodes back-filled with 4 M potassium acetate and 150 mM KCl (Figure 1B) were less noisy than electrodes back-filled with graphite-epoxy and that successful contact with the fiber was made more often with the electrolyte back-fill. Because of the high solubility of potassium acetate, we had no problem from salt crystal formation with evaporation of the back-fill solution, as seen with concentrated NaCl or KCl. The material of the contact wire was found to be important also; for example nickel-plated copper wire caused an additional (cathodic) potential to be added into the potentiostat circuit. AgCl-plated Ag gave the most stable responses; KCl was added to the back-fill solution for maintenance of a constant Ag/AgCl potential.

Elimination of these three major sources of noise, which were the result of our electrode fabrication procedure, markedly improved the quality of CFVM measurements. Other noise sources were not considered in the present study.

**Effect of Coating CFVMs with Nafion.** Calibration profiles for uncoated CFVMs (Figure 3A) indicated that the inherent selectivity ratio for DA:AA of the carbon fibers used was 20–50:1 (30  $\pm$  8, mean  $\pm$  SEM,  $N = 4$ ) and that this ratio was increased to better than 2000:1 (2200  $\pm$  620,  $N = 6$ ; Figure 3C) after a single dip-coating with Nafion during which a small anodic potential was applied to a freshly exposed CFVM surface. Only such surfaces were used because lower selectivity ratios (160  $\pm$  30,  $N = 4$ ) were seen with CFVMs which were previously calibrated, rinsed with distilled water, and dried before coating. This suggested that repetitive exposure to the cycling voltage waveform during calibration was sufficient to alter the surface functionalities of the carbon fiber, so that Nafion had less affinity for the used surface. This might explain why our coating procedure appeared to be more effective than previously reported dip-coating (500:1, DA:AA) (11) or high-potential electroplating (1400:1) (7) procedures. After use in brain tissue (9, 27), the selectivity of our Nafion film CFVMs was maintained, although the sensitivity was reduced by 50–60% (unpublished observations), as seen with other CFVMs (28).

Subtraction voltammograms of cumulative DA additions recorded with Nafion film CFVMs (Figure 3A) had anodic and cathodic peak potentials which were unchanged from those of uncoated CFVMs (Figure 3C). The addition of 100  $\mu\text{M}$  AA altered only slightly the cumulative DA voltammogram at CFVMs coated with Nafion (Figure 3D), but the same addition

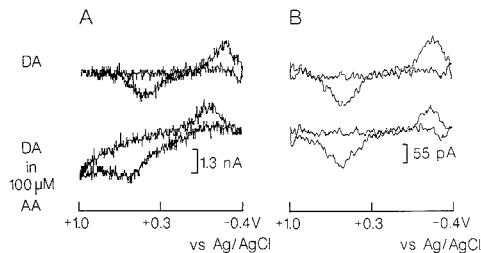


**Figure 4.** DA subtraction voltammograms in the absence and presence of AA. Scan rate, 900 V/s. (A) Uncoated CFVM, 1  $\mu\text{M}$  DA increment in PBS before and after the addition of 200  $\mu\text{M}$  AA. Voltammograms were not averaged. (B) Nafion film CFVM (different electrode than in part A), 200 nM DA increment in PBS before and after 200  $\mu\text{M}$  AA addition. Voltammograms were averaged ( $N = 16$ ). See text for further discussion.

produced a large increase in anodic current monitored with uncoated electrodes (Figure 3A,B, see below for discussion of the AA subtraction voltammogram, labeled 4–3). Further, with uncoated CFVMs, subsequent DA additions in the presence of AA produced higher anodic peak currents than those seen for similar increments in the absence of AA (Figure 4A). With Nafion film CFVMs, this regenerative (29) current was not seen at the high scan rates used (Figure 4B); however, some reduction of voltammetrically oxidized DA by ascorbate may account for the smaller cathodic peak of DA voltammograms recorded in the presence of AA (Figure 4B).

**Signal Processing.** The elimination of most electrode-derived noise revealed system noise (mostly aliased 60 Hz) as the limiting factor in the detection of nanomolar DA. Background fluctuations in the sample-and-hold output could be seen by substituting a 10-M $\Omega$  resistor for an electrochemical cell (Figure 5A,B). This limiting noise was diminished by averaging sequentially recorded traces (Figure 5A) and was further diminished by using a curve-smoothing operation on the data before averaging (Figure 5B). The same smoothing operation performed on voltammetric data traces recorded during the iontophoresis of DA (Figure 5C) also improved the appearance of diffusion profiles (Figure 5E) without adding a time constant to the measurement, indicated by the values of  $D$  (the free solution diffusion coefficient) determined from the smoothed ( $D = 4.8 \times 10^{-6} \text{ cm}^2 \text{ s}^{-1}$ ) and nonsmoothed ( $4.9 \times 10^{-6} \text{ cm}^2 \text{ s}^{-1}$ ) averaged curves (Figures 5C,E). Recognizable voltammograms for 36  $\mu\text{M}$  DA (Figure 5D) were obtained by subtracting averaged ( $N = 16$ ) base-line voltammograms from averaged voltammograms at the DA concentration maxima.

**pH Interference.** One major advantage of high-speed cyclic voltammetry over other voltammetric techniques is that the identity of a substance, like DA, released into the complex environment of the brain can be established by its characteristic cyclic voltammogram. This feature requires that the shape of the background voltammogram is relatively constant, which in turn depends on relatively constant electrolyte composition and pH. Changes in these factors can alter the capacitance of the electrode and affect background oxidation processes, either of which could cause a current increase that might be misinterpreted without a diagnostic cyclic voltammogram.

For example, we found that pH changes interfered with our measurements of DA diffusion in agarose under certain conditions. DA iontophoresis pipets required a "warm-up" period of several iontophoresis cycles during which diluted DA in the tip was replaced by the concentrated solution in the shank and became the major charge carrier. During this early period, a current increase was recorded at the adjacent CFVM (Figure 5F); however the charge carrier was primarily some substance

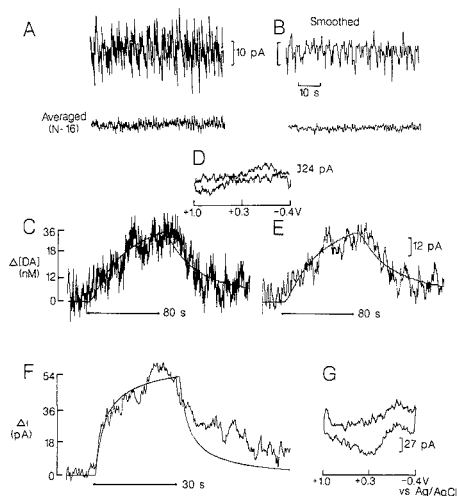


**Figure 5.** Noise reduction and pH interference in high-speed cyclic voltammetry measurements. (A) Sample-and-hold output of system noise (mostly 60 Hz) with a 10-M $\Omega$  resistor as a dummy cell. Upper trace is a single record; lower trace illustrates the noise reduction from signal averaging ( $N = 16$ ). (B) Upper trace shows the effect of smoothing (see text) on the upper record in part A; the lower trace is with the result of averaging ( $N = 16$ ) smoothed records. (C) Averaged ( $N = 16$ ), but unsmoothed dopamine concentration-time curves. Calculated dopamine  $D = 4.9 \times 10^{-6} \text{ cm}^2 \cdot \text{s}^{-1}$  ( $T = 17^\circ \text{C}$ ). Iontophoresis bias current was 4 nA with a 0.4-nA current step applied for 80 s. Electrode spacing ( $r$ ) was 186  $\mu\text{m}$ , transport number ( $n$ ) was 0.02. Solid line is the fitted theoretical curve from which the parameters were derived. Sample-and-hold potential was +0.7 V vs Ag/AgCl. (D) Subtraction voltammogram averaged ( $N = 16$ ) from voltammograms taken near the concentration maximum (36 nM) of one dopamine concentration-time curve. (E) Effect of smoothing each experimental curve before averaging ( $N = 16$ ).  $D = 4.8 \times 10^{-6} \text{ cm}^2 \cdot \text{s}^{-1}$  for the smoothed curve. (F) Concentration-time profile of presumed pH interference during iontophoresis (30 s, 10 nA iontophoresis step on 1-nA bias current). Calculated  $D = 5.5 \times 10^{-5} \text{ cm}^2 \cdot \text{s}^{-1}$  ( $T = 17^\circ \text{C}$ ). Spacing  $r = 162 \mu\text{m}$ . Concentration maximum was about 100 nM in DA equivalents. Sample-and-hold potential was +0.3 V vs Ag/AgCl. (G) Averaged ( $N = 16$ ) subtraction voltammogram from concentration maximum of part F. The peak at +0.3 V indicated that the current increase was not from an increase in DA (compare to part D). The duration of the iontophoresis step for each diffusion record is indicated by the bar beneath the curve. All CFVMs were coated with Nafion.

other than DA, as indicated by the subtraction voltammogram (compare Figure 5G with Figure 5D for DA) and the value of the diffusion coefficient, which was nearly an order of magnitude faster ( $5.5 \times 10^{-5} \text{ cm}^2 \cdot \text{s}^{-1}$ ) than that of DA. The probable iontophoretic charge carrier was  $\text{H}^+$  (or  $\text{H}_3\text{O}^+$ ), because no  $\text{Na}^+$  was present in the iontophoresis back-fill solution. The lack of fit on the falling phase of the diffusion curve (Figure 5F) was perhaps the result of a long-lasting effect on the electrode surface from the local pH change. The subtraction voltammogram (Figure 5G) may reflect the pH sensitivity of carbon functionalities on the electrode surface or of solution background processes such as  $\text{O}_2$  reduction. A similar contaminating peak at +0.3 V vs Ag/AgCl was sometimes seen after the addition of AA (10  $\mu\text{L}$  of 250 mM AA in 0.1 M  $\text{HClO}_4$ ) to 25 mL of nondeoxygenated PBS (Figure 3B).

It should be noted that pH transients do occur in brain tissue as the result of neuronal stimulation (30), with alkaline-going and acid-going shifts of several tenths pH under some conditions (31, 32). The pH and other ion shifts asso-

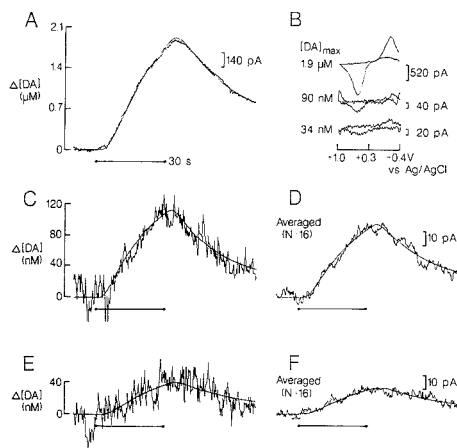


**Figure 6.** Dopamine diffusion curves. The solid line through each is the fitted theoretical curve. Each point is the peak current of a DA voltammogram (scan rate 900 V/s) recorded every 100 ms. (A) Single DA concentration-time profile, no smoothing, 1.9  $\mu\text{M}$  maximum.  $D = 5.2 \times 10^{-6} \text{ cm}^2 \cdot \text{s}^{-1}$ ;  $T = 17^\circ \text{C}$ ;  $r = 186 \mu\text{m}$ ; transport number ( $n$ ) = 0.014; bias current = 2 nA, step = 10 nA. (B) Representative DA subtraction voltammograms for illustrated concentration-time curves: 1.9  $\mu\text{M}$ , unaveraged; 90 nM, averaged ( $N = 16$ ); 34 nM, averaged ( $N = 16$ ). (C) Single, smoothed DA profile, 110 nM maximum.  $D = 5.5 \times 10^{-6} \text{ cm}^2 \cdot \text{s}^{-1}$ ;  $T = 20^\circ \text{C}$ ;  $r = 162 \mu\text{m}$ ;  $n = 0.003$ ; bias = 1 nA, step = 10 nA. (D) Average ( $N = 16$ ) of smoothed profiles with the same parameters as part C, 90 nM average maximum. Averaged record  $D = 5.1 \times 10^{-6} \text{ cm}^2 \cdot \text{s}^{-1}$ . (E) Single record, 38 nM maximum.  $D = 5.1 \times 10^{-6} \text{ cm}^2 \cdot \text{s}^{-1}$ ;  $T = 18^\circ \text{C}$ ;  $r = 186 \mu\text{m}$ ;  $n = 0.004$ ; bias = 2 nA, step = 3 nA. (F) Average ( $N = 16$ ) of smoothed records with parameters as in part E, 34 nM average maximum. Averaged record  $D = 5.2 \times 10^{-6} \text{ cm}^2 \cdot \text{s}^{-1}$ . Iontophoresis step duration was 30 s, indicated by the bar beneath each diffusion record. All CFVMs were coated with Nafion.

ciated with electrical stimulation of the dopaminergic pathways of rat striatum are apparently small enough not to interfere in the measurement of DA release using high-speed voltammetry (20, 21). Larger changes in tissue pH and ion shifts, however, accompany other brain phenomena, including anoxia, hypoxia, and spreading depression (33), and should be considered in studies of these events. The power of difference-voltammogram confirmation under such conditions should not be underestimated. In addition to the interference effects described above, changes in ionic composition can alter the extraction coefficient, and hence peak current, of DA in a Nafion film (11, 34).

**Diffusion Measurements of Nanomolar Dopamine.** The diffusion of DA in agarose could be reliably monitored over a DA concentration range of several orders of magnitude (Figure 6) using the techniques described in this report. Micromolar DA concentration-time profiles could be recorded without curve-smoothing and analyzed without averaging (Figure 6A). Similarly, it was not necessary to average the subtraction voltammograms to identify DA in the micromolar range (Figure 3A); however averaging was routinely done to improve the quality of the voltammograms (Figure 6B). Single smoothed 100 nM DA concentration profiles could be fitted fairly accurately (Figure 6C); however, averaging records (generally 16 times) enhanced the signal-to-noise ratio (Figure 6D). Voltammogram averaging was necessary below 0.5  $\mu\text{M}$ . Averaging was also essential to analyze diffusion records with DA maxima below 100 nM. With this signal processing, averaged concentration-time profiles for around 35 nM (Figures 5C,E and 6F) could be readily fitted to the diffusion equation,

whereas single record concentration increases were hard to distinguish from background (6E).

As well as demonstrating DA detection in the tens of nanomoles range, diffusion analysis (23) provided a relevant evaluation of the response time of the untreated CFVMs to DA concentration change. The value of  $D$  determined by using these CFVMs was about  $5.0 \times 10^{-6} \text{ cm}^2 \text{ s}^{-1}$  (17 °C) (Figure 5C,E and Figure 6), which, when temperature corrected (35), agreed well with previously reported values determined by using a flow injection method (24). The accurate monitoring of the 30-s rising portion of the concentration profile suggests that even shorter intervals could be evaluated if such data were needed. Smaller values for  $D$  ( $(3-4) \times 10^{-6} \text{ cm}^2 \text{ s}^{-1}$ ) seen with some electrodes suggested that adsorption and slow desorption of DA were increasing the CFVM time constant. Similar slow responses were seen when the CFVM was exposed to the air after measuring DA in agarose and was not rinsed before continuing measurements. In that case, a thin layer of dried agarose could be acting as a diffusion barrier to the CFVM surface.

In conclusion, the rational design of low-noise CFVMs can be accomplished by addressing possible noise sources that are the result of the VM fabrication process. The features of the electrodes described here have been optimized for high-speed cyclic voltammetry; however the design principles are generally applicable for other materials and techniques. Concern about possible interferences, including pH changes, is also pertinent to all voltammetric techniques used to study changes of neuroactive compounds in brain and mandates access to cyclic voltammograms throughout the progress of the experiment.

#### ACKNOWLEDGMENT

We are grateful to Dr. F. G. Gonon for his gift of 8- $\mu\text{m}$  Le Carbone Lorraine fibers and to Dr. R. M. Wightman for his gift of 8-10- $\mu\text{m}$  Thornell fibers. We also thank Mr. A. Benedek for electronic support and Ms. S. Sleet for assistance with photography and graphics.

#### LITERATURE CITED

- (1) Kissinger, P. T.; Hart, J. B.; Adams, R. N. *Brain Res.* **1973**, *55*, 209-312.
- (2) Ponchon, J. L.; Cespuoglio, R.; Gonon, F.; Jouviet, M.; Pujol, J. F. *Anal. Chem.* **1979**, *51*, 1483-1486.

- (3) Armstrong-James, M.; Millar, J. J. *Neurosci. Methods* **1979**, *1*, 279-287.
- (4) Dayton, M. A.; Brown, J. C.; Stutts, K. J.; Wightman, R. M. *Anal. Chem.* **1980**, *52*, 946-950.
- (5) Maidment, N. T.; Marsden, C. A. *Brain Res.* **1985**, *338*, 317-325.
- (6) Meulemans, A.; Poulain, B.; Baux, G.; Tauc, L.; Henzel, D. *Anal. Chem.* **1986**, *58*, 2088-2091.
- (7) Brazell, M. P.; Kasser, R. J.; Renner, K. J.; Feng, J.; Moghaddam, B.; Adams, R. N. *J. Neurosci. Methods* **1987**, *22*, 167-172.
- (8) Rice, M. E.; Nicholson, C. *J. Neurochem.* **1987**, *49*, 1096-1104.
- (9) Nicholson, C.; Rice, M. E. *NeuroMethods Vol. 9: Neuronal Microenvironment*; Boulton, A. A., Baker, G. B., Walz, W., Eds.; Humana Press: Clifton, NJ, 1988; pp 247-361.
- (10) Gerhardt, G. A.; Oke, A. F.; Nagy, G.; Moghaddam, B.; Adams, R. N. *Brain Res.* **1984**, *290*, 390-395.
- (11) Kristensen, E. W.; Wightman, R. M. *Anal. Chem.* **1987**, *59*, 1752-1757.
- (12) Crespi, F.; Martin, K. F.; Marsden, C. A. *Neuroscience* **1988**, *27*, 865-896.
- (13) Armstrong-James, M.; Fox, K.; Millar, J. J. *Neurosci. Methods* **1980**, *3*, 37-48.
- (14) Gonon, F. G.; Fombarlet, C. M.; Buda, M. J.; Pujol, J. F. *Anal. Chem.* **1981**, *53*, 1386-1389.
- (15) Gonon, F. G.; Buda, M. *Neuroscience* **1985**, *14*, 765-774.
- (16) Gonon, F. G. *Neuroscience* **1988**, *24*, 19-28.
- (17) Feng, J.-X.; Brazell, M.; Renner, K.; Kasser, R.; Adams, R. N. *Anal. Chem.* **1987**, *59*, 1863-1867.
- (18) Armstrong-James, M.; Kruk, Z. L.; Millar, J. *Nature* **1980**, *288*, 181-183.
- (19) Millar, J.; Stamford, J. A.; Kruk, Z. L.; Wightman, R. M. *Eur. J. Pharmacol.* **1985**, *109*, 341-348.
- (20) Kuhr, W. G.; Wightman, R. M. *Brain Res.* **1986**, *381*, 168-171.
- (21) Stamford, J. A.; Kruk, Z. L.; Millar, J. *Brain Res.* **1986**, *381*, 351-355.
- (22) May, L. J.; Kuhr, W. G.; Wightman, R. M. *J. Neurochem.* **1988**, *51*, 1060-1069.
- (23) Nicholson, C.; Phillips, J. M. *J. Physiol.* **1981**, *321*, 225-257.
- (24) Gerhardt, G. A.; Adams, R. N. *Anal. Chem.* **1982**, *54*, 2618-2620.
- (25) Kelly, R. S.; Wightman, R. M. *Anal. Chim. Acta* **1986**, *187*, 79-87.
- (26) Fox, K.; Armstrong-James, M.; Millar, J. J. *Neurosci. Methods* **1980**, *3*, 37-48.
- (27) Rice, M. E.; Nicholson, C. *Soc. Neurosci. Abstr.* **1988**, *14*, 742.
- (28) Stamford, J. A. *J. Neurosci. Methods* **1986**, *17*, 1-29.
- (29) Dayton, M. A.; Ewing, A. G.; Wightman, R. M. *Anal. Chem.* **1980**, *52*, 2392-2396.
- (30) Kraig, R. P.; Ferreira-Filho, C. R.; Nicholson, C. *J. Neurophysiol.* **1983**, *49*, 831-850.
- (31) Chesler, M.; Chan, C. Y. *Neuroscience* **1988**, *27*, 941-948.
- (32) Rice, M. E.; Nicholson, C. *Brain Res.* **1988**, *461*, 328-334.
- (33) Hansen, A. *J. Physiol. Rev.* **1985**, *65*, 101-148.
- (34) Nagy, G.; Gerhardt, G. A.; Oke, A. F.; Rice, M. E.; Adams, R. N.; Moore, R. B., III; Szentirmai, M. N.; Martin, C. R. *J. Electroanal. Chem.* **1985**, *189*, 85-94.
- (35) Meites, L. *Polarographic Techniques*; 2nd ed.; Interscience: New York, 1965; p 139.

RECEIVED for review April 17, 1989. Accepted June 12, 1989.  
This work was supported by USPHS Grant NS-13742.

## Transient Infrared Emission Spectroscopy by Pulsed Laser Excitation

Roger W. Jones and John F. McClelland\*

Center for Advanced Technology Development, Iowa State University, Ames, Iowa 50011

**Transient infrared emission spectroscopy (TIRES) produces analytically useful emission spectra from optically thick samples by reducing self-absorption of the emitted radiation. Use of a pulsed laser in the TIRES technique allows the observed emission from samples to be limited to a sufficiently thin surface layer of the material that self-absorption is nearly eliminated and the resulting spectra are close to being saturation free. Pulsed-laser TIRES emittance spectra are presented for various plastics and inorganic materials, and these spectra are compared to conventional emittance spectra and photoacoustic absorbance spectra.**

#### INTRODUCTION

Applications of conventional infrared emission spectroscopy have long been limited to optically thin materials because of the phenomenon of self-absorption. When a material is heated to a uniform elevated temperature, all parts of it both emit and reabsorb infrared radiation, and this self-absorption of previously emitted light severely truncates and alters features in the emission spectra of optically thick samples. The resulting emission spectra closely resemble blackbody spectra and contain very little structure characteristic of sample composition ( $I$ ). Recently a new technique called transient

infrared emission spectroscopy (TIRES) that produces analytically useful emission spectra from optically thick samples was introduced (2). In TIRES a laser is used to rapidly heat a thin surface layer of the sample and emission from this layer is gathered before it thickens and cools by thermal diffusion. This effectively minimizes self-absorption by limiting the emitting and reabsorbing to an optically thin volume. In the previous paper on TIRES (2) the background and characteristics of performing TIRES using both continuous-wave (CW) lasers with moving samples and pulsed lasers with both moving and stationary samples were discussed, but only results obtained by using a CW laser were presented and discussed. This paper reports TIRES experiments involving a pulsed, KrF-excimer laser and moving samples.

Since emission induced with a pulsed laser is itself pulsed, TIRES done with a pulsed laser and a Fourier-transform infrared (FT-IR) spectrometer requires both the addition of an integrator circuit into the spectrometer signal path and the synchronization of laser firing with signal sampling by the spectrometer, as described in the Experimental Section. CW-laser TIRES has the advantage of simplicity since no synchronization is required and any FT-IR spectrometer fitted with a HgCdTe (or similarly sensitive) detector and adaptable to emission spectroscopy may be used without modification. Pulsed-laser TIRES, however, produces spectra with less self-absorption than CW-laser TIRES does under typical conditions. The amount of self-absorption in a spectrum is related to the emitting-layer thickness,  $l$ , in the sample while it is being observed by the spectrometer. As was described previously (2), a reasonable estimate for  $l$  is  $(4Dt)^{1/2}$ , where  $D$  is the thermal diffusivity of the sample and  $t$  is the time since laser heating occurred. Accordingly, how long an area of the sample is observed after heating governs how thick the observed emitting layer becomes. It was also previously shown that the maximum observed layer thickness,  $l_{\max}$ , is  $(4Dr/v)^{1/2}$  for CW-laser TIRES, where  $r$  is the width of the sample region behind the laser beam observed by the spectrometer and  $v$  is the sample velocity. For pulsed-laser TIRES the absolute maximum limit on  $t$  is the period between laser shots, which would give  $l_{\max} = (4DR)^{1/2}$ , where  $R$  is the repetition rate of the laser. When an integrator is inserted into the circuitry, however, the maximum  $t$  at which observations are made is controlled by the integrator gating, and so  $l_{\max} = (4Dt_{\max})^{1/2}$ , where  $t_{\max}$  is the time between the laser pulse and the end of the observation gate of the integrator. This is the advantage of pulsed-laser TIRES over CW-laser TIRES—the size of  $l_{\max}$  can be changed simply by altering  $t_{\max}$ , and so smaller values of  $l_{\max}$  are readily achieved. In CW-laser TIRES, reducing  $l_{\max}$  requires either raising the sample speed or reducing the spectrometer field of view, or both, but neither adjustment may be practical in a given application. For example, all of the spectra reported here were observed with a  $t_{\max}$  of 110  $\mu$ s. If  $D$  is taken to be 0.002 cm<sup>2</sup>/s, which is typical of organic solids, this results in an  $l_{\max}$  of 9  $\mu$ m. Such a small  $l_{\max}$  can be difficult to produce by CW-laser TIRES. If  $D$  were the same and  $r$  were 0.4 cm, as it was for the earlier CW-laser TIRES work (2), a sample velocity of 40 m/s would be needed to attain a 9- $\mu$ m  $l_{\max}$ . The small values of  $l_{\max}$  that are readily achieved with pulsed-laser TIRES result in spectra suffering from only minimal self-absorption. Such low- $l_{\max}$  spectra have a larger fraction of the total emission in the structured portion of the emission (at the expense of the blackbody-like portion) and have better spectral contrast (that is, less apparent saturation) in the resulting emission spectra.

## EXPERIMENTAL SECTION

Figure 1 is a diagram of the setup used for observing pulsed-laser TIRES spectra. The physical and optical arrangements were

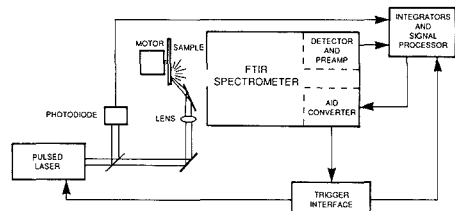


Figure 1. Experimental arrangement used for pulsed-laser TIRES.

very similar to those used for CW-laser TIRES (2), but the electronic arrangement and signal treatment were modified in a manner similar to that used by Leone and co-workers (3, 4) to study chemical kinetics by infrared emission. A disk either made of or covered with the sample material was mounted on the shaft of a variable-speed motor and placed at the normal source position of a Perkin-Elmer 1800 Fourier transform spectrophotometer. The beam from a Lambda Physik EMG 105i excimer laser operating on KrF (248 nm) at 10 mJ/pulse was focused onto the sample disk at a 45° angle within the 8-mm-wide field of view of the spectrometer. A NaCl window covered the entry port of the spectrometer, which viewed the sample normal to the sample surface. The size of the laser beam spot on the sample was optimized for each sample with a single 25-cm-focal-length lens. No other optics were used to better match the emitting area to the spectrometer field of view. The sample disks were spun at 1000 rpm so that the area irradiated by a single laser pulse had left the spectrometer field of view before the next laser pulse. The spectrometer used a wide-band HgCdTe detector ( $D^* = 1 \times 10^{10}$  cm-Hz<sup>1/2</sup>/W) and accumulated 256 interferograms (128 round-trip cycles of the interferometer mirror with an interferogram collected in each direction of mirror travel) at a 0.09 cm/s optical-path-difference velocity and 8 cm<sup>-1</sup> nominal resolution. Each TIRES spectrum appearing in this paper required about 13 min to record.

Because of the pulsed nature of the emission produced by the laser irradiation, it was necessary both to synchronize the laser firing with the signal sampling by the spectrometer analog-to-digital (A/D) converter and to insert an integrator between the output of the detector preamp and the A/D converter. The pulse used internally by the spectrometer to trigger its A/D converter was fed through a trigger interface to fire the laser. At a 0.09 cm/s optical-path-difference velocity, the spectrometer sampled at a 2845-Hz rate, but the laser had a maximum repetition rate of 1000 Hz. The trigger interface prevented overdriving of the laser by firing the laser only on every fourth signal sampling.

The output signal of the detector preamp showed a sharp onset (accompanied by some rapidly damped ringing) when the laser fired, that then decayed away over typically a few hundred microseconds. This output was fed to a boxcar integrator (SRS Model SR250) which was modified to produce a 100- $\mu$ s sampling gate that started 10  $\mu$ s after the laser fired to avoid the initial ringing. The integrator was adjusted so that each laser shot was integrated independently, with no averaging among successive shots. In experiments where the emission strength was not strongly sensitive to pulse-to-pulse fluctuations in the laser energy, the output of the integrator was fed directly to the A/D converter of the spectrometer. The integrator was triggered by the same pulse as the laser and so the four spectrometer samplings between successive laser shots all recorded the same output value from the integrator. In effect, this lowered the Nyquist frequency; however, under these conditions the Nyquist wavenumber was still 3951 cm<sup>-1</sup>.

The pulses from the laser fluctuated in energy by approximately the  $\pm 15\%$  specification of the laser. Usually this fluctuation caused the emission from the sample to vary by a similar amount, resulting in excessive noise. In such cases additional signal processing was done before the signal was fed to the spectrometer A/D converter. A quartz flat was placed in the laser beam to reflect a small portion of the light onto a photodiode, as shown in Figure 1. The output of the diode was fed to a second integrator adjusted and triggered like the first to integrate each laser pulse separately, without averaging successive pulses. The outputs of

the two integrators were then ratioed together to reduce the effect of laser fluctuations. This ratioed signal was then fed to the spectrometer A/D converter. This two-integrator method was used for all of the pulsed-laser TIRES spectra presented here except for that of the polycarbonate.

The emission spectra fall off in intensity with increasing wavenumber in the same manner as blackbody emission curves. To compensate for this, the emission spectra were converted to emittance spectra by ratioing them against blackbody spectra in the same manner as was used previously (2). Since the samples did not have single, uniform temperatures when the TIRES spectra were recorded, temperature could not be used as the criterion for selecting which blackbody curve was to be used with a particular emission spectrum. Instead, since the emittance of an object cannot exceed one, the blackbody curve was chosen in each case so that the resulting apparent emittance of the strongest feature in the spectrum was between 0.8 and 0.95. The blackbody curves were produced by placing a plastic plate covered with carbon black at the source position of the spectrometer and heating it to a series of temperatures in the range 30–80 °C. The spectra were recorded with the same signal processing as was used for the pulsed-laser TIRES emission spectra (with only one integrator). Since carbon black acts as a "gray body" with an emittance less than one and since the selection of a blackbody spectrum described above is somewhat arbitrary, only the relative emittances that result are valid; the absolute values of the emittances are not meaningful. Accordingly, no ordinate scales are provided for any of the TIRES spectra.

As the size of the laser-beam spot on a sample is reduced by more sharply focusing the beam, the intensity of the structured portion of the emission increases substantially due to the higher transient-layer temperature while the blackbody-like portion from the cooler bulk increases more slowly. The signal-to-noise ratios of the emittance spectra increase with decreasing spot size, while the degree of saturation is usually not affected. Accordingly, optimum focusing in most cases corresponded to an irradiation intensity slightly below the threshold for rapid damage to the sample. Slate is the one exception. The emittance spectra of slate, which has a high damage threshold, show increasing saturation as the threshold is neared. Optimum focusing for slate corresponded to a point having both sufficient spectral contrast and a sufficient signal-to-noise ratio.

Conventional emittance spectra are included in the figures for comparison purposes. For these spectra the sample disks were placed at the source position of the spectrometer and heated from behind with heating tape. Because the non-blackbody structure was very weak in such emission spectra, they were recorded under the conditions described elsewhere for CW-laser TIRES spectra (2), which result in reduced noise. Briefly, no integrator was used and 256 cycles were accumulated at a 1.50 cm/s optical-path-difference velocity and 4-cm<sup>-1</sup> nominal resolution. Blackbody spectra required to calculate emittances from these emission spectra were recorded under the same conditions.

Also for comparison with the TIRES results, infrared absorbance spectra were recorded by means of photoacoustic detection. An MTEC Model 200 photoacoustic detector was mounted in the FT-IR spectrophotometer (with its normal light source) and 32 cycles were accumulated at a 0.05 cm/s optical-path-difference velocity and 8-cm<sup>-1</sup> resolution.

## RESULTS AND DISCUSSION

Figure 2 shows the emission from a 3.2-mm-thick disk of polycarbonate. At the top is the pulsed-laser TIRES emission spectrum resulting from a laser-beam fluence per pulse of 30 mJ/cm<sup>2</sup>. Below that is the conventional emission spectrum from the same disk heated to 45 °C. For comparison, a blackbody emission curve from carbon black at 44 °C is shown at the bottom. The measurement conditions for the two polycarbonate spectra were such that the spectrometer observed the same total emission intensity for both, and all three spectra were recorded with the same signal handling. (Only one integrator was used.) The spectra have not been corrected for the response function of the spectrometer and detector. In the pulsed-laser TIRES spectrum the strongest features

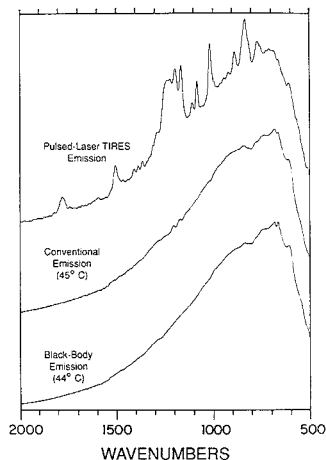


**Figure 2.** Emission spectra from a polycarbonate disk acquired by pulsed-laser TIRES (top) and conventional means (middle). A featureless (blackbody) emission spectrum is included for comparison (bottom).

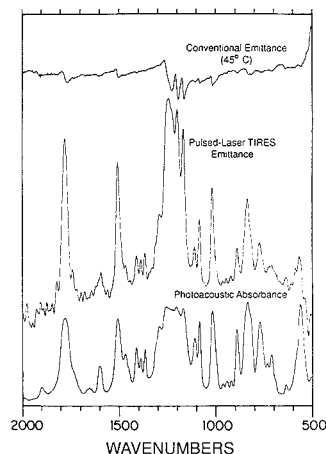


**Figure 3.** Emission spectra from a polycarbonate disk acquired by conventional means (top) and by pulsed-laser TIRES (middle). An absorbance spectrum of the polycarbonate is included for reference (bottom).

have intensities comparable to the blackbody background above which they appear. In contrast, the conventional emission spectrum has very small features and is very similar in appearance to the blackbody spectrum. The difference between TIRES and the conventional technique is equally striking when the emittance spectra are compared. Figure 3 contains emittance spectra derived from the TIRES spectrum in Figure 2 and from a conventional emission spectrum of the sample disk at 45 °C (recorded under better signal-to-noise conditions than the spectrum in Figure 2, as described in the Experimental Section). The two emittance spectra are shown on the same vertical scale, except for an offset. Included for reference in Figure 3 is a photoacoustic absorbance spectrum of polycarbonate, which has been scaled so that small (and therefore low-saturation) features appear the same size in the absorbance and TIRES spectra. The conventional

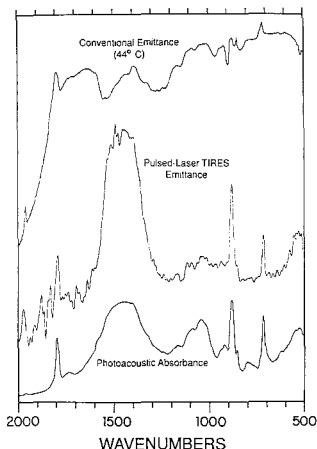


**Figure 4.** Emission spectra of blackboard chalk acquired by conventional means (top) and by pulsed-laser TIRES (middle). An absorbance spectrum of the chalk is included for reference (bottom).

emittance spectrum demonstrates the severe effects of self-absorption. Only the strongest features are observable, and they correspond to small (less than 0.1) changes in emittance. In addition, they have taken on a derivative-like shape. The pulsed-laser TIRES spectrum, on the other hand, is so free of self-absorption that it appears even less saturated than the photoacoustic spectrum. All of the large features are sharper, and the broad feature at  $1200\text{ cm}^{-1}$  is much better resolved into its components in the TIRES spectrum than in the absorbance spectrum. The one characteristic in which the TIRES spectrum is lacking is its signal-to-noise ratio, although it is adequate for observing all but the smallest features.

It should be noted that the surface of the irradiated area of the polycarbonate disk slowly turned dark brown while the TIRES spectrum was being taken. This damage, however, had no effect on the observed spectrum. During the recording of the TIRES spectrum the laser fired approximately 500 000 times, which corresponds to roughly 7000 laser shots on every point within the sampled area of the disk. The observed damage, therefore, was the result of repeated irradiations and would not occur in situations where there is a continuous flow of new material, such as on a production line. We have not investigated whether the damage was photochemical or was thermally induced by the high instantaneous laser intensity (approximately  $2\text{ MW/cm}^2$ ).

Figures 4 and 5 show TIRES and conventional emittance spectra, as well as reference absorbance spectra, of white blackboard chalk and of slate, respectively. In each figure the two emittance spectra were recorded under conditions resulting in the same total emission intensity, and all three spectra are scaled in the same manner as those in Figure 3. These materials were chosen because they allowed higher laser fluences per pulse than the polycarbonate without observable damage ( $96$  and  $82\text{ mJ/cm}^2$  for chalk and slate, respectively) and because their irregular surfaces would test the effects on pulsed-laser TIRES of motion in space of the laser spot. The chalk sample disk consisted of 6-mm-thick sticks of chalk glued to an aluminum disk and planed flat so that the laser tracked over a continuous path of chalk. Variations in the surface caused the laser spot to move 1 to 2 mm as the disk spun. The slate disk was a single piece of stone cut from approximately 4-mm-thick roofing slate. Its surface followed the natural grain of the stone and was therefore irregular,

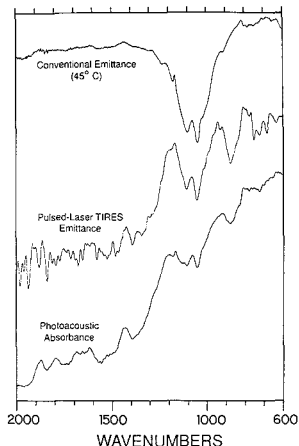


**Figure 5.** Emission spectra from a slate disk acquired by conventional means (top) and by pulsed-laser TIRES (middle). An absorbance spectrum of the slate is included for reference (bottom).

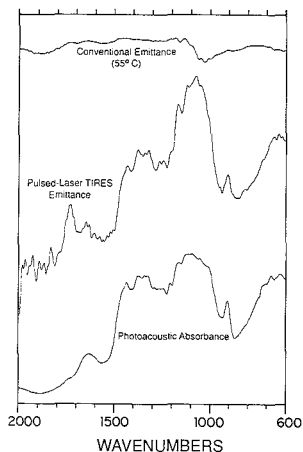


**Figure 6.** Emission spectra from a phenolic-plastic disk acquired by conventional means (top) and by pulsed-laser TIRES (middle). An absorbance spectrum of the plastic is included for reference (bottom).

causing the laser spot to shift by about as much as with the chalk disk. The TIRES spectra in Figures 4 and 5 again show better spectral contrast than the absorbance spectra (however, the structure atop the broad  $1450\text{-cm}^{-1}$  feature in the chalk spectrum is not reproducible), while the conventional emittance spectra are not related in an analytically useful way to the absorbance spectra. The poorer signal-to-noise ratio of these two pulsed-laser TIRES spectra are the results of their irregular surfaces. The pulsed-laser version of TIRES, at least as implemented here, is apparently more sensitive to surface irregularities than CW-laser TIRES which was not affected by modest surface features (2).

The earlier article on TIRES (2) presented results for several samples with a CW laser. Spectra for two of the same samples with a pulsed laser are shown in Figures 6 and 7, again with emission intensities matched and scaling done as in the other illustrations. Figure 6 contains the spectra from a 3-

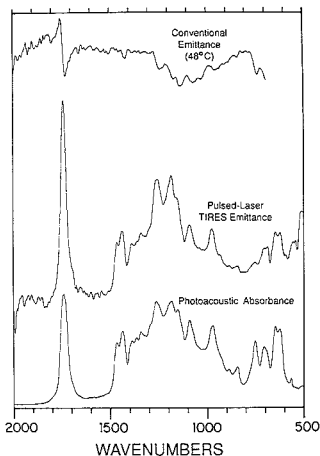


**Figure 7.** Emission spectra of electrical tape acquired by conventional means (top) and by pulsed-laser TIRES (middle). An absorbance spectrum of the tape is included for reference (bottom).

mm-thick, red, filled-phenolic-plastic disk, and Figure 7 shows the results for electrical tape (0.18-mm-thick, black, plasticized poly(vinyl chloride) sheet) attached by its own adhesive to an aluminum disk. The results are qualitatively the same as those in the other figures; the TIRES spectra show less saturation than the absorbance spectra, and the conventional emission spectra show structure that either is not easily related to the absorbance spectra or is reduced in strength and has a derivative shape. Like the polycarbonate, the phenolic plastic darkened during the laser irradiation. The electrical tape being black could not darken, but it lost its glossy finish, turning dull. The TIRES spectrum of the phenolic plastic in Figure 6 has an extra peak at  $1724\text{ cm}^{-1}$  that is caused by the laser irradiation, probably because of the production of carbonyl species. No change definitely related to laser damage appears in the electrical tape spectrum, although some of the increase in the peak at  $1735\text{ cm}^{-1}$  may be the result of carbonyl production instead of reduced self-absorption.

These last two pulsed-laser TIRES spectra may be compared to the CW-laser TIRES spectra appearing in the previous paper on TIRES (2). The spectra observed by using the two types of TIRES differ in only two important ways—the amount of feature saturation and the signal-to-noise ratio. The CW-laser TIRES spectra have roughly the same amount of saturation as the photoacoustic absorbance spectra, while the pulsed-laser spectra have less saturation. As discussed briefly in the Introduction and in more detail elsewhere (2), the degree of self-absorption, and hence the amount of saturation, is governed by the maximum emitting-layer thickness,  $l_{\text{max}}$ , which in turn increases approximately as  $t_{\text{max}}^{1/2}$ , where  $t_{\text{max}}$  is the maximum time after irradiation that the spectrometer observes sample emission. For all of the pulsed-laser TIRES spectra presented in this paper,  $t_{\text{max}}$  is  $11.0\text{ }\mu\text{s}$ , which for phenolic plastic corresponds to an  $l_{\text{max}}$  of  $9\text{ }\mu\text{m}$  ( $D = 0.0020\text{ cm}^2/\text{s}$  (5)). The previously published CW-laser TIRES spectra of the phenolic plastic (spectra 2D and 5F of ref 2) were recorded with a 13-ms  $t_{\text{max}}$ , giving a  $100\text{-}\mu\text{m}$   $l_{\text{max}}$ . Another factor that may also reduce  $l_{\text{max}}$  for the pulsed-laser TIRES spectra is the laser wavelength involved. The above estimates of  $l_{\text{max}}$  assume that the laser light is fully absorbed in a negligibly thin layer at the sample surface, that is, that the absorption coefficient of the sample is effectively infinite at the

laser wavelength. The lower the absorption coefficient actually is, the deeper the laser light will penetrate, and the thicker the emitting layer will be. The CW-laser TIRES spectra were made with a multiline argon-ion laser operating in the blue and green regions of the visible spectrum, while the pulsed laser was operated on KrF at  $248\text{ nm}$ . Since for many materials the absorption coefficient is greater in the ultraviolet region than in the visible region, the pulsed-laser light was normally absorbed within a thinner layer than the CW-laser light. The superior contrast in the pulsed-laser TIRES spectra is the direct result of the smaller  $l_{\text{max}}$  produced by the above factors.

The signal-to-noise ratios of all emission spectra, both TIRES and conventional, decrease with increasing wavenumber since the strengths of the original emission spectra decrease at higher wavenumbers, as Figure 2 shows. Beyond that, though, the signal-to-noise ratios of the pulsed-laser TIRES spectra are more than an order of magnitude less than those of the CW-laser spectra. These reduced ratios are the results of both less signal and more noise. The ease with which sample damage could be induced with the KrF laser necessitated limiting the average beam intensity to a maximum of roughly  $0.4\text{ W/cm}^2$ . The CW-laser experiments were limited to a maximum of about  $2\text{ W/cm}^2$ . The lower intensities allowed with the pulsed laser generally produced lower average sample temperatures and smaller signals. The increased noise in the pulsed-laser case comes from several sources, including the pickup of electromagnetic noise from the laser discharge, the increased bandwidth of the infrared-detector amplifier required in order to accommodate the pulsed emission signal, and the reduced Nyquist frequency that results in the folding of more noise into the spectrum. The principal noise source, however, is the shot-to-shot fluctuations in the laser-pulse energy. The fluctuations were partially compensated for by ratioing the observed signal against the laser-pulse energy, as described in the Experimental Section; however, this approach assumes the signal is linearly related to the pulse energy, which is at best only approximately true. Better compensation could be achieved if the signal were ratioed against the total observed emission intensity (prior to modulation by the interferometer) instead of the laser-pulse energy. This approach should also reduce the sensitivity of pulsed-laser TIRES to surface irregularities.

The pulsed-laser TIRES spectra presented here show that nearly saturation-free emission spectra can be obtained from optically thick samples by synthetically limiting emission to a sufficiently thin layer. For these experiments the spectrometer was modified to only the minimum extent necessary; the normal light source was replaced with the irradiated samples, an integrator was inserted in the signal path to capture the pulsed emission response, and certain band-pass filters were bypassed. Numerous further changes could be made to improve the modest signal-to-noise ratios observed. Better optical matching between the irradiated sample and the spectrometer and the use of an optimum laser wavelength (which would be sample dependent) that would permit higher average laser intensities would increase the signal, while better compensation for laser fluctuations, use of a laser with a higher repetition rate so that the Nyquist frequency could be raised, and better tailoring of the signal-path bandwidth to the TIRES technique would reduce the noise.

#### ACKNOWLEDGMENT

We wish to thank Robert Hoult of the Perkin-Elmer Corp. for many discussions and much essential information. We gratefully acknowledge the generous loan by A. P. D'Silva and Stephan Weeks of Ames Laboratory of integrators and other electronic equipment used in this study. We thank David



Eckels of Ames Laboratory for his advice and assistance.

(5) Erk, S.; Keller, A.; Poltz, H. *Phys. Z.* 1937, 38, 394-402.

#### LITERATURE CITED

- (1) Griffiths, Peter R. *Appl. Spectrosc.* 1972, 26, 73-76.
- (2) Jones, Roger W.; McClelland, John F. *Anal. Chem.* 1989, 61, 850-856.
- (3) Donaldson, D. J.; Leone, Stephen R. *Chem. Phys. Lett.* 1986, 132, 240-246.
- (4) Fletcher, T. Rick; Leone, Stephen R. *J. Chem. Phys.* 1988, 88, 4720-4731.

RECEIVED for review March 10, 1989. Accepted May 12, 1989. This work was funded by the Center for Advanced Technology Development (formerly the Center for New Industrial Materials) which is operated for the U.S. Department of Commerce by Iowa State University under Grant No. ITA 87-02.

## Element Selective Detection after Supercritical Fluid Chromatography Using a Radio Frequency Plasma Detector

R. J. Skelton, Jr.,<sup>1</sup> P. B. Farnsworth,\* K. E. Markides, and M. L. Lee\*

Department of Chemistry, Brigham Young University, Provo, Utah 84602

**A radio frequency plasma was evaluated as an element selective detector for capillary supercritical fluid chromatography. Atomic emission from S and Cl was detected at 921.3 and 837.6 nm, respectively. The analytical performance of the detector was evaluated by monitoring its response to components of several mixtures introduced chromatographically, and to test solutes introduced by using an exponented dilution flask. Minimal spectral interferences were found for the CO<sub>2</sub> and N<sub>2</sub>O doped plasmas. Detection limits and sensitivities were dependent on the mass flow of CO<sub>2</sub> into the detector. The detection limits ranged from 50 to 300 pg/s.**

### INTRODUCTION

Element selective detectors, such as the flame photometric and thermionic ionization detectors, have been important to the development of gas chromatography as an analytical technique. These detectors are known to be very selective and relatively easy to operate on a routine basis. In addition, the thermionic ionization detector is among the most sensitive detectors used for chromatographic detection. Although these detectors are well established, they are not without shortcomings. The investigation of element selective detectors has continued, with much attention given to the use of atomic emission as a basis for detection.

Detection based on atomic emission offers many potential advantages. First, atomic emission lines are narrow and often intense, affording high selectivity and sensitivity. In addition, the atomic-emission-based detectors are tunable. A single detector can be used for several elements, instead of only one or two as with conventional selective detectors. Also, all emission lines are present in the plasma simultaneously, and either single or multichannel detection is possible. The most common device based on this principle is the microwave induced plasma detector (MIP), which was first reported by McCormack et al. (1) and Bache and Lisk (2). The number of workers using MIPs is significant, and many excellent applications have been described (3-6). Other detectors based on plasmas have also been investigated. These include direct current discharge (7), glow discharge (8, 9), and inductively

coupled plasmas (10-15). Rice et al. have worked extensively with afterglow detectors (16), and they have recently reported some encouraging results from a helium afterglow detector based on a primary discharge generated by a radio frequency (rf) power source (17). More recently, we reported the use of a helium radio frequency generated plasma as a gas chromatographic detector (18). This detector is based on an rf discharge formed directly between a pointed metal electrode and a ground, and it has shown promise as a simple, tunable multielement selective detector for gas chromatography. This detector differs from that described by Rice et al. (17) in that emission is observed from the interelectrode region through the wall of a quartz tube. No attempt is made to divide the discharge into a primary discharge and afterglow. Small quantities of oxygen are doped into the plasma to create an ideal environment for sample decomposition and atomic emission. Intense emission lines for the nonmetals of chromatographic interest exist in this portion of the spectrum, and background emission from the plasma arising from molecular species is much less intense than in the UV region. Because of this spectral simplicity, low-resolution light sorting can be used. The combination of a doped helium plasma and the use of the near-infrared emission allows for a simple, low-cost detector.

Because of the good operational characteristics of this plasma for gas chromatographic detection, its use as a detector for supercritical fluid chromatography (SFC) was investigated. Other element selective detectors, such as the thermionic ionization and the flame photometric detectors, have been employed with SFC (19, 20), but their use has not yet become popular because of problems of detector incompatibility with the SFC mobile phases. Recently, the use of surface-wave-sustained microwave induced plasma system was evaluated for the detection of sulfur-containing compounds after SFC (21, 22). In like manner, this paper is intended as an evaluation of the potential use of the radio frequency plasma detector with SFC, including its inherent advantages and limitations.

### EXPERIMENTAL SECTION

**Supercritical Fluid Chromatography.** The supercritical fluid chromatograph consisted of a Hewlett-Packard 5890 gas chromatographic oven (Hewlett-Packard, Avondale, PA) equipped with a flame ionization detector. A varian 8500 syringe pump (Varian Associates, Palo Alto, CA) controlled by an Apple IIe computer was used to deliver the supercritical fluid. The CO<sub>2</sub> and N<sub>2</sub>O used were of SFC grade (Scott Specialty Gases, Plum-

\* Authors to whom correspondence should be addressed.

<sup>1</sup> Current address: Shell Development Co., P.O. Box 1380, Houston, TX 77251.

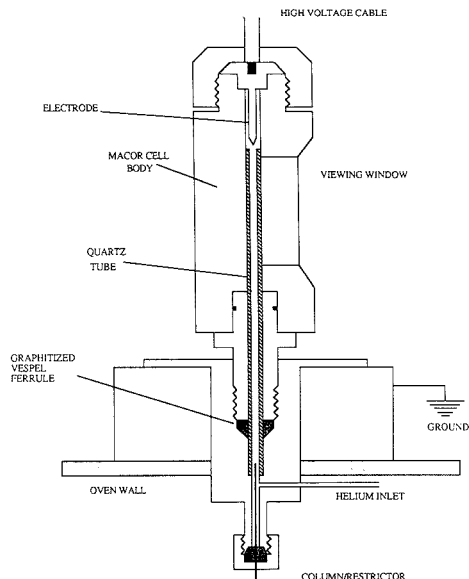


Figure 1. Schematic diagram of the radio frequency plasma detector cell.

steadsville, PA). The columns employed were either purchased from Lee Scientific (Salt Lake City, UT) or made in our laboratory by procedures described in previous publications (23). Capillaries were 50  $\mu\text{m}$  in internal diameter and were coated with film thicknesses between 0.25 and 0.5  $\mu\text{m}$ . The stationary phases used are listed appropriately in the text. Injection into the capillary column was achieved by using a VICI (Houston, TX) valve with a 0.2- $\mu\text{L}$  sample loop. Either split or delayed split (24) techniques were used for sample introduction. The solute mass on the column was in the range of 40–100 ng per solute for the applications shown in this publication.

**Radio Frequency Plasma Detector.** The configuration for the radio frequency plasma detector (RPD) was very similar to the one reported for gas chromatography. Figure 1 shows a schematic diagram of the detector used in this work. The radio frequency power source (ENI Power Systems, Rochester, NY) was connected to the stainless steel electrode by a high-voltage cable. This cable was heavily insulated to prevent arcing to any instrumentation. The ground from the power supply was connected to the mounting block for the detector. The stainless steel electrode was held in place above the quartz discharge tube by a ceramic cell body machined from Macor (Corning Glass Works, Corning, NY), which also acts as an electrical insulator. The quartz discharge tube had an internal diameter of 1 mm. This was held in place by a graphitized vespel ferrule seated in the detector base. High-purity helium (99.9999%, Scott Specialty Gases, Plumsteadville, PA) entered from the side of this base and passed up through the quartz tube. Flow regulation was accomplished by a bellows type needle valve placed between a high-purity gas regulator and the detector base. This helium passed up and around the frit restrictor, which was placed about 1 cm into the plasma. The helium flow rate was optimized around 65 mL/min for GC experiments and around 100 mL/min for SFC. The dopant gases used in GC were unnecessary for the SFC experiment. The plasma power source was tuned to minimize reflected power at a frequency around 330 KHz. Power levels employed ranged between 60 and 100 W, with the higher power levels suited better for the SFC experiments. A slot window in the side of the Macor body allowed for observation of the atomic emission through the quartz tube.

A 0.32-m-focal-length monochromator (Model HR-320, Instruments S. A., Metuchen, NJ) equipped with a 1200 groove/mm

grating was mounted on an x,y translating stage. The monochromator was equipped with continuously variable entrance and exit slits. Most experiments utilized slit widths of 0.5 mm, which maximized optical throughput without seriously affecting selectivity. The spectral bandpass was approximately 1.3 nm. The optics were held in an anodized aluminum tube mounted directly on the entrance slit housing of the monochromator. The optics consisted of a pair of 12.7-mm-diameter achromatic lenses ( $f = 50.8$  mm, Newport Corp., Fountain Valley, CA) and a 12.7-mm-diameter UV cutoff filter (595-nm cutoff, Oriel Corp., Stratford, CT).

The translating stage allowed for easily controlled viewing of the discharge. Detection of the near-infrared radiation was accomplished with a red-sensitive photomultiplier tube (R2658, Hamamatsu, Middlesex, NJ). This InGaAs tube had a red response extending to 1010 nm and was operated at approximately 1000 V. The current generated by the photomultiplier was fed into an electrometer (Keithley Model 602, Cleveland, OH). The output was filtered with a low-pass filter and recorded with a strip chart recorder (Houston Instruments, Houston, TX). Figure 2 illustrates the complete SFC-RPD system.

**Exponential Dilution.** Exponential dilution experiments were done with a mass flow meter (Sierra Instruments, Carmel Valley, CA) and a gas handling syringe. The dilution flask was constructed from a glass sample bulb purchased from Chrompack (Bridgewater, NJ). Dead volume was minimized by use of 320- $\mu\text{m}$ -i.d. fused silica tubing to transfer the gas to the detector. The effluent from the exponential dilution flask was added to the plasma support gas through a tee connection. Mobile phase was introduced into the plasma through a capillary chromatographic column configured as described above. A digital oscilloscope (Nicolet Instruments, Madison, WI) was used to collect and process the data. Further details of this experiment are given later.

**Reagents.** Supracide and Chlorpyrifos were obtained from Ciba Geigy, Greensboro, NC. DDT,  $\alpha$ -BHC,  $\beta$ -BHC, and chlordane were obtained from the Pesticides Repository, Perrine, FL. Carbofuran was obtained from FMC Corp., Middleport, NY. Spectroscopic grade  $\text{CS}_2$  (Fisher, Fairlawn, NJ) and  $\text{CH}_2\text{Cl}_2$  (EM Science, Cherry Hill, NJ) were used in the exponential dilution experiments.

## RESULTS AND DISCUSSION

The mobile phases commonly used in SFC are molecular fluids. Because the plasma does not differentiate between molecular species, energy from the active species in the plasma is used for decomposition and excitation of both the mobile phase and the analyte. In addition, when passive restrictors such as frits are used, the mass flow rate of the mobile phase into the detector increases as the supercritical fluid is density-programmed. These complications are the primary reasons for incompatibility of SFC with traditional element selective detectors.

To be useful, the detector must be insensitive to the increasing amounts of fluid entering the system. Because the RPD is based on atomic emission, the detector would not be expected to respond to a fluid like  $\text{CO}_2$  unless carbon or oxygen were being monitored. Plasma sources, however, usually exhibit emission arising from molecular species such as  $\text{CO}$ ,  $\text{C}_2$ , and  $\text{CN}$ . In our case, emission in the near-infrared portion of the spectrum is utilized for element selective detection, and  $\text{CO}$  and  $\text{C}_2$  emissions, which lie primarily in the UV and visible regions, are not a serious problem. Emission from the  $\text{CN}$  molecule is a potential problem in the near-infrared, however, since several bands exist in this spectral region. In the case of  $\text{CO}_2$ , the large amount of oxygen in the plasma limits the formation of  $\text{CN}$  because  $\text{CO}$  is somewhat more stable. The formation of  $\text{CN}$  in significant amounts should not occur because only trace amounts of nitrogen exist in a clean system.

The presence of  $\text{CO}_2$  in the system gives a green appearance to the otherwise orange-pink color of the pure helium plasma. The presence of  $\text{N}_2\text{O}$  in the system gives a purple hue to the plasma. These colors, from the green  $\text{C}_2$  band the blue  $\text{N}_2^+$

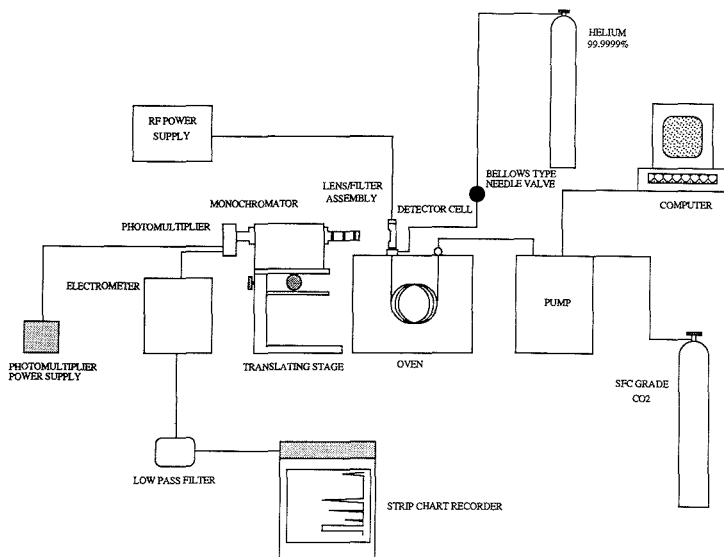


Figure 2. Schematic diagram of the SFC-RPD system.

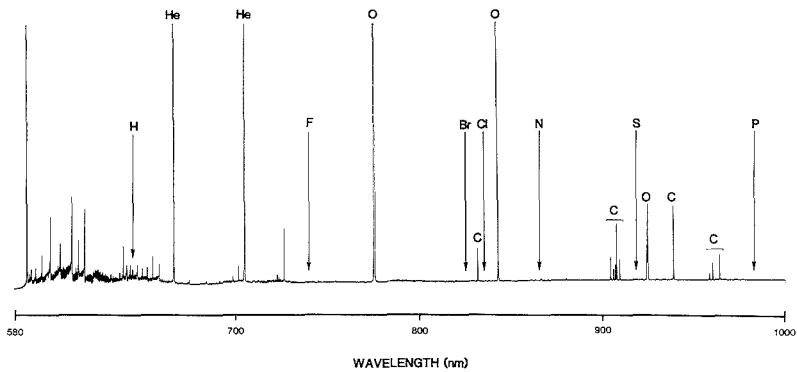


Figure 3. Spectrum of the near-infrared region of the helium radio frequency plasma containing  $\text{CO}_2$ .

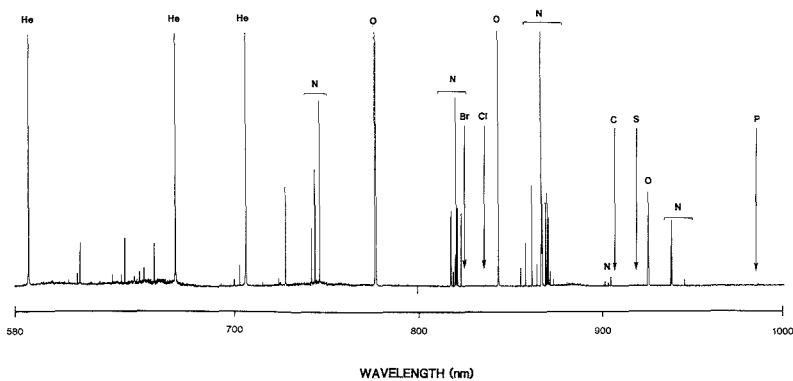


Figure 4. Spectrum of the near-infrared region of the helium radio frequency plasma containing  $\text{N}_2\text{O}$ .

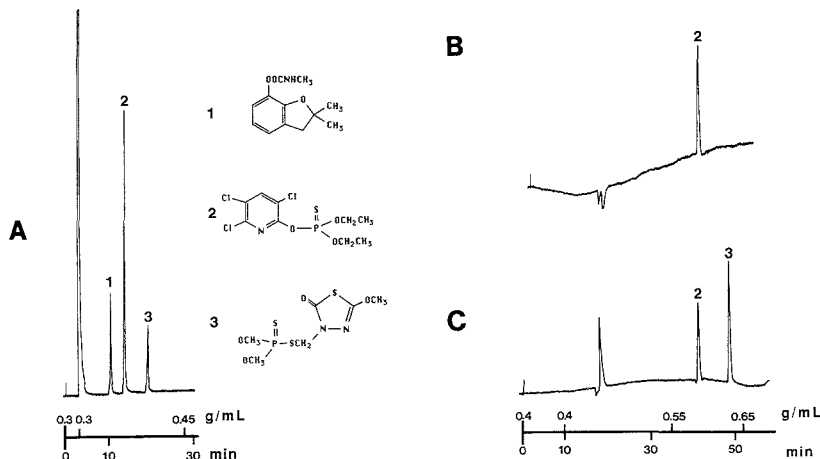


Figure 5. Supercritical fluid chromatograms of a standard pesticide mixture. Conditions: 2.5 m  $\times$  50  $\mu$ m i.d. biphenyl capillary column (0.5- $\mu$ m film thickness); CO<sub>2</sub> at 100 °C. Key: (A) FID; (B) RPD (837.6 nm for chlorine); (C) RPD (921.3 nm for sulfur).

band, are indicative of significant concentrations of these species. Fortunately they produce little emission in the near-infrared region. Figures 3 and 4 show spectra of the near-infrared portions of the spectra for systems containing CO<sub>2</sub> and N<sub>2</sub>O, respectively. The atmospheric pressure flow rate for both gases was approximately 1 mL/min. Major features of the spectra are labeled, with the emission lines for the major nonmetals of chromatographic interest labeled in the locations where they would occur. It can be seen that for many elements, these fluids do not create major background interferences.

Although these spectra indicate that the potential exists for element selective detection with these fluids as mobile phases, other possible problems exist. As discussed earlier, the energetic species in the plasma attack the mobile phase molecules as readily as the analyte. If too much of the mobile phase is in the plasma, the plasma will be quenched and sensitivity will be lost. In an effort to reduce this problem, 50- $\mu$ m-i.d. capillary columns of 2–3 m in length and mobile phase flow rates near the optimum linear velocity were used to carry out the separations. These columns afforded good separations due to the efficiencies obtained at the low linear velocities. The short lengths of the columns kept the total analysis times within reason. This combination allowed the use of only slightly higher than normal plasma support gas flows of 100 mL/min (compared with GC). This is important, since sensitivity drops as the support gas flow increases beyond approximately 50 mL/min. The 100 mL/min helium flow allowed reasonable sensitivity while maintaining a robust plasma, even when the mobile phase was programmed to high densities. The frit restrictors used to maintain flow control from the capillary columns did not show any signs of degradation during these experiments, although the polyimide coating on the columns was stripped from the 1-cm length inserted into the plasma. The atmospheric pressure flow rate of mobile phase varied from 0.8 to 3 mL/min during a density program from 0.3 to 0.7 g/mL.

Figure 5 shows three chromatograms of a pesticide test mixture. The first chromatogram (A) is a flame ionization detector (FID) trace of the separation. The second (B) was generated by using the RPD, monitoring 837.6 nm for chlorine selective detection. The third chromatogram (C) was from the RPD by monitoring 921.3 nm for sulfur selective detection. It can be seen that the selectivity obtained is excellent. In

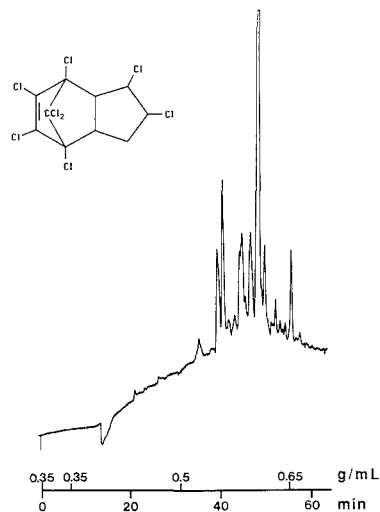
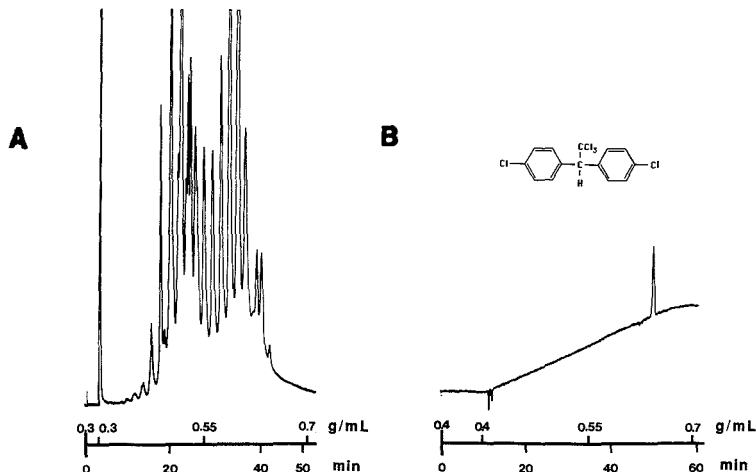


Figure 6. Supercritical fluid chromatogram of chlordane and impurities. Conditions: 2.5 m  $\times$  50  $\mu$ m i.d. biphenyl capillary column (0.5- $\mu$ m film thickness); CO<sub>2</sub> at 100 °C; chlorine detection (837.6 nm).

the case of chlorine, even the large amount of solvent resulted in a negative response. The base line in each case drifted somewhat as a function of density programming. Slight adjustments to the support gas flow allowed this drift to be minimized. Also, the drift was reproducible for given parameters so that base-line compensation, such as that used with UV detection after SFC, could be used.

Figure 6 is a chromatogram of chlordane and its related impurities. The chlordane used to make the standard was of technical grade, and many isomers and degradation products of the compound exist. The detection of these compounds with chlorine selectivity (notice the negative solvent response) suggests that they contain chlorine. The polychlorinated nature of chlordane would seem to support this result.

Figure 7 shows the selective detection of DDT in a milk extract containing primarily triglycerides. The presence of



**Figure 7.** Supercritical fluid chromatogram of a milk extract containing DDT. Conditions: 2.5 m  $\times$  50  $\mu$ m i.d. biphenyl capillary column (0.5- $\mu$ m film thickness); CO<sub>2</sub> at 100 °C. Key: (A) FID; (B) chlorine detection (837.6 nm).

triglycerides in the sample makes difficult the analysis of this mixture by gas chromatography under normal conditions. It should be noted here that the linear velocity used with the SFC-RPD experiments was less than that used with the FID. In practice, the lower flows were more compatible with the detector, and the corresponding frit was left installed in each detector during the duration of the experiment. Therefore, even though the samples are the same, retention times cannot be compared directly.

Figure 8 shows a chromatogram of four chlorine-containing pesticides eluted by using N<sub>2</sub>O as the mobile phase. The chromatogram here shows a normal profile with a large solvent response, since methylene chloride was used to dissolve the sample. Base-line drift in this case was still acceptable. Although solute detection with N<sub>2</sub>O in the plasma was successful, the selectivity is probably poorer than would be obtained with CO<sub>2</sub> because of interference at the analytical wavelengths from CN bands. No base-line compensation was employed for any of the chromatograms shown.

Selectivity measurements were not made for the elements studied here. In practice, only solvent interferences were observed. This is consistent with selectivity measurements observed with gas chromatography (18). The main limitation to the system as described is probably sensitivity. Although the use of 50- $\mu$ m-i.d. columns limits the amount of CO<sub>2</sub> entering the detector, the sample capacity is still good (50–100 ng per component). One advantage of a plasma emission detector is that the response of the detector to the amount of element present has little to do with the molecular structure of the analyte. However, because a passive restrictor was used in these experiments, it is likely that the sensitivity of the detector changed as a function of retention time in density-programmed runs due to the increased flow of mobile phase.

**Exponential Dilution.** In order to characterize detector performance, exponential dilution experiments were carried out to measure sensitivity, linearity, and detection limits as a function of CO<sub>2</sub> density (25, 26). The apparatus used in the experiment is shown in Figure 9. When a known quantity of compound was introduced into the dilution flask, the amount of that compound entering the detector could be accurately calculated on the basis of the flow rate through the flask and the volume of the flask. A mass flow meter was used

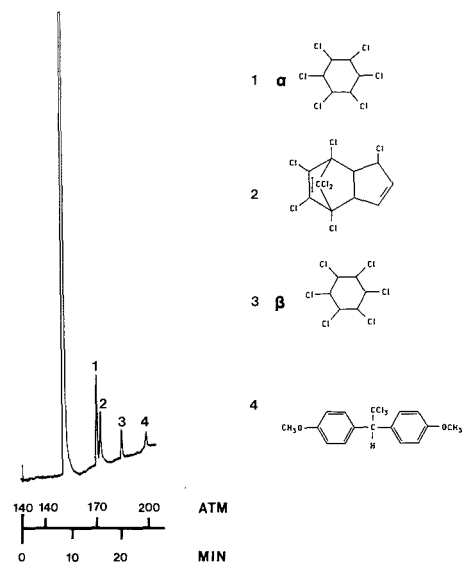


**Figure 8.** Supercritical fluid chromatogram of a pesticide standard mixture. Conditions: 1.5 m  $\times$  50  $\mu$ m i.d. biphenyl capillary column (0.5- $\mu$ m film thickness); N<sub>2</sub>O at 100 °C; chlorine selective detection (837.6 nm).

to measure the flow rate of helium into the flask. The volume of the flask was measured exactly by weight, using a liquid of known density. The compound containing the element of choice was first diluted in helium by using a 100-mL sample bulb so that the weight and concentration could be accurately known. The gas handling syringe was then used to transfer the gas into the dilution flask. The concentration as a function of time could be derived from the equation

$$C_t = C_0 \exp(-Ft/V) \quad (1)$$

where  $C_t$  is concentration at time  $t$ ,  $C_0$  is the initial concen-

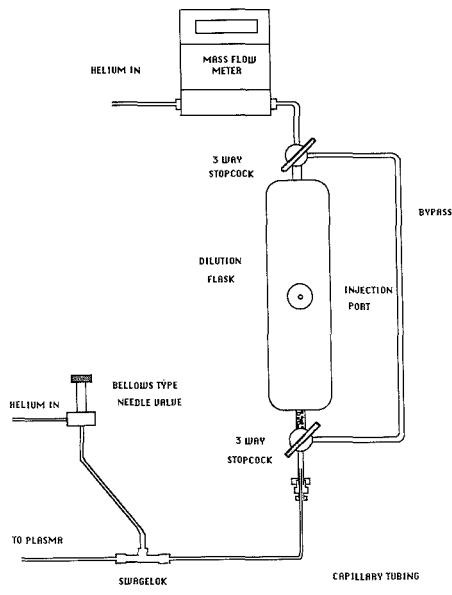


Figure 9. Schematic diagram of the exponential dilution system.

Table I. Detection Limits and Relative Sensitivities of SFC-RPD as a Function of Density

element	100 atm	200 atm	300 atm	400 atm
Detection Limits <sup>a</sup>				
sulfur	59.6	61.2	114	178
chlorine	116	148	152	260
Relative Sensitivity				
sulfur	67.5	64.8	54.9	42.6
chlorine	32.6	23.3	19.6	15.7

<sup>a</sup> Detection limits given in pg/s.

tration, and  $F$  is the flow through the flask. Relative sensitivity and linearity could then be determined from a plot of

$$\ln(x_t) = \ln(C_0) + \ln(S) - Ft/V \quad (2)$$

where  $x_t$  is the signal at time  $t$  and  $S$  is the relative sensitivity. Such a plot would be a straight line over the linear range of the detector. The detection limit could be calculated by deriving the concentration that gave a signal twice the standard deviation of the background. These expressions were thus used to derive the operational characteristics from the experimentally generated exponential dilution curve, which maps detector response as a function of time. Comparison of the theoretical curve with the experimentally observed one and calculations of the response of the detector as a function of time yielded the desired information.

The detector was evaluated by using methylene chloride and carbon disulfide to determine the response for Cl and S, respectively. The experiments were repeated at increasing densities to determine the effect of increasing amounts of  $\text{CO}_2$  on detector response. Figure 10 shows exponential dilution curves for four sulfur determinations. Also included is a derived linear log plot on which the upper limits of linearity and the detection limits are indicated. The sensitivity data obtained from these experiments are given in Table I. It can be seen that the relative sensitivity ( $S$  in eq 2) of the detector

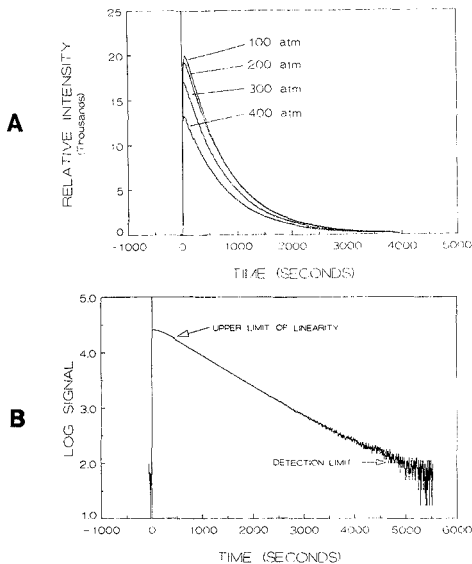


Figure 10. Results from exponential dilution: (A) exponential dilution curves for sulfur determinations at different pressures and (B) a derived linear plot (from eq 2) for 100-atm curve showing the detection limits and upper limits of linearity. The atmospheric pressure flow rates of  $\text{CO}_2$  ranged from approximately 1 mL/min at 100 atm to approximately 3 mL/min at 400 atm.

greatly depends on the flow of  $\text{CO}_2$  into the detector. Sensitivities, however, are good for these elements when  $\text{CO}_2$  is used as the mobile phase. Certainly there are some restrictions of use for the detector operating in its present form. Constant mass flow restriction would be a great asset to this technique. Further work, including the varying of electrode geometry to optimize this unit for SFC, must still be carried out to determine the ultimate utility of the RPD coupled to SFC.

Registry No. DDT, 50-29-3;  $\text{CO}_2$ , 124-38-9;  $\text{N}_2\text{O}$ , 10024-97-2; chlordane, 12789-03-6.

#### LITERATURE CITED

- (1) McCormack, A. J.; Tong, S. C.; Cooke, W. D. *Anal. Chem.* **1965**, *37*, 1470.
- (2) Bache, C. A.; Lisk, O. J. *Anal. Chem.* **1965**, *37*, 1477.
- (3) Carnahan, J. W.; Mulligan, K. J.; Caruso, J. A. *Anal. Chim. Acta* **1981**, *130*, 227.
- (4) Haas, D. L.; Caruso, J. A. *Anal. Chem.* **1985**, *57*, 846.
- (5) Cebus, C. S.; Gluck, J. A. *Spectrochim. Acta* **1983**, *38B*, 387.
- (6) Ke-Wei, Z.; Qing-Yu, O.; Guo-Chuen, W.; Wei-Lu, Y. *Spectrochim. Acta* **1985**, *40B*, 349.
- (7) Evans, G. L. *Anal. Chem.* **1968**, *40*, 1142.
- (8) Tomkins, B. A.; Feldman, C. *Anal. Chim. Acta* **1980**, *119*, 283.
- (9) Treybig, D. S.; Elebracht, S. R. *Anal. Chem.* **1980**, *52*, 1633.
- (10) Windsor, D. L.; Denton, M. B. *Anal. Chem.* **1979**, *51*, 1116.
- (11) Somer, D.; Ohls, K. *Fresenius' Z. Anal. Chem.* **1979**, *295*, 337.
- (12) Brown, R. M.; Northway, S. J.; Fry, R. C. *Anal. Chem.* **1981**, *53*, 934.
- (13) Eckhoff, M. A.; McCarthy, J. P.; Caruso, J. A. *Anal. Chem.* **1982**, *54*, 165.
- (14) Wolnick, K. A.; Miller, D. C.; Seliskar, C. J.; Fricke, F. L. *Appl. Spectrosc.* **1985**, *39*, 930.
- (15) Fujimoto, C.; Yoshida, H.; Jinno, K.; *J. Microcol. Sep.* **1989**, *1*, 19.
- (16) Rice, G. W.; Richard, J. J.; D'Silva, A. P.; Fassel, V. A. *Anal. Chim. Acta* **1982**, *142*, 47.
- (17) Rice, G. W.; D'Silva, A. P.; Fassel, V. A. *Spectrochim. Acta* **1985**, *40B*, 1573.
- (18) Skilton, R. J., Jr.; Markides, K. E.; Farnsworth, P. B.; Yang, F. J.; Lee, M. L. *HRC CC, J. High Resolut. Chromatogr. Chromatogr. Commun.* **1988**, *11*, 75.
- (19) West, W. R.; Lee, M. L. *HRC CC, J. High Resolut. Chromatogr. Chromatogr. Commun.* **1986**, *9*, 161.
- (20) Markides, K. E.; Lee, E. D.; Bolick, R.; Lee, M. L. *Anal. Chem.* **1986**, *58*, 740.
- (21) Galante, L. J.; Selby, M.; Luffer, D. R.; Hietfle, G. M.; Novotny, M. *Anal. Chem.* **1988**, *60*, 1370.

- (22) Luffer, D. R.; Galante, L. J.; David, P. A.; Novotny, M.; Hietje, G. M. *Anal. Chem.* **1988**, *60*, 1365.
- (23) Woolley, C. L.; Tarbet, B. J.; Markides, K. E.; Bradshaw, J. S.; Bartle, K. D.; Lee, M. L. *HRC CC, J. High. Resolut. Chromatogr. Chromatogr. Commun.* **1988**, *11*, 113.
- (24) Lee, M. L.; Xu, B.; Huang, E. C.; Djordjevic, N. M.; Tuominen, J. P.; Chang, H.-C. K.; Markides, K. E. *J. Microcol. Sep.* **1989**, *1*, 7.
- (25) Beenaker, C. I. M. *Spectrochim. Acta* **1977**, *32B*, 173.
- (26) van Dalen, J. P. J.; de Lezenen Coulander, P. A.; de Galan, L. *Anal. Chim. Acta* **1977**, *94*, 1.

RECEIVED for review October 21, 1988. Accepted May 15, 1989.  
This work was funded by the State of Utah, Centers of Excellence Program.

## Spin Dynamics in the Analysis of Carbonaceous Deposits on Zeolite Catalysts by Carbon-13 Nuclear Magnetic Resonance with Cross Polarization and Magic-Angle Spinning

Benny R. Richardson and James F. Haw\*

Department of Chemistry, Texas A&M University, College Station, Texas 77843

The potential of solid-state  $^{13}\text{C}$  nuclear magnetic resonance spectroscopy with cross polarization and magic-angle spinning (CP/MAS) for the characterization of the carbonaceous deposits that form on zeolite catalysts during hydrocarbon processing is explored. Particular attention is given to the extent to which the results can be regarded as quantitative. The samples considered in this investigation were prepared by reaction of butadiene on catalyst pellets containing zeolite HY in a flow reactor at temperatures between 150 and 600 °C. The NMR studies performed included relaxation measurements to characterize the spin dynamics relevant to quantitation and a variable-temperature  $^{13}\text{C}$  CP/MAS experiment. Comparison of carbon spin counting results with carbon content from combustion analysis revealed that although 78% of the carbon was detected by NMR for the sample obtained from the 150 °C reactor run, significantly less carbon was detected for samples coked in the reactor at higher temperatures. This result correlated with the observation of organic free radicals in the samples, but it could also be due in part to inefficient cross polarization in hydrogen-deficient regions.

### INTRODUCTION

Aluminosilicate catalysts such as zeolites are used in a number of important industrial processes including the cracking of fuel oil to yield gasoline-range products, hydrocarbon synthesis from methanol, and a number of isomerization and disproportionation reactions (1-3). A limiting factor in all of these processes is the formation of carbonaceous deposits (termed coke), which eventually deactivates the catalyst and necessitates regeneration (4-6). It has been stated that coke formation is one of the least understood phenomena in catalytic cracking (7). The chemical structure of coke deposits and the mechanisms by which they form have been, therefore, of considerable interest.

As a result of the low solubility of coke deposits, especially those formed at higher temperatures, most efforts to characterize the deposits have focused upon the coked catalyst particles themselves, without a prior attempt to separate the carbonaceous material from the inorganic catalyst and/or binder, although degradative methods involving either acid

(8, 9) or base (6) digestion of the catalyst matrix have also been proposed. Techniques previously applied to the characterization of coked catalyst samples have included elemental analysis (10), electron microscopy and X-ray diffraction (11), and IR spectroscopy (12, 13). There have also been several previous studies that have reported  $^{13}\text{C}$  CP/MAS spectra of carbonaceous residues on zeolites. For example, Derouane and co-workers have studied the residues formed in zeolites H-ZSM-5 and mordenite during the reactions of  $^{13}\text{C}$ -enriched methanol or  $^{13}\text{C}$ -enriched ethylene (14). The entrapped reaction products observed in that study were predominantly low molecular weight alkanes and simple alkylaromatics such as ethylbenzene and were therefore not properly termed carbonaceous deposits. Carlton and co-workers published  $^{13}\text{C}$  CP/MAS spectra of coked ZSM-5 samples that had each been subjected to one of several reactivation procedures (15). Weitkamp and Maixner studied the residues formed at relatively low temperatures by isobutane/butene alkylation on a  $\text{NaNH}_4\text{Y}$  zeolite (16). That study reported an increase in aromatics as the reaction temperature was increased from 80 to 314 °C. In none of those studies was there an investigation of the optimum conditions for the study of coke deposits on zeolites by  $^{13}\text{C}$  CP/MAS NMR, nor was there an investigation of the more complex deposits that are known to form on acidic Y zeolites at elevated temperatures (7, 8).

At first glance, the application of  $^{13}\text{C}$  CP/MAS NMR to the characterization of coke deposits on oxide catalysts might appear to be a straightforward task. The experience of workers familiar with the application of CP/MAS NMR to coals (17, 18), lignins (19), and other complex carbonaceous materials (20-23), however, suggests that analogous studies of coke deposits be approached cautiously, especially if quantitative results are important. The cross polarization experiment is prone to errors in quantitation, especially for samples that are hydrogen deficient. Furthermore, the presence of paramagnetic sites can complicate efforts at quantitation by severely broadening resonances due to carbons in the vicinity of radical sites or by adversely affecting relaxation phenomena central to cross polarization dynamics.

In this contribution, we have taken one catalyst (zeolite HY) and coked it with a single feed (butadiene) at six different temperatures under otherwise identical conditions. We have then performed the detailed measurements necessary to evaluate the reliability of  $^{13}\text{C}$  CP/MAS NMR for these samples. We find that the  $^{13}\text{C}$  CP/MAS spectral intensities de-

\* Author to whom correspondence should be addressed.

terminated for these samples are sufficiently quantitative to be useful, especially for samples coked at the lower temperatures.

### EXPERIMENTAL SECTION

**Sample Preparation.** Type Y molecular sieves were obtained from Strem as extruded pellets consisting of 80% zeolite (in the sodium form as received) and 20% inorganic binder. The Si:Al ratio of the zeolite component was 2.4, and the pore volume was reported to be 0.6 cm<sup>3</sup>/g. The catalyst was converted to the acidic HY form by ion exchange with 0.5 M NH<sub>4</sub>NO<sub>3</sub> followed by activation in a quartz flow reactor at 500 °C under a flow of dry N<sub>2</sub>. Five grams of activated catalyst pellets was used in each reactor run. Following activation, the reactor temperature was changed to the desired reaction temperature, and 110 cm<sup>3</sup>/min of 1,3-butadiene (Matheson) was metered into the nitrogen flow stream, which was kept at 150 cm<sup>3</sup>/min. The reaction was allowed to proceed under these conditions for 1 h, after which the sample was cooled under a N<sub>2</sub> purge prior to grinding and storage in a glovebox under N<sub>2</sub>. Samples were prepared at reaction temperatures of 150, 200, 300, 400, 500, and 600 °C.

**Sample Characterization.** Except where stated otherwise, all NMR experiments were performed on a Chemagnetics M-100S spectrometer operating at a <sup>13</sup>C frequency of 25.02 MHz. Magic-angle spinning was carried out at a rate of 3–4 kHz. Kel-F spinners were loaded with approximately 0.4 g of sample in a glovebox under dry N<sub>2</sub> gas. Chemical shifts were referenced externally to hexamethylbenzene and are reported relative to tetramethylsilane. Pulse delays of 1 s and contact times of 2 ms were used in all cross polarization experiments except for selected relaxation measurements. In general, 40 000 scans were acquired per spectrum. Proton spin-lattice relaxation times (*T*<sub>1</sub>(H)) were determined by using the method described by Maciel et al. (24). Cross polarization time constants (*T*<sub>CH</sub>) were determined from variable-contact-time experiments, and rotating frame proton spin-lattice relaxation times (*T*<sub>ρ</sub>(H)) were determined by holding the proton magnetization in a spin-lock field for a variable delay prior to cross polarization. Generally, seven or more data points were used in all relaxation measurements.

Carbon spin-counting experiments were performed by using the method previously described by Hageman (20). Essentially, this method involves measuring spectra of a weighed amount of the sample of interest mixed with a known quantity of glycine. Integrated intensities, corrected for spectral overlap from the methylene carbon of glycine and *T*<sub>1</sub>(H) values provide a measure of the weight percent of NMR-observable carbon in the sample, which is then compared with the weight percent carbon determined by combustion analysis.

Variable-temperature <sup>13</sup>C CP/MAS experiments (25) were also performed on the 150 °C coked zeolite sample by using methods previously described (26).

Electron spin resonance (ESR) measurements were performed on a Varian E-6S spectrometer. The spectrometer was standardized for quantitative measurements with a standard sample of α,γ-bis(diphenylene)-β-phenylallyl free radical (Aldrich). The standard material was diluted with dicarboxy-terminated polystyrene to a spin concentration of 2.02 × 10<sup>19</sup> spins/g. Standardization was performed at liquid nitrogen temperatures. All ESR sample spectra were also collected at liquid nitrogen temperatures, under vacuum, to minimize extraneous signals from molecular oxygen.

Weight percent carbon was determined for all coked catalyst samples by combustion analysis using a Perkin-Elmer Model 240 elemental analyzer that was standardized with acetanilide. Weight percent hydrogen was also determined on that instrument, but blank determinations on uncoked zeolite samples gave variable percent hydrogen results that, in some cases, were comparable to those for the coked catalyst samples. Large variations were also observed for the coked catalyst samples. These problems were attributed to variable sorption of atmospheric water during sample loading. Therefore, the weight percent hydrogen data were concluded to be unreliable and are not reported.

### RESULTS AND DISCUSSION

Other solid-state NMR studies have shown that simple olefins such as propene (27) undergo rapid acid-catalyzed reactions on zeolite HY at room temperature to give long-chain

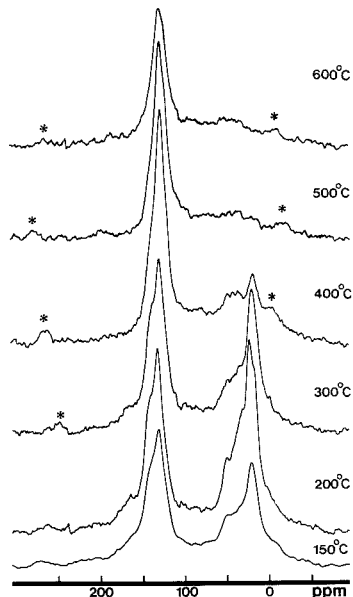


Figure 1. 25.02-MHz <sup>13</sup>C CP/MAS NMR spectra of samples of HY catalyst coked at various temperatures with 1,3-butadiene. The asterisks denote spinning sidebands. All spectra were obtained at room temperature.

oligomeric products with primarily aliphatic carbons and also some olefinic functionality. Furthermore, a number of reaction pathways to aromatic products are available to hydrocarbon species on acidic catalysts at the elevated temperatures used in this study (6, 28), and previous studies of coke deposits formed at elevated temperatures have established their aromatic or even graphitic nature (9, 11). Butadiene is expected to be even more reactive than propene, in accordance with the predicted order of stability of reactive intermediates. In addition to acid-catalyzed reactions, butadiene can also undergo thermally activated Diels-Alder cycloaddition at temperatures of 350 °C or higher (28). Clearly, a complex spectrum of reaction pathways is available to butadiene and oligomeric coke precursors under the reaction conditions used in this study. The mechanisms by which butadiene reacts on zeolite catalysts will not be considered in this contribution; the focus of the present investigation is to ascertain the extent to which <sup>13</sup>C CP/MAS spectra of coked catalyst samples can be regarded as quantitative.

<sup>13</sup>C CP/MAS spectra of the carbonaceous deposits formed by reaction of butadiene on zeolite HY catalyst at six different temperatures are shown in Figure 1. To a first approximation, these spectra are characterized by two broad spectral features: an aliphatic carbon resonance band (10–50 ppm) and an aromatic carbon resonance band (110–160 ppm). Olefinic carbons, if present, could also contribute to the latter band. The possibility of improving spectral resolution by operating at a higher static magnetic field strength was assessed by obtaining a <sup>13</sup>C CP/MAS spectrum of the sample coked at 150 °C on a Bruker MSL-300 spectrometer at a <sup>13</sup>C frequency of 75.47 MHz (Figure 2). Only a very modest improvement in resolution was observed, in accordance with established ideas about spectral resolution in <sup>13</sup>C MAS NMR (29).

Inspecting the spectra in Figure 1, one notes that the relative intensity of the aromatic band is strongly dependent on the reactor temperature. The relative fraction of aromatic



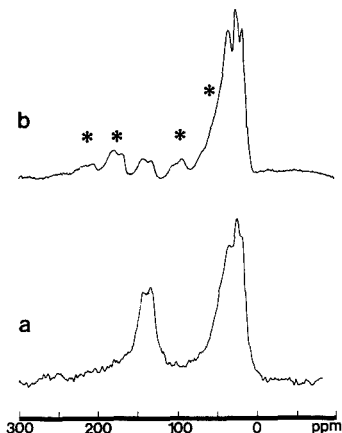


Figure 2.  $^{13}\text{C}$  CP/MAS NMR spectra of the sample of HY catalyst coked at  $150^\circ\text{C}$ , obtained at (a) 25.02 and (b) 75.47 MHz. The asterisks denote spinning sidebands in the high-field spectrum.

Table I. Percent Carbon Analysis and Apparent Aromaticities for Samples of HY Catalyst Coked with Butadiene at Various Temperatures

coking temp, $^\circ\text{C}$	% carbon <sup>a</sup> (by wt)	aromaticity, <sup>b</sup> %
150	13.7	31.5
200	15.3	44.3
300	15.1	50.7
400	18.2	57.2
500	21.2	>90
600	27.0	>90

<sup>a</sup> Determined by combustion analysis. <sup>b</sup> Determined from the integrated intensities of the NMR spectra in Figure 1.

carbon signal intensity in  $^{13}\text{C}$  NMR spectra of coals and analogous samples is described quantitatively by the apparent aromaticity, which is calculated from the ratio of the integrated area of the aromatic peak to that of the total integrated carbon intensity. Apparent aromaticity values for the six coked catalyst samples are reported in Table I. The coke deposit formed at  $150^\circ\text{C}$  has an apparent aromaticity of 0.31, and this ratio increased monotonically to approximately 0.90 for reactor temperatures of  $500^\circ\text{C}$  or greater. The degree to which these apparent aromaticity values can be accepted as accurate will be discussed later in this contribution.

The sample from the reactor run at  $150^\circ\text{C}$  was subjected to Soxhlet extraction using first methylene chloride and then toluene. The  $^{13}\text{C}$  CP/MAS spectrum of the sample following extraction was identical with that obtained prior to extraction. The failure of extraction to remove any significant fraction of the carbon deposit was confirmed by mass spectra of the concentrated extracts, which had insufficient signal-to-noise ratio for the detection of molecular ion peaks. These results suggest that the carbonaceous deposits are not simply low molecular weight products but are instead high molecular weight species that are either insoluble or are too large to be extracted through the pores of the zeolite. The presence of species with condensed aromatic rings in coked catalyst samples obtained from reactor runs at higher temperatures can be inferred from the interrupted-decoupling (dipolar dephasing) spectra (30) reported in Figure 3. The interrupted-decoupling spectrum of the sample coked at  $500^\circ\text{C}$  combined with chemical shift assignments strongly suggests that much of the carbon in this sample is at bridgehead sites in

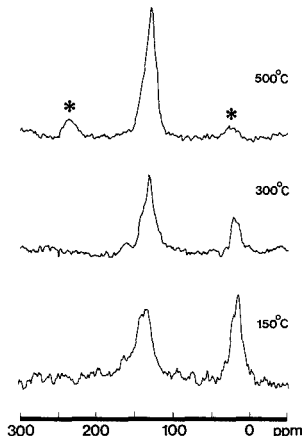


Figure 3. 25.02-MHz interrupted-decoupling spectra ( $\tau = 50 \mu\text{s}$ ) of HY catalyst coked with butadiene at various temperatures. The asterisks denote spinning sidebands. All spectra were obtained at room temperature.

highly condensed aromatic species.

An important criterion for obtaining a quantitative response in cross polarization spectra is that it must be possible to choose a cross polarization contact time ( $t_{\text{cp}}$ ) that satisfies the inequalities

$$T_{\text{CH}} \ll t_{\text{cp}} \ll T_{1\rho}(\text{H})$$

for all of the signals.  $T_{\text{CH}}$  is the time constant for transfer of magnetization from protons to  $^{13}\text{C}$ . Each  $^{13}\text{C}$  environment will have its own characteristic  $T_{\text{CH}}$  value, so in spectra of complex materials such as coked catalysts, the growth of any particular spectral feature will generally be a sum of contributions from different species with approximately the same chemical shift. The time constant for proton spin-lattice relaxation in the rotating frame,  $T_{1\rho}(\text{H})$ , characterizes the loss of spin-locked proton magnetization. For homogeneous, diamagnetic solids such as pure polycrystalline compounds, proton spin diffusion equalizes the proton relaxation time constants to common values for all protons in the sample, regardless of chemical environment. Such solids thus have a single  $T_{1\rho}(\text{H})$  and a single  $T_1(\text{H})$  for all protons. If a uniform  $T_{1\rho}(\text{H})$  is observed, then the right side of the above inequality can be relaxed somewhat as the decay of spin-locked proton magnetization will affect all  $^{13}\text{C}$  cross polarization signals equally. It has previously been demonstrated (17, 31) however that complex carbonaceous materials such as coals can have some degree of heterogeneity, which is reflected in small differences between  $T_{1\rho}(\text{H})$  values determined from the aromatic and aliphatic carbon signals, respectively. Measuring the time constant for proton spin-lattice relaxation in the laboratory frame,  $T_1(\text{H})$ , is also important for establishing the degree to which a  $^{13}\text{C}$  CP/MAS experiment is quantitative, since heterogeneous materials can also display a distribution of  $T_1(\text{H})$  values, and a too-short pulse delay will result in the preferential saturation of the protons which relax more slowly.

The results of these relaxation measurements are summarized in Table II. These results are generally consistent with efficient proton spin diffusion in the samples studied, although the  $T_{1\rho}(\text{H})$  data for the sample coked at  $300^\circ\text{C}$  are suggestive of some degree of heterogeneity over the time scale of that measurement. From the results in Table II, it is apparent that accurate measurements of the relative intensities of observable aromatic and aliphatic carbons can be obtained with cross

**Table II. Summary of Relaxation Data for Samples of HY Catalyst Coked with Butadiene at Various Temperatures**

	$T_{CH}$ , ms	$T_{1\rho}(H)$ , ms	$T_1(H)$ , ms
150 °C run			
aromatic signal	0.679	10.1	304
aliphatic signal	0.123	10.5	291
300 °C run			
aromatic signal	0.233	16.6	242
aliphatic signal	0.083	9.6	277
500 °C run			
aromatic signal	0.341	5.2	71

**Table III.  $^{13}C$  CP/MAS Spin-Counting Results for Samples of HY Catalyst Coked with Butadiene**

reactor temp, °C	% carbon	% carbon, corrected <sup>a</sup>
150	69.5	78.2
300	42.9	57.0
500	31.3	42.7

<sup>a</sup> Corrected for the differences in  $T_{1\rho}(H)$  values (ref 31) between the internal standard (glycine) and the coke sample.

polarization time constants of approximately 2 ms and pulse delays of greater than or equal to 1 s. But it is known that in complex carbonaceous materials such as coal a significant fraction of the total carbon can be *unobservable* in cross polarization experiments (20, 21). For coals, unobservable carbon is believed to be the result of two different problems. Carbon in hydrogen-deficient domains (e.g., graphitic phases) will have minimal dipolar coupling to remote protons and hence will not cross polarize efficiently. Secondly, a fraction of the carbon in coals is believed to be near free radical sites which either broaden the resonances due to nearby  $^{13}C$  nuclei beyond detectability or greatly reduce the  $T_{1\rho}(H)$  in the vicinity of the radical. Since pseudographitic structures have been proposed for some coked catalyst samples (9) and previous ESR measurements have shown that organic free radicals can exist in coke deposits (32, 33), both possibilities must be considered for our samples.

The spin-counting procedure of Hagaman and co-workers (20) was used in order to quantify the fraction of detectable carbon in selected coked-catalyst samples. Basically, this procedure involves measuring a  $^{13}C$  CP/MAS spectrum of a weighed quantity of the sample of interest co-ground with a weighed quantity of a suitable quantitation standard, glycine in this case. From the weight percent carbon (from combustion analysis of the coked catalyst) and the integrated peak intensities, it is possible to calculate the fraction of detectable carbon. The integrated intensities used in the calculations were corrected for their  $T_{1\rho}(H)$  values. Samples from three reactor runs were selected for  $^{13}C$  spin counting. The results (Table III) show that 78% of the carbon was observed for the sample from the reactor run at 150 °C, while a lower percentage of carbon was observed for the 300 °C sample (57%). This trend continued for the sample coked at 500 °C, for which only 43% of the carbon was observed. These values are similar to those found in analogous spin-counting experiments on coals of various rank (31).

The similarities between the above results and those from analogous experiments on coals motivated an examination of the ESR spectra of several of the coked catalyst samples. Quantitative ESR spectroscopic measurements (34) revealed that the sample coked at 150 °C had a free-radical content of  $9.5 \times 10^{18}$  spins/g while that which was coked at 500 °C had a radical content of  $7.3 \times 10^{20}$  spins/g. These values are similar to those obtained for coals of varying rank (35) and account, at least in part, for a fraction of unobserved carbon in the  $^{13}C$  CP/MAS spectra.

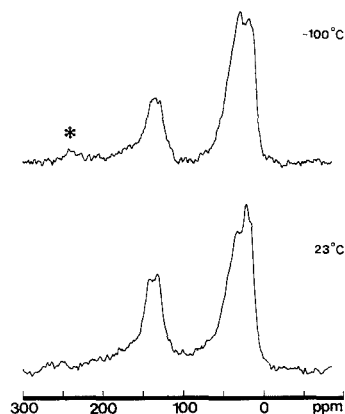


**Figure 4.** Variable-temperature  $^{13}C$  CP/MAS NMR spectra of the sample of HY catalyst coked at 150 °C. Spectra were recorded at 23 and -100 °C. The asterisks denote spinning sidebands.

Of the possible sources of unobserved signal intensity in  $^{13}C$  CP/MAS spectra, the presence of both hydrogen-deficient graphitic domains and organic free radicals would be expected to result in inaccurately low estimates of the fraction of aromatic carbons. To test this possibility, a Bloch decay spectrum of the sample from the 200 °C reactor run was obtained by using  $90^\circ$   $^{13}C$  pulses (8600 scans). A pulse delay of 10 s was used to ensure that saturation of the  $^{13}C$  magnetization did not occur (previous studies on coals suggested that this delay value would be sufficient). The resulting spectrum (not shown) was similar to the cross polarization spectrum of that material (Figure 1) with the exception that the aromaticity determined from the Bloch decay spectrum (0.49) was slightly higher than that from the cross polarization spectrum (0.44). This result is consistent with the view that aromatic carbon is more likely to be underestimated in cross polarization spectra of coked catalyst samples than aliphatic carbon as a result of inefficient cross polarization in graphitic domains as well as the presence of free radicals.

The above sources of uncertainty in the quantitative significance of  $^{13}C$  CP/MAS spectra of coked catalyst samples are similar to those encountered in analogous studies of coals and other complex carbonaceous materials. There is, however, an additional source of uncertainty that might be encountered for coked catalyst samples. Molecular motion of oligomeric compounds on or in the catalyst framework (e.g., in the supercages of a Y-type zeolite) could result in an attenuated signal due to inefficient cross polarization dynamics, or a very broad resonance for mobile components in the special case (36) of molecular motion at the rotating-frame precessional frequency of the  $^1H$  spin-lock field ( $\gamma B_1 = 45$  kHz in this experiment). The possibility that these effects might have a significant effect on the  $^{13}C$  CP/MAS spectra of coked catalyst samples was investigated by obtaining a low-temperature spectrum of the sample coked at 150 °C, which was selected on the premise that it was more likely to contain mobile, oligomeric species than samples coked at higher temperatures. Indeed, the somewhat long  $T_{CH}$  value for the aromatic carbons in this sample (Table II) is suggestive of some degree of molecular motion. Figure 4 compares the  $^{13}C$  CP/MAS NMR spectrum obtained at -100 °C with the room-temperature spectrum. No significant differences are observed between the two spectra. In particular, the aromaticities obtained from the two spectra are identical within experimental error when contributions from spinning sidebands are taken into account for the low-temperature spec-

conclude that either the aliphatic coke molecules do not possess enough molecular motion in the sample matrix over the temperature range studied or carbon has appeared in the CD/MAS spectra. The latter possibility is ruled out because molecular motion is so broad as to preclude a noticeable appearance in the spectral band shapes.

#### CONCLUSIONS

zeolite catalyst HV has an aromaticity that is strongly dependent upon reaction temperature. Samples coked at 500 °C are predominantly aromatic, whereas samples coked at 700 °C are predominantly aliphatic. Since negligible organic matter was extractable from even the sample prepared with the lowest reactor temperature (500 °C), the high aromaticity observed in the CD/MAS spectra of coked catalysts is appropriate. The results of this study indicate that the CD/MAS spectra of coked catalyst samples prepared at lower reactor temperatures. Cross polarization contact times of 2 ms and pulse delays of 1 s are generally sufficient to observe carbons of low mobility. For samples coked at higher temperatures, however, the fraction of aromatic carbon will increase and hydrogen-deficient regions. Molecular motion of aliphatic coke molecules in the catalyst is apparently not significantly different from that of aliphatic carbons in graphite.

#### LITERATURE CITED

- (1) Gates, B. C.; Katzer, J. R.; Schuit, G. C. A. *Chemistry of Catalytic Processes*; McGraw-Hill: New York, 1968; p 100.
- (2) Satterfield, C. N. *Heterogeneous Catalysis in Practice*; McGraw-Hill: New York, 1970; p 100.
- (3) Venuto, D. B.; Habib, E. T. *Fluid Catalytic Cracking with Zeolite Catalysts*; Marcel Dekker: New York, 1974; p 100.
- (4) Wolf, E. E.; Alfani, F. *Catal. Rev. Sci. Eng.* **1982**, *24*, 329-371.
- (5) *Catalysis by Acids and Bases*; Imelik, B. et al., Eds.; Elsevier Science Publishers: Amsterdam, 1981; p 100.
- (6) Appleby, W. G.; Gibson, J. W.; Good, G. M. *Ind. Eng. Chem. Process Des. Dev.* **1981**, *20*, 1000-1004.
- (7) Langner, B. E. *Ind. Eng. Chem. Process Des. Dev.* **1981**, *20*, 1000-1004.
- (8) Magnoux, P.; Roger, P.; Canaff, C.; Fouche, V.; Gnep, N. S.; Guisnet, M. *J. Catal.* **1987**, *106*, 100-104.

- (9) Gates, B. C.; Katzer, J. R.; Schuit, G. C. A. *Chemistry of Catalytic Processes*; McGraw-Hill: New York, 1968; pp 317-331.
- (10) Appleby, W. G.; Gibson, J. W.; Good, G. M. *Ind. Eng. Chem. Process Des. Dev.* **1987**, *26*, 190-192.
- (11) Halifman, R. G.; Roff, M. G. *J. Phys. Chem.* **1980**, *84*, 480-488.
- (12) Blackmond, D. G.; Goodwin, J. G.; Lester, J. E. *J. Catal.* **1982**, *72*, 100-104.
- (13) Derouane, E. G.; Gilson, J. P.; Naey, J. R. *Zeolites* **1982**, *2*, 42-46.
- (14) Derouane, E. G.; Gilson, J. P.; Naey, J. R. *Chem. Commun.* **1986**, *13*, 1008-1009.
- (15) Sullivan, M. J.; Maciel, G. E. *Anal. Chem.* **1982**, *54*, 1615-1623.
- (16) Hatfield, G. R.; Maciel, G. E.; Erbart, O.; Erbart, G. *Anal. Chem.* **1986**, *58*, 1000-1004.
- (17) Hagaman, E. W.; Chambers, R. R.; Wood, M. C. *Anal. Chem.* **1986**, *58*, 1000-1004.
- (18) Vassallo, A. M.; Wilson, M. A.; Collin, P. J.; Oades, J. M.; Waters, A. *J. Catal.* **1987**, *106*, 100-104.
- (19) Wilson, M. A. *NMR Techniques and Applications in Geochemistry and Petrology*; Elsevier: Amsterdam, 1987; p 100.
- (20) Axelson, D. E. *Solid State Nuclear Magnetic Resonance of Fossil Fuels*; American Institute of Physics: New York, 1981; pp 317-317.
- (21) Haw, J. F. *Anal. Chem.* **1988**, *60*, 559A-570A.
- (22) Haw, J. F. *J. Am. Chem. Soc.* **1989**, *111*, 2052-2058.
- (23) *Zeolite Catalysis*; Delmon, B.; Froment, G. F., Eds.; Elsevier: Amsterdam, 1981; p 100.
- (24) VanderHart, D. L.; Earl, W. L.; Garroway, A. N. *J. Magn. Reson.* **1979**, *30*, 585A-586A.
- (25) Opella, S. J.; Frey, M. H. *J. Am. Chem. Soc.* **1979**, *101*, 5854-5856.
- (26) Kalinina, N. G.; Poluboyarov, V. A.; Anufrienko, V. F.; Ione, K. G. *Kiurg. Khim.* **1982**, *59*, 240-242.
- (27) Kalinina, N. G.; Ryabov, Y. V.; Korobitsyna, L. L.; Poluboyarov, V. A.; *Int. J. Chem. Kinet.* **1988**, *20*, 1699-1704.

RECEIVED for review March 6 1989 Accepted May 15 1989  
 THE SUPPORT OF THE NATIONAL SCIENCE FOUNDATION THROUGH

# Characteristics of Aerosols Produced by the Spark Discharge

Robert L. Watters, Jr.,\* James R. DeVoe, Francis H. Shen, John A. Small, and Ryna B. Marinenko

Center for Analytical Chemistry, National Institute of Standards and Technology, Gaithersburg, Maryland 20899

**A detailed study of the physical properties and the chemical composition of spark-produced aerosol and corresponding erosion craters has been undertaken. A high repetition rate (1 kHz), electronically controlled waveform spark source was used to generate the aerosol from samples of Standard Reference Materials (SRMs). The feasibility of using an on-line electrical mobility analyzer to monitor real-time particle concentrations was examined. Consistent bias in the Zn/Cu ratios of aerosols from a series of brass SRMs corresponded to a reverse bias in the Zn/Cu ratios measured in the spark erosion pits. Collected particles were dissolved and analyzed by inductively coupled plasma spectrometry. A predominance of small particles ( $\approx 10$  nm) was observed, and confirming analyses were performed with the analytical electron microscope on individual particles.**

Analytical techniques such as inductively coupled plasma (ICP) and atomic absorption spectrometry (AAS) are usually applied to the analysis of liquid samples or solid samples that have been dissolved. Over the past several years there has been increased interest in developing direct solid sample introduction systems for use with these techniques. Lasers have been used to sample both electrically conducting and non-conducting samples, but matrix effects have been observed that may be due to the thermal nature of the laser sampling event and differences in matrix constituent volatility (1, 2). Electrical discharges have been used since 1907 for production of aerosols from conducting materials (3). More recently, arc and spark discharges have been used as sampling devices for ICP and other spectrometric techniques (4-14), and the suitability of a variety of discharge types has been reviewed recently (15). The advantages of wide dynamic range, relative freedom from matrix effects, and simultaneous multielement analysis capability have made the ICP a logical choice for this approach. Spark-ICP analytical results in our laboratory show that several elements in ferrous materials fall on the same linear calibration curve spanning over 4 orders of magnitude (9, 10). The spark-ICP combination has been applied to the analysis of aluminum alloys (12), and a commercial spark-ICP (13) has been successfully applied to the analysis of coal fly ash (8) and nickel alloys (14). Although these and other studies have demonstrated that the spark-ICP combination is a convenient means of direct conductive solid analysis, universal attainment of accurate analyses has not always been realized. Often it is necessary that calibration standards and samples need to be of the same alloy type to achieve acceptable accuracy.

Since the use of the spark to generate sample aerosol separates the sampling and excitation processes into two distinct events, systematic errors in each step should be examined to explain any analytical bias in the combined spark-ICP technique. Therefore, it is useful to study the sampling process itself by examining physical and chemical characteristics of the aerosol produced by the spark discharge and correlating these results with the characteristics of the sample erosion crater. Although a few studies have considered the analytical

aspects of spark sampling, it is difficult to reach a unified set of conclusions leading to the definition of causes of bias. This is due in part to the wide variety of spark sources used or the lack of state-of-the-art microanalysis instrumentation. In other cases, only the aerosol or the craters were analyzed, but not both.

For example, Brewer and Walters (16) have examined the effects of 1 to 16 oscillatory and unipolar discharges on brass, aluminum, and mild steel by microscopic and X-ray analysis of the erosion craters. Multiple sampling points were evident even for a single oscillatory or unipolar spark. Pb and Bi in aluminum and Pb in brass samples exhibited some migration to the cathode spot, but concentration or depletion of Cr, Mo, and Ni in mild steel was not evident. The authors note, however, that these elements were near the detection limit for the X-ray analysis technique used. The Zn/Cu ratio measured in the sampled area of the brass material was not significantly different from that obtained from unsparked areas, although long-term heating of this material was shown to cause volatilization of Zn. Although the sampling process appeared to be accurate, the small number of sparks used would not produce enough sample aerosol for subsequent ICP excitation. The aerosol produced was not analyzed, but critical spark source conditions were described fully.

Emission characteristics and electrode erosion phenomena for a long train of spark discharges were reported by Ekimoff and Walters (17). They have shown conclusive evidence that marked changes occur in the physical appearance of electrode surfaces during the first 20-30 s of spark sampling. The progressive formation and coalescence of pitted structures on the sample surface suggest that melting occurs as the number of sparks increases. Emission vs time characteristics for a given element also depend on peak current, spark repetition rate, and sample matrix. Semiquantitative X-ray analysis of the surface of a stainless steel electrode could detect no major changes in Cr/Fe or Ni/Fe ratios between sampled and unsampled surface points. These data underscore the complex changes caused by continuous sampling of the discharge. There was clear evidence of melting of the electrode material, which would be expected to cause bias in the composition of sample aerosol. However, the melting points of the major elements Cr (1615 °C) and Ni (1452 °C) in the stainless steel may not be sufficiently different to exhibit sampling bias.

Light scattering and electron microscopy were used by Scheeline et al. (18) to detect the formation and examine the physical size distribution of spark-produced aerosol. Collection of aerosol from the outlet of a closed spark stand may have preferentially retained large particles of 0.5-2  $\mu\text{m}$  in diameter. There was some evidence of clusters of smaller particles, the smallest unit being about 0.01  $\mu\text{m}$  in diameter. These observations are similar to those of Helmer and Walters (19), but Helmer and Walters offer the first evidence that stable sparks produce particles in the larger size ranges of somewhat different appearance from those produced by unstable sparks. Differences in size range were also reported by Ono et al. (20) for different spark current waveforms. A detailed mass balance of total sampled material partitioned into that which is carried into an ICP vs that which is deposited on the counter

electrode on a per spark basis was provided. None of these groups of authors attempted to obtain an independent chemical analysis of the spark-produced particles.

The application of spark sampling of aluminum alloys and nonconducting powders has been reported by Aziz et al. (12). Although the calibration curves for a number of elements in some alloys were linear, the high silicon content of other alloys caused significant deviations in the calibration curves for the same elements. The authors used the scanning electron microscope (SEM) to examine the physical appearance of Al-alloy aerosol collected on a Nuclepore filter, but no detailed study of electrode erosion or aerosol composition was undertaken. The particles collected on a Nuclepore filter were chiefly from 0.3 to 3  $\mu\text{m}$ . Collection conditions were not optimized to ensure detection of smaller particles that have been observed in other studies. Furthermore, the visibility of small particles on filter media observed in the SEM may not be sufficient to permit reliable measurements below 0.1  $\mu\text{m}$  (21).

Transport efficiencies and physical properties of spark-generated aerosols were recently reported by Prell and Koirtiyohann (22). They found similar ranges of particle sizes, which depended on the type of gas flow used to sweep the spark chamber. Particles were collected on filters, dissolved, and analyzed by ICP to determine the total transport rate. Although Standard Reference Materials (SRMs) were used as samples for sparking, the relative concentrations of analytes in the particles were not compared to the original SRM compositions.

Raeymaekers et al. (23) have recently examined the composition of spark-produced particles by using electron probe microanalysis (EPMA). The particles were also collected on Nuclepore filters, classified by size and shape, and analyzed by EPMA with energy dispersive spectrometry (EDS) detection. Their interpretation of the results indicated that most of the particles were similar in composition to the electrode material, but close inspection of their data reveals evidence of bias between the composition of the aerosol and that of the electrode material. The particles collected and examined were principally from 1 to 2  $\mu\text{m}$  in diameter, and it is correctly concluded that complete vaporization of such particles in the ICP is likely to occur. In contrast to a number of other studies, no significant number of particles less than 0.05  $\mu\text{m}$  was observed. Whether this is related to the details of the current waveform of the spark discharge (which were not communicated), the collection method used, or limitations of the EPMA instrument is not clear.

Since a variety of spark discharge types, alloy types, and collection methods have been used, it is difficult to present a coherent picture of the physical and chemical characteristics of the spark aerosol production. What is known about the characteristics of spark-produced aerosol can be summarized as follows: A few spark discharges do not significantly alter the chemical composition of the cathode surface (16), implying that the composition of the aerosol produced may match that of the electrode material. However, insufficient analyte aerosol is produced to be independently analyzed or to be useful for ICP excitation. Aerosol is produced from each discharge in the spark gap within 150  $\mu\text{s}$  after spark current has ceased (19). When a longer train of spark discharges samples the cathode, changes occur in both electrode surface composition and spark-emitted light. This implies that aerosol composition may be affected by repetitive sparking, but the sample alloy type, whether or not the spark is allowed to wander over the cathode surface, and the details of the current waveform may also be important parameters.

The size distributions of particles produced by the spark fall into at least two groups. The first consists of spheres 0.01

$\mu\text{m}$  in diameter and the second consists of spheres of up to several micrometers in diameter that are formed from melted material. It appears that the repetition rate and spark current waveform may play an important role in determining the relative population of these groups, but most reports do not contain these particular details. Production of aerosol in an open spark gap or a closed chamber may also affect the physical characteristics of the aerosol, but unless the spark is contained in a closed system, it is difficult to transport the aerosol to the ICP for efficient analysis. The type of sample alloy or even the details of phase composition in a particular alloy may be critical to the physical and chemical nature of the spark-produced aerosol. Whatever the important details are, it is clear that accuracy of ICP analysis may suffer from certain biases in the spark sampling step. Whenever there is evidence of melting, distillation effects will cause systematic error, requiring that calibration standards and samples be closely matched.

In light of these points, we have studied the effects of certain parameters of a train of unidirectional discharges on the characteristics of spark-produced aerosols. Experiments were designed such that size distribution and chemical composition measurements were directly related to the type of aerosol produced by commercially available spark-ICP instrumentation. To increase sampling efficiency, the spark discharge repetition rate (1000 Hz) was set higher than is normally used in commercial instruments. The feasibility of measuring physical size distributions "on-line" with an electrical mobility analyzer was examined, and particles were also collected for SEM examination. Chemical analysis of the aerosol was performed by dissolving collected aerosol and analyzing the solutions by conventional ICP spectrometry. Additional analyses were performed on single particles using the analytical electron microscope (AEM). The experiments were designed to focus on possible shifts in chemical composition of the aerosol from that of the electrode material. Corresponding analyses of the electrode erosion craters were carried out by using EPMA. Physical size distributions were measured for a variety of pure single-element metals. Major and minor constituents of the collected aerosols were determined for a series of brass and ferrous SRMs. The brass SRMs were chosen to provide a simple homogeneous chemical system consisting of two major elements, Cu and Zn, that have significantly different melting points. Electrostatic particle collection for AEM analysis was used to avoid losses of particles smaller than the pore size of typical collection filters. Back-up filter collection was used to check for the presence of large particles.

## EXPERIMENTAL SECTION

**Spark Source.** The spark source is an electronically controlled, adjustable-waveform unit similar to a general design previously described by Coleman and Walters (24). This specific circuit is designed for relatively low peak currents and high repetition rates. The schematic diagram is presented in Figure 1, with component specifications listed in Table I. The resulting current waveform, which is presented in Figure 2, ensures that the sample electrode is cathodic during each discharge. The basic triangular shape of the waveform enables it to be described adequately by designation of the peak current and the duration of current conduction in the spark gap. A principal feature of this particular spark source is that the main storage capacitor is charged by a three-phase, 208 V ac rectified power supply that allows continuously variable spark repetition rates to be selected without regard to the phase of the power mains. The circuitry and specifications of the power supply have been published by Coleman et al. (25).

The spark gap and chamber were designed to the approximate dimensions of a commercially available spark-ICP analytical instrument (8, 13, 14). A diagram of the spark electrode region is presented in Figure 3. Argon support gas for the discharge is supplied through the flow-jet counter electrode. This gas flow

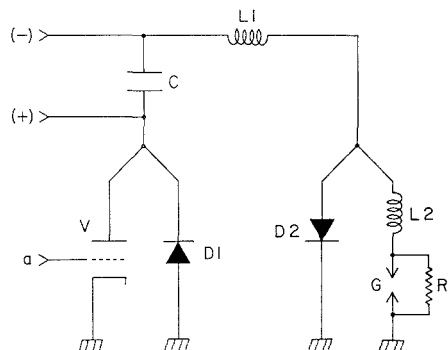


Figure 1. Schematic diagram of controlled waveform spark source. Components and their values are listed in Table I.

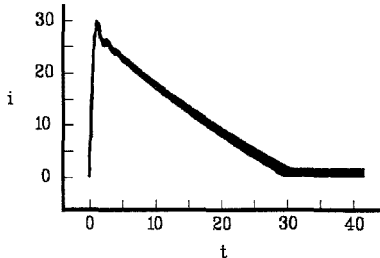


Figure 2. Spark current waveform,  $i$  (A) vs  $t$  ( $\mu$ s).

Table I. Spark Source Components and Specifications (Refer to Figure 1).

component	description
C	capacitor, Aerovox type 1940-311, 0.007 $\mu$ F, 25 kV; two in parallel, total = 0.014 $\mu$ F
V	Thyratron EG&G type HY-6
L1	inductor, wire wound, air core, adjustable 0 to 143 $\mu$ H (set to 0 $\mu$ H for the waveform in Figure 2)
L2	Inductor, wire wound, air core, adjustable 0 to 53 $\mu$ H (set to 53 $\mu$ H for the waveform in Figure 2)
D1, D2	diode stack assembly, Thermo Jarrell-Ash No. 003674
R	Resistor, 1 M $\Omega$ , 5 W, ceramic noninductive
a	Thyratron trigger input

provides the carrier gas for the spark-produced aerosol as it exits the spark chamber. Although previous studies with the controlled waveform spark discharge used the argon flow-jet to stabilize the spark in an open research spark stand (26), the spark is somewhat destabilized by being enclosed in the ceramic spark chamber. This destabilization occurs because the chamber fills with argon, and there is no defined flow boundary between the spark support gas and air.

**Particle Size Measurement.** The feasibility of measuring particle size distributions and number densities on-line was examined by using an electrical aerosol analyzer (EAA). Details of the EAA design and the theory that relates differences in electrical mobility to particle diameter have been published by Liu et al. (27, 28). Aerosol is passed into the EAA where it is exposed to gaseous ions produced by an electrostatic diffusion charger. Aerosol particles become singly charged in this region and are deflected by a clean air sheath through a laminar air stream in a cylindrical condenser. A voltage is placed on the collector rod in the center of the condenser that precipitates particles of a certain mobility. Charged particles that are not precipitated pass downstream where they are detected by an electrometer.

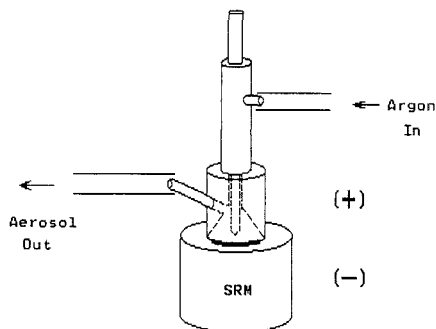


Figure 3. Diagram of the spark gap chamber consisting of the flow jet counter electrode and the sample cathode.

Particle size measurements were also obtained by using the AEM. Aerosol from the spark chamber was passed through an electrostatic precipitator (29) that was designed to collect ultrafine particles directly onto 20-nm carbon films. The carbon films are supported by gold transmission electron microscope grids, allowing the collected particles to be analyzed directly in the AEM without further sample preparation. The precipitator is contained in a particle sampling device made from a Lucite cylinder 6 cm in diameter by 20 cm long. The sampler consists of an electrostatic precipitator, a thermal precipitator, and a back-up filter. Only the electrostatic precipitator and the back-up filter were used to collect the particles for these studies. Particles are charged to between -3 and -5 kV in the throat of the sampler by a corona discharge using a tungsten needle. The aerosol is passed through the sampler at the spark discharge argon gas support flow rate of 175  $\text{cm}^3/\text{min}$ . Four grounded carbon film grids are placed downstream from the tungsten needle ionizer to collect the sample aerosol. Preliminary tests of the sampler indicate an efficiency of approximately 80% for particles smaller than 0.5  $\mu\text{m}$  in diameter.

**Chemical Analysis.** Batch collections of aerosol for chemical analysis were obtained by drawing the spark chamber output stream through a double filter cassette. The filter cassette was designed as part of a portable ambient aerosol sampler by Bright and Fletcher (30). The first filter is a Nuclepore filter with a 6.8- $\mu\text{m}$  pore size, coated with Apiezon-L grease. This filter collects most of the particles above 3  $\mu\text{m}$  in diameter. The final filter is a Teflon fiber filter with 3- $\mu\text{m}$  nominal pore size that has a collection efficiency of more than 98% for submicrometer particles. Particles collected from the spark aerosol stream were dissolved off the filter in acid and analyzed by ICP spectrometry. Particles were also analyzed on an individual basis by X-ray microanalysis. Since the particle sizes are less than 0.2  $\mu\text{m}$ , the analysis was accomplished with an AEM. This instrument provides quantitative elemental ratios for isolated particles as small as 10 nm in diameter.

The compositions of collected particles were compared to the elemental compositions of the spark-induced crater regions of a series of brass SRMs. The analysis of the craters was accomplished by EPMA. This instrument uses a high-energy focused electron beam to excite characteristic X-rays in the specimen. The  $K\alpha$  lines for Cu and Zn were simultaneously observed by using two wavelength dispersive spectrometers (WDS). An electron beam of 20 kV and 113 nA was focused to a diameter of 0.5  $\mu\text{m}$  at the specimen surface. Quantitative information is derived for material on the sample surface to 3  $\mu\text{m}$  deep. EPMA is calibrated by using pure Cu and Zn standards, and calculations for quantitative analysis were accomplished by using FRAME (31), a data reduction program developed at NIST. Scans across the spark erosion craters were recorded and the results were reduced to weight percent of a given element at each integrated spot.

## RESULTS AND DISCUSSION

The physical properties of spark-produced aerosols were investigated by using the EAA to monitor total output and

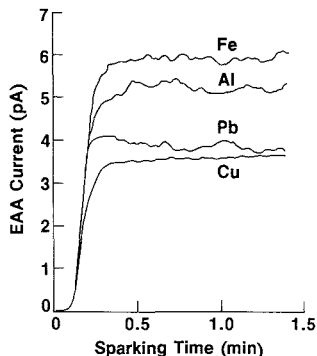


Figure 4. Electrical aerosol analyzer (EAA) response vs time for Al, Cu, Fe, and Pb electrode materials.

particle size distributions. The collector voltage of the EAA was set to detect all particles within the effective measuring range of 0.003 to 1.000  $\mu\text{m}$  in diameter. It should be noted that although some micrometer-size particles have been observed in spark aerosols (17-19, 22, 23), they would not be detected by the EAA. The output stream from the spark chamber was diluted in two stages to reduce particle concentrations to within the range accepted by the EAA. The first stage was a 15-fold dilution with clean filtered air, and the second stage involved splitting the aerosol stream into two branches. The high-flow branch was passed through an absolute filter and the flow rate of the other branch was set with a pinch valve. The two branches were recombined so that the total gas flow remained constant, but only the particles passing through the low-flow branch were passed to the EAA input. The overall dilution rate of both stages was about 1:225. The low-flow branch through the pinch valve was checked to ensure that no large particles or agglomerates were trapped by the valve during the course of the measurement. The EAA response vs sparking time for a number of pure metals is plotted in Figure 4. After the initial increase in number density, the particle concentration for each metal levels off for a period of a few minutes. If sparking is allowed to continue for several minutes, the number density slowly decreases. It is during this relatively stable plateau, that both spark emission and ICP emission from spark-sampled metals are measured for analytical spectrometry. Although all metals exhibit similar profile shapes, the absolute number densities in the plateau region are quite different. A comparison between the average particle concentrations and weight of collected aerosol for each metal will be discussed later.

Occasionally, the number density peaks after the initial increase and then stabilizes. A similar profile in spark emission vs time for Mn and Al in mild steel was noted by Ekimoff and Walters (17). A peak in the particle concentration profile supports their statement that such peaks are most likely related to total sampling rate, rather than time-dependent compositional changes. The fact that particle concentration peaks were observed infrequently for Fe, brass alloys, and a stainless steel (SRM 1151) also relates to the data of Ekimoff and Walters (17). The data presented here are for peak spark currents between 30 and 60 A. This range is near the lowest current used by Ekimoff and Walters, which resulted in the smallest peaks observed in their emission-time profiles.

We observe the most prominent number density vs time peaks when sparking conditions are not optimal. That is, when good electrical contact exists between the tungsten anode and the flow jet, between the flow jet and the jaw of the spark

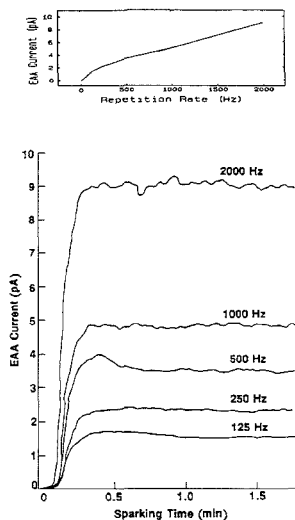


Figure 5. EAA response vs time for SRM 1265 electrode at various spark repetition rates. Top inset is EAA current vs repetition rate after 1 min of sparking.

stand, and between the cathode sample and the spark stand, the occurrence of number density vs time peaks is minimized. When good contact does not exist, there is an increase in radio frequency (rf) interference observed on the current waveform. This change is quite subtle, however, and the overall  $di/dt$  of the lead edge of the current waveform is not significantly changed. We feel that under such conditions there may be insufficient coupling of the sampling energy of the spark with the microscopic sampling site of the electrode to effectively erode the bulk material. The spark wanders to a greater extent over the cathode surface, sampling only the electrical "high-spots", much the same as atmospheric lightning seeks the highest point at ground potential. Once these points have been sampled, the unstable spark becomes increasingly ineffective at boring down deeper into the electrode material. The rate of sampling decreases, and the number density vs time begins to decline.

We have also examined the effect of spark repetition rate on the particle concentration-time profiles. A series of profiles for SRM 1265 (99.9% Fe) at five different repetition rates is presented in Figure 5. Each of these profiles has the same basic shape, and the aerosol number density (measured after 1 min of sparking) is found to be an increasing function of the repetition rate. A plot of particle concentration vs repetition rate is presented in the inset of Figure 5. It is apparent that the number of particles produced by a train of spark discharges is not linear with repetition rate over the entire range of this plot. Although it is reasonable to expect that higher repetition rates cause more sampling, changes in the number of particles sampled may or may not reflect changes in the mass of material sampled. Differences in the fundamental type of sampling, as indicated in the discussion of number density vs time profiles above, and the formation of agglomerates of particles can affect the number density measurements. Particle collection efficiencies may also depend on the absolute quantities of particles formed.

In addition to serving as a real-time monitor of particle number densities, the EAA has been also used to define particle size distributions under carefully controlled sampling conditions. The application of this device for measuring

**Table II. Sampling Rates Measured by Particle Collection and Calculated from EAA Current<sup>a</sup>**

metal	meas rate, <sup>b</sup> μg/min	calcd rate from EAA, μg/min
Pb	720	85
Fe	95	95 <sup>c</sup>
Cu	50	65
Al	45	30

<sup>a</sup>The EAA data were normalized to the Fe current, which was taken as the current for 95 μg/min. <sup>b</sup>The uncertainty of these data is about ±5%, relative. <sup>c</sup>Normalized.

particle size distributions was examined by waiting for the aerosol concentration in the output stream to stabilize and stepping the analyzer voltage of the EAA. The analyzer current is recorded at each voltage setting and the data are reduced following the procedures given by Liu et al. (27, 28). The resulting size distribution plots indicate a relatively monodisperse aerosol with a peak mean diameter of 0.1 μm. Similar distributions were obtained for pure metal samples of Al, Cu, Fe, Mo, Pb, W, and a few other ferrous and nickel alloys. Furthermore, the measured size distributions were not significantly affected by changing the repetition rate of the spark discharge. This would indicate that for analytical spectrometry using spark sampling followed by independent excitation, the excitation source need only vaporize and excite 0.1-μm particles. It is, therefore, likely that the ICP performs this task with nearly 100% efficiency.

Since the particle size distributions appeared to be the same for each of the pure metals sparked, one would expect that the relative steady-state particle concentrations taken from Figure 4 could be combined with the density factors for each of the pure metals to obtain relative sampling rates for each metal in terms of weight per unit time. In order to measure directly the sampling rates for each of the metals, the output of the spark chamber was passed through a Teflon filter to collect all of the particles in the stream for a fixed collection period. Particles of a pure metal sample were collected on a filter for 5 min, and the filter was transferred to a beaker containing a 1:1 dilution of acid in water. The choice of acid was determined by the particular metal aerosol collected. The particles on each filter were quantitatively dissolved and the solutions were analyzed by ICP spectrometry to determine the total weight collected for each metal. The results are listed in Table II.

These data can be used to evaluate the steady-state EAA signal as a monitor for the spark sampling rate of metals. The expected relative sampling rates are calculated by multiplying the EAA analyzer current by the density for each metal and normalizing the results so that the calculated rate for Fe matches its measured rate. The results of these calculations are also listed in Table II. It is apparent that although the aerosol size distributions for each metal appear to be the same, the overall number densities do not relate to the measured sampling rates in terms of weight. The underlying reason for the discrepancy between the sets of data in Table II can be deduced from the TEM photomicrograph in Figure 6. This image of collected Fe aerosol clearly shows that the fundamental units of spark-produced aerosol are approximately 0.01 μm in diameter and that the EAA registers populations of agglomerated units whose characteristic size is approximately 0.1 μm in diameter. Occasionally, a spherical particle of a few micrometers in diameter can be observed with the SEM for the sparking conditions used in this study. Such a particle would weigh approximately 10 million times more than a 0.01-μm particle of the same material and could account for a significant fraction of total material sampled. The observation of such large particles was very rare in these studies,

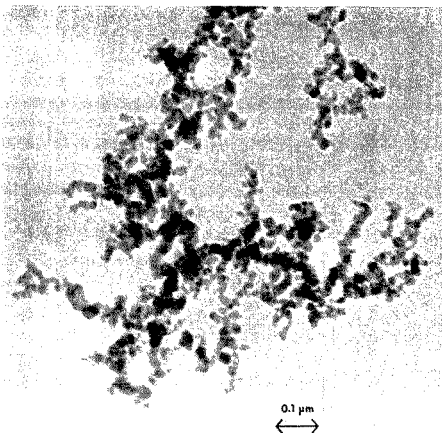


**Figure 6.** Scanning electron microscopic image of collected iron aerosol. The smallest visible units are approximately 0.01 μm in diameter.

except in the case of lead, in contrast to a number of previous studies discussed in the introduction above. The large difference between the measured sampling rate and the EAA calculated rate for lead is probably due more to the upper size limit of the EAA than to agglomerate formation. However, the tendency of lead to form large particles is not detected at all by the number density vs size profile within the size range registered by the EAA. It is also clear that in order to relate number densities of agglomerated units to the weight-based sampling rate, the density of a characteristic chain of particles must be taken into account instead of the density of the pure metal. Such densities are not easily obtained, and it must be concluded that direct mass-based measurement of collected aerosol is the only reliable way to obtain sampling rates.

The importance of an on-line measure of sampling rate is evident in the application of the spark discharge to analytical spectrometry. Two methods for normalization of different sampling rates of alloys in atomic spectrometry are currently in use. Spark emission spectrometry has traditionally used the ratio of the analyte emission intensity to an appropriate spectral line intensity of a matrix element as an internal standard. This approach is also used in spark sampling ICP spectrometry; however the wide linear dynamic range of the spark-ICP spectrometry may complicate the choice of the internal standard element. For example, in the determination of Ni in ferrous alloys, Fe is a suitable standard at the low end of the calibration curve. The high end of the curve can cover Ni concentrations of up to 60% by weight where the Fe concentration may be only 5% by weight (SRM 1245). It is questionable whether Fe is a suitable monitor for total sampling in such an alloy, since it is no longer the principal chemical matrix component.

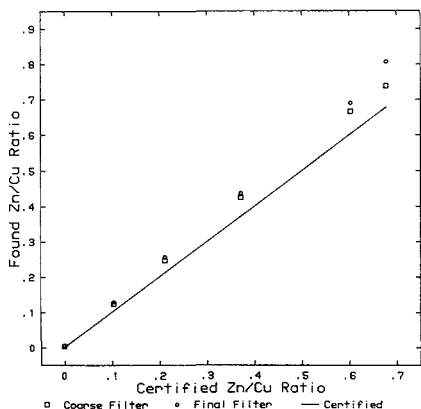
The second normalization method for total sampling rate is to determine simultaneously every significant constituent in the sample of interest in terms of weight percent. These concentrations are the normalized to sum to 100% (13). It is essential that the determinations of the major elements be very accurate in this scheme so that errors in the minor and trace elements are not amplified by the normalization.

Perhaps even a more important question is the comparison of chemical concentrations between the bulk material and the aerosol. If a solid sampling device were found to transform quantitatively the bulk sample material to vapor or even



**Table III. Brass SRMs Used To Examine Chemical Composition of Spark-Produced Aerosol**

SRM	type	% Cu	% Zn	Zn/Cu ratio
1102	cartridge brass C	72.85	27.10	0.372
1103	free cutting A	59.23	35.7	0.603
1106	naval brass A	59.08	40.08	0.678
1109	red brass A	82.2	17.40	0.212
1116	commercial bronze	90.37	9.44	0.104
1122	beryllium copper	97.45	0.01	$1 \times 10^{-4}$



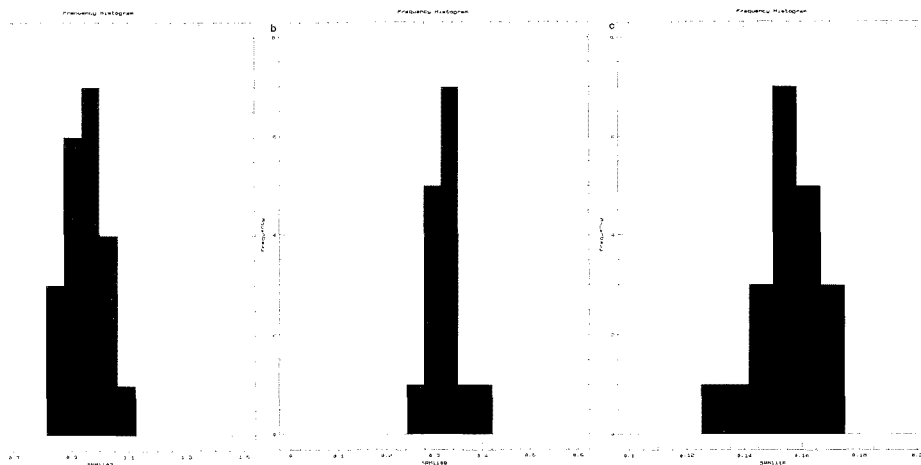


Figure 9. Distributions of Zn/Cu ratios found for individual particles analyzed by the AEM: a, SRM 1103; b, SRM 1109; c, SRM 1116.

Figure 7, but there were no large particles ( $>1 \mu\text{m}$ ) found on the grids for AEM analysis or the back-up filters. The highest Zn/Cu ratios were observed by the AEM, which examined particles that were predominantly  $100 \text{ \AA}$  in diameter but were also representative of a much smaller sampling of material than the ICP results. These details need to be examined more closely with a larger number of analyses using the AEM to unambiguously define this point.

To examine the question of material balance between the sampled electrode material and that which remains on the electrode surface, EPMA was used to analyze the sparked electrode surface. In this analysis, the  $1\text{-}\mu\text{m}$  electron beam was stepped in  $100\text{-}\mu\text{m}$  increments across the center of the spark erosion crater, beginning and ending on unsampled regions on either side of the pit. Two scans across the spark erosion crater were recorded for each SRM electrode material. The characteristic X-rays from the  $K\alpha$  lines of Cu and Zn were recorded by two WDS analyzers. Count rates for samples and standards were corrected for background and dead time. Corrected count rate ratios ( $k$  ratios) of samples to standards were then corrected for matrix effects and concentrations in weight percent were calculated by using FRAME. Although SRM 1103 contains 3.73 wt % lead, no inhomogeneities were apparent in the EPMA scans of this or the other SRM materials. No significant differences between duplicate scans for each SRM were evident.

The results of a single scan of elemental concentration vs relative position on the electrode surface for the each of the three brass SRMs are plotted in Figure 10. The horizontal lines plotted through the data indicate the SRM certified concentrations. Only Zn is plotted for SRM 1116, since the small relative changes in the Cu concentration at this high level are masked by the measurement variance. In each case, the Zn concentration is depleted in the center of the spark erosion pit, and for SRMs 1103 and 1109 the Cu concentration is appreciably enhanced. That is, the enhanced Zn/Cu ratios observed for collected particles correlate with depleted Zn relative to Cu left on the sample electrode surface.

### CONCLUSIONS

We have found that peaks in number density vs time plots correspond to the peaks in element spectral intensities often observed in "sparking off" or "burn-out" experiments for spark emission spectrometry. This indicates an initial efficiency of sampling that diminishes after some amount of erosion.

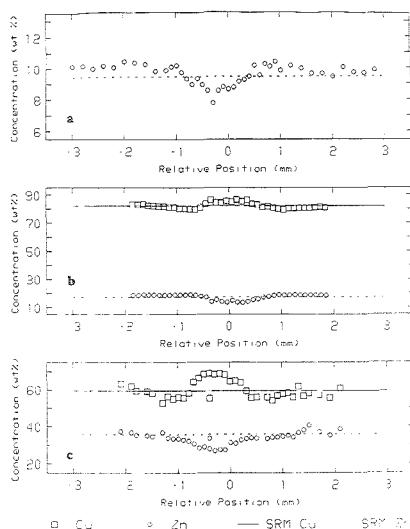


Figure 10. EPMA scans of SRM electrode surfaces. Horizontal lines represent the certified concentrations. Spark erosion pits are approximately  $\pm 1 \text{ mm}$  either side of the nominal electrode center: a, SRM 1116; b, SRM 1109; c, SRM 1103.

Similar observations have been noted for other types of discharges (34–36). After this period, if the train of spark discharges is sufficiently stable, sample melting becomes an increasingly important mechanism. Conversion from the liquid to the gaseous phase is followed by nucleation and condensation to form small particles. These agglomerate into chains and clusters, which are held together by weak electrostatic forces. Although the EAA has been found to be a suitable monitor for such relative measurements of number density vs time, any significant change in the degree of agglomeration of small particles will significantly affect this type of measurement.

If allowed to continue, stable spark sampling amplifies the degree of partitioning of elements by melting point in the aerosol formed. More volatile elements are concentrated in

the aerosol and depleted in the erosion pit relative to the original concentration in the sample.

For accurate, effective sampling for aerosol introduction into the ICP, it would seem that rapid transfer of energy from the spark into the solid is required. That is, the processes causing rapid vaporization while minimizing the time that material exists in the molten liquid state should dominate. Rapid vaporization of "high spots" may avoid chemical biases due to melting point differences, but these microscopic locations on the sample surface may or may not be truly representative of bulk concentrations. Höller (34) called the thin layer from which sampling takes place the "actual specimen", and Herberg et al. (35, 36) referred to these spots as "preferential" cathodes and found evidence that sampling depended on their composition and structure. If the degree of sampling is limited to preferential cathode points, sufficient aerosol for reexcitation by the ICP is not produced. More extensive (deeper) sampling is required, which may risk more significant melting.

The critical questions that remain are as follows: (1) What details of the spark current waveform promote more accurate sampling? Scheeline and Coleman (15) indicate that the initial  $di/dt$  may be more critical than the  $i$  vs  $t$  integral. (2) What sample matrix and analyte element combinations are most susceptible to sampling biases with a fixed type of spark current waveform and repetition rate? We have observed measurable bias for two elements of widely differing melting points (Cu, 1083 °C, and Zn, 419 °C). (3) What details of grain boundaries and microstructure affect sampling accuracy or rate? Compositional mapping techniques (37) will be important for characterizing the original sample surface on a more microscopic scale than was possible in previous studies (34-36).

The object of studies that address these questions will be to define the limiting conditions for analyzing complex alloys by using simple calibration standards with spark-ICP spectrometry.

#### LITERATURE CITED

- Thompson, M.; Goulter, J. E.; Sieper, F. *Analyst* **1981**, *106*, 32.
- Carr, J. W.; Horlick, G. *Spectrochim. Acta, Part B* **1982**, *37B*, 1.
- Hemsalech, G. A.; de Watteville, M. C. C. *R. Hebd. Seances Acad. Sci.* **1907**, *144*, 1338.
- Monvoisin, J.; Mavrodineanu, R. *Spectrochim. Acta* **1951**, *4*, 396.
- Human, H. G. C.; Scott, R. H.; Oakes, A. R.; West, C. D. *Analyst* **1976**, *101*, 265.
- Dahlquist, R. L.; Knoll, J. W. *ICP Inf. Newsl.* **1975**, *1*, 15.
- Coleman, D. M.; Sainz, M. A.; Butler, H. T. *Anal. Chem.* **1980**, *52*, 746.
- Beckwith, P. M.; Mullins, R. L.; Coleman, D. M. *Anal. Chem.* **1987**, *59*, 163.
- Norris, J. A.; Watters, R. L., Jr. *Federation of Analytical Spectroscopy Societies (FACSS) V*, Boston, MA, 1978, Paper no. 85.
- Walters, R. L., Jr. Paper presented at Institut für Spektrochemie und angewandte Spektroskopie, Dortmund, Germany, 1978.
- Helmer, D. J. C.; Walters, J. P. *Appl. Spectrosc.* **1984**, *38*, 392.
- Aziz, A.; Broekaert, J. A. C.; Laqua, K.; Leis, K. *Spectrochim. Acta, Part B* **1984**, *39B*, 1091.
- Beaty, J. S.; Belmore, R. J. *J. Test. Eval.* **1984**, *12*, 212.
- Marks, J. Y.; Fornwald, D. E.; Yungik, R. E. *Spectrochim. Acta, Part B* **1983**, *38B*, 107.
- Scheeline, A.; Coleman, D. M. *Anal. Chem.* **1987**, *59*, 1185A.
- Brewer, S. A.; Walters, J. P. *Anal. Chem.* **1969**, *41*, 1980.
- Ekimoff, D.; Walters, J. P. *Anal. Chem.* **1981**, *53*, 1644.
- Scheeline, A.; Norris, J. A.; Travis, J. C.; DeVoe, J. R. *Spectrochim. Acta, Part B* **1981**, *36B*, 373.
- Helmer, D. J. C.; Walters, J. P. *Appl. Spectrosc.* **1984**, *38*, 399.
- Omo, A.; Saeki, M.; Chiba, K. *Appl. Spectrosc.* **1987**, *41*, 970.
- Goldstein, J. I.; Newbury, D. E.; Joy, D. C.; Fiori, C. E.; Echlin, P.; Lifshin, E. *Scanning Electron Microscopy and X-ray Microanalysis*; Plenum: New York, 1981; pp 172-175.
- Prell, L. J. and Koptyonann, S. R. *Appl. Spectrosc.* **1988**, *42*, 1221.
- Raeymaekers, B.; Van Espen, P.; Adams, F.; Broekaert, J. A. C. *Appl. Spectrosc.* **1988**, *42*, 142.
- Coleman, D. M.; Walters, J. P. *Spectrochim. Acta, Part B* **1976**, *31B*, 547.
- Coleman, D. M.; Walters, J. P.; Watters, R. L., Jr. *Spectrochim. Acta, Part B* **1977**, *32B*, 287.
- Walters, J. P.; Goldstein, S. A. *ASTM Spec. Tech. Publ.* **1973**, *540*, 45.
- Liu, B. Y. H.; Whitby, K. T.; Pui, D. Y. H. *APCA J.* **1974**, *24*, 1067.
- Liu, B. Y. H.; Pui, D. Y. H. *J. Aerosol. Sci.* **1975**, *6*, 249.
- Small, J. A. "The Efficiency Tests of a Particle Collector for Microanalysis"; Annual Meeting of the American Association for Aerosol Research, Seattle, WA, 1987.
- Bright, D. S.; Fletcher, R. A. *Am. Ind. Hyg. Assoc.* **1983**, *44*, 528.
- Yakowitz, H.; Myklebust, R. L.; Heinrich, D. F. J. "FRAME: An On-Line Correction Procedure for Quantitative Electron Probe Microanalysis"; *Natl. Bur. Stds. (U.S.) Tech. Note* **1973**, *No. 796*, 46 pp.
- Cliff, G.; Lorimer, G. W. *J. Microsc.* **1975**, *103*, 203.
- Sheridan, P. J. The Use of Analytical Electron Microscopy for the Individual Particle Analysis of Arctic Haze Aerosol. Ph.D. Thesis, University of Maryland, 1986, p 220.
- Höller, P. *Spectrochim. Acta, Part B* **1967**, *23B*, 1.
- Herberg, G.; Höller, P.; Köster-Pflugmacher, A. *Spectrochim. Acta, Part B* **1967**, *23B*, 101.
- Herberg, G.; Höller, P.; Köster-Pflugmacher, A. *Spectrochim. Acta, Part B* **1967**, *23B*, 363.
- Marinenko, R. B.; Myklebust, R. L.; Bright, D. S.; Newbury, D. E. *J. Microsc.* **1987**, *145*, 207.

RECEIVED for review December 8, 1988. Revised manuscript received May 12, 1989. Accepted May 19, 1989. In order to describe adequately certain experimental procedures, products or instruments may be identified by specific manufacturer. This does not imply that these products may be the best for the purpose intended, nor does it imply endorsement by the National Institute of Standards and Technology.

# Determination of Silicon in National Institute of Standards and Technology Biological Standard Reference Materials by Instrumental Epithermal Neutron Activation and X-ray Fluorescence Spectrometry

Ernest S. Gladney\*

Health and Environmental Chemistry, Group HSE-9, MS K-484, Los Alamos National Laboratory, Los Alamos, New Mexico 87545

Peter E. Neifert and Nathan W. Bower

Chemistry Department, Colorado College, Colorado Springs, Colorado 80903

**The measurement of silicon in biological standard reference materials has been investigated by both boron-filtered epithermal neutron activation analysis and wavelength dispersive X-ray fluorescence. Good agreement between the methods was obtained for 11 different materials ranging from the methods' detection limits of about 100  $\mu\text{g/g}$  to the highest concentration in these samples of 12 000  $\mu\text{g/g}$  silicon.**

## INTRODUCTION

Silicon has been recognized as an essential micronutrient since 1972 (1). It plays an important role in the development of young bones and is also important in some plants. However, rapid and accurate methods for the determination of silicon in biological materials have proven to be difficult to develop. This is evidenced by the general scarcity of silicon data on biological reference materials in the literature. We have located only 27 reported values for the 11 different biological standard reference materials (SRMs) that the U.S. National Institute of Standards and Technology (NIST—the new name for the former National Bureau of Standards) has produced since 1972. Although silicon has traditionally been measured by gravimetric or colorimetric methods in many environmental matrices, the concentrations are too low for gravimetric work, and interferences from other elements (especially phosphorus) are too severe for colorimetry in biologicals. Thermal, epithermal, 14-MeV, and thermal neutron capture prompt  $\gamma$ -ray neutron activation methods have all been applied to the problem with widely varying results. Similarly, energy dispersive, wavelength dispersive, and charged-particle X-ray fluorescence have produced divergent data, though the reasons for this are unclear. Inductively coupled plasma atomic emission spectrometry and spark-source mass spectrometry have seen limited application, although the sensitivity of the latter is competitive with that of radiochemical neutron activation for silicon in biological samples. Atomic absorption has been utilized, but with only limited success and sensitivity. High background for all three stable silicon masses from molecular ions probably precludes the trace determination of this element by inductively coupled plasma mass spectrometry.

An excellent paper by Jones et al. (2) has described the nuclear basis of silicon determination via epithermal neutron activation analysis. The displacement of a proton by a high-energy neutron on the two most abundant isotopes of

silicon produces radioactive aluminum isotopes with useful half-lives, abundances, and  $\gamma$ -ray decay energies. The first of these is the  $^{28}\text{Si}(n,p)^{28}\text{Al}$  reaction. Unfortunately,  $^{28}\text{Al}$  is also produced by capture of slower neutrons by stable  $^{27}\text{Al}$  via the  $^{27}\text{Al}(n,\gamma)^{28}\text{Al}$  reaction and by the fast neutron  $^{31}\text{P}(n,\alpha)^{28}\text{Al}$  reaction on stable phosphorus. Aluminum is not particularly abundant in most biological materials, but phosphorus frequently occurs in concentrations of 0.1–1% or more. There are no nuclear reaction interferences with the  $^{28}\text{Si}(n,p)^{28}\text{Al}$  reaction, but the overall sensitivity for silicon determination with this reaction is limited by the low  $^{28}\text{Si}$  natural abundance. High-resolution  $\gamma$ -ray detectors are required to separate the 1273-keV  $^{28}\text{Al}$   $\gamma$ -ray from the 1268-keV single escape line of the more intense 1779-keV  $\gamma$ -ray of  $^{28}\text{Al}$ . However, detectors with resolutions of less than 2.0 keV fwhm are generally adequate to achieve base-line separation between these two transitions. Therefore, the preferred method of analysis would be to use the  $^{28}\text{Si}(n,p)^{28}\text{Al}$  reaction, although the silicon concentration may also be determined from the  $^{28}\text{Si}(n,p)^{28}\text{Al}$  reaction if the phosphorus and aluminum concentrations are first determined. A number of methods would be applicable for the determination of phosphorus and aluminum, including neutron activation analysis and colorimetry.

Wavelength dispersive X-ray fluorescence (XRF) readily resolves the silicon peak from both the aluminum and the much larger phosphorus peak usually found in biological materials. In fact, there are few interferences expected, other than the general scatter background usually found for particulate samples. The XRF analysis of light elements in plant matrices has been adequately demonstrated elsewhere (3, 4). However, a simplified procedure that requires less handling and equipment and no cellulose binder or diluent is described here.

## EXPERIMENTAL SECTION

**Instrumental Epithermal Neutron Activation.** The boron-filtered facility at the Los Alamos Omega West Reactor has been described in detail previously (5). Samples of the various NIST SRMs weighing approximately 0.1 g were packaged in small polyethylene snap-cap vials and irradiated in plastic rabbits inside the  $^{10}\text{B}$  enriched boron-shielded epithermal neutron facility fixed near the core of the reactor. Following a 5-min irradiation, the samples are extracted pneumatically. After decaying for 5 min the samples are counted for 5–10 min at the face of a large intrinsic Ge  $\gamma$ -ray detector coupled to a 4096-channel pulse-height analyzer. The  $\gamma$ -ray spectrum may be transferred to magnetic tape for off-line data reduction or digitally integrated directly on the cathode ray tube display of the multichannel analyzer. The analyses were standardized against 500- $\mu\text{g}$  quantities of silicon

\* Author to whom correspondence should be addressed.

Table I. Results of the Analysis of Silicon in Biological NIST Standard Reference Materials (Concentration in  $\mu\text{g/g}$ )

This Study												
method	1549	1566	1567	1568	1569	1570	1571	1572	1573	1575	1577	1577A
$^{28}\text{Al}$	<50	1360 $\pm$ 70	<200	120 $\pm$ 15	11 000 $\pm$ 1000	3080 $\pm$ 300	2360 $\pm$ 100	2150 $\pm$ 400	10 100 $\pm$ 100	1360 $\pm$ 70	<400	<300
$^{29}\text{Al}$	<100	1500 $\pm$ 90	<100	160 $\pm$ 30	13 100 $\pm$ 300	2600 $\pm$ 400	2120 $\pm$ 190	2100 $\pm$ 400	10 800 $\pm$ 100	1300 $\pm$ 200	<150	<150
XRF	<200	1330 $\pm$ 100	<100	150 $\pm$ 150	11 900 $\pm$ 530	2500 $\pm$ 250	2800 $\pm$ 300	1900 $\pm$ 400	9 800 $\pm$ 1000	1310 $\pm$ 200	225 $\pm$ 150	<100
Previous Work <sup>a</sup>												
method	1566	1570	1571		1572	1573	1575		1577			
XRF		2800 $\pm$ 500 <sup>b</sup>	1800 $\pm$ 500 <sup>b</sup>	480 $\pm$ 14 <sup>d</sup>	2080 <sup>e</sup>		9600 $\pm$ 500 <sup>b</sup>	820 $\pm$ 240 <sup>f</sup>	1200 $\pm$ 400 <sup>b</sup>		246 <sup>e</sup>	
CPXRF								248 $\pm$ 36 <sup>f</sup>	1380 <sup>e</sup>			
ICPES	1100 $\pm$ 100 <sup>g</sup>	2900 $\pm$ 900 <sup>g</sup>					3000 <sup>g</sup>					
IENA	2000 <sup>h</sup>		2000 <sup>h</sup>		2340 $\pm$ 60 <sup>h</sup>							
NAA			476 $\pm$ 12 <sup>i,j</sup>		750 <sup>k</sup>						16.7 $\pm$ 0.7 <sup>j</sup>	
14NAA			500 $\pm$ 200 <sup>l</sup>		1000 $\pm$ 160 <sup>m</sup>							
SSMS			2400 <sup>n</sup>								19 <sup>n</sup>	
TCGS						1900 $\pm$ 600 <sup>o</sup>						
unknown			600 <sup>p</sup>									

<sup>a</sup> CPXRF = charged particle XRF; ICPES = inductively coupled plasma emission spectroscopy; IENA = instrumental epithermal neutron activation; NAA = neutron activation analysis; 14NAA = 14-MeV neutron activation analysis; SSMS = spark source mass spectrometry; TCGS = thermal neutron prompt  $\gamma$ -ray spectrometry. <sup>b</sup> Reference 8. <sup>c</sup> Reference 19. <sup>d</sup> Reference 11. <sup>e</sup> Reference 16. <sup>f</sup> Reference 6. <sup>g</sup> Reference 7. <sup>h</sup> Reference 2. <sup>i</sup> Reference 9. <sup>j</sup> Reference 10. <sup>k</sup> Reference 14. <sup>l</sup> Reference 12. <sup>m</sup> Reference 15. <sup>n</sup> Reference 17. <sup>o</sup> Reference 18. <sup>p</sup> Reference 13.

standard solutions (SPEX Industries) pipetted onto Whatman-41 filters that were folded to match the geometry of the samples. Silicon concentrations in the samples were calculated directly from this standard using  $^{28}\text{Al}$ . To determine silicon via the  $^{28}\text{Al}$  isotope, standards for Al and P were prepared similarly and run along with several filter paper blanks. Contributions to the observed  $^{28}\text{Al}$  from the  $(n,\gamma)$  and  $(n,\alpha)$  reactions were measured from these latter standards and corrected for in the samples by using the certified or literature concentrations of these elements in each material. Typically, 1000  $\pm$  50 net counts ( $1\sigma$ ) were observed for the 500- $\mu\text{g}$  standard, where the uncertainty is due purely to counting statistics. In the biological matrices, the  $1\sigma$  counting statistics uncertainty rose to approximately 10%.

**Wavelength Dispersive X-ray Fluorescence.** The XRF measurements were made by using a Rigaku 3070 spectrometer with a Rh end-window tube operated at 40 kW and 50 mA. The  $K\alpha$  line was counted under a He atmosphere for 80 s at 109.04°, and the background was calculated from the average of 40-s counts obtained at 2 $\theta$  angles of 105.00° and 112.00° with the use of a 3-cm diaphragm and an EDDT (PET) crystal. No overlaps with other peaks were noted, and no matrix corrections were used, as these matrices were relatively uniform, consisting largely of organic matter. The responsivity under these conditions was 8 (kcunts/s)/1% Si, with background counts of 30 counts/s. This gives a detection limit based on counting statistics of 3  $\mu\text{g/g}$  by using the formula

$$C_1 = \frac{t_\alpha}{m} \left( \frac{2r_b/t}{n_m} \right)^{1/2}$$

where  $C_1$  is the detection limit,  $m$  is the slope of the calibration curve and  $n_m$  is how many times it is measured,  $t_\alpha$  is the one-sided  $t$  statistic with  $\alpha = 0.05$  and with  $n - 2$  degrees of freedom ( $n$  is the number of standards used to obtain the calibration graph),  $r_b$  is the background count rate, and  $t$  is the counting time.

The data were calculated from quintuplicate counts of three samples of each of the SRMs except for 1549, 1566, and 1571, for which there was only enough powder for duplicate samples. Samples of approximately 5 g were hand-packed in 3-cm Spex cells (No. 3527) and covered with 0.2 mil thick polycarbonate film (Spex 3522). Although it is important to pack the cells reproducibly for good precision in the analysis, this method avoids the need for a high-pressure press or a cellulose binder to hold the samples together in the spectrometer, as the polycarbonate film holds the sample in and is transparent to the X-rays. Although a vacuum may be used with some care with these cells, occasional

explosive failure of the film suggested use of a He atmosphere. It should be noted that the binder method also sometimes fails under a vacuum, and that such failures led to the development of this procedure.

Calibration curves were constructed from Whatman Ashless cellulose chromatography powder (standard grade) and reagent grade sodium metasilicate. A slurry of 5 g of the cellulose was mixed with 20 mL of doubly deionized water (Millipore 18 M $\Omega$ ) for each of the five sodium metasilicate standards, and these were then dried under a heat lamp before being packed in the Spex cells. The calibration curve that resulted showed a small negative deviation from linearity.

## RESULTS AND DISCUSSION

The results of the analyses are presented in Table I for the silicon concentrations in the NIST biological SRMs determined, using the two different isotopes, by instrumental epithermal neutron activation (IENA) and by XRF, as well as the average of the data available in the literature. Excellent agreement was obtained for this work with no significant differences apparent over the entire range of concentrations and matrices. The difference between the two methods (results averaged 4% higher with IENA) was not significant ( $P = 0.25$ ). This slight difference might be due to inadequate matrix or geometry matching between the standards and the samples.

The comparison with the literature at first appears to be less perfect. The major differences would appear to be for orchard leaves 1571 (an average of 2520 for this study versus 1310 for the literature), tomato leaves 1573 (10 125 versus 6300), and pine needles 1575 (1320 versus 912). However, if the comparison is made with the most recent analyses for these samples, the differences disappear. It is interesting to note the time dependence of the values from the literature. Whether this is due to the contamination of the standards as they abrade their glass containers or whether it is due to improved analyses or to some other factor is difficult to say.

The relative contributions from stable aluminum and phosphorus and silicon to the total aluminum signal are shown in Table II for five SRMs. In most vegetable SRMs the silicon concentration is high enough so that the contributions from aluminum and phosphorus do not seriously affect the accuracy. However, in tissue SRMs, the contribution from

**Table II. Relative Percent Contributions of P and Al to the <sup>28</sup>Si Peak**

SRM	P	Al	Si
1570	32	17	51
1571	20	10	70
1572	14	3	83
1573	9	9	82
1577	95	<1	5

phosphorus overwhelms that from silicon.

Although the methods employed here are theoretically capable of determining concentrations near 10  $\mu\text{g/g}$  (the limitation of the blank's variability), the samples themselves seem to have inhomogeneities or contaminations that are nearer 100  $\mu\text{g/g}$ . This is in good agreement with the detection limits reported previously for XRF (3) of 120  $\mu\text{g/g}$  for silicon in biological matrices. Based on the XRF data, which was not limited by counting statistics even for those samples with the lowest levels of silicon, the precision of sampling seems to be about 10% relative standard deviation (RSD) for most of these samples. Some SRMs, such as citrus leaves (1572), have significantly worse precision by XRF (possibly due to the fact that it also has the largest particle size). Some of the imprecision is due to the hand-packing method, but the more homogeneous samples such as 1569 with a 5% RSD imply that this should not be the limiting factor. A constant-pressure press might improve the packing precision, but the use of a binder is not recommended as it dilutes the sample as well as providing a potential source of contamination. Instead, the polycarbonate film and He flush should be used for the maximum accuracy and precision.

### CONCLUSIONS

The efficacy of both IENA and XRF for the determination of silicon in a variety of biological matrices has been amply demonstrated, especially considering the simplicity of the sample preparation. Analytical methods that require sample dissolution are especially vulnerable to systematic errors due to contamination while handling and to volatility losses, silicon

tetrafluoride being a well-known example. Neither of these methods requires such dissolution, offering distinct advantages in terms of accuracy as well as simplicity. The results also suggest that contaminations at the level of 100  $\mu\text{g/g}$  are ubiquitous, and extra care in the preparation, packaging, and handling of SRMs will be necessary if they are ever to be certified below this concentration.

### LITERATURE CITED

- (1) Valkovic, V. *Analysis of Biological Materials for Trace Elements Using X-ray Spectroscopy*; CRC Press, Inc.: Boca Raton, FL, 1980; pp 95, 96.
- (2) Jones, J. D.; Kaufman, P. B.; Rigot, W. L. *J. Radioanal. Chem.* **1979**, *50*, 251-275.
- (3) Evans, C. C. *Analyst* **1970**, *95*, 919-929.
- (4) Norrish, K.; Hutton, J. T. *X-ray Spectrom.* **1977**, *6*, 6-11.
- (5) Gladney, E. S.; Perrin, D. R.; Balagna, J. P.; Warner, C. L. *Anal. Chem.* **1980**, *52*, 2128-2132.
- (6) Nadkarni, R. A. *Anal. Chem.* **1984**, *56*, 2233-2237.
- (7) Williamson, T. G.; Benneche, P.; Hosticka, B.; Brenizer, J.; Nguyen, T. *J. Radioanal. Nucl. Chem.* **1987**, *114*, 387-392.
- (8) Rethfeld, H. *Fresenius' Z. Anal. Chem.* **1986**, *324*, 720-727.
- (9) Guzzi, G.; Pietra, R.; Sabbioni, E. *J. Radioanal. Chem.* **1976**, *34*, 35-57.
- (10) Pietra, R.; Sabbioni, E.; Girardi, F. *Radiochem. Radioanal. Lett.* **1975**, *22*, 243-250.
- (11) Kirchner, S. J.; Oona, H.; Perron, S.; Fernando, Q.; Lee, J.; Zeitlin, H.; *Anal. Chem.* **1980**, *52*, 2195-2201.
- (12) Faanhof, A.; Das, H. A.; Zonderhuis, J. *J. Radioanal. Chem.* **1980**, *56*, 173-184.
- (13) Nonaka, N.; Higuchi, H.; Hamaguchi, H.; Tomura, K. *Bunseki Kagaku* **1981**, *30*, 599-604.
- (14) Gangadharan, S.; Velgnasubramanian, S. *J. Radioanal. Chem.* **1978**, *42*, 455.
- (15) Seegade, C. *Fresenius' Z. Anal. Chem.* **1977**, *284*, 23-29.
- (16) Kaufmann, H. C.; Steenblik, J. *Nucl. Instrum. Methods Phys. Res.* **1984**, *231*, 198-202.
- (17) Vos, L.; Van Grieken, R. *Fresenius' Z. Anal. Chem.* **1985**, *321*, 32-36.
- (18) Anderson, D. L.; Gordon, G. E.; Walters, W. B.; Zoller, W. H.; Lindstrom, R. M. Neutron-capture Prompt Gamma-ray Activation Analysis. In *NBS Reactor: Summary of Activities July 1981 through June 1982*; Shorten, F. J., Ed.; NBS Technical Note, 1983; pp 159-164.
- (19) Rachetti, A.; Wegscheider, W. *Anal. Chim. Acta* **1986**, *188*, 37-50.

RECEIVED for review February 7, 1989. Accepted May 22, 1989. This work was funded in part by the U.S. Department of Energy and in part by a Faculty Research and Development Grant from Colorado College.

# Thin-Specimen X-ray Fluorescence Analysis of Major Elements in Silicate Rocks

Lewis H. Cohen\*

*Department of Earth Sciences, University of California, Riverside, Riverside, California 92521*

David K. Smith

*Earth Sciences Department, Lawrence Livermore National Laboratory, Livermore, California 94550*

**The concentrations of major elements in silicate rocks—Na, Mg, Al, Si, K, Ca, Ti, and Fe—are readily determined via wavelength-dispersive X-ray fluorescence analysis by fine grinding, adding an internal standard, and producing a monolayer of particles. Matrix absorption corrections are attenuated such that calibrations of count rate versus concentration are linear for all elements but Si. Linearity of calibration for K and heavier elements is theoretically expected from particles  $\leq 1 \mu\text{m}$ ; linearity for Al and lighter elements is partially due to the systematics of silicate rock chemistry. The calibration of Si departs from linearity because of the particle size and the wide range (47–100 wt %) of concentrations used. Nonuniformity of grain size causes scatter, particularly for Al and Si. The thin-specimen procedure described here thus allows for simple and accurate determination of major elements in small volume samples. Since the sensitivity, (counts per second)/(weight percent), follows theoretical predictions for thin films, the technique can be generalized to other materials.**

## INTRODUCTION

X-ray fluorescence (XRF) analysis of thin specimens prepared from bulk solids has been attempted only infrequently, although the technique promises theoretically linear calibration due to attenuation of matrix effects (1). A further advantage to analyzing suitably thin samples is a decrease in background relative to the analyte peak, allowing increased sensitivity of analysis. Commonly, there also exists a need to analyze the bulk chemistry of small volumes of sample (2). These analytical advantages and situations suggest that further work is warranted in developing a thin-specimen XRF technique.

We present here a method of producing thin specimens of particulate samples which is also applicable for analysis of small volumes of solids, and we also demonstrate the utility of such thin specimens for calibration of the major elements (Na, Mg, Al, Si, K, Ca, Ti, and Fe) in silicate rocks by wavelength-dispersive XRF.

The relatively low energies of the  $K\alpha$  emission lines of the lighter silicate rock major elements make these elements particularly difficult to analyze by thin-specimen XRF analysis. Chung et al. (3) give a criterion for the thickness  $d_1$  of a continuous thin specimen that, with a relative error of  $\leq 1\%$ , yields count rates proportional to analyte concentration

$$d_1 \leq 0.135/\mu\rho \quad (1)$$

where  $\rho$  is the density of the sample,  $\text{g}/\text{cm}^3$ , and  $\mu = \mu_1 \csc \phi_1 + \mu_2 \csc \phi_2$ , with  $\mu_1$  and  $\mu_2$  being the mass absorption coefficients for primary and characteristic X-rays and  $\phi_1$  and  $\phi_2$  X-ray incident and takeoff angles. Chung et al. (3) also show that a sample is infinitely thick to X-rays, within 1%, if it has a thickness,  $d_c$ , of  $4.62/\mu\rho$ . Hence by this criterion,

$d_c/d_1 \approx 34$ . For 2% departures from linearity,  $d_c/d_1 \approx 21$ .

By use of mass absorption coefficients calculated via sub-routines from the NBSGSC fundamental parameters program (4), the geometry of the X-ray fluorescence unit employed ( $\phi_1$  and  $\phi_2 = 60^\circ$  and  $45^\circ$ , respectively), and the simplifying assumption that the exciting radiation is 0.1 Å shorter than the absorption edge for the  $K\alpha$  characteristic line excited, Table I gives the maximum thickness of continuous mineral specimens that depart no more than 1% from being ideal thin samples. This table contains a range of the common igneous-rock-forming minerals and is representative rather than exhaustive. A monolayer of individual mineral grains that exceeds thicknesses given in Table I is not ideally "thin"; a grain that approaches infinite thickness ( $d_c$ ) for Na or Mg may still be infinitely thin for Fe. Thicknesses given in Table I are very similar to those calculated for 1% error using the particle size effect formula of Criss (6).

Samples that are significantly thicker than those given in Table I complicate thin-specimen analysis by introducing matrix absorption of the characteristic X-rays and potentially introducing enhancement from secondary excitation. Regarding enhancement, Van Dyck et al. (7) calculated that for geological materials, a sample of  $2 \text{ mg}/\text{cm}^2$ , i.e.  $\approx 0.7 \text{ mm}$  thick, would increase Mg  $K\alpha$  emission by some 10%. Since this thickness is much greater than the grain sizes used in this experimentation and those shown in Table I, the predominant departure from linearity of calibration for finely ground materials will be caused by matrix absorption.

Thin-specimen analysis thus requires sample loading great enough to yield suitable count rates but not so thick as to introduce matrix absorption from the vehicle used to produce the thin specimens, or introduce effects due to a sufficient thickness of overlapping grains (8). A further and significant complexity is introduced by the fact that most common minerals consist of several major elements in addition to Si. Routine grinding techniques usually do not produce grain sizes uniformly  $< 1 \mu\text{m}$ ; hence a single mineral or glass grain may be "thin" with regard to more energetic characteristic X-rays of rock-forming elements but of intermediate thickness with respect to characteristic radiation from the lighter of such elements. This inherent departure from linearity of calibration can be accommodated, but not eliminated, by employing similar grain sizes in all samples.

Our technique extends the work of McGinness et al. (9) and Chung et al. (3) to the light elements that constitute silicate rocks. Finely ground material is mixed with a solid internal standard, the mixture is spread with reproducible thickness using a dilute organic vehicle on an inorganic-free substrate, and the resulting samples are analyzed by wavelength-dispersive XRF.

## EXPERIMENTAL SECTION

**Sample Preparation.** Chemically diverse U.S. Geological Survey and National Institute of Standards & Technology reference rocks, which are supplied as finely ground, homogeneous materials, were used in this calibration; consensus values for their

**Table I. Maximum Thickness ( $\mu\text{m}$ ) of Continuous Mineral Films That Cause  $\leq 1\%$  Deviation from Linearity in Counts per Second vs Concentration<sup>a</sup>**

mineral	Na K $\alpha$	Mg K $\alpha$	Al K $\alpha$	Si K $\alpha$	K K $\alpha$	Ca K $\alpha$	Ti K $\alpha$	Fe K $\alpha$
quartz				0.15				
albite	0.07		0.15	0.13				
orthoclase	0.07		0.16	0.14	0.54			
labradorite	0.07		0.14	0.13		0.70		
NBS-278 (glass)	0.07		0.16	0.14	0.54			3.1
muscovite			0.14	0.12	0.53			
biotite		0.07	0.10	0.11	0.52		1.0	1.8
hornblende		0.07	0.10	0.11		0.62	0.9	1.9
pigeonite		0.06		0.10		0.60		1.7
enstatite		0.08		0.10				2.9
forsterite (F <sub>096</sub> )		0.07		0.10				2.9

<sup>a</sup> Mineral composition data are from Deer et al. (5). Geometry of the incident and takeoff angles of the X-ray fluorescence unit are included in the above calculation. Only those minerals containing  $>1$  wt % of the element as an oxide have thicknesses tabulated.

compositions are tabulated by Abbey (10). Both the  $\text{La}_2\text{O}_3$  used as the internal standard and the silicic acid used in calibration were reagent grade, with the latter having a composition  $<0.06\%$  nonvolatile with HF. The  $\text{La}_2\text{O}_3$  and silicic acid were ignited at  $850^\circ\text{C}$  before use. All samples were ground under acetone in an automated rotary alumina mortar and pestle for 20–30 min and dried at  $120^\circ\text{C}$ . Comparison of the Al count rate for  $\text{SiO}_2$  ground in the alumina and in an agate mortar and pestle showed no detectable Al contamination. Scanning electron microscopy indicates that both  $\text{La}_2\text{O}_3$  and  $\text{SiO}_2$  grain sizes are  $<1\ \mu\text{m}$ .

$\text{La}_2\text{O}_3$  was chosen as an internal standard for analysis of major elements because it has minimal potential for emission line overlap, as demonstrated by its routine use as a heavy element absorber in borate fusion XRF analysis of rocks.  $\text{La}_2\text{O}_3$  was mixed with the ground rock in a ratio of 1 part by weight  $\text{La}_2\text{O}_3$  to 4 parts rock and thoroughly homogenized in a plastic vial in a shaker mill. The ratio of  $\text{La}_2\text{O}_3$  to rock chosen here gives a convenient La counting rate without significant atomic dilution of the sample; the greater density of  $\text{La}_2\text{O}_3$  than the rock also minimizes dilution.

The substrate upon which the thin specimen was subsequently drawn was cleaned and then flattened by capillary adhesion to a glass plate. Both  $13\ \mu\text{m}$  (0.0005 in.) and  $25\ \mu\text{m}$  (0.001 in.) thick Mylar were used as substrates and found to be suitable; little difference in scattered radiation background count rates was found between the two thicknesses of Mylar. Each lot of film has to be checked for measurable quantities of undesirable inorganics (11), however, since Ca was found to be in unacceptably high concentrations in some Mylar.

A 60-mg sample of powder was placed in a 3-mL Wheaton V-vial and the powder wetted with  $3/4$  mL of acetone. A  $3/4$ -mL portion of a commercial, major-element-free alkyl resin spar varnish was added with a disposable syringe, and the resulting mixture was vigorously mixed and homogenized by drawing the slurry in and out of the V vial using another disposable syringe with an 18-gauge pipetting needle. The vial and its contents were kept near  $0^\circ\text{C}$  in an ice water bath to increase the viscosity of the organic vehicle.

While the powder/varnish mixture was still very well dispersed in the syringe, several drops were applied on the Mylar substrate before the opening of a Gardner/Neotec Bird film applicator. With slight downward pressure, a thin-specimen film was created by quickly drawing the applicator by hand for a distance of at least 12 cm along the Mylar. The sample was then transferred to a lint-free cardboard backing, covered to prevent contamination, and dried at  $\approx 50^\circ\text{C}$ . An applicator with  $13\ \mu\text{m}$  (0.0005 in.) "wet film thickness" was used to produce the films analyzed; a  $38\text{-}\mu\text{m}$  (0.0015 in.) applicator was found to yield unsatisfactory results since it created specimens that showed light element X-ray absorption. The manufacturer of the applicator, which is commonly used for quality control in the paint industry, notes that the actual clearance of the casting knife is approximately double the "wet film thickness" specification.

The undiluted spar varnish used in this experimentation had  $\approx 55$  wt % nonvolatile material; several other commercial clear gloss finishes were also determined to have minimal or no content of the inorganics to be analyzed and thus would also potentially be suitable for this purpose. These commercial finishes typically

are nitrocellulose and/or alkyl-modified polyurethane in a variety of solvents. The 1:1 dilution chosen is not critical insofar as X-ray absorption is concerned, since experiments with 5 parts varnish to 3 parts acetone as a vehicle had no effect on the count rate of Na versus the more energetic X-rays from heavier elements.

Scanning electron microscopy of the samples thus prepared showed that more than 90% of the area of the film produced was composed of a monolayer of particles  $<1\text{--}2\ \mu\text{m}$  in maximum dimension dispersed in the organic vehicle. Occasional mineral grains  $>2\ \mu\text{m}$  in maximum dimension were noted; rarer were clots composed of several grains.

**XRF Analytical Procedure and Data Reduction.** An automated Siemens SRS-1 sequential wavelength XRF spectrometer with 10-position sample changer was operated with a Cr tube at 41 kV and 36 mA. Samples were cut from the Mylar film with a scalpel, placed sample-side toward the beam, and held in place with plastic retainers. Scatter of radiation to the detector was minimized by using carbon sample cups with no tops and a 23 mm diameter mask over the tube window that limited the irradiation area to the opening in the sample cups.

The K $\alpha$  peak and one background position were counted for 100 s for all elements but Na and Mg; the K $\alpha$  peak, two background positions, and 200-s counts were employed for Na and Mg. Any instrumental count-rate drift was compensated by ratioing to the temporal change in counts of a high count-rate element in a synthetic counting standard in the sample changer. Multiple thin-specimen films of each standard were prepared and two samples from each film counted. Standard pulse height discrimination was employed.

The thin-sample films were robust in the beam: repeated ratioing of Na counts in a silicate mineral to La counts in the internal standard in a single film for  $1\ 1/2$  h showed only statistical variations in counts recorded.

After subtraction of the off-peak background, a correction was applied to the data on an element-by-element basis to take into account contamination by or additional scatter from the varnish and  $\text{La}_2\text{O}_3$  potential additional absorption by the sample of X-rays scattering from behind the sample, and/or potential additional scattering by the sample. This correction was determined from counting blanks which consisted of thin-specimen films containing only  $\text{SiO}_2$  (with and without  $\text{La}_2\text{O}_3$ ), and films with  $\text{La}_2\text{O}_3$  only but in the same proportion as in the thin-specimen films with sample. In each case, counts from the blanks were subtracted from the background-corrected intensities; these corrections were relatively minor and made slight statistical improvement in calibration.

The average counts per second of the La internal standard for all samples was then determined, and all intensities were subsequently normalized to this average to remove variations inherent to producing the thin specimens. Consistent procedure yielded the same La average counts per second from month to month, within one standard deviation.

## RESULTS AND DISCUSSION

Parameters derived from linear regression analysis for the major elements in silicate rocks except for Si are given in Table II. The ranges of concentrations for the elements shown in



**Table II. Detection Limits and Results of Linear Regression Analysis on Counting U.S. Geological Survey Reference Rocks BCR-1, DNC-1, DTS-1, and GSP-1, National Institute of Standards & Technology Standard Reference Material 278, and SiO<sub>2</sub><sup>a</sup>**

oxide	range of concn, wt %	range of normalized count rate, counts/s	detection limit, wt %	slope [sensitivity], (counts/s)/wt %	intercept, counts/s	corr coeff
Na <sub>2</sub> O	0-4.84	-2.0-39.2	0.17	8.05	-1.4	0.999 69
MgO	0-49.80	-0.2-730.7	0.13	14.1	-5.3	0.999 10
Al <sub>2</sub> O <sub>3</sub>	0-18.36	0.5-562.5	0.06	24.0	11.4	0.993 23
K <sub>2</sub> O	0-5.51	-6.1-2637	0.003	471.2	7.4	0.999 49
CaO	0-11.31	4.7-4155	0.005	366.4	2.9	0.999 69
TiO <sub>2</sub>	0-2.26	-5.4-863.8	0.007	377.5	-7.6	0.999 66
Fe <sub>2</sub> O <sub>3</sub>	0-13.41	-2.6-562.5	0.08	40.9	-5.2	0.999 03

<sup>a</sup> Linear regression data for SiO<sub>2</sub> are omitted, due to curvature in the calibration (see text). The range of SiO<sub>2</sub> covered in experimentation is 47.20-100 wt %, and its normalized count rate was 614.0-2022 counts/s. The detection limit for SiO<sub>2</sub> was ≈0.08 wt %. All regressions are on 36 data points.

Table II span the range commonly encountered in silicate rocks. Compositions of the major elements in silicate rocks are conventionally given as oxides, and that convention is followed here.

Fe and Ti K $\alpha$  characteristic radiation are energetic enough such that maximum thicknesses  $d_1$  for thin film behavior (Table I) are greater than the grain sizes employed here; a linear response of counts per second versus weight percent is thus expected. Table II shows the data from one calibration; Ti, being in lower concentration than Fe in most rocks but being much more efficiently excited by the Cr XRF tube, shows much greater sensitivity.

Thicknesses for K and Ca given in Table I are less than or approximately equal to the dimensions of our grains as seen under the scanning electron microscope. Although thicknesses  $\approx d_1$  increase the possibility of nonlinear response, analyzing similar grain sizes in all samples offsets the tendency toward nonlinearity of response. A typical calibration is shown for Ca (Figure 1); results of linear regression analysis for both K and Ca are given in Table II. Regression shows that the responses by K and Ca are indeed satisfactorily represented by linear fits.

Na, Mg, Al, and Si are all within the range of thickness between  $d_1$  and  $d_c$  and thus may give nonlinear response. For Na, as for K, only a limited number of common rock-forming minerals have significant (>1 wt % as oxide) concentrations; hence in materials ground to similar grain sizes, the signal generated will largely be in response to the number of fluoresced grains and only secondarily influenced by varying mineralogy. The necessity for similar grain size is implicit in the work of Holmes (12). Even as mineralogy of igneous rocks changes, the data in Table I show that the  $\mu\rho$  of the Na-containing minerals remains approximately constant. Linear response might thus be expected for uniform grain size samples, and the data in Table II show that to be the case.

Although a number of minerals tabulated in Table I contain Mg, only a limited number of them will occur in a single rock. The calculated  $d_1$  values of Mg-bearing minerals in Table I are almost identical. Hence grinding grains to similar dimensions will give X-ray counting rates that respond primarily to dilution of the very few Mg-bearing phases and will tend to yield linear responses. The data presented in Table II bear this out. There is a gap in the calibration between ≈10 and ≈43 wt % MgO, reflecting the fact that whole rock compositions within that range, and hence available standards, are uncommon.

Si is an essential component in a wide variety of phases in a single silicate rock and thus grinding to uniform grain size will not completely overcome the problem of grain dimensions larger than  $d_1$ . Al may be similarly affected. Since the rocks used in our calibration span a very wide range of the compositions of silicate rocks commonly encountered, there will

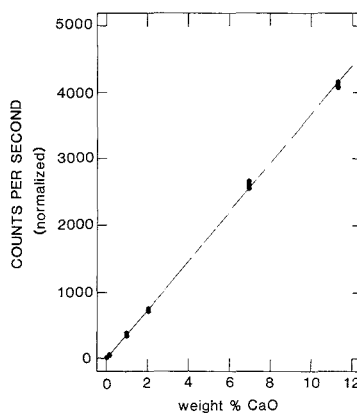


**Figure 1.** Calibration for Ca expressed as weight percent CaO. Counts per second in this and Figure 2 are normalized to the average counts per second of the internal standard, La. Line in this figure is a linear regression. Samples, in increasing concentration, are SiO<sub>2</sub>, DTS-1, NBS-278, GSP-1, BCR-1, and DNC-1.

be a maximum variation in mineralogy in the rocks used here. The variety of mineralogy includes NBS-278, which is largely a silicate glass. The data in Table I reflect this variation in  $\mu\rho$  by showing a 50% range in  $d_1$  for Si and Al.

Although the number of major Si-bearing phases in a given rock will be limited, the mineralogy of silicate rocks is such that the lower the SiO<sub>2</sub> content of the rock, the greater the content of minerals that have lesser  $d_1$ . As the grain dimension increasingly exceeds  $d_1$ , the count rate will not increase proportional to the content of the lighter elements Si and Al. The sensitivity, i.e. the (counts per second)/(weight percent), will decrease. The slope of the curve that best fits the data will thus decrease as the SiO<sub>2</sub> content decreases. This is reflected in Figure 1. Linear regression data for Al are given in Table II, since no curvature was found for that element, but linear regression data for Si are not shown in Table II because the expected curvature was encountered.

Since the Si data show nonlinearity due to thickness exceeding the criterion for  $d_1$ , a nonlinear regression was performed by using both the first and second terms in the power series expansion of  $(1 - \exp[-\mu\rho d])/\mu$  (3). The expression, of the form  $y = a_0 + a_1x(1 + a_1b)$ , was fit to the data by using a commercial statistical software package, and the resulting curve, which reduces the mean square of the residuals, is shown in Figure 2.

Optimal thin-specimen calibration for Al and Si in rocks will be obtained from reference rocks containing only similar

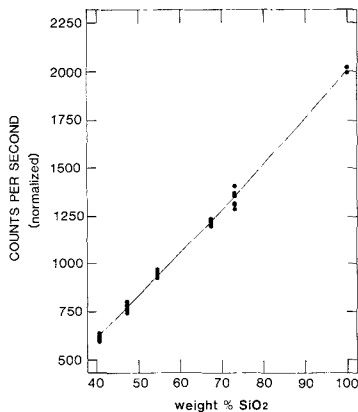


**Figure 2.** Calibration for Si expressed as weight percent  $\text{SiO}_2$ . Line shown is a nonlinear regression (see text). Samples, in increasing concentration, are DTS-1, DNC-1, BCR-1, GSP-1, NBS-278, and  $\text{SiO}_2$ .

mineralogies. Such a limited-range linear calibration for Si and Al should yield as satisfactory results as the full-range calibrations shown for the other major rock-forming elements. For such calibrations, however, the linear regressions will not necessarily pass through the origin. This will be especially so for Si, since silicate rocks rarely have <40 wt %  $\text{SiO}_2$ ; linear extrapolation to the origin will be considerably outside the range of calibration.

Lower limits of detection shown in Table II are calculated according to Tertian and Claisse (ref 13, p 351). These are to be compared with detection limits tabulated for analysis of whole rock pressed powders (14) with thickness  $\gg d_c$ . Detection limits in Table II are comparable to those for infinitely thick samples for Ti and lighter, i.e. those elements for which our grain thickness is similar to or greater than  $d_i$ . Only for Fe is the lower limit of detection significantly better for infinitely thick samples.

Tertian and Claisse (ref 13, p 302) calculate sensitivity for thin specimens for a excitation at 45 kV with a Cr target, conditions almost identical with those adopted here for experimentation. In order to compare our experimental data with their predictions, sensitivities given in Table II in (counts per second)/(weight percent) oxide were converted to (counts per second)/(weight percent) of the element. Linear regressions were fit to the Si data of Figure 1 in order to compare sensitivities; 22.8 (counts/s)/wt % oxide sensitivity (with correlation coefficient 0.997 44) was found.

Tertian and Claisse (13) present their data as the reciprocal of sensitivity and normalize to Ti as 1. Our sensitivities are greater than their predictions (Figure 3), except for Si which is equal, regardless of whether our thicknesses are less than or greater than  $d_i$ . Nevertheless, our sensitivities are quite close to the theoretical predictions and show that the Tertian and Claisse calculations can be used to assess sensitivities for elements not covered in this investigation. Similarly, these predictions can be used in extending the technique of thin-

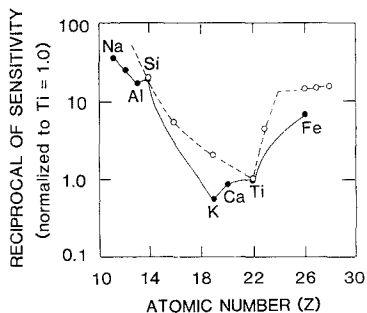


**Figure 3.** Reciprocal of sensitivity, normalized to Ti = 1, as a function of atomic number. Solid symbols with solid line are derived from sensitivities given in Table II. Sensitivity for Si is discussed in the text. Open symbols with dashed line are predicted sensitivities for approximately the same experimental conditions from Tertian and Claisse (13).

specimen XRF to bulk materials other than silicate rocks.

The technique developed here provides a versatile method for analyzing for the major elements in silicate rocks and, with due attention to the limiting effects of mass absorption, for accurately analyzing many other bulk and heterogeneous solids. Preparation is minimized, with the critical factor being similar grain size distributions for both reference standards and unknowns. The samples produced are durable to the vacuum and X-rays of the spectrometer; even Na, which is difficult to analyze by XRF fusion (15), is readily determined due to enhanced signal to background ratios, and calculations are minimized due to linear calibrations.

#### LITERATURE CITED

- (1) Birks, L. S. *X-ray Spectrochemical Analysis*; Interscience Publishers: New York, 1959; p 59.
- (2) Schroeder, B.; Thompson, G.; Sulanowska, M. *Am. Lab.* **1982**, *14*(3), 66, 68, 70-72.
- (3) Chung, F. H.; Lentz, A. J.; Scott, R. W. *X-Ray Spectrom.* **1974**, *3*, 172-175.
- (4) Tao, G. Y.; Pella, P. A.; Rousseau, R. M. *Natl. Bur. Stand. (U.S.) Tech Note* **1985**, No. 1213, 117 pp.
- (5) Deer, W. A.; Howie, R. A.; J. Zussman, J. *An Introduction to the Rock Forming Minerals*; London: Longman, 1966; 528 pp.
- (6) Criss, J. W. *Anal. Chem.* **1976**, *48*, 179-186.
- (7) Van Dyck, P. M.; Torok, S. B.; Van Grieken, R. E. *Anal. Chem.* **1986**, *58*, 1761-1766.
- (8) Rhodes, J. R.; Hunter, C. B. *X-Ray Spectrom.* **1972**, 113-117.
- (9) McGinness, J. D.; Scott, R. W.; Mortensen, J. S. *Anal. Chem.* **1969**, *41*, 1858-1861.
- (10) Abbey, S. *Geol. Surv. Can. Pap.* **1983**, No. 83-15, 121 pp.
- (11) Solazzi, M. J. *Am. Lab.* **1985**, *17*(11), 124, 126-131.
- (12) Holmes, G. S. *Chem. Geol.* **1981**, *33*, 333-353.
- (13) Tertian, R.; Claisse, F. *Principles of X-ray Fluorescence Analysis*; London: Heyden, 1982.
- (14) Rose, W. I.; Bornhorst, T. J.; Sivonen, S. J. *X-Ray Spectrom.* **1986**, *15*, 55-60.
- (15) Stork, A. L.; Smith, D. K.; Gill, J. B. *Geostand. Newsl.* **1987**, *11*, 107-113.

RECEIVED for review March 8, 1989. Accepted June 1, 1989. The Committee on Research, University of California, Riverside, generously sponsored this investigation. Work also performed under the auspices of the U.S. Department of Energy under Contract W-7405-Eng-48 to Lawrence Livermore National Laboratory.

# Determination of Total Inorganic Carbon in Aqueous Samples with a Flame Infrared Emission Detector

S. Wayne Kubala, David C. Tilotta, Marianna A. Busch, and Kenneth W. Busch\*

Department of Chemistry, Baylor University, Waco, Texas 76798

A specially designed system, using a flame infrared emission (FIRE) detector, was developed to permit the determination of total inorganic carbon (TIC) in water samples. Carbon dioxide, released from 1.0-mL samples upon acidification, was purged from solution with He and excited in a hydrogen/air flame. The carbon dioxide emission intensity at 4.42  $\mu\text{m}$  (2264  $\text{cm}^{-1}$ ) was monitored by use of a lead selenide detector in conjunction with a 4.4- $\mu\text{m}$  band-pass optical filter. Peak emission intensity measurements from multiple injections of 1.0-mL water samples gave a relative standard deviation of 1.35%. The average relative standard deviation of the TIC measured with the FIRE system was found to be 0.89%. The accuracy of the FIRE technique was determined by comparing the FIRE-TIC results with those obtained by total alkalinity titrations for five natural water samples and was found to be 1.22%. The detection limit for the system was found to be equivalent to  $3.05 \times 10^{-2}$  mM  $\text{Na}_2\text{CO}_3$  and calibration curves were linear up to 50 mM  $\text{Na}_2\text{CO}_3$ . Elevated levels of purgeable organic compounds were found to be a potential interference in the determination of TIC with the FIRE system.

## INTRODUCTION

Carbonate ( $\text{CO}_3^{2-}$ ), bicarbonate ( $\text{HCO}_3^-$ ), and dissolved carbon dioxide ( $\text{H}_2\text{CO}_3^*$ ) are found in natural water sources and originate primarily from soluble minerals, the action of microorganisms, and the atmosphere, which contains carbon dioxide from many sources including photosynthesis and the combustion of fossil fuels (1). The sum of these three carbon-containing species,  $C_T$

$$C_T = [\text{H}_2\text{CO}_3^*] + [\text{HCO}_3^-] + [\text{CO}_3^{2-}] \quad (1)$$

(where  $[\text{H}_2\text{CO}_3^*]$  represents the total analytical concentration of dissolved  $\text{CO}_2$ , whether hydrated or not) is generally referred to as total inorganic carbon (TIC).

The presence of soluble carbonates and bicarbonates increases the capacity of water to neutralize acid and, thus, affects the pH and mineral content of the water. Since the concentrations of carbonate and bicarbonate also determine the scale-forming, corrosive, and coagulation/flocculation properties of water (2), the measurement of TIC is of fundamental importance in many environmental and industrial areas including oceanography (3, 4), water resource management (5), and water/wastewater treatment (2, 6).

Numerous analytical methods have been developed for the determination of TIC in water samples. Direct methods for TIC include chromatographic separation procedures (7, 8), spectrophotometric titrations (9-11), and nondispersive infrared absorption measurements of evolved  $\text{CO}_2$  gas (12, 13). However, since these direct methods tend to be time-consuming, tedious, and/or expensive, the most commonly used method for TIC determination is indirect and involves the measurement of the total alkalinity present in the solution.

Total alkalinity is defined as the quantitative capacity of water to neutralize strong acid (6). If it is assumed that the only Brønsted bases in the water sample are hydroxide,

carbonate, and bicarbonate (as is the case for many surface waters), then the total solution alkalinity will be given by [total alkalinity] =  $C_T(\alpha_1 + 2\alpha_2) + [\text{OH}^-] - [\text{H}^+]$  (2)

where  $\alpha_1$  and  $\alpha_2$  represent the fraction of total inorganic carbon present as bicarbonate and carbonate, respectively

$$\alpha_1 = \frac{[\text{HCO}_3^-]}{C_T} = \frac{[\text{H}_3\text{O}^+]K_1}{[\text{H}_3\text{O}^+]^2 + K_1[\text{H}_3\text{O}^+] + K_1K_2} \quad (3)$$

$$\alpha_2 = \frac{[\text{CO}_3^{2-}]}{C_T} = \frac{K_1K_2}{[\text{H}_3\text{O}^+]^2 + K_1[\text{H}_3\text{O}^+] + K_1K_2} \quad (4)$$

and  $K_1$  and  $K_2$  are the first and second dissociation constants of carbonic acid.

Previously developed methods for total alkalinity determination include measurement of the specific conductance of the solution (14) and titration of the water sample to a preselected end point using a strong acid and an indicator such as methyl orange or a potentiometer (5, 15). For natural water samples, the preselected end point may vary between 5.1 and 4.5 pH units and depends on a number of factors including the concentration of  $\text{CO}_2$  expected at the final stage of the titration (5). For some complex industrial wastewater samples, however, the titration end point may be as low as 3.7 pH units (5). Knowledge of the solution alkalinity (i.e., milliequivalents of acid added to the sample to obtain the desired pH) and the pH of the solution prior to titration allows the TIC to be determined from the equilibrium relationships between  $\text{CO}_2$ ,  $\text{HCO}_3^-$ , and  $\text{CO}_3^{2-}$  or from a graphical representation of these relationships, as in a Deffeyes diagram (16).

In order to maintain standards of taste, odor, and levels of dissolved minerals, the EPA has established a primary drinking water regulation that requires monitoring of total alkalinity by every municipal water treatment plant in the country (2). Solution alkalinity is also routinely monitored in many applications where the corrosive and scale-forming tendencies of water must be controlled. It should be borne in mind, however, that because alkalinity is an aggregate property of the water, alkalinity determinations are subject to many interferences, and the results can be strictly related to TIC only when the entire chemical composition of the water is known. Furthermore, since proper selection of the end-point pH requires prior knowledge of the water composition, the great variation in sample characteristics introduces a considerable uncertainty in the final results. For example, the flocculating properties of clay-based drilling muds used in petroleum recovery is highly dependent on TIC, but alkalinity titrations provide only a very approximate idea of the true TIC content of such complex samples (17). Thus, there is a real need for a direct method of TIC determination which is quick, simple, inexpensive, reproducible, and not subject to the uncertainties resulting from sample variability.

This paper reports the development of a new method for the direct determination of TIC based on the principle of flame infrared emission (FIRE) detection first described by Busch and Hudson (18, 19). In essence, the FIRE-TIC instrument consists of two commercially available purge devices coupled to a FIRE detector. Water samples are acidified in

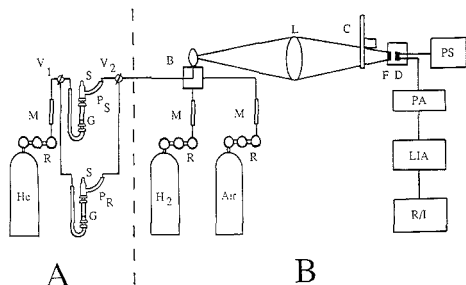


**Figure 1.** Schematic diagram of FIRE instrument for determination of total inorganic carbon in water samples: purge section (1A), FIRE detector (1B); He, helium cylinder; R, regulator; M, flowmeter;  $V_1$ ,  $V_2$ , three-way valves; S, rubber septum; G, glass frit;  $P_S$ , sample purge device;  $P_R$ , reference purge device;  $H_2$ , hydrogen cylinder; Air, air cylinder; B, burner; L,  $CaF_2$  lens; C, chopper; F, band-pass filter; D, PbSe detector; PS, power supply; PA, preamplifier; LIA, lock-in amplifier; R/I, recorder-integrator.

the purge device to convert bicarbonate and carbonate to carbon dioxide. The total  $CO_2$  is then purged from the sample cell by using an inert carrier gas and introduced into a low-background hydrogen/air flame where vibrational excitation of the  $CO_2$  molecule occurs. Direct determination of total inorganic carbon, as carbon dioxide, is accomplished by monitoring the  $4.42\text{-}\mu\text{m}$  infrared emission intensity from the excited  $CO_2$  molecule. Previous work in this laboratory has demonstrated that the  $4.42\text{-}\mu\text{m}$  asymmetric stretching vibration of carbon dioxide is analytically useful due to its relatively high emission intensity and its freedom from other strong overlapping infrared emission bands produced by the hydrogen/air flame (18, 19). The FIRE detector consists of a miniature capillary-head hydrogen/air burner, an optical collection lens, a band-pass filter to isolate the  $4.42\text{-}\mu\text{m}$   $CO_2$  emission band, and a PbSe photoconductive detector.

### EXPERIMENTAL SECTION

**Apparatus.** A schematic diagram of the FIRE-TIC instrument, shown in Figure 1, has been divided into two principal sections for purposes of discussion. Figure 1A shows the  $CO_2$  generation and purging portion of the apparatus, and Figure 1B shows the FIRE detection system.

**Purge Apparatus.** Two purge devices (Model 991710, Wheaton Scientific, Millville, NJ) were connected together in parallel with 3.2 mm o.d. polyethylene tubing and two, three-way valves (Model B-42XS4, Whitey Co., Highland Heights, OH). Each purge device consisted of a 5-mL, demountable glass tube, equipped with a fritted glass disk, and an inlet and outlet opening for the purge gas. A third opening at the top of the purge device was fitted with a rubber septum (Model Z12,433-8, Aldrich Co., Milwaukee, WI) and used for sample introduction. The purge tube with its associated frit was attached to the purge device with plastic screw-caps and could be disconnected for cleaning between sample injections. Water samples and sulfuric acid aliquots were injected into the purge tubes with a glass syringe (water sample syringe, Model 1002, Hamilton Co., Reno, NV; acid syringe, Model 2300, Becton-Dickinson & Co., Rutherford, NJ).

The pressure of the helium purge gas was regulated at 0.75 atm with a three-stage regulator constructed by coupling a single-stage regulator (Model 6200, Rexarc Co., West Alexandria, OH) to a conventional dual-stage unit (Model 2068, Rexarc). The helium flow rate was monitored with a Brooks Instrument flowmeter (Model 1110-05F1A1A Brooks Instrument Division, Emerson Electric Co., Hatfield, PA) corrected for helium. The output of the helium flowmeter was connected to the purge device with 6.4 mm o.d. polyethylene tubing and Swagelok fittings (Crawford Fitting Co., Solon, OH).

**FIRE Detection System.** The components of the FIRE detection system were mounted on a  $39.5 \times 29.1 \times 2.0$  cm aluminum plate and consisted of a hydrogen/air burner, collection lens,

optical chopper, optical band-pass filter, and PbSe detector. The associated electronics included a preamplifier, lock-in amplifier, and recorder/integrator.

The premixed hydrogen/air, capillary-head burner was fabricated from an aluminum block and has been described previously (19). The burner head consisted of a circular array of six stainless-steel capillary tubes surrounding a seventh capillary, each having a 0.6 mm i.d. Fuel and oxidant gases were premixed within the burner body and introduced through the six outer capillaries. The center capillary was connected to the outlet valve of the purge assembly with a modified Swagelok male connector and 3.2 mm o.d. Teflon tubing. With this design, the sample and purge gases could be introduced directly into the flame without premixing with the fuel and oxidant gases. The burner was enclosed with an aluminum shield and chimney assembly to minimize signal fluctuations resulting from air drafts and changes in ambient temperature conditions.

As in the case of the helium purge gas, pressure regulation of the fuel and oxidant gases was accomplished through three-stage regulation. A hydrogen dual-stage regulator (Model 2067HY, Rexarc) was coupled to a hydrogen-line regulator (Model 6203, Rexarc), and an air dual-stage regulator (Model 2067A, Rexarc) was coupled to an air-line regulator (Model 6200, Rexarc). The hydrogen and air flow rates were controlled with variable area flowmeters (Models J3216-06 and J3216-16, respectively, Cole-Parmer Instrument Co., Chicago, IL). Fuel and oxidant gases were used without purification to remove residual carbon dioxide which might be present.

The optimum flow rates for hydrogen and air were determined to be 324 and 754 mL/min, respectively. These flow rates correspond to a fuel-to-air ratio of 3:7 and were chosen because they produced the lowest flame background noise signal without flame lift-off from the burner head.

The infrared emission from the flame was collected and directed onto the detector by using an F/2, 5-cm focal-length,  $CaF_2$  lens (part 43150, Oriol Corp., Stratford, CT). A laboratory-constructed chopper modulated the infrared radiation at 575 Hz. The  $4.42\text{-}\mu\text{m}$   $CO_2$  emission band was isolated optically by means of a  $4.4\text{-}\mu\text{m}$  optical band-pass filter (part 58300, Oriol) placed immediately before the detector. A PbSe photoconductive cell (part P2038-01, Hamamatsu Corp., San Jose, CA), operated at a 30-V bias potential, served as the infrared detector.

The preamplifier circuit used with the PbSe detector has been previously described (18). The preamplified signal was demodulated by a lock-in amplifier (Model 3962, Ithaco Corp., Ithaca, NY) and recorded on a plotter/integrator (Model HP3396A, Hewlett-Packard Corp., North Hollywood, CA). A 1-s time constant was employed in the lock-in amplifier for all measurements.

**Reagents.** All chemicals were A.C.S. reagent grade and were used without further purification. Stock solutions of 4.0 and 10.0 mM  $Na_2CO_3$  (Mallinckrodt, Inc., St. Louis, MO) were prepared by dissolving primary standard  $Na_2CO_3$ , dried at  $110^\circ C$  for 24 h, in deionized water. The laboratory deionized water was further conditioned by passing it through two mixed-bed deionizing columns. Standard  $Na_2CO_3$  solutions, having concentrations of 0.1, 0.5, 1.0, 2.0, 4.0, 5.0, 8.0, and 10 mM, were prepared immediately before use by diluting aliquots of the stock solutions to the appropriate volumes.

**Procedure.** Natural water samples were obtained from several local sources and stored according to standard procedures (5). For alkalinity-determined TIC, the water samples were titrated with 0.0219 N  $H_2SO_4$  to an end point of 4.8 pH units. A Fisher Accumet Model 825MP pH meter was used for all measurements.

For TIC determinations performed with the FIRE-TIC system, one of the purge devices (Figure 1A) served as the sample chamber while the other served as the reference chamber. As part of the warm-up procedure, He purge gas was directed through the sample purge tube by using the dual, three-way valve system, and a 2-mL volume of deionized water was injected onto the frit of the reference purge tube with a syringe. The He gas was then rerouted through the reference purge tube, the flame lit, and the FIRE-TIC instrument allowed to warm up until a stable base line was obtained on the chart recorder.

When the instrument had stabilized, a 0.5-mL volume of 3 M  $H_2SO_4$  (Mallinckrodt) was introduced onto the frit of the sample

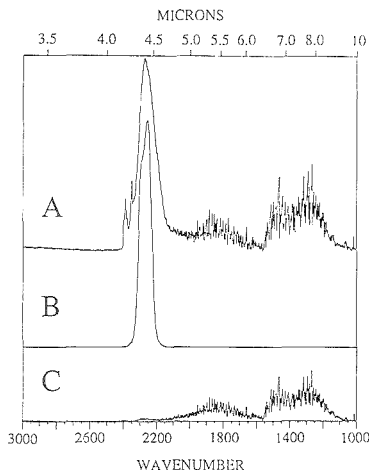


**Figure 2.** Fourier-transform infrared spectra from 3000 to 1000  $\text{cm}^{-1}$ . (A) and (C) are emission spectra plotted on the same relative intensity scale (not corrected for instrument response). (A) Flame infrared emission from a hydrogen/air flame containing carbon dioxide showing the strong  $\text{CO}_2$  asymmetric stretching vibration at 2264  $\text{cm}^{-1}$ . (B) Transmission spectrum of the band-pass filter used in the FIRE detector (maximum transmission at 4.42  $\mu\text{m}$  75% T, <0.10% T elsewhere). (C) Flame infrared emission from a hydrogen/air flame in the absence of carbon dioxide showing the background emission from water.

purge tube. The He flow was then switched from the reference to the sample chamber, and the acid was purged with helium for approximately 30 s. With He flow maintained, a 1.0-mL volume of a carbonate-containing water sample was injected onto the 3 M sulfuric acid aliquot contained in the sample purge tube. The carbon dioxide resulting from sample acidification was purged from the solution and carried into the flame where vibrational excitation occurred. Once the resulting infrared emission peak profile had been recorded, the sample purge tube was disconnected and rinsed with deionized water to remove the residual acid, and the process was repeated with subsequent standards to permit the preparation of a calibration curve of peak emission intensity versus concentration.

Sample determinations were carried out with 1.0-mL sample volumes using the same procedure as used in preparing the calibration curve. Sample concentrations were read from the calibration curve by using measured peak heights.

## RESULTS AND DISCUSSION

**Instrumental Configuration.** The FIRE-TIC detection system described in this paper has evolved over several years of development and represents the best of the various configurations that have been studied in this laboratory. The basic detection system, shown in Figure 1B, was similar to that described earlier (19) with several modifications. As shown in Figure 1B, a  $\text{CaF}_2$  lens was added to improve the collection efficiency of the infrared radiation emitted by the flame. The location of this lens was determined experimentally by optimizing the signal-to-noise ratio (SNR) obtained with the system.

The optical band-pass of the FIRE detector was also modified over the previous design by replacing the short-wavelength cutoff filter (18, 19) with a narrow band-pass optical filter. With the short wavelength cutoff filter in place, the system had an optical band-pass that extended from 3.5 (the cutoff for the filter) to 5.5  $\mu\text{m}$  (the cutoff for the  $\text{PbSe}$  detector). This band-pass, which was much wider than the 4.42- $\mu\text{m}$  asymmetric-stretching band of carbon dioxide (Figure

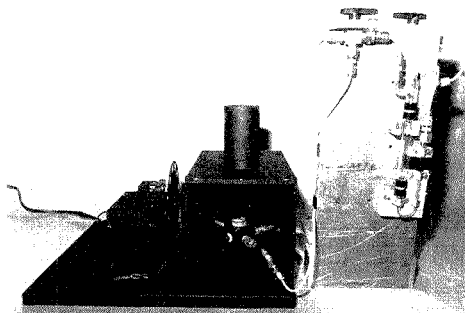


**Figure 3.** Photograph of the FIRE-TIC instrument showing the chimney and enclosure used to shield the flame. The front plate of the enclosure/chimney assembly has been removed to show the burner and lens.

2A), included significant amounts of unwanted water emission bands (Figure 2C) and raised the detector background level considerably.

A 4.4- $\mu\text{m}$  optical band-pass filter with a full-width at half maximum height (fwhm) of 0.15  $\mu\text{m}$  was selected to reduce the effect of unwanted flame background. Tilotta et al. (20) have shown by means of Fourier transform infrared spectroscopy that at hydrogen/air flame temperatures (approximately 2000  $^{\circ}\text{C}$ ) the carbon dioxide atmospheric emission bandhead is centered at 4.42  $\mu\text{m}$  with a fwhm of 0.21  $\mu\text{m}$  and the water emission bands occur in the 4.04–8.70- $\mu\text{m}$  spectral region. Figure 2B shows the spectrum of the 4.4- $\mu\text{m}$  band-pass filter over the spectral region from 3.33 to 10.00  $\mu\text{m}$ . Use of this band-pass filter was found to significantly reduce the detector signal arising from the flame background, thereby lowering the minimum detectable level of carbon dioxide that could be observed.

Finally, the housing and chimney assembly shown in Figure 3 were added to enclose the burner and the optical path to the  $\text{CaF}_2$  lens. This shielding was found to significantly reduce flame-flicker noise due to air drafts as well as long-term drift arising from extraneous organic contaminants found in the laboratory air.

**Sample Introduction.** Although it is clear from previous studies (18, 19) that the FIRE detector should be capable, in principle, of determining the carbon dioxide liberated from an aqueous sample upon acidification, a key factor in the successful application of FIRE measurements to the determination of TIC in water samples is the means used to introduce the liberated carbon dioxide into the flame. During the course of this study, two basic approaches were tested—the first employing a static equilibrium method and the second employing a rapid purge method.

In the static equilibrium approach (21), a 100-mL sample of the TIC-containing water was acidified, and a mechanically driven propeller was used to equilibrate the resulting carbon dioxide between the solution and the head space above the liquid. After the propeller had been activated for a fixed time period, the head-space gas was flushed into the flame with an inert carrier gas. However, because the amount of carbon dioxide reaching the flame did not equal the total amount of carbon dioxide present in the system, sample sizes on the order of 100 mL were required for good detection limits. Furthermore, difficulties encountered in fabricating a "leak-proof" head-space analysis chamber resulted in reproducibilities of only about 3%.

In contrast, the purge-tube approach is a stripping method that is capable of removing dissolved carbon dioxide both

rapidly and quantitatively. Rapid degassing produced more reproducible peak shapes, and quantitative stripping of the dissolved carbon dioxide allowed the sample size to be reduced by a factor of 100 compared with the head-space equilibration approach.

The commercially available purge devices used in this study were readily interfaced to the FIRE detector and were found to be effective in stripping the carbon dioxide gas from the aqueous samples. In addition to the sample purge device containing the water sample for TIC determination, a reference purge device filled with degassed water was installed in order to maintain a constant flow of helium and water vapor to the FIRE detector between sample injections (Figure 1A). The reference purge device was found to be useful in minimizing the difference between the base-line signal obtained with the helium purge gas flowing into the flame (during actual TIC determinations) and the signal obtained while the sample purge tube was disconnected. This base-line difference is presumably due to the cooling effects of both the helium purge gas and the water vapor on the hydrogen/air flame.

The concentration of  $\text{CO}_2$  in the flame, which gives rise to the total  $\text{CO}_2$  emission signal, is a function of the TIC in the water sample, the rate of  $\text{CO}_2$  degassing from the acidified water sample (which depends upon the sample introduction method), the transport rate of  $\text{CO}_2$  out of the purge device, and the dead-space volume in the purge apparatus. The dead-space volume was kept to a minimum by using small volume purge tubes and short lengths of narrow inside diameter polyethylene tubing for interconnections.

The  $\text{CO}_2$  arising from the TIC present in these aqueous samples was purged into the FIRE detector by using helium gas. Faster helium flow rates produced more rapid stripping of the dissolved carbon dioxide, thereby increasing peak heights and SNR's, but also tended to force the sample out of the purge tube during the analysis. For the particular purge device used in this study, a helium flow rate of 55 mL/min was found to minimize the time required for removal of the  $\text{CO}_2$  from the water sample without risking sample loss.

Poor regulation of the He flow rate was found to cause instability in the transport rate of the  $\text{CO}_2$  into the FIRE detector and resulted in increased variability in the measured peak emission signal. In order to maintain a stable helium flow rate, a line regulator was installed at the outlet of the two-stage helium regulator to provide additional regulation. Carbon dioxide gas purged into the flame under this triple-stage helium regulation produced peak emission signals with a variability of 30–50% less than those signals that were obtained under dual-stage regulation.

**System Performance.** With the prototype system described in this paper, the total time required for signal acquisition from a sample was approximately 2.5 min (from sample injection to purge-tube disconnection and cleanup). Figure 4 shows typical  $\text{CO}_2$  peak shapes obtained from acidifying equivalent volume sample injections of different concentration  $\text{Na}_2\text{CO}_3$  solutions with 0.5 mL of 3 M  $\text{H}_2\text{SO}_4$ . The small negative signals (below the base line) which precede the positive  $\text{CO}_2$  emission peaks coincide with the injection of the water samples and do not impair the measurement of peak height. Although the exact cause of the negative pen deflections is not known, these "inverse" signals may arise from the rapid injection of the water samples, which causes an amount of He proportional to the sample volume to be instantaneously displaced into the flame. The increase in helium may momentarily cool the flame and also displace the vertical height at which the maximum emission of the water background occurs. Both of these factors reduce the flame water-band background emission signal. The slight tailing at the trailing edge of each of the peaks may result from

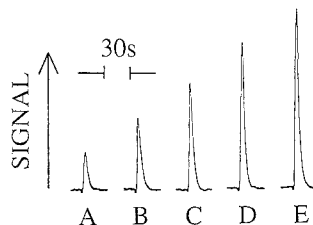


**Figure 4.** Carbon dioxide signal profiles obtained by acidification for a series of 1.0-mL injections of  $\text{Na}_2\text{CO}_3$  solutions with different concentrations: A, 1.0 mM; B, 2.0 mM; C, 3.0 mM; D, 4.0 mM; E, 5.0 mM.

mixing effects (exponential dilution) in the dead-space volume of the purge assembly.

The reproducibility of the FIRE-TIC system was studied by recording the  $\text{CO}_2$  signals obtained from acidifying eight 1.0-mL injections of a 4.0 mM  $\text{Na}_2\text{CO}_3$  standard. Since the FIRE detector has been reported to exhibit a mass flow-rate response (19), the area under the emission peak should be proportional to the total amount of  $\text{CO}_2$  gas liberated from the TIC in the water sample. As a result, it was anticipated that emission peak area measurements would be more reproducible than the corresponding emission peak height measurements.

This was not the case, however, for measurements made with the present system. By use of the Hewlett-Packard HP3396A plotter/integrator, it was determined that the relative standard deviation (RSD) for the eight emission peak height measurements (measured from the base line "zero" level and ignoring the initial slight negative pen deflection) was 1.35%. By contrast, the RSD for the eight emission peak area measurements was 2.11%. Since the signal profiles resulting from the purge-tube sample introduction system have nearly vertical leading edges, the difference between the reproducibility in the peak area measurements and peak height measurements most probably occurs in the trailing edge of the peak profiles. This additional error apparently affects only the peak areas and may arise from irreproducibility in the mixing of the purged  $\text{CO}_2$  with the helium purge gas, pressure and flow rate fluctuations in the purge gas, or electronic difficulties in either measuring the peak area or recording the signal from the lock-in amplifier.

Since the peak height measurements were consistently more reproducible for the standards and aqueous samples tested in this study, peak height measurements were used exclusively. For  $\text{CO}_2$  signals obtained after acidifying 1.0-mL injections of 4 mM  $\text{Na}_2\text{CO}_3$ , signal-to-noise ratios were approximately 262:1 ( $\text{SNR}_{\text{rms}}$ ). Based on these SNR's, it is believed that the reproducibility of the FIRE-TIC system is not limited by the FIRE detector itself, but rather by the sample introduction and/or purge steps.

The rubber septa at the column inlet joints allowed sample aliquots to be conveniently introduced into the purge tubes with a syringe. Similar to sample injections performed in gas chromatography, the reproducibility in sample injection volume and injection speed was found to be important in determining the reproducibility of the emission peak-height signal. The manufacturer's reported mechanical reproducibility of the syringe used for water sample introduction was one percent and may partially account for the RSD in the peak height replications. Also, since peak heights were measured by using a millimeter scale, a reading error of  $\pm 0.5$  mm is expected. Since the peak heights that resulted from the 4 mM  $\text{Na}_2\text{CO}_3$  injections were about 59 mm, this reading error amounts to approximately 1%.

Calibration curves for  $\text{CO}_2$  were prepared from acidified 0.10–50 mM  $\text{Na}_2\text{CO}_3$  standards and were found to be linear

Table I. Comparison of TIC Results for Selected Water Samples

water sample	method I <sup>a</sup>	method II <sup>b</sup>			method III <sup>c</sup>		
	mM	mM	% RSD	% rel error	mM	% RSD	% rel error
Hewitt tap	7.21 ± 0.01 <sup>d</sup>	7.26 ± 0.08 <sup>d</sup>	1.10	+0.69	6.65 ± 0.10 <sup>d</sup>	1.50	-7.77
Waco tap	2.13 ± 0.01	2.11 ± 0.00	0.00	-0.94	1.75 ± 0.00	0.00	-17.84
Lake Brazos	2.93 ± 0.01	2.96 ± 0.03	1.01	+1.02	2.61 ± 0.03	1.15	-10.92
Brazos River	3.65 ± 0.01	3.73 ± 0.04	1.07	+2.19	3.32 ± 0.05	1.51	-9.04
Bosque River	3.93 ± 0.01	3.98 ± 0.05	1.26	+1.27	3.56 ± 0.07	1.97	-9.41

<sup>a</sup> TIC from total alkalinity determination. <sup>b</sup> FIRE-TIC; aqueous sample added to purged acid. <sup>c</sup> FIRE-TIC; acid added to aqueous sample. <sup>d</sup> Standard deviation of four determinations.

(correlation coefficient of 0.9996). The linear regression equation for a typical calibration curve possessed a slope of 14.65 mm/mM with a  $y$  intercept of 0.08 mm. The TIC detection limit for the FIRE-TIC system, defined as a concentration producing a signal equivalent to twice the root mean square noise, was found to be 0.366 ppm C (corresponding to 1.34 ppm CO<sub>2</sub>). This detection limit is believed to be governed by the noise present in the flame water-band background emission, which slightly overlaps the 4.42- $\mu$ m CO<sub>2</sub> emission band.

**Precision and Analytical Accuracy.** The analytical performance of the FIRE-TIC system was evaluated with five natural water samples collected from various locations around the Waco area. These water samples included tap water from the city of Waco and the nearby community of Hewitt, and water from Lake Brazos, the Brazos River, and the Bosque River. Tap water for the city of Waco can be classified as a surface water and is taken from Lake Waco, an artificial lake formed by damming the North Bosque River. Hewitt tap water is a groundwater that is taken from a deep water well supplied from the Hosston aquifer. These water samples are characteristic of those commonly found in Central Texas and are classified as very hard (hardness levels often in excess of 300 mg of CaCO<sub>3</sub>/L).

Table I shows a comparison of the TICs determined by alkalinity titration (method-I) with those obtained by the FIRE system for four replications of the five natural water samples described above. The alkalinity titration measurements were converted into TIC values by using eq 2 and the initial pH values of the water samples measured prior to the titration. As shown in the table, each water sample was analyzed with the FIRE system by using two different sample introduction methods. In Table I, the method II denotes the TIC determined by introducing the sample according to the sequence outlined in the Experimental Section while method III denotes the TIC determined by introducing the acid into the purged aqueous sample.

From the table, it can be seen that the precision of the TIC values obtained with the FIRE system is quite good regardless of the method of sample introduction, although method II values have a slightly better precision (average RSD 0.89%) than method III values (average RSD 1.23%). The accuracy obtained with the two methods of sample introduction is dramatically different, however. Taking the alkalinity TIC values as the "true" measurement of the solution TIC, it can be seen that the average relative error for the five water samples obtained by using method III is 11.00% low. By use of the sample introduction procedure denoted in method II, the average relative error for the five water samples is only 1.22%.

The low TIC values obtained by purging the water samples before acidification (method III) undoubtedly result from the loss of CO<sub>2</sub> by degassing. This loss was unavoidable with this sample introduction method because the purge gas must be allowed to flow through the sample purge device for a time period sufficient to give a stable base line before the acid is

added. While addition of NaOH prior to purging would convert dissolved CO<sub>2</sub> to carbonate and so avoid losses from degassing, this procedure is subject to interferences from carbonate contamination in the NaOH solution and from further solubilization of carbon dioxide present in the air. Alternatively, degassing loss can be avoided with the present system by adding the sample to the acid (method II). With this procedure, the sulfuric acid in the purge tube is stripped of any dissolved CO<sub>2</sub> and a stable base line is obtained prior to injecting the water sample.

To assess the accuracy of the FIRE system, it should be emphasized that the reference method (alkalinity titration, method I) is not totally error free. Even in the absence of interferences (other Brønsted bases), TIC determinations based on alkalinity titrations require an additional measurement (usually pH) to convert the titration value into TIC. The need for two measurements increases the errors associated with alkalinity titrations as a means of TIC determination. With this in mind, the agreement between the TIC values obtained by titration with method II is quite good.

**Interferences.** It is well-known that the presence of other protolysis systems such as borates, phosphates, and ammonia can lead to errors in TIC determinations by means of alkalinity titrations (5). The presence of additional unsuspected Brønsted bases invalidates the proton condition given in eq 2 and leads to incorrect TIC values by titration. Since the concentrations of borate, phosphate and ammonia present in natural water samples can reach levels as high as 5 mg/L B (5), 0.4 mg/L P (22), and 30 mg/L N (5), respectively, the effect of these potential interferents on the FIRE-TIC determinations was studied.

To determine the effect of these non-carbonate bases on the TIC measurements performed with the FIRE system, TIC determinations were performed on 4 mM Na<sub>2</sub>CO<sub>3</sub> standards which had been spiked with each of these three bases in amounts 10 times greater than the maximum concentration expected for natural waters using the sequence outlined in the Experimental Section. Since no differences were observed between the peak height signals in the spiked water samples compared with the unspiked samples, it was concluded that the presence of ammonia, phosphate, and borate in natural water samples will not give rise to an interference with the FIRE-TIC system.

Although the presence of ammonia, phosphate, and borate does not lead to interferences with the FIRE-TIC determinations, the presence of purgeable organic compounds (POC's) could lead to errors with the FIRE system if the organics are stripped from solution and combusted to CO<sub>2</sub> in the flame. In order to determine the extent to which POC's may interfere with the TIC determinations performed with the FIRE system, 1.0-mL aliquots of water saturated with cyclopentane were injected into the purge tube and purged with He, and the resulting gases were introduced into the hydrogen/air flame. (The solubility of cyclopentane in water is 0.01% (w/w) (23), giving a solution concentration of approximately 100 ppm.) The resulting carbon dioxide emission signals were

equivalent to those signals obtained from 1.0-mL injections of 12 mM Na<sub>2</sub>CO<sub>3</sub> solutions. This demonstrates that the presence of elevated levels of POC's in contaminated water can lead to significant positive errors in the TIC values obtained with the FIRE system. However, as indicated by the data in Table I, under normal conditions and using natural water samples, this interference does not appear to be too severe. Since the maximum contaminant level (MCL), for most volatile organics is regulated at levels well below 1 ppm (24), the positive error in the TIC values obtained with the FIRE system should not exceed 2% for drinking water.

For those samples where elevated levels of POC's are expected, some means of obtaining a corrected TIC signal must be used. One possibility is installation of an in-line hydrocarbon trap to prevent the organics from reaching the flame. Alternatively, a carbon dioxide trap (Ascarite) could be installed between the purge assembly and the flame. If two injections of the water sample were made, one with and one without the trap, the difference between the two carbon dioxide emission signals should give the corrected TIC measurement. These, and other approaches are currently being studied in this laboratory and will be presented in a future paper.

### CONCLUSIONS

The FIRE detection system described in this paper has been shown to be a sensitive, reproducible, accurate, and direct means of determining total inorganic carbon in water samples. It is easy to use and requires only a 1-mL sample for each determination. In its present stage of development in the laboratory, the time required for signal acquisition from a sample is 2.5 min from sample injection to purge-tube disconnection and cleanup. The system is easily amenable to automation, however, and a multiple purge-tube version can easily be envisioned. The interference caused by purgeable organics in water opens up the possibility of developing a combined TIC/POC monitor, and we are currently investigating this possibility.

### LITERATURE CITED

- (1) Stumm, W.; Morgan, J. J. *Aquatic Chemistry*, 2nd ed.; John Wiley: New York, 1981; Chapter 4.

- (2) *Introduction to Water Treatment: Principles and Practices of Water Supply Operations*; American Water Works Association: Denver, CO, 1984, Vol. 2, and 1982, Vol. 4.
- (3) Almgren, T.; Dyrssen, D.; Fonselius, S. In *Methods of Seawater Analysis*, 2nd ed.; Grasshoff, K., Ehrhardt, M., Kremling, K., Eds.; Verlag Chemie: Weinheim, Germany, 1983; Chapter 8.
- (4) Dyrssen, D.; Wedborg, M. *Mar. Chem.* **1982**, *98*, 183-185.
- (5) *Standard Methods for the Examination of Water and Wastewater*, 15th ed.; Greenberg, A. E., Connors, J. J., Jenkins, D., Eds.; American Public Health Association, American Water Works Association, and Water Pollution Control Federation: Washington, DC, 1980; pp 235-257.
- (6) *Basic Science Concepts and Applications: Principles and Practices of Water Supply Operations*; American Water Works Association: Denver, CO, 1984.
- (7) Brandt, G.; Matuschek, G.; Ketrup, A. *Fresenius' Z. Anal. Chem.* **1985**, *321*, 653-654.
- (8) Park, K.; Kennedy, G. H.; Dobson, H. H. *Anal. Chem.* **1964**, *36*, 1686.
- (9) Stuart, W. A.; Lister, A. R. *Desalination* **1970**, *8*, 69-72.
- (10) Graneli, A.; Anfalt, T. *Anal. Chim. Acta* **1977**, *91*, 175-180.
- (11) Underwood, A. L.; Howe, L. H. *Anal. Chem.* **1962**, *34*, 692-694.
- (12) Van Hall, C. E.; Stenger, V. A. *Anal. Chem.* **1967**, *39*, 503-507.
- (13) Pobiner, H. *Anal. Chem.* **1962**, *34*, 878-879.
- (14) Kramer, J. R. In *Water Analysis*; Minear, R. A., Keith, L. H., Eds.; Academic Press: New York, 1982; Vol. 1, Part 1, Chapter 3.
- (15) Faust, S. D.; Aly, O. M. *Chemistry of Natural Waters*; Ann Arbor Science: Ann Arbor, MI, 1981; pp 128-139.
- (16) Defeyes, K. S. *Limnol. Oceanogr.* **1965**, *10*, 412.
- (17) Garrett, R. L. *J. Pet. Technol.* **1978**, (June), 860-868.
- (18) Hudson, M. K.; Busch, K. W. *Anal. Chem.* **1967**, *59*, 2603.
- (19) Hudson, M. K.; Busch, K. W. *Anal. Chem.* **1988**, *60*, 2110.
- (20) Tlotta, D. C.; Busch, K. W.; Busch, M. A. *Appl. Spectrosc.* **1989**, *43*, 704-709.
- (21) Busch, K. W.; Busch, M. A.; Kubala, S. W.; Ravishanker, M. 39th Pittsburgh Conference on Analytical Chemistry and Applied Spectroscopy, New Orleans, LA, 1988; Abstract 709.
- (22) Manahan, S. E. *Environmental Chemistry*; Willard Grant Press: Boston, MA, 1979.
- (23) *High Purity Solvent Guide*, 2nd ed.; Przybytek, J. T., Ed.; Burdick and Jackson Laboratories: Muskegon, MI, 1982; p 34.
- (24) *Water Treatment Principles and Design*; J. M. Montgomery, Consulting Engineers, Inc.; John Wiley: New York, 1985; Chapter 4.

RECEIVED for review January 30, 1989. Accepted May 1, 1989. This work was supported by Baylor University Research Grants 012-S85-URC, 006-S87-URC, 007-F87-URC, and 11.510. Portions of this paper were presented at the 39th Pittsburgh Conference & Exposition on Analytical Chemistry & Applied Spectroscopy (paper No. 709, February 24, 1988, New Orleans) and the 15th Annual Federation of Analytical Chemistry & Spectroscopy Societies Meeting (paper No. J05, October 31, 1988, Boston).



# Limitations of Spectrophotometric Multicomponent Analysis of Metal Ions with Mixed Reagents

Matthias Otto\*

Department of Chemistry, Bergakademie Freiberg, Akademiestrasse 6, 9200 Freiberg, German Democratic Republic

Wolfhard Wegscheider

Institute for Analytical Chemistry, Micro- and Radiochemistry, Graz University of Technology, Technikerstrasse 4, A-8010 Graz, Austria

**Simultaneous analysis of metal ions is explored by means of a two-component reagent consisting of Tiron and 2-pyridine-aldoxime. The influence of experimental conditions, i.e. pH and metal and reagent concentrations, on the spectral system is studied by computer simulations in a model system containing six metal analytes and 24 equilibrium species in total. From this study an analytical procedure on the basis of multivariate calibration and data reduction with the partial least-squares algorithm is derived that enables copper, iron, and titanium to be determined simultaneously in aluminum reference samples with mean relative errors of less than 15%.**

Multicomponent analysis (MCA) by means of spectrophotometry in the UV-visible spectral range is used nowadays mainly for determining UV-absorbing compounds that are of practical importance in the pharmaceutical and clinical laboratory. For analyzing metal ions simultaneously by computer-aided spectrophotometric MCA, only few procedures have been proposed (1-4). This is reasoned by the fact that atomic spectrometric methods, ion chromatography, or also to some extent electroanalytical methods provide a powerful alternative to spectrophotometric determinations. However, the huge number of proposed spectrophotometric methods, their readiness for automation, and the need for dedicated systems in analytical process control, especially by using fiber-optical chemical sensors, justify further efforts for developing spectrophotometric methods of MCA for determining metal ions in solutions.

There are several problems with simultaneous determinations of metal ions in general. On the one hand, spectrophotometric reagents may be rather unselective; i.e., plenty of metals form complexes with very similar absorption spectra. Since such multicomponent systems have a very bad conditioning (in a mathematical sense), these systems are not appropriate for selective determination of metal ions by MCA. Typical reagents with such properties are derivatives of azo dyes, e.g. 4-(2-pyridylazo)resorcinol (PAR) or 4-(2-thiazolylazo)resorcinol (TAR), and of triphenylmethane dyes, such as Xylon Orange or Bromophenol Blue.

On the other hand, there are complex forming agents, such as 1,10-phenanthroline, that form complexes with several metal ions, but only a few of them highly absorb in the visible spectral range. This again limits the number of simultaneously determinable metal species to say, two or three, which might even have quite similar absorption spectra.

In order to provide a basic means for spectrophotometric MCA of several metal ions, in this work the use of mixed organic reagents is proposed. The possibility of applying several reagents for spectrophotometric MCA of metal ions is derived from computer simulation of all the simultaneous equilibria in such a system. Optimum conditions are evaluated

for MCA of metal ions with the combined reagents Tiron (1,2-dihydroxybenzene-3,5-disulfonic acid, disodium salt) and 2-pyridinealdoxime, and the possibilities of a PLS (partial least squares) (5-7) based determination of titanium, iron, and copper in aluminum alloys are reported.

## EXPERIMENTAL SECTION

**Apparatus and Computations.** Digital values for absorbances were obtained from recording the spectra by means of a two-channel Model SPECORD M40 spectrophotometer (VEB Carl Zeiss Jena).

Simulations of simultaneous metal-ligand equilibria were run on an Atari 260ST computer with a BASIC version of the algorithmically improved program COMICS (8).

Multicomponent analysis was performed with the PLS algorithm (5, 2) on an IBM/AT computer in compiled Basic. The eigenvalues for reporting the condition number were calculated according to ref 9. Autoscaling was applied to all data before analysis.

**Reagents.** Analytical reagent grade chemicals were used throughout the work. Buffer solutions were prepared from sodium acetate (saturated solutions) and diluted as appropriate.

For preparation of stock metal ion solutions standard procedures were applied.

The titanium solution (0.16 mg of Ti/mL) was obtained from 0.1668 g of TiO<sub>2</sub> treated with a 10-fold amount of K<sub>2</sub>S<sub>2</sub>O<sub>8</sub> in a Pt crucible and heated up to dissolution in the melt. At the end of digestion some drops of concentrated sulfuric acid are added. The cooled melt is dissolved in 2 M H<sub>2</sub>SO<sub>4</sub> and made up to a volume of 100 mL. The final stock solution is prepared by further dilution of 8 mL of the titanium solution to 50 mL.

Copper stock solutions (1 mg of Cu/mL) were prepared by dissolving 0.2683 g of CuCl<sub>2</sub>·H<sub>2</sub>O in 100 mL of water.

The iron solution (0.32 mg of Fe/mL) was made in a 250-mL flask from 0.968 g of FeCl<sub>3</sub>·H<sub>2</sub>O dissolved in 0.1 N hydrochloric acid. Before use the solution is diluted by a factor of 2.5.

**Aluminum Solution.** For analysis in aluminum alloys 6 g of pure Al foil (for calibration) or aluminum alloy (as sample) is dissolved in a 1:1 diluted hydrochloric acid solution by gentle heating. In order to accelerate the dissolution, one to two drops of 1% HgCl<sub>2</sub> solution can be added. After evaporation to near dryness the residue can be dissolved in water and transferred to a 100-mL volumetric flask made up with redistilled water to the final volume.

**Procedure.** In a 100-mL beaker to the analyte solution (10 mL of the aluminum sample solution or for calibration 10 mL of dissolved aluminum foil and the appropriate metal ion solutions (cf. Table I)) is added 15 mL of buffer solution, and the pH is adjusted at 4 with diluted hydrochloric acid (diluted 1:1 with water). This solution is transferred to a 100-mL volumetric flask that contains 5 mL of the 2-pyridinealdoxime solution and 10 mL of Tiron solution, and the flask is made up with water. After 5 min the solution is transferred to a 0.5-cm cuvette, and the absorbances are recorded between 340 and 630 nm every 10 nm. The digitized absorbances are used for the computations as described above.

## RESULTS AND DISCUSSION

**Choice of Spectrophotometric System.** The suitability of a spectrophotometric metal complex system is to be judged

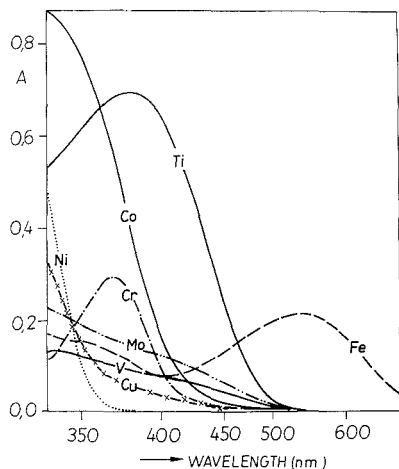


Figure 1. Absorption spectra of eight metal ions with the mixed reagents Tiron and 2-pyridinealdoxime at pH 6. Concentrations: metal ion,  $5 \times 10^{-5}$  M each; reagent,  $1.5 \times 10^{-3}$  M each.

Table I. Typical Condition Numbers for Characterizing the Selectivity of the Spectrophotometric System with the Reagents Tiron/2-Pyridinealdoxime

analyte	cond (K)
Ti, Fe	4.61
Ti, Fe, Co	11.86
Ti, Fe, Co, Mo	374
Ti, Fe, Co, Mo, Cr	1910
Ti, Fe, Co, Mo, Cr, Cu	2934
Ti, Fe, Co, Mo, Cr, Cu, Ni	544163
Ti, Fe, Co, Mo, Cr, Cu, Ni, V	(neg eigenvalues)

at first from its selectivity, i.e. the degree of overlap between the different spectral component bands. This can be quantitatively characterized by the condition number (4) as described elsewhere (10).

Secondly, compromise conditions have to be found for complex formation of the different metal ions with the spectrophotometric reagents with respect to pH, ionic strength, and reagent concentrations.

With these restraints taken into account, the number of suitable systems is rather limited. As potential reagents we studied pyrogallol red, bathocuproin disulfonic acid, 7,8-dihydroxy-4-methylcumarin, 5,7-dibromoquinoline, Tiron, and 2-pyridinealdoxime and  $\alpha$ -benzildioxime. A system that simultaneously responds to 2- and higher-valued metal ions was found with the reagents Tiron and 2-pyridinealdoxime. Tiron forms colored complexes of high absorption with Fe(III), Ti(IV), V(V), or Mo(VI). The second reagent, 2-pyridinealdoxime, reacts with Fe(III), Mn(II), Ni(II), V(V), Co(II), or Cu(II) to form light-absorbing species.

Typical spectra of the reagent mixture with eight metals are given in Figure 1. As expected there is a strong overlap of absorption bands so that it will be not possible to determine all of the eight metals simultaneously. This can also be seen from the conditioning of the system by using the condition number (10). The condition number increases with increasing number of metals to be determined, as shown in Table I. Empirically one knows (cf ref 10) that condition numbers much higher than 1000 do not enable precise determinations to be carried out. Of course, the analytical system can be optimized with respect to the experimental conditions as

Table II. Equilibrium Model for Computation of Complex Formation of Metal Ions with Tiron (T) and 2-Pyridinealdoxime (P)

species	log stability constant	species	log stability constant
HT	12.7 <sup>a</sup>	HP	10.0
H <sub>2</sub> T	20.4	H <sub>2</sub> P	13.4
FeT	20.7	CoP	8.6
FeT <sub>2</sub>	35.9	CoP <sub>2</sub>	17.2
FeT <sub>3</sub>	46.9	CuP	8.9
FeHT	22.7	CuP <sub>2</sub>	14.55
TiO(HT) <sub>2</sub>	40.5	NiP	9.4
TiT <sub>3</sub>	58	NiP <sub>2</sub>	16.5
VO <sup>+</sup> T	16.74	NiP <sub>3</sub>	22.0
CuT	14.5		
CuHT	18.2		
CoT	9.5		
CoHT	15.8		
NiT	9.96		
NiHT	15.7		

<sup>a</sup> At 25 °C and 0.1 M ionic strength.

evaluated here on the basis of a physicochemical model for practical analysis of the elements copper, titanium, and iron in light metal alloys.

**Chemical Equilibria in the Tiron/2-Pyridinealdoxime System.** To evaluate optimum conditions for simultaneous complex formation of the metal ions, a model system was studied that contained the metal ions Co(II), Cu(II), Ni(II), Fe(III), Ti(IV), and V(V) and the two ligands Tiron and 2-pyridinealdoxime as well.

The protolysis and complex formation constants used for the equilibrium simulations were taken from the literature (11) and are summarized in Table II. This system is to be taken as an approximate model only since it is based on standardized equilibrium constants, i.e. at a temperature of 25 °C and at 0.1 M ionic strength. The possibility of the occurrence of ternary complexes cannot be ruled out although no stability constants were found in the related literature. The model, however, is adequate to draw important conclusions for spectrophotometric MCA.

With respect to the metal ion complexes given in Table II one can differentiate between complexes that are analytically of importance, as they show high absorption in the visible range, and other species in which absorbance is negligible if their concentrations are lower than about  $10^{-3}$  M.

Analytically important complexes are formed by Co(II), Cu(II), and Ni(II) with 2-pyridinealdoxime and by Fe(III), Ti(IV), and V(V) with Tiron. Thus with the use of equilibrium simulations those experimental conditions are to be selected that guarantee the analytically important complexes to be present at their highest feasible concentrations.

At first, the influence of the pH value on the simultaneous equilibria was investigated at typical concentrations of the organic reagents Tiron and 2-pyridinealdoxime, i.e. 0.0075 M concentrations in each. The six metal ion concentrations were set at  $5 \times 10^{-5}$  M each. The species distributions between pH 2 and 8 are given in Figure 2 for every metal ion separately although in the computations all metal ions have been present simultaneously.

Cobalt forms complexes with 2-pyridinealdoxime (P) at pH values higher than 3.5. Since the 1:1 complex (CoP) exists at most for 30% of the total cobalt concentration, for the analytical procedure the pH should be at least 4 since the 1:2 CoP<sub>2</sub> complex is formed quantitatively (96%) only at pH 5. The formation of complexes of cobalt with Tiron is negligible.

The colored copper complexes with P exist only in a narrow pH range, and the main species is a 1:1 complex that is formed at about pH 4 by 66% of the total copper concentration. This

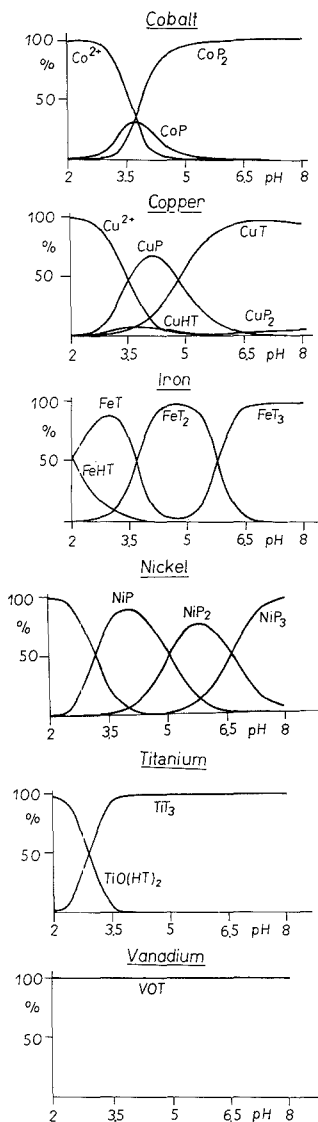


**Figure 2.** Equilibrium distribution of metal ion complexes in dependence on pH in solutions of Co(II), Cu(II), Fe(III), Ni(II), Ti(IV), and V(V) (each  $5 \times 10^{-5}$  M) and Tiron (T)/2-pyridinealdehyde (P) (each 0.0075 M).

is reasoned by the competing complex formation with Tiron (CuT). Thus, copper is bound quantitatively to Tiron at pH values higher than 6.5.

The three known colored Tiron complexes of iron (12) are distributed over the whole pH range studied. The blue 1:1 complex is mainly formed at a pH of about 3, the purple 1:2 Fe(III)-Tiron complex at about pH 5, and the red 1:3 complex at about pH 6.5. Thus, with respect to the best conditions for copper, the measuring of the 1:2 complex would be appropriate for the MCA.

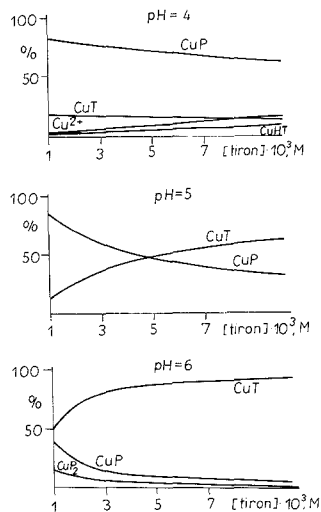


**Figure 3.** Influence of the total Tiron concentration on copper complex species in the spectrophotometric system of Tiron/2-pyridinealdehyde in the presence of six metal ions (conditions as in Figure 2).

A similar picture is obtained for nickel-P complexes that are formed step by step between pH 2 and 8. The 1:1 complex of NiP is best developed at pH 4, i.e. by 88% of total nickel ion concentrations. With respect to titanium and vanadium it can be followed from Figure 2 that pH values higher than 3.5 would be appropriate for their analytical determination.

In conclusion, since the choice of pH is mainly dictated by the existence of an absorbing species of copper (CuP), as a compromise pH a value of about 4 should be adjusted for simultaneous complex formation of all of the metal ions of interest.

As a second variable the Tiron concentration was changed between 0.001 and 0.01 M in order to vary the ratio of the two reagents in solution. No influence was found with respect to the analytically important complexes of Ni(II), Co(II), V(V), and Ti(IV). However, for Fe(III) complexes the dominating species depend on the actual Tiron concentration; e.g. at pH 4 for low Tiron concentrations (0.001 M) 70% of Fe(III) is bound to the 1:1 complex and 30% to the 1:2 complex, but at high Tiron concentrations (0.01 M) only 14% is in the 1:1 complex and 86% in a 1:2 Fe(III)-Tiron complex. Therefore, the Tiron concentration cannot be set too low if the 1:2 complex is to be monitored (cf. above).

On the other hand, it is to be expected that the Tiron concentration directly affects the presence of copper-P complexes since both of the reagents compete for Cu(II) in the pH range studied. Figure 3 gives the dependence of species distribution of Cu(II) on the Tiron concentration for three different pH values. As seen from the figure the decrease in the analytically important CuP complex concentration is especially affected at higher pH values. In order to keep a substantial amount of Cu(II) bound to P, the optimal pH value will be again 4 where only a slight dependence on the Tiron concentration exists.

To further explore the applicability of the system for MCA the dependences of absorbing species on the total metal ion concentrations were evaluated.

At pH 4 the change of the absorbing complexes was negligible if the concentration of the total metal ion was increased to 10 times the initial concentration ( $5 \times 10^{-5}$  to  $5 \times 10^{-4}$  M).

**Table III. Mixture Concentrations for Calibration of a Three-Component System with the Reagents Tiron/2-Pyridinealdoxime**

mixture	mL of metal ion soln <sup>a</sup> per 100 mL of final soln		
	Ti	Fe	Cu
1	1.5	5	0.2
2	4.5	5	0.2
3	4.5	9	0.2
4	1.5	9	0.2
5	1.5	5	0.5
6	4.5	5	0.5
7	4.5	9	0.5
8	1.5	9	0.5

<sup>a</sup> For concentrations, see Experimental Section.

For example, the relative CuP complex concentration decreased by less than 1%. However, at a 100-fold concentration of the initial one the concentration of this complex decreased by 8%. For cobalt and iron the following changes were found: CoP (+6%), CoP<sub>2</sub> (-15%), NiP (+7%), NiP<sub>2</sub> (-7%), FeT (+7%), FeT<sub>2</sub> (-7%).

Thus, in case of wide variations of total metal ion concentrations nonlinear absorbance-concentration dependences are to be taken into account in the MCA.

**Calibration of the Multicomponent System.** In order to account for interactions between the different (equilibrium) species and for the strong overlap of absorption bands, multivariate calibration based on the use of the whole spectral range (multiwavelength spectroscopy) becomes obligatory for MCA of the metal ions.

Preliminary tests in aqueous solutions for calibrating versus all absorbing complexes of Ti, Fe, Mo, Co, Cu, Cr, Ni, and V individually with 13 mixtures of the metal ions based on a Box-Behnken experimental design (13) revealed that only three elements (Ti, Fe, and Co) out of eight could be determined with mean relative errors less than 14%. This was to be expected from the bad conditioning of the system as explained above with the increase in the condition number with increasing number of components in the system (cf. Table I). However, this does not mean that not all of these metals could be present in a sample. The consequence is that only a limited number of metal components can be determined with good precision and the other metal ions are to be calibrated in the model as "abstract" principal components. Predictions of the elements Fe(III), Ti(IV), and Co(II) at concentrations between 0.1 and  $4 \times 10^{-5}$  M with the used model gave mean relative prediction errors of 5.8%, 5.9%, and 13.5%, respectively. Thus, in the following experiments a dedicated system was studied for simultaneous determination of titanium, iron, and copper in aluminum alloys. Table III reveals the mixtures used for calibrating the spectrophotometric system. The composition of these mixtures is based on a three-factor, two-level full factorial experimental design, i.e. a 2<sup>3</sup> design (14).

In addition, all the solutions contained the adequate amount of dissolved aluminum as described in the Experimental Section. For calibrating the system the spectra are recorded between 340 nm and 630 nm every 10 nm. The absorbances at all the 30 wavelengths are used for calibrating the system versus the concentration matrix in Table III with the PLS method.

The results for predicting the three components within the calibrated concentration range in aluminum-containing solutions are given in Table IVA. The analysis of Fe(III) is highly precise (0.402%). The prediction errors for elements with lower concentrations, i.e. titanium and copper, are both less than 10%. The same calibration model was used then for analysis of three reference samples of the ASMW (Amt

**Table IV. Aluminum Sample Solutions Analyzed for Ti(IV), Fe(III), and Cu(II)**

	Fe	Ti	Cu
A. Simulated Sample Solutions			
sample concn range, mass %	0.098-0.46	0.01-0.089	0.011-0.049
mean rel error, %	0.402	9.02	7.47
B. Al Reference Samples			
NP 4.16/2, mass %			
certified	0.31	0.089	0.049
determined	0.26	0.096	0.042
rel error, %	16.13	7.8	14.3
NP 4.16/3, mass %			
certified	0.098	0.044	0.029
determined	0.087	0.042	0.028
rel error, %	8.7	4.55	3.45
NP 4.16/4, mass %			
certified	0.46	0.01	0.011
determined	0.43	0.0072	0.021
rel error, %	6.52	28.0	91.0

für Standardisierung, Messwesen und Warenprüfung, Berlin, GDR).

The results are also given in Table IVB and are compared with the certified metal contents. As can be seen, most of the relative prediction errors are less than 10%. However, at the lowest concentrations of Ti (0.01%) and of Cu (0.011%) in the third sample the MCA failed since the excess of iron over the components copper and titanium is obviously too high to enable precise analysis of all components to be performed.

The reason for this limitation in the accuracy of the method not only is an experimental one but is mainly due to the bad conditioning of the aluminum-containing system at the compromise conditions. As condition number one computes for the three absorbing metal ion complexes Cu-2-pyridinealdoxime, Fe- and Ti-Tiron complexes a value of 2250 (based on the molar absorptivities). This high condition number is caused by the weak absorption of the copper complex compared to the absorption of iron and titanium complexes because the latter two complexes would reveal a much lower condition number of only 50.9.

It also should be recognized that the investigated spectrophotometric system is still very sensitive to additional unknown components in the sample as well as to a change in the main component aluminum in the reagent solution. This is reasoned by the complicated equilibria in the reaction solution. If analysis is to be carried out in wide concentration ranges, it will even be necessary to calibrate with extended concentration models where, i.e. quadratic or mixed concentration terms are to be included into the calibration/prediction model in order to account for nonlinear absorbance-concentration dependences as mentioned in the simulation section for copper. This, of course, will further increase the labor for calibrating the spectrophotometric system because an experimental design based on three or more factor levels will become obligatory.

## CONCLUSIONS

Mixed reagents can be considered an alternative means to extend the applicability of spectrophotometric multicomponent analysis of metal ions. Limitations, however, arise from the necessity of finding compromise conditions with respect to the existence of absorbing metal complexes in the then highly complex chemical systems. Because of these complicated metal-ligand equilibria it is difficult to adjust the experimental conditions such that all the analytes exist completely in the complex with the highest possible ligand coordination number. This is a main difference compared to single-component spectrophotometric analysis, where the

metal ions are determined in excess of reagents. Therefore, MCA with mixed reagents may include deviations from linear absorbance-concentration (total) relationships.

#### ACKNOWLEDGMENT

We thank V. Brendler, I. Klimant, and H. Walter for their help in the equilibrium simulations with the computer program COMICS and K. Sporreiter and S. Zimmermann for experimental assistance (all of the Department of Chemistry, Bergakademie Freiberg).

Registry No. Cu, 7440-50-8; Fe, 7439-89-6; Ti, 7440-32-6; Tiron, 149-45-1; 2-pyridinealdoxime, 873-69-8.

#### LITERATURE CITED

- (1) James, G. E. *UV/VIS Technical Paper UV-4*; Hewlett-Packard Company: Palo Alto, CA, 1981.

- (2) Otto, M.; Wegscheider, W. *Anal. Chem.* **1985**, *57*, 63.  
 (3) Otto, M.; George, T. *Anal. Chim. Acta* **1987**, *200*, 379.  
 (4) Jochum, C.; Jochum, P.; Kowalski, B. R. *Anal. Chem.* **1981**, *53*, 85.  
 (5) Wold, S.; Wold, H.; Dunn, W. J.; Ruhe, A. *Report UMINF-83*; Department of Chemistry, University of Umea: Sweden, 1980.  
 (6) Beebe, K. R.; Kowalski, B. R. *Anal. Chem.* **1987**, *59*, 1007A.  
 (7) Lindberg, W.; Persson, J.-A.; Wold, S. *Anal. Chem.* **1983**, *55*, 643.  
 (8) Ferrin, D. D.; Sayce, G. I. *Talanta* **1967**, *14*, 833.  
 (9) Wilkinson, J. H.; Reinsch, C. *Handbook for Automatic Computation*; Springer: Heidelberg, New York, 1980; Vol. II, pp 21.  
 (10) Otto, M.; Wegscheider, W. *Anal. Chim. Acta* **1986**, *180*, 445.  
 (11) Martell, A. E.; Smith, R. M. *Critical Stability Constants*; Plenum Press: New York, 1978; Vol. 1-5.  
 (12) Schwarzenbach, G.; Willi, A. *Helv. Chim. Acta* **1951**, *34*, 528.  
 (13) Sporreiter, K. Diplomarbeit, Department of Chemistry, Bergakademie Freiberg, Freiberg, G.D.R., 1985.  
 (14) Deming, S. N.; Morgan, S. L. *Experimental Design: a Chemometric Approach*; Elsevier: Amsterdam, 1987.

RECEIVED for review February 15, 1989. Accepted May 5, 1989.

## Determination of Iron, Cobalt, Copper, Zinc, Rubidium, Molybdenum, and Cesium in Human Serum by Inductively Coupled Plasma Mass Spectrometry

Hans Vanhoe, Carlo Vandecasteele,\* Jacques Versieck,<sup>1</sup> and Richard Dams

Laboratory of Analytical Chemistry, Rijksuniversiteit Gent, Institute for Nuclear Sciences, Proeftuinstraat 86, B-9000 Gent, Belgium

A method was developed for the determination of seven trace elements (Fe, Co, Cu, Zn, Rb, Mo, and Cs) in human serum by inductively coupled plasma mass spectrometry (ICP-MS). Sample preparation was kept as limited as possible. As the only sample pretreatment serum samples were diluted with nitric acid and indium was added as an internal standard. The results for iron, cobalt, copper, and zinc were corrected for interferences from polyatomic ions by using a blank solution containing the same concentration of sodium, sulfur, chlorine, and calcium as human serum. For copper and zinc the corrections are small, whereas for iron and cobalt they are important. No interferences occur for the considered isotopes of rubidium, molybdenum, and cesium. In order to test the accuracy and precision of the analytical technique, a "second-generation biological reference material (human serum)" was analyzed. The results obtained by ICP-MS for the seven elements considered showed good agreement with the certified values.

#### INTRODUCTION

Because of their biochemical importance and their easy accessibility, human blood plasma and serum attracted the attention of many trace element researchers. Thus far, neutron activation analysis (NAA) and atomic absorption spectrometry (AAS) were the main techniques used to perform trace element determinations in this matrix (1). Both techniques, however, have some serious drawbacks. The use of NAA is limited to specialized laboratories having access to

a nuclear reactor; the technique has a relatively low sample throughput and, for some elements, results only become available after about 1 month. AAS, which is available in more laboratories, is also relatively slow since only one element can be determined at a time. In addition, interferences (chemical, background, ...) may be serious and not easy to correct.

Inductively coupled plasma mass spectrometry (ICP-MS), although a relatively novel technique (2), seems a powerful alternative for the determination of trace elements in serum. Detection limits are below 1 µg/L for more than 60 elements in a multielement determination (3). In the literature, several attempts to analyze serum have been described. Serfass et al. (4), first ashed the samples and measured zinc-isotope ratios after extraction of the zinc; Janghorbani et al. (5) carried out an ion-exchange separation before measuring bromine-isotope ratios; Lyon et al. (6) performed a chromatographic separation before measuring selenium; Lyon et al. (7) measured several elements (aluminum, vanadium, chromium, manganese, iron, nickel, copper, zinc, selenium, molybdenum, and barium) in a "synthetic serum". However, the concentration levels for various elements were much higher than those in real serum samples.

This paper describes the determination of iron, cobalt, copper, zinc, rubidium, molybdenum, and cesium in human serum by ICP-MS. Sample preparation was limited as much as possible, in order to avoid contamination and losses of trace elements. Sample pretreatment consisted merely of dilution with 0.14 M nitric acid and addition of indium as an internal standard. Sample dilution is necessary to avoid rapid blockage of the torch and of the pneumatic nebulizer and to reduce the extent of signal suppression due to the matrix. Indeed, experiments showed that signal suppression occurs in the presence of sodium chloride (8). Nine grams per liter sodium chloride, equivalent to the total cation concentration in human

<sup>1</sup>Department of Internal Medicine, Division of Gastroenterology, University Hospital, De Pintelaan 185, B-9000 Gent, Belgium.

Table I.

PlasmaQuad Operating Conditions	
plasma	
rf power	forward, 1.35 kW reflected, <10 W
gas flows	plasma, 13 L/min auxiliary, 1 L/min nebulizer, 0.72 L/min
peristaltic pump	Minipuls 2-Gilson pumped at 0.9 mL/min
nebulizer	Meinhard concentric glass nebulizer (type: Tr-30-A3)
spray chamber	double pass Scott type, water cooled (10 °C)
ion sampling	
sampling cone	nickel, 1.0 mm orifice
skimmer cone	nickel, 0.75 mm orifice
sampling depth	10 mm (from load coil)
vacuum	
expansion stage	2.3 mbar
intermediate	$1.0 \times 10^{-4}$ mbar
analyzer	$1.6 \times 10^{-6}$ mbar
Data acquisition	
quantitative scanning	
sweeps	120
dwelt time	250 $\mu$ s
channels	4096
mass region	50–140 u
acquisition time	123 s

serum, causes a signal suppression of 30–40%. In addition, it was shown that the suppression effect does not in the case of a sodium chloride matrix depend critically on the analyte element considered. The use of indium ( $^{115}\text{In}$ ) as an internal standard thus corrects for the matrix effect and also partly for instability of the ion signal. In order to correct for polyatomic interferences, which occur when iron, cobalt, copper, and zinc are determined in serum, a simulated blank solution is used, containing the same concentration of sodium, sulfur, chlorine, and calcium as serum. For the elements rubidium, molybdenum, and cesium no polyatomic interferences could be detected for the nuclides selected.

To check the accuracy and precision of the analytical procedure, the "second-generation biological reference material (human serum)", prepared by Versieck et al. (9, 10), was used. This material was collected and conditioned under rigorously controlled conditions to avoid contamination. So, concentrations of different elements are fairly similar to those expected in normal human serum. The values obtained by ICP-MS are compared with the certified values obtained by other analytical techniques. Our results are based on the analysis of liquid serum. The reference material is, however, available to the scientific community in freeze-dried form, but reconstitution of the freeze-dried human serum seems not to be a problem. To our knowledge this is the first extensive study of the accuracy of ICP-MS as an analytical technique for ultratrace elements in serum.

## EXPERIMENTAL SECTION

**Instrumentation.** A commercially available ICP-MS instrument, the VG PlasmaQuad (VG Elemental, Winsford, U.K.), was used in its standard configuration with a Meinhard nebulizer and a spray chamber made of borosilicate glass. Details of the operating conditions are given in Table I.

**Reagents and Solutions.** All solutions were prepared with 0.14 M nitric acid obtained by a hundred-fold dilution of concentrated nitric acid, purified by sub-boiling distillation, with Millipore Milli Q water. Pre-cleaned polyethylene volumetric flasks and glass pipets were used throughout.

For the quantitative analysis two different standard solutions were prepared: the first containing 100  $\mu\text{g/L}$  of iron, cobalt, copper, zinc, and indium (internal standard); the second containing 100  $\mu\text{g/L}$  of rubidium, molybdenum, indium (internal standard),

Table II. Composition of the Simulated Blank Solution for the Determination of Fe, Co, Cu, and Zn in Human Serum

	10-fold diluted	5-fold diluted
NaCl	0.60 g/L (370 mg/L Cl and 240 mg/L Na)	1.2 g/L (730 mg/L Cl and 470 mg/L Na)
Na NO <sub>3</sub>	0.33 g/L (88 mg/L Na)	0.65 g/L (180 mg/L Na)
cysteine-HCl-H <sub>2</sub> O	0.66 g/L (120 mg/L S)	1.3 g/L (240 mg/L S)
Ca(NO <sub>3</sub> ) <sub>2</sub> ·4H <sub>2</sub> O	0.057 g/L (9.7 mg/L Ca)	0.11 g/L (19 mg/L Ca)
internal standard	100 $\mu\text{g/L}$ In	100 $\mu\text{g/L}$ In
solvent	0.14 M nitric acid	0.14 M nitric acid

and cesium. They were all prepared from commercial 1 g/L solutions and stored in polyethylene flasks.

Sodium chloride and sodium nitrate solution, cysteine solution, and calcium nitrate solution were prepared respectively by dissolving 1.5 g of sodium chloride (reagent grade, UCB), 0.81 g of sodium nitrate (reagent grade, Carlo Erba), 1.6 g of cysteine chloride monohydrate (reagent grade, Merck), and 0.14 g of calcium nitrate tetrahydrate (reagent grade, UCB) in 0.14 M nitric acid and diluting to 250 mL. The reagents used were of the highest purity available to us. When the content of impurities was indicated (Fe in sodium chloride, Fe and Zn in sodium nitrate and calcium nitrate), it was negligible compared to the apparent concentration due to polyatomic species.

Use was also made of solutions containing a sodium chloride concentration of 0.9, 1.8, 2.7, 4.5, 7.2 and 9 g/L and of solutions containing a potassium bromate concentration corresponding to 0.88, 1.3, 2.2, 3.5, and 4.4 mg/L of bromine.

**Sample Preparation.** Liquid serum, obtained by defrosting serum stored in a polyethylene container in a deep freezer, was diluted 10-fold for the quantitative determination of iron, copper, zinc, and rubidium and 5-fold for the quantitative determination of iron, cobalt, copper, zinc, rubidium, molybdenum, and cesium with 0.14 M nitric acid. To 2.5 or 5 mL of serum 2.5 mL of a 1 mg/L indium solution was added and the volume was adjusted with 0.14 M nitric acid to obtain 25 mL of the serum solution with an indium concentration of 100  $\mu\text{g/L}$ . Pre-cleaned polyethylene pipets and volumetric flasks were used to prepare the diluted serum samples. All manipulations were carried out on a clean-bench to avoid contamination.

**Blank Solutions.** For the quantitative determination of iron, cobalt, copper, and zinc in human serum a simulated blank solution was prepared to correct for interferences from polyatomic ions, whereas for rubidium, molybdenum, and cesium 0.14 M nitric acid containing 100  $\mu\text{g/L}$  of indium used as an internal standard was applied as blank solution. The simulated blank solution contains the following components: 0.14 M nitric acid, internal standard (100  $\mu\text{g/L}$  of indium), sodium chloride, sodium nitrate, cysteine, and calcium nitrate. The latter four components yield the same concentration of sodium, chlorine, sulfur, and calcium as in human serum. The corresponding concentrations are given in Table II. Nitric acid (0.14 M) with 100  $\mu\text{g/L}$  of indium as internal standard was used as blank for the multielement standard.

**Measurements.** Quantitative analyses were performed by using the scanning mode of data acquisition. The scan conditions are summarized in Table I. The following analysis sequence was applied: first the blanks were measured, then several samples, and, only at the end of the sequence, the standard. Three repeated measurements were made on each solution, and the analysis sequence was repeated twice.

In previous experiments it was observed that for some elements, rinsing with distilled water was not sufficient to reach low blank levels after measurement of a standard. This memory effect is illustrated in Figure 1 for molybdenum. Each experimental point was obtained as follows: a standard solution containing 100  $\mu\text{g/L}$  of molybdenum was nebulized for 4 min and measured. After a variable rinsing time, a blank solution (0.14 M nitric acid) was measured and the corresponding concentration of the blank solution calculated. Millipore Milli Q water and 0.14 M and 1.4 M nitric acid were used as rinsing liquids. The blank signal remained high following rinsing with water (around 0.16  $\mu\text{g/L}$  after 1 h of rinsing). Rinsing with 0.14 M or 1.4 M nitric acid,

**Table III. Polyatomic Ions Interfering with the Nuclides of Fe, Co, Cu, and Zn<sup>a</sup>**

element	nuclide (isotopic abundance)	polyatomic ions
iron	<sup>54</sup> Fe (5.8%)	<i><sup>40</sup>Ar<sup>14</sup>N</i> , <i><sup>38</sup>Ar<sup>16</sup>O</i> , <i><sup>36</sup>Ar<sup>18</sup>O</i> , <i><sup>36</sup>Ar<sup>17</sup>OH</i> , <i><sup>38</sup>Ar<sup>15</sup>NH</i> <i><sup>40</sup>Ca<sup>14</sup>N</i> , <i><sup>42</sup>Ca<sup>12</sup>C</i> <i><sup>37</sup>Cl<sup>17</sup>O</i> , <i><sup>37</sup>Cl<sup>16</sup>OH</i> <i><sup>36</sup>S<sup>18</sup>O</i> , <i><sup>38</sup>S<sup>17</sup>OH</i>
	<sup>56</sup> Fe (91.7%)	<i><sup>40</sup>Ar<sup>16</sup>O</i> , <i><sup>38</sup>Ar<sup>18</sup>O</i> , <i><sup>38</sup>Ar<sup>17</sup>OH</i> , <i><sup>40</sup>Ar<sup>15</sup>NH</i> <i><sup>40</sup>Ca<sup>16</sup>O</i> , <i><sup>42</sup>Ca<sup>14</sup>N</i> , <i><sup>44</sup>Ca<sup>12</sup>C</i> , <i><sup>43</sup>Ca<sup>13</sup>C</i> <i><sup>37</sup>Cl<sup>18</sup>OH</i>
	<sup>57</sup> Fe (2.19%)	<i><sup>40</sup>Ar<sup>17</sup>O</i> , <i><sup>40</sup>Ar<sup>16</sup>OH</i> , <i><sup>38</sup>Ar<sup>18</sup>OH</i> <i><sup>40</sup>Ca<sup>17</sup>O</i> , <i><sup>40</sup>Ca<sup>16</sup>OH</i> , <i><sup>42</sup>Ca<sup>15</sup>N</i> , <i><sup>44</sup>Ca<sup>13</sup>C</i>
cobalt	<sup>59</sup> Co (100%)	<i><sup>40</sup>Ar<sup>18</sup>OH</i> <i><sup>36</sup>Ar<sup>23</sup>Na</i> <i><sup>42</sup>Ca<sup>16</sup>O</i> , <i><sup>42</sup>Ca<sup>17</sup>O</i> , <i><sup>44</sup>Ca<sup>15</sup>N</i> , <i><sup>46</sup>Ca<sup>13</sup>C</i> , <i><sup>40</sup>Ca<sup>18</sup>OH</i>
copper	<sup>63</sup> Cu (69.1%)	<i><sup>40</sup>Ar<sup>23</sup>Na</i> , <i><sup>23</sup>Na<sup>39</sup>Na<sup>17</sup>O</i> <i><sup>48</sup>Ca<sup>15</sup>N</i> , <i><sup>46</sup>Ca<sup>17</sup>O</i> , <i><sup>46</sup>Ca<sup>16</sup>OH</i> <i><sup>33</sup>S<sup>16</sup>O<sup>16</sup>O</i> , <i><sup>32</sup>S<sup>33</sup>S</i> , <i><sup>32</sup>S<sup>18</sup>O<sup>17</sup>O</i>
	<sup>65</sup> Cu (30.9%)	<i><sup>48</sup>Ca<sup>17</sup>O</i> , <i><sup>48</sup>Ca<sup>16</sup>OH</i> <i><sup>32</sup>S<sup>16</sup>O<sup>16</sup>O</i> , <i><sup>32</sup>S<sup>32</sup>S</i>
zinc	<sup>64</sup> Zn (48.9%)	<i><sup>48</sup>Ca<sup>18</sup>O</i> , <i><sup>48</sup>Ca<sup>16</sup>O</i> , <i><sup>46</sup>Ca<sup>17</sup>OH</i> <i><sup>23</sup>Na<sup>23</sup>Na<sup>18</sup>O</i>
	<sup>66</sup> Zn (27.8%)	<i><sup>32</sup>S<sup>16</sup>O<sup>18</sup>O</i> , <i><sup>32</sup>S<sup>34</sup>S</i> , <i><sup>32</sup>S<sup>17</sup>O<sup>17</sup>O</i> , <i><sup>33</sup>S<sup>16</sup>O<sup>17</sup>O</i> , <i><sup>34</sup>S<sup>16</sup>O<sup>16</sup>O</i> , <i><sup>33</sup>S<sup>33</sup>S</i> <i><sup>48</sup>Ca<sup>18</sup>O</i> , <i><sup>48</sup>Ca<sup>17</sup>OH</i>

<sup>a</sup>The main interfering species are italicized.

however, yields lower blank signals (around 0.07 µg/L after 1 h of rinsing) corresponding to the blank level obtained without previous measurement of a standard (0.08 ± 0.03 µg/L). Cobalt, rubidium, and cesium are rapidly removed even with a water rinse, whereas the apparent blanks for iron, copper, and zinc are not significantly affected by the various rinsing fluids because they mainly originate from polyatomic interferences. For this reason the sample introduction system was rinsed for 30 min with 0.14 M nitric acid after each analysis sequence. As an additional precaution each time before serum samples were analyzed the skimmer, the sampling cone, the plasma torch and the spray chamber were cleaned thoroughly.

**Calculations.** For each solution the signals—peak area integrated over 0.8 µ around the peak maximum—of the analyte elements were divided (normalized) by the signal of the internal standard (<sup>115</sup>In). The mean and the standard deviation of the

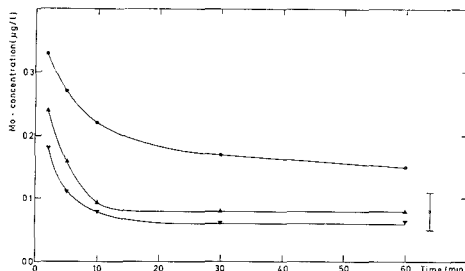


**Figure 1.** Blank signal of molybdenum as a function of the rinsing time for different rinsing solutions (●, H<sub>2</sub>O; ▲, 0.14 M HNO<sub>3</sub>; ▼, 1.4 M HNO<sub>3</sub>). A molybdenum standard solution (100 µg/L) was nebulized for 4 min, before time 0. The mean ± standard deviation of the blank signal of molybdenum without previous nebulization of a molybdenum standard solution is indicated with an X and vertical bar.

three resulting normalized signals of each solution were calculated. For each element the average normalized signal of the blank was subtracted from the average normalized signal of the diluted serum solution. To calculate the corresponding concentration, a multi-element standard containing 100 µg/L of the analyte elements was employed.

## RESULTS AND DISCUSSION

**Choice of Nuclides.** When biological material is analyzed by ICP-MS, potential interferences from polyatomic ions must be considered (7). The interfering polyatomic ions produced from the plasma gases and from nitric, hydrochloric, and sulfuric acids are fairly well-known qualitatively (11). Those interfering with the isotopes of iron, cobalt, copper, and zinc on analysis of human serum are given in Table III. The occurrence of some of the species indicated in Table III has not actually been proven. A study is however under way to unambiguously assign the interferences to the various polyatomic species. They originate mainly from argon, nitrogen, and/or oxygen in combination with sodium, sulfur, chlorine, and calcium, which are present respectively at concentrations of 3251 (3130–3370), 1197 (1120–1270), 3655 (2940–4120), and 97 mg/L (92–109 mg/L) in human serum (12). The values in parentheses give the range due to the natural variation of the element considered.

**Table IV. Apparent Concentration (µg/L) of Fe, Co, Cu, and Zn in a Simulated Blank Solution Containing the Same Concentration of Na, Cl, S, and Ca as a 10-Fold and a 5-Fold Diluted Serum Solution<sup>a</sup>**

nuclide (isotopic abundance)	main polyatomic interferences	10-fold diluted	5-fold diluted	concn in human serum <sup>d</sup>
<sup>57</sup> Fe (2.19%)	total	210 ± 16 <sup>c</sup>	330 ± 27	2350 ± 140
	<i><sup>40</sup>Ar<sup>16</sup>OH</i>	51 ± 1	48 ± 1	
	<i><sup>40</sup>Ca<sup>16</sup>OH</i>	166 ± 16	286 ± 39	
<sup>59</sup> Co (100%)	total		0.080 ± 0.020	0.33 ± 0.05
	<i><sup>36</sup>Ar<sup>23</sup>Na</i>		0.035 ± 0.005	
	<i><sup>48</sup>Ca<sup>16</sup>O</i>		0.030 ± 0.007	
	<i><sup>40</sup>Ar<sup>18</sup>OH</i>		0.020 ± 0.004	
	background <sup>b</sup>		<0.1	
<sup>63</sup> Cu (69.1%)	total	120 ± 35	420 ± 50	1009 ± 36
	total	4.4 ± 0.5	8.2 ± 1.0	
<sup>65</sup> Cu (30.9%)	<i><sup>33</sup>S<sup>16</sup>O<sup>16</sup>O</i> , <i><sup>32</sup>S<sup>33</sup>S</i>	4.0 ± 0.5	7.1 ± 0.7	
	<i><sup>48</sup>Ca<sup>16</sup>OH</i>	<0.1	<0.1	
	background <sup>b</sup>	0.46 ± 0.16	0.43 ± 0.15	
<sup>64</sup> Zn (48.9%)	total	26 ± 4	62 ± 6	873 ± 18
	total	4.3 ± 0.3	9.7 ± 1.0	
<sup>66</sup> Zn (27.8%)	<i><sup>32</sup>S<sup>16</sup>O<sup>18</sup>O</i> , <i><sup>32</sup>S<sup>34</sup>S</i>	3.0 ± 0.2	7.1 ± 0.9	
	<i><sup>48</sup>Ca<sup>18</sup>O</i>	0.43 ± 0.08	0.70 ± 0.09	
	background <sup>b</sup>	0.80 ± 0.03	0.76 ± 0.03	

<sup>a</sup> For <sup>57</sup>Fe, <sup>59</sup>Co, <sup>65</sup>Cu, and <sup>66</sup>Zn the contribution of the various polyatomic species is also given. <sup>b</sup> Concentration corresponding to the signal in pure water. <sup>c</sup> 95% confidence limits. <sup>d</sup> Reference 10, this concentration must be divided by 10 or 5 for comparison with the values in columns 3 and 4, respectively.

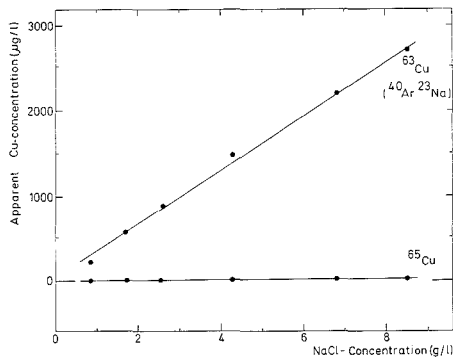


**Figure 2.** Apparent copper concentration at mass 63 and 65 in a sodium chloride solution as a function of the sodium chloride concentration.

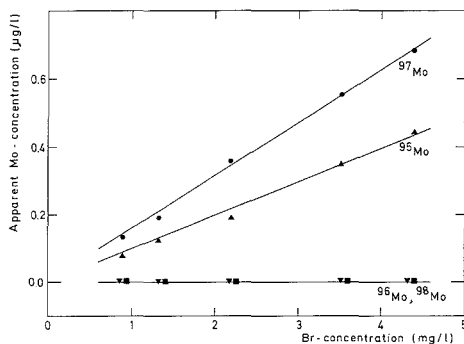


**Figure 3.** Apparent molybdenum concentration at mass 95, 96, 97, and 98 in a potassium bromate solution as a function of the bromine concentration ( $\blacktriangle$ ,  $^{95}\text{Mo}$ ;  $\blacklozenge$ ,  $^{96}\text{Mo}$ ;  $\bullet$ ,  $^{97}\text{Mo}$ ;  $\blacksquare$ ,  $^{98}\text{Mo}$ ).

In order to estimate the importance of the polyatomic interferences, sodium chloride and sodium nitrate solutions, cysteine solutions, calcium nitrate solutions, and simulated blank solutions (containing all the components) were measured. The results are given in Table IV. Whereas the relative contributions of these interferences to the total signal obtained for 5- or 10-fold diluted human serum are relatively small for the nuclides  $^{65}\text{Cu}$  and  $^{66}\text{Zn}$ , they are important for  $^{57}\text{Fe}$ ,  $^{58}\text{Co}$ ,  $^{63}\text{Cu}$ , and  $^{64}\text{Zn}$ .

No polyatomic interferences from phosphorus or potassium, present respectively at concentrations of 142 (115–163) and 191 mg/L (160–211 mg/L) in human serum (12) could be detected for the nuclides considered.

**Iron.** Iron has four isotopes:  $^{54}\text{Fe}$  (5.8%),  $^{56}\text{Fe}$  (91.7%),  $^{57}\text{Fe}$  (2.14%) and  $^{58}\text{Fe}$  (0.31%). The determination of iron by ICP-MS is difficult because for all its isotopes significant interferences occur. Determinations were made at mass 57, the same nuclide as used by Lyon et al. (7). In fact, measurements at mass 56 always gave low results when compared to the certified value. The reason for this observation is not clear: Experiments, however, showed that the signal for  $^{40}\text{Ar}^{16}\text{O}$  decreased more rapidly than the signal for the  $^{115}\text{In}$  internal standard with increasing sodium chloride concentration. At mass 54 the interference from  $^{40}\text{Ar}^{14}\text{N}$  is sometimes too high to allow meaningful results to be obtained for iron.

**Cobalt.** Cobalt is monoisotopic as  $^{59}\text{Co}$ . The contribution of the various polyatomic interferences to the signal at mass 59 for a 5-fold diluted serum solution corresponds to a cobalt

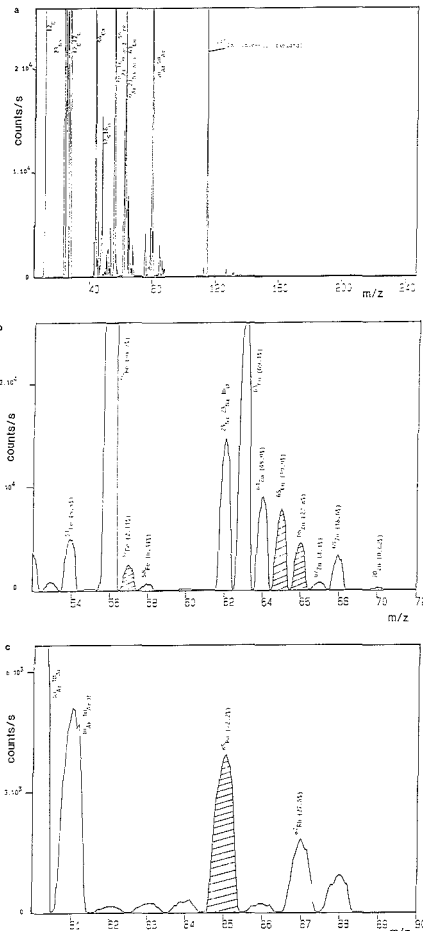


**Figure 4.** (a) Mass spectrum from 54 and 255 u of a 5-fold diluted serum solution to which 100  $\mu\text{g/L}$  In as internal standard was added. (b) Mass spectrum between 52 and 72 u of a 5-fold diluted serum solution which shows the isotopes of Fe, Cu, and Zn. The shaded peaks are used for the quantitative determination of the elements considered. For the polyatomic interferences reference is made to Table III. (c) Mass spectrum between 80 and 90 u of a 5-fold diluted serum solution which shows the two isotopes of Rb. The shaded peak ( $^{85}\text{Rb}$ ) is used for the quantitative determination of Rb.

concentration of  $0.080 \pm 0.020 \mu\text{g/L}$  (Table IV).

**Copper.** Copper has two isotopes:  $^{63}\text{Cu}$  (69.1%) and  $^{65}\text{Cu}$  (30.9%). Determinations were made at mass 65 rather than at mass 63, because  $^{40}\text{Ar}^{23}\text{Na}$  interferes as shown in Figure 2, where the apparent copper concentration in a sodium chloride solution obtained at masses 63 and 65 is given as a function of the sodium chloride concentration. The apparent copper concentration at mass 63 increases linearly with the sodium chloride concentration. The polyatomic species interfering at mass 65 ( $^{33}\text{S}^{16}\text{O}^{16}\text{O}$ ,  $^{32}\text{S}^{33}\text{S}$ ,  $^{32}\text{S}^{16}\text{O}^{17}\text{O}$ ) do not constitute a major problem as the interference corresponds to a copper concentration of only  $4.4 \pm 0.5$  and of  $8.2 \pm 1.0 \mu\text{g/L}$  in 10-fold and 5-fold diluted serum solution, respectively.

**Zinc.** Zinc has five isotopes:  $^{64}\text{Zn}$  (48.9%),  $^{66}\text{Zn}$  (27.8%),  $^{67}\text{Zn}$  (4.1%),  $^{68}\text{Zn}$  (18.6%), and  $^{70}\text{Zn}$  (0.62%). All of these are interfered by polyatomic ions containing sulfur and oxygen.



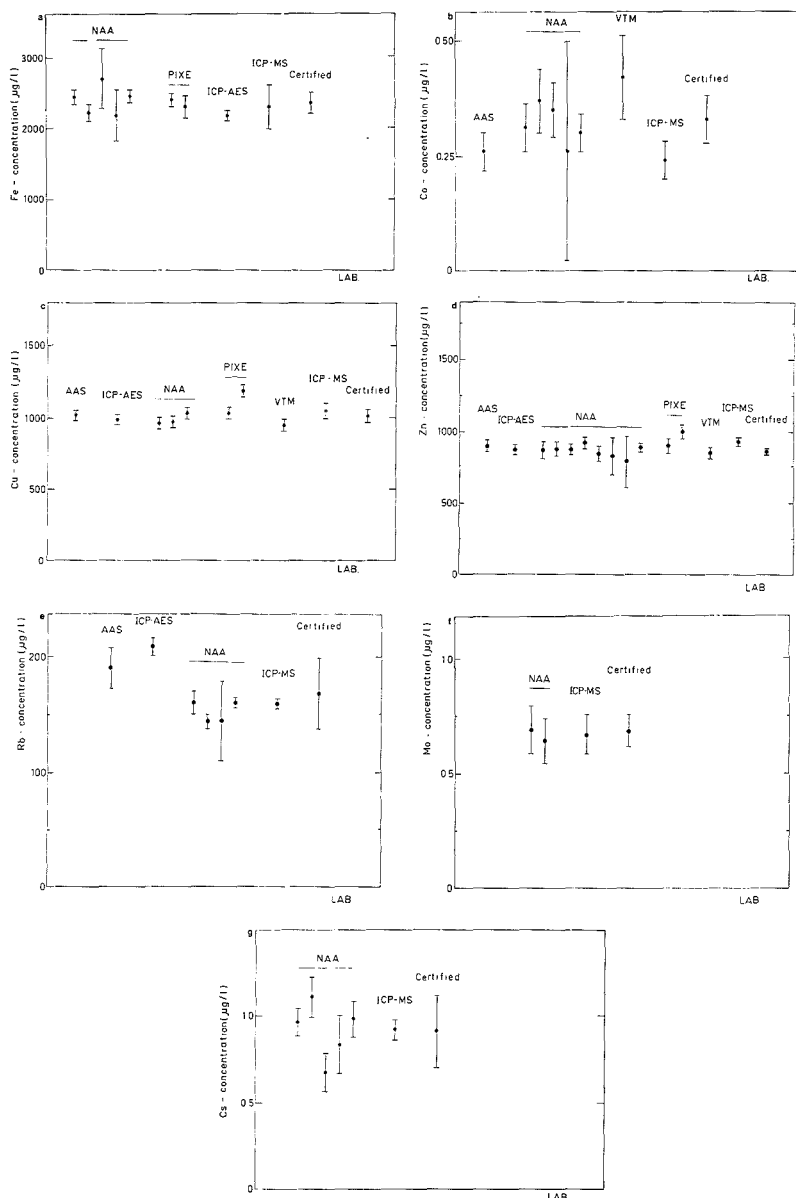


**Figure 5.** Results of the determination of seven trace elements in the human serum reference material obtained by various analytical techniques. The ICP-MS value is the result of this work. For each laboratory mean  $\pm$  standard deviation is given. (a) Fe, (b) Co, (c) Cu, (d) Zn, (e) Rb, (f) Mo, (g) Cs.

Determinations were made at mass 66, since  $^{64}\text{Zn}$ , although the most abundant isotope, is interfered to a larger extent (Table IV).

**Rubidium.** Rubidium has two isotopes:  $^{85}\text{Rb}$  (72.2%) and  $^{87}\text{Rb}$  (27.8%). Determinations were made at mass 85, because of an isobaric interference on  $^{87}\text{Rb}$  by  $^{87}\text{Sr}$  (7.0%).

**Molybdenum.** Molybdenum has seven isotopes:  $^{92}\text{Mo}$  (14.8%),  $^{94}\text{Mo}$  (9.1%),  $^{95}\text{Mo}$  (15.9%),  $^{96}\text{Mo}$  (16.7%),  $^{97}\text{Mo}$

(9.5%),  $^{98}\text{Mo}$  (24.4%), and  $^{100}\text{Mo}$  (9.6%). Some of these are interfered by polyatomic ions containing bromine and oxygen:  $^{79}\text{Br}^{16}\text{O}$  interferes with  $^{96}\text{Mo}$ ,  $^{79}\text{Br}^{17}\text{O}$  with  $^{96}\text{Mo}$ ,  $^{79}\text{Br}^{18}\text{O}$  and  $^{81}\text{Br}^{16}\text{O}$  with  $^{97}\text{Mo}$ ,  $^{81}\text{Br}^{17}\text{O}$  with  $^{98}\text{Mo}$ . Figure 3 shows the apparent molybdenum concentration in a potassium bromate solution at mass 95, 96, 97, and 98 as a function of the bromine concentration (the bromine concentration in human serum is ca. 4.4 mg/L (10)). The apparent molybdenum concen-

Table V. Comparison of the Results of the Second-Generation Biological Reference Material (Human Serum)

element	selected nuclide	ICP-MS results		certified value
		10-fold diluted	5-fold diluted	
iron	<sup>57</sup> Fe	2360 ± 330 <sup>a</sup> µg/L	2210 ± 350 µg/L	25.9 ± 1.5 µg/g
		26.0 ± 3.6 µg/g	24.3 ± 3.9 µg/g	
cobalt	<sup>58</sup> Co	916 ± 14 µg/L	0.24 ± 0.05 µg/L	3.6 ± 0.6 ng/g
		10.1 ± 0.2 µg/g	2.6 ± 0.6 ng/g	
copper	<sup>65</sup> Cu	1040 ± 49 µg/L	1047 ± 52 µg/L	11.1 ± 0.4 µg/g
		11.4 ± 0.5 µg/g	11.5 ± 0.6 µg/g	
zinc	<sup>68</sup> Zn	916 ± 14 µg/L	939 ± 21 µg/L	9.6 ± 0.2 µg/g
		10.1 ± 0.2 µg/g	10.3 ± 0.2 µg/g	
rubidium	<sup>85</sup> Rb	158.3 ± 1.5 µg/L	159.8 ± 1.0 µg/L	1.85 ± 0.33 µg/g
		1.74 ± 0.02 µg/g	1.76 ± 0.01 µg/g	
molybdenum	<sup>96</sup> Mo	158.3 ± 1.5 µg/L	0.67 ± 0.08 µg/L	7.5 ± 0.8 ng/g
		1.74 ± 0.02 µg/g	7.4 ± 0.9 ng/g	
cesium	<sup>133</sup> Cs	158.3 ± 1.5 µg/L	0.92 ± 0.05 µg/L	10.0 ± 2.3 ng/g
		1.74 ± 0.02 µg/g	10.1 ± 0.6 ng/g	

<sup>a</sup>95% confidence limits.

tration at mass 95 and mass 97 increases linearly with the bromine concentration, whereas at mass 96 and 98 the signals observed do not differ significantly from that of the solution without potassium bromate. The apparent molybdenum concentration in a potassium bromate solution, containing the same amount of bromine as a 5-fold diluted serum solution (ca. 0.88 mg/L), at mass 95 and at mass 97 is, for instance, respectively ca. 0.07 µg/L and ca. 0.13 µg/L, whereas the molybdenum concentration in a 5-fold diluted serum solution is ca. 0.13 µg/L. Therefore, determinations were made at mass 98.

**Cesium.** Determinations were made at mass 133 (<sup>133</sup>Cs, 100%) where no interferences from polyatomic ions were expected.

**Analysis of the Second-Generation Human Serum Reference Material.** Figure 4 shows spectra of a 5-fold diluted serum solution to which a 100 µg/L indium solution was added. A full mass range spectrum (5–255 u) is shown in Figure 4a. From this spectrum it is clear that the most intense peaks occur beneath mass 80. The mass regions between 1 and 5 u, between 12 and 22 u, and between 28 and 44 u were skipped. The part of the mass spectrum containing the isotopes of iron, copper, and zinc is shown in Figure 4b (mass range between 52 and 72 u), whereas the one containing the isotopes of rubidium (<sup>85</sup>Rb, 72.2% and <sup>87</sup>Rb, 27.8%) is shown in Figure 4c (mass range between 80 and 90 u).

Table V summarizes the results for the reference serum obtained by analysis of a 10-fold and a 5-fold diluted serum solution. The results are expressed in micrograms per liter of liquid serum and are also given in micrograms per gram in the lyophilized material. The latter values were obtained by multiplying the values in micrograms per liter by a factor of 0.011 and are compared with the certified values (10). Each result obtained by ICP-MS was based on two samples, each analyzed 6 times, i.e. a total of 12 analyses. The uncertainty given corresponds to the 95% confidence limits.

The random errors (corresponding to the 95% confidence limits on the mean of 12 analyses) amount to 16% for iron, 21% for cobalt, 5.0% for copper, 2.2% for zinc, 0.6% for rubidium, 12% for molybdenum, and 5.4% for cesium. These random errors are significantly smaller than the uncertainty on the certified value for rubidium and for cesium. For cobalt, copper, zinc, and molybdenum both are comparable, and for iron the random error of ICP-MS is larger than the uncertainty on the certified value. For iron, the precision of the results obtained by ICP-MS is rather limited, because of the large interference correction required (Table IV). For cobalt the results of ICP-MS are somewhat imprecise because of the low concentration of cobalt.

For iron, copper, zinc, and rubidium, the results obtained on 10- and 5-fold diluted serum samples do not differ significantly. In general, the results agree also within the experimental uncertainty with the certified values.

Figure 5 compares for seven elements the results obtained by ICP-MS with those obtained by other analytical techniques (10), such as atomic absorption spectrometry (AAS), inductively coupled plasma atomic emission spectrometry (ICP-AES), neutron activation analysis (NAA), particle-induced X-ray emission (PIXE), voltammetry (VTM), and with the certified value. For iron, copper, and zinc the agreement is excellent. The values for cobalt obtained by AAS, NAA, VTM, and ICP-MS are somewhat imprecise, but still the agreement is satisfactory in view of the large correction for polyatomic interferences and of the low cobalt concentration. For rubidium the agreement with NAA is almost complete, although AAS and ICP-AES yield somewhat higher values. For molybdenum thus far certification (10) was only based on NAA. ICP-MS yielded results in excellent agreement with the certified value. For cesium the results obtained by NAA—up to now the only available method—showed an important spread (0.56–1.23 µg/L). The value obtained by ICP-MS lies in the middle of the range.

#### ACKNOWLEDGMENT

We thank J. Hoste for his interest in this work and L. Vanballenberghe and A. Wittoek for their contribution in the preparation of the serum samples.

**Registry No.** Fe, 7439-89-6; Co, 7440-48-4; Cu, 7440-50-8; Zn, 7440-66-6; Rb, 7440-17-7; Mo, 7439-98-7; Cs, 7440-46-2.

#### LITERATURE CITED

- Versieck, Jacques; Cornelis, Rita *Anal. Chim. Acta* **1980**, *116*, 217–254.
- Houk, Robert S.; Fassel, Velmer A.; Fleisch, Gerald D.; Svec, Harry J.; Gray, Alan L.; Taylor, Charles E. *Anal. Chem.* **1980**, *52*, 2283–2289.
- Douglas, D. J.; Houk, R. S. *Prog. Anal. At. Spectrosc.* **1985**, *8*, 1–13.
- Serfass, Robert E.; Thompson, Joseph J.; Houk, R. S. *Anal. Chim. Acta* **1986**, *188*, 73–84.
- Janghorbani, Morteza; Davis, Terri A.; Ting, Bill T. G. *Analyst* **1988**, *113*, 405–411.
- Lyon, Thomas D. B.; Fell, Gordon S.; Hutton, Robert C.; Eaton, Andrew N. J. *Anal. At. Spectrom.* **1988**, *3*, 601–603.
- Lyon, Thomas D. B.; Fell, Gordon S.; Hutton, Robert C.; Eaton, Andrew N. J. *Anal. At. Spectrom.* **1988**, *3*, 265–271.
- Vandecasteele, C.; Nagels, M.; Vanhoe, H.; Dams, R. *Anal. Chim. Acta* **1988**, *211*, 91–98.
- Versieck, J.; Hoste, J.; Vanballenberghe, L.; De Kesel, A.; Van Renterghem, D. J. *Radioanal. Nucl. Chem.* **1987**, *113*, 299–304.
- Versieck, Jacques; Vanballenberghe, Lidia; De Kesel, Antoine; Hoste, Julien; Wallays, Bart; Vandenhoute, Joris; Baeck, Nicole; Sunderman, F. William, Jr. *Anal. Chim. Acta* **1986**, *204*, 63–75.

- (11) Tan, S. H.; Horlick, G. *Appl. Spectrosc.* 1986, 40, 445-460.  
(12) Iyengar, G. V.; Kollmer, W. E.; Bowen, H. J. M. *The Elemental Composition of Human Tissues and Body Fluids*, 1st ed.; Verlag Chemie: Weinheim, New York, 1978.

RECEIVED for review January 25, 1989. Accepted May 15, 1989. We thank the National Fund for Scientific Research (Belgium,

NFWO) and the Interuniversity Institute for Nuclear Sciences (IIKW) for financial support. The PlasmaQuad was acquired by a grant of the "Fund for Medical Scientific Research (FGWO)". H. Vanhoe is indebted to the Institute for Scientific Research in Industry and Agriculture (IWONL) for a research fellowship. C. Vandecasteele is Research Director of the National Fund for Scientific Research (Belgium).

## Determination of Trace Metals in Reference Water Standards by Inductively Coupled Plasma Mass Spectrometry with On-Line Preconcentration

Diane Beauchemin\*<sup>1</sup> and S. S. Berman

Analytical Chemistry Section, Chemistry Division, National Research Council of Canada, Ottawa, Ontario K1A 0R9, Canada

**A preliminary implementation of on-line preconcentration in inductively coupled plasma mass spectrometry (ICP-MS) improved the detection limits of several elements by a factor of 2-7 compared to ICP-MS alone. The on-line preconcentration system was first assessed by using the method of standard additions to determine Mn, Co, Ni, Cu, Pb, and U in the certified riverine water SLRS-1 whose salt content was low enough to allow monitoring both the preconcentration and the elution processes. Results in good agreement with the certified values were obtained for all but Ni, because of a spectral interference by CaO from coeluted Ca. The system was successfully applied to the determination of Mn, Mo, Cd, and U in the reference open ocean water NASS-2 by using an isotope dilution technique and the method of standard additions.**

### INTRODUCTION

Although the use of inductively coupled plasma mass spectrometry (ICP-MS) is rapidly expanding because of the many features of this technique (summarized in four review articles (1-4)), its application to the analysis of saline waters remains limited. This is largely due to the low tolerance of the technique to dissolved solids with the highest recommended level being of 0.2%, if a solution is to be continuously nebulized without inducing undue instrumental drift caused by solid deposition on the orifice (3, 5). Another restriction comes from effects of concomitant elements that are non-spectroscopic interferences often resulting in a suppression of analyte signals (e.g., ref 6-8). Thus, the analysis of seawaters requires a preliminary treatment in order to reduce their salt content prior to analysis by ICP-MS. This can be accomplished by, for instance, preconcentration on silica-immobilized 8-hydroxyquinoline (I-8-HOQ) (9), a technique that allows the concentration of a number of trace metals while separating them from the univalent major ions and, to some extent, the divalent ions such as Ca and Mg. This technique was successfully applied to the analysis of the coastal seawater reference material CASS-1 (10) and the open ocean water ref-

erence material NASS-2 (11). It presents, however, the disadvantages of being time-consuming and of using large volumes of sample.

Flow injection analysis (FIA) can be used to both speed up the preconcentration process and reduce sample consumption (e.g. ref 12-13). The first on-line application of FIA to the preconcentration of trace metals in seawater was realized by Olsen and co-workers (14). They used a miniature ion-exchange column of Chelex-100 resin to determine Pb, Cd, Cu, and Zn by flame atomic absorption spectrometry (FAAS). Hartenstein and co-workers (15, 16) used a similar setup to enhance the sensitivity of inductively coupled plasma atomic emission spectrometry (ICP-AES), improving the detection limits by over 20 times for Ba, Be, Cd, Co, Cu, Mn, Ni, and Pb (15) compared to conventional continuous aspiration. A detailed study of on-line preconcentration systems in FAAS was performed by Fang and co-workers (17) who compared different types of resins (among them, Chelex-100 and I-8-HOQ). Their observation was that, owing to the smaller exchange capacity of I-8-HOQ and the comparatively high stability of the magnesium complexes, the recoveries of most of the heavy metals from a seawater matrix were not acceptable with I-8-HOQ, even if this material almost always had the highest concentration factor; good recoveries were however obtained with Chelex-100. Nonetheless, Malamas and co-workers (18), as well as Marshall and Mottola (19) successfully used I-8-HOQ for on-line preconcentration in FAAS. They found that the excellent resistance to swelling of silica with changes in solvent composition was an advantage of I-8-HOQ over polymer-based ion exchangers such as Chelex-100.

This work will describe the implementation of the on-line preconcentration technique in ICP-MS, using a miniature column packed with I-8-HOQ (20); a preliminary assessment of the system with the analysis of the riverine water reference material SLRS-1, which has a low salt content and can be run continuously (as was done for its direct analysis in another work (21)) without clogging the torch and/or the interface; and, finally, the application of this system to the analysis of open ocean water NASS-2, a reference material whose salt content precludes its direct analysis by ICP-MS.

### EXPERIMENTAL SECTION

**Instrumentation.** The inductively coupled plasma mass spectrometer used for this work was the Perkin-Elmer SCIEX

\* Author to whom correspondence should be sent.

<sup>1</sup> Present address: Department of Chemistry, Queen's University, Kingston, ON K7L 3N6, Canada.

Table I. ICP-MS Operating Conditions

Plasma Conditions	
torch	conventional ICP-AES
rf power	1.2 kW
reflected power	≤5 W
plasma gas flow	14 L/min
auxiliary gas flow	2.0 L/min
nebulizer gas flow	0.9 L/min
Mass Spectrometer Settings	
Bessel box stop	-6.1 to -6.7 V
Bessel box barrel	3.1-3.5 V
Einzel lenses 1 & 3	-15.1 V
Einzel lens 2	-13.0 V
Bessel box end lenses	-8.6 V
skimmer orifice diameter	1.14 mm
skimmer orifice diameter	0.89 mm
interface pressure	0.8-1.2 Torr
mass spectrometer pressure	(2.5-5.5) × 10 <sup>-5</sup> Torr

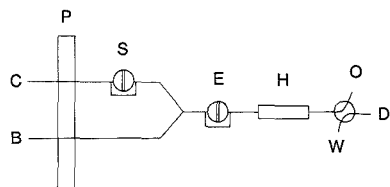


Figure 1. On-line preconcentration setup: C, carrier (deionized distilled water); B, buffer (0.1 M ammonium acetate, pH 5.0); P, peristaltic pump; S, sample injection loop; E, eluent injection loop; H, short column of I-8-HOQ; O, output to the nebulizer; W, to waste; D, deionized distilled water.

ELAN 250 (Thornhill, ON, Canada). Four modifications were made to the originally supplied instrument. A mass flow controller (Model 5850, Brooks Instrument Division, Emerson Electric, Hatfield, PA) was added to the nebulizer gas line, and a peristaltic pump (Minipuls II, Gilson Medical Electronics Inc., Middleton, WI) was used to maintain the sample delivery to the nebulizer at 1.1 mL/min. Also, a conventional ICP-AES torch was used instead of the approximately 15 mm longer one that was provided with the instrument. Finally, an x,y,z translation stage (22) was installed under the torch box to allow the precise and reproducible translation of the torch box in three dimensions. The operating conditions used throughout this work are summarized in Table I. The elutions were recorded in real time and stored on the hard disk with the "multiple elements" software provided with the instrument. With this software, up to 4 masses could be monitored from the same injection. The measurements were made using the multichannel mode by peak hopping rapidly from one mass to the other, staying only a short time (dwell time) of 20 ms at each mass, until the total measurement time of 0.06 s was reached. Three measurements (of 20 ms each) were made per peak (one measurement being done at the central mass while two others were done at ±0.05 u from the assumed peak center). A resolution of 0.8 u (peak width) at 10% peak height was maintained throughout the study. Under these measuring conditions, a data point was generated only every second because of data processing (to plot the points in real time) and dead time.

**On-Line Preconcentration Setup.** Three Teflon sample injection valves (Rheodyne, Inc., Cotati, CA) were installed between a peristaltic pump and the nebulizer, as shown in Figure 1, in a fashion similar to that in ref 19. One ("S" in Figure 1) was used for injecting the sample in a flow of carrier; another ("E" in Figure 1) was for the eluent; and the last one served as a bypass valve, to direct the output from the column either to the nebulizer of the ICP-MS or to waste (in which case, an alternative flow of deionized distilled water (DDW) could be fed to the nebulizer). The preconcentration procedure was the following. The sample was injected (using interchangeable loops with injection volumes from 100 μL to 10 mL) in a flow of carrier (DDW for most of the work) and neutralized by using a buffer of 0.1 M ammonium acetate at pH 5.0 (adjusted with HCl). It then passed through

a short column (3.0 mm i.d. × 4.5 cm long) of silica-immobilized 8-hydroxyquinoline (ca. 80 mg dry weight, 37-75 μm particle size) which was described in detail in ref 20. After a suitable wash time (of at least 1 min), elution was accomplished (in slightly less than 1 min) by injecting 1 mL of eluent (2 M HCl/0.1 M HNO<sub>3</sub>). The flow rate of the carrier line was equal to that of the buffer line of 1.1 mL/min, which produced a flow rate of 2.2 mL/min through the column. This was the maximum flow rate that was allowed because of the back pressure produced in the system. Tygon tubing of 0.76 mm i.d. (Mandel Scientific Co., Ltd., Rockwood, ON, Canada) was used to feed the carrier and buffer, while Teflon tubing of 1 mm i.d. was used for the other flow lines.

**Reagents.** All acids were purified by subboiling distillation in a quartz still (23). Purified ammonia was prepared by isothermal distillation of reagent grade stock. The enriched <sup>62</sup>Ni, <sup>68</sup>Cu, <sup>100</sup>Mo, <sup>111</sup>Cd, and <sup>207</sup>Pb isotopes used for the stable isotope dilution analysis were purchased from the Oak Ridge National Laboratory. The <sup>235</sup>U was the National Bureau of Standards SRM U-930. All the stable isotopes were dissolved as described previously (24) and their concentrations were checked by reverse spiking.

The marine reference waters SLRS-1 and NASS-2 were acidified to pH 1.6 immediately after collection. The riverine water SLRS-1 was gathered in the St. Lawrence River at 2-3 m depth, several kilometers upstream from Québec City (Québec, Canada) and about 30-40 km upriver from the saltwater mixing zone. The seawater NASS-2 was collected at a depth of 1300 m, southeast of Bermuda. (Complete information on the procurement of these water reference materials and other marine reference materials can be obtained from S. Berman, Marine Analytical Chemistry Standards Program, Division of Chemistry, National Research Council of Canada, Ottawa, ON, Canada K1A 0R6.)

**Analysis Procedure. Instrument Operating Conditions.** Both the ion lens voltages of the instrument and the plasma operating conditions (Table I) were chosen while continuously aspirating a multielement standard solution through the bypass valve (while the effluent of the column is being routed to waste), so as to provide a compromise between high sensitivity and low oxide levels.

**Data Treatment.** The raw count rates were transferred to a VAX-11 computer (Digital Equipment Corp., Maynard, MA) and processed by using programs written in FORTRAN. The count rates recorded for each elution peak were first smoothed with a seven-point Savitzky-Golay (25) moving window; background correction was performed by using points on both sides of each peak. The area and height of each peak were then measured. For the determination of the detection limit, the mean and standard deviation of several (typically eight) injections of the eluent were calculated. Isotope ratios were obtained by either ratioing the areas or the heights of the isotopes considered.

**Isotope Dilution Calculations.** The analyte concentration in the waters was calculated by using the following formula:

$$C = \frac{M_S K (A_S - B_S R)}{V(BR - A)}$$

where C is the analyte concentration in the water sample (microgram per liter), M<sub>S</sub> is the mass of the stable isotope spike (nanogram), V is the volume of water sample to which the isotopic spikes were added (milliliter), A is the natural abundance of the reference isotope, B is the natural abundance of the spike isotope, A<sub>S</sub> is the abundance of the reference isotope in the spike, B<sub>S</sub> is the abundance of the spike isotope in the spike, K is the ratio of the natural and spike atomic weights, and R is the measured ratio (reference isotope/spike isotope) corrected for mass discrimination where needed (as explained later) measured after the addition of the spike. It should be noted that the ratio used in the isotope dilution calculations was obtained by first subtracting the intensities of the column blank from those of the reference and spike isotopes and by then ratioing the resulting blank-subtracted intensities.

## RESULTS AND DISCUSSION

**Preliminary Assessment of On-Line Preconcentration ICP-MS.** The miniature column of I-8-HOQ used in this work was developed by Nakashima and co-workers (20) for off-line

**Table II. Detection Limits ( $\mu\text{g/L}$ ) for Mn, Co, Ni, and Cu under Different Preconcentration Conditions**

Mn	Co	Ni	Cu	conditions
0.9	0.2	0.2	3	no buffer <sup>a</sup>
0.09	0.03	0.06	0.9	1/4 buffer <sup>b</sup>
0.05	0.05	0.03	0.2	1/2 buffer <sup>c</sup>
0.03	0.05	0.09	0.3	all buffer <sup>d</sup>

<sup>a</sup>Carrier = buffer = DDW at 1.1 mL/min. <sup>b</sup>Carrier = DDW at 2 mL/min; buffer = 0.1 M ammonium acetate, pH 5.0, at 0.5 mL/min. <sup>c</sup>Carrier = DDW at 1.1 mL/min; buffer = 0.1 M ammonium acetate, pH 5.0, at 1.1 mL/min. <sup>d</sup>Carrier = buffer at 2 mL/min; buffer = 0.1 M ammonium acetate, pH 5.0, at 0.5 mL/min.

preconcentration of trace metals from seawater in a flow-system prior to their determination by graphite furnace atomic absorption spectrometry (GFAAS). The main purpose of their work was to decrease the sample consumption. The procedure followed was essentially the same as the column method described in ref 9, but on a smaller scale. Briefly, the sample was pumped through the column at 2 mL/min. The column was washed with a small volume of DDW and the elution was then carried out by pumping 1.7 mL of 2 M HCl/0.1 M HNO<sub>3</sub> (at 1 mL/min) through the column. The pH of the sample was adjusted prior to its preconcentration (no buffer was used). In contrast, when the same miniature column was installed on-line (as shown in Figure 1), it appeared that neutralization of the sample with a buffer was mandatory if reproducible elutions were to be obtained. This is illustrated in Table II where the effect of different proportions of buffer/carrier on the detection limits of Mn, Co, Ni, and Cu is summarized. There was a dramatic improvement as soon as the ammonium acetate buffer was introduced, which leveled off when the proportion of buffer became equal or greater than that of the carrier (DDW). Since, according to the results in Table II, it was not necessary to use an all buffered system (i.e. buffer as the carrier), a buffer flow rate of 1.1 mL/min, equal to that of the carrier (DDW), was used thereafter.

The blank signals (i.e. injection of eluent without prior injection of samples), sensitivities, and detection limits obtained in these preconcentration conditions, using peak area and peak height, are compared in Table III. They are based on 100- $\mu\text{L}$  injections of an aqueous 10  $\mu\text{g/L}$  multielement standard (with subsequent elutions with 1 mL of eluent). In general, the detection limits using peak height were better or similar to those using peak area. (It should be noted that similar results could be obtained by using 1-mL injections of an aqueous 1  $\mu\text{g/L}$  multielement standard; the 100- $\mu\text{L}$  injection loop was preferred for this preliminary characterization of the system, because of the shorter loading time required.) The most important reproducible blanks were observed for

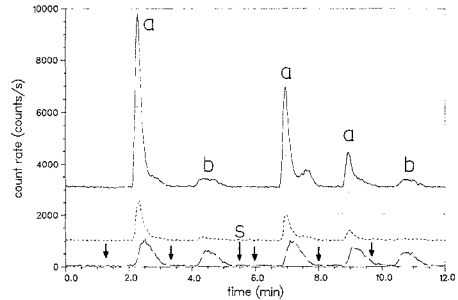


**Figure 2.** Preconcentration and elution processes of <sup>55</sup>Mn (—), <sup>59</sup>Co (···), <sup>60</sup>Ni (---), and <sup>65</sup>Cu (-·-·), showing that with too short a wash time, two elutions are required for a complete recovery of the elements. Injections of 1 ng (as 100  $\mu\text{L}$  of 10  $\mu\text{g/L}$ ) of each element were done at time 0.0 and that indicated by the "S" arrow. Injections of 1-mL eluents (2 M HCl/0.1 M HNO<sub>3</sub>) are indicated by the other arrows. "a" and "b" indicate respectively analyte elutions and column blank elutions.

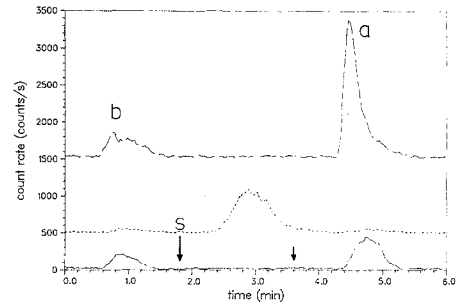


**Figure 3.** Preconcentration and elution processes of <sup>96</sup>Mo (—), <sup>114</sup>Cd (···), <sup>121</sup>Sb (---), and <sup>208</sup>Pb (-·-·). An injection of 1 ng (as 100  $\mu\text{L}$  of 10  $\mu\text{g/L}$ ) of each element was done at the time indicated by the "S" arrow. Injections of 1 mL of eluent (2 M HCl/0.1 M HNO<sub>3</sub>) were done at time 0.0 and that indicated by the other arrow. "a" and "b" indicate respectively analyte elution and column blank elution.

Sn, Pb (see Figure 4), and especially Cu. (The same observation was made for Fe and Zn; in their case however, the blank was much higher and quite irreproducible so that no reliable results could be obtained.) Measurements of isotope ratios during the elution of column blanks revealed that these elements were released by the column (they were probably preconcentrated from the reagents used).

Typical elutions of 1 ng of each of several elements, as well as column blanks, are illustrated during the first 5.5 min of

**Table III. Figures of Merit with On-Line Preconcentration ICP-MS (Carrier = DDW at 1.1 mL/min; Buffer = 0.1 M Ammonium Acetate, pH 5.0, at 1.1 mL/min)**

element	peak area			peak height		
	blank, <sup>a</sup> counts	sensitivity, counts/( $\mu\text{g/L}$ )	DL, <sup>b</sup> $\mu\text{g/L}$	blank, counts/s	sensitivity, (counts/s)/( $\mu\text{g/L}$ )	DL, $\mu\text{g/L}$
Mn	181 $\pm$ 24 <sup>c</sup>	1557 $\pm$ 56	0.05	296 $\pm$ 22	6500 $\pm$ 130	0.01
Co	46 $\pm$ 15	927 $\pm$ 39	0.05	123 $\pm$ 73	4020 $\pm$ 310	0.05
Ni	37 $\pm$ 5	480 $\pm$ 110	0.03	93 $\pm$ 26	1660 $\pm$ 410	0.05
Cu	296 $\pm$ 16	217 $\pm$ 58	0.2	555 $\pm$ 43	578 $\pm$ 57	0.2
Mo	36 $\pm$ 13	120 $\pm$ 41	0.3	97 $\pm$ 14	247 $\pm$ 72	0.2
Cd	23 $\pm$ 3	282 $\pm$ 13	0.03	43 $\pm$ 2	1042 $\pm$ 78	0.006
Sn	150 $\pm$ 5	208 $\pm$ 21	0.07	262 $\pm$ 11	618 $\pm$ 27	0.05
Pb	151 $\pm$ 6	357 $\pm$ 48	0.05	266 $\pm$ 14	1400 $\pm$ 180	0.03
U	2 $\pm$ 2	226 $\pm$ 15	0.03	19 $\pm$ 6	790 $\pm$ 100	0.02

<sup>a</sup>Signal observed for the column blank (1.4–2.0-min interval). <sup>b</sup>Detection limit (based on 3 $\sigma$ ) which could be reproduced over at least a month. <sup>c</sup>Precision expressed as the standard deviation ( $n = 3-5$ ).

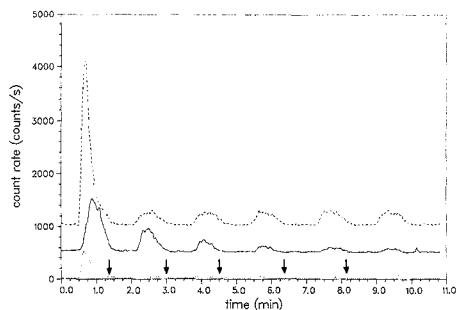


**Figure 4.** Peaks observed with the injection of six consecutive 1-mL aliquots of eluent following the injection of 1 ng (as 100  $\mu\text{L}$  of 10  $\mu\text{g/L}$ ) of each of  $^{98}\text{Mo}$  (—),  $^{114}\text{Cd}$  (···), and  $^{209}\text{Pb}$  (---). The first injection of the eluent was carried out at time 0.0 (about 1 min following the sample injection).

Figure 2, and in Figure 3. Figure 2 shows results for Mn, Co, Ni, and Cu. It is interesting to see (looking at the 0.0–5.5-min interval) that Mn, Co, and Ni came out at essentially the same time (1 min after injection of eluent), whereas Cu eluted about 30 s later. This behavior is in good agreement with the stability constants of 8-HOQ complexes (26), with  $\text{Cu}^{2+}$  forming the strongest one. The 5.5–12-min interval illustrates the importance of a preelution wash with this on-line preconcentration system. When too short a time (in this instance, 30 s) was allowed after injection of the sample and before elution, disproportioned elution peaks were obtained and more than one injection of eluent was required for a complete recovery of analyte. However, when the wash time was increased to at least 1 min, reproducible peaks (such as those obtained in the 0.0–5.5-min interval) were seen. This wash time, which is longer than that required to simply traverse the column, probably accounts for diffusional processes as well as actually washing the column. (During the analysis of seawater, if the wash time was too short (i.e. less than 1 min), a bright yellow Na emission was seen in the plasma as soon as the bypass valve was switched to monitor the elution.)

Figure 3 illustrates the cases of Mo, Cd, Sb, and Pb. Sb is obviously not retained (this was true at both pH 5.0 and 8.0). The elution pattern of Mo was different from that of the other elements considered in this work. Like Cu, Mo eluted later, but several injections of eluent were required (Figure 4) in order to recover Mo completely. It should be noted that symmetrical peaks were observed only for unrestrained elements (Sb) or molecular species, such as  $^{40}\text{Ar}^{36}\text{Cl}$  at  $m/z$  75, and  $^{36}\text{Cl}^{16}\text{OH}$  at  $m/z$  52, resulting from the coelution of chlorine-containing compounds. These peaks were wide and symmetrical, in contrast to the elution peaks which were, in general, tall, narrow, and tailing toward the end of the elution. A similar behavior was observed in FAAS by Olsen and co-workers (14) who reported that nonselective absorption of light by Na from the matrix gave a low and wide peak during the preconcentration period, whereas a high and narrow peak was obtained during elution of the analyte.

The detection limits and sensitivities obtained for Mn, Co, Cu, Cd, and Pb by direct aspiration are compared to those obtained with on-line preconcentration in parts a and b of Table IV, respectively. Standard solutions in the range 1–100  $\mu\text{g/L}$  were used for direct aspiration while a maximum of 100  $\mu\text{L}$  of 10  $\mu\text{g/L}$  was used for the on-line preconcentration. Except for Cu whose column blank is the limiting factor, peak area detection limits were similar to those obtained by continuous nebulization (Table IVa), which was to be expected since the same measurement period was used in both cases. The results obtained by using peak height showed a different

**Table IV**

a. Comparison of Some Typical Detection Limits ( $\mu\text{g/L}$ ) Observed with Direct Aspiration vs On-Line Preconcentration

element	continuous aspiration	on-line preconcn		ratios	
		height	area	continuous/height	continuous/area
Mn	0.04	0.01	0.05	4	0.8
Co	0.04	0.05	0.05	0.8	0.8
Cu	0.07	0.2	0.2	0.4	0.4
Cd	0.03	0.006	0.03	5	1.0
Pb	0.07	0.03	0.05	2	1.4

b. Comparison of Some Typical Sensitivities ((counts/s)/( $\mu\text{g/L}$ )) Observed with Direct Aspiration vs On-Line Preconcentration

element	continuous aspiration	on-line preconcn height	ratio height/continuous
Mn	3701	6500	1.8
Co	3149	4020	1.3
Cu	1436	578	0.4
Cd	783	1042	1.3
Pb	745	1400	1.9

behavior. The detection limits for Cu and Co were the same as with peak area, but those for Pb and especially Mn and Cd were improved with on-line preconcentration (even with a preconcentration factor of 1). These improvements can be explained (at least partly) by considering the elution process. Although 1 mL of eluent is injected, the analyte is mostly eluted near the front of this volume. As can be seen in Figures 2–4, 1 ng of analyte came out over about 1 min but most of it was already out in the first 30 s. This generally resulted in an enhancement of the signal compared to that of 1 ng/mL aspirated directly, as can be seen from the change in peak height sensitivities reported in Table IVb. However, on comparison of the changes in sensitivities (Table IVb) to the corresponding changes in detection limits (Table IVa), it appears that they are similar for Co, Cu, and Pb whereas the improvement in detection limit is much greater than that in sensitivity for Mn and Cd. This means that the increased sensitivity is cancelled by increased noise (resulting from the shorter measurement time used for peak heights) in the case of Co, Cu, and Pb, whereas there would seem to actually be a reduction in noise for Mn and Cd. Although the difference between the results of Co and Mn can partly be explained by the lower recovery of Co experienced with 1-8-HOQ (9), future work will aim at accounting for the above observations (which were reproducible over several months).

**Analysis of SLRS-1.** The first application of the on-line preconcentration system was made to the certified riverine water SLRS-1. The method of standard additions was used (additions were made to an aliquot of SLRS-1, prior to injection, in order to double the concentrations of the analytes). A 1-fold preconcentration was performed for Mn, Ni, and Cu (i.e. 1-mL aliquots of the unspiked and spiked SLRS-1 were injected) while a 10-fold preconcentration was done for Co, Pb, and U. (In each case, the three elements stated were monitored from the same injection.) The results, computed by using both peak height and peak area, are summarized in Table V. A good agreement with the certified values was achieved by either peak area or peak height for Mn and Co, whereas peak area gave the best results for Pb and U, and peak height gave the most accurate and precise result for Cu. Overall, it seems that within each pair of results (area vs height), the result of highest precision is also the most accurate. (These observations were also true for seawater.) However, high results (by both peak height and peak area) were obtained for Ni. It should be noted that, although the

**Table V. Concentration ( $\mu\text{g/L}$ ) of Some Trace Metals in the Riverine Water SLRS-1 As Determined by the Method of Standard Additions with On-Line Preconcentration ICP-MS,<sup>a</sup> with Peak Area and Peak Height**

element	peak area	peak height	certified value <sup>b</sup>
Mn	1.79 $\pm$ 0.54 <sup>c</sup>	1.81 $\pm$ 0.55	1.77 $\pm$ 0.23
Co	0.047 $\pm$ 0.011	0.044 $\pm$ 0.014	0.043 $\pm$ 0.010
Ni	1.41 $\pm$ 0.40	1.26 $\pm$ 0.38	1.07 $\pm$ 0.06
Cu	4.0 $\pm$ 1.5	3.60 $\pm$ 0.88	3.58 $\pm$ 0.30
Pb	0.099 $\pm$ 0.018	0.082 $\pm$ 0.020	0.106 $\pm$ 0.011
U	0.295 $\pm$ 0.012	0.243 $\pm$ 0.048	0.28 $\pm$ 0.03

<sup>a</sup>The preconcentration factor was 1 for Mn, Ni, and Cu, and 10 for Co, Pb, and U. <sup>b</sup>The uncertainties for the accepted values are 95% tolerance limits—not standard deviations. <sup>c</sup>Standard deviation ( $n = 3$ ).

most abundant isotope was monitored for all the other elements, <sup>60</sup>Ni was used to avoid the isobaric interference of <sup>58</sup>Fe on <sup>58</sup>Ni.

One plausible explanation for the higher Ni result would be an isobaric interference from <sup>44</sup>Ca<sup>16</sup>O, which may result from a coelution of Ca. It was noted during the analysis of SLRS-1 that some Ca went through the column during the preconcentration. This is illustrated in Figure 5 where a 1-fold preconcentration of SLRS-1 was accomplished by injecting 1 mL of SLRS-1 (as four 250- $\mu\text{L}$  injections) followed by elution with 1 mL of eluent and an additional injection of eluent to check if elution was complete (i.e. if the column blank was observed). Four symmetrical peaks appeared during the preconcentration which were not due to Ni and may be attributed to <sup>44</sup>Ca<sup>16</sup>O because they remained identical during the injection of SLRS-1 spiked with Ni, whereas the taller asymmetrical peak observed during the elution increased. However, although some of the Ca was obviously not retained by the column, there was probably some Ca that was retained as well. This assertion is supported by the fact that the alkaline earths are complexed by I-8-HOQ (for instance, 8-HOQ can be used for the determination of Mg (26)) but to a smaller extent than the transition metals. This smaller retention can become significant when high concentrations of alkaline earths are present with traces of metals. For instance, Fang and co-workers (17) reported unacceptable recoveries of most of the heavy metals from a seawater matrix because of the high concentrations of alkaline earths, in particular magnesium which had a concentration of 1300 mg/L.

**Analysis of NASS-2.** The on-line preconcentration system was really put to the test by performing the analysis of the open ocean reference water NASS-2. This time, isotope dilution was more specifically considered, the method of standard additions being mostly reserved for monoisotopic elements. The isotopic spikes were chosen so as to obtain isotopic ratios close to unity. During each preconcentration of NASS-2, the effluent was directed to waste to prevent the

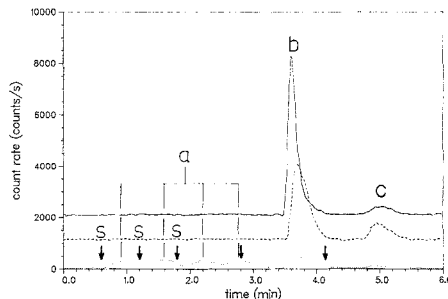


**Figure 5.** Preconcentration and elution processes of <sup>55</sup>Mn (—), <sup>60</sup>Ni (···), and <sup>68</sup>Cu (---) from riverine water SLRS-1. Injections of 4  $\times$  250  $\mu\text{L}$  (1 mL) SLRS-1 were done at time 0.0 and those indicated by the "S" arrows. Injections at 1-mL eluent (2 M HCl/0.1 M HNO<sub>3</sub>) are indicated by the other arrows. "a" indicates the peaks observed during the preconcentration period, "b" the elution, and "c" a column blank.

high salt content from reaching the nebulizer and the interface. The effluent was only monitored during elutions (performed after a wash period of at least 1 min). The natural isotopic ratios of standard solutions of Ni, Cu, Mo, and Cd were first measured (by on-line preconcentration) to assess the extent of mass discrimination. The ratios were compared to IUPAC values (27) and found to all be in good agreement. Therefore, no correction for mass discrimination was made. In the case of Pb, a solution of NBS 981 was used. The <sup>207</sup>Pb/<sup>208</sup>Pb ratio of the NBS standard solution came out higher than expected for no apparent reason. Also, no reliable result could be obtained for Pb by isotope dilution analysis, for any of the reference waters considered in this work, whereas good results were obtained in previous works (11, 21), using the original column preconcentration with I-8-HOQ.

The results obtained by isotope dilution analysis are summarized in Table VI, along with the results obtained by standard additions, those obtained in a previous work (11) by isotope dilution analysis with off-line preconcentration, and the certified values. The isotope dilution determination with on-line preconcentration of Mo, Cd, and U yielded results in good agreement with the certified values, as did the method of standard additions for monoisotopic Mn. However, isotope dilution with on-line preconcentration gave results too high for Ni and Cu, although the method of standard additions (using <sup>68</sup>Cu) gave a Cu result in closer agreement with the certified value. On comparison of the on-line preconcentration results with those obtained with the off-line method, it appears that isotope dilution yields good results for Ni and Cu but not Mo when used off-line. Since the major difference between the on-line and off-line preconcentration techniques is the neutralization of the ammonium acetate buffer (which is not used with the off-line method), it would appear that neutralization of the sample with a buffer improved the

**Table VI. Concentration ( $\mu\text{g/L}$ ) of Some Trace Metals in the Open Ocean Water NASS-2 As Determined by Isotope Dilution and the Method of Standard Additions with On-Line Preconcentration ICP-MS<sup>a</sup>**

element	isotope dilution	standard addition	previous work <sup>b</sup>	certified value <sup>c</sup>
Mn		0.022 $\pm$ 0.007 <sup>d</sup>		0.022 $\pm$ 0.007
Ni	0.332 $\pm$ 0.001		0.268 $\pm$ 0.005	0.257 $\pm$ 0.027
Cu	0.190 $\pm$ 0.020	0.095 $\pm$ 0.011	0.116 $\pm$ 0.011	0.109 $\pm$ 0.011
Mo	12.1 $\pm$ 0.9		8.90 $\pm$ 0.64	11.5 $\pm$ 1.9
Cd	0.033 $\pm$ 0.001		0.027 $\pm$ 0.001	0.029 $\pm$ 0.004
U	2.91 $\pm$ 0.17	3.06 $\pm$ 0.56	2.92 $\pm$ 0.04	3.00 $\pm$ 0.15

<sup>a</sup>The preconcentration factor was 1 for Mo and U and 10 for Mn, Ni, Cu, and Cd. <sup>b</sup>See ref 11. Determined by the isotope dilution technique with a 50-fold off-line preconcentration. <sup>c</sup>The uncertainties for the accepted values are 95% tolerance limits—not standard deviations. <sup>d</sup>Precision expressed as the standard deviation ( $n = 3$ –12).

loading of Mo, whereas it was a source of interferences for the determination of Ni and Cu. It is interesting to note that different sample injection volumes (i.e. preconcentration factors) can be used to speed up the analysis. For instance, only 1 mL was needed for Mo and U, while 10 mL was required for the lower concentrations (Mn, Ni, Cu, and Cd).

### CONCLUSIONS

The implementation of on-line preconcentration in ICP-MS can both speed up the sample pretreatment of seawater and decrease the sample consumption drastically. With the original procedure (9), the preconcentration of NASS-2 required 500-mL aliquots (11) whereas only 10-mL aliquots were needed by on-line preconcentration. Furthermore, a preconcentration by a factor of 50 was found necessary with the original procedure in order to get reliable values for Cd, whereas a factor of 10 was quite sufficient with on-line preconcentration because of the additional enhancement in sensitivity (see Table IV) which results when elutions are followed in real time (most of the analyte coming out in the first half of the eluent reaching the column). Finally, at least 8 h (for the preconcentration as well as the actual analysis by ICP-MS) was required with the original procedure for the analysis of three samples of NASS-2 and three column blanks; only 45 min was needed with on-line preconcentration. In terms of "concentration efficiency" (CE), defined as the product of the enrichment (or preconcentration) factor (EF) and the sampling frequency in number of samples analyzed per minute (28), this converts to a CE value of 0.31 EF/min with the original procedure and of 0.67 EF/min with on-line preconcentration. This preliminary on-line preconcentration setup thus improved the concentration efficiency by a factor of 2. However, it was not applicable to all the elements normally determined with the original procedure (for instance, huge column blanks precluded the determination of Fe and Zn). Future work will deal with a more thorough application of this system to the analysis of saline waters as well as the optimization of several parameters of the setup in order to improve even more the concentration efficiency. These parameters will include the column dimensions, sampling frequency (which could probably be doubled if the buffer line was eliminated and 0.05 M ammonium acetate was used as the carrier, at a rate of 2.2 mL/min), pH of the buffer, column blanks, etc.

### ACKNOWLEDGMENT

The authors are grateful to J. W. McLaren for his helpful comments during the preparation of the manuscript.

**Registry No.** Mn, 7439-96-5; Co, 7440-48-4; Ni, 7440-02-0; Cu, 7440-50-8; Mo, 7439-98-7; Cd, 7440-43-9; Sn, 7440-31-5; Pb, 7439-92-1; U, 7440-61-1; water, 7732-18-5; 8-hydroxyquinoline, 148-24-3.

### LITERATURE CITED

- (1) Douglas, Donald J.; Houk, Robert S. *Prog. Anal. At. Spectrosc.* **1985**, *8*, 1-18.
- (2) Gray, Alan L. *Spectrochim. Acta, Part B* **1985**, *40B*, 1525-1537.
- (3) Houk, Robert S. *Anal. Chem.* **1986**, *58*(1), 97A-105A.
- (4) Gray, A. L. *Fresenius' Z. Anal. Chem.* **1986**, *324*, 561-570.
- (5) Douglas, D. J.; Kerr, L. A. *J. Anal. At. Spectrom.*, in press.
- (6) Beauchemin, D.; McLaren, J. W.; Berman, S. S. *Spectrochim. Acta, Part B* **1987**, *42B*, 467-490.
- (7) Tan, S. H.; Horlick, G. J. *Anal. At. Spectrom.* **1987**, *2*, 745-763.
- (8) Gillson, George R.; Douglas, Donald J.; Fulford, John E.; Halligan, Kenneth W.; Tanner, Scott D. *Anal. Chem.* **1988**, *60*, 1472-1474.
- (9) Sturgeon, R. E.; Berman, S. S.; Willie, S. N.; Desaulniers, J. A. H. *Anal. Chem.* **1981**, *53*, 2337-2340.
- (10) McLaren, J. W.; Myktyiuk, A. P.; Willie, S. N.; Berman, S. S. *Anal. Chem.* **1985**, *57*, 2907-2911.
- (11) Beauchemin, Diane; McLaren, James W.; Myktyiuk, Alex P.; Berman, Shier S. J. *Anal. At. Spectrom.* **1988**, *3*, 305-308.
- (12) McLeod, Cameron W. J. *Anal. At. Spectrom.* **1987**, *2*, 549-552.
- (13) Christian, Gary D.; Ruzicka, Jaromir. *Spectrochim. Acta, Part B* **1987**, *42B*, 157-167.
- (14) Olsen, Svend; Pessenda, Luiz, C. R.; Ruzicka, Jaromir; Hansen, Eio H. *Analyst* **1983**, *108*, 905-917.
- (15) Hartenstein, Steven D.; Ruzicka, Jaromir; Christian, Gary D. *Anal. Chem.* **1985**, *57*, 21-25.
- (16) Hartenstein, Steven D.; Christian, Gary D.; Ruzicka, Jaromir. *Can. J. Spectrosc.* **1985**, *30*, 144-148.
- (17) Fang, Zhaolun; Ruzicka, J.; Hansen, E. H. *Anal. Chim. Acta* **1984**, *164*, 23-39.
- (18) Malamas, Fottis; Bengtsson, Mats; Johansson, Gillis. *Anal. Chim. Acta* **1984**, *160*, 1-10.
- (19) Marshall, Monte A.; Mottola, Horacio A. *Anal. Chem.* **1985**, *57*, 729-733.
- (20) Nakashima, S.; Sturgeon, R. E.; Willie, S. N.; Berman, S. S. *Fresenius' Z. Anal. Chem.* **1988**, *330*, 592-595.
- (21) Beauchemin, Diane; McLaren, J. W.; Myktyiuk, A. P.; Berman, S. S. *Anal. Chem.* **1987**, *59*, 778-783.
- (22) Beauchemin, Diane; McLaren, J. W.; Berman, S. S. *J. Anal. At. Spectrom.* **1988**, *3*, 775-780.
- (23) Dabeka, R. W.; Myktyiuk, A. P.; Berman, S. S.; Russel, D. S. *Anal. Chem.* **1976**, *48*, 1203-1207.
- (24) McLaren, J. W.; Beauchemin, Diane; Berman, S. S. *Anal. Chem.* **1987**, *59*, 610-613.
- (25) Savitzky, Abraham; Golay, Marcel J. E. *Anal. Chem.* **1964**, *36*, 1627-1639.
- (26) Burger, K. "Organic Reagents in Metals Analysis" In *International Series of Monographs in Analytical Chemistry*; Beicher, R., Freiser, H., General Eds.; 1973; Vol. 54.
- (27) De Bièvre, Paul; Gallet, Marc; Holden, Norman E.; Barnes, I. *Lynus J. Phys. Chem. Ref. Data* **1984**, *13*, 809-891.
- (28) Fang, Zhaolun; Xu, Shukun; Zhang, Suchun. *Anal. Chim. Acta* **1987**, *200*, 35-49.

RECEIVED for review July 1, 1988. Resubmitted February 27, 1989. Accepted June 2, 1989. This is NRCC Publication No. 30431.



# Development of an Optical Relative Humidity Sensor. Cobalt Chloride Optical Absorbency Sensor Study

Francisca Boltinghouse\* and Kenneth Abel

The ABEL Company, SR 774 Box 192-A, Pembroke, Virginia 24136

**Cellulose impregnated with cobalt chloride was investigated for use in quantitative relative humidity (RH) measurements. Two cellulose substrates were tested: (a) unmodified cellulose chromatography paper and (b) the same paper after acetylation. Decreasing the amount of cobalt chloride in the cellulose matrix decreases both hysteresis effects and the effective RH range over which the salt/substrate combination can be used for RH measurement. Acetylation of the cellulose extends the effective RH range, increases reproducibility, and decreases hysteresis effects.**

## INTRODUCTION

Relative humidity can be measured by using various techniques including infrared spectrometry (1), wet/dry thermometers (2), chilled mirror dew point depression (3), and a variety of sensors based on various electrical properties hygroscopic materials. Some inexpensive hygrometers use the extension of a natural or synthetic fiber, the length of which is proportional to the surrounding water vapor concentration. The most common sensors are those that measure the change in capacitance of dielectric material or the change in resistance of a conductive material as a function of relative humidity. A novel detector for moisture in gases employing a quartz crystal coated with hydroscopic material has been described in which weight changes are measured to determine water gain or loss (4). A recent report describes a sensor based on a poly(tetrafluoroethylene) (PTFE) film in which the impedance of the grafted film decreases as the humidity increases (5). Since Winkler (6) first noted a blue solution when dissolving the anhydrous salt of cobalt chloride in absolute ethanol and reported a color change when water is added, colorimetric sensors have been suggested using metal salt hydrates of cobalt, copper, and vanadium (7). Cobalt chloride has six states of hydration and exhibits progressive color changes with corresponding changes in hydration state. Recent reports indicate that with excess exposure to moisture cobalt chloride can exist in even higher states of hydration (8) although no further color change can be noted. As the initially anhydrous cobalt salt bonds with each water molecule, it exhibits a color change from blue to a fully hydrated pink (9). Figure 1 illustrates the transmission absorbing spectra of fully hydrated and anhydrous cobalt chloride on filter paper. The scattering/absorbency spectrum, corrected for substrates' reflectance, is essentially identical.

From a practical standpoint, measurement of the change in intensity of light reflected from a sensor element surface is easier to develop into an optrode than is measurement of the change in intensity of light transmitted through a sensor element. Both absorbency measurements and reflectance measurements were taken. The results were equivalent except at relative humidity values from 90 to 100% where water absorption into the cellulose substrate results in increased transparency, which in turn reduces the reflected/scattered

signal in a nonreproducible manner. Because the absorbency experiments were more comprehensive, the majority of the data reported herein was taken from experiments using the transmission mode of optical absorbency.

In the earliest literature reports, cobalt chloride was utilized primarily as a qualitative indicator of the presence or absence of moisture, an application for which it is still used in determining the residual capacity of solid desiccants. In recent years, attempts to turn the principle into a quantitative method for monitoring relative humidity have appeared in the literature. An optical waveguide humidity detector employing a cobalt chloride-gelatin film on silica optical fibers has been reported (10). An even more recent report describes the application of a porous optical fiber segment impregnated with cobalt chloride to measure relative humidity with the goal of developing a fiber-optic RH sensor (11). This recent work has apparently been prompted by the many reports of fiber-optic sensors being developed for measuring a variety of physical and/or chemical variables. Fiber-optic sensors have been reported for measuring ammonia (12), pH (13), CO<sub>2</sub> (14), O<sub>2</sub> (15), temperature (16, 17), and pressure (18). In spite of the advances in fiber-optic-sensor development at the laboratory level, only the fiber-optics temperature probe appears to have been successfully commercialized.

The work described herein is part of an ongoing investigation into the possible application of optical methods for quantitative moisture and relative humidity sensor systems. This report is based on two methods: optical absorbency and reflectance of cellulose-based substrates impregnated with cobalt chloride as a function of relative humidity.

## EXPERIMENTAL SECTION

**Control of Relative Humidity.** A Shimadzu UV-160 double-beam recording spectrophotometer with computerized data reduction was used to measure the optical absorbency of the sample. A specially designed sample cell replaced the cell supplied by the manufacturer. The entire cell chamber is fabricated from a block of aluminum, which is attached to a water bath circulator for temperature control. Relative humidity in the test chamber is controlled by mixing dry air and water saturated air streams, using identical, calibrated rotometers and fine control valves to vary the volumetric ratios of the two air streams. The two air streams are mixed within the cell block, passed sequentially through the sample and reference cell, and exhausted through a Rotronic RH sensor ( $\pm 1\%$  reported reproducibility within the range of 5%-95% RH). The saturated air stream is produced by bubbling dry air through a water chamber built into the cell block to ensure isothermal temperature control. The water chamber incorporates a channel-grooved, highly porous fire brick as an auxiliary wick to fully saturate the wet air stream. Figure 2 is a three-dimensional representation of the cell chamber.

The design of the optical path of the UV-160 includes matched silicon photodetectors located close to the sample. This feature makes it particularly useful for translucent or turbid samples having high scattering coefficients: The design provides excellent results in transmission absorbency of highly absorbing cellulose paper substrates, allowing reproducible data acquisition across the visible spectrum.

For the reflectance studies, a single-beam system was fabricated utilizing a Beckman DU quartz prism monochromator, a 12-V tungsten halogen light source operating at 6 V from a constant

\* Author to whom correspondence and reprint requests should be addressed.

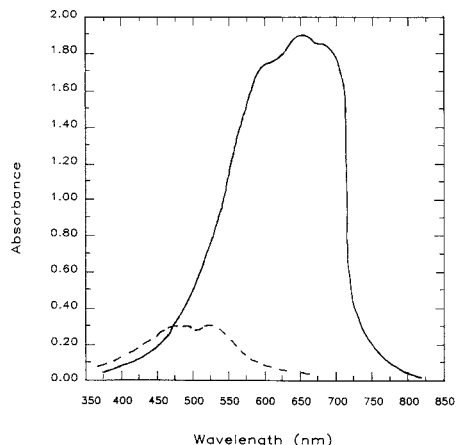


**Figure 1.** Absorbency spectra of  $\text{CoCl}_2$  on cellulose filter paper: solid line, anhydrous; broken line, hexahydrate.

voltage regulator, and an amplified silicon diode as the reflected light detector. The stability of this single-beam system was sufficient to allow noise-free, reproducible readings to four decimal places. Figure 3 is a schematic of this system.

**Acetylated Substrate Preparation.** Whatman Chr2 cellulose filter paper (Whatman Labsales, Hillsboro, OR) was immersed at room temperature in distilled water for 5 min to initiate swelling of the cellulose structure; it was then immersed in a second mixture of 30% pyridine and 70% water (by volume) for another 5 min. This was followed by immersion in a third solution of 70% pyridine and 30% water for an additional 5 min. The fourth and final solution consisted of 70% pyridine and 30% acetic anhydride. The cellulose paper was left for 24 h in the final solution and then dried in a HEPA-filtered laminar flow hood prior to treatment with cobalt chloride solution. For comparison, Whatman Chr2 without acetylation was used directly as received from the manufacturer.

**Sample Preparation.** The cobalt chloride was dissolved in methanol at the following concentrations: 5, 10, 25, 50, and 75 mg/mL. Each substrate was soaked in a specified solution for 1–2 min. For each sample treated with the  $\text{CoCl}_2$  solutions, a second was treated with pure methanol for use in the reference beam of the spectrophotometer. All samples were allowed to dry in a clean laminar flow hood for a minimum of 1 h. Each sample was screened at room temperature by measuring its optical absorbency spectrum at 0 and at 95% RH prior to extensive data

**Table I.** Conversion of Solution Concentration to Paper Concentration

Solution Concentration (mg $\text{CoCl}_2$ /ml MeOH)	Paper Concentrations:	
	Acetylated Chr.2 ( $g_s/g_p$ )	Unmodified Chr.2 ( $g_s/g_p$ )
75	0.200	0.180
50	0.173	0.130
25	0.115	0.073
10	0.061	0.046
5	0.042	0.036
Weight of paper	1.80 mg/sq mm	1.79 mg/sq mm
paper thickness	0.229 mm	0.190 mm

collection. Table I outlines the cobalt chloride paper concentration in grams of solution per gram of paper ( $g_s/g_p$ ) for both substrates, the weight of the paper, and the paper thickness.

Triplicate sets of data were measured at 10% RH increments both from 0 to 80% RH and from 80 to 0% RH for each sample. The UV-160 was operated in the double-beam kinetic mode, which allowed determination of response times for each incremental RH step. The RH steps were not changed until the kinetic mode response curve showed no more than a 1% change in total step response over a 30-min time period. All optical absorbency and reflectance measurements were taken at the incident wavelength of 675 nm corresponding to the maximum absorbency for the concentrations of interest.

## RESULTS

**Unmodified Cellulose Results.** The concentration of cobalt chloride deposited within the cellulosic substrates has a significant effect on the optical properties as a function of relative humidity. Samples prepared from the following cobalt chloride/methanol solutions were tested thoroughly: 5, 10, 25, 50, and 75 mg/mL. Higher concentrations (150 and 300 mg/mL) were briefly examined, but did not provide useful responses and were not tested further. The cobalt chloride paper concentrations that covered the maximum percent relative humidity range were between 0.180 and 0.130  $g_s/g_p$ . Although this concentration range provides the greatest usable percent relative humidity range, it exhibits poor reproducibility. At and above these cobalt chloride concentration levels,

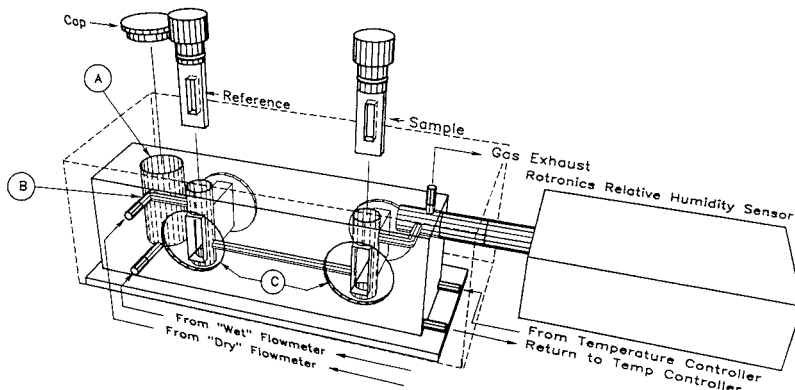


**Figure 2.** 3-D representation of RH control and test block: A, humidity generating chamber; B, dry/wet air mixing junction; C, two of four quartz optical windows.

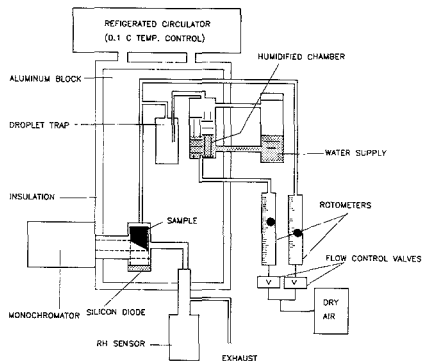


Figure 3. Reflectance mode system schematic.

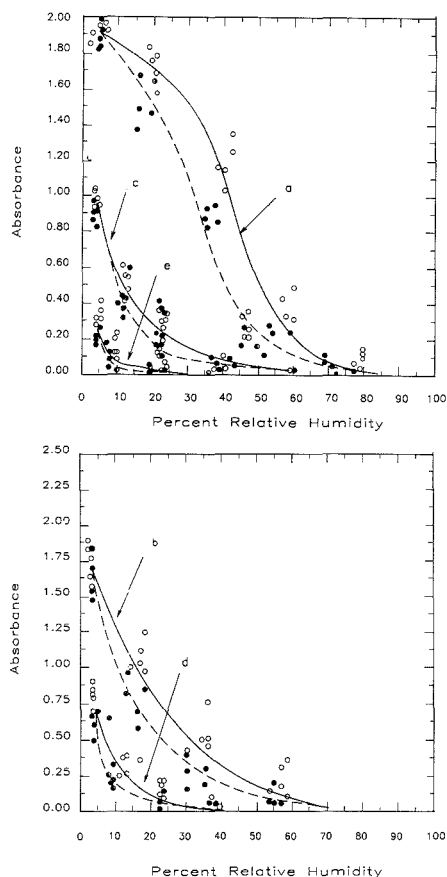


Figure 4. Effects of cobalt chloride concentration and hysteresis effects on untreated cellulose. (A, top panel) a, 0.180  $g_g/g_p$ ; c, 0.073; e, 0.036. (B) b, 0.130  $g_g/g_p$ ; d, 0.046.

it appears that crystals of the salt precipitate into the cellulose matrix, a factor that results in distinct steps between hydration states becoming evident in the response curve with each step exhibiting a different hysteresis effect.

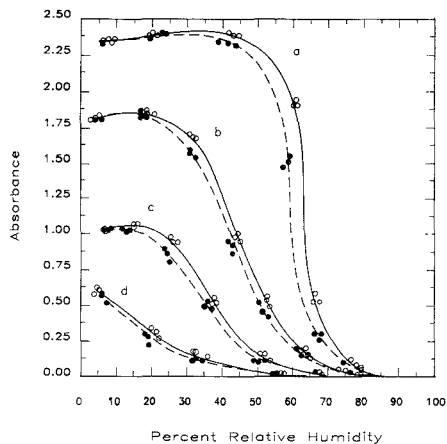


Figure 5. Effects of cobalt chloride concentration and hysteresis effects on acetylated Chr2: a, 0.173  $g_g/g_p$ ; b, 0.155; c, 0.061; d, 0.042.

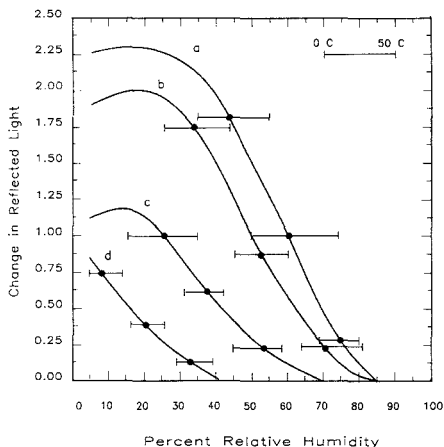
The lowest concentration (0.042  $g_g/g_p$  on nontreated and 0.036  $g_g/g_p$  on the treated) provides the highest reproducible response. This concentration, however, has a very short usable range with most of the change occurring between 0% and 20% RH for the nontreated and between 0% and 40% RH for the acetylated. In fact, samples prepared from each concentration of cobalt chloride/methanol solution have their own response characteristics over specific ranges of absorbency and humidities.

Figure 4 illustrates the low reproducibility, the shift in RH range with cobalt chloride concentration, and the hysteresis effect at each concentration on untreated cellulose filter paper. A solid line (open circles) is the test data obtained upon starting at 0% RH and ending at approximately 90% RH; the dashed line (closed circles) is the test data obtained upon starting at 90% RH and ending at 0% RH. The open circles represent the actual data points collected from dry to wet, and the closed circles represent the wet to dry data points.

The 97% response times (the time required for 97% of the final equilibrium value to be obtained following a step change in relative humidity) for 10% RH incremental steps for each concentration starting at 0% RH and progressing to 80% RH were monitored. Response times ranged from 16 to 35 min for increasing RH incremental steps. For the reverse response time were typically longer, ranging from 25 min to almost 1 h for equilibration.

Response times going from wet to dry are appreciably longer than these going from dry to wet, implying that the removal of water from either (or both) the cellulosic matrix or the salt hydrate microcrystals is more difficult than the addition of water vapor to the matrix.

**Modified Cellulose Results.** The most striking difference between acetylated and untreated cellulose was the decreased scatter and the improved reproducibility of the data. These samples also possessed much shorter response times than did the nonmodified cellulose samples. In addition, acetylation of the cellulose also results in lower hysteresis effects as compared to unmodified cellulose. On the acetylated cellulose, the concentrations that cover the maximum percent relative humidity range lie between 0.173 and 0.115  $g_g/g_p$ . These concentrations cover the same percent relative humidity range: 15%–70% RH with the higher concentration absorbing more light at each percent RH. Figure 5 illustrates the effect of concentration on RH range, reproducibility, and hysteresis



**Figure 6.** Temperature dependency on acetylated Chr2: a, 0.173  $g_s/g_p$ ; b, 0.155; c, 0.061; d, 0.042.

effects. The two higher concentrations exhibited overlapping response characteristics and hysteresis effects; due to the similarity the 0.200  $g_s/g_p$  concentration data was omitted from the figure. As in Figure 4 the solid line (open circle) represents the dry to wet test data and the dashed line (closed circle) the wet to dry data points.

Response times for the acetylated samples were monitored. Reproducibility of response times was excellent: Identical response time values were collected during repetitive testing. Dry to wet equilibration required between 5 and 19 min (depending on the RH step range), while the wet to dry required between 7 and 20 min. Acetylation clearly leads to reduction of response times; however, no clear trends appeared to exist from the data collected.

**Temperature Dependency.** Because of the lower degree of reproducibility obtainable with the unmodified cellulose, temperature dependency studies were made only with samples prepared from acetylated cellulose. There is a substantial shift in response toward higher RH values with increasing temperature, as is illustrated in Figure 6. As observed in the room-temperature studies, the two higher concentrations exhibit quite similar characteristics, and the response characteristics are only shown for the concentrations in the 0.0180–0.0036  $g_s/g_p$  range.

The change in response versus temperature in the linear response RH ranges at any given percent relative humidity approximates a straight line relationship fitted to the equation  $y = 0.034x + 0.30$ .

## DISCUSSION AND CONCLUSIONS

Studies have been reported on the interaction of the cellulose water vapor over long periods of time (19–21). Cellulose is an imperfect hygroscopic crystalline polymer that readily absorbs water vapor, causing morphological changes within the matrix. Existing theories (22) on the sorption characteristics of cellulose account for at least four major phenomena and related effects. These are (a) the magnitude of sorption, (b) heat effects accompanying sorption, (c) swelling, and (d) hysteresis. It is generally accepted that the unbounded cellulose hydroxyls act as sorption sites capable of sorbing water with bonding energy greater than that of water. The first water molecules adsorbed at low relative humidity are principally adsorbed by hydrogen bond formation with hydroxyl groups in the cellulose matrix. This sorption of water causes the structure to swell, and it continues to swell with increasing humidity. The hydrogen bonds of the cellulose break due to

the swelling of the structure and thus increase the number of sorption sites as more water is absorbed. Equilibration time for sorption of water on filter paper was reported to be as long as 14 h at 79% RH (5).

Acetylation of cellulose reduces the interaction of water vapor and the cellulose matrix, thereby allowing more rapid equilibration with subsequent reduction in response time. The acetylation reaction, if carried to completion, results in the substitution of the three hydroxyl groups with three acetyl groups for each cellulose unit (24). Low-power microscopy showed that the cellulose acetylated in our laboratory possesses a more grossly porous structure than that of the unmodified cellulose, which may also be a factor in the more rapid equilibration of water vapor through the acetylated matrix.

With unmodified cellulose, lowering the concentration of cobalt chloride decreases the usable percent relative humidity response range. Although having decreased usable RH ranges, the lowest concentrations have the highest reproducibility and least hysteresis effect. The acetylation of the cellulose causes a shift in the usable percent relative humidity response range from that observed with unmodified cellulose at the same concentration values. Acetylation not only shifts the percent relative humidity range, but also increases it; this is clearly observed in Figure 5 for the 0.042  $g_s/g_p$  concentration. The  $CoCl_2$  on unmodified cellulose possesses a percent relative humidity range that covers from 4% to 20% RH, while the acetylated cellulose at approximately the same concentration possesses a range from 4% to 60% RH. The concentration range from 5 to 25 mg/mL is also the range with minimal hysteresis effect and high reproducibility.

The response to relative humidity of  $CoCl_2$  on cellulose is strongly temperature dependent. This dependency, combined with the hysteresis effects at constant temperature and the limited RH range over which a given concentration of  $CoCl_2$  will function, does not allow this system to act as a substitute for conventional, nonoptical, full-range RH sensors. Because of the very short range over which a substantial change in optical properties occurs, and because this range can be shifted by changing the concentration of  $CoCl_2$  in the cellulose matrix, the method could find application in optical control of RH in facilities requiring constant relative humidity levels.

## LITERATURE CITED

- (1) Husband, R. M.; Peters, P. J. *Tappi* **1966**, (December), 49.
- (2) Wexler, A.; Brombacher, G. *Natl. Bur. Stand. Circ. (U.S.)* **1951**, No. 512.
- (3) Davey, F. R. *Humidity and Moisture*; Ruskin, R. E., Ed.; Reinhold: New York, 1965; Vol. 11, pp 571–577.
- (4) King, W. H., Jr. *Res. Dev.* **1969**, **21**, 28–33.
- (5) Seaki, Y.; Sadaoka, Y.; Ikeuchi, K. *Sens. Actuators* **1986**, **9**(2), 125–132.
- (6) Winkler, C. J. *Prakt. Chem.* **1964**, **91**, 209–211.
- (7) King, W. H., Jr. *Humidity and Moisture*; Ruskin, R. E., Ed.; Reinhold: New York, 1965; Vol. 11, pp 578–589.
- (8) Russell, A. P.; Fletcher, K. S. *Anal. Chim. Acta* **1985**, **170**, 209–216.
- (9) Katzin, L. I.; Ferraro, J. R. *J. Am. Chem. Soc.* **1952**, **74**, 2752.
- (10) Ballantine, D. S.; Wohltjen, H. *Anal. Chem.* **1966**, **38**, 2883–2885.
- (11) Siegel, G. H., Jr.; Kriz, D.; Shahriari, M. R.; Zhou, Q. *Anal. Chem.* **1988**, **60**, 2317–2320.
- (12) Giulian, J. F.; Wohltjen, H.; Jarvis, N. L. *Opt. Lett.* **1983**, **54**, 281.
- (13) Saari, L. A.; Seitz, W. R. *Anal. Chem.* **1962**, **54**, 821.
- (14) Vurek, G. G.; Feustel, P. J.; Severinghass, J. W. *Ann. Biomed. Eng.* **1983**, **11**, 499–509.
- (15) Peterson, J. I.; Fitzgerald, R. V.; Buckhold, D. K. *Anal. Chem.* **1984**, **56**, 62–70.
- (16) Wickersham, K. A.; Alves, R. V. *Ind. Res. Dev.* **1979**, **21**(12), 82.
- (17) Cetas, T. C.; Connor, W. G. *Med. Phys.* **1978**, **5**, 79–83.
- (18) Giallorenzini, T. G. *Opt. Laser Technol.* **1981**, April, 73–77.
- (19) Bull, H. B. *J. Am. Chem. Soc.* **1944**, **66**, 576–588.
- (20) Dole, M. J. *Chem. Phys.* **1948**, April, 73–76.
- (21) White, H. J., Jr.; Eyring, H. *Tex. Res. J.* **1947**, **17**, 523.
- (22) *Cellulose Chemistry and Its Application*; Albin, F., Ed.; Interscience Publishers: New York, 1965.

RECEIVED for review February 15, 1989. Accepted June 15, 1989. This work was supported by the U.S. Department of Energy under SBIR Contract No. DE-AC01-85ER80299.

# Atomic Absorption Determination of Lead at Picogram per Gram Levels by Ethylation with in Situ Concentration in a Graphite Furnace

R. E. Sturgeon,\* S. N. Willie, and S. S. Berman

Division of Chemistry, National Research Council of Canada, Montreal Road, Ottawa, Ontario K1A 0R9, Canada

**A method is described for the atomic absorption spectrometric determination of lead in natural waters and biological tissues based on the generation of  $Pb(C_2H_5)_4$  using  $NaB(C_2H_5)_4$  with its subsequent trapping in a graphite furnace at 400 °C. Quantitation is achieved by using a simple calibration graph prepared from aqueous standards having a sensitivity of  $0.150 \pm 0.006 A ng^{-1}$ . An absolute detection limit ( $3\sigma$ ) of 14 pg is achieved. Precision of determination at 100 pg/mL is 4% relative standard deviation. Results are reported for the determination of Pb in a suite of marine reference materials.**

Impressive advances in the detection of ionic alkyllead compounds (1–2 ng/L range) have been obtained by using derivatization techniques (butylation) to form volatile tetraorganolead compounds followed by chromatography with atomic absorption detection (1, 2). These procedures involve sample preconcentration (using 500-mL to 1-L volumes) and solvent phase transfers, which lead to potential losses, restrictions on maximum volumes used for analysis, and considerable time and effort.

Rapsomanikis et al. (3) recently reported a novel derivatization purge and trap atomic absorption spectrometric procedure based on the solution ethylation of aqueous methyllead ions by sodium tetraethylborate ( $NaBEt_4$ ) which eliminated the need for prior analyte concentration while permitting the entire sample to be derivatized, trapped, and determined with a minimum of handling. Detection limits obtained for  $Me_3Pb^+$  and  $Me_2Pb^{2+}$ , viz. 0.18 ng/L and 0.21 ng/L, respectively (based on a 50 mL sample), are the lowest values reported to date.

More reliable atomic spectrometric methods for detection of inorganic lead are required in order to access the extreme trace levels present in many samples of environmental interest. Hydride generation procedures are commonly resorted to in an effort to enhance concentration detection limits for several elements; varying success has been reported in the case of lead (4–13) using both continuous flow and purge and trap techniques. Early studies by Vijan and Wood (6) noted the instability of plumbane and the poor reaction efficiency with  $NaBH_4$  reagent. Use of various oxidizing and complexing agents appears necessary for efficient generation (12) but even with these, reported conversion efficiencies of inorganic lead to plumbane range from 27 to 91% (8–10, 13) often accompanied by severe interelement interferences (7, 10, 11).

The accuracy of such analyses in the picogram to nanogram per gram range depends primarily on the ability of the analyst to obtain a true estimate of contamination blanks introduced during the collection, transport, and handling of samples (14). In the laboratory, the latter step must be kept to an absolute minimum. Although the possibilities of  $Pb^{2+}$  contamination

are much greater than for the alkyllead species, its ease of ethylation and the absence of significant sample manipulation make this approach attractive for coupling with in situ concentration and atomization procedures using a graphite furnace (15–19). The latter offers substantial advantages over conventional purge and trap methodologies with furnace or heated quartz cell detection systems including simplicity of operation and use of small sample volumes, high sensitivity, and a substantial increase in detection power. The application of such in situ metal trapping to the determination of lead in natural waters and biological materials is presented here.

## EXPERIMENTAL SECTION

**Apparatus.** A Perkin-Elmer Model 5000 atomic absorption spectrometer was fitted with an HGA-500 graphite furnace and Zeeman effect background correction. A Perkin-Elmer lead electrodeless discharge lamp operated at 10 W was used as the line source. Absorption was measured at the 283.3-nm line. A nominal spectral band-pass of 0.7 nm was used. Standard Perkin-Elmer pyrolytic graphite coated tubes were modified for use by increasing the diameter of the sample introduction hole to  $\approx 2$  mm.

A custom-made Pyrex cell was used to generate  $Pb(Et)_4$ , which was transferred, via a quartz delivery tube, into the sample introduction hole of a preheated furnace tube. The design and operation of the cell have been detailed elsewhere (16–19).

**Reagents.** A 1000 mg/L stock solution of inorganic lead was prepared by dissolving high-purity lead granules (Johnson Matthey) in concentrated  $HNO_3$  and diluting to 1 M  $HNO_3$ . Working standards were prepared by serial dilution in deionized distilled water (DDW) (Barnstead Nanopure system) containing 0.1 M  $HNO_3$ .

High-purity subboiling distilled  $HNO_3$ ,  $CH_3COOH$ , and  $HClO_4$  were prepared in-house. Isothermal distillation of reagent grade  $NH_4OH$  into a receiver vessel of cold DDW was used to produce a high-purity 12 M product. A 1 M buffer solution of ammonium acetate was prepared from high-purity reagents and adjusted to a pH of 5.5 using excess acid.

A 0.5% (m/v) solution of  $NaB(Et)_4$  in DDW was prepared as required.

A Sure/Pac cylinder of  $B(Et)_3$  (Aldrich), a lecture bottle of  $EtCl$  (Matheson), sodium metal (Fisher), and anhydrous ether (Fisher) were used to synthesize  $NaB(Et)_4$ .

Several marine reference materials were analyzed for total Pb including National Research Council of Canada (NRC) open ocean seawater (NASS-2), coastal seawater (CASS-2), estuarine water (SLEW-1), river water (SLRS-1), dogfish muscle (DORM-1), and proposed nondefatted lobster hepatopancreas tissue LUTS-1 (20). Additionally, a sample of water collected from the Western Scheldt estuary (salinity 12‰) as part of the International Council for Exploration of the Seas (ICES) 6th Round Intercalibration for Trace Metals in Seawater (21) was analyzed.

**Procedures.** Sodium tetraethylboron was synthesized according to the procedure outlined by Honeycutt and Riddle (22). Approximately 14 mL of  $B(Et)_3$  was transferred under  $N_2$  pressure, using a septum inlet T and stainless steel needle tubing, into a  $N_2$ -purged 250-mL round-bottom three-necked flask containing 30 mL of anhydrous ether. The flask was continuously purged with dry  $N_2$  through one neck. A second neck was fitted with an angled side arm containing 5 g of freshly prepared sodium sand in ether. The third neck supported a reservoir for anhydrous ether

\* Author to whom all correspondence should be addressed.

Table I. HGA Program

program	step	temp, °C	time, s		int gas, mL/min
			ramp	hold	
generation-collection	1	400	1	14	300
	2 <sup>a</sup>	400	1	29	100
	3	400	1	119	150
atomization	1	400	1	9	0
	2	1600	0	3	0
	3	2700	1	1	300

<sup>a</sup> 0.5% NaB(Et)<sub>4</sub> added at 4 mL/min.

and bypass line for escaping N<sub>2</sub>. Ethyl chloride was bubbled continuously into the solution at a rate of about 200 mL/min. The flask was suspended in an ultrasonic bath and chilled to 5–10 °C by periodic addition of ice. The sodium sand was added in four portions over approximately a 5-h period. The purple product mixture was then allowed to warm to room temperature and transferred to 30-mL vials for centrifugation at 2500 rpm for 20 min to remove NaCl. The filtrate was evaporated down to about 20 mL under a stream of N<sub>2</sub> and chilled at –78 °C to crystallize sodium tetraethylboron etherate which on heating at 110–115 °C and 1 mmHg gave ether-free sodium tetraethylboron. Estimated yield was 60%, assuming the product was pure. No further purification was attempted. The reagent was transferred, under a N<sub>2</sub> atmosphere, to sealed vials in 1-g aliquots which were subsequently stored at 4 °C in the dark. CAUTION: B(Et)<sub>3</sub> is pyrophoric.

All sample and analytical manipulations were conducted in a class 100 clean room environment. Ten-milliliter aliquots of CASS-2, NASS-2, and SLEW-1 were transferred directly to the generator cell, and 200 µL of acetate buffer was added. Five-milliliter aliquots of SLRS-1 and ICES water were used together with 5 mL of DDW and 200 µL of buffer.

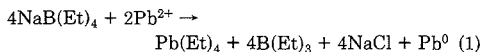
The biological reference materials DORM-1 and LUTS-1 were solubilized in PFA pressure vessels by using a HNO<sub>3</sub>-HClO<sub>4</sub> mixture with heating in a microwave oven, as described elsewhere (23). Nominal 0.5-g subsamples (dry weight) were taken and following dissolution were diluted to 50.0 mL in 1 M HNO<sub>3</sub>. Blanks were run concurrently with each set of sample decompositions. Total lead was determined by using 1.00-mL and 100-µL aliquots, respectively, of the dissolved LUTS-1 and DORM-1 samples. These were diluted to 10.0 mL in the generation flask and 200 µL of buffer was added.

The sequence of operations describing generation, collection, and atomization of Pb(Et)<sub>4</sub> is similar to that reported for the hydride-forming elements (16–19) and will not be repeated here with the exception of details pertinent to the Pb system. The graphite furnace program is given in Table I. Lead is collected at 400 °C. Two milliliters of NaB(Et)<sub>4</sub> was metered into the cell at a flow rate of 4 mL/min with a peristaltic pump.

Peak-height absorbance measurements were found adequate in all cases. Measurement of integrated absorbance was less precise (12% relative standard deviation vs 4% at 1 ng absolute). Standard calibration curves prepared from spikes of inorganic Pb added to 10 mL of DDW containing 200 µL of buffer were used to permit quantitation of samples.

## RESULTS AND DISCUSSION

The ease with which inorganic lead salts can be ethylated in good yield in aqueous solution was noted by Honeycutt and Riddle (22) and Rapsomanikis et al. (3). An autooxidation-reduction reaction occurs with production of Pb(IV) and Pb, i.e.



The reaction proceeds to 50% efficiency with respect to quantitative conversion of inorganic lead to tetraethyllead (TEL). Triethylborane is also reported to be capable of ethylating Pb<sup>2+</sup> to TEL, thus the stoichiometry of the above equation is not exact (24).

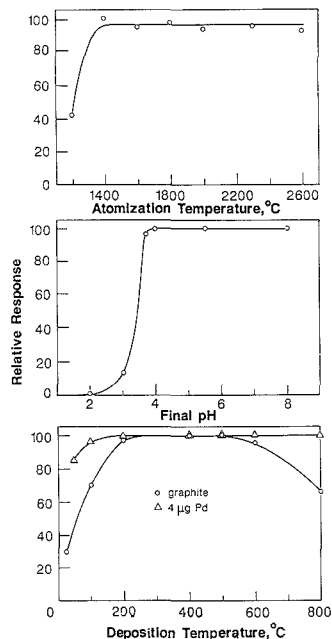


Figure 1. Effect of system variables on the generation, deposition, and atomization of TEL (see text for details).

Figure 1 shows the relative peak height signals obtained in response to changes affecting generation, trapping, and atomization of TEL. Generation efficiency was independent of pH provided the latter was >4. Rapsomanikis et al. (3) reported an optimum pH of 4.1 in their studies.

Scavenging of TEL (or its decomposition products) on the graphite tube surface was relatively insensitive to temperature over the range 200–600 °C. Both new pyrolytic graphite coated tubes and older worn tubes (over 200 heating cycles) exhibited the same collection characteristics. The range of deposition temperatures could be extended considerably (100 to >800 °C) in the presence of 4 µg of reduced Pd, which had been previously aliquoted, dried, and reduced (at 800 °C) on the tube surface. Similar observations have been noted when Pd was used to aid in the sequestering of analyte hydrides in the preheated graphite tube (25). Since Pd did not significantly enhance the performance characteristics of the system (peak absorbance and integrated signal increased by 10 and 12%, respectively), its use was discontinued in favor of a less complex procedure.

Maximum power heating to an optimum atomization temperature of 1600 °C was used. The abrupt decline in response below a setting of 1400 °C favored the selection of 1600 °C as a compromise between extended tube lifetime and assurance of a robust technique.

All experiments were conducted by using 2 mL of a 0.5% (m/v) solution of NaB(Et)<sub>4</sub>. With up to 10-mL sample volumes, generation of TEL was independent of NaB(Et)<sub>4</sub> concentration above 0.2% (m/v). As sample volumes increased to 20–40 mL, the optimum reagent concentration was found to increase to 0.5% (m/v). Concurrently, the cell purging time (step 3 of the furnace program) had to be increased from 120 s for 10-mL sample volumes to 240 s for 40-mL sample volumes. Relative to that obtained with 10-mL volumes, signal response decreased as sample volume increased, i.e., 87% at

**Table II. Analytical Results<sup>a</sup>**

sample	result	accepted value
SLRS-1 (ng/mL)	0.110 ± 0.008 (5)	0.106 ± 0.011
SLEW-1 (ng/mL)	0.030 ± 0.002 (5)	0.028 ± 0.007
CASS-2 (ng/mL)	0.021 ± 0.003 (5)	0.019 ± 0.006
NASS-2 (ng/mL)	0.038 ± 0.003 (8)	0.039 ± 0.006
ICES (ng/mL)	0.20 ± 0.01 (5)	0.19 ± 0.04 <sup>b</sup>
DORM-1 (μg/g)	0.45 ± 0.02 (5)	0.40 ± 0.12
LUTS-1 (μg/g)	0.074 ± 0.003 (10)	0.078 ± 0.016 <sup>c</sup>

<sup>a</sup> Mean and one standard deviation; numbers in parentheses are numbers of replicate samples. <sup>b</sup> Mean result of 20 participating ICES laboratories (21). <sup>c</sup> GFAAS direct analysis results.

**Table III. Figures of Merit**

sensitivity, A/ng	0.150 ± 0.006
cell blank, ng	0.074 ± 0.0042
3σ detection limit, pg	14
concentration LOD (10-mL sample), ng/mL	0.001
linear range, ng	0.014–2
reproducibility, % RSD at 1 ng	4
system efficiency, %	58 ± 3

20 mL, 77% at 30 mL, and 74% at 40 mL.

Aqueous NaB(Et)<sub>4</sub> solutions were stable for about 1 week when stored at 4 °C in darkened polypropylene screw-capped bottles. Signals equivalent to ~75% of those obtained by using freshly prepared 0.5% (m/v) solutions of NaB(Et)<sub>4</sub> were observed for 1 week old reagent.

**Analytical Blanks.** The primary source of the blank was determined to be the NaB(Et)<sub>4</sub>. Absolute cell (reagent and manipulation) blanks were found to be 74 ± 4 and 77 ± 5 pg when two different batches of NaB(Et)<sub>4</sub> were synthesized and used. It was noted that, when freshly prepared, the blank level from aqueous solutions of this reagent was about twice this value. Permitting the solution to stand overnight presumably allowed volatile TEL impurities to degas.

**Analytical Results.** Table II summarizes the analytical results for the determination of total Pb in a number of marine reference materials. In all cases, calibration was against simple working curves prepared by generating TEL from spiked 10-mL aliquots of buffered DDW. The accuracy of this approach is evident from a comparison of these data with the certified, accepted, or consensus values given for these samples in Table II.

The procedure used for the ethylation of lead is remarkably free of interferences in comparison to current hydridization techniques (11). The latter technique suffers marked signal reduction in the presence of such cations as Ca, Mg, Na, and the first-row transition elements. Signals from 1 ng of Pb(II) were found to be unaffected by the presence of 10<sup>6</sup>-fold excesses of Ca<sup>2+</sup>, Na<sup>+</sup>, and Mg<sup>2+</sup> and 5000-fold excesses of Fe<sup>3+</sup>, Cr<sup>6+</sup>, Ni<sup>2+</sup>, Mn<sup>2+</sup>, As<sup>3+</sup>, and Zn<sup>2+</sup>. Copper was the only element tested for which a signal suppression was noted (~15% at 1000-fold excess (1 μg absolute)). The procedure is thus sufficiently robust that direct calibration against external standards may be made for most natural waters as well as solutions of dissolved sediments and biological materials.

**Figures of Merit.** Table III summarizes analytical figures of merit. Absolute peak absorbance sensitivity as determined from the slopes of calibration curves run in several tubes, using two different lots of synthesized NaB(Et)<sub>4</sub> reagent, averaged 0.150 ± 0.006 A/ng (i.e. 28 pg/0.0044 A). This figure is 58 ± 3% of that obtained by direct injection of 1 ng of Pb as an aqueous solution (20 μL) into the furnace with atomization under identical conditions. Comparison of both peak height and integrated absorbance measurements resulted in the same estimate of overall efficiency. Inspection of eq 1 reveals that

the overall efficiency of the ethylation reaction is expected to be 50%. However, subsequent ethylation of any redissolved Pb<sup>0</sup> by NaB(Et)<sub>4</sub> or B(Et)<sub>3</sub> reagent in solution would be expected to increase this yield. The generation system is thus 58% efficient overall (generation, transfer, trapping), but this appears to be the maximum that can theoretically be achieved.

With signal integration, an absolute sensitivity of 90 ± 11 pg/0.0044 A-s was obtained. Atomization conditions were not optimized for signal integration.

The estimated procedural detection limit for inorganic lead, based on the variability of the blank (3σ), is 14 pg. This corresponds to a concentration detection limit of 1 pg/mL in natural water, assuming a 10-mL sample. Sub-picogram-per-milliliter detection limits may be readily achieved by taking larger sample aliquots. Precision of determination is better than 5% RSD on determinations 70-fold (i.e., 1 ng) above the LOD.

The linear working range spans over 2 decades, extending to 2 ng. Higher analyte concentrations are accessible by working with smaller sample volumes or by introducing an internal purge gas flow during atomization.

## CONCLUSION

Extreme trace concentrations of lead in environmental samples become accessible on a routine basis utilizing ethylation-in situ graphite furnace atomic absorption spectrometry (GFAAS) trapping procedures. Concentration factors of 500 are readily achieved in 3–4 min (10-mL samples vs conventional 20-μL aliquots for GFAAS techniques) and sample volume requirements are significantly curtailed. The detection limit achieved (1 pg/mL) is, to our knowledge, the lowest reported for inorganic lead.

## LITERATURE CITED

- (1) Chau, Y. K.; Wong, P. T. S.; Kramar, O. *Anal. Chim. Acta* **1983**, *146*, 211–217.
- (2) Chakraborti, D.; DeJonghe, W. R. A.; Van Mol, W. E.; Van Cleuvenbergen, R. J. A.; Adams, F. C. *Anal. Chem.* **1984**, *56*, 2692–2697.
- (3) Rapsomanikis, S.; Donard, O. F. X.; Weber, J. H. *Anal. Chem.* **1986**, *58*, 35–38.
- (4) Thompson, K. C.; Thomerson, D. R. *Analyst* **1974**, *99*, 595–601.
- (5) Flennig, H. D.; Ide, R. G. *Anal. Chim. Acta* **1976**, *83*, 67–82.
- (6) Vijan, P. N.; Wood, G. R. *Analyst* **1976**, *101*, 966–973.
- (7) Vijan, P. N.; Sadana, R. S. *Talanta* **1980**, *27*, 321–326.
- (8) Yamauchi, H.; Arai, F.; Yamamura, Y. *Ind. Health* **1981**, *19*, 115–124.
- (9) Ikeda, M.; Nishibe, J.; Hamada, S.; Tujino, R. *Anal. Chim. Acta* **1981**, *125*, 109–115.
- (10) Jin, K.; Taga, M. *Anal. Chim. Acta* **1982**, *143*, 229–236.
- (11) Castillo, J. R.; Mir, J. M.; Val, J.; Colón, M. P.; Martínez, C. *Analyst* **1985**, *110*, 1219–1221.
- (12) Castillo, J. R.; Mir, J. M.; Martínez, C.; Val, J.; Colón, M. P. *Mikrochim. Acta* **1985**, *1*, 253–263.
- (13) D'Ulivo, A.; Fuoco, R.; Papoff, P. *Talanta* **1986**, *33*, 401–405.
- (14) Patterson, C. C.; Settle, D. M. *Accuracy in Trace Analysis: Sampling, Sample Handling and Analysis*; *Natl. Bur. Stand. (U.S.) Spec. Publ.*, **1976**, No. 422, Vol. 1, pp 321–351.
- (15) Lee, D. S. *Anal. Chem.* **1982**, *54*, 1682–1686.
- (16) Sturgeon, R. E.; Willie, S. N.; Berman, S. S. *Anal. Chem.* **1985**, *57*, 2311–2314.
- (17) Willie, S. N.; Sturgeon, R. E.; Berman, S. S. *Anal. Chem.* **1986**, *58*, 1140–1143.
- (18) Sturgeon, R. E.; Willie, S. N.; Berman, S. S. *J. Anal. At. Spectrom.* **1986**, *1*, 115–118.
- (19) Sturgeon, R. E.; Willie, S. N.; Berman, S. S. *Anal. Chem.* **1987**, *59*, 2441–2444.
- (20) Berman, S. S.; Sturgeon, R. E. *Fresenius' Z. Anal. Chem.* **1988**, *332*, 546–548.
- (21) Berman, S. S.; Boyko, V. J. *ICES 6th Round Intercalibration for Trace Metals in Seawater (6/TM/SW)*; ICES Coop. Res. Report No 152; National Research Council of Canada: Ottawa, ON, Canada, 1987.
- (22) Honeycutt, J. B., Jr.; Riddle, J. M. *J. Am. Chem. Soc.* **1961**, *83*, 369–373.
- (23) Nakashima, S.; Sturgeon, R. E.; Willie, S. N.; Berman, S. S. *Analyst* **1988**, *113*, 159–163.
- (24) Honeycutt, J. B., Jr.; Riddle, J. M. *J. Am. Chem. Soc.* **1960**, *82*, 3051–3052.
- (25) Sturgeon, R. E.; Willie, S. N.; Sproule, G. I.; Robinson, P. T.; Berman, S. S. *Spectrochim. Acta, Part B*, in press.

RECEIVED for review March 17, 1989. Accepted June 2, 1989.  
This is NRCC No. 30432.

# Characterization of Single-Ply and Poly laminate Films by Nuclear Magnetic Resonance Spectroscopy

Galen R. Hatfield<sup>1</sup>

Corporate Technology, Allied-Signal, Inc., Morristown, New Jersey 07960

The ability of solid-state NMR to obtain detailed information on structure and morphology in poly laminate films is demonstrated for the first time. The poly laminates studied here contained layers of polyethylene, Nylon 6, Surlyn, and/or ethylene-vinyl acetate copolymers. The multilayer films examined were chosen with the intent of illustrating the relative strengths and weaknesses of this analytical approach. The most notable strength is the ability of NMR to obtain morphological information on the interior layers of poly laminates without resorting to ply dissolution or separation.

## INTRODUCTION

Single-ply and poly laminate films are important materials with major applications in the packaging industry (1, 2). Physical properties such as permeability, strength, clarity, and dimensional stability are directly related to the polymer and its morphology in each layer. Unfortunately, these systems have often proven to be difficult and/or tedious to study due to their complexity and physical construction. Most approaches involve separation or dissolution of laminate plies by refluxing in solution and subsequent analysis (2). Unfortunately, this procedure is time-consuming and, more importantly, may jeopardize the structural integrity of the system. In addition, morphological information such as crystalline content is lost in solution or may be altered during separation. Finally, these films are frequently thick, often prohibiting an examination of the interior layers by traditional methods such as infrared (IR) and X-ray diffraction (XRD).

High-resolution solid-state nuclear magnetic resonance (NMR) has quickly become one of the more powerful tools available for the study of polymer morphology (3, 4). The purpose of this paper is to demonstrate, for the first time, the ability of solid-state NMR in characterizing both single ply and poly laminate films. Examples are chosen specifically to illustrate the relative strengths and weaknesses of this analytical approach.

## EXPERIMENTAL SECTION

**NMR Spectroscopy.** NMR experiments were carried out at 75.3 MHz on a Chemagnetics CMX300 NMR spectrometer using standard cross-polarization (CP) and magic angle spinning (MAS) techniques (5-7). The films were packed into rotors and spun at roughly 5.0 kHz. The magic angle was adjusted to within 0.1° by using the <sup>79</sup>Br spectrum of KBr (8). The spectra shown in Figures 1-6 were acquired by using a 0.8-ms contact time and a 2-s repetition time.

For the purposes of measuring the  $\alpha$  crystallinity of Nylon 6 in sample F, data were also acquired with a 240-s pulse delay. The length of this delay was chosen to ensure total magnetization recovery and therefore accurate quantitative data. Cross-polarization ( $T_{CH}$ ) and proton rotating frame spin-lattice relaxation ( $T_{1\rho}(H)$ ) rates were measured (3, 4, 9) for the peaks at 43 and 40 ppm (see text).  $T_{CH}$  was determined to be 0.03 ms for both resonances. Values of  $T_{1\rho}(H)$  were found to be 5.09 and 4.38 ms

<sup>1</sup> Current address: Washington Research Center, W.R. Grace & Co., 7379 Route 32, Columbia, MD 21044.

Table I. Film Structure and Composition

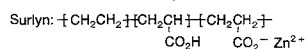
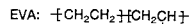
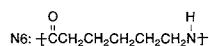
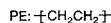
sample	total plies	ply	thickness, $\mu$ m	composition	comment
A	1	1	243.8	PE	milk bottle grade
B	1	1	25.4	N6	
C	1	1	27.9	EVA	12% VA
D	1	1	25.4	Surlyn	
E	2 + ADH	1	140.6	Surlyn adhesive	
F	3	2	90.6	N6	
		1	12.6	EVA	2% VA
		2	22.2	N6	
		3	20.6	EVA	2% VA

for the peaks at 43 and 40 ppm, respectively. Spectral deconvolutions were carried out with software by New Methods Research, Inc., and Lorentzian line shapes.

**Samples.** The films studied in the text were reference-type research samples, which had been previously characterized by combining the information obtained from a number of analytical techniques. The relevant information for each sample is given in Table I. Each film was examined "as received", with no experimental preparation.

## RESULTS

**Single-Ply Films.** Four common materials used in the formation of poly laminate films are polyethylene (PE), Nylon 6 (N6), ethylene-vinyl acetate copolymers (EVA), and Surlyn. Structures for each of these are given below. <sup>13</sup>C NMR spectra of typical PE, N6, EVA, and Surlyn films are given in Figures 1-4. Peaks labeled with an asterisk in Figures 1-6 are due to spectral features called spinning sidebands and should be ignored.



Polyethylene (PE) is the most common material used in the production of plastic bottles and other multilayer containers (1). The properties of PE films are strongly dependent upon morphology, density, and branching. PE has been extensively studied by solid-state <sup>13</sup>C NMR (10-31). Spectra of PE typically contain a sharp resonance at 34 ppm and a peak or broad shoulder at 32 ppm. Both of these can be seen for sample A in Figure 1. The peak at 34 ppm has been assigned to "crystalline" methylenes while the peak at 32 ppm has been assigned to those methylenes in the "amorphous" phase (10-31). Thus, the ratio of these two peaks can be used to measure the crystallinity of any PE sample, including films.

Nylons (or polyamides) are another class of materials commonly used in the production of films. These films are



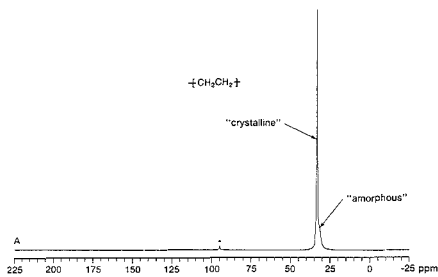


Figure 1. Solid-state  $^{13}\text{C}$  CP-MAS NMR spectrum of a single-ply PE film (sample A) (asterisk denotes spinning sideband).

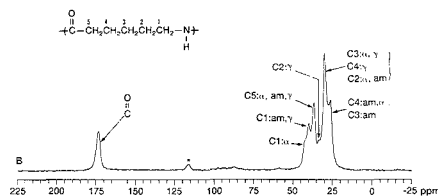


Figure 2. Solid-state  $^{13}\text{C}$  CP-MAS NMR spectrum of a single-ply N6 film (sample B) (asterisk denotes spinning sideband).

characterized by high strength, high water absorption, and good gas barrier properties (2). Several solid-state  $^{13}\text{C}$  NMR studies of Nylon 6 (N6) have recently appeared in the literature (32–37) and have shown that the various structural forms of N6 can be distinguished by chemical shift differences in the  $^{13}\text{C}$  NMR spectra. N6 can crystallize into two forms, classified as alpha ( $\alpha$ ) and gamma ( $\gamma$ ) (38). The thermodynamically stable structure is the  $\alpha$  phase and consists of molecules in an extended chain conformation. In the  $\gamma$  phase structure the molecules are in the form of pleated sheets. The  $^{13}\text{C}$  NMR spectrum of a typical Nylon 6 film (sample B) is given in Figure 2. While definitive NMR assignments for each carbon in each phase are not yet available, certain resonances have been clearly shown (32, 33) to be representative of specific phases. For example, the peak at 43 ppm can be assigned to the methylene adjacent to the nitrogen in the  $\alpha$  phase. This same carbon appears at 40 ppm in the  $\gamma$  and amorphous phases. The peak at 34 ppm, on the other hand, has been shown (32, 36) to be indicative of the methylene  $\beta$  to the nitrogen in only the  $\gamma$  phase. Since these resonances can be readily observed and resolved, it is possible to accurately quantitate the percent of each phase present in any N6 sample (33), including films.

Ethylene-vinyl acetate copolymers (EVA) are another common material used in poly laminate films. EVA films may be considered as modified low density polyethylene and can be blow extruded to be tough or cast for clarity (2). The  $^{13}\text{C}$  NMR spectrum of a typical EVA film (sample C) is given in Figure 3. This sample has been previously shown to contain 12% vinyl acetate (VA). There are, apparently, no solid-state NMR studies of EVA morphology in the literature. However, on the basis of the NMR studies of the analogous PE system (10–31), the two major peaks at 34 and 32 ppm are tentatively assigned to methylenes in "crystalline" and "amorphous" environments, respectively. The vinyl acetate (VA) functionality can be seen in the carbonyl peak at 171 ppm, the methine resonance at 74 ppm, and the methyl peak at 22 ppm. The chemical shift of the VA methylene appears as the shoulder at roughly 40 ppm. These assignments have been confirmed by separate studies on poly(vinyl acetate) (not shown) and  $^{13}\text{C}$  NMR studies of EVA copolymers in solution

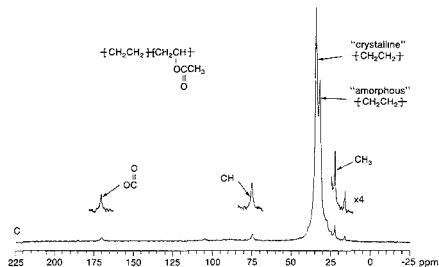


Figure 3. Solid-state  $^{13}\text{C}$  CP-MAS NMR spectrum of a single-ply EVA film (sample C).

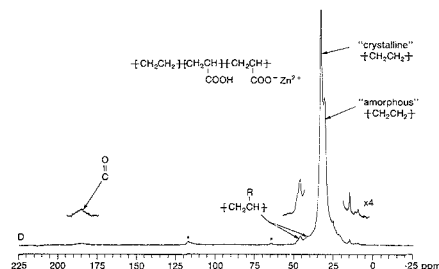


Figure 4. Solid-state  $^{13}\text{C}$  CP-MAS NMR spectrum of a single-ply Surlyn film (sample D) (asterisk denotes spinning sideband).

(39, 40). The small peak at 16 ppm can be assigned to terminal methyl groups on the PE chain and are an indication of the extent of branching present (41).

Surlyn is the common name for one system in a class of polymers called ionomers, which contain both covalent and ionic bonds. Surlyn is based on polyethylene and contains ionic cross-links between neighboring chains. These links stiffen and toughen the polymer, which provides increased melt strength in films (2). The  $^{13}\text{C}$  NMR spectrum of a typical Surlyn film (sample D) is given in Figure 4. There are apparently no solid-state NMR studies of Surlyn structure and morphology in the literature. However, the spectrum is dominated by peaks at 34 and 32 ppm, which can be tentatively assigned to "crystalline" and "amorphous" type methylenes. The acid carbonyls can be seen at 187 ppm. The peaks at roughly 47 and 40 ppm are tentatively assigned to the various zinc acrylate and acrylic acid (42) type CH and  $\text{CH}_2$  carbons. The small peak at 16 ppm is again indicative of terminal methyl groups in the branching PE chains (41).

**Poly laminates.** In order to illustrate the ability of NMR for examining poly laminates, two multilayer films will be discussed. Each of these has been previously characterized by combining the information gained from a multitude of techniques including gas chromatography (GC), infrared (IR), X-ray diffraction (XRD), optical microscopy (OM), and various thermal methods (DSC, DMA). The relevant information for each sample is given in Table I.

The  $^{13}\text{C}$  NMR spectrum of a two-ply film is given in Figure 5. This film (sample E) is a forming web made by either coextrusion or extrusion coating. It contains layers of Nylon 6 (N6) and Surlyn that are held together with a very thin (less than 1  $\mu\text{m}$ ) adhesive tie layer. Figure 5 can be readily seen as a composite of Figures 2 and 4. From the major resonances at 34 and 32 ppm, it is clear that a polyolefin is present that can be identified as Surlyn by the peak at 185 and the asymmetric resonance at 48 ppm. Nylon 6 features are observable at 172, 43, 40, and 37 ppm. Note that there is a lack

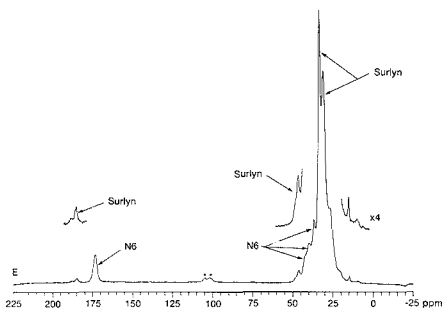


**Figure 5.** Solid-state  $^{13}\text{C}$  CP-MAS NMR spectrum of a two-ply film containing Surlin, an adhesive layer, and N6 (sample E) (asterisk denotes spinning sideband).

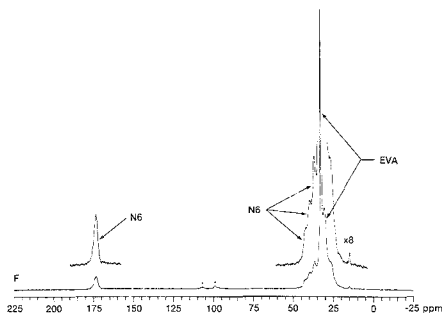


**Figure 6.** Solid-state  $^{13}\text{C}$  CP-MAS NMR spectrum of a three-ply film containing EVA, N6, and EVA (sample F) (asterisk denotes spinning side-band).

of signals attributable to the adhesive layer. The weight percent adhesive present, although unknown, is very small and apparently below the current detection limit.

A more complex system exists in the case of a three-ply film and an example is given Figure 6. Sample F is a three-layer blown film that contains (in order) layers of EVA, N6, and EVA. There are no adhesive tie layers. Polyolefin signals can be seen at 34 and 32 ppm. Nylon 6 signals, similar to those in Figure 2, can be seen at 172, 43, 40, and 37 ppm. From the NMR data alone, one can only draw the conclusion that the film contains a polyolefin and N6. It is not clear that the polyolefin is EVA since no appreciable vinyl acetate (VA) signals are observed. The VA content has been determined (by IR) to be 2%, or roughly 1% of the entire polylaminate. This appears to be below the detection limit in the current experiment. The total experiment time used to obtain Figure 6 was 1 h. We would expect to observe resonances due to the 1% components after an overnight acquisition. Finally, it should be noted that the NMR data alone do not identify the existence of two separate polyolefin layers.

## DISCUSSION

The examples above illustrate many of the strengths and weaknesses of NMR for characterizing single-ply and poly-laminate films. A major strength is that spectra can be acquired "as is" and interpreted in a short time, providing a rapid method of analysis. For example, one can easily characterize the films in Figures 5 and 6 as containing N6 and a polyolefin. However, a clear identification of the PE-based copolymer present is not as straightforward. This is generally not the case for other polymeric systems. For example, one could quickly distinguish Nylon 6 from Nylon 12. Another significant weakness of NMR is its inability to observe low levels

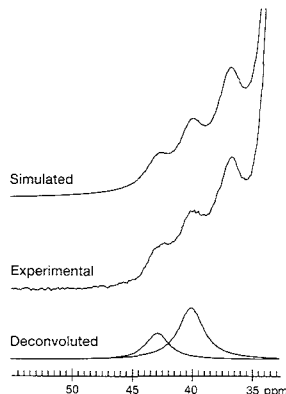


**Figure 7.** Partial deconvolution of Figure 6 for determination of the  $\alpha$ -crystalline content of N6 in the center ply.

of copolymer content, which can have a dramatic effect on the physical properties of the film. However, a major advantage is that NMR can be used to quickly determine the morphology of many polymers (4), including the four given here.

Solid-state NMR spectroscopy is a bulk-sensitive technique. In the experiments carried out here, the observed signals are indicative of the entire sample and do not contain any spatial information. As a result, NMR cannot easily distinguish between a blend of two components and a two-ply film. It should be noted, however, that other experiments (43-46) can be performed which are capable of probing the molecular level interaction present (if any) between two components. Solid-state NMR spectroscopy also cannot determine the physical ordering of plies by distinguishing an "ABC" film from an "ACB" one. These are clearly disadvantages for the complete characterization of a polylaminate by solid-state NMR spectroscopy. However, this transparency to physical construction also creates a significant and unique advantage.

While NMR cannot determine the order of layering, it can probe the structure, morphology, and molecular dynamics of all layers without resorting to dissolution or separation of plies. This is most significant for examining the interior layer(s). Other traditional methods such as infrared (IR) and X-ray diffraction (XRD) are limited or complicated by problems with sampling depth (IR, XRD), sample thickness (IR, XRD), interfering strong X-ray scatter (XRD), and orientation (IR, XRD). Thus, NMR represents a unique "as is" approach that does not suffer from the experimental limitations imposed on many other techniques.

Consider, for example, the three-ply film in Figure 6. Here, Nylon 6 is the central layer and accurate determination of the percent  $\alpha$ -crystalline phase present by most traditional methods would require ply separation or dissolution. This is not the case for NMR, where the  $\alpha$ -crystalline content can be determined by comparing the integrated intensities at 43 and 40 ppm (32-37) and using the correct analytical approaches (3, 4, 9). The spectrum in Figure 6 can be deconvoluted into its individual components, and a portion is shown in Figure 7. With this approach, the  $\alpha$ -crystalline content has been determined to be 19%. This type of morphological information can be obtained on many polymers including PE and PET.

Although it has not been illustrated here, NMR is also a powerful method for characterizing molecular motion and dynamics in polymers (3, 4, 47, 48). Experiments designed to probe these behaviors are also possible on interior layers.

The ability to obtain detailed structural, morphological, and dynamic information on interior layers has the clear potential to provide critical insights into the changes induced by processing and their effect on film performance.

#### ACKNOWLEDGMENT

The following should be acknowledged for contributing to the initial characterization of the poly(laminate) films: R. Bray, J. Belles, J. Hanrahan, N. Murthy, K. O'Brien, A. Szollosi, E. Szollosi, and E. Walsh. In addition, I would like to acknowledge K. O'Brien and A. Signorelli for providing the samples and K. O'Brien for many helpful discussions. Finally, I would like to thank R. D. Sedgwick for his continued support of this work.

**Registry No.** PE, 9002-88-4; N6, 25038-54-4; EVA, 24937-78-8; Surlyn, 9078-96-0.

#### LITERATURE CITED

- (1) Sacks, W. *CHEMTECH* **1988**, 480.
- (2) Briston, J. H. *Plastics Films*; Longman Scientific and Technical: Essex, 1986.
- (3) Fyfe, C. A. *Solid-State NMR for Chemists*; CFC Press: Guelph, 1983.
- (4) *High Resolution NMR Spectroscopy of Synthetic Polymers in Bulk*; Komoroski, R. A., Ed.; VCH Publishers: Deerfield Beach, FL, 1986.
- (5) Pines, A.; Gibby, M. G.; Waugh, J. J. *Chem. Phys.* **1973**, *59*, 569.
- (6) Schaeffer, J.; Stejskal, E. O. *J. Am. Chem. Soc.* **1976**, *98*, 1031.
- (7) Schaeffer, J.; Stejskal, E. O. *In Topics in Carbon-13 NMR Spectroscopy*; Levy, G. C., Ed.; Wiley and Sons: New York, 1979.
- (8) Frye, J. S.; Maciel, G. E. *J. Magn. Reson.* **1982**, *48*, 125.
- (9) Hatfield, G. R.; Maciel, G. E.; Erbateur, O.; Erbateur, G. *Anal. Chem.* **1987**, *59*, 172.
- (10) Schroter, B.; Posern, A. *Makromol. Chem.* **1981**, *182*, 675.
- (11) Dekmezian, A.; Axelson, D. E.; Dechter, J. J.; Borah, B.; Mandelkern, L. *J. Polym. Sci., Polym. Phys. Ed.* **1985**, *23*, 367.
- (12) Komoroski, R. A.; Maxfield, J.; Sakaguchi, F.; Mandelkern, L. *Macromolecules* **1977**, *10*, 550.
- (13) Kitamaru, R.; Horii, F.; Murayama, K. *Polym. Bull.* **1982**, *7*, 583.
- (14) Dechter, J. J.; Mandelkern, L. *J. Polym. Sci., Polym. Phys. Ed.* **1979**, *17*, 317.
- (15) Schroter, B.; Posern, A. *Macromol. Chem. Rapid Commun.* **1982**, *3*, 623.
- (16) Earl, W. L.; VanderHart, D. L. *Macromolecules* **1979**, *12*, 762.
- (17) Fyfe, C. A.; Lyerla, J. R.; Volksen, W.; Yannoni, C. S. *Macromolecules* **1979**, *12*, 764.
- (18) VanderHart, D. L. *Macromolecules* **1979**, *12*, 1232.
- (19) VanderHart, D. L. *J. Chem. Phys.* **1976**, *64*, 830.
- (20) Opella, S. J.; Waugh, J. S. *J. Chem. Phys.* **1977**, *66*, 4919.
- (21) Axelson, D. E.; Mandelkern, L.; Popli, R.; Mathieu, P. J. *Polym. Sci., Polym. Phys. Ed.* **1983**, *21*, 2319.
- (22) Axelson, D. E. *J. Polym. Sci., Polym. Phys. Ed.* **1982**, *20*, 1427.
- (23) VanderHart, D. L. *J. Magn. Reson.* **1973**, *24*, 4671.
- (24) Axelson, D. E.; Mandelkern, L. *J. Polym. Sci., Polym. Phys. Ed.* **1978**, *16*, 1135.
- (25) VanderHart, D. L.; Khoury, F. *Polymer* **1984**, *25*, 1589.
- (26) VanderHart, D. L. *J. Magn. Reson.* **1981**, *44*, 117.
- (27) Ando, I.; Yamanobe, T.; Sorita, T.; Komoto, T.; Sato, H.; Deguchi, K.; Imanari, M. *Macromolecules* **1984**, *17*, 1955.
- (28) VanderHart, D. L.; Garroay, A. N. *J. Chem. Phys.* **1979**, *71*, 2773.
- (29) Kitamaru, R.; Horii, F.; Nakagawa, M. *Polym. Prepr. (Am. Chem. Soc., Div. Polym. Chem.)* **1987**, *28*, 58.
- (30) Ando, I.; Yamanobe, T.; Akiyama, S.; Komoto, T.; Sato, H.; Fujito, T.; Deguchi, K.; Imanari, M. *Solid State Commun.* **1987**, *62*, 785.
- (31) Dechter, J. J.; Komoroski, R. A.; Axelson, D. E.; Mandelkern, L. *J. Polym. Sci., Polym. Phys. Ed.* **1981**, *19*, 631.
- (32) Hatfield, G. R.; Glans, J. H.; Hammond, W. B., submitted for publication in *Macromolecules*.
- (33) Weeding, T. L.; Veeman, W. S.; Angad Gaur, H.; Huysmans, W. G. B. *Macromolecules* **1988**, *21*, 2028.
- (34) Weeding, T. L.; Veeman, W. S.; Jenneskens, L. W.; Angad Gaur, H.; Schuur, H. E. C.; Huysmans, W. G. B. *Macromolecules* **1989**, *22*, 706.
- (35) Ketels, H.; Van de Ven, L.; Aerds, A.; Van der Velden, G. *Polym. Commun.* **1989**, *30*, 80.
- (36) Okada, A.; Kawasumi, M.; Tajima, I.; Kurauchi, T.; Kamigaito, O. *J. Appl. Polym. Sci.* **1989**, *37*, 1363.
- (37) Kubo, K.; Yamanobe, T.; Komoto, T.; Ando, I.; Shilbashi, T. *J. Appl. Polym. Sci., B: Polym. Phys.* **1989**, *27*, 929.
- (38) Reimschuessel, H. *In Handbook of Fiber Science and Technology*; Marcel Dekker: New York, 1985; Vol. 4.
- (39) Ibrahim, B.; Kalitzky, A. R.; Smith, A.; Weiss, D. E. *J. Chem. Soc., Perkin Trans 2* **1974**, 1537.
- (40) Wu, T. K.; Ovenall, D. W. *Macromolecules* **1974**, *7*, 776.
- (41) Bovey, F. A. *Chain Structure and Conformation of Macromolecules*; Academic Press: New York, 1982.
- (42) Fyfe, C. A.; McKinnon, M. S. *Macromolecules* **1986**, *19*, 1909.
- (43) Perez, E.; Vanderhardt, D. L.; Crist, B.; Howard, P. R. *Macromolecules* **1987**, *20*, 78.
- (44) Caravatti, P.; Delli, J. A.; Bodenhausen, G.; Ernst, R. R. *J. Am. Chem. Soc.* **1982**, *104*, 5506.
- (45) Stejskal, E. O.; Schaefer, J.; Sefcik, M. D.; McKay, R. A. *Macromolecules* **1981**, *14*, 188.
- (46) Schaefer, J.; Sefcik, M. D.; Stejskal, E. O.; McKay, R. A. *Macromolecules* **1981**, *14*, 275.
- (47) Bovey, F. A.; Jelinski, L. W. *J. Phys. Chem.* **1985**, *89*, 571.
- (48) Hatfield, G. R.; Aharoni, S. M. *Macromolecules*, in press.

RECEIVED for review March 9, 1989. Accepted May 19, 1989.

# Gas Chromatographic Sample Introduction into the Collision Cell of a Triple Quadrupole Mass Spectrometer for Mass Selection of Reactant Ions for Charge Exchange and Chemical Ionization

Mark E. Hail,<sup>1</sup> David W. Berberich,<sup>1</sup> and Richard A. Yost\*

Department of Chemistry, University of Florida, Gainesville, Florida 32611

A gas chromatograph (GC) has been interfaced to the collision cell of a triple quadrupole tandem mass spectrometer for performing mass-selected ion-molecule reactions. Reactant ions are selected with the first quadrupole and are allowed to react in the second quadrupole collision cell with the effluent from a short open tubular GC column. The ion-molecule reaction product ions are mass analyzed by the third quadrupole. Charge exchange (CE) and chemical ionization (CI) reactions have been studied. The advantages of using mass-selected reactions for controlling the selectivity of charge exchange and chemical ionization are demonstrated. In addition, this configuration is shown to provide both structural information and molecular weight information in the same chromatogram by alternating between different reactant ions. The possibility of searching CE spectra against the NBS EI library has also been investigated. With the benzene molecular ion as a charge exchange reactant and benzophenone as the analyte, the system is shown to detect 100 pg of the analyte utilizing a full scan (comparable to or better than the detection limit obtainable with conventional gas chromatography/mass spectrometry) and 15 pg with selected reaction monitoring.

Tandem mass spectrometry (MS/MS) has proven to be a powerful analytical method for both structure elucidation and mixture analysis (1, 2). The enhanced selectivity of MS/MS over that of MS has been shown to reduce the need of extensive sample preparation and the lengthy chromatographic steps often needed in trace mixture analysis (2). In fact, theory and practice have shown that short open tubular columns under vacuum outlet conditions can provide extremely rapid analyses in gas chromatography/mass spectrometry (GC/MS) and GC/MS/MS (3-8). The increased optimum carrier gas velocities and the short column length allow for the analysis of thermally labile compounds and/or compounds normally thought to be too polar to pass through conventional-length (e.g., 30 m) columns (4-8).

The maximum selectivity of any analytical technique can be realized if all of the variable parameters of the method are considered. These variable parameters can be considered as resolution elements that affect the informing power (i.e., the amount of information available) in the analytical method (9). In mass spectrometry, two resolution elements that may be varied are mass analysis and ionization. The informing power of mass analysis can be augmented by increasing the mass range, increasing the mass resolution, or increasing the number of stages of mass analysis (i.e., tandem mass spectrometry). Since the ionization method is a resolution element, it too will affect the informing power. A certain degree of "resolution" (or selectivity) can be obtained with ionization by employing

techniques that allow ionization of only the desired components of a mixture, thereby excluding the ionization (and hence detection) of undesirable interferences. This selectivity of ionization is less frequently exploited but can be taken advantage of if careful consideration is made for the selection of reactant ions for charge exchange (CE) ionization or chemical ionization (CI) (10).

The selectivity of charge exchange (CE) and chemical ionization (CI) techniques arises from control of the energetics of the ion-molecule reactions between reactant ions and sample molecules (11). A CE reaction may occur if the ionization energy of the compound of interest,  $IE[M]$ , is less than the recombination energy of the reactant ion,  $RE[R^{**}]$ . For monatomic species, the recombination energy of an ion is the same as the ionization energy of the neutral. However, polyatomic ions may possess excess vibrational/rotational energy; therefore, this equality cannot always be assumed. The amount of internal energy deposited into  $M^{**}$  is equal to the difference between  $IE[M]$  and  $RE[R^{**}]$ . Similarly, proton transfer CI reactions may occur if the proton affinity of the sample molecule,  $PA[M]$ , is greater than the proton affinity of the conjugate base,  $R$ , of the reactant ion  $[R + H^+]$ ,  $PA[R]$ . The amount of internal energy deposited into  $[M + H]^+$  is equal to the difference in the proton affinities of  $R$  and  $M$ .

Traditionally, ion-molecule reactions are performed in a high-pressure (e.g., 1 Torr) ion source (10-13). However, there are limitations to performing these reactions in the ion source. When a reactant gas is introduced into the ion source, it is rare that only a single  $m/z$  reactant ion is formed. Since other undesirable reactant ions may be present, the ionization process is not well-controlled. In fact, many ionization processes including CE, CI (each with various reactant ions), and even EI may compete with the ionization technique of interest. This mixed-mode ionization certainly limits the selectivity of the ionization process. In addition, instrumental parameters such as ion source pressure affect the relative abundances of the various reactant ions, and reproducible CE or CI spectra are often not easily obtained.

An approach that eliminates the mixed-mode ionization discussed above is to mass-select the desired reactant ion before allowing it to react with the sample. Mass selection of reactant ions has previously been used for studying ion-molecule reactions and reactive collisions. A variety of tandem mass spectrometers have been used, including sector instruments (14), a double quadrupole instrument (15), quadrupole ion traps (16-19), and triple quadrupole mass spectrometers (19-27). Crawford and co-workers have used Kr as a charge exchange collision gas in a triple quadrupole mass spectrometer (TQMS) for monitoring carbon monoxide in the presence of hydrocarbons (28). However, to date there has been no demonstration of the analytical utility of mass selecting the reactant ion for mixture analysis or of the combination of such mass-selected reactions with GC.

In the work described here, a gas chromatograph has been interfaced to the collision cell of a TQMS. Reactant ions are

<sup>1</sup>Current address: Finnigan MAT, 355 River Oaks Parkway, San Jose, CA 95134-1991.

selected with the first quadrupole mass filter (Q1) and are allowed to react with neutral sample molecules that elute from a GC column into the second quadrupole collision cell (Q2). The third quadrupole is scanned for the products of the ion-molecule reactions. For both CE and proton transfer CI, the exothermicity of the ion-molecule reaction and the resulting extent of fragmentation can be controlled by the selection of the reactant ion. These ionization processes can be used to enhance selectivity by choosing reactant ions that will only ionize targeted compounds or by excluding the ionization of undesirable interferents. For example, if the molecular ion of benzene ( $C_6H_6^+$ , IE = 9.2 eV) is chosen as a CE reactant, only compounds with ionization energies less than 9.2 eV are ionized (typically only aromatic compounds). The energetics of ion-molecule reactions can also be used to obtain the desired amount of fragmentation. For example, if CE is used and molecular weight information is desired, then reactant ions may be chosen that have REs just above the IEs of the analytes. Alternatively, if structural information is desired, a reactant ion may be chosen that has a RE much larger than the IE of the sample molecules. The same logic can be applied to proton transfer CI, except that the difference in proton affinities determines the degree of fragmentation. Here the selectivity and sensitivity of a TQMS system combining short-column GC with mass-selected reactions are presented. Also, the capability of obtaining both molecular weight and structural information in the same chromatogram is demonstrated.

### EXPERIMENTAL SECTION

**Mass Spectrometry.** A Finnigan MAT TSQ70 triple quadrupole mass spectrometer was used in these studies. All reactant gases, except for benzene and acetone, were introduced into the ion source through the gas line normally used for introduction of CI gas. Benzene and acetone were introduced into the ion source via a variable leak valve (Granville-Phillips), which was mounted on a  $1/2$  in. o.d. stainless steel probe that could be inserted into the ion source through the probe inlet assembly. Reactant gases were ionized in the source with electron energies of 70–100 eV and emission currents of 200  $\mu$ A. Reactant gas pressures of less than 0.3 Torr were used in all cases. For experiments utilizing argon and benzene as a reactant gas mixture, the pressures of the two reactant gases were adjusted to yield approximately the same signal intensity for the  $Ar^{++}$  ( $m/z$  40) and  $C_6H_6^{++}$  ( $m/z$  78) reactant ions. The continuous dynode electron multiplier was operated at 1000–1200 V, and the preamplifier gain was set at  $10^8$  V/A. The mass spectrometer vacuum cradle was maintained at 100 °C to minimize sample memory effects in the collision cell.

The TQMS was tuned in the normal fashion with perfluorotributylamine (FC43) to optimize ion transmission and calibrate the mass assignment. An additional tuning procedure, described in detail elsewhere (20), was used to optimize the ion optics for maximum transmission of the ion-molecule reaction products. This was performed by introducing Ar into the source and *n*-butylbenzene into Q2. The first quadrupole (Q1) was set to pass  $Ar^+$  and the resulting charge exchange products of  $Ar^{++}$  with *n*-butylbenzene were monitored. The ion optics were optimized for the appearance of the product ions. Relatively low Q2 ion energies (typically 0–2 eV) were required for optimum product ion formation. This could be expected, considering that the Q2 ion energy effectively controls ion residence times within Q2.

**Gas Chromatography.** A Varian 3400 gas chromatograph with a split/splitless injector was used. A 2.1 m  $\times$  0.25 mm i.d. DB-5 (0.25- $\mu$ m film) or a 3 m  $\times$  0.18 mm i.d. (0.4- $\mu$ m film) fused-silica open tubular (FSOT) column (J&W Scientific) was used, depending on the analysis. Carrier gas flow rates were controlled with a mass flow controller (MKS Model 1159A) and a flow control system described previously (6). This flow control system allows the injection port to be operated at subambient pressures such that low carrier gas flow rates (1–2 mL/min) can be used with short columns with a vacuum outlet. It was necessary to limit the flow rates to less than 2 mL/min in the collision cell to avoid

exceeding the normal operating pressure of the analyzer region of the TSQ70. The pressure in the analyzer region, with <2 mL/min of He carrier gas flowing into the collision cell, was typically  $2 \times 10^{-6}$  Torr, as indicated by a Bayard-Alpert ionization gauge. It should be noted that longer columns could be used (instead of short columns with reduced inlet pressures) to restrict the column flow rates, at the expense of longer analysis times. Split injections were performed by injecting the sample directly into the low pressure injection port, which was connected to a mechanical pump via the splitter line. During the splitless mode of operation, the samples were injected with the split valve closed and the injection port slightly above atmospheric pressure. The inlet pressure was then sharply reduced after allowing approximately 10 s for the sample to enter the column. At the flow rates used, the injection port was completely flushed with carrier gas in approximately 3 s. Final inlet pressures of 420 and 710 Torr were used for the 0.25 mm i.d. and the 0.18 mm i.d. column, respectively. Temperature programming was used for all analyses. A GC test mixture (J&W P/N 2000110) consisting of 250 ng/ $\mu$ L of each of seven components in hexane was employed to evaluate the chromatographic integrity of the GC and GC/MS transfer line.

It was important to select a carrier gas that would not be ionized by mass-selected reactant ions, since the ionized carrier gas could interfere with the ion-molecule reactions of interest. Helium was chosen for this work, since it has an ionization energy well above the recombination energies of the reactant ions used. In addition, it was expected that the small collision cross section of helium would reduce the probability of collisionally activated dissociation (CAD) of reactant or product ions in the collision cell; however, helium does serve as a buffer gas, which is able to absorb energy during collisions with reactant or product ions.

**GC/MS Interface.** Two different transfer lines were used for GC/MS interfaces. In both cases the effluent from the GC column was introduced directly into the collision cell of the TQMS. For one transfer line, a 1-m section of the polyimide-clad FSOT column was passed through a 1-m length of  $1/16$  in. o.d. stainless steel tubing. The second transfer line consisted of a 0.9 m  $\times$  0.32 mm i.d. BP-5 aluminum-clad FSOT column with a 0.5- $\mu$ m film thickness (SGE). The 2.1-m FSOT column was coupled to the Al-clad column with a glass-lined zero-dead-volume fitting. Both transfer lines were resistively heated by applying an ac voltage across the tubing. This was accomplished by connecting the line voltage (120 V ac) across an adjustable autotransformer (Variac), and connecting the output of the autotransformer to a step-down transformer (rated at 34 V, 10 A, with 120 V input). The voltage developed across the secondary of the transformer was placed across the transfer line. The temperature of the transfer line was adjusted by varying the voltage output of the autotransformer. Approximately 5–6 V ac was required to heat either transfer line to 175 °C. The transfer lines were covered with glass braid insulation to minimize temperature fluctuations. The transfer line temperatures were monitored with a digital temperature sensor utilizing a low thermal mass type K thermocouple (Omega Engineering). Small alligator clips were used to make electrical connections to the transfer lines. The transfer line being used was inserted through a feedthrough into the mass spectrometer vacuum chamber. A Viton ferrule and a 5 cm piece of Teflon tubing were used to electrically isolate the transfer line from the vacuum manifold of the mass spectrometer. Grounding for the transfer line was made inside the vacuum chamber, which allowed all but the last 5 cm of the column to be heated. The end of the column was inserted into the collision chamber through the same opening used for introduction of collision gas. The TSQ70 vacuum manifold has a removable glass top that allows easy access to the collision chamber. The procedure of installing the column outlet into Q2 requires about the same amount of time as normal installation of a column into the ion source. The transfer lines are mechanically simple and can be rapidly heated (or cooled) to the desired temperature. Details of the performance and merits of direct resistive heating of Al-clad GC columns are presented in a separate publication (29).

### RESULTS AND DISCUSSION

**Mass-Selected Reactions for Obtaining Structural and Molecular Weight Information.** Electron ionization (EI)

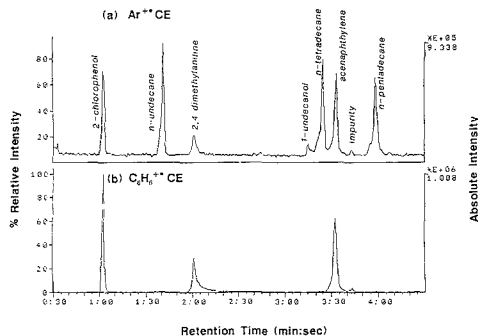


**Figure 1.** Mass-selected reaction chromatogram of GC test mixture with (a)  $\text{Ar}^{++}$  charge exchange and (b)  $\text{C}_6\text{H}_6^{++}$  charge exchange. The reactant ions were mass selected with Q1 during alternate scans. The impurity in the mixture is acenaphthene.

typically provides structural information; however, in many cases low intensity molecular ions (or no molecular ions at all) are obtained. Chemical ionization (CI) is then used to obtain pseudo molecular ions (e.g.,  $[\text{M} + \text{H}]^+$ ) for molecular weight confirmation. There are a number of commercially available mass spectrometers that provide the capability of acquiring EI and CI spectra during alternating scans. For mass spectrometers not equipped with this capability, a physical change in the ion source region (e.g., an ion volume or a different ion source) is required to switch from EI to CI. In the latter case, EI and CI spectra cannot be obtained simultaneously; consequently, molecular weight and structural information are not readily obtained in a single chromatographic run. With mass-selected reactions, however, the energetics of the ionization process can be tailored to the type of information desired. As a result, structural information and molecular weight information can be simultaneously acquired. This can be accomplished by sequentially selecting different reactant ions from the same reactant gas or by introducing a mixture of reactant gases in the source and selecting the reactant ions during alternating scans that have different recombination energies or proton affinities. It is also possible to acquire alternating CI and CE spectra by selecting different reactant ions.

Figure 1 shows CE reconstructed ion chromatograms of 1  $\mu\text{L}$  of a GC test mixture that were obtained by selecting the  $\text{Ar}^{++}$  and  $\text{C}_6\text{H}_6^{++}$  reactant ions during alternating scans. This mixture contains a variety of compound types (alkanes, aromatics, alcohols, and an amine), as noted in the figure. The wide range of polarity and reactivity of these components makes this mixture useful for evaluating the chromatographic performance of the capillary column/transfer line (e.g., to indicate the presence of active sites), as well as for investigating a variety of ion-molecule reactions. The chromatogram was obtained with the  $3\text{ m} \times 0.18\text{ mm}$  i.d. column (1 m of which served as the transfer line) operated with a 25:1 split.

Ionization energies of aliphatic compounds are typically above 11 eV, while those of aromatics are typically below 10 eV. As shown in Figure 1,  $\text{Ar}^{++}$  ( $\text{RE} = 15.8\text{ eV}$ ) ionizes all of the compounds of the mixture, while the  $\text{C}_6\text{H}_6^{++}$  ion ( $\text{RE} = 9.2\text{ eV}$ ) only ionizes the aromatic components. Fenselau et al. have previously evaluated benzene as a charge exchange reactant (13). However, their results showed that species not ionized by the  $\text{C}_6\text{H}_6^{++}$  reactant ion were ionized by EI in the source. Clearly, the ability to mass-select the desired reactant ion and carry out these reactions in a region without the presence of ionizing electrons yields the maximum selectivity obtainable with the ionization process.

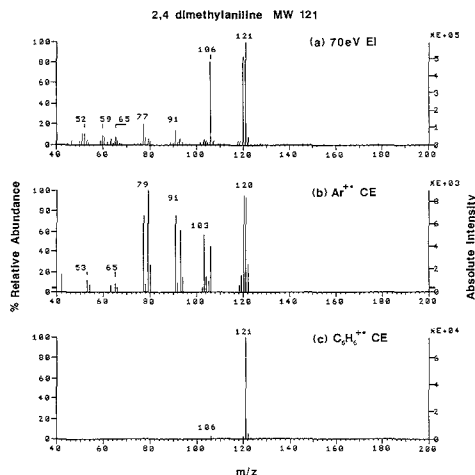


**Figure 2.** Mass spectra of 2,4-dimethylaniline: (a) 70 eV EI, (b)  $\text{Ar}^{++}$  CE, and (c)  $\text{C}_6\text{H}_6^{++}$  CE. The CE spectra were obtained from the chromatogram in Figure 1. The EI spectrum was acquired separately.

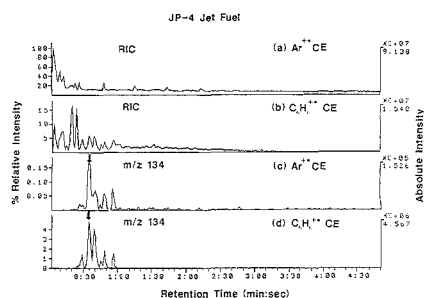
Figure 2 shows a comparison of the spectra of 2,4-dimethylaniline obtained from  $\text{Ar}^{++}$  and  $\text{C}_6\text{H}_6^{++}$  CE from the chromatogram in Figure 1, as well as an EI spectrum acquired separately for comparison. The CE spectra illustrate the capability of simultaneously obtaining molecular weight and structural information. Our experience has shown that the  $\text{C}_6\text{H}_6^{++}$  reactant ion yields predominantly the molecular ion for aromatic compounds with little or no fragmentation. Conversely, the  $\text{Ar}^{++}$  CE spectra are more energetic than 70-eV EI spectra. This can be better understood by considering the internal energy imparted upon ionization. The internal energy deposited during CE ionization is well-defined (11), whereas the internal energy deposited during ionization by EI is not well-defined due to the wide range of energies imparted during EI with 70-eV electrons (30). Since the distribution of internal energies imparted by CE and EI is different, the spectra will generally be different, even if the average internal energy deposited is the same.

It is also possible for some reactant ion kinetic energy to be transferred to product ion internal energy during the ion-molecule reactions. As a result, it would be expected that the relative ion abundances of the product ion spectra would be dependent on the Q2 ion energy. In these experiments, relatively low Q2 ion energies were used (e.g., 0–2 eV) with the presence of helium (acting as a buffer gas) in the collision cell; therefore, the amount of kinetic energy transferred from the reactant ions to internal energy of the product ions is expected to be small.

Charge exchange ionization produces odd-electron species as does EI (31, 32). It has previously been shown that CE spectra can be searched against the NBS EI library with acceptable results (32). These concepts were investigated by using mass-selected reactions in the TQMS. An advantage of mass-selected reactions is that two (or more) different CE reactant ions can be used, one resulting in EI-type spectra and another yielding very little fragmentation. Thus, the CE spectra could provide an added dimension for simultaneously providing structural and molecular weight information for the classification of unknowns. Charge exchange spectra from  $\text{Ar}^{++}$ ,  $\text{CO}_2^{++}$  ( $\text{RE} = 13.8\text{ eV}$ ), and  $\text{CH}_3^+$  ( $\text{RE} = 13.5\text{ eV}$ ) with the components in the GC test mixture were compared with EI library spectra. The results of the library searches obtained with the TSQ70 ICIS system from the three CE reactant ions

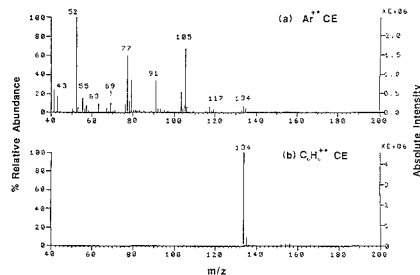
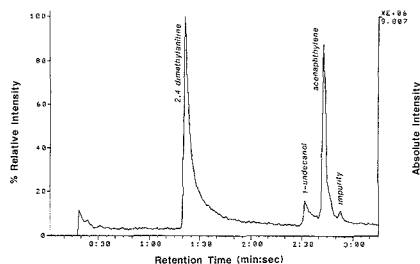
**Table I.** Comparison of EI Library Search Results for CE with Various Reactant Ions and EI of Compounds in GC Test Mixture

compound	library search match number				MW filter
	EI	CE Ar <sup>+</sup>	CE CO <sub>2</sub> <sup>+</sup>	CE CH <sub>3</sub> <sup>+</sup>	
2-chlorophenol	1	3	3	2	off
	1	3	3	2	on
undecane	N <sup>a</sup>	N	N	N	off
	5	5	2	1	on
2,4-dimethylaniline	5	3	N	4	off
	5	3	3	3	on
1-undecanol	N	N	N	N	off
	1	3	2	1	on
tetradecane	4	9	1	1	off
	2	1	1	1	on
acenaphthylene	1	7	N	N	off
	1	4	10	2	on
pentadecane	N	N	N	1	off
	1	3	1	1	on

<sup>a</sup>N, Not found among the top ten best fits of the library search.**Figure 3.** Mass-selected reaction chromatogram of JP-4 jet fuel on a 2.1-m column. Reconstructed ion chromatograms were (a) Ar<sup>+</sup> CE and (b) C<sub>6</sub>H<sub>6</sub><sup>+</sup> CE. Mass chromatograms of the *m/z* 134 M<sup>+</sup> of 10-carbon alkylbenzenes were (c) Ar<sup>+</sup> and (d) C<sub>6</sub>H<sub>6</sub><sup>+</sup> CE. The arrows indicate where spectra were obtained for Figure 4.

as well as from EI are shown in Table I. As shown in the table, the success rate of the library search for the CE spectra was comparable to that obtained with EI. In general, among the charge exchange reactants studied, the CH<sub>3</sub><sup>+</sup> CE spectra yielded the most reliable match with the EI library spectra. This might be expected, since the CH<sub>3</sub><sup>+</sup> charge exchange reactant ion deposits the least amount of energy of the three reactant ions studied and yielded the most abundant molecular ions. In cases where the compound was not found, knowledge of the molecular weight (obtainable by CE with a less energetic reactant ion) led to more accurate classification. Once the molecular weight was known, the molecular weight filter could be applied before the library search was carried out. In addition, in cases where the compound was not correctly matched, information about the compound class could be obtained from the best hits of the CE spectra, as is commonly done with EI spectra.

**Selectivity of Ionization.** The chromatograms in Figure 1 illustrate the selectivity of C<sub>6</sub>H<sub>6</sub><sup>+</sup> CE for a relatively simple mixture. A more dramatic illustration of the selectivity of the C<sub>6</sub>H<sub>6</sub><sup>+</sup> reactant ion is its use as a means of rapidly screening for the aromatic components of a complex mixture without high-resolution chromatographic separation. An example of these concepts is presented in Figure 3, which shows reconstructed ion chromatograms (RICs) of JP-4 jet fuel on a 2.1 m × 0.25 mm i.d. FSOT column (1 m of this column served as the transfer line). The top two traces of the figure show

**Figure 4.** Spectra obtained from the chromatogram marked by arrows in Figure 3: (a) Ar<sup>+</sup> CE and (b) C<sub>6</sub>H<sub>6</sub><sup>+</sup> CE. Only aromatic species of the jet fuel are ionized with benzene charge exchange, with no fragmentation.**Figure 5.** Mass-selected reaction chromatogram of GC test mixture obtained with mass selection of the protonated acetone dimer (*m/z* 117) reactant ion. The impurity in the mixture is acenaphthene.

the RICs resulting from Ar<sup>+</sup> and C<sub>6</sub>H<sub>6</sub><sup>+</sup> CE, respectively. The bottom two traces show mass chromatograms for the *m/z* 134 ion obtained via CE from the two different reactant ions. The *m/z* 134 ion is the molecular ion produced from a number of different isomers of alkylbenzenes containing a total of ten carbons. Figure 4 shows Ar<sup>+</sup> and C<sub>6</sub>H<sub>6</sub><sup>+</sup> CE spectra that were obtained from the chromatogram of Figure 3. The points at which these spectra were taken are indicated by the arrows in Figure 3. The Ar<sup>+</sup> CE spectrum of Figure 4a is not easily interpreted, since molecular ions and fragment ions from both aliphatic and aromatic constituents of the jet fuel are produced. However, in the C<sub>6</sub>H<sub>6</sub><sup>+</sup> CE spectrum of Figure 4b, only the molecular ion (*m/z* 134 and the <sup>13</sup>C peak at *m/z* 135) from the alkylbenzene(s) is produced.

Mass-selected ion-molecule reactions can be performed by using unique, highly specific reactant ions. Often, selection of reactant gases for chemical ionization in the ion source is limited to low molecular weight gases (e.g., methane, ammonia, etc.), as reactant gases of higher molecular weight (e.g., 100 amu), present in a large excess compared to the sample, can produce ions due to adducts, dimers, and/or fragment ions that obscure the presence of sample ions. With mass-selected reactions, virtually any reactant ion can be used, provided that the reactant ion can be produced in the ion source and does not have the same *m/z* as the sample under study. An example of a unique reactant ion for chemical ionization is the protonated acetone dimer (*m/z* 117). A chromatogram of the GC test mixture obtained by mass selected reaction with the protonated acetone dimer is shown in Figure 5. The 2.1-m FSOT column was used with the 0.9-m FSOT Al-clad transfer line. It was discovered that selection of the *m/z* 117 ion with Q1 resulted in the production of the protonated acetone (*m/z* 59) in Q2. The *m/z* 59 ion, which was the result of metastable decomposition of *m/z* 117 or CAD of *m/z* 117 with the helium carrier gas, has an intensity of 30% relative to the *m/z* 117

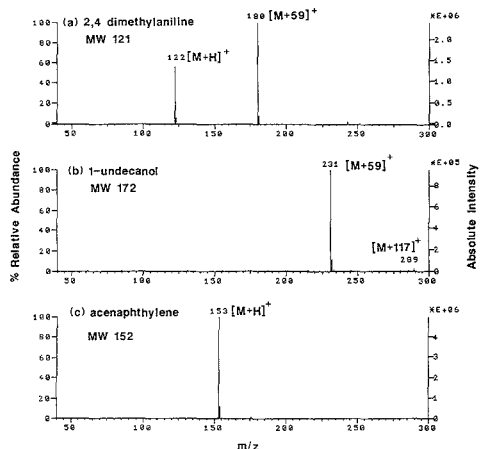


**Figure 6.** Acetone CI spectra obtained from chromatogram in Figure 5: (a) 2,4-dimethylaniline, (b) 1-undecanol, (c) acenaphthylene. Only components with hydrogen-bonding sites reacted to form acetone adducts.

ion. Only three of the seven components were ionized by the acetone reactant ions. Spectra for the components ionized are shown in Figure 6. The acetone reactant ions can react via proton transfer to form  $[M + H]^+$  ions if the reaction is energetically favorable. Acenaphthylene and 2,4-dimethylaniline were the only mixture components protonated by the acetone reactant ions. Compounds may also form adducts with protonated acetone to yield  $[M + 59]^+$  ions or with the protonated acetone dimer to produce  $[M + 117]^+$  ions. For the components of the GC test mixture, only compounds with hydrogen bonding sites reacted to form the acetone adduct ions (e.g., 2,4-dimethylaniline, and 1-undecanol). Note that 2-chlorophenol, which does have a hydrogen bonding site, was not ionized by the acetone reagent ions. All of the spectra obtained from acetone CI exhibited no fragmentation, as shown in Figure 6.

**Detection Capabilities of GC/MS/MS with Mass-Selected Reactant Ions.** The ability of GC/MS/MS with mass-selected reactions to detect low levels of analyte was also examined. Initially, it was not expected that products of ion-molecule reactions in Q2 could be efficiently extracted and mass analyzed. The products of the ion-molecule reactions have little or no axial kinetic energy when they are formed; thus, the collection efficiency of the product ions is dependent on the extraction capabilities of the Q2 ion exit lens. In fact, Enke et al. have found it necessary to fill and trap ions in Q2 for a period of time and then pulse them out with the Q2 ion exit lens in order to obtain adequate sensitivity (25). Nevertheless, we have found that detection limits with GC/MS/MS and mass-selected reactions (without ion trapping techniques) are comparable or better than those obtained with GC/MS. For these experiments, benzophenone was the analyte and  $C_6H_6^{+}$  was the CE reactant ion. The same column and transfer line, described previously with the acetone CI studies, were used for these experiments. Similar to the spectra of other aromatic compounds studied, benzophenone was ionized by CE with the  $C_6H_6^{+}$  reactant ion to produce only the molecular ion ( $m/z$  182). Figure 7a shows the mass chromatogram for the  $m/z$  182 ion of 100 pg of benzophenone for a full scan of Q3 (80–240 amu in 0.5 s). Figure 7b shows the chromatogram obtained from 15 pg of benzophenone when Q3 was scanned from 181–183 amu in 0.5 s. The signal-to-noise ratios for parts a and b of Figure

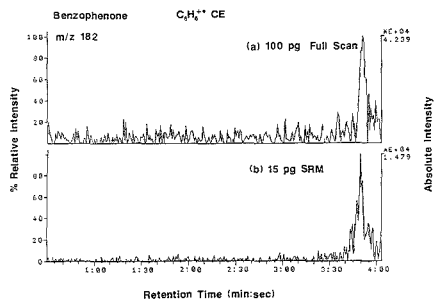


**Figure 7.** Benzene CE mass chromatograms for (a) 100 pg of benzophenone obtained with a full scan of Q3 and (b) 15 pg of benzophenone obtained with selected reaction monitoring (SRM) of the  $m/z$  182 ion.

7, estimated by dividing the peak height by the average background noise level of the  $m/z$  182 ion, are approximately 9:1 and 30:1, respectively. For comparison, the specifications for the full scan sensitivity of the TSQ70 with GC/MS are quoted as 200 pg for EI with signal to noise ratio (S/N) of 10:1 and 100 pg with methane CI with a S/N of 25:1. Benzene CE experiments were attempted in the ion source for comparison with the mass-selected reaction results. With benzene CE in the ion source and a full scan of Q1, 600 pg of benzophenone could be detected at a S/N of 10:1 with GC/MS. However, the spectra obtained from carrying out the reactions in the ion source resembled EI spectra instead of benzene CE spectra (due to mixed-mode ionization) and thus do not represent a valid comparison. The ability to obtain the molecular ion (or pseudo molecular ion) with little or no fragmentation for an analyte provides the maximum sensitivity for trace analysis. Since such "soft ionization" is easily performed with mass-selected reactions, the GC/MS/MS approach provides the opportunity to "tune" the ionization to obtain the best limits of detection.

**Chromatographic Integrity.** The chromatographic peak shape obtained from introducing the effluent from the GC column into the collision cell is not quite as good as that normally obtained when the GC effluent is introduced into the ion source. The tailing of the 2,4-dimethylaniline peak (Figure 1 and Figure 5) is most likely due to active sites and insufficient heating of the collision cell. Since the temperature of the collision cell was controlled by radiant heating from the vacuum manifold heater, the maximum temperature was limited to 100 °C to avoid damage to the electron multiplier. It is expected that better chromatographic peak shape could be obtained if the collision cell were heated separately and to higher temperatures than 100 °C. The best peak shape was obtained when a polyimide-clad FSOT column was used as a transfer line (Figure 1) instead of the Al-clad column (Figure 5). Although the Al-clad column is more easily heated resistively, the polyimide-clad column can be inserted closer to the quadrupole rods of the collision cell without danger of electrical arcing, minimizing sample adsorption on the stainless steel walls of the collision cell. The introduction of the GC column into the collision cell did not appear to reduce ion transmission or decrease the performance of the instrument and has not required cleaning of any of the ion optics beyond routine maintenance.

## CONCLUSIONS

A new technique in which samples are introduced via GC into the collision cell of a TQMS system has been described. This GC/MS/MS approach utilizing mass-selected reactions offers significant advantages over GC/MS for control of the



selectivity and energetics of the ionization process. Molecular ions, pseudo molecular ions, or characteristic fragment ions can be obtained depending on the reactant ion and the amount of internal energy deposited during ionization of the sample. The utility of searching charge exchange spectra against EI library spectra has also been demonstrated. When combined with short-column open tubular GC, mass-selected reactions can be used to rapidly screen for particular classes of compounds. For example, the aromatic content of a jet fuel can be investigated with  $C_6H_6^{*+}$  charge exchange, without interference from aliphatic constituents. The detection limits of GC/MS/MS with mass-selected reactions are in the picogram range, which are comparable to those that can be obtained with GC/MS. The simple, resistively heated GC/MS transfer lines described here should make these types of experiments readily accessible on any TQMS system. With this technique, it should be possible to devise highly specific ion-molecule reactions for mixture analysis.

#### ACKNOWLEDGMENT

The authors gratefully acknowledge fruitful discussions with Douglas W. Kuehl of the U.S. EPA.

#### LITERATURE CITED

- (1) *Tandem Mass Spectrometry*; McLafferty, F. W., Ed.; John Wiley & Sons: New York, 1983.
- (2) Johnson, J. V.; Yost, R. A. *Anal. Chem.* **1985**, *57*, 758A-764A.
- (3) Yost, R. A.; Fetterolf, D. D.; Hass, J. R.; Harvan, D. J.; Weston, A. F.; Skotnicki, P. A.; Simon, N. M. *Anal. Chem.* **1984**, *56*, 2223-2228.
- (4) Trehy, M. L.; Yost, R. A.; Dorsey, J. G. *Anal. Chem.* **1986**, *58*, 14-19.
- (5) Trehy, M. L.; Yost, R. A.; McCreary, J. J. *Anal. Chem.* **1984**, *56*, 1281-1285.
- (6) Hail, M. E.; Yost, R. A. *Proceedings of the 36th ASMS Conference on Mass Spectrometry and Allied Topics* **1988**, 803-804.
- (7) McClellen, W. H.; Richards, J. M.; Meuzelaar, H. L. C. *Proceedings of the 36th ASMS Conference on Mass Spectrometry and Allied Topics* **1988**, 403-404.
- (8) Richards, J. M.; McClellen, W. H.; Bunker, J. A.; Meuzelaar, H. L. C. *Proceedings of the 36th ASMS Conference on Mass Spectrometry and Allied Topics* **1988**, 547-548.
- (9) Fetterolf, D. D.; Yost, R. A. *Int. J. Mass Spectrom. Ion Processes* **1984**, *62*, 33-49.
- (10) Jesus, B. L.; Munson, B.; Fenselau, C. *Biomed. Mass Spectrom.* **1974**, *1*, 96-102.
- (11) Harrison, A. G. *Chemical Ionization Mass Spectrometry*; CRC Press, Inc.: Boca Raton, FL, 1983; Chapter 2.
- (12) Einolf, N.; Munson, B. *Int. J. Mass Spectrom. Ion. Phys.* **1972**, *9*, 141-160.
- (13) Subba Rao, S. C.; Fenselau, C. *Anal. Chem.* **1978**, *50*, 511-515.
- (14) Hsu, C. S.; Cooks, R. G. *Org. Mass Spectrom.* **1976**, *11*, 975-983.
- (15) Busch, K. L.; Kruger, T. L.; Cooks, R. G. *Anal. Chim. Acta* **1980**, *119*, 153-156.
- (16) Van Berkel, G. J.; Glish, G. L.; McLuckey, S. A. *Proceedings of the 36th ASMS Conference on Mass Spectrometry and Allied Topics* **1988**, 300-301.
- (17) Van Berkel, G. J.; Glish, G. L.; McLuckey, S. A. *Proceedings of the 36th ASMS Conference on Mass Spectrometry and Allied Topics* **1988**, 639-640.
- (18) Glish, G. L.; Van Berkel, G. J.; Asano, K. G.; McLuckey, S. A. *Proceedings of the 36th ASMS Conference on Mass Spectrometry and Allied Topics* **1988**, 1112-1113.
- (19) Berberich, D. W.; Hail, M. E.; Yost, R. A. *Proceedings of the 36th ASMS Conference on Mass Spectrometry and Allied Topics* **1988**, 1110-1111.
- (20) Berberich, D. W.; Hail, M. E.; Johnson, J. V.; Yost, R. A. *Int. J. Mass Spectrom. Ion Processes*, in press.
- (21) Schmit, J. P.; Dawson, P. H.; Beaufileu, N. *Org. Mass Spectrom.* **1985**, *20*, 269-275.
- (22) Schmit, J. P.; Beaudet, S.; Brisson, A. *Org. Mass Spectrom.* **1986**, *21*, 493-498.
- (23) Jalonen, J. J. *Chem. Soc., Chem. Commun.* **1985**, 872-873.
- (24) Fetterolf, D. D.; Yost, R. A.; Eyster, J. R. *Org. Mass Spectrom.* **1984**, *19*, 104-105.
- (25) Dolnikowski, G. G.; Kristo, M. J.; Erke, C. G.; Watson, J. T. *Int. J. Mass Spectrom. Ion Processes* **1988**, *82*, 1-15.
- (26) Beauprand, C.; Devant, G.; Jaouen, D.; Mestdag, H.; Rolando, C. *Proceedings of the 35th ASMS Conference on Mass Spectrometry and Allied Topics* **1987**, 345-346.
- (27) Beauprand, C.; Devant, G.; Jaouen, D.; Mestdag, H.; Rolando, C.; Supérieure, E. N. *Proceedings of the ASMS Conference on Mass Spectrometry and Allied Topics* **1988**, 811-812.
- (28) Crawford, R. W.; Alcaraz, A.; Reynolds, J. G. *Anal. Chem.* **1988**, *60*, 2439-2441.
- (29) Hail, M. E.; Yost, R. A., submitted for publication in *Anal. Chem.*
- (30) Mark, T. D. *Gaseous Ion Chemistry and Mass Spectrometry*; John Wiley & Sons: New York, 1986; Chapter 3.
- (31) Lee, E. D.; Hsu, S.; Henion, J. D. *Anal. Chem.* **1988**, *60*, 1990-1994.
- (32) Hunt, D. F.; Gale, P. J. *Anal. Chem.* **1984**, *56*, 1111-1114.

RECEIVED for review November 16, 1988. Accepted May 19, 1989. This research was sponsored in part by the U.S. Air Force Engineering and Services Center, Environics Division (HQ-AFESC/RDVS), at Tyndall Air Force Base and by the U.S. Army Chemical Research Development and Engineering Center (CRDEC).

## Radio Frequency Powered Glow Discharge Atomization/Ionization Source for Solids Mass Spectrometry

Douglas C. Duckworth and R. Kenneth Marcus\*

Department of Chemistry, Howard L. Hunter Chemical Laboratories, Clemson University, Clemson, South Carolina 29634-1305

A radio frequency (rf) powered glow discharge atomization/ionization source has been developed for solids mass spectrometry. By use of a 13.56-MHz generator to supply the discharge operating potential, a pseudocontinuous plasma is produced that permits the sputtering of electrically insulating materials such as glasses and ceramics. The rf-powered source operates at argon pressures of 100-500 mTorr and powers of 5-50 W. The effect of discharge parameters on the observed analyte ion signals is explained in part as a spatial, ion sampling effect. Mass spectra are presented for alloy, metal oxide, and glass matrix samples. For each of the matrix types, analyte ion currents for the major species are on the order of  $10^{-11}$  A, a value similar to those observed in the conventional dc glow discharge ion sources.

#### INTRODUCTION

Over the last 25 years there has been phenomenal growth in the number, and capabilities, of spectrochemical methods for the elemental analysis of solution-based sample types. Flame and furnace atomic absorption (1) and inductively coupled plasma emission and mass spectrometry (2) are prime examples of such methods. A wide variety of dissolution procedures has been investigated for those samples that do not occur naturally as aqueous solutions (3). Unfortunately, dissolution schemes are as varied as the possible solid sample types. The complexity of dissolution procedures, the loss of desirable spatial (homogeneity) information, and the inherent analyte dilution of transformed solids have led to a renewed emphasis in the area of direct solids elemental analysis. In

addition, the developments occurring in the field of materials science pose ever increasing challenges to and requirements on the traditional solution phase methods. The majority of the new approaches to solids analysis has incorporated some means of thermal vaporization, generally followed by transport of the produced gaseous species to a secondary excitation/ionization source. For example, atomic populations have been created for inductively coupled plasma atomic emission spectrometry/mass spectrometry (ICP-AES/MS) analysis by arc and spark atomization (4, 5), electrothermal atomizers (6, 7), direct insertion (8, 9) and laser ablation (10, 11). Research continues in the use of lasers as atomization sources with subsequent optical (12) or mass spectrometric (13) analysis in the resultant plasma plume. Research emphasis in support of the laser atomization methods is placed on the efficient vapor transport to auxiliary spectrochemical sources (14) and the compensation for laser- and matrix-based irreproducibilities (15).

The application of glow discharge devices for direct solids elemental analysis is increasing (16). These reduced pressure, inert atmosphere plasma sources rely on a cathodic sputtering step to produce atomic populations from conductive solids such as metals, alloys, and semiconductors. Sputtered material subsequently diffuses into the collision-rich negative glow region where collisions with electrons and metastable discharge gas atoms produce excited-state and ionic species. Glow discharges are currently employed for elemental analysis by atomic absorption (17, 18), emission (19, 20), mass spectrometry (21, 22), and a number of laser-based spectroscopic methods (23, 24).

One of the factors that has tended to limit the application of glow discharges has been the requirement that the sample be conductive in nature. Nonconducting powder samples have in fact been efficiently atomized for subsequent optical and mass analysis (25-27) by mixing with a conducting powder matrix. The resulting powder is pressed into the form of a disk of appropriate dimensions, in a manner similar to the preparation of an IR spectrophotometry sample pellet. While this procedure is compatible for many powder samples, many bulk solids are not easily transformed into powders. In addition, this process precludes any depth-resolved analyses.

The research described here is focused on expanding the analytical utility of glow discharge spectroscopies to include bulk solid insulating (nonconducting) materials. By use of a radio frequency (13.56-MHz) potential to sustain the glow discharge plasma, samples ranging from metal alloys to high-temperature ceramics can be sputter-atomized for subsequent spectrochemical analysis. Radio frequency (rf) plasmas have been applied extensively in the production of specialized thin film and semiconductor (28, 29) systems. Spectroscopic investigations of these plasmas have been approached primarily as means of process monitoring (30, 31) and diagnostics of fundamental plasma chemistry (32-40). In terms of the application to bulk solids analysis, the principal advantages of rf operation are the ability to analyze insulating materials directly without matrix modification and to operate in a lower pressure regime than their dc cousins (50-500 mTorr vs 1-5 Torr). The latter feature is expected to result in lower amounts of molecular species being formed in the gas phase and the possibility for enhanced resolution in depth-profiling applications (41).

The mass spectrometric sampling of rf powered glow discharge devices, to date, has been pursued from principally a fundamental point of view. These studies have been performed in order to understand better the operating principles of these devices as they are employed in semiconductor device fabrication. Coburn and co-workers (37-40) pioneered mass spectrometric sampling of rf plasmas as a diagnostic tool.

They employed mass spectrometry along with atomic absorption to study the ionization mechanisms in rf glow discharges, concluding that Penning collisions are the dominant process (37, 38). Other studies identified the existence of species of the form  $M^{2+}$ ,  $MAr^+$ ,  $M^+Ar$ , and  $MO^+$  (39). Finally, these researchers illustrated that mass spectrometric sampling of rf glow discharges allows for the generation of element vs depth profiles in thin film systems (40). As will be discussed later, the discharge pressures of the sources employed in these earlier studies were much lower (generally much less than 100 mTorr) than those employed in the work described here (100-500 mTorr).

Given the possible benefits of rf glow discharge operation, the application of this operating mode has not been investigated to a great extent in analytical chemistry. Donohue and Harrison (42) applied the rf (500-kHz) potential from a spark source (mass spectrometer) generator to power a hollow cathode discharge ion source. Their studies indicated that the analytical capabilities of the rf powered hollow cathode were quite similar to dc powered devices, with the ability to sputter insulating materials (Pyrex glass) directly as an added advantage. Of note was the absence in the mass spectrum of oxide and hydroxide species of the glass materials, suggesting that these "molecular" analyte species are efficiently dissociated by the plasma processes. Oeschner (43) has developed the technique of sputtered neutral mass spectrometry (SNMS) in which a high-frequency plasma is employed either as the primary sputter/ionization source or as a secondary ionization source for neutral sputtered species. The 27-MHz plasma operates in the  $10^{-3}$ - $10^{-4}$  Torr regime with the power applied through inductive coupling. In the direct bombardment mode (DBM), a relatively small dc potential (a few hundred electronvolts) is applied to the sample. This potential extracts ions produced in the plasma and accelerates them to the cathode surface, resulting in sputtering. A commercial version of this instrument (INA 3, Leybold-Heraeus Vacuum Products, Export, PA), having depth resolution powers reported on the order of a nanometer, is sold as an alternative to conventional secondary ion mass spectrometry. Both radio frequency (44) and microwave (45) radiation have been employed to boost the spectral output of glow discharge emission devices. The purpose of these couplings is the enhancement of electron impact collisions in the gas phase, but not necessarily the primary sputter atomization processes. Of these analytical implementations of rf power (energy), only that of Donohue (42) incorporates the direct coupling of rf power to sputter atomize solid samples.

We present here a description of early developmental work on a radio frequency powered glow discharge atomization/ionization source for solids mass spectrometry (rf-GDMS). After a discussion of the principles that permit rf sputtering of insulating materials, and the attainment of proper electrode biasing, the results of rf plasma diagnostic studies which have produced number densities of analytically relevant plasma characteristics will be summarized. The design considerations of the rf powered glow discharge source and its interfacing to a quadrupole mass filter system will be presented. The parametric dependencies of plasma ionic species will be illustrated for source operation with copper alloy samples. The applicability of this source to the analysis of insulating materials is demonstrated through mass spectra obtained for a mixture of transition-metal oxides and a simulated nuclear defense waste glass. While not intended to define the ultimate powers of such a device, it is believed that the demonstration of these basic qualities is indicative of the possible wide-ranging applicability of the rf-GDMS source to a number of areas requiring bulk solids elemental analysis.

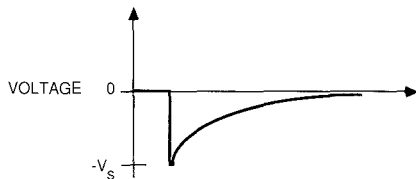


Figure 1. Temporal response of an insulating material to a negative voltage pulse.

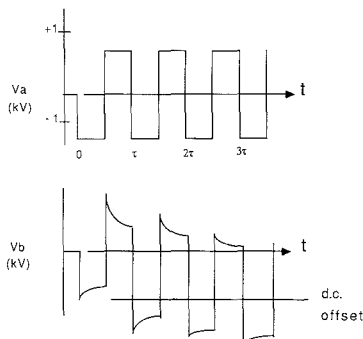


Figure 2. Electrode response to an applied square wave potential.

### THEORY

The principles by which direct current (dc) glow discharge devices operate have been detailed in a number of texts (46, 47). The atomization/excitation/ionization processes (i.e. cathodic sputtering, electron impact, and Penning collision) which make the devices useful tools for direct solids analysis have also been reviewed (16). These collisional processes are those occurring when analyzing metals, semiconductors, and suitably modified nonconducting powders. If one of the electrodes in the system is an electrically insulating material, the required flow of current cannot occur. The application of a high-voltage pulse to an insulating surface can be considered analogous to the charging of a capacitor, as shown in Figure 1. As a high negative voltage ( $-V_s$ ) is applied, the electrode surface potential drops to  $-V_s$  followed by a charging to more positive potentials as a function of time. This is not due to the accumulation of positive charges at the surface, but rather the loss of electrons through ion neutralization reactions at the surface (46). A short-lived discharge will exist only until the surface potential drops below the threshold value. For this reason, dc power will not sustain the discharge. The time scale of this process is such that the application of voltage pulses at frequencies on the order of 1 MHz and above results in a pseudocontinuous plasma. Wehner and co-workers (48) used this rationale in demonstrating the use of rf powered glow discharges as sputtering sources.

A key aspect of the application of rf glow discharges to the sputtering of insulating surfaces (true also for conductors) is the self-biasing that occurs between the plasma electrodes. Consider the application of a 2-kV peak-to-peak square wave potential ( $V_a$ ) to a pair of electrodes, as illustrated in Figure 2. In the initial half-cycle, the voltage of the primary cathode ( $V_b$ ) goes to  $-1$  kV and then begins positive charging to approximately  $-0.7$  kV. As the applied voltage is switched to  $+1$  kV, a surface potential of  $+1.3$  kV is produced. During this half-cycle, electrons are accelerated to the electrode's surface. The greater mobility of the plasma electrons (compared to the much heavier positive ions) results in a faster

Table I. Comparison of Analytically Relevant Plasma Characteristics of Radio Frequency (rf) and Direct Current (dc) Glow Discharge Plasmas

	rf	dc
sputtered atom density, $\text{Cu}/\text{cm}^3$	$10^{10}$ - $10^{11}$ (36)	$10^{10}$ - $10^{13}$ (51, 52)
electron density, $\text{cm}^{-3}$	$10^{15}$ - $10^{18}$ (27)	$10^{14}$ (52, 53)
average electron energy, eV	4-6 (27)	2-5 (54, 55)
metastable atom density, $\text{cm}^{-3}$	$10^{10}$ - $10^{11}$ (37)	$10^{10}$ - $10^{12}$ (51, 52)
excitation temperature, K		3000-6000 (53, 56)
mean free path, cm	$5 \times 10^{-2}$	$5 \times 10^{-3}$
collision frequency, $\text{s}^{-1}$	$8 \times 10^5$	$8 \times 10^6$

surface charging during this half-cycle such that the electrode surface potential approaches zero much faster than the previous half-cycle, thus reaching a value of  $+0.2$  kV. When the voltage polarity is switched at the start of the second full cycle, the potential on this electrode will reach  $-1.8$  kV ( $+0.2 - 2$  kV). As successive cycles proceed, the waveform of  $V_b$  will reach a constant offset value, which is significantly displaced in the negative direction. This negative dc offset (self-biasing), generally having a value of half of the applied peak-to-peak potential, is for all intents and purposes continuous. The electrode is bombarded alternately by high-energy ions and low-energy electrons and is therefore employed as the sputtering target (cathode). While the potentials applied to the electrodes are alternating, a time-averaged cathode and anode are established. Self-biasing is also a function of the respective electrode sizes. Studies by Koenig and Maissel (49) and Coburn and Kay (50) have shown that the potential developed at the smaller of the electrodes is much larger than that of the larger one. It is therefore advantageous to apply the rf potential to the sputtering target and to make its exposed area much smaller than the metal vacuum chamber which, for experimental simplicity, is usually held at ground potential.

While the vast majority of spectroscopic studies of rf glow discharge plasmas has been pursued as means of process monitoring, a large number of more fundamental studies have been undertaken to gain a more thorough understanding of collisional processes in the plasma negative glow (32-40). Gotscho and Miller (32) have reviewed the optical techniques that have been applied to rf plasma diagnostics. These techniques include actinometry (33), laser-induced fluorescence (34), and optogalvanic spectroscopy (35). Charged species in these devices have been sampled by use of electrostatic probes (36) and mass spectrometry (37-40). Ranges of the analytically relevant characteristics in rf and dc glow discharge devices are compared in Table I. Because comparisons of such values will also depend on discharge geometry and operating conditions, the figures should not be taken as absolute. As can be seen, the values given for the respective plasma types are in fairly close agreement. Therefore, one would expect that the analytical characteristics of rf and dc glow discharges should not be terribly different. In addition to the more common particle characteristics, the mean free path and collision frequency for argon atoms are given for the respective sources based on an rf operating pressure of 200 mTorr and a dc value of 2 Torr. These values are important in understanding the extent of molecular species observed in the mass spectra and the role of redeposition in the sputtering process.

The preliminary data presented here indicate that the analytical characteristics are indeed similar. The key difference is of course the fact that the rf discharge is capable of direct atomization of insulating materials. Other advantages that are yet to be investigated may result from the lower operating pressures of the rf devices. Lower discharge gas pressures would be expected to produce lower amounts of

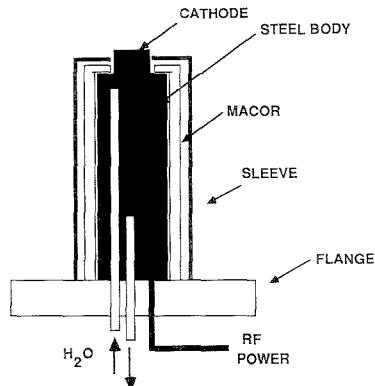


Figure 3. Diagrammatic representation of the rf glow discharge ion source.

possible molecular mass spectral interferences and a higher degree of depth resolution for thin-film analyses.

### EXPERIMENTAL SECTION

**Ion Source Design.** The design criteria for radio frequency powered glow discharge devices are similar to those of the more common dc plasmas. Key points include (1) discharge source housing configuration and material, (2) vacuum and discharge gas delivery systems, and (3) cathode (sample) holder geometry, power coupling, and cooling. The requirements for the latter set (3) are far more complex than in the dc case. Morgan (29) and Kumagi (57) have discussed the design considerations for rf powered glow discharge sputtering/deposition systems. The basic criteria described by these authors, along with experience in this laboratory in the design of more conventional dc glow discharge devices, have been incorporated in the design presented here. Other design considerations important for the analytical spectroscopic application of rf plasmas include the size and shape of the sample, the ease of sample interchange, and the ability to interface the device to both mass and optical spectrometers.

The design of the sample holder must allow for the application of the discharge maintenance potential and the passage of cooling water. The mounting of the sample to the holder needs to be such that there is efficient electrical and thermal conductivity between the sample and holder. Figure 3 is a diagram of the rf glow discharge sample holder designed in this laboratory. The body of the holder is a stainless steel cylinder capped at one end by a plate containing the electrical and cooling water connections. The opposite end is enclosed by the cathode mounting plate which has a 0.5 in. diameter, 0.125 in. deep recession into which the sample is press fit. Incoming cooling water is delivered close to the backside of the cathode mount. The rf discharge potential is simply applied to the cylinder through a stainless steel setscrew in the base. The cathode holder is encased in a glass ceramic (Macor) sleeve which acts to reduce the amount of sputtering of the holder assembly. Since the ceramic sleeve and metal holder are in direct contact, the Macor itself may be subject to sputtering collisions. To further restrict the discharge to the sample surface, an electrically grounded stainless steel sleeve (shutter) is flange mounted within one dark space distance ( $\sim 0.1$  in.) from the holder assembly. The location of this "anode", less than one dark space from the holder, prohibits the formation of a plasma in the enclosed regions. The complete sample holder/shutter apparatus is mounted on a 2.75-in. conflat-type flange that mates with the six-way cross ion source region described below. The mass spectrometric samples described here are nominally 0.5 in. in diameter, which are press fit into the holder. (Sample disks of this size result in a cathode/anode area ratio of  $\sim 0.05$ , which is quite favorable in terms of the self-biasing phenomenon (44, 50).)

In the studies described here, the rf glow discharge plasma was powered by an RF Plasma Products (Marlton, NJ) Model RF-10 radio frequency generator. This unit has a maximum power

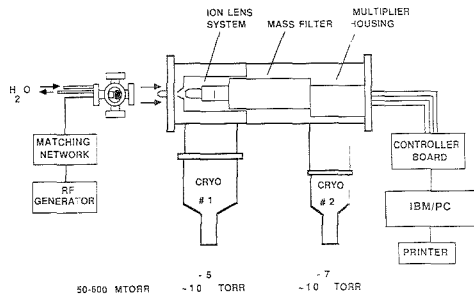


Figure 4. Rf glow discharge mass spectrometer system.

output of 1 kW at a frequency of 13.56 MHz. In this application, discharge powers of 5–50 W were found to be optimum for mass spectrometric signal intensity. In order to achieve efficient energy transfer to the plasma, an rf impedance matching network must be incorporated in series with the rf generator. Chapman (44) has discussed the rationale of using rf matching networks by analogy to the dc power theorem. Basically, the power dissipated in a load (plasma) is maximized when the resistance in the load is equal to that of the voltage source. In practice, the matching network is an LC circuit which is tuned such that the total impedance of the network and the plasma equals the output impedance of the rf generator. An RF Plasma Products AM-10 automatching network has been employed here. It cannot be emphasized too much that thorough electrical grounding must be achieved for proper impedance matching and to obtain proper mass spectrometer operation.

**Mass Spectrometer System.** A diagrammatic representation of the complete rf-GDMS system is shown in Figure 4. The ion source assembly is constructed from a standard six-way cross (MDC, Hayward, CA) equipped with 2.75 in. conflat-type flanges. The rf glow discharge ion source is mounted coaxial with the mass spectrometer axis. The remaining ports of the cross are utilized for the mounting of fused silica optical windows, vacuum and gas inlet attachments, and pressure monitoring thermocouples. The mass filter system assembled in this laboratory consists of Extrel (Pittsburgh, PA) C-50 components housed in a differentially pumped vacuum chamber. Two Leybold-Heraeus (Export, PA) cryopumps, rated at pumping speeds of 1150 and 640 L/s for argon, provide efficient pumping of the discharge gas and residual vapors without the possibility of contamination from pump oils. Ions exiting the source region pass through an intermediate vacuum region ( $10^{-6}$  Torr) and into the analyzer region ( $10^{-7}$  Torr) where they are collected by an ion lens system consisting of an immersion lens and a Bessel Box energy analyzer. Ions entering the high vacuum region are focused by the immersion lens into the Bessel Box, which is equipped with a neutral beam stop in its center. The energy analyzer serves to select (and normalize to some extent) a band-pass of ion kinetic energies which will be transmitted to the quadrupole. Employment of the Bessel Box is necessary to achieve proper resolution in the quadrupole mass filtering process. The neutral beam stop serves to impede the flight path of neutral atoms and fast ions down the quadrupole axis as well as to deflect photons exiting the ion source, each of which are sources of spectral noise. Tuning of the Bessel Box elements was performed to maximize the ion signal of the sputtered sample material while maintaining proper mass resolution and peak shapes. The Bessel Box may also be employed as a tool to map ion kinetic energies for plasma diagnostics.

The mass filter employs  $3/4$  in. diameter, 9 in. long quadrupole rods which are powered by a 200-W, 1.2-MHz generator. This combination of quadrupole dimensions and power supply is chosen for maximum ion transmission and resolution over the mass range required for elemental mass spectrometry (i.e.,  $\sim 1$ –250 amu). Resonant ions passing through the filter are detected by a conversion dynode-continuous dynode pair. The system allows for detection of both positive and negative ions in the analog mode, with ion counting also possible. The mass spectra displayed here are recorded in the analog mode on a laboratory X-Y recorder

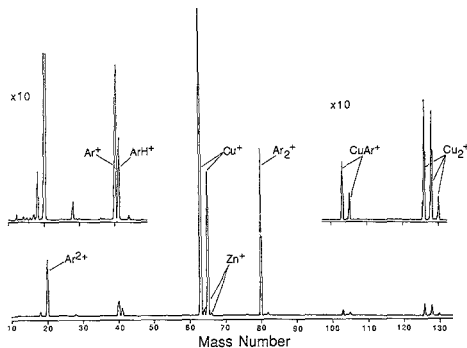


Figure 5. Rf glow discharge mass spectrum of a stock copper alloy (0.20 Torr, 10 W).

as single mass scans with typical sweep rates of 0.5 amu/s and time constants of 0.3 s.

## RESULTS AND DISCUSSION

**Plasma Operating Characteristics.** The preliminary evaluation of the operating parameters of the rf glow discharge ion source was performed employing a stock copper cathode. The copper metal matrix was chosen because of its ease of sputtering and prior experience in this laboratory with the dc glow discharge mass spectrometric characteristics of this material. Figure 5 is a rf-GDMS spectrum of the stock copper sample under discharge conditions of 0.2 Torr argon pressure and 10 W rf power. (It should be mentioned that in all of the work presented here, the reflected rf power is 1 W or less.) As can be seen, the spectrum is very similar to dc glow discharge spectra. The rf spectra are atomic in nature, with the spectrum dominated by ions of the matrix species and the various discharge gas species (e.g.,  $\text{Ar}^+$ ,  $\text{Ar}^{2+}$ ,  $\text{Ar}_2^+$ ). Of fundamental interest is the fact that the  $\text{Ar}^+$  ions have significantly different kinetic energies than the rest of the ions observed in the spectrum. Marcus et al. (58) observed a similar phenomena with the hollow cathode plume glow discharge ion source. The ion signal for the  $\text{Ar}^+$  maximizes at more negative Bessel Box ion energy settings implying that they are formed by a less energetic process than the other species (electron impact rather than a Penning-type collision). Optimization of the energy analyzer throughput for argon ions results in a  $^{40}\text{Ar}^+ / ^{63}\text{Cu}^+$  ratio of approximately 4 to 1.

Scale expansion of the spectrum reveals the existence of species related to residual gases due to nonideal vacuum conditions:  $\text{H}_2\text{O}^+$  at mass 18,  $\text{N}_2^+$  at 28, and  $\text{CO}_2^+$  at mass 44. Also observed are the isotopic distributions of ions of the form  $\text{CuAr}^+$  and  $\text{Cu}_2^+$ . These species are far more prevalent in the rf-GDMS spectra than in normal dc spectra. One would expect that the formation mechanism of these species is a gas-phase associative collision (46). The relative extent of molecular ions is surprising in light of the lower operating pressures of the rf source. In fact, the degree of dissociation,  $\text{Cu}^+ / \text{Cu}_2^+$  and  $\text{Cu}^+ / \text{CuAr}^+$ , increases with higher pressures (collision frequencies) with very little dependency on discharge power. King and co-workers (59) also found that molecular species, particularly dimers, tend to be reduced relative to analytes at increased pressure. The data presented here seem to indicate that once formed, molecular species are not likely to be dissociated. The point of origin of these species may well be the cathode dark space/negative glow interface, were the mass spectrometric ion sampling is performed. Ions formed in this active region may have a range of kinetic energies where atom/ion collision cross sections are maximized. Total collision cross sections of electrons in rare gases are

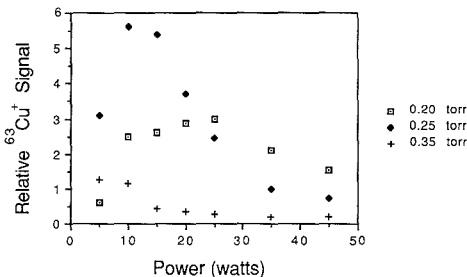


Figure 6. Effect of discharge power and pressure on  $^{63}\text{Cu}^+$  signal.

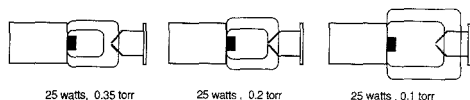


Figure 7. Illustration of the influence of discharge pressure and power on the cathode dark space/negative glow interface location.

known to have such energy maxima (60). Argon metastable species, which are also partners in associative ionization processes (46), may also be at a maximum in this region. Studies of the formation and dissociation of molecular ion species are currently under way.

Certainly, molecular species pose problems in performing elemental analysis. Their contribution may be decreased by sampling in other regions of the plasma or by judicious choice of discharge parameters. King and Harrison (61) have employed a triple quadrupole mass spectrometer to demonstrate that collision-induced dissociation (CID) is a viable option in the reduction of molecular isobaric interferences. A recent upgrade of this instrument to a simple double quadrupole geometry will permit investigations into the use of CID to remove these interferences.

A key point at this stage of the source's development is the fact that the raw ion currents of the matrix ion species reaching the detector are on the same order of magnitude ( $10^{-11}$  A) as those observed for the more thoroughly developed dc sources. Further source design optimization is expected to yield even higher rf signals relative to the dc sources.

**Parametric Evaluation.** The complex interdependence of the pressure/current/voltage conditions of the dc plasma sources makes parametric evaluations quite complex; however, the rf source is powered by a constant power generator, which makes evaluation somewhat more straightforward. Certainly, both the voltage and current change at fixed powers with different pressures, but these values are not directly accessible at this point. The response of the copper matrix ion signal, specifically  $^{63}\text{Cu}^+$ , to changes of discharge power is shown for a range of pressures in Figure 6. For each fixed-pressure data set an rf power is observed where a maximum amount of matrix ion signal is detected. It can be seen that as the discharge pressure increases, the point of the maximum signal shifts to lower power settings. Earlier work by Coburn et al. (37-40) did not mention such dramatic parametric dependencies with respect to the anode-cathode separation. This trend in responses seems to be related to the physical relationship between the plasma negative glow/dark space interface and the ion sampling orifice.

Figure 7 illustrates the effect of discharge pressure on the dark space thickness and the relationship between the interfacial region and the sampling cone. As discharge pressures decrease, electron mean free paths increase such that the cathode fall (potential drop) occurs over longer distances away from the cathode surface extending the interfacial region

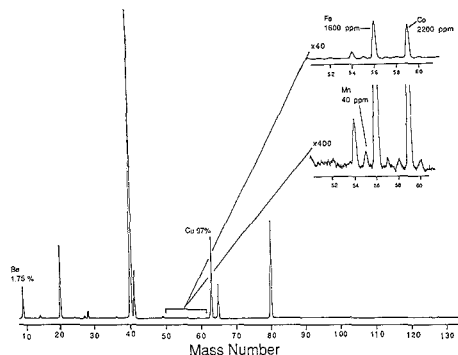


Figure 8. Rf glow discharge mass spectrum of NBS C1122 Cu-Be alloy (0.15 Torr, 20 W).

toward the exit orifice. Decreases in discharge power (voltage) produce analogous changes, though to a much lower degree. Visual observation of the plasma shows a correlation between the position of the negative glow/dark space interface and the matrix ion signal detected. The discharge conditions in which maximum signal is observed are those where the interfacial region is at the sampling cone orifice (as shown in the center portion of Figure 7). The reason for this spatial relationship would seem to be due to the fact that at this point secondary electrons emitted from the cathode surface will have lost sufficient energy to be effective in direct electron impact ionization collisions with sputtered atoms. In addition, one would also expect that this would be the region of highest argon metastable atom density. Coburn and co-workers (37) have shown that the ion signal of sputtered atoms in an rf glow discharge is proportional to the product of the sputtered atom density (copper in this case) and the discharge gas metastable atom density (argon). Studies of dc discharges by Hess and Harrison (62) have also shown the importance of metastable species in glow discharge ionization of metal atoms. Sampling from within the dark space is hindered by the fact that the cathode fall potential will tend to draw ions formed in that region back to the cathode surface. Lower ion signals further into the negative glow are likely due to lower metastable densities and an increasingly diffuse sputtered atomic population. Clearly, spatially resolved atomic absorption measurements to determine sputtered and metastable atom number densities would aid in defining these mechanisms. There is also a need to be able to vary the cathode-to-sampling cone distance to determine the optimum mass spectrometric sampling conditions.

**Exemplary Analytical Matrices.** While the previous discussion has illustrated that there is work to be done in terms of further refinements of the discharge source parameters and configuration, the possible scope of applicability of the source merits further study. We have investigated what might be thought of as a cross section of the possible bulk solid analytical matrices requiring elemental analyses. The matrices investigated were metal alloys, metal oxide powders, glass frit, and a vitrified glass. The latter two of these matrices were obtained from the Savannah River Plant in Aiken, SC, where they are part of studies involving the Defense Waste Processing Facility (DWPF) (63).

The application of the rf glow discharge ion source to the analysis of metal alloy (conducting) materials is demonstrated in Figure 8. The mass spectrum of the NBS SRM C1122 copper-beryllium alloy illustrates the simplicity of the rf-GDMS spectra. Clearly seen are the isotopic signals for the Cu and Be matrix species. The exaggerated response of the

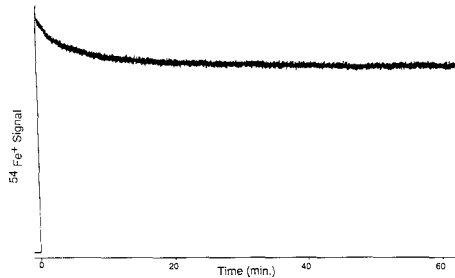


Figure 9. Temporal character of the  $^{54}\text{Fe}^+$  signal in NBS C1122 (0.15 Torr, 20 W).

beryllium signal is a function of the throughput characteristics of the quadrupole at these mass filter settings and possibly a high relative ion yield due to its low ionization potential. While the discharge source is far from achieving what we believe is optimum performance, the copper matrix ion current of  $\sim 7 \times 10^{-11}$  A is on the same order of magnitude as that produced in the more developed dc sources. An expansion of the intensity scale in the mass region between 50 and 61 amu reveals the presence of minor transition-metal constituents at the concentrations indicated in the inset. The relative sensitivity factors (RSF's) for the iron, cobalt, and manganese in the sample are quite similar to those observed in this and other laboratories (64) with dc glow discharge sources. The single scan detection of the Mn at 40 ppm in the sample, at these nonoptimal discharge conditions, is quite encouraging at this early stage of development.

The rf ion source operates quite stably over extended periods of time. Figure 9 is a single ion monitoring trace of the  $^{54}\text{Fe}$  (93 ppm) ion signal. After an initial 20-min plasma induction period, the measured ion signal varies by only  $\sim 3\%$  over the following 40-min time period. This type of temporal stability is important in quadrupole mass spectrometry which is a sequential analysis technique. On the basis of the observed temporal profile and associated noise, a 2 ppm detection limit of iron is estimated for the current system. Improvements in the source design, ion optics, and multiple scan averaging, which would be possible with microcomputer instrument control, would be expected to yield much lower values.

The major impetus for the development of the rf glow discharge source is the ability to analyze insulating materials directly, without matrix modification. In addition to their inability to conduct electrical current, analysis of these types of samples is complicated by the fact that the analytes are actually in molecular form (generally oxides). Therefore, the plasma must also act to dissociate these species for atomic spectroscopic analysis. The applications of ceramic and glass matrix materials are a rapidly expanding area in the material sciences. High-temperature, high-strength ceramics, such as silicon nitride based materials, are finding increased usage as fabrication materials. Another expanding field of application of ceramic materials is their implementation as electrooptic devices. In both of these applications, quantitative analyses are necessary to characterize the level of desired dopants and potential pollutant species (65, 66). The amorphous nature of glass matrices has led to the increased usage of these materials in a wide range of industries. One of the most important of these applications is the immobilization of high-level nuclear waste (63). The borosilicate glasses employed at the defense waste processing facility (DWPF) are being developed with the goal of safe storage of radioactive waste in geological environments for millions of years.

The first matrix type used to investigate the rf sputtering of nonconductors was a mixture of transition-metal oxides

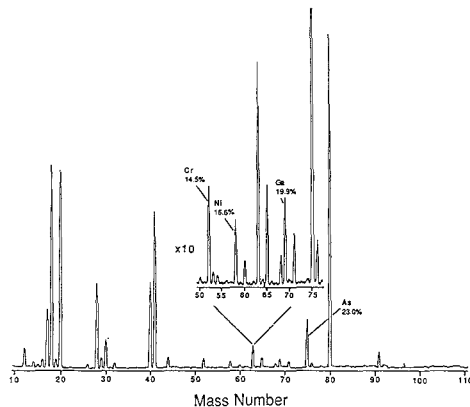


Figure 10. Rf glow discharge mass spectrum of a mixture of transition-metal (Cr, Ni, Ga, As) oxides (0.30 Torr, 25 W).

prepared from Spex (Edison, NJ) Hi-Pure powders pressed into the form of a disk, without binder. The sample disk was in turn mounted on a copper backing disk to achieve the proper sample positioning with respect to the sampling cone. The plasma produced while employing the oxide mixture as the cathode was quite stable. A mass spectrum obtained from the mixture of the chromium, nickel, gallium, and arsenic oxides is shown in Figure 10. As can be seen clearly in the  $\times 10$  scale expansion, these oxides seem to be efficiently sputtered, dissociated, and ionized in elemental form. (This is not to say that all oxides would be dissociated.) It is not clear at this point whether the dissociation occurs in the sputtering process or in the gas phase. Given the relative energetics of the two possibilities and the previously discussed low collision frequency, the former seems more plausible.

Some other important characteristics are displayed in the spectra obtained from this sample. Even though the sample itself is nonconducting, the measured ion currents for the metal ions are on the same order of magnitude as the brass alloy shown previously. This indicates that the oxygen (as oxides) in the sample simply represents an additional element in the matrix which will in fact be sputter atomized like the metal atoms. The spectrum shown also indicates, through the presence of water and related residual gases, that care should be taken to properly dry and degas the oxide powder samples prior to analysis. This is also evidenced by the  $\text{AsH}^+$  signal at mass 76. The spectrum shows little evidence of the formation of complex ions of the form  $\text{ArO}^+$  and  $\text{ArOH}^+$ , which would be present at masses 56 and 57, respectively. Such species tend to appear at these signal levels in dc glow discharge mass spectra. It may be that sputtered oxygen atoms, because of the low discharge pressure, do not form such species in the rf device. The ability to produce atomic ions from a sample of this type is indicative of the applicability of the rf-GDMS source to the analysis of ceramic and cement powders.

To investigate the ability of the rf glow discharge to sputter glass matrix samples, mass spectra were obtained from a glass frit precursor and a vitrified simulated defense waste glass. As in the case of the metal oxide powders, the frit sample was prepared by compacting it into disk form (again, without binder). Mass spectra of this sample indicate the efficient atomization of the glass components with both the major and minor frit components observed. Figure 11 is an rf glow discharge mass spectrum of the vitrified (solid) simulated DWPF glass. As was the case for the other nonconducting

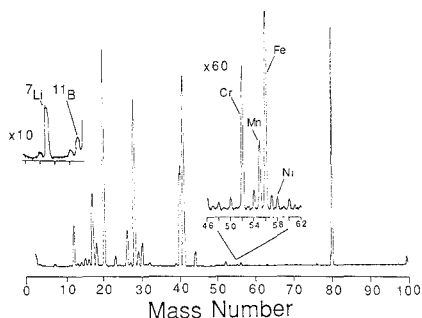


Figure 11. Rf glow discharge mass spectrum of vitrified simulated DWPF glass (0.15 Torr, 20 W).

matrices, the plasma was quite stable. Also consistent with the previous insulating species, the measured ion currents of the sputtered species are in the  $10^{-12}$ – $10^{-11}$  A range. The scale expansions in the figure display the signals observed for lithium and boron, basic matrix components, and the minor first-row transition metals.

One of the features of GDMS that make it particularly attractive for metal alloy analysis is the relative insensitivity of the elemental relative sensitivity factors (RSF's) (64) to the sample matrix identity. This methodology can be taken to an extreme by comparing RSF's between metallic and insulating materials. On the basis of the generated RSF's of iron and manganese in the C1122 copper-beryllium alloy, the concentration ratio between iron and manganese (Fe/Mn) in the glass sample is calculated to be 5.0. A listing of the starting materials for this glass (given in kilograms per component) indicates a Fe-to-Mn ratio of 4.2. While this represents only a single case, the possibility of employing elemental RSF's between vastly different matrices, for at least semiquantitative analyses, is encouraging.

## CONCLUSIONS

The design and operation of a radio frequency (13.56 MHz) powered glow discharge atomization/ionization source have been described. The source operates stably at rf powers up to  $\sim 50$  W at argon gas pressures of 0.05–1 Torr. The dependence of the sputtered atom ion signal on the power/pressure parameters seems to suggest a spatial component in either the actual ion population or the ion extraction. The mass spectra of metal samples, having sample matrix ion currents on the order of  $10^{-11}$  A, are quite similar to those produced by the more common dc powered devices. Analysis of aluminum-based alloys by both dc and rf glow discharge mass spectrometry indicates that the interelement relative sensitivity factors are quite comparable. Also of note is the fact that the rf source is more than 1 order of magnitude more sensitive than its dc counterpart for this matrix (67).

Exemplary mass spectra have been obtained for a mixture of metal oxides and a defense waste glass matrix. These spectra too are atomic in nature and have measured ion currents on the same order of magnitude as their metal counterparts. These preliminary data suggest that rf powered glow discharge ion sources have a great deal of potential for the analysis of a wide range of sample matrices, both conducting and insulating.

Future studies will involve the development of a direct insertion probe sample introduction system. This device will allow for rapid sample interchange and the performance of pressure/power/distance studies to determine optimum sampling conditions. It is believed that the ability to work at lower discharge pressures, and thus higher powers, will

prove to be beneficial in terms of analytical sensitivity and the desired depth profiling application. Once completed, methods of quantitation such as RSP's will be developed with a particular emphasis placed on the analysis of glass and ceramic materials.

#### ACKNOWLEDGMENT

The loan of the rf power supply and matching network from RF Plasma Products (Marlboro, NJ) is gratefully acknowledged as is financial and instrumentation support from Extrel Corporation. We also acknowledge Dr. J. C. Fanning of the Clemson University Chemistry Department for supplying the simulated defense waste glass.

#### LITERATURE CITED

- (1) Weiz, B. *Atomic Absorption Spectrometry*, 2nd. ed.; VCH Publishers: New York, 1986.
- (2) *Inductively Coupled Plasmas in Analytical Atomic Spectrometry*; Montaser, A., Golightly, D. W., Eds.; VCH Publishers: New York, 1987.
- (3) Nadkarni, R. *Anal. Chem.* **1984**, *56*, 2233-2237.
- (4) Ohls, K.; Sommer, D. *Fresenius' Z. Anal. Chem.* **1979**, *296*, 241-246.
- (5) Marks, J. Y.; Fornwalt, D. E.; Yungk, R. E. *Spectrochim. Acta, Part B* **1983**, *38*, 107-113.
- (6) Alvarado, J.; Cavalli, P.; Omenetto, N. *J. Anal. At. Spectrom.* **1987**, *2*, 357-363.
- (7) Park, C. J.; Van Loon, J. C.; Arrowsmith, P.; French, J. B. *Anal. Chem.* **1987**, *59*, 2191-2196.
- (8) Shao, Y.; Horlick, G. *Appl. Spectrosc.* **1986**, *40*, 386-393.
- (9) Boomer, D. W.; Powell, M.; Sing, R. L. A.; Salin, E. D. *Anal. Chem.* **1988**, *58*, 975-976.
- (10) Gui-Chen, S.; Sou-Lin, L. *J. Anal. At. Spectrom.* **1988**, *3*, 841-847.
- (11) Arrowsmith, P. *Anal. Chem.* **1987**, *59*, 1437-1444.
- (12) Cremers, D. A.; Romero, D. J. *Proc. SPIE—Int. Soc. Opt. Eng.* **1986**, *644*, 7-12.
- (13) Moenke-Blankenburg, L. *Prog. Anal. Spectrosc.* **1986**, *9*, 335-427.
- (14) Chen, G.; Yeung, E. S. *Anal. Chem.* **1988**, *60*, 2258-2263.
- (15) Arrowsmith, P.; Hughes, S. K. *Appl. Spectrosc.* **1988**, *42*, 1231-1239.
- (16) Hess, K. R.; Marcus, R. K. *Spectroscopy* **1987**, *2*(9), 24-31.
- (17) Ohls, K. *Z. Anal. Chem.* **1987**, *327*, 111-118.
- (18) Winchester, M. R.; Marcus, R. K. *Appl. Spectrosc.* **1988**, *42*, 941-944.
- (19) Wagatsuma, K.; Hirokawa, K. *Spectrochim. Acta, Part B* **1987**, *42*, 523-531.
- (20) *Improved Hollow Cathode Lamps for Atomic Spectroscopy*; Caroli, S., Ed.; John Wiley & Sons: New York, 1985.
- (21) Bentz, B. L.; Harrison, W. W. *Prog. Anal. At. Spectrosc.* **1988**, *11*, 53-110.
- (22) Jakubowski, N.; Stuewer, D.; Vieth, W. *Anal. Chem.* **1987**, *59*, 1825-1830.
- (23) Patel, B. M.; Winefordner, J. D. *Spectrochim. Acta, Part B* **1986**, *41*, 469-474.
- (24) Tong, W. G.; Chen, D. A. *Appl. Spectrosc.* **1987**, *41*, 586-590.
- (25) Marcus, R. K.; Harrison, W. W. *Anal. Chem.* **1987**, *59*, 2369-2373.
- (26) Brenner, I. B.; Laqua, K.; Dvorachek, M. *J. Anal. At. Spectrom.* **1987**, *2*, 623-627.
- (27) Tong, S. L.; Harrison, W. W. Presented at the 35th ASMS Conference on Mass Spectrometry and Allied Topics, Denver, CO, May 24-29, 1987.
- (28) Sugano, T. *Applications of Plasma Processing to VLSI Technology*; Wiley-Interscience: New York, 1985.
- (29) Morgan, R. A. *Plasma Etching in Semiconductor Fabrication*; Elsevier: Amsterdam, 1985.
- (30) Savage, R. N. *Spectroscopy* **1987**, *2*(8), 40-42.
- (31) Bolker, B. F. T. *Solid State Technol.* **1983**, *26*(Dec), 115-119.
- (32) Gottscho, R. A.; Miller, T. A. *Pure Appl. Chem.* **1984**, *56*, 189-208.
- (33) Coburn, J. W.; Chen, M. J. *Appl. Phys. Chem.* **1980**, *51*, 3134-3136.
- (34) Gottscho, R. A.; Mandich, M. L. *J. Vac. Sci. Technol. A* **1985**, *3*, 617-624.
- (35) Walkup, R. E.; Dreyfus, R. W.; Avouris, P. *Phys. Rev. Lett.* **1983**, *50*, 1846-1849.
- (36) Cox, T. I.; Deshmukh, V. G. I.; Hope, D. A. O.; Hydes, A. J.; Braithwaite, N. St. J.; Benjamin, N. M. P. *J. Phys. D* **1987**, *20*, 820-831.
- (37) Eckstein, E. W.; Coburn, J. W.; Kay, E. *Int. J. Mass Spectrom. Ion Phys.* **1975**, *17*, 129-138.
- (38) Coburn, J. W.; Kay, E. *Appl. Phys. Lett.* **1971**, *18*, 435-438.
- (39) Coburn, J. W.; Kay, E. *J. Chem. Phys.* **1976**, *64*, 907-908.
- (40) Coburn, J. W.; Eckstein, E. W.; Kay, E. *J. Appl. Phys.* **1975**, *46*, 2828-2830.
- (41) Pons-Corbeau, J.; Cazet, J. P.; Moreau, J. P.; Berneron, R.; Charbonnier, J. C. *Surf. Int. Anal.* **1986**, *9*, 21-25.
- (42) Donoue, D. L.; Harrison, W. W. *Anal. Chem.* **1975**, *47*, 1528-1531.
- (43) Geiger, J. F.; Lopnarski, M.; Oeschner, H.; Paulus, H. *Mikrochim. Acta (Wein)* **1987**, *1*, 497-506.
- (44) Walters, P. E.; Human, H. G. C. *Spectrochim. Acta, Part B* **1981**, *36*, 585-589.
- (45) Leis, F.; Broekert, J. A. C.; Laqua, K. *Spectrochim. Acta, Part B* **1987**, *42*, 1169-1176.
- (46) Chapman, B. N. *Glow Discharge Processes*; John Wiley & Sons: New York, 1980.
- (47) Weston, G. F. *Cold Cathode Discharge Tubes*; Iliff: London, 1968.
- (48) Anderson, G. S.; Mayer, W. N.; Wehner, G. K. *J. Appl. Phys.* **1962**, *33*, 2991-2992.
- (49) Koenig, H. R.; Maisel, L. I. *IBM J. Res. Dev.* **1970**, *14*, 168-171.
- (50) Coburn, J. W.; Kay, E. *J. Appl. Phys.* **1972**, *43*, 4965-4971.
- (51) Marcus, R. K. Ph.D. Dissertation, University of Virginia, Charlottesville, VA, 1986.
- (52) Ferreira, N. P.; Strauss, J. A.; Human, H. G. C. *Spectrochim. Acta, Part B* **1983**, *38B*, 899-911.
- (53) Brackett, J. M.; Mitchell, J. C.; Vickers, T. J. *Appl. Spectrosc.* **1984**, *38*, 136-140.
- (54) Borodin, V. S.; Kagan, Yu. M. *Sov. Phys.—Tech. Phys. (Engl. Transl.)* **1966**, *11*, 131-134.
- (55) Mehs, D. M.; Niemczyk, T. M. *Appl. Spectrosc.* **1978**, *32*, 269-272.
- (56) Mehs, D. M.; Niemczyk, T. M. *Appl. Spectrosc.* **1981**, *35*, 66-69.
- (57) Kumagi, H. Y. *J. Vac. Sci. Technol.* **1986**, *4A*, 1800-1804.
- (58) Marcus, R. K.; King, F. L.; Harrison, W. W. *Anal. Chem.* **1986**, *54*, 972-974.
- (59) King, F. L.; McCormack, A. L.; Harrison, W. W. *J. Anal. At. Spectrom.* **1988**, *3*, 883-886.
- (60) Massey, H. S. W.; Burhop, E. H. S. *Electronic and Ionic Impact Phenomena*; Oxford Press: London, 1969; Vol. 1.
- (61) King, F. L.; Harrison, W. W. *Int. J. Mass. Spectrom. Ion Process* **1989**, *89*, 171-185.
- (62) Hess, K. R.; Harrison, W. W. *Anal. Chem.* **1988**, *60*, 691-696.
- (63) *Scientific Basis for Nuclear Waste Management*; Jantzen, C. M., Stone, J. A., Ewing, R. C., Eds.; Materials Research Society Proceedings: Pittsburgh, PA 1985.
- (64) Sanderson, N.; Hall, E.; Clark, J.; Charalambous, P.; Hall, D. *Mikrochim. Acta* **1987**, *1*, 275-290.
- (65) Pašto, A. E. *MRS Bull.* **1987**, *12*(7), 73-78.
- (66) Klein, M. B.; Schwartz, R. N. *J. Opt. Soc. Am. B* **1986**, *3*, 293-305.
- (67) Marcus, R. K.; Duckworth, D. C. Presented at the 1989 Pittsburgh Conference and Exposition, March 6-10, 1989, Atlanta, GA.

RECEIVED for review February 8, 1989. Accepted June 1, 1989.



# Determination of the Concentration and Stable Isotopic Composition of Oxygen in Organic Matter Containing Carbon, Hydrogen, Oxygen, Nitrogen, and Sulfur

Michael J. DeNiro\*<sup>1,2</sup> and Samuel Epstein

Division of Geological and Planetary Sciences, California Institute of Technology, Pasadena, California 91125

**A method for the quantitative production of carbon dioxide from oxygen in organic matter consisting of carbon, hydrogen, oxygen, nitrogen, and sulfur has been developed. Manometric and mass spectrometric analysis of the CO<sub>2</sub> permit direct determination of the concentration and isotopic composition of oxygen in CHONS compounds with accuracy comparable to that previously achievable for CHO and CHON compounds. Samples containing as little as 187 μmol of oxygen with S/O ratios as high as 0.16 have been analyzed by using this method.**

## INTRODUCTION

Stable isotope ratios of modern, historic, and fossil organic matter record biological and environmental information of potential interest to a variety of researchers (e.g., ref 1-3). Extraction of this information requires the use of analytical procedures that permit quantitative conversion of an element in an organic sample to a gas, which can then be analyzed mass spectrometrically. Almost all of the published work utilizing oxygen isotope ratios in this manner has involved organic matter consisting of carbon, hydrogen, and oxygen, such as sucrose or cellulose (e.g., ref 4-6). Two reports of <sup>18</sup>O/<sup>16</sup>O ratios of a CHON compound, glucosamine, isolated from arthropod exoskeletons, have appeared (7, 8). However, the bulk of naturally occurring organic matter, both modern and fossil, consists of carbon, hydrogen, oxygen, nitrogen, and sulfur. Such compounds have not been subjected to oxygen isotopic analysis because the available techniques for determining <sup>18</sup>O/<sup>16</sup>O ratios in organic matter do not work when sulfur is present. Santrock and Hayes (9) have reported a procedure for determining <sup>18</sup>O/<sup>16</sup>O ratios in CHONS compounds, but, as discussed below, this procedure requires the use of special equipment and the application of a number of correction factors. In this paper we report a method that permits quantitative conversion of oxygen in CHONS compounds to CO<sub>2</sub>, which can then be analyzed manometrically and mass spectrometrically to determine both the concentration and <sup>18</sup>O/<sup>16</sup>O ratio of the oxygen.

We review briefly below the analytical procedures that have been used to determine <sup>18</sup>O/<sup>16</sup>O ratios in organic matter.

Three methods for high precision (±0.5%) measurements of δ<sup>18</sup>O values (see Experimental Section for definition of δ<sup>18</sup>O values) in organic matter consisting of C, H, and O have been developed. The first (10), which involved pyrolysis of carbohydrates (CHO compounds), in the presence of diamonds, has not been used since its introduction, to our knowledge. Epstein et al. (5) introduced two other methods that have been widely used to measure δ<sup>18</sup>O values of cellulose, a CHO compound. One involved pyrolysis of the sample at 1100 °C in a nickel reaction vessel, through which all of the H in the

sample diffused into the atmosphere. The products that remained in the reaction vessel were CO<sub>2</sub> and CO. After spark discharge was used to disproportionate the CO to CO<sub>2</sub> plus C, all of the O in the cellulose had been converted to CO<sub>2</sub>, which was analyzed mass spectrometrically. The other method used by Epstein et al. (5) involved pyrolysis of cellulose in the presence of HgCl<sub>2</sub>, at 550 °C in Vycor tubes, a modification of a procedure introduced by Rittenberg and Ponticorvo (11) to measure <sup>18</sup>O contents of isotopically spiked samples. The products of the pyrolysis reaction were CO<sub>2</sub>, CO, and HCl. After the HCl was removed by reaction with benzoquinoline to form benzoquinoline hydrochloride, the CO and CO<sub>2</sub> were processed as for the Ni tube pyrolysis method prior to mass spectrometric analysis.

In 1985, Schimmelmann and DeNiro (12) published a paper in which the HgCl<sub>2</sub> pyrolysis technique was modified to allow for <sup>18</sup>O/<sup>16</sup>O ratio determinations of glucosamine, a CHON compound. The products of the pyrolysis reaction were CO<sub>2</sub>, CO, N<sub>2</sub>, and HCl. After HCl was removed with benzoquinoline (as above), the CO<sub>2</sub>, CO, and N<sub>2</sub> were sealed into a Vycor tube containing finely dispersed Ni powder. The tube was heated to 275 °C, causing the CO to disproportionate to CO<sub>2</sub> and C. The N<sub>2</sub> did not react. The CO<sub>2</sub> in the tube, which now contained all the O from the glucosamine, was separated cryogenically from the N<sub>2</sub> prior to mass spectrometric determination of the δ<sup>18</sup>O value.

The HgCl<sub>2</sub> technique introduced by Epstein et al. (5) for analysis of CHO compounds does not work for organic compounds that contain S. Milburn and DeNiro (13) demonstrated that pyrolysis of methionine, a CHONS compound, in the presence of HgCl<sub>2</sub> produced substantial amounts of CS<sub>2</sub>, COS, and SO<sub>2</sub>, along with CO<sub>2</sub>, CO, and N<sub>2</sub>. The presence of oxygen in two sulfur-containing gases would render oxygen isotope ratios based on analysis of oxygen in CO and CO<sub>2</sub>, done as discussed above, artifactual even if the CO and CO<sub>2</sub> were separated from the COS and SO<sub>2</sub> prior to the isotopic analysis.

Santrock and Hayes (9) showed that a modified version of the Unterzaucher procedure can be used for determining δ<sup>18</sup>O values in organic matter. Organic matter is pyrolyzed, the pyrolysis products are equilibrated with elemental C at 1060 °C to produce CO, and the CO is oxidized with I<sub>2</sub>O<sub>5</sub> to produce CO<sub>2</sub>, which is analyzed in the mass spectrometer. Corrections must be made for contributions of oxygen to the final CO<sub>2</sub> from an oxygen blank, oxygen from previous samples, and oxygen from I<sub>2</sub>O<sub>5</sub> (since half the oxygen in CO<sub>2</sub> produced from CO comes from the iodine pentoxide). Evaluation and monitoring of the correction factors require analysis of multiple standards in parallel with the samples. Moreover, achievement of reproducible results practically requires the use of automated equipment. If hundreds of samples are to be processed at a rate of 20 per day or more, the method has advantages of speed and convenience. Otherwise, a procedure requiring lower investments in calibration and equipment may be favored.

We report here a method that permits quantitative conversion of O in CHONS compounds to CO<sub>2</sub>, which can then be analyzed mass spectrometrically. We found that pyrolysis

<sup>1</sup> Also Department of Earth and Space Sciences and Institute of Geophysics and Planetary Physics, University of California, Los Angeles, CA 90024.

<sup>2</sup> Current address: Department of Earth Sciences, University of California, Santa Barbara, CA 93106.

of CHONS compounds in nickel reactions vessels, as was done for CHO compounds by Epstein et al. (5), converts all the oxygen in the sample to CO<sub>2</sub> and CO. The other gaseous product of this reaction is N<sub>2</sub>. Apparently the S in the sample reacts with the nickel pyrolysis vessel to form nickel sulfide, while the H in the sample diffuses out through the nickel reaction vessel into the atmosphere. CO<sub>2</sub> was separated from CO and N<sub>2</sub> by cryogenic condensation. Since CO cannot be quantitatively disproportionated to CO<sub>2</sub> and C by spark discharge in the presence of N<sub>2</sub> because NO<sub>2</sub> forms as well (14), we used a nickel catalyst described by Clayton and Epstein (15) to accomplish the disproportionation. N<sub>2</sub> does not react in this system. Analysis of a CHONS compound and of a CHO compound doped with a CHNS compound indicates that the precision and accuracy of the δ<sup>18</sup>O values determined with the method presented here are as good as that determined for CHO and CHON compounds with previously available techniques.

### EXPERIMENTAL SECTION

Glucose, cysteine, and thioguanine were purchased from Sigma. Nickel oxide was purchased from Baker.

Organic samples (cysteine, glucose, or glucose and thioguanine mixtures) were pyrolyzed according to the technique introduced by Epstein et al. (5), which is described in detail in ref 16. Briefly, the sample was weighed in a platinum boat, which was then inserted into a reaction vessel made of nickel 200, which was closed at one end and had an internal volume of ~20 cm<sup>3</sup>. After the vessel was evacuated, it was heated at 100 °C for 6 h while being pumped. A piston was then lowered in vacuo, crushing a gold gasket and sealing off the interior of the nickel reaction vessel from the vacuum system. The vessel was heated at 1100 °C for 3 h and then allowed to cool to 350 °C over 2 h. With the vessel then maintained at 350 °C, the piston was raised, breaking the gold gasket seal and allowing the gaseous pyrolysis products to pass into the vacuum system. The gases were passed through a trap cooled with liquid nitrogen, in which CO<sub>2</sub> condensed out. If the sample did not contain N (for glucose, a CHO compound), the noncondensable gas (CO) was admitted to a high-voltage discharge chamber (10), in which CO was quantitatively disproportionated to CO<sub>2</sub> and C. The discharge chamber was cooled with liquid nitrogen, which caused the CO<sub>2</sub> to condense out as it formed. If the sample contained N (for cysteine or for glucose doped with thioguanine), the noncondensable gases (CO and N<sub>2</sub>) were collected with a Toepfer pump and then circulated through a tube made of nickel 200 maintained at 400 °C containing finely divided nickel powder (which was prepared by passing hydrogen through nickel oxide powder at 450 °C as described in ref 15) and through a liquid nitrogen cooled trap until disproportionation of CO to CO<sub>2</sub> and C was complete (20 min or less for all samples reported here). The noncondensable gas (N<sub>2</sub>) that remained after the disproportionation was pumped away. The two CO<sub>2</sub> aliquots (that formed directly during pyrolysis and that formed during the disproportionation of CO) were combined. The amount of CO<sub>2</sub> was determined manometrically, after which the CO<sub>2</sub> was analyzed mass spectrometrically.

Isotopic compositions are given in the δ notation relative to the V-SMOW standard (Vienna Standard Mean Ocean Water) as

$$\delta^{18}\text{O} = \left[ \frac{(^{18}\text{O}/^{16}\text{O})_{\text{sample}}}{(^{18}\text{O}/^{16}\text{O})_{\text{V-SMOW}}} - 1 \right] \times 10^3\text{‰}$$

### RESULTS AND DISCUSSION

Mass spectral scans indicated no or negligible amounts of S-containing gases (COS, CS<sub>2</sub>, SO<sub>2</sub>) present in the CO<sub>2</sub> samples generated from CHONS compounds or mixtures. In the worst case, the largest peak at a mass for any of these three gases was <3 mV, compared to a 9-V signal at mass 46 for <sup>12</sup>C<sup>18</sup>O<sup>16</sup>O.

The concentrations and isotopic compositions of oxygen determined for cysteine (a CHONS compound), glucose (a CHO compound), and mixtures of glucose and thioguanine (a CHNS compound) are given in Table I. The concentration

**Table I. Oxygen Concentrations and Isotopic Compositions for Pure and Composite Substrates**

		% theoretical concn	δ <sup>18</sup> O <sub>SMOW</sub> , ‰
cysteine, mg			
23.5		97.2	+17.7
26.8		96.0	+17.7
19.8		99.6	+17.7
27.2		98.6	+17.7
22.2		99.0	+17.8
21.0		95.7	+17.8
24.1		98.0	+17.5
22.6		98.1	+17.9
		97.8 ± 1.4	+17.7 ± 0.1
glucose, mg			
12.2		96.7	+26.1
13.2		96.6	+26.3
14.1		96.9	+25.9
12.9		96.4	+26.9
12.5		100.7	+26.3
17.1		99.5	+26.0
13.1		102.4	+25.8
		98.5 ± 2.4	+26.2 ± 0.4
glucose, mg		thioguanine, mg	
13.2	2.6	96.2	+26.7
11.1	5.6	96.0	+26.4
12.6	3.6	99.4	+25.4
10.2	4.3	98.2	+26.1
8.6	3.0	94.2	+26.8
9.2	5.8	97.3	+26.4
12.7	6.7	101.4	+26.9
11.6	4.4	95.2	+26.7
5.6	5.0	109.5	+26.0
11.2	0.7	98.9	+25.9
		98.6 ± 4.4	+26.3 ± 0.5

data indicate that O in CHONS compounds or mixtures is quantitatively converted to CO<sub>2</sub> by the procedures described above. The ranges and standard deviations of the δ<sup>18</sup>O values obtained for CHONS compounds or mixtures are similar to those obtained for CHO compounds here and elsewhere (4–6, 10), indicating the precision of the method presented here is comparable to that used for CHO compounds. Finally, there is no significant difference between the mean δ<sup>18</sup>O values obtained for glucose and for glucose doped with thioguanine (Mann-Whitney test at *P* = 0.05 level), indicating that δ<sup>18</sup>O values determined for CHONS compounds or mixtures with the method described herein are as accurate as those determined for CHO compounds using previously described methods (5, 10).

We note that another method for disproportionating CO to CO<sub>2</sub> has been presented (12) and see no reason why it could not be employed instead of the method we used in the work reported here for that purpose.

We have not run samples smaller than those discussed in this report. We expect, however, that it will be possible to use the method presented herein to determine oxygen concentration and isotopic composition in samples containing 1 to 2 orders of magnitude less oxygen (say down to a few micromoles) than the samples we analyzed. Minimum sample size will be dictated not by the limitations of manometric and mass spectrometric analyses of the CO<sub>2</sub> produced from small samples but rather by the background contribution of CO<sub>2</sub> coming from the vacuum system.

### ACKNOWLEDGMENT

We thank Joop Goris and Dave Winter for performing the mass spectrometric analyses and Lee Cooper for providing statistical assistance.

## LITERATURE CITED

- (1) Epstein, S.; Yapp, C. J.; Hall, J. H. *Earth Planet. Sci. Lett.* **1976**, *30*, 241-251.
- (2) Brenninkmeijer, C. A. M.; Geel, B.; Mook, W. G. *Earth Planet. Sci. Lett.* **1982**, *61*, 283-290.
- (3) Wedeking, K. W.; Hayes, J. M. *Isot. Geosci.* **1983**, *1*, 357-370.
- (4) Doner, L. W.; Aje, H. O.; Sternberg, L. da S. L.; Milburn, J. M.; DeNiro, M. J.; Hicks, K. B. *J. Agric. Food Chem.* **1987**, *35*, 610-612.
- (5) Epstein, S.; Thompson, P.; Yapp, C. *J. Science* **1977**, *198*, 1207-1215.
- (6) Sternberg, L. S.; DeNiro, M. J. *Science* **1983**, *220*, 947-949.
- (7) Schimmelmann, A.; DeNiro, M. J. *Geochim. Cosmochim. Acta* **1986**, *50*, 1485-1496.
- (8) Schimmelmann, A.; DeNiro, M. J.; Poulicek, M.; Voss-Foucart, M.-F.; Goffinet, G.; Jeuniaux, Ch. *J. Archaeol. Sci.* **1986**, *13*, 553-566.
- (9) Santrock, J.; Hayes, J. M. *Anal. Chem.* **1987**, *59*, 119-127.
- (10) Hardcastle, K. G.; Friedman, I. *Geophys. Res. Lett.* **1974**, *1*, 165-167.
- (11) Rittenberg, D.; Ponticorvo, L. *Int. J. Appl. Radiat. Isot.* **1956**, *208-214*.
- (12) Schimmelmann, A.; DeNiro, M. J. *Anal. Chem.* **1985**, *57*, 2644-2646.
- (13) Milburn, J. M.; DeNiro, M. J., unpublished work, University of California, Los Angeles, 1985.
- (14) Mook, W. G.; Grootes, P. M. *Int. J. Mass Spectrom. Ion Phys.* **1973**, *12*, 273-298.
- (15) Clayton, R. N.; Epstein, S. *J. Geol.* **1958**, *66*, 352-373.
- (16) Thompson, P.; Gray, J. *Int. J. Appl. Radiat. Isot.* **1977**, *28*, 411-415.

RECEIVED for review February 21, 1989. Accepted May 24, 1989. This work was supported by National Science Foundation Grants EAR 85-04096, BNS 84-18280, and DMB 84-05003. This is contribution number 4706 from the Division of Geological and Planetary Sciences at Caltech.

## Isomer Discrimination of Disubstituted Benzene Derivatives through Gas-Phase Iron(I) Ion Reactions in a Fourier Transform Mass Spectrometer

Asgeir Bjarnason<sup>1</sup> and James W. Taylor\*

Department of Chemistry, University of Wisconsin—Madison, Madison, Wisconsin 53706

James A. Kinsinger,<sup>2</sup> Robert B. Cody, and David A. Weil

Nicolet Analytical Instruments, Madison, Wisconsin 53711

Gas-phase reactions of  $\text{Fe}^+$  with the isomers of several disubstituted benzene derivatives were studied in a Fourier transform mass spectrometer. The electron impact mass spectra of these compounds are generally too similar for routine isomer identification. The iron ion complexes and their fragments produce spectra that reveal isomer differentiation. The method presented here fundamentally relies on the ability of  $\text{Fe}^+$  to form a bridge between the two substituents. Where such a bridging reaction is observed, an ion unique to that isomer is produced and identifies the isomer. In all the cases studied but one (xylene), the ortho isomer can easily be identified, and in some cases all three isomers can be differentiated with this method. Pressure variations within the normal operating range of the mass spectrometer were found not to interfere with the isomer identification.

### INTRODUCTION

Gas-phase reactions of metal ions with neutral molecules, most commonly small organic compounds, have received considerable interest in recent years. The study of these reactions became particularly feasible and appealing with the advent of Fourier transform mass spectrometers. Freiser and co-workers (1-8) produced metal ions by focusing a laser beam onto a piece of the metal in the Fourier transform mass spectrometer, and this method has been used by other workers although alternative methods for metal ion generation exist,

such as electron impact on volatile metal carbonyls and heating metal salts (9, 10). As pointed out by Freiser (3), the laser ionization has several advantages over other methods for Fourier transform mass spectrometry (FT-MS). The method is convenient and "clean", and because FT-MS is inherently a pulsed technique, the use of a pulsed ionization source is straightforward. Many of the volatile carbonyls are poisonous and the neutral carbonyl may be highly reactive with the sample and/or the ions present and may thus complicate analysis. A drawback to laser ionization is that it produces metal ions with an unknown distribution of electronic states such that an unknown, and possibly significant, fraction of the ions may be in excited states.

A few researchers have commented on the selectivity of metal ions as chemical ionization agents (3-9, 11). Limited effort appears to have been made to demonstrate or harness the analytical potential of these types of reactions with the exception of the elegant work by Gross and co-workers (9), who found that  $\text{Fe}^+$  could be used to locate double bonds in olefins, and the work of Forbes et al. (7, 8) on pattern recognition methods for metal ion chemical ionization mass spectra.

The study reported here is an effort to explore the method of  $\text{Fe}^+$  chemical ionization in the gas phase for the analytical purpose of distinguishing between isomers of disubstituted benzene derivatives. The criteria for their selection in this preliminary study were that (a) the electron impact (EI) spectra of the isomers were too similar for routine discrimination and (b) the compounds were volatile. (Methods for analyzing isomers of solid samples are under investigation now.)

The EI spectra of the chosen compounds show the same ions for all three isomers. Occasionally, some intensity var-

<sup>1</sup> Present address: Science Institute, University of Iceland, Dunhaga 3, IS-107 Reykjavik, Iceland.

<sup>2</sup> Present address: Industrial Laboratories, Denver, CO.

iations may be shown between the isomers in library spectra, but these intensity variations can be instrument dependent and are generally not well suited for routine isomer discrimination. Relying on small variations in peak intensities for isomer identification is difficult when using hyphenated techniques, such as gas chromatography/mass spectrometry, due to impurities that may be present from previous eluents. The method presented here usually relies on an abundance of a characteristic ion which is present in the spectrum of one isomer but shows very low intensity or is absent in the spectra of the other isomers.

### EXPERIMENTAL SECTION

All measurements were done by use of a Nicolet FTMS-2000 Fourier transform mass spectrometer with a 3.0-T superconducting magnet and equipped with a Nicolet laser desorption interface. The laser was a Tachisto Model 215 CO<sub>2</sub> laser operating as an aperture-controlled stable resonator. Maximum output energy for this arrangement is on the order of 1 J in a 40 ns wide (fwhm) pulse. Typical output energy used in these experiments was estimated to be ca. 0.01–0.05 J/pulse. Metal ions were made by focusing the laser pulses onto the stainless steel tip of the direct insertion probe.

As pointed out by Jacobson et al. (5), it is good practice to isolate the laser-produced iron ions by ejecting all other ions prior to monitoring the reactions in order to eliminate effects of other, uncharacterized species which are produced by the interaction of the laser pulse with the metal target. It is clear that an abundance of electrons of unknown energies is produced, and they may ionize neutral species present in the FT-MS cell and thereby interfere with the analysis. It was found that although negative ions are abundantly produced for most species containing highly electronegative atoms, positive ions were not produced by these laser-generated electrons except in the case of compounds containing iodine (e.g. iodobenzene). Nevertheless, a triple resonance experimental sequence was used that ejected all ions except iron prior to the variable delay (reaction time). This sequence also eliminated the other metal ions from the stainless steel target (mostly Cr, Mn, and Ni) and made the analysis of the spectra more straightforward. The triple resonance experimental sequence is part of the standard software provided by Nicolet, but briefly, the sequence of events in the experiment is as follows. Following the generation of the metal ions by the laser pulse, Fe<sup>+</sup> is isolated by employing two ejection events that eject all other ions from the cell. The iron ions are stored in the cell during a programmable delay event and react with the sample. The ions generated in the primary reactions of Fe<sup>+</sup> with the sample react again with the neutral sample molecules and the product ions of these secondary reactions react again and so on. A particular ion may be isolated by using another set of ejection pulses after an appropriate reaction time when its intensity is relatively high. The reactions of this ion with the neutral sample molecules can then be monitored by using a second variable delay event as a reaction time. Reaction paths can be elucidated in this manner, and exact mass measurements aid in the identification of each ion. The mass measurement accuracy achieved was on the order of 10 ppm.

The pressure of the reagent gas was generally  $\sim 3 \times 10^{-7}$  Torr but was varied for a few test compounds from  $3 \times 10^{-8}$  to  $1 \times 10^{-6}$  Torr. The identification process described below could be employed over the entire pressure range. Reaction time was varied from 0.003 to 25.6 s. Normally, ten transients were collected and averaged to minimize effects of laser power fluctuations.

The effect of the laser power output was of interest, especially on the relative intensity of the ions produced in the ion–molecule reactions. Varying the laser power resulted in only very slight changes in the relative intensity of the observed ions, except for M<sup>+</sup> (the molecular ion), whose intensity increased with increased laser power. This, presumably is because of increased charge transfer reactions. At higher laser power the average kinetic energy of the iron ions produced is increased. This was supported by examining the total intensity of Fe<sup>+</sup> at different trapping voltages as the laser power was increased. Larger trapping potentials were required to trap the majority of iron ions produced as the laser power was increased. These observations are in agreement with the results of Kang and Beauchamp (12) who studied the rela-

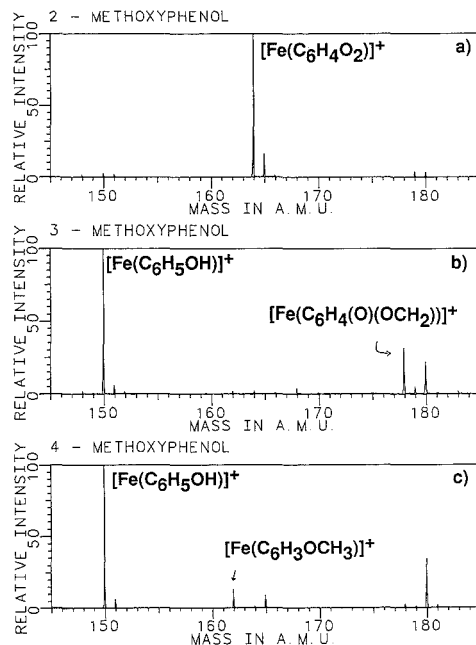


**Figure 1.** Mass spectra obtained after reactions of Fe<sup>+</sup> with the (a) ortho, (b) meta, and (c) para isomers of methoxyphenol for 0.4 s. Pressure of the neutral methoxyphenol gas in the cell was  $8 \times 10^{-8}$  Torr in each case.

tionship between laser power and kinetic energy of laser-generated metal ions. It was observed in our study that the molecular ion was produced not only in charge transfer reactions with kinetically excited Fe<sup>+</sup> but also, to some extent, through charge transfer reactions with some of the product ions from the Fe<sup>+</sup> reactions with the sample—presumably those produced in collisions with iron ions of higher kinetic energies. The use of relatively low laser energy in this study and low trapping voltages minimized effects of excess kinetic energy.

The internal energy distribution of the laser desorbed iron ions was of concern. The reactions of a few samples were analyzed while maintaining a pressure of nitrogen collision gas at 10 times the pressure of the reagent gas with both present in the cell during the reaction period. No significant differences were observed between the mass spectra obtained with or without the nitrogen gas present. This suggests either that a very small fraction of the iron ions are in excited states or that the reactions of Fe<sup>+</sup> in the different excited states are identical with those in the ground state.

The compounds investigated in this study were the isomers of xylene, methoxyphenol (Figure 1), fluoroacetophenone (Figure 2), fluoroanisole (Figure 3), and methylanisole. All reagents were commercially obtained and used without further purification except for a few freeze–pump–thaw cycles to remove dissolved gases.

### RESULTS AND DISCUSSION

The spectra obtained for the reactions of Fe<sup>+</sup> with disubstituted benzene derivatives reveal that for analytical purposes these reactions can be separated into three classes. The first class exhibits complex reactions, and identification of each isomer can be readily accomplished. The second class exhibits very similar reactions of the meta and para isomers which are too similar for routine discrimination. The ortho isomer, however, can be easily distinguished from the other two, as its reactions are vastly different. The third class, which only

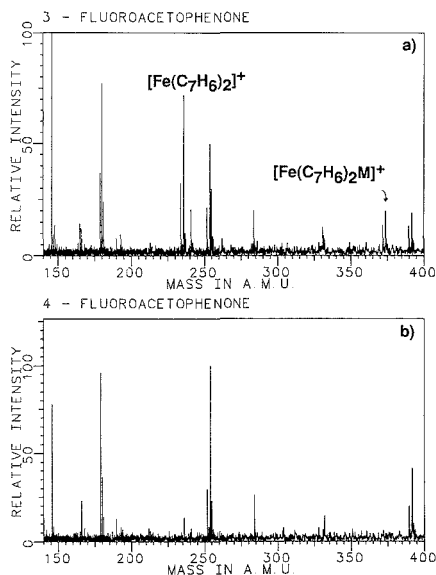


Figure 2. Mass spectra obtained after reactions (following the isolation) of the ionic species at  $m/z$  146 with the (a) meta and (b) para isomers of fluoroacetophenone for 1.0 s (see text).

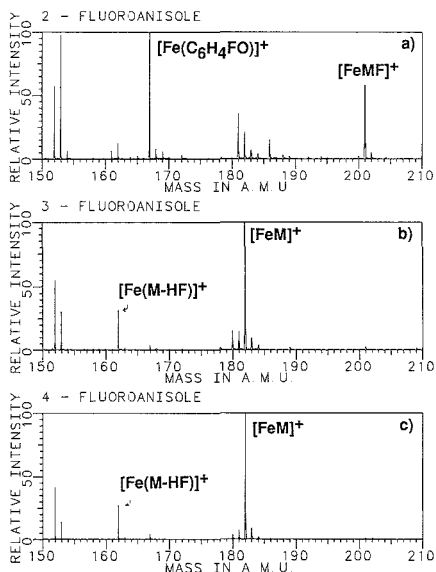


Figure 3. Mass spectra obtained after the reactions of  $\text{Fe}^+$  with the (a) ortho, (b) meta, and (c) para isomers of fluoroanisole for 0.4 s. Pressure of the neutral fluoroanisole gas in the cell was  $3 \times 10^{-7}$  Torr in each case.

xylene is representative of those compounds studied, showed very simple reactions and very similar reaction rates for all three isomers so that none of the isomers could be identified. It appears that electronegative substituents and, in particular, those containing oxygen facilitate the greatest variety in reactions with  $\text{Fe}^+$ . Further, the primary reactions of  $\text{Fe}^+$  with

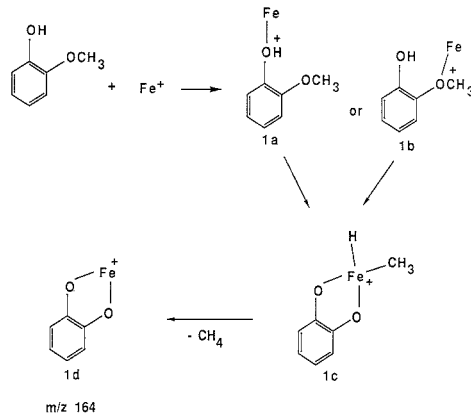


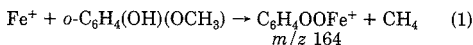
Figure 4. A proposed reaction mechanism for the reaction of  $\text{Fe}^+$  with *o*-methoxyphenol.

the sample usually differentiate immediately between the ortho isomer and the other two. In those cases where differentiation of the meta and para isomers is possible, the differences sometimes appear in the primary reactions in some cases in secondary or higher order reactions.

In the discussion below, we present several speculative reaction mechanism schemes in an attempt to explain *why* isomer differentiation is achieved with this technique. It should be emphasized that the reaction schemes are not directly supported by experimental results, but they are believed to be reasonable in view of the reaction products and the fact that isomer specificity is observed.

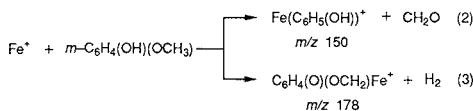
**Methoxyphenol.** It should be noted that library EI mass spectra for the isomers of methoxyphenol vary from one source to another and identification should not be attempted without obtaining mass spectra for the pure compounds first. According to the Wiley/NBS Mass Spectral Database (3rd ed.) the EI mass spectrum of the ortho isomer of methoxyphenol can be used for identification due to the high abundance of the ionic species at  $m/z$  109. The meta and the para EI spectra are too similar for routine identification.

All three isomers of methoxyphenol could be differentiated through primary  $\text{Fe}^+$  reactions. The main reaction for the ortho isomer proceeds according to



A possible mechanism for this reaction is presented in Figure 4.  $\text{Fe}^+$  attaches to either oxygen and the proximity of the second oxygen atom results in bridge forming with elimination of methane.

The meta isomer shows two dominant primary reactions (eq 2 and 3). Mechanisms for these reactions are presented



in Figure 5. Reaction 2 is analogous to the main reaction of  $\text{Fe}^+$  with anisole (13). After attachment to the oxygen of the methoxy group, the  $\text{Fe}^+$  can insert into the bonds on either side of the oxygen. If it inserts on the phenyl side, elimination of formaldehyde ( $\text{CH}_2\text{O}$ ) follows and the ion labeled 2c is formed. After attachment to the oxygen of the hydroxyl group, the bridge to the carbon of the methoxy group can form with

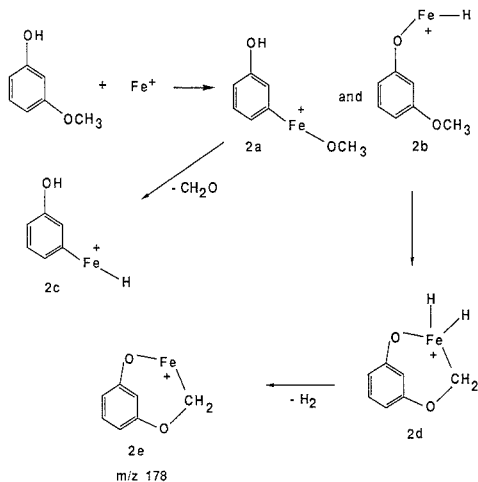
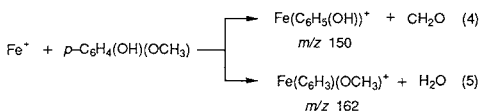


**Figure 5.** A proposed reaction mechanism for the reaction of  $\text{Fe}^+$  with *m*-methoxyphenol.

the elimination of hydrogen ( $\text{H}_2$ ) forming the ion labeled 2e.

The reactions of  $\text{Fe}^+$  with the para isomer yield mainly two reaction products of interest, according to reactions 4 and 5.



A suggested mechanism for reaction 5 is presented in Figure 6. The elimination of water is one of the main reactions of  $\text{Fe}^+$  with phenol (13) and is only observed here for the para isomer. The elimination of formaldehyde, which is analogous to the reaction of  $\text{Fe}^+$  with anisole, is the other main reaction here, as was the case with the meta isomer. This is in accordance with the expected behavior. Greater distance between the two functional groups reduces the possibility of  $\text{Fe}^+$  interacting with both at the same time. This means that the reactions of the para isomer would be expected to most resemble the reactions of the monosubstituted derivatives. The ortho isomer is the other extreme. The proximity of the two functional groups gives rise to an entirely different behavior, because of the possibility of  $\text{Fe}^+$  forming a bridge between the two groups. None of the major reactions of the monosubstituted species are observed for the ortho isomer. The meta isomer reactions are in-between the other two. The elimination of formaldehyde is observed as in the case of anisole, but none of the reactions analogous to those of phenol are observed. A reaction path involving bridging between the two functional groups is observed, unique to the meta isomer.

To summarize, the ortho isomer reacts to form the ion at  $m/z$  164 but no ions at  $m/z$  150, 162, or 178. The meta isomer reacts to form ions at  $m/z$  150 and 178, but the ion at  $m/z$  162 can only be seen in negligible amounts. The para isomer predominantly reacts to form two ions, at  $m/z$  150 and 162. Figure 1 shows the pertinent portion of the spectra for each isomer. The spectra in Figure 1 were all obtained after a reaction time of 0.4 s at a pressure of  $8 \times 10^{-8}$  Torr. All spectra show, in addition to the ions discussed above, an ion at  $m/z$  180, which is  $\text{Fe}(\text{M})^+$ , where M stands for the neutral methoxyphenol molecule. From these observations it is clear that isomer differentiation can be accomplished via  $\text{Fe}^+$  reactions in gas phase.

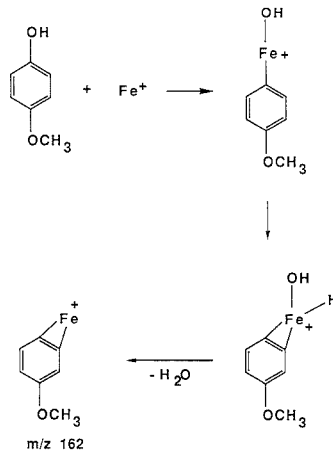
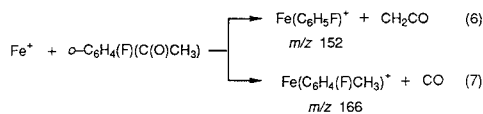


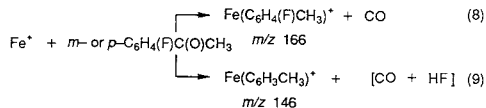
**Figure 6.** A proposed reaction mechanism for the reaction of  $\text{Fe}^+$  with *p*-methoxyphenol.

**Fluoroacetophenone.** This compound is another example where all three isomers can be identified through  $\text{Fe}^+$  reactions. The ortho isomer can easily be identified through the primary iron ion reactions, but the other two react in a similar manner. A closer examination of the reactions of the meta and para isomers, in particular the secondary reactions, does reveal differences that can be used for identification. The reactions of  $\text{Fe}^+$  with the ortho isomer proceed according to eq 6 and 7. Suggested mechanisms for these reactions are



presented in Figure 7. The elimination of CO is observed in the reactions of acetophenone (13) but not the elimination of  $\text{CH}_2\text{CO}$ , indicating that the presence of the fluorine facilitates that reaction. The ion at  $m/z$  166 reacts further to eliminate  $\text{FeF}$  and form the stable ion  $(\text{C}_7\text{H}_7)^+$  at  $m/z$  91. It is not clear whether the ion at  $m/z$  91 is the tropylium ion (ionization potential (IP) = 6.24 eV (14)) or the benzyl cation (IP = 7.20 eV (14)). In either case it has a lower ionization potential than  $\text{FeF}^+$  ( $\text{FeI}^+$ , for example, has an IP of 7.8 eV (14)) and thus retains the charge upon fragmentation. The ion at  $m/z$  152 reacts further to form  $\text{FFe}(\text{M})^+$ , where M stands for the neutral fluoroacetophenone molecule. These secondary reactions suggest that the structures labeled 4e and 4h may rearrange so that the iron inserts into the C-F bond.

The main reactions of the meta and para isomers are shown in reactions 8 and 9. Double resonance studies reveal that



the ionic species at  $m/z$  146 is not produced from the ionic product of reaction 8. Instead, it appears that the metal ion interacts with both functional groups simultaneously to eliminate CO and HF. A similar phenomenon has been observed in a study of the chemistry of  $\text{Co}^+$  with 1,4-disubstituted butanes by Tzarpopoulos and Allison (15). Despite the long chain, abstraction from both functional groups through

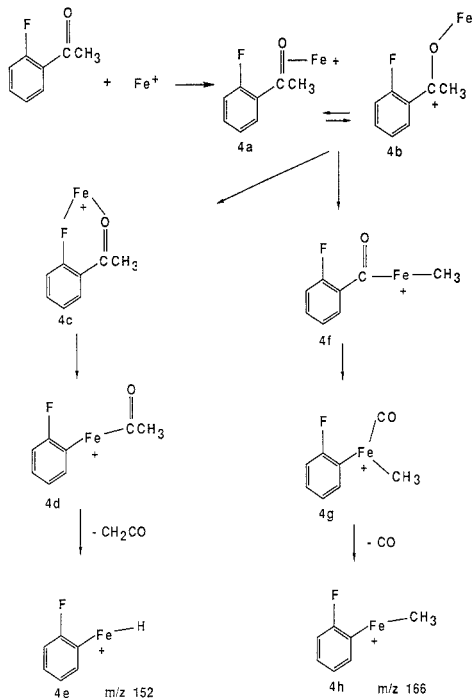


Figure 7. A proposed reaction mechanism for the reaction of  $\text{Fe}^+$  with *o*-fluoroacetophenone.

the interaction of a single cobalt ion was observed.

As with the reactions of the *ortho* isomer, the elimination of CO is observed analogous with the reactions of acetophenone (13). Reaction 6 is not observed for either the meta or the para isomers and is therefore unique to the *ortho* isomer.

At longer reaction times, when secondary reactions have occurred, some differences in the spectra of the meta and para isomers become apparent. An example of this is illustrated in Figure 2. The ion at  $m/z$  146 was isolated through the use of double ejection pulses. It was then allowed to react with the neutral fluoroacetophenone for 1 s at a pressure of  $3 \times 10^{-7}$  Torr prior to ion detection. Parts a and b of Figure 2 show the mass spectra for the meta and the para isomers, respectively, obtained after the reactions of the ion at  $m/z$  146 ( $\text{Fe}(\text{C}_7\text{H}_6)^+$ ). Characteristic is the formation of an ion at  $m/z$  236, which is present in high abundance in the meta isomer spectrum but in low abundance in the para spectrum. Exact mass measurements support that the formula for this ion is  $\text{Fe}(\text{C}_7\text{H}_6)_2^+$ , but the reaction mechanism is not obvious. Further differences between the meta and the para mass spectra are observed in the abundance of the ionic species at  $m/z$  374, which has the formula  $\text{Fe}(\text{C}_7\text{H}_6)_2\text{M}^+$ , where M stands for the neutral fluoroacetophenone molecule. Because this ion is produced from  $\text{Fe}(\text{C}_7\text{H}_6)^+$  at  $m/z$  236, it is observed in high abundance in the mass spectrum of the meta isomer but in minor abundance in the para isomer mass spectrum. The meta and para isomers can be differentiated based on the abundance of the ion species at  $m/z$  236 produced from the isolated ion at  $m/z$  146.

**Fluoroanisole.** The EI spectra of the isomers of fluoroanisole are indistinguishable and, thus, cannot be used for isomer identification. These isomers represent the second class

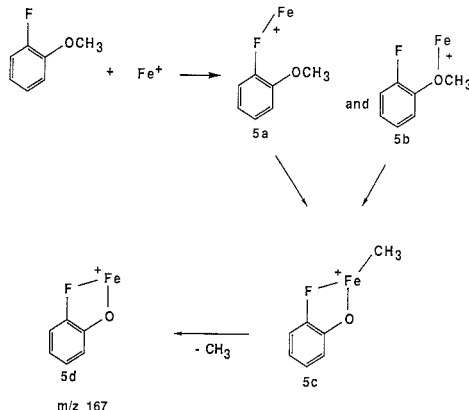
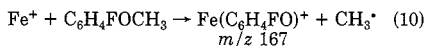


Figure 8. A proposed reaction mechanism for the reaction of  $\text{Fe}^+$  with *o*-fluoroanisole.

of compounds with respect to their reactions with  $\text{Fe}^+$ . The *ortho* isomer can easily be identified, but the other two react in a very similar manner making isomer identification difficult. Figure 3 shows the mass spectra obtained after a reaction time of 0.4 s for the *ortho*, *meta*, and *para* isomers. Although the differences between the *ortho* spectrum and the others are obvious, the most characteristic ions at shorter reaction times are at  $m/z$  167 and 201. Both of these ions are in high abundance in the *ortho* spectrum but absent or in minor abundance in the spectra of the other isomers. The reaction producing these ions is believed to be



The ion at  $m/z$  167 then reacts again with the neutral molecule to produce an ion at  $m/z$  201 ( $\text{FeFe}(\text{M})^+$ ), which suggests that the iron may be bonded to the fluorine in the former ion. A possible mechanism for reaction 10 is shown in Figure 8.

Dehydrofluorination, analogous to reactions of  $\text{Fe}^+$  with fluorobenzene (13) is observed for the meta and para isomers to produce  $(\text{Fe}(\text{M} - \text{HF})^+)$  at  $m/z$  162 as is elimination of formaldehyde, analogous to the anisole reactions (13) to produce  $(\text{Fe}(\text{M} - \text{CH}_2\text{O})^+)$  at  $m/z$  152. In the case of the *ortho* isomer, the latter reaction is observed, but the former only as a minor side reaction. Identifying the *ortho* isomer from the other two isomers is the abundance of the ions at  $m/z$  167 and 201. Some variations in the abundance of several ion species can be seen in the spectra of the meta and the para isomers. These differences are not readily recognizable for routine isomer identification.

A similar behavior was observed in the case of *methylanisole*. The *ortho* isomer reacted uniquely with  $\text{Fe}^+$  to form a complex ion with the elimination of methane. A suggested mechanism for this reaction is shown in Figure 9. As in the case of fluoroanisole, the iron ion is believed to form a bridge between the functional groups in the case of the *ortho* isomer, but, the increased distance between these groups in the meta and the para isomers does not allow the formation of such a bridge. Thus, the *ortho* isomer reacts uniquely and can be identified through the  $\text{Fe}^+$  reactions, whereas the meta and the para isomers cannot be distinguished.

**Xylene.** The reactions of  $\text{Fe}^+$  with the xylenes were very simple. Production of  $\text{Fe}(\text{M})^+$  was observed followed by the generation of  $\text{Fe}(\text{M})_2^+$ , where M stands for the neutral xylene molecule. At higher laser power  $\text{M}^+$  and  $(\text{M} - \text{CH}_3)^+$  could also be detected. No significant differences between the re-

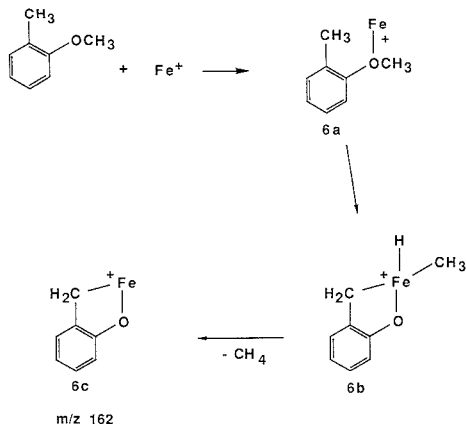


**Figure 9.** A proposed reaction mechanism for the reaction of  $\text{Fe}^+$  with *o*-methylanisole.

actions of the isomers could be established. These reactions are analogous to the reactions of toluene (13).

Of the compounds studied, only xylene belonged to class three, where none of the isomers could be differentiated. Methoxyphenol and fluoroacetophenone were in class one, where all three isomers could be differentiated. The other compounds, methylanisole and fluoroanisole, belong to class two, where one isomer can readily be differentiated from the other two.

### CONCLUSIONS

This study on several disubstituted benzene derivatives reveals that the iron-ion reactions can be diagnostic for isomer identification for a number of compounds where the electron impact spectra at 70 eV of these compounds are not. In all but one case (the xylenes) the ortho isomer can easily be identified through these iron-ion/molecule reactions, but in some cases the spectra for the meta and para isomers are too similar for routine discrimination and careful attention and reliance on peak intensity variations are required for identification.

The isomer discrimination method presented here fundamentally relies on the ability of  $\text{Fe}^+$  to form a bridge between the two substituents. Where such a bridging reaction is observed, an ion unique to that isomer is produced and identifies the isomer. Where there is no possibility of such bridging reactions, identification of the isomer must rely on intensity variations between the spectra of the isomers. Although transition-metal ions have the ability to form bonds to more than one functional group and are therefore suitable for this

application, various other ionic species, organic as well as inorganic, singly as well as multiply charged, may prove to be equally or better suited for this purpose. The size, shape, and composition of the reactant ion would be determined by the nature of the isomer system to be identified.

On the basis of the results presented here, predictions can be made for what other isomer systems the method may be useful. For example, in the case of dihydroxybenzene one would expect an iron bridge to form between the two oxygens, with the elimination of  $\text{H}_2$  in the case of the ortho isomer. Such a bridge would not be expected either in the case of the meta or the para isomers due to the increased distance between the functional groups and, thus, only the ortho isomer could be identified by using this method.

A similar study of the reactions of other transition-metal ions (in some cases doubly charged ions as well as singly charged) is under way to determine if other metals may provide better discrimination in some cases and if a matrix of a several metals may be the best choice for general applications. Also in progress is a systematic study of the reactions of a wide range of isomer systems to reveal the generality of this method.

### ACKNOWLEDGMENT

A.B. and J.W.T. thank Nicolet Analytical Instruments, and especially Mr. Mark Johnston, for access to the FTMS-2000.

### LITERATURE CITED

- (1) Burnier, R. C.; Carlin, T. C.; Reents, W. D.; Cody, R. B.; Lengel, R. K.; Freiser, B. S. *J. Am. Chem. Soc.* **1979**, *101*, 7127.
- (2) Cody, R. B.; Burnier, R. C.; Reents, W. D.; Carlin, T. J.; McCrery, D. A.; Lengel, R. K.; Freiser, B. S. *Int. J. Mass Spectrom. Ion Phys.* **1980**, *33*, 37.
- (3) Freiser, B. S. *Anal. Chim. Acta* **1985**, *178*, 137.
- (4) Freiser, B. S. *Talanta* **1985**, *32*, 697.
- (5) Jacobson, D. B.; Byrd, G. D.; Freiser, B. S. *Inorg. Chem.* **1984**, *23*, 553.
- (6) Burnier, R. C.; Byrd, G. D.; Freiser, B. S. *Anal. Chem.* **1980**, *52*, 1641.
- (7) Forbes, R. A.; Tews, E. C.; Freiser, B. S.; Wise, M. B.; Perone, S. P. *Anal. Chem.* **1986**, *58*, 684.
- (8) Forbes, R. A.; Tews, E. C.; Huang, Y.; Freiser, B. S.; Perone, S. P. *Anal. Chem.* **1987**, *59*, 1937.
- (9) Peake, D. A.; Gross, M. L. *Anal. Chem.* **1985**, *57*, 115.
- (10) Armentrout, P. B.; Hodges, R. V.; Beauchamp, J. L. *J. Am. Chem. Soc.* **1981**, *103*, 784.
- (11) Lombarski, M.; Allison, J. *Int. J. Mass Spectrom. Ion Phys.* **1983**, *49*, 281.
- (12) Kang, H.; Beauchamp, J. L. *J. Phys. Chem.* **1985**, *89*, 3364.
- (13) Bjarnason, A.; Taylor, J. W., submitted for publication in *J. Am. Chem. Soc.*
- (14) Lias, S. G.; Bartmess, J. E.; Liebman, J. F.; Holmes, J. L.; Levin, R. D.; Mallard, W. G. *J. Phys. Chem. Ref. Data* **1988**, *17*, Suppl. 1.
- (15) Tzaropoulos, A.; Allison, J. *Organometallics* **1984**, *3*, 86.

RECEIVED for review December 21, 1988. Accepted June 7, 1989. The authors gratefully acknowledge the support from the Wisconsin Alumni Research Foundation, the Center for X-Ray Lithography, the Olin-Hunt Corporation, The Upjohn Company, and the National Science Foundation through Grant CHE-8508731.



# Amino Acid and Tripeptide Mixture Analysis by Laser Desorption Fourier Transform Mass Spectrometry

M. Paul Chiarelli and Michael L. Gross\*

Midwest Center for Mass Spectrometry, Department of Chemistry, University of Nebraska, Lincoln, Nebraska 68588

Laser desorption (LD) at 1064 nm and Fourier transform mass spectrometry (FTMS) were investigated as a means of analyzing mixtures of amino acids and tripeptides. LD mass spectra were obtained of a 15-component amino acid mixture consisting of 3 ng of each in admixture. The mixture was desorbed from a copper probe at a power density of  $2 \times 10^6$  W/cm<sup>2</sup>. All components yield sample-specific ions of the  $(M - H + 2Na)^+$  type, but the relative abundances are not proportional to concentration. The most important factors influencing the disproportionate ion abundances are the differences in the individual amino acid sublimation enthalpies. A five-component mixture of tripeptides with widely varying solubilities was also analyzed successfully. Fast atom bombardment mass spectrometry is a less successful approach than LD/FTMS for analysis of amino acid and tripeptide mixtures.

## INTRODUCTION

Many molecules of biochemical interest are thermally labile and do not volatilize without decomposing. Mass spectrometric analysis of these molecules must be preceded by a sputtering or a desorption ionization process that preserves the structural integrity of the analyte molecule. Such "soft ionization" techniques have permitted the mass spectrometric analysis of many important biomolecules, particularly polynucleotides, polypeptides, and small proteins.

One of the next major challenges in mass spectrometry is the analysis of complex mixtures, such as those that might result from the digest of a large protein. The most common type of desorption ionization employed for digest analysis has been fast atom bombardment (FAB) (1). FAB coupled with tandem mass spectrometry (MS/MS) has also proven to be a powerful tool for the sequencing of proteins (2). Collisional activation of peptide constituents of the digest and analysis by MS/MS can be used to determine the amino acid sequence.

The utility of FAB is limited, however, because a liquid matrix is necessary for analyte solvation, and the nature of the matrix can have a profound effect on analyte response (3). Furthermore, the surface activities of the peptides in a given mixture also influence the relative responses (4). The more surface-active components of the peptide mixture preferentially desorb with respect to those peptides having greater matrix solubility, and the latter can be suppressed to the point where they are not observed in a mass spectrum at all (5). The discrimination may be minimized somewhat by the addition of other reagents to the matrix, as was shown for liquid secondary ion mass spectrometry (SIMS) (6). The development of continuous flow FAB is promising because the on-line coupling of a FAB probe to a high-performance liquid chromatograph (HPLC) appears to minimize the effects of competitive ionization (7). Some of these issues are discussed in a recent comprehensive review of peptide analysis by FAB mass spectrometry (8).

Other desorption ionization techniques for peptide analysis appear to be less plagued by the discrimination problems of

FAB. Field desorption (FD) was successful in identifying 28 amino acids in the digest of a 29 amino acid peptide (9). Plasma desorption (PDMS) is also a powerful means of analyzing peptides. PDMS was employed to determine the molecular weight of human interleukin-2. Moreover, digestion of this protein with CNBr gave five peptide fragments, all of which showed sample-specific ions after dithiothreitol reduction on the sample substrate (10). A comprehensive review of PDMS was also published recently (11). Solid secondary ion mass spectrometry (SIMS) is also an effective approach for analyzing peptides. Detection limits of  $10^{-14}$  mol of the peptide bradykinin were established by using SIMS and time-of-flight mass analysis (12).

The purpose of this study is to investigate the utility of laser desorption at 1064 nm and Fourier transform mass spectrometry (FTMS) for analyzing mixtures of amino acids and small peptides. The first portion of this investigation is focused on the mixture analysis of single amino acids because their chemical and physical properties are better known than those of peptides. The second part of the paper deals with the analysis of tripeptide mixtures.

To date, most laser desorption (LD) studies of amino acids and small peptides have been directed at understanding the nature of the desorption process itself. The desorption thresholds of amino acids and dipeptides resonant at a desorbing wavelength of 266 nm were shown to be proportional to their absorptivities (13). Selectively deuterated amino acids were studied to distinguish functional-group-specific protonation reactions from "random" protonation reactions (14). Amino acids and small peptides were employed to show that UV LD analysis can be carried out on a few monolayers of sample (15) and that matrix assisted laser desorption can also be utilized (16). The latter research has produced particularly spectacular results for desorption of very high molecular weight proteins. Peptides were also used to study the desorption time profiles of ions and neutral molecules under IR desorption conditions (17). Infrared LD/FTMS was demonstrated to be successful for determining the peptide bradykinin (18). No peptide mixture analysis, however, has been undertaken by using LD mass spectrometry.

## EXPERIMENTAL SECTION

Laser desorption spectra were obtained by using a Quanta-Ray DCR-2 Nd:YAG laser and a FT mass spectrometer constructed in this laboratory (19) and interfaced to a Nicolet 1000 data system. The sample probe was interfaced to the analyzer cell through a 6.35-mm hole at the intersection of the excitation and receiver plates (20). The cell was a cubic design of 5.08-cm dimensions. The laser beam entered the cell along the opposing diagonal, striking the probe normal to the surface. The magnetic field was 1.2 T. A specially designed vespel cone was inserted into the opening of the FTMS cell to ensure reproducible probe placement.

The laser probes were made of oxygen-free copper and were prepared by facing off in a mechanical lathe and subsequent sonication in methanol and dichloromethane for 15 min in each solvent. All the amino acids and tripeptides employed in this study were combined with an equal weight of NaCl prior to LD/FTMS analysis. No NaCl was used in the FAB determinations. Except for the amino acid detection limit determination,

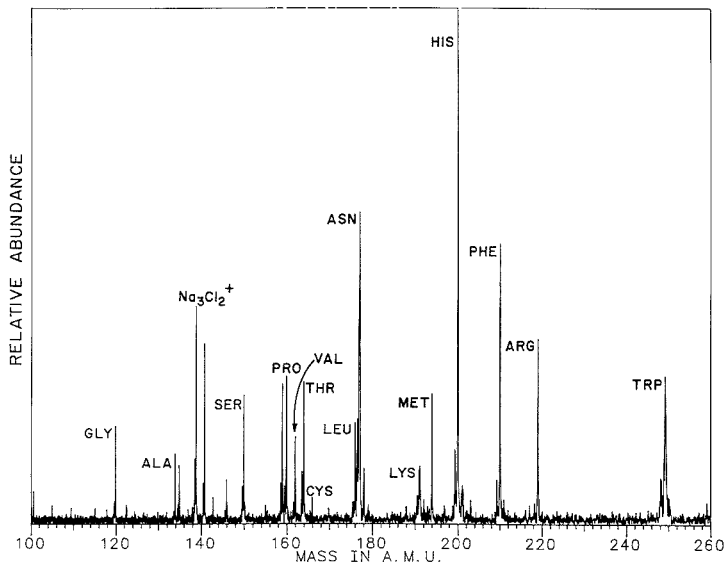


**Figure 1.** LD/FTMS spectrum of a 15-component amino acid mixture combined with an equal total weight of NaCl acquired at a wavelength of 1064 nm and a power density of  $2 \times 10^6$  W/cm<sup>2</sup>. The  $(M - H + 2Na)^+$  ions are labeled by the three-letter codes of the corresponding amino acids.

a total of 10  $\mu$ g of sample was applied to the laser probe.

Singlet-shot LD spectra were obtained at a wavelength of 1064 nm. The area of the laser spot was  $1.6 \times 10^{-3}$  cm<sup>2</sup>. The pulse width of the laser was 140  $\mu$ s. The power of the laser was measured immediately prior to the experiment by using a Scientech Model 362 meter and measuring the average powder output when the laser was operated at 10 pulses/s.

The FAB MS experiments were conducted with a Kratos MS-50 triple analyzer equipped with a standard Kratos FAB source (27). The primary beam was 6–8-keV argon atoms at a total current of 2 mA at the cathode of the gun.

All amino acids and tripeptides used in this investigation were obtained from Sigma Corp. and were used without further purification.

## RESULTS AND DISCUSSION

**Amino Acid Mixture Analysis.** It is necessary to evaluate the generality and detection limits of 1064-nm LD/FTMS for amino acid mixture analysis. Figure 1 shows a 15-component amino acid mixture with 10 ng of each applied to the laser probe. The best sensitivity was found under more nearly "thermal" desorption conditions (22) at a power density of  $2 \times 10^6$  W/cm<sup>2</sup>; 3 ng of each amino acid gave a detectable signal. All the amino acids give sample-specific ions of the  $(M - H + 2Na)^+$  type. Some of the larger amino acids also desorb as  $(M + Na)^+$  ions (e.g., tryptophan and phenylalanine). FAB mass spectra were obtained for comparison. The best results were found with FAB by using a glycerol matrix; 10 of the 15 amino acids gave  $(M + H)^+$  ions when 350 ng of each was present in the matrix (Figure 2). In these experiments, LD/FTMS is superior to FAB/MS in sensitivity and relative response for the analysis of amino acid mixtures.

The relative ion abundances observed in the LD/FTMS spectra indicate that mixture component discrimination is operative. Because the amino acids were applied in equal weights, one would expect the glycine ion molar response or abundance to be 2.7 times that of tryptophan if their LD characteristics are the same. The larger amino acids, however, are desorbed more abundantly in general (e.g., compare the abundances of glycine and alanine to those of histidine and

**Table I.** Ion Abundance Ratios from the Laser Desorption of Glycine and Other Alkyl Amino Acids in Binary Mixtures in a NaCl Matrix at a Wavelength of 1064 nm and a Power Density of  $2 \times 10^6$  W/cm<sup>2</sup>

amino acid	R group	ratio on probe	ion abundance ratio <sup>a</sup>
Ala	CH <sub>3</sub>	1.2	$0.37 \pm 0.07$
Val	CH(CH <sub>3</sub> ) <sub>2</sub>	1.5	$0.24 \pm 0.07$
Leu	CHCH <sub>2</sub> (CH <sub>3</sub> ) <sub>2</sub>	1.6	$0.29 \pm 0.05$

<sup>a</sup> Ratio of abundance of Gly to the abundance of the other amino acid.

tryptophan in Figure 1). In order to improve the utility of LD/FTMS, we decided to investigate the mechanism(s) responsible for the discrimination. Binary mixtures of amino acids of differing chemical and physical properties were desorbed, and their relative sample-specific ion abundances were compared to obtain insight into the mechanisms responsible for the discrimination.

**Role of Amino Acid Mass.** In the first set of experiments, binary mixtures of glycine and other alkyl amino acids were codesorbed under the same conditions as for the 15-component mixture to test if molecular mass affects the desorption efficiency. These amino acids possess similar side chains (Table I) and  $pK_a$ 's. All the ions were of the  $(M - H + 2Na)^+$  type. The glycine/alkyl amino acid ion abundance ratios tend to decrease as the size of the alkyl side chain on the amino acid increases (Table I). The results are consistent with the apparent trend seen for the 15-component mixture. The implications are discussed later in the text.

**Role of Acid/Base Characteristics.** In the next set of experiments, binary mixtures of amino acids of different  $pK_a$ 's were desorbed. One might expect that tendencies for the individual amino acids to form  $(M - H + 2Na)^+$  ions are dictated at least in part by the relative carboxyl group acidities; that is, the smaller the  $pK_a$  the larger the  $(M - H + 2Na)^+$  abundance. Binary mixtures of cysteine, valine, and threonine were chosen for these experiments because the  $pK_{a1}$ 's are quite

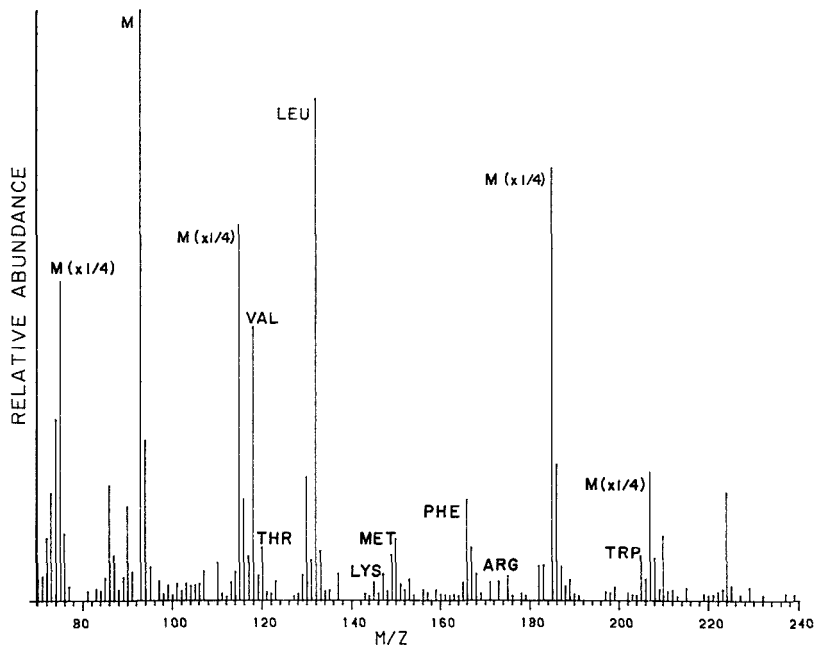


**Figure 2.** FAB MS spectrum of a 15-component amino acid mixture in a glycerol matrix. The  $(M + H)^+$  ions of the 10 amino acids detected are labeled by the three-letter codes. Ions from the matrix are labeled as "M".

**Table II**

A. $pK_a$ Values for the Amino Acids Cys, Val, and Thr			
amino acid	$pK_{a1}$	$pK_{a2}$	$pK$ side chain
cysteine	1.71	8.18	10.28
valine	2.32	9.62	
threonine	2.71	9.62	

B. Ion Abundance Ratios of $(M - H + 2Na)^+$ Ions Desorbed from Binary Mixtures of Cys, Val, and Thr in an NaCl Matrix		
amino acids	ions ratioed	abundance ratios <sup>a</sup>
Val/Thr	$(m/z\ 162)/(m/z\ 164)$	$0.24 \pm 0.06$
Cys/Thr	$(m/z\ 166)/(m/z\ 164)$	$0.21 \pm 0.02$
Cys/Val	$(m/z\ 166)/(m/z\ 162)$	$0.77 \pm 0.05$

<sup>a</sup>  $N = 8$  determinations.

different for the amino acids, and their masses are approximately equal (Table II). The conditions employed and the types of ions desorbed are the same as discussed above.

On the basis of the trend in  $pK_{a1}$ , cysteine should yield the largest ion abundance and threonine the smallest, but just the opposite trend is observed. This is good evidence that the acid/base characteristics of the amino acids have little influence on their tendency to form  $(M - H + 2Na)^+$  ions under thermal laser desorption conditions. The relative ion abundances, however, do suggest that the desorption characteristics of the amino acids are governed by intrinsic properties rather than by intermolecular interactions. Because the Cys/Thr and the Val/Thr ion abundance ratios are similar (Table II), the Cys/Val ratio is expected to be close to unity, and it is. Because the desorption characteristics of the three amino acids are not governed principally by their  $pK_a$ 's, some other physical property must be responsible for the observed results. Some "thermal" decompositions may be competing, as was

found for sulfur-containing amino acids (methionine and cysteine) in Tian-Calvet calorimetry studies (23). For example, cysteine does not sublime at ca. 400 K because it decomposes.

**Role of Sublimation Enthalpy.** At this point it seemed logical to consider the role of sublimation enthalpy in amino acid desorption. The temperature dependence of the sublimation enthalpies of glycine, alanine, and proline was previously investigated with Tian-Calvet calorimetry (24, 25). To obtain an estimate of the sublimation enthalpies of these amino acids under the conditions employed for laser desorption, the temperature of the irradiated copper probe must be known. The temperature rise on the copper surface may be estimated by the expression in eq 1

$$T(0,t) = [2(1 - R)F_0/K][\kappa t/\pi]^{1/2} \quad (1)$$

(26) where  $R$  is the reflectivity of the copper at 1064 nm,  $F_0$  the power density of the laser,  $\kappa$  the thermal diffusivity,  $K$  the thermal conductivity, and  $t$  the length of the laser pulse in seconds. The values (27) of these physical parameters for copper are  $R = 0.92$ ,  $K = 3.74$  W/(deg cm), and  $\kappa = 1$  cm<sup>2</sup>/s. The calculation yields a maximum surface temperature at 800 K. This value is undoubtedly higher than the actual desorption temperature for several reasons. The expression assumes the laser beam is of infinite radial extent so it does not account for the diffusion of energy into the nonirradiated area around the laser spot or for diffusion of energy into the bulk copper during the time of irradiation. The desorption of ions and neutrals may also proceed before all the energy is absorbed; time-resolved studies under conditions similar to those used here (22) show that ion desorption proceeds on a microsecond timescale, and the laser pulse length used here was 140  $\mu$ s.

There is a relation between the relative ion abundance ratios obtained from laser desorption of binary mixtures and the

Table III

## A. Enthalpies of Sublimation Estimated for Gly, Ala, and Pro at 800 K

amino acids	enthalpy, kJ/mol	ref
Gly	108.9	24
Ala	91.0	24
Pro	22.1	25

B.  $(M - H + 2Na)^+$  Ion Abundance Ratios of Gly, Ala, and Pro Desorbed from Binary Mixtures in an NaCl Matrix

amino acids	ion abundance ratios	$N^a$
Gly/Ala	$0.37 \pm 0.07$	8
Gly/Pro	$0.08 \pm 0.01$	12
Ala/Pro	$0.45 \pm 0.09$	10

<sup>a</sup>  $N$  = number of determinations.

difference in sublimation enthalpies of the amino acid constituents of the mixtures (see Table III). Estimates of the sublimation enthalpies at 800 K were made from literature trends (Table IIIA), and the relative ion abundances were obtained under the laser desorption conditions described earlier in the paper (Table IIIB). Because proline has the lowest sublimation enthalpy, the ion abundance ratios of Gly/Pro and Ala/Pro should be less than unity, and the Gly/Pro ratio should be smaller than Ala/Pro. These predictions are in accord with the experimental data. We also expect that the Gly/Ala abundance ratio should be less than unity; a value of 0.37 is obtained. On a quantitative basis, however, the Gly/Ala abundance ratio should be nearly equal to unity, and, on the basis of the Gly/Pro abundance ratio, the Ala/Pro is expected to be smaller than 0.45 and nearly equal to that of Gly/Pro.

We conclude that the model gives semiquantitative predictive capability. A possible weakness in the correlation is that the sublimation enthalpy measurements may include some contribution from decomposition of the amino acids. The extent of decomposition, however, cannot be assessed on the basis of the literature studies of sublimation. Furthermore, there is not a necessary parallel between the thermodynamic quantity (sublimation enthalpy) and the kinetics of desorption. The results of the sublimation study of cysteine (23) mentioned above suggest that no  $(M - H + 2Na)^+$  should desorb under these conditions if LD were governed only by thermodynamic factors. The low-abundance  $(M - H + 2Na)^+$  ions that are observed probably arise by means of nonequilibrium, rapid desorption. The desorption may be evidence for a kinetically driven, nonequilibrium component of the overall desorption. This component is minor for most of the amino acids (except cysteine), but it becomes more important at higher laser powers.

If sublimation enthalpies have a major influence on desorption characteristics of amino acids, then the desorption behavior at other temperatures should be predictable on the basis of trends of sublimation enthalpies as a function of temperature. Knudsen cell calorimetry was previously employed to determine the sublimation enthalpies of many of the amino acids at 455 K (see Table IVA for values for the alkyl amino acids (28)). At this temperature, glycine has the smallest sublimation enthalpy. The Tian-Calvet calorimetry studies discussed above were conducted for the purpose of extrapolating the sublimation enthalpies of proline, alanine, and glycine to 298 K under standard conditions; the resulting enthalpies are  $149 \pm 4.0$ ,  $144 \pm 4.2$ , and  $138.2 \pm 4.6$  kJ/mol, respectively.

On the basis of the Tian-Calvet and the Knudsen cell data, the sample-specific ion abundance of glycine is expected to

Table IV. Enthalpies of Sublimation for Alkyl Amino Acids Determined at 455 K by the Knudsen Cell Effusion Method<sup>a</sup>

amino acid	enthalpy, kJ/mol
Gly	136.5
Ala	138.1
Val	162.8
Leu	150.7

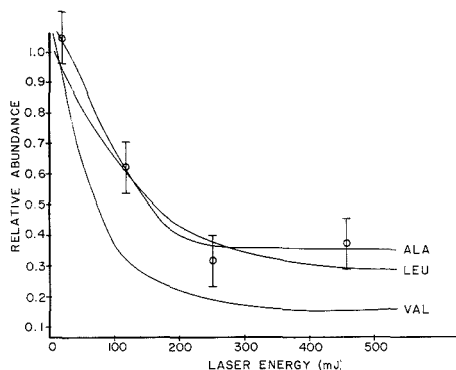
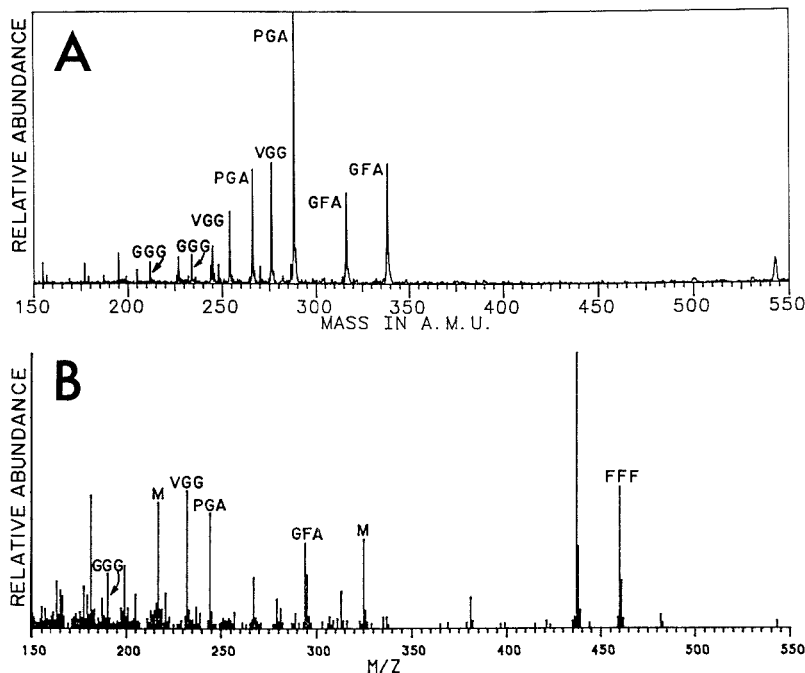
<sup>a</sup> Reference 28.

Figure 3. Plot of the ratios of the total sample-specific ion abundances (those of  $(M - H + 2Na)^+$ ,  $(M + Na)^+$ , and  $(M + H)^+$ ) of glycine to alanine, valine, and leucine against laser energy at a wavelength of 1064 nm. For simplicity, points and error bars are shown only for alanine to illustrate typical data.

increase with respect to the ion abundances of the other amino acids as the laser power is decreased. The alkyl amino acids were chosen for these determinations because their  $pK_a$ 's are similar, and therefore the energies of formation for each type of sample-specific ion should also be similar. The trends in ion abundance ratios shown in Figure 3 are consistent with the variation of sublimation energies of the three alkyl amino acids. Three types of ions,  $(M + H)^+$ ,  $(M + Na)^+$ , and  $(M - H + 2Na)^+$ , were observed over this power density range; the first two show increasing abundances at lower laser energies, consistent with the results of UV laser desorption on a time-of-flight mass spectrometer (13).

**Tripeptide Mixture Determinations.** The success obtained with the amino acid mixture analyses prompted the application of 1064-nm LD and FTMS to tripeptide mixtures. First, two binary mixtures of tripeptides were desorbed to ascertain the effect of amino acid sequence on the relative sample-specific ion abundances. Then four- and five-component mixtures of tripeptides were analyzed to assess the influence of solubility and surface activity on ion formation. The LD conditions that were utilized in the analysis of the 15-component amino acid mixture were employed throughout these investigations. Most of the sample-specific ions observed are of either the  $(M - H + 2Na)^+$  or  $(M + Na)^+$  type, the former being generally more abundant.

Each of the tripeptides Ala-Pro-Gly (APG) and Pro-Gly-Ala (PGA) was mixed with Val-Gly-Gly (VGG) to give two binary mixtures, and the relative sample-specific ion abundances,  $(VGG)/(APG)$  and  $(VGG)/(PGA)$ , were compared for amino acid sequence effects on ion formation. The ion abundance ratios should be equal if no sequence effects exist. These ratios,  $0.28 \pm 0.03$  and  $0.39 \pm 0.05$  for  $(VGG)/(APG)$  and  $(VGG)/(PGA)$ , respectively, (12 determinations each) show a small but significant difference. This difference may be



**Figure 4.** (A) LD/FTMS spectrum of a four-component tripeptide mixture combined with an equal weight of NaCl acquired at a wavelength of 1064 nm and a power density of  $2 \times 10^9$  W/cm<sup>2</sup>. All sample-specific ions are of the  $(M - H + 2Na)^+$  or  $(M + Na)^+$  type. (B) FAB MS spectrum of a five-component mixture in a thioglycerol matrix. All sample-specific ions are of the  $(M + H)^+$  type. The tripeptide ions are identified by the combinations of the one-letter codes of their constituent amino acids. Matrix ions are labeled with an "M".

attributed to the changes in the conformation of the peptide as a function of the position of the proline residue. Proline is known to cause bends in peptide chains (29).

Sublimation enthalpies may also play an important role in determining abundance differences, but these enthalpies are not known for tripeptides. Sensitivity of sublimation enthalpy to temperature is theoretically proportional to the difference in the heat capacities of the material in the gas and solid states:  $C_p(g) - C_p(s)$  (30). Because the heat capacity difference should increase with the number of atoms (number of vibrational modes), sublimation enthalpies of peptides should decrease more rapidly as temperature is increased than those of amino acids. This effect forecasts opportunities for large peptide analysis by laser desorption.

A four-component mixture of tripeptides was also desorbed to see if differences in solubility and surface activity influence the observed ion abundances, as does occur for FAB (4). Bull-Breese indices (free energies) have been employed to describe relative differences in amino acid and peptide surface activities (4, 5, 31). The percent total ion abundances of the peptides employed in this study and their Bull-Breese indices are given in Table V. Good precision is seen for these relative ion abundances. The good reproducibility is taken to indicate that the composition of the solid is homogeneous across the probe surface, and a selective crystallization upon evaporation of the solvent is not apparent. A typical spectrum is given in Figure 4A. The larger percent total ion abundances associated with the larger tripeptides are consistent with the sublimation enthalpy theory proposed above. The large relative ion abundance of PGA with respect to GFA, however, suggests other mechanisms of desorption may also be operative.

**Table V. Bull-Breese Indices and Relative Percent Ion Abundances for the Four Tripeptides Used in This Investigation**

tripeptide	B + B indices, <sup>a</sup> cal	% ion abundance <sup>b</sup>
Gly-Phe-Ala	-843	0.25 ± 0.01
Gly-Pro-Ala	-393	0.47 ± 0.04
Val-Gly-Gly	-520	0.22 ± 0.02
Gly-Gly-Gly	0	0.05 ± 0.01

<sup>a</sup> Calculated in the same manner as in ref 4. <sup>b</sup>  $N = 8$  determinations.

A decidedly more surface-active peptide (FFF) was added to the four-component mixture, and the mixture was desorbed to see if the precision of the relative total ion abundances is maintained. Triphenylalanine (FFF) has a Bull-Breese index of -2.33 kcal, which indicates that the solubility properties of FFF are different from those of the four tripeptides in the original mixture. Desorption of the five-component mixture gave relative ion abundances that are much more erratic than those observed for the four-component mixture. Some observations, however, are consistent with those seen in the analysis of the four-component mixture. The largest total ion abundances are due to either PGA or FFF; when the latter is dominant, the other components are of greatly reduced abundance. The trend in relative ion abundance among the other three peptides is the same as for the four-component mixture analysis. All five tripeptides were observed for each laser shot.

The erratic relative ion abundances may be due to the selective crystallization and segregation of FFF as the solvent is pumped away. To verify this hypothesis, the five tripeptides

were mixed in water, rather than in a 60:40 mixture of water and acetonitrile, because FFF is insoluble in water alone when added in the same proportions as the other tripeptides. The mixture to be deposited on the probe was withdrawn while it was stirred to maintain homogeneity. This mixture should simulate that formed as acetonitrile evaporates from the acetonitrile/water solution. The LD results are similarly as erratic as those obtained with the first solvent mixture, thus providing evidence for the selective precipitation of the FFF from the solvent. Because of the greater surface activity of FFF, it may aggregate in islands on top of the solid phase.

FAB spectra of this five-component mixture were also acquired, and the best results were obtained when a thioglycerol matrix was used. All five tripeptides gave  $(M + H)^+$  ions, and less discrimination was found than for the LD determinations (Figure 4B) when equal amounts of the mixture were analyzed. In glycerol, the discrimination expected from the previously proposed surface activity hypothesis was observed, but thioglycerol appears to be a less discriminating matrix for peptide analysis, at least on the basis of the limited number of measurements made here.

There may be at least two ways of improving the utility of LD/FTMS for peptide mixture analysis. Increasing the total laser power and area irradiated should minimize the effects that an inhomogeneous solid phase has on the observed ion abundances. Another approach is to use a nitrocellulose binder as is employed for PDMS (10). Rinsing this binder with dilute peptide solutions may yield a more representative and uniform distribution of the peptides on the sample surface.

### CONCLUSION

LD/FTMS can be used for the mixture analysis of amino acids and small peptides at higher sensitivity than can be obtained by standard FAB MS. Variations in sublimation enthalpy and inhomogeneous solid phases formed by selective precipitation of peptide components of widely varying surface activity are problems. When peptides of widely differing solubilities (surface activities) are in the mixture, as in peptide mapping, mass spectra from several laser shots need to be acquired across the substrate surface to ensure that all peptides in the mixture are desorbed.

The correlation of relative abundances of desorbed amino acid  $(M - H + 2Na)^+$  ions with sublimation enthalpies of the pure amino acids can be rationalized as follows. The amino acids exist in the solid state as zwitterions,  $^+H_3NCHRCOO^-$ . In the presence of excess NaCl, the most likely species to desorb is not the zwitterion but neutral  $H_2NCHRCOONa$ . This neutral salt molecule is cationized with gas-phase  $Na^+$  in the selvage region close to the surface. The desorption tendencies of neutral  $H_2NCHRCOONa$  species correlate with sublimation enthalpies of the amino acids themselves because the sublimation enthalpy of  $H_2NCHRCOONa$  can be viewed as a sum of the sublimation enthalpy of the amino acid and that of the reaction to exchange a sodium ion for  $H^+$ . The latter quantity is approximately a constant for the amino acids.

As a result, the former quantity accounts for the variations. As the laser power is decreased, there is insufficient gas-phase  $Na^+$  for the cationization reaction, and other species such as  $(M + Na)^+$  and  $(M + H)^+$  become important, as was observed.

### ACKNOWLEDGMENT

We thank Enrico Davoli and Kenneth Caldwell for their assistance in obtaining the FAB spectra, Don Rempel for his design of the vespel guide cone for the laser desorption studies, and Richard Grese for the artwork.

### LITERATURE CITED

- Barber, M.; Bordoli, R. S.; Sedgwick, R. D.; Tyler, A. N. *J. Chem. Soc., Chem. Comm.* **1981**, 325-327.
- Biemann, K.; Scoble, H. A. *Science* **1987**, *237*, 992.
- Lehmann, W. D.; Kessler, M.; König, W. A. *Biomed. Mass Spectrom.* **1981**, *11*, 217-222.
- Clench, M. R.; Garner, G. V.; Gordon, D. B.; Barber, M. *Biomed. Mass Spectrom.* **1985**, *12*, 355-357.
- Naylor, S.; Findels, A. F.; Gibson, B. W.; Williams, D. H. *J. Am. Chem. Soc.* **1986**, *108*, 6359-6363.
- Petti, G. R.; Cragg, G. M.; Holzapfel, C. W.; Tuinman, A. A.; Gieschen, D. P. *Anal. Biochem.* **1987**, *162*, 236-241.
- Caprioli, R. M.; Fan, T.; Cottrell, J. S. *Anal. Chem.* **1986**, *58*, 2949-2954.
- Biemann, K.; Martin, S. A. *Mass Spectrom. Rev.* **1987**, *6*, 1-76.
- Shimomishi, Y.; Hong, Y.-M.; Kitagishi, T.; Matsuo, T.; Matsuda, H.; Kakuse, I. *Eur. J. Biochem.* **1980**, *112*, 251-264.
- Jardine, I.; Scanlan, G. F.; Tsarbobopoulos, A.; Liberato, D. *J. Anal. Chem.* **1988**, *60*, 1086, 1087.
- Cotter, R. *J. Anal. Chem.* **1988**, *60*, 781A-793A.
- Steffens, P.; Niehuis, E.; Frieze, T.; Benninghoven, A. In *Secondary Ion Mass Spectrometry, SIMS IV*; Springer Series in Chemical Physics; Benninghoven, A., Ed.; Springer Verlag: New York, 1983; Vol. 25, pp 111-117.
- Karas, M.; Bachmann, D.; Hillenkamp, F. *Anal. Chem.* **1985**, *57*, 2935-2939.
- Parker, C. D.; Hercules, D. M. *Anal. Chem.* **1986**, *58*, 25-30.
- Karas, M.; Hillenkamp, F. *Anal. Chem.* **1988**, *60*, 2299-2301.
- Karas, M.; Bachmann, D.; Bahr, U.; Hillenkamp, F. *Int. J. Mass Spectrom. Ion Processes* **1987**, *78*, 53-68.
- Tabet, J.-C.; Cotter, R. *J. Anal. Chem.* **1984**, *56*, 1662-1667.
- Wilkins, C. L.; Wiel, D. A.; Yang, C. L. C.; Ijames, C. F. *Anal. Chem.* **1985**, *57*, 520-524.
- Ledford, E. B., Jr.; White, R. L.; Ghaderi, S.; Wilkins, C. L.; Gross, M. L. *Anal. Chem.* **1980**, *52*, 2450, 2451.
- McCreary, D. A.; Ledford, E. B., Jr.; Gross, M. L. *Anal. Chem.* **1982**, *54*, 1435-1437.
- Gross, M. L.; Chess, E. K.; Lyon, P. A.; Crow, F. W.; Evan, S.; Tudge, H. *Int. J. Mass Spectrom. Ion Phys.* **1982**, *42*, 243-254.
- Cotter, R. J.; Van Breemen, R. B.; Snow, M. *Int. J. Mass Spectrom. Ion Phys.* **1983**, *49*, 35-50.
- Sabbah, R.; Minadakis, C. *Thermochim. Acta* **1981**, *43*, 269-277.
- Ngauv, S. N.; Sabbah, R.; Laffitte, M. *Thermochim. Acta* **1977**, *20*, 371-380.
- Sabbah, R.; Laffitte, M. *Bull. Chim. Soc.* **1978**, *1-2*, 50-52.
- Ready, J. F. *Effects of High Power Laser Radiation*; Academic Press: New York, 1971; 405 pp.
- Goldsmith, A.; Waterman, T. E.; Hirschhorn, H. J. *Handbook of Thermophysical Properties of Solid Materials*; MacMillan: New York, 1961.
- Svec, H. J.; Clyde, D. D. *J. Chem. Eng. Data* **1965**, *10*, 151, 152.
- Zubay, G. *Biochemistry*; Addison-Wesley: Reading, MA, 1983; 1268 pp.
- Berry, R. S.; Rice, S. A.; Ross, J. *Matter in Equilibrium: Statistical Mechanics*; Wiley and Sons: New York, 1980; p 804ff.
- Bull, H. B.; Breese, K. *Arch. Biochem. Biophys.* **1974**, *161*, 665-670.

RECEIVED for review December 6, 1988. Revised manuscript received May 11, 1989. Accepted June 1, 1989. This work was supported by the Midwest Center for Mass Spectrometry (NSF Grant CHE-8620177).

# Dual-Column Immunoassays Using Protein G Affinity Chromatography

Linda J. Janis and Fred E. Regnier\*

Departments of Chemistry and Biochemistry, Purdue University, West Lafayette, Indiana 47907

**Tandem protein G affinity and reversed-phase chromatography (RPC) columns, coupled with a switching valve, were used for on-line immunoassays of antibodies and antigens. Columns with reversibly immobilized antibodies were prepared by adsorbing antibodies on the protein G column. Following antigen capture in the immunoaffinity column, antigen-antibody complexes were desorbed, dissociated, and transferred to the RPC column where they were separated and quantified. This system was used to determine the titer of a rabbit anti-human transferrin antibody sample with a precision of  $\pm 2\%$ . Quantitation of human transferrin in human serum had a precision of  $\pm 6\%$  and showed good agreement with rate nephelometry. The linear dynamic range for the transferrin, antigen immunoassay was  $5 \times 10^1$  to  $1 \times 10^5$  ng with a precision of  $\pm 3.5\%$ .**

## INTRODUCTION

There is a great need in biotechnology for methods that monitor concentration and purity of recombinant protein products and the immune response of patients using these proteins therapeutically. In contrast to clinical chemistry, where the analyte may be present in relatively low concentrations and has a known structure, the protein product in biotechnology can be present in relatively high amounts but be contaminated with product variants of unknown structures. These variants can arise from many sources such as expression errors, faulty posttranslational modification, and/or chemical or proteolytic degradation during biosynthesis and purification.

Analytical immunology would appear to be an ideal technique for biotechnology because of the great specificity of immunoglobulins. Dual-column immunoassay (DCIA), described in this paper, is a versatile method that was developed for use in biotechnology. It can be used for (i) determination of the concentration of a protein in a complex mixture, (ii) determination of the purity of a protein contaminated with variant species of similar structure, and (iii) determination of antibody titer of an antiserum.

Although immunoaffinity chromatography is widely used as an analytical technique, there are several problems that compromise the sensitivity of the method. The first is slow desorption kinetics. Dissociation of the antigen-antibody complex can be sufficiently slow that eluted antigen peaks are broad and asymmetric. This reduces peak height and makes it more difficult to detect antigens at low concentrations. A second problem is that of solvent interference with detection. The large concentration of desorption buffer necessary to dissociate the antigen-antibody complex can produce drastic shifts in the refractive index and absorbance of the effluent. Unfortunately, this desorption buffer pulse occurs as the antigen is eluted and diminishes the spectral difference between the mobile phase and the antigen. While this base-line perturbation can be minimized by using longer wavelengths ( $>280$  nm) and low detector gain, high sensitivity

requires detection at shorter wavelengths ( $<240$ ) and high detector gain.

Several approaches have been suggested to circumvent these limitations of immunoaffinity chromatography. One was the use of affinity columns prepared on nonporous particles and operated at elevated temperatures. This produced sharper peaks by enhancing desorption kinetics (1). Unfortunately, operating columns at elevated temperatures introduces the risk of compromising antibody half-life.

Solutions proposed for the base line disturbance problem, which also offered increased sensitivity, involved either competitive binding or sandwich immunoassays with indirect detection schemes using immunological reagents labeled with tags such as enzymes or fluorophores. For example, enzyme tags that generated a colored or electroactive product have been used (2-4). Unfortunately, preparation of labeled reagents can cause a loss of antigenicity and new reagents must be synthesized for each antigen assayed. This paper will demonstrate that DCIA overcame many of the problems of immunoaffinity chromatography and that sensitive immunoassays could be carried out without labeled immunological reagents.

The DCIA method involved two columns, an affinity and reversed-phase chromatography (RPC) column, in this case, coupled with a switching valve (5-10). The essential steps of the DCIA technique were (i) purification of antigen(s) on an immunoaffinity column, (ii) direct transfer of antigen(s) to a second chromatography column operating in a different mode, (iii) separation of antigen(s) on the second column, and (iv) direct detection of antigen(s) eluted from the second column.

For the work reported here, antibodies were not covalently attached to a chromatographic support; instead immunoaffinity columns were prepared for each analysis by reversible adsorption of antibodies (11) on a column with covalently immobilized protein G. Protein G is a bacterial protein that binds to immunoglobulins. The binding of IgG to protein G does not interfere with antigen binding (12). It has the advantage of binding to a wider range of immunoglobulin (IgG) species and subclasses than other bacterial IgG Fc binding proteins such as protein A (13). Antigens were captured by the adsorbed antibodies. Antigen-antibody complexes were desorbed from the protein G column and dissociated by using acidic conditions and then transferred to the RPC column where both components were separated.

A big advantage of this approach is that a different immunoassay could be performed for each run by using a different antiserum for the antibody loading step. The system hardware and operating conditions remain the same. A protein G affinity column provides a versatile, "universal support" (14) for immunoassays because it binds to antibodies from a wide range of species.

Previous work (8, 10) focused on the ability of DCIA to discriminate qualitatively among structural variants by using covalently immobilized antibodies. The goal of this paper was to demonstrate the utility of a protein G column for DCIA and to evaluate the technique quantitatively by determining

both antigen concentrations in complex samples and specific antibody concentrations in an antiserum (titer).

Many methods have been developed for titer measurements. Classically, titer refers to the highest dilution of the antiserum (e.g. 1/16) which reacts with a constant amount of antigen to give a detectable change such as precipitation, agglutination, complement fixation, or lysis. Many of these measurements are useful only for rough titer quantitations. Large differences have been reported when comparing titers measured free in solution (homogeneous) with those determined in gels or using solid supports (heterogeneous) (15). The units used to express titer vary from method to method. Some report amount of antiserum that reacted with a constant amount of antigen; others specify amount of antigen bound to a constant volume of antiserum. Antibody titers, although expressed in identical units, cannot be directly compared unless the measurement method is identical (15). Many investigators have found that high-affinity antibodies are measured preferentially in some assays including hemagglutination, complement fixation, virus neutralization, and enzyme-linked immunosorbent assays (ELISA) (16–20). Studies using monoclonal antibodies have demonstrated that ELISA exhibits both affinity-dependent and -independent behavior (20). Affinity dependence occurs at low antigen concentrations and large interepitope distances of the antigen immobilized on the solid surface. Affinity-independent behavior predominates at high antigen concentrations and small interepitope distances.

Antibody titers determined by DCIA could be measured by using affinity-independent or -dependent conditions. Since antigen was not immobilized on a solid phase with limited protein capacity, as is the case for ELISA, a large excess of antigen was used in this flow-through system, and epitope density was not a factor. Another advantage of DCIA is that all sides of the antigen could react with the antibody because it was free in solution. Immobilization of an antigen may cover up a face of the antigen so that antibodies recognizing the covered epitopes do not bind, resulting in titers that are smaller than the actual value.

## EXPERIMENTAL SECTION

**Materials.** Crystalline rabbit IgG (RiGG), human transferrin (HT<sub>r</sub>), and human serum albumin (HSA) were obtained in the purest grade available from Sigma Chemical Co. (St. Louis, MO). The rabbit anti-HT<sub>r</sub> was obtained as an immunoglobulin G (IgG) fraction of antiserum from Boehringer Mannheim Biochemicals (Indianapolis, IN). Human serum samples were donated by St. Elizabeth's Hospital (Lafayette, IN). The Bradford reagent for protein assays was purchased from Biorad Laboratories (Richmond, CA). HPLC-grade trifluoroacetic acid (TFA), acetic acid (Pierce Chemical Co., Rockford, IL), and acetonitrile and water (American Burdick & Jackson, Muskegon, MI) were used in the chromatographic analyses. All other reagents were analytical grade.

**Apparatus.** The experimental setup used for the assays is shown in Figure 1. All chromatography was performed at ambient temperature (22–25 °C). The automatic switching valve, V<sub>4</sub> (Rheodyne, Model 7010 attached to a Rheodyne Model 5701 pneumatic actuator), contained the analytical reversed-phase C-4 column (Supelco C304, 300 Å, 5 μm, 5 × 0.41 cm i.d.) in place of the sample loop. This allowed the protein G affinity column (500 Å, 30 μm, 10 × 0.46 cm i.d., a generous gift from Chromatchem, Inc., Missoula, MT) and the RPC column to be used either in series or separately depending on the position of the switching valve. Timing of the automatic switching valve was controlled by pump C (Hewlett-Packard Binary Gradient Liquid Chromatograph, Model 1090L) fitted with a manual injector, V<sub>5</sub> (Rheodyne, Model 7125), used to load samples onto the RPC column. Valve V<sub>1</sub> (Rheodyne, Model 7010) allowed the mobile phase for the affinity column to be switched rapidly between loading buffer in pump A (Beckman, Altex, Model 110) and desorption buffer in pump B (Eldex, Model 1011/B-100-S). Valve V<sub>2</sub> (Rheodyne, Model 7120) was used to load samples onto the

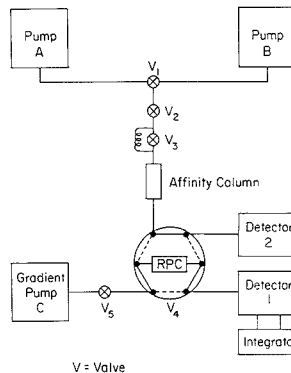


Figure 1. Apparatus for dual-column immunoassays.

protein G column and valve V<sub>3</sub> (Valco, Model C6U), equipped with a 3-mL injection loop, enabled the affinity column to be washed between each analysis. Absorbance of the eluent from both columns was monitored separately, using detector 1 (Kratos Spectroflow Variable Wavelength Detector, Model 773) at 280 or 215 nm for the RPC column and detector 2 (Altex, Model 153) at 254 nm for the affinity column. Both detectors were connected to a dual-pen recorder (Linear, Model 1200) and the output from detector 1 was also connected to an integrator (Waters, Model 740) which calculated peak areas for quantitation.

**Optimization of Loading and Desorption Conditions for Protein G Column.** The immobilized protein G is a recombinant product, GammaBind G (Genex Corp.). Nonspecific binding of 1 mg (100 μL, 10 mg/mL) of HT<sub>r</sub> and HSA on the protein G column was evaluated by measuring the percent recovery of these proteins in the loading buffer, 0.01 M sodium phosphate, 0.15 M NaCl (pH 7.4) at 2 mL/min. Triplicate samples and controls of each protein were collected in 10-mL volumetric flasks. The protein content was measured by using a Bradford assay (21).

The recovery of RiGG from the protein G column was evaluated by using various flow rates and desorption buffers recommended by the column manufacturer (22). Triplicate samples and controls of 800 μg of RiGG (100 μL, 8 mg/mL) were collected in 25-mL volumetric flasks. Bradford protein assays confirmed that percent recoveries could be calculated from peak area data if the sample peak areas were corrected for the small peak appearing in the desorption buffer blank. The loading buffer was 0.01 M sodium phosphate, 0.15 M NaCl (pH 7.4) in all cases except when 2% acetic acid, 0.25 M NaCl (pH 2.4) was the desorption buffer. In this instance, the NaCl concentration was increased to 0.25 M to keep the ionic strength constant. Recovery studies evaluating different desorption buffers were done by using a flow rate of 2 mL/min. Flow rate recovery studies were done by using 0.10 M glycine, 2% acetic acid (pH 2.9) as the desorption buffer. Both loading and desorption steps were at the same flow rate (0.5–4 mL/min). The affinity column was cleaned with 3 mL of 20% acetic acid between analyses.

**Method for Antibody Titer Quantitation by Off-Line Incubation.** A schematic diagram for this method of antibody titer quantitation is shown in Figure 2. Anti-HT<sub>r</sub> was incubated with an excess of HT<sub>r</sub> before the mixture was injected onto the protein G column. For incubation time experiments, triplicate samples of 20 μL of anti-HT<sub>r</sub>, 1 mg of HT<sub>r</sub>, in 1 mL of loading buffer, 0.01 M sodium phosphate, 0.15 M NaCl (pH 7.4) were incubated at 4 °C for 1 to 72 h. A control was run using nonimmune RiGG (100 μg) in place of the anti-HT<sub>r</sub> and 1 mg of HT<sub>r</sub> incubated for 24 h. Excess antigen experiments were conducted in triplicate using samples of 20 μL anti-HT<sub>r</sub> in 1 mL of loading buffer, incubated for 48 h with antigen amounts ranging from 80 to 1000 μg. The valve switching sequence for the assays is listed in Table I. The protein G column was equilibrated in loading buffer using pump A at 2 mL/min. The antigen-antibody mixture was injected onto the protein G column, via the 3-mL loop of valve V<sub>3</sub> (event 1). After 5 min, when absorbance of the eluent from



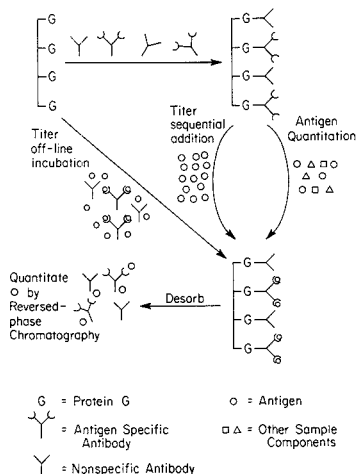


**Figure 2.** Schematic diagram of antibody titer determinations and antigen quantitation.

**Table I.** Valve Switching Sequence for DCIA

event	time, min	valve	description
1	0		titer, off-line incubation
		V <sub>3</sub>	inject antigen/antibody mixture
			titer, sequential addition
		V <sub>2</sub>	inject antibody, then antigen
			antigen quantitation
		V <sub>3</sub>	inject antibody
		V <sub>2</sub>	inject standards or samples
2	5	V <sub>4</sub>	affinity and RPC switched in series
3	5	V <sub>1</sub>	switched to pump B (desorption buffer)
4	15	V <sub>4</sub>	RPC switched back in-line with gradient pump and RPC analysis started
5	15	V <sub>1</sub>	switched to pump A (loading buffer)
6	17	V <sub>3</sub>	inject 3 mL of 20% acetic acid

the affinity column, monitored by detector 2, had returned to base line, the automatic switching valve, V<sub>4</sub>, was switched to place the affinity and RPC columns in series (event 2). Valve V<sub>1</sub> was switched (event 3) and pump B delivered desorption buffer (0.10 M glycine, 2% acetic acid at 2 mL/min) into the affinity column, desorbing the antigen-antibody complexes from the affinity column and concentrating them on the head of the RPC column. After 10 min, V<sub>4</sub> was switched (event 4), connecting the RPC column back to the gradient pump C and valve V<sub>1</sub> was switched (event 5) to pump A (loading buffer). The chromatographic conditions for the reversed-phase analyses started with an 8-min linear gradient from 0 to 35% of 0.1% TFA in acetonitrile at 1 mL/min. These conditions were held until 11 min, followed by a 5-min linear gradient up to 100% of 0.1% TFA in acetonitrile. Between analyses, a 5-min linear gradient from 0 to 100% of 0.1% TFA in acetonitrile was used to wash the RPC column. Absorbance was monitored at 280 nm. During the reversed-phase analyses, the protein G column was washed with 3 mL of 20% acetic acid, using valve V<sub>3</sub> (event 6) reequilibrated and reloaded with sample (event 1). The amount (micrograms) of HTr bound to the antibody was quantitated by peak area using a calibration curve generated with HTr standards (20  $\mu$ L, 1.25, 2.50, 3.75, 5.00 mg/mL) on the RPC column alone.

**Method for Antibody Titer Quantitation by Sequential Addition.** In this method, antibodies and antigen are bound sequentially onto the protein G column as illustrated in Figure 2. Excess antigen studies were performed in triplicate as follows. The valve switching for this assay is listed in Table I. Anti-HTr (20  $\mu$ L) was injected onto the protein G column via valve V<sub>2</sub> (event

**Table II.** Effect of Desorption Buffer on Rabbit IgG Recovery from Protein G Column

desorption buffer	% RIgG recovery
0.10 M glycine (pH 2.2)	26.0 $\pm$ 6.0
0.01 M glycine, 0.15 M NaCl (pH 2.2)	62.4 $\pm$ 4.2
2% acetic acid, 0.15 M NaCl (pH 2.4)	94.9 $\pm$ 2.3
2% acetic acid, 0.25 M NaCl (pH 2.4)	40.9 $\pm$ 4.0
20% acetic acid (pH 2.1)	93.6 $\pm$ 6.7
0.05 M sodium citrate (pH 2.2)	75.3 $\pm$ 4.4
0.10 M glycine, 2% acetic acid (pH 2.9)	102.1 $\pm$ 1.7

1). Then, successive 20- $\mu$ L injections of HTr solutions of concentrations ranging from 1.25 to 10 mg/mL were injected onto the protein G column at 1 mL/min and monitored by detector 2 until two successive injections attained the same peak height (event 1). This ensured that antibodies bound to the protein G column were saturated with antigen. The antigen-antibody complexes were desorbed from the protein G column using the same sequence of events described in the preceding section, and the amount of HTr was quantitated.

The titer of the antibody fraction was determined by quantitating the amount (micrograms) of HTr that bound to different volumes of antibody sample. Triplicate samples of 10, 20, and 30  $\mu$ L of the same solution of anti-HTr were injected into the protein G column and then saturated with antigen using successive injections of HTr (20  $\mu$ L, 10 mg/mL).

**Antigen Quantitation.** For this method, the antiserum was loaded first on the protein G column, followed by the sample containing the antigen as illustrated in Figure 2. The sequence of events for the rest of the analysis is also listed in Table I and was the same as described in the previous section. Both flow rate and antiserum equivalent studies were done in triplicate using 25  $\mu$ g of HTr (20  $\mu$ L, 1.25 mg/mL). For the flow rate studies, HTr was loaded onto 30  $\mu$ L of anti-HTr using flow rates ranging from 0.2 to 2.0 mL/min. Antiserum equivalent experiments were performed by using equivalents of antiserum ranging from 1 to 5 (11 to 55  $\mu$ L). One equivalent of antiserum contained the exact amount of antibody, based on its titer, that should have reacted with all of the antigen.

The amount of HTr present in two human serum samples was quantitated by DCIA using a calibration curve generated by duplicate injections, using valve V<sub>3</sub> of HTr standards (20  $\mu$ L, 1.25, 2.50, 3.75, and 5.00 mg/mL) and an antiserum equivalent of 2.5. Duplicate 20- $\mu$ L aliquots of each human serum sample were analyzed.

A second calibration curve was generated by monitoring the RPC column with detector 1 at 215 nm. Duplicate injections of HTr standards in amounts ranging from 0.50 to 100  $\mu$ g (20  $\mu$ L, 0.0025–5.0000 mg/mL) were analyzed.

## RESULTS AND DISCUSSION

**Optimization of Loading and Desorption Conditions for Protein G Column.** Variable mobile phases and flow rates were evaluated in order to determine which gave the least amount of nonspecific binding of proteins and the highest amount of binding and recovery of RIgG from the protein G column. The manufacturer's reported capacity of the protein G column was 27.4 mg of human IgG per column. All of the recovery studies were done using less than 1 mg of RIgG, hence never exceeding  $1/27$  of the column IgG capacity.

The percent recovery of HTr and HSA from the protein G column was 98.7  $\pm$  0.3% and 97.5  $\pm$  1.0%, respectively. This showed no significant binding of both proteins when the loading buffer 0.01 M sodium phosphate, 0.15 M NaCl (pH 7.4) was used. As shown in Table II, desorption of RIgG from the protein G column was dependent on ionic strength. A change in ionic strength of 0.10 M (0.15–0.25 M) NaCl in 2% acetic acid (pH 2.4) resulted in a drastic decrease in percent recovery (from 94.9 to 40.9). Of all the desorption buffers listed in Table II, 0.10 M glycine, 2% acetic acid (pH 2.9) gave the highest percent recovery of RIgG (102  $\pm$  1.7%). This buffer was used throughout the rest of this work.

**Table III. Effect of Flow Rate on Rabbit IgG Recovery from Protein G Column**

flow rate, <sup>a</sup> mL/min	% RIgG recovery <sup>b</sup>	flow rate, <sup>a</sup> mL/min	% RIgG recovery <sup>b</sup>
0.5	100.0 ± 6.8	3.0	100.8 ± 2.6
1.0	97.8 ± 4.0	4.0	102.1 ± 3.5
2.0	102.1 ± 1.7		

<sup>a</sup>Flow rate for loading and desorption. <sup>b</sup>Recoveries measured by using 0.10 M glycine, 2% acetic acid (pH 2.9) as desorption buffer.

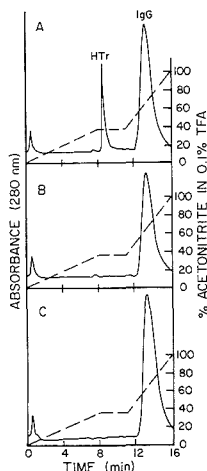


**Figure 3.** Reversed-phase separation of antigens and antibodies captured and desorbed from protein G column: (A) anti-HTr (10  $\mu$ L), HTr (1 mg); (B) anti-HTr (10  $\mu$ L); (C) nonimmune RIgG (100  $\mu$ g), HTr (1 mg). Chromatographic conditions are given in text.

The amount of RIgG bound and recovered from the protein G column was not influenced by loading and desorption flow rate as shown in Table III. Consequently, these assays can be performed rapidly by using high flow rates. However, the back pressure of the protein G and RPC columns in tandem may limit the flow rate that can be used. An intermediate mobile phase velocity of 2 mL/min was chosen for these studies.

**Antibody Titer Quantitation.** Two methods were used to measure the antibody titer as illustrated in Figure 2. The off-line incubation method involved incubating the antibody fraction with a large excess of antigen prior to injection onto the protein G column. In the sequential addition method, antibody and excess antigen were sequentially loaded onto the protein G column. In both cases, antigen-antibody complexes were desorbed and dissociated from the protein G column and concentrated on the RPC column. Dissociation of the antigen-antibody complexes was also aided by the reversed-phase mobile phases (0.1% TFA and acetonitrile). Antigen (HTr) and antibody (anti-HTr) were then separated by RPC as shown in Figure 3A. The broad IgG peak is typically found in the reversed-phase chromatography of polyclonal antibodies due to the heterogeneous mixture of IgG subclasses (23).

Figure 3 illustrates the results of three DCIAs by using different samples to prove that HTr only bound to the protein G column in the presence of anti-HTr (Figure 3A). When anti-HTr was injected alone, only IgG was bound (Figure 3B). However, when nonimmune RIgG and HTr were injected, only RIgG (no HTr) was bound (Figure 3C). Additional evidence

**Table IV. Influence of Incubation Time on Off-Line Antibody Titer Quantitation**

incubation time, h	HTr, $\mu$ g	incubation time, h	HTr, $\mu$ g
0	63.9 ± 1.9	10	74.8 ± 2.1
1	73.9 ± 6.8	15	72.4 ± 7.2
2	82.4 ± 4.0	20	77.9 ± 0.1
3	75.2 ± 5.8	24	78.1 ± 5.7
5	73.7 ± 10.1	72	75.2 ± 1.4

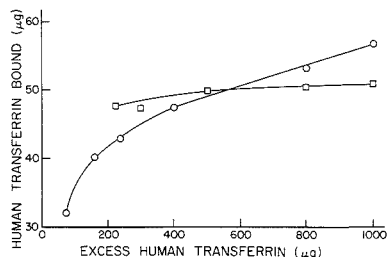


**Figure 4.** Influence of excess antigen concentration on the antibody titer: O, off-line incubation; □, sequential addition.

for minimal nonspecific binding of HTr was the high percent recovery of HTr from the protein G column previously reported.

For the off-line incubation method, the influence of incubation time and excess antigen concentration on the amount of HTr bound to anti-HTr was studied. The amount of HTr (micrograms) bound to the affinity column was determined from a HTr calibration curve generated by using the RPC column alone. The least-squares regression equation was  $y$  (HTr peak area) =  $1.69x$  ( $\mu$ g of HTr) - 3.3 with correlation coefficient of 0.997 and relative standard deviation (RSD) values of  $\pm 2\%$ . This calibration curve was regenerated for every study, and the correlation coefficient and RSD remained the same.

Table IV lists the influence of incubation time. Overall, after 1 h, the amount of HTr bound does not appear to be influenced by incubation time. Experimental precision was very poor with RSD values ranging from  $\pm 0.1\%$  to  $\pm 13.7\%$ . Variations in incubation temperature, and temperature of the antigen-antibody mixture at injection, probably caused some of these fluctuations. Also, the amount of HTr bound to antibody varied with the amount of excess antigen incubated with the antiserum, as shown in Figure 4. The precision of these values was also poor, with RSD values ranging from  $\pm 1.6\%$  to  $\pm 11.2\%$ . The shape of the curve demonstrated that this method is dependent on the equilibrium between antibody and antigen. The amount of HTr bound increased as the amount of excess HTr increased. (The curve would eventually reach a plateau.) No precipitation of the antibody and antigen was noted in any of the mixtures prior to injection onto the protein G column.

Figure 4 shows that unlike the off-line incubation method, the amount of HTr bound for the sequential addition method was not as dependent on the excess antigen concentration. This method was also more precise, with all measurements having RSD values of  $\pm 2\%$ . The sequential addition method reported smaller antibody titers than the off-line method at excess antigen concentrations greater than 600  $\mu$ g. Although these experiments used conditions (antigen excess) reported to be antibody affinity independent for ELISA, this system does not operate under equilibrium conditions. The off-line incubation method is equilibrium dependent and was consequently able to detect very low affinity antibodies present

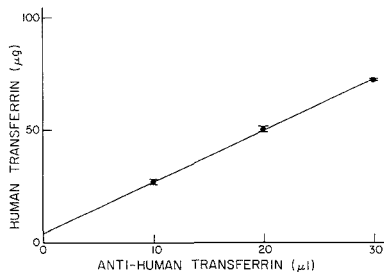


Figure 5. Determination of titer of anti-HTr by sequential addition.

Table V. Influence of Flow Rate on Antigen Quantitation

flow rate, mL/min	HTr peak area	flow rate, mL/min	HTr peak area
0.2	21.61 ± 0.49	1.0	20.58 ± 1.77
0.5	21.22 ± 1.32	2.0	21.70 ± 0.61

in the antibody fraction by using a large excess of antigen. Therefore, off-line incubation is the method of choice for titer measurements made early in the immune response, when low affinity antibodies predominate.

The sequential addition method, which was more precise and less dependent on excess antigen concentration, was used to determine the titer of the anti-HTr antibody fraction as shown in Figure 5. The plot of the amount (micrograms) of HTr bound versus the amount (microliters) of anti-HTr yielded a least-squares regression equation of  $y(\mu\text{g of HTr}) = 2.27x(\mu\text{L of anti-HTr}) + 4.60$  with a correlation coefficient of 0.999 and RSD  $\pm 2.8\%$ . The slope of the line,  $2.27 \mu\text{g of HTr}/\mu\text{L of anti-HTr}$  was the titer of the antibody sample. The manufacturer's reported titer, determined by single radial immunodiffusion (24), was  $2.0 \pm 0.2 \mu\text{g of HTr}/\mu\text{L of anti-HTr}$ . (Good agreement between these values may actually be because neither method measured very low affinity antibodies.) The major difference is that single radial immunodiffusion requires precipitating antiserum and DCIA does not. DCIA is much more flexible and can be used for monoclonal antibodies as well.

Determination of antibody titers by DCIA may have many useful applications, such as the measurement of the immune response in patients using therapeutic recombinant proteins. When higher sensitivity is required, antigens labeled with a tag, such as a fluorophore or an enzyme could be used.

**Antigen Quantitation.** DCIA was also used to quantitate antigen as illustrated in Figure 2. Antibodies were loaded onto the protein G column, creating an immunoaffinity support. The sample was injected and antigen was captured, desorbed, and quantitated by RPC.

The influence of flow rate and amount of antibody on the amount of HTr bound was studied in order to determine optimum conditions for the assay. Table V shows that the amount of HTr bound by the antibody was the same for flow rates ranging from 0.2 to 2.0 mL/min. A flow rate of 2 mL/min was chosen for the same reason stated previously.

The influence of the amount of antibody on the amount of antigen bound was studied by loading the protein G column with increasing equivalents of anti-HTr and a constant amount (25  $\mu\text{g}$ ) of HTr. One equivalent of anti-HTr (11  $\mu\text{L}$ ) contained the exact amount of antibody, based on its titer (2.27  $\mu\text{g of HTr}/\mu\text{L of anti-HTr}$  measured by dual-column immunoassay in the previous section) which should react with all 25  $\mu\text{g}$  of the antigen. Figure 6 shows that 2 equiv of anti-HTr were sufficient to obtain maximal antigen binding. No increased

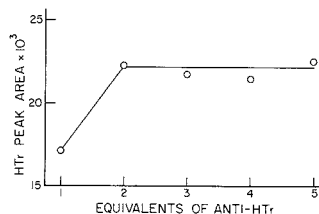


Figure 6. Influence of antiserum equivalents on antigen quantitation.

Table VI. Comparison of Values Obtained for HTr Concentrations in Human Serum Determined by DCIA and Rate Nephelometry

sample	DCIA, <sup>a</sup> mg/mL	rate nephelometry, <sup>b</sup> mg/mL
1	1.43 ± 0.09	1.35
2	1.71 ± 0.10	1.65

<sup>a</sup>RSD is  $\pm 6.0\%$ . <sup>b</sup>Manufacturer's reported RSD is  $\pm 5\%$ .

binding of HTr was gained by using antiserum equivalents. The rest of this work was done with 2.5 equiv of antiserum.

The concentration of HTr in human serum samples was quantitated by DCIA. A plot of peak area versus the concentration of HTr yielded a least-squares regression equation of  $y(\text{peak area HTr}) = 17.94x(\text{HTr, mg/mL}) - 1.026$  with a correlation coefficient of 0.9996 and RSD values  $\pm 5.6\%$ . The values obtained by DCIA were compared (Table VI) to those obtained by rate nephelometry using a Beckman Analyzer II (Brea, CA) at St. Elizabeth Hospital (Lafayette, IN). Rate nephelometry measures the increase in light scatter resulting from the antigen-antibody reaction. Within error, both methods showed good agreement. The RSD of the DCIA method was slightly higher ( $\pm 6\%$ ) than the manufacturer's reported value for rate nephelometry ( $\pm 5\%$ ).

The detection limits and linear dynamic range of the HTr DCIA were measured. The calibration curve showed that the assay had a detection limit of 50 ng (0.7 pmol) at 215 nm and was linear over approximately 4 orders of magnitude from  $5 \times 10^1$  to  $1 \times 10^5$  ng. The calibration curve had a correlation coefficient of 0.999 and RSD values of  $\pm 3.5\%$ .

DCIA was more sensitive than conventional immunoaffinity chromatography. The antigen, which eluted from the immunoaffinity column as a broad peak, was concentrated on the second more efficient column. Also the second column, unlike the immunoaffinity column, could be monitored at shorter wavelengths (e.g. 215 nm) and high detector gain and improved the sensitivity of the assay by at least 2 orders of magnitude.

DCIA had better precision and a wider linear dynamic range than standard ELISA. Typical RSD values for ELISA range from 5 to 15% (25) while the values obtained for DCIA were  $\pm 3.5\%$ . ELISA generally has a range of 2-3 orders of magnitude. The linear dynamic range of DCIA covered approximately 4 orders of magnitude. A much wider range of sample volumes (0.001-2.000 mL) could be used for DCIA because it was a flow-through system. ELISA sample volumes are limited to  $<0.200$  mL because of the size of the microtiter plate well.

The limit of detection is lower for ELISA (nanograms to picograms) (26) than for DCIA (micrograms to nanograms). However the discriminating ability of DCIA is superior to ELISA. Nonspecific binding and nonspecificity of the antisera can cause great interferences in ELISA. The second column in DCIA adds another separation step which can help distinguish species which cross reacted or bound nonspecifically

to the immunosorbent from the analyte of interest. Conventional chromatographic methods have been able to discriminate variants that were indistinguishable by an immunological method (7, 8, 10). A simultaneous immunoassay of multiple antigens can also be performed by DCIA provided the antigens can be separated by RPC or another chromatographic mode.

Both ELISA and DCIA can be automated. The throughput of DCIA was 40-50 samples/day with each assay requiring 30 min. ELISA usually requires 24 h for completion; however the throughput can be up to 1000 samples/day if the system is automated. DCIA was intended for use in biotechnology for research and required a skilled technician, whereas ELISA does not.

The biggest advantages of DCIA were its simplicity, versatility, and ease of implementation. The protein G column served as a universal support for immobilizing mammalian antibodies. A different antigen could be assayed for each run. Antibodies were not covalently immobilized, so loss of antigen binding capacity was not a concern as it is in conventional immunoaffinity analysis. The protein G column had a long lifetime. Most of the analyses were done by using less than 1/90 of the total IgG column capacity. A gradual decrease in capacity over time would not cause a problem because of the large excess of protein G over IgG. After 5 months of use (>500 cycles) the protein G column was still in good condition.

Reagent preparation or synthesis was not required for DCIA. The protein G column could selectively bind and purify IgG from whole serum, so purification of the antiserum was not required. Also since relatively low detection limits were easily obtained by DCIA, without using labeled immunological reagents, antigen specific reagent synthesis was not required before a new immunoassay could be performed (as is the case for ELISA and other methods).

#### ACKNOWLEDGMENT

We thank R. Hammen from Chromatochem, Inc., for the timely gift of the protein G column. We also thank St. Eli-

zabeth Hospital for human serum samples and the rate nephelometry data.

#### LITERATURE CITED

- (1) Varady, L.; Kalghatgi, K.; Horvath, C. J. *Chromatogr.* **1988**, *458*, 207.
- (2) Heineman, W. R.; Halsall, H. B. *Anal. Chem.* **1985**, *57*, 1321A.
- (3) De Alwis, W. U.; Wilson, G. S. *Anal. Chem.* **1985**, *57*, 2756.
- (4) De Alwis, W. U.; Wilson, G. S. *Anal. Chem.* **1987**, *59*, 2786.
- (5) Nilsson, B. J. *Chromatogr.* **1983**, *276*, 413.
- (6) Johansson, B. J. *Chromatogr.* **1986**, *381*, 107.
- (7) Rybacek, L.; D'Andrea, M.; Tarnowski, S. J. *J. Chromatogr.* **1987**, *397*, 355.
- (8) Janis, L. J.; Regnier, F. E. *J. Chromatogr.* **1988**, *444*, 1.
- (9) Farjam, A.; De Jong, G. J.; Fre, R. W.; Brinkman, U. A. Th.; Haasnoot, W.; Hamers, A. R. M.; Schilt, R.; Huf, F. A. *J. Chromatogr.* **1988**, *452*, 419.
- (10) Janis, L. J.; Grott, A.; Smith-Gill, S. J.; Regnier, F. E. *J. Chromatogr.*, in press.
- (11) Mattiasson, B.; Borrebaeck, C. In *Proceedings of the International Symposium on Enzyme Labeled Immunoassay of Hormones and Drugs*; Pal, S., Ed.; Walter de Gruyter: Berlin, 1978; p 91.
- (12) Reiss, K. J.; Von Mering, G. O.; Karis, M. A.; Faulmann, E. L.; Lotenber, R.; Boyle, M. D. P. *J. Immunol. Methods* **1988**, *107*, 273.
- (13) Akerstrom, B.; Brodin, T.; Reiss, K. J.; Björck, L. *J. Immunol.* **1985**, *135*, 2569.
- (14) Phillips, T. M.; Queen, W. D.; More, N. S.; Thompson, A. M. *J. Chromatogr.* **1985**, *327*, 213.
- (15) Harcoe, N. M. G.; Ingild, A. *Scand. J. Immunol., Suppl.* **1983**, *17*, 10, 345.
- (16) Butler, J. E.; Feldbush, McGivern, P. L.; Stewart, N. *Immunochimistry* **1978**, *131*.
- (17) Peterly, F.; Kuusela, P.; Makela, O. *J. Immunol.* **1983**, *130*, 1809.
- (18) Lew, A. M. *J. Immunol. Methods* **1984**, *72*, 171.
- (19) Nimmo, G. R.; Lew, A. M.; Stanley, C. M.; Steward, M. W. *J. Immunol. Methods* **1984**, *72*, 177.
- (20) Griswold, W. R. *Mol. Immunol.* **1987**, *24*, 1291.
- (21) Bradford, M. M. *Anal. Biochem.* **1976**, *72*, 243.
- (22) *HIPac Protein G Affinity Chromatography: Guideline*; Chromatochem, Inc.: Missoula, MT.
- (23) Thevenon, G.; Regnier, F. E. *J. Chromatogr.*, in press.
- (24) Becker, W. *Immunochimistry* **1969**, *539*.
- (25) Clark, B. R.; Engvall, E. In *Enzyme Immunoassay*; Maggio, E. T., Ed.; CRC Press, Inc.: Boca Raton, FL, 1980; p 177.
- (26) Monroe, D. *Anal. Chem.* **1984**, *56*, 920A.

RECEIVED for review May 6, 1989. Accepted May 19, 1989. This work was supported by NIH Grant GM25431-10. This is journal paper no. 11,977 from the Purdue University Agricultural Experiment Station.

## Direct Coupling of Planar Chromatography to Gas Chromatography by Laser Desorption

Jianzhong Zhu and Edward S. Yeung\*

Ames Laboratory—USDOE and Department of Chemistry, Iowa State University, Ames, Iowa 50011

**A method of direct coupling of thin-layer chromatography (TLC) to gas chromatography (GC) is demonstrated with pesticide samples. Laser desorption with a special TLC cell was used for the interface. Factors affecting the transfer efficiency and the parent peak ratio were studied. The fragmentation pattern in the gas chromatogram provides a fingerprint for each TLC separated compound. For TLC separations of complex mixtures, GC provides one more dimension of separation and sensitive detection. Laser desorption with electron capture detection (no GC column) was also demonstrated as a universal quantitative technique for TLC. The limit of detection was in the low nanogram range. The scan speed was 5 times faster, the detection limit was 20 times lower, and the resolution was 2 times better than the analogous laser pyrolysis method.**

Thin-layer chromatography (TLC) is a widely employed

analytical technique that provides a simple, rapid, and inexpensive separation method. In terms of instrumentation, detection, separation and identification, TLC is not as well developed as column liquid chromatography, although some aspects have been improved by the recent development of high-performance TLC and novel methods of detection (1-15). TLC still plays an important role in the separation of complex samples. For example, highly retained compounds may eventually degrade a column but are compatible with TLC since the plates are disposable. Because TLC is capable of handling multiple samples in short time, it is extensively used in routine clinical and drug testing, where hundreds of samples are analyzed every day and only a few TLC-test-positive samples are sent to HPLC or GC/MS for confirmation (16-19). Also, many GC analyses of environmental and biomedical samples directly or indirectly rely on TLC for sample cleanup to protect the GC column or to avoid background interference. Therefore, direct coupling of TLC to

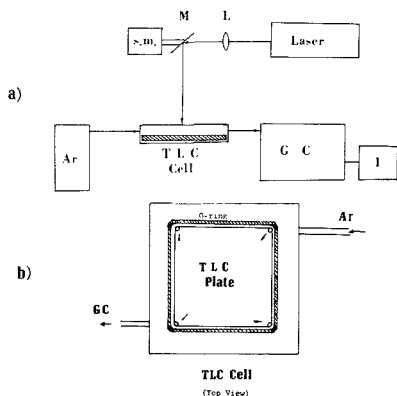


**Figure 1.** (a) Schematic diagram of the laser desorption interface. (b) Details of the TLC cell. Key: L, lens (focal length = 50 cm); M, mirror; s.m., stepping motor; I, integrator.

GC should find broad applications in many areas of analysis.

On-line multidimensional chromatography has attracted increasing attention recently because of increased separation efficiency. The on-line combinations of HPLC/GC, HPLC/TLC, and GC/TLC were reported (20–24). In off-line combinations, the TLC spot was scraped off, redissolved, and then injected into LC or GC. Direct coupling of TLC to GC or to HPLC has not been reported in the literature, probably because of the sample transfer difficulties, where a solid to gas or solid to liquid transition with spatial resolution (on the TLC plate) is required.

An ion source has been used for direct solid-gas phase transfer in TLC/secondary ion mass spectrometry (SIMS) to extract samples from the plate without loss of resolution (25–27). However, SIMS is only sensitive to the first few atomic layers of the sample and thus most of the sample on the TLC plate (buried in the silica particles) was inaccessible unless it is first extracted. Some other techniques including fast atom bombardment (FAB) and laser microprobe analyzer (LMA) were also applied in TLC/MS for direct identification of the TLC spotted compounds (8, 28). High TLC adsorbent backgrounds were observed. Identification becomes even more difficult if the compounds are not well separated. The combination of TLC/GC to MS should be free from most of these problems, since GC would further discriminate against the TLC background and distinguish between unseparated compounds.

The purpose of present work is to develop an interface for direct coupling of TLC to high-resolution GC based on laser desorption. Without the GC column, this technique should also work as a universal quantitative scanning method for TLC by taking advantage of any of the existing GC detectors.

#### EXPERIMENTAL SECTION

**Apparatus.** The schematic diagram of the TLC/GC interface is shown in Figure 1a. The laser was a Model HyperEX 460 (Lumonics, Ottawa, Canada) and operates at 308 nm. The laser repetition rate was varied from 10 to 200 Hz. The pulse energy ranged from 10 to 18 mJ as measured by radiometer (Laser Precision, Utica, NY, Model Rj-7200) with an energy probe (Laser Precision, Utica, NY, Model Rjp-734). The laser beam was focused to about  $2 \times 3$  mm with a quartz lens (focal length = 50 cm) and directed by a mirror driven by a stepping motor.

The TLC cell was constructed with copper and consisted of either a 50 mm (long)  $\times$  50 mm (wide)  $\times$  8 mm (deep) or a 50 mm (long)  $\times$  10 mm (wide)  $\times$  8 mm (deep) chamber to accommodate the TLC plate. The top of the chamber was covered by a quartz window sealed with an O-ring. The details of the TLC

cell are shown in Figure 1b. The carrier gas (argon + 10% methane) enters from three corners of the chamber, passes above the surface of the TLC plate, and then flows out of the other corner to a GC inlet or directly to a GC detector. The flow rate was about 100 mL/min during the sample collection or the laser desorption process and was reduced to 15 mL/min during GC separation.

**Thin-Layer Chromatography.** Normal-phase silica gel plates (Alltech, Deerfield, IL, Adsorbisil HPTLC) were used. The plates were cut to the sizes required and cleaned with methanol only. A 0.2- $\mu$ L portion of the pesticide sample was spotted on the plate by a 1.0- $\mu$ L Hamilton microsyringe.

In the experiments involving quantitative scanning without GC separation, for a lower background, the plate was prescanned with the laser and the sample introduction and TLC separation were performed in a glovebox filled with nitrogen to avoid contact with air. Plates were developed with hexane and dried under a 200-W infrared lamp for 2 min to evaporate the solvents. A carrier gas flow rate of 300 mL/min was used.

**Gas Chromatography.** A Model 550 gas chromatograph (Tracor, Austin, TX) with an electron capture detector was equipped with a 30 m  $\times$  0.53 mm (i.d.) DB-1701 fused silica column (J&W Scientific, Folsom, CA). The oven temperature was programmed at 30  $^{\circ}$ C for 5 min and then raised 10  $^{\circ}$ C/min to 200  $^{\circ}$ C. The data collection was accomplished with an integrator (LDC, Riviera Beach, FL, CI 3000). The column was directly connected to the TLC cell through a stainless steel tubing via the GC inlet. The tubing was heated by a heating tape to around 250  $^{\circ}$ C to prevent sample deposition.

**Chemicals.** The pesticide standards were purchased from Alltech Associates, Inc. (Deerfield, IL), and used as received. They were dieldrin, *p,p*-DDT, lindane, and methoxychlor. Samples were dissolved in hexane and diluted to various concentrations. All solvents used were HPLC grade.

#### RESULTS AND DISCUSSION

Laser desorption (LD), particularly with pulsed lasers, is an attractive technique for rapid vaporization of solid molecular samples. It has been widely investigated as a sampling method in mass spectrometry for both volatile and nonvolatile organic compounds (29, 30). Laser desorption is simply based on the rapid heating effect in which the molecules desorb before they have time to kinetically decompose (11, 25). However, certain kinds of fragmentation processes have also been observed. These are related to laser power density, laser wavelength, and the thermal stability of the compounds (31). The same mechanism is expected in the laser desorption of TLC adsorbed molecules, although the experimental requirements may be very different. Quantitative transfer and the production of neutral molecules are the main concerns in TLC/GC, while enhancements of ionization processes are more important in laser desorption mass spectrometry (LDMS). Therefore, low laser power density ( $5 \times 10^6$  W/cm $^2$ ) and multiple pulses (around 1000 pulses) were used in this experiment instead of the high power density and single shot conditions in LDMS.

The gas chromatograms of four pesticides directly removed from TLC plates by laser desorption are shown in Figure 2. The experimental conditions of GC have not been optimized. For the first 5 min, the column was left at room temperature to trap the material from a given spot. This effectively provides a small injection volume. There are two intriguing features in the TLC/GC results shown in Figure 2. First, it demonstrates sensitive detection for TLC by GC detectors without TLC adsorbent background interference. The background peaks were marked by "b" and they were identified by their GC retention times. There were four major background peaks. They correspond to the peaks at 9.03, 10.57, 11.68, and 13.15 min in Figure 2b,c. These are derived from breakdown of the TLC stationary phase by the laser. No attempts were made to identify them, however. The background peak at 9.03 increased dramatically at high laser



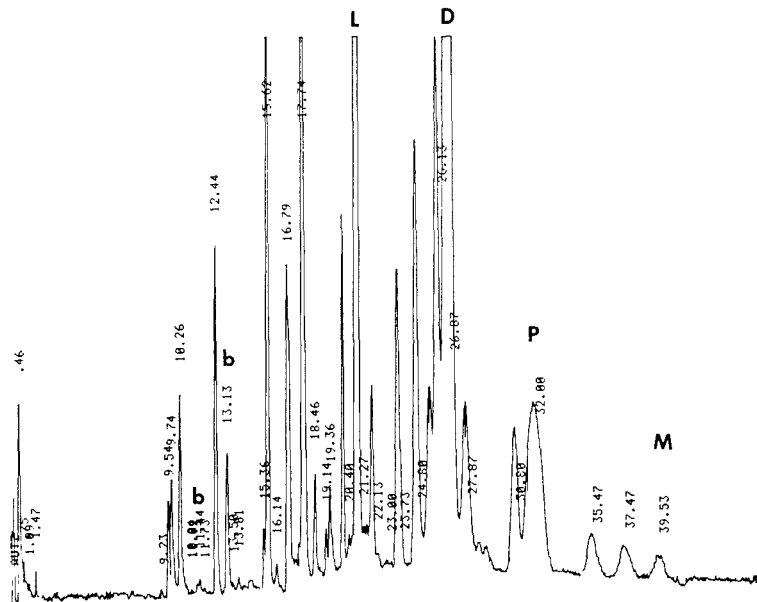


**Figure 3.** Gas chromatogram of a TLC spotted mixture (without separation) by laser desorption. The mixture contains L, lindane (200 ng), D, dieldrin (200 ng), P, *p,p*-DDT (200 ng), and M, methoxychlor (200 ng); laser 14 mJ/50 Hz, 1000 shots; and ECD detector attenuation  $\times 32$ .

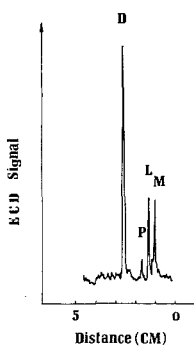


**Figure 4.** Thin-layer chromatogram of four pesticides with laser desorption scanning and electron capture detection (no GC separation): D, dieldrin (12.6 ng); P, *p,p*-DDT (6.8 ng); L, lindane (5.0 ng); M, methoxychlor (6.8 ng); laser energy, 16.5 mJ/pulse; repetition rate, 50 Hz; scan speed, 10 cm/min; flow rate of carrier gas, 300 mL/min; ECD output attenuation,  $\times 8$ ; TLC plate,  $5 \times 5$  cm. A  $0.1\text{-}\mu\text{L}$  portion of sample was introduced by a  $1.0\text{-}\mu\text{L}$  syringe and developed with hexane.

with a higher carrier gas flow should minimize this problem. The distance between the TLC plate and the window is also critical. With a distance of 1 mm, less than 10% of lindane was detected, even though the linear flow rate in the chamber was higher with the smaller chamber volume. A distance of 5 mm was optimal for the flow rate used here. Still higher flow rates were not compatible with GC and the resulting pressure is too high for our particular TLC cell.

TLC/GC coupling offers one more dimension of separation. Figure 3 presents a well separated GC chromatogram of a mixture of four pesticides which was spotted on the TLC plate with no separation. This simulates overlapping components

causing a loss of signal. A proper design of the TLC chamber on the TLC plate. Here the analytes and their fragmentation fingerprints can be easily identified based on the individual chromatograms in Figure 2.

**Quantitative Scanning.** For laser scanning alone, the TLC cell was directly connected to a GC detector without the GC column. Quantitative scanning of TLC plates for detecting amino acids and pesticides by a continuous wave infrared laser with a flame ionization detector (FID) or an electron capture detector (ECD) has been demonstrated in an earlier paper (LPS, laser pyrolysis scanning) (6). The system here represents laser desorption scanning (LDS). The advantage of LDS is brought about by pulsed laser operation, which provides high power density, fast heating, and rapid cooling, leading to better scanning resolution and fewer fragments. For efficient transfer of the analytes, a higher laser power density is needed. But a high power continuous wave laser would easily break the TLC plates. The scanning speed and spatial resolution are increased due to fast vaporization and less heat conduction to the neighboring spots. Figure 4 shows a demonstration of LDS for the four TLC separated pesticides: dieldrin, *p,p*-DDT, lindane, and methoxychlor. The detection limit is in the 1 ng range and the scan rate was 10 cm/min. The detection limit is about a factor of 20 better than LPS reported earlier (8). To achieve this level of performance, the TLC plate was precleaned, developed, and detected in a nitrogen environment to avoid oxygen, moisture, and other laboratory contamination.

The signal dependence on laser energy and the laser pulse frequency in a scanning mode is shown in Figure 5 for 250 ng of lindane. It should be noted that the signal level was also position dependent. When the spot was in a location close to the outlet of the chamber, it produces larger signals, particularly for a  $50 \times 50$  mm TLC plate. Readsorption and peak dispersion may be the causes of this spatial dependence. Samples were spotted at the same position in Figure 5 for

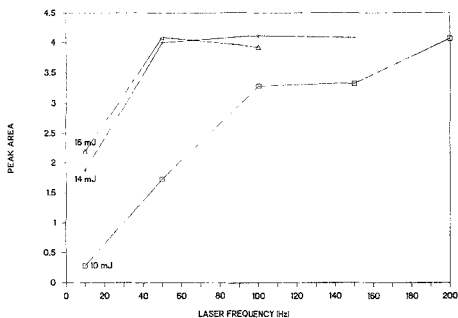


Figure 5. ECD signal dependence on laser energy and repetition rate in laser desorption scanning TLC of 250 ng of lindane: attenuation,  $\times 512$ .

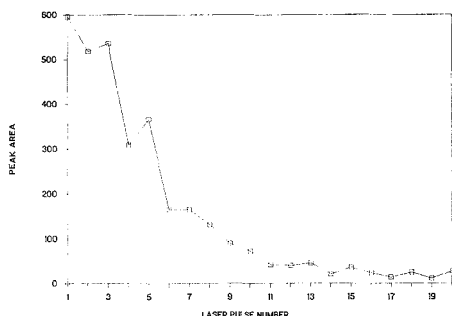


Figure 6. ECD signal for consecutive laser pulses: sample, lindane (200 ng); laser energy, 16 mJ/pulse; repetition rate, 0.05 Hz.

comparisons. The results indicate that complete vaporization of the sample spot occurs above 40 Hz for 14 and 16 mJ/pulse. On the other hand, it takes 200 Hz to vaporize the entire sample at 10 mJ/pulse. The thermal effects at higher repetition rates compensate for the lower powers of the pulses. Therefore, for maximum vaporization at low powers and low repetition rates, the scan rate will have to be reduced. However, the signal (Figure 4) may not increase because the material vaporized will then be more dilute at the detector. Figure 6 shows the amount of material desorbed over a series of laser pulses at 0.05 Hz without scanning. The slow repetition rate guarantees that very little heat is generated by the

laser on the plate itself. The primary vaporization mechanism is therefore desorption and not thermal pyrolysis (8). It is interesting that less than 1% of the sample (out of the integrated area in Figure 6) was detected in the first laser shot. The profile in Figure 6 will naturally be different at higher repetition rates, since surface temperatures will then be higher.

#### LITERATURE CITED

- (1) Kirchner, J. G. *Thin-layer Chromatography*; Wiley: New York, 1978.
- (2) Sherma, J. *Anal. Chem.* **1988**, *60*, 74R-86R.
- (3) Bertsch, W.; Hara, S.; Kaiser, R. E.; Zlatkis, A. *Instrumental HPTLC*; Huthig: Heidelberg, 1980.
- (4) Morris, M. D.; Chen, I. I. *Anal. Chem.* **1984**, *56*, 19-22.
- (5) Ma, Y.; Yeung, E. S. *Anal. Chem.* **1988**, *60*, 722-724.
- (6) Zhu, J.; Yeung, E. S. *J. Chromatogr.* **1989**, *463*, 139-145.
- (7) *Proceedings of the 3rd International Symposium on Instrumental High Performance Thin Layer Chromatography*; Kaiser, R. E., Ed.; Institute of Chromatography: Bad Duerkheim, FRG, 1985; 509 pp.
- (8) Novak, F. P.; Hercules, D. M. *Anal. Lett.* **1985**, *18(A4)*, 503-518.
- (9) Ramaley, L.; Vaughan, M. E. *Anal. Chem.* **1985**, *57*, 353-358.
- (10) Iwabuchi, H.; Nakagawa, A.; Nakamura, K. *J. Chromatogr.* **1987**, *414*, 139-148.
- (11) Unger, S. E.; Vincze, A.; Cooks, R. G. *Anal. Chem.* **1981**, *53*, 976-981.
- (12) Busch, K. L.; Stanley, M. S. *Anal. Chim. Acta* **1987**, *194*, 199-209.
- (13) Ramaley, L.; Nearing, M. E.; Vaughan, M. A. *Anal. Chem.* **1983**, *55*, 2285-2289.
- (14) Belchamber, R. M.; Read, H.; Roberts, J. D. M. *J. Chromatogr.* **1987**, *395*, 47-53.
- (15) Belenkii, B. C.; Gankina, E. S.; Adamovich, T. B.; Lobazov, A. F.; Nechaev, S. V.; Solonenko, M. G. *J. Chromatogr.* **1988**, *365*, 315-320.
- (16) Stahr, H. M.; Hyde, W.; Pfeiffer, R.; Domoto, M. *Proc. Int. Symp. Instrum. High Perform. Thin Layer Chromatogr.*, 3rd **1985**, 447-468.
- (17) Scott, R. M. *Clinical Analysis by Thin-layer Chromatography Techniques*; Humphrey Science: Ann Arbor, MI, 1969; 227 pp.
- (18) Touchstone, J. C. *Advances in Thin Layer Chromatography: Clinical and Environmental Applications*; Wiley: New York, 1982.
- (19) Garrett, E.; Tsan, J. J. *Pharm. Sci.* **1974**, *64*, 1563-1566.
- (20) Raglione, T. V.; Hartwick, R. A. *Anal. Chem.* **1986**, *58*, 2680-2683.
- (21) Hofstraat, J. W.; Engelsma, M.; Van De Nesse, R. J.; Gooijer, C.; Velthorst, N. H.; Brinkman, U. A. *Anal. Chim. Acta* **1986**, *186*, 247-259.
- (22) Casu, B.; Cavallotti, L. *Anal. Chem.* **1962**, *34*, 1514-1516.
- (23) Janak, J. J. *Gas Chromatogr.* **1964**, *15*, 15-28.
- (24) Humphrey, A. M. *J. Chromatogr.* **1970**, *53*, 375-378.
- (25) DiDonato, G. C.; Busch, K. L. *Anal. Chem.* **1986**, *58*, 3231-3232.
- (26) Stanley, M. S.; Busch, K. L.; Vincze, A. *J. Planar Chromatogr.—Mod. TLC* **1988**, *1*, 76-78.
- (27) Stanley, M. S.; Busch, K. L. *J. Planar Chromatogr.—Mod. TLC* **1988**, *1*, 135-140.
- (28) Bare, K. J.; Read, H. *Analyst (London)* **1987**, *112*, 433-436.
- (29) Kolaitis, L.; Lubman, D. M. *Anal. Chem.* **1986**, *58*, 2137-2142.
- (30) Tembreull, R.; Lubman, D. M. *Anal. Chem.* **1986**, *58*, 1299-1303.
- (31) Hillenkamp, F. *Int. J. Mass Spectrom. Ion Phys.* **1982**, *45*, 305-313.
- (32) Irwin, W. J. *Analytical Pyrolysis*; Dekker: New York, 1982.

RECEIVED for review February 6, 1989. Accepted May 11, 1989. The Ames Laboratory is operated by Iowa State University for the U.S. Department of Energy under Contract No. W7405-Eng-82. This work was supported by the Director of Energy Research, Office of Basic Energy Sciences, Division of Chemical Sciences.



# Resonant Two-Photon Ionization Spectroscopic Analysis of Thin-Layer Chromatography Using Pulsed Laser Desorption/Volatilization into Supersonic Jet Expansions

Liang Li and David M. Lubman\*

Department of Chemistry, The University of Michigan, Ann Arbor, Michigan 48109

Pulsed laser desorption has been used as a means of directly vaporizing thin-layer chromatography (TLC) spots into the gas phase. The resulting neutral plume of molecules is then entrained into a supersonic jet expansion of CO<sub>2</sub> and transported into a time-of-flight mass spectrometer (TOFMS) where resonant two-photon ionization (R2PI) is performed. By use of this method, various thermally labile biological molecules, including indoleamines, catecholamines, peptides, and drugs have been detected from silica gel TLC plates with production of the molecular ion in a TOFMS device. The spectroscopic nature of R2PI has been used to obtain cold sharp wavelength spectra in the TOFMS of several compounds desorbed from the TLC plate into the jet expansion. The combination of wavelength selectivity and mass spectrometric identification has allowed us to uniquely identify components that have not been completely separated by TLC. In addition, quantitation has been achieved for indole-3-acetic acid and imipramine over 4 orders of magnitude using this method with detection limits in the low nanogram range.

## INTRODUCTION

Thin-layer chromatography (TLC) has become a widely used separation method for qualitative analysis of mixtures in both chemistry and biology (1-3). This is due to TLC's experimental simplicity, ability to separate several samples simultaneously, and applicability to a wide range of samples and problems. However, identification of separated components is generally performed photometrically, using either absorbance or fluorescence where the TLC plate is developed with substances that form visible or UV fluorescing spots from which retention times can be visually determined. Under these conditions unambiguous identification may not be possible without the use of other methods that provide molecular structure information.

A number of spectroscopic detectors have been developed for TLC that provide enhanced identification based upon spectral information. These include such methods as multidimensional detection via imaging detectors (4, 5), diffuse reflectance detection (6), and Fourier transform infrared photoacoustic spectroscopy (7). In recent work, laser induced fluorescence (LIF) has been used by Zare and co-workers (8) as a means of achieving sensitive and selective detection for TLC adsorbates. In related work, Seybold and co-workers (9) demonstrated the use of laser induced two-photon excited fluorescence (TPEF) and sequentially excited fluorescence (SEF) as a means of obtaining additional spectral selectivity and of reducing the optical background level compared to conventional LIF. Detection limits in the 100-200-pg region were reported for these fluorescence methods. The work performed by these groups illustrated the unique advantages of laser radiation for detection of adsorbates on TLC plates including: (a) the high power, coherent nature of pulsed laser radiation, which allows it to be focused on a spot for sensitive

detection of a specific substance, and (b) the use of time-resolved or wavelength-resolved detection, which may permit the analysis of a mixture of fluorescent species although the chromatographic spots may not be completely resolved. The obvious drawback of LIF and other fluorescence methods though is that they work well only for molecules that exhibit a reasonable quantum yield in fluorescence. Also the wavelength selectivity available for distinguishing different substances may be limited due to the broad spectral features characteristic of large polyatomic molecules at room temperature.

Alternative means of detecting adsorbates on TLC include mass spectrometric methods (10-26). In particular, particle desorption methods such as secondary ion mass spectrometry (SIMS) (15-19) and fast atom bombardment mass spectrometry (FABMS) (21-23) have been used to interface TLC directly with mass spectrometry without requiring extensive sample preparation and with the capabilities of volatilizing thermally labile samples. Unger et al. (15) for example used secondary ion mass spectrometry (SIMS) to detect quaternary alkaloids on silica gel and cellulose plates directly in the ion source of a mass spectrometer. Although mass spectra were observed, the analysis required long periods of time and required 10- $\mu$ g spots. The problem here is that SIMS is sensitive to only the first few atomic layers of sample and thus most of the sample on the TLC plate is not probed. Also a high background was observed at low mass due to the plate material. Similar problems may also exist with FABMS (23). However, both SIMS and FABMS used for detection of adsorbates on TLC plates have been shown to offer great potential for solving practical problems and for on-line applications (15-23).

Laser desorption methodology has been shown to be a powerful means of volatilizing samples from TLC plates directly into a mass spectrometer. This method was first used by Ramaley and co-workers (24, 25) to desorb various compounds from TLC plates, which were subsequently swept by a chemical ionization (CI) gas into a mass spectrometer. The detection limit for substances such as phenanthrene was about 10 ng, although more polar compounds were often difficult to detect. Amino acids, for example, could not be detected. In addition, as the molecular weight increased and the volatility decreased, detection also became more difficult. In related work, Novak and Hercules (26) applied the laser microprobe method for direct detection from TLC plates in a mass spectrometer. They demonstrated that the inherent lateral resolution of the laser microprobe device ( $\sim 5 \mu\text{m}$ ) could be used to resolve multiple components in broad chromatographic spots so that components can be identified even if they are not completely resolved chromatographically. However, they observed increased fragmentation at the increased power density needed to obtain spectra from a TLC plate relative to a zinc foil support and also a large number of peaks due to the chromatographic support below  $m/z$  100.

In this work, we present a method of detecting and identifying TLC adsorbates that uses a pulsed laser desorp-

tion/volatilization method for production of gas-phase neutral molecules with subsequent detection using laser-induced resonant two-photon ionization (R2PI) in supersonic jet expansions (27–30). This method is a spectroscopic-based technique that allows simultaneous detection of ions in a mass spectrometer, thus taking advantage of the best aspects of both these methodologies. Spectroscopic detection is based upon monitoring the resonant cross section of a molecule as a function of wavelength as a tunable pulsed dye laser is scanned. Although ions are ultimately detected, the ionization signal reflects the absorption spectrum of the electronic state in resonance with the first absorbed photon. In combination with the supersonic jet technique, unique identification can be achieved with R2PI based upon the resulting sharp spectral features characteristic of each molecule. The selectivity obtained by optical analysis can be combined with the soft ionization capabilities of R2PI for mass spectrometric detection and the separation capabilities of TLC so that a tandem method for enhanced discrimination is obtained. In addition, the highly efficient R2PI method allows for sensitive detection and for ionization of many samples that cannot be detected by using LIF due to low quantum yields in fluorescence (29).

In order to interface R2PI directly to detection of TLC spots, pulsed laser desorption (27–34) has been used to volatilize the eluent spots from a TLC substrate into the gas phase in a mass spectrometer. A relatively low-powered CO<sub>2</sub> laser (~10<sup>6</sup> W/cm<sup>2</sup>) is used to desorb both the eluent spots and TLC matrix together as mainly neutral species that are entrained in a supersonic jet. The analyte molecules are then selectively detected by R2PI in a time-of-flight mass spectrometer (TOFMS) while the background matrix remains transparent to the laser radiation and is thus not detected. In the present study, we examine the capabilities of this method for detecting analytes directly from a TLC matrix in a mass spectrometer with little prior sample preparation. We demonstrate the power of this method for detecting and uniquely identifying eluents that are not completely separated by thin-layer chromatographic procedures.

### EXPERIMENTAL SECTION

The experimental apparatus is a supersonic beam time-of-flight mass spectrometer (TOFMS) setup which has been described in detail previously (28). Sample introduction in these studies was performed by using pulsed laser induced desorption/volatilization followed by subsequent entrainment into a supersonic jet expansion (27–29). Laser desorption (LD) is performed with a CO<sub>2</sub> laser (Spectra Physics, EXC-1, 20–40 mJ/pulse) focused onto a ~1 mm diameter spot on the TLC substrate with a 10 cm focal length germanium lens. We estimate a power density on the surface of ~5 × 10<sup>6</sup> W/cm<sup>2</sup> (28). The TLC substrate is situated on a Macor-tipped probe which is located 4 mm downstream of the orifice and 1 mm from the molecular beam axis in order to optimize the entrainment of the desorbed material in the jet and to obtain maximum cooling as described previously (29). The samples are prepared by dissolving the analyte in a suitable solvent such as methanol or water to provide a solution that is 100 nmol/μL. A 1-μL sample is then introduced with a microliter syringe onto the TLC plate and the plate is developed with 50/50 EtOH/ethyl acetate. A UV lamp is used to visualize the spot which is then cut out into a 0.5 cm × 0.5 cm piece. This small section of TLC plate is then connected to the probe tip with double-stick tape. In order to obtain R2PI induced mass spectra, no further preparation of the sample is required. However, in order to obtain wavelength spectra, ~5–10 μL of glycerol is coated onto the TLC spot to allow an even, renewable source of molecules upon each desorption pulse (29). The samples were obtained from Sigma Chemical Co. and used without further purification. The TLC plates were Whatman 250 μm layer silica gel coated plates with aluminum backing (catalog no. 4420221).

Upon desorption, the plume of neutral molecules vaporized from the TLC plate is entrained into a pulsed supersonic jet pulse

**Table I. Compounds Detected Directly from Silica Gel TLC Plate Using Pulsed Laser Desorption/Volatilization with Detection by R2PI at 266 nm**

1. PAHs:	5. Catecholamines:
(1) phenanthrene	(1) DOPA
(2) pyrene	(2) dopamine
(3) pentacene	(3) synephrine
2. Carboxylic Acids:	6. Drugs:
(1) anthranilic acid	(1) papaverine
(2) indole-3-acetic acid	(2) nalorphine
(3) 2-naphthylacetic acid	(3) codeine
3. Amino acids:	(4) morphine-3-β-D-glucuronide
(1) tyrosine	(5) dibucaine
(2) tryptophan	(6) diphenhydramine
(3) phenylalanine	(7) fentanyl
4. Peptides:	(8) chlorpromazine
(1) Trp-Leu	(9) naphazoline
(2) Tyr-Gly-Gly	(10) amitriptyline
(3) CBZ-Leu-Gly	

of CO<sub>2</sub> carrier gas and transported into the TOFMS acceleration region. Laser ionization (R2PI) was then performed by using the frequency doubled dye output from a Quanta-Ray DCR-3 Nd:YAG pumped dye laser system or the fourth harmonic of the Nd:YAG laser at 266 nm. The sequence of events was controlled by several delay generators as described in earlier work (27). The 6 mm output beam was collimated with a combination 30 cm focal length positive lens and a 10 cm focal length negative lens to produce a laser beam 2–3 mm in diameter. The power density of the 266-nm beam used for obtaining mass spectra is ~5 × 10<sup>6</sup> W/cm<sup>2</sup>, while the doubled dye laser beam used to obtain scanning spectra is ~1 × 10<sup>6</sup> W/cm<sup>2</sup>. The laser power was measured with a Scientech Model 365 power meter. The distance from the nozzle to the excitation point was generally ~16 cm, which provided a Mach number of ~20, which corresponds to a translational temperature of 5 K using 1 atm reservoir pressure of CO<sub>2</sub> carrier gas (27). Laser induced R2PI wavelength spectra were obtained by using a SRS 250 gated integrator to monitor only the molecular ion as the dye laser was scanned and mass spectra were obtained with a LeCroy 9400 digital oscilloscope.

### RESULTS AND DISCUSSION

In this work, laser desorption/volatilization has been used to evaporate various compounds including polycyclic aromatic hydrocarbons (PAHs), carboxylic acids, amino acids, peptides, and drugs into a supersonic jet expansion with detection by R2PI as shown in Table I. In these experiments desorption was performed by a pulsed CO<sub>2</sub> laser in a 1 mm diameter spot ( $P \sim 5 \times 10^6$  W/cm<sup>2</sup>) and ionization was performed at 266 nm ( $P \sim 5 \times 10^6$  W/cm<sup>2</sup>). In each case, the molecular ion can be detected, although some fragmentation generally results at the above laser power. Under these conditions where ~100 nmol of sample is spotted onto the TLC plate, a signal level between 50 and 100 mV of the molecular ion is observed with a peak width (fwhm) of ~15 ns through a 50-Ω oscilloscope input. The background noise level is <0.05 mV so that one would expect the detection limit to be in the low nanogram range for these compounds. In addition, the molecular ion only, with little or no fragmentation, can be observed for most of these compounds if the laser power is reduced. However, a reduction in the signal level also results.

A comparison of the R2PI results obtained by desorption of compounds directly from a Macor tipped probe shows the same mass spectra as those obtained from the silica gel TLC plates. Thus, although some of the TLC substrate may also be volatilized in the desorption step, it does not appear to affect either the desorption or ionization process for the compounds studied in Table I. The silica gel substrate is not observed in the R2PI process either because the matrix does not absorb the radiation or because the ionization potential of the matrix components is too high for efficient two-photon ionization. The selectivity of R2PI is an important advantage

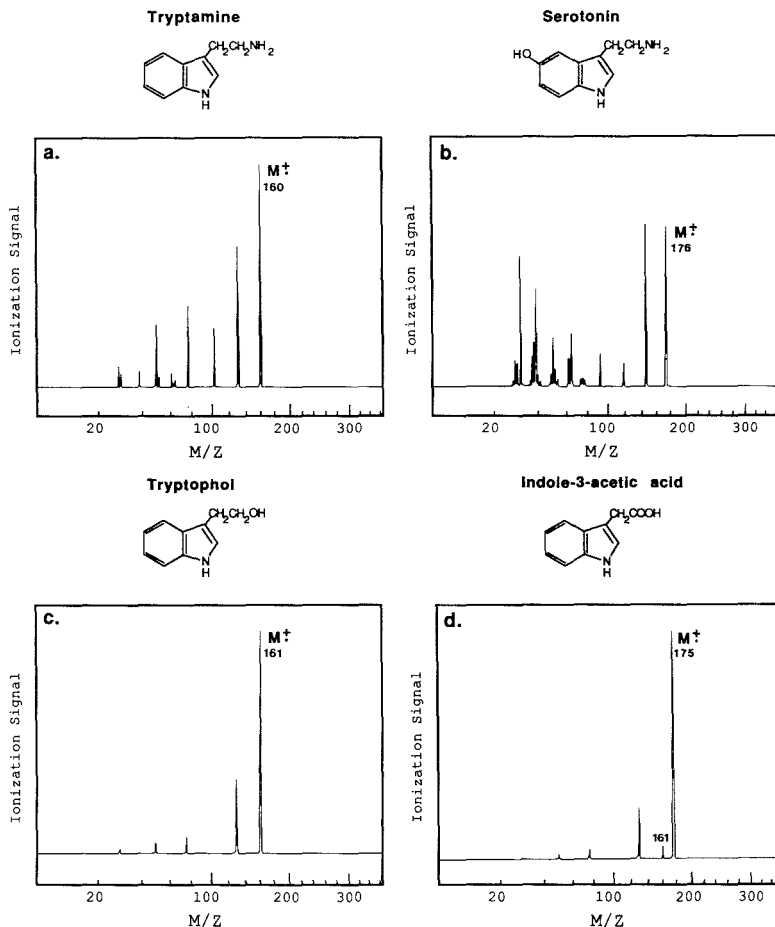


**Figure 1.** R2PI/MPI mass spectra of tryptamine analogues after TLC separation: (a) tryptamine and (b) serotonin (obtained by using 266-nm laser ionization ( $P = 5 \times 10^6 \text{ W/cm}^2$ )), (c) tryptophol (obtained by selective laser ionization at 285.75 nm ( $P = 5 \times 10^6 \text{ W/cm}^2$ )), (d) indole-3-acetic acid (obtained by selective laser ionization at 285.30 nm ( $P = 5 \times 10^6 \text{ W/cm}^2$ )).

over other ionization methods such as FABMS (21), SIMS (15), laser microprobe (26), etc. where significant background ions are observed below  $m/z$  100. In addition, the sensitivity of the method, in terms of the typical signal levels observed, does not appear to be significantly affected by the TLC matrix as compared to desorption directly from a Macor surface with the same sample spot size. However, the desorption in these experiments is performed by focusing the IR laser beam to a 1 mm diameter spot on a 3 mm diameter sample spot. In the case of the desorption directly from the ceramic rod, the sample can be placed in a very small spot (<0.5 mm diameter) so that total sample desorption can be achieved in one laser pulse. Thus, the overall sensitivity will be somewhat lower for these TLC plate experiments due to diffusion of the spot size. However, there is no apparent dependence of the desorption process or sensitivity on the molecular weight or polarity of the compound on the TLC plate as in the LD/CI work of Ramaley (25).

One of the unique features of this technique is the use of the supersonic jet method for obtaining sharp spectral features in R2PI spectroscopy (30) for identification of unseparated

species on the TLC plate. An example of the capabilities of this method is shown in Figures 1 and 2. As a demonstration an experiment was performed where an equimolar mixture of four indole derivatives was spotted on a TLC plate, separated, and developed using 50/50 ethanol/ethyl acetate. The  $R_f$  values obtained were tryptophol 0.83, indole-3-acetic acid 0.83, tryptamine 0.16, and serotonin 0.53. In this case, the separation between tryptophol and indole-3-acetic acid is incomplete. The spots were then cut out and placed on the probe tip and inserted into our TOFMS device. Laser desorption/volatilization was performed on each spot and the sample desorbed from the spot was probed by R2PI using UV radiation from a tunable dye laser. The resulting R2PI mass spectra of each spot is shown in Figure 1. Each compound can be identified by its molecular ion peak including the unresolved tryptophol/indole-3-acetic acid spot where the presence of the two compounds is observed in the mass spectrum. The detection of tryptophol can be optimized by tuning into a sharp absorption peak at 285.75 nm (see Figure 1c) at the expense of the indole-3-acetic acid signal, which is not observed in the mass spectrum since it does not absorb

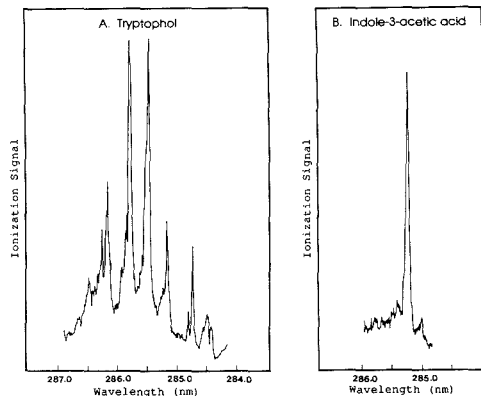


**Figure 2.** R2PI jet-cooled spectra of (A) tryptophol and (B) indole-3-acetic acid desorbed from a TLC plate.

at this wavelength. The detection of indole-3-acetic acid can be optimized by tuning the laser to 285.30 nm (see Figure 1d). At this wavelength the tryptophol signal is minimized and appears as a small peak at  $m/z$  161 in Figure 1d. This is the molecular ion peak of tryptophol and some ionization results due to absorption of the UV light by the wings of a relatively weak tryptophol absorption band in the cold jet.

The idea of selective spectroscopic detection is illustrated in Figure 2. These spectra were obtained by placing a 2- $\mu$ L sample solution containing 10  $\mu$ g each of indole-3-acetic acid and tryptophol onto the TLC plate with a microliter syringe and developing the plate with 50/50 EtOH/ethyl acetate. The unresolved TLC spot is then prepared as before for the mass spectrometer system; however, in this case  $\sim$ 5–10  $\mu$ L of glycerol is coated onto the spot. The glycerol dissolves the spot and allows for repetitive desorption for performing spectroscopy as described in our earlier work (29). By monitoring the molecular ion intensity produced by R2PI in the TOFMS as a function of wavelength using a gated integrator, we obtain sharp wavelength spectra of tryptophol (Figure 2a) and indole-3-acetic acid (Figure 2b). These spectra can unambiguously identify these compounds in combination with mass spectrometry. In addition, R2PI can be used to obtain spectra for these molecules which have relatively low quantum yields in fluorescence.

There are three other advantages of the supersonic jet in these experiments in addition to the spectroscopic cooling effect. The sample desorbed from the TLC plate is carried away immediately so that sample condensation can be avoided and the optimum sample is transported into the TOFMS. A second advantage of the jet is that the collisional cooling effect may prevent thermal decomposition of the laser desorbed plume of neutral molecules. A third advantage is the increase in resolution of the TOFMS device that results from a narrowing of the energy spread as discussed in previous work (35).

The question of quantitation has been examined for indole-3-acetic acid using tryptophol as an internal standard. A set of solutions was made with between 1 and 100  $\mu$ g of indole-3-acetic acid and 10  $\mu$ g of tryptophol as a standard and a second set was made with between 25 ng and 1  $\mu$ g of indole-3-acetic acid and 50 ng of tryptophol standard. Each mixture was applied to the TLC plate and developed until the solvent front migrated 4 cm. Each spot was prepared for the desorption probe as described previously and desorbed into the TOFMS. The mass spectrum was signal averaged over 10 pulses (1 s) ( $P \sim 5 \times 10^6$  W/cm<sup>2</sup>) and the height of the molecular ion peak was measured in the TOFMS for

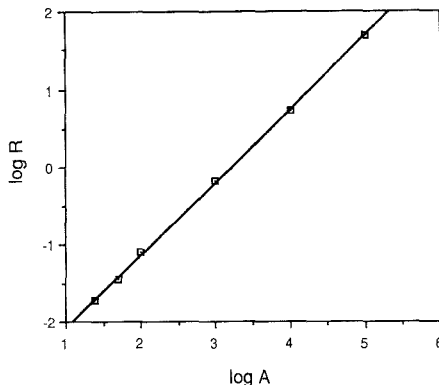


**Figure 3.** Quantitation of indole-3-acetic acid with tryptophol as an internal standard. A is the amount of indole-3-acetic acid in nanograms. R is the relative intensity between indole-3-acetic acid and tryptophol. The ionization laser wavelength is 266 nm at  $P = 5 \times 10^6$  W/cm<sup>2</sup>.

indole-3-acetic acid and tryptophol. The ratio between these peaks was compared and the same procedure followed for all the spots. An internal standard is required for comparison in these experiments because of the limited number of laser pulses available for signal averaging before the sample is completely desorbed. The pulse-to-pulse stability of the signal generated by laser desorption from the TLC matrix followed by R2PI may only be  $\pm$ 50%, so that an internal standard is necessary to compensate for these signal fluctuations when a large number of pulses are not available for averaging. A plot of the relative signal intensity between indole-3-acetic acid and tryptophol versus the amount of indole-3-acetic acid in nanograms is shown in Figure 3. Each point shown in Figure 3 represents the mean relative intensity from three mass spectra (error <8%). The plot is linear between 10 ng and 100  $\mu$ g. The ultimate detection limit for indole-3-acetic acid under these circumstances is  $\sim$ 12 ng with a signal to noise ratio ( $S/N$ ) of 3.

Quantitation experiments were also similarly performed with imipramine using [<sup>2</sup>H<sub>3</sub>]imipramine as the internal standard. The TLC plate of course does not resolve the isotopic species but since the mass spectrometer has sufficient resolution to resolve the two isotopic peaks, the deuterated compound serves as an excellent internal standard. The plot of signal intensity versus concentration was linear over the range of 5 ng to 50  $\mu$ g with a detection limit of  $\sim$ 3 ng with a  $S/N$  of 3. These detection limits are quite comparable to those obtained by other direct detection methods from TLC using various mass spectrometric or spectral methods that also provide molecular structure information.

In conclusion, pulsed laser desorption is a powerful means of directly vaporizing thin-layer chromatography spots into the gas phase for analysis by R2PI spectroscopy and mass spectrometry. Using this method, we have been able to detect a variety of thermally labile biological molecules from TLC plates without significant thermal decomposition. The production of intact gas-phase neutral molecules allows us to use R2PI as a means of producing the molecular ion for exact mass identification in a TOF device. Although the TLC substrate is also desorbed in the desorption step, it is not observed in the mass spectrum due to the selective nature of the R2PI process. By expansion of the desorbed molecules in a supersonic jet expansion, cold sharp R2PI wavelength spectra can be obtained for unique identification in the TOFMS. The combination of wavelength selectivity and mass spectrometric identification has allowed us to uniquely identify components

that have not been completely separated by TLC. In addition, the method has been quantitated over at least 4 orders of magnitude between 10 ng and 100 µg using an internal standard. The detection limit achieved is typically in the low nanogram regime.

**Registry No.** Trp-Leu, 13123-35-8; Tyr-Gly-Gly, 21778-69-8; CBZ-Leu-Gly, 2706-38-9; phenanthrene, 85-01-8; pyrene, 129-00-0; pentacene, 135-48-8; anthranilic acid, 118-92-3; indole-3-acetic acid, 87-51-4; 2-naphthylacetic acid, 581-96-4; L-tyrosine, 60-18-4; L-tryptophan, 73-22-3; L-phenylalanine, 63-91-2; DOPA, 59-92-7; dopamine, 51-61-6; synephrine, 94-07-5; papaverine, 58-74-2; nalorphine, 62-67-9; codeine, 76-57-3; morphine-3-β-D-glucuronide, 20290-09-9; dibucaine, 85-79-0; diphenylhydramine, 58-73-1; fentanyl, 437-38-7; chlorpromazine, 50-53-3; naphazoline, 835-31-4; amitriptyline, 50-43-6; imipramine, 50-49-7; tryptamine, 61-54-1; serotonin, 50-67-9; tryptophol, 526-55-6.

#### LITERATURE CITED

- Poole, C. F. *Trends Anal. Chem.* **1985**, *4*, 209-213.
- Smith, R. V. *Trends Anal. Chem.* **1984**, *3*, 179-181.
- Brinkman, V. A. Th. *Trends Anal. Chem.* **1986**, *5*, 178-182.
- Callis, J. B. *ACS Symp. Ser.* **1984**, *No. 250*, 171.
- Warner, I. M.; Patonay, G.; Thomas, M. P. *Anal. Chem.* **1985**, *57*, 463A-483A.
- Zuber, G. E.; Warren, R. J.; Begosh, P. P.; O'Donnell, E. L. *Anal. Chem.* **1984**, *56*, 2935-2939.
- White, R. L. *Anal. Chem.* **1985**, *57*, 1819-1822.
- Berman, M. R.; Zare, R. N. *Anal. Chem.* **1975**, *47*, 1200-1201.
- Seybold, P. G.; Hinckley, D. A.; Heinrichs, T. A. *Anal. Chem.* **1983**, *55*, 1992-1994.
- Dekker, D. J. *Chromatogr.* **1979**, *168*, 508-511.
- Nilsson, C. A.; Norstrom, A.; Andersson, K. J. *Chromatogr.* **1972**, *73*, 270-273.
- Henion, J.; Maylin, G. A.; Thomson, B. A. J. *Chromatogr.* **1983**, *271*, 107-124.
- Down, G. J.; Gwyn, S. A. J. *Chromatogr.* **1975**, *103*, 208-210.
- Kaiser, R. *Chem. Br.* **1969**, *5*, 54-61.
- Unger, S. E.; Vincze, A.; Cooks, R. G.; Christian, R.; Rothman, L. D. *Anal. Chem.* **1981**, *53*, 976-981.
- Kushi, Y.; Rokukawa, C.; Handa, S. *Anal. Biochem.* **1988**, *175*, 167-176.
- Iwabuchi, H.; Nakagawa, A.; Nakamura, K. J. *Chromatogr.* **1987**, *44*, 139-148.
- Stanley, M. S.; Duffin, K. L.; Doherty, S. J.; Busch, K. L. *Anal. Chim. Acta* **1987**, *200*, 447-458.
- Stanley, M. S.; Busch, K. L. *Anal. Chim. Acta* **1987**, *194*, 199-209.
- Busch, K. L. *Trends Anal. Chem.* **1987**, *6*, 95-100.
- Chang, T. T.; Lay, J. O., Jr.; Francel, R. J. *Anal. Chem.* **1984**, *56*, 109-111.
- Bare, K. J.; Read, H. *Analyst* **1987**, *112*, 433-436.
- Tamura, J.; Sakamoto, S.; Kubota, E. *JEOL News* **1987**, *23A*, 20-25.
- Ramaley, L.; Vaughan, M. A.; Jamieson, W. D. *Anal. Chem.* **1985**, *57*, 353-358.
- Ramaley, L.; Nearing, M. E.; Vaughan, M. A.; Ackman, R. G.; Jamieson, W. D. *Anal. Chem.* **1983**, *55*, 2285-2289.
- Novak, F. P.; Hercules, D. M. *Anal. Lett.* **1985**, *18(A4)*, 503-518.
- Li, L.; Lubman, D. M. *Anal. Chem.* **1988**, *60*, 2591-2598.
- Li, L.; Lubman, D. M. *Anal. Chem.* **1988**, *60*, 1409-1415.
- Li, L.; Lubman, D. M. *Rev. Sci. Instrum.* **1988**, *59*, 557-561.
- Lubman, D. M. *Anal. Chem.* **1986**, *58*, 31A-40A.
- Engelke F.; Hahn, J. H.; Henke, W.; Zare, R. N. *Anal. Chem.* **1987**, *59*, 909-912.
- Hahn, J. H.; Zenobi, R.; Zare, R. N. *J. Am. Chem. Soc.* **1987**, *109*, 2842-2843.
- Grote Meyer, J.; Boesi, U.; Walter, K.; Schlag, E. W. *Org. Mass Spectrom.* **1986**, *21*, 595-597.
- Grote Meyer, J.; Boesi, U.; Walter, K.; Schlag, E. W. *Org. Mass Spectrom.* **1988**, *23*, 388-396.
- Lubman, D. M.; Jordan, R. M. *Rev. Sci. Instrum.* **1985**, *56*, 373-376.

RECEIVED for review March 13, 1989. Accepted May 11, 1989. We acknowledge financial support of this work under NSF Grant CHE 8419383 and NSF Grant DMR 8418095 for the acquisition of the Chemistry and Materials Science Laser Spectroscopy Laboratory. David M. Lubman is an Alfred P. Sloan Foundation Research Fellow.

## Examination of the Automated Solute-Independent Calibration Technique

Curtiss N. Renn and Robert E. Synovec\*

Center for Process Analytical Chemistry, Department of Chemistry, BG-10, University of Washington, Seattle, Washington 98195

The solute independent calibration (SICAL) method is used to simultaneously measure analyte concentration and to provide information, namely, the equivalent ionic conductance, leading to solute identification. The SICAL method was fully automated for sampling, chromatographic separation, data collection, and analysis and applied to ion chromatography using conductivity detection. Theoretical predictions for the precision and accuracy of the fully automated method are presented and experimentally validated. The sample was varied with respect to analyte concentration and identity, with the automated method successfully monitoring real-time changes. Over a 24-h period under steady-state sample conditions (26 measurements), the relative standard deviation of concentration was 2.5% for fluoride and 3.9% for chloride, while the relative standard deviation of the SICAL calculated equivalent ionic conductance was 0.9% for fluoride and 1.7% for chloride. Precision of automated injection for a single chromatographic system over the 24-h period was better than 0.7%. Potential use of the method as a process monitor is discussed.

#### INTRODUCTION

Process control in the chemical industry has entered a new

phase of research and development for more reliable and useful information (1). In the past, a wide variety of analytical techniques have been developed for chemical analysis. Many of the older techniques involve manual sampling and wet chemical analysis (ASTM procedures), thereby limiting the utility of these methods in the fast-paced, continuous, and potentially harsh environments of the chemical industries. Previously established techniques have largely given way to faster, automated analysis methods such as automated titration (2), ion selective electrodes and sensors (1), gas chromatography (2, 3), and flow injection analysis (4). Robotics (5, 6) has also been successful in the automation of chemical analysis in both on-line and off-line process monitoring.

The use of high-performance liquid chromatography (HPLC) as an analytical technique for process control and monitoring has already found wide use (3, 7-10). More specifically, ion chromatography has recently been implemented in process control for both on-line and off-line analysis (3, 11, 12). Implicit in standard methods of analysis is the assumption that the information necessary for control decisions is encoded in the chemical identity and concentrations of components in a process stream. Therefore, in process control two phases of development would be employed. The first step would be the correlation of analyte identity and concentration to the

behavior of the chemical process (13). The second step would then involve the use of the analytical information to monitor and control the chemical process. Although, in principle a process is well understood and the subsequent analysis should be straightforward, in practice a process that goes "out of control" may do so for a number of reasons. In the HPLC analysis, an out-of-control process will result in chromatographic peaks where analyte peaks have potentially changed in qualitative or quantitative nature, or both simultaneously. The need for confident and reliable analytical information is, therefore, paramount in monitoring and the control of chemical processes.

The typical HPLC procedure involves identifying analytes in a sample via retention time of the chromatographic peaks and comparing the retention time with that of known standards, constructing a calibration curve with known standards, and then quantitating the analytes in the process via the calibration curve (3). Many assumptions are made with this standard method of chromatographic analysis. First, is the assumption that the resolution is adequate to identify the analytes of interest. In process control, the need for fast HPLC (14) compromises the validity of this first assumption. A second assumption is that the chemical matrix is well characterized and is known at all times during the analysis. When this assumption is not valid, the possibility of coeluting species greatly increases, and the quantitation of analytes is adversely effected (1). A third assumption is that the standards are stable and readily available. Obviously these conditions are not always met. A fourth assumption is that the conditions for the calibration and analysis remain exactly the same. Of particular concern are temperature drift (2), instrumental drift (2), eluent composition (3), and column performance (3). The ramifications of these assumptions is magnified as a limitation of standard analytical methodology as applied in process HPLC. The problem reduces to the need to improve current approaches taken to calibrate and quantitative process HPLC data.

With the present limitation of standard analytical methodology in mind, an approach for confident calibration in off-line HPLC was introduced by Yeung and co-workers (15-21), referred to as solute independent calibration (SICAL). The SICAL method allows one to calculate the concentration and chemical properties of solutes without the use of solute calibration curves or the use of internal standards. SICAL is accomplished by simultaneously injecting the sample to be analyzed into two chromatographic systems and measuring peak areas in both chromatographic systems. In addition, two arbitrary calibrating ions are then injected into both chromatographic systems and peak areas are again measured. The peak areas are then used to provide a universal calibration scale to quantitate the chromatographic analytes of interest. A basic requirement of the SICAL method is the order of the peaks in both chromatograms must be known. For ion chromatography, this is trivial since the elution order is relatively invariant of the type of eluent (22). For other types of chromatography, a system for correlating the order of peaks was developed (21). With the goal of obtaining reliable analytical information for process control, we have investigated and evaluated the precision and accuracy of the SICAL method using a fully automated, continuous monitoring system. Ion chromatography (IC) followed by conductivity detection, as described earlier (16), was used. The method was first described for refractive index detection (15). Other areas for application of the method include, size exclusion chromatography with refractive index detection (17), IC with absorbance detection (18), microbore HPLC with optical activity detection (19), and gas chromatography with ultrasonic detection (20). Thus, the future of applying the SICAL method

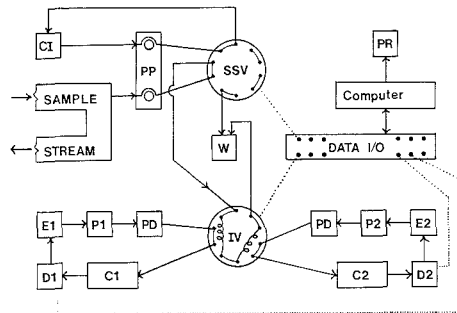


**Figure 1.** SICAL-automated monitor using two ion chromatograph systems in parallel, shown in the position loading the injection valve with sample stream material: CI, calibrating ions (arbitrary); SAMPLE STREAM; PP, peristaltic pump; SSV, sample selection valve; W, waste; IV, injection valve (two 5- $\mu$ L loops); C1, C2, ion chromatography columns; D1, D2 conductivity detectors; E1, E2, eluents (different); P1, P2, pumps; PD, pulse dampeners; PR, printer or recording of data for processing. Dotted lines represent computer and data I/O interactions with system.

to chemical analysis is founded in several separation and detection principles.

In the automated HPLC system described here, SICAL uses the "same" sample injected into two independent chromatographic systems to provide a universal calibration (16), in order to simultaneously calculate the concentration and equivalent ionic conductance of analytes in a sample stream. In this work, the sample stream consists of a 1-L vessel containing fluoride and chloride as process analytes. Analysis is accomplished without assumption of the analyte identity. The first study conducted was to test the reproducibility of the automated system toward sampling, injection of the sample into the two systems in parallel, and chromatographic peak area measurements. Next, the precision of the method was investigated experimentally and compared to theoretical expectations based on propagation of error. Third, response to solute change was evaluated by systematically varying the analyte concentrations in the sample stream. Potential use of the SICAL method for process analysis is discussed. It should be pointed out that the method provides both quantitative analysis and qualitative analysis, *simultaneously*, that in principal is of interest in process analysis verification. In general, our studies point toward the need to evaluate the precision of automated, multistep chemical analysis procedures, particularly in HPLC.

#### EXPERIMENTAL SECTION

A diagram of the experimental configuration for the automated SICAL monitor is shown in Figure 1, and consisted of synchronous sampling, ion chromatographic separation, instrument control, data acquisition, and analysis. In Figure 1, a Nalgene 1-L reservoir was used to simulate a batch process or continuous process stream (sample stream), and a Nalgene 1-L reservoir was used for the calibrating ions (CI). Both the sample stream (SS) and the calibrating ions were pumped continuously by a peristaltic pump (Isco, Tris, Lincoln, NE) through intake and delivery lines of 0.065 in. i.d.  $\times$  0.194 in. o.d. silicone tubing. The calibrating ion solution was recirculated to the calibrating ion reservoir without introducing noticeable error in the method. The sample stream consisted of 10.0 mequiv/L KF and 10.0 mequiv/L NaCl prepared from dried reagent grade KF and NaCl (J. T. Baker Chemical Co., Baker Analyzed, Phillipsburg, NJ) and in-house deionized water. The calibrating ions consisted of 25.0 mequiv/L NaIO<sub>3</sub> and 25.0 mequiv/L NaBr prepared from dried reagent grade NaIO<sub>3</sub> and NaBr (Baker) and in-house deionized water. The sample stream and calibrating ions were pumped through a two-position electric-actuated HPLC sample selection valve (SSV)

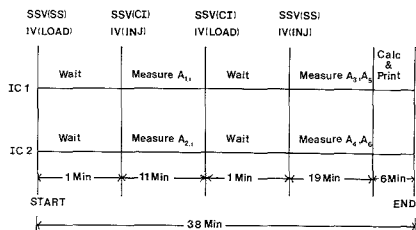


**Figure 2.** SICAL-automated monitor sequencing of data acquisition, instrument control, and data analysis. See Figure 1, the Experimental Section, and eq 1-6 for explanation of sequencing.

(Valco, Model EC10W, Houston, TX) and then to the second electric-actuated HPLC injection valve (IV) (Valco, Model EC10W, Houston, TX) or to waste.

The sample stream and calibrating ions were synchronously diverted to the injection valve (IV) from the sample selection valve (SSV) via 0.007 in. i.d. Teflon tubing. The injection valve was equipped with two 5.0- $\mu$ L injection loops made in-house from 10 cm lengths of 0.010 in. i.d. stainless steel HPLC tubing. Both injection loops were loaded simultaneously, thus within the chromatographic time frame essentially defined two "identical" volumes injected. The separation and detection of ions in the sample stream were accomplished via two independent IC systems. Both systems were identical with the exception of the eluents used. System 1 used 1.25 mequiv/L benzoic acid (E1) adjusted to pH 7.0 with NaOH while system 2 used 4.0 mequiv/L formic acid (E2) adjusted to pH 7.0 with NaOH. Reciprocating piston pumps (P1 and P2) (Milton Roy, Model 396-31, Riviera Beach, FL) delivered eluents 1 and 2 at a flow rate of 1.2 mL/min through pulse dampeners with pressure gauges (PD1 and PD2) (Alltech, Free-Flow Pulse Dampener, Deerfield, IL), through resin-based anion exchange columns (C1 and C2) (Wescan, Model 269-031 Anion/R-HS 4.6 mm  $\times$  100 mm, Santa Clara, CA), and subsequent detection via conductivity detectors (D1 and D2) (Milton Roy, Model ConducoMonitor III, Riviera Beach, FL), each equipped with a 0.5- $\mu$ L volume flow cell. The effluents from D1 and D2 were recirculated to E1 and E2 reservoirs, respectively, to provide a closed-loop IC system necessary for continuous, long-term operation. No adverse affects were observed due to the recirculation procedure.

The data acquisition and instrument control were facilitated via a laboratory interface (MetraByte, DASH-16, Taunton, MA) under the control of a personal computer (IBM-XT, Armonk, NY). The data from D1 and D2 were simultaneously collected via the laboratory interface on two separate analog-to-digital (A/D) input channels at the rate of 1000 points/s, boxcar averaged to 1 s to minimize A/D conversion noise and provide a 2-s time constant, and stored in the computer for further analysis. Four TTL digital-to-analog (D/A) output channels from the laboratory interface were used to independently control the sample selection valve and injection valve. All computer software was written in-house for data acquisition, instrument control, and data analysis. The results of the data analysis were then output to a printer (IBM, Proprinter, Armonk, NY) for inspection and for permanent record.

The sequencing of data acquisition, instrument control, and data analysis is shown in Figure 2. IC1 refers to IC system 1 and IC2 refers to IC system 2. In the initial phase of the sample monitoring cycle, the sample selection valve delivered a portion of the sample stream to the injection valve, which was in the "load" position. A period of 1 min was sufficient to flush the Teflon tubing and to load the injection loops in the injection valve with no apparent carryover from previous samples. At the end of the loading interval, the sample selection valve and injection valves were simultaneously switched to inject the sample into IC1 and IC2 and to begin delivering the calibrating ions to the injection valve. This configuration minimized the lag time of loading samples in the injection valve. The sample stream chromatographic data from IC1 and IC2 were simultaneously collected for 11 min to allow complete elution of all ions. At the end of

collecting the sample stream chromatograms, the injection valve was returned to the "load" position to load the calibrating ions into the injection loops. At the end of this time period, the sample selection valve and injection valve were simultaneously switched to inject the calibrating ions into IC1 and IC2 and to begin delivering the sample stream to the injection valve. The calibrating ion chromatograms were collected for 19 min to allow complete elution of the calibrating ions. At the end of the chromatographic data collection, the automated monitor entered the data analysis phase.

The raw chromatographic data were first base-line corrected about a numerical value of zero by choosing two portions of the chromatograms where no peaks should appear (before the injection disturbance and after the last peak has eluted) and applying a linear correction, i.e., calculating a line from the initial and final base-line portions of the chromatograms and subtracting the line from the raw chromatographic data. After the chromatograms were base-line corrected, the data were stored on the hard disk of the computer for later data analysis. Next the parameters for peak integration were read from a file on the hard disk. The parameters include the number of peaks and the integrating boundaries for each peak in each chromatogram. The peaks in the chromatograms were then integrated by using a trapezoidal rule algorithm utilizing the appropriate boundaries for integration of each peak. The integrated areas were then input into the appropriate equations for calculation of the normality and equivalent ionic conductance for each integration interval by the SICAL method. The areas and integration intervals of each peak in each chromatogram were output to the printer along with the normalities and equivalent ionic conductances. This completed one full cycle and the automated monitor was then returned to the start position for execution of the next cycle. The cycle time was 38 min for our system, but could easily be shortened by further optimization of the IC separations. The cycle time did not detract from the objectives of our investigation.

## RESULTS AND DISCUSSION

It is useful to summarize the basic equations for the signal from a differential conductivity detector employed in SICAL, as previously described (16) and defined in terms of Figures 1 and 2, namely the two IC systems, IC1 and IC2

$$A_{1,i} = C_i K_1 (\lambda_i - \lambda_1) \quad (1)$$

$$A_{2,i} = C_i K_2 (\lambda_i - \lambda_2) \quad (2)$$

$$A_3 = CK_1 (\lambda_3 - \lambda_1) \quad (3)$$

$$A_4 = CK_2 (\lambda_3 - \lambda_2) \quad (4)$$

$$A_5 = CK_1 (\lambda_4 - \lambda_1) \quad (5)$$

$$A_6 = CK_2 (\lambda_4 - \lambda_2) \quad (6)$$

where  $A_{1,i}$  is the area of analyte,  $i$ , in IC1,  $A_{2,i}$  is the area of the analyte in IC2,  $A_3$  and  $A_5$  are the areas of the calibrating ions in IC1,  $A_4$  and  $A_6$  are the areas of the calibrating ions in IC2,  $K_1$  and  $K_2$  are the instrumental factors for D1 and D2, respectively,  $\lambda_1$ ,  $\lambda_2$ ,  $\lambda_3$ ,  $\lambda_4$ ,  $\lambda_i$  are the equivalent ionic conductances of E1, E2, C1, C2, and analyte, respectively,  $C$  is the concentration (mequiv/L) of the arbitrary calibrating species, and  $C_i$  is the concentration (mequiv/L) of an analyte. Equations 1-6 apply only for retained solutes in the case of IC.

There are three advantages of using peak area instead of peak height. First, the precision and accuracy of peak quantitation are better for peak area than peak height (23). Second, the height of a peak is dependent on retention time, while, peak area is independent of retention time (23). Third, peak area is proportional to the flow rate and data acquisition rate so the calibration ion and sample injected into both eluents accounts not only for any difference in instrumental response factors but also for any differences in flow rates, allowing the method of SICAL using peak areas to become self-calibrating with no assumptions necessary for instrumental factors or flow rates.

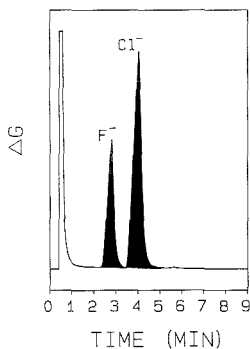


Figure 3. Relative conductance,  $\Delta G$ , measured for fluoride and chloride in the benzoate eluent ion chromatographic system, represented individually by eq 1, 5.0  $\mu\text{L}$  of 10.0 mequiv/L of each injected.

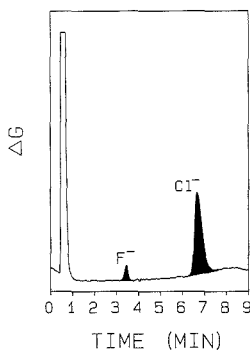


Figure 4. Relative conductance,  $\Delta G$ , measured for fluoride and chloride in the formate eluent ion chromatographic system, represented individually by eq 2. Quantities injected as in Figure 3.

Solving eq 1-6 as a set of simultaneous equations yields an expression for the concentration of analyte (16)

$$C_i = C \left[ \frac{A_{1,i} - A_{2,i} \left[ \frac{A_3 - A_5}{A_4 - A_6} \right]}{A_3 - A_4 \left[ \frac{A_3 - A_5}{A_4 - A_6} \right]} \right] \quad (7)$$

In this experiment, both of the CI are used at the same injected concentration,  $C$ , to simplify eq 7 and 8 (16). With the additional information of the equivalent ionic conductances of the calibrating ions, it is possible to derive eq 8 for the equivalent ionic conductance of an analyte

$$\lambda_i = \left[ \frac{A_{2,1} \left[ \frac{C}{C_i} \right] - A_4}{A_4 - A_6} \right] (\lambda_3 - \lambda_4) + \lambda_3 \quad (8)$$

where  $C_i$  is first calculated from eq 7.

Figures 3 and 4 are ion chromatograms of the sample stream in benzoate and formate, respectively, as eluents. The darkened portions of the chromatograms signify the peak areas containing the analytical information of interest. Referring back to the basic ion chromatographic signal as given by eq 1 and 2, it becomes clear why the signals from chloride and fluoride in formate are less than those obtained in benzoate. One must recognize that the analytical signal is a differential

Table I. Limiting Equivalent Ionic Conductance,  $\lambda^\circ$ , of Ions Used in Process Automated SICAL Method

ion	$\lambda^\circ, \Omega^{-1} \text{cm}^2 \text{equiv}^{-1}$	ion	$\lambda^\circ, \Omega^{-1} \text{cm}^2 \text{equiv}^{-1}$
fluoride <sup>a</sup>	54.5	bromide <sup>b</sup>	78.1
chloride <sup>a</sup>	76.4	benzoate <sup>c</sup>	32.4
iodate <sup>b</sup>	40.5	formate <sup>c</sup>	54.6

<sup>a</sup>Analyte. <sup>b</sup>Calibrating ion. <sup>c</sup>Eluent.

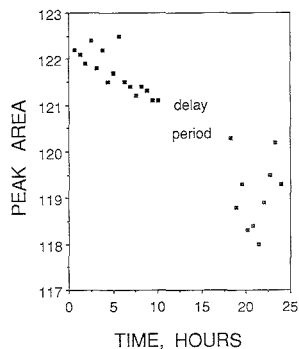


Figure 5. Ion chromatographic peak areas, in arbitrary units, for fluoride (■) measured with benzoate as eluent over a 24-h continuous period including a 6-h delay period (system shut off and restarted). A representative chromatogram is shown in Figure 3.

signal relative to the background signal of the eluent. In the case of formate as an eluent, formate has a higher equivalent ionic conductance than benzoate (see Table I); thus, the difference between the analyte and eluent conductivities is less in formate, resulting in a smaller analytical signal. Chromatograms providing the data for eq 3-6 are not shown for brevity.

The first consideration under study was the precision of an automated monitor. The automated monitor was programmed to analyze a steady-state concentration of chloride and fluoride ions, in a conventional manner by measuring the area of the chloride and fluoride peaks with sodium benzoate as the eluent, in order to evaluate the precision of the method. The automated monitor was operated for 11 h, shut down for 6 h (delay period), and then restarted and operated for 7 h to check the resiliency of the system over a full 24-h period. The peak areas of fluoride are shown in Figure 5 with a root-mean-square (rms) value of 1.40 with an average of 120.73 (arbitrary area units), or a relative uncertainty of 1.16%, which was calculated by assuming normal Gaussian statistics (24). Clearly, the magnitude of the peak area drifts with time, thus distorting the relative uncertainty. In principle, the drifting may be due to several factors, such as instrument stability (temperature and mechanical), or a changing fluoride concentration. The dilemma in conventional calibration approaches is in understanding and overcoming problems such as the drift, so data may be properly interpreted. After correction for the linear drift, the relative uncertainty of the fluoride area measurements in Figure 5 was only 0.67%. Thus, the 0.67% accounts for the random fluctuations primarily associated with the automated injection technique. Chloride in benzoate yielded similar results. In comparison, a typical rms value of 3% for peak area measurement is attainable by manual injection techniques (17, 23). Other than the obvious advantage of reducing labor intensive analysis via automation, clearly, the precision of the automated injection technique is much better.



**Table II. Absolute Standard Deviation,  $s$ , of the Predicted<sup>a</sup> Concentration, SICAL-Measured Average Concentration,  $\bar{C}$ , and Absolute Standard Deviation of the SICAL-Measured Concentration for Analytes Chloride and Fluoride Monitored over a 24-h Period Including the Delay Period (see Figure 5)**

ion	$s(C_i)^a$ , mequiv/L	$\bar{C}^b$ , mequiv/L	$s(C_i)^c$ , mequiv/L
chloride	0.76	10.93	0.43
fluoride	0.37	9.24	0.23

<sup>a</sup>Standard deviation calculated from propagation of error analysis of the SICAL equations using precision of area measurements ( $n = 26$ ). <sup>b</sup>Average for SICAL-measured concentration ( $n = 26$ ); in both cases  $\bar{C}$ (true) was 10.00 mequiv/L. <sup>c</sup>Standard deviation calculated from  $C_i$  values after applying SICAL method in an automated fashion using peak areas ( $n = 26$ ).

After investigation of the operation of the automated monitor, the next step was to investigate the predicted precision of the automated SICAL method and compare the prediction to the actual precision of the method. Equation 7 is first expanded to simplify the propagation of error calculation

$$C_i = C \left[ \frac{A_{1,i}}{A_5 - (A_3A_6/A_4)} + \frac{A_{1,i}}{A_3 - (A_4A_5/A_6)} + \frac{A_{2,i}}{A_6 - (A_4A_5/A_3)} + \frac{A_{2,i}}{A_4 - (A_3A_6/A_5)} \right] \quad (9)$$

Through propagation of error using eq 9, eq 10 can be derived

$$[dC_i]^2 = \left[ \frac{\delta C_i}{\delta C} dC \right]^2 + \left[ \frac{\delta C_i}{\delta A_{1,i}} dA_{1,i} \right]^2 + \left[ \frac{\delta C_i}{\delta A_{2,i}} dA_{2,i} \right]^2 + \left[ \frac{\delta C_i}{\delta A_3} dA_3 \right]^2 + \left[ \frac{\delta C_i}{\delta A_4} dA_4 \right]^2 + \left[ \frac{\delta C_i}{\delta A_5} dA_5 \right]^2 + \left[ \frac{\delta C_i}{\delta A_6} dA_6 \right]^2 \quad (10)$$

where each variance term with regard to area measurements in eq 10 is given by eq 11–16. Note that the statistical

$$\left[ \frac{\delta C_i}{\delta A_{1,i}} \right] = C \left[ \left[ A_5 - \frac{A_3A_6}{A_4} \right]^{-1} + \left[ A_3 - \frac{A_4A_5}{A_6} \right]^{-1} \right] \quad (11)$$

$$\left[ \frac{\delta C_i}{\delta A_{2,i}} \right] = C \left[ \left[ A_6 - \frac{A_4A_5}{A_3} \right]^{-1} + \left[ A_4 - \frac{A_3A_6}{A_5} \right]^{-1} \right] \quad (12)$$

$$\left[ \frac{\delta C_i}{\delta A_3} \right] = C \left[ A_{1,i} \left[ A_5 - \frac{A_3A_6}{A_4} \right]^{-2} \frac{A_6}{A_4} - A_{1,i} \left[ A_3 - \frac{A_4A_5}{A_6} \right]^{-2} \frac{A_4A_5}{A_6} - A_{2,i} \left[ A_6 - \frac{A_4A_5}{A_3} \right]^{-2} \frac{A_4A_5}{A_3^2} + A_{2,i} \left[ A_4 - \frac{A_3A_6}{A_5} \right]^{-2} \frac{A_6}{A_5} \right] \quad (13)$$

$$\left[ \frac{\delta C_i}{\delta A_4} \right] = C \left[ -A_{1,i} \left[ A_5 - \frac{A_3A_6}{A_4} \right]^{-2} \frac{A_3A_6}{A_4^2} + A_{1,i} \left[ A_3 - \frac{A_4A_5}{A_6} \right]^{-2} \frac{A_5}{A_6} + A_{2,i} \left[ A_6 - \frac{A_4A_5}{A_3} \right]^{-2} \frac{A_5}{A_3} - A_{2,i} \left[ A_4 - \frac{A_3A_6}{A_5} \right]^{-2} \right] \quad (14)$$

$$\left[ \frac{\delta C_i}{\delta A_5} \right] = C \left[ -A_{1,i} \left[ A_5 - \frac{A_3A_6}{A_4} \right]^{-2} + A_{1,i} \left[ A_3 - \frac{A_4A_5}{A_6} \right]^{-2} \frac{A_4}{A_6} + A_{2,i} \left[ A_6 - \frac{A_4A_5}{A_3} \right]^{-2} \frac{A_4}{A_3} - A_{2,i} \left[ A_4 - \frac{A_3A_6}{A_5} \right]^{-2} \frac{A_3A_6}{A_5^2} \right] \quad (15)$$

$$\left[ \frac{\delta C_i}{\delta A_6} \right] = C \left[ A_{1,i} \left[ A_5 - \frac{A_3A_6}{A_4} \right]^{-2} \frac{A_3}{A_4} - A_{1,i} \left[ A_3 - \frac{A_4A_5}{A_6} \right]^{-2} \frac{A_4A_5}{A_6^2} - A_{2,i} \left[ A_6 - \frac{A_4A_5}{A_3} \right]^{-2} + A_{2,i} \left[ A_4 - \frac{A_3A_6}{A_5} \right]^{-2} \frac{A_3}{A_5} \right] \quad (16)$$

uncertainty in  $C$ , namely the standard deviation of  $C$  written as  $\delta C$ , is assumed to be equal to zero, although a systematic error in  $C$  may occur. Equations 11–16 were programmed on the computer to predict the propagation of error from the precision of the area measurements, where, for instance,  $dA_3$  stands for the standard deviation of the 26  $A_3$  measurements. Averages of the 26 peak area measurements were used in applying eq 9 to predict the uncertainty in  $C_i$  for fluoride and chloride based on the uncertainty of peak area measurements, with the results shown in Table II. Thus, using the precision of the measured peak areas, one would expect the SICAL method to calculate concentration with an absolute standard deviation of 0.76 mequiv/L for chloride (7.6% relative uncertainty) and 0.37 mequiv/L for fluoride (3.7% relative uncertainty). These relative uncertainties,  $s(C_i)$ , are somewhat high, but note that any correlated drift increases  $dA$ , such as for fluoride in Figure 5, and will necessarily increase the value of  $s(C_i)$  calculated via propagation of error.

After the predicted precision of the method was determined through the propagation of error analysis, the actual accuracy and precision of the automated SICAL method were examined. The SICAL calculated concentrations for chloride and fluoride were essentially constant over the 24-h period. The SICAL calculated precisions of chloride and fluoride are also reported in Table II. It is interesting to compare  $s(C_i)$  values in Table II calculated by propagation of error, and by the usual approach after applying the method to calculate  $C_i$ . Referring to Table II, when calibration and quantitation are performed on-line by an internally consistent method, the relative precisions of the concentration calculations for chloride and fluoride are only 51% and 68%, respectively, of the relative precision calculated through propagation of error. Thus, an  $F$  test is not appropriate, since SICAL internally corrects for correlated linear drift, while the propagation of error prediction cannot. Furthermore, the precision data in Table II suggest that the SICAL method is correcting for systematic drift.

The accuracy of the SICAL method was also examined. Results are reported in Table II. Both of the ions in the sample stream were formulated at 10.0 mequiv/L, while the calculated concentrations for chloride and fluoride were 10.9 and 9.2 mequiv/L, respectively, using the average of 26 measurements. Using 3 standard deviations as the boundary limits, the measured precision for each analyte, and a true value of 10.0 mequiv/L, one can calculate the boundary limits as 8.7 and 11.3 mequiv/L for chloride and 9.3 and 10.7 mequiv/L for fluoride. The SICAL measured average concentration values are, therefore, on the outer limits for the two analytes. The sample stream and calibrating ions were made

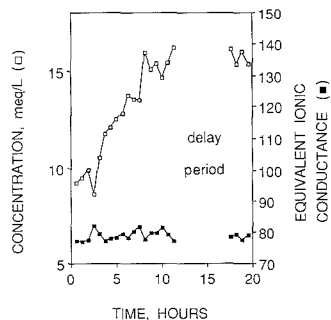


**Figure 6.** SICAL-calculated concentration (□) and equivalent ionic conductance (■), as continuously monitored for a programmed chloride concentration change (as explained in the text), including a 5-h delay period (system shut off and restarted).

from dried reagent grade materials to minimize contamination; however, potassium fluoride is hygroscopic and could have absorbed water from the air causing the fluoride concentration to be low. The signals from the detector were well within the linear range of operation. The inaccuracy more than likely stems from the implicit assumption that activity equals concentration (25). In the derivation of eq 1-6, it is assumed that the concentrations are at an activity coefficient of one and that the equivalent ionic conductances are completely independent of concentration. A slight modification of the experimental configuration could alleviate this problem by using eluents with similar ionic strength. Another assumption in deriving eq 1-6 is the absence of matrix effects in the two different eluents. Again, eluent choice could minimize these effects. Meanwhile, the SICAL calculated equivalent ionic conductances (average for 26 trials) for chloride and fluoride were 69.3 (1.7% relative uncertainty) and 55.4 (0.9% relative uncertainty), respectively. From Table I, these equivalent ionic conductances for chloride and fluoride are in reasonable agreement with the limiting equivalent ionic conductances, considering the experiments were not performed at infinite dilution. Being able to calculate the equivalent ionic conductance on-line may be a valuable diagnostic tool, particularly in process analysis. Again, this principle is not limited to conductivity detection (15-21). Another consideration of the method as applied was the relatively long time constant for new information, on the order of 38 min. As evident by Figure 2, the bulk of the time for the analysis is the acquisition of the chromatographic data. For a given chemical process, the makeup of the process will remain fairly constant and, therefore, the process monitor can be further optimized by reducing analysis time. An appropriate choice of the eluents could speed up the separation considerably (23). High-speed and superspeed HPLC may be employed (14). Another possibility is to reduce the rate at which the CI are analyzed.

The next study of interest was to monitor a changing chemical sample. The system investigated was the same sample stream as before, but now the chloride concentration was increased while keeping the fluoride concentration constant. This was accomplished by steadily adding 50.0 mL of 50.0 mequiv/L NaCl and 10.0 mequiv/L KF to 200 mL of the stream by a syringe pump over a 8.33-h time period at which time the process stream conditions level off. Recirculation of the process stream and negligible injection volume essentially kept the final sample stream reservoir volume at 250 mL with no adverse effects. Thus, chloride should ideally begin at 10.0 mequiv/L and reach 18.0 mequiv/L after 8.33 h and remain at steady state, while fluoride should ideally remain constant throughout at 10.0 mequiv/L. During this

study, as in the steady-state concentration study, there was a delay period. The system was shut off at the 12-h point and restarted after 5 h. The SICAL measured concentration and equivalent ionic conductance of chloride are shown in Figure 6. Original chromatograms in the two eluents are also not shown, for the sake of brevity. The SICAL method was successful in monitoring the changing chloride concentration without the use of a calibration curve. The next question of interest was what happens to the equivalent ionic conductances during this same exercise? There should be no change in the SICAL measured equivalent ionic conductances as it is an intensive property of the ions that does not depend on concentration (25). Figure 6 also shows the measured equivalent ionic conductance for chloride. For chloride, the concentration changed as "programmed", but the equivalent ionic conductance did not change as predicted by eq 8. For fluoride, neither the concentration nor the equivalent ionic conductance changed as anticipated, and for the sake of brevity, are not shown.

The results of Figure 6 point toward the potential of the SICAL method, or some similar method, that simultaneously performs qualitative and quantitative analysis. Conventional HPLC quantitative procedures assume qualitative analysis by performing analyte calibration in a separate step, i.e., measure a standard, then measure the unknown. With the SICAL method, the unknown is measured twice in an internally consistent fashion, thus providing a built-in consistency test that indicates whether or not the qualitative or quantitative nature of a particular analyte response has changed. This feature was clearly demonstrated for chloride in Figure 6. Likewise, the qualitative nature of a solute response may be charged, as in coelution interference. The method has also been tested for coelution problems and succeeded in diagnosing the problem. Thus, the method provides more information than the conventional single-column HPLC calibration procedure. Furthermore, the method indicates whether or not a change in the sample component is qualitative or quantitative in nature. This feature of the SICAL method may be useful in purity testing, evaluation of true unknowns, and process analysis if redundancy testing is required. Further developments in the instrumentation and deconvolution techniques (26) coupled with real process testing will be required in future developments in order to circumvent the cumbersome nature of the present SICAL method.

## LITERATURE CITED

- (1) Hirschfeld, T.; Callis, J. B.; Kowalski, B. R. *Science* **1984**, *226*, 312-318.
- (2) Mix, P. E. *The Design and Applications of Process Analyzer Systems*; Wiley-Interscience: New York, 1984; Vol. 70.
- (3) Baker, G. L.; Miller, T. E.; Mowery, R. A., Jr. In *Automated Stream Analysis for Process Control*; Manika, D. P., Ed.; Academic Press: New York, 1982; Vol. 1 and 2.
- (4) Ruzicka, J.; Hansen, E. H. *Flow Injection Analysis*; Wiley: New York, 1988.
- (5) Dong, M. C. *J. Liq. Chromatogr.* **1986**, *9*(14), 3063-3092.
- (6) Little, J. N. *J. Liq. Chromatogr.* **1986**, *9*(14), 3033-3062.
- (7) Moller, J.; Hiddessen, R.; Niehoff, J.; Schuriger, K. *Kanal. Chim. Acta* **1986**, *190*, 195-203.
- (8) Apffel, J. A.; Alfredson, T. V.; Majors, R. E. *J. Chromatogr.* **1981**, *206*, 43-57.
- (9) Erni, F.; Keller, P. H.; Morin, C.; Schmitt, M. *J. Chromatogr.* **1981**, *204*, 65-76.
- (10) Johnson, E. L.; Gloor, R.; Majors, R. E. *J. Chromatogr.* **1978**, *149*, 571-585.
- (11) Fuller, E. N.; Porter, G. T.; Roof, L. B. *J. Chromatogr. Sci.* **1979**, *17*, 661-665.
- (12) Borman, S. A. *Anal. Chem.* **1980**, *52*, 1409A-1410A.
- (13) Sharaf, M. A.; Illman, D. L.; Kowalski, B. R. *Chemometrics*; Wiley-Interscience: New York, 1986; Vol. 82.
- (14) Renn, C. R.; Synovec, R. E. *Anal. Chem.* **1988**, *60*, 200-204.
- (15) Synovec, R. E.; Yeung, E. S. *Anal. Chem.* **1983**, *55*, 1599-1603.
- (16) Wilson, S. A.; Yeung, E. S.; Bobbitt, D. R. *Anal. Chem.* **1984**, *56*, 1457-1460.
- (17) Synovec, R. E.; Yeung, E. S. *J. Chromatogr.* **1984**, *283*, 183-190.
- (18) Wilson, S. A.; Yeung, E. S. *Anal. Chim. Acta* **1984**, *157*, 53-63.
- (19) Bobbitt, D. R.; Yeung, E. S. *Anal. Chem.* **1984**, *56*, 1577-1588.
- (20) Skogerboe, K. J.; Yeung, E. S. *Anal. Chem.* **1984**, *56*, 2684-2686.

- (21) Synovec, R. E.; Yeung, E. S. *Anal. Chem.* **1984**, *56*, 1452-1457.
- (22) Gjerde, D. T.; Fritz, J. S.; Pohland, T. C. *Chromatographic Methods: Ion Chromatography*, Hühig; Heidelberg, 1982; pp 84-130.
- (23) Karger, B. L.; Snyder, L. R.; Horvath, C. *An Introduction to Separation Science*; Wiley-Interscience: New York, 1973; pp 235-236.
- (24) Smit, H. C.; Heuvel, E. J. In *Topics in Current Chemistry*; Springer-Verlag: Berlin, 1987; Vol. 141.
- (25) Atkins, P. W. *Physical Chemistry*; Oxford University Press: Oxford, Great Britain, 1978; pp 819-848.
- (26) Sharaf, M. A.; Kowalski, B. R. *Anal. Chem.* **1982**, *54*, 1291-1296.

RECEIVED for review February 8, 1989. Accepted May 26, 1989. C.N.R. and R.E.S. thank the NSF Center for Process Analytical Chemistry for support of this work (Project Number 87-1).

## Polyamine Detection System for High-Performance Liquid Chromatography Involving Enzymatic and Chemiluminescent Reactions

Sachiko Kamei\* and Akiyuki Ohkubo

Department of Laboratory Medicine, Faculty of Medicine, University of Tokyo, 7-3-1 Hongo, Bunkyo-ku, Tokyo 113, Japan

Shin Saito and Shigeyuki Takagi

The Medical Equipment Technical and Engineering Division, JEOL, Ltd., 1418, Nakagami-cho, Akisima-shi, Tokyo 196, Japan

We have developed a new specific detection system for polyamines, separated by high-performance liquid chromatography, to replace the usual *o*-phthalaldehyde (OPA) postlabeling method. This system utilizes a chemiluminescent reaction to determine the amount of hydrogen peroxide generated through the enzymatic oxidation of polyamines. With this method, as little as 5 pmol of putrescine could be accurately determined ( $S/N = 4$ ), and linearity between the amount of this polyamine and the relative chemiluminescence intensity was observed up to 500 pmol. In the cases of cadaverine, spermidine, and spermine, the linearity continued to 1 nmol. The within-assay coefficients of variation for these four polyamines ranged between 0.97% and 2.03%. As compared with the OPA method, the new method is highly specific for polyamines due to the high specificity of the enzyme used. Another advantage of the new method is the direct determination of polyamines in urine samples that contain various compounds that interfere with the OPA method.

The measurement of polyamine concentrations in urine is very useful for following the progress of cancer patients because increases in polyamine concentrations are often noted in the urine of patients with cancer as well as in cancer tissues and body fluids. The amounts of polyamines are currently determined by high-performance liquid chromatography (HPLC) employing either the ion exchange column (1-3) or the ion-paired reversed-phase column of octadecylsilane (4-6). Usefulness of the latter column is especially remarkable since free and monoacetylated polyamines, as well as metabolites of polyamines, can be separated within a fairly short time when the column is developed by a gradient elution program (6). After separation, polyamines are usually detected by the fluorescence detection system, utilizing an *o*-phthalaldehyde (OPA) postlabeling method (7). This detection method is sufficiently sensitive and reproducible for estimating the

amount of purified polyamines. However, it is not satisfactorily specific for the determination of polyamines in biological materials because OPA reacts with various amino compounds other than polyamines and generally the quantity of polyamines in biological materials is very low compared to those of various interfering amino compounds. Thus, in the analysis of polyamines in biological materials, it is essential to choose very strict conditions in the elution program to separate each polyamine from many other amino compounds (1, 3, 6) or to treat the samples prior to the analysis to remove interfering materials. From this point of view, it is desirable to develop a simple detection system, which is highly specific for polyamines. With such a system, the conditions for HPLC to separate polyamines become rather simple, because the separation of polyamines from each other is only required for the direct measurement of polyamines in biological materials.

Generally speaking, luminescence photometry is highly sensitive within wide dynamic ranges and has the advantage that it requires no light source or spectroscopy. Application of a chemiluminescence (CL) reaction on HPLC has been reported for the detection of fluorescent compounds (8, 9), in which the CL generated through the reaction between the compound to be determined, an oxalic ester, and hydrogen peroxide ( $H_2O_2$ ) was measured. With the aim of applying a CL reaction to determine polyamines, which are not fluorescent compounds, we developed a new CL detection system. The system is based on the specific enzymatic oxidation of polyamines and separation with a fully automated HPLC, to produce  $H_2O_2$ . The amount of  $H_2O_2$  is then determined by using a CL reaction. Employing a flow system, we determined the conditions for the new CL detection method to obtain the highest precision and sensitivity. Then, we applied this method for the determination of free polyamines by HPLC and compared it with the OPA postlabeling method (10, 11).

### EXPERIMENTAL SECTION

**Materials.** Bis(2,4-dinitrophenyl) oxalate (DNPO), 8-anilino-naphthalenesulfonate (ANS), and OPA were obtained from Wako Pure Chemical Industries, Ltd., Osaka, Japan. Amino-

propyl-controlled-pore glass was obtained from Pierce Chemical Co., Rockford, IL. Glutaraldehyde and a packed column of octadecylsilane (ODS) for HPLC were obtained from Seikagaku Kogyo Co., Ltd., Tokyo, Japan. Putrescine, cadaverine, spermidine, and spermine were obtained from Nakarai Co., Kyoto, Japan. Putrescine oxidase (EC 1.4.3.10, PUOD) from *Micrococcus flavidus* was donated by Tokuyama Soda Co., Ltd., Kanagawa, Japan. Polyamine oxidase (PAOD) from *Aspergillus terreus* analogous to amine oxidase (flavin containing) (EC 1.4.3.4) was donated by Amano Seiyaku Co., Ltd., Aichi, Japan.

**Procedures. Preparation of Immobilized Enzymes.** PUOD and PAOD were immobilized separately on aminopropyl-controlled-pore glass (particle size, 125–177  $\mu\text{m}$ ; 80–120 mesh; mean pore diameter, 5  $\mu\text{m}$ ) by the glutaraldehyde method (12). Briefly, 2 g of aminopropyl-controlled-pore glass was stirred in a 1.0% aqueous solution of glutaraldehyde for 30 min at 0  $^{\circ}\text{C}$ . The derivatized beads obtained were rinsed with 50 mL of 10 mM phosphate buffer, pH 7.2, and then suspended in 10 mL of the same buffer containing 45 mg (900 units) of PUOD or PAOD. After the mixture was stirred for 2 h at 4  $^{\circ}\text{C}$ , the beads were washed thoroughly with the 10 mM phosphate buffer containing 0.8 M NaCl until no enzymatic activity was detectable in the washings.

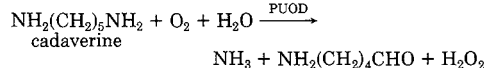
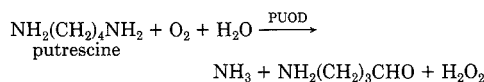
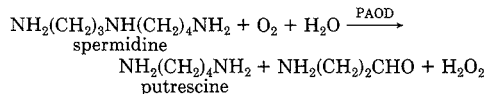
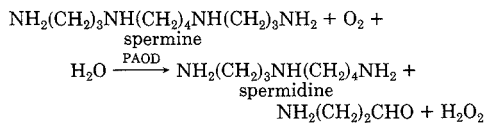
**Preparation of Test Samples from Urine.** Urine was collected from apparently healthy volunteers and stored at  $-70^{\circ}\text{C}$  until use. Test samples were prepared from the urine as follows: 1.0 mL of urine was mixed with the same volume of 6 N HCl, and then the mixture was heated for 12 h at 100  $^{\circ}\text{C}$ . After the pH was adjusted to 7.0 with 3 N NaOH, the mixture was used as a test sample.

**Apparatus.** A fully automated HPLC, type JLC 300, with a luminescence detector, type LC 30-DPC10, from JBOL Co., Ltd., Tokyo, Japan, was used.

## RESULTS AND DISCUSSION

### Principle Underlying the Detection of Polyamines.

Polyamines separated by HPLC were oxidized with a combination of PAOD and PUOD to generate  $\text{H}_2\text{O}_2$ , aminoaldehyde, and ammonia, as follows:



Thus, spermine, spermidine, putrescine, and cadaverine yield three, two, one, and one molecule of  $\text{H}_2\text{O}_2$ , respectively. Furthermore, acetyl derivatives of polyamines such as acetylspermine and  $N^1$ -acetylspermidine, which are suggested to have a biological significance, generate  $\text{H}_2\text{O}_2$  with PAOD in a similar manner.

As proposed by Rauhut (13), it is possible to generate CL with the  $\text{H}_2\text{O}_2$  produced through these steps in the presence of an oxalic ester and a fluorophore according to the following reactions.  $\text{H}_2\text{O}_2$  reacts with the oxalic ester DNPO to yield dioxetanedione, which is immediately degraded to two molecules of carbon dioxide, simultaneously exciting the coexisting fluorescent compound, ANS. ANS in the excited state, then returns spontaneously to the ground state, being ac-

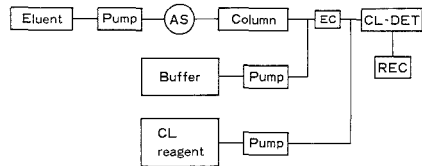
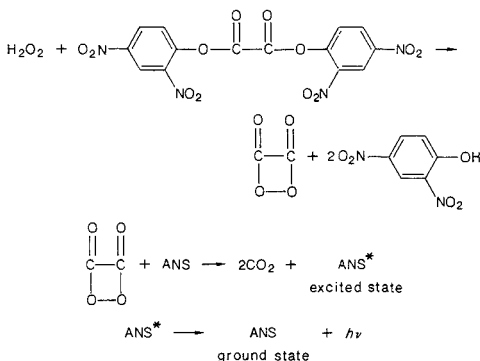


**Figure 1.** Flow diagram of the complete system for polyamine determination: CL reagent, chemiluminescence reagent; CL-DET, chemiluminescence detector; REC, recorder. The complete system can be separated into three parts.

companied by the emission of a photon,  $h\nu$ . The emitted photons are detected by a photomultiplier tube with a photon counter, and the relative luminescence intensity is recorded.



To make these steps occur in order, we constructed the system illustrated in Figure 1. The complete system can be separated into three parts. The first part is HPLC to separate the polyamines, which is composed of eluent, a pump, an autosampler (AS), and a column for HPLC (Column). The second part is an enzymatic oxidation system for the polyamines, which is composed of buffer, a pump, and an immobilized enzyme column (EC). The third part is the CL generating system with a detector, which is composed of chemiluminescence reagent (CL reagent), a pump, a chemiluminescence detector (CL-DET), and a recorder (REC).

**Studies on the Conditions for CL Detection.** At the CL detection step, we examined various conditions by means of flow injection analysis, employing the system without an AS, a Column, and an EC shown in Figure 1. We found that after injection of  $\text{H}_2\text{O}_2$  into the system, followed by introduction of 0.2 M imidazole–0.05 M borate buffer (pH 7.5, containing 75 mM sodium azide; flow rate, 0.75 mL/min) and the CL reagent (composed of 0.63 mM DNPO and 0.63 mM ANS in acetonitrile; flow rate, 0.8 mL/min), the relative luminescence intensity decreased with the lapse of time, while the signal to noise ratio (S/N) reached a maximal level at 10 s after the onset of mixing. On the basis of this maximal level of 10 s, we chose a corresponding flow path length for the CL reaction of 10 s. Although the maximal S/N value was observed at pH 6.5 in the CL reaction, we decided to adopt pH 7.5 for the following experiments because both PUOD and PAOD are known to have optimal pH values of about 8. Furthermore, we found that the S/N value became maximal at 0.63 mM DNPO, whereas the relative luminescence intensity increased with an increase in the concentration of ANS. Since the sensitivity of the CL reaction seemed to be sufficient with 0.63 mM ANS, we used 0.63 mM DNPO and 0.63 mM ANS in further experiments. From these results we chose the following standard conditions: (i) as the HPLC step, we adopted

**Table I. With-Assay Precision of Peak Area<sup>a</sup>**

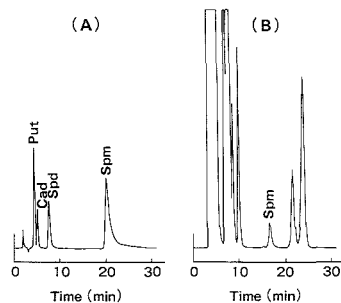
	putrescine	cadaverine	spermidine	spermine
max, pmol	306.3	305.1	300.6	304.2
min, pmol	293.7	288.3	280.2	281.1
mean, pmol	299.7	294.3	291.3	291.9
SD, <sup>b</sup> pmol	2.91	4.41	4.71	5.91
CV, <sup>c</sup> %	0.97	1.49	1.62	2.03

<sup>a</sup>  $n = 20$  throughout. 300 pmol of each polyamine was injected.  
<sup>b</sup> SD, standard deviation. <sup>c</sup> CV, coefficient of variation.

pentanesulfonic acid ion-paired, reversed-phase chromatography on an ODS column (2.6 mm diameter  $\times$  150 mm; maintained at 37 °C), which has been reported to be able to separate spermine, spermidine, putrescine, and cadaverine within 25 min (8, 11, 14), (ii) conditions for the enzymatic oxidation step were the same as in previous work (using an immobilized enzyme column, 2.1 mm diameter  $\times$  35 mm; maintained at 37 °C) (15) except that the pH was 7.5, and (iii) the CL detection step was carried out as described above, except that the pH of the buffer solution (flow rate, 0.25 mL/min) was raised from 7.5 to 8.42 in order to adjust the low pH of the eluent buffer for HPLC (composed of 10 mM sodium phosphate, pH 2.0, containing sodium chloride, 6.0 g/L; flow rate, 0.5 mL/min) to 7.5 before it entered the immobilized enzyme column.

**Evaluation of the New Method.** The capability of the new method under these conditions was examined by applying standard polyamines. A linear relationship between the amount of the polyamine applied and the relative luminescence intensity was observed up to 500 pmol in the case of putrescine, and up to 1 nmol in the cases of cadaverine, spermidine, and spermine. The detection limit ( $S/N = 4$ ) was 6 pmol of spermine, 7 pmol of spermidine, and 5 pmol of putrescine. On comparison of these values with those obtained with the OPA method (16) (i.e., 12–15 pmol, 3–6 pmol, and 3–6 pmol, respectively), the sensitivity for spermine was found to be higher, which seemed to be the result of three molecules of  $H_2O_2$  being generated from one molecule of spermine as described above. The detection limit for cadaverine is relatively high at 30 pmol, which may be due to the low reactivity of the PUOD to cadaverine. These observations indicate that the new method has a wide dynamic range and is as useful as the OPA method except for cadaverine, which is thought to be a less significant polyamine in biological materials. The within-assay precision of the peak area was examined by applying a standard solution containing 300 pmol of each polyamine 20 times, and calculating the mean value, the standard deviation, and the coefficient of variation. As summarized in Table I, the coefficient of variation was less than 2%, indicating that the precision of the new method is satisfactory. Among monoacetyl derivatives of the polyamines which have been demonstrated to be excreted in urine (17),  $N^1$ -acetylspermidine and acetylspermine are able to be detected by this method because they are oxidized with PAOD. The disadvantage of this method is that acetylputrescine, acetylcadaverine, and  $N^8$ -acetylspermidine are not detected. However, an enzymatic chemiluminescent detection system for polyamines, together with their monoacetyl derivatives, should be possible if we utilize acylpolyamine amidohydrolase (18) in combination with PAOD and PUOD. This should be studied as a next step.

**Advantages of the New Method over the OPA Method.** The new method shows comparable capability to the OPA method when it is used for the analysis of a mixture of pure standard polyamines (not shown). However, the advantage of the new method over the OPA method is obvious for the analysis of polyamines in biological materials such as tissue

**Figure 2.** Chromatograms of a hydrolyzed urine sample.**Table II. Precision of the Urine Assay<sup>a</sup>**

	mean (SD), pmol/20 $\mu$ L	CV, %
putrescine	286 (3.7)	1.3
cadaverine	118 (3.4)	2.9
spermidine	204 (4.5)	2.2
spermine	42 (4.1)	9.7

<sup>a</sup>  $n = 8$  each.

extracts, body fluids, and urine, which contain many OPA reactive substances. The new method detects only polyamines as a result of the strict substrate specificity of PUOD and PAOD. Figure 2 shows two typical chromatograms of a hydrolyzed urine sample, which was subjected to HPLC under simple isocratic separation conditions. The detection system employed was the new method in Figure 2A and the OPA method in Figure 2B. In part A, four sharp peaks were identified as corresponding to putrescine (Put), cadaverine (Cad), spermidine (Spd), and spermine (Spm), respectively, on the basis of their retention times. In part B, only the peak of spermidine could be identified. This clearly indicates the usefulness of the new method for the determination of polyamines, especially in clinical samples. We expect its further application to many other fields including the diagnosis of cancer. The retention times are different in A and B, because of the degeneration of the separation column from repeated use.

**Analytical Variables for Urine Assay. Linearity.** A linear relationship between the amount of the polyamine in urine sample and the relative luminescence intensity was ascertained up to 320 pmol in the case of putrescine, and up to 155, 60, and 115 pmol in the cases of cadaverine, spermidine, and spermine, respectively, which represent the content of polyamine in an urine sample without dilution.

**Precision.** The results for studies of within-run precision ( $n = 8$ ) obtained with urine samples are shown in Table II.

**Analytical Recovery.** We added 10  $\mu$ M of each polyamine to a normal fresh urine sample to determine the recovery. Recovery rates ranged between 87% (cadaverine) and 103% (putrescine).

**Method Comparison.** The correlation coefficient ( $r$ ) between the values of putrescine determined with this method ( $y$ ) and those with an OPA method ( $x$ ) was 0.906, the regression equation being  $y = 1.24x - 0.90 \mu\text{M}$  ( $n = 17$ ). A good correlation ( $r = 0.983$ ) was also observed between both methods as to cadaverine, the regression equation being  $y = 1.47x + 0.05 \mu\text{M}$  ( $n = 17$ ), whereas a reduced correlation ( $r = 0.763$ ) was observed between the values of spermidine determined with both methods, the regression equation being  $y = 0.818x - 3.80 \mu\text{M}$  ( $n = 14$ ). It seemed to be due to the possible positive error caused by some interferent(s) with method  $x$ , and relatively low amount of spermidine in most

samples. Since spermine was the lowest in concentration in urine samples and lower than detection limit in many samples, we could not present any helpful information about method comparison.

Finally, we should point out the possibility of utilizing the electrochemical detector for HPLC (19) recently developed for the direct determination of  $H_2O_2$ , with the conditions that (i) its sensitivity is comparable to that of our CL method or the usual OPA method and (ii) it is sensitive to only  $H_2O_2$ , and not to coexisting oxidoreductive compounds in biological materials. If these conditions can be satisfied, it would be interesting to compare the determination of polyamines in biological materials with this system and with the CL detection system.

#### ACKNOWLEDGMENT

The authors wish to thank Dr. K. Iwasaki for his critical reading of the manuscript and Miss K. Hiramatsu for her technical assistance. They are also grateful for the support of this research by a Grant-in-Aid for Scientific Research (No. 62571033) from the Ministry of Education, Science and Culture of Japan.

#### LITERATURE CITED

- (1) Mach, M.; Kersten, H.; Kersten, W. *J. Chromatogr.* **1981**, *223*, 51-57.
- (2) Bondy, P. K.; Canellakis, Z. N. *J. Chromatogr.* **1981**, *224*, 371-379.

- (3) Russell, D. H.; Ellingson, J. D.; Davis, T. P. *J. Chromatogr.* **1983**, *263*-274.
- (4) Selier, N.; Knodgen, B. *J. Chromatogr.* **1980**, *221*, 227-235.
- (5) Wagner, J.; Danzin, C.; Mamont, P. *J. Chromatogr.* **1982**, *227*, 349-368.
- (6) Selier, N.; Knodgen, B. *J. Chromatogr.* **1985**, *339*, 45-57.
- (7) Roth, M.; Hampai, A. *J. Chromatogr.* **1973**, *83*, 353-356.
- (8) Kobayashi, S.; Imai, K. *Anal. Chem.* **1980**, *52*, 424-427.
- (9) Kobayashi, S.; Sekino, J.; Honda, K.; Imai, K. *Anal. Biochem.* **1981**, *112*, 99-104.
- (10) Kamei, S.; Ohkubo, A.; Yamanaka, M.; Saito, S.; Takagi, S. *Abstracts of International Conference on Polyamines in Life Sciences 1986*, 261-262.
- (11) Kamei, S.; Saito, S.; Ohkubo, A.; Yamanaka, M.; Okaji, M. *Abstracts of the World Congress of Anatomic and Clinical Pathology 1987*, *14*, 80.
- (12) Robinson, P. J.; Dunnill, P.; Lilly, M. D. *Biochem. Biophys. Acta* **1971**, *242*, 659-661.
- (13) Rauhut, M. M. *Acc. Chem. Res.* **1969**, *2*, 80-87.
- (14) Murakita, H.; Watanabe, Y.; Fujiwara, M. *Abstracts of International Conference on Polyamines in Life Sciences 1986*, 253-254.
- (15) Kamei, S.; Mashige, F.; Ohkubo, A.; Yamanaka, M.; Okada, M.; Imahori, K. *Jpn. J. Clin. Chem.* **1984**, *13*, 66-73.
- (16) Seiler, N. *J. Chromatogr.* **1986**, *379*, 157-176.
- (17) Abdel-Moneim, M. M.; Ohno, K. *J. Pharm. Sci.* **1977**, *66*, 1195.
- (18) Okada, M.; Yoshimura, Y.; Imahori, K. *Polyamines: Basic and Clinical Aspects*; Imahori, et al., Eds.; 1985 VNU Science Press: 1985; pp 73-80.
- (19) Watson, B.; Stiffl, D. N.; Semersky, F. E. *Anal. Chim. Acta* **1979**, *106*, 233-242.

RECEIVED for review September 14, 1987. Resubmitted September 26, 1988. Revised manuscript received May 15, 1989. Accepted May 15, 1989.

## Determination of Chloride in Platinum-Rhenium Alumina-Based Reforming Catalyst by Ion Chromatography

Raj P. Singh,\* Khurshid Alam, Dawoud S. Redwan, and Nureddin M. Abbas

The Research Institute, King Fahd University of Petroleum & Minerals, Dhahran 31261, Saudi Arabia

An ion chromatographic method was developed for the fast and accurate determination of chloride in Pt-Re/Al<sub>2</sub>O<sub>3</sub> catalysts using a Dionex Model 2120i ion chromatograph. Extraction of chloride was carried out with sodium hydroxide solution in a Teflon Parr bomb at 150 °C. After filtration, ion chromatographic analyses were made by injecting 100 μL of the diluted solution into the sample port. Separation of chloride was achieved on a Dionex AS-4 separator and AG-4 guard column with sodium carbonate-bicarbonate eluent. The proposed method is free from interferences of sulfide and halides generally encountered in conventional potentiometric and spectrophotometric methods. The total analysis time of less than 1 h was considerably shorter than that reported for conventional methods. The minimum detectable chloride in a catalyst sample was 0.1% by weight with a relative standard deviation of about 3%.

#### INTRODUCTION

Pt-Re/Al<sub>2</sub>O<sub>3</sub> reforming catalysts are used for upgrading low octane naphthas to high octane gasoline as well as for the production of important feedstocks for the petrochemical industry (1-5). Reforming catalysts are bifunctional, and their performance largely depends on the correct balance between

the metallic (Pt-Re) and acidic (alumina support) functions. Practically, the balance is monitored by the addition of chlorinating agent and water in the feed. Changes in this balance heavily affect both the product quality and quantity. Low chloride content of the catalyst will cause a drop in its acidity, and consequently slowing down the desired reaction affected by the acidic properties of the catalyst (isomerization, and dehydrocyclization), which will result in reformat of low octane number. On the other hand, if chloride content uncontrollably increases, the acid strength of the catalyst support increases and thus favors the undesired reactions such as hydrocracking and coke deposition. To overcome these problems, the chloride content of the catalyst should be continuously monitored and controlled.

The methods of chloride determination in bimetallic reforming catalysts have not been well established. In practice, the analysis of chloride is carried out by digesting the catalyst in sulfuric acid, for 2-26 h (depending on the carbon content) and titrating the chloride against silver nitrate using a silver or chloride ion selective electrode. A spectrophotometric method (6) has also been reported recently, by measuring the absorbance of the colored complex of Cl<sup>-</sup> with Hg(SCN)<sub>2</sub>-Fe<sup>3+</sup>. Extraction of chloride in the later method was carried out by digesting the catalyst in 1.0 mol L<sup>-1</sup> sodium hydroxide, for about 2 h, in three steps. However, due to lack of availability of either a standard method of chloride analysis in these

**Table I. Ion Chromatography Conditions**

analytical column	Dionex AS-4
guard column	Dionex AG-4
suppressor column	Dionex Anion Micro Membrane Suppressor
eluent	0.003 mol L <sup>-1</sup> NaHCO <sub>3</sub> + 0.0024 mol L <sup>-1</sup> Na <sub>2</sub> CO <sub>3</sub>
regenerant	0.0125 mol L <sup>-1</sup> H <sub>2</sub> SO <sub>4</sub>
flow rate	2.0 mL min <sup>-1</sup>
regenerant flow rate	2-2.5 mL min <sup>-1</sup>
injection volume	100 µL
detector sensitivity	30 µS full scale
detector	conductivity, Dionex
integrator	Dionex Model 4217

catalysts or a standard catalyst sample with certified chloride value, the accuracy of the extraction of chloride in sodium hydroxide could not be assessed. In addition, both methods may also suffer from the interferences of other ions, present in the catalyst extracts.

Ion chromatography, the method of choice for the determination of common anions, offers certain advantages over other techniques (7-9). In the literature few reports (10-15) have been published on the ion chromatographic analysis of ions in the inorganic materials but none have appeared on its use for the analyses of catalysts. The objective of this work was to develop an ion chromatographic (IC) method for the rapid and accurate determination of chloride in bimetallic reforming catalysts. We were also interested in assessing the extraction (liberation) of chloride from the catalyst in 1 mol L<sup>-1</sup> sodium hydroxide at 150 °C in a Parr bomb, since Parr bomb methodology allows fast and efficient digestions.

#### EXPERIMENTAL SECTION

**Reagents.** Doubly distilled deionized water (Nanopure II) was used to prepare solutions. Sodium hydroxide (Reidel Certified) and sulfuric acid (Fluka) were of >99% purity and contained less than 0.0005 and 0.0001% chloride, respectively. Chloride standards for IC were prepared from a 500 mg L<sup>-1</sup> solution supplied by RICCA Chemical Co., Arlington, TX.

**Catalyst Sample Preparation.** All the analyses were carried out on the platforming catalyst R-50. The catalyst samples taken out of the reactor always contain a considerable amount of petroleum hydrocarbons in varying amounts. Therefore, to have the analytical results free from hydrocarbons, all the samples were heated at 150 °C in a mechanical convection oven for 4 h. After cooling in a desiccator, the samples were finally ground in an agate mortar to a 100 mesh size.

**Parr Bomb.** The Parr bomb (4745, Parr Instrument Co.) consisted of a sealable bomb lined with Teflon which contained a 25-mL Teflon cup with cover. The bomb can operate up to 275 °C and pressures up to 5000 psi without corrosion or loss of volatile elements.

**Carbon Analyzer.** A Strohhlein Model Coulomat 702 carbon sulfur analyzer was used for the determination of total carbon.

**Titration.** A microprocessor-controlled Mettler DL 40RC Memotitrator fitted with Mettler's GM 141 combination silver ring electrode, GA 44 printer, and GA 15 chart recorder was used to carry out the silver chloride precipitation titrations in sulfuric acid extracts.

**X-ray Fluorescence Spectrometer.** A Phillips PV 9500 energy dispersive fluorescence spectrometer with a Si(Li) detector was used. The detector had a resolution of 164 eV at 5.9 kV and active area of 10 mm<sup>2</sup>. The samples were analyzed in powder form with a rhodium target excited at 30 kV and 500 mA. The spectra were collected for 400 live seconds with an aluminum filter. The specimen chamber was flushed with helium gas during the data collection.

**Ion Chromatograph.** Ion chromatographic analyses were made with a Dionex 2120i ion chromatograph at a constant temperature of 20 ± 1 °C under the conditions summarized in Table I. The ion chromatograph was calibrated with chloride standards at 1.0, 2.0, and 4.0 mg L<sup>-1</sup>. A computerized linear regression routine was used to determine the chloride concen-

tration of catalyst samples. The slope of the calibration curve, peak height versus concentration, remained constant throughout the analysis with a linear correlation coefficient of 0.9998.

**Extraction of Chloride in Sulfuric Acid and Its Determination by Titration and IC Methods.** One gram of catalyst was weighed to the nearest 0.1 mg and transferred to a 250-mL round-bottom flask. After 30 mL of 3.5 mol L<sup>-1</sup> sulfuric acid was added, the mixture was refluxed with a water condenser for 10-16 h. Although preliminary studies have shown a complete extraction of chloride in 1 h from a used catalyst sample (containing 8.1% coke), all the used catalyst samples were refluxed at least for 10 h to ensure complete dissolution of alumina. On the completion of the extraction step, the flasks were cooled and the solution was quantitatively transferred to a 100-mL volumetric flask and diluted up to the mark with water. This solution "A" was used for the determination of chloride.

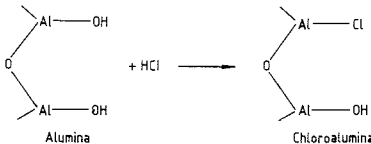
In the titration method (TM), 10 mL of A was titrated with standard silver nitrate solution.

For IC, solution A was diluted 500 times and neutralized (pH 6-7) by the addition of 1.0 mol L<sup>-1</sup> sodium hydroxide. One hundred microliters of diluted solution was injected into the column.

**Extraction of Chloride in Sodium Hydroxide and Determination by IC.** A 200-mg powdered catalyst sample was weighed to the nearest 0.1 mg in the Teflon cup (30 mL capacity) of the Parr bomb. Four milliliters of 1.0 mol L<sup>-1</sup> sodium hydroxide was then added to it and mixed well. The cap was placed on the cup and the bomb, preheated to 150 °C, was assembled. Preliminary tests showed that the extraction was completed in 30 min at 150 °C. During this period the bombs were shaken to agitate the mixture inside the Teflon cup. Finally, the bombs were cooled and the extract was transferred quantitatively to a 50-mL volumetric flask and diluted with water up to the mark. A portion of this solution was filtered through 0.45 µm (Millipore) or #42 (Whatman) filters and diluted 10 times for the chloride analysis by IC.

#### RESULTS AND DISCUSSION

**Extraction and Determination of Chloride by IC.** Chloroalumina, the acidic function of the bifunctional reforming catalyst, is generally prepared by replacing the OH<sup>-</sup> groups of alumina with Cl<sup>-</sup> ions, by the ion-exchange method (1)



The ion-exchange properties of the hydrous alumina have been extensively studied (16-19) and depend upon the pH of the ion-exchange medium. At pH values greater than the isoelectric point (iep) i.e., 6.8 for  $\gamma$ -alumina, the oxide behaves as a cation exchanger, while below the iep it possesses anion exchange properties.

Stability of alumina is weak in acidic solutions (below pH 2) and it can be dissolved in reasonably high concentrations of sulfuric or hydrochloric acids. Thus, one way of determining chloride in these catalysts is to digest the sample in sulfuric acid and titrate the extracts for chloride ions against silver nitrate solution. This method, though seeming to be simple and accurate, may suffer from the interferences of ions that precipitate with silver. As can be seen in Figure 1, ion chromatography can be used for the separation and accurate determination (Table II) of the chloride in sulfuric acid extracts; however, due to the presence of large concentration of sulfate ions, a long analysis time of about 10 min per sample is required.

The presence of sulfate ions in the catalyst extracts can be eliminated by eluting the chloride ions in alkaline solutions, since, alumina loses its affinity for anions at high pH values.

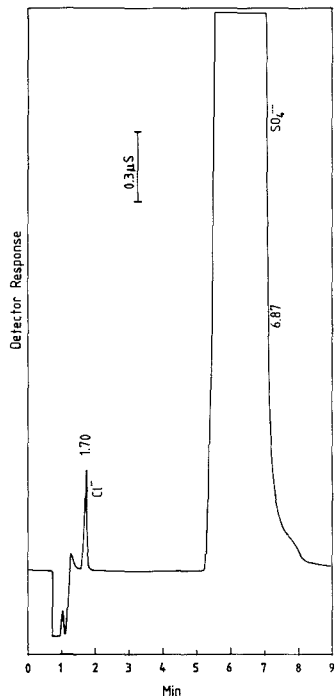


**Figure 1.** Typical ion chromatograph of the sulfuric acid extract after neutralization and dilution. Chloride elutes at 1.7 min. Large peak (6.87 min) is due to sulfate. Conditions are mentioned in the Experimental Section.

**Table II.** Results of the Analysis of Chloride in Sulfuric Acid Extracts by IC and TM

catalyst sample no.	Cl <sup>-</sup> , wt %		% bias [(X - Y)/X]100
	by TM (X)	by IC (Y)	
1	0.76	0.76	0.00
2	0.76	0.72	+5.26
3	0.73	0.70	+4.11
4	0.95	0.94	+1.05
5	0.81	0.81	0.00

mean = 2.08  
std dev = 2.45  
Student *t* = 2.28

Student *t* at 95% confidence interval = 2.78

This approach was used by Koshy and Garg (6) by digesting the catalyst samples in 1.0 mol L<sup>-1</sup> sodium hydroxide solution. However, these workers failed to make a quantitative assessment of chloride recovery. Moreover, their digestion procedure as a whole is quite cumbersome. In the present method, we used a Parr bomb, which allowed fast (30 min) digestion of the catalyst samples. Figure 2 shows the typical ion chromatograph of sodium hydroxide extracts. The chloride peak was well separated from the large negative peak of hydroxyl ions. The accuracy of the chloride determination by IC, following the extraction in sodium hydroxide, was assessed by comparing the results with those obtained by the sulfuric acid extraction/silver nitrate titration method. These results are reported in Table III.

The application of null hypothesis (paired *t* test) has shown that the bias between the two methods does not differ sig-

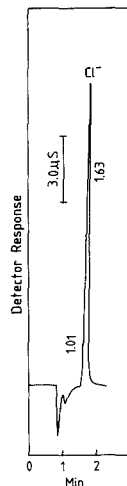


**Figure 2.** Ion chromatograph showing the separation of chloride (1.63 min) from sodium hydroxide extract. Negative peak is due to the hydroxyl ions.

**Table III.** Concentration of Chloride in Bimetallic Catalysts Containing Varying Percent Carbon (Coke Deposit) As Determined by TM and IC from Sodium Hydroxide Extracts

catalyst sample	carbon, wt %	Cl <sup>-</sup> , wt %		bias [(X - Y)/X]100
		by TM (X)	by IC (Y)	
1 <sup>a</sup>	0.0	0.94	0.95	-1.06
2	19.3	0.63	0.59	+6.35
3	2.3	0.96	0.98	-2.08
4	7.3	0.75	0.75	0.0
5	2.8	0.99	1.01	-2.02
6	8.1	0.76	0.74	+2.63
7	2.9	1.00	1.02	-2.00
8	9.0	0.78	0.77	+1.30
9	3.6	1.03	1.03	0.0
10	10.1	0.76	0.74	+2.63

mean = 0.58  
std dev = 2.71  
Student *t* = 0.50

Student *t* at 95% confidence interval = 2.26

<sup>a</sup> Fresh catalyst sample.

nificantly from zero. For comparison studies, sulfuric acid extraction/titration method was chosen as a reference method because (i) alumina, the base of the catalyst samples, was almost completely dissolved in sulfuric acid, releasing all the chloride into solution, and (ii) the ions such as bromide and iodide, which can interfere by precipitating with silver, were either absent or present in trace amounts in all the catalyst samples analyzed in the present studies, as determined by X-ray fluorescence (XRF).

**XRF Analysis.** Further confirmation of the chloride recovery by a Parr bomb/sodium hydroxide extraction method can be derived from the XRF analysis of catalyst samples. Figure 3 shows the typical XRF spectrum of a sample containing 8.1% C before and after the sodium hydroxide extraction. Absence of the Cl<sup>-</sup> peak in the XRF spectrum of the sample after sodium hydroxide treatment clearly shows that the chloride was eluted out of the catalyst by sodium hydroxide. The calculated detection limit of Cl<sup>-</sup> determination



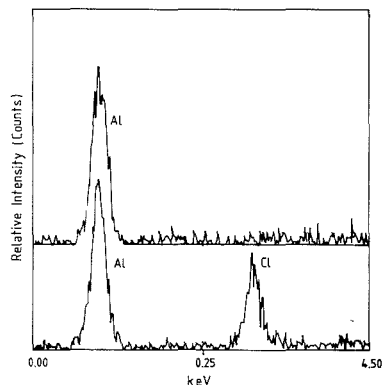


Figure 3. X-ray fluorescence spectra of catalyst sample containing 8.1% C, before (lower) and after (upper) sodium hydroxide extraction.

Table IV. Reproducibility of the Ion Chromatography Determination of Chloride in Bimetallic Reforming Catalysts

	n	mean, wt %	std dev, wt %	rel std dev, %
intrarun variation (chromatography)	10	0.74	0.009	1.2
intrarun variation (chromatography)	10	1.01	0.005	0.5
intrarun variation (overall)	5	0.74	0.02	2.7

by the XRF method indicated that at least 97% of the total  $\text{Cl}^-$  eluted out of the catalyst samples, with a 99% certainty.

**Reproducibility of the IC Method.** Table IV shows the reproducibility of the estimation of chloride by ion chromatography. On an intrarun basis, the maximum relative standard deviation is 1.2% for the ion chromatographic part of the method alone. For the overall procedure (i.e., including the sodium hydroxide extraction in the Parr bomb and dilution of the sample) the intrarun coefficient of variation increased to 2.7%.

**Accuracy of the Ion Chromatographic Part of  $\text{Cl}^-$  Analysis and Its Detection Limit.** Table V shows the recovery of  $\text{Cl}^-$  added to the sodium hydroxide extracts of five different catalysts. The application of null hypothesis has shown that the recovery was quantitative ( $p > 0.25$ ). This reveals that hydroxyl ions present in the extract do not interfere in the IC determination of chloride ions. These results also indicate that under the experimental conditions the present method can detect up to 0.1%  $\text{Cl}^-$  by weight in the catalyst samples with a relative standard deviation less than 3%. The recovery of  $\text{Cl}^-$  from the sodium hydroxide extracts at lower concentrations of chloride was not found to be quantitative.

In conclusion, with the ability to extract  $\text{Cl}^-$  from the catalyst samples in 1.0 mol  $\text{L}^{-1}$  sodium hydroxide in the Parr

Table V. Recovery of 4.5 mg  $\text{L}^{-1}$  of Chloride Added to Sodium Hydroxide Extracts of Different Catalysts

sample no.	% carbon	initial $\text{Cl}^-$ , mg $\text{L}^{-1}$	final $\text{Cl}^-$ , mg $\text{L}^{-1}$	% recovery
1	0.0	37.8	42.2	97.8
2	2.8	40.3	44.6	95.6
3	8.1	30.1	34.6	100.0
4	7.3	29.5	34.1	102.2
5	2.3	39.2 ± 0.6	43.8 ± 0.54	102.2

mean = 99.6 ± 2.9

% RSD = 2.9

Student  $t$  = 0.31

Student  $t$  at 75% confidence interval = 0.73

bomb and to resolve the  $\text{Cl}^-$  peak in less than 2 min by ion chromatography, the present method was found to be considerably faster than the presently used methods of chloride analysis in reforming bimetallic catalysts. Method comparison and XRF analyses have confirmed that a 30-min extraction of chloride in sodium hydroxide solution at 150 °C in a Parr bomb was quantitative. In addition, the present method is free from the interference of sulfide, bromide, or iodide ions, which may interfere in titration and spectrophotometric methods.

#### ACKNOWLEDGMENT

Authors are thankful to E. R. Pambid for his technical assistance.

**Registry No.** Cl, 16887-00-6; Pt, 7440-06-4; Re, 7440-15-5;  $\text{Al}_2\text{O}_3$ , 1344-28-1.

#### LITERATURE CITED

- Gates, B. C.; Katzer, J. R.; Schult, G. C. A. *Chemistry of Catalytic Processes*; McGraw-Hill: New York, 1979, pp 184-324.
- Grau, J. M.; Jablonski, E. L.; Pleck, C. L.; Verderone, R. J.; Parera, J. M. *J. Chem. Technol. Biotechnol.* **1987**, *38*, 105-113.
- Jossens, L. W.; Petersen, E. E. *J. Catal.* **1982**, *76*, 265-273.
- Parera, J. M.; Jablonski, E. L.; Cabrol, R. A.; Figoli, R. A.; Musso, J. C.; Verderone, R. *J. Appl. Catal.* **1984**, *12*, 125-139.
- Goughlin, R. W.; Hasan, A.; Kawakami, K. *J. Catal.* **1984**, *88*, 163-176.
- Koshiy, V. J.; Garg, V. N. *Talanta* **1987**, *34*, 905-908.
- Small, H. *Anal. Chem.* **1983**, *55*, 235A-242A.
- Smith, F. C.; Cheng, R. C. *CRC Rev. Anal. Chem.* **1980**, *9*, 197-217.
- Pohl, C. A.; Johnson, E. L. *J. Chromatogr. Sci.* **1980**, *18*, 442-452.
- Evans, K. L.; Moore, C. B. *Anal. Chem.* **1980**, *52*, 1908-1912.
- Gustafson, F. J.; Markell, C. G.; Simpson, S. M. *Anal. Chem.* **1985**, *57*, 621-624.
- Tan, L. K.; Dutrizac, J. E. *Anal. Chem.* **1985**, *57*, 2615-2620.
- Tan, L. K.; Dutrizac, J. E. *Anal. Chem.* **1986**, *58*, 1383-1389.
- Stallings, E. A.; Candelaria, L. M.; Gladney, E. S. *Anal. Chem.* **1986**, *60*, 1246-1248.
- Wiishire, J. P.; Brown, W. A. *Anal. Chem.* **1982**, *54*, 1647-1650.
- Vesely, V.; Pekarek, V. *Talanta* **1972**, *19*, 219-262.
- Williams, K. C.; Daniel, J. L.; Thomson, W. J.; Kaplan, R. I. *J. Phys. Chem.* **1965**, *69*, 250-253.
- Schmitt, G. L.; Pietrzyk, D. J. *Anal. Chem.* **1985**, *57*, 2247-2253.
- Clearfield, A. *Inorganic Ion Exchange Materials*; CRC Press: Boca Raton, FL, 1982; pp 161-273.

RECEIVED for review March 13, 1989. Accepted May 15, 1989. This work was supported by the Research Institute of King Fahd University of Petroleum and Minerals in Dhahran, Saudi Arabia.

# Chemically Bonded Liquid Crystals as Stationary Phases for High-Performance Liquid Chromatography. Effects of Mobile-Phase Composition

Joseph J. Pesek\*

Department of Chemistry, San Jose State University, San Jose, California 95192

Antoine M. Siouffi

Laboratoire de Chimie Appliquee, Universite d'Aix-Marseille, F13390 Marseille Cedex 13, France

The compound [4-(allyloxy)benzoyl]-4-methoxyphenyl (ABMP), shown to possess liquid crystal properties when bonded to a polysiloxane backbone, was covalently attached to silica and tested chromatographically for similar properties by mobile-phase-composition studies. Methanol, acetonitrile, and tetrahydrofuran are mixed with water in various proportions in order to determine the bonded material's reverse-phase behavior. The separation of anthracene and phenanthrene as well as that of carvone and pulegone is used to monitor the mobile-phase effects on the stationary phase. In all cases a plot of  $\log k'$  vs percentage of organic solvent in the mobile phase is not completely linear. At higher percentages of organic solvent the plot is linear without separation of either pair of solutes. At lower percentages of organic solvent the plot is nonlinear and the two pairs of compounds are separated. This observation is attributed to a phase transition in the bonded material. Variable-temperature experiments also support the possibility of a phase transition.

## INTRODUCTION

The use of liquid crystals as stationary phases in gas chromatography was first established over 25 years ago (1, 2). They are used quite extensively for many difficult separations, and a typical review (3) may contain hundreds of references. In contrast, the early studies (4, 5) using liquid crystals as stationary phases for high-performance liquid chromatography were rather incomplete, and no conclusion could be drawn about their potential usefulness. There is, however, one important difference between the use of liquid crystals as stationary phases in gas chromatography and liquid chromatography. In GC the liquid crystal can be coated directly on a solid support or capillary wall. The low volatility of these materials leads to long column lifetimes. In HPLC such a procedure would result in rapid loss of the stationary phase due to solubility in the mobile phase or to removal by shear forces. Therefore, the only practical solution for HPLC is to produce a chemically bonded material that possesses liquid crystal properties. This situation was never properly addressed in the earlier studies, so no conclusion could be made concerning the effectiveness of bonded liquid crystals as stationary phases for HPLC.

However, several recent studies (6-8) have shown that certain liquid crystals or structurally similar compounds when bonded to a polysiloxane backbone retain or develop liquid crystalline behavior. Therefore it seems possible that similar compounds bonded to silica may have the same liquid crystalline behavior. An earlier report (9) described the synthetic approach for producing a chemically bonded material that might possess liquid crystal properties. The preliminary tests

of this bonded phase, particularly the thermal and retention index studies, indicated that liquid crystal properties could be present. In this report we further test the bonded material by subjecting it to a varying mobile-phase composition and monitoring the separation of two pairs of solutes. Ordinary reverse-phase behavior should result in a linear relationship between  $\log k'$  and the percentage of organic solvent in the mobile phase (10). In contrast, it is known that molecular orientation of crystals is a function of solvent type (11). Therefore, mobile-phase-composition studies might be able to detect phase transitions that occur in the bonded material. These results would provide substantial evidence that a bonded liquid crystal with useful chromatographic properties could be produced. This report is a preliminary study of the solvent effects observed on the ABMP phase which could be used to determine whether further investigations on bonded liquid crystals as stationary phases for HPLC are warranted. Some variable-temperature studies are also included in this report.

## EXPERIMENTAL SECTION

**Bonded Liquid Crystal Column.** The synthesis of the bonded liquid crystal material has been described previously (9). The bonded phase on Nucleosil 300-10 was packed into a  $150 \times 4.6$  mm stainless steel column using a Haskel pneumatic amplification pump with methanol as the driving solvent.

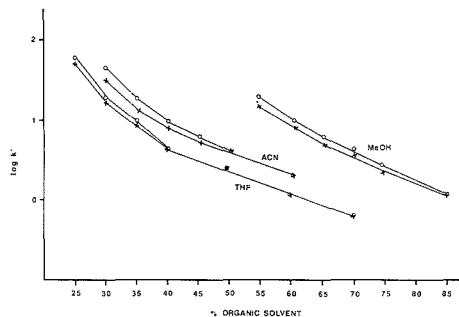
**Materials.** Acetonitrile (ACN), tetrahydrofuran (THF), and methanol (MeOH) (Merck) were all chromatographic grade solvents. The water was triply distilled and filtered through a  $0.45\text{-}\mu\text{m}$  filter. The solutes used in this study, anthracene, phenanthrene, carvone, and pulegone (Aldrich), were used without further purification. Each compound gave only a single peak in all chromatograms.

**Apparatus.** One liquid chromatography system consisted of a Waters Model 6000A pump, a Rheodyne Model 7125 injector with a  $50\text{-}\mu\text{L}$  sample loop, and a Merck variable-wavelength monitor. Variable-temperature experiments were done on a Hewlett-Packard Model 1050 LC system equipped with a Model 1046B fluorescence detector. Two C-18 columns were employed; both were  $150 \times 4.6$  mm with one containing Lichrosphere RP-18e (Merck) on  $5\text{-}\mu\text{m}$  particles and a second containing the product of Nucleosil 300-10 and octadecyldimethylchlorosilane.

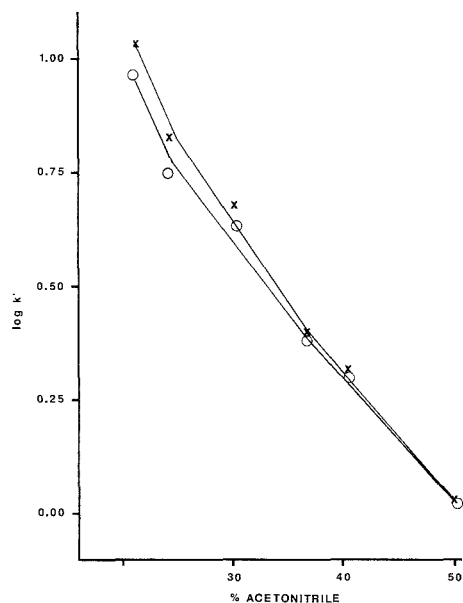
**Procedures.** The solutes anthracene and phenanthrene were monitored at 254 nm while carvone and pulegone were monitored at 230 nm. Fluorescence of anthracene was monitored at 405 nm with an excitation wavelength of 365 nm. The mobile phases were prepared by using standard volumetric glassware and were degassed before use with helium. The void volumes for both the C-18 and liquid crystal columns were determined by nitrate injection.

## RESULTS AND DISCUSSION

The primary pair of test solutes chosen for monitoring retention properties of the bonded liquid crystal was an-



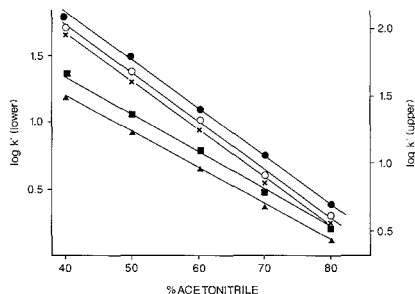
**Figure 1.**  $\log k'$  vs percentage of organic solvent in the mobile phase for phenanthrene (X) and anthracene (O) on ABMP column. Key: THF, tetrahydrofuran; ACN, acetonitrile; MeOH, methanol.



**Figure 2.**  $\log k'$  vs percentage of acetonitrile in the mobile phase for carvone (O) and pulegone (X) on ABMP column.

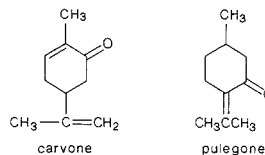
thracene and phenanthrene. This pair can be separated by a number of different stationary phases (12, 13) including liquid crystals coated on a capillary column for GC (3). Therefore the chromatographic behavior of these solutes may serve as a useful indicator of the presence of liquid crystal properties in the ABMP bonded phase.

Figure 1 shows a plot of  $\log k'$  for both anthracene and phenanthrene as a function of percentage of organic solvent in the mobile phase using three different solvents. In each case there is a linear portion in which the two solutes are not separated and a nonlinear portion where the  $k'$  values of the two compounds begin to diverge. The point of divergence occurs at a higher percentage of organic solvent as the polarity of the solvent increases, i.e. as the solvent strength in the reverse-phase system decreases. For each solvent, the linear portion occurs at relatively high solvent strength and the nonlinear portion at relatively low solvent strength.



**Figure 3.**  $\log k'$  vs percentage of acetonitrile in the mobile phase on C-18 columns. Merck RP-18e: phenanthrene (X) and anthracene (O) using scale on right side of plot and carvone (A) and pulegone (M) using scale on left side of plot. C-18 on Nucleosil 300-10: anthracene (●) using scale on left side of plot.

Figure 2 shows a similar plot for the pair of solutes carvone and pulegone in acetonitrile. Like anthracene and phenanthrene, this pair of solutes differs only slightly in structure as shown below:



The same behavior is observed for this pair of components as for anthracene and phenanthrene, i.e. a linear portion with no separation at high solvent strength and a nonlinear portion with separation at low solvent strength.

Figure 3 shows the behavior of both pairs of solutes on a commercial endcapped C-18 phase as well as the retention of anthracene on a C-18 column made from the identical support used for the liquid crystal phase. In contrast to the behavior of these solutes on the ABMP phase, the ODS phase exhibits linear behavior over the entire mobile-phase-composition range. In addition, both pairs of solutes are separated over the 40–80% acetonitrile range on the commercial column. Similar behavior is observed for the C-18 material bonded to Nucleosil 300-10, so that the silica support does not appear to have any effect on the retention characteristics of these solutes under these experimental conditions. Therefore, the differences observed between the ABMP and C-18 retention vs mobile-phase composition must be due to the properties of the bonded material and not the silica support.

It is evident from an examination of the  $\log k'$  variations of either pair of solutes in the organic and aqueous mobile phases studies that there is a fundamental difference between retention on the ABMP phase and that on a conventional reverse-phase material such as C-18. The behavior exhibited by the two pairs of solutes on the C-18 phase (Figure 3) is the predicted response for variations in solvent strength (10), i.e.  $\log k'$  varies linearly as a function of percentage of organic solvent in the mobile phase. Therefore the unusual characteristic exhibited by the ABMP phase must be due to some other effect besides or in addition to normal reverse-phase behavior. Silanophobic interactions are probably not responsible for the retention behavior observed since there is no minimum in the plot of  $\log k'$  vs percentage of organic solvent in the mobile phase at high solvent strengths (14, 15). In addition, all the solutes used in this study as well as *N,N*-diethylaniline gave symmetric peaks indicating no substantial

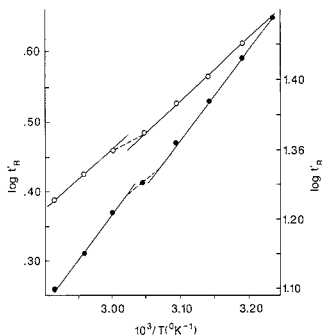


**Figure 4.**  $\log t_R'$  of anthracene vs  $1/T$  on the ABMP phase for acetonitrile:water (55/45) (O, scale on left side of plot) and for acetonitrile:water (35/65) (●, scale on right side of plot) mobile-phase composition.

number of residual silanols.

If it is postulated that some type of liquid crystal property (ordering) is possible for the ABMP phase, then an explanation of the solvent strength variations can be formulated. It has been demonstrated that in the presence of a "hostile" (polar) solvent, ordinary brush phases collapse in order to minimize the surface area in contact with the mobile phase (16). In the studies reported here, the mobile phase becomes more "hostile" as the percentage of organic solvent decreases. Figure 1 also demonstrates that this point of collapse is variable, depending on the polarity of the organic modifier. Therefore, the percentage of organic solvent required to reach this critical point is greater for methanol (the most polar of the organic solvents used) than for acetonitrile which is greater than that for THF (the least polar of the organics used). Under these conditions the collapse could lead to an ordering of the organic moiety on the silica because of the closer proximity of the bonded phase molecules and the partial expulsion of the solvent. This new ordered phase may have a more favorable environment for the solute, which leads to a greater increase in  $\log k'$  than predicted from solvent strength considerations alone. The fact that the slope is changing as opposed to attaining a single new value indicates that the process is a gradual change rather than a sudden phase transition. This interpretation is in agreement with the thermal data (9), which shows a phase change over a broad temperature range rather than a sudden sharp transition.

Another interesting comparison between ordinary reverse-phase behavior and the retention characteristics of the ABMP phase involves the  $\alpha$  values of the solute pairs. As shown in Figure 3, the  $\alpha$  value for anthracene and phenanthrene (1.14) and carvone and pulegone (1.36) remains constant on the C-18 phase. For the ABMP phase these values change with solvent composition. With a constant  $\log k' = 1.5$ , the  $\alpha$  values are 1.15, 1.29, and 1.33 for anthracene and phenanthrene in THF, ACN, and MeOH, respectively. It is interesting to note that  $\alpha$  becomes larger as the overall polarity of the mobile phase increases. As discussed previously, the increasing polarity may force the bonded phase into a more ordered environment, which leads to greater efficiency in the separation process. If the  $\alpha$  value of carvone and pulegone (1.16) is compared to the value for anthracene and phenanthrene (1.24), then it can be seen that the larger  $\alpha$  value occurs for the higher molecular weight pair. This may reflect the overall distance between the bonded moieties, indicating not only that there is greater degree of interaction for the pair anthracene and phenanthrene (higher percentage of ACN needed to achieve a  $\log k' = 1$ ) but that the differential in-

teraction between this pair is greater than that for carvone and pulegone. If the spacing between brushes is too large, then the maximum degree of interaction cannot be achieved. The lack of separation for either of these solute pairs at high percentage of organic solvent is not unusual. Normal phase separations using a variety of stationary phases containing aromatic and substituted aromatic groups result in  $\alpha$  values for anthracene and phenanthrene varying from 1.0 to 1.3 (17). Our own experiments with a theobromine bonded phase resulted in an  $\alpha = 1.0$  over a solvent composition range of 30–70% ACN in water.

Further support for the possibility of a phase transition in the bonded material is shown in Figure 4. At both high and low solvent strength, there is a discontinuity in the plot of  $\log t_R'$  vs  $1/T$ . The presence of the discontinuity is supported by the fact that the differences between the two straight lines drawn at each solvent strength are much greater than the error in the measurement of  $t_R'$  ( $\leq 0.7\%$ ). Derivative analysis by comparison of successive experimental points indicates a change in slope so that representation of the data by a single straight line is not possible. The presence of a discontinuity is characteristic of a phase transition and has been observed for this material bonded to polysiloxane (8). The transition temperature observed in these experiments (between 55 and 60 °C) is quite similar to the transition temperature (61 °C) measured on polysiloxane (8). A lowering of the transition temperature might be expected in these studies due to the presence of an impurity (mobile phase). It is interesting to note that the variable-temperature studies reveal a transition occurring in both the linear and nonlinear portions of the solvent strength plot. The difference in slope is probably reflective of the relative amount of ordering that exists in the bonded material. Only additional variable-temperature experiments with more bonded liquid crystal materials utilizing a variety of solutes and mobile phases will elucidate the exact nature of the bonded-phase transitions that are possible on silica.

In conclusion, it appears that solvent-induced changes occur in the structure of the ABMP bonded phase that are likely related to their ability to form a liquid crystalline structure. Such mobile-phase effects result in nonlinear plots for  $\log k'$  vs solvent strength and could provide a powerful means of controlling retention in complex systems. Current work focuses on determining whether these phenomena are present in other liquid crystal materials bonded to silica as well as formulating other bonded reactions and elucidating surface, temperature, and solvent strength effects.

#### ACKNOWLEDGMENT

We acknowledge the assistance of Ms. Sally Swedberg in obtaining the variable-temperature chromatographic measurements.

#### LITERATURE CITED

- (1) Kelker, H. Z. *Anal. Chem.* **1963**, *198*, 254.
- (2) Kelker, H. *Ber. Bunsen-Ges. Phys. Chem.* **1963**, *80*, 698.
- (3) Witkiewicz, Z. *J. Chromatogr.* **1982**, *251*, 311.
- (4) Taylor, P. J.; Sherman, P. L. *J. Liq. Chromatogr.* **1980**, *3*, 21.
- (5) Aratskova, A. A.; Vetrova, Z. P.; Yoshin, Y. I. *J. Chromatogr.* **1986**, *365*, 27.
- (6) Jones, B. A.; Bradshaw, J. S.; Nishida, M.; Lee, M. L. *J. Org. Chem.* **1984**, *49*, 4947.
- (7) Morkida, K. E.; Chang, H. C.; Schregenberger, C. M.; Tolbert, B. J.; Bradshaw, J. S.; Lee, M. L. *HRC CC. J. High Resolut. Chromatogr. Chromatogr. Commun.* **1985**, *8*, 516.
- (8) Apfel, M. A.; Finkelman, H.; Janini, G. M.; Laub, R. J.; Luhmann, B. H.; Price, A.; Roberts, W. L.; Shaw, T. J.; Smith C. A. *Anal. Chem.* **1985**, *57*, 651.
- (9) Pesek, J. J.; Cash, T. *Chromatographia*, in press.
- (10) Snyder, L. R.; Quarry, M. A.; Glajch, J. L. *Chromatographia* **1987**, *24*, 33.
- (11) Ohgawara, M.; Uchida, T. *Jpn. J. Appl. Phys.* **1981**, *20*, L237.
- (12) Jinno, K.; Kawasaki, K. *Chromatographia* **1983**, *17*, 445.
- (13) Jinno, K.; Kawasaki, K. *Chromatographia* **1984**, *18*, 44.
- (14) Nahum, A.; Horvath, C. *J. Chromatogr.* **1981**, *203*, 53.

- (15) Klaas, B.; Horvath, C.; Melander, W. R.; Nahum, A. J. *Chromatogr.* **1981**, *203*, 65.  
(16) Lochmuller, C. H.; Kersey, M. T. *Anal. Chem.* **1988**, *60*, 1910.  
(17) Bertrand-Molard, Cecile. Ph.D. Thesis, Universite de Bordeaux, 1988.

RECEIVED for review October 26, 1988. Revised manuscript

received May 8, 1989. Accepted May 20, 1989. J.J.P. was supported by a grant from the French Ministry of Education while at the Universite d'Aix-Marseille. Partial support of this research was also provided by a grant from the National Science Foundation (CHE-8814849).

## Laser-Based Indirect Fluorometric Detection and Quantification in Thin-Layer Chromatography

Yinfa Ma, Lance B. Koutny, and Edward S. Yeung\*

Ames Laboratory—USDOE and Department of Chemistry, Iowa State University, Ames, Iowa 50011

**A laser-based indirect fluorometric detection method for thin-layer chromatography is described. The new technique can be easily used for quantitative measurements because of its two-dimensional scanning capability. Since it is based on the indirect fluorescence mode, universal detection is possible without derivatization. Also, it takes only 35 s for acquiring a data array of  $256 \times 64$  points with this technique to achieve a detection limit of 6 pg. This is 100 times lower than when the human eye is used as a detector for the same samples based on indirect fluorometry. The linearity in indirect fluorometric detection is found to be over 2 orders of magnitude.**

### INTRODUCTION

Since thin-layer chromatography (TLC) was described by Kirchner and his group (1), many improvements in all aspects of operation have been made, including high quality, high performance, and multimodal TLC plates, accurate and precise spotting techniques, instrumentalized development devices, and sophisticated detectors (2-6). These improvements have transformed TLC into a modern separation technique.

Detection and quantification on TLC plates are important considerations. The simplest detection method is based on the human eye aided by a vast array of selective spray reagents, or by the use of plates impregnated with fluorescent indicators to allow components to be detected by absorption at the excitation or emission wavelength. For quantitative analysis, traditionally the plates were scanned by mechanically driven densitometers (7). This is usually a slow procedure. Recently, various methods have been suggested for improving the detection limit, speed, and scope of application. These include photoacoustic spectrometry (8-10), flame ionization (11), photothermal deflection (12, 13), laser fluorometry (14, 15), mass spectrometry (16-19), and computer-aided videodensitometry (5, 20, 21). All these detection methods respond to a specific property of the analyte. If the analyte does not possess that specific property, difficulties in detection will arise. There is thus a need for a sensitive universal detection scheme for TLC.

Recently, quite a few indirect detection methods for liquid chromatography (LC) have been demonstrated (22-26). The detection mechanisms have been clearly identified (27, 28). Briefly, the detector responds to some physical property of the chromatographic eluent. A constant background signal

is then maintained when the analytes are absent. When the analytes elute, displacement of the eluent causes a change in the background signal. So, analytes can be detected indirectly. Following the same principles, the indirect fluorometric detection of anions (29), cations (30), and nonelectrolytes (31) in TLC has also been achieved. However, the results so far have not been optimized. The visual observation of the TLC plates (which are illuminated by a UV lamp) is obviously not sensitive compared to instrumental detection methods. Also, visual observation cannot be reliably used for quantitative measurements. In this paper, we describe a laser-based indirect fluorometric detection scheme for TLC with high sensitivity (picograms) and wide linear dynamic range (more than 2 orders). Reliable scanning is easily performed because the TLC plates and detector are fixed while the excitation laser beam is moved. In this system, a microcomputer controls the X-Y scanning and at the same time collects the data. This allows a total data acquisition time of 35 s for a data array of  $256 \times 64$ . There is also an improvement in the signal-to-noise ratio (S/N) resulting from data averaging.

### EXPERIMENTAL SECTION

**Apparatus.** The experimental setup for two-dimensional TLC scanning in laser-based indirect fluorometric detection is shown in Figure 1. A He-Ne laser (Uniphase, Manteca, CA) was used as an excitation light source at 633 nm at a power of 8 mW. In order to maintain a constant laser power, a laser power stabilizer (Cambridge Research and Instrumentation, Cambridge, MA, LS 100) was used. An acoustooptic modulator (Andersen Laboratories, Inc., Bloomfield, CT), which was controlled by a radio frequency (rf) driver, was used to deflect the laser beam. The change in the frequency of rf input to the acoustooptic device causes deflection of the first-order laser beam (32, 33).

The acoustooptic modulator and a rotating mirror combine to scan the laser beam in the horizontal and vertical directions, respectively. To obtain the optimum spatial resolution, we introduced a cylindrical beam expander with  $L_1$  and  $L_2$  and used long focal length lenses  $L_3$  and  $L_4$ . The focused image onto a microscope eyepiece (12 $\times$  magnification) was enlarged to an area of  $40 \times 50$  mm (horizontal  $\times$  vertical) with a laser spot size of about 1.5 mm on the TLC plate.

The fluorescence signal was collected by a camera lens (28-105 mm, f/2.8-f/3.8, Vivitar Corp., Santa Monica, CA), passed through a cutoff filter (to remove scattered 633-nm light), and directed into a R928 photomultiplier tube (PMT) (Hamamatsu, Middlesex, NJ) operated at 850 V. The output of the PMT was converted into voltage via a resistor and was fed into a data acquisition system consisting of an analog to digital I/O interface (Data Translation, Marlborough, MA, DT 2827) and a microcomputer (IBM, Boca Raton, FL, PC/AT). This system was also used to control the rf output and the stepping motor in order to syn-

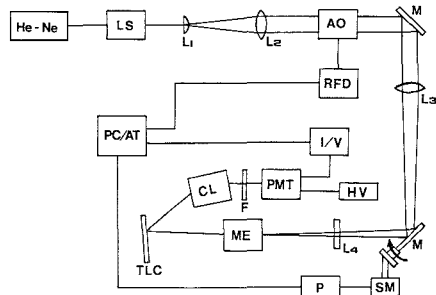


**Figure 1.** Schematic diagram of laser-based indirect fluorometric detector for thin-layer chromatography: He-Ne, helium-neon laser; LS, laser stabilizer; AO, acoustooptic modulator; M, mirror; RFD, radio frequency driver; PC/AT, personal computer/AT compatible; I/V, current-voltage converter; PMT, photomultiplier tube; HV, high voltage; CL, camera lens; ME, microscope eyepiece; SM, stepping motor; P, power for stepping motor; F, cutoff filter; TLC, thin-layer chromatographic plate;  $L_1$ , 25 mm focal length cylindrical lens;  $L_2$ , 400 mm focal length spherical lens;  $L_3$ , 1000 mm focal length spherical lens;  $L_4$ , 250 mm focal length cylindrical lens.

chronously scan the laser beam. After each horizontal measurement, the laser beam was moved vertically to the next horizontal line by the stepping motor. For our experiment, a data array of  $256 \times 64$  points (horizontal  $\times$  vertical) was acquired from the entire scan area. Each point was averaged 256 times. Data acquisition takes 35 s. Six additional minutes was needed for data averaging and reduction. The final data array was  $64 \times 64$  points. The data was then normalized to minimize the fluctuations in the background signal.

**Chromatography.** A  $K_8$  silica gel plate (Whatman, Clifton, NJ) was pretreated with  $2 \times 10^{-6}$  M Nile Blue A perchlorate in methanol for 20 min. The plate was then dried with a heat gun. A 0.1–1.0- $\mu$ L methanol solution of test sample containing crocein orange G and orange G (Aldrich, Milwaukee, WI) was spotted by a microsyringe (Hamilton, Reno, NV). The thin-layer plate was developed to a distance of about 40 mm from the origin in a developing solution containing 2-butanol/acetone/water (75:15:10 (v/v)). After drying, the TLC plate was placed in the apparatus for measurements. For comparison with the detection limit obtained visually, the TLC plate was put under a sodium lamp.

## RESULTS AND DISCUSSION

In indirect fluorometric detection, the limit of detection can be estimated from the following equation (24, 25):

$$C_{\text{lim}} = C_F / DR \cdot TR \quad (1)$$

where  $C_{\text{lim}}$  is the molar concentration of analytes at the detection limit,  $C_F$  is the molar concentration of the fluorophore, DR is the dynamic reserve (which is defined as the ratio of the background signal to the noise level), and TR is the transfer ratio (which is defined as the number of fluorescing molecules transferred by one analyte molecule). From eq 1, it is easy to see that if one wants to decrease the detection limit, a more stable background signal (large DR) and a lower concentration of the fluorophore (smaller  $C_F$ ) are needed. Even though a large transfer ratio can improve the detection limit, it is generally fixed by the stationary phase, the developing solvent system, and the analyte. In our previous papers (29, 31), even though we demonstrated indirect fluorometric detection in TLC, the detection limit was not optimum. The human eye has a low contrast, which lowers the DR. In this work, we can easily stabilize the background signal (increase DR) and use lower concentrations of the fluorophore in the pretreating solution (smaller  $C_F$ ) due to the high sensitivity of phototubes. These conditions help to improve the detection limit.

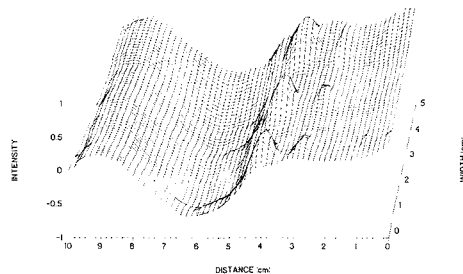


**Figure 2.** Two-dimensional chromatogram obtained by indirect fluorometric detection of orange G and crocein orange G without data normalization. The left series of peaks are crocein orange G; the right series of peaks are orange G. The amounts spotted are 80, 120, and 150  $\mu$ g, counting from bottom to top for each sample.

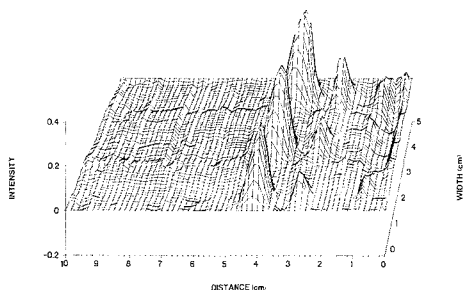


**Figure 3.** Two-dimensional chromatogram of indirect fluorometric detection of orange G and crocein orange G with data normalization. The peak orders and amounts are the same as in Figure 2.

In this work, we chose Nile Blue as the fluorophore because it can be excited by a He-Ne laser. This will greatly enhance cost and convenience considerations in an eventual instrument. Since detection is by indirect fluorescence, the choice of the fluorophore is quite arbitrary. The analytes were chosen so that they do not absorb at the He-Ne laser wavelength or the fluorescence wavelength, to emphasize the indirect detection mode. Before the TLC plate is developed, the analyte spots do not show any signal. This confirms that displacement of Nile Blue on the plate is responsible for the indirect fluorometric response. The colored analytes also allow us to compare indirect fluorescence with conventional visualization of the spots on TLC plates.

Figure 2 shows a two-dimensional chromatogram of the indirect fluorometric detection of orange G and crocein orange G. The response is dependent on the analyte because TR is a function of  $R_f$  (25). We can see from the figure that 80  $\mu$ g of each can be detected. However, the conditions are not perfect for quantification because of the fluctuating background. The systematic fluctuations in the background fluorescence signal are caused by variations in the intensity of the laser spot with the angle of deflection and inconsistencies in fluorophore concentration due to the development. To compensate for these fluctuations, the signal can be normalized based on the background levels in a lane in between the sample lanes. The normalized data is shown in Figure 3. The data in Figure 2 and Figure 3 have been inverted to facilitate viewing. Thus, "zero" corresponds to background fluorescence, and "1" would correspond to no fluorescence. Figure 3 shows that the signal-to-noise ratio is readily improved by normalization. The detection limit of crocein orange G is approximately 6  $\mu$ g. This detection limit is over 100 times lower than when the eye is used to view the same dark spots

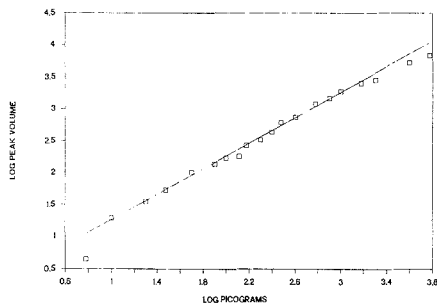


Figure 4. Analytical calibration curve for indirect fluorometric detection based on peak volumes. The test sample is crocein orange G. A line with unit slope is drawn for comparison.

under a sodium lamp (visual indirect fluorometry). This is also 1000 times lower than those limits reported earlier (31) that were obtained with a near-UV fluorophor, about 1000 times better than using the eye to look at the colored spots in room light (direct densitometry) without Nile Blue pretreatment, and 100 times better than photoacoustic detection of the same two analytes (8, 9). It should be noted that the detection limit depends on the square root of the number of data points averaged. It is thus possible to reduce the total scan time to 1 s and still achieve detectability in the 40-pg level.

Because of the optical medium, a nonlinear response is usually observed for direct densitometry measurements (34, 35). This can be corrected by applying the Kubelka-Munk function. If the detection mode is based on fluorescence or absorbance, for example, higher concentrations of analytes will lead to nonlinear calibration plots due to self-absorption, self-quenching, and detector saturation. In indirect fluorometric detection, the response is not based on the analyte itself. A linear response is therefore easier to obtain. Figure 4 shows a calibration curve for crocein orange G. A line with unit slope is shown for comparison. Based on the linear regression criteria described by Johnson (36), linearity was observed over 2 orders of magnitude with relative deviations of approximately 10%. Note that the calibration curve was based on the peak volume of the TLC spots in Figure 3. This properly accounts for band broadening due to development. The peak volume can be estimated by determining the peak area under a single scan through the peak raised to the  $3/2$  power. Due mostly to variations in the concentrations of the fluorophor from plate to plate, and partly due to variations in light collection geometry, it was necessary to include a standard spot on each TLC plate to allow normalization among different plates. If the concentration of the analyte is too high (beyond 3.2 in Figure 4), the calibration plot begins to show nonlinearity. This happens because the TR in eq 1 will change at higher concentrations. The signal also falls off at the low-concentration end, probably because of difficulties in integration and in background normalization for small signals. However, the linear range achieved is large enough for this approach to be broadly applicable.

## CONCLUSION

We have developed a laser-based indirect fluorometric detection scheme for TLC. The method is universal, is very sensitive, and has a large linear dynamic range. The laser and the optics used should allow the construction of a rugged, fully automated instrument eventually. At present, commercial TLC plates have to be pretreated with the fluorophor to allow indirect detection. It is conceivable that this step can be incorporated into the manufacturing process. The entire process of TLC separations is then substantially simplified; i.e. one can avoid the tedious and unreliable derivatization steps completely.

## LITERATURE CITED

- (1) Kirchner, J. G.; Miller, J. M.; Keller, G. J. *Anal. Chem.* **1951**, *23*, 420-425.
- (2) Donovan, J.; Gould, M.; Majors, R. E. *LC-GC* **1987**, *5*, 1024-1028.
- (3) Jaenchen, D. E.; Issaq, H. J. *J. Liq. Chromatogr.* **1988**, *11*, 1941-1965.
- (4) Jaenchen, D. E.; Issaq, H. J. *J. Liq. Chromatogr.* **1988**, *11*, 1941-1965.
- (5) Jaenchen, D. E. *Am. Lab.* **1988**, *3*, 66-73.
- (6) Dallas, F. A. A.; Read, H.; Ruane, R. J.; Wilson, I. D. *Recent Advances in Thin-Layer Chromatography*; Plenum: New York, 1988.
- (7) Touchstone, J. C.; Sherna, J. *Densitometry in Thin-Layer Chromatography: Practice and Applications*; Wiley: New York, 1979.
- (8) Kawazumi, H.; Yeung, E. S. *Appl. Spectrosc.* **1988**, *42*, 1228-1231.
- (9) Kawazumi, H.; Yeung, E. S. *Appl. Spectrosc.* **1989**, *43*, 249-253.
- (10) Imaeda, K.; Ohsawa, K.; Uchiyama, K.; Nakamura, S.; Tokieda, T. *Anal. Sci.* **1986**, *2*, 9-13.
- (11) Ranny, M. *Thin-Layer Chromatography with Flame Ionization Detection*; Reidel: Boston, 1987.
- (12) Chen, I. I.; Morris, M. D. *Anal. Chem.* **1984**, *56*, 19-21.
- (13) Chen, I. I.; Morris, M. D. *Anal. Chem.* **1984**, *56*, 1674-1677.
- (14) Huff, P. B.; Sepaniak, M. J. *Anal. Chem.* **1983**, *55*, 1992-1994.
- (15) Belenki, B. G.; Gankina, E. S. *J. Chromatogr.* **1986**, *365*, 315-320.
- (16) *Proceedings of the Third International Symposium on Instrumental HPLC*; Chang, T. T.; Andrews, F.; Kaiser, R. E., Eds.; Institute for Chromatography, Bad Burkheim, West Germany, 1985; pp 427-433.
- (17) Chang, T. T.; Lay, J. O.; Francel, R. J. *Anal. Chem.* **1984**, *56*, 109-111.
- (18) Ramaley, L.; Vaughn, M.-A.; Jamieson, W. D. *Anal. Chem.* **1985**, *57*, 353-358.
- (19) Kraft, R.; Otto, A.; Zoepfl, H. J.; Etzold, Gerhard. *Biomed. Environ. Mass Spectrom.* **1987**, *14*, 1-4.
- (20) Ford-Holevinski, T. S.; Radin, N. S. *Anal. Biochem.* **1985**, *150*, 359-363.
- (21) Belchamber, R. M.; Read, H.; Roberts, J. D. M. *J. Chromatogr.* **1987**, *395*, 47-53.
- (22) Bobbitt, D. R.; Yeung, E. S. *Anal. Chem.* **1984**, *56*, 1577-1581.
- (23) Mho, S. I.; Yeung, E. S. *Anal. Chem.* **1985**, *57*, 2253-2256.
- (24) Takeuchi, T.; Yeung, E. S. *J. Chromatogr.* **1986**, *370*, 83-92.
- (25) Takeuchi, T.; Yeung, E. S. *J. Chromatogr.* **1986**, *366*, 145-152.
- (26) Pfeffer, W.; Takeuchi, T.; Yeung, E. S. *Chromatographia* **1987**, *24*, 123-126.
- (27) Ishii, D.; Takeuchi, T. *J. Liq. Chromatogr.* **1988**, *11*, 1865-1874.
- (28) Yeung, E. S. *Acc. Chem. Res.* **1989**, *22*, 125-130.
- (29) Ma, Y.; Yeung, E. S. *Anal. Chem.* **1988**, *60*, 722-724.
- (30) Ma, Y.; Yeung, E. S. *Mikrochim. Acta* **1988**, *III*, 327-332.
- (31) Ma, Y.; Yeung, E. S. *J. Chromatogr.* **1988**, *455*, 382-390.
- (32) Lekavich, J. *Lasers Appl.* **1986**, *4*, 59-64.
- (33) Young, M. *Optics and Lasers*; Springer-Verlag: Berlin, 1986; p 193.
- (34) Ebel, S.; Glaser, E. *HRC CC, J. High Resolut. Chromatogr. Chromatogr. Commun.* **1979**, *2*, 36-38.
- (35) Costanzo, S. J.; Cardone, M. J. *J. Liq. Chromatogr.* **1984**, *7*, 2711-2718.
- (36) Johnson, D. C. *Anal. Chim. Acta* **1988**, *204*, 1-5.

RECEIVED for review March 10, 1989. Accepted June 5, 1989. The Ames Laboratory is operated by Iowa State University for the U.S. Department of Energy under Contract No. W-7405-Eng-82. This work was supported by the Office of Basic Energy Science, Division of Chemical Sciences, and by the Office of Health and Environmental Research.

# Density Determination of Low-Density Polymer Latexes by Sedimentation Field-Flow Fractionation

D. J. Nagy

Air Products and Chemicals, Inc., Corporate Research Services, 7201 Hamilton Boulevard, Allentown, Pennsylvania 18195

Particle density must be accurately known to characterize particle size distributions of polymeric latexes by sedimentation field-flow fractionation (SFFF). In this work, it is demonstrated that SFFF can be used to determine *in situ* density of copolymer latexes in the range from 1.00 to 1.02 g/cm<sup>3</sup>. To perform these measurements the density of the SFFF mobile phase is decreased to less than 1.00 g/cm<sup>3</sup> with the use of methanol as an eluant modifier. Retention data are measured for the latexes by using several low-density mobile phase solutions. This method is feasible for low-density polymers since particle retention time by SFFF is directly related to the density difference between the particles and the mobile phase. This technique has been successfully applied to narrow distribution styrene-butadiene and to narrow and broad particle size distribution vinyl acetate-acrylic copolymer latexes.

## INTRODUCTION

Sedimentation field-flow fractionation (SFFF) is a sub-technique of field-flow fractionation (FFF) used to characterize mixtures of high molecular weight polymers, emulsions, latexes, and other suspensions. SFFF technology combines the principles of single-phase chromatography and centrifugation to separate submicrometer-sized particles according to size (1, 2). The size separation occurs in a circular channel of a spinning, continuous-flow centrifuge rotor. An imposed centrifugal force applied perpendicular to the laminar flow in the channel causes particulates heavier than the liquid mobile phase to sediment radially outward against the channel wall. This buildup of particles near the wall is resisted by normal diffusion in the opposite direction. The particles establish a steady-state concentration zone whose mean concentration is at a height,  $l$ , which is dependent on the force field and diffusion coefficient of the particles away from this wall. Particles of different masses reach sedimentation equilibrium with different characteristic layer thicknesses. This results in different mean distances from the wall and is shown in Figure 1 for mean distances  $l_A$  and  $l_B$  (3). The average particle velocity will increase or decrease depending on the degree of zonal compression. Heavier and bigger particles are intercepted by slower moving flow streamlines near the channel wall and will elute from the channel after the smaller particles. This order of elution is the basis for size separation by SFFF and has been used successfully for a variety of submicrometer-sized materials (3-5).

Particle density must be known accurately to determine quantitative particle size distribution information from SFFF turbidity-time fractograms. However, if the particle density is unknown, it is still possible to determine the density from SFFF measurements. Kirkland and Yau demonstrated the usefulness of this approach to determine densities of polymer latexes from 1.05 g/cm<sup>3</sup> (polystyrene) to 1.22 g/cm<sup>3</sup> (polychloroprene), utilizing glycerine as a mobile phase modifier (3). This method is feasible since particle retention by SFFF

is directly related to the density difference between the particles and the mobile phase. The use of SFFF under nonaqueous conditions has also been described by Yonker et al. (6). Binary mixtures of ethanol and 1,1,2-trichlorotrifluoroethane were used to measure the density of silica particles.

Many commercial latex products are copolymers whose densities are less than that of polystyrene (1.05 g/cm<sup>3</sup>). Classical methods for density measurement such as densitometry and weight per gallon exhibit poor accuracy and precision for low density polymer latexes. This is due to the fact that the dispersed polymer phase is at or near the density of the continuous aqueous phase. The presence of residual monomer, surfactant, salt, and/or initiators complicates the situation. SFFF, by providing an alternative means to examine *in situ* polymer density, circumvents these types of problems. In addition, SFFF provides the capability to examine polymer density homogeneity. This is not possible with the methods mentioned above. For particle size calculations of copolymers which exhibit suspected bimodal or broad distributions, it is important to establish that separation is by size alone and not the result of polymer compositional heterogeneity.

In this paper, we wish to show the usefulness of SFFF for *in situ* density characterization of low-density copolymers in the range from approximately 1.00 to 1.02 g/cm<sup>3</sup>. For these low-density polymers, we used methanol-modified mobile phases with densities less than 1.00 g/cm<sup>3</sup>. As in the case for higher density polymers and related materials, SFFF is equally well suited for low-density polymer characterization. This will be shown for styrene-butadiene and vinyl acetate-acrylic copolymers.

## BACKGROUND

Kirkland and Yau have shown that under normal operating conditions (where the particles are more dense than the mobile phase), the mobile phase density,  $\rho_0$ , can be expressed as (3)

$$\rho_0 = \rho_s - (1/\bar{D}_p^3)[(\rho_{s,0} - \rho_0)\bar{D}_{p,0}^3] \quad (1)$$

where  $\rho_s$  is the density of the particle (g/cm<sup>3</sup>),  $\rho_{s,0}$  is an assumed particle density,  $\bar{D}_{p,0}$  is the calculated particle diameter value based on the assumed  $\rho_{s,0}$  value for particle density, and  $\bar{D}_p$  is the true average particle diameter of the same statistical averaging type. To determine particle density by SFFF, a plot of  $\rho_0$  values versus the quantity  $(\rho_{s,0} - \rho_0)\bar{D}_{p,0}^3$  is constructed, with the intercept at the density axis ( $x$  axis), to be that of the density of the particle in question (i.e., where  $\rho_{s,0} = \rho_0$ ). The validity of the above equation is based on the fact that the fundamental SFFF separation parameter is the effective particle mass, which is directly proportional to the product  $(\Delta\rho \cdot \bar{D}_p^3)$ , where

$$\Delta\rho = |\rho_s - \rho_0| \quad (2)$$

This  $(\Delta\rho \cdot \bar{D}_p^3)$  value always appears as an inseparable quantity in all SFFF retention equations. Each retention time on an SFFF elution fractogram is in direct correspondence with a single value for  $(\Delta\rho \cdot \bar{D}_p^3)$ . The value of this quantity remains



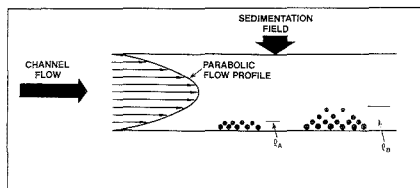


Figure 1. SFFF separation process.

Table I. Latexes Used for Density Determination

latex code	polymer type	particle size type
A	styrene-butadiene ( $T_g = -6^\circ\text{C}$ )	narrow
B	styrene-butadiene ( $T_g = +1^\circ\text{C}$ )	narrow
C	vinyl acetate-acrylic ( $T_g = -40^\circ\text{C}$ )	narrow
D	vinyl acetate-acrylic ( $T_g = -40^\circ\text{C}$ )	broad

the same regardless of different  $\Delta\rho$  values in the SFFF particle size calculations (3). Thus, for an assumed particle density,  $\rho_{s,0}$

$$(\Delta\rho)_0 = |\rho_{s,0} - \rho_0| \quad (3)$$

and

$$(\Delta\rho)_0 D_{p,0}^3 = \Delta\rho D_p^3 \quad (4)$$

A rearrangement of eq 4 gives

$$D_{p,0} = \left| \frac{\rho_s - \rho_0}{\rho_{s,0} - \rho_0} \right|^{1/3} D_p \quad (5)$$

The importance of eq 5 above is as follows: the effect of using an assumed density instead of the accurate particle density in the particle size calculation causes the calculated  $D_{p,0}$  values to differ from the true  $D_p$  values by a simple factor containing the density term. For particles of homogeneous density  $\rho_s$ , the ratio between the  $D_{p,0}$  and  $D_p$  values is expected to be constant for all particle sizes at every retention time on the SFFF fractogram. The average values for  $D_p$  should also differ by a constant factor

$$\bar{D}_{p,0} = \left| \frac{\rho_s - \rho_0}{\rho_{s,0} - \rho_0} \right|^{1/3} \bar{D}_p \quad (6)$$

which is the basis for eq 1 for determining in situ particle densities by SFFF. Theory for density determination by SFFF has been described previously in greater detail (3, 7, 8).

Experimentally, SFFF measurements are made on an unknown sample by using four or five different mobile phase densities. The sample is analyzed under identical SFFF operating conditions for each density. A reasonable value of  $\rho_{s,0}$  is then assumed. This  $\rho_{s,0}$  value is used with the known  $\rho_0$  values for the various mobile phases employed, to calculate the  $\bar{D}_{p,0}$  value of the sample for any statistical particle size average (number, weight, turbidity, peak maximum, etc.).

In this investigation, methanol-modified aqueous mobile phases were used to lower the mobile phase density to values less than  $1.00\text{ g/cm}^3$  (at  $25^\circ\text{C}$ ). This was necessary to keep the mobile phase density less than that of the polymer latexes studied.

## EXPERIMENTAL SECTION

**Polymer Latexes.** The polymer latexes used in this study are all free-radical polymerized, commercially available copolymers. The properties of the latexes are summarized in Table I. A monodisperse  $0.330\text{-}\mu\text{m}$  polystyrene latex (Duke Scientific) was also used in this study. Polystyrene has a well-known polymer density of  $1.05\text{ g/cm}^3$  (3, 9).

Table II. SFFF Operating Conditions

	polystyrene $0.330\text{ }\mu\text{m}$	latex A	latex B	latex C	latex D
initial rpm	5000	12000	12000	12000	12000
field decay	4	6	4	4	8
constant, min					
equilibration	5	5	5	5	10
time, min					
decay delay	4	6	4	4	8
time, min					

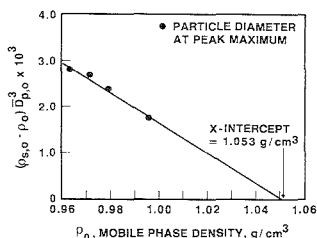


Figure 2. Density plot for polystyrene latex standard,  $0.330\text{-}\mu\text{m}$  particle size. Mobile phase densities used:  $0.9973$ ,  $0.9795$ ,  $0.9715$ , and  $0.9633\text{ g/cm}^3$ .

**Instrumentation.** All measurements were made on a Du Pont Model 1000 SFFF (Du Pont Instrument Systems) with a Hewlett-Packard 9000/216 data processing system. The standard SFFF aqueous mobile phase contained  $0.1\%$  Aerosol-OT emulsifier (Fisher Scientific) in HPLC-equivalent water (Milli-Q Water Systems). All measurements were performed on the SFFF system at  $25^\circ\text{C}$  with a flow rate of  $2.00\text{ mL/min}$ . Latex samples were prepared by dilution in the mobile phase to approximately  $0.5\text{--}1.0\%$  (by weight) and prefiltered through an  $8.0\text{-}\mu\text{m}$  Teflon Millipore membrane to remove any aggregates or other particulate debris prior to injection into the SFFF channel. Samples were injected immediately after preparation in the appropriate mobile phase. Injection volumes were  $50\text{-}\mu\text{L}$ . Detection was by turbidity at  $254\text{ nm}$ .

**Operating Procedures.** The SFFF operating conditions for the latex copolymers and the polystyrene standard are summarized in Table II. The same conditions were employed for each mobile phase and each individual sample. Time delayed, field-decay programming was used in all cases. The methanol-modified mobile phases were prepared by adding a known amount of HPLC methanol (Fisher Scientific) to the standard aqueous mobile phase and degassing under house vacuum for  $1\text{--}2\text{ min}$ . Actual densities of the methanol-modified mobile phases were determined on a Mettler/Parr DMA-55 density meter. Methanol-modified mobile phases at  $25^\circ\text{C}$  were of the following densities:  $0.9633$ ,  $0.9715$ ,  $0.9795$ , and  $0.9882\text{ g/cm}^3$ . The density of the standard  $0.1\%$  Aerosol-OT mobile phase was  $0.9973\text{ g/cm}^3$  at  $25^\circ\text{C}$ . Normal laboratory safety precautions were applied for the above procedures.

## RESULTS AND DISCUSSION

The usefulness of determining polymer density with methanol-modified mobile phases was first verified by using a  $0.330\text{-}\mu\text{m}$  polystyrene latex standard. Experience in our laboratory has shown that polystyrene and latexes of the type used for this study do not exhibit swelling in aqueous solutions of methanol. Methanol is an excellent mobile phase modifier even for mobile phase densities as low as  $0.9633\text{ g/cm}^3$ , the lowest density solution we used.

The SFFF density plot for polystyrene is shown in Figure 2, where the  $x$  intercept indicates a density of  $1.053\text{ g/cm}^3$ . This value compares favorably with the generally accepted density value of  $1.05\text{ g/cm}^3$  for polystyrene. For this measurement the  $95\%$  confidence limit for the  $x$  intercept is  $1.030\text{--}1.114\text{ g/cm}^3$ . The linear regression  $R$  square value is

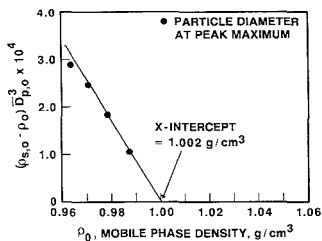


Figure 3. Density plot for latex A. Mobile phase densities used: 0.9882, 0.9795, 0.9715, and 0.9633 g/cm<sup>3</sup>.

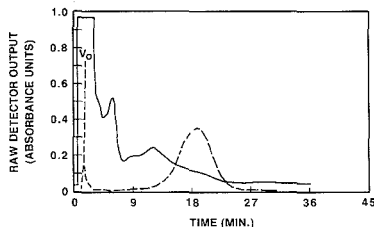


Figure 4. Turbidity-time fractograms for latex A using standard mobile phase of 0.1% Aerosol-OT (solid line; density = 0.9973 g/cm<sup>3</sup>) and methanol-modified mobile phase (broken line; density = 0.9882 g/cm<sup>3</sup>).

0.979. The assumed density used for the calculations was 1.100 g/cm<sup>3</sup>. It should be noted that the wide range for the 95% tolerance limit is due to the fact that the data were taken for mobile phase densities less than 1.00 g/cm<sup>3</sup>. This requires a lengthy extrapolation of the data to the  $x$  axis. The use of glycerine-modified mobile phases for polystyrene, where  $1.00 \leq \rho_0 < 1.05$ , yields better precision as shown by Kirkland and Yau (3).

The particle diameter used in Figure 2 (and in the data that follow) was the peak maximum diameter of the turbidity-elution time fractogram. Any one of the normally reported diameter averages such as number, weight, volume, or turbidity could be used in the calculations and subsequent plot of density versus  $(\rho_{s,0} - \rho_0) D_{p,0}^3$ .

The density plot for latex A (styrene-butadiene copolymer) is shown in Figure 3. The density of the polymer as given by the  $x$  intercept is 1.002 g/cm<sup>3</sup>. The 95% confidence limit for the  $x$  intercept is 0.997–1.009 g/cm<sup>3</sup> and the linear regression  $R$  square value is 0.996. The assumed density used for the calculations was 1.080 g/cm<sup>3</sup>. Initially, this low polymer density was qualitatively verified when an attempt was made to sediment the latex by using the normal mobile phase of the SFFF (density = 0.9973 g/cm<sup>3</sup>). With a speed of 15 000 rpm, the fractogram indicated that the sample did not effectively sediment due to a lack of significant difference between the sample and mobile phase density. This is shown in Figure 4. Excellent sedimentation and separation were achieved for this sample by using a methanol-modified mobile phase of 0.9882 g/cm<sup>3</sup>. Note that for the case where poor sedimentation occurred using the standard mobile phase, most of the sample eluted near  $V_0$  (the channel void volume). Particle size averages for latex A (and latex B, C, and D to follow) were calculated by using the particle density value determined from the density plot and are summarized in Table III.

Latex B (styrene-butadiene copolymer) exhibited a higher density value determined by the  $x$  intercept of its density plot, as shown in Figure 5. The density of latex B was found to be 1.019 g/cm<sup>3</sup>, with a 95% confidence limit of the  $x$  intercept from 1.009 to 1.036 g/cm<sup>3</sup>, and a linear regression  $R$  square

Table III. Latex Particle Size Data from in Situ SFFF Density Determination

latex	$\bar{D}_w^a$ , $\mu\text{m}$	$\bar{D}_n^b$ , $\mu\text{m}$	$\bar{D}_w/\bar{D}_n^c$
A	0.205	0.175	1.2
B	0.110	0.105	1.1
C	0.175	0.150	1.2
D	0.375	0.160	2.3

<sup>a</sup>  $\bar{D}_w$ , weight average. <sup>b</sup>  $\bar{D}_n$ , number average. <sup>c</sup>  $\bar{D}_w/\bar{D}_n$ , polydispersity index.

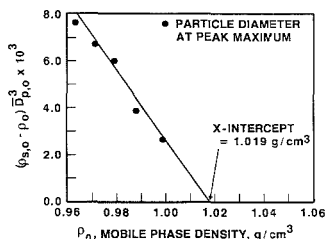


Figure 5. Density plot for latex B. Mobile phase densities used: 0.9973, 0.9882, 0.9795, 0.9715, and 0.9633 g/cm<sup>3</sup>.

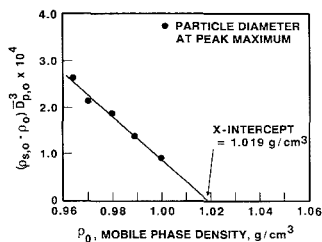


Figure 6. Density plot for latex C. Mobile phase densities same as in Figure 5.

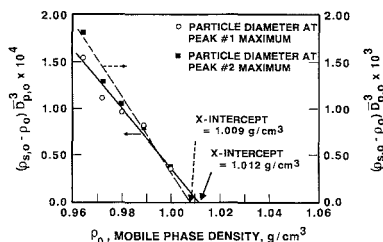
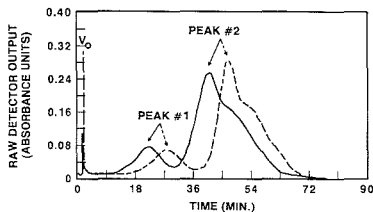


Figure 7. Density plot for latex D. Mobile phase densities same as in Figure 5.

value of 0.973. The assumed density used for the calculations was 1.080 g/cm<sup>3</sup>. As expected, this latex sedimented adequately and was well-resolved by using the standard mobile phase density. It was determined by DSC analysis that the  $T_g$  of latex A was  $-6^\circ\text{C}$  and the  $T_g$  of latex B was  $+1^\circ\text{C}$  (measured at onset of the  $T_g$  transition). The slightly higher  $T_g$  of latex B, presumably due to lower butadiene content, would account for the higher polymer density of latex A compared to latex B.

The density plots for latex C and latex D (vinyl acetate-acrylic copolymers) are shown in Figures 6 and 7, respectively. Latex C was known to be a narrow particle size distribution material, while latex D was known to be bimodal in character. The measured density for latex C was found to be 1.019 g/cm<sup>3</sup>,



**Figure 8.** Turbidity-time fractograms for latex D using standard mobile phase of 0.1% Aerosol-OT (solid line; density = 0.9973 g/cm<sup>3</sup>) and methanol-modified mobile phase (broken line; density = 0.9882 g/cm<sup>3</sup>).

with a 95% confidence limit of the  $x$  intercept from 1.014 to 1.025 g/cm<sup>3</sup>. The linear  $R$  square value was 0.995. An assumed particle density value of 1.080 g/cm<sup>3</sup> was used for latex C. For latex D, the density was measured by using the calculated particle size at the maximum of each of the two peaks in the fractogram shown in Figure 8. An assumed particle density value of 1.080 g/cm<sup>3</sup> was used. Fractograms are shown for the standard mobile phase and the methanol-modified mobile phase of 0.9882 g/cm<sup>3</sup>. As expected, the fractograms are unchanged in shape and character for the two mobile phases. The sample in the methanol-modified mobile phase elutes approximately 7 min later than that of the one in the standard mobile phase.

The densities of peaks 1 and 2 for latex D in the fractogram are statistically equal, with measured values of 1.012 and 1.009 g/cm<sup>3</sup>, respectively. The 95% confidence limits of the  $x$  intercept for peak 1 are 1.003-1.032 g/cm<sup>3</sup> and for peak 2, 1.009-1.019 g/cm<sup>3</sup>. The linear  $R$  square values are 0.980 and 0.960, respectively. This result demonstrates that for this particular vinyl acetate-acrylic latex, the copolymer composition is constant over the entire particle size distribution, although a distinct bimodal character is indicated. The lack of particle heterogeneity coupled with in situ determination

of sample density enables accurate particle size distribution characterization of broad distribution latexes of this type.

### CONCLUSION

The use of methanol-modified mobile phases with SFFF expands the utility of this technique for characterizing densities of copolymer latexes with values near 1.00 g/cm<sup>3</sup>. Mobile phase densities from approximately 0.96-1.00 g/cm<sup>3</sup> have been successfully used for characterization of these types of polymers. For particle size calculations of copolymers that exhibit suspected bimodal or broad distributions, it is important to establish that separation is by size alone and not due to polymer density heterogeneity.

### ACKNOWLEDGMENT

The author wishes to express his appreciation to S. C. Voth for assistance in these experiments and W. F. Tiedge and J. V. Martinez for helpful discussions.

**Registry No.** Polystyrene, 9003-53-6; (styrene)(butadiene) (copolymer), 9003-55-8.

### LITERATURE CITED

- (1) Yang, F. J.; Myers, M. N.; Giddings, J. C. *Anal. Chem.* **1974**, *46*, 1924.
- (2) Giddings, J. C.; Caldwell, K. D.; Fisher, S. R.; Myers, M. N. *Methods Biochem. Anal.* **1980**, *26*, 79.
- (3) Kirkland, J. J.; Yau, W. W. *Anal. Chem.* **1983**, *55*, 2165.
- (4) Levy, G. B. *Amer. Lab.* **1987**, *19*, 84.
- (5) Kirkland, J. J.; Yau, W. W. *Science* **1982**, *218*, 121.
- (6) Yonker, C. R.; Jones, H. K.; Robertson, D. M. *Anal. Chem.* **1987**, *59*, 2574.
- (7) Giddings, J. C.; Karaiskakis, G.; Caldwell, K. D. *Sep. Sci. Technol.* **1981**, *16*, 607.
- (8) Yau, W. W.; Kirkland, J. J. *Sep. Sci. Technol.* **1981**, *16*, 577.
- (9) *Polymer Handbook*; Brandrup, J., Immergut, E. H., Eds.; John Wiley & Sons: New York, 1967.

RECEIVED for review March 13, 1989. Accepted May 23, 1989. This work was presented in part at the First International Symposium on Field-Flow Fractionation, June 15, 1989, Park City, UT.

## A Different Perspective on the Theoretical Plate in Equilibrium Chromatography

Paul J. Karol

Department of Chemistry, Carnegie Mellon University, Pittsburgh, Pennsylvania 15213

The differential rate model for equilibrium chromatography is used to derive both the continuous (Martin and Synge) plate model and the stepwise (Craig) plate model. The latter have previously been regarded as severely deficient because of the ad hoc manner in which the plate height is related to the chemistry and physics of the chromatographic process. However, it is demonstrated that the "height equivalent to a theoretical plate" arises naturally from a finite difference approach to solving the rate equation. It is also argued that the much maligned step model is a phenomenologically valid approximation to the continuous plate model and also to the rate model.

### INTRODUCTION

For the past 25 years the theoretical plate model has been viewed as failing to describe the physical and molecular events occurring in chromatography (1). In contrast to this point

of view, we will try to demonstrate that the plate concept is a phenomenologically and mathematically sound approximation to the chromatographic process and that its use is partially exonerated.

After separately reviewing the differential rate model and the plate model, the link between them will be discussed. In so doing, it will be argued that the literature on this topic (1-7) routinely handicaps the plate model by prematurely invoking a unidirectional transport restraint in deriving chromatogram equations. It is that act which is the source of discord with the current procedure.

### THEORY

The (simplified) rate model for continuous flow equilibrium chromatography (1), ignoring velocity profiles, usually starts with a differential rate equation such as

$$\frac{\partial c(z,t)}{\partial t} = -u_e \frac{\partial c(z,t)}{\partial z} + D_e \frac{\partial^2 c(z,t)}{\partial z^2} \quad (1)$$

which describes the simultaneous drift and dispersion of the eluting species. With convenient boundary conditions, eq 1 yields a normalized chromatogram as a function of time  $t$  for a column of length  $L$  (8)

$$c(t) = \frac{c_0}{(4\pi D_e t)^{1/2}} \exp\left[-\frac{(L - u_e t)^2}{4D_e t}\right] \quad (2)$$

On occasion, reference in the literature to the function of eq 2 incorrectly terms it a Gaussian function. Statistical moments of the equilibrium chromatogram have also been derived (9, 10) for a column of finite length  $L$ . Below are the mean, variance, and skewness taken from previous work (10)

$$\begin{aligned} t_1 &= L/u_e \\ \sigma_t^2 &= 2D_e L/u_e^3 \\ \gamma_1 &= 3(2D_e/u_e L)^{1/2} \end{aligned} \quad (3)$$

Implicit in eq 1 for equilibrium chromatography is the stipulation that the mobile phase velocity is low enough to justify ignoring interphase kinetic effects. Kinetic considerations would necessitate additional terms and additional equations. In the above equations,  $u_e$  is the elute velocity (the mobile phase velocity divided by  $1 + k'$  where  $k'$  is the capacity factor).  $D_e$  is the longitudinal dispersion constant divided by  $1 + k'$  and  $c(z,t)$  is the concentration of solute at position  $z$  and time  $t$  on the column. What we will show is that the solution to the differential rate equation can lead cleanly to the so-called plate model and that there is no prerequisite for a large number of plates.

**Finite Difference Solution.** Equation 1 is a second-order linear differential equation which, although it has an exact analytical solution, will be solved for our ultimate purposes by numerical approximation. For convenience, we will abbreviate eq 1 as

$$c_t = D_e c_{zz} - u_e c_z$$

The numerical solution to the above equation will be accomplished by use of the finite difference method (11, 12). Briefly, multidimensional variable space is replaced by a grid whose mesh size can be made smaller and smaller. As is usually done, the mesh sizes in the  $z$  and  $t$  directions are labeled  $h$  and  $k$ , respectively. Any point in  $z,t$  space can be represented by the number of mesh steps from the origin:  $z_m = mh$  and  $t_n = nk$ . A Taylor series expansion replaces partial derivatives with corresponding difference quotients

$$\begin{aligned} c(z+h,t) &= c(z,t) + hc_z(z,t) + \frac{h^2}{2}c_{zz}(z,t) + \dots \\ c(z-h,t) &= c(z,t) - hc_z(z,t) + \frac{h^2}{2}c_{zz}(z,t) - \dots \end{aligned}$$

Subtraction and addition of the above truncated equations give the following approximations with errors of order  $O(h^2)$

$$\begin{aligned} c_z &\sim \frac{1}{2h}[c(z+h,t) - c(z-h,t)] \\ c_{zz} &\sim \frac{1}{h^2}[c(z+h,t) - 2c(z,t) + c(z-h,t)] \end{aligned}$$

Additionally

$$c(z,t+k) = c(z,t) + kc_t(z,t) + \dots$$

yields

$$c_t \sim \frac{c(z,t+k) - c(z,t)}{k}$$

The grid coordinates can be identified by just their indices. For example,  $z-h$ ,  $z$ , and  $z+h$  become  $m-1$ ,  $m$ , and  $m+1$ , respectively.

Substitution of the above finite difference approximations into the partial differential equation 1 then gives

$$\begin{aligned} c_{m,n+1} &= \lambda \left( D_e + \frac{1}{2}u_e h \right) c_{m-1,n} + [1 - 2D_e \lambda] c_{m,n} + \\ &\quad \lambda \left( D_e - \frac{1}{2}u_e h \right) c_{m+1,n} \end{aligned} \quad (4)$$

in which  $\lambda = k/h^2$ . In this approximation, the concentration at grid point  $m$  at time step  $n+1$  on the left is equal to the sum of three terms on the right, all determined at the previous time step  $n$ : a forward-feed term from the previous grid point  $m-1$ , a retention at the given grid point  $m$ , and a backward-feed from the next grid point  $m+1$ . By "feed", we imply a combination of a forward-only velocity effect and a forward-and-backward diffusion effect. Traditional finite difference developments of the rate model using the Taylor series (1, 2) invariably exclude the last term corresponding to backward feeding. Our approach is thus a departure from the conventional one.

Equation 4 can be used to generate the approximate on-column profile even in the diffusion-only limit,  $u_e \rightarrow 0$ . This observation is relevant to the criticism (1) that plate treatments do not include effects of longitudinal diffusion. However, we will defer further discussion of the finite element solution until the plate models are addressed.

**Plate Models.** Martin and Synge's plate model (3) envisions the chromatographic column as being a linear sequence of hypothetical cells or plates, each of which consists of identically repeating proportions of stationary phase and mobile phase. The loading plate, numbered zero, contains the sample solute which partitions between the two phases according to the equilibrium retention ratio,  $R$ .  $R$ , the fraction of solute in the mobile phase, is related to the capacity factor  $k' = (1-R)/R$ . Mobile phase is then transferred downstream to the next plate, numbered 1; a portion of what was in 1 is similarly transferred to 2; etc. Simultaneously, pure mobile phase is added to the original cell containing stationary phase with retained solute. We will symbolize the time step for this transfer by  $\tau$ . Whether these transfers are truly stepwise or infinitesimally stepwise (continuous) can be dealt with according to a very simple argument presented below.

Picture each cell as being divided into  $\nu$  identical (hypothetical) "subcells". For  $\nu = 1$ , we will have the stepwise (Craig) plate model, whereas for  $\nu \rightarrow \infty$  we will have the (Martin and Synge) continuous plate model describing the transfers at equilibrium. The amount being transferred will be calculated from the equilibrium concentration in a volume of one subcell and is identical with the concentration in all other subcells in the given plate. Such a picture is consistent with the plate definition as "the length of a cell whose mean concentration is in equilibrium with its own effluent" (1). It is similar to the rectangular step approximation used in numerically integrating smooth functions that actually vary over the step's width. In terms of fractions of the original sample amount, the zero-numbered plate's total solute amount after the first transfer is calculated from the sum of  $1-R$ , the fraction remaining in the stationary phase, and  $R(1-(1/\nu))$ , the fraction remaining in the mobile phase. Here we introduce the abbreviation

$$\rho = R/\nu$$

for the fraction of solute in a subcell, and

$$T = \tau/\nu$$

for the steps to transfer a volume of mobile phase equal to that in a complete plate. Note that  $RT = \rho\tau$ . The letter " $p$ " has frequently been used to represent  $R$  or  $\rho$  or sometimes

both (4). To avoid this ambiguity, we have chosen not to use "p".

With the above definitions, the zeroth plate contains a solute fraction  $1 - \rho$  after the first partial transfer. At equilibrium, repartition yields fractional compositions of  $R(1 - \rho)$  and  $(1 - R)(1 - \rho)$  in the mobile and stationary phases, respectively. In the first plate down the sequence, the transferred total fraction is  $\rho$  and repartitioning yields fractions  $R\rho$  and  $(1 - R)\rho$  in the mobile and stationary phases, respectively. After a second partial transfer and equilibration, the original, first, and second plates contain total fractions  $(1 - \rho)^2$ ,  $2\rho(1 - \rho)$ , and  $\rho^2$ , respectively. In terms of amounts rather than fractions, the continued development as above corresponds to a recursion relationship for  $c_{m,n+1}$ , the amount of solute in plate  $m$  following the  $(n + 1)$ st transfer. In terms of  $c_{m-1,n}$  and  $c_{m,n}$ , the amounts in the given and upstream plates prior to the transfer, we have for the continuous plate model

$$c_{n,n+1} = \rho c_{m-1,n} + [1 - \rho]c_{m,n} \quad (5)$$

and, parenthetically

$$c_{m,n+1} = R c_{m-1,n} + [1 - R]c_{m,n} \quad (6)$$

for the step plate model. After a third transfer, four plates have total compositions given sequentially by the terms on the left in the sum below

$$(1 - \rho)^3 + 3\rho(1 - \rho)^2 + 3\rho^2(1 - \rho) + \rho^3 = 1$$

After a total of  $\tau$  transfers, plates 0 through  $\tau$  have total compositions corresponding to the  $\tau + 1$  terms in the binomial expansion generalized as

$$[(1 - \rho) + \rho]^\tau = 1$$

Each of the  $\tau + 1$  terms in the binomial expansion can be written as

$$\frac{\tau!}{j!(\tau - j)!} \rho^j (1 - \rho)^{\tau - j}$$

with plate index  $j$  running from 0 to  $\tau$ . This is identical with what has been given in most developments of the plate model where attention is immediately drawn to the binomial distribution and its mathematical properties. In particular, the Craig stepwise model in which  $\nu = 1$ ,  $\rho = R$ , and  $T = \tau$  gives

$$f(j, T = \text{constant}) = \binom{T}{j} R^j (1 - R)^{T - j} = \frac{T!}{j!(T - j)!} R^j (1 - R)^{T - j} \quad (7)$$

and has a mean  $\mu_j = RT$  and a variance  $\sigma_j^2 = RT(1 - R) = \mu_j(1 - R)$ . The normalization condition would be the finite summation

$$\sum_{j=0}^T \binom{T}{j} R^j (1 - R)^{T - j} = 1$$

In the Martin and Syngde continuous flow model,  $\nu \rightarrow \infty$  and the binomial distribution becomes exactly the Poisson distribution

$$f(j, \tau = \text{constant}) = \frac{(\rho\tau)^j}{j!} \exp(-\rho\tau) = \frac{(RT)^j}{j!} \exp(-RT) \quad (8)$$

For large, fixed time  $\tau$ , the usual Gaussian approximation is indeed appropriate for the continuous, on-column spatial profile in this model

$$f_G(j, \tau = \text{constant}) = \frac{1}{(2\pi\sigma_j^2)^{1/2}} \exp\left[-\frac{(\mu_j - j)^2}{2\sigma_j^2}\right] \quad (9)$$

The on-column plate model profile corresponds to what an elute detector would be expected to see in a semiinfinite column if the detector, at a fixed time, instantaneously

scanned the column as a function of distance from the load point.

It is incorrect, however, to conclude the derivation at this stage as is occasionally done. The binomial and Poisson distributions pertain only to the on-column development. That is, those distributions express the column spatial profile for fixed number of transfers and with plates  $j$  ranging between 0 and  $\tau$ . The chromatogram develops off the column and the elution (time) profile is a different function, one which properly involves a fixed plate index  $j$  which we will now call  $r$ . Then  $\tau$  for the chromatogram ranges from  $r$  through  $\infty$ .

If the last plate is  $r$ , determined by the length of the column, then the elution chromatogram is determined by the fraction of solute in the  $r$ th plate. Equilibrium following transfer  $\tau = r$  determines that a fraction  $\rho$  of the amount in cell  $r$  is in the mobile phase and will move out of the column on the next transfer. Consequently, the effluent chromatogram is functionally given by terms of the form

$$\rho \frac{\tau!}{r!(\tau - r)!} \rho^r (1 - \rho)^{\tau - r} \quad (\text{for } r = \text{constant})$$

which are to elute beginning with the  $(r + 1)$ st transfer. The elution profile is neither a binomial nor Poisson distribution. Nor is the Gaussian approximation necessarily valid for large transfer numbers as is evident in eq 2 or in the nonzero third central moment of the chromatogram (9, 10).

## RESULTS

**Stepwise Plate Model Result.** Bearing in mind that the terms with  $0 \leq T < r$  are explicitly equal to zero, reflecting the displacement of the interstitial volume that precedes the original load in the Craig model, the normalized chromatogram,  $f(j = r, T) = c(T + 1)$ , for the stepwise case and the normalization constraint are correctly given by the infinite series

$$\sum_{T=r}^{\infty} c(T + 1) = 1 \quad (10)$$

where

$$c(T + 1) = 0 \quad \text{for } 0 < T < r$$

$$c(T + 1) = R \left\{ \frac{T!}{r!(T - r)!} R^r (1 - R)^{T - r} \right\} \quad \text{for } r \leq T < \infty \quad (11)$$

The mean  $k$ th moments of the number of transfers into a fixed, final plate  $r$  are given by

$$\langle T^k \rangle = R \sum_{T=r}^{\infty} T^k \frac{T!}{r!(T - r)!} R^r (1 - R)^{T - r}$$

The following identities are employed in conjunction with the substitutions  $w = T - r$  and  $q = 1 - R$ :

$$TT! = (T + 1)! - T!$$

$$T^2T! = (T + 2)! - 3(T + 1)! + T!$$

$$T^3T! = (T + 3)! - 6(T + 2)! + 7(T + 1)! - T!$$

$$\frac{1}{(1 - q)^{s+1}} = \sum_{w=0}^{\infty} \frac{(s + w)!}{s!w!} q^w \quad 0 \leq q < 1, s = r, r + 1, r + 2 \dots$$

to give the (Craig) elution profile mean, mean squared, and mean cubed transfer numbers

$$\langle T \rangle = \frac{r + 1}{R} - 1 \quad (12)$$

$$\langle T^2 \rangle = \frac{(r + 2)(r + 1)}{R^2} - \frac{3(r + 1)}{R} + 1$$

$$\langle T^3 \rangle = \frac{(r+3)(r+2)(r+1)}{R^3} - \frac{6(r+2)(r+1)}{R^2} + \frac{7(r+1)}{R} - 1$$

The peak variance is given by

$$\sigma_{\tau^2} = \langle T^2 \rangle - \langle T \rangle^2 = \frac{(r+1)(1-R)}{R^2} \quad (13)$$

and the skewness

$$\gamma_1 = \frac{\langle T^3 \rangle - 3\langle T^2 \rangle \langle T \rangle + 2\langle T \rangle^3}{\sigma^3} = \frac{2-R}{(r+1)^{1/2}(1-R)^{1/2}}$$

Higher order moments can easily be calculated.

**Continuous Plate Model Result.** The convenient feature about the above stepwise development is that it can be applied directly to the continuous process. The equations that result would be identical with  $T$  replaced by  $\tau$  and  $R$  replaced by  $\rho$ . One would then reexpress the results taking limits when  $\nu \rightarrow \infty$  as was done in eq 8. Then

$$c(\tau+1) = \rho \left\{ \frac{(\rho\tau)^r}{r!} \exp(-\rho\tau) \right\} = \rho \left\{ \frac{(RT)^r}{r!} \exp(-RT) \right\} \quad (14)$$

$$\text{for } r \leq T < \infty$$

Although eq 14 resembles the Poisson distribution 8, it is not the Poisson distribution but rather the *gamma distribution* (13). Note the distinction between what is varying and what is constant in the two distributions 14 and 8.

The moments of the gamma distribution are particularly straightforward to calculate.

$$\langle \tau^k \rangle = \frac{\rho}{r! \rho^k} \int_0^{\infty} (\rho\tau)^{r+k} \exp(-\rho\tau) d\tau = \frac{(r+k)!}{r! \rho^k}$$

giving

$$\begin{aligned} \langle \tau \rangle &= \frac{r+1}{\rho} \\ \langle \tau^2 \rangle &= \frac{(r+2)(r+1)}{\rho^2} \\ \langle \tau^3 \rangle &= \frac{(r+3)(r+2)(r+1)}{\rho^3} \\ \sigma_{\tau^2} &= \frac{r+1}{\rho^2} \\ \gamma_1 &= \frac{2}{(r+1)^{1/2}} \end{aligned}$$

In comparing the above equations to those from the step result, one should recall that  $T = \nu\tau$  and  $\rho = R/\nu$ . The expression for  $\langle \tau \rangle$  for example can be rewritten as  $\nu\langle \tau \rangle = (r+1)/(\rho/\nu) = \langle T \rangle = (r+1)/R$ . It is easy to demonstrate that the previous (Craig) stepwise results for mean, variance, and skewness all converge to the continuous results above when  $R = 1/(1+k') \ll 1$  as expected. The means and variances in both plate results are identical with what Klinkenberg and Sjenitzer derived (4). Those authors drew attention to the difference in the variances for the two plate models. However, since their derivation was achieved essentially by allowing  $R \rightarrow 0$ , the differences become insignificant and the comparison is academic.

## DISCUSSION

First, we will return to the finite difference approximation for the rate eq 4. Equation 4 is, in every sense, a plate model, but one in which forward and backward transfers are both

possible in contrast to other discussions on the topic. The rate of convergence and consequently the truncation error in using this equation are determined not only by how small  $k$  (time step) and  $h$  (distance step) are but also by the factor  $\lambda = k/h^2$ .

We can resort to the physical picture of the chromatographic process to guide us in choosing the step sizes. During a small unit of time  $\delta t$ , the elute is diffusing with respect to its centroid in the mobile phase such that  $\langle \delta z^2 \rangle = 2D\delta t$ . Simultaneously, the mobile phase is carrying the elute downstream a distance  $u\delta t$ . A measure of the net displacement downstream is  $u\delta t + \langle \delta z^2 \rangle / u\delta t$ . Similarly,  $u\delta t - \langle \delta z^2 \rangle / u\delta t$  is a measure of the net upstream displacement. The distance that the mobile phase moves downstream can be identified with step size  $h$  since  $\delta t$  is arbitrary. We can eliminate the arbitrariness by resorting to a choice that simplifies the ensuing mathematics. That is, we can choose  $h (=u\delta t)$  such that there is no net upstream displacement on the average due to diffusion:  $u\delta t - (\langle \delta z^2 \rangle / u\delta t) = u\delta t - (2D\delta t / u\delta t)$  is then zero. Consequently, by a choice large enough to mitigate the backward (upstream) contributions to the chromatographic development, we identify the step size in the column with  $2D/u$ . This convenient choice of nonzero stepsize corresponds to equating  $h$  to what has been called the height equivalent to a theoretical plate and within which the partitioning of solute between mobile phase and stationary phase is approximated (rectangularized) by the theoretical equilibrium result. Equation 4 now begins to resemble eq 6 in becoming approximated as

$$c_{m,n+1} = 2D_e \lambda c_{m-1,n} + [1 - 2D_e \lambda] c_{m,n}$$

The remaining grid direction corresponds to time with step size  $k$ . To an extent,  $k$  determines how rapidly the finite difference equation 4 converges. The largest that  $k$  logically can be is just the time it takes for mobile phase from one complete plate (or  $\nu$  subcells) to move distance  $h$ . That is,  $0 < k \leq h/u$  where  $u = u_e/R$  is the mobile phase velocity. Substituting this maximum time step and  $h = 2D/u = 2D_e/u_e$  into eq 4 gives eq 6. In other words, the Craig stepwise plate model with the plate height defined in terms of both the dispersion constant and the flow rate follows directly from the finite difference approach to the differential rate equation. If higher order terms are kept, the recursion relationship 4 will then more realistically have solute breaking through the end of the column in fewer than  $\tau+1$  transfers. On the other hand, if fewer terms in the Taylor series are used, the ideal chromatogram (no band broadening) will be obtained (14). No ad hoc assumptions are necessary other than conveniently adjusting to zero the net contribution for backward transfers. If just the time step is contracted to zero in the limit, the continuous (Martin and Syngé) plate result is obtained. This was demonstrated indirectly by invoking a subcell picture in which the number of subcells  $\nu$  per plate approached  $\infty$  corresponding to an infinitesimal time step for transfer.

The approach used in this work appears to complement the developments recently presented by Guiochon et al. (14, 15). In their "semiideal" model, longitudinal diffusion is assumed to be negligible. This allows use, in more complex rate equations, of a numerical solution which favors just the forward direction of propagation. Kinetics of mass transfer are approximated in a way that leads to an artificial dissipation coefficient. Their numerical procedure yields stable and optimized solutions when the step size is equated to the conventional theoretical plate height. That result is equivalent to what we have obtained, but the conditions and interpretations are somewhat different. In each case, they seem valid under the assumptions implicitly invoked.

A brief critique of the major phenomenological approximation to the plate model developed here is warranted. In

getting from eq 4 to eq 6 we had let the average contribution from backward feeding due to diffusion be identically cancelled by mobile phase downstream drift. This forward-only assumption is also imposed, but ab initio, in stochastic models of the chromatographic process (16-18), although attention is not drawn to it. It appears similarly in derivations of the differential equation based on mass balance where only downstream feeding is taken into consideration (1, 2, 19), that is, when longitudinal diffusion is neglected. The forward-only assumption is valid, on the other hand, for the Craig model of countercurrent distribution separations (20).

In continuing the critique, let us examine the consequences had we not made the forward-only hypothesis but rather used the complete finite difference equation 4 to give a more accurate relationship between step  $h$  and the physical parameters  $R$ ,  $D_e$ , and  $u_e$ . We can express this relationship simply as a correction to the previous one; that is,  $h = (2D/u) + \epsilon$ . The term  $\epsilon$  is not necessarily small nor is it necessarily constant. Substituting  $h$  into the last term in eq 4 gives, for that backward-feed term's coefficient

$$\lambda \left( D_e - \frac{1}{2} u_e h \right) = \frac{-R\epsilon/2}{(2D/u) + \epsilon}$$

The above coefficient with  $\epsilon \neq 0$  legitimately approaches zero in three possible ways: (i) the trivial situation where  $D \rightarrow \infty$  in which case the solute is diffused uniformly over the entire column and no "chromatography" occurs, (ii) when  $u_e$ , the mobile phase velocity, approaches 0 where again no "chromatography" occurs, and (iii) when  $R$ , the equilibrium retention ratio, approaches zero. In this third case, the neglect of backward feed is identified as the chromatographically relevant assumption. Both plate models based on it become justifiable under this condition. This is true regardless of the number of theoretical plates in a column.

In assessing how well the plate models do, one can compare their statistical moments with those obtained by using the differential rate model 4. Below are the latter, transformed from eq 3 which had time  $t$  as the continuous variable, into transfers  $\tau$  as the variable

$$\begin{aligned} \langle \tau \rangle &= \frac{r+1}{\rho} \\ \langle \sigma_\tau^2 \rangle &= \frac{r+1}{\rho^2} \\ \langle \gamma_1 \rangle &= \frac{3}{(r+1)^{1/2}} \end{aligned}$$

The mean and variance from the exact differential rate model are identical with what is obtained from the plate approximations (when  $R$  is necessarily small, irrespective of the number of plates,  $r+1$ ). It is not until the skewness is evaluated that the approximations display any significant deviation from the exact result. Even here, the deviation  $1/(r+1)^{1/2}$  is small for large plate numbers. An assertion frequently made concerning large plate numbers is that both the

step and continuous plate models then provide Gaussian chromatograms. A quick probe of the non-Gaussian character of a chromatogram is the skewness parameter, which should be zero. The step plate model skewness for a large number of plates is not negligible if  $R \approx 1$ , although this is rarely of practical interest.

We will put the above discussion in a more succinct perspective in order to summarize this paper. First, we have shown that the Craig step model and the Martin and Synge continuous plate model are both derivable directly from the differential rate equation as approximate solutions to equilibrium chromatography. Our method reveals that the approximations employed to accomplish this inherently bring about the relationship between plate height and physicochemical variables for equilibrium chromatography. Furthermore, both plate models are shown to be equally valid in the limit  $R \ll 1$  (or capacity factor  $k' \gg 1$ ) and, as we have seen, give equivalent results in that limit. The "equality" is not a new conclusion (2, 4, 21) but the validity claim is. However, we have also concluded something at odds with the literature (2, 4). There is no a priori justification for employing the continuous plate model in preference to the step model when  $R$  is not  $\ll 1$  since then both are inappropriate. For small  $R$  (large  $k'$ ) the continuous and step plate models are equally valid even for inefficient columns; but, neither can be justified for large  $R$  (small  $k'$ ) regardless of the number of theoretical plates. The often quoted claim that they give different results here is moot.

#### LITERATURE CITED

- Giddings, J. C. *The Dynamics of Chromatography*; Marcel Dekker, Inc.: New York, 1965; pp 20-26.
- Gleuckauf, K. *Trans. Faraday Soc.* **1955**, *51*, 34-44.
- Martin, A. J. P.; Synge, R. L. M. *Biochem. J.* **1941**, *35*, 1358-1368.
- Klinkenberg, A.; Sjenitzer, F. *Chem. Eng. Sci.* **1966**, *5*, 258-270.
- Keulemans, A. I. M. *Gas Chromatography*, 2nd ed.; Reinhold Publishing Corp.: New York, 1959; pp 112-129.
- Dal Nogare, S.; Juvet, R. S., Jr. *Gas-Liquid Chromatography Theory and Practice*; John Wiley & Sons Interscience: New York, 1962; pp 55-69.
- Brown, P. R.; Hartwick, R. A. *High Performance Liquid Chromatography*; John Wiley & Sons Interscience: New York, 1989; pp 100-103.
- Jönsson, J. A. *Chromatographia* **1984**, *18*, 427-433.
- Kucera, E. J. *Chromatogr.* **1965**, *19*, 237-248.
- Karol, P. J. J. *Chromatogr.* **1988**, *445*, 207-210.
- Kreuzig, E. *Advanced Engineering Mathematics*, 5th ed.; John Wiley & Sons: New York, 1983; Chapter 21.
- Lapidus, L.; Pinder, G. F. *Numerical Solutions of Partial Differential Equations in Science and Engineering*; John Wiley & Sons: New York, 1982; Chapter 2.
- Kendall, M.; Stewart, A. *The Advanced Theory of Statistics*, 4th ed.; Chas. Griffin & Co.: London, 1977; Vol. 1, p 64.
- Lin, B.; Guiochon, G. *Sep. Sci.* **1989**, *24*, 31-40.
- Rouchon, P.; Schonauer, M.; Valentin, P.; Guiochon, G. *Sep. Sci.* **1987**, *22*, 1793-1833.
- Giddings, J. C.; Eyring, H. J. *Phys. Chem.* **1955**, *59*, 416-421.
- Giddings, J. C. *J. Chem. Phys.* **1957**, *26*, 169-173.
- Dondi, F.; Remelli, M. J. *Phys. Chem.* **1966**, *90*, 1885-1891.
- Aris, R.; Arundson, N. R. *Mathematical Methods in Chemical Engineering*; Prentice-Hall: Englewood Cliffs, NJ; Vol. 2, pp 33-36.
- Grushka, E. *Sep. Sci.* **1971**, *6*, 331-344.
- van Deemter, J. J.; Zuideweg, F. J.; Klinkenberg, A. *Chem. Eng. Sci.* **1956**, *5*, 271-289.

RECEIVED for review February 27, 1989. Accepted June 15, 1989.

# Robust Statistics and Functional Relationship Estimation for Comparing the Bias of Analytical Procedures over Extended Concentration Ranges

Michael Thompson

Department of Chemistry, Birkbeck College, Gordon House, 29 Gordon Square, London WC1H 0PP, U.K.

Kane's Kjeldahl protein data were assembled to compare the efficacy of a copper sulfate catalyzed procedure with that of the standard procedure employing mercury(II) oxide. The original data analysis was carried out by a conventional analysis of variance at each level, after the rejection of outliers. The data have now been reexamined by a functional relationship method after the estimation of robust means and standard deviations. The combined methods gave the rapid and unambiguous result that there was no measurable relative bias between the two procedures.

In 1984 Kane (1) reported parallel collaborative trials of two variants of the manual Kjeldahl procedure for the determination of protein in feedstuffs. The same test and reference materials were used in both procedures. The purpose of the trial was to determine whether a variant procedure, which used a copper sulfate catalyst, gave the same results as the standard procedure requiring a mercury(II) oxide catalyst.

The parallel trials were designed in the normal manner, with 22 laboratories participating. Twenty-six test materials were analyzed in each laboratory by each procedure, with blind duplication. Two reference materials were also included, but were analyzed without duplication. The test materials were organized as 13 closely matched Youden pairs, so that a split level interpretation could be undertaken (2).

The interpretation reported by Kane was carried out in the normal manner, consisting of a separate one-way analysis of variance for each analytical procedure and each Youden pair, after outliers had been identified and excluded from the data. The purpose of the trial, namely the detection of bias (if any) between the two procedures, was addressed by a separate comparison of the means for each material. The general conclusion was that, as significant differences between procedures were observed in only four of the 26 materials at the 95% confidence level, and those differences were small, the variant procedure with the copper catalyst could be adopted.

In this study some newer statistical methods were used for the interpretation of this large suite of published interlaboratory data. The purpose was to test the applicability and power of the functional relationship for a comparison of the results of two analytical procedures carried out on a number of materials of the same class but with widely varying analyte levels. In addition the use of a robust method for estimating means and standard deviations of analytical data was also tested.

## STATISTICAL METHODS

**Robust Mean and Standard Deviation.** Robust methods are designed for use with parametric data that might be contaminated with outliers (3). The potential applicability to analytical data is therefore obvious. The aim of robust statistics is to describe the parametric or "good" part of the data set. This is similar in intention to the rejection of outliers

before using classical statistics. However, robust methods accomplish this by downweighting rather than rejecting the outlying results. Unlike their classical counterparts, robust estimates cannot be calculated directly from a formula. Nevertheless, they can be readily obtained by numerical methods that can be simply implemented on a microcomputer.

Many different robust methods have been proposed, but the one used in this study is based on the "Huber Proposal 2" (4). Suppose that the data  $x_1, x_2, \dots, x_n$  come from a Gaussian population  $N(\mu, \sigma^2)$  but are contaminated with outliers subsequently. The "Winsorized" values ( $\tilde{x}_i$ ) of the variate are defined as follows:

$$\tilde{x}_i = x_i \text{ if } |x_i - m| < cs$$

or

$$\tilde{x}_i = m + \text{sign}(x_i - m)cs \text{ if } |x_i - m| > cs \quad (1)$$

The value of the constant  $c$  depends on the expected proportion of outliers. A value of  $c = 1.5$  seems widely accepted, protecting against up to 5% of outliers, and was used in this study.

The robust estimates of mean ( $m$ ) and standard deviation ( $s$ ) are obtained from the equations

$$m = \text{average}(\tilde{x}_i) \quad (2)$$

$$s^2 = \text{var}(\tilde{x}_i)/B \quad (3)$$

where  $B$  is a function of  $c$ . However, the Winsorized values are not defined until  $m$  and  $s$  are evaluated, so eq 1-3 have to be iterated to a suitable degree of convergence. Suitable initial estimates of  $m$  and  $s$  are

$$m_0 = \text{median}(x)$$

$$s_0 = 1.483 \text{ median}(|x_i - \text{median}(x)|)$$

The function  $B$  is defined as

$$B = E[\min(c^2, X^2)]$$

where  $X$  is a standard normal deviate. This function can be evaluated from the equivalent expression

$$B = p(|X| < c) + c^2 p(|X| > c) - 2c \cdot \exp(-c^2/2)/(2\pi)^{1/2}$$

where the probabilities ( $p$ ) are obtained from tabulations of the area of the Gaussian curve. Some corresponding values of  $c$  and  $B$  are as follows:

$c$	1.0	1.1	1.2	1.3	1.4	1.5	1.6	1.7
$B$	0.516	0.578	0.635	0.688	0.736	0.778	0.816	0.849
$c$	1.8	1.9	2.0					
$B$	0.877	0.900	0.920					

**Functional Relationship.** The obvious course to pursue in this study was to assume a linear relationship between the results of the two procedures. Other types of relationship are sometimes encountered (5), but in this case a glance at the scatter plot (Figure 1) shows that a linear model is a good initial assumption.



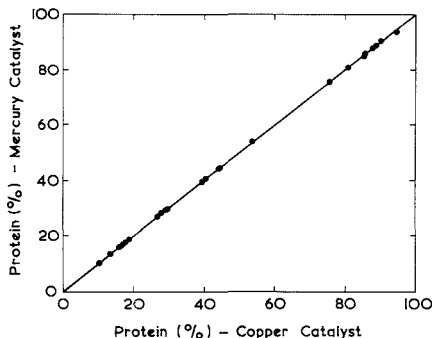


Figure 1. Comparison of robust means for the two procedures for protein determination.

The functional relationship approach is similar to weighted linear regression in that it provides estimates ( $a$  and  $b$ ) of the intercept and the slope coefficient together with their standard errors ( $se(a)$  and  $se(b)$ , respectively). However, it differs from regression in an important way: It produces unbiased values of  $a$  and  $b$  when both of the variables are subject to errors, as in the comparison of analytical methods. A corollary of this advantage is that the interpretation of variables as "dependent" or "independent" is purely nominal, and the method gives the same relationship whichever way the two variables are designated.

Methods of estimating the parameters of linear functional relationships have been suggested since the work of Adcock (6). A maximum likelihood treatment by York (7) obtained  $b$  by minimizing the expression

$$\sum_i [(x_i - u_i)^2/k_i + (y_i - \alpha - \beta u_i)^2/l_i]$$

where  $x_i$  is the mean result of the first method on the  $i$ th material,  $y_i$  is the corresponding result by the second method,  $k_i$  and  $l_i$  are the respective variances of  $x_i$  and  $y_i$ ,  $u_i$  is the (unknown) population mean of  $x_i$ , and  $\alpha$  and  $\beta$  are the parameters to be estimated by  $a$  and  $b$ . Note that  $k_i^{1/2}$  and  $l_i^{1/2}$  are the standard errors of the means  $x_i$  and  $y_i$ . The minimization was carried out by an iterative method, after setting the derivatives to zero. Ripley and Thompson (8), concerned with accuracy comparisons in analytical science, showed that the problem was equivalent to minimizing

$$\sum_i w_i(\beta) [y_i - a(\beta) - \beta x_i]^2$$

where the weight  $w_i(\beta)$  is given by

$$w_i(\beta) = w_i = 1/(l_i + \beta^2 k_i)$$

and

$$a(\beta) = \sum_i w_i y_i - \beta \sum_i w_i x_i$$

to find the value of  $b$ . The minimization was undertaken by a linear search with parabolic inverse interpolation, a method thought to have superior performance to setting the derivatives to zero (9). The iteration starts with a preliminary estimate of  $\beta$  obtained by normal regression. Expressions such as  $a(\beta)$  indicate that the estimate  $a$  depends on the estimate of  $\beta$  in the current iteration. The standard errors are given by

$$se(a) = [\sum_i w_i x_i^2 / \sum_i w_i \sum_i w_i (x_i - \bar{x}_w)^2]^{1/2}$$

$$se(b) = [\sum_i w_i (x_i - \bar{x}_w)^{-2}]^{1/2}$$

where the weighted mean is given by

$$\bar{x}_w = \sum_i w_i x_i / \sum_i w_i$$

A FORTRAN program for the maximum likelihood functional relationship method used in this study can be obtained from Prof. B. D. Ripley, Department of Mathematics, University of Strathclyde, Glasgow G1 1XH, U.K.

If there is no overall bias between the two analytical procedures, then  $E(a) = 0$  and  $E(b) = 1$ . Bias is demonstrated by a significant deviation from these criteria and is formalized by an examination of the values of  $a/se(a)$  and  $(b-1)/se(b)$ , which are distributed approximately according to the  $t$  distribution. The adequacy of the linear model can be tested by an examination of the scaled residuals. Ideally they should be randomly positive or negative and show no trend in absolute magnitude when plotted against concentration and be approximately distributed as a sample from a standard normal deviate.

Additionally the degree of fit of the model can be gauged by forming the sum of the squares of the scaled residuals, i.e.

$$S = \sum_i w_i (y_i - a - \beta x_i)^2$$

For a perfect fit to the model  $S$  should have a chi-squared distribution with  $n - 2$  degrees of freedom. Lack of fit is indicated by a value of  $S$  greater than that shown for the chi-squared distribution at  $p = 0.05$ . This circumstance might arise if the true relationship were curvilinear, or alternatively if cumulatively there were enough biases between individual pairs of results. In the present study this latter effect could conceivably arise from occasional failure of one or other of the two analytical procedures for particular trial materials. A significantly high value of  $S$  could also be obtained when no bias were present if the precisions of the analytical procedures were underestimated. This last feature is a common failing in within-laboratory analytical data. In this study, however, underestimated precision would not be expected, as the data originated independently from different laboratories.

## RESULTS AND DISCUSSION

**Comparison of Means.** The data from Table 2 of Kane's paper, as outlined above, were used without any omission. The results for each blind duplicate were averaged. Then the robust means and standard deviations were estimated over all 22 laboratories, for each of the 28 materials and both analytical procedures. The "Youden pairs" of similar materials were treated as two independent materials. The reference materials were included in the data set and treated as were the test materials, except that there was no analytical duplication. The statistics are shown in Table I and II. The functional relationship between the two sets of 28 means for each procedure was then investigated by the method of Ripley and Thompson, with the arbitrary selection of the results of the copper-catalyzed procedure as the "independent" variable.

The results obtained were as follows: intercept,  $a = 0.005$ ,  $se(a) = 0.040$ ,  $t = 0.12$ ; coefficient,  $b = 0.9997$ ,  $se(b) = 0.0015$ ,  $t = 0.20$ .

The results indicate that overall there is no measurable bias between the two methods, as the respective  $t$  values are not significantly high. (In fact the  $t$  values are unusually low, perhaps indicating that the original analytical data from the two methods were not completely independent). The scaled residuals showed no trends or unusual features when plotted against concentration (Figure 2). The distribution showed no obvious excess of outlying points, showing that the general conclusion (of no bias between the results of the procedures) applied equally to the individual trial materials. The sum of the squared residuals was 18.5, less than the critical level of  $\chi^2$  (38.9 for  $p = 0.05$  and 26 degrees of freedom), demonstrating the absence of significant lack of fit.

The residuals from some of the "Youden pairs" seemed systematically close by visual inspection, suggesting small matrix effects for particular materials. However, an analysis

**Table I. Robust and Classical Means (% Protein) of Results from 22 Laboratories**

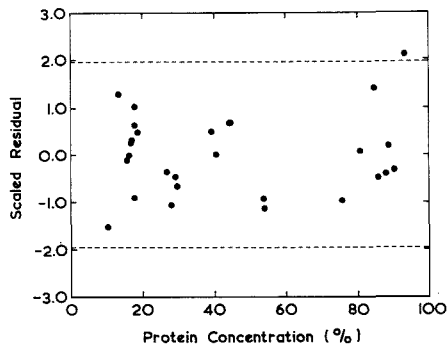
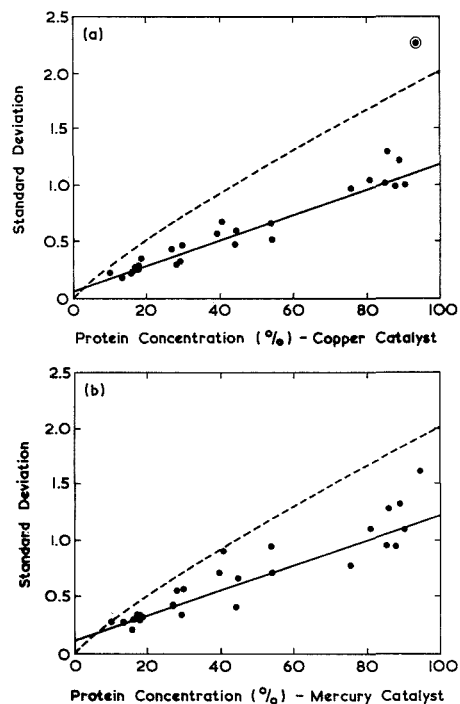
material	mean, Cu method		mean, Hg method	
	classical	robust	classical	robust
dehydrated alfalfa meal	18.74	18.74	18.75	18.79
dehydrated alfalfa meal	16.86	16.86	16.86	16.88
soy protein concentrate	87.66	87.92	87.60	87.77
soy protein concentrate	88.89	88.81	88.82	88.86
pullet grower	15.69	15.73	15.70	15.72
layer	16.13	16.20	16.17	16.20
meat and bone meal	54.20	54.21	53.92	53.97
meat and bone meal	53.83	53.92	53.55	53.68
custom mix cattle feed	13.36	13.39	13.44	13.48
beef feed	10.11	10.19	10.08	10.08
swine base mix	29.76	29.76	29.73	29.65
swine base mix	29.27	29.32	29.24	29.26
dry dog food	26.97	26.97	26.88	26.92
dry puppy food	28.10	28.17	27.99	28.02
hydrolyzed poultry feathers	85.85	85.84	85.75	85.63
hydrolyzed poultry feathers	90.18	90.30	90.06	90.18
cottonseed meal	39.43	39.40	39.38	39.49
cottonseed meal	40.40	40.52	40.38	40.52
blood meal	84.82	84.84	84.94	85.23
blood meal	80.61	80.73	80.57	80.73
swine developer	17.00	17.02	17.02	17.05
swine grower	17.92	17.95	17.94	18.05
milk replacer	17.75	17.79	17.67	17.70
milk replacer	17.79	17.78	17.87	17.83
soybean meal	44.02	44.08	44.11	44.16
soybean meal	44.41	44.54	44.59	44.66
NH <sub>4</sub> H <sub>2</sub> PO <sub>4</sub>	-	75.78	-	75.50
lysine HCl	-	93.38	-	94.59

**Table II. Robust and Classical Standard Deviations (% Protein) of Results from 22 Laboratories**

material	std dev, Cu method		std dev, Hg method	
	classical	robust	classical	robust
dehydrated alfalfa meal	0.30	0.35	0.40	0.32
dehydrated alfalfa meal	0.25	0.28	0.27	0.31
soy protein concentrate	0.94	0.99	0.88	0.94
soy protein concentrate	0.98	1.26	1.13	1.33
pullet grower	0.20	0.22	0.22	0.20
layer	0.33	0.23	0.27	0.30
meat and bone meal	0.50	0.56	0.77	0.75
meat and bone meal	0.55	0.68	1.00	0.94
custom mix cattle feed	0.25	0.19	0.27	0.28
beef feed	0.20	0.23	0.20	0.27
swine base mix	0.46	0.47	0.48	0.60
swine base mix	0.36	0.33	0.32	0.34
dry dog food	0.38	0.44	0.35	0.42
dry puppy food	0.35	0.30	0.44	0.55
hydrolyzed poultry feathers	0.93	1.30	0.89	1.28
hydrolyzed poultry feathers	1.08	0.99	1.05	1.10
cottonseed meal	0.50	0.56	0.71	0.71
cottonseed meal	0.82	0.67	0.62	0.90
blood meal	0.91	1.01	1.14	0.95
blood meal	0.85	1.05	0.99	1.10
swine developer	0.20	0.26	0.26	0.34
swine grower	0.20	0.26	0.28	0.34
milk replacer	0.24	0.26	0.29	0.34
milk replacer	0.20	0.29	0.26	0.29
soybean meal	0.42	0.48	0.34	0.40
soybean meal	0.52	0.59	0.51	0.66
NH <sub>4</sub> H <sub>2</sub> PO <sub>4</sub>	-	0.96	-	0.77
lysine HCl	-	2.26	-	1.61

of variance of the residuals between and within "Youden pairs" did not support this conclusion ( $F = 1.18$  with 12 and 13 degrees of freedom;  $p = 0.384$ ).

**Precision and Concentration.** The relationship between precision and concentration for both analytical procedures was

**Figure 2.** Scaled residuals from the functional relationship plotted against concentration.**Figure 3.** Robust standard deviation vs concentration (a) for the copper-catalyzed procedure and (b) for the mercury-catalyzed procedure. The solid lines show the weighted regression lines. The broken curves show the Horwitz function. The circled point in (a) was omitted from the regression.

investigated by weighted regression of the robust standard deviations against the robust means. The model fitted was

$$\sigma_c = \sigma_0 + \theta_c$$

where  $\sigma_c$  is the standard deviation at concentration  $c$  and  $\sigma_0$  and  $\theta$  are constants. The weights were estimated by  $2n/s_c^2$  where  $s_c$  is the estimate of  $\sigma_c$ .

The data are shown in Figure 3, together with the regression lines. For the copper-catalyzed results, the circled point was excluded from the regression. The regression statistics were as follows (%): CuSO<sub>4</sub>,  $a = 0.064$ ,  $b = 0.0112$ ,  $S = 23.6$ , dof = 24; HgO,  $a = 0.109$ ,  $b = 0.0111$ ,  $S = 52.4$ , dof = 26 where

$a$  estimated  $\sigma_0$  and  $b$  estimates  $\theta$ . Overall, the levels of precision indicated by these values were virtually identical for the two procedures over the whole concentration range. Apart from the result for the reference material lysine (excluded from the regression), the copper-catalyzed procedure gave a good fit to the model, as shown by the  $\chi^2$  test. In contrast the mercury-catalyzed procedure showed significant lack of fit ( $\chi^2 = 38.9$  for 26 degrees of freedom and  $p = 0.05$ ). This demonstrates that the mercury-catalyzed method gave somewhat less predictable values of precision from material to material. In both instances the precision function is noticeably lower than that predicted by Horwitz's conjecture (10) that reproducibility should follow the relationship

$$\sigma_c = 0.02c^{0.8495}$$

#### Comparison of Robust and Classical Estimates. Means.

The means produced by the robust estimation were very close to those produced by classical statistics after outlier rejection (Table I). The average difference between the methods amounted to only 0.15%, well below the relative standard deviation of the procedures (about 1.1%).

**Standard Deviations.** In contrast to the means, the standard deviations produced by robust estimation were noticeably greater on average than those produced by classical statistics after outlier rejection as implemented by Kane (Table II). The average increases amounted to 10% for the copper-catalyzed procedure and 13% for the mercury-catalyzed procedure. This difference probably reflects the unwarranted rejection of data by the outlier tests, i.e., a small proportion of "errors of the first kind". While this has a relatively small effect on the mean, the standard deviation is more strongly affected.

This difference may be of some importance if it is general in analytical data. Collaborative trial data are currently processed after outlier rejection, and values of repeatability and reproducibility may subsequently be used as standards for data quality control schemes. If these statistics are underestimated, then an unduly large proportion of data may be unnecessarily rejected by failing the precision tests. If the standard were set 13% lower than the true level, for example, about 9% of the observations would fall outside the putative 95% confidence limits.

## CONCLUSIONS

Two nonclassical methods of statistical estimation have been used to examine an existing data set. The trial showed that the robust method used gave appropriate values of mean and standard deviation without the need for outlier tests. The maximum likelihood functional relationship provided a (statistically) unbiased comparison of the relative accuracy of the two methods over the whole range of materials analyzed, including the reference materials, and provided a validated fitting to a model with only two parameters. A comparison of the parameter estimates with their theoretical values showed that there was no significant (analytical) bias between the two procedures. Examination of the residuals showed that there were no individual materials that deviated from this overall conclusion.

It seems that much greater consideration should be given to the possibilities in analytical science of statistical procedures such as robust estimation and functional relationship. Despite the apparent complexities of the iterative methods of estimation, both methods can be easily implemented on a microcomputer.

## ACKNOWLEDGMENT

The author thanks B. D. Ripley for the programs and expert advice.

Registry No.  $N_2$ , 7727-37-9.

## LITERATURE CITED

- (1) Kane, P. F. *J. Assoc. Off. Anal. Chem.* **1984**, *67*, 869.
- (2) Youden, W. J.; Steiner, E. H. *Statistical Manual of the AOAC*; AOAC: Arlington, VA; pp 22, 23.
- (3) Hampel, F. R.; Ronchetti, E. M.; Rousseeuw, P. J.; Stakel, W. A. *Robust Statistics: The Approach Based on Influence Functions*; Wiley: New York, 1986.
- (4) Huber, P. J. *Robust Statistics*; Wiley: New York, 1981.
- (5) Thompson, M. *Analyst* **1982**, *107*, 1169.
- (6) Adcock, R. J. *The Analyst (Des Moines, Iowa)* **1878**, *5*, 53.
- (7) York, D. *Can. J. Phys.* **1966**, *44*, 1079.
- (8) Ripley, B. D.; Thompson, M. *Analyst* **1987**, *112*, 377.
- (9) Nash, J. C. *Compact Numerical Methods for Computers: Linear Algebra and Function Minimization*; Adam Hilger: Bristol, U.K., 1979; pp 129, 130.
- (10) Horwitz, W.; Kamps, L. R.; Boyer, K. W. *J. Assoc. Off. Anal. Chem.* **1980**, *63*, 1344.

RECEIVED for review August 26, 1988. Accepted May 1, 1989.

# Factors Affecting Precision and Accuracy in Quantitative Analysis by Secondary Ion Mass Spectrometry

Ray-Chern Deng and Peter Williams\*

Department of Chemistry, Arizona State University, Tempe, Arizona 85287-1604

**In quantitative analysis by secondary ion mass spectrometry (SIMS) using external standards, precision and accuracy are affected by sample misalignment and different secondary ion energy distributions. To investigate this, depth profiles of four pieces of a B-implanted silicon wafer were obtained with samples mounted flat, or intentionally misaligned. The B<sup>+</sup> signal was referenced to <sup>30</sup>Si<sup>+</sup> and <sup>28</sup>Si<sub>3</sub><sup>+</sup>. In comparative analyses of four nominally identical samples, the relative standard deviation (RSD) was 5.9% for nominally flat samples compared to 13% for misaligned samples for the <sup>30</sup>Si<sup>+</sup> reference ion. When <sup>28</sup>Si<sub>3</sub><sup>+</sup> was used as the reference species, internal agreement was much worse (150% for misaligned samples compared to 13% for flat samples). The best results (RSD 1.9%) were obtained for analyses from the center of one large sample with <sup>30</sup>Si<sup>+</sup> as a reference. This study has shown that random sample misalignments lead to discrimination between analyte and reference ion species with differing energy distributions, which cause significant errors in the comparison of two samples.**

## INTRODUCTION

Secondary ion mass spectrometry (SIMS) has been used widely for depth profiling ion-implanted impurities in semiconductor materials in the electronics industry. For quantification, the average count rate in the implant profile is compared with an average concentration over the analyzed depth, calculated from the implant dose (*I*). When one implanted sample is used as a standard for a second sample, it is usual to normalize the implant count rate to a signal for the matrix element, to minimize errors arising from differing instrumental sensitivity (transmission) between samples. It is generally felt that SIMS analyses obtained in this way should be accurate to about ±10% (standard deviation of a single comparison); detailed measurements using replicate analyses gave a precision of 5–7% (2), again for a single comparison. The question arises: what is the source of this sample to sample variation? Counting statistics on most depth profiles should yield errors much less than 1%. Matrix effects and ion yields should be constant for a given dilute impurity in, say, Si, and these effects should not contribute any error in the final results. We suspected that the sample to sample variation arises from small misorientations of the samples with respect to the secondary ion optic axis of the instrument, together with differences in energy distribution between implant and matrix ion species. Together, these effects can result in a misregistration of the secondary ion beams for the two species at the entrance aperture of the secondary ion mass spectrometer, so that the entrance aperture, if aligned to maximize the matrix ion signal, may not be aligned accurately for the implant ion signal. Note that the secondary ions move slowest in the initial portion of their trajectory, so that electric fields near the sample have a particularly strong effect on ion

trajectories. Thus a random fraction of the signal for the implanted element may be rejected by the entrance aperture which leads to random errors in the results.

If the secondary mass spectrometer must be operated at highest sensitivity to detect a weak impurity signal, the signal for the matrix element is often too high to be measured with an electron multiplier. Under such circumstances, one often looks for a matrix-related signal of lower intensity; cluster ions, e.g. Si<sub>3</sub><sup>+</sup>, Si<sub>3</sub><sup>-</sup>, or multiply charged ions, e.g. Si<sup>2+</sup>, are often used. If the initial kinetic energy distribution for the reference ion is markedly different from that for the analyte species, as is the case for the cluster ions, then the effects of sample misorientation are increased. For negative ion analysis, multiply charged ions are not formed, so that cluster ions offer the only low-intensity matrix reference signal.

To evaluate the effects of sample misorientation and initial kinetic energy differences on analytical precision, we have compared depth profiles for a set of samples cut from the same boron-implanted silicon wafer. Four mounting conditions were compared. Sample set I used our normal four-hole sample holder. This sample holder has a thin metal faceplate with four holes against which samples are pressed by small springs; some slight distortion of the faceplate, and small misorientation of the samples was therefore possible. For set II the samples were deliberately misaligned using small shims. For sample set III analyses from different areas on a large single wafer piece were compared to simulate identically aligned samples. Finally (set IV), four samples were mounted in a one-hole sample holder separately and introduced into the instrument successively for analysis. <sup>30</sup>Si<sup>+</sup> and <sup>28</sup>Si<sub>3</sub><sup>+</sup> were used as reference signals.

## EXPERIMENTAL SECTION

All the depth profiles were obtained by using a Cameca IMS 3f secondary ion mass spectrometer. An O<sub>2</sub><sup>+</sup> primary ion beam with an impact energy of 8 keV was used. Secondary ion signals were taken from a 62 μm diameter circular area in the center of a 250 × 250 μm raster area, eliminating signals from the crater edge. The chosen sample was a B-implanted silicon wafer with an implant energy of 40 keV and a nominal dose of 1 × 10<sup>15</sup> ions/cm<sup>2</sup>. For each set of analyses, pieces slightly larger than 1 cm square were cut from adjacent areas on the wafer. The different sample sets were analyzed under different sets of conditions as follows.

**Sets I and II.** For these analyses our standard four-position sample holder for multiple sample holding was used. This sample holder has a thin (0.5 mm) tantalum faceplate containing four 1 cm diameter holes. For set I, four samples taken from adjacent areas were placed one over each hole and pressed against the rear of the faceplate by small springs. This mounting procedure could induce some small sample misorientations if the tantalum faceplate flexed slightly, and such misorientations were suspected as the source of sample-to-sample variation encountered in normal analyses. For set II, two of the four samples were deliberately misaligned by loading with a 0.5 mm shim (another piece of the wafer) inserted between the sample holder and one end of the sample as shown in Figure 1. These two samples were tilted in opposite directions, each by an angle between 4° and 6°. Sample sets I and II were each analyzed by using two reference ion species, <sup>30</sup>Si<sup>+</sup> and <sup>28</sup>Si<sub>3</sub><sup>+</sup>, leading to the results labeled conditions 1–4 in Table I.

\*To whom correspondence should be addressed.

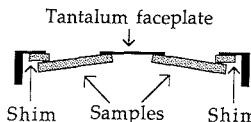


Figure 1. Detail of sample holder showing the Ta faceplate and mounting of the tilted samples. The angle of the tilting is between 4° and 6°.

Table I. Analytical Results for the Four Sample Sets

condition	sample set and loading	reference ion	% RSD	% RSDM
1	I, flat	$^{30}\text{Si}^+$	5.9	1.7
2	I, flat	$^{28}\text{Si}_3^+$	13	3.8
3	II, tilted	$^{30}\text{Si}^+$	13	3.8
4	II, tilted	$^{28}\text{Si}_3^+$	150	44
5	III, one piece	$^{30}\text{Si}^+$	3.9	1.0
6	III, one piece	$^{30}\text{Si}^+$	1.9	0.55
7	IV, flat	$^{30}\text{Si}^+$	2.9	0.84

**Set III.** Sample set III was actually a single flat piece of wafer, about  $2 \times 2$  cm, cut from the starting wafer and attached with silver paint to a flat copper mounting block held in a sample holder without a faceplate. The height difference measured from each edge of this sample to the back of the copper block was less than  $75 \mu\text{m}$ . Analyses in four regions of this sample corresponding to the four analysis positions in the four-hole sample holder were intended to simulate analyses of identically aligned samples (condition 5).  $^{30}\text{Si}^+$  was used as the reference ion species. A further set of analyses was obtained from a small region near the center of this sample to avoid any electric field perturbations near the edges of the sample holder (condition 6). Again  $^{30}\text{Si}^+$  was used as the reference ion species.

**Set IV.** These samples (again taken from adjacent areas on the wafer) were each mounted separately in a sample holder having a single 1 cm diameter hole in the center, and introduced successively into the instrument for analysis. Analyses were obtained from regions close to the center of the sample holder.  $^{30}\text{Si}^+$  was used as the reference ion species (condition 7).

Depth profiles were taken in each case after the secondary current was maximized for the reference ion by adjusting the primary ion beam position and the mass spectrometer entrance aperture. At least three depth profiles were taken for each sample. Each depth profile was obtained in 10 min. Integrals of the  $\text{B}^+$  signal were normalized to the reference ion signals before the relative standard deviations were calculated. Simulation of the secondary ion trajectories was performed by using the SIMION PC/PS2 computer program (Idaho National Engineering Laboratory, Idaho Falls, ID).

## RESULTS AND DISCUSSION

In the Cameca IMS 3f secondary ion mass spectrometer ions are accelerated by a 4500-V electrostatic potential applied between the sample and a grounded extraction plate. Leaving the acceleration space through a hole in the extraction plate, the beam is focused by a pair of einzel lenses (transfer optics) to a beam waist or crossover in the plane of the mass spectrometer entrance aperture. The width of the crossover is a function of the initial trajectories and kinetic energies of the secondary ions; its mean position reflects the alignment of the primary ion impact area with the optical axis of the transfer optics, and the alignment of the sample surface normal to this axis (3). The circular entrance aperture is known also as the contrast diaphragm (CD), because it allows improvement of contrast and lateral resolution in the secondary ion image by limiting the angular and energy spread of the ions entering the mass spectrometer. The smallest CD (diameter  $20 \mu\text{m}$ ) was used for the present study; this CD transmitted an estimated 0.1% of the sputtered ions. It was noted that to maximize the reference ion signal when moving from sample to sample in set I, the primary beam position and/or the CD

position needed to be adjusted. This effect was much stronger for the intentionally tilted samples (set II).

Table I contains the results of the seven study conditions and shows the relative standard deviations (RSD) of the normalized ratios of the integrals, calculated for 12 replicate analyses (three from each of four sample positions in the set). Also shown are the relative standard deviations of the means (RSDM) of the seven data sets. Data from the intentionally misaligned samples were treated as a single set as they would be in a normal analytical situation where misalignment was not suspected. As expected, the agreement for the misaligned samples was particularly bad when  $^{28}\text{Si}_3^+$  was used as a reference species. The use of  $^{30}\text{Si}^+$  as a reference for this sample set gave much better internal agreement (13% RSD rather than 150%). For the nominally flat set of four separate samples (set I), the results were significantly better. Again, the use of the  $^{28}\text{Si}_3^+$  reference gave demonstrably worse results (RSD 13%) than did  $^{30}\text{Si}^+$  (RSD 5.9%). Mounting samples separately in the single-hole sample holder and restricting analyses to the center of the holder gave even better results (RSD 2.9%, condition 7), even though the possibility remained of sample-to-sample variations in alignment. For the single, large sample (III), analyses at points distant from the center of the sample (RSD 3.9%, condition 5) were better than for individual samples at these positions (RSD 5.9%, condition 1) but were less accurate than analyses that were restricted to the center of the sample holder. Analyses on sample III performed at the center of the sample gave the best results in the set (RSD 1.9%, condition 6).

This study clearly shows that sample misalignment is a significant source of error in SIMS analyses that use an external standard. The results also substantiate our initial suggestion that the error arises from a misregistration of the secondary ion beam crossovers for the analyte and reference species at the position of the contrast diaphragm. This causes discrimination against the analyte signal if, as is usually the case, the CD and primary ion beam positions are adjusted to maximize transmission of the reference signal. Alternatively, if the analyte signal were maximized, discrimination against the reference signal would result. The effect of the misregistration is exaggerated if the analyte and reference signal have markedly different initial kinetic energy distributions. The effect was observed in reductions of the  $\text{B}^+$  signals by as much as 40% for conditions 3 and 4, where the  $^{28}\text{Si}_3^+$  signal was maximized for the tilted sample. Although initial kinetic energy differences are most often encountered when an atomic analyte signal is compared to a cluster reference signal, the effect can also occur even if two atomic signals are compared.  $\text{H}^+$  and  $\text{F}^+$  in particular have energy distributions very different from the majority of atomic secondary ions (4, 5).

In some cases it is necessary to operate the secondary ion mass spectrometer at high mass resolving power to distinguish the analyte signal from that of an interfering cluster ion. A typical entrance slit width for such analyses is comparable to the size of the contrast aperture used in the present study ( $20 \mu\text{m}$  diameter). Depending on the quality of the magnet power supply, it can be difficult to switch reproducibly between the analyte and reference peaks, so that an additional source of error is introduced. If, instead of peak switching, the analyte signal alone is monitored, with the reference signal being recorded only at the end of the analysis, then the stability of the primary ion current may limit the analytical accuracy. In general, the analytical accuracy would be expected to degrade at high mass resolution, but the extent of this degradation will vary depending on the stability of the instrument being used. The effects of sample tilt examined here would also be present to about the same extent in high mass resolution analyses. In addition, a tilted sample can

degrade the mass resolution of the mass spectrometer, because ions are initially directed away from the ion-optical axis of the instrument.

The crystal orientation of the sample is not expected to affect the analytical results for semiconductor samples because the ion bombardment rapidly amorphizes the sample surface to a depth on the order of the ion projected range. For heavy ion bombardment (e.g.  $O_2^+$ ) the dose required to fully amorphize the surface region of a silicon sample at room temperature is  $\sim 10^{15}$  ions/cm<sup>2</sup>; such a dose sputters no more than one to two monolayers of silicon, so that over essentially the entire analysis the sample surface is amorphous. The good results from the individually loaded samples (condition 7), which were loaded with random orientations, confirm that variations in sample orientation for silicon do not introduce major errors. For metals, many of which do not amorphize fully under ion bombardment, changes in sample orientation may well introduce sizable errors in analyses which use external standards.

It is not clear where the residual 3.9% RSD for widely spaced analyses on the flat sample (condition 5) arises. Counting statistics in the B<sup>+</sup> and silicon signals would account for only a 0.3% RSD. A portion of the variation might result from nonuniform implantation across the wafer. The wafer used was 10 cm in diameter, and implant doses should be uniform to at least 5% across the wafer area, assuming proper operation of the implanter. A 5% nonuniformity could produce a 1% variation across the 2 cm wide sample. A possible source of error is misalignment of the sample holder in the instrument, which could have caused the entire sample to have been tilted and changed the path length through the acceleration field from one side of the sample to the other. We believe that the major source of variation is the finite extent of the sample holder which gives rise to fringe field effects that slightly distort the acceleration field. The sample holder has a finite size (approximate 2.8 cm × 3.4 cm) and is situated 5 mm from an extraction electrode at ground potential. Within about 4–6 mm of the edge of the sample holder, the accelerating field is not accurately normal to the sample surface, and this can cause deviations of the ion trajectories which vary depending on the initial kinetic energies of the different ion species. Trajectory simulations using the SIMION ray-tracing program of the secondary ions ejected from the edge and from the center of the sample holder show that the distorted acceleration field near the edge does alter the

ion trajectories to some extent. When a set of replicate measurements were all obtained in the central region of the large flat sample (condition 6), the reproducibility improved to 1.9% RSD, suggesting that samples should be centered in the sample holder for the most accurate SIMS analysis. The *relative standard deviation of the mean* for condition 6 was only 0.6% (0.8% for condition 7 and 1.7% for condition 1), so that the precision of a set of 12 measurements compares well with other precise microanalytical or thin film techniques (electron probe or Rutherford backscattering spectrometry).

The results of this study suggest that for the most accurate quantitative SIMS analysis, the sample should be mounted as flat as possible in the center of a sample holder having a rigid faceplate, and the analyzing area should be restricted to the center of the sample to minimize the effects of nonuniform accelerating fields near the edges of the sample holder. In situations where sample orientation is not under ideal control, for example if the sample itself is not flat, or is very small, it is worth noting that careful selection of the reference ion species to have a closely similar energy distribution to the analyte species gives the best chance of analytical accuracy.

### CONCLUSIONS

Quantitative analysis by SIMS is an important requirement, particularly in the electronic industry, and because standards are always required to calibrate elemental sensitivities in each sample type, it is important to know the factors affecting the accuracy with which two samples can be compared. This study has shown that differences in initial kinetic energy distributions between analyte and reference species, combined with small, random sample misalignments, may be a significant source of error in the comparison of two samples. When care is taken to minimize sample misalignments, and analyte and reference ion species are chosen to have similar initial energy distributions, the present results demonstrate that the precision of a comparative SIMS analysis can be better than  $\pm 3\%$  for a single comparison of standard and unknown.

### LITERATURE CITED

- (1) Leta, D. P.; Morrison, G. H. *Anal. Chem.* **1980**, *52*, 514–519.
- (2) Williams, P.; Baker, J. E.; Davies, J. A.; Jackman, T. E. *Nucl. Instrum. Methods* **1981**, *191*, 318–322.
- (3) Slodzian, G. *Surf. Sci.* **1975**, *48*, 161–186.
- (4) Wittmaack, K. *Phys. Rev. Lett.* **1979**, *43*, 872–875.
- (5) Williams, P. *Phys. Rev. B: Condens. Matter* **1981**, *23*, 6187–6190.

RECEIVED for review January 26, 1989. Accepted May 25, 1989.

# Linearized Model for Error-Compensated Kinetic Determinations without Prior Knowledge of Reaction Order or Rate Constant

Jan A. Larsson and Harry L. Pardue\*

Department of Chemistry, Purdue University, West Lafayette, Indiana 47907

This paper describes a new algorithm for calculation of reaction orders, rate constants, and initial and final values of detector signal from several signal vs time data points. The algorithm utilizes a linearized version of the rate equation and is intended primarily to provide initial estimates of these kinetic parameters for other curve-fitting methods. However, under some circumstances, the linearized model can provide sufficiently reliable results that subsequent processing by other methods is not needed. Simulated data with different levels of superimposed noise, data densities, reaction orders, rate constants, and signal change are used to evaluate the algorithm both for its primary purpose of providing initial estimates for other curve-fitting methods and as an independent method. Results are compared with those obtained with a nonlinear least-squares method and two initial-rate methods. The new algorithm provides less reliable results than those obtained by the nonlinear curve-fitting method for some situations (e.g. reaction orders greater than two, low data densities) but has the advantage that it is applicable to reaction orders at and near unity where the nonlinear method to which it is compared fails.

Several papers have described kinetic methods based on the use of regression methods to fit suitable model equations to time-dependent data (1-4). Most of these methods require initial estimates of the fitting parameters that may include the signals at the beginning ( $t = 0$ ) and end ( $t = \infty$ ) of the process as well as the rate constant and reaction order. Approaches used to obtain these initial estimates have ranged from educated guesses based on prior experience with the system to the use of some experimental datum such as the last measured value of signal as an estimate of the final value. However, because the success of the fitting process often depends on the initial estimates of the fitting parameters (5), a more systematic method for obtaining the initial estimates is needed.

In an earlier study, a predictive method based on a linearized model was developed and used to obtain initial estimates of parameters for a nonlinear predictive method (6). Preliminary work with the algorithm indicated that it had potential as an independent kinetic method in its own right. This paper describes that algorithm and results of a study designed to evaluate its capabilities and limitations.

The algorithm is based on a linearized version of a general rate equation and uses time-dependent rates in addition to time-dependent signal values. Simulated data for different values of signal change, rate constants, reaction order, data density, and noise are used to evaluate the algorithm. Results obtained with this new algorithm are compared with results obtained with two rate methods and a nonlinear curve-fitting method. These comparisons show that in some situations, results obtained with the new algorithm are as reliable as results obtained with the other methods. Therefore, although the primary focus was on a method to obtain initial estimates of fitting parameters for other curve-fitting methods, it is

concluded that the new algorithm can be used as an independent kinetic method in some situations.

## MATHEMATICAL DESCRIPTION

This section describes the primary algorithm as well as mathematical procedures used to obtain best estimates of reaction order and the signal at the start of the process.

**Linearized Rate Equation.** As described earlier (6), it is assumed that the rate of change of concentration can be represented by the equation

$$-dc_t/dt = kc_t^n \quad (1)$$

in which  $k$  is a rate constant,  $n$  is the reaction order, and  $c_t$  is the concentration of the species monitored (reactant or product) at time,  $t$ . It is also assumed that the time-dependent concentration is related to measured signal by

$$c_t = (D/q)(S_\infty - S_t) \quad (2)$$

in which  $D$  is  $\pm 1$  and accounts for the direction of signal change and  $q$  accounts for stoichiometry (6) and  $S_t$  and  $S_\infty$  are values of signal at time  $t$  and at  $t = \infty$ , respectively.

By differentiating eq 2, equating the result for  $dc_t/dt$  to eq 1, and substituting for  $c_t$  from eq 2, one can see that

$$D(dS_t/dt) = kq[(D/q)(S_\infty - S_t)]^n \quad (3)$$

Assuming that  $S_t$  is unidirectional, the product on the left side of the equation can be replaced by an absolute value operation, and the resulting equation can be rewritten in the form

$$|dS_t/dt|^{1/n} = D(q^{1-n}k)^{1/n}(S_\infty - S_t) \quad (4)$$

Substituting  $k_s = q^{1-n}k$ , eq 4 can be written as

$$|dS_t/dt|^{1/n} = Dk_s^{1/n}S_\infty - Dk_s^{1/n}S_t \quad (5)$$

in which  $k_s$  is viewed as a signal-based rate constant. Thus, a plot of  $|dS_t/dt|^{1/n}$  vs  $S_t$  should be linear with the rate constant and signal value at  $t = \infty$  being related to the slope,  $b_1$ , and intercept,  $a_1$ , by  $k_s = (-Db_1)^n$  and  $S_\infty = -a_1/b_1$ .

**Reaction Order.** The proposed plot based on eq 5 will be linear only if the correct value of reaction order is used, and this is the basis for obtaining the best estimate of  $n$ . Briefly stated, the procedure is to find the value of  $n$  that gives the "best" linear relationship between  $|dS_t/dt|^{1/n}$  and  $S_t$ .

The criteria and procedures used to accomplish this are discussed later.

**Zero-Time Signal.** The integrated form of the kinetic equation is used to evaluate the signal at  $t = 0$ . To do this, the integrated form of equation (6)

$$S_t = S_\infty - D[k_s(n-1)t + [D(S_\infty - S_0)]^{1-n}]/(1-n) \quad (6)$$

is arranged into the form

$$[D(S_\infty - S_t)]^{1-n} = (n-1)k_s t + [D(S_\infty - S_0)]^{1-n} \quad (7)$$

Because  $S_\infty$  and  $n$  have been determined as described above, the term on the left can be plotted vs time, yielding a straight line with the signal at  $t = 0$  being related to the intercept,  $a_2$ , by  $S_0 = S_\infty - D(a_2)^{1/(1-n)}$ .

## EXPERIMENTAL SECTION

**Instrumentation.** A supermicrocomputer (MC5500 work station, Massachusetts Computer Corp., Westford, MA) was used

to generate and process simulated data. This computer runs under a UNIX operating system, and all software used is written in C language.

**Simulated Data.** Simulated kinetic responses with superimposed noise were produced as described in a previous study (6). Each signal value was computed as the sum of the perfect value (no noise added) plus the product of the desired standard deviation times a noise factor. The noise factor was obtained from the sum of 100 random numbers normalized to the range (1 to 32 767) of the random number generator to give an approximate Gaussian distribution with a mean value of zero and a variance of unity. All simulated responses were for an increasing signal with the same background value (0.1 signal unit). Most cases covered the time interval from 1 to 200 s with a data rate of one point per second, corresponding to 85% of the steady-state signal change,  $\Delta S_{\infty}$ .

**Data Processing.** A linear least-squares program was used to fit the linearized model to kinetic data as described above (eq 5 and 7). A minimum of seven data points covering the desired time range was used, and the program automatically determined the signal direction,  $D$ , and the four desired parameters ( $k_b$ ,  $n$ ,  $S_{\infty}$ ,  $S_0$ ). When the nonlinear predictive method was used, the parameters determined with the linearized model were automatically passed on as initial estimates to another program section in which the nonlinear least-squares algorithm (6) was implemented.

The method of Savitzky and Golay (7) was used with convoluting integers given by them to compute rates used in the linearized predictive method. The size of the moving data range (window) for the derivatization process was selected automatically by the program by using the square of the correlation coefficient,  $r^2$ , as a diagnostic of fit. The data window was selected as the smallest range that gave a final value of  $r^2$  of 0.98 or larger in the procedure described later for selecting the best value of  $n$ .

Results obtained with the linearized predictive (LP) method described herein and the nonlinear predictive (NLP) method described earlier (6) were compared with two rate methods, herein called an ordinary initial rate method and an extrapolated rate method. For these comparisons, 200 data points were used with each of the predictive methods. In the *ordinary rate method*, the rate was computed as the linear-least-squares slope for the first eight data points. In the *extrapolated-rate method*, the method of Savitzky and Golay (7) with a seven-point window was applied to each response, and the resulting values of rate vs time were fit over points 4–19 by a linear least-squares model to obtain the extrapolated rate at  $t = 0$ .

Data used for comparisons involved fits of five data sets each for six values of simulated signal change,  $\Delta S_{\infty}$ , ranging from 0.1 to 0.9, three reaction orders (0.75, 1.25, 2.25) and three rate constants (0.006, 0.02, 0.3). The reaction orders and rate constants were selected so that the 200 data points used with the predictive methods corresponded to about 85% completion for the midlevel signal change (0.3) and the eight data points used with the ordinary rate method corresponded to no more than about 10% of completion except for a reaction order of 2.25. For  $n = 2.25$ , an 8-s data range would have corresponded to up to 34% completion for some cases, and instead a 10-fold faster data acquisition rate ( $10 \text{ s}^{-1}$ ) and shorter dead time (0.1 s) were used for the rate methods for this reaction order; numbers of data points processed for the rate methods were the same as stated above.

To facilitate comparisons, rates computed by these two methods were converted to equivalent values of determined signal change,  $\Delta S_{\infty}$ , by using expected values of reaction order and rate constant for each case.

## RESULTS AND DISCUSSION

Unless stated otherwise, the expected signal change,  $\Delta S_{\infty}$ , was 0.500 with superimposed noise corresponding to a standard deviation of 0.0007 signal unit and 200 data points were processed, corresponding to 85% of the total change expected. All noise levels are quoted as the values corresponding to one standard deviation. All evaluations of statistical significance by  $t$  tests and  $F$  test were made at the 95% confidence level.

**Reaction Order.** As explained earlier, the best estimate of reaction order was taken as the value that gave the most

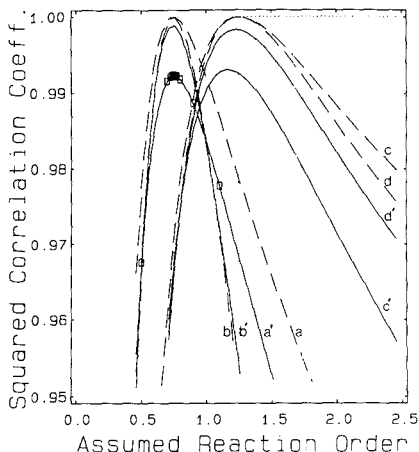


**Figure 1.** Relationships between squared correlation coefficients ( $r^2$ ) and assumed reaction order for selected conditions: noise,  $1 \times 10^{-6}$  (—),  $7 \times 10^{-4}$  (---); reaction order 0.75 (a–b'), 1.25 (c–d'); rate constant 0.01 (a, a'), 0.02 (b–d'); signal change ( $\Delta S_{\infty}$ ) 0.5 (a–c'); 0.9 (d, d'); trial values ( $\square$ ).

nearly linear relationship between  $|dS/dt|^{1/n}$  and  $S_0$  (eq 5). Initially, we attempted to use the standard error of the estimate,  $s_{y,x}$ , to test for goodness of fit of the linear model. However, changes in the standard error were too gradual in the range of correct values of  $n$  to make this a useful diagnostic. On the other hand, as shown in Figure 1, the squares of the correlation coefficients,  $r^2$ , were smooth and passed through reasonably sharp maxima in the region of correct values of  $n$ . Thus,  $r^2$  was used as the test diagnostic in the selection of the best estimates of reaction order.

Curve  $a'$  in Figure 1 is used to describe an optimization program used to obtain best estimates of  $n$ . The boxes on the plot correspond to test values used in the computerized selection of the best estimate of  $n$ . An initialization step is used to select two values of  $n$  and to calculate the corresponding two values of  $r^2$  for the fit described by eq 5. These initial values of  $n$  are then temporarily ranked as  $n_h$  and  $n_m$ , where  $n_h$  and  $n_m$  correspond to the highest and lowest values of  $r^2$ . Thereafter a multistep loop is used to select the best value of  $n$ . The first step in the loop is to compute the next value,  $n_a$ , to be tested by using the equation

$$n_a = n_h + I(n_h - n_m) \quad (8)$$

in which  $I$  is a variable with the value 1.0 for the initial trial inside the loop. The second step is to obtain the new value,  $r_a^2$ , and to rank the latest three values of  $n$  ( $n_h$ ,  $n_m$ ,  $n_a$ ) as the new  $n_h$ ,  $n_m$ , and  $n_i$  according to which gave the highest, medium, and lowest values of  $r^2$ . The third step is to determine the next value of  $I$ , which can be  $-0.5$ ,  $1.0$ , or  $2.0$ . The value of  $I$  is equal to  $-0.5$  anytime  $n_h$  is between  $n_m$  and  $n_i$ ; it is equal to  $1.0$  when  $n_h$  and  $n_i$  are on opposite sides of  $n_m$ ; and it is  $2.0$  when this latter situation continues. After the correct value of  $I$  is selected,  $n_i$  is discarded and the process is repeated by returning to the first step in the loop. This looping process is continued until  $I$  is  $-0.5$  and the difference between  $n_m$  and  $n_i$  is smaller than a predetermined value, such as 0.001. The best  $n$  is then selected as the latest value of  $n_h$ .

For data with moderate noise such as those from which curves  $a'$ – $d'$  in Figure 1 were produced, this process gives very good values of  $n$ ; in the particular case of curve  $a'$  used to illustrate the process, the true value of  $n$  was 0.750 and the determined value was 0.753. Effects of signal noise are shown



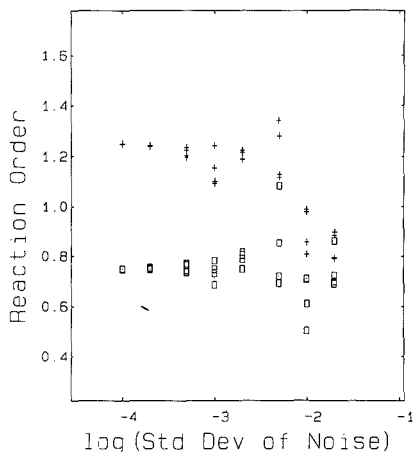


**Figure 2.** Effects of noise on values of reaction order computed with the linearized method: reaction order, 0.75 ( $\square$ ), 1.25 (+); signal change, 0.5; rate constant, 0.0065 ( $\square$ ), 0.015 (+); processing range,  $0.85 \Delta S_{\infty}$ ; expected values (---).

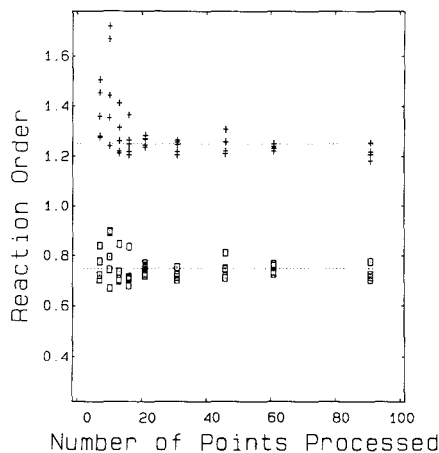


**Figure 3.** Effects of number of points processed per kinetic curve on computed values of reaction order: signal change, 0.5;  $n = 0.75$ ,  $k_s = 0.0072$  ( $\square$ );  $n = 1.25$ ,  $k_s = 0.017$  (+); processing range,  $0.85 \Delta S_{\infty}$  (181 s, number of points, 7-91); expected values (---).

in Figures 1 and 2. For the plots a-d in Figure 1, produced from kinetic data with very low noise, the peak maxima occur exactly at the correct values of  $n$ ; for higher levels of noise, the maxima are sometimes shifted away from the true value. For results in Figure 2, errors (peak positions) are relatively low for noise levels up to about  $5 \times 10^{-4}$ , with values for  $n < 1$  being more randomly distributed about the true values than is the case for  $n > 1$ . Effects of noise on the results for  $n$  when the values of  $n$  and other parameters determined with the linearized method were used as initial estimates in the nonlinear program have been discussed previously (6).

Effects of data density on computed values of  $n$  are shown in Figure 3. For moderate noise levels, reliable results are obtained for 20 or more data points; errors increase rapidly for fewer than 20 data points. When these values were used as initial estimates for the nonlinear method (6), only slight

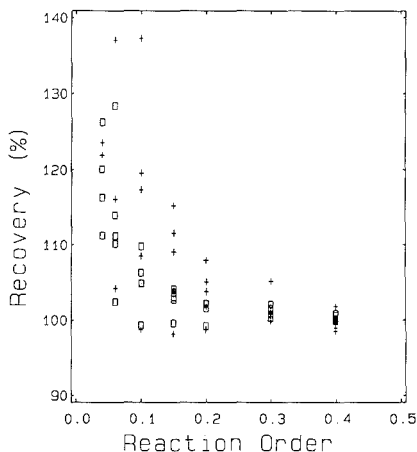


**Figure 4.** Effects of reaction order on results obtained by linearized predictive method: signal change, 0.5; noise, 0.0007;  $k_s$  selected to give  $t_{95} = 200$  s; processing range,  $0.95 \Delta S_{\infty}$  ( $\square$ )  $0.85 \Delta S_{\infty}$  (+).

improvements were obtained for the lower values of  $n$  but errors for the larger value of  $n$  became more randomly distributed about the true value and the scatter was slightly less than that for the lower plot in Figure 3.

**Signal Change.** Effects of different values of reaction order, data range, data density, and signal noise on computed values of signal change were evaluated.

**Reaction Order.** Figure 4 shows effects of reaction orders between 0.04 and 0.4 on the signal change, expressed as percentage recovery of the expected value of 0.5. As expected, errors are quite large for reaction orders near zero, but drop to reasonable values as the order increases. For a processing range of 95% completion, errors are 5% or less for reaction orders above 0.15; for a processing range of 85% completion, errors are 5% or less for orders larger than 0.3. For reaction orders close to unity ( $n = 0.98-1.02$ , not shown), the average recovery was  $99.3 \pm 0.1\%$  for data processed over 95% completion and  $98.4 \pm 0.9\%$  for data processed over 80 to 85% completion. Herein lies a principal advantage of this algorithm relative to that described earlier (6); whereas the previously reported model fails for orders near unity, the present algorithm suffers no such limitation.

When rate data are used, as in eq 3-5, there are no mathematical restrictions for  $n$  at or near unity. However, in eq 7 in which signal-versus-time data are used, the calculation of  $S_0$  will be indeterminate when  $n$  is at or near unity because of the  $1/(1-n)$  term. This problem was resolved by preventing the absolute value of  $1-n$  from becoming smaller than a preselected value. In this study, the value used was  $1-n \geq 0.008$ , which is the same as the value used for other restrictions in an earlier study (6). This restriction does not affect the calculation of any of the other parameters ( $S_{\infty}$ ,  $k_s$ ,  $n$ ).

Effects of reaction order on results obtained with the nonlinear method were presented earlier (6).

**Data Range.** The effect of data range was evaluated for an unfavorable reaction order of 0.20. For data ranges between 75 and 90% completion, results were consistent among the different ranges, being systematically high, with errors ranging from -2 to +10% and averaging about +5%; for a range of 95% completion, the average error was about 2%.

**Data Density.** Effects of data density on  $\Delta S_{\infty}$  values are analogous to those shown in Figure 3 for reaction order. For

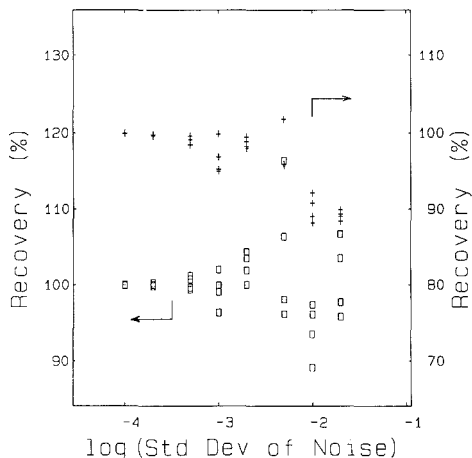


**Figure 5.** Effects of noise on computed values of signal change: signal change, 0.5; left ordinate (□)  $n = 0.75$  and  $k_s = 0.0065$ ; right ordinate (+)  $n = 1.25$  and  $k_s = 0.015$ ; processing range,  $0.85 \Delta S_{\infty}$ .

7 to 20 data points, errors ranged up to +10% for  $n = 0.75$  and up to +12% for  $n = 1.25$ ; for more than 20 points, the errors were distributed about zero with a maximum range of -3 to +4%, with a slight bias toward negative values. When these values were used as initial estimates for the nonlinear method, results were randomly distributed about expected values with maximum errors ranging from about 5% for 7 to 20 data points to about 3% for 30 to 90 data points.

**Signal Noise.** Figure 5 shows effects of signal noise on the error in the computed value of  $\Delta S_{\infty}$ . For noise levels below about  $5 \times 10^{-4}$ , maximum errors are less than 2%; above this level, maximum errors increase to about 10%. Effects of signal noise when these values were used as initial estimates in the nonlinear program were discussed earlier (6).

**Comparison of Methods.** Results for responses corresponding to six values of expected signal change (0.1, 0.2, 0.3, 0.5, 0.7, 0.9), three values of reaction order (0.75, 1.25, 2.25), and three values of rate constant (0.006, 0.02, 0.3) are compared here for the two predictive and two rate methods described above.

**Rate Methods.** Some preliminary studies were done to evaluate the properties of the rate methods, especially the extrapolated rate method because there have been no previous reports of such an approach. Some typical data for the effect of data range on the recovery of expected signal change are shown in Figure 6. As expected, the rate computed as the slope of a linear-least-squares fit of  $S_t$  vs  $t$  decreases as the range of data included in the fit increases. A range of eight data points was chosen as a compromise between systematic and random error. The extrapolated-rate method is much less susceptible to this problem because rates analogous to those shown for the ordinary rate method are extrapolated to the value at  $t = 0$ , with those involving a seven-point smooth having less systematic bias than those for the 13-point smooth. The larger scatter among the results for the extrapolated-rate method is not surprising because intercepts of least-squares fits are expected to have large uncertainties associated with them.

**Comparisons.** Results for three combinations of reaction order and rate constant are shown in Figure 7 as residuals which represent differences between computed and expected values of signal change. For the lower values of  $n$  and  $k_s$  (Figure 7A), results for both predictive methods and the ex-

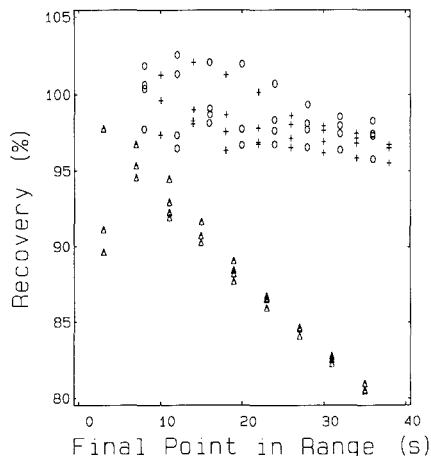


**Figure 6.** Effects of data range on computed results by ordinary and extrapolated rate methods: ordinary method (Δ); extrapolated method, 7-point (O) and 13-point (+) windows; first data point, 1 s; data rate,  $1 \text{ s}^{-1}$ ;  $\Delta S_{\infty} = 0.5$ ;  $n = 1.25$ ;  $k_s = 0.015$ .

trapolated-rate method are randomly distributed about the expected values, whereas results for the ordinary rate method appear to exhibit some bias at higher values of signal change. For the higher values of  $n$  and  $k_s$  (Figure 7C), only the nonlinear predictive method yields unbiased results throughout the signal range examined. A  $t$  test for each set indicates that apparent biases in the figures are statistically significant at the 95% confidence level. More specifically, for the lower values of  $n$  and  $k_s$ , neither approach exhibits a statistically significant additive bias and only the ordinary rate method exhibits a significant proportional bias. For the higher values of  $n$  and  $k_s$ , the nonlinear-predictive and ordinary rate methods exhibited additive bias while all methods exhibit proportional bias. Results for the predictive methods with intermediate values of  $n$  (1.25) and  $k_s$  (0.02) are shown in Figure 7B. These results are better than those in either part A or C of Figure 7. Analysis of variance (ANOVA) methods (8) indicate significant deviations from linearity only for the linearized predictive and extrapolated-rate methods at the higher values of  $n$  and  $k_s$  (Figure 7C). It is apparent from these results that the nonlinear predictive method supplemented with initial estimates from the linearized predictive method yields superior results for the conditions examined.

The point-by-point scatter for the different methods can be visualized in Figure 7. The average imprecision along each calibration plot was evaluated as the mean square pure error (MSPE) of residuals. Values ( $10^{-6}$  signal units) at the low, medium, and high values of  $n$  and  $k_s$  were 19, 3, and 8 for the nonlinear predictive method, 64, 10, and 71 for the linear predictive method, 340, 22, and 133 for the extrapolated rate method, and 350, 33, and 105 for the ordinary rate method. By comparison, the analogous MSPE for "equilibrium" results computed as the difference between averages of 20 noise points each at the beginning and end of each process was 0.03 or about 2 orders of magnitude below the best values obtained for any of the kinetic methods. Also, additive and proportional bias were not statistically significant for the equilibrium results.

These results show that of the four kinetic methods tested, the nonlinear predictive method yields highest quality results. The principal limitation of this latter method is the relatively longer data-processing time required. The average processing

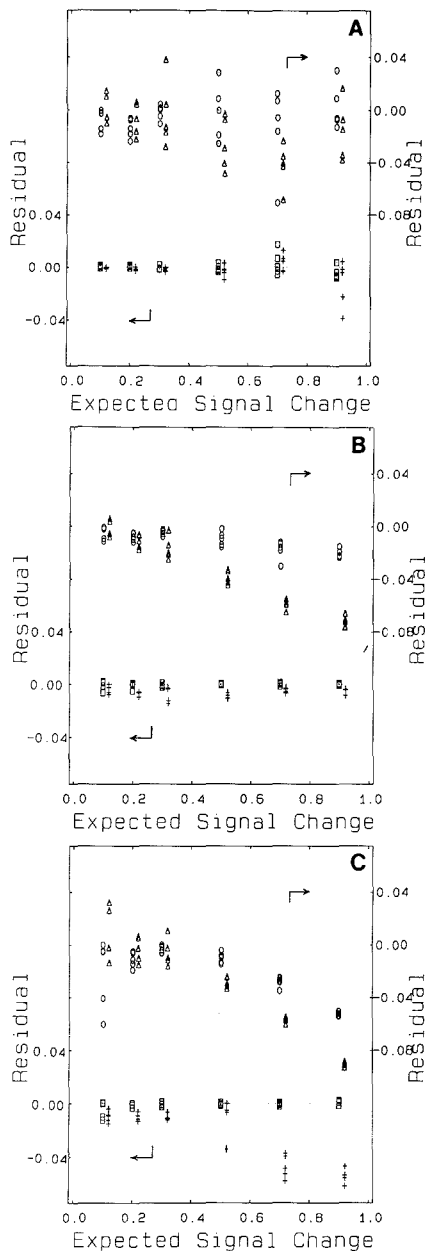


**Figure 7.** Effects of signal change and noise on results obtained by different methods: ordinary rate method ( $\Delta$ ); extrapolated rate method (seven-point window, (O)); linearized predictive method (+); and nonlinear predictive method ( $\square$ ). Five replicates at each of six simulated concentrations. Signal change, 0.1–0.9; noise, 0.0007; data interval, 1 s; dead time, 1 s; results for ordinary rate and linearized predictive methods offset 0.02 unit to right for clarity. (A)  $n = 0.75$ ;  $k_s = 0.006$ ; processing range 76–94%  $\Delta S_{\infty}$ . (B)  $n = 1.25$ ;  $k_s = 0.02$ ; processing range 82–91%  $\Delta S_{\infty}$ . (C)  $n = 2.25$ ;  $k_s = 0.3$ ; processing range 71–84%  $\Delta S_{\infty}$ ; data interval and dead time for rate methods, 0.1 s.

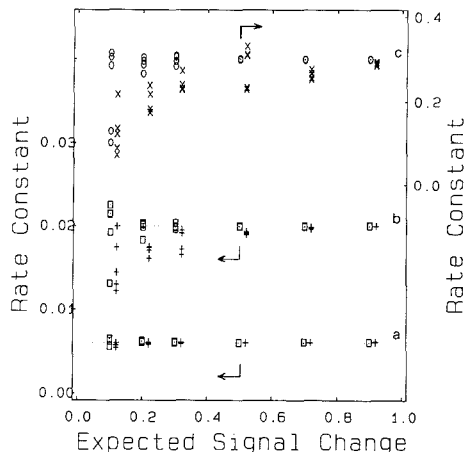


**Figure 8.** Effects of signal change and noise on computed values of rate constant. Conditions are given in Figure 7.

times per data set for the four methods were 16, 6.7, 0.4, and 0.3 s for the nonlinear predictive, linearized predictive, extrapolated rate, and ordinary rate methods, respectively. The time for the nonlinear predictive method includes that for the linearized predictive method that is used to obtain initial estimates of fitting parameters. The linearized predictive method is not optimized for speed, and if it were, data processing times for both the predictive methods could be reduced. For example, by changing the termination criterion for selection of the best value of  $n$  from 0.001 to 0.05 and manually entering a suitable range for the derivatization window (seven points), the average processing time for the linearized predictive method was 1.9 s per run.

**Rate Constants/Reaction Order.** These data were also used to evaluate the combined effects of signal change, reaction order, and rate constant on the reliability with which the latter two parameters were computed by the two predictive methods. Results for rate constant are shown in Figure 8. Both methods yield very good results throughout the range of signal changes examined for the lower values of  $n$  and  $k$ . Results are degraded at higher values of these parameters, with the largest scatter and bias (negative) resulting at the smallest values of signal change. Analogous plots for reaction order have similar shapes and can be visualized reasonably reliably by relabeling the left-hand ordinate as reaction order ranging from 0.5 to 2.5, bottom to top.

**Discussion.** Of the four kinetic methods tested in this study, the nonlinear predictive method yields the most reliable results for the widest range of conditions. As noted earlier (6), a principal limitation of that method is that it fails for values of  $n$  at and near unity. Although the linearized predictive method exhibits somewhat larger systematic errors at higher values of reaction order, rate constant, and signal change, those errors are in the range 4–10%, relative, and this method gives satisfactory results for reaction orders at and near unity. The main source of error for the linearized predictive method lies in the determination of  $n$ . The reaction order is determined first, and if it is incorrect, its subsequent use in eq 5 and 7 leads to errors in the three other parameters ( $k_s$ ,  $S_{\infty}$ ,  $S_0$ ). The method is least reliable for low and high values of  $n$ . When the reaction order is close to zero, the  $1/n$  term in eq 5 gives very small numerical values for the dependent variable, which makes  $n^2$  less ideal as a criterion for goodness of fit. The noise is also amplified. When the reaction

order is greater than about 2, the initial rate is very high relative to rates after the first half-life of the reaction. This high initial rate causes a larger loss of detector signal before the first data point is acquired. When this curve segment is extrapolated to obtain  $\bar{S}_0$  (eq 7), even a small error in the signal data is amplified by the high slope to give a larger error in the intercept ( $S_0$ ). This effect is seen only for high reaction orders at high concentrations (Figure 7C), even though the determined values for reaction order and rate constant (Figure 8) improve as the concentration increases.

Although the linearized predictive method may appear more complex because reaction order and the signal at  $t = 0$  are quantified separately, these operations are easily automated. Because the method determines the rate constant and reaction order separately for each sample, it should exhibit the same ability to compensate for changes in chemical and physical variables that affect these parameters. Accordingly, the linearized predictive method merits consideration, not only as a

way to obtain initial estimates of parameters for nonlinear iterative methods but also as an independent method in its own right.

#### LITERATURE CITED

- (1) Harris, R. C.; Hulman, E. *Clin. Chem. (Winston-Salem)* **1983**, *29*, 2079-2081.
- (2) Wentzell, P. D.; Crouch, S. R. *Anal. Chem.* **1986**, *58*, 2855-2858.
- (3) Pardue, H. L. *Anal. Chim. Acta* **1989**, *216*, 69-107.
- (4) Matheson, I. B. C. *Anal. Inst.* **1987**, *16*, 345-373.
- (5) Rutan, S. C.; Fitzpatrick, C. P.; Skoug, J. W.; Weiser, W. E.; Pardue, H. L. *Anal. Chim. Acta*, in press.
- (6) Larsson, J. A.; Pardue, H. L. *Anal. Chim. Acta*, in press.
- (7) Savitzky, A.; Golay, M. L. *Anal. Chem.* **1964**, *36*, 1627-1639.
- (8) Neter, J.; Wassermann, W.; Kutner, M. H. *Applied Linear Statistical Models*, 2nd ed.; Richard D. Irwin, Inc.: Homewood, IL, 1985; p 129.

RECEIVED for review April 10, 1989. Accepted June 8, 1989. This work was supported in part by Grant No. GM 13326-21 from the National Institutes of Health and in part from Grant No. CHE-8319014 from the National Science Foundation.

## Electrochemical Behavior of *N*-Acetylpenicillamine Thionitrite at Glassy Carbon and Carbon Fiber Electrodes

Michael J. Nuwer and Janet Osteryoung\*

Department of Chemistry, State University of New York at Buffalo, Acheson Hall, Buffalo, New York 14214

Optimization of square-wave voltammetric parameters increases the sensitivity ( $0.27 \mu\text{A}/\mu\text{M}$ ) 8-fold and decreases the detection limit ( $3 \mu\text{M}$ ) an order of magnitude below that of the previously reported method for *N*-acetylpenicillamine thionitrite at a glassy carbon electrode. The construction of and pretreatment procedure for the carbon fiber microcylinder electrode (CFME) are described. The current density at the CFME was 5 times larger than at the glassy carbon electrode, with about 15% of the enhancement due to nonplanar diffusion. The kinetics of the irreversible electron transfer at a glassy carbon electrode was examined by analyzing normal pulse (NP) voltammetric data with a nonlinear least-squares fit employing a simplex search routine for the optimal values of the kinetic parameters. The mean value for the transfer coefficient is 0.457 and that of the standard rate constant referred to  $E = -0.4 \text{ V}$  is  $7.8 \times 10^{-5} \text{ cm/s}$ . The diffusion coefficient calculated from the limiting NP current is  $8.5 \times 10^{-6} \text{ cm}^2/\text{s}$ .

*N*-Acetylpenicillamine thionitrite (NAPTn) and organic thionitrites (RSNO) in general are currently being investigated for their vasodilating effect in mammals (1, 2) and as tools for synthetic organic chemists. The sulfur-nitrogen bond in *S*-nitroso compounds is weak compared with the corresponding oxygen-nitrogen bond in nitrites (*O*-nitroso). Therefore, compounds containing *S*-NO bonds would be expected to be more reactive and more useful as sulfenylating and nitrosating agents (3). It is this reactivity that makes thionitrites so difficult to study from an analytical point of view. However, NAPTn is an unusually stable representative of this class of compounds; in fact, it is the only one that is stable in the crystalline form.

The first analytical method for NAPTn was described by Takeuchi and Osteryoung (4), who examined the electrochemistry of NAPTn at mercury and glassy carbon electrodes (GCE). They found that the voltammetric behavior at a mercury electrode is similar to that of the parent compounds *N*-acetylpenicillamine (RSH) and penicillamine (R'SH). The reaction is the one-electron oxidation of mercury in the presence of a thiol (or thionitrite) to form the mercury mercaptide. Upon further investigation, we have found the reactions at mercury to be very complicated due to overlapping anodic (of mercury) and cathodic (of nitrogen) waves as well as adsorptive prewaves.

Electrochemical and spectroscopic evidence suggests that at a carbon electrode RNSO is reduced irreversibly according to the reaction



The value of  $\alpha n_2$  (charge-transfer coefficient times apparent number of electrons transferred) for reaction 1 has been determined from linear scan voltammetry to be 0.53, using the diffusion coefficient value of  $7.8 \times 10^{-6} \text{ cm}^2/\text{s}$  reported for penicillamine (5). By making use of this reaction, one can determine NAPTn selectively in the presence of other sulfur-containing organics.

This report focuses on the reduction at carbon electrodes with the dual aims of better characterizing the charge-transfer process and achieving superior analytical performance through optimization. We have employed normal pulse voltammetry to determine the value of the diffusion coefficient for NAPTn. These data are used also to verify the value of the transfer coefficient ( $\alpha$ ) by means of the curve-fitting procedure described by O'Dea et al. (6), as well as to determine the heterogeneous rate constant ( $k_h$ ).

In the original investigation, square-wave voltammetry (SWV) was chosen over linear scan voltammetry for its in-

creased sensitivity and discrimination against background current. By the use of a large ( $0.283 \text{ cm}^2$ ) glassy carbon electrode, a square-wave frequency ( $f$ ) of 5 Hz, a step height ( $\Delta E_s$ ) of 5 mV, and a square-wave amplitude ( $E_{sw}$ ) of 25 mV, the sensitivity was found to be  $3.2 \times 10^{-2} \mu\text{A}/\mu\text{M}$  with a detection limit of  $40 \mu\text{M}$ . Typically an irreversible process might yield only one-tenth the current found for a corresponding reversible process if the optimal values of parameters for the reversible process ( $nE_{sw} = 50 \text{ mV}$ ,  $n\Delta E_s = 10 \text{ mV}$ ) are used. We have found that optimization of the square-wave parameters ( $\Delta E_s$ ,  $E_{sw}$ , and  $f$ ) and use of a microelectrode each gave a greater sensitivity and lower detection limit. A complete discussion of SWV and the optimal parameters to choose for reversible and totally irreversible reactions can be found in ref 7. The square-wave response is considered to be optimal when the resolution has maximum value. The resolution is the net peak current ( $\Delta i = i_t - i_b$ ) divided by the peak width at half-height ( $W_{1/2}$ ). Inspection of the resolution vs the parameter under investigation allows the experimenter empirically to determine the best choice.

Because of their many advantages, microelectrodes would seem an automatic choice in any electroanalytical investigation. In particular microcylinder electrodes have been shown both theoretically (8) and experimentally (9) to have an enhanced signal due to nonplanar diffusion at all experimental times (scan rate or frequency). Their small area results in lower background currents. However the area, in contrast with that of a microdisk electrode with similar mass transport properties, is typically large enough that currents can be measured with conventional instrumentation. Therefore a microcylinder electrode made from a single carbon fiber is used here for the determination of NAPTIN.

#### EXPERIMENTAL SECTION

**Materials.** *N*-Acetylpenicillamine thionitrite (NAPTIN) was prepared from its parent compound, *N*-acetylpenicillamine (Sigma Chemical Co.) as prescribed by Field et al. (10). Recrystallization was required to transform the powdery, pale green product into the dark green crystals that reflect red light described in the original paper. The procedure is to dissolve the crude product in a minimal amount of methanol, add water dropwise until the solution becomes slightly cloudy (the total amount of water added is about 30% that of the methanol), filter the solution, and place it in a freezer until the crystals fall out of solution. The recrystallized product is retrieved by filtration through a sintered glass funnel and may be stored indefinitely in a refrigerator. The crystalline NAPTIN product was characterized by Fourier transform infrared spectroscopy (Nicolet 7199). Broad band absorbances were observed at  $\nu_{\text{max}} = 1510$  and  $1940 \text{ cm}^{-1}$ , which have been reported (11) to be characteristic of the thionitrite functionality. Also, the absence of an absorbance at  $2600\text{--}2550 \text{ cm}^{-1}$ , characteristic of the thiol function, was noted.

NAPTIN stock solutions were prepared daily by dissolving NAPTIN crystals in the supporting electrolyte, an aqueous solution 0.1 M in potassium chloride (Mallinckrodt) and 0.1 M in hydrochloric acid (Fisher Scientific). The very low pH was chosen to eliminate any complications due to the preceding or follow-up protonation reaction that must occur. Under these chemical conditions no wave is seen for reduction of NO (cf. eq 1) at a carbon electrode. Water was purified by passing distilled water through a Millipore Milli-Q purification system. To prevent light-catalyzed decomposition, amber-colored glassware, including the electrochemical cell, was used for NAPTIN solutions. Solution concentrations were confirmed with visible spectroscopy (Shimadzu, Model 260) by measuring the absorbance at 590 nm, specific to NAPTIN. The absorbance and nominal concentrations yielded the value of molar absorptivity previously determined (2),  $12.4 \text{ L mol}^{-1} \text{ cm}^{-1}$ .

All electrochemical experiments employed a three-electrode configuration using a platinum wire auxiliary electrode, saturated calomel reference electrode (all potentials are reported versus the SCE), and a glassy carbon ( $A = 0.1963 \text{ cm}^2$ , IBM Instruments) or carbon fiber ( $8\text{-}\mu\text{m}$  diameter) working electrode. The auxiliary

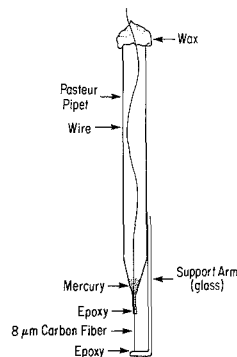


Figure 1. Carbon fiber microelectrode.

electrode was contained in a compartment separated from the analyte solution by a Vycor frit. Isolation of the auxiliary electrode is essential since the oxidation product produced at this electrode drastically changes the background signal at the working electrode. The glassy carbon electrode was lightly polished with  $1.0\text{-}\mu\text{m}$  alumina on a Microcloth polishing cloth (both from Buehler, Ltd.) by using a Buehler Minimet mechanical polisher and only was rinsed with distilled water prior to use.

**Fabrication of Carbon Fiber Cylindrical Electrodes.** Carbon fibers (polyacrylonitrile (PAN) type) were obtained from Aesar (Johnson Matthey, Inc.). They were cleaned chemically by placing them in a vial of acetone and sonicating for 10 min. This procedure was repeated with 1:1 nitric acid and again with distilled water. The fibers were retrieved on a piece of filter paper, which was subsequently placed in a  $100^\circ\text{C}$  oven to dry the fibers. The batch cleaning provides a hearty supply of fibers that can be stored in a desiccator indefinitely.

Figure 1 is a diagram of the carbon fiber electrode. The device costs about a dime and takes approximately 5 min to construct (with practice). A 9-in. Pasteur pipet is used as a mechanical support. The capillary portion of the tip is removed from the body about  $1/2$  in. past the taper by simply pulling the two pieces apart after heating in a gentle flame. The tip of the pipet is filled off by using a rotating piece of sandpaper to provide an opening about  $0.1 \text{ mm}$  in diameter. The capillary that was pulled off is heated and molded into the side arm, which is held in place with cellophane tape. With the aid of a microscope ( $20\times$ ) the fiber is threaded into the tip of the pipet to a distance of about  $0.3 \text{ mm}$ , making sure the opposite end touches the side arm. The exposed fiber length is  $1\text{--}2 \text{ cm}$ , yielding an area of  $0.0025\text{--}0.0050 \text{ cm}^2$ . At this time the epoxy (5-Minute Epoxy, Devcon Co.) can be mixed. A small drop is gently placed on the tip of the pipet; capillary action will pull the epoxy inside, making an adequate seal. Another drop is placed on the point where the fiber touches the side arm, and few drops are used to secure the side arm to the pipet. The purpose of the side arm is not only to provide the needed mechanical support but to prevent the fiber from twitching during electrochemical pulse experiments. The device is placed in a  $120^\circ\text{C}$  oven for 1 h to cure the epoxy (epoxy cured at room temperature swells more readily when placed in the electrolyte solution). When the pipet has cooled, the fabrication can be completed by making electrical contact with a drop of mercury and a length of wire. The open end of the pipet is sealed with paraffin.

**Electrochemical Instrumentation.** Cyclic linear scan voltammetry was performed with an IBM 225 electrochemical analyzer. The data were collected on a Houston Instruments X-Y recorder.

All pulse voltammetric data were collected with a system designed for real-time voltammetry. The major components include a PDP-8/e minicomputer (DEC) and an EG&G PARC Model 273 potentiostat/galvanostat. This automated system allows for the execution of reproducible experiments and facilitates signal averaging and batch analysis. The scheme for a normal pulse experiment incorporates a purging cycle after each pulse to renew the boundary conditions at the initial potential. These experi-

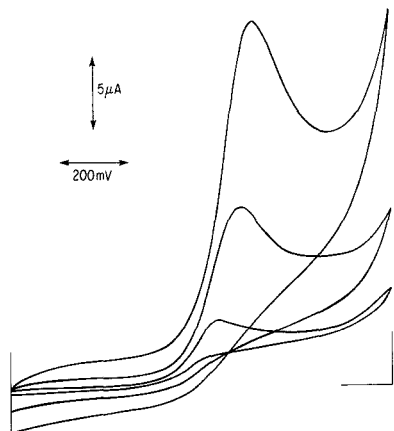


**Figure 2.** Cyclic linear scan voltammograms at the glassy carbon electrode for 0.6 mM NAPTN at scan rates of 5, 50, and 200 mV/s (bottom to top).

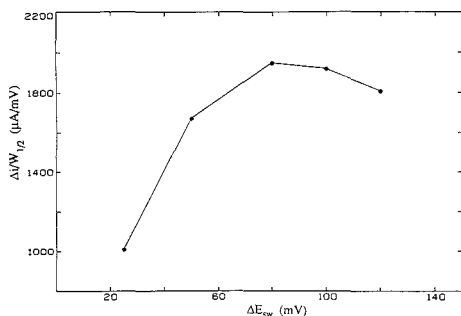


**Figure 3.** Resolution of the square-wave response versus the square-wave amplitude:  $\Delta E_s = 5$  mV,  $f = 260$  Hz, 1.0 mM NAPTN, glassy carbon electrode.

ments can be carried out in a batch mode, which permits the experiment to be run unattended for the extended periods of time required to acquire significant amounts of data. This same computer is used for calculations and data analysis.

Experimental results were compared with theoretical models by means of the COOL algorithm (6), which finds the best-fitting theoretical curve by a procedure equivalent to the method of maximum likelihood.

## RESULTS AND DISCUSSION

Typical linear scan voltammograms at the glassy carbon electrode for various scan rates are shown in Figure 2. From their shape it is clear the overall reaction is totally irreversible. A plot of peak current versus the square root of scan rate is linear, implying the process is diffusionally controlled. Voltammograms were obtained by purging the solution with argon for 15 s, allowing 10 s for the solution to equilibrate, and then scanning from 0.0 to -1.1 V. With a freshly polished electrode it is necessary to repeat this procedure about 50 times in the electrolyte solution to provide a constant background signal. Peak currents were measured from the extrapolation of the base line before the wave. The calibration curve obtained by using this procedure at a scan rate of 10 mV/s was linear over the entire range studied (10–1500  $\mu M$ ) with a correlation coefficient of 0.999 and a sensitivity of 0.014  $\mu A/\mu M$ . The detection limit, defined as 3 times the standard deviation of the  $y$ -intercept of the calibration function divided

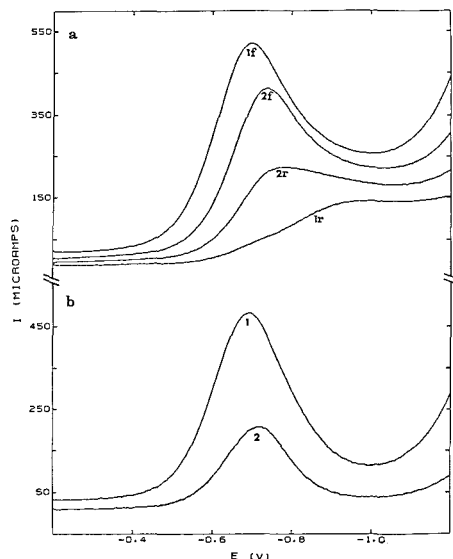


**Figure 4.** (a) Forward (f) and reverse (r) and (b) net square-wave currents for square-wave amplitudes of 80 (1) and 25 (2) mV:  $\Delta E_s = 5$  mV,  $f = 260$  Hz, 1 mM NAPTN, glassy carbon electrode.

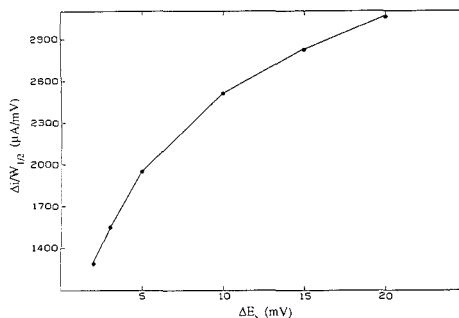


**Figure 5.** Resolution of the square-wave response versus the square-wave step height:  $E_{sw} = 80$  mV,  $f = 260$  Hz, 1 mM NAPTN, glassy carbon electrode.

by its slope, calculated for concentrations less than 100  $\mu M$ , is 4.6  $\mu M$ .

Square-wave voltammetry at the glassy carbon electrode was found to have an optimal response for a square-wave amplitude of 80 mV as seen in Figure 3. Figure 4 shows how the individual forward and reverse (4a) as well as the net (4b) square-wave currents are affected by changing the amplitude from 25 to 80 mV. The shapes of the voltammograms are typical of those for a totally irreversible electron transfer in which there is no anodic contribution to the reverse current. This is true even at frequencies as high as 620 Hz. The considerable advantage attained at larger pulse amplitudes arises from the resulting decrease in the reduction current on the reverse step.

The step height was optimized in a similar manner with results as shown in Figure 5. In this case the resolution of the square-wave response continues to increase monotonically with step height. Since a larger step height results in fewer data points, a step of 10 mV was chosen as a reasonable value to give a well defined voltammogram.

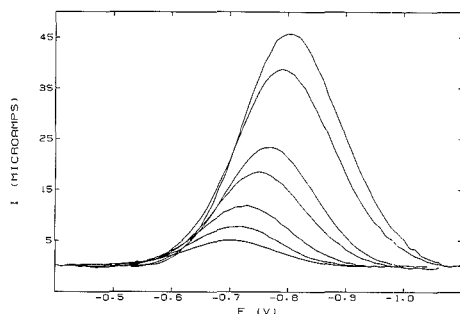


**Figure 6.** Square-wave voltammograms at 10, 20, 40, 100, 180, 400, and 600 Hz, (bottom to top):  $\Delta E_s = 10$  mV,  $E_{sw} = 80$  mV, 0.166 mM NAPTN, glassy carbon electrode.

Theoretically, the response increases indefinitely with increasing square-wave frequency, but of course there are instrumental or chemical limitations to consider. Square-wave voltammograms at various frequencies up to 600 Hz are shown in Figure 6. Background currents have been subtracted, and then a tangent, fit to the wings of each voltammogram, has been subtracted. The peak shifts to more negative potential as the frequency is increased, as expected for a slow electron transfer. It is this phenomenon that limits the square-wave frequency to 600 Hz, since at higher frequencies the peak due to NAPTN begins to overlap with the next peak (probably for reduction of  $\text{NO}_2$  or  $\text{H}_2\text{O}^+$ ). The square-wave net current is proportional to the square root of frequency over this range.

Calibration curves for the square-wave experiments were done with a step height of 10 mV, an amplitude of 80 mV, and a frequency of 5 or 260 Hz. The 5- and 260-Hz cases gave detection limits of 5.5 and 3.5  $\mu\text{M}$  with sensitivities of 0.039 and 0.27  $\mu\text{A}/\mu\text{M}$ , respectively.

**The Microcylindrical Electrode.** Experiments using a carbon fiber working electrode require electrochemical conditioning at +1.4 V for 10 s prior to each scan. The scan begins at +1.3 V and proceeds slowly (5 Hz) (or alternatively begins with a 10-s delay at 0.0 V) to -1.3 V. Employing higher square-wave frequencies results in irreproducible background current. When a new carbon fiber is used, it must be activated by repeating the above procedure 50–60 times. This procedure may be monitored by watching the analytical peak shift to more positive potential (about a 200-mV shift in this case) until its position and magnitude remain constant. This routine was developed on the basis of previous studies (12, 13) and empirical observations of what was necessary to achieve a background signal suitable for studying reductions at these very negative potentials.

This method gave a detection limit of 2.7  $\mu\text{M}$  with a sensitivity of  $2.92 \times 10^{-3}$   $\mu\text{A}/\mu\text{M}$  and a linear correlation coefficient of 0.9996. The calibration is linear up to 1.6 mM.

The normalized ( $i/\Delta i(\text{peak})$ ) square-wave responses for a carbon fiber and a glassy carbon disk are shown in Figure 7. In Figure 7a we observe the dramatic change in shape for the forward and reverse current, where the additional flux at the fiber (in comparison with the disk) is seen clearly at potentials negative of the peak. Although it has been shown that the net square-wave response is independent of electrode geometry (14) for a reversible system, we observe a shift in peak potential and difference in peak width (7b) which is attributed to the interaction of time-dependent diffusion with the kinetics of the electron transfer. Some portion of the difference may be due also to the different electrode materials.

Deciding which of these methods provide the best means of analysis is not straightforward. The detection limits are

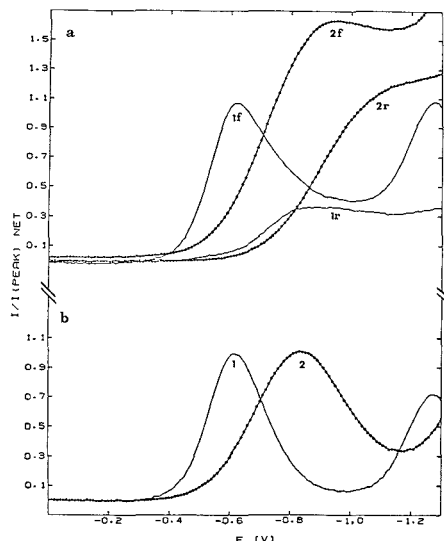


**Figure 7.** (a) Normalized forward (f) and reverse (r) and (b) net square-wave voltammograms at the glassy carbon electrode (1) and at a carbon fiber microelectrode (2,  $A = 3.55 \times 10^{-3}$   $\text{cm}^2$ ): 0.166 mM NAPTN,  $f = 5$  Hz,  $E_{sw} = 80$  mV,  $\Delta E_s = 5$  mV.

comparable, but the sensitivities vary widely, that for the 260-Hz square wave at the disk being almost 20 times greater than for the 5 mV/s linear scan. Since the background signal at a CFME can be orders of magnitude lower than at the GCE, the sensitivity of the instrument measuring the current may be adjusted to measure currents orders of magnitude lower with the same accuracy and precision. With this rationale, it is reasonable to compare current density per concentration unit. The current density per unit concentration for the 5-Hz square-wave experiment at the glassy carbon disk was 0.123  $\mu\text{A}/(\mu\text{M cm}^2)$  compared with 0.646  $\mu\text{A}/(\mu\text{M cm}^2)$  at the CFME. About 15% of the increase in current density can be attributed to nonplanar diffusion. The reason for the additional current is not known. Specific effects of differing carbon surfaces are well documented (12). It would be reasonable also to suspect the intensive initial conditioning, since drastic chemical and topographical changes have been observed with chemically and electrochemically oxidized carbon fibers (15). The enhanced sensitivity at the carbon fiber does not result in a comparable decrease in the detection limit because the background noise also increases.

**Kinetic Investigation.** Normal pulse experiments were carried out using the glassy carbon electrode with a 10- or 15-mV step height over the potential range of 0.0 to -1.0 V. The pulse width was varied between 20 and 400 ms, which required a 15–20-s delay between pulses in order to renew the boundary conditions. The delay time can be cut in half, from a total of 22 to 11 min per voltammogram, by purging the solution for the first 3 s after each pulse. The voltammograms analyzed were an average of three repetitive experiments with background subtracted. Linear base-line correction could not be used, since the wave of interest merges into the background. For all experiments the limiting current increased linearly with concentration.

Kinetic parameters were obtained from normal pulse voltammetric data by means of the COOL algorithm, which provides nearly real time data analysis (6). The experimental data (after background subtraction) are used directly without

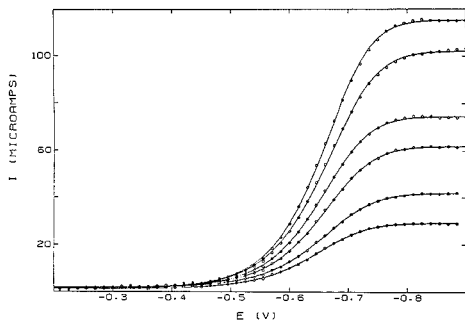


**Figure 8.** Normal pulse voltammograms at various concentrations of NAPTN (circles). The solid line is the best-fitting voltammogram (see text). Conditions: concentration,  $0.225 \leq C \text{ (mM)} \leq 0.985$ ;  $t_p = 50$  ms; glassy carbon electrode.

normalization, eliminating operator bias in choosing a normalizing factor (here the limiting current). The experimental current is expressed as a linear function of the dimensionless current function,  $\psi$ :

$$i_{\text{exp}} = a\psi + b \quad (2)$$

For normal pulse voltammetry under the present conditions (initial conditions renewed before each pulse), the dimensionless current function for slow electron transfer, based on the Butler-Volmer relation, is given by the well-known expression

$$\psi = (\pi^{1/2}(1 + \epsilon)^{-1}x) \exp(x^2) \operatorname{erfc}(x) \quad (3)$$

where

$$x = \kappa(1 + \epsilon)\epsilon^{-\alpha}t_p^{1/2}$$

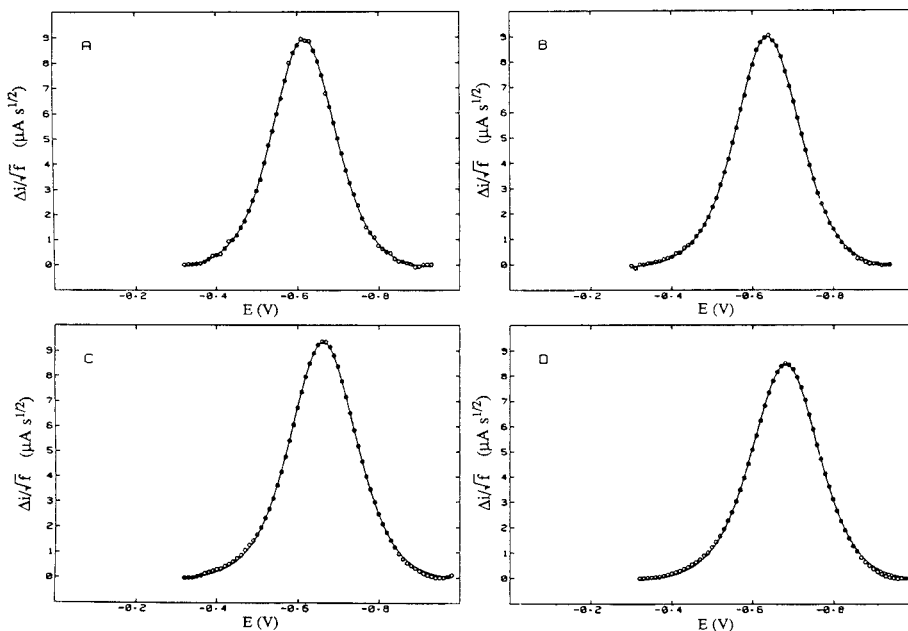


**Figure 9.** Square-wave voltammograms at frequencies (Hz) of (A) 10, (B) 20, (C) 50, (D) 100. Experimental data points are circles and the best-fitting theoretical curve is the solid line. Conditions:  $0.566 \text{ mM NAPTN}$ ;  $E_{\text{sw}} = 50 \text{ mV}$ ,  $\Delta E_s = 5 \text{ mV}$ .

$$\epsilon = \exp\{nF(E - E_{1/2}^r)/RT\}$$

$$\kappa = k_a^\circ / D_O^{(1-\alpha)/2} D_R^{(\alpha/2)}$$

$t_p$  is the pulse width,  $\alpha$  is the charge-transfer coefficient,  $E_{1/2}^r$  is the reversible half-wave potential,  $D_O$  and  $D_R$  are diffusion coefficients of the oxidized and reduced forms, respectively, and  $k_a^\circ$  is the standard heterogeneous rate constant.

Extracting kinetic and thermodynamic information from totally irreversible voltammetric waves is limited by the degenerate nature of the standard potential,  $E^\circ$ , and the apparent heterogeneous rate constant,  $k_a^\circ$  (16). Knowledge of the standard potential, which is not accessible in this case, is required in order to determine the rate constant. Similarly, the curve-fitting procedure will have inseparable degenerate pairs of values for the reversible half-wave potential  $E_{1/2}^r$  and  $\kappa$ . The diffusion coefficients of the oxidized and reduced forms,  $D_O$  and  $D_R$ , respectively, are assumed equal, and therefore  $E_{1/2}^r$  equals  $E^\circ$ . Because of this degeneracy, we report a formal rate constant,  $k_r$ , referenced to an arbitrary reference potential,  $E_r$ . The value of the charge-transfer coefficient is unaffected by these considerations.

With the value of  $E_{1/2}^r$  fixed at  $-0.4 \text{ V}$  (which is more positive than the  $E_{1/2}$  value for the longest time scale experiment), the arbitrary reference potential, the algorithm searches for the optimal values of  $\kappa$  and  $\alpha$  using a simplex search routine and evaluates the fit to the experimental data by computing the correlation coefficient ( $R$ ) of eq 2. The optimal values of the kinetic parameters correspond to the minimal value of the complement of the correlation coefficient ( $1 - R$ ).

Figure 8 shows normal pulse data points (circles) along with the best fit voltammogram (solid line) for a 50-ms pulse width at various NAPTN concentrations. To evaluate the quality of the fit, there are two parameters to consider, the correlation coefficient ( $R$ ) or the signal-to-noise ratio ( $S/N = a/s_y$ , where  $a$  is the slope and  $s_y$  the standard deviation about the line



according to eq 2). For the fitted voltammogram in Figure 8,  $R \geq 0.9998$  and  $S/N$  increases from 123 to 237 as the concentration is changed from 225  $\mu\text{M}$  (lower curve) to 985  $\mu\text{M}$  (upper curve). From a data bank representing 56 voltammograms over 11 days of experimentation, at pulse widths from 20 to 400 ms, the mean value of  $-\log \kappa$  was determined to be 1.57 (range = 0.41, standard deviation = 0.11) with a mean  $\alpha$  value of 0.457 (range = 0.13, standard deviation = 0.012). Rejection of data was done with a  $Q$ -test at the 90% confidence level on a daily basis. A day of experiments represent a series of voltammograms at increasing concentrations of NAPTIN. The large range of values greatly exceeds both the uncertainty of each individual fit and the consistency within a given day but is nevertheless anticipated, since the data were collected at a solid electrode whose electroactive surface area as well as surface work function depends on polishing as well as chemical and electrochemical conditioning (4, 17).

The mean value of the diffusion coefficient determined from the limiting current is  $8.50 \times 10^{-6} \text{ cm}^2/\text{s}$ . When one uses this value of  $D$  and  $0.0269 \text{ s}^{-1/2}$  for  $\kappa$ , the value of the rate constant referenced to  $-0.40 \text{ V}$  is  $7.8 \times 10^{-5} \text{ cm/s}$ .

Square-wave voltammetry can be used also to extract the same kinetic information (6, 18). Figure 9 shows four square-wave voltammograms at 10, 20, 50, and 100 Hz (i.e. a pulse width from 50 to 5 ms) for which the experimental data points are the circles and the optimal theoretical curve is the solid line. The correlation coefficients are 0.9998, 0.9999, 0.9998, and 0.9987, respectively, and the values of kinetic parameters agree well with those obtained from normal pulse data. The average value of  $\log \kappa$  is  $-1.62$  and the average value of  $\alpha$  is 0.463. The cycle time for one square-wave experiment (at 10 Hz and a step height of 10 mV, range 1.0 V) is 10 s plus 3 s of purge time and 5 s of delay time for a total of 18 s. Compare this with the 50-ms normal pulse experiment (the same characteristic time), which would take 14 min and 10 s, or 45 times as long.

To complete our investigation, the linear scan data (from Figure 2, as well as at 20, 100, and 300 mV/s) were analyzed by using the treatment for a totally irreversible heterogeneous electron transfer (19). Using our value of the transfer coefficient ( $\alpha = 0.457$ ), we obtain a diffusion coefficient of  $5.38 \times 10^{-6} \text{ cm}^2/\text{s}$  and rate constant of  $4.8 \times 10^{-5} \text{ cm/s}$ , corresponding to a value of  $-1.68$  for  $\log \kappa$ , which agree well with the data presented above.

Thus we conclude that even at these very negative potentials either glassy carbon or carbon fiber electrodes can be used

to determine *N*-acetylpenicillamine thionitrite voltammetrically with a detection limit of ca. 3  $\mu\text{M}$ . The vasodilating properties of NAPTIN have been studied over the range  $10^{-10}$  to  $10^{-5} \text{ M}$ . The voltammetric measurement described here could not be used directly in complex biological fluids. However, it could be adapted readily to detection following appropriate sample pretreatment. Under the proper conditions the kinetic process (reaction 1) is extremely well-behaved. Thus examination of this reduction may be a useful technique for characterizing unstable thionitrites of physiological interest.

#### ACKNOWLEDGMENT

Discussions with John O'Dea and Stanley Bruckenstein are greatly appreciated. We thank James Schmidt for assistance with the FTIR work.

#### LITERATURE CITED

- (1) Edward, J. C.; Ignarro, L. J.; Hyman, A. L.; Kadowitz, P. J. *J. Pharm. Exp.* **1984**, *1*, 33.
- (2) Ignarro, L. S.; Lipton, H.; Edwards, J. C.; Borros, W. H.; Hyman, A. L. *J. Pharm. Exp.* **1981**, *3*, 739.
- (3) Oae, S.; Shinhama, K. *Org. Prep. Proced. Int.* **1983**, *15*, 165-198.
- (4) Takeuchi, E. S.; Osteryoung, J.; Fung, H.-L. *Anal. Chim. Acta* **1985**, *175*, 69-77.
- (5) Jemal, M.; Knevel, A. M. *J. Electroanal. Chem. Interfacial Electrochem.* **1979**, *95*, 201.
- (6) O'Dea, J.; Osteryoung, J.; Lane, T. J. *Phys. Chem.* **1986**, *90*, 2761.
- (7) Osteryoung, J.; O'Dea, J. *Electroanalytical Chemistry*; Bard, A. J., Ed.; Marcel Dekker: New York, 1986; Vol. 14, pp 209-303.
- (8) Aoki, K.; Honda, K.; Tokuda, K.; Matsuda, H. *J. Electroanal. Chem. Interfacial Electrochem.* **1985**, *182*, 267.
- (9) Singleton, S. T.; O'Dea, J. J.; Osteryoung, J. *Anal. Chem.* **1989**, *61*, 1211.
- (10) Field, L.; Dolts, R. V.; Ravichandran, R.; Lenhart, P. G.; Carnahan, G. E. *J. Chem. Soc., Chem. Commun.* **1978**, 249.
- (11) Bonnet, R.; Nicolaidou, P. *J. Chem. Soc., Perkin Trans. 1* **1979**, 1969.
- (12) Edwards, T. E. *Anal. Chim. Acta* **1985**, *175*, 1-22.
- (13) Gonon, F.; Fombarlet, C. M.; Buda, M.; Pujol, J. F. *Anal. Chem.* **1981**, *53*, 1386-1389.
- (14) Aoki, K.; Tokuda, K.; Matsuda, H.; Osteryoung, J. *J. Electroanal. Chem. Interfacial Electrochem.* **1986**, *107*, 25-39.
- (15) Kozlowski, C.; Sherwood, P. M. A. *J. Chem. Soc., Faraday Trans. 1* **1984**, *80*, 2099-2107.
- (16) Oldham, K. B.; Parry, E. P. *Anal. Chem.* **1968**, *40*, 65.
- (17) Poon, M.; McCreery, R. *Anal. Chem.* **1988**, *60*, 1725.
- (18) O'Dea, J. J.; Osteryoung, J.; Osteryoung, R. A. *Anal. Chem.* **1981**, *53*, 695-701.
- (19) Bard, A. J.; Faulkner, L. R. *Electrochemical Methods*; John Wiley and Sons: New York, 1980; p 223.

RECEIVED for review March 24, 1989. Accepted May 19, 1989. This work was supported in part by Grant No. CHE8521200 from the National Science Foundation, by donations of equipment from EG&G PARC, and by financial support from the Office of Naval Research for purchase of the FTIR spectrometer.

# Influence of Mass Transfer Kinetics on the Separation of a Binary Mixture in Displacement Liquid Chromatography

Sadroddin Golshan-Shirazi, Bingchang Lin, and Georges Guiochon\*

*Department of Chemistry, University of Tennessee, Knoxville, Tennessee 37996-1600, and Division of Analytical Chemistry, Oak Ridge National Laboratory, Oak Ridge, Tennessee 37831-6120*

The derivation and properties of the system of equations describing a nonlinear, nonideal model of chromatography are discussed in the case of the separation of the components of a binary mixture by displacement chromatography. This is a three-component problem and the system of equations includes three mass balance equations and three kinetic equations, one mass balance equation and one kinetic equation for each component of the binary mixture and for the displacer. The nature of the specific problem (displacement) is accounted for in the boundary conditions: a rectangular pulse of the sample is injected in a column containing only the pure mobile phase. After the injection, a stream of a solution of displacer is passed through the column. The procedure for calculating numerical solutions of the system of nonlinear partial differential equations obtained is explained and justified. A series of simulated chromatograms is presented, corresponding to various combinations of the mass transfer coefficients of the three compounds involved, covering a wide range of numerical values. When the values of the three mass transfer coefficients become large, the results approach those derived from a semiequilibrium model of displacement chromatography. It is shown, however, that displacement chromatography remains possible when the kinetics of mass transfer between phases is slow, provided long columns are used at low flow velocity of the mobile phase. The critical parameters for a displacement separation are the displacer concentration, the loading factor (ratio of sample size to column saturation capacity), and the number of theoretical plates as measured in linear elution, for a very small sample size.

## INTRODUCTION

Displacement chromatography was first introduced by Tiselius in 1943, as a new mode of carrying out chromatographic separations (1). A chromatographic phase system is selected so that the components of the sample have large retention volumes and the proper column is prepared. A volume of sample is introduced in the column. This volume can be rather large compared to the column volume if the sample is dilute, but it should remain moderate compared to the retention volume, so that frontal analysis does not take place. Elution is then carried out with a displacer, i.e., a solution of a compound that is more retained than any component of interest in the sample. The front of the displacer moves along the column, sweeping the sample components in front of it. These components are stacked in neat zones, ordered after their increasing retention in the phase system selected. Under proper conditions, the separation of these zones is complete, and the corresponding components can be recovered at a high degree of purity. The displacer must be

purged out of the column, and only after this regeneration step has been completed, can another separation be attempted on the original column.

In displacement chromatography, the elution of the sample out of the column exhibits a series of zones, with thin boundaries, where two neighbor zones interfere, with wide concentration plateaus in between, during which a pure component of the sample is eluted at a constant concentration. These series of zones are called "isotachic displacement trains", because, once formed, they move at constant velocity and profile. Therefore, the optimum conditions for a separation are those for which the isotachic train is just formed when it exits the column, or, possibly, slightly before that moment, if analysis time or production rate are of serious concern. The retention data (time or volume) do not mean much in displacement chromatography: they depend on the composition of the sample. The maximum concentration of the band of a given compound does not depend on its concentration. The width or duration of this band, on the other hand, is proportional to the compound concentration in the sample.

In the 1940s, analytical instrumentation was very rudimentary. Analysts would collect fractions at the exit of the column and analyze them by combinations of chemical reactions and colorimetry. A separation process such as displacement chromatography, which delivers fractions more concentrated than elution chromatography, was highly valuable. When analytical instrumentation progressed and the liquid chromatograph was developed in the 1960s, displacement was abandoned because it does not give well-resolved bands, which can be turned into easily handled signals by the very sensitive detectors now available. On-line detection of the isotachic train is not suitable for analytical purposes. Horvath et al. brought displacement chromatography back to the limelight in the early 1980s, as a possible implementation of preparative liquid chromatography, when it became obvious that the pharmaceutical industry was in need for a general purpose, highly selective method of separation for its intermediates (2).

In spite of the publication of a number of important contributions (2-8), the lack of theoretical understanding of the kinetics of the displacement process still hinders experimental studies of the optimization of the experimental conditions under which displacement chromatography is run. Most theoretical investigations of displacement chromatography are based on the use of an equilibrium or ideal model (2-6). The rates of mass transfers of the components of the sample between the two phases of the chromatographic system are assumed to be infinite, while axial dispersion is neglected. This amounts to assuming the column efficiency to be infinite. Under such an assumption, the bands in an isotachic train are completely resolved and merely touch each other. The boundaries of each zone are vertical. Helfferich and Klein have presented an analysis of the phenomenon based on the coherence concept (i.e., isotachic migration of two components) and using the h-transform (4). They have shown how to predict the progressive formation of the isotachic train and the characteristics of that train. Rhee et al. have analyzed

\* Author to whom correspondence should be addressed at the University of Tennessee.

the details of multicomponent ideal displacement chromatography, when the adsorption isotherms are given by the classical competitive Langmuir equations (5, 6).

In spite of the very high column efficiencies available today in high-performance liquid chromatography (HPLC), the ideal model permits only first-order approximations. The nonlinear effects due to the curvature of the equilibrium isotherms and the coupling between the isotherms of the various components are properly taken into account. On the other hand, however, the ideal model predicts razor-sharp boundaries between the displacement zones of an isotachic train and this is not realistic. Using a semiideal model, in which the finite column efficiency is taken into account, Katti and Guiochon have shown that the ideal model assumption grossly overestimates the recovery yield of a separation and its production rate, because it neglects the losses due to the zone boundaries which are significant (7). The semiideal model gives excellent results, which account very well for the experimental profiles obtained, when the chromatographic system and the sample used provide for rapid mass transfers between phases, and especially for a fast kinetics of the retention process (7).

There are cases of practical importance, however, where mass transfers between phases are not fast, especially when proteins are concerned. In a number of practical applications of bioaffinity chromatography, or even of adsorption chromatography, the kinetics of the retention and/or of the mass transfers between phases are slow, and their effect on the band profiles must be taken into account. This can be done through the use of a kinetic model. Recently, Philips et al. presented a numerical solution of such a model (8). This approach has some limitations, which will be discussed in the present paper. We have recently described a procedure for the computer calculation of numerical solutions of the classical kinetic model, in the case of a single compound (9) and of a binary mixture (10), in isocratic elution chromatography.

The purpose of the present paper is in the extension of our previous results to the solution of a multicomponent problem and in the application of these results to the investigation of the influence of the kinetics of mass transfers between phases on the profiles of zones in displacement chromatography, on the rate of formation of the isotachic train, and on the recovery yields in a separation. The following discussion is limited to the case of a binary mixture, with a single component used as a displacer (three-component problem). Extensions to the case of multicomponent mixtures appear rather straightforward.

## MATHEMATICAL MODEL AND NUMERICAL SOLUTION

The problem investigated here involves a three-component chromatographic system, with particular boundary conditions simulating the experimental conditions under which a displacement run is carried out. In the following, subscripts 1 and 2 refer to the two components of the binary mixture to be separated, in the order of their elution, and subscript d refers to the displacer.

**1. The Mass Balance Equations.** The mass balance equations for the three components involved are written in exactly the same way as for a single compound

$$\frac{\partial C_1}{\partial t} + u \frac{\partial C_1}{\partial z} + F \frac{\partial \bar{q}_1}{\partial t} = D_1 \frac{\partial^2 C_1}{\partial z^2} \quad (1a)$$

$$\frac{\partial C_2}{\partial t} + u \frac{\partial C_2}{\partial z} + F \frac{\partial \bar{q}_2}{\partial t} = D_2 \frac{\partial^2 C_2}{\partial z^2} \quad (1b)$$

$$\frac{\partial C_d}{\partial t} + u \frac{\partial C_d}{\partial z} + F \frac{\partial \bar{q}_d}{\partial t} = D_d \frac{\partial^2 C_d}{\partial z^2} \quad (1c)$$

In these equations  $t$  and  $z$  are the time and abscissa along the

column, respectively,  $C$  and  $\bar{q}$  are the concentrations of the compounds indicated by the subscript in the mobile and stationary phase, respectively,  $F = (1 - \epsilon)/\epsilon$  is the phase ratio of the column, and  $\epsilon$  is the column porosity,  $u$  is the mobile phase velocity, which is constant along the column and during the experiment, and  $D$  is the axial dispersion coefficient, which accounts for the effects of the molecular diffusion of the corresponding compound, of the column tortuosity and of the lack of homogeneity of the packing on the axial dispersion of the chromatographic bands.

A similar set of equations has been previously discussed (9, 10). It contains two functions for each compound, the concentrations in the mobile and the stationary phases. These functions must be related. In the ideal and the semiideal models, the relationship is derived by assuming that the two phases are always at equilibrium (ideal model) or near equilibrium (semiideal model). In the present work, we employ a kinetic model to account for the rate of mass transfer between the two phases.

**2. Kinetic Equations.** Several models are conceivable for the kinetic equation relating the concentration of a compound in the mobile and the stationary phase. Thomas (11), Goldstein (12), and Wade et al. (13) used the Langmuir kinetics of adsorption/desorption in their investigations. Since the Langmuir kinetics cannot account for the mass transfer kinetics, which is the main source for deviation from equilibrium in most chromatographic separations, we have preferred the solid film driving force model (9). The corresponding equation assumes that the rate of mass transfer is proportional to the difference between the actual concentration in the stationary phase and the one that would correspond to thermodynamic equilibrium between the two phases. Accordingly, we have

$$\partial \bar{q}_1 / \partial t = -k_{t1}(\bar{q}_1 - q_1) \quad (2a)$$

$$\partial \bar{q}_2 / \partial t = -k_{t2}(\bar{q}_2 - q_2) \quad (2b)$$

$$\partial \bar{q}_d / \partial t = -k_{td}(\bar{q}_d - q_d) \quad (2c)$$

In these equations  $k_{ti}$  stands for the lumped mass transfer coefficient of the compound  $i$  and  $q_i$  is the concentration of the corresponding compound,  $i$ , in the stationary phase, at equilibrium with the concentration  $C_i$  in the mobile phase.  $q_i$  is given by the appropriate isotherm equation.

**3. Isotherm Equations.** In principle any isotherm equation can be used to complete the system of equations. Special difficulties arise, however, when the phenomenon popularly referred to by experimentalists as "isotherm intersection" takes place (14, 15). In the present work, we have used the competitive Langmuir isotherms for three compounds

$$q_1 = \frac{a_1 C_1}{1 + b_1 C_1 + b_2 C_2 + b_d C_d} \quad (3a)$$

$$q_2 = \frac{a_2 C_2}{1 + b_1 C_1 + b_2 C_2 + b_d C_d} \quad (3b)$$

$$q_d = \frac{a_d C_d}{1 + b_1 C_1 + b_2 C_2 + b_d C_d} \quad (3c)$$

These ternary isotherms account for what is probably the most important single feature of multicomponent nonlinear chromatography, the competition between the different compounds involved for interaction with the stationary phase. More complex isotherm equations are available, which accounts for the nonideal behavior of the mobile and the stationary phases.

**4. Boundary and Initial Conditions.** The initial conditions correspond to a column initially filled with pure mobile phase and empty of either the binary mixture or the displacer

$$C_i(x, 0) = \bar{q}_i(x, 0) = 0 \quad (i = 1, 2) \quad x > 0 \quad (4a)$$

$$C_d(x, 0) = \bar{q}_d(x, 0) = 0 \quad x > 0 \quad (4b)$$

At time  $t = 0$ , a rectangular pulse of the binary mixture is injected. The duration of the pulse is  $t_p$  and its concentrations,  $C_1^0$  and  $C_2^0$ , and the amounts of components 1 and 2 injected are respectively  $C_1^0 t_p F_v$  and  $C_2^0 t_p F_v$ , where  $F_v$  is the volume flow rate of mobile phase; hence the boundary conditions for the binary mixture are

$$C_i(0, t) = C_{0i} \quad 0 < t \leq t_p \quad (5a)$$

$$C_i(0, t) = 0 \quad t > t_p \quad (5b)$$

After the injection is finished, a step of constant concentration,  $C_d$ , of the displacer in the mobile phase is introduced in the column at constant flow velocity, until the experiment ends

$$C_d(0, t) = 0 \quad t \leq t_p \quad (6a)$$

$$C_d(0, t) = C_{0d} \quad t > t_p \quad (6b)$$

The problem is now fully determined and ready for solution.

**5. Numerical Analysis.** The mathematical model involves the three mass balance equations, eq 1, the three kinetic equations, eq 2, the three isotherm equations, eq 3, the initial condition, eq 4, and the boundary conditions, eq 5 and 6. It is impossible at present to obtain an analytical solution for this system. Even the numerical analysis is not simple, because the convergence of a numerical algorithm toward the exact solution of the system has not been demonstrated, so that stability conditions of the numerical procedures are unknown. The convergence, stability, and truncation errors of several numerical procedures used for the calculation of solutions of the kinetic model have been discussed (16, 17).

In the present work we have replaced the set of partial differential equations 1 and 2 by the following equivalent finite difference equations ( $i = 1, 2, d$ ):

$$u \frac{(C_i)_{n+1}^{j+1} - (C_i)_n^{j+1}}{h} + \frac{(C_i)_{n+1}^{j+1} - (C_i)_n^j}{\tau} + F \frac{(\bar{q}_i)_{n+1}^{j+1} - (\bar{q}_i)_n^j}{\tau} = 0 \quad (7a)$$

$$\frac{(\bar{q}_i)_{n+1}^{j+1} - (\bar{q}_i)_n^j}{\tau} = -k_i((\bar{q}_i)_{n+1}^{j+1} - (q_i)_{n+1}^{j+1}) \quad (7b)$$

where  $h$  and  $\tau$  are the space and time increments and  $n$  and  $j$  are the space and time indices, respectively.

In order to minimize the impact of the truncation errors on the numerical solution, we have carried out the calculations assuming that the axial dispersion coefficients are all equal to 0. Under such conditions, the truncation errors introduce an artificial dispersion term which can be made to compensate exactly for the lost axial dispersion term, if the space and time integration increments are properly chosen (16). The error analysis shows that, in the linear case, the error made in replacing each eq 1 by a finite difference equation introduces an artificial dispersion term that is equal to  $D_a \partial^2 C / \partial x^2$ , where  $D_a$  is the apparent or artificial dispersion coefficient introduced by the truncation errors.  $D_a$  is equal to  $(a-1)hu_0/2$ , where  $a$  is the Courant number, equal to  $u_0\tau/h(1+k_0)$ , which must be kept larger than 1 to avoid numerical instabilities and negative values of the concentration.

In the present work, we have taken  $a = 2$  and the space integration increment equal to  $2D/u_0$ , where  $D$  is the axial dispersion coefficient. Under these conditions,  $\tau = 4D(1+k_0)/u_0^2$  and the apparent dispersion coefficient,  $D_a$ , is equal to  $D$ , as required. The axial dispersion coefficient includes the axial molecular diffusion, the column tortuosity, and the unevenness of the flow pattern in the packed column. Thus it corresponds to the sum of the first two terms of the classical Knox equation,  $(2\gamma D_m/u) + Au^{1/3}$  (18). The third term of

the HETP equation,  $Cu_0$ , the resistance to mass transfer in the stationary phase is accounted for here by the kinetic equations (eq 2). The importance of the truncation errors was ignored in ref 8, which may affect the validity of some of the conclusions of that work, and certainly results in the prediction of profiles which are smoother than they should.

A computer program implementing this algorithm has been written and numerical calculations have been carried out on the VAX 8750 at the Computer Center of the University of Tennessee.

## RESULTS AND DISCUSSION

Using the mathematical model, the calculation procedure, and the computer program described above, we have studied systematically the influence of the displacer concentration, the column length, the mobile phase velocity, the axial dispersion, and the mass transfer coefficients on the characteristics of the separation achieved. The results are described in Figures 1 to 20.

**1. Influence of the Displacer Concentration.** The influence of the displacer concentration has already been discussed in detail by Rhee et al., using the ideal model (5, 6). They have shown that there is a threshold concentration, below which displacement of a compound band can never take place. More precisely, displacement is possible only if the slope of the chord between the origin and the point on the isotherm of the pure displacer corresponding to its concentration in the mobile phase,  $C_d$ , is lower than the slope of the origin tangent to the isotherm of the compound studied. This condition can be written (6)

$$\frac{q_d}{C_d} = \frac{a_d}{1 + b_d C_d} < a_i \quad (8)$$

Therefore, the critical concentration of the displacer during a chromatographic development is

$$C_{d_c} = \frac{1}{b_d} \left( \frac{a_d}{a_i} - 1 \right) \quad (9)$$

and a successful displacement requires that  $C_d > C_{d_c}$ . Thus, for a multicomponent mixture, the critical displacer concentration for displacement of the whole band system depends only on the adsorption isotherms of the pure displacer and of the pure lesser retained component of the mixture. It does not depend on the other components of the mixture, except that, of course, the displacer must also be more strongly retained than the more retained component of the mixture. It does not depend on the composition of the feed either.

The use of the kinetic model permits a more detailed investigation, since it predicts the exact profile of the component zones at the end of the displacement, when they elute from the column. If needed, it can also predict the progressive changes in the zone profiles which accompany the formation of the isotactic train (7). We can investigate three types of displacement experiments, depending on the value of the displacer concentration. Let  $l$  be the subscript which stands for the last eluted component of a mixture and  $f$  the subscript for the first eluted one.

*a.  $a_l < q_d/C_d$ . The Chord Slope Exceeds the Slope of the Origin Tangent of the Most Retained Component.* In this case the displacer concentration is lower than the threshold concentration for the last component

$$C_d < \frac{1}{b_d} \left( \frac{a_d}{a_l} - 1 \right) \quad (10)$$

The displacer has no influence on the behavior of any of the mixture components. Their migration along the column is too fast and the displacer front can never take over and in-

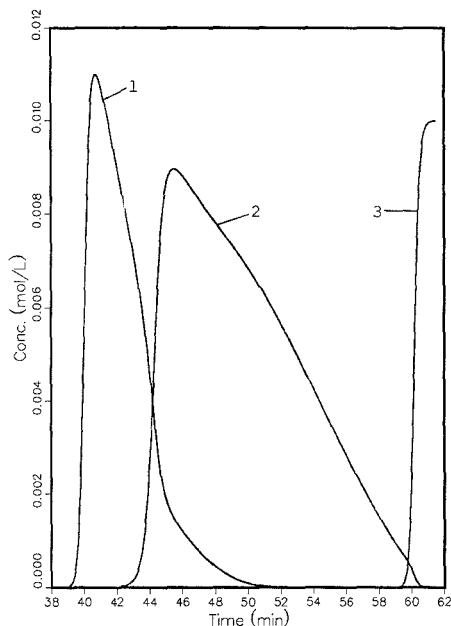


**Figure 1.** Simulated zone profile for displacement chromatography. Experimental conditions: column length, 25 cm; phase ratio, 0.25; flow velocity, 0.05 cm/s. Curve 1, first component; curve 2, second component; curve 3, displacer. Isotherms: first component,  $q_1 = 18.75C_1/(1 + 12.5C_1 + 15C_2 + 18C_d)$ ; second component,  $q_2 = 22.5C_2/(1 + 12.5C_1 + 15C_2 + 18C_d)$ ; displacer,  $q_d = 27C_d/(1 + 12.5C_1 + 15C_2 + 18C_d)$ . Relative retention of the two components of the feed:  $\alpha = 1.20$ . Sample size: injection duration,  $t_p = 250$  s; concentration in the feed,  $C_1^0 = 0.01$  M,  $C_2^0 = 0.02$  M. Loading factors:  $L_1 = 1.333\%$ ,  $L_2 = 2.666\%$ . Displacer concentration:  $C_d = 0.01$  M. Mass transfer coefficients:  $k_{1f} = k_{2f} = k_{df} = 1$  s $^{-1}$ . Axial dispersion coefficient:  $D_a = 1.25 \times 10^{-4}$  cm $^2$ /s.

interact with them. A conventional chromatogram, typical of elution or overloaded elution, is recorded. For example, Figure 1 has been obtained with  $C_d = 10$  mM, a concentration for which the inequality 10 is satisfied. Although there is some interference between the bands of the two components of the binary mixture, there is none between the second component and the displacer, as expected.

b.  $a_f < q_d/C_d < a_f$ . *The Chord Slope Is Intermediate between the Slopes of the Origin Tangents of the Two Components.* In this case the displacer concentration is higher than the threshold concentration for the last component, but lower than the threshold concentration for the first one

$$\frac{1}{b_d} \left( \frac{a_d}{a_1} - 1 \right) < C_d < \frac{1}{b_d} \left( \frac{a_d}{a_f} - 1 \right) \quad (11)$$

The displacer has no influence on the behavior of the first component but does displace the second component. Figure 2 has been simulated with the same parameters as Figure 1, except that the displacer concentration is now 20 mM. It shows that the zone profile of the second component is very different from the one on Figure 1. A displacement effect is taking place, although the isotachic train has not had time to fully form. In agreement with theory, the formation of an isotachic train is possible for the second component and it is nearly achieved under the conditions of Figure 2. As theory also predicts, it is impossible to ever incorporate the band of the first component in an isotachic train. In fact, the first

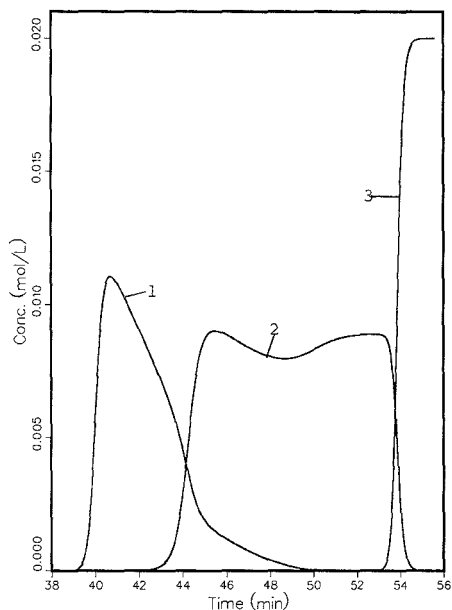


**Figure 2.** Simulated zone profile for displacement chromatography. Same conditions as for Figure 1, except displacer concentration  $C_d = 0.02$  M.

component profile is almost the same as on Figure 1, except that at its very end its tail is shorter and ends 2 min earlier, because of the increased concentration of the second component in the corresponding time zone, enhancing the competition with the first component molecules.

Under the experimental conditions simulated by Figures 1 and 2, the critical displacer concentration for displacement of the sample mixture is 24.5 mM.

c.  $q_d/C_d < a_f$ . *The Chord Slope Is Lower Than the Slope of the Origin Tangent of the Lesser Retained Component.* In this case the displacer concentration is higher than the threshold concentration for a successful displacement (i.e.,  $C_d > (1/b_d)((a_d/a_f) - 1)$ ). Figure 3 corresponds to a displacer concentration of 40 mM, which satisfies this condition. Rather sharp boundaries appear on both sides of each zone and on the displacer front. An isotachic displacement train is formed.

The ideal model predicts that a concentration shock should take place on both sides of each profile (5, 6). In actual columns, which have a finite efficiency, the true concentration discontinuities are replaced by shock layers, which have a finite thickness, proportional to the column HETP. The length of the plateau is shorter than that predicted by the ideal model: the actual zone profiles are not rectangular. The ideal model also predicts the height of each plateau,  $C_i^P$ , which is given by (5)

$$C_i^P = \frac{1}{b_i} \left( \frac{a_i}{a_d} - 1 \right) + \frac{a_i b_d}{a_d b_i} C_d \quad (12)$$

The plateau concentration for each component of the mixture is independent of the feed composition, but depends only on the equilibrium isotherm of the corresponding component, as a pure compound (only  $a_i$  and  $b_i$  enter in eq 12, not the  $b_j$ 's ( $j \neq i$ )), and on the displacer concentration and isotherm. For example, eq 12 predicts for the plateau concentrations of the two components of the binary mixture, under the experimental

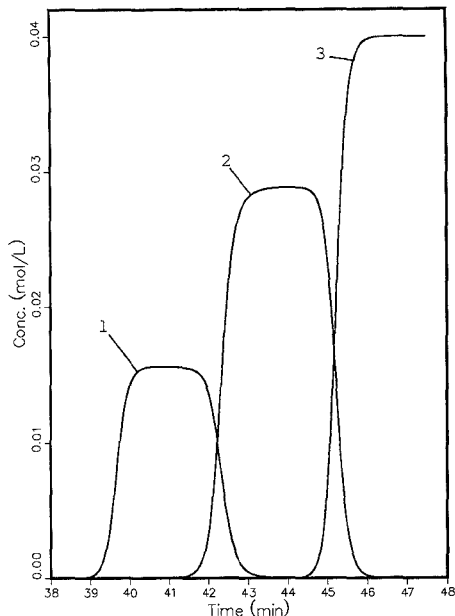


Figure 3. Simulated zone profile for displacement chromatography. Same conditions as for Figure 1, except displacer concentration  $C_d = 0.04$  M.

conditions simulated on Figure 3,  $C_1^P = 0.015556$  M and  $C_2^P = 0.028889$  M respectively. The values predicted by the computer calculations are identical, 0.015556 M and 0.02889 M, respectively. Thus, the finite column efficiency, i.e., the axial dispersion and the finite mass transfer kinetics, narrows the plateaus, smooths their edges, and turns the shocks into shock layers. It does not change the maximum concentration of the zones, if a plateau can be formed. As we show later, when the mass transfer kinetics decreases excessively, the plateau narrows and disappears. As long as the plateau exists, however, its concentration is given by eq 12.

d. *Optimization of the Displacer Concentration.* As we have shown in the previous section, the minimum concentration for the formation of an isotachic train involving the bands of all the mixture components is given by eq 9. However, the ideal model predicts that the best results are obtained if the displacer concentration is chosen so that the ratio  $q_d/C_d$  is smaller than the smallest root,  $\phi_1$ , of the equation

$$\sum_{i=1}^2 \frac{b_i q_i}{a_i - \phi} = 1 \quad (13)$$

In this case, the shocks between the two components and between the last component and the displacer appear as soon as the displacer is injected and are stable and propagate as such. Thus a short column is needed for the formation of an isotachic displacement train of fully separated zones, a column shorter than in the previous cases (6).

If we use a displacer concentration higher than the one given by eq 9, we can, within the framework of the ideal model, increase the plateau heights (see eq 12). The zone width decreases, which is not detrimental with an ideal column of infinite efficiency, but is with a real column. The actual boundary between displacement zones is always a shock layer, as explained above, and a mixed, interference boundary zone, with a finite thickness, appears between each successive pair of bands. The recovery yield may never approach 100%. As

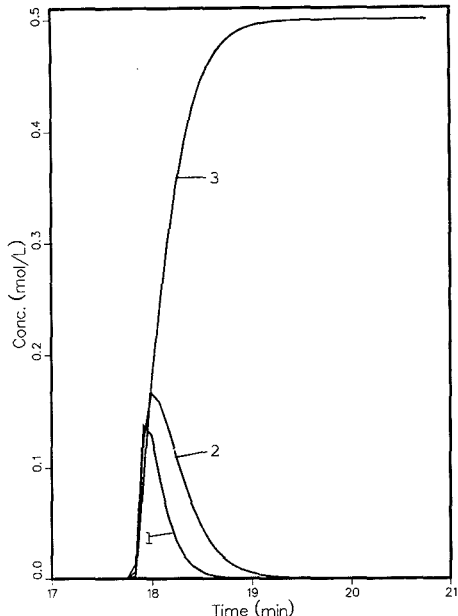


Figure 4. Simulated zone profile for displacement chromatography. Same conditions as for Figure 1, except displacer concentration  $C_d = 0.5$  M.

the displacer concentration rises above the critical value (eq 9), the plateau at the top of each band narrows and the ratio of the width of the interference regions to the band widths increases. The recovery yield decreases. For a while, the production rate increases, because the cycle time decreases. At still higher displacer concentrations, the plateaus disappear, the separation between the two components degrades, and eventually the two bands are eluted on the front of the displacer without any significant degree of resolution (see Figure 4). The recovery yield and the production rate are negligible.

Thus, the optimum displacer concentration in displacement chromatography with real columns is slightly higher than the critical threshold concentration (eq 9), but not as large as the optimum value predicted by the ideal model ( $C_d$  corresponding to the smallest root of eq 13). For example, in the experimental case investigated above (see Figures 1 to 4), the critical displacer concentration, for the phenomenon to take place is 24.4 mM. Simulation with a displacer concentration of 30 mM fails to show an adequate isotachic train developed for columns shorter than 35 cm. This is why we have chosen a concentration of 40 mM for the rest of the investigation.

2. *Influence of the Column Length.* In order for the isotachic train to fully develop, the sample size should not exceed a value corresponding to a certain, optimum loading factor. The loading factor is inversely proportional to the column length (19). Thus, if the sample is too large or the column length too short, the isotachic train will not have time to form, but with the same sample size, it will develop with another, longer column. Alternatively, if the sample is smaller than the optimum loading factor, the isotachic train will be formed before the end of the column. Increasing the column length will result in no change in the band profiles of the mixture components, their resolution, or the displacer front at the column exit but will decrease the production rate.

Figures 5-7 show the concentration profiles observed at the exit of columns having lengths of 10, 25, and 50 cm, respec-

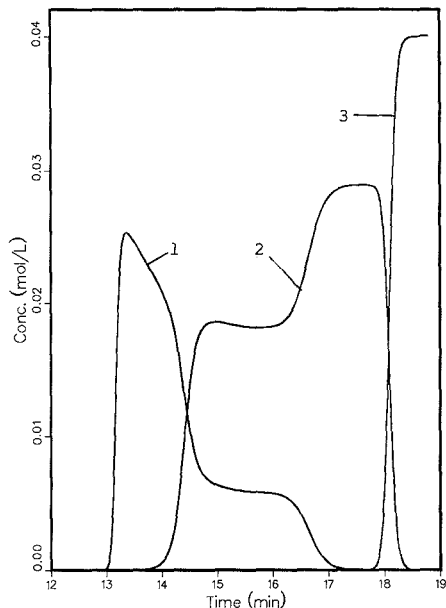


**Figure 5.** Simulated zone profile for displacement chromatography. Same conditions as for Figure 3, except (i) mass transfer coefficients  $k_{f1} = k_{f2} = k_{f3} = 50 \text{ s}^{-1}$  and (ii) column length  $L = 10 \text{ cm}$ . Since the sample size is the same, the loading factors are now  $L_{t1} = 3.33\%$  and  $L_{t2} = 6.65\%$ , respectively.

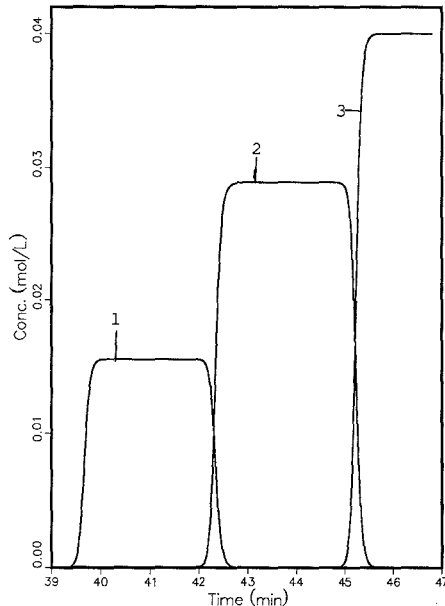


**Figure 6.** Simulated zone profile for displacement chromatography. Same conditions as for Figure 5, except column length  $L = 25 \text{ cm}$ , hence  $L_{t1} = 1.33\%$ ,  $L_{t2} = 2.66\%$ .

tively, for the same sample size. At the end of the first column (Figure 5), the isotachic displacement train is not formed; the loading factor was too large. At the end of the second column (Figure 6), it is formed.

The band profiles are identical at the exit of the last two columns (see Figures 6 and 7). This observation confirms the existence of a constant pattern behavior, as demonstrated in the case of convex isotherms, such as the Langmuir isotherm, by Cooney and Lightfoot (20). In the initial region of the column, the finite kinetics of mass transfer spreads the bands as the front progresses. At some distance from the column inlet, however, the band front approaches an asymptotic form and moves as a stable profile thereafter, with no further change in its shape. Such a concentration profile is called a constant pattern profile (20).

Finally, the profile shown in Figure 8 has been obtained with the same column and under the same conditions as the one in Figure 5, except that the sample size was 2.5 times smaller. Thus, the loading factor was the same as for Figure 6, and the band profiles of these two figures are identical (constant pattern profiles). This demonstrates that, in order to obtain an isotachic train just fully developed at the column exit with a displacer of constant concentration, the critical parameters are not the column length, or the injection bandwidth, or the mobile phase velocity, or the composition of the feed, but the loading factor. As shown below, the column efficiency, i.e., the value of the mass transfer coefficients, also has some effect. Since the loading factor is inversely proportional to the column length, and since the residence time of the displacer front is proportional to the column length, the maximum production rate of a chromatographic system in displacement chromatography is independent of the column length, when the column is operated at its optimum loading factor.

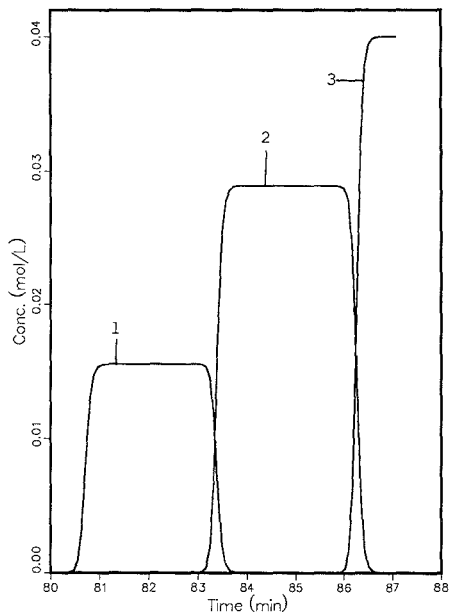


**Figure 7.** Simulated zone profile for displacement chromatography. Same conditions as for Figure 5, except column length  $L = 50 \text{ cm}$ ; hence  $L_{t1} = 0.666\%$  and  $L_{t2} = 1.333\%$ .

**3. Influence of the Axial Dispersion.** In the numerical analysis section, we use the truncation error caused by the finite nature of the space and time integration increments to

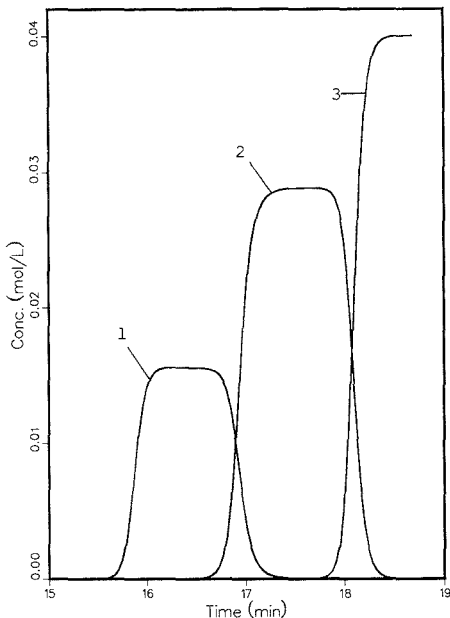


**Figure 8.** Simulated zone profile for displacement chromatography. Same conditions as for Figure 5, except sample size and loading factors  $L_{t_1} = 1.333\%$  and  $L_{t_2} = 2.666\%$ .

simulate the effect of the axial dispersion in the calculations. This effect smooths the band profiles, as seen in Figures 1 to 8 and in the following ones.

The numerical dispersion effect in Figures 5 to 8 corresponds to a space integration increment  $h$  of  $50 \mu\text{m}$  (i.e., a numerical dispersion coefficient  $D_a = 1.25 \times 10^{-4} \text{ cm}^2/\text{s}$ ) and to a mass transfer coefficient equal to  $50 \text{ s}^{-1}$ . In classical mass transfer terminology, the height of a mixing stage is equal to  $2D/u_0$  and the height of a mass transfer stage is given by  $2u_0k_0'/(1+k_0')^2k_t$  (10, 21). They are respectively equal to 0.005 and 0.00029 for these figures. The two curves in Figure 9, on the other hand, have been calculated by using the same mass transfer coefficient ( $k_t = 1000$ ), and two values of the numerical dispersion coefficient, the same as before (corresponding to a height of a mixing stage equal to  $50 \mu\text{m}$ ) and a second one 10 times smaller (mixing stage height,  $5 \mu\text{m}$ ). When the kinetics of mass transfer are not very slow, which is true with the columns discussed so far, the band profiles under linear conditions (small sample sizes) are Gaussian and their variances correspond to a HETP given by (21)

$$H = \frac{2D}{u_0} + \frac{2u_0k_0'}{(1+k_0')^2k_t} \quad (14)$$

The numerical values corresponding to the two curves on Figure 9 are  $50.1$  and  $5.15 \mu\text{m}$ , respectively, corresponding to theoretical plate numbers of 4990 and 48550. The shock layers are much thinner, the plateaus broader and their ends more abrupt on the second curve (Figure 9) than they are on the first one (see captions).

Comparison between these two curves illustrates the importance of column efficiency in displacement chromatography. It also illustrates the potentially very important effect of numerical errors if they are not properly accounted for. In this work, we have adjusted the truncation errors so that they account exactly for the axial dispersion effects, and therefore our numerical results are correct. In some previous work the

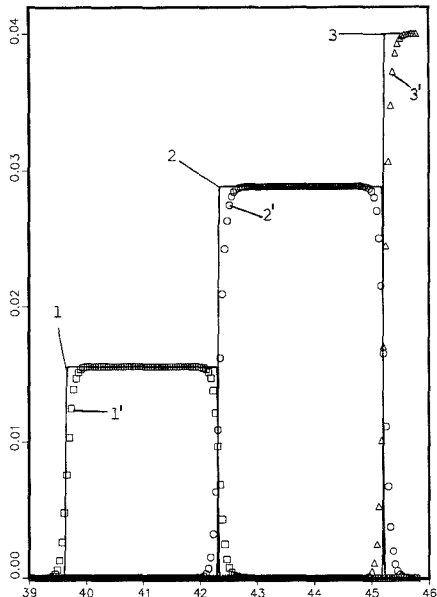


**Figure 9.** Simulated zone profile for displacement chromatography. Same conditions as for Figure 6, except (i) mass transfer coefficients:  $k_{t_1} = k_{t_2} = k_{t_3} = 1000 \text{ s}^{-1}$ . Curves 1, 2, and 3: elution profiles of the first and second components and the displacer, respectively, with a mixing stage height of  $5 \mu\text{m}$ . Curves 1', 2', 3', same profiles, but with a numerical dispersion coefficient corresponding to a height of a mixing stage equal to  $50 \mu\text{m}$ .

truncation errors have been neglected. Since they cannot be avoided, the numerical results obtained are inaccurate and cannot be used for quantitative predictions of production rates and recovery yields (8). The width of the mixed regions, between the different component zones, is proportional to the thickness of the shock layer, itself a function of the column HETP. The recovery yield and the production rate increase with increasing column efficiency.

**4. Influence of the Mass Transfer Kinetics ( $k_{t,1} = k_{t,2}$ ).** In this subsection, we assume that the mass transfers proceed at the same rate for the two components of the binary mixture investigated and for the displacer. In the next subsection, we investigate the influence of widely different mass transfer coefficients for these three compounds and the resulting effects of these differences on the profiles of the displaced bands.

Figures 9 (curve 1), 6, and 3 above, and Figures 10–13 show a series of displacement chromatograms that have been simulated under identical conditions, except for the value of the mass transfer coefficient, which decreases in the following order:  $1000 \text{ s}^{-1}$  (Figure 9);  $50 \text{ s}^{-1}$  (Figure 6);  $1 \text{ s}^{-1}$  (Figure 3);  $0.5 \text{ s}^{-1}$  (Figure 10);  $0.2 \text{ s}^{-1}$  (Figure 11);  $0.05 \text{ s}^{-1}$  (Figure 12);  $0.01 \text{ s}^{-1}$  (Figure 13). The corresponding value of the column HETP is given in Table I.

The factor that determines the profile shape is the ratio of the column length to the height equivalent to a theoretical plate (i.e., the sum of the height of a mass transfer stage,  $2u_0k_0'/(1+k_0')^2k_t$  and the height of a mixing stage,  $2D/u_0$ ). The heights of the mass transfer stage corresponding to the series of mass transfer coefficients used for Figures 9, 6, 3, and 10–13 range from  $1.45 \text{ cm}$  (Figure 13) to  $1.5 \times 10^{-5} \text{ cm}$  (Figure 9). In the worst case, the column contains only 17 stages.

When  $k_t$  decreases from 1000 to  $0.5 \text{ s}^{-1}$  (i.e., the plate number decreases from 5000 to 735), the plateau at the top



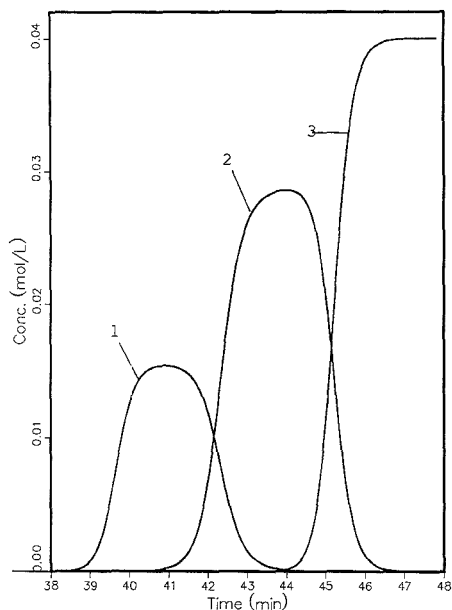


**Figure 10.** Simulated zone profile for displacement chromatography. Same conditions as for Figure 6, except mass transfer coefficients:  $k_{t1} = k_{t2} = k_{t3} = 0.5 \text{ s}^{-1}$ .

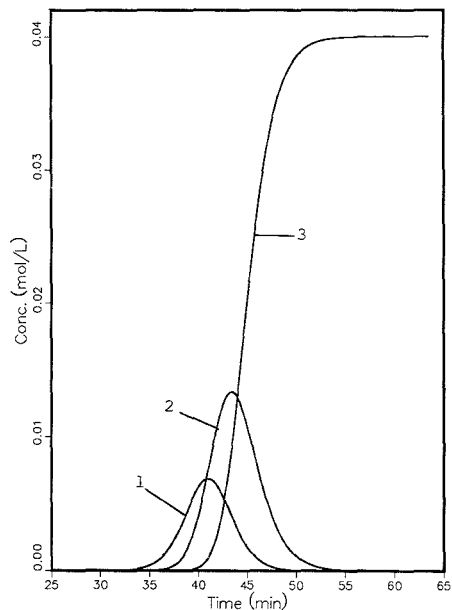


**Figure 12.** Simulated zone profile for displacement chromatography. Same conditions as for Figure 6, except mass transfer coefficients:  $k_{t1} = k_{t2} = k_{t3} = 0.050 \text{ s}^{-1}$ .

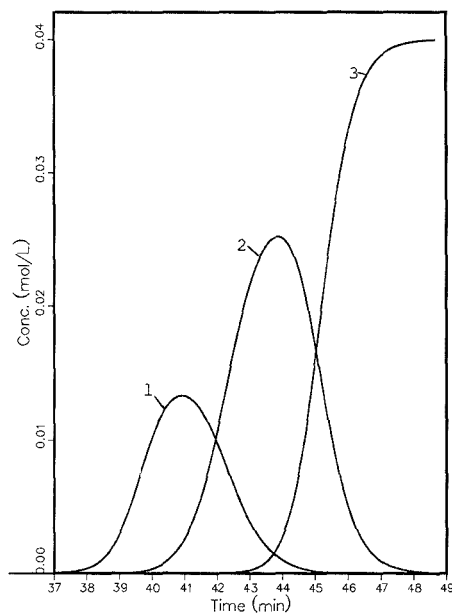


**Figure 11.** Simulated zone profile for displacement chromatography. Same conditions as for Figure 6, except mass transfer coefficients:  $k_{t1} = k_{t2} = k_{t3} = 0.2 \text{ s}^{-1}$ .

of the displacement zones predicted by the ideal model remains present and its height is constant. Its width decreases steadily, however, while the thickness of the shock layers

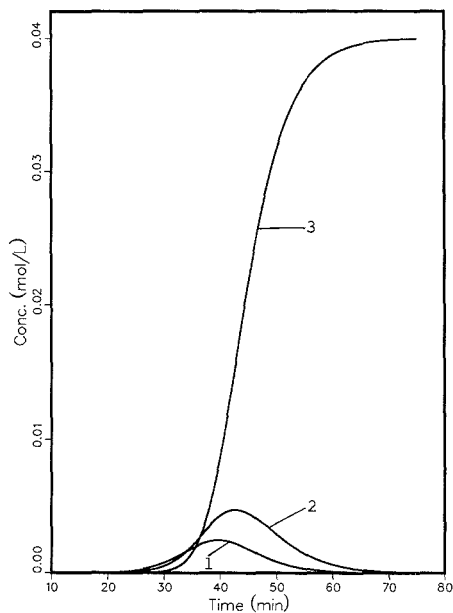


**Figure 13.** Simulated zone profile for displacement chromatography. Same conditions as for Figure 6, except mass transfer coefficients:  $k_{t1} = k_{t2} = k_{t3} = 0.010 \text{ s}^{-1}$ .

increases, and the plateau disappears when  $k_t$  becomes smaller than  $0.5 \text{ s}^{-1}$ . The degree of interference between bands increases and the recovery yield decreases. Further decrease

**Table I. Correspondence between Column Efficiency and Coefficient of Mass Transfer**

mass transfer coeff, $s^{-1}$	height of a mixing stage, <sup>a</sup> cm	height of a mass transfer stage, <sup>b</sup> cm	column height equiv to a theoretical plate <sup>c</sup>
1000	0.00050	0.000015	5.1
1000	0.0050	0.000015	50.1
50	0.0050	0.00030	53
1.0	0.0050	0.0145	195
0.50	0.0050	0.029	340
0.20	0.0050	0.0725	775
0.050	0.0050	0.29	2950
0.010	0.0050	1.45	14550

<sup>a</sup> $2D_d/u_0$ , <sup>b</sup> $2u_0k'_{0,2}/(1+k'_{0,2})^2k_f$ , <sup>c</sup>In micrometers.

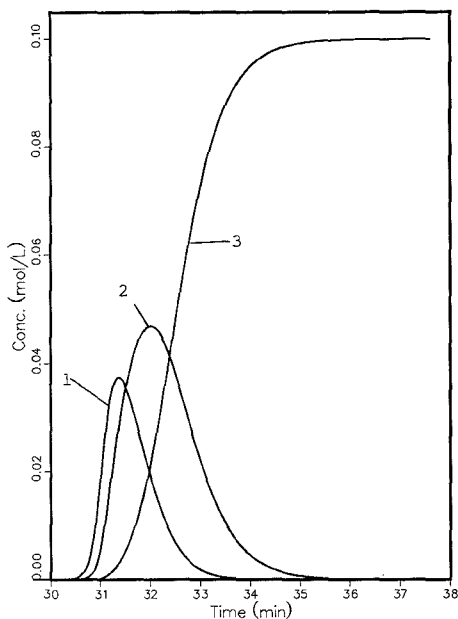


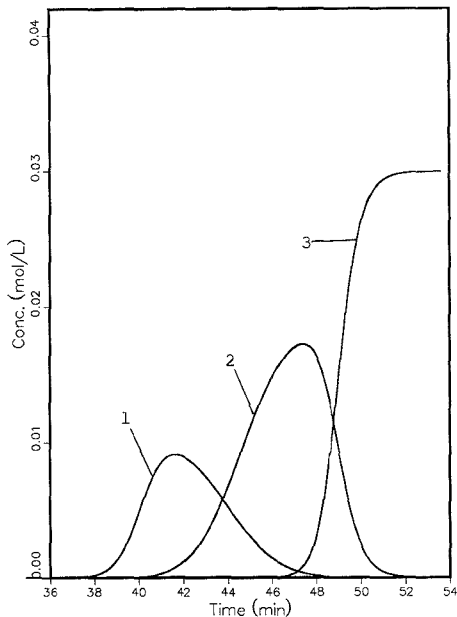
**Figure 14.** Simulated zone profile for displacement chromatography. Same conditions as for Figure 11, except displacer concentration  $C_d = 0.10$  M.

of the mass transfer coefficient to  $0.2 s^{-1}$  and below gives bell-shaped bands. The plateau has disappeared and the band height decreases with decreasing mass transfer coefficient (see Figures 11 to 13). The displacement process just does not take place anymore. The mass transfer kinetics has become too slow.

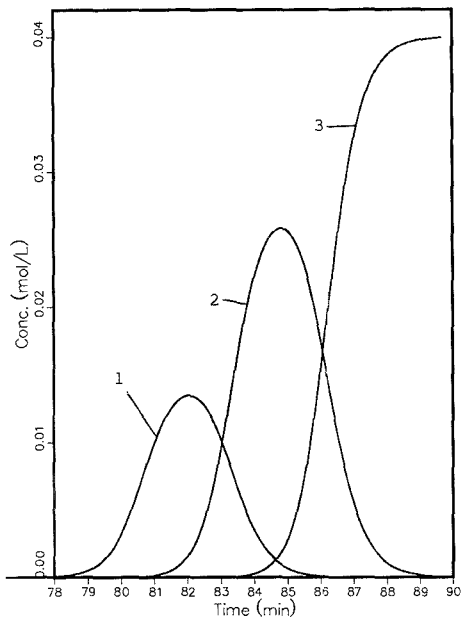
The experimentalist placed in such a difficult situation may try one of three things in order to attempt to improve the experimental results: increase the displacer concentration, increase the column length, or decrease the mobile phase velocity.

Figure 14 shows that increasing the displacer concentration has no significant effect on the displaced zone profiles and certainly does not improve the separation. The overdisplacement effect shown on Figure 4 appears (compare Figures 4 and 14), as was expected. Figure 15 shows that a reduction of the displacer concentration (from 0.04 to 0.03 M) very slightly improves the separation.

Figures 16 and 17 show that increasing the column length and keeping the same loading factor permits a serious im-



**Figure 15.** Simulated zone profile for displacement chromatography. Same conditions as for Figure 11, except displacer concentration  $C_d = 0.03$  M.



**Figure 16.** Simulated zone profile for displacement chromatography. Same conditions as for Figure 11, except column length  $L = 50$  cm, hence loading factors  $L_1 = 0.667\%$  and  $L_2 = 1.333\%$ .

provement of the performance achieved. For Figure 16, the experimental conditions, including the sample size, have been kept constant (as for Figure 11), except for the column length,

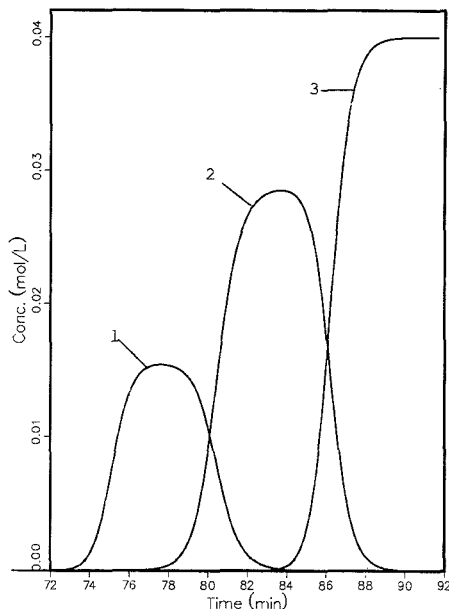


**Figure 17.** Simulated zone profile for displacement chromatography. Same conditions as for Figure 16, except sample size and loading factors,  $L_{n1} = 1.333\%$  and  $L_{t2} = 2.667\%$ .

which has been multiplied by 2, thus, effectively decreasing by half the loading factor. The zone profiles are very comparable to those in Figure 11 and there is no improvement in the separation. The separation time is double, but the zone widths and heights remain nearly the same. For Figure 17, the experimental conditions remain the same as for Figure 16, except the sample size is double, so the loading factor is now the same as for Figure 11. Although there is not yet a detectable plateau, the maximum of the zone profile is now at the plateau concentration predicted by the ideal model and the separation is improved. The displacement train profile is nearly identical with the one obtained on Figure 10, with the same loading factor, a column twice as short but a mass transfer coefficient 2.5 times as large (number of mass transfer stages in the columns, 645 for Figure 17, instead of 735 for Figure 10). Figure 17 shows that, when the mass transfer is slow, the separation and the production rate of displacement chromatography can be improved by increasing the column length, and injecting proportionally more solute (so as to keep constant the loading factor and the throughput).

We note that the improvement observed above (cf. Figure 16 and 17) in the separation performance when doubling the loading factor is contrary to what is expected in ideal chromatography, which predicts that there should be no sample size effect, as long as the loading factor is smaller than the optimum. In real columns, concentration shocks do not appear on both sides of a large size displacement zone, but shock layers, whose width is proportional to the column HETP. When the sample size decreases, the plateau narrows down, but the shock layer thickness remains constant. Eventually, the plateau disappears when the tops of both shock layers come into contact.

Finally, Figure 18 shows the result obtained by decreasing the mobile phase velocity, at constant column length. It has been assumed here that the velocity has no effect on the height of a mixing stage ( $2D/u_0$ ). The results of the displacement

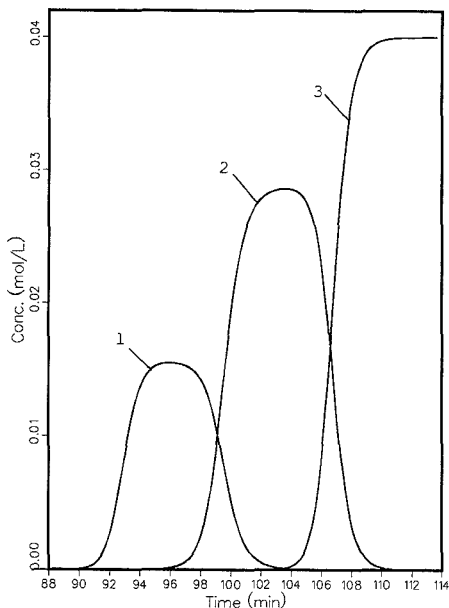


**Figure 18.** Simulated zone profile for displacement chromatography. Same conditions as for Figure 11, except mobile phase flow velocity:  $u_0 = 0.02$  cm/s, and loading factors  $L_{n1} = 1.66\%$  and  $L_{t2} = 3.33\%$ .

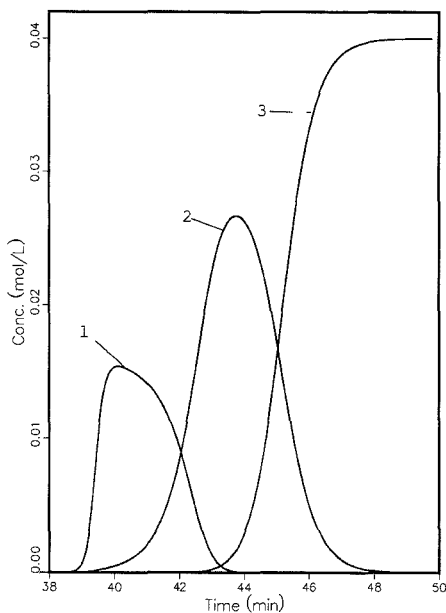


**Figure 19.** Simulated zone profile for displacement chromatography. Same conditions as for Figure 11, except mass transfer coefficients  $k_{t2} = 0.20$  s<sup>-1</sup> and  $k_{t1} = k_{t0} = 1.0$  s<sup>-1</sup>.

experiment are much better, because a reduction in the mobile phase velocity results in a proportional decrease of the height of the mass transfer stage (compare Figures 11 and 18). We

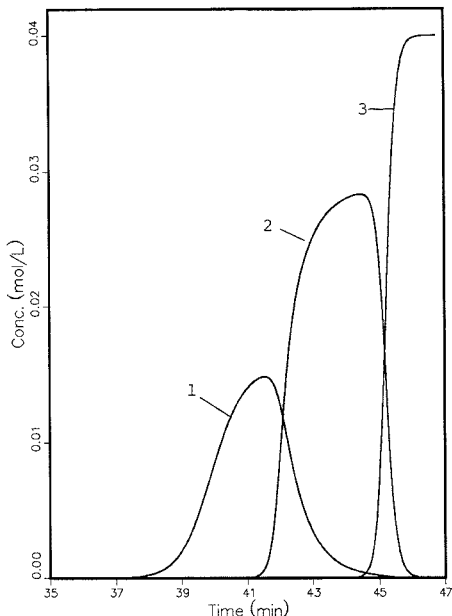


**Figure 20.** Simulated zone profile for displacement chromatography. Same conditions as for Figure 11, except mass transfer coefficients  $k_{t1} = 0.20 \text{ s}^{-1}$  and  $k_{t2} = k_{t3} = 1.0 \text{ s}^{-1}$ .

must emphasize, however, that this result is valid only if the mobile phase diffusion coefficient of the compounds studied is small (e.g., proteins). Otherwise, the improvement could be only marginal.

The critical parameter for the onset of a displacement train appears to be the ratio of the column length to the height equivalent to a theoretical plate; i.e., a minimum value of the column plate number is required for a successful displacement experiment.

**5. Influence of the Mass Transfer Kinetics ( $k_{t1} \neq k_{t2}$ ).** All the results presented here have been obtained with the assumption that the mass transfer coefficients of the two components of the binary mixture studied and the displacer are equal (Figures 1 to 18).

When the kinetics of mass transfers proceed at different rates for these three compounds, the fronts of the zone profiles of the compounds that transfer rapidly from one phase to the other are much steeper than those of the compounds that exchange more slowly. The compounds that have a high mass transfer rate cannot, however, separate easily from those that have a slow mass transfer kinetics, and this may result in paradoxical situations. These effects are illustrated by Figures 19 and 20.

For Figure 3, the mass transfer coefficients were all equal to  $1 \text{ s}^{-1}$ . For Figure 11, they were all equal to  $0.2 \text{ s}^{-1}$ . These figures should be compared to Figure 19 ( $k_{t1} = k_{t2} = 1 \text{ s}^{-1}$ ,  $k_{t3} = 0.2 \text{ s}^{-1}$ ) and Figure 20 ( $k_{t2} = k_{t3} = 1 \text{ s}^{-1}$ ,  $k_{t1} = 0.2 \text{ s}^{-1}$ ). The

first separation (Figure 3) is the best. Surprisingly enough, the other three separations are almost equally bad, except that, on Figure 20, the first component, which has the slower mass transfer kinetics, can be produced with a somewhat better yield under the conditions of Figure 20 than under the other two sets of conditions. In these three cases, there is an interference between the first component and the displacer band, so the second component cannot be prepared at a high degree of purity with any significant recovery yield. Increasing the mass transfer coefficient from 1 to  $50 \text{ s}^{-1}$  for the two components which have fast mass transfers does not change the profiles significantly.

## CONCLUSION

As results from the work described here, high production rates and satisfactory recovery yields in preparative liquid chromatography can be obtained only by using chromatographic systems for which mass transfer between phases is sufficiently fast, and efficient, well-packed columns. The successive development of applications of displacement chromatography, especially in the life sciences, requires some understanding of the factors that influence kinetic phenomena in chromatographic columns.

The relationships between the kinetics of mass transfer in chromatographic systems, the nature of the retention mechanisms involved, and the nature of the components of the mixture whose separation is studied are largely unknown. It is also likely that the kinetics depends on the mobile phase concentration of the compounds that are to be separated.

A solution to these important problems would help considerably in the development of strategies for the rapid optimization of separation schemes by preparative liquid chromatography.

## LITERATURE CITED

- (1) Tiselius, A., *Ark. Kemi, Mineral. Geol.* **1943**, *18*, 1.
- (2) Horvath, Cs.; Nahum, A.; Frenz, J. H., *J. Chromatogr.* **1981**, *218*, 365.
- (3) Glueckauf, E., *Discuss. Faraday Soc.* **1949**, *7*, 12.
- (4) Helfferich, F.; Klein, G., *Multicomponent Chromatography. A Theory of Interference*; Marcel Dekker: New York, 1970.
- (5) Rhee, H. K.; Aris, R.; Amundson, N. R., *Proc. R. Soc. London, A* **1970**, *A267*, 419.
- (6) Rhee, H. K.; Amundson, N. R., *AIChE J.* **1982**, *28*, 423.
- (7) Katti, A. M.; Guiochon, G., *J. Chromatogr.* **1988**, *449*, 25.
- (8) Philips, M. W.; Subramanian, G.; Cramer, S. M., *J. Chromatogr.* **1988**, *454*, 1.
- (9) Lin, B.; Golshan-Shirazi, S.; Guiochon, G., *J. Phys. Chem.* **1989**, *93*, 3363.
- (10) Golshan-Shirazi, S.; Lin, B.; Guiochon, G., *J. Phys. Chem.*, in press.
- (11) Thomas, H. C., *J. Am. Chem. Soc.* **1944**, *66*, 1664.
- (12) Goldstein, S., *Proc. R. Soc. London, A* **1953**, *A219*, 151.
- (13) Wade, J. L.; Bergold, A. F.; Carr, P. W., *Anal. Chem.* **1987**, *59*, 1786.
- (14) Huang, J. X.; Guiochon, G., *J. Colloid Interface Sci.* **1989**, *128*, 577.
- (15) Horvath, Cs.; Lee, A., Communication to HPLC'88, Washington, DC, June 1988.
- (16) Lin, B.; Guiochon, G., *Sep. Sci. Technol.* **1989**, *24*, 31.
- (17) Lin, B.; Ma, Z.; Guiochon, G., *J. Chromatogr.*, in press.
- (18) Knox, J. H.; Saleem, M., *J. Chromatogr. Sci.* **1969**, *7*, 745.
- (19) Golshan-Shirazi, S.; Guiochon, G., *Anal. Chem.* **1988**, *60*, 2364.
- (20) Cooney, D. O.; Lightfoot, E. N., *Ind. Eng. Chem. Fundam.* **1966**, *5*, 212.
- (21) Van Deemter, J. J.; Zuiderweg, F. J.; Klinkenberg, A., *Chem. Eng. Sci.* **1956**, *5*, 271.

RECEIVED for review March 6, 1989. Accepted May 23, 1989. This work has been supported in part by Grant CHE-8715211 of the National Science Foundation and by the cooperative agreement between the University of Tennessee and the Oak Ridge National Laboratory.

# Ionic Equilibria of Picric Acid in Mixed Amphiprotic Solvents. The 2-Methoxyethanol/Water Solvent System

Andrea Marchetti, Emanuele Picchioni, Lorenzo Tassi, and Giuseppe Tosi\*

University of Modena, Department of Chemistry, via G. Campi, 183, 41100 Modena, Italy

Picric acid is the guide solute used in our studies in order to verify the applicability of an empirical treatment that describes the dependence of the dissociation constant on temperature and composition of the solvent mixture ( $\chi$  is mole fraction). The 2-methoxyethanol/water solvent system has been employed in this work operating at 19 temperatures ranging from  $-10$  to  $+80$  °C; by use of the conductometric method the dissociation constant values of picric acid have been evaluated by the Fuoss-Hsia equation. The data have been fitted by three empirical equations that represent the functions  $K = K(T)$ ,  $K = K(\chi)$ , and  $K = K(T, \chi)$ . The  $K = K(T, \chi)$  equation in its complete form is composed of 20 terms, some of which can be eliminated because of small statistical weight; the number and type of these terms vary on passing from one solvent system to another, and the best-fitting form, which in this case represents 13 terms, is suggested. The possibility of extrapolating  $K$  values of picric acid in a pure water solution is investigated and compared with similar previous calculations.

## INTRODUCTION

The importance of the study of dissociating behavior of weak electrolytes is demonstrated by the increasing interest and noticeable effort of many research workers. However, the role of the solvents in ionization and dissociation processes of weak solutes is still not well understood, because of the complexity of physicochemical phenomena that take place in solution (1). The use of binary solvent systems (or higher mixtures of miscible components) apparently can make this problem difficult. On the contrary, it represents an useful and powerful tool of experimental investigation, making possible the continuous variation of some physicochemical properties such as density, viscosity, and dielectric constant; all these parameters play, in fact, a significant role in the ionization and dissociation processes.

As regards our specific interest in obtaining a calculation model able to predict acid-base titration curves in nonaqueous solvents, in their mixtures and in mixtures with water (2-7), we need to know at first some characteristic properties of the systems under study, such as the dissociation constants of the utilized electrolytes, the association constants of the adducts formed during the titrations, and the ionic mobilities in solution.

Recently we have performed a series of preliminary investigations on picric acid, chosen as the guide solute, in some solvents, i.e. pure 1,2-ethanediol (Gliet), pure 2-methoxyethanol (Gliem), their binary mixtures (8-10), and the binary system Gliet/water (11). The dissociation constants of the above solute were evaluated by the conductometric method at 19 temperatures in the range between  $-10$  and  $+80$  °C. In connection with our previous studies we report here the dissociation constant determination of the same solute in the binary system Gliem/water using the same conductometric technique in the temperature range above mentioned in the pure solvents and in their six mixtures. In the case of pure

water and of another particularly water rich mixture we have encountered some difficulties in evaluation and interpretation of experimental data (see the discussion below). This study is, consequently, a part of systematic research regarding both the influence of the solvents on the dissociation constants of weak electrolytes and the correlation between the feasibility of conductometric titrations of such solutes under suitable experimental conditions and the properties of the solvent systems employed (2-11).

## EXPERIMENTAL SECTION

**Materials.** The 2,4,6-trinitrophenol (picric acid), supplied by BDH (purity ca. 95%), was twice purified by recrystallization from hot ethanol and diethyl ether (mp 122 °C; lit. 122-3 °C) (12).

The solvent 2-methoxyethanol (containing <0.05% water found by Karl-Fischer titration) was of Carlo Erba high-purity grade. Twice distilled water, utilized for the preparation of the mixed solvents and as pure solvent, gave conductivities of  $<2.36 \times 10^{-6}$  S at 25 °C.

**Apparatus.** Conductances of the solutions were measured with an Amel Model 134 digital conductivity bridge operating in the  $0.1 \times 10^{-6}$  to 0.3 S (scale-end) range, with a sensitivity of  $\pm 1.0\%$ , and using platinumized platinum electrodes (cell constant 9.12 cm). The temperature control was provided by a Lauda K2R thermostatic bath maintained to  $\pm 0.02$  °C. Viscosity measurements were performed by using a Schott-Geräte AVS 400 viscosity measuring system, equipped with a series of Ubbelohde viscometers. The densities were determined with a digital density meter, Anton Paar Model DMA 60, equipped with a density measuring cell, Model DMA 602, with a sensitivity up to 0.000001 g cm<sup>-3</sup>. The dielectric constants were measured with a WTW-DM01 dipolemeter equipped with two stainless-steel cylindrical cells: MFL2 ( $7 < \epsilon < 21$ ) was calibrated with dichloromethane ( $\epsilon = 9.08$  at 20 °C), pyridine ( $\epsilon = 12.30$  at 25 °C), butan-1-ol ( $\epsilon = 17.80$  at 20 °C), and acetone ( $\epsilon = 20.70$  at 25 °C) (12); MFL3 ( $21 < \epsilon < 90$ ) was calibrated with ethanol ( $\epsilon = 24.30$  at 25 °C), methanol ( $\epsilon = 32.63$  at 25 °C), glycerol ( $\epsilon = 42.50$  at 25 °C), and water ( $\epsilon = 80.37$  at 20 °C) (12). A frequency of 2.0 MHz was used. Karl-Fischer titrations were performed with an automatic titration system (Crison Model KF431) equipped with a digital buret (Crison Model 738).

**Procedure.** The solvent mixtures were prepared by weight. The solutions of picric acid at different concentrations were obtained by successive dilution of stock solutions, freshly prepared by weight; concentrations in volume were then calculated from weight concentrations and densities. Conductance readings were recorded when they became invariant with time; this took about 30 min for each measurement. Solvent conductance corrections were applied to all the data at different temperatures.

## RESULTS AND DISCUSSION

Tables 1-6 (available as supplementary material; ordering information is given in the last paragraph of this paper) report the equivalent conductance values obtained from conductometric measurements at 19 temperatures (ranging from  $-10$  to  $+80$  °C) for at least six different concentrations of picric acid in pure 2-methoxyethanol (Gliem) and in five binary Gliem/water mixtures. The solvent systems employed were identified by means of the water mole fraction, i.e.: H, 0.0000 (pure Gliem); G, 0.3244; F, 0.5208; E, 0.7436; D, 0.8673; C, 0.9457. It must be noted that for the two solvent systems B (0.9751) and A (1.0000; pure water) many difficulties appeared

Table I. Dissociation Constant Values<sup>a</sup> for Picric Acid in the 2-Methoxyethanol/Water Solvent System at Different Temperatures

<i>t</i> , °C	system H <sup>b</sup> <i>K</i> × 10 <sup>6</sup>	system G <i>K</i> × 10 <sup>2</sup>	system F <i>K</i> × 10	system E <i>K</i> × 10	system D <i>K</i> × 10	system C <i>K</i> × 10	system B	system A
-10	8.482 ± 0.010	1.530 ± 0.002	0.6191 ± 0.0128	0.7799 ± 0.0089	0.9703 ± 0.0166	-	-	-
-5	7.656 ± 0.010	2.121 ± 0.002	0.8142 ± 0.0238	0.9668 ± 0.0114	1.188 ± 0.014	1.823 ± 0.198	-	-
0	6.637 ± 0.010	1.985 ± 0.002	1.026 ± 0.100	1.201 ± 0.017	1.421 ± 0.050	2.101 ± 0.279	-	-
5	5.494 ± 0.010	1.669 ± 0.002	1.177 ± 0.006	1.409 ± 0.027	1.604 ± 0.046	2.262 ± 0.257	-	-
10	4.646 ± 0.010	1.531 ± 0.002	1.262 ± 0.005	1.604 ± 0.049	1.937 ± 0.044	2.414 ± 0.404	-	-
15	4.191 ± 0.010	1.351 ± 0.002	1.334 ± 0.007	1.775 ± 0.068	2.197 ± 0.091	2.650 ± 0.238	-	-
20	3.591 ± 0.010	1.244 ± 0.002	1.322 ± 0.007	1.939 ± 0.082	2.525 ± 0.132	2.853 ± 0.442	-	-
25	2.975 ± 0.010	1.121 ± 0.001	1.268 ± 0.006	2.001 ± 0.090	2.572 ± 0.135	3.029 ± 0.471	-	-
30	2.470 ± 0.010	0.9938 ± 0.0102	1.115 ± 0.006	2.010 ± 0.076	2.709 ± 0.127	3.165 ± 0.761	-	-
35	2.170 ± 0.010	0.8767 ± 0.0089	0.9404 ± 0.0393	1.906 ± 0.075	2.723 ± 0.165	3.191 ± 0.710	-	-
40	1.748 ± 0.010	0.7624 ± 0.0080	0.8429 ± 0.0307	1.663 ± 0.069	2.700 ± 0.164	3.189 ± 0.779	-	-
45	1.472 ± 0.010	0.6974 ± 0.0067	0.7220 ± 0.0249	1.532 ± 0.065	2.588 ± 0.146	3.146 ± 0.506	-	-
50	1.260 ± 0.010	0.6588 ± 0.0064	0.6232 ± 0.0194	1.349 ± 0.049	2.473 ± 0.170	3.122 ± 0.526	-	-
55	1.075 ± 0.010	0.6252 ± 0.0060	0.5034 ± 0.0135	1.193 ± 0.039	2.225 ± 0.110	3.009 ± 0.545	-	-
60	0.8646 ± 0.0002	0.5950 ± 0.0057	0.4157 ± 0.0100	1.014 ± 0.067	2.055 ± 0.117	2.860 ± 0.585	-	-
65	0.6525 ± 0.0003	0.5259 ± 0.0050	0.3464 ± 0.0074	0.8608 ± 0.0226	1.876 ± 0.095	2.575 ± 0.437	-	-
70	0.4778 ± 0.0002	0.4215 ± 0.0038	0.2706 ± 0.0050	0.7243 ± 0.0170	1.566 ± 0.057	2.356 ± 0.370	-	-
75	0.3126 ± 0.0001	0.3482 ± 0.0031	0.1941 ± 0.0029	0.5913 ± 0.0119	1.215 ± 0.035	2.005 ± 0.235	-	-
80	0.1715 ± 0.0002	0.2869 ± 0.0024	0.1451 ± 0.0019	0.4872 ± 0.0085	0.9498 ± 0.0216	1.718 ± 0.184	-	-

<sup>a</sup> All *K* values are reported on the molar scale. <sup>b</sup> From ref 10.

in the computing treatment (see below), and as a consequence, the conductance data of these last mixtures have not been utilized and the relative tables have been omitted. The specific conductances of the solvents at each temperature were used in order to correct the experimental data. The so corrected values were analyzed by the method of Fuoss and Hsia (13, 14), modified in order to take into account the variation with density of the solutions' concentrations. The equation

$$\Lambda = \Lambda_0 - S(C\gamma)^{1/2} + EC\gamma \log(C\gamma) + J_1 C\gamma - \frac{J_2(C\gamma)^{3/2} - K_A C\gamma f_{\pm}^2 \Lambda}{(1)}$$

was used, whose symbols have the following significance (15):

$$S = \alpha\Lambda_0 + \beta$$

$$\alpha = (8.204 \times 10^5) / (\epsilon T)^{3/2}$$

$$\beta = 82.43 / \eta(\epsilon T)^{1/2}$$

$$E = E_1\Lambda_0 - 2E_2$$

$$E_1 = 2.303k^2\alpha^2b^2/24C$$

$$E_2 = 2.303kab\beta/16C^{1/2}$$

$$b = \frac{e^2}{\alpha\epsilon k_B T}$$

$$k = \left( \frac{8\pi N_0 z^2 e^2 C}{1000\epsilon k_B T} \right)^{1/2}$$

$$J_1 = \sigma_1\Lambda_0 + \sigma_2$$

$$J_2 = \sigma_3\Lambda_0 + \sigma_4$$

$$\sigma_1 = [(kab)^2/24C][1.8147 + 2 \ln(ka/C^{1/2}) + (2/b^3)] / (2b^2 + 2b - 1)$$

$$\sigma_2 = \alpha\beta + \beta(ka/C^{1/2}) - \beta[(kab)/16C^{1/2}][1.5337 + (4/3b) + 2 \ln(ka/C^{1/2})]$$

$$\sigma_3 = [b^2(ka)^3/24C^{3/2}][0.6094 + (4.4748/b) + (3.8284/b^2)]$$

$$\sigma_4 = [\beta(kab)^2/24C][(2/b^3)(2b^2 + 2b - 1) - 1.9384] + \alpha\beta(ka/C^{1/2}) + [\beta(ka)^2/C] - [\beta b(ka)^2/16C][1.5405 + (2.2761/b)] - (\beta^2 kab/16\Lambda_0 C^{1/2})[(4/3b) - 2.2194]$$

where the following are defined: *C*, concentration (equivalents/dm<sup>3</sup>); *T*, absolute temperature;  $\epsilon$ , dielectric constant of

the solvent;  $\eta$ , solvent viscosity; *z*, valencies of the ions; *N*, Avogadro's number;  $k_B$ , Boltzmann constant; *e*, electronic charge;  $K_A$ , association constant;  $\gamma$ , degree of association;  $f_{\pm}$ , mean ionic activity coefficient; *a* =  $\bar{a}$ , interionic distance parameter.

An initial value of  $\Lambda_0$  is estimated from a  $\Lambda$  vs  $C^{1/2}$  plot, and then a few iterations allow us to obtain the limiting ionic conductivity  $\Lambda_0$ , the association constant  $K_A$  ( $K = 1/K_A$ ), and the interionic distance parameter  $\bar{a}$ .

The Fuoss-Hsia analysis does not involve difficulties for the choice of the electrolyte or of the solvents; however, as already mentioned and observed also in a previous paper (11) for the water solvent system, any attempt to calculate *K* values by the conductometric method fails when one is working with water (system A) and with water-rich solvent mixtures (system B). Similar difficulties were found by other authors working by the potentiometric method (16, 17). This lack is probably due to the characteristic property of picric acid which is a nearly strong electrolyte in these media. In fact, picric acid is almost completely dissociated in 10<sup>-2</sup> M aqueous solutions, and *K* and  $\Lambda_0$  values evaluated are unreliable (*K* values, for example, are in disagreement with those obtained by other methods (12, 16-18)); the same behavior was observed in our previous work (11). The formation of triple ions or dimers, observed by other authors (19, 20), may be excluded by the experimental evidence of conductometric titrations performed at various temperatures in the same solvent system (21).

The experimental *K* values for picric acid in the Gliem/water solvent system in the temperature range between -10 and +80 °C are reported in Table I, with the exception of the data regarding the mixtures B and A owing to the above-mentioned problems, while Table II reports the  $\bar{a}$  parameters obtained.

Each set of *K* data for all the mixtures was fitted by the equation

$$\ln K = a_0 + a_1 T + a_2/T + a_3 \ln T \quad (2)$$

Figure 1 reports the experimental *K* values and the best-fit curves for the systems from C to H. The *a*<sub>i</sub> values, calculated by analyzing the experimental data with the multilinear regression package TSP (22), are presented in Table III, while Table IV reports the *K* data calculated from eq 2. The average difference of 3.7% between calculated and experimental values indicates that the integrated Van't Hoff equation (2) well reproduces the experimental *K* values.

**Table II. Interionic Distance Center-to-Center ( $\text{\AA}$ ) for Picric Acid in the 2-Methoxyethanol/Water Solvent System at Different Temperatures**

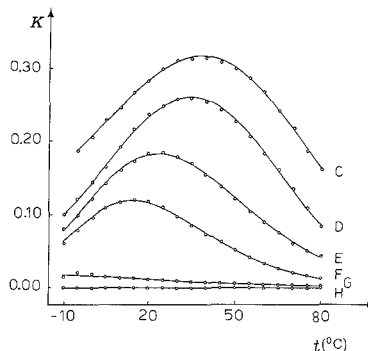
$t, ^\circ\text{C}$	system H	system G	system F	system E	system D	system C	system B	system A
-10	2.614	4.968	5.477	2.299	1.484	-	-	-
-5	2.600	6.603	6.831	2.707	1.653	1.410	-	-
0	2.579	6.531	7.989	3.270	1.854	1.557	-	-
5	2.544	5.952	8.709	3.811	2.038	1.670	-	-
10	2.518	5.817	9.157	4.334	2.377	1.792	-	-
15	2.513	5.530	9.549	4.796	2.677	1.970	-	-
20	2.494	5.442	9.719	5.229	3.061	2.150	-	-
25	2.469	5.277	9.792	5.485	3.189	2.330	-	-
30	2.447	5.080	9.569	5.654	3.409	2.502	-	-
35	2.440	4.893	9.149	5.645	3.517	2.615	-	-
40	2.416	4.694	8.939	5.353	3.595	2.717	-	-
45	2.401	4.642	8.520	5.242	3.586	2.798	-	-
50	2.392	4.685	8.098	4.972	3.574	2.895	-	-
55	2.385	4.742	7.325	4.716	3.402	2.931	-	-
60	2.366	4.810	6.641	4.336	3.303	2.938	-	-
65	2.334	4.697	6.029	3.971	3.180	2.826	-	-
70	2.302	4.396	5.192	3.618	2.860	2.754	-	-
75	2.275	4.207	4.257	3.241	2.453	2.539	-	-
80	2.245	4.051	3.698	2.955	2.158	2.365	-	-

**Table III.  $a_i$  Coefficients of Eq 2 for Picric Acid in the 2-Methoxyethanol/Water Solvent System**

system	$a_0$	$a_1$	$a_2$	$a_3$
A	-	-	-	-
B	-	-	-	-
C	-2430.2	-0.80279	57347	434.58
D	-2176.1	-0.80359	45815	396.78
E	1406.7	0.19549	-50519	-227.67
F	3208.8	0.68536	-99188	-541.03
G	774.7	0.16693	-22774	-132.08
H	-5663.0	-1.74210	145109	997.85

From examination of the trends of Figure 1, some features are apparent:

- (i) The shape of the curves  $K$  vs  $t$  ( $^\circ\text{C}$ ) changes progressively from convex (mixture C) to concave (mixture H). The decreasing trend of the curve H is not very evident upon examining the figure because all the curves have been reported in a unique compressed scale that makes curve H quite flat, but if we consider the  $K$  data as they appear in Table I, the decreasing trend is evident.
- (ii) The curves from C to F show a maximum in  $K$  values, which shifts toward lower temperatures as the  $X_{\text{water}}$  decreases.

**Figure 1.** Dissociation constants of picric acid in 2-methoxyethanol/water solvent system as a function of the temperature.

A particular case is that of system G where the experimental observations, as they appear from Table I, suggest the presence of a maximum at ca.  $-5^\circ\text{C}$ , but the integrated Van't Hoff equation (2) does not adequately represent the trend. In fact,

**Table IV. Dissociation Constant Values<sup>a</sup> for Picric Acid in the 2-Methoxyethanol/Water Solvent System Calculated by Eq 2 at Different Temperatures**

$t, ^\circ\text{C}$	system H $K \times 10^5$	system G $K \times 10^2$	system F $K \times 10$	system E $K \times 10$	system D $K \times 10$	system C $K \times 10$	system B	system A
-10	9.197	1.883	0.6279	0.7489	0.9633	-	-	-
-5	7.463	1.813	0.8228	0.9822	1.182	1.852	-	-
0	6.216	1.723	1.008	1.224	1.422	2.046	-	-
5	5.295	1.619	1.161	1.455	1.675	2.249	-	-
10	4.588	1.505	1.262	1.653	1.933	2.457	-	-
15	3.997	1.387	1.308	1.806	2.178	2.567	-	-
20	3.497	1.268	1.295	1.901	2.397	2.843	-	-
25	3.057	1.152	1.232	1.932	2.576	3.006	-	-
30	2.651	1.040	1.133	1.905	2.699	3.132	-	-
35	2.271	0.9342	1.010	1.825	2.754	3.212	-	-
40	1.920	0.8358	0.8764	1.703	2.740	3.243	-	-
45	1.593	0.7453	0.7428	1.551	2.653	3.217	-	-
50	1.295	0.6626	0.6164	1.381	2.502	3.134	-	-
55	1.027	0.5880	0.5030	1.205	2.296	2.995	-	-
60	0.7932	0.5210	0.4046	1.032	2.050	2.805	-	-
65	0.5963	0.4610	0.3211	0.8689	1.781	2.577	-	-
70	0.4058	0.4114	0.2619	0.7316	1.466	2.249	-	-
75	0.3062	0.3606	0.1970	0.5888	1.238	2.039	-	-
80	0.2087	0.3190	0.1528	0.4752	0.9901	1.756	-	-

<sup>a</sup> All  $K$  values are reported on the molar scale.

Table V.  $K_{\max}^a$  and  $t$  ( $^{\circ}\text{C}$ ) Corresponding Values for the Dissociation of Picric Acid in the 2-Methoxyethanol/Water Solvent System

system	eq 2		$pK$ vs $1/\epsilon$	
	$K_{\max}$	$t_{\max}$	$K_{\max}$	$t_{\max}$
A	—	—	—	—
B	—	—	—	—
C	0.3427	40.3	0.3426	42.2
D	0.2821	36.5	0.3325	36.1
E	0.1963	25.2	0.2375	26.7
F	0.1289	16.4	0.1633	18.2
G	—	—	—	—
H	—	—	—	—

<sup>a</sup> All  $K_{\max}$  values are reported on the molar scale.

the fitting procedure gives probably little statistical weight to the terminal points of the curve, which as a consequence, appears continuously decreasing also at lower temperatures (see Table IV).

(iii) If we consider that the composition of the solvent system varies with continuity and that the curves in the  $\pi(K, T)$  plane change in shape with continuity, it is reasonable to think that the dissociation constant too varies with continuity with the mixture composition. If this hypothesis is true, we may think to the existence of a particular mixture that defines the limit between convex and concave curves, called "limiting mixture", as already observed for similar binary systems (8-10).

The possibility of the existence of this "limiting mixture" may appear also by examining the trend of the  $\bar{d}$  values reported in Table II. In fact, while the trend vs  $T$  for each solvent system reflects that observed for the experimental  $K$  values, the  $\bar{d}$  vs  $\chi$  trend ( $T$  being constant) shows increasing values from the H to G or F system and then decreasing values up to C; this behavior could suggest that any phenomenon depending on the properties of the solvent mixture occurs between the G and F solvent systems.

Taking into account the above considerations and in particular ii, it is possible to perform a  $pK$  vs  $1/\epsilon$  correlation in order to check the  $K_{\max}$  and  $T_{\max}$  values for the various mixtures calculated by the best-fit  $K$  vs  $T$  equations. Good agreement is observed for the results of these procedures (Table V). The  $pK$  vs  $1/\epsilon$  correlation has been performed by using the dielectric constant values experimentally determined for pure solvents and for the mixtures at all the temperatures under investigation; the  $\epsilon$  data were optimized by the relation  $\log \epsilon = \alpha t + \beta$  ( $t$  in  $^{\circ}\text{C}$ ) (12) and are reported in Table 7 of the supplementary material.

The relation between  $pK$  and  $\epsilon^{-1}$  is normally linear, but in some cases smooth curves and deviations from linearity were found, particularly in mixed solvents (23, 24). A probable explanation of these deviations lies in the fact that the effective microscopic dielectric constant cannot be identified with the macroscopic and measured quantity. In fact, particularly in mixed solvents, the dielectric constants effective on molecules, ion pairs, and ions are influenced by selective solvation phenomena (25) that happen in the immediate neighborhood of the species. In the present case the two branches of the smooth curves relative to the systems from C to F have been approximated as straight lines, their linear correlation coefficients being quite acceptable (26, 27):  $r = 0.987$  and  $0.961$  for C;  $r = 0.975$  and  $0.970$  for D;  $r = 0.986$  and  $0.996$  for E;  $r = 0.987$  and  $0.994$  for F. For the systems G and H a linear increase is observed ( $r = 0.986$  for G and  $r = 0.993$  for H) (see Figure 2).

Starting from eq 2, the standard thermodynamic equations could be used to determine the thermodynamic  $\Delta G^{\circ}$ ,  $\Delta H^{\circ}$ , and  $\Delta S^{\circ}$  parameters even if many uncertainties due either

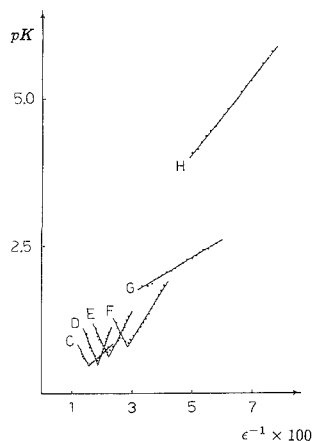


Figure 2.  $pK$  vs  $1/\epsilon$  plot for picric acid in 2-methoxyethanol/water solvent system.

to experimental errors in  $K$  values determination and/or to the method of calculating the integrated Van't Hoff equation could probably affect the obtained values (9).

Let us consider now the  $a_i$  coefficients of Table III; taking into account the above iii hypothesis, we may think that the dependence of  $K$  on the solvent system composition is implicitly present in the  $a_i$  parameters whose graphs show characteristics of "self similarity (28, 29) or omotetia interna (30)", i.e.

$$a_i = a_i(\chi) \quad \text{for } i = 0, 1, 2, 3 \quad (3)$$

No model equation expliciting the  $a_i$  function is available in the literature. We proposed in previous papers (10, 11) an empirical equation that correlates  $K$  with  $\chi$ :

$$\ln K = b_0 + b_1\chi + b_2\frac{(1-\chi)}{(1+\chi)} + b_3\chi^2 + b_4\frac{(1-\chi^2)}{(1+\chi^2)} \quad (4)$$

Also in the present case eq 4 fits the experimental  $K$  values better than many other tested empirical relations; in fact, the experimental  $K$  values of Table I are reproduced by eq 4 with good approximation (average difference 2.4%).

The  $b_j$  coefficients, determined as  $a_i$  (22), are reported in Table VI and refer to all the isothermal  $K = K(\chi)$  curves, some of which are presented in Figure 3; the  $K$  values calculated by eq 4 are in Table VII. Similarly to  $a_i$ , the  $b_j$  adjusting parameters should contain an implicit dependence on the temperature and we may write

$$b_j = b_j(T) \quad \text{for } j = 0, 1, 2, 3, 4 \quad (5)$$

The two empirical equations, (2) and (4), were simply combined (10, 11) in order to propose an empirical approach to solving the problem of a single function  $K = K(T, \chi)$ :

$$f(T, \chi) = [f(T) \cdot f(\chi)]^{1/2} \quad (6)$$

where  $f(T)$  and  $f(\chi)$  are eq 2 and 4, respectively. The above equation, written in its expanded form, is composed of 20 terms which have been evaluated together with their statistical weights by fitting the set of experimental dissociation constant values of Table I with the use of the computing program mentioned above (22).

As already done in our previous papers (10, 11) the terms having negligible statistical weight have been omitted. In general the statistical weight of the polynomial coefficients provided by the TSP fitting procedure (22) varies between 0 and 100 ca. and it is reasonable to omit all the terms having statistical weight less than 1 ca. In this way the importance



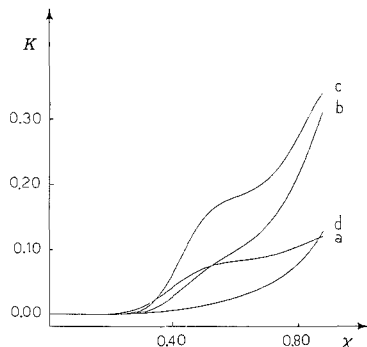


Figure 3. Dissociation constants of picric acid in 2-methoxyethanol/water solvent systems as a function of the composition of the binary solvent system: (a) -10, (b) 20, (c) 50, (d) 80 °C.

Table VI.  $b_i$  Coefficients of Eq 4 for Picric Acid in the 2-Methoxyethanol/Water Solvent System

$t, ^\circ\text{C}$	$b_0$	$b_1$	$b_2$	$b_3$	$b_4$
-10	-687.50	931.73	474.12	-246.56	204.00
-5	-840.78	1136.45	579.13	-297.38	252.17
0	-1130.30	1532.65	786.56	-404.03	334.12
5	-1388.98	1887.19	972.49	-499.95	406.68
10	-1435.91	1952.85	1007.06	-518.64	418.97
15	-1572.48	2140.06	1105.39	-569.24	457.01
20	-1511.44	2058.04	1062.63	-548.18	438.57
25	-1491.32	2030.55	1048.17	-541.05	432.42
30	-1326.99	1807.55	931.57	-481.98	384.81
35	-1162.76	1583.83	814.66	-422.43	337.36
40	-1297.36	1766.46	909.81	-469.90	377.10
45	-1161.51	1580.16	812.10	-419.90	338.28
50	-1090.26	1481.62	760.06	-392.55	318.91
55	-834.17	1131.72	576.60	-298.67	246.14
60	-686.39	929.45	470.07	-243.63	205.16
65	-606.33	818.82	411.67	-213.59	182.72
70	-528.14	711.51	355.24	-184.54	160.64
75	-197.58	260.63	118.75	-64.25	66.26
80	65.59	-98.96	-70.57	31.92	-8.40

of the remaining terms is emphasized and the expression is simplified. The omitted terms vary in dependence of the solvent system under study, so that every system is charac-

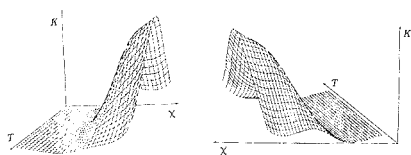


Figure 4. Plot of  $K = K(T, \chi)$  for picric acid in 2-methoxyethanol/water solvent system (two points of view are presented).

terized by its own best fitting  $K = K(T, \chi)$  equation. For the Gliem/water solvent system 13 terms are present:

$$(\ln K)^2 = c_0 + c_1 T + c_2 \frac{1}{T} + c_3 \chi + c_4 T \chi + c_5 \frac{\chi}{T} + c_6 \frac{(1-\chi)}{(1+\chi)} + c_7 T \frac{(1-\chi)}{(1+\chi)} + c_8 \frac{(1-\chi)}{(1+\chi)T} + c_9 \chi^2 + c_{10} T \chi^2 + c_{11} \frac{\chi^2}{T} + c_{12} \frac{(1-\chi^2)}{(1+\chi^2)} \quad (7)$$

where  $c_0 = 22817.2$ ;  $c_1 = -38.0176$ ;  $c_2 = -3193576$ ;  $c_3 = -37900.9$ ;  $c_4 = 63.2231$ ;  $c_5 = 5374304$ ;  $c_6 = -23913.8$ ;  $c_7 = 41.0047$ ;  $c_8 = 3392922$ ;  $c_9 = 15201.9$ ;  $c_{10} = -25.4167$ ;  $c_{11} = -2196784$ ;  $c_{12} = -356.199$ . When eq 7 is applied, the calculated  $K$  values of Table VIII are obtained in satisfactory agreement with the experimental ones (average difference of 9.0%).

Equation 7 can also provide the three-dimensional plot of Figure 4 (two points of view), which represents the  $K = K(T, \chi)$  function; the intersections of the surface with planes  $\pi\{K, T\}$  and  $\pi\{K, \chi\}$  provide the curves of Figures 1 and 3, respectively.

In recent papers (10, 11) the same evaluation of the function  $K = K(T, \chi)$  was made for the ethane-1,2-diol/2-methoxyethanol and ethane-1,2-diol/water systems; the best fitting equations, corresponding to eq 7 of the present work, differ in the number and in the type of the terms of the equation, as well as in magnitude of the coefficients. The choice of the best equation was made on the basis of the lowest difference between calculated and experimental  $K$  values; however, another probably more appropriate way should be the reduction as much as possible of the number of the terms, the percent differences being acceptable. While in a previous work (11) it was possible to obtain an equation with only nine terms and acceptable percent differences, in the present case only eq 7 may be suggested.

Table VII. Dissociation Constant Values<sup>a</sup> for Picric Acid in the 2-Methoxyethanol/Water Solvent System Calculated by Eq 4 at Different Temperatures

$t, ^\circ\text{C}$	system H $K \times 10^9$	system G $K \times 10^9$	system F $K \times 10$	system E $K \times 10$	system D $K \times 10$	system C $K \times 10$	system B	system A
-10	8.482	1.530	0.6190	0.7800	0.9700	-	-	-
-5	7.637	2.158	0.8002	0.9162	1.344	1.704	-	-
0	6.618	2.026	1.006	1.128	1.641	1.942	-	-
5	5.476	1.708	1.151	1.321	1.888	2.070	-	-
10	4.636	1.555	1.243	1.527	2.166	2.271	-	-
15	4.182	1.372	1.314	1.694	2.445	2.500	-	-
20	3.586	1.257	1.309	1.878	2.175	2.742	-	-
25	2.969	1.136	1.252	1.920	2.826	2.878	-	-
30	2.466	1.004	1.104	1.946	2.918	3.040	-	-
35	2.168	0.8836	0.9331	1.862	2.871	3.100	-	-
40	1.747	0.7641	0.8407	1.649	2.753	3.155	-	-
45	1.472	0.6981	0.7209	1.525	2.616	3.128	-	-
50	1.260	0.6582	0.6238	1.354	2.451	3.137	-	-
55	1.075	0.6246	0.5033	1.195	2.215	3.016	-	-
60	0.8652	0.5923	0.4179	1.029	1.989	2.912	-	-
65	0.6534	0.5211	0.3492	0.8864	1.756	2.870	-	-
70	0.4781	0.4189	0.2723	0.7352	1.512	2.402	-	-
75	0.3126	0.3479	0.1941	0.5918	1.212	2.008	-	-
80	0.1714	0.2883	0.1444	0.4804	0.9801	1.689	-	-

<sup>a</sup> All  $K$  values are reported on the molar scale.

Table VIII. Dissociation Constant Values<sup>a</sup> for Picric Acid in the 2-Methoxyethanol/Water Solvent System Calculated by Eq 7 at Different Temperatures

$t, ^\circ\text{C}$	system H $K \times 10^5$	system G $K \times 10^2$	system F $K \times 10$	system E $K \times 10$	system D $K \times 10$	system C $K \times 10$	system B	system A
-10	7.264	1.847	0.6760	0.7330	0.9719	-	-	-
-5	6.961	1.809	0.8020	0.9542	1.198	1.746	-	-
0	6.497	1.744	0.9230	1.217	1.453	1.944	-	-
5	5.916	1.657	1.026	1.514	1.732	2.147	-	-
10	5.265	1.553	1.101	1.823	2.016	2.353	-	-
15	4.591	1.439	1.137	2.110	2.293	2.554	-	-
20	3.929	1.319	1.130	2.327	2.519	2.745	-	-
25	3.306	1.198	1.084	2.427	2.670	2.921	-	-
30	2.740	1.079	1.008	2.391	2.732	3.063	-	-
35	2.241	0.9649	0.9123	2.234	2.687	3.176	-	-
40	1.811	0.8572	0.8064	1.998	2.545	3.249	-	-
45	1.448	0.7576	0.6998	1.729	2.345	3.269	-	-
50	1.148	0.6665	0.5988	1.459	2.105	3.267	-	-
55	0.9020	0.5841	0.5063	1.210	1.860	3.206	-	-
60	0.7040	0.5102	0.4245	0.9930	1.619	3.127	-	-
65	0.5462	0.4443	0.3536	0.8080	1.398	3.002	-	-
70	0.4215	0.3861	0.2930	0.6542	1.196	2.877	-	-
75	0.3239	0.3349	0.2420	0.5282	1.021	2.720	-	-
80	0.2479	0.2900	0.1993	0.4256	0.8668	2.568	-	-

<sup>a</sup> All  $K$  values are reported on the molar scale.

**Data Extrapolation.** The correlation procedures for the experimental data enable us to extrapolate  $K$  values for picric acid in the B and A systems, taking into account the hypothesis previously announced regarding the continuity properties of eq 2, 4, and 7.

For comparison purposes only, the data relative to system A (pure water) at 25 °C are discussed, and this is also because at temperatures higher than 50 °C great difficulties appear, probably due to the lack of experimental data for two systems (B and A) causing an excessive variance of the coefficients of eq 7. The data of the extrapolation at 25 °C, i.e.  $2.573 \times 10^{-1}$  (pK vs 1/ε),  $2.187 \times 10^{-1}$  (eq 4),  $3.327 \times 10^{-1}$  (eq 7), are in good agreement with those reported in our previous paper, i.e.  $2.00 \times 10^{-1}$  (pK vs 1/ε),  $1.90 \times 10^{-1}$  (eq 4),  $2.68 \times 10^{-1}$  (eq 7,  $K = K(T, \chi)$ ) (11), and with literature data, i.e.  $4.6 \times 10^{-1}$  (12) and  $2.00 \times 10^{-1}$  (18).

### CONCLUSIONS

The three proposed empirical equations, which represent the functions  $K = K(T)$  (eq 2),  $K = K(\chi)$  (eq 4), and  $K = K(T, \chi)$  (eq 7), well reproduce the experimental  $K$  values; the average differences between experimental and calculated values are in fact quite acceptable (3.7% for eq 2, 2.4% for eq 4, and 9.0% for eq 7).

In particular for eq 7, on the basis of our present and previous experiences (10, 11) we may conclude that any extrapolation outside the  $T$  and  $\chi$  experimentally investigated ranges is at least hazardous. However, for  $K$  values in the range  $10^{-6}$  to  $10^{-2}$  mol dm<sup>-3</sup> the use of equations like (7) may be considered as an acceptable tool in extrapolating  $K$  values, either in the experimentally studied  $T$  and  $\chi$  ranges or shortly outside the ranges.

The limits affecting the proposed  $K = K(T, \chi)$  model equation are evident if we consider in particular the failure in extrapolating the  $K$  values for the B and A systems. This fact surely arises from the impossibility of obtaining reliable conductance data for nearly strong electrolytes, such as picric acid in very high dielectric constant solvent systems; the lack of data for two mixtures out of eight makes excessive the variance of the coefficients obtained by the multilinear regression.

At the moment, each investigated solvent system is characterized by its own best-fitting model equation even if they are all derived from the same general equation (6). The same equation was proposed in previous works for other solvent

systems, and its validity is now extended to the Gliem/water system.

The next step in our studies should be to set up a unique general equation that gives acceptable percent differences between calculated and experimental  $K$  values, consists of a few simple terms, and is able to predict the  $K$  values of the solutes as a function of  $T$  and  $\chi$ . In addition, the availability of a three-dimensional model  $K = K(T, \chi)$  for several solutes in many solvent systems makes it possible to select the most appropriate conditions, i.e. the best solvents and the best  $T$  and  $\chi$  values, for obtaining the most accurate analytical results and the clearest evidence in acid-base titration curves.

### ACKNOWLEDGMENT

We thank Prof. M. Goffredi for the kind supply of a computing program and the Centro Interdipartimentale di Calcolo Automatico ed Informatica Applicata (CICAIA) of Modena University for the computing facilities.

**Registry No.** Picric acid, 88-89-1.

**Supplementary Material Available:** Tables 1–6, listing conductance values of picric acid solutions, and Table 7, listing calculated dielectric constant values (7 pages). Photocopies of the supplementary material from this paper or microfiche (105 × 148 mm, 24× reduction, negatives) may be obtained from Microforms & Back Issues Office, American Chemical Society, 1155 16th Street, N.W., Washington, D.C. 20036. Orders must state whether for photocopy or microfiche and give complete title of article, names of authors, journal issue date, and page numbers. Prepayment, check or money order for \$16.00 for photocopy (\$18.00 foreign) or \$10.00 for microfiche (\$11.00 foreign), is required and prices are subject to change.

### LITERATURE CITED

- Harned, H. S.; Owen, B. B. In *The Physical Chemistry of Electrolytic Solutions*, 3rd ed.; Reinhold Publishing Corp.: New York, 1958.
- Preti, C.; Tosi, G. *Anal. Chem.* **1981**, *53*, 48–51.
- Preti, C.; Tassi, L.; Tosi, G. *Anal. Chem.* **1982**, *54*, 798–799.
- Nevisani Gliberti, E.; Preti, C.; Tassi, L.; Tosi, G. *Ann. Chim. (Rome)* **1983**, *73*, 527–532.
- Preti, C.; Tassi, L.; Tosi, G. *Ann. Chim. (Rome)* **1985**, *75*, 201–206.
- Franchini, G. C.; Preti, C.; Tassi, L.; Tosi, G. *Anal. Chem.* **1988**, *60*, 2358–2364.
- Franchini, G. C.; Marchetti, A.; Preti, C.; Tassi, L.; Tosi, G. *Anal. Chem.* **1989**, *61*, 177–184.
- Franchini, G. C.; Ori, E.; Preti, C.; Tassi, L.; Tosi, G. *Can. J. Chem.* **1987**, *65*, 722–726.
- Franchini, G. C.; Tassi, L.; Tosi, G. *J. Chem. Soc., Faraday Trans. 1* **1987**, *83*, 3129–3138.
- Franchini, G. C.; Marchetti, A.; Preti, C.; Tassi, L.; Tosi, G. *J. Chem. Soc., Faraday Trans. 1*, in press.

- (11) Franchini, G. C.; Marchetti, A.; Tassi, L.; Tosi, G. *J. Chem. Soc., Faraday Trans. 1* **1988**, *84*, 4427-4438.
- (12) *Handbook of Chemistry and Physics*, 66th ed.; Weast, R. C., Ed.; The Chemical Rubber Co.: Cleveland, OH, 1985-1986.
- (13) Fuoss, R. M.; Hsia, K. L. *J. Am. Chem. Soc.* **1968**, *90*, 3055-3060.
- (14) Goffredi, M. *J. Chem. Soc., Faraday Trans. 1* **1987**, *83*, 1437-1447.
- (15) Roberts, J. H. In *The Chemistry of Nonaqueous Solvents*; Lagowski, J. J., Ed.; Academic Press: New York, 1976.
- (16) Davis, M. M.; Paabo, M. *J. Res. Natl. Bur. Std.* **1963**, *A* **67**, 244-246.
- (17) Willi, A. V.; Möri, P. *Helv. Chim. Acta* **1964**, *47*, 155-158.
- (18) Kortüm, G.; Vogel, W.; Andrusow, K. In *Dissociation Constants of Organic Acids in Aqueous Solution*; Butterworths: London, 1981.
- (19) Ives, D. J. G.; Moseley, P. G. N. *J. Chem. Soc. B* **1966**, *13*, 757-761.
- (20) Shammim, M.; Spiro, M. *J. Chem. Soc., Faraday Trans. 1* **1970**, *66*, 2863-2871.
- (21) Marchetti, A.; Picchioni, E.; Tassi, L.; Tosi, G., unpublished work.
- (22) *Time Series Processor-TSP-User's Guide*; Hall, Bronwyn H., Ed.; TSP International: Stanford, CA, July 1983.
- (23) Accascina, F.; Petrucci, S.; Fuoss, R. M. *J. Am. Chem. Soc.* **1959**, *81*, 1301-1305.
- (24) Bodenseh, H. K.; Ramsey, J. B. *J. Phys. Chem.* **1963**, *67*, 140-143.
- (25) Frölich, H. In *Theory of Dielectrics*; Clarendon Press: Oxford, U.K., 1958.
- (26) Green, J. R.; Margerison, D. In *Statistical treatment of experimental data*; Elsevier Publ.: Amsterdam, 1977.
- (27) Shorter, J. In *Correlation analysis of organic reactivity*; J. Wiley and Sons, Ltd.: Letchworth, U.K., 1982.
- (28) Mandelbrot, B. B. In *Fractals, Form, Chance and Dimension*; W. H. Freeman and Co.: San Francisco, CA, 1977.
- (29) Peitgen, H. O.; Richter, P. H. In *The beauty of fractals*; Springer-Verlag: Berlin, 1986.
- (30) Mandelbrot, B. B. In *Gli oggetti frattali*; Einaudi: Torino, Italy, 1987.

RECEIVED for review January 17, 1989. Accepted May 22, 1989. The Ministero della Pubblica Istruzione (MPI) of Italy is acknowledged for financial support.

## CORRESPONDENCE

### Voltammetric Detection with Gradient Elution for Open Tubular Liquid Chromatography

Sir: Electrochemical detection has become an important tool in liquid chromatography. However, the acceptance of this detection method for LC has been hindered by the belief that it does not work well with gradient elution (1-3). As recently as 1980, it was thought that "gradient elution cannot be used with electrochemical detectors" (2). Since that time many researchers have found that the two can be compatible (4-14). To our knowledge, all of the published work on this topic has involved amperometric detection. While data obtained at a single potential can be very valuable, voltammetric detection can yield a great deal more information since it provides electrochemical as well as chromatographic data. This can be useful for complex mixtures, in which analytes may not be resolved chromatographically but do have different oxidation or reduction potentials. They can thus be resolved voltammetrically but not amperometrically under the same chromatographic conditions. An excellent example of the utility of voltammetric detection is found in the analysis of individual snail neurons (15, 16). The added resolution obtained by combining voltammetry with chromatography allowed for the quantitative determination of several neurotransmitters present in single cells. Without voltammetric detection it would have been impossible to resolve all of the compounds present. Unfortunately, a gradient was not available to these workers, and they were thus affected by the general elution problem. The combination of a gradient with voltammetry in this case would have provided an even more powerful technique.

This report describes the use of voltammetric detection with gradient elution in an open tubular LC system. The value of the technique is demonstrated by using a sample of brewed tea.

#### EXPERIMENTAL SECTION

**Apparatus.** The chromatographic system used in this work has been described in detail elsewhere (14, 17). Briefly, the gradient was provided to the column by a Waters 600E Multisolute Delivery System used at a flow rate of 1 mL/min. The flow rate on the column is typically 60 nL/min, so a splitting system was employed to divert the majority of the mobile phase

to waste. The analytical column had an inner diameter of 15  $\mu$ m, was 150 cm long, and had octadecylsilane bound to its porous glass walls.

The electrochemical detector used here has also been described previously (17, 19, 20). A carbon fiber, 0.4 mm long and 9  $\mu$ m in diameter, serves as the working electrode. It is inserted directly into the outlet end of the capillary column. The electrode potential was scanned from 0 to +1.5 V vs a Ag/AgCl reference electrode at a rate of 1 V/s. Data were acquired at 100 points/s through the use of a microcomputer. A Model 427 current amplifier (Keithley Instruments, Inc., Cleveland, OH) with a 30 ms rise time and a Model 3341 low pass filter (Krohn-Hite Corp., Avon, MA) set at 40 Hz were also used.

**Materials.** HPLC grade acetonitrile and methanol (Fisher Scientific Co., Fair Lawn, NJ) were used as received. All water used was purified by a Milli-Q Water Purification System (Millipore, Bedford, MA). Standards were purchased from Sigma (St. Louis, MO). Naphthalene-2,3-dicarboxaldehyde (NDA) was purchased from Molecular Probes, Inc. (Eugene, OR), while reagent grade sodium cyanide was obtained from Aldrich (Milwaukee, WI).

Phosphate buffer (0.1 M), pH 3.1, was mixed with acetonitrile to form the mobile phases. All mobile phases were filtered before use. Sample solutions were made by using the initial mobile phase as the solvent and were prepared fresh each day.

**Procedures.** *Preparation of Tea.* Tea samples were prepared by boiling 2.4 g of tea leaves (Nifda Golden Brew Tea) in 60 mL of 0.1 M phosphate buffer for 5 min. After cooling, the solution was filtered through a Whatman No. 42 filter (Whatman Paper, Ltd., Maidstone, England), and then through a 0.45- $\mu$ m filter (Micon Separations, Inc., Westbrook, MA).

*Derivatization of Leucine.* Leucine was derivatized to form an electroactive compound using NDA (14, 21-23). To 100  $\mu$ L of  $10^{-2}$  M leucine was added 100  $\mu$ L of 0.1 M cyanide, followed by 200  $\mu$ L of 0.01 M borate buffer (pH 9.5) containing 20% methanol. Finally, 100  $\mu$ L of 0.1 M NDA (dissolved in methanol) was added. The reaction was allowed to proceed at room temperature for 10 min and was then diluted 1:1 with the initial mobile phase.

#### RESULTS AND DISCUSSION

The viability of voltammetric detection with gradient elution was determined by using a set of standards. Figure 1

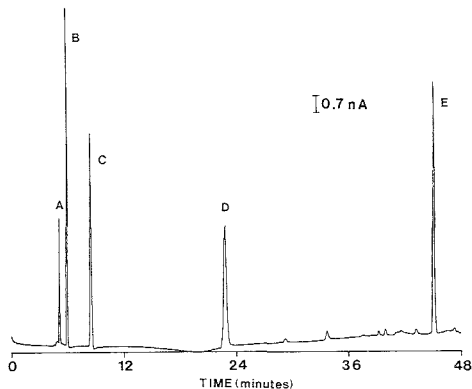


**Figure 1.** Chromatogram at +1.2 V vs Ag/AgCl of an equimolar mixture (0.1 mM) of tyrosine (A), catechol (B), 4-methylcatechol (C), 2,3-dihydroxynaphthalene (D), and NDA-tagged leucine (E).

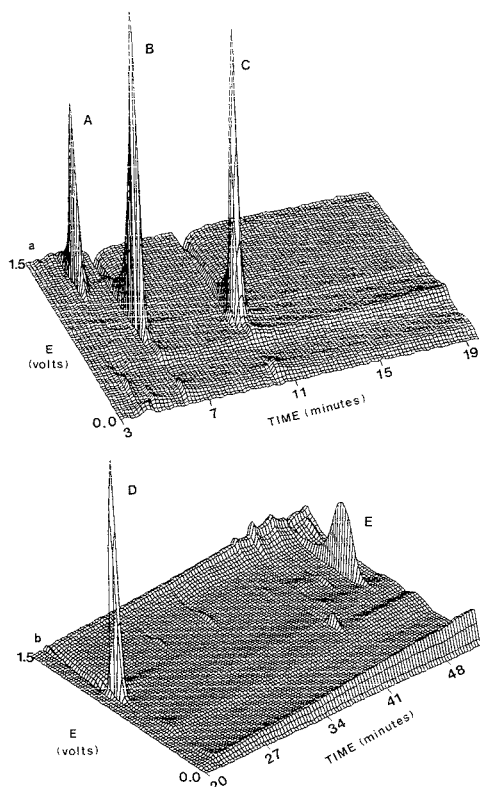


**Figure 2.** Chromatovoltammograms of the standard run shown in Figure 1: (A) includes the first 20 min; (B) covers the remaining 30 min. Labeled peaks correspond to those given in Figure 1.

shows results that were obtained voltammetrically but with only the current from a single potential (+1.2 V) plotted. The mixture consists of  $10^{-4}$  M tyrosine, catechol, 4-methylcatechol, 2,3-dihydroxynaphthalene, and NDA-leucine. The chroma-

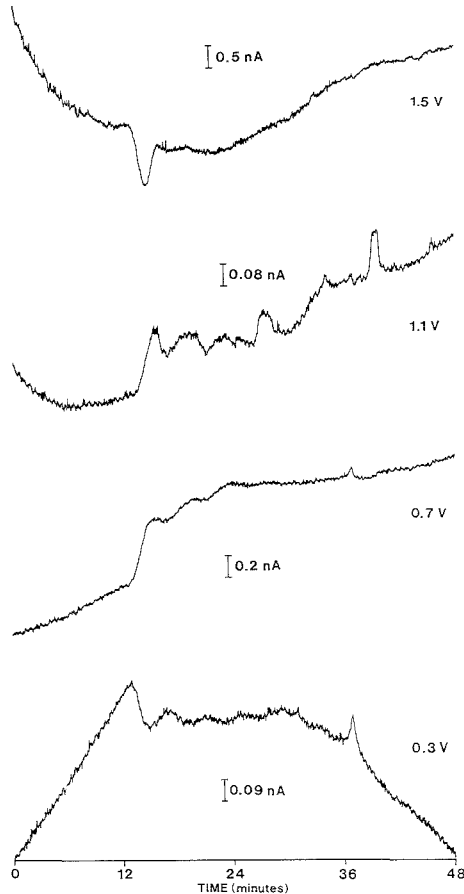


**Figure 3.** Chromatograms of four voltages from a single blank run: (A) chromatogram at +1.5 V vs Ag/AgCl; (B) chromatogram at +1.1 V; (C) chromatogram at +0.7 V; (D) chromatogram at +0.3 V.

togram of this group of standards demonstrates that the base line is relatively flat over a wide range of organic content. The gradient used here began with 100% phosphate buffer and changed linearly to 80% phosphate with 20% acetonitrile over the first 20 min. During the following 30 min the mobile phase composition changed linearly to 30/70 phosphate/acetonitrile.

Chromatovoltammograms of two parts of the standard run are given in Figure 2. Prior to converting all data to the three-dimensional domain, the mathematical derivative was taken of each electrochemical wave (20). Figure 2a is taken from the first 20 min (0 to 20% acetonitrile) and shows a few ripples but is, in general, very flat. Figure 2b contains the part of the run that involves an increase in acetonitrile content of the mobile phase from 20 to 70%. While a rise in the base line is evident at very low potentials, again the background is quiet. The valleys seen behind the peaks in the chromatovoltammograms are a result of taking the mathematical derivative of the peaks and are not due to the gradient or the detection method (20).

Evaluation of the extent of base-line drift due to the gradient was done by means of a blank run, in which no solutes were injected. Data-taking was initiated when the gradient

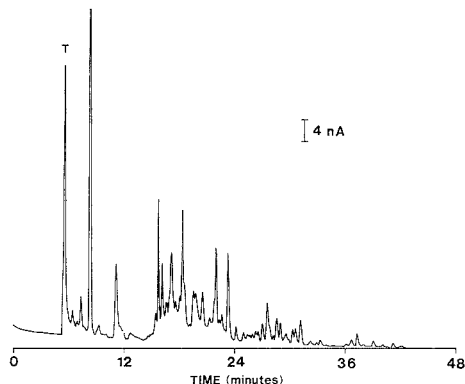


Figure 4. Chromatogram at +1.3 V vs Ag/AgCl of a sample of brewed tea. Peak labeled "T" is theophylline.

began. The gradient used was a linear change from 0 to 40% acetonitrile in phosphate buffer over 50 min. Figure 3 shows the base line obtained at four different potentials. The background current is the highest at +1.5 V, as might be expected. The large dip present from approximately 15 to 20 min is thought to be due to electroactive contaminants present in the mobile phase that build up at the head of the column during the early part of the gradient. As the organic content increases, these contaminants are eluted. Certainly the base-line drift seen here would be detrimental if very low analyte concentrations were used, but for routine analyses the change in base line is acceptable, as demonstrated by the standard run shown in Figure 1.

The detection limit for voltammetric detection with gradient elution was estimated for catechol. The signal to root mean square noise ratio for catechol at a concentration of  $1.9 \times 10^{-5}$  M was found to be 47. A concentration of  $1.2 \times 10^{-6}$  M would therefore yield a signal to noise ratio of three. This is equivalent to approximately 7 fmol injected onto the column. This estimated detection limit is about 100 times higher than that found for voltammetric detection without the gradient, which is about  $10^{-8}$  M (20). However, the increased analytical utility of the combination of the gradient with voltammetry will certainly outweigh the disadvantage of a higher detection limit in many cases.

The resolving power of voltammetric detection in conjunction with gradient elution is demonstrated for tea, a complex sample containing many electroactive species. Figure 4 is a chromatogram of brewed tea, obtained voltammetrically but with only the current from +1.3 V plotted. The gradient used in this case is the same as that for the blank run, a linear change from 0 to 40% acetonitrile over 50 min. Two major components of tea, theophylline and caffeine, should be present in the chromatogram. Theophylline is the first peak to elute. The voltammetric wave of this compound peaks at approximately +1.5 V. Caffeine, however, has a voltammetric wave that peaks very sharply at +1.7 V. It cannot be determined until this potential is reached, and so is not evident in Figure 4. When the potential was scanned up to +1.7 V in order to oxidize caffeine, severe disturbances in the base line were produced due to the massive oxidation of water that occurs at this potential. Caffeine was found to elute at approximately 22 min under these chromatographic conditions, however.

Chromatovoltammograms of this tea sample are given in Figure 5. The first 15 min of the chromatogram are contained in Figure 5a. Theophylline is the first peak seen. Figure 5b

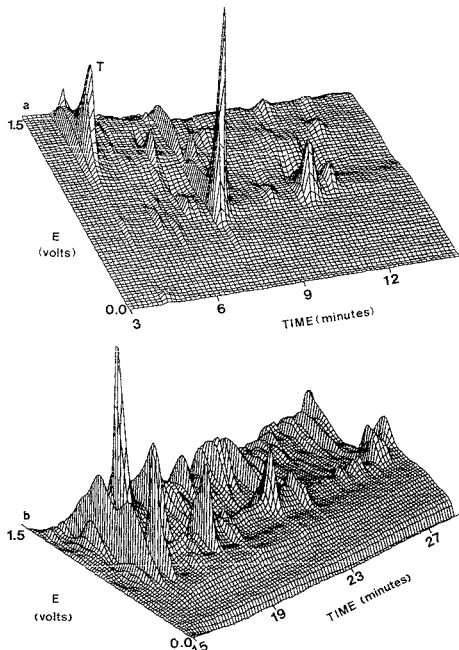


Figure 5. Chromatovoltammograms of portions of Figure 4: (A) includes the first 15 min of the run; (B) covers the second 15 min of the chromatogram. Theophylline is labeled "T".

covers the second 15 min. Many peaks present at lower potentials are observed in the chromatovoltammogram that cannot be seen in Figure 4, which is plotted at a single potential (although obtained voltammetrically). Much more information and greater resolving power are available due to the use of voltammetric detection rather than amperometric detection.

Voltammetric detection with gradient elution has thus been shown to be a valuable technique for use with liquid chromatography. It provides important electrochemical information that cannot be obtained with amperometric detection, and excellent chromatographic and voltammetric resolution are both possible.

#### ACKNOWLEDGMENT

The authors wish to thank Waters Associates (Milford, MA) for the gift of the 600E Multisolvent Delivery System.

#### LITERATURE CITED

- (1) Lores, E. M.; Bristol, D. W.; Moseman, R. F. *J. Chromatogr. Sci.* **1978**, *16*, 358-362.
- (2) Rucki, R. *J. Talanta* **1980**, *27*, 147-156.
- (3) Stulik, K.; Pacakova, V. *CRC Crit. Rev. Anal. Chem.* **1984**, *14*, 297-351.
- (4) Khaledi, M. G.; Dorsey, J. G. *Anal. Chem.* **1985**, *57*, 2190-2196.
- (5) Malliaros, D. P.; DeBenedetto, M. J.; Guy, P. M.; Tougas, T. P.; Jahng, E. G. *Anal. Biochem.* **1988**, *169*, 121-131.
- (6) Hadj-Mohammadi, M. R.; Ward, J. L.; Dorsey, J. G. *J. Liq. Chromatogr.* **1983**, *6*, 511-526.
- (7) Gunasingham, H.; Tay, B. T.; Ang, K. P.; Koh, L. L. *J. Chromatogr.* **1984**, *285*, 103-114.
- (8) Tjaden, U. R.; deJong, J. *J. Liq. Chromatogr.* **1983**, *6*, 2255-2274.
- (9) Drumheller, A. L.; Bachelard, H.; St-Pierre, S.; Jolicoeur, F. B. *J. Liq. Chromatogr.* **1985**, *8*, 1829-1843.
- (10) Meinsma, D. A.; Radzik, D. M.; Kissinger, P. T. *J. Liq. Chromatogr.* **1983**, *6*, 2311-2335.
- (11) St. Claire, R. L., III; Ansari, G. A. S.; Abell, C. W. *Anal. Chem.* **1982**, *54*, 186-189.
- (12) Allison, L. A.; Mayer, G. S.; Shoup, R. E. *Anal. Chem.* **1984**, *56*, 1089-1096.

- (13) Pallister, D. *Curr. Sep.* **1987**, *8*, 53-57.  
 (14) Oates, M. D.; Jorgenson, J. W. *Anal. Chem.* **1989**, *61*, 432-435.  
 (15) Kennedy, R. T.; Jorgenson, J. W. *Anal. Chem.* **1988**, *60*, 1521-1524.  
 (16) Kennedy, R. T.; Jorgenson, J. W. *Anal. Chem.* **1989**, *61*, 436-441.  
 (17) Knecht, L. A.; Guthrie, E. J.; Jorgenson, J. W. *Anal. Chem.* **1984**, *56*, 479-482.  
 (18) St. Claire, R. L., III Ph.D. Thesis, University of North Carolina, Chapel Hill, North Carolina, 1986.  
 (19) White, J. G.; St. Claire, R. L., III; Jorgenson, J. W. *Anal. Chem.* **1986**, *58*, 293-298.  
 (20) White, J. G.; Jorgenson, J. W. *Anal. Chem.* **1986**, *58*, 2992-2995.  
 (21) Roach, M. C.; Harmony, M. D. *Anal. Chem.* **1987**, *59*, 411-415.  
 (22) de Montigny, F.; Stobaugh, J. F.; Givens, R. S.; Carlson, R. G.; Srinivasachar, K.; Sternson, L. A.; Higuchi, T. *Anal. Chem.* **1987**, *59*, 1096-1101.  
 (23) Matuszewski, B. K.; Givens, R. S.; Srinivasachar, K.; Carlson, R. G.;

Higuchi, T. *Anal. Chem.* **1987**, *59*, 1102-1105.

Mary D. Oates  
 James W. Jorgenson\*

Department of Chemistry  
 University of North Carolina  
 Chapel Hill, North Carolina 27599-3290

RECEIVED for review December 12, 1988. Accepted May 19, 1989. Support for this work was provided by the donors of the Petroleum Research Fund, administered by the American Chemical Society.

## Crystal-Face-Specific Response of a Single-Crystal Cadmium Sulfide Based Ion-Selective Electrode

*Sir:* The approach to characterization of ion-selective electrodes (ISEs) has been to pull together thermodynamic and kinetic principles and apply them to response interpretation. The extensive studies by Buck, Eisenman, Simon, Morf, Pungor, Cammann and others have solved major thermodynamic and kinetic problems in the theory and mechanism of ISE responses (1-6). However, not much has been achieved in the way of microscopic characterization of ISEs, particularly of solid membrane ISEs. Although ion-exchange reaction is considered to be one of the processes responsible for permselectivity and charge separation for solid ISE/electrolyte interfaces, conventional solid membrane ISEs such as pressed-pellet types do not necessarily satisfy rigorous analysis of experimental results in terms of the relation between surface structure on the atomic scale and potential response.

It appeared to us that the study of the ion-selective response of a well-defined surface of a single-crystal ISE would provide direct atomic/molecular information for understanding the basic principle of potential generation. Since the introduction of  $\text{LaF}_3$  single-crystal ISEs (7), several attempts have been made to use single crystals for ISEs. However, the purpose for utilizing a single-crystal membrane has been limited to improving bulk electrical conductance and reducing the dissolution of solid matrix. Thus, no control of the crystallographic polarity has been attempted aiming at the atomic/molecular basis for the potential response (8-12).

Here we report for the first time the crystal-face-specific response of single-crystal ISEs. As a representative example of the system, we have chosen CdS, which has been known for a long time as an active component of Cd(II) ISEs (see, for example, ref 13). The lack of inversion symmetry in the [0001] direction of wurtzite CdS single crystals gives rise to a crystallographic polarity of this compound (14). One face (0001) terminates with Cd and the other (000 $\bar{1}$ ) with S. Fortunately, crystal-face controlled single crystals of CdS are easily available because of its use as a photocell component. Also, the historical background that CdS has been well studied in terms of solid-state physics, semiconductor electrochemistry, and photoelectrochemistry further justifies the choice of CdS for the above objective. Striking differences between these two faces have been observed in some of the physical, electrical, and chemical properties (15-20).

To correlate the surface compositions with the response characteristics, the surface of ISE membranes should be characterized. X-ray photoelectron spectroscopy (XPS),

Auger, and Fourier transform infrared (FT-IR) techniques are often employed (21, 22). Another potential technique for characterization of ISEs seems to be ion-scattering spectroscopy (ISS) (23-25), particularly impact collision ion-scattering spectroscopy (ICISS) (26, 27). ISS gives stoichiometric information about an exclusively top layer (monolayer) of solid surfaces and is most suitable for this study. Here we demonstrate for the first time the use of ICISS for the surface characterization of a CdS single-crystal ISE. Theoretical analysis of the potential response of the (0001)Cd and (000 $\bar{1}$ )S surfaces of a single-crystal CdS ISE suggests the imperfection of surface composition, which is confirmed by ICISS measurements.

The results and approach of this study will be of value for the atomic/molecular level characterization and design of solid membrane ISEs.

### EXPERIMENTAL SECTION

CdS single-crystal slices (thickness  $\sim 1$  mm) cut perpendicularly to the *c* axis were purchased from Teikoku Tsushin Kogyo Co., Ltd. (Kanagawa, Japan). The crystals were not intentionally doped, and their carrier density was  $\sim 10^{17}$   $\text{cm}^{-3}$ . Two types of electrodes were prepared. One has a (0001)Cd face and the other has a (000 $\bar{1}$ )S face as electrode surfaces, respectively. Two faces were distinguished by chemical etching in 6 M HCl in this study. The difference in etching characteristics of these two faces has been noted many times (16-20). The (0001)Cd face is etched much faster than the (000 $\bar{1}$ )S face and gives a brighter face by the etching (17). The faces thus determined were confirmed by many methods including X-ray reflection (16), ISS (14), and piezoelectric (15) techniques. An ohmic contact was obtained by indium metal at the back face. Except for the front face, all other parts were covered with epoxy resin and shielded in a glass tubing.

Sample solutions were prepared by using reagent grade chemicals (Wako Pure Chemicals Co., Ltd., Tokyo) and purified water (Milli-Q water purification system, Millipore Corp.). Solutions used were  $10^{-2}$  to  $10^{-6}$  M CdSO<sub>4</sub> plus 0.1 M NaNO<sub>3</sub> and  $10^{-2}$  to  $10^{-6}$  M Na<sub>2</sub>S plus 0.3 M CH<sub>3</sub>COONH<sub>4</sub> (pH = 9.0). Since the  $\text{p}K_{a1}$  and  $\text{p}K_{a2}$  for sulfur species are 7.0 and 12.9, respectively, the solution species at pH = 9.0 is almost exclusively (>99%) SH<sup>-</sup>.

Potentiometric measurements were carried out at room temperature in complete darkness by using a millivolt meter (Model COM-20R, Denki Kagaku Keiki Co., Ltd., Tokyo) with Ag/AgCl as a reference electrode. Prior to each run, the electrode surface was etched in 6 M HCl followed by exhaustive rinsing. The measurements were carried out from dilute to concentrated solutions unless otherwise stated.

Flat band potentials were determined by analyzing measured impedance data (28). Impedance measurements were carried out

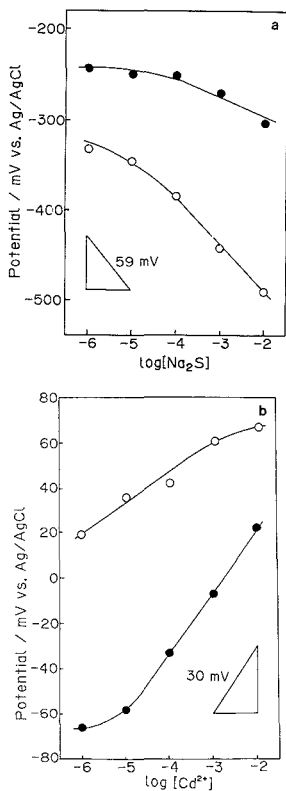


**Figure 1.** Crystal-face specific response of single-crystal CdS electrodes toward  $\text{SH}^-$  and  $\text{Cd}^{2+}$  ions: O, (0001)Cd face; ●, (0001)S face. (a) Response to  $\text{SH}^-$  ions. Solution composition was  $\text{Na}_2\text{S}$  in 0.3 M  $\text{CH}_3\text{COONH}_4$  (pH = 9). (b) Response to  $\text{Cd}^{2+}$  ions. Solution composition was  $\text{CdSO}_4$  in 0.1 M  $\text{NaNO}_3$ .

by using a potentiostat (Model NPG-301S, Nikko Keisoku Co., Ltd., Tokyo) and a frequency response analyzer (Model S-5720B, NF Electronic Co., Ltd., Tokyo) which was controlled by a personal computer (Model PC-8801 mkII, NEC Corp., Tokyo) via a GP-IB interface. All data were transferred to and stored on a floppy disk. In these measurements, the three-electrode configuration with a large Pt auxiliary electrode and a Ag/AgCl reference electrode was employed.

ISS and ICISS measurements were carried out by a Model ADES 400 spectrometer (V.G. Co., U.K.) operating at  $5 \times 10^{-11}$  Torr vacuum. Attempts were made to remove surface impurities from the CdS single-crystal samples, such as Zn, Na, and O atoms that still existed at negligible levels after the chemical etching in HCl, by flash-heating at 400–500 °C.

## RESULTS AND DISCUSSION

Figure 1a shows a remarkable preferential response of  $\text{SH}^-$  ions (pH = 9) to the (0001)Cd plane over the (0001)S plane of a CdS single-crystal ion-selective electrode. The slope of the  $\log c$  vs  $E$  curve was found to be 53 mV/decade at the (0001)Cd plane, which is close to the theoretical value (=59 mV) at 25 °C, whereas the (0001)S plane exhibits a very poor response to  $\text{SH}^-$  ions (<20 mV). On the other hand, the (0001)S plane responded to  $\text{Cd}^{2+}$  ions in the Nernstian manner, but the (0001)Cd plane responded poorly to  $\text{Cd}^{2+}$  ions (Figure 1b). A large decrease in the potential in  $\text{CH}_3\text{COONH}_4^+$  media (Figure 1a) compared to that in  $\text{NaNO}_3$

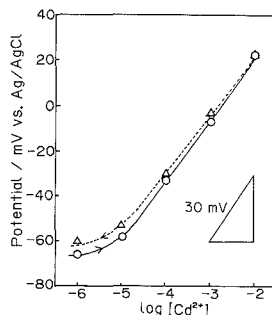


**Figure 2.** Potential response of (0001)S face of a CdS single-crystal electrode toward  $\text{Cd}^{2+}$  ions. The potentials were measured from dilute to concentrated (O) and then back from concentrated to dilute ( $\Delta$ ). The solution composition was  $\text{CdSO}_4$  in 0.1 M  $\text{NaNO}_3$ .

media (Figure 1b) even at very dilute sample solutions may be due to adsorption or complexation of  $\text{CH}_3\text{COO}^-$  ions with the Cd sites of the surface, which appears to be more appreciable for the (0001)Cd face than for the other. The response was quite reversible, virtually free from hysteresis (memory effect) regardless of the direction of concentration change. This is shown in Figure 2 for the (0001)S face electrode toward  $\text{Cd}^{2+}$  ions as an illustrative example. One must note that although the potential with respect to a Ag/AgCl electrode differs from sample to sample, the reproducibility of the slope was quite high.

To investigate the mechanism of the above potentiometric response, it is essential to understand how the potential is generated. It is known that the flat band potential ( $V_{fb}$ ) measurement which is carried out under potentiostatic conditions provides the information on the potential distribution at semiconductor/electrolyte interfaces. Since CdS is an n-type semiconductor, it is useful to compare the potentiometric response with the activity (concentration) dependence of  $V_{fb}$ . Thus, we also measured the flat band potentials ( $V_{fb}$ ) of the (0001)Cd and (0001)S faces of each CdS single-crystal electrode in the same solution in which the potentiometric response was studied. Dependence of  $V_{fb}$  of the (0001)Cd face and (0001)S face on the concentrations of  $\text{Cd}^{2+}$  and  $\text{S}^{2-}(\text{SH}^-)$  ions was found parallel to the above potentiometric results: The observed slopes of  $V_{fb}$  vs  $\log c$  plots were virtually identical with those of  $E$  vs  $\log c$  plots. Thus, these ions seem to affect both  $V_{fb}$  and  $E$  in the same manner. It has been well-known that  $V_{fb}$  shifts positively or negatively depending on the sign of excess surface charge which is caused by specific adsorption of ionic species and is represented as (29)

$$V_{fb} = V_{fb,0} + \Delta V_H \quad (1)$$

where  $V_{fb,0}$  is the value of  $V_{fb}$  without specific adsorption, which does not depend on the concentration of noninteracting ionic species including different kinds of redox systems, and  $\Delta V_H$  is the amount of potential change within the inner Helmholtz layer due to the specific adsorption (29). Some examples of  $V_{fb}$  shift due to specific adsorption are hydroxide adsorption onto  $\text{TiO}_2$  (29), InP (30), and CdSe (31) and sulfide adsorption on CdSe (29). In these cases,  $V_{fb}$  values shift negatively when  $\text{OH}^-$  or  $\text{S}^{2-}(\text{SH}^-)$  concentration increases. The values of  $V_{fb}$  of CdS also depend on the concentration of  $\text{Cd}^{2+}$  and  $\text{S}^{2-}(\text{SH}^-)$  ions (32–35). This shift is also explained by adsorption of  $\text{Cd}^{2+}$  or  $\text{SH}^-$  ions onto the CdS surface. If  $\text{Cd}^{2+}$  is adsorbed,  $V_{fb}$  shifts toward positive potential, and if  $\text{SH}^-$  is adsorbed,  $V_{fb}$  shifts toward negative potential. As mentioned above,  $V_{fb}$  and  $E$  have yielded essentially the same magnitude of response for the concentration change of  $\text{Cd}^{2+}$

and  $\text{SH}^-$  ions. Also, the change in  $V_{\text{H}}$  is attributable solely to  $\Delta V_{\text{H}}$  (see eq 1). From these, it is concluded that the potential changes observed in the potentiometric measurement are equal to  $\Delta V_{\text{H}}$  and potential distribution at interfaces other than the CdS/electrolyte interface is not affected by a change of ion concentration. Thus, the present potentiometric response can be explained by the preferential adsorption of  $\text{Cd}^{2+}$  ions to the (0001)S face and  $\text{SH}^-$  ions to the (0001)Cd face, respectively. This proposed mechanism is, in a sense, similar to that operated at fixed site ion-exchange membranes, Cd being a site for  $\text{SH}^-$  and S being a site for  $\text{Cd}^{2+}$ . The analogy between the doped semiconductors and solid-state ion exchangers is suggested by Buck (2). We must point out here, however, that the present adsorption/desorption model appears to be more general than the ion-exchange mechanism. If the adsorption/desorption process of ions determines the response, the response should be reversible, and the results of Figure 2 confirm this.

It should be noted here that in both the  $\text{Cd}^{2+}$  and  $\text{SH}^-$  cases, complete failure of the response to the (0001)Cd and (0001)S surfaces, respectively, was not observed. The most plausible mechanism for this will be discussed in terms of a theoretical analysis and the data for ISS as in the following. The magnitude of the potential change that occurs within the inner Helmholtz layer,  $\Delta V_{\text{H}}$ , is given by (36)

$$\Delta V_{\text{H}} = Q_{\text{ad}}/C_{\text{H}} \quad (2)$$

where  $Q_{\text{ad}}$  is surface excess charge due to specific adsorption of ions and  $C_{\text{H}}$  is the double-layer capacitance. By assuming a simple adsorption equilibrium in which no interaction between adsorbates exists, one gets the Nernst equation (29). There were many cases, however, where the Nernst equation did not hold as the present case. Recently, Licht and Marcu proposed the following general equation to explain the activity (concentration) dependence of the flat band potential, assuming a Frumkin isotherm for adsorption (37):

$$d\Delta V_{\text{H}}/d \ln (a) = ZF\Gamma/[1/\{\theta(1-\theta)\} + f + g]C_{\text{H}} \quad (3)$$

where  $a$  is the activity of the adsorbing ion,  $Z$  the charge,  $F$  the Faraday constant,  $\Gamma$  the number of adsorption sites,  $\theta$  the surface coverage of adsorbates,  $f$  the interaction energy between adsorbed species, and  $g$  a parameter given by

$$g = Z^2 F^2 \Gamma / C_{\text{H}} RT \quad (4)$$

It must be mentioned here that when  $1/\{\theta(1-\theta)\}$  is small compared to  $(f+g)$ , a linear dependence of  $\Delta V_{\text{H}}$  with  $\ln(a)$  is obtained, and if  $g \gg f$ , eq 3 becomes

$$d\Delta V_{\text{H}}/d \ln (a) = RT/ZF \quad (5)$$

which is the Nernst equation. Typical values of  $d\Delta V_{\text{H}}/d \ln (a)$ , i.e., responses to concentration changes, are calculated by using values of  $Z = 1$ ,  $C_{\text{H}} = 20 \mu\text{F cm}^{-2}$ ,  $\theta = 0.5$ , and various values of  $\Gamma$  and  $f$ . The results are shown in Figure 3 as a function of  $f$ . The larger the  $\Gamma$ , the larger the response. When the number of adsorption sites is close to that of the exposed atom ( $\sim 10^{14} \text{ cm}^{-2}$ ) at the solid surface,  $dV_{\text{H}}/d \ln (a)$  is ca. 50 mV and is close to Nernstian slope. When  $\Gamma$  is  $10^{13}$ ,  $10^{12}$ , and  $10^{11} \text{ cm}^{-2}$ , the slope is ca. 20, a few, and almost 0 mV, respectively. Since values of  $C_{\text{H}}$  at semiconductor electrodes are not known (29), a typical value at metal electrodes ( $C_{\text{H}} = 20 \mu\text{F cm}^{-2}$ ) was used for the calculation shown in Figure 3. It is generally believed that values of  $C_{\text{H}}$  at semiconductor electrodes are not much different from those at metal electrodes (29). The larger  $C_{\text{H}}$  value gives the smaller slope, but the values shown above are not much affected as far as  $10\text{--}30 \mu\text{F cm}^{-2}$ , which are typical values of metal electrodes and are used as  $C_{\text{H}}$ . The effect of  $\theta$  on the slope is quite small in the region of  $0.2 < \theta < 0.8$ . When  $\theta$  approaches either 0 or 1, the slope approaches zero. This happens when the concentration

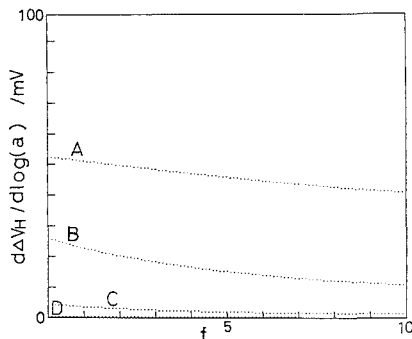


**Figure 3.** Calculated value of  $d\Delta V_{\text{H}}/d \ln (a)$  as a function of  $f$  based on eq 3.  $C_{\text{H}} = 20 \mu\text{F cm}^{-2}$ ,  $\theta = 0.5$ , and  $Z = 1$  were used for the calculation. Key: A,  $\Gamma = 10^{14} \text{ cm}^{-2}$ ; B,  $\Gamma = 10^{13} \text{ cm}^{-2}$ ; C,  $\Gamma = 10^{12} \text{ cm}^{-2}$ ; D,  $\Gamma = 10^{11} \text{ cm}^{-2}$ .

is very high ( $\theta \rightarrow 1$ ) or very low ( $\theta \rightarrow 0$ ). Based on this calculation, the experimental results are interpreted as follows. At the (0001)Cd face, exposed Cd atoms acted as adsorption sites for  $\text{SH}^-$  and Nernstian behavior was observed. Due to surface imperfections, there were a small number of S atoms at the (0001)Cd face which acted as adsorption sites for  $\text{Cd}^{2+}$  and the (0001)Cd face responded to  $\text{Cd}^{2+}$  although poorly. A similar explanation is valid for the (0001)S face. A comparison of results of Figure 1a and Figure 3 (see curve B) suggests that about 10% of the (0001)S surface is actually Cd atoms.

To confirm the above, surface atomic composition was analyzed by ISS. The best available means for determining surface composition has been known to be ISS (23–25). Here the term “surface” shall denote that region of a solid which is, at most, a few atomic dimensions in depth (38). ISS utilizes low-energy (<3 keV) ion beam scattering to characterize the surface properties of solids. The elemental composition of the first monolayer of surface atoms can be derived from the energy spectrum of back-scattered noble gas or alkali-metal ions. In the present experiment, ISS spectra were taken with the impact collision mode (ICISS), which is a type of ISS technique known as the most quantitative approach of this kind (26, 27). The results are shown in Figure 4. In this measurement, a  $\text{Na}^+$  ion beam of 1 keV was incident at an angle of  $\alpha$ , from the (0001)Cd or (0001)S direction. Then the intensities of  $\text{Na}^+$  ions scattered by surface Cd atoms at an angle of  $160^\circ$  with respect to the direction of the primary ion beam were analyzed as a function of  $\alpha$  (see inset of Figure 4). The critical angle  $\alpha_0$  where the intensity starts to decrease is calculated assuming a perfect crystal structure and is shown as crosses in Figure 4;  $\alpha_0$  is higher at the (0001)S face than at the (0001)Cd face. This means that the content of Cd atoms at the top layer is lower at the (0001)S face than the other. If the top layer of the (0001)S face consists of only S atoms, the intensity of ICISS for the (0001)S plane is supposed to decrease sharply to zero at a relatively large  $\alpha$  value compared that for the (0001)Cd plane, as shown by the dotted curve (shadowing effect) (26, 27). Contrary to this, the present experimental result (solid curve) shows that the intensity of ICISS scattered by surface Cd atoms for the (0001)S surface decreased very gradually with the decrease of  $\alpha$ . The difference between experimental and calculated results is shown in Figure 4 as a shaded portion. This means that there are a certain number of Cd atoms at the outermost layer of the (0001)S face. This residual cadmium may be due to either the defect or the step at the surface of the (0001)S plane.

In summary, the (0001)Cd face of a CdS single-crystal ISE was found to respond essentially to  $\text{SH}^- (\text{S}^{2-})$  rather than  $\text{Cd}^{2+}$



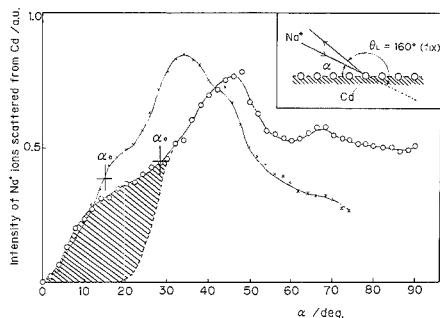


**Figure 4.** ICISS intensity scattered from Cd atoms measured in the [1010] azimuth of (0001)S face (O) and (0001)Cd face (X). The measurements were carried out under the conditions shown schematically in the inset. The intensity of the ICISS spectrum for the (0001)S face was multiplied by 3 so that the comparison between the intensity at the (0001)Cd face and that at the (0001)S face becomes more accurate for smaller values of  $\alpha$  ( $\alpha < 40$ ). The shadowing critical angles calculated ( $2\theta$ ) for the surface without disorder are indicated by crosses. The difference between calculated (---) and experimental (—) values at  $\alpha < \alpha_0$  (shaded portion) is due to Cd atoms exposed as a result of steps and/or sulfur atom defects at the surface.

and the (0001)S face to  $\text{Cd}^{2+}$  rather than  $\text{SH}(\text{S}^{2-})$ . These results were explained by a reversible adsorption/desorption model together with the data for flat-band potentials. ICISS measurements demonstrated the existence of Cd atoms at the (0001)S face and S atoms at the (0001)Cd face, which led to a poor but measurable response of the (0001)S face to  $\text{SH}(\text{S}^{2-})$  and the (0001)Cd face to  $\text{Cd}^{2+}$ . The smaller slope is considered to be due to the failure of co-ion exclusion in the classical ion-exchange mechanism without quantitative treatment (2). The employment of a single-crystal CdS ISE with the adsorption/desorption model makes it possible to treat the response of the ISE to specific ions quantitatively.

#### ACKNOWLEDGMENT

The experimental assistance of M. Kataoka at Department of Chemistry, Hokkaido University, is gratefully acknowledged.

#### LITERATURE CITED

- Buck, R. P. In *Theory, Design, and Biomedical Applications of Solid State Chemical Sensors*; Cheung, P. W., et al., Eds.; CRC Press: Boca Raton, FL, 1978; p 3.
- Buck, R. P. In *Ion-Selective Electrodes in Analytical Chemistry*; Freiser, H., Ed.; Plenum Press: New York, 1978; Vol. 1, Chapter 1.
- Morf, W. E. *The Principles of Ion-Selective Electrodes and of Membrane Transport*; Elsevier: Amsterdam, 1981.
- Lakshminarayanaiah, N. *Membrane Electrode*; Academic Press: New York, 1976.
- Ammann, D.; Morf, W. E.; Anker, P.; Meier, P. C.; Pretsch, E.; Simon, W. *Ion-Sel. Electrode Rev.* **1983**, *5*, 3-92.
- Buck, R. P. In *Ion-Selective Electrodes 4*; Pungor, E., Ed.; Akademiai Kiado: Budapest, 1985; pp 3-34.
- Frant, M. S.; Ross, J. W. *Science* **1966**, *154*, 1553, 1554.
- Van Der Linden, W. E. In *Comprehensive Analytical Chemistry XI*; Svehla, G., Ed.; Elsevier Press: Amsterdam, 1981; Chapter 3, pp 275-392.
- Hulanicki, A.; Trojanowicz, M.; Cichy, M. *Talanta* **1976**, *23*, 47-50.
- Vesely, J. *Collect. Czech. Chem. Commun.* **1971**, *36*, 3364-3369.
- Ross, J. W. In *Ion-Selective Electrodes*; Durst, R. A., Ed.; National Bureau of Standards Special Publication 314; NBS: Washington, DC, 1969; Chapter 2.
- Adametzova, H.; Vadura, R. J. *Electroanal. Chem. Interfacial Electrochem.* **1974**, *55*, 53-58.
- Cammann, K. *Working with Ion-Selective Electrodes*; Springer-Verlag: 1979; p 58.
- Strehlow, W. H.; Smith, D. P. *Appl. Phys. Lett.* **1968**, *13*, 34, 35.
- Wolff, G. A.; Frawley, J. J.; Hietanen, J. R. J. *Electrochem. Soc.* **1964**, *111*, 22-27.
- Warekoi, E. P.; Lavine, M. C.; Mariano, A. N.; Gatos, H. C. J. *Appl. Phys.* **1962**, *33*, 690-696.
- Sullivan, M. V.; Bracht, W. R. J. *Electrochem. Soc.* **1967**, *114*, 295-297.
- Coster, D.; Knol, K. S.; Prins, J. A. Z. *Phys.* **1930**, *63*, 345-369.
- Reynolds, D. C.; Cryzak, S. J. *J. Appl. Phys.* **1960**, *31*, 94-98.
- Zave, R.; Cook, W. R., Jr.; Shiozawa, L. R. *Nature* **1961**, *189*, 217-219.
- Harsanyi, E. G.; Toth, K.; Pungor, E.; Ebel, M. F. *Microchim. Acta* **1967**, *11*, 177-186 and references therein.
- Kellner, R.; Zippel, E.; Pungor, E.; Toth, K.; Lindner, E. *Fresenius' Z. Anal. Chem.* **1987**, *328*, 464-468.
- Buck, T. M. *Methods of Surface Analysis*; Czanderna, A. W., Ed.; Elsevier Press: Amsterdam, 1975.
- Taglauer, E.; Heiland, W. *Appl. Phys.* **1976**, *9*, 261-275.
- Heiland, W. *Appl. Surf. Sci.* **1982**, *13*, 282-291.
- Aono, M.; Souda, R. *Jpn. J. Appl. Phys.* **1985**, *24*, 1249-1262.
- Aono, M. *Nucl. Instrum. Methods Phys. Res.* **1984**, *B2*, 374-383.
- Myrtilin, V. A.; Pleskov, Yu. V. *Electrochemistry of Semiconductors*; Plenum Press: New York, 1967.
- Morrison, S. R. *Electrochemistry at Semiconductor and Oxidized Metal Electrodes*; Plenum: New York, 1980.
- Ellis, A. B.; Bots, J. M.; Wrighton, M. S. J. *Electrochem. Soc.* **1977**, *124*, 1603-1610.
- Fresse, K. W., Jr.; Confield, P. G. J. *Electrochem. Soc.* **1984**, *131*, 2614-2618.
- Minoura, H.; Tsukui, M.; Oki, T. *Bar. Bunsen <<hpGes. Phys. Chem.* **1977**, *81*, 588-592.
- Minoura, H.; Watanabe, T.; Oki, T.; Tsukui, M. *Jpn. J. Appl. Phys.* **1977**, *16*, 865-866.
- Ginley, D. S.; Butler, M. A. J. *Electrochem. Soc.* **1978**, *125*, 1968-1973.
- Feiner, A. S.; McEvoy, A. J.; Infelta, P. P. *Surf. Sci.* **1987**, *189/190*, 411-419.
- Bockris, J. O'M.; Reddy, A. K. N. *Modern Electrochemistry*; Plenum: New York, 1970; Vol. 2.
- Licht, S.; Marou, V. J. *Electroanal. Chem. Interfacial Electrochem.* **1986**, *210*, 197-204.
- Smith, D. P. *Surf. Sci.* **1971**, *25*, 171-191.

Kohei Uosaki  
Yasuyuki Shigematsu  
Hideaki Kita  
Yoshio Umezawa\*

Department of Chemistry  
Faculty of Science  
Hokkaido University  
Sapporo 060, Japan

Ryutarou Souda  
National Institute for Research in Inorganic Materials  
Namiki, Tsukuba 305, Japan

RECEIVED for review September 13, 1988. Revised manuscript received January 3, 1989. Accepted June 6, 1989. This work was partially supported by the Ministry of Education, Science and Culture.

## Pseudo Molecular Ions in Ion Trap Detector Electron Impact Mass Spectra: Practical Consequences

Sir: Self chemical ionization (self-CI) (1) and space charge effects (2) have been proposed as alternative explanations for the occurrence of pseudo molecular ions,  $(M + 1)^+$ , in ion trap

detector (ITD) electron impact (EI) mass spectra. From a practical point of view, however, there is a more fundamental question. Does the formation of pseudo molecular ions, for

whatever reason, compromise the utility of the ITD as a tool for routine gas chromatography/mass spectrometry (GC/MS) analysis?

We have recently used a Finnigan-MAT ITD-800 (Revision 3.15 software) coupled to a Carlo Erba 4160 gas chromatograph for the routine analysis of natural triglycerides after transesterification to form the fatty acid methyl ester derivatives (3). Such long chain fatty acid esters have earlier been used as model compounds to study self-CI effects in Fourier transform mass spectrometers (4) where, like the ion trap, ions are held for a given time before analysis. We therefore felt that fatty acid methyl esters would provide a good test of potential interference from pseudo molecular ions on the analytical capabilities offered by the ITD.

For ITD spectra of methyl stearate, a typical long chain fatty acid ester, run in the EI mode, we observed: (a) full scan spectra from as little as 2  $\mu$ g of analyte entering the ion trap; (b) a steady increase of the pseudo molecular ion with increasing sample quantity for sample levels >10 ng: in a 225-ng spectrum,  $(M + 1)^+$  at  $m/z$  229 was the base peak; (c) statistically similar values of library comparison parameters for a given sample size whether ITD spectra of methyl stearate or literature EI spectra from a variety of conventional mass spectrometers were used as library reference spectra; (d) no statistically significant change in values of library comparison parameters, even at sample levels where the pseudo molecular ion became the base peak.

Using an ITD library of fatty acid methyl ester EI reference spectra which we created from pure standards, we have been able to routinely analyze fatty acid methyl ester mixtures from lipids of both animal and vegetable origin, including human milk and blood plasma lipids. Generally, target compounds

are identified in rank 1 of the library hit list, and a combination of GC retention data with the mass spectrum systematically gives an unambiguous identification.

We conclude that even in conditions where self-CI or another phenomenon leads to the formation of pseudo molecular ions in ITD EI mass spectra, these still retain enough EI character to be readily recognizable by library algorithms. The ITD offers the sensitivity and selectivity required for routine GC-MS analysis of fatty acid methyl esters over a  $10^4$ - $10^5$  dynamic range. Although of theoretical interest, pseudo molecular ions in the ITD would appear to be of little practical detriment to the analyst and may even be advantageous in providing "molecular ion" information (5).

#### LITERATURE CITED

- (1) Eichelberger, J. W.; Budde, W. L. *Biomed. Environ. Mass Spectrom.* **1987**, *14*, 357-362.
- (2) Eichelberger, J. W.; Budde, W. L.; Silvon, L. E. *Anal. Chem.* **1987**, *59*, 2732-2734.
- (3) Horman, I.; Traitter, H.; Aeschlimann, J.-M. *J. High Res. Chromatogr.* **1989**, *12*, 308-315.
- (4) Gihaderi, S.; Kulkarni, P. S.; Ledford, E. B., Jr.; Wilkins, C. L.; Gross, M. L. *Anal. Chem.* **1981**, *53*, 428-437.
- (5) Olson, E. S.; Diehl, J. W. *Anal. Chem.* **1987**, *59*, 443-448.

Ian Horman\*  
Helmut Traitter

Nestlé Research Centre  
Nestec Ltd.  
Vers-chez-les-Blanc  
CH-1000 Lausanne 26  
Switzerland

RECEIVED for review April 10, 1989. Accepted June 13, 1989.

## Optical Resolution of Enantiomers with Chiral Mixed Micelles by Electrokinetic Chromatography

*Sir:* Hydrophobic interactions contribute principally to substrate binding in enzymes and to the self-association of surfactants in micelles (1, 2). This paper reports the recognition of molecular chirality based on hydrophobic entanglement of enantiomers with chiral mixed micelles. Many micellar enzyme models, particularly chiral imidazole catalysts in the presence of surfactant micelles for affecting the hydrolysis of enantiomeric substrates (3-8), have been investigated for greater clarification of the nature of enzyme reactions. Hydrophobic substrate binding to micellar systems is essential for their enantioselective hydrolysis. A comicellar system composed of chiral surfactants with L-amino acid residues and sodium dodecyl sulfate (SDS) was found to vary in its binding affinity to enantiomeric amino acid derivatives, thus becoming a means for their optical resolution. This was confirmed by using the electrokinetic capillary chromatography devised by Terabe et al. (9-15), which provides a sophisticated means for assessing micellar enantioselectivity without any solid support to hold the stationary liquid phase in place. In capillary zone electrophoresis, metal-chelate complexation using a chiral copper(II)-aspartylphenylalanine methyl ester has been successfully applied to the resolution of enantiomeric dansylated amino acid mixtures (16). The chiral recognition discussed here is primarily based on hydrophobic entanglement of amino acid derivatives with the micellar interior core.

There are numerous reports on enantioselective hydrophobic entanglement that accompanies the formation of the inclusion complex, i.e., mutual hydrophobic binding of a solute to a chiral molecular cavity such as that of cyclodextrin (17-21). In such a case, there may be enantioselectivity by which a solute becomes bound by hydrogen bonds to hydroxy groups at the rim of a cyclodextrin cavity. Chiral recognition of enantiomers is possible when a chiral hydrogen-bonding functionality, such as an amide unit induced from an optically active amino acid, becomes embodied in the micellar hydrophobic core to entangle enantiomers. This was achieved by the comicellization of *N*-dodecanoyl-L-amino acid sodium salts as chiral surfactants and SDS. Enantioselective interactions between the chiral comicelle and solute should thus be incapable of a tight fit, as seems to be the case in the inclusion complex.

#### EXPERIMENTAL SECTION

**Synthesis of Sodium *N*-Dodecanoyl-L-valinate (SDVal).** *N*-Dodecanoyl-L-valine was prepared from L-valine by treatment with the dodecanoic acid *N*-hydroxysuccinimide ester (mp 87 °C; lit. (22) mp 75 °C) according to a procedure of the literature (21): mp 103-105 °C (recrystallized from ethyl acetate),  $[\alpha]_D^{26} = -2.6^\circ$  ( $c = 1.00$ , methanol). This carboxylic acid was then converted to the corresponding sodium salt by methanolic sodium hydroxide; the slightly residual carboxylic acid was extracted with acetone by the Soxhlet apparatus.

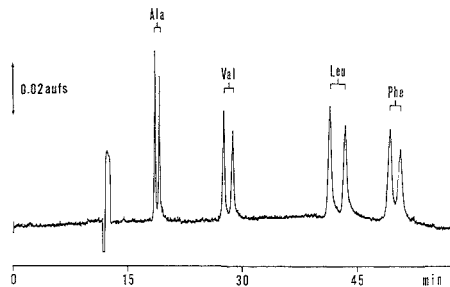


**Figure 1.** Optical resolution of a mixture containing four enantiomeric pairs of amino acids as their *N*-(3,5-dinitrobenzoyl) *O*-isopropyl ester derivatives in electrokinetic capillary chromatography. Chromatographic conditions: column, fused silica tubing 40 cm in length (50  $\mu\text{m}$  i.d.) for effecting the separation; micellar solution, 0.0125 M SDVal and SDS each in 0.025 M borate–0.05 M phosphate buffer (pH 7.0) containing 10% (v/v) methanol; samples, 2.5% methanol solution in each solute; total applied voltage, ca. 10.5 kV; current, 26  $\mu\text{A}$ ; detection, UV at 254 nm; temperature, ambient (ca. 20  $^{\circ}\text{C}$ ). The  $k'$  of the first-eluted D enantiomer and  $\alpha$  for each derivative are as follows:  $k'_{\text{D}}$  0.79 ( $\alpha$  1.09) for the alanine,  $k'_{\text{D}}$  1.97 ( $\alpha$  1.09) for the valine,  $k'_{\text{D}}$  4.38 ( $\alpha$  1.10) for the leucine, and  $k'_{\text{D}}$  6.24 ( $\alpha$  1.06) for the phenylalanine derivatives.

**Chromatographic Procedure.** Electrokinetic capillary chromatography was performed according to Terabe et al. (9, 10). The capillary column consisted of a fused silica tubing 64 cm in length (situated 40 cm from the detection cell, 50- $\mu\text{m}$  i.d. and 375- $\mu\text{m}$  o.d.; Gasukuro Kogyo, Inc.). A regulated dc power supply delivering a maximal 25 kV (Model HEL-25R0.1-TYU; Matsuda Precision Devices, Otsu, Japan) provided high voltage between the ends of the column filled with a chiral comicellar solution. The chromatography was carried out at a constant electric current of 26  $\mu\text{A}$ . The elution of a solute injected at the positive end of the column was monitored by on-column UV detection (254 nm) through a slit of 0.05  $\times$  3 mm at the negative end. SDS (Tokyo Kasei) was recrystallized from ethanol prior to use. Chiral comicellar solutions were prepared by dissolving equimolar amounts of the chiral surfactant and SDS in the borate–phosphate buffer (pH 7.0) solution consisting of 0.025 M sodium tetraborate and 0.05 M sodium dihydrogen phosphate solution. In all cases, the micellar solution was filtered through a 0.45  $\mu\text{m}$  pore membrane filter and degassed in an ultrasonic bath for 3 min.

The capacity factor ( $k'$ ) for a solute was calculated as follows (9, 10):

$$k' = (T_{\text{R}} - T_0) / [T_0(1 - (T_{\text{R}}/T_{\text{MC}}))] ]$$

where  $T_{\text{R}}$  is the retention time of the solute,  $T_0$  that determined with methanol as the solute unsolubilized into a micelle, and  $T_{\text{MC}}$  that with Sudan III as the solute completely solubilized into a micelle. Sudan III indicates migration of the micellar phase, i.e., a capacity factor of infinity.

**Fluorescence Measurements in Microenvironmental Polarity.** Steady-state fluorescence spectra were obtained with a Hitachi 650-60 spectrometer, using an excitation and emission slit width of 5 nm. Emission intensity was measured during excitation at 337 nm and at both 373 and 383 nm, using pyrene (Tokyo Kasei; recrystallized from ethyl acetate) as the probe in SDVal–SDS mixtures dissolved in the borate–phosphate buffer solution.

## RESULTS AND DISCUSSION

It was possible by use of a comicellar system consisting of equimolar amounts of sodium *N*-dodecanoyl-L-valinate (SDVal) and SDS to effectively bring about the enantiomeric resolution of *N*-3,5-dinitrobenzoylated amino acid isopropyl esters, as shown in Figure 1. The negatively charged micellar phase migrates at a velocity slower than that of the aqueous phase toward the negative end of the column, since the electroosmotic velocity of the aqueous phase is much greater than the electrophoretic velocity of the micelle in the opposite

direction. The separation is thus based on distribution processes between two phases. The 3,5-dinitrobenzoyl derivatives provided the most effective resolution for all examined solutes containing the corresponding 4-nitrobenzoyl and benzoyl derivatives. Among the different amino acid derivatives used, the alanine derivatives were the least hydrophobic and thus eluted first. When a comicellar solution of 0.1 M (total concentration) was used, the capacity factor of the first-eluted D enantiomer ( $k'_{\text{D}}$ ) and separation factor ( $\alpha$ ) between enantiomers for each derivative were as follows:  $k'_{\text{D}}$  7.42 ( $\alpha$  1.12) for the 3,5-dinitrobenzoyl,  $k'_{\text{D}}$  5.76 ( $\alpha$  1.05) for the 4-nitrobenzoyl, and  $k'_{\text{D}}$  3.59 ( $\alpha$  1.05) for the benzoyl derivative. Decreasing the micellar total concentration from 0.1 to 0.025 M led to a smaller  $k'$  and virtually constant  $\alpha$  values for these derivatives. The  $k'_{\text{D}}$  and  $\alpha$  values observed for the 3,5-dinitrobenzoylalanine derivative were 1.19 and 1.11, respectively, in 0.025 M solution. In contrast, the corresponding phenylalanine derivative was the most hydrophobic and thus had the largest  $k'_{\text{D}}$  value of 13.07, but its resolution even in the 0.025 M solution was poor. In electrokinetic chromatography, the resolution ( $R_s$ ) is very much dependent on  $k'$  of the solute, as has been reported by Terabe et al. (10), and a large  $k'$  value is unfavorable for obtaining good resolution. Resolution of the enantiomeric mixtures was improved by adding methanol to the comicellar solution at 5–10% (v/v) (15), leading to a greater total elution range, as is evident from the values of  $T_0/T_{\text{MC}}$  (10). With the 0.025 M comicellar solution, an increase in the organic modifier concentration decreased  $T_0/T_{\text{MC}}$  from 0.20 in the absence of methanol to 0.10 in 10% (v/v) methanol. This corresponded to a decrease in  $k'$  of the enantiomers and an increase in resolution ( $R_s$ ), as was noted in particular for the phenylalanine derivative with the largest retention.

In the elution order of the amino acid derivatives resolved, the D enantiomer eluted faster than the corresponding L enantiomer in all cases, indicating that the chiral comicelle binds to the L enantiomer having the same configuration as its chiral component to a greater extent than the D enantiomer. Such a difference in binding capacity has been reported in kinetic measurements in the enantioselective hydrolysis of enantiomeric *N*-acyl amino acid esters using a cationic comicellar system containing *N*-acyl-L-histidine; the binding constant for the L enantiomer was less than that of the corresponding D enantiomer (3). This finding is at variance with our observations.

The critical micelle concentration (cmc) of the comicellar system was determined at  $2 \times 10^{-3}$  M by using the intensity ratio of pyrene fluorescence peaks at 383 nm ( $I_{383}$ ) relative to that at 373 nm ( $I_{373}$ ), which reflected the micropolarity around pyrene as a probe (23). The intensity ratio ( $I_{383}/I_{373}$ ) increased from 0.69–0.70 (in the borate–phosphate buffer solution, 0.68) to 1.10–1.11 at cmc and remained virtually constant above cmc owing to the solubilization of pyrene in the interior core of the comicelle. This comicellar micropolarity was lower than that observed for the SDS micelle in the borate–phosphate buffer solution (1.00–1.03). The smaller extent of water penetration into the chiral comicelle than into the SDS micelle (22) may be the explanation for this. Thus possibly, the comicellar system may provide a favorably ordered medium for hydrogen bonding with the solute enantiomers since chiral recognition of the enantiomers should be induced, at least to some degree, by hydrogen bonding between the chiral surfactant and the enantiomers in the shallow hydrophobic region, near the Stern layer, in which hydrogen bonding sites exist. The addition of methanol to the comicellar solutions resulted in no change, as expected, in the micropolarity of the interior core. The intensity ratio of pyrene fluorescence peaks appeared essentially constant ( $I_{383}/I_{373} =$

1.10-1.12) at 0-20% (v/v) methanol. This appears to support the notion that water soluble alcohols predominantly dissolve in the water phase, causing the aggregation number of a surfactant to change according to the alcohol concentration (24). Thus, the main effect of an organic modifier may be to change micellar size, as well as electroosmotic flow, as suggested by Gorse et al. (15).

We are now examining better chiral surfactants containing SDVal congeners and *N*-acyldipeptide sodium salt. The results will be presented in detail in the near future.

#### ACKNOWLEDGMENT

We are greatly indebted to Shigeru Terabe for his valuable suggestions in setting up the electrokinetic capillary chromatographic apparatus.

#### LITERATURE CITED

- (1) *Surfactant Systems*; Attwood, D., Florence, A. T., Eds.; Chapman and Hall, Ltd.: New York, 1985.
- (2) *Ordered Media in Chemical Separations*; Hinze, W. L., Armstrong, D. W., Eds.; ACS Symposium Series 342; American Chemical Society: Washington, DC, 1987.
- (3) Ueoka, R.; Murakami, Y. *J. Chem. Soc., Perkin Trans. 2* **1983**, 219.
- (4) Ihara, Y.; Hosaka, R.; Nango, M.; Kuroki, N. *J. Chem. Soc., Perkin Trans. 2*, **1983**, 5.
- (5) Ihara, Y.; Kunikiyo, N.; Kunimasa, T.; Kimura, Y.; Nango, M.; Kuroki, N. *J. Chem. Soc., Perkin Trans. 2* **1983**, 1741.
- (6) Ueoka, R.; Matsumoto, Y.; Nagamatsu, T.; Hirohata, S. *Tetrahedron Lett.* **1984**, 25, 1363.
- (7) Kim, G.-C.; Cho, I. *J. Org. Chem.* **1988**, 53, 5187.
- (8) Ueoka, R.; Matsumoto, Y.; Moss, R. A.; Swarup, S.; Sugii, A.; Harada, K.; Kikuchi, J.; Murakami, Y. *J. Am. Chem. Soc.* **1988**, 110, 1588.
- (9) Terabe, S.; Otsuka, K.; Ichikawa, K.; Tsuchiya, A.; Ando, T. *Anal. Chem.* **1984**, 56, 111.
- (10) Terabe, S.; Otsuka, K.; Ando, T. *Anal. Chem.* **1985**, 57, 834.
- (11) Otsuka, K.; Terabe, S.; Ando, T. *J. Chromatogr.* **1985**, 348, 39.
- (12) Terabe, S.; Utsumi, H.; Otsuka, K.; Ando, T.; Inomata, T.; Kuze, S.; Hanaoka, Y. *HRC CC, J. High Resolut. Chromatogr. Chromatogr. Commun.* **1986**, 9, 666.
- (13) Otsuka, K.; Terabe, S.; Ando, T. *J. Chromatogr.* **1987**, 396, 350.
- (14) Sepaniak, M. J.; Cole, R. O. *Anal. Chem.* **1987**, 59, 472.
- (15) Gorse, J.; Balchunas, A. T.; Swalle, D. F.; Sepaniak, M. J. *HRC CC, J. High Resolut. Chromatogr. Chromatogr. Commun.* **1988**, 11, 554.
- (16) Gozel, P.; Gassman, E.; Michelsen, H.; Zare, R. N. *Anal. Chem.* **1987**, 59, 44.
- (17) Ward, T. J.; Armstrong, D. W. *Chromatographic Chiral Separations*; Zief, M., Crane, L. J., Eds.; Marcel Dekker, Inc.: New York, 1988; p 131.
- (18) Armstrong, D. W.; Yang, X.; Han, S. M.; Menges, R. A. *Anal. Chem.* **1987**, 59, 2594.
- (19) Seeman, J. I.; Secor, H. V.; Armstrong, D. W.; Timmono, K. D.; Ward, T. J. *Anal. Chem.* **1988**, 60, 2120.
- (20) Armstrong, D. W.; Han, Y. I.; Han, S. M. *Anal. Chim. Acta* **1988**, 208, 275.
- (21) Guttman, A.; Paulus, A.; Cohen, A. S.; Grinberg, N.; Karger, B. L. *J. Chromatogr.* **1988**, 448, 41.
- (22) Lapidot, Y.; Rappoport, S.; Wolman, Y. *J. Lipid Res.* **1967**, 8, 142.
- (23) Kalyanasundaram, K.; Thomas, J. K. *J. Am. Chem. Soc.* **1977**, 99, 2039.
- (24) Backlund, S.; Rundt, K.; Birdi, K. S.; Dalager, S. *J. Colloid Interface Sci.* **1981**, 79, 578.

Akira Dobashi  
Tamami Ono  
Shoji Hara\*

Tokyo College of Pharmacy  
1432-1 Horinouchi, Hachioji  
Tokyo 192-03, Japan

Junko Yamaguchi

Gasukuro Kogyo, Inc.  
237-2 Sayamagahara, Iruma  
Saitama 358, Japan

RECEIVED for review February 22, 1989. Accepted June 1, 1989. This research was supported by the Ministry of Education of Japan (Grant-in-Aid for Scientific Research No. 62570973).

## Quantitative Supercritical Fluid Extraction/Supercritical Fluid Chromatography of a Phosphonate from Aqueous Media

*Sir:* There are several problems associated with supercritical fluid extraction (SFE) of analytes from aqueous samples. Water is soluble in CO<sub>2</sub> to approximately 0.3% at supercritical conditions (1). For a dynamic type of extraction where fresh fluid is continually passed over the sample to be extracted, the removal of 0.3% water over time can cause problems such as restrictor plugging and activation of the trapping or chromatographic phase. Aside from these problems should the resulting stream be collected into a nonpolar solvent for further chromatographic analysis, a two-phase system would result. Clearly very little constructive extraction can be realized in this manner since the sample and matrix would simply have been moved from one container to another. Equilibrium static extractions on the other hand, wherein the vessel is pressurized for a time and then analyzed, may be inefficient and slow.

The vast majority of the work that has been reported for SFE of aqueous systems has been performed on large scales such as for wastewater treatment purposes (1-4). Many applications for SFE of aqueous samples at the analytical scale can be envisioned, such as the analysis of pesticides and herbicides from field drainage, municipal wastewater, and drugs/drug metabolites from biological fluids. We, therefore, offer here a preliminary description of an on-line extraction system for performing trace analysis of phosphonates in an

aqueous matrix. To our knowledge, this constitutes the first study of this type reported.

#### EXPERIMENTAL SECTION

The extraction vessel currently in use was acquired from Suprex Corp. (Pittsburgh, PA) and is 1 cm i.d. × 10 cm in length (8 mL volume). The supercritical CO<sub>2</sub> (Scott Specialty Gas, Plumsteadville, PA) was delivered by and subsequent chromatography was done with a Suprex SFC 200 (Suprex Corp., Pittsburgh, PA). The system shown in Figure 1 in the recirculation mode consists of three six-port valves (Rheodyne, Inc., Cotati, CA), a recirculating pump (Micropump, Inc., Concord, CA), extraction vessel, and associated plumbing in a temperature-controlled oven. A three-port switching valve (VICI, Houston, TX) was used to allow for easy conversion of the instrument for conventional SFC analysis. A 1-m length of 100 μm deactivated fused silica was used to interface the extraction apparatus to either a 1.0 mm or 4.6 mm (i.d.) × 250 mm DELTABOND cyanopropyl packed column (Keystone Scientific, Inc., Bellefonte, PA). The results stated herein were obtained with a 20-μL sample loop. The volume of extracted phase was determined to be 6 mL when using 3-mL aqueous samples. Each 20-μL injection represents only 0.3% of the total extracted phase, so that multiple injections could be run on the sample without significantly depleting the extracted phase of analyte. Fourier transform infrared (FT-IR) data were acquired from a Nicolet (Madison, WI) supercritical fluid chromatography/infrared (SFC/IR) interface.

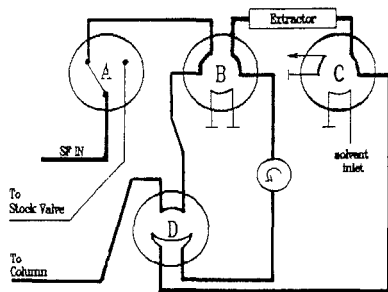


Figure 1. Extraction setup showing the recirculation and injection modes.

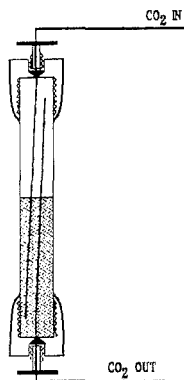


Figure 2. Aqueous extraction vessel.

## RESULTS

The extraction apparatus shown in Figure 1 was designed and built for the purpose of extracting species from aqueous samples for quantitative analysis. The same type of system could be used on a semipreparative or preparative scale for the extraction of products or waste from reaction mixtures. Many of the valves used are extraneous and allow the system to perform many different types of extractions other than the aqueous technique which is described here. There are two points at which the extraction apparatus in Figure 1 differs from existing SFE systems. They are a recirculating pump and the design of the extraction vessel, Figure 2. Once pressurized the extraction system can be isolated to form a loop. The recirculation pump then acts to move the supercritical fluid trapped in the loop. For example, the fluid enters the vessel as shown. It is then brought into intimate contact with the sample and being less dense than water rises in the vessel and exits through a second line. After an appropriate time the extract can be sampled and analyzed via the attached 20- $\mu$ L loop.

Figure 3 shows a comparison of the flame ionization and Gram-Schmidt reconstruction (GSR) (i.e. essentially total infrared absorbance) traces of a supercritical fluid extraction/supercritical fluid chromatography (SFE/SFC) run of 834 ppm diisopropyl methylphosphonate (DIMP) in water. FT-IR detection was used to provide positive identification of the eluting peak as DIMP. The large peak at the beginning of the GSR is due to a relatively small amount of water (carried over with the phosphonate during the extraction)

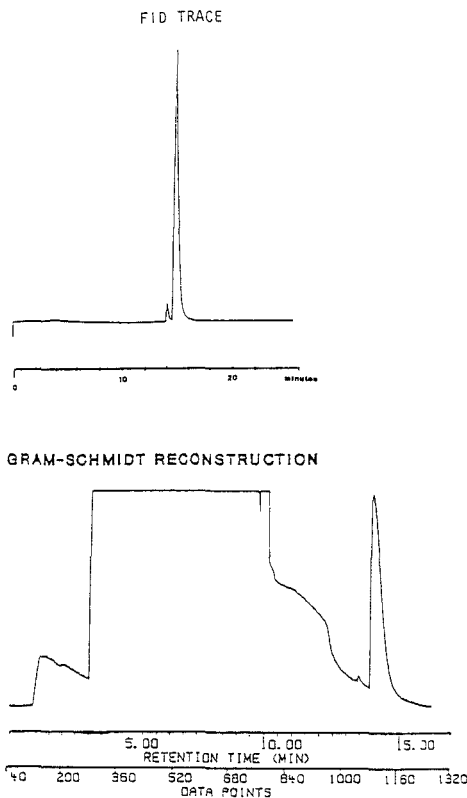


Figure 3. Comparison of FID and GSR traces for SFE/SFC of an 834 ppm solution of DIMP in water, DELTABOND CN column (25 cm) at 100 atm for 10 min ramped to 350 atm in 10 min. The column temperature was 75 °C. Extraction was done at 350 atm for 1 h.

being injected onto the column. The relatively long hold time in the chromatographic pressure program was used to allow the water to completely elute from the column prior to the phosphonate. Figure 4 compares the spectrum of the major eluting peak from SFE/SFC with the spectra of DIMP taken from a standard. At all frequencies the spectra match.

In order to be a useful extraction technique, the method must be fast (less than 30 min). A time study was done to determine the rate of extraction of DIMP from the water. The results are shown in Figure 5. As expected, there is an initial equilibration time where there is a slow increase in the amount extracted with time. After 1.5 h the system reaches equilibrium and there is no change in the SFC/FID area response. However, when 0.1 mg of NaCl is added to the sample before extraction, the equilibration time is reduced to less than 5 min as shown in Figure 5.

A calibration curve was made to determine the viability of the static extraction method as a quantitative technique. The FID response for four concentrations of DIMP in H<sub>2</sub>O was measured. The total analysis time for each concentration was less than 45 min. This time included cleaning and loading of the extraction system, pressurization, extraction of the sample as well as five replicate injections, and SFC analysis of each aliquot. The calibration curve is linear over the range measured (834 ppb to 834 ppm). The relative standard de-

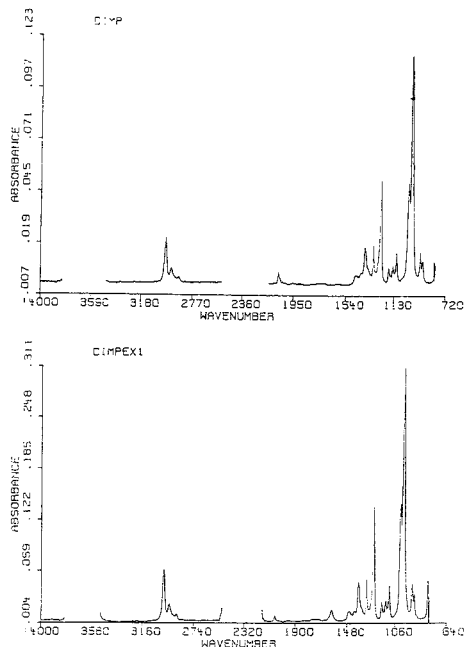


Figure 4. Comparison of spectra for actual DIMP and the major peak from SFE/SFC of aqueous solution (DIMPEX).

viation for peak area is less than 1.5% for concentrations greater than 8.34 ppm and 15% for 834 ppb DIMP.

The technique has also been extended for the qualitative study of various hydrochloride salts of drugs. Figure 6 shows the results of triprolidine hydrochloride analyzed by SFE/SFC. An aqueous solution of the drug was added to 1 mL of tetrabutylammonium hydroxide (TBAH) in the extraction vessel. In the extraction vessel the free triprolidine base was formed and subsequently extracted. Chromatographic separation of the free base from the residual water was then accomplished by eluting with a gradient of CO<sub>2</sub> and methanol-containing TBAH. The qualitative success of SFE/SFC of triprolidine suggests that the technique described may be extended to many relatively polar materials on a quantitative basis.

#### LITERATURE CITED

- (1) Kuk, M. S.; Montagna, J. C. *Chemical Engineering at Supercritical Fluid Conditions*; Paultis, M. E., Penninger, J. M., Gray, R. D., Davison, K. P. Eds.; Ann Arbor Science: Ann Arbor, MI, 1983; pp 101-111.
- (2) Ehntholt, D. J.; Thrun, K.; Eppig, C.; Ringhand, P. J. *Environ. Anal. Chem.* **1983**, *13*, 219-235.

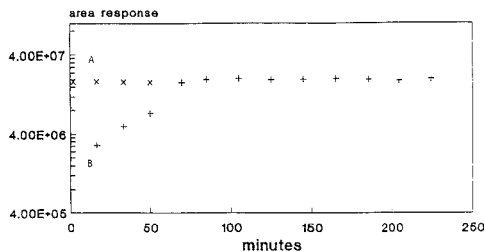


Figure 5. Relative amount of DIMP extracted vs time with (A) and without (B) NaCl added to the aqueous matrix: 100% CO<sub>2</sub>, 350 atm, 50 °C.

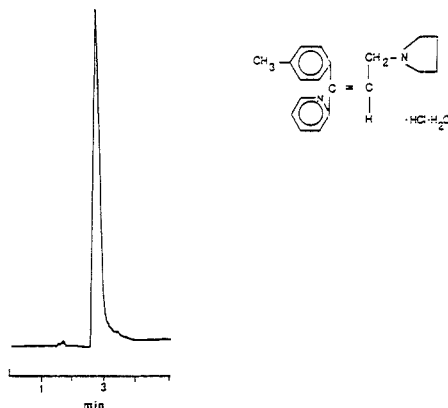


Figure 6. SFE/SFC/UV of 1 mg/mL aqueous solution of triprolidine: extraction, 50 °C, 100% CO<sub>2</sub>, 340 bar; chromatography, DELTABOND CN, 60 °C, 290 nm, 2 mL/min CO<sub>2</sub> and 150 μL/min MeOH/TBAH for 1.0 min then 150 to 450 μL/min in 3.0 min and hold.

- (3) Eckert, C. A.; Van Alsten, J. G.; Stoicos, T. *Environ. Sci. Technol.* **1986**, *20*, 319-325.
- (4) Roop, R. K.; Akgerman, A.; Irvin, T. R.; Stevens, E. K. J. *Supercrit. Fluid* **1988**, *1*, 31-36.

J. Hedrick  
L. T. Taylor\*

Department of Chemistry  
Virginia Polytechnic Institute and State University  
Blacksburg, Virginia 24061-0212

RECEIVED for review April 3, 1989. Accepted June 19, 1989.  
The financial assistance of the Environmental Protection Agency is greatly appreciated.

## TECHNICAL NOTES

### In Situ Laser Activation of Glassy Carbon Electrochemical Detectors for Liquid Chromatography: Demonstration of Improved Reversibility and Detection Limits

Kent Sternitzke and Richard L. McCreery\*

Department of Chemistry, The Ohio State University, 120 West 18th Avenue, Columbus, Ohio 43210

Craig S. Bruntlett and Peter T. Kissinger

Bioanalytical Systems, 2701 Kent Avenue, West Lafayette, Indiana 47906

#### INTRODUCTION

The development of liquid chromatography/electrochemistry (LCEC) provided a very sensitive technique for a variety of redox compounds, many of which are biologically important. The marriage of the separation ability of LC and the selectivity and low detection limits of amperometric flow detectors has made LCEC the method of choice for many neurotransmitters, vitamins, pharmaceuticals, and a variety of other systems (1, 2). With the advent of capillary zone electrophoresis, electrochemical detectors have extended detection limits to femtomole levels, with analytical volumes in the subnanoliter range (3). In addition to the high sensitivity resulting from Faraday's law, LCEC has an additional advantage of variable applied potential. Selectivity beyond that already provided by the chromatographic process may be realized for analytes having different redox potentials. Several technological approaches for exploiting these advantages have been discussed (4-7).

The LCEC experiment is dependent on heterogeneous electron-transfer kinetics at the electrode/solution interface and can be adversely affected by changes in the electrode surface. Kinetic effects in LCEC have two common manifestations in detector sensitivity and stability. First, slow kinetics may result in poor sensitivity for certain analytes. An example of relevance to this report is the oxidation of glutathione (GSH) at carbon electrodes. Slow heterogeneous kinetics require a high oxidation potential at the detector, leading to high background current and poor detection limits. Stated more generally, there is a variety of important redox systems that could be detected with LCEC if their charge-transfer kinetics were more favorable. Second, the sensitivity of an LCEC detector may degrade with time due to electrode passivation, usually by irreversible deposition of solution species or electrolysis products on the electrode surface. The resulting film may inhibit electron transfer and decrease detector response. Selectivity is dependent upon kinetics as well. The ability to resolve analytes at the detector on the basis of redox potential is an important aspect of LCEC (5). Whether the detector sensitivity and selectivity are low because of inherently slow charge-transfer kinetics or because of passivation, a means to improve the electron-transfer rate constant ( $k^0$ ) would be valuable.

Due to several practical advantages such as wide potential range, low background current and desirable mechanical properties, glassy carbon (GC) has been used widely for LCEC. The electron-transfer kinetics of a GC electrode are known to vary greatly with pretreatment history, and several methods have been demonstrated for improving electrochemical kinetics on glassy carbon. These include rigorous polishing

procedures (8-10), flame, inert atmosphere, vacuum, and low-pressure heat treatments (11-13), radio frequency plasmas (14, 15), electrochemical pretreatments (16-24), and laser irradiation (25-28). While any of these may be done prior to cell assembly, the activated surface is sensitive to pollution, and deactivation is likely during cell mounting and startup. Only the last two methods can be carried out in situ during LCEC analysis, thus reducing contamination. Electrochemical pretreatments (ECP) have been developed for LCEC, to result in a repeatable, in situ activation technique (23, 24). It was demonstrated that passivated GC electrodes could be restored repeatedly by using ECP directly in the LCEC cell. A very different approach to activation is exposure of the GC surface to intense laser pulses, also in situ. Not only did laser activation restore passivated GC surfaces, but it also increased  $k^0$  greatly for several redox systems with very slow kinetics (26, 27).

This work was undertaken to address several questions. First, can the advantages demonstrated for laser activation in conventional electrochemical experiments be realized in an LCEC detector? Second, can a passivated LCEC electrode, specifically GC, be renewed in situ with laser activation? Third, can a wider range of analytes be detected with laser-assisted LCEC?

#### EXPERIMENTAL SECTION

Activation was conducted with a Quantel 580-10 Nd:YAG laser, using the same optical arrangement and alignment procedure described previously (26, 27). Unless noted otherwise, three pulses of the Nd:YAG fundamental (1064 nm, 7-10 ns) were employed for activation, and the center of the laser beam covered the entire GC working electrode surface. Three laser pulses were used to average out the significant spatial and pulse-to-pulse variation in laser power density, which was approximately  $\pm 20\%$ . Power densities were determined by dividing average power through a known aperture by the pulse duration, repetition rate, and aperture area.

The electrode was a single 3.2-mm glassy carbon disk in a Kel-F block. A modified Model TL-5A cell (Bioanalytical Systems, West Lafayette, IN) held the working electrode block and Ag/AgCl reference electrode (3 M in NaCl). All potentials reported are relative to this reference electrode. A window was mounted in the cell block across from the working electrode to allow entry of laser light, as shown in Figure 1. All laser activation was conducted in the LCEC cell, with solvent present and flowing. Prior to cell assembly the GC was polished successively with 1.0-, 0.3-, and 0.05- $\mu\text{m}$  alumina and ultrasonicated. The detector unit was a BAS LC-4B potentiostat operated at constant potential, and output from the detector was recorded by a Labmaster analog-to-digital converter (Scientific Solutions, Solon, OH) and IBM PC compatible computer. The working electrode was switched off during laser irradiation to avoid overloading the detector with the large electromagnetic interference and current spikes accompanying laser activation.

\* Author to whom correspondence should be addressed.

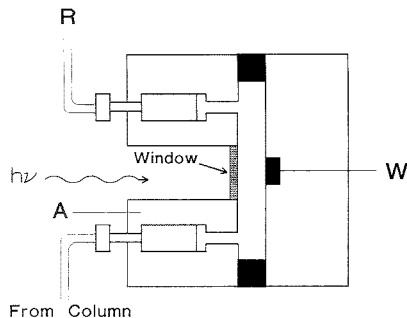


Figure 1. Design of the thin-layer cell used for experiments. See text for details.

An unmodified Model BAS PM-30A pump was used with a 10- $\mu\text{m}$  silica C-18 bonded phase column (Alltech Associates), 25  $\times$  0.46 cm. All separations were isocratic, and injections were made with a 20- $\mu\text{L}$  sample loop. A Teflon tube delivered the column eluent to the cell block mounted in front of the laser on an optical table. Mobile phases were made with NANOpure II water (Sybron Barnstead) and filtered with 0.45- $\mu\text{m}$  membranes (Gelman Scientific). Degassing was performed by bubbling argon through the mobile phase for 20 min prior to use. All chemicals and solvents were of reagent grade and used as received.

### RESULTS AND DISCUSSION

The optical and electrochemical aspects of the apparatus depicted in Figure 1 are very similar to those of previous work on laser activation, with the exception of the thin-layer hydrodynamic cell and high current sensitivity. The most pronounced effect of laser activation on the LCEC response is an increase in the heterogeneous electron-transfer rate constant,  $k^{\circ}$ , particularly for GC electrodes. The effect of improved kinetics on the LCEC chromatogram is an increase in observed peak current for systems exhibiting slow kinetics on unactivated electrodes. The result of increased  $k^{\circ}$  of important to LCEC is detection of redox systems at applied potentials closer to the thermodynamic  $E^{\circ}$ . As will be demonstrated, increased  $k^{\circ}$  provides advantages in selectivity and detection limits.

An example of laser activation for LCEC is shown in Figure 2 for the case of a chromatogram of a mixture of three oxidizable species. At an applied potential of +0.05 or +0.6 V, glutathione (GSH), resorcinol, and 5-hydroxytryptamine (5-HT) exhibit small chromatographic peaks on a conventional GC electrode, due to slow electron transfer. Laser activation significantly improves the peak currents for these systems by improving the electron-transfer rate. At the same time, background has not increased in proportion to signal and settles quickly after laser activation. For unactivated GC, GSH and resorcinol are barely observable above background but exhibit well-defined peaks at either +0.5 or +0.6 V after in situ laser activation.

GSH is a tripeptide with a thermodynamic redox potential of -0.57 V vs Ag/AgCl (at pH 7.4;  $E^{\circ}$  is ca. -0.15 V vs Ag/AgCl at pH 0) and should be amenable to oxidative LCEC detection. However, very slow electron-transfer kinetics on GC inhibit oxidation to the disulfide within the available potential range. The potential dependence of the LCEC response for GSH is shown in the hydrodynamic voltammogram (HDV) of Figure 3. The points in Figure 3 are the peak heights for equal amounts of GSH injected at a range of  $E_{\text{app}}$  values. Figure 3, curve B shows that GSH does not oxidize on polished GC, until  $E_{\text{app}}$  is greater than +1.0 V vs Ag/AgCl, with an  $E_{1/2}$  above +1.2 V. In order to obtain a useful LCEC response on unactivated GC, the high  $E_{\text{app}}$  required will lead

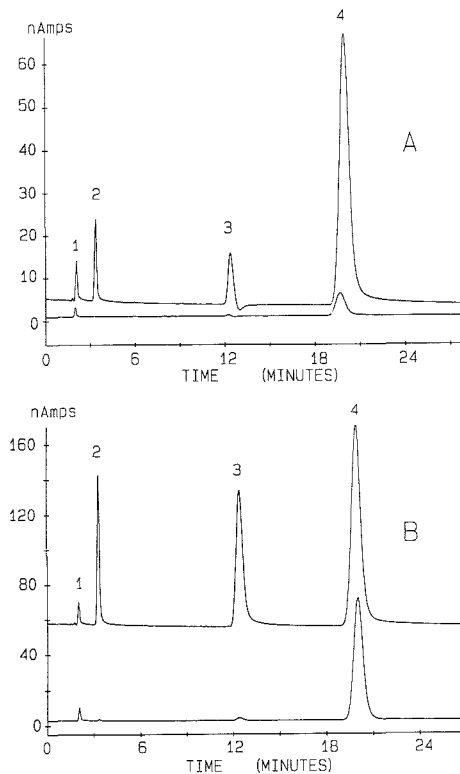


Figure 2. LCEC chromatograms for the separation of glutathione (GSH), resorcinol, and 5-HT after injection of 0.60, 60.0, and 0.60 nmol, respectively. Mobile phase: 0.050 M monochloroacetic acid (MCAA)-methanol (25:1), pH 2.9, flow rate 1.5 mL  $\text{min}^{-1}$ . (A)  $E_{\text{app}}$  +0.50 V; (B) +0.60 V. Lower traces are for polished GC; upper traces were obtained 5 min after three 30 MW  $\text{cm}^{-2}$  laser pulses. Upper trace in Figure 2B was displaced upward by 50 nA for clarity. Peak identities: 1, solvent front; 2, GSH; 3, resorcinol; 4, 5-HT.

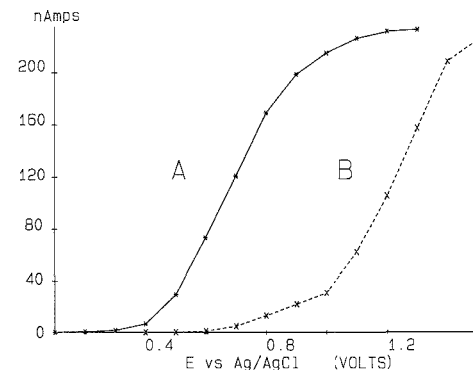
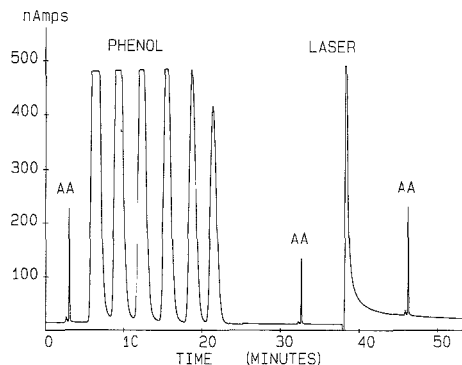


Figure 3. Hydrodynamic voltammograms for the oxidation of glutathione on GC injections of 0.40 nmol in 20  $\mu\text{L}$ . Mobile phase: 0.040 M MCAA-methanol (100:1), pH 2.9, flow rate 1.0 mL  $\text{min}^{-1}$ . A is for three 30 MW  $\text{cm}^{-2}$  pulses applied initially, with one renewal pulse at each potential. B is for conventionally polished GC.

to high background and low signal-to-background ratio. Laser activation leads to a more useful hydrodynamic voltammogram





**Figure 4.** Renewal of an electrode fouled with phenol. Conditions: ascorbic acid injections of 0.20 nmol, phenol 160 nmol; mobile phase, 0.050 M MCAA-methanol (20:1), pH 2.95, flow rate 1.5 mL min<sup>-1</sup>; laser, three 35 MW cm<sup>-2</sup> pulses at 38 min;  $E_{app}$  +0.900 V.

with an  $E_{1/2}$  of +0.76 V vs Ag/AgCl, and thus more easily quantified LC peaks. Although the charge-transfer kinetics are still slow and the  $E_{1/2}$  is still much more positive than the thermodynamic  $E^\circ$ , the electron-transfer rate has been increased to a point where LCEC analysis is tremendously improved. The resulting improvement in the detection limit for GSH is discussed below.

The benefits of laser activation for LCEC applications presented thus far are dependent on improved electron-transfer kinetics. As reported previously, an additional aspect of laser activation is removal of surface films, which may foul solid electrodes. For the case of passivating films produced from phenol oxidation, laser treatment in a conventional cell restored an inactive electrode apparently indefinitely (25). Phenol oxidation results in a passivating film similar to irreversibly adsorbed products that may form from a variety of common analytes and nonelectroactive biomolecules. This film deters the mass transport of some analytes to the electrode surface, or the electron transfer itself. The resulting decreased response to a common analyte and the removal of this passivating film are both demonstrated in Figure 4. Initially, ascorbic acid (AA) exhibits an LCEC response on a laser-activated GC electrode with a peak height of 210 nA. After six injections of large amounts of phenol, the ascorbic acid peak current is reduced to 120 nA. Three laser pulses restored the peak current to 202 nA. This increase in current is due exclusively to film removal since at 0.90 V ascorbic acid is already at its diffusion limit before electrode activation.

As mentioned in the Introduction, the LCEC detector can, in principle, resolve analytes on the basis of their redox potentials, through the use of different applied potentials. For example, AA and dihydroxyphenylacetic acid (DOPAC) have thermodynamic potentials that differ by 0.18 V, with DOPAC more positive. Based on thermodynamic  $E^\circ$ , an LCEC detector operating at 0.3 V vs Ag/AgCl should detect only AA, while one at +0.5 or greater should detect both compounds. Unfortunately, the electron-transfer kinetics for both systems are so slow that their voltammetric peaks are shifted positive by several hundred millivolts, to the point where they severely overlap. As shown by the series of chromatograms in Figure 5A, it is difficult to find an  $E_{app}$  where only one component is detected. If  $E_{app}$  is low enough so DOPAC is not detected, (e.g. +0.3 V), the AA response is greatly diminished. As demonstrated for conventional voltammetry (26), laser activation can greatly improve resolution by increasing  $k^\circ$  to the point where redox systems appear near their thermodynamic potentials. On the laser-activated surface (Figure 5B), AA

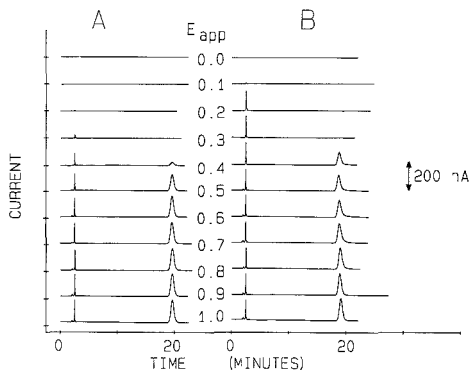


**Figure 5.** Chromatograms of mixtures of AA (0.30 nmol) and DOPAC (1.80 nmol) at various applied potentials. Mobile phase: 0.050 M MCAA-methanol (17:1), pH 2.9, flow rate 1.5 mL min<sup>-1</sup>. (A) polished GC; (B) following three 30 MW cm<sup>-2</sup> laser pulses. Single laser pulses occurred after each chromatogram in series B.  $E_{app}$  values indicated are positive relative to Ag/AgCl.

**Table I.** GSH Detection Limits

$E_{app}$	p-p noise, pA	sensitivity, <sup>a</sup> pA/pmol <sup>b</sup>	detectn lim, pmol <sup>b</sup> ( $S/N = 3$ )
+1.0 V, no laser	18.3	41.5	1.32
+1.5 V, no laser	784	366	6.43
+0.6 V, laser activated	16.5	96.1	0.52
+1.0 V, laser activated	39.5	304	0.39

<sup>a</sup> Determined from five or more injections covering at least an order of magnitude of GSH injection amount. <sup>b</sup> Picomoles of injected GSH.

and DOPAC exhibit  $E_{1/2}$  values that are well separated (by ca. 0.25 V). At an  $E_{app}$  of +0.2-0.3 V on the activated surface, AA exhibits a diffusion-limited response, while the DOPAC peak is negligible. Clearly the activated GC surface permits resolution on the basis of redox potential.

As demonstrated in Figure 3 for GSH, a consequence of increased  $k^\circ$  is detection of redox systems at values closer to their thermodynamic potentials. In the case of GSH, LC detection is feasible at 0.6-0.9 V rather than 1.0-1.3 V vs Ag/AgCl. Since background current from both GC surface oxidation and interferences generally increases with more positive potentials, a higher signal-to-background ratio would be expected at +0.6 than at +1.0 V. The effects of potentials and laser activation on GSH detection limits are listed in Table I. Noise is defined as the peak-to-peak variation in detector response with no peaks eluting; signal is the LC peak height above the average base line. For an unactivated surface, the high  $E_{app}$  required to detect GSH led to higher background and noise, and a relative poor detection limit. With  $E_{app} = 1.0$  V, laser activation increased the noise, but increased the signal by a greater factor, resulting in improved signal-to-noise ratio and a lower detection limit. At +0.6 V, where an unactivated electrode showed negligible response, the laser-activated surface exhibited a significantly lower detection limit than that of the conventional GC electrode operating at higher applied potential. It should be noted that this comparison was carried out with synthetic GSH samples. For actual analytical samples, interferences that may oxidize at high potentials may not appear at +0.6 V. Thus laser activation may reduce contributions to background from oxidizable inter-

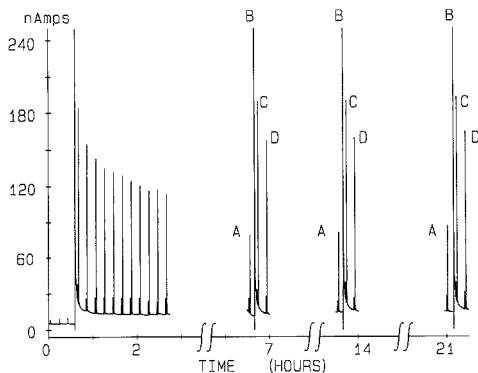


**Figure 6.** Chromatograms showing decay of activation for GSH on GC: injections, 0.40 nmol; mobile phase as in Figure 3. At  $t = 0$ , the electrode was conventionally polished GC. At  $t = 40$  min, 10 30 MW  $\text{cm}^{-1}$  laser pulses were applied. Single renewal pulses were applied at  $t = 6.7, 13.5,$  and  $21.2$  h.  $E_{\text{app}} = +0.800$  V. Peaks are labeled as follows: A, last GSH peak before laser; B, laser pulse; C, first GSH injection after laser; D, second injection after laser.

ferents, as well as improve the signal-to-noise ratio. The principal motivation for the activation of GC toward GSH oxidation is to provide an alternative to mercury film electrodes for GSH in biological materials (29).

The duration and reproducibility of laser activation on LCEC chromatograms were examined in more detail for the case of glutathione on GC. Loss of surface activity would be exhibited in the HDV (similar to Figure 3) as a shift to more positive potential. Deactivation is accelerated by the passage of mobile phase over the electrode surface, presumably because of enhanced mass transport of adsorbates. We observed that loss of surface activity is extremely slow under static conditions in a thin-layer cell. Several factors were observed to affect activation lifetime, including laser power, purity of mobile phases, filtering, and flow rate. Figure 6 shows a series of chromatograms for GSH at four different times after activation. At 0.8 V, the applied potential is below the mass transport limit with or without laser activation and laser activation yields a significant increase in GSH peak height. Although the peak height decays slowly after activation, it may be restored with additional laser pulses, as shown in Figure 6 for a period covering 23 h. Although the GSH peak height decreased by 58% over a 6-h period after activation, it was completely restored by a single laser pulse. Peak heights are reproducible following subsequent activations within the margin of error expected from injection to injection. The laser also induces an increase in background current, which decays to base line. Apparently the background current is due to activation to surface faradaic reactions which are pronounced at 0.80 V. The magnitude of the laser-induced background increase depends on potential and detector sensitivity, with larger backgrounds always appearing at higher potential. For low potential or relatively high analyte concentrations, laser-induced background is negligible, but for very low analyte concentrations, the passivation period following laser treatment was significantly shorter than that following polishing, in some cases a few seconds instead of many minutes. From the practical standpoint, the principal advantage of laser activation is the ability to activate analyte redox processes to a greater extent than background processes.

The longevity of laser activation depends on the redox system being detected, for reasons related to the electron-transfer rate constant. GSH is a case where  $E_{1/2}$  on the activated surface is still far from the thermodynamic  $E^{\circ}$ . Laser

activation increases  $k^{\circ}$  by several orders of magnitude, but the applied oxidation potential for LCEC detection of GSH is still very positive of  $E^{\circ}$ . As activity gradually decreases with time,  $k^{\circ}$  decreases and the peak response is reduced. GSH represents a difficult case where LC response is sensitive to  $k^{\circ}$  and therefore to electrode surface stability. A different situation arises with ascorbic acid, for which the activated  $E_{1/2}$  is close to the thermodynamic  $E^{\circ}$ . For the large  $k^{\circ}$  values exhibited by AA on activated GC, the LC response is not charge-transfer-limited and variations in  $k^{\circ}$  no longer affect LCEC response. After laser activation, the surface must deactivate substantially before charge-transfer kinetics again become a factor and the LCEC response suffers. The practical ramification of this effect is variable sensitivity of different redox systems to the time elapsed after electrode activation. For GSH detected at 1.0 V, the LCEC response decreased by 21% during a 130-min period following laser activation. For AA detected at +0.250 V, the LCEC peak height decreased by less than 5% over a 70-min period, and no decrease was observed for 75 min if  $E_{\text{app}} = +0.450$  V. Thus  $k^{\circ}$  appears to decrease for many systems following laser activation, as would be expected from surface adsorption of impurities. However, the LCEC responses of some systems (e.g. GSH) are more sensitive to  $k^{\circ}$  changes than others, and the charge-transfer-limited systems exhibit the greatest variation with time after activation. Even with these difficult systems, however, electrode activity may be restored by an additional laser activation pulse.

In situ laser activation of LCEC detectors has objectives similar to those of the electrochemical activation methods for GC (16–24) and metal electrodes (30). While electrochemical pretreatments have the advantage of simplicity and low cost, there are fundamental differences in the effects on surface chemistry. Potential pulses applied to Au and Pt electrodes (30) are very effective for a variety of electrocatalytic reactions, but are not applicable to GC because they rely on reversible oxide film formation. The oxidation of GC is a more complex and irreversible process, with the surface of the oxidized GC currently being uncharacterized at the molecular scale (31, 32). Of particular importance to the LCEC application is the potentially high background current observed on oxidized GC, which apparently results from surface redox groups (28). In contrast, laser activation reduces oxides and enhances  $k^{\circ}$  by exposing graphitic edge plane (28, 31). Although the comparative efficacy of laser vs electrochemical activation will be application dependent, it is important to recognize that they are fundamentally different processes.

## CONCLUSIONS

All of the effects of laser activation of GC electrodes used for LCEC result from the enhanced electron-transfer rate following laser treatment. Laser activation is fast and repeatable, and can be carried out in situ without cell disassembly. Enhanced  $k^{\circ}$  permits detection for several example analytes to be conducted at less extreme potentials and may reduce interferences. Although laser activation may increase background current on GC, the increased sensitivity to analyte often more than compensates, and both selectivity and detection limits may be better. For analytes exhibiting high  $k^{\circ}$  on activated GC (e.g. AA), laser activation yields a long-lived improvement in response, while the response for kinetically slow analytes (e.g. GSH) slowly decreases with time. In either case, response can be restored immediately with additional laser pulses. The degree of these improvements will depend on the nature of the analyte, other substances in the sample, and the properties of the mobile phase (pH, solvent, etc.). While not examined here, other electrodes of value for LCEC, such as metals and composite electrodes, may also exhibit improved performance upon laser activation, particularly with

respect to the removal of passivating films. On a final note regarding practicality, the Nd:YAG laser employed for this work is a versatile research laser with high cost compared to that of the LCEC detector. However, initial experiments with a small  $N_2$  laser have demonstrated activation with a much lower cost laser (ca. \$3500).

#### ACKNOWLEDGMENT

We acknowledge Jan Pursely of BAS for valuable advice on chromatographic conditions and crucial equipment repairs.

#### LITERATURE CITED

- Shoup, R. E. In *High Performance Liquid Chromatography*; Academic Press: 1986; Vol. 4, p 91.
- Stuflik, K.; Pacakova, V. *CRC Crit. Rev. Anal. Chem.* **1984**, *14*, 297.
- Knecht, L. A.; Guthrie, E. J.; Jorgenson, J. W. *Anal. Chem.* **1984**, *56*, 479.
- Lunte, C. E.; Kissinger, P. T.; Shoup, R. E. *Anal. Chem.* **1985**, *57*, 1541.
- White, J. G.; St. Claire, R. L.; Jorgenson, J. W. *Anal. Chem.* **1986**, *58*, 293.
- Lavrich, C.; Kissinger, P. T. *Chromatogr. Sci.* **1985**, *32*, 191.
- Roston, D. A.; Shoup, R. E.; Kissinger, P. T. *Anal. Chem.* **1982**, *54*, 1417A.
- Hu, I. F.; Karweik, D. H.; Kuwana, T. *J. Electroanal. Chem. Interfacial Electrochem.* **1985**, *188*, 59.
- Kumau, G. N.; Willis, W. S.; Rusling, J. F. *Anal. Chem.* **1985**, *57*, 545.
- Thornton, D. C.; Corby, K. T.; Spindel, V. A.; Jordan, J.; Robbot, A.; Rustron, D. J.; Gross, M.; Ritzler, G. *Anal. Chem.* **1985**, *57*, 150.
- Stutts, K. J.; Kovach, P. M.; Kuhr, W. G.; Wightman, R. M. *Anal. Chem.* **1983**, *55*, 1632.
- Fagan, D. T.; Hu, I. F.; Kuwana, T. *Anal. Chem.* **1985**, *57*, 2759.
- Wightman, R. M.; Deakin, M. R.; Kovach, P. M.; Kuhr, W. G.; Stutts, K. J. *J. Electrochem. Soc.* **1984**, *131*, 1578.
- Miller, C. W.; Karweik, D. H.; Kuwana, T. *Anal. Chem.* **1981**, *53*, 2319.
- Evans, J.; Kuwana, T. *Anal. Chem.* **1979**, *51*, 358.
- Engstrom, R. C. *Anal. Chem.* **1982**, *54*, 2310.
- Engstrom, R. C.; Strasser, V. A. *Anal. Chem.* **1984**, *56*, 136.
- Wang, J.; Hutchins, L. D. *Anal. Chim. Acta* **1985**, *50*, 1056.
- Moiroux, J.; Elving, P. J. *Anal. Chem.* **1978**, *50*, 1056.
- Falat, L.; Cheng, H. Y. *J. Electroanal. Chem. Interfacial Electrochem.* **1983**, *157*, 393.
- Nonon, F. G.; Fombarlet, C. M.; Buda, M. J.; Pujol, J. F. *Anal. Chem.* **1981**, *53*, 1386.
- Wang, J. *Anal. Chem.* **1981**, *53*, 2280.
- Wang, J.; Tuzhi, P. *Anal. Chem.* **1986**, *58*, 1787.
- Wang, J.; Lin, M. S. *Anal. Chem.* **1988**, *60*, 499.
- Hershenhart, E.; McCreery, R. L.; Knight, R. D. *Anal. Chem.* **1984**, *56*, 2256.
- Poon, M. J.; McCreery, R. L. *Anal. Chem.* **1986**, *58*, 2745.
- Poon, M. J.; McCreery, R. L. *Anal. Chem.* **1987**, *59*, 1616.
- Poon, M. J.; Engstrom, R. C.; McCreery, R. L. *Anal. Chem.* **1988**, *60*, 1725.
- Allison, L. A.; Shoup, R. E. *Anal. Chem.* **1983**, *55*, 8.
- Neuburger, G. C.; Johnson, D. C. *Anal. Chem.* **1987**, *59*, 203.
- Bowling, R. J.; Packard, R. T.; McCreery, R. L. *Langmuir* **1989**, *5*, 683.
- Kepley, L. J.; Bard, A. J. *Anal. Chem.* **1988**, *60*, 1459.

RECEIVED for review December 30, 1988. Accepted May 1, 1989. This work was supported by the Air Force Office of Scientific Research and the donors of the Petroleum Research Fund, administered by the American Chemical Society.

## Diffusion Apparatus for Trace Level Vapor Generation of Tetramethyllead

P. R. Fielden\* and G. M. Greenway<sup>1</sup>

Department of Instrumentation and Analytical Science, UMIST, P.O. Box 88, Manchester M60 1QD, U.K.

The generation of vapor standards and measurement of the diffusion coefficients of vapors is an important aspect of the development and calibration of methods for trace vapor analysis in atmospheres. Dynamic vapor generation systems can be based on a wide range of production methods such as gas stream mixing (1), injection methods, evaporation and chemical reactions (2), permeation devices (3), diffusion apparatus (4), electrolytic methods (5), and gas-phase titrations (6).

The toxicity of the compound must be considered when deciding which method should be employed. Usually for toxic compounds the vapor standards required will be of very low concentrations. In this work vapor samples of tetramethyllead (TML) were prepared near the Occupational Exposure Limit of 0.15 mg m<sup>-3</sup> (7). Permeation devices and diffusion apparatus are the most appropriate methods for the production of low vapor concentrations; however permeation devices are difficult to develop and construct for toxic compounds because of their basic design (8). Diffusion apparatus provides a simple method for preparing mixtures of vapor-containing atmospheres and determining diffusion data (4).

The apparatus works by maintaining the liquid phase of a vapor in a reservoir which is kept at constant temperature. The liquid is then allowed to evaporate and the vapor diffuses through a capillary tube into a flowing gas stream. If the rate of diffusion of the vapor and the flow rate of the diluent gas are known, the vapor concentration in the resultant mixture can be calculated.

More recent designs allow for rapid changes in the concentration of the vapor standards by altering the diffusion path length (9, 10). These methods require syringes or taps to alter the volume of liquid present. This is not suitable for toxic compounds because there is a danger of the pure liquid leaking, and the need for significant volumes of liquid renders such an approach potentially hazardous.

Another important consideration when handling toxic compounds is the method of measuring the diffusion rate. The gravimetric method is not always practicable. Alternatively the diffusion rate can be found by monitoring the position of the liquid meniscus in an open precision capillary tube as a function of time (11). The gradient (X) of a graph of the square of the variation in diffusional path length (l<sup>2</sup>) vs time is given by

$$X = \frac{2DMP}{RT\rho} \ln \left[ \frac{P}{P-p} \right] \quad (1)$$

where  $\rho$  is the density of the liquid at temperature  $T$ ,  $P$  is pressure in diffusion cell at the open end of the capillary (Pa),  $p$  is the partial pressure of the diffusing vapor at temperature  $T$  (Pa),  $M$  is relative molecular mass of the vapor,  $R$  is the gas constant (8.314 J K<sup>-1</sup> mol<sup>-1</sup>),  $D$  is the diffusion coefficient (m<sup>2</sup> s<sup>-1</sup>), and  $T$  is the temperature (K). At a fixed temperature and pressure the diffusion rate can be calculated from

$$S = XA\rho/2l \quad (2)$$

where (S) is rate of diffusion of vapor out of the capillary tube (kg s<sup>-1</sup>), and  $l$  is diffusion path length (m).  $A$  is the cross sectional area of the diffusion tube (m<sup>2</sup>).

<sup>1</sup>Present address: Department of Chemistry, University of Hull, Cottingham Road, Hull HU6 7RX, U.K.

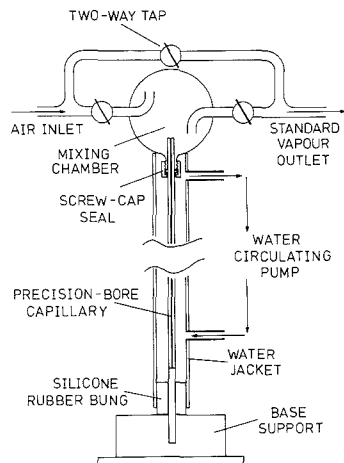


Figure 1. Diagram to show the construction of the diffusion apparatus.

The diffusion rate can be determined at any time from a knowledge of  $X$ ,  $A$ ,  $T$ , and  $l$ . For eq 2 the change in path length ( $l$ ) with time is negligible in comparison to the actual diffusion path length and therefore does not affect results. To obtain precise results, control of the temperature to within  $\pm 0.2$  °C is considered necessary (9). A difference of  $0.4$  °C would cause an error in the diffusion rate of  $0.01 \times 10^{-11}$  kg  $s^{-1}$ . Once the system has been calibrated, the vapor concentration produced can be altered by varying the temperature of the system or by altering the diffusion path length. Sufficient time must be allowed for equilibrium to be obtained after adjustment. Changing the flow rate of the diluent gas will also alter the concentration but should not exceed ca.  $1$  dm<sup>3</sup> min<sup>-1</sup> or turbulence will occur (12), which would reduce the effective diffusion path length. Since the diffusion rate is also governed by the length and diameter of the capillary column, a judicious selection of these parameters will contribute to the range of concentrations that may be obtained.

### EXPERIMENTAL SECTION

**Apparatus.** In the design of the apparatus, eq 1 and 2 were utilized to set the parameters so that a suitable diffusion rate could be obtained. To use the equations, it was necessary to obtain an approximate value for the diffusion coefficient of the compound in question. When this is not readily available in tables, it can be calculated by using (13)

$$D = \frac{0.0043T^{3/2} \left[ \frac{1}{M_A} + \frac{1}{M_B} \right]}{[V_A^{1/3} + V_B^{1/3}]^2 P} \quad (3)$$

where  $M_A$  is molecular mass of vapor,  $M_B$  is molecular mass of diluent gas,  $V_A$  is molal volume of A ( $M_A/\rho$  at boiling point) of vapor (m<sup>3</sup>),  $V_B$  is molal volume of B ( $M_B/\rho$  at boiling point) of diluent gas (m<sup>3</sup>), and  $P$  is total pressure (Pa). An approximate value of  $6.3 \times 10^{-6}$  m<sup>2</sup> s<sup>-1</sup> was calculated for TML by using the available data (the density of TML at 25 °C and the density of nitrogen at its boiling point). This approximation could then be used to construct the apparatus and find the experimental diffusion coefficient.

The apparatus that was constructed is illustrated in Figure 1. The pure tetramethyllead was obtained from Associated Oel (Port Sunlight, U.K.). One end of a precision capillary tube (2 mm i.d.) was sealed and the compound was introduced directly into the capillary bore. This meant the liquid was contained and could only escape up the capillary bore. Introduction was accomplished by a glass syringe with a 60 cm length of poly(tetrafluoroethylene) (PTFE) tube attached which could be passed

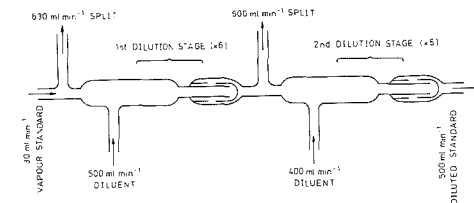


Figure 2. Diagram showing design of the dilution manifold.

down the capillary tube. All glassware was previously silanized with hexamethyldisilazane to prevent loss of sample on the glass walls. The temperature of the system was controlled by enclosing the capillary tube in a water jacket, and a water circulating pump (Churchill, Surrey, U.K.) was used to keep the capillary tube at the required temperature.

When the apparatus was designed, it was necessary to ensure that the drop in the meniscus would be sufficiently large to be monitored. If the system was set up so that there was a diffusion path length of 40 cm and the temperature was 50 °C, then, using eq 3, the theoretical diffusion rate was calculated to be  $4.87 \times 10^{-11}$  kg s<sup>-1</sup>. This value was then used to estimate the drop in meniscus height over an 8-h period. With this diffusion rate,  $1.403 \times 10^{-3}$  g would have diffused from the tube over an 8-h period. The density of TML is  $1.99$  g cm<sup>-3</sup> at 25 °C, so the volume of TML that would be lost from the tube over 8 h is  $7.04 \times 10^{-4}$  cm<sup>3</sup>. With the cross-sectional area of the capillary being  $3.14 \times 10^{-2}$  cm<sup>2</sup>, the drop in the meniscus would be 0.22 mm. This change in meniscus level could be monitored precisely to within  $\pm 5\%$  by using a cathetometer (Precision Instruments, Ltd.), which could be read to  $\pm 0.01$  mm.

**Calibration of the Diffusion Apparatus.** The system was assembled by using the capillary dimensions described in the calculation given above and the temperature was maintained at 50 °C. The diluent gas was air, which was first pumped through a glass microfiber filter tube (grade 10 minifilter, Whatman) to remove particulate matter. A mass flow controller (flow range, 281–1160 cm<sup>3</sup> min<sup>-1</sup>, Brookes, Stockport, U.K.) was utilized to alter the flow rate entering the dilution chamber. The position of the meniscus was then monitored with time. The cathetometer was placed on a stable base as near as possible to the meniscus.

**Dilution of Vapor Standard.** The apparatus used for dilution is shown in Figure 2. Stainless steel valves are often used in gas dilution apparatus but with the very low concentrations that were involved in this experiment, the sample could not be allowed to come in contact with such surfaces. The system was designed so that the sample was only in contact with glass walls that had been silanized previously with hexamethyldisilazane. The dilution occurred in two stages and was achieved by using mass flow controllers, (Brookes, Stockport, U.K.). The errors in this type of system are typically  $\pm 5\%$  (11). At each mixing stage a proportion of the gas flow was removed leaving  $100$  cm<sup>3</sup> min<sup>-1</sup> to dilute, otherwise high flows would have resulted. The flow was split with a mass flow controller, which meant that the amount removed was always constant and not affected by back pressure; an adsorption tube or gas bubbler was required at the end of the system to generate a back pressure or the gas would take the path of least resistance and travel straight out of the open end. The diluent gas flow was also controlled by a mass flow controller, and therefore when all the flow controllers were fixed at the correct values, a known dilution was obtained. These flow controllers were shown to have a maximum error of  $\pm 3\%$  by observing the fluctuations of the float and by taking into account the scale reading errors. The dilution process occurred in the following steps: (i)  $730$  cm<sup>3</sup> min<sup>-1</sup> standard atmosphere entered the dilution apparatus; (ii) split  $630$  cm<sup>3</sup> min<sup>-1</sup> standard atmosphere, leaving  $100$  cm<sup>3</sup> min<sup>-1</sup>; (iii) added  $500$  cm<sup>3</sup> min<sup>-1</sup> air thus diluting by 6; (iv) split  $500$  cm<sup>3</sup> min<sup>-1</sup> diluted standard, leaving  $100$  cm<sup>3</sup> min<sup>-1</sup>; (v) added  $400$  cm<sup>3</sup> min<sup>-1</sup> air thus diluting by 5; (vi)  $500$  cm<sup>3</sup> min<sup>-1</sup> standard atmosphere, which had been diluted 30 times, left the dilution apparatus.

The diluted vapor standard was collected either on adsorption tubes packed with Porapak Q or in a gas bubbler containing nitric

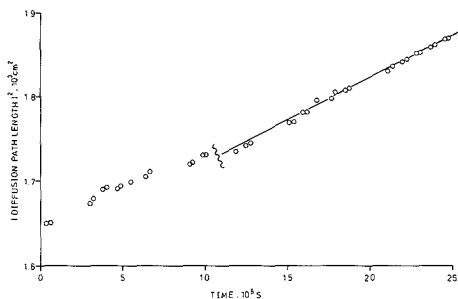


Figure 3. Graph of diffusion path length squared vs time, for determination of the diffusion rate at 50 °C.

acid (70% (w/v)). With the system set up in this manner, a total dilution of 30 was achieved. The system could easily be adjusted to give different dilutions. The baffle mixers incorporated after each split/dilution stage, ensured adequate mixing between the standard vapor and diluent gas. Dilutions of up to 400 times would be possible with two dilution steps.

**Validation of Diffusion Method by Anodic Stripping Voltammetry.** Anodic stripping voltammetry was used for the determination of the lead in the vapor standards because of its inherent sensitivity. For the analysis a static mercury drop electrode was utilized (Model 303 static mercury drop electrode, Princeton Applied Research) with a Ag/AgCl reference electrode. The experiment was controlled by a polarographic analyzer/stripping voltammeter (Model 264, Princeton Applied Research). The instrument was set up as follows: medium drop size; scan rate 5 mV s<sup>-1</sup>; pulse repetition interval 0.2 s; and pulse amplitude 50 mV. Under these conditions, the potential at peak maximum (differential pulse stripping voltammetry mode) for lead was found to occur between -0.67 and -0.73 V vs Ag/AgCl reference electrode.

The system then had to be calibrated for lead determination. For trace analysis in electrochemistry it is essential to use ultrapure water to keep the blank value low. The water was prepared by circulating doubly distilled water through a water purifier containing a mixed bed ion exchange column (Water-I Gelman Sciences, Inc., Ann Arbor, MI) until its resistance was above 18 MΩ. The standards were prepared from lead nitrate (AnalaR Grade, BDH, Dorset) and were made up in the pure water to which nitric acid (70% (w/v) Aristar Grade, BDH, Dorset) had been added (5% (v/v)). A stock solution of 1000 ppm Pb<sup>2+</sup> was prepared from which fresh standards were made daily. The standards were stored in nitric acid washed polythene bottles.

## RESULTS AND DISCUSSION

The results obtained for the calibration of the diffusion apparatus were plotted as a graph of diffusion path length squared vs time (Figure 3). It can be seen from Figure 3 that the precision of the results improves after 1.18 × 10<sup>6</sup> s. After this point to reduce errors due to slight movement of the apparatus, the readings were taken relative to a fixed mark on the capillary tube. The equation for the line after 1.18 × 10<sup>6</sup> s was  $y = 1.02x + 1620$  and the correlation coefficient was 0.998 (the standard deviation of the (y) residuals was 2.7). It was decided to take the gradient of the final part of the line,  $(1.02 \pm 0.01) \times 10^{-8} \text{ m}^2 \text{ s}^{-1}$  (95% confidence limits) where there was greater precision in the readings for the calculation of the diffusion rate from eq 1 and 2. The diffusion rate was found as  $(7.97 \pm 0.14) \times 10^{-13} \text{ kg s}^{-1}$ . The diffusion coefficient was calculated to be  $(1.03 \pm 0.02) \times 10^{-5} \text{ m}^2 \text{ s}^{-1}$ . When the diffusion rate was calculated, care had to be taken to use the correct diffusion path length. This was because the graph covers readings taken over 31 days. The meniscus dropped approximately 1 mm per day and therefore over this time period the diffusion path length would alter considerably (ca. 31 mm). By use of the diffusion coefficient calculated, a difference of

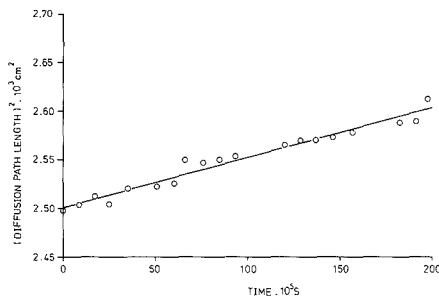


Figure 4. Graph of diffusion path length squared vs time, for determination of the diffusion rate at 30 °C.

1 mm would cause the diffusion rate to alter by  $0.13 \times 10^{-11} \text{ kg s}^{-1}$ . This experiment also showed the stability of the system to be good because the error in the gradient of the line over a 31-day period was only  $\pm 1.5\%$ .

The experiment was repeated with the temperature set at 30 °C, Figure 4. The equation of the line was  $y = 0.52x + 2500$  and the correlation coefficient was 0.981 (the standard deviation of the y residuals was 6.7). The results obtained at this temperature were less precise because it was more difficult to keep the temperature constant to within  $\pm 0.2$  °C and the change in the meniscus level was smaller. The percent relative standard deviation for the gradient at 50 °C was 1.3% compared to 4.5% for 30 °C. The diffusion rate obtained at 30 °C was  $3.26 \times 10^{-11} \text{ kg s}^{-1}$ .

The temperature of the system was returned to 50 °C and the diffusion rate was calculated by using the experimental diffusion coefficient and a diffusion path length of 49.5 cm. The diffusion rate was calculated to be  $(6.44 \pm 0.01) \times 10^{-11} \text{ kg s}^{-1}$ . This meant that when the flow rate of the diluent gas was 730 cm<sup>3</sup> min<sup>-1</sup>, the concentration of TML in air was  $5.3 \pm 0.18 \text{ mg m}^{-3}$ . This concentration is approximately 30 times greater than the occupational exposure limit for TML (0.15 mg m<sup>-3</sup> as lead).

The concentration could be altered by changing the diffusion rate, but this was undesirable as the only easily variable parameter was the diffusional path length, which meant handling the toxic tetramethyllead. A more acceptable solution was the quantitative dilution of the gas standard using the apparatus described. In order to assess the dilution process, the gas standard collected in the bubblers was determined for total lead content by anodic stripping voltammetry. The value obtained by this method was compared with the calculated value.

For analysis, the polarographic conditions were as previously described and the electrode cell was cleaned with dilute nitric acid. A blank of 10 mL of ultrapure water was then run with a supporting electrolyte of 5 μL of Aristar nitric acid. Purging was carried out for 4 min with "oxygen free" nitrogen. This resulted in a low blank signal with less than 10 nA variation in stripping current over the electroactive region for lead. For this initial calibration, 5-μL aliquots of a 100 ppm solution of lead were successively added to the blank and after each addition a run was taken. Figure 5 shows these data as a series of stripping peaks of increasing magnitude. All results were triplicated to check reproducibility (within 2%) and the blank value was subtracted from each result. A linear calibration curve was obtained for 0 to 40 ng cm<sup>-3</sup> and the equation of the line was  $y = 1.04x - 0.4$ ; the correlation coefficient was 0.999 and the standard deviation of the y residuals was 0.43.

Once a suitable calibration curve had been obtained, the vapor standard could be analyzed. TML was collected in concentrated nitric acid. To ensure that no TML was lost,

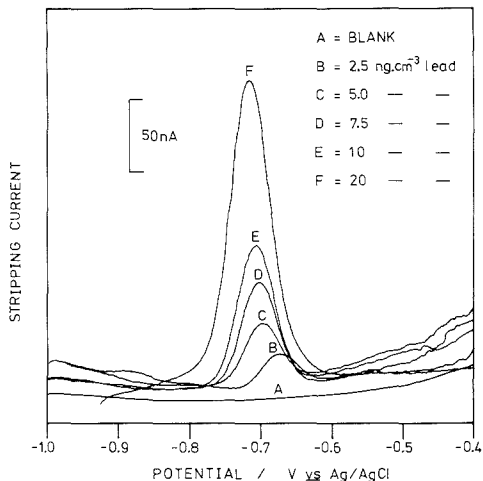
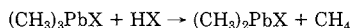
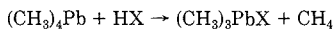


Figure 5. Figure to show the stripping voltammograms obtained for the blank and a series of lead calibration solutions.

three bubblers in series were used to collect it. In each bubbler there was 100 cm<sup>3</sup> of acid. In subsequent determinations most of the lead was found in the first bubbler and none was found in the last bubbler. The nitric acid destroys the TML



Under extreme conditions inorganic lead(II) compounds are formed (14). It is essential that all the organolead be converted to inorganic lead, because anodic stripping voltammetry only detects inorganic lead. After several experiments it was found that all the TML could be converted to inorganic lead by placing it in a sealed digestion vessel, lined with Teflon (Berghol, West Germany) and heating it in an oven at 100 °C for 3 h.

Once it was known that all the lead could be converted to inorganic lead, a sample of the diluted vapor standard could be analyzed. The standard atmosphere was generated with an air throughput of 730 cm<sup>3</sup> min<sup>-1</sup>. After dilution, the sample flow rate through the collection solution was 500 cm<sup>3</sup> min<sup>-1</sup>. A 0.5-cm<sup>3</sup> portion of the sample that had been collected in acid and digested was diluted to 10 cm<sup>3</sup>. This was then determined and the concentration of lead in the acid was found

to be 6.75 ng cm<sup>-3</sup>. The sample had been collected for 5 min and the diffusion rate was 6.44 × 10<sup>-11</sup> kg s<sup>-1</sup>. There was a 30 times dilution before collection of the sample in 100 cm<sup>3</sup> nitric acid. This meant that theoretically there should have been 6.44 ng cm<sup>-3</sup> lead present. The error in the result was therefore 4.8%.

The ASV analysis confirmed that the vapor generator was operating successfully. The stability of the system was also shown to be acceptable with the error in the slope of the calibration curve being 1.5% over 31 days.

## CONCLUSIONS

The apparatus described here is capable of providing very low vapor concentrations of toxic compounds. For this type of apparatus with a diffusion path length of 49.5 cm, a calibration range of approximately 4 mg m<sup>-3</sup> to 10 μg m<sup>-3</sup> TML would be possible at 50 °C. At 30 °C the range would be 2 mg m<sup>-3</sup> to 5 μg m<sup>-3</sup> TML. The equipment ensures that the toxic liquid is safely contained but, rapid production of different vapor concentrations is still possible by gas stream mixing. In using this method the diffusion coefficient of the compound may also be determined without making an extra measurement. Although the system was designed for tetramethyllead, it can be easily adapted to other compounds by altering the appropriate parameters.

Registry No. Tetramethyllead, 75-74-1.

## LITERATURE CITED

- Lucro, D. P. *Calibration in Air Monitoring*, 7; A.S.T.M.S., Special Techniques Publication 568; ASTM: Philadelphia, PA, 1976; p 301.
- Nelson, G. C. *Controlled Test Atmospheres, Principles and Techniques*; Ann Arbor Publishers: Ann Arbor, MI, 1971.
- O'Keefe, A. E.; Ortman, G. C. *Anal. Chem.* **1966**, *38*, 760.
- Fortuin, J. M. *Anal. Chim. Acta* **1966**, *15*, 521.
- Methods for the Preparation of Gaseous Mixtures*; BS4559; British Standard Institution: London, U.K., 1970.
- Selected Methods of Measuring Air Pollutants*; WHO Offset Publication No. 249; World Health Organisation: Geneva, Switzerland, 1976.
- Farmer, D.; Humphrey, J. *Safe to Breathe*; Kingwood Publications Ltd.: 1984; p 78.
- Lucero, D. P. *Anal. Chem.* **1971**, *43*, 1744.
- Barratt, R. S. *Analyst (London)* **1981**, *106*, 187.
- Savitsky, A. C.; Sigga, S. *Anal. Chem.* **1972**, *44*, 1712.
- Desty, D. N.; Geach, C. J.; Goldup, A. *Gas Chromatography*; Butterworth: London, 1960.
- Atschuller, A. P.; Cohen, I. R. *Anal. Chem.* **1960**, *32*, 802.
- Gilliland, E. R. *Ind. Eng. Chem.* **1934**, *26*, 681.
- Willemsens, L. C. *Organolead Chemistry*; International Zinc Research Organisation: New York, 1964.

RECEIVED for review November 30, 1988. Revised May 10, 1989. Accepted May 15, 1989. The authors wish to acknowledge the Occupational Medicine and Hygiene Laboratories of the Health and Safety Executive (Sheffield, U.K.) for supporting this research.

## Preparation of Organic Matter for Stable Carbon Isotope Analysis by Sealed Tube Combustion: A Cautionary Note

Michael H. Engel\* and Rick J. Maynard

School of Geology and Geophysics, The Energy Center, 100 East Boyd Street, The University of Oklahoma, Norman, Oklahoma 73019

### INTRODUCTION

The utilization of sealed tube combustion methods (1, 2) continues to increase in popularity as a more time-efficient and less costly method for the conversion of organic carbon to carbon dioxide for stable carbon isotope analysis. Com-

parisons of dynamic combustion and sealed tube combustion have demonstrated that, with appropriate precautions, both methods provide comparable results (1-3).

In the course of preparing several samples of reference material NBS 22 for stable carbon isotope analyses using sealed tube combustion, it was observed that with increasing elapsed time subsequent to combustion, the δ<sup>13</sup>C values of

\* Author to whom correspondence should be addressed.

these samples became up to 3% lighter (i.e., depleted in carbon-13). In this paper, we report the results of a series of experiments that document this observed carbon isotope depletion effect and suggest a strategy for sample preparation to avoid this problem.

### EXPERIMENTAL SECTION

One hundred eleven samples of NBS 22 (~3  $\mu$ L each) were placed in individual Pyrex tubes (22 cm  $\times$  7 mm i.d.) that contained 5.5 g of copper oxide wire. The tubes and copper oxide were preheated (to 550 and 850  $^{\circ}$ C, respectively) and then cooled to room temperature prior to loading the samples. Next, the tubes were evacuated, sealed, and combusted at 550  $^{\circ}$ C for 2.5 h. Subsequent to combustion, the tubes were stored at room temperature. At various times, ranging from 1 to 274 days after combustion (Table I), several tubes were opened with a tube cracker (4) and the CO<sub>2</sub> gas was cryogenically isolated from the individual tubes for stable carbon isotope analysis as previously described (5). The sampling ampules containing the CO<sub>2</sub> samples were transferred directly to the inlet system of a Finnigan Delta E mass spectrometer for stable carbon isotope analysis. On several occasions some of the sealed tubes were reheated for 2.5 h at 550  $^{\circ}$ C just prior to stable carbon isotope analysis.

It has been speculated that, subsequent to combustion, copper carbonate may precipitate as a surface film via prolonged contact of CO<sub>2</sub> and H<sub>2</sub>O with the copper oxide wire in a sealed tube. Additional experiments were conducted to verify this phenomenon and to evaluate its possible effect on the stable carbon isotope composition of CO<sub>2</sub>. After analysis of the CO<sub>2</sub> gas isolated from the 259 and 274 day old tubes (Table I), the individual copper oxide samples isolated from these tubes were reheated to 550  $^{\circ}$ C. The resultant CO<sub>2</sub> samples were isolated and analyzed for their respective stable carbon isotope compositions as described above. Also, three additional tubes containing NBS 22 and copper oxide wire were combusted and, after being kept at room temperature for 112 days, were pinched in half. The bottom halves, containing gas and copper oxide, and the top halves, containing only gas, were reheated (550  $^{\circ}$ C) prior to the stable isotope analysis of their respective CO<sub>2</sub> components.

Assuming that the observed carbon isotope depletion effect for CO<sub>2</sub> is directly associated with the reaction of CO<sub>2</sub> and H<sub>2</sub>O with the copper oxide wire, an attempt was made to evaluate whether this apparent CO<sub>2</sub> fractionation could be diminished by increasing the volume of the combustion tube. Aliquots of NBS 22 and copper oxide (approximately identical with the amounts used in the above experiments) were placed in 34 cm  $\times$  0.7 mm i.d. Pyrex tubes and combusted as described above. Two of these samples were analyzed for their stable carbon isotope compositions immediately subsequent to combustion. After storage at room temperature for 96 days, the CO<sub>2</sub> gas in 11 of the tubes was analyzed for stable carbon isotope compositions. The copper oxide wire in the bottom half of each tube was resealed while the tube was still under vacuum in the tube cracker and then reheated for 2.5 h at 550  $^{\circ}$ C. The resultant CO<sub>2</sub> was isolated and analyzed as above. Three of the long tubes were reheated just prior to stable isotope analysis of the CO<sub>2</sub> gas.

### RESULTS AND DISCUSSION

Stable carbon isotope values for samples of NBS 22 that were combusted and then stored for 1–274 days prior to analysis are compiled in Table I. The average  $\delta^{13}\text{C}$  value for samples that were stored for up to 22 days prior to analysis was  $-29.80 \pm 0.03\%$ . However, the average  $\delta^{13}\text{C}$  value for samples that were stored for 37–274 days prior to analysis was  $-30.83 \pm 1.0\%$ . The combusted NBS 22 samples that were stored for 274 days prior to analysis were depleted by more than 3% relative to average  $\delta^{13}\text{C}$  values for NBS 22 that have been reported in the literature, i.e.,  $-29.81 \pm 0.06\%$  (3) and  $-29.73 \pm 0.09\%$  (6). Statistical analysis revealed that a linear relationship exists between the stable carbon isotope values of the NBS 22 samples and storage time subsequent to combustion (Pearson's correlation coefficient = 0.98). It is important to note, however, that the average  $\delta^{13}\text{C}$  value for samples that had been stored for up to 259 days, but were

Table I. Stable Carbon Isotope Values for NBS 22 Samples

time elapsed after initial combustn, days	$\delta^{13}\text{C}$ , ‰	$\delta^{13}\text{C}$ , ‰, for samples reheated just prior to anal.
1	$-29.82 \pm 0.04$ (13) <sup>a</sup>	– <sup>b</sup>
2	$-29.85 \pm 0.01$ (3)	–
3	$-29.81 \pm 0.03$ (13)	–
4	$-29.82 \pm 0.02$ (6)	–
5	$-29.81 \pm 0.05$ (3)	–
6	$-29.76$ (1)	–
7	$-29.80 \pm 0.03$ (5)	–
8	$-29.79 \pm 0.03$ (11)	–
10	$-29.85$ (1)	–
12	$-29.77 \pm 0.03$ (3)	–
13	$-29.77 \pm 0.01$ (2)	–
21	$-29.80 \pm 0.04$ (5)	–
22	$-29.83 \pm 0.04$ (2)	–
31	$-30.08 \pm 0.13$ (4)	–
34	–	$-29.82$ (1)
37	$-30.06 \pm 0.15$ (2)	–
39	$-29.92 \pm 0.01$ (2)	–
40	$-30.04 \pm 0.01$ (3)	–
41	$-29.85 \pm 0.01$ (2)	–
46	$-29.99$ (1)	–
55	$-30.36 \pm 0.02$ (3)	–
61	$-30.30$ (1)	–
68	$-30.83 \pm 0.15$ (3)	$-29.83 \pm 0.01$ (2)
69	$-30.87 \pm 0.01$ (3)	$-29.82 \pm 0.01$ (4)
88	$-31.08$ (1)	$-29.81$ (1)
89	–	$-29.85 \pm 0.01$ (2)
259	$-33.27$ (1)	$-29.82 \pm 0.01$ (2)
274	$-33.21 \pm 0.42$ (5)	–

<sup>a</sup> The number in parentheses indicates the number of samples that were analyzed. <sup>b</sup> –, sample not analyzed.

Table II. Stable Carbon Isotope Values for NBS 22 Samples

combustn tube length, cm	time elapsed after initial combustn, days	$\delta^{13}\text{C}$ , ‰	
		CO <sub>2</sub> gas <sup>a</sup>	reheated CuO wire <sup>b</sup>
22	259	$-33.27$ (1)	$-25.98$ (1)
22	274	$-33.21 \pm 0.42$ (5)	$-26.15 \pm 0.21$ (4)
34	1	$-29.84 \pm 0.00$ (2)	–
34	96	$-29.89 \pm 0.05$ (11)	$-24.16 \pm 0.42$ (7)
34	96	$-29.86 \pm 0.02^d$ (3) <sup>e</sup>	–

<sup>a</sup>  $\delta^{13}\text{C}$  value for CO<sub>2</sub> gas present in tube. <sup>b</sup>  $\delta^{13}\text{C}$  value for CO<sub>2</sub> gas that was recovered by reheating the CuO wire. <sup>c</sup> –, sample not analyzed. <sup>d</sup> Sample reheated just prior to stable carbon isotope analysis. <sup>e</sup> The number in parentheses indicates the number of samples that were analyzed.

reheated to 550  $^{\circ}$ C just prior to analysis, was  $-29.83 \pm 0.01\%$  (Table I).

Subsequent to the analysis of the NBS 22 gas samples that were stored for 259 and 274 days, the copper oxide wire that remained in the tubes was resealed under vacuum and heated to 550  $^{\circ}$ C. Whereas the original CO<sub>2</sub> components isolated from these tubes were depleted in carbon-13 relative to NBS 22 samples that were stored for shorter time intervals (Table I), the CO<sub>2</sub> samples recovered by reheating the copper oxide wire were enriched by several parts per mil (Table II). Furthermore, stable carbon isotope analyses of the CO<sub>2</sub> recovered subsequent to the reheating of tubes that were pinched in half revealed that the gas in the top portions of the tubes was depleted in carbon-13 relative to NBS 22 ( $-31.69 \pm 0.41\%$ ) and the gas in the bottom portions of the tubes that remained in contact with the copper oxide was enriched in carbon-13 relative to NBS 22 ( $-28.66 \pm 0.04\%$ ). Assuming that the

observed stable carbon isotope depletion for NBS 22 that occurs with prolonged storage is a consequence of the interaction of the gaseous products of combustion with the copper oxide wire, it is not surprising that an increase in the size (34 cm) of the combustion tubes diminished the isotope depletion effect that was observed for the shorter (22 cm) combustion tubes (Table II).

The synthesis of copper carbonate minerals such as malachite results in an isotope fractionation such that the carbonate carbon becomes enriched in carbon-13 relative to the CO<sub>2</sub> starting material (7). Also, the fact that copper carbonate minerals such as malachite and azurite decompose at 200 and 220 °C, respectively, well below the combustion temperature employed in this study (i.e., 550 °C), lends credence to the hypothesis that (1) the formation of a copper carbonate phase is responsible for the observed isotope depletion of CO<sub>2</sub> with prolonged storage of the NBS 22 samples subsequent to combustion and (2) reheating of older NBS 22 samples prior to stable isotope analysis results in the destruction of this copper carbonate mineral phase and the release of this <sup>13</sup>C-enriched component back into the CO<sub>2</sub> reservoir.

X-ray diffraction analysis of the preheated (850 °C) copper oxide wire indicated that the dominant mineral present was, as expected, tenorite (CuO). X-ray analysis of the wire subsequent to the combustion and storage of NBS 22 samples was apparently not sensitive enough to detect the copper carbonate phase. It was observed, however, that a significant percentage of the tenorite had been converted to cuprite (Cu<sub>2</sub>O), which is at an appropriate oxidation state for the formation of copper carbonate (Cu<sub>2</sub>CO<sub>3</sub>).

In summary, the sealed tube combustion method is rapidly becoming the method of choice for the conversion of organic

matter to CO<sub>2</sub> for stable carbon isotope analysis. Unlike those who use dynamic combustion, scientists who employ static (sealed tube) combustion are typically combusting 30 or more individual samples at a time. As indicated above, the storage of samples for prolonged time intervals (i.e., several weeks) subsequent to combustion will result in δ<sup>13</sup>C values that are depleted by up to 1-3‰ relative to what would have been observed had the samples been analyzed within several days subsequent to combustion. For situations that arise (such as instrument down time) when combusted samples must be stored prior to analysis, it is possible to avoid this problem by isolating the CO<sub>2</sub> gas from the copper oxide wire. A more practical solution, however, is to simply reheat the tubes immediately prior to analysis.

#### ACKNOWLEDGMENT

We thank D. Powell (OU) for performing the X-ray diffraction analyses and Z. Sofer (Amoco Production Co.) for his critical review of this manuscript.

#### LITERATURE CITED

- (1) Stuermer, D. H.; Peters, K. E.; Kaplan, I. R. *Geochim. Cosmochim. Acta* 1978, 42, 989-997.
- (2) Sofer, Z. *Anal. Chem.* 1980, 52, 1389-1391.
- (3) Schoell, M.; Faber, E.; Coleman, M. L. *Org. Geochem.* 1983, 5, 3-6.
- (4) DesMarais, D. J.; Hayes, J. M. *Anal. Chem.* 1976, 48, 1651-1652.
- (5) Bonilla, J. V.; Engel, M. H. *Org. Geochem.* 1986, 10, 181-190.
- (6) Hut, G. Report to Director General, International Atomic Energy Agency; Vienna, 1987, 42 pp.
- (7) Smith, A. W. *Archaeometry* 1978, 20, 123-133.

RECEIVED for review January 24, 1989. Accepted June 1, 1989. We acknowledge the National Science Foundation, Division of Earth Sciences (Grant No. EAR-8352055) for partial support of this research.

## Foam Countercurrent Chromatography of Bacitracin with Nitrogen and Additive-Free Water

Hisao Oka,<sup>1</sup> Ken-ichi Harada,<sup>2</sup> Makoto Suzuki,<sup>2</sup> Hiroyuki Nakazawa,<sup>3</sup> and Yoichiro Ito\*

Laboratory of Technical Development, National Heart, Lung, and Blood Institute, National Institutes of Health, Bethesda, Maryland 20892

Foam separation has long been used for separation of a broad spectrum of samples ranging from metal ions to mineral particles (1). The separation is based on a unique parameter of foaming capacity and/or foam affinity of samples in an aqueous solution and bears a great potential for application to biological samples. Utility of the method in research laboratories, however, has been extremely limited mainly due to a lack of efficient instruments to fully exploit versatility of the method.

Recently, an innovation of the foam separation technology has been achieved by development of foam countercurrent chromatography (CCC), which utilizes a true countercurrent movement between foam and its mother liquid through a long, narrow coiled tube by the aid of a particular mode of planetary motion generated by a coil planet centrifuge (2). Introduction of a sample mixture into the coil results in separation of the

sample components: Foam-active materials quickly move with the foaming stream and are collected through the foam outlet while the rest are carried with the liquid stream in the liquid outlet. The method has been applied to various test samples including ionic compounds collected with suitable surfactants and surface-active proteins separated in a phosphate buffer solution to prevent denaturation of the molecule (2-4).

This paper describes a successful application of the foam CCC technology to chromatographic fractionation of bacitracin complex using nitrogen gas and distilled water entirely free of surfactant or other additives. Bacitracin (BC) is a basic, cyclic peptide antibiotic commonly used as a feed additive of livestock all over the world. It consists of more than 20 components, each with different antimicrobial activities, and chemical structures of these components other than BCs-A and -F are still unknown. Because of its strong foaming activity, BC is an ideal test sample to demonstrate capability and usefulness of the present method.

#### EXPERIMENTAL SECTION

The apparatus used for the present study is a multilayer coil planet centrifuge, which produces a synchronous planetary motion of the gear-driven column holder and has been described pre-

<sup>1</sup> Visiting Scientist from the Aichi Prefectural Institute of Public Health Nagoya, Japan.

<sup>2</sup> Permanent address: Faculty of Pharmacy, Meijo University, Tempaku, Nagoya 468, Japan.

<sup>3</sup> Permanent address: The Institute of Public Health, Tokyo 108, Japan.



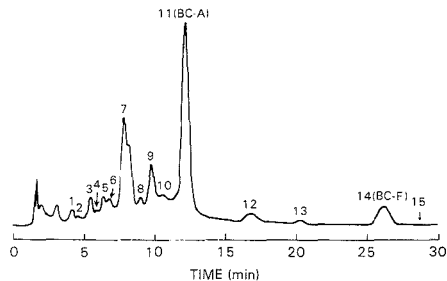


Figure 1. HPLC analysis of bacitracin in the original sample. The experimental conditions are given in the text.

viously (2, 3). Although our prototype was originally designed and fabricated at NIH, the apparatus may be duplicated in a reasonable time period by the following two companies: Pharma-Tech Research Corp., Baltimore, MD, and P.C., Inc., Potomac, MD. Also, interested readers may try to use their commercial high-speed CCC models with a 10 cm revolutionary radius by modifying the column holder and the separation column.

Separation was initiated by simultaneous introduction of distilled water at a flow rate of 3.2 mL/min from the tail and nitrogen gas pressured at 80 psi from the head into the rotating coil at 500 rpm while the needle valve on the liquid collection line was fully open (13.5 turns). After a steady-state hydrodynamic equilibrium was reached, the pump was stopped and 0.5 mL of a sample solution containing bacitracin (Sigma Chemical Co., St. Louis, MO), 1% (w/v) in distilled water, was injected through the sample port. After a standing time of 5 min, the opening of the needle valve was adjusted (0.8 turn) to bring the volume ratio of foam and liquid fractions to 1:5–6, and the pumping resumed at 3.2 mL/min. Effluents through the foam and liquid outlets were each manually fractionated at 30-s intervals. An aliquot of each fraction was analyzed by reversed-phase high-performance liquid chromatography (HPLC). The HPLC analysis was performed with a Shimadzu HPLC set consisting of a Model LC-6A pump, a manual injector kit, a Model SPD-6A detector, and a Model C-R5A recording data processor (Shimadzu Corporation, Kyoto, Japan) using a Capcell Pak  $C_{18}$  column, 0.46 cm i.d.  $\times$  15 cm (Shiseido, Tokyo, Japan). The mobile phase, composed of methanol and 0.04 M  $\text{Na}_2\text{HPO}_4$  (pH 9.4) at a volume ratio of 62:38, was isocratically eluted at a flow rate of 1 mL/min, and the effluent was monitored at 234 nm.

## RESULTS AND DISCUSSIONS

HPLC analysis of the original BC sample revealed major component BC-A, its oxidation product BC-F, and over 20 UV-absorbing minor components as shown in Figure 1. In the present foam CCC method, all these components were divided into two groups based on their foam activity: BC-A and several components with higher hydrophobicity (or longer retention time in Figure 1) were eluted through the foam collection line while the rest of the components were eluted through the liquid collection line.

In the foam fraction, hydrophobic components corresponding to peaks 10 through 15 (Figure 1) were eluted in such a manner that the most hydrophobic component (peak 15) emerged first near the foam front followed by the rest of the components exactly in decreasing order of hydrophobicity or retention time. Furthermore, each component in the foam fractions showed substantial enrichment relative to that in the original sample solution. In the first foam fraction, most hydrophobic components corresponding to peaks 15 and 14 (BC-F) were enriched 2.8 and 2.2 times, respectively (Figure 2). Peak 15 is hardly visible in Figure 1 due to the low solute concentration in the original sample solution, whereas the same peak is clearly observed in Figure 2 after near 3-fold enrichment in the foam fraction. In the 11th fraction, BC-A (peak 11) was enriched 1.8 times and almost entirely isolated

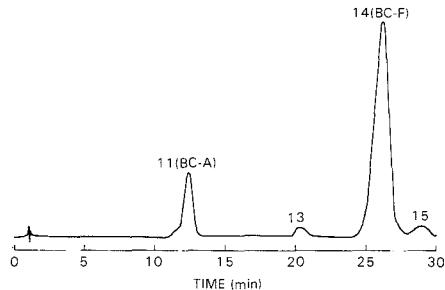


Figure 2. HPLC analysis of the first foam fraction.

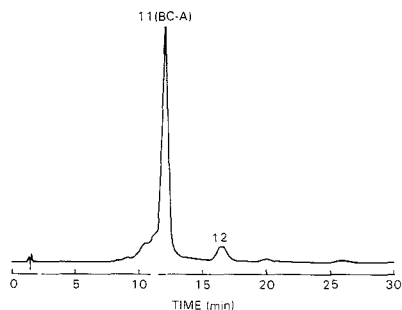


Figure 3. HPLC analysis of the 11th foam fraction.

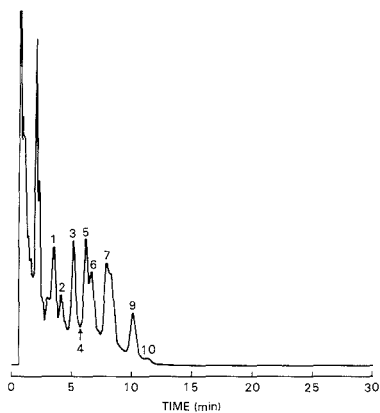


Figure 4. HPLC analysis of the second liquid fraction.

from other components (Figure 3). It should be noted that these separations were achieved within 6 min of elution or 11 min after sample injection.

On the other hand, much less efficient separation was observed in liquid fractions as shown in the HPLC analysis of the second fraction (Figure 4). Nevertheless, the components corresponding to peaks 1 through 9 appear to be eluted in decreasing order of their polarity, and more hydrophobic components (peaks 11–15) are almost entirely eliminated from all liquid fractions.

The above results were obtained by optimizing various operational parameters such as liquid feed rate, needle valve opening on the liquid collection line, standing time after sample injection, etc., while  $\text{N}_2$  feed pressure and revolution

speed of the centrifuge were kept constant. Liquid feed rates lower than 3.2 mL/min failed to elute foam, while higher feed rates yielded less efficient foam separation. The opening of the needle valve determined the relative volume between the foam and liquid fractions. Opening the valve over 1.2 turns gave no foam fraction, while less than 0.5 turn lowered separation efficiency in foam fraction. By manipulation of the needle valve opening between the above critical range, the components with intermediate hydrophobicity can be eluted from either the foam or liquid outlet. Standing time after sample injection was also an important factor affecting both the foam elution pattern and the separation efficiency. Long standing time improved separations between peaks 10 and 15 (Figure 1), but when it exceeded 5 min, foam elution became intermittent. Pumping was stopped during the standing time because even low flow rates of 0.2–0.5 mL/min delayed foam elution resulting in longer separation times required.

As described above, we were able to separate BC components in the order of hydrophobicity by using foam CCC without any surfactant or buffer solution. The combined use of nitrogen gas and distilled water in an open column provides a number of advantages over other chromatographic methods such as (1) minimum decomposition or deactivation of bio-

logical samples, (2) nonadsorptive sample loss onto the solid support matrix, (3) no risk of contamination, (4) easy recovery of samples after fractionation, (5) low cost in operation, etc. In addition, the method is capable of enrichment of foam active samples so that a minute amount of compounds can be effectively concentrated and detected in the foam fraction. The system also permits continuous operation by continuous sample feeding. Efficiency of the method may be increased in many folds by the use of a longer coil and the sample loading capacity by the use of a larger-bore coil.

We believe that the present method has a great potential in enrichment, stripping, and isolation of various natural and synthetic products in research laboratories.

**Registry No.** BC, 1405-87-4; BC-A, 22601-59-8; BC-F, 22601-63-4; nitrogen, 7727-37-9; water, 7732-18-5.

#### LITERATURE CITED

- (1) Somasundaran, P. *Sep. Purif. Methods* **1972**, *1*, 117.
- (2) Ito, Y. *J. Liq. Chromatogr.* **1985**, *8*, 2131.
- (3) Bhatnagar, M.; Ito, Y. *J. Liq. Chromatogr.* **1988**, *11*, 21.
- (4) Ito, Y. *J. Chromatogr.* **1987**, *403*, 77.

RECEIVED for review December 29, 1988. Accepted May 24, 1989.

# For Over Six Decades...



## The Leader in the Field.

*ANALYTICAL CHEMISTRY*, the world's foremost publication in the vital field of measurement science, comes to you semi-monthly packed with *more* research articles, special features and application papers.

Keeping pace with the changes has continued to make *ANALYTICAL CHEMISTRY* the pinnacle of publications in the field . . . for over 6 decades.

For your personal subscription:

**CALL TOLL FREE (800) 227-5558 (U.S. only)**  
**Outside U.S. (202) 872-4363**

**Telex: 440159 UI**  
**89 2582 ACSPUBS**



American Chemical Society  
1155 16th St., NW  
Washington, DC 20036

# TITRATION SYSTEMS FOR EVERY APPLICATION FROM "ROUTINE" TO "RESEARCH".



A single burette Titration System.



A 12 burette Titration System.

multi-user R&D laboratory making a complex variety of measurements.

And with the aid of our half century of applications experience, anyone can implement the full gamut of titrations including acid base, redox, complexometric, halogenide, Karl Fischer, COD and others.

Don't buy a titration system until you've talked to us.

For a TitraLab brochure and a complete list of applications literature, call (800) 321-9484 or, in Ohio, (216) 871-8900. Or return the completed coupon to Radiometer America Inc., 811 Sharon Drive, Westlake, Ohio 44145.

Acid/Base  
Acid Rain  
COD  
Complexometric  
Halogenide  
ISE Measurements

Karl Fischer  
pH Stat Titration  
pK  
Redox  
TAN/TBN

TitraLab Systems can meet a wide variety of applications.

We have dozens of TitraLab® systems and the broadest applications experience in the automatic titration business.

TitraLab is a modular titration system offering a choice of two data systems, up to 12 automatic burettes, a single sample station or a sample changer with a capacity of up to 20 samples, dozens of electrodes and interfaces for balances, robotics, a printer/plotter and LIMS.

TitraLab systems can be configured for applications ranging from the single user QA/QC laboratory making one type of measurement to the

**RADIOMETER**  
**COPENHAGEN** 

Please send literature on the new TitraLab® system to:

Name: \_\_\_\_\_

Title: \_\_\_\_\_

Organization: \_\_\_\_\_

Street & No.: \_\_\_\_\_

City: \_\_\_\_\_

State: \_\_\_\_\_ Zip: \_\_\_\_\_

Phone: \_\_\_\_\_

Application: \_\_\_\_\_

2076